



3rd International Iron & Steel Symposium



UDCS'17

<http://udcs17.karabuk.edu.tr>

3-5 April 2017 - Karabuk University Iron and Steel Institute



UDCS'17

The Proceedings of Third International Iron and Steel Symposium (UDCS'17)
April 3-5, 2017, Karabuk University, Karabuk, Turkey.

Edited by

Dr. Mustafa YAŞAR (Chairman)

Copyright

ISBN 978-605-9554-0-60

© 2017, UDCS'17, Karabuk University
Karabuk, Turkey
<http://udcs17.karabuk.edu.tr/>
udcs17@karabuk.edu.tr

This proceedings include the original papers submitted to UDCS'17. It is accessed in free of charge.
All scientific and linguistic responsibilities of the published articles belong to their authors.

**The Third International Iron and Steel
Symposium (IIS'17)**

3-5 April 2017

Karabuk University, Karabuk, Turkey

HONORARY COMMITTEE

Dr. Refik POLAT, Rector of Karabuk University
Dr. Erol ARCAKLIOĞLU, TÜBİTAK
Dr. Türky DERELİ, İskenderun Technical University
Dr. Arif KARADEMİR, Bursa Technical University
Ercüment ÜNAL, Kardemir A.Ş.
Namık EKİNCİ, Steel Exporters Association

UDCS'17 CHAIRMAN

Dr. Mustafa YAŞAR

ORGANISING COMMITTEE

Dr. Mustafa YAŞAR
Dr. Yavuz SUN
Dr. Yasin KANBUR
Dr. Erkan KOÇ
Dr. Engin CEVİK
Dr. Betül USTA
Dr. Ali GÜNGÖR
Dr. Hayrettin AHLATCI
Dr. Hüseyin ÇİMENOĞLU
Dr. Mehmet Baki KARAMIŞ
Dr. Veysel YAYAN
Dr. Yunus TÜREN
Dr. Erkan KOÇ
Dr. Yasin KANBUR
Dr. Engin ÇEVİK
Dr. Betül USTA
Alper İNCESU
Yasin AKGÜL
Fatih AYDIN
M. Emre TURAN
Fazıl HÜSEM
Yüksel AKINAY
Safa POLAT
Savaş AĞDUK
M. Yunus AŞKIN

SCIENTIFIC COMMITTEE

Dr. A. Macit ÖZENBAŞ
Dr. Adem KURT
Dr. Ahmet DURGUTLU
Dr. Ahmet EKERİM

Middle East Technical University
Gazi University
Gazi University
Yıldız Technical University

Dr. Ahmet GÜRAL
Dr. Ali ARSLANTAŞ
Dr. Ali GÜNGÖR
Dr. Ali KALYON
Dr. Anthony D. ROLLETT
Dr. Ali KONAK
Dr. Alper ERGÜN
Dr. Ali RAMAZANI
Dr. Bahattin TÜRETKEN
Dr. Behçet GÜLENG
Dr. Betül USTA
Dr. Bilge DEMİR
Dr. Bülent Aydemir
Dr. Bülent Bostan
Dr. Bülent KURT
Dr. Carl D. LUNDIN
Dr. Cemal ÇARBOĞA
Dr. Cemal MERAN
Dr. Cemil Hakan GÜR
Dr. Cihan MIZRAK
Dr. David K. MATLOCK
Dr. Emrah DENİZ
Dr. Engin ÇEVİK
Dr. Enver OKTAY
Dr. Erhan DEMİRBAŞ
Dr. Erkan KOÇ
Dr. Ertugrul ESMERAY
Dr. Eyüp Sabri KAYALI
Dr. Fatih HAYAT
Dr. Fatma MEYDANERİ TEZEL
Dr. Ferhat GÜL
Dr. Filiz ERSÖZ
Dr. Fuat ŞİMŞİR
Dr. Hakan ATEŞ
Dr. Hakan AYDIN
Dr. Halil KULLUK
Dr. Hani HENEIN
Dr. Hasan GÖKKAYA
Dr. Hasan HASIRCI
Dr. Hasan KARABULUT
Dr. Hatem AKBULUT
Dr. Hatice EVLEN
Dr. Hayrettin AHLATÇI
Dr. Hüseyin ÇİMENOĞLU
Dr. Hüseyin DEMİREL
Dr. Hüseyin DEMİRTAŞ
Dr. Hüseyin KURT
Dr. Ivan Enrique Campos SILVA
Dr. İdris KABALCI
Dr. İhsan KORKUT
Dr. İhsan ULUER
Dr. İnan KESKİN
Dr. Irinei RADOMİR
Dr. İsmail EKMEKÇİ
Dr. Jahan RASTY
Dr. Kerim ÇETİNKAYA
Dr. Kiyotaka MATSUURA
Dr. Mahdi MAHFOUF
Dr. M. Akif ERDEN
Dr. M. Hüseyin ÇETİN

Gazi University
Karabuk University
Karabuk University
Karabuk University
Carnegie Mellon University
Karabuk University
Karabuk University
University of Michigan-Ann Arbor
Karabuk University
Gazi University
Karabuk University
Karabuk University
TUBITAK
Gazi University
Nevsehir Hacı Bektas Veli University
The University of Tennessee Knoxville
Nevsehir Hacı Bektas Veli University
Pamukkale University
Middle East Technical University
Karabuk University
Colorado School of Mines
Karabuk University
Karabuk University
Istanbul University
Gebze Technical University
Karabuk University
Karabuk University
Istanbul Technical University
Karabuk University
Karabuk University
Gazi University
Karabuk University
Karabuk University
Gazi University
Uludag University
Intekno Group of Companies Chairman of the Board
University of Alberta
Karabuk University
Gazi University
Karabuk University
Sakarya University
Karabuk University
Karabuk University
Istanbul Technical University
Karabuk University
Karabuk University
Karabuk University
Instituto Politecnico Nacional
Karabuk University
Gazi University
Karabuk University
Karabuk University
Transilvania University of Brasov
Istanbul Commerce University
Texas Tech University
Karabuk University
Hokkaido University
Sheffield University
Karabuk University
Karabuk University

Dr. M.Kelami ŞEŞEN
Dr.Mehmet AKBABA
Dr. Mehmet EROĞLU
Dr. Mehmet Baki KARAMIŞ
Dr. Mehmet KARA
Dr. Mehmet KOBYA
Dr. Mehmet ÖZALP
Dr. Mehmet ÖZKAYMAK
Dr. Mehmet TÜRKER
Dr. Melik ÇETİN
Dr. Metin ZEYVELİ
Dr. Mihai Alin POP
Dr. Mihai CERNAT
Dr. Muhammet KAYFECİ
Dr. Muharrem DÜĞENCİ
Dr. Murat VURAL
Dr. Mustafa ACARER
Dr. Mustafa AKTAŞ
Dr. Mustafa ANUTGAN
Dr. Mustafa AYDIN
Dr. Mustafa BOZ
Dr. Mustafa GÜNAY
Dr. Mustafa KURT
Dr. Mustafa ÜRGEN
Dr. Mustafa YAŞAR
Namık EKİNCİ
Dr. Necmi Serkan TEZEL
Dr. Niyazi ÖZDEMİR
Dr. Nizamettin KAHRAMAN
Dr. Oğuz BORAT
Dr. Oğuz KOÇAR
Dr. Oktay ERKOCA
Dr. Ömer BUCAK
Dr. Özden İŞBİLİR
Dr. P. A. DEARNLEY
Dr. Raif BAYIR
Dr. Ramazan KAÇAR
Dr. Sakıp KÖKSAL
Dr. Salim ASLANLAR
Dr. Selami SAĞIROĞLU
Dr. Selçuk SELİMLİ
Dr. Serdar SALMAN
Dr. Süheyla AYDIN
Dr. Süleyman GÜNDÜZ
Dr. Süleyman YAŞIN
Dr. Şenol GÜRSOY
Dr. Tamila ANUTGAN
Dr. Tanju TEKER
Dr. Tayfur ÖZTÜRK
Dr. Ulaş MATİK
Dr. Ulvi ŞEKER
Dr. Veli ÇELİK
Dr. Virgil GEAMAN
Dr. Volkan KILIÇLI
Dr. Yakup Kaya
Dr. Yasin KANBUR

Istanbul Technical University
Karabuk University
Fırat University
Erciyes University
Karabuk University
Gebze Technical University
Karabuk University
Karabuk University
Gazi University
Karabuk University
Karabuk University
Transilvania University of Brasov
Transilvania University of Brasov
Karabuk University
Karabuk University
Istanbul Technical University
Selçuk University
Karabuk University
Karabuk University
Dumlupınar University
Karabuk University
Karabuk University
Marmara University
Istanbul Technical University
Karabuk University
Steel Exporters Union Chairman of the Board of Directors
Karabuk University
Fırat University
Karabuk University
Istanbul Commerce University
Bulent Ecevit University
ArcelorMittal Global R&D
Hochschule Furangewandte Wissenschaften Munchen
Karabuk University
University of Leeds
Karabuk University
Karabuk University
Karabuk University
Sakarya University
Sakarya University
Karabuk University
Karabuk University
Marmara University
Istanbul Technical University
Karabuk University
Karabuk University
Karabuk University
Karabuk University
Adiyaman University
Middle East Technical University
Karabuk University
Gazi University
Yildirim Beyazıt University
Transilvania University of Brasov
Gazi University
Karabuk University
Karabuk University

Dr.Yaşar YETİŐKEN
Dr.Yavuz SUN
Dr.Yılmaz YILDIRIM
Dr.Yunus TÜREN
Dr.Yusuf ÖZÇATALBAŐ
Dr.Zehra Őule GARİP

Karabuk University
Karabuk University
Bulent Ecevit University
Karabuk University
Gazi University
Karabuk University

SYMPOSIUM SECRETARIAT

Tuğba AVŐAR
Gözde GÜNEY
Tuğba COŐKUN

SYMPOSIUM SECTION COORDINATORS

Metallurgy &

Materials

Dr. Ali GÜNGÖR
Dr. Oncu AKYILDIZ
Dr. Necmi TEZEL
Dr. Fatma Meydaneri TEZEL

Heat Treatment

Dr. Mehmet EROGLU
Dr. Bilge DEMİR

Welding & Cutting

Dr.Mustafa ACARER
Dr. Fatih HAYAT
Dr. Erkan KONCA
Dr.Harun CUG

Energy & Environment

Dr. Mehmet OZALP
Dr. Harun CUG
Dr. Suleyman YASIN

Materials Testing Machines

Dr.Engin CEVIK

Recycling

Dr. Yunus TUREN

Accreditation&Certification

Dr. Bulent AYDEMİR

Casting

Dr.Erkan KOC
Dr.Kazım TUR

Coating & Corrosion

Dr. Yasin KANBUR
Dr.Hasan KOTAN
Dr. Hamza Yasar OCAK
Dr. M. Akif ERDEN

Forming&Machining

Dr.Cemal CARBOGA
Dr.Yavuz SUN
Dr. Mustafa GUNAY
Dr.Engin CEVIK

Forming &Machining

Dr. Mehmet YAZ

Tribology

Dr.Nizamettin KAHRAMAN
Dr. Ulas MATIK

Marketing& Finance

Dr. Ali KONAK
Dr. Filiz ERSOZ

**METALLURGY AND MATERIALS STUDENT ASSOCIATION
KARABUK UNIVERSITY**

Onur ALTAY
Meral ERDİL
Saime AÇIKGÖZ
Elif SEYMEN
Anıl İNCE
Hilal TORUN
Nurdan OZTURK
Sakine OBUZ
Sinan EKŞİ
Özgür DURGUN
Gülcan CETİN
Neslihan ERKEK
Ceyda ALBAYRAK
Cemre GOZUTOK
Gamze ALTUNER

**UDCS'17 is organised by
Iron and Steel Institute**

**Karabuk University
78050 Karabuk, Turkey
T: +90 370 433 88 33
F: +90 370 433 88 32
E-mail: dce@karabuk.edu.tr
<http://dce.karabuk.edu.tr>
<http://udcs17.karabuk.edu.tr>**

**Third International Iron and Steel
Symposium (UDCS'17)
3-5 April 2017
Karabuk University, Karabuk, Turkey**

PREFACE

The 3rd International Iron and Steel Symposium (UDCS'17) organised by Iron and Steel Institute, Karabuk University is held in April 3-5, 2017 in Karabuk, Turkey. The former symposium took place in April 1-3, 2015 (<http://iiss15.karabuk.edu.tr>). This succeeding symposium is aimed at bringing together academics, researchers and engineers, iron and steel manufacturers, exporters and importers, suppliers, technology producers and non-governmental organizations around the World to share and discuss their latest works and the new methodologies to improve the structure and properties of iron and steel products. The topics of UDCS'17 covered are Metallurgy and materials, Casting, Heat treatment, Coating and corrosion, Welding and cutting, Forming and machining, Energy and environment, Marketing and finance, Automation, Occupational health and safety.

Special panels from industry experts, "*Heat Treatments In Iron Steel Industry*" and "*Simulation Solutions in Materials and Metallurgy*", and the panels from directors and CEOs, "*Strategies On R&D, Accreditation, Certification, And Skilled Workforce Training In Iron & Steel Industry*" and "*Strategies On Increasing International Marketing And Competitiveness In Iron & Steel Industry*" are organised. Thanks to NGO Associations and the companies work in iron and steel industry for their helps in making the panels are successful. The Symposium includes invited papers of national and international academicians and the papers submitted by academia in all aspects of the iron and steel industries.

We would like to express our sincere thanks to those who spend great effort to make this event take place. We sent our special thanks to Prof. Dr. Refik Polat as the Rector of KBÜ, Ercüment ÜNAL, General Manager of KARDEMİR A.Ş. as being main sponsor of the UDCS17.

We would also like to thank to ERDEMİR Group and other sponsors of UDCS'17 as their names and company logos stated. We also express our gratitude to the members of Honorary Committee, Scientific Committee, Organizing Committee, Industrial Committee, Secretarial Assistance, and Student Association for their great effort to make the event successful. Last but not least, we would like to thank to academicians, practitioners, and the experts who were joined to UDCS'17 in order to share their knowledge.

With the wishes to see you all at the next International Symposium...

Editor

Dr. Mustafa YAŞAR

**The Third International Iron and Steel
Symposium (UDCS'17)**

**3-5 April 2017
Karabuk University, Karabuk, Turkey**

ACKNOWLEDGEMENTS

We wish to thank the following co-organisers Universities and associations as panellists for their contribution to the success of this symposium.

CO-ORGINISER UNIVERSITIES



PANELIST ASSOCIATIONS

The Third International Iron and Steel
Symposium (UDCS'17)

3-5 April 2017
Karabuk University, Karabuk, Turkey

ACKNOWLEDGEMENTS



KARDEMİR A.Ş.
<http://kardemir.com>



ERDEMİR GRUBU
<http://erdemir.com.tr>



MARZINC
<http://marzinc.com.tr>



ZEISS TÜRKİYE
<http://zeiss.com.tr>



ZİRAAT BANKASI
<http://ziraat.com.tr>



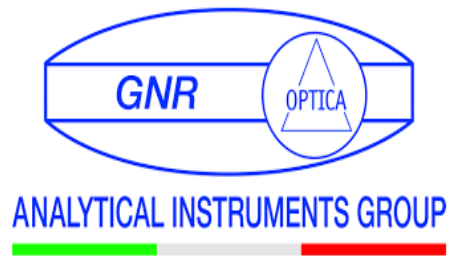
ANKA ANALİTİK
<http://ankaanalitik.com.tr>



MAK ELEKTRONİK
<http://makelektronik.com.tr>



GALDABINI
<http://galdabini.it>



GNR
<http://gnr.it>



METALS
<http://mdpi.com>



**JOURNAL OF THE BALKAN
TRIBOLOGICAL ASSOCIATION**
<http://scibulcom.net>

UDCS'17 SYMPOSIUM PROGRAMME

DAY 1	3 APRIL MONDAY			LOCATION
8.30-10.00	Registration			Hamit Çepni Conference Hall
10.00-10.15	Turkish National Anthem and Musical Notation			
10.15-10.30	Presentation of Karabuk University and Iron & Steel Institute			
10.30-10.45	Speech of Protocol			
10.45-11.15	Oktay Elkoca: Abrasion Resistant Steels			
11.15-11.45	Coffee Break			
11.45-12.15	Young Pyun: Reduction of operation cost and improvement of production by utilizing advance surface modification technology "UNSM (Ultrasonic Nanocrystal Surface Modification)"			
12.15-12.45	Mehmet Eroglu: An innovative study: Developing of a continuous coating method for steel sheets or plates			
12.45-13.30	Lunch			
13.30-15.00	Oral Presentations 1	Majid Pouranvari: Metallurgical Challenges in Resistance Spot Welding of Advanced High Strength Steels Panel 1 <u>Research and Development, Human Resources in Iron and Steel Industry</u> Mehmet Ordukaya (Professional Qualification Institution) Didem Tunc (Professional Qualification Institution) Hüseyin Soykan (MATIL Inc.) Oguz Gunduz (ERDEMIR Inc.)	Poster Presentations 1	Iron & Steel Institute
15.00-15.30	Coffee Break			
15.30-17.00	Fatih Hayat: Steel Trend in Automotive Industry <u>Presentations</u> Sponsor Companies			
17.00-19.30	Touristic Travel – Bulak Mencilis Cave			
19.30-20.30	Gala Dinner			
DAY 2	4 APRIL TUESDAY			LOCATION
9.00-10.30	Oral Presentations 2			Iron & Steel Institute
10.30-11.00	Coffee Break			
11.00-12.30	Oral Presentations 3	Mehmet Baki Karamis: Tribological Damages On Projectile Steel Tip Surface After Ballistic Impact Panel 2 <u>Raw Material Markets</u> Murat Demirci (ERDEMIR Inc.) Nazım Çapraz (KAHDER) Zeki Cizmecioglu (Istanbul Commerce University)	Poster Presentations 2	
12.30-13.30	Lunch			
13.30-15.00	Oral Presentations 4	Hüseyin Cimenoglu: Wear Characteristics of H13 Hot Work Tool Steel at Elevated Temperatures Panel 3 <u>Global Steel Industry and Expectations</u> Ercument Unal (KARDEMIR Inc.) Ugur Dalbeler (Colakoglu Metallurgy Inc.)	Poster Presentations 3	Iron & Steel Institute
15.00-15.30	Coffee Break			

15.30-17.00	Oral Presentations 5	<u>Seminar</u> Bülent Aydemir Tensile Test for Metallic Materials according to ISO 6892-1:2016	
17.00-19.30	Touristic Travel – Safranbolu Glass Terrace		
19.30-20.30	Dinner		
DAY 3	5 APRIL WEDNESDAY		LOCATION
9.00-10.30	Oral Presentations 6		Iron & Steel Institute
10.30-11.00	Coffee Break		
11.00-12.30	Oral Presentations 7		
12.30-13.30	Lunch		
13.30-17.00	Technical and Touristic Travel – KARDEMİR Inc. and Yenice Seker Canyon		

ORAL PRESENTATIONS

1. SESSION

Parallel Session – Room : Hematite -- 03.04.2017 – (13:30 – 15:00)		
Paper ID	Title	Speaker
127	EFFECT OF GRAIN BOUNDARY CHARACTERISTICS ON THE IMPACT PROPERTIES OF THERMOMECHANICALLY ROLLED API X70 PIPELINE STEELS	Semih ENGÜN
105	USE OF STEEL SLAG IN RUBBLE-MOUND MARINE STRUCTURES	V.S. KIRCA
14	EFFECTS OF SLAG OPTIMIZATION ON STEEL CLEANLINESS IN SECONDARY METALLURGY PROCESS	Emre ALAN
125	PURE BENDING FATIGUE BEHAVIOUR OF 80 C STEEL CORD FLAMENTS	Hüseyin KOYMATCIK
54	DYNAMICS STRESS ANALYSIS IN 120 MM SMOOTH BORE TANK BARREL	Mehmet Fatih YAŞAR
88	INVESTIGATION OF GAS PRESSURE EFFECT ON POWDER CHARACTERIZATION OF AL12SI ALLOY PRODUCED BY GAS ATOMIZATION METHOD	Kamal Mohamed Em AKRA

Parallel Session – Room : Magnetite -- 03.04.2017 – (13:30 – 15:00)		
Paper ID	Title	Speaker
39	EFFECT OF ION-NITRIDING PROCESS ON THE MECHANICAL PROPERTIES OF AISI 4140 LOW ALLOY STEEL	M. Anıl KAYA
43	EFFECT OF HOMOGENIZATION HEAT TREATMENT ON MICROSTRUCTURE, HARDNESS AND TOUGHNESS PROPERTIES OF G18NICRMO3-6 STEEL	Funda GÜL KOÇ
178	THE EFFECT OF THE SINTERING TEMPERATURE ON HARDNESS AND WEARING BEHAVIORS OF THE STEEL	Ramazan YILMAZ
138	INVESTIGATION OF STRAIN HARDENING IN AISI 430 FERRITIC STAINLESS STEELS	Gökhan ARICI
247	EFFECT OF DEFORMATION ON THE MECHANICAL PROPERTIES OF HOT ROLLED AISI 4140 STEEL	Gökhan ATAY
65	PRODUCTION OF DUAL-PHASE STEEL USING VERY RAPID HEATING AND SHORT ANNEALING TIME	Bilge DEMİR

Parallel Session – Room : Wustite – 03.04.2017 – (13:30 – 15:00)		
Paper ID	Title	Speaker
12	EFFECT OF NORMALIZATION PROCESS ON ADHASIVE WEAR BEHAVIOR OF DUCTILE IRON	Ferhat GÜL
46	AN INTEGRATED PROCESS DESIGN FOR MAGNESIUM ALLOY PART MANUFACTURING IN TURKEY	Ali Serdar VANLI
213	THE FLASH BUTT WELDING APPLICATION AND INSPECTION IN RAILWAY IN KARABUK TRAIN STATION	Mustafa DURSUNLAR
50	SOLIDCAST CASTING SIMULATION SOFTWARE REVISION OF SAMPLE PIECE MOLD DESIGN BY SAND CASTING	Mustafa ERCAN
52	SIMULATION INVESTIGATION OF EFFECTS ON PRODUCT QUALITY OF THE ROUTING DESIGN PARAMETERS IN HIGH PRESSURE CASTING METHOD	Mustafa ERCAN
133	DETERMINATION OF PHASE EQUILIBRIA IN HIGH ALLOY WHITE CAST IRONS	Öncü AKYILDIZ

Parallel Session – Room : Limonite – 03.04.2017 – (13:30 – 15:00)		
Paper ID	Title	Speaker
123	THE IMPROVEMENT OF CORROSION RESISTANCE OF ZINC-COATED STEEL WIRES BY CHROMATING PROCESS	Ömer Faruk ÖZKAN
103	SYNTHESIS, CHARACTERIZATION AND TRIBOLOGICAL STUDIES OF CHROMIUM-NANO DIAMOND COMPOSITE COATING	Nima ZOGHIPOUR
25	WEAR BEHAVIOUR OF INDUCTION HARDENED 100CR6 STEEL	Gülcan TOKTAŞ
18	VANADIUMBORIDE COATING OF A LOW CARBON STEEL BY PLASMA TRANSFERRED ARC (PTA) METHOD	Yusuf DONAT
19	BORIDE COATINGS ON A LOW CARBON STEEL USING SHIELDED METAL ARC WELDING ELECTRODE WITH BORONCARBIDE	Mehmet EROĞLU
119	EFFECT OF ADDITIONAL BORON ON CORROSION RESISTANCE OF AISI4140 (42CRMO4)	Cemal ÇARBOĞA

Parallel Session – Room : Siderite – 03.04.2017 – (13:30 – 15:00)		
Paper ID	Title	Speaker
30	EFFECT OF MULTIPASS WELDING ON MICROSTRUCTURAL AND MECHANICAL PROPERTIES OF AISI 2205 DUPLEX STAINLESS STEEL	Alptekin KISASÖZ
38	X-RAY RADIOGRAPHY OF P460-ST52 STEEL COUPLES WELDED BY SUBMERGED ARC WELDING	Uğur ÇALIGÜLÜ
41	AN EFFECT OF STRESS RELIEF ANNEALING ON THE RESISTANCE SPOT WELDED TRIP STEEL JOINT	Hayriye Ertek EMRE
42	AN INVESTIGATION OF RESISTANCE SPOT WELDABILITY OF DP600/TRIP800 DISSIMILAR STEEL COUPLE	Hayriye Ertek EMRE
45	JOINING GR2 AND GR5 TITANIUM ALLOYS WITH DIFFUSION BONDING METHOD USING COPPER INTERLAYER	Uğur ÇALIGÜLÜ
48	EFFECT OF PROCESS PARAMETERS AND PRODUCTIVITY OF WELDING TECHNIQUE OF ALUMINUM ALLOY (AA5182 H111) PLATES USING TIG AND MIG	Musa KILIÇ

2. SESSION

Parallel Session – Room : Hematite – 04.04.2017 – (09:00 – 10:30)		
Paper ID	Title	Speaker
256	INVESTIGATION OF THE EFFECT OF VANADIUM ADDITION AND CYCLING HEAT TREATMENT ON MECHANICAL PROPERTIES AND WEAR BEHAVIORS OF CASTING STEEL	Harun ÇUĞ
115	COMPARİSON OF THE MECHANİCAL PROPERTİES OF DIFFERENT QUALITY AUSTENİTİC STAİNLESS STEELS AFTER WİRE DRAWİNG	Yılmaz YILDIRIM
9	INVESTIGATION OF DYNAMIC STRAIN AGING PROPERTIES OF HOT WORK TOOL STEELS	Demet TAŞTEMUR
91	DEVELOPMENT OF HIGH VALUE ALLOYS WITHOUT CRITICAL RAW MATERIALS THROUGH HIGH ENTROPY ALLOYS	Hakan YILMAZER
164	DESIGN AND SIMULATION OF AN APPARATUS FOR THE POST-WELD CONTROLLED ACCELERATED COOLING OF R350HT HEAD HARDENED RAIL JOINTS	Nizar RAMADAN
210	CALCULATION OF (HKL) PLANE ENERGY OF BCC AND BCT IRON USING ANALYTICAL METHOD	Hamza Yaşar OCAK

Parallel Session – Room : Magnetite – 04.04.2017 – (09:00 – 10:30)		
Paper ID	Title	Speaker
173	PARAMETER DETERMINATION OF YOSHIDA-UJEMORI AND CHABOCHE KINEMATIC HARDENING MODEL OF DUAL PHASE STEELS	İlyas KAÇAR
174	COMPARISON OF YOSHIDA-UJEMORI AND CHABOCHE KINEMATIC HARDENING MODEL'S PREDICTION ABILITIES	İlyas KAÇAR
185	MICROSTRUCTURAL EVOLUTION AND MECHANICAL PROPERTIES OF FRICTION STIR PROCESSED TRIP780 STEEL	İmren ÖZTÜRK YILMAZ
186	ACHIEVING ULTRAFINE GRAIN STRUCTURE WITH SUPERIOR MECHANICAL PROPERTIES BY FRICTION STIR PROCESSING OF INTERSTITIAL-FREE STEEL (IF-STEEL) SHEETS	Mumun YILMAZ
163	AN INVESTIGATION INTO THE MACHINABILITY OF COLD WORK TOOL STEEL (DIN 1.2312)	İbrahim ÇİFTÇİ
26	UTILIZATION OF FLUE DUST IN ZINC AND STEEL PRODUCTION PROCESSES AS RAW MATERIALS	Ömer ÖZAL

Parallel Session – Room : Wustite – 04.04.2017 – (09:00 – 10:30)		
Paper ID	Title	Speaker
220	INVESTIGATION OF MACHINABILITY OF HARDOX STEEL EXPOSED TO HEAT TREATMENT PROCESSES IN WEDM	Mehmet ALTUĞ
222	INCREASING COLD FORGING TOOL LIFE OF M10X1.25 WELDING FLANGE NUT BY USING FINITE ELEMENT SIMULATION	Sezgin YURTDAS
121	THE INVESTIGATION OF THE EFFECT OF TEMPCORE PROCESS ON STRUCTURAL FORM AND MECHANICAL PROPERTIES OF THE HOT ROLLED STEEL NPU AND EQUAL ANGLE TYPE OF PROFILES	Tuna TOK
122	ANALYSIS AND OPTIMIZATION OF ROLLING PARAMETERS IN STEEL PROFILE HOT ROLLING PROCESS	Didem KILIÇ
10	THE EFFECT OF FUZZY LOGIC SPEED CONTROL OF SPINDLE MOTOR ON SURFACE ROUGHNESS IN MACHINING	Metin ZEYVELİ
207	MACHINING OF INCONEL 718 USING TAGUCHI METHODOLOGY WITH ABRASIVE WATER JET MACHINING PARAMETERS	Fuat KARTAL

Parallel Session – Room : Limonite – 04.04.2017 – (09:00 – 10:30)		
Paper ID	Title	Speaker
240	CORROSION BEHAVIOUR OF STEEL WIRE ROD	Gülseher DOĞANCIK
100	INFLUENCE OF VARIOUS ZN COATING AMOUNT OF FORMED GALVANIZED STEELS ON CORROSION PERFORMANCE	Aras KARTUN
89	AFFECTING FACTORS ON GLOSS VALUE FOR GALVANIZED COLD ROLLED SHEETS	Erkan PÜGE
64	FORMATON OF TRIANGLE SHAPED TIB2 BORIDES IN COATED SURFACE PRODUCED BY GTAW	Mehmet YAZ
31	ASSESSMENT OF MATERIAL SELECTION AND CORROSION PERFORMANCES FOR PLATE HEAT EXCHANGERS	Haluk ERDEMİR
62	THE WEAR PERFORMANCE OF TOOLS STEEL (AISI M2) COATED TIALN BY DC REACTIVE MAGNETRON SPUTTERING TECHNIQUE	Şengül DANIŞMAN

Parallel Session – Room : Siderite – 04.04.2017 – (09:00 – 10:30)		
Paper ID	Title	Speaker
66	THE EFFECT OF NANO-SIZED ADDITIVES ON IGNITION TEMPERATURE OF THERMITE WELDING	Ömer GÜLER
67	WELDABILITY OF SIMILAR AISI 1040 MEDIUM CARBON STEELS USING FRICTION WELDING	İhsan KIRIK
85	AN INVESTIGATION OF THE INFLUENCE OF KEYHOLE LASER WELDING PARAMETERS ON WELD BEAD SHAPE AND INTEGRITY	Ömer EKİNCİ
96	INVESTIGATION OF WELDABILITY OF DP 1000-DP 1000 STEEL USING ELECTRON BEAM WELDING	Cihangir Tevfik SEZGİN
106	AN EXPERIMENTAL STUDY ON EFFECTS OF LASER WELDING SPEED AND LASER POWER ON WELD BEAD SHAPE AND HEAT AFFECTED ZONE IN KEYHOLE LASER WELDING	Ömer EKİNCİ
128	THE EFFECT OF THE ELECTRODE TYPE ON TENSILE PROPERTIES OF THE RESISTANCE SPOT WELDED JUNCTIONS OF DP STEEL	Öznur DİNÇEL

3. SESSION

Parallel Session – Room : Hematite – 04.04.2017 – (11:00 – 12:30)		
Paper ID	Title	Speaker
219	INVESTIGATION OF MACHINABILITY OF THE HARDOX STEEL	Mehmet ALTUĞ
206	APPLICATION OF TAGUCHI METHOD FOR OPTIMIZATION AWJ MACHINING OF 316 STAINLESS STEEL	Fuat KARTAL
134	AN INVESTIGATION OF OPTIMUM INSERT DIAMETER / MOLDING DIAMETER RATIO OF PARTS PRODUCED BY INSERTED POWDER INJECTION MOLDING	Oğuz YILMAZ
137	MODELING OF THREE-DIMENSIONAL FRACTURE PROBLEMS USING FCPAS	M. Faruk YAREN
156	AN INVESTIGATION INTO THE MACHINABILITY OF HOT WORK TOOL STEEL (TOOLOX 44)	Halil DEMİR
162	AN INVESTIGATION ON MACHINABILITY OF HARDENED AISI H10 STEEL WITH CBN INSERT	Gültekin UZUN

Parallel Session – Room : Magnetite -- 04.04.2017 – (11:00 – 12:30)		
Paper ID	Title	Speaker
221	THE EFFECTS OF HEAT TREATMENT ON THERMAL, MECHANICAL AND MICROSTRUCTURAL PROPERTIES OF AL BASED SB - 42.4% MG - 57.6% AL EUTECTIC ALLOY	Fatma MEYDANERİ TEZEL
246	INVESTIGATION OF HOT ROLLED AISI 4140 STEELS SUBJECT TO LARGE STRAINS	Sedef SIŞMANOĞLU
175	ASSESSMENT OF THE AUSTEMPERING PROCESS PARAMETERS TO IMPROVE THE WEAR RESISTANCE OF GG-25 GRAY CAST IRON	Abdulsamet YILDIRIM
255	BAINITIC RAIL STEEL PRODUCTION FROM PERLITIC RAILS IN EUTECTOID ALLOY AND INVESTIGATION OF WEAR BEHAVIOUR	Derya BULGAN
53	THERMAL STABILITY AND PHASE TRANSFORMATION OF NANOCRYSTALLINE STAINLESS STEELS PREPARED BY MECHANICAL ALLOYING	Hasan KOTAN
16	RAPID SURFACE HARDENING OF AISI 1045 STEEL FOR AUTOMOTIVE APPLICATION BY ELECTROLYTIC PLASMA TREATMENT	Gözdenur KURT

Parallel Session – Room : Wustite -- 04.04.2017 – (11:00 – 12:30)		
Paper ID	Title	Speaker
11	OPTIMIZATION OF ABRASIVE WEAR BEHAVIOR OF BORON AND MILD STEEL BY TAGUCHI METHOD	Ferhat GÜL
110	EFFECT ON THE FORMATION OF BORIDE LAYER OF INCREASING AMOUNT OF NIOBIUM IN PURE IRON	Eyyüp Murat KARAKURT
28	CHARACTERIZATION OF BORIDE LAYER FORMED ON FE-NI ALLOYS	Naim Murat MAÇKAN
113	RELATION BETWEEN MICROSTRUCTURE AND HARDNESS IN HARDOX 450+FEW BASED COMPOSITE COATING FABRICATED BY PLASMA TRANSFERRED ARC CLADDING	Eyyüp Murat KARAKURT
151	INVESTIGATION OF DRY SLIDING WEAR RESISTANCE OF AISI 52100 STEELS UNDER DIFFERENT TRIBOLOGICAL CONDITIONS	Merve YILMAZ
158	EXPERIMENTAL STUDY ON TRIBOLOGICAL PERFORMANCE OF SIC COMPOSITE COATING LAYERS	Koray KILIÇAY

Parallel Session – Room : Limonite -- 04.04.2017 – (11:00 – 12:30)		
Paper ID	Title	Speaker
129	THE EFFECTS OF THE ELECTRODE TYPE ON MICROSTRUCTURE AND HARDNESS OF THE RSW OF DP600 STEEL	Muhammed ELİTAŞ
131	INVESTIGATING MECHANICAL PROPERTIES OF HARDOX 400 AND ST52 STEEL COUPLE JOINED BY MIG/MAG WELDING	Musa KILIÇ
142	AN INVESTIGATION INTO THE EFFECT OF WELDING PARAMETERS ON MECHANICAL PROPERTIES OF DISSIMILAR RESISTANCE SPOT WELDED DP1000–QP1180 STEEL JOINTS	Abdullah Yasin BİLİCİ
211	MICROSTRUCTURE CHARACTERIZATION AND MECHANICAL PROPERTIES OF 9CR-1,2W WELD METAL	Fikret KABAĞCI
193	INVESTIGATION OF CUTTING FORCES AND SURFACE ROUGHNESS IN HARD TURNING OF BEARING RING WITH CBN INSERT	Mehmet BOY
203	ACTIVATED FLUX TIG WELDING OF AUSTENITIC STAINLESS STEELS	Ahmet İrfan YÜKLER

Parallel Session – Room : Siderite – 04.04.2017 – (11:00 – 12:30)		
Paper ID	Title	Speaker
51	BARKHAUSEN NOISE AS A MAGNETIC NONDESTRUCTIVE TESTING TECHNIQUE	Oğuz KOÇAR
198	EFFECT ON CUTTING FORCES OF MINIMUM QUANTITY LUBRICATION METHODS IN HARD TURNING OF 90MNCRV8 COLD WORK TOOL STEELS	Nihat YILMAZ
90	DETECTION OF SURFACE RAIL DEFECTS WITH USING IMAGE PROCESSING METHOD	Cihan MIZRAK
116	EFFECTS OF BIMETALLIC MATERIAL PROPERTIES ON APPLICATIONS FOR RELIABILITY OF DESIGN	Ahmet ÇETİN
176	PHASED ARRAY INDUSTRIAL APPLICATIONS OF IRON-ROAD ULTRASONIC INSPECTION METHOD	Ramazan YILMAZ
179	EFFECTS OF ALLOYING ELEMENTS (MO, NI AND CU) ON THE AUSTEMPERABILITY OF GGG-60 DUCTILE CAST IRON	Erkan KONCA

4. SESSION

Parallel Session – Room : Hematite – 04.04.2017 – (13:30 – 15:00)		
Paper ID	Title	Speaker
160	INVESTIGATION OF TRIBOLOGICAL AND MECHANICAL PERFORMANCE OF CRYOGENIC TREATED MEDIUM CARBON STEEL, 38MNV56	Esad KAYA
169	EFFECT OF CARBON CONTENT ON THE WEAR BEHAVIOUR OF EUTECTOID STEEL WIRE ROD	Melike BİRİNCİ
183	EFFECT OF THERMAL FACTORS ON ABRASIVE WEAR BEHAVIOR OF DIE CASTING MOLD MATERIALS	Ferhat GÜL
201	INFLUENCE OF GRAIN SIZE ON SUSCEPTIBILITY TO INTERGRANULAR CORROSION OF AISI 316 AUSTENITIC STAINLESS STEEL	Hüseyin ZENGİN
167	EXAMINATION OF SOLID STATE NITROGEN ABSORPTION FOR PRODUCTION OF NICKEL FREE STAINLESS STEEL	Oğuz Gürkan BİLİR
172	DETERMINING RETAINED AUSTENITE QUANTITY AND COMPOSITION WITH HEAT TREATMENT PARAMETERS IN SAE52100 STEELS	Ahmet Efe GEZMİŞOĞLU

Parallel Session – Room : Magnetite – 04.04.2017 – (13:30 – 15:00)		
Paper ID	Title	Speaker
177	GTAW WELDING OF AUSTENITIC STAINLESS STEEL AND ITS CORROSION PROPERTIES	Ramazan YILMAZ
182	USING A NICKEL-COATED MOLD WALL IN CONTINUOUS CASTING MACHINE	Mehmet Fatih KAHRAMAN
215	AN INVESTIGATION ON MECHANICAL PROPERTIES AND MICROSTRUCTURE OF AISI 304L AND 316Ti STAINLESS STEELS WELDED BY TIG	Gökhan Emre KÜKÜRTÇÜ
180	USE OF SUBMERGED ARC WELDING TECHNIQUE IN IRON AND STEEL INDUSTRY FOR COATING	Mehmet Fatih KAHRAMAN
237	MICROSTRUCTURAL AND MECHANICAL CHARACTERIZATION OF 9 CR - 1 MO - 1 W WELD METAL	Emin SALUR
60	X-RAY DIFFRACTION INVESTIGATION OF WELDING CHARACTERISTICS OF AISI304-HARDOX 400 STEEL COUPLES WELDED BY PLASMA TRANSFERRED ARC WELDING	Uğur ÇALIGÜLÜ

Parallel Session – Room : Wustite – 04.04.2017 – (13:30 – 15:00)		
Paper ID	Title	Speaker
199	EXPERIMENTAL INVESTIGATION OF EFFECT OF PROCESSING PARAMETERS ON THE SURFACE ROUGHNESS DURING THE BRASS ALLOY TURNING WITH ABRASIVE WATER JET	Fuat KARTAL
200	OPTIMIZATION OF PROCESS PARAMETERS FOR ABRASIVE WATER JET OF CAST ALUMINUM ALLOY A319 BY TAGUCHI METHOD	Fuat KARTAL
124	THE IMPROVEMENT OF WEAR RESISTANCE OF STEEL DESCALING ROLLERS BY BORIDING PROCESS IN WIRE DRAWING INDUSTRY	Ahmet POLAT
228	EFFECT OF FRICTION STIR PROCESS ON ULTIMATE STRENGTH OF SHIP HULL GIRDER STEEL PLATES ESTIMATED BY FEM APPROACH	Dursun Murat SEKBAN
209	EFFECT OF FORGING AND HEAT TREATMENT ON MICROSTRUCTURE AND MECHANICAL PROPERTIES OF SAE 4140 STEEL	Secarettin AKDI
181	EFFECT OF FRICTION STIR PROCESSES ON MECHANICAL PROPERTIES OF DP600 STEEL	Onur SAYAR

Parallel Session – Room : Limonite – 04.04.2017 – (13:30 – 15:00)		
Paper ID	Title	Speaker
2	REVISION OF THE ROLLING MILL ROLLER BEARING	Bilal ÇOLAK
5	THE EXPERIMENTAL INVESTIGATION OF SPRINGBACK PHENOMENON IN DP600 SHEET METAL MATERIAL AND ESTIMATION WITH FUZZY LOGIC	Tahsin ÖNEL
32	HYDROFORMABILITY OF ADVANCED HIGH STRENGTH STEELS THROUGH FEA	Doğan ACAR
69	COMPARISON OF VARIOUS CRITICAL PLANE APPROACHES UNDER PROPORTIONAL AND NON-PROPORTIONAL MULTIAXIAL STRESS STATES	Tuğçe LEBLEBİCİ
75	COMPARISON OF ENERGY ABSORBING MEMBERS FOR PASSENGER COACHES	Ramazan ÖZMEN
76	STRESS DISTRIBUTION ANALYSIS AND TOPOLOJİ OPTIMIZATION FOR SEMI-TRAILER	Şükrü ŞEN

Parallel Session – Room : Siderite – 04.04.2017 – (13:30 – 15:00)		
Paper ID	Title	Speaker
6	INVESTIGATION OF HEAT RECOVERY AND SAVING POTENTIAL OF HOT STOVES IN BLAST FURNACES	Erhan KAYABAŞI
36	ENERGY SAVING IN INDUSTRIAL ANNEALING FURNACES	Durmuş KAYA
44	EVALUATION OF ENERGY SAVING POTENTIAL IN INDUSTRIAL FURNACES USED IN IRON-STEEL SECTOR	Şaban PUSAT
47	ELECTRICITY GENERATION WITH ORGANIC RANKINE CYCLE FROM WASTE GASES	Emrecan ERCAN
120	THE EXPERIMENTAL INVESTIGATION OF THE EFFECTS OF IRON STEEL PLANT WASTE (SLAG) IN BIOGAS PURIFICATION	Nuri TUNÇ
188	INVESTIGATION OF THE EFFECT OF IMPROVED WASTE FUSEL OIL USING IN A SPARK IGNITED ENGINE TO DETERMINE THE ENGINE PERFORMANCE AND EMISSIONS	Süleyman ŞİMŞEK

5. SESSION

Parallel Session – Room : Hematite – 04.04.2017 – (15:30 – 17:00)		
Paper ID	Title	Speaker
77	THE INFLUENCE OF TOOL HELIX ANGLE ON TOOL WEAR WHEN END MILLING AISI 8640 STEEL	İbrahim ÇİFTÇİ
82	MECHANICAL CHARACTERIZATION OF THIN SHEET METALS FOR SUSPENSION SYSTEM FORMING DESIGN	Ali Murtaza RUTCI
87	THE INVESTIGATION OF TRIBOLOGICAL PROPERTIES OF THERMAL AGED CUAL10FE ALLOYS	Anıl İMAK
95	INVESTIGATION OF SHEET METAL FORMING PROCESS BASED ON FINITE ELEMENT SIMULATION	Ali Murtaza RUTCI
101	2D MODELING OF RESIDUAL STRESSES IN HARD TURNING OF AISI 4140 STEEL	Mehmet Erdi KORKMAZ
102	MODELLING OF ROUND ROLLING PROCESS BY USING FINITE ELEMENT METHOD	Emre EROL

Parallel Session – Room : Magnetite – 04.04.2017 – (15:30 – 17:00)		
Paper ID	Title	Speaker
194	AN APPLICATION EXAMPLE FOR ELECTRIC POWER PRODUCTION WITH ORGANIC RANKINE CYCLE FROM WASTE HEAT OF BASIC OXYGEN FURNACE PROCESS	Aytaç AYDIN
195	AN APPLICATION EXAMPLE FOR DEMINERALIZED WATER PRODUCTION FROM WASTE HEAT OF BASIC OXYGEN FURNACE PROCESS	Aytaç AYDIN
204	IMPROVING THE ENERGY EFFICIENCY IN IRON AND STEEL INDUSTRY BY ELECTRIC MOTOR RETROFIT	Mehmet AKBABA
244	IRON POWDER RECOVERY FROM STEEL PLANT RED MUD	Çağrı KOYMATÇIK
218	HEAT TRANSFER ANALYSIS OF A REHEAT FURNACE IN IRON AND STEEL INDUSTRY	Hüseyin YAĞLI
234	PRECIPITATING OF SINTER POWDER BY ESP AND EFFECTS OF SINTER POWDER ON ESP EFFICIENCY	Muhammed Esad ÇAYIR

Parallel Session – Room : Wustite – 04.04.2017 – (15:30 – 17:00)		
Paper ID	Title	Speaker
205	FROM WASTE MANAGEMENT IN IRON AND STEEL SECTOR TO ZERO WASTE	Esmâ YILMAZ
98	INDUSTRIALIZATION AND CANCER RISKS; A REVIEW	Kasım YILMAZ
17	AN EXAMPLE IMPLEMENTATION FOR THE LOWEST REDUCTION OF ENVIRONMENTAL EFFECTS OF CHEMICAL ORIENTED DISASTERS: THE REACH SYSTEM	Gazanfer ERBAY
94	AN OBSERVATION ON NATURAL WEATHERING EFFECT ON COLOR AND GLOSS PROPERTIES OF PPG COILS BASED ON DÖRTYOL HATAY TURKEY REGION COMPARED WITH FLORIDA	Tuğçe TOP
80	A RESEARCH ON BUSINESS SATISFACTION LEVELS OF OCCUPATIONAL HEALTH AND SAFETY SPECIALISTS IN OCCUPATIONAL HEALTH AND SAFETY PRACTICE	Volkan SANCI
93	REMOVAL AND ABSORPTION OF AMMONIA BY AN AIR STRIPPING PROCESS USING WATER-SPRAYING AERO-COLUMN REACTOR	Fuat ÖZYONAR

Parallel Session – Room : Limonite – 04.04.2017 – (15:30 – 17:00)		
Paper ID	Title	Speaker
49	THE EFFECTS OF REAL EXCHANGE RATES ON IRON & STEEL INDUSTRY	Ömer Faruk ÖZYALÇIN
81	LONG-TERM STEEL CONSUMPTION IN TURKEY	Hüseyin KARAMELİKLİ
139	ESTIMATION OF STRENGTH PROPERTIES IN CONCRETE STEEL BARS BY MULTIPLE REGRESSION METHOD	Hande VURŞAN
84	A FORECASTING ANALYSIS OF EXPORTS OF RAIL AND RAIL EQUIPMENTS IN TURKEY BY GREY PREDICTION AND EXPONENTIAL SMOOTHING	Ahmet Ziyaeddin BULUM
154	THE NUMERICAL SIMULATION OF THE FATIGUE ANALYSIS OF UIC60 AND 49E1 RAILS FOR HIGH SPEED MOVING TRAINS	Mehmet Akif KOÇ
108	THE DEVELOPMENT OF A DECISION SUPPORT SYSTEM FOR IRON AND STEEL INDUSTRY IN TURKEY	Muharrem DÜĞENÇİ

Parallel Session – Room : Siderite – 04.04.2017 – (15:30 – 17:00)		
Paper ID	Title	Speaker
238	ENERGY BALANCE RELATION FOR A BATCH TYPE FURNACE, A THEORETICAL STUDY	Selçuk SELİMLİ
243	ENHANCEMENT OF ENGINE OIL LIFE WITH VACCINATION METHOD	İsmail TARAKÇI
55	INVESTIGATION OF NANOCRYSTALLINE STAINLESS STEELS AS A FUNCTION OF MILLING TIME	Ahmet Burçin BATIBAY
223	EXPERIMENTAL INVESTIGATION ON SELF-LOOSENING OF PRELOADED STAINLESS STEEL FASTENERS	Barış TANRIKULU
259	THE INTEGRATION OF PLATE HEAT EXCHANGERS TO HEATING SYSTEM IN AN IRON & STEEL PLANT	Mutlucan BAYAT
8	INVESTIGATION OF PHYSICAL, CHEMICAL AND METALLURGICAL PROPERTIES OF DOMESTIC AND IMPORTED PELETS	Neslihan ATALAY

6. SESSION

Parallel Session – Room : Hematite – 05.04.2017 – (09:00 – 10:30)		
Paper ID	Title	Speaker
37	FATIGUE STRENGTH ASSESSMENT USING FINITE ELEMENTS AND INTERNATIONAL STANDARDS: APPLICATION EXAMPLES FROM RAILWAY WAGON CERTIFICATION	Emin SÜNBÜLOĞLU
59	INTERLABORATORY COMPARISONS OF TENSILE TEST FOR REINFORCING STEEL RELATED TO TS EN ISO 6892-1	Alper INCESU
68	ANALYSIS OF ACCREDITED LABORATORIES IN THE STEEL SECTOR IN TURKEY	Murat KAVRUK
126	MEASUREMENT UNCERTAINTY CALCULATION FOR CHARPY IMPACT TEST OF S275JR QUALITY STEEL	Alper INCESU
208	THE LIMITATIONS FOR PLANE-STRAIN FRACTURE TOUGHNESS TEST OF STEEL COMPACT TENSION SPECIMENS	Oğuzhan DEMİR
79	INTERLABORATORY COMPARISONS OF CHARPY IMPACT TEST FOR S275JR STEEL ACCORDING TO ISO 148-1	Betül USTA

Parallel Session – Room : Magnetite -- 05.04.2017 – (09:00 – 10:30)		
Paper ID	Title	Speaker
225	RESEARCH AND DEVELOPMENTS IN IRON AND STEEL INDUSTRY	Aslan ÜNAL
241	A LITERATURE REVIEW TO DESIGN OF 60 METRES AERIAL WORK PLATFORM	Yasin YAMAN
148	DETERMINATION OF THE INDIVIDUAL LEVEL OF FINANCIAL LITERACY: A STUDY IN KARDEMIR INC.	Murat YILDIRIM
149	A STUDY ON THE FINANCIAL BEHAVIOR OF KARDEMIR INC. EMPLOYEEER	Gülay GÜNAY
155	THE EUROPEAN COAL AND STEEL COMMUNITY AS A TRIVET FOR PEACE AFTER THE SECOND WORLD WAR	Umut KEDİKLİ
147	STEEL AND DEFENSE: SUCCESS TO THE SUCCESSFUL	Bahar AŞÇI

Parallel Session – Room : Wustite -- 05.04.2017 – (09:00 – 10:30)		
Paper ID	Title	Speaker
157	SIMULATION AND ANALYSIS OF THE SOLIDIFICATION CHARACTERISTICS OF A CAST AUSTENITIC STAINLESS STEEL	Gülşah AKTAŞ ÇELİK
171	ANALYSIS OF THE EFFECT OF THE CONTINUOUS SLAB CASTING PARAMETERS ON MOULD FRICTION	Hakan KAPUSUZ
229	UNPRESSURIZED GATING SYSTEM DESIGN AND SIMULATION IN SAND CASTING OF DUCTILE IRON	Ali Serdar VANLI
7	INVESTIGATION OF THE WETTING BEHAVIORS OF SAC305 AND SAC405 TERNARY LEAD-FREE SOLDER ALLOYS ON CU SUBSTRATE	Hasan ABUT
258	CLIMATE CHANGE EFFECT BY ROAD TRANSPORTATION IN KARABUK PROVINCE	Ali CAN
3	ALUMINUM INGOT FEEDING SYSTEM DESIGN FOR BASIC OXYGEN FURNACE	Ahmet KAYRAK
239	FEEDER DESIGN OPTIMIZATION FOR ALUMINUM SAND CASTING	Mustafa ERCAN

7. SESSION

Parallel Session – Room : Hematite -- 05.04.2017 – (11:00 – 12:30)		
Paper ID	Title	Speaker
153	INFLUENCE OF COOLING CONDITIONS ON FRACTURE TOUGHNESS OF 1040 QUALITY STEEL	Fazıl HÜSEM
248	INFLUENCE OF AGING ON RESIDUAL STRESS, WEAR AND HARDNESS BEHAVIOUR IN AL-CU-NI HEUSLER ALLOYS	Fazıl HÜSEM
197	INVESTIGATION OF THE EFFECT OF YTTRIA CONTENT ON THE MECHANICAL PROPERTIES OF THE ALUMINUM/TIC COMPOSITES	Yasin AKGÜL
135	NANO-SIZED IRON OXIDE PRODUCTION AND CHARACTERIZATION BY ARC DISCHARGE METHOD	Safa POLAT
152	INFLUENCE OF HEAD HARDENING PROCESS ON FRACTURE TOUGHNESS IN RAILS	Fazıl HÜSEM
196	FABRICATION AND MECHANICAL BEHAVIOR OF ALUMINUM-MATRIX COMPOSITES REINFORCED WITH BORON NITRIDE PARTICLES	Yasin AKGÜL

Parallel Session – Room : Magnetite -- 05.04.2017 – (11:00 – 12:30)		
Paper ID	Title	Speaker
227	THE OPTIMIZATION OF THE COATING PROCESS PARAMETERS BY ELECTRO-SPARK DEPOSITION (ESD) TECHNIQUE USING STEEL/INCONEL COUPLE	Mustafa Safa YILMAZ
166	THE EFFECT OF PRIOR AUSTENITE GRAIN SIZE ON MICROSTRUCTURE OF MEDIUM CARBON DUAL PHASE STEELS	Özge ARARAT
214	INVESTIGATION OF RESISTANCE SPOT WELDING CONNECTION IN DP600 STEEL	Burak Emre YAPANMIŞ
27	EFFECT OF CHROMIUM ON THE BORONIZING BEHAVIOR OF IRON	Mehmet TARAKÇI
29	CHARACTERIZATION OF BIODEGRADABLE FE-CO ALLOYS	Mehmet TARAKÇI
230	EFFECT OF NB CONTENT ON MICROSTRUCTURE TENSILE STRENGTH PROPERTIES OF NB-V ADDED MICROALLOYED STEEL PRODUCED BY POWDER METALLURGY METHOD	Ferhat KAHVECİGİL
232	THE MECHANICAL PROPERTIES OF CARBURIZED AND UNCARBURIZED AISI 8620 STEEL BY POWDER METALLURGY METHOD	Özcan TOPÇU

Parallel Session – Room : Wustite -- 05.04.2017 – (11:00 – 12:30)		
Paper ID	Title	Speaker
143	EFFECT OF TEMPERING TIME AND TEMPERATURE ON WEAR PERFORMANCES OF CR-W STEELS	Fatih AYDIN
184	TRIBOLOGICAL BEHAVIORS OF NITRIDED AND NITROXED TOOL STEELS	M. Emre TURAN
1	INFLUENCE OF STRAIGHTENING PROCESS ON MECHANICAL PROPERTIES OF PRE-STRAIN PEARLITIC STEELS	Alper INCESU
191	THE INFLUENCE OF HEAT TREATMENT ON STRUCTURAL TRANSFORMATIONS OF NITI ALLOY	Yüksel AKINAY
146	DRY SLIDING AND CORROSIVE WEAR PERFORMANCES OF HEAD HARDENED RAILS	M. Emre TURAN
136	ENHANCED SYNTHESIS AND FUNCTIONALIZATION OF BORON NITRIDE NANOPLATES	Safa POLAT

POSTER PRESENTATIONS

1. SESSION

Location : Poster Hall - 03.04.2017 - (13:30 – 17:00)		
Paper ID	Title	Presenter
4	CORROSION-RESISTANT HIGH ENTROPY STAINLESS STEELS — A PERSPECTIVE	Burak DİKİCİ
86	INVESTIGATION FRICTION WELDING PROCESS OF HIGH SPEED STEEL TO SPRING STEEL	İhsan KIRIK
20	FRICTION STIR SPOT WELDING FOR DIFFERENT METALS: A REVIEW	Melike ŞAŞMAZ
33	HIGH PERFORMANCE COPPER AND COPPER ALLOYS FABRICATED BY SEVERE PLASTIC DEFORMATION	Aslıhan GÖKDUMAN
34	HIGH PRESSURE TORSION APPLICATIONS ON DILUTE COPPER ALLOYS	Hasan KÖKLÜ
57	A METHOD FOR ASSESMENT OF RUST PREVENTIVE OIL ON GALVANIZED STEEL	Özgür KARAKAŞ
63	THE CHANGES IN ISO 6892-1:2016 METALLIC MATERIALS TENSILE TESTING STANDARD	Bülent AYDEMİR
70	A NEW HARD COPPER ALLOY ALTERNATIVE TO CUCONIBE ALLOY FOR STEEL WIRE MESH WELDING	Tuba ÖZEREN
71	AN INVESTIGATION ON CUTTING BEHAVIOR OF CONIAL SHAPE MEMORY ALLOY BY ABRASIVE WATER JET	Ali GÜNEN
72	APPLICATION OF DIFFERENT COATING METHODS TO EXTERNAL COOLING ROLLER AND CHARACTERIZATION OF APPLIED COATINGS	Ali GÜNEN
78	IMPORTANCE OF FORCE MEASUREMENTS AND THEIR TRACEABILITY IN STEEL INDUSTRY	Haldun DİZDAR
74	DETERMINING THE CORROSION BEHAVIOUR OF EN 1.4462 DUPLEX STAINLESS STEEL IN FECL3 MEDIA FOR VARIOUS SOLUTION TREATMENT CONDITIONS	Alptekin KISASÖZ

2. SESSION

Location : Poster Hall - 04.04.2017 - (09:00 – 12:30)		
Paper ID	Title	Presenter
92	CHANGE IN CHLORIDE CONTENT OF REGENERATED RED IRON OXIDE PARTICLES IN ACCORDANCE WITH PARTICLE SIZES	Alper AKÜN
97	AGING OF A356 ALUMINUM BILLETS PRODUCED BY SEMI-SOLID METAL PROCESSING	Rıdvan GECU
99	SAFE BEHAVIOR CHANGE TO RELEASE OF OHS CULTURE IN THE IRON AND STEEL SECTOR	Cumhur KOCAMAN
107	EFFECT OF REDUCTION RATE IN FORMABILITY OF TITANIUM + NIOBIUM ALLOYED IF STEEL	Muhammed Mustafa ERŞEN
114	EFFECT OF HEAT TREATMENT PARAMETERS APPLIED TO AA7075 ALLOY ON CORROSION BEHAVIOR	Gökhan ÖZER
117	MAGNESIUM METAL PRODUCTION WITH MAGNETERM PROCESS BY USING ALUMINIUM	Yahya BAYRAK
130	INVESTIGATION OF MECHANICAL PROPERTIES OF PIPES USED IN OIL AND GAS PIPELINES	Osman AKTAŞ
132	ELECTROSTATIC POWDER PAINTING PLANT CONVEYOR SYSTEM AND ENERGY EFFICIENCY	Demet TAŞKAN
140	ENERGY SAVING BY USING BLAST FURNACE TOP PRESSURE RECOVERY TURBINE (TRT) SYSTEM	Selcuk KUŞOĞLU
141	THE INVESTIGATION OF MICROSTRUCTURE OF DUBLEX STAINLESS STEEL WELDED BY FCAW METHOD	Mustafa TÜMER
144	INVESTIGATION OF DETERMINATION THE NON-RECRYSTALLIZATION TEMPERATURE (TNR) BY THERMO-MECHANICAL SIMULATION METHODS	Ekrem AKÇA
189	THE TRIBOLOGICAL CHARACTERISTICS OF ELECTROLESS NI-P COATED AISI1020 CARBON STEEL	Ulaş MATİK
251	RECYCLING AND REUSE POTENTIAL OF SOLID WASTES PRODUCED IN IRON AND STEEL INDUSTRY	Sakine UĞURLU KARAAĞAÇ

3. SESSION

Location : Poster Hall - 04.04.2017 - (13:30 – 17:00)		
Paper ID	Title	Presenter
150	TURKEY'S MAGNESITE FOR PRODUCTION OF FUSED MAGNESIA, PROPERTIES AND USES IN REFRACTORY APPLICATIONS	Asım BİLGE
165	THE EFFICIENT USE OF NOISE PRODUCED IN ENERGY FACILITIES OF INTEGRATED IRON AND STEEL PLANTS	Hasan KAHRAMAN
187	STUDY OF THE COMPACTING AND PRE-SINTERING OF DENTAL ZIRCONIA WASTE POWDERS	Handan TURAN MATİK
192	EFFECT OF SIC PARTICLE SIZE ON THE TRIBOLOGICAL PROPERTIES OF AA6061-SICP COMPOSITE PREPARED BY HOT PRESSING	Mert YAKIŞIK
145	RESIDUAL STRESS DISTRIBUTION IN R220 AND R260 GRADE GROOVED RAILS	M. Emre TURAN
216	IMPROVEMENT OF 16MNCR5 STEEL WEAR RESISTANCE BY DEFORMATION	Hüseyin DEMİRTAŞ
231	EFFECT OF CR CONTENT ON MICROSTRUCTURE AND TENSILE STRENGTH PROPERTIES OF NONALLOYED STEEL PRODUCED BY POWDER METALLURGY METHOD	Rifat GÜNDÜZ
233	EFFECT OF GRAPHITE CONTENT ON MICROSTRUCTURE AND MECHANICAL PROPERTIES OF MO ADDED STEEL PRODUCED BY POWDER METALLURGY METHOD	Mehmet Akif ERDEN
236	RESIDUAL STRESS MEASUREMENT IN EN ISO / IEC 17025 STANDARD AND HARDNESS-RESIDUAL STRESS RELATIONS IN HOT ROLLED SQUARE AND ROUND SHAPED PROFILES	Tolga TURANLI
245	ACCELERATED COOLING HEAT TREATMENT OF EQUILATERAL ANGLE AND HEA-HEB PROFILES	Fatma KÖZ
249	INVESTIGATION OF WEAR AND MECHANICAL BEHAVIORS OF DAMASCUS STEELS	Eren SALIS
56	ECONOMIC CRISES IN TURKEY AND IN THE WORLD AND THEIR EFFECTS ON IRON AND STEEL MARKET	Nazmi SARIKAYA

Influence of Straightening Process on Mechanical Properties of Pre-Strain Pearlitic Steels

Alper INCESU¹, Yasin AKGUL¹, Muhammet Emre TURAN¹, Ahmet GULLU²

¹Karabuk University, Iron and Steel Institute

²Gurmak Çelik

correspond e-mail: yasinakgul@karabuk.edu.tr

ABSTRACT

In this study, effect of straightening process on mechanical properties of pre-strain pearlitic steels was investigated. The material employed in this study has 0,83 % Carbon content. Tensile test, Vickers hardness test and Wear tests under load of 10N and 20N were performed for samples (straightened and non-straightened) to determine mechanical properties. Also, Scanning Electron Microscope (SEM) was used for microstructure characterization. Tensile test results revealed that yield strength and tensile strength increased with straightening process.

Keywords: Straightening, Pre-strain steel, SEM analysis, Wear Behavior

Revision of The Rolling Mill Roller Bearing

Bilal ÇOLAK*, Ahmet EREN⁺, Naci KURGAN*

[#]Karabuk University, Eskipazar Vocational School
Bahcepinar Mah. Hastane Cad. No:37 Eskipazar, Karabuk, Turkey
bilalcolak@karabuk.edu.tr

Ondokuz Mayıs University, Engineering Faculty
Kurupelit Kampusu, Atakum, Samsun, Turkey
naci.kurgan@omu.edu.tr

⁺aarena@gmail.com

Abstract— Generally, 4-row cylindrical roller bearings are used as roll neck bearing in rolling mills. The inner ring of these bearings must be fitted as a tight fit to the roll neck according to the structure of the bearing. This concomitantly requires a great deal of labor, time and equipment. In addition to this hardship, roller bearing damages and time lost are in question because of difficulties encountered when mounting the chock to the roll. It was provided an improvement in bearing life and an increase in production speed and quantity by being eliminated these problems with the use of tapered roller bearings instead of cylindrical roller bearings.

Keywords— 4-high, rolling, roller bearing, rolling force, axial force, radial force, chock

I. INTRODUCTION

This revision has been performed in the finishing mill of a hot rolling mill producing flat rolled products in Turkey. The finishing mill consists of 7 stands finishing train, side guides and with looper tables between each pair of stands (Fig. 1). Finishing mill is equipped with the high technology systems to achieve proper surface condition, narrow dimension tolerances and good shape. There are AGC (Automatic Gauge Control), roll bending and roll shifting systems in this mill. Each stand reduces strip thickness according to calculated setup to produce ordered dimensions at the exit of last stand. Each stand has a 4-high rolling mill with two work rolls and two support rolls [1] (Fig. 2). The revision has been held on the last three stands (F5, F6, F7) of the finishing mill.



Fig. 1 Finishing mill

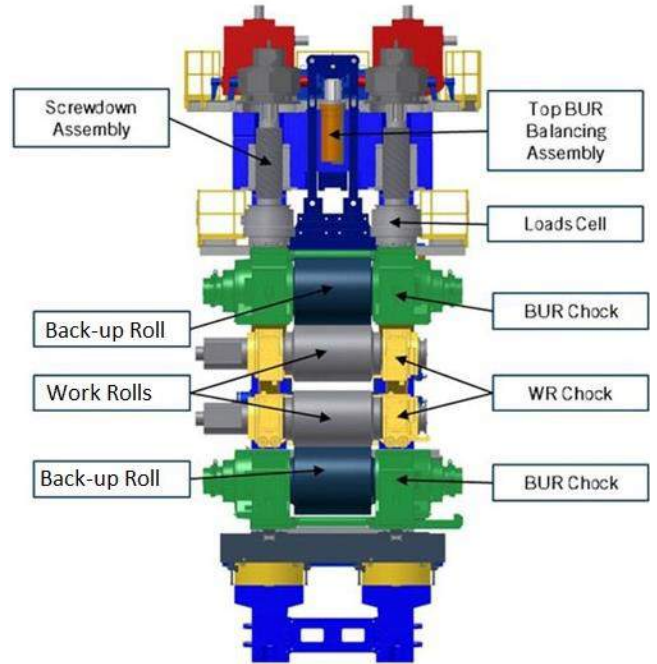
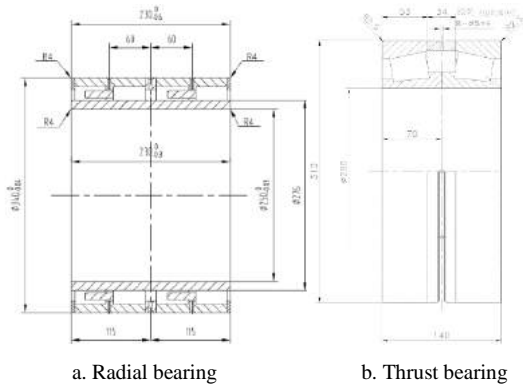


Fig. 2 4-high rolling mill [2]

4-row cylindrical roller bearing (Fig. 3a) is used on work roll in the mill. These bearings have high stiffness and can accommodate only radial loads. For this reason, they are mounted together with double row tapered roller bearing shown in Fig. 3b.



a. Radial bearing b. Thrust bearing

Fig. 3 Original roller bearings [1]

Roll barrel surfaces are deteriorated during rolling. They are ground to remove residual work hardening wear and minor damage. After grinding of the barrel surfaces, chocks must be remounted on the roll neck. Assembled chocks are fitted to the roll neck via chock mounting device shown in Fig. 4 and operating principle of this device is schematized in Fig. 5. This process is performed many times in every shift. It is important to make the settlement process as soon as possible to prevent interruption of production.



Fig. 4 Chock mounting device



Fig. 5 Main steps for dismounting and mounting of chocks [3]

II. AVAILABLE ROLLER BEARING TROUBLES

A. Inner Race Mounting Problem

The inner ring of the 4-row cylindrical roller bearing illustrated in Fig. 3a can be completely separated from the bearing. The cylindrical roller bearing inner rings are mounted on the roll neck with tight fit (Fig.6). In this process, the selection of the fitting temperature is important so that the properties of the ring material are not adversely affected. The size difference between the roll neck and the bearing inner race varies between 0.084 mm and 0.143 mm [1]. For mounting the inner races on the necks, they must be heated to approximately 100 to 120°C. The races are dimensionally stable up to 160°C, i.e. this temperature must not be exceeded, not even partly. A temperature presetting device is available so that the maximum temperature not to be exceeded. The heated races are centrally pushed onto the roll until they abut. They should be left on the roll to cool down and shrink on. While cooling down, the races must on no account be axially adjusted [4]. The work roll before mounting is shown in Fig. 7a and it is shown after mounting in Fig. 7b.

During mounting, physical damage of the ring depends on the degree of mastery of the person. The ring mounting is another disadvantage of the cylindrical roller bearing when it is remembered that the life of the roller bearing depends largely on the mounting conditions.



a. Heating of the rings b. Mounting of the rings

Fig. 6 Mounting process of the rings

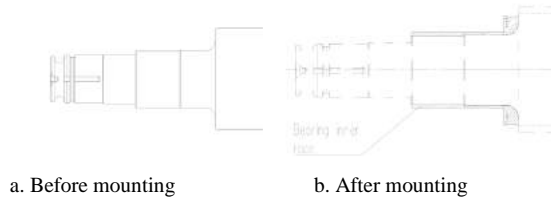


Fig. 7 Work roll [1]

Inner rings must be finish ground after mounting on the roll neck to minimize eccentricity of the roll neck to the roll body (Fig.8.). Thanks to this skin grind, bearings have extended useful life in the mill.



Fig. 8 Ring grinding

Sturdy rings on scrap rolls are removed by an induction heater and remounted to new rolls (Fig. 9). But in this reheating operation, the bearing material may be impaired and result in physical damage to the bearing. This process also causes labor and time loss.



a) Heating of the ring b) Extracting of the ring

Fig. 9 Dismounting of the ring

B. Roller Drop

Rolls that have been ground in certain periods need to chock with the aid of the chock mounting system shown in Fig. 4. This process is as shown in Fig. 10.

The four-row cylindrical roller bearings are provided with a double pronged brass cage that cannot properly control the roller drop during the bearing life cycle. With high roller drop, the mounting process can be very tricky. Due to the tight dimensions, care must be paid to avoid damaging bearing components. In fact, by hitting the inner ring, the resulting tilting moment on the rollers can

damage the cage or outer ring integral ribs as shown in Fig. 11 [3]. Besides the bearing damage, the installation time is also extended. Repeatedly performing this assembly process in a busy working environment can cause the production to be interrupted.

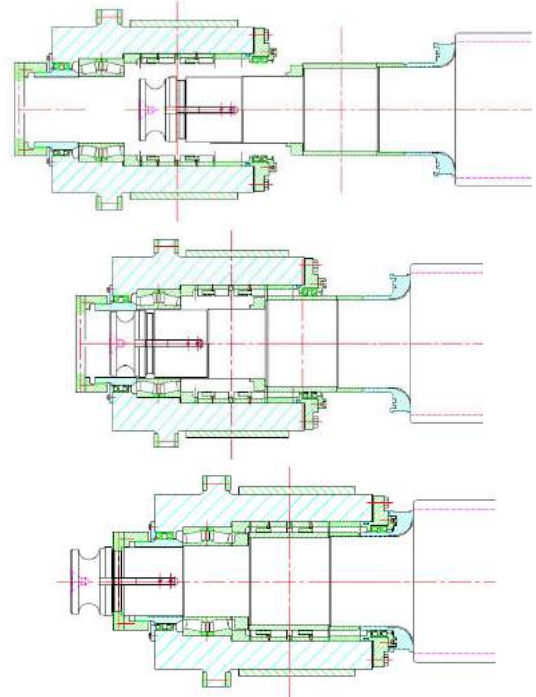


Fig. 10 Mounting of the CRB to the roll (Original type bearing) [1]



Fig. 11 Roller drop [3]

III. REVİZYON

Although cylindrical roller bearings take only the radial loads, tapered roller bearings have the inherent ability to carry combinations of radial and thrust

loads, depending on the angle of the rollers. This angle is indicated by the K factor (Fig. 12). The bearing with small K factor has high thrust load rating, low radial load rating; the bearing with large K factor has high radial load rating and low thrust load rating [5]. The selected tapered roller bearing in this revision has been chosen to have high K factor (K = 1.89) to accommodate as a radial bearing.

$K = \text{dynamic radial load rating} / \text{dynamic thrust load rating}$

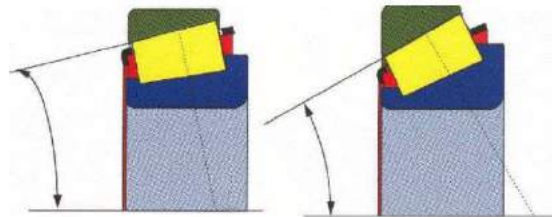


Fig. 12. K factor [6]

The radial load carriage capacity of tapered roller bearings is lower than the radial load carriage capacity of the same-sized CRBs. A tapered roller bearing of the same size was needed to carry the same amount of radial load. To find the most suitable bearing to meet the need, the theme was passed with Timken regional sales manager. In making bearing selections for the hot strip mill chock, Timken representatives have assisted us in load and life calculation methods that have taken full advantage of tapered roller bearing operating characteristics. In this stage rolling loads (radial, axial, bending), operating speed, working temperature, material type, lubrication condition, environmental factors, bearing and roller dimensions and tolerances have been considered. This information required in the calculation and selection of the bearing is given in Table I, Table II and Table III.

TABLE I
WORKING CONDITIONS [1]

Stand	Max. Radial Force (kN)	Max. Bending Force (kN)	Max. Rolling Speed (m/sec)	Lube
F5	5.000	800	4,57-11,43	Grease
F6	5.000	800	6,03-15	Grease
F7	5.000	800	7,22-15	Grease

The forces given in Table 1 are the forces per bearing.

TABLE II
DIMENSIONS OF THE MILL [1]

Stand	Bearing Centre				Roll Dia. (mm)

	Distance (mm)	Barrel Width (mm)	Bearing Temp. (°C)	Internal Clearance (mm)	Max	Min
F5	1860	1150	50	0,28	460	410
F6	1860	1150	50	0,28	460	410
F7	1860	1150	50	0,28	460	410

TABLE III
INFORMATION OF ROLLED MATERIAL [1]

Stand	Max. Width of Rolled Material (mm)	Max. Reduction (Δh) (mm)	Rolling Temp. (°C)	Material Grade
F5	1000	1	900-1000	Low carbon steel
F6	1000	1	900-1000	
F7	1000	1	900-1000	

As a result of the evaluations, it is concluded that the TQOW type 4-row tapered roller bearing shown in Fig. 13 is the most suitable bearing in the present conditions. The type TQOW is particularly suited to roll necks not having a separate fillet ring, where the cone is backed directly against the roll shoulder [6].

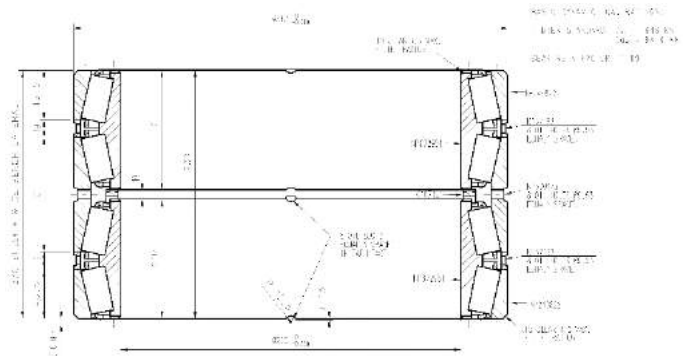


Fig. 13 4-row tapered roller bearing (New type bearing) (TRB)

The static and dynamic load ratings of the old and new type bearings are given in Table 4.

TABLE IV
LOAD RATINGS

Bearing Type	Static Load Rating (C ₀) (kN)	Dynamic Load Rating (C) (kN)
Original Roller Bearing (CRB)	5220	2030
New Kind of Bearing (TRB) – Timken	C ₀₉₀ (kN) 98,8	C ₉₀ (kN) 648

IV. LOAD DISTRIBUTION

The distribution of load in each work roll bearing is dependent not only on the magnitude of radial and axial loads but also their relative values. That is, when the radial load is relatively large compared to the axial load, then all the four rows will be loaded, to differing values. If the axial load is significant compared to the radial load, then two of the four rows will be very lightly loaded or even unloaded. But this is not the case in the revised bearing. Even

if the thrust loads increase, the new type radial bearing (TRB) will not carry thrust loads. Because bearing in which has the least internal clearance takes the load. Due to the structure of the tapered roller bearings, the radial and axial clearances can be adjusted during mounting. Axial clearance of the radial TRB (Fig. 13) is set larger than axial clearance of the 2-row tapered roller bearing (Fig. 3b) in the same chock. Thus, the radial TRB only carries radial loads. Because of this, axial loads were not considered in life calculation of the TRB.

Due to the plastic deformation of the material, the pressure distribution occurred between the work roll and the material is shown in Fig. 14. It is assumed that the resultant force of this pressure distribution (F_r) acts from the neutral point (N) where there is no relative motion between the roll and the material. This whole resultant force isn't taken by the radial TRB. This force is divided into vertical (F_v) and horizontal (F_h) components at varying rates depending on the ϕ angle. Since the horizontal component is taken by the radial TRB, only this component has been considered in the life calculation.

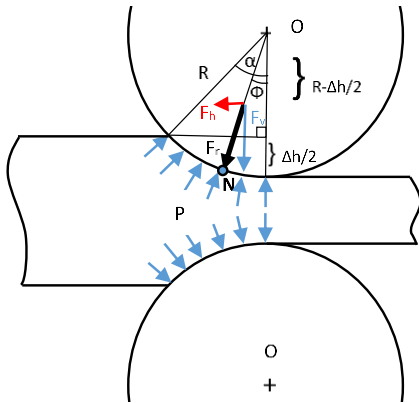


Fig. 14 The components of the rolling force

The maximum radial force is 5.000kN in the mill (Table 1). The horizontal component of this force (F_h) is taken by the TRB. The maximum value of this component ($F_{h_{max}}$) occurs when the angle ϕ is maximum. This means that the diameter of the roll is the smallest (410 mm) (Table II) and the reduction is the largest ($\Delta h=1$ mm) (Table III). The roll bite angle (α) is calculated as 4° with the aid of trigonometric relations as shown below.

$$\cos^{-1} \alpha = \frac{\left(R - \frac{\Delta h}{2}\right)}{R} = \frac{205 - 0,5}{205} = 4^\circ$$

The angle Φ is theoretically 25% of angle α .

$$\phi \cong 0,25 \times \alpha \cong 0,25 \times 4 = 1^\circ$$

Here the angle is 1° and the force $F_{h_{max}}$ is 87kN.

$$F_{h_{max}} = F_r \times \sin \phi = 5.000 \times \sin 1 \cong 87kN$$

The vertical component of the radial load (F_v) is transmitted to the back-up roll barrel over the work roll barrel and then to the back-up roll bearings (Fig. 15).

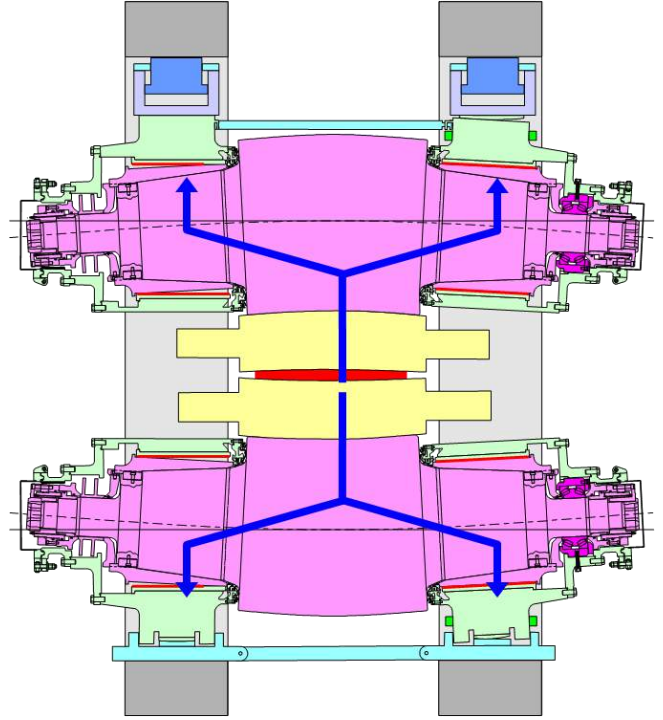


Fig. 15 Transmission of the separating force [7]

The main forces acting on the work roll bearings are the bending forces which are occurred by the bending system (Fig. 16). This rolling mill is equipped with a positive bending system and bending forces are around 800kN per bed (Table I). The bending force (F_b) is perpendicular to the horizontal component of the radial force (F_h). With the help of trigonometric relations, the compound of these two forces (F) is found to be 805kN as shown below.

$$F_{h_{max}} = 87kN$$

$$F_b = 800kN \text{ (Table I)}$$

$$F = \sqrt{(F_{h_{max}})^2 + F_b^2} = \sqrt{(87^2 + 800^2)} = 805kN$$

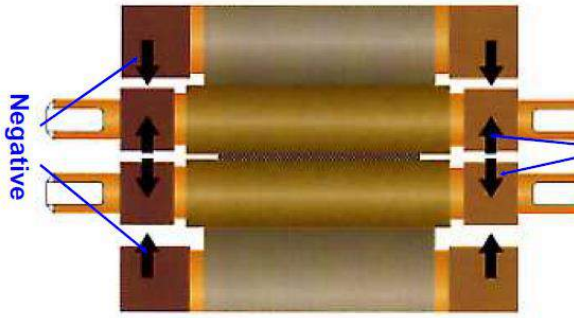


Fig. 16 Bending system [8]

There is also a horizontal component of the roll force caused by the offset of the work roll to the backup roll. This force, as well as the friction force between the roll and the material, is neglected in the bearing lifetime calculation.

A. Bearing Life Calculation

According to ISO and AFBMA (Anti-Friction Bearing Manufacturers Association), the dynamic load ratings used in bearing life calculation are given for 1 million cycles. Table 4 shows the number of dynamic load ratings of the original CRB for 1 million cycles. However, for Timken bearings this value is given for 90 million cycles (500rpm, 3000h) [5]. The life calculation that has been made considering this difference is given below.

1) Original Bearing (CRB) Life Calculation

$$L = \left(\frac{C}{F}\right)^{\frac{10}{3}} \times 10^6 = \left(\frac{2030}{805}\right)^{\frac{10}{3}} \times 10^6 = 21,8.10^6 \text{ cycle}$$

2) Life Calculation of the New Kind Bearing (TRB)

$$L = \left(\frac{C_{90}}{F}\right)^{\frac{10}{3}} \times 90.10^6 = \left(\frac{648}{805}\right)^{\frac{10}{3}} \times 90.10^6 = 43,6.10^6 \text{ cycle}$$

Although the dynamic load rating of the TRB is lower than that of the CRB, the life of the Timken bearings is higher than that of 90 million rpm.

When the speed reaches 2 times in the roller bearings, the life is reduced to about half [5]. Since the life of Timken bearings is given for 500rpm and the current bearing speeds are also approximately the same with this speed, negative impact of speed on bearing life isn't in question.

V. CONCLUSIONS

As a result of this revision, the disadvantages in using cylindrical roller bearings have been abolished by the use of tapered roller bearings. The advantages have been gained in this revision are below.

- 1) Tapered roller bearings components are assembled into the chock with their rings and assembled onto the roll neck. So, roller drop

problem encountered in cylindrical roller bearing assembly is not experienced in tapered roller bearing assembly. So, the mounting process is performed more quickly and efficiently, with a low incidence of bearing damages.

- 2) Since there is no ring mounting in the use of tapered roller bearings, there are no ring mounting-disassembly problems experienced with the use of cylindrical roller bearings.
- 3) As roller bearings work, their rollers are worn out and their diameter gets smaller. Thus, load distribution in the bearing does not show homogeneity and the bearing life is reduced. This problem can be solved using tapered roller bearings. In the case of tapered roller bearings, when the rollers are worn, the spacer rings between the cones are grinded to ensure that all the cones and rollers are evenly loaded. So, that the actual life of the bearings has prolonged.
- 4) With the commence using of tapered roller bearings, damage to the bearings was largely avoided and a considerable reduction in bearing costs was seen. In addition, shortening of the chock assembly duration leads to reduce downtime, thus contributing to increase the annual production volume.
- 5) Rolling mills need bearings to perform effectively at high speeds, under heavy loads, and in severely contaminated environments. At the same time, there's constant pressure to increase production while reducing cost-per-ton rolled. Maintenance budgets are often being reduced, allowing for less time and resources available for bearing maintenance.
- 6) Because of its tapered construction and hard wearing surfaces, the Timken bearing has the capacity to tolerate a reasonable amount of dirt. This results from a tendency for the dirt along with the lubricant to be worked through the bearing, minimizing the lapping effect that would otherwise be created by dirt trapped in the bearing [6].
- 7) The on-apex construction that assures true rolling motion of a Timken bearing, combined with its fine surface finish, keeps friction to a minimum. This is of significance on machines that are continually started and stopped under heavy loads [6].
- 8) Timken bearings can be depended upon to deliver their full rated capacity because the rib-guided rollers are positively aligned, permitting them to carry load over the full length of the rollers. Even with a significant amount of deflection and misalignment, the roller in a Timken bearing line up squarely. The cage doesn't guide the rollers. Its only operating function is to keep the rollers from rubbing against each other. Timken bearings truly "roll the load" with ease and dependability [6].

REFERENCES

- [1] Rolling Mill Manuals
- [2] (2017) [Online]. Available www.aptint.com/
- [3] RKB Multi-Row Roller Bearing Brochure
- [4] Made by SKF, Mounting and Maintenance Instructions for 4-row Taper Roller Bearing, SKF GmbH, Schweinfurt
- [5] Timken Tapered Roller Bearing Guide
- [6] Rolling Mill Equipment Supplement, The Timken Company
- [7] Morgoil Symposium, Sept. 2004
- [8] Timken Rolling Mill Industry Training Notes

Aluminium Ingot Feeding System Design for BOF

Ahmet Kayrak*, Mesut Tural+, İsa Keskin*

Ereğli Iron and Steel Works Co., Steelmaking and Casting Tech. R&D
Zonguldak, Turkey
{akayrak, ikeskin}@erdemir.com.tr

+ Erdemir Engineering, Portfolio and Project Management Dept.
Hatay, Turkey
mtural@erdemir.com.tr

Abstract— Aluminium is usually used for de-oxidation of liquid-steel production in Basic Oxygen Furnaces. For this process, Aluminium ingots that have 5 kg nominal weight are feeding manually in a ladle for this kind of Plant. This situation can lead to some problems such as quality error and loss of efficiency. The problem was solved by designing automatic aluminium ingot feeding system. Hereby feeding system performance variables had improved considerably and also risks caused by occupational health and safety aspects have been eliminated.

Keywords— Basic Oxygen Furnace, Aluminium ingot, De-oxidation, automatic feeding

I. INTRODUCTION

During the tapping process of steel from converter to ladle in steel making shop, due to the deoxidation of liquid steel defined amount of aluminium is added to stream. The aim of ideal deoxidation practices is preventing the CO gas formation during casting by binding free oxygen in liquid steel and removing oxide inclusions which are formed in deoxidation during tapping and increasing the efficiency of deoxidant materials. For being supplied easily, high affinity to oxygen and cost advantage reasons, aluminium is one of the most common used deoxidizer in steelmaking process. The amount of soluble oxygen can be measured between 400 – 1400 ppm at the end of blowing process in converter. According to affinity diagram the soluble oxygen amount can be decreased till 5 ppm levels in steel [1].

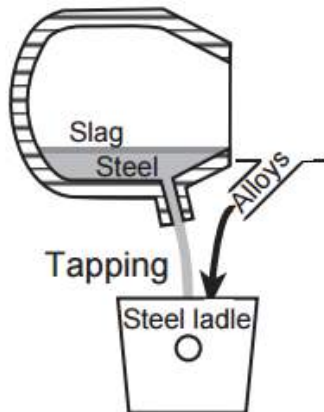


Figure 1: Tapping Poces [2]

As seen in figure 1, the shape of aluminium added for steel deoxidation can be ingot, pyramit and granulated. Although material additon system is used for feeding the pyramit and granulated aluminium, the ingot aluminium is fed by manually in steelmaking processes. In this study, the deoxidation efficiency and cost optimization of ingot aluminium's amount of 5 kg, fed by automated feeding system or manually was investigated. Moreover, during the startup of automated aluminium feeding system the ratio of work accidents and operation risks were aimed least as possible.

In steelmaking process, deoxidizers are always used to decrease the dissolved oxygen in liquid steel [1]. Dissolved metal reacts with the dissolved oxygen according to the precipitation reaction to generate metal oxide and this deoxidation product Al_2O_3 not only can affect the cleanness of steel, but also is the main cause for nozzle clogging during continuous casting. The most common used deoxidation agents are FeSi and Aluminium [3]. According to Ellingham diagram, the commercial element which has the highest affinity to oxygen is aluminium [4]. The deoxidation product of process can be FeO. Al_2O_3 when the aluminium activity is lower or Al_2O_3 when Al activity is higher. The FeO. Al_2O_3 and Al_2O_3 phases are in equilibrium condition at the specific temperature on the equilibrium lines of FeO. Al_2O_3 and Al_2O_3 (Figure 2).

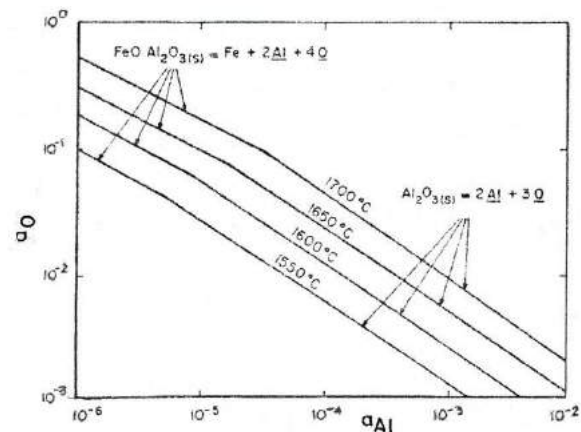


Figure 2: Equilibrium diagram of Al Deoxidation [1]

In equilibrium conditions at 1600°C, the deoxidation product will be $\text{FeO} \cdot \text{Al}_2\text{O}_3$ when the aluminium feed to liquid steel which has 0.058% soluble oxygen [5].

There are several risks while feeding of aluminum manually during the tapping process. It is well known that the unstable movements of body will cause some problems to back pains and other risks [6]. The statistical results show that 71% of work accidents related with environmental reasons and 29% is related with body actions during the working time. The highest risky group in working conditions is manually loading activities [7]. In general, most of the injuries are underlined as low risky activities [8].

II. MATERIAL & METHOD

In this study, automated aluminum feeding system was designed. The milestones of project were listed below;

- The general overview of system design was defined while discussing with related operation groups.
- The potential benefits of automated feeding system were investigated in literature and similar operations.
- Preliminary design studies were finished according to possible requirements during the real operation of system.
- After the assessment of preliminary design of system, detailed mechanisms of feeding system finalized. The system includes connectors, weighing systems, and transfer chutes (Figure 3).
- The prototype of automated feeding system was manufactured and tested with different feeding scenarios. The optimization studies were implemented with that prototype system in terms of mechanical and automation systems.
- After the commissioning phase was finalized the performance tests were applied and operation started successfully.

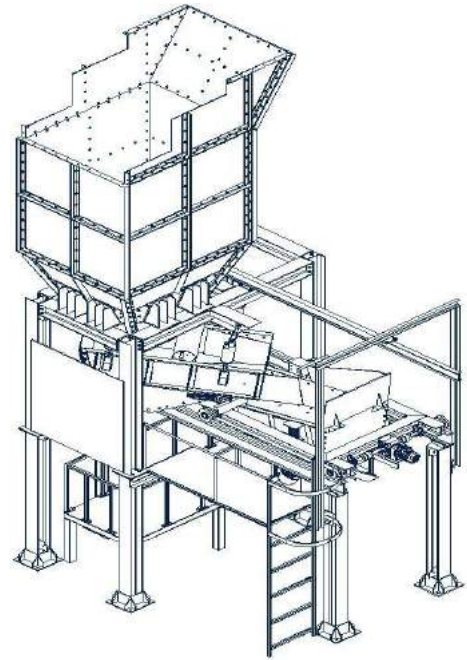


Figure 3: Aluminum Ingot Feeding System

B. Systems Operation Principle

The aluminium ingot feeding system is able to charge uniform and smooth geometry ingots within 4 minutes. The amount of the aluminium to be charged automatically received from the automation system according to the steel grade or entered manually by the operator. aluminium feeding rate of the system which is provided that the error limit at each feed is maximum +/- 10 kg, is between 50 kg minimum and 200 kg maximum per minute. Therefore, in these conditions, system is capable of weighing, feeding and communicate with automation system. The block diagram of the system operation can be seen in Fig. 4.

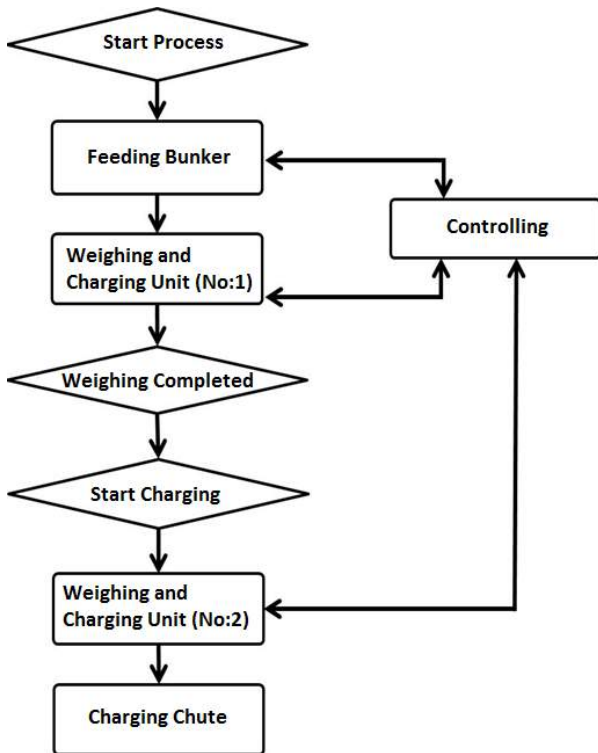


Figure 4: Aluminum Ingot Feeding System Flow Diagram

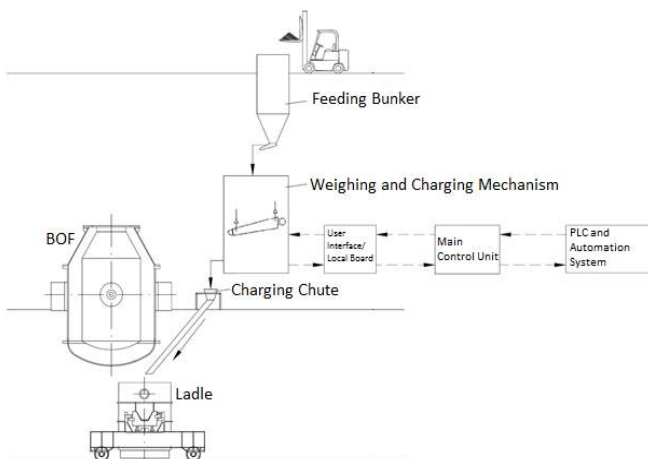


Figure 5: Aluminum Ingot Feeding System Process Chart

The system contains 3 basic subcomponents:

1. Aluminum Feeding Bunker
2. Weighing and Charging Unit
3. Control Unit

3) *Aluminium Feeding Bunker*: It is a subsystem which is ingot aluminium are stored before weighing. It allows to ingot aluminium transferred uniformly from feeding bunker to weighing unit. The bunker is designed to have about 9 tons of aluminium capacity. The ingot aluminium feeding bunker is produced from St37-2 material (HARDOX 400) which is

resistant to wear and impact. Wear plates are designed as modular and easily changeable.

4) *Weighing and Charging Unit*: This unit allows to the ingot aluminium move through from feeding bunker to charging chute. The weighing system consists of load cells, original mounting apparatus, weighing indicator and junction box. The unit also have mechanical stoppers for the weighing platform not to be affected or tilted from side and vertical loads. The weighing system weigh and transfer the aluminium ingots which is pouring the uniformly to the control system. When the exact amount of aluminium coming from the control system, the cut-off damper automatically closes and the aluminium flow is cut off. After the tapping has been started, second command is given to the mechanism and aluminium ingot which has been weighed flows to the direction of the charging chute.

5) *Control Unit*: There is a control unit on the system that allows the feedstep to be controlled automatically or manually via a panel.

- When the system is in automatic mode, it takes the amount of aluminium from the automation system and proportionally feeds to the charging chute which is near the converter, then reports back to the system the actual amount of discharged aluminium after charging.
- In the manual mode, the amount of aluminium entered by the operator from the operator panel is fed to the material grooves next to the converter with a maximum ± 10 kg error and the amount of actual aluminium discharged after charging is reported back to the system.

If the system fails in any way, the control unit will be able to determine the cause of the fault and relay the error message to the user for describing the fault. The system works in the maximum tolerance range of ± 10 kg fault tolerance and preventing less or overfeeding from this amount. User inputs are convenient to be made from a remote terminal or automation system.

III. RESULT & DISCUSSION

After the system design and the optimization studies on the prototype, the system is installed in the Basic Oxygen Furnace and the automation integration is completed.

To make he experiments for Feeding System, St22 steel grade which have just aluminium addition for alloying, was choosen. The results obtained by casting 249 in total are compared with the same quality castings made by manual aluminium feed. 249 heat were made using the machine system

and heats are compared with the same quality castings made from the manual aluminium feeding.

TABLE I
ST22 TARGET CHEMICAL SPECIFICATION

Steel Grade	%C	%Mn	%P	%S	%Si	%Al	%Cu
St22	0.020 0.050	0.15 0.25	0.018	0.014	0.030	0.020 0.050	0.012

The amount of aluminium required for stoichiometry to remove oxygen in the liquid steel is calculated according to reaction 3.1.



However, in practice it is known that the converter blowing oxygen value can be deoxidized by the carbon contained in the liquid steel by the reaction given in 3.2.



Figure 6 shows the data obtained by using the values of the converter blowing end and the secondary metallurgical input %C and %Al amount before and after the aluminium ingot feeding system. By using the stoichiometric calculations (using the equations 3.1 and 3.2) the amounts of oxygen deoxidized by aluminium and carbon in kg were determined.

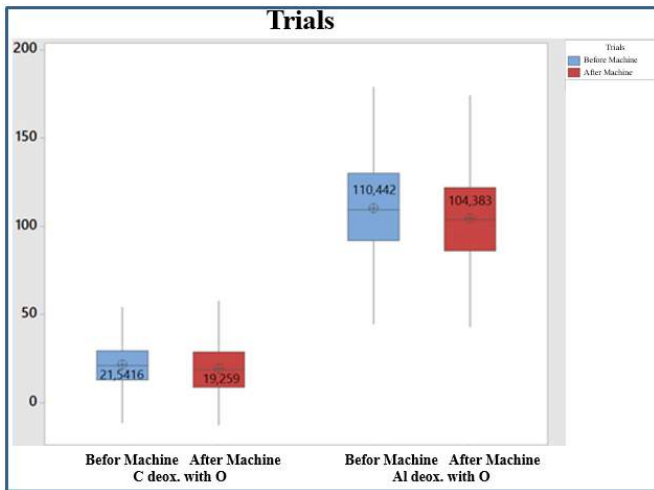


Figure 6: Before and After Machine Deoxidising Al and C Values

As shown in the graph, the results of the converter end blowing oxygen amount were deoxidized with Al by 82-85% when 15-18% deoxidisation with C. The summary table of the total 498 heats done in the experiments was as shown in table 2.

TABLE VI
TRIALS SUMMARY TABLE

200 ton Liquid Steel	Before Machine	After Machine
Heat Number	249	249
Average End Blow %C	0.035	0.035

Average End Blow O ppm	663.55	618.43
Average Al Consumption	0.020 0.050	0.15 0.25

	Al Consumption Per Year	Saving Rate
Saving Amount	5000 ton	%1.16
Total	58 ton saving	

1 dollar = 3,66 TL (16.02.2017)
Cost advantage = 58 * 1870\$ (Official Al prize [9])
= 108.460 \$ (=108.460*3,66 = 369.964 TL)

The cost analysis of the results is shown in table 3.

Problems caused by workers error during manual feed operation can affect the quality negatively. Via Automated feeding system, as a result of chancing the stability of feeding system the aluminium yield of tapping process was increased 1.16% compared to manually feeding (Figure 7). After trial results it was seen that according to calculations one of the major alloying agents, aluminium consumption amount can be decreased in remarkable amount.

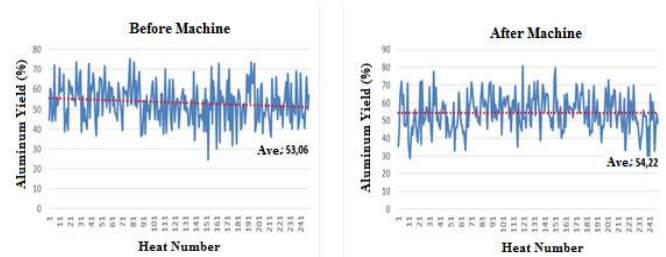


Figure 7. Aluminium Yields for Before and After Machine

TABLE VIII
SAVING ALUMINUM AMOUNT

IV. CONCLUSIONS

In the work done, the Aluminum Ingot Feeding System which can be used in an integrated manner with Basic Oxygen Furnaces has made the process more controlled and stable. It was supported by statistical analyzes that it was an advantageous application in terms of efficiency and costwise compared to the manual feeding process. At the same time, the aluminum ingot feeding process, which was carried out completely manually before, has been automated. Thus, the hazards that could arise at aluminum feeding work have been removed.

REFERENCES

- [1] Sevinç, N., 1995. Chemical Metallurgy of Steel Lecture Notes. ODTÜ, Ankara.
- [2] Miller, T.W., Jimenez J., Sharan A., Goldstein D.A., 1998. Oxygen Steelmaking Processes. The AISE Steel Foundation, 475-524, Pittsburgh.
- [3] Türkdogan, E.T., 1996. Fundamentals of Steelmaking, London.

- [4] Kloppers, C., Fedotova, T., 2001. Primary De-Oxidation Of Basic Oxygen Furnace Steel By Means Of Carbon, South Africa
- [5] Tetik, Y., 2015. The Coke Preoxidation Process and The Principle for Reducing Aluminum Consumption, Istanbul Technical University, Master Degree Thesis
- [6] Riihimaki, H., 1991. Low "Back Pain: Its Origin and Risk Indi-Cators" Scandinavian Journal of Work, Environment and Health 17, 81-90.
- [7] Lortie, M., Pelletier, R., 1996. Incidents In Manual Handling Activities", Safety Science, 21(3), pp. 223-237
- [8] Frostick, S.P., Davies, J.C., Kemp, G.J., Manning, D.P., 1999. Manual Handling Injuries to Workers Attending the Royal Liverpool University Hospital, HSE Contract Research Report CRR 213, HSE Books, Sudbury, Suffolk, UK.
- [9] (2017) London Metal Exchange website [Online]. Available: <https://www.lme.com/en-gb/metals/non-ferrous/aluminium/>

Corrosion - Resistant High Entropy Stainless Steels — A Perspective

Burak Dikici, Hakan Yilmazer**

[*burakdikici@gmail.com*](mailto:burakdikici@gmail.com)

*+Mechanical Engineering, Yuzuncu Yil University
Van, Turkey*

ABSTRACT

Recently, new generation, promising functional alloys for different applications, developed via high entropy (HE) alloying method, have gained attention both from academia and industry. This technique is mainly alloying of at least five major elements in equiatomic or near equiatomic ratios and positioning all the elements in the same lattice using the high entropy of mixing of the system. These unique HE alloys can be obtained using the suitable combinations of almost all the metallic elements present on the periodic table. The main question is, “what is the most important property for a stainless steel?” Clearly, the answer is corrosion resistance. In addition, it is well known that protective surface films play a key role in corrosion resistance of the stainless steels. HE alloys are innovative and promising materials due to their excellent corrosion properties. Key documents on the corrosion behaviour of the high entropy stainless steels have been reviewed under this study.

Keywords: High entropy alloying, Stainless steel, Corrosion resistance

The Experimental Investigation of Springback Phenomenon in DP600 Sheet Metal Material and Estimation with Fuzzy Logic

Tahsin ÖNEL^a, İbrahim KARAAĞAÇ^b

^aGraduate School of Natural and Applied Sciences, Department of Manufacturing Engineering
Gazi University Teknikokullar, Ankara, TURKEY
tahsinonel@hotmail.com

^bDepartment of Manufacturing Engineering, Gazi University
Teknikokullar, Ankara, TURKEY
ibrahimkaraagac@gazi.edu.tr

Abstract— in the first stage of this study, the process parameters that affect the springback which occurs after DP600 sheet metal is bent with V die were investigated experimentally. For the second stage of the study, the results from the first stage were transferred to a fuzzy logic system and the springback was estimated according to the experiment parameters that were not determined with the fuzzy logic method. Die angle, holding time and punch radius were determined as the experiment parameters. It was observed that a 15 degree increase in die's angle raised the springback by average 0.61 degree, a 2 mm increase in punch's radius raised the springback by average 0.13 degree, and a 10 second increase in holding time decreased the springback by average 0.12 degree. A 98.5% similarity was found when the results from the actual experiment and the estimations made with the fuzzy logic method were compared. It is determined that the fuzzy logic method can be used successfully for springback estimations in V bending operations.

Keywords—Springback, DP600, fuzzy logic

I. INTRODUCTION

Due to the global warming and the necessity for less fuel consumption, the automotive industry has been searching for effective methods to manufacture the vehicles with more durable and lighter materials in order to reduce the weight of the vehicle while ensuring the passenger safety [1]. Also; the industry is now more interested in advanced high strength steels due to the increasing concerns about the environment and safety [2]. However; the formability of sheet metal materials dynamically decreases when the strength increases. In addition to the significant changes in formability with the increased strength, there is also an increase in springback during the forming of high strength steels [3]. Dual phase (DP) steels are common types of advanced high strength steels (AHSS) [4], and their use in the automotive industry has been gradually increasing because of their high hardening rate and their perfect combination that has advanced formability [5]. DP steels which are types of advanced high strength steels are low carbon materials with hard martensite and soft ferrite [6]. DP steels have perfect ductility and work hardening rates and this gives them a superiority in strength ductility balance. Because of the

increasing work hardening exponent of DP steels, these parts have higher strain levels and advanced formability. In return the springback amount increases [7].

Springback can be described as the change in the shape of the workpiece after the punch is removed from the piece due to the unbalanced stress that occurs in the moulded piece during the forming process [8]. The amount of springback is substantially related to estimation of the remaining stress in the workpiece after the forming process [9]. Springback depends on many parameters such as forming conditions, tool geometry, sheet thickness, yield strength, elastic module, work hardening, strain rate sensitivity [10-11]. In recent years, many studies have been conducted on reducing the springback and these studies have two approaches. The first approach is reducing the springback to a minimum by increasing the plastic deformation to decrease the stress changes along the sheet thickness, and the second approach is springback compensation through die design [12].

In the literature, there have been many studies on determining and estimating the springback of high-tensile steels. Anderson, in his study, investigated the springback behaviour and its estimation of DP600, TRIP700 and complex phase (CP) materials in elastic rail geometry both experimentally and quantitatively. They made the sheet metal forming simulations in LS-Dyna software. They discovered that although rail geometry exhibited complex springback behaviour, the springback estimation was very proper for little sections of bending [13]. Öztürk et al. investigated the tensile and springback behaviour of DP600 advanced high strength steel in warm temperature. They conducted their study in 0-45 and 90 degree rolling direction parameters for 60 degree die in 300 °C temperature. They determined that the formability of DP600 steel material is lower in 300 °C than it is in room temperature and that the optimal condition for moulding is room temperature [6]. Padmanabhan et al. investigated the effect of the force that draw beads -which is the tensile limiter of springback- create. In the study, in the tensile-bending test, tensile limiting force was imitated with the back force that hydraulic press water hammer. For DP600, DP800 and DP980

which are three types of dual phase steels, it was observed that the springback decreased when the back force was increased [7]. Lim et al. studied the time-dependent changes in the springback behaviour for advanced high strength steels such as DP600, DP800, DP980 and TRIP780. They determined that the springback of DP600 steel material increased in accordance with time [14].

In the literature, there have been many studies in which both warm forming and numeric analysis methods are investigated in order to determine or reduce the springback for DP600 steel materials. However, when each parameter is taken into consideration in experimental studies, the number of studies that are conducted increase, and this results in waste of material, time and energy.

In this study, in the first stage, the aim is to investigate the springback behaviour of DP600 steel material after it is bent by

V die in room temperature experimentally. In the second stage, the aim is to transfer the results obtained from the experiments to a fuzzy logic system and estimate the springback for the parameters of the experiments that are not conducted.

II. MATERIAL AND METHOD

C. Experimental Setup

The experimental studies were conducted in an electrically operated experimental setup that was engineered and calibrated. The experimental setup consisted of hydraulic control unit, mechanical construction, die unit and electronic control software. The experimental working environment and the V die unit are illustrated in Figure 1.



Fig. 1 Experimental working environment

D. The Characterization of Experiment Material

During the characterization of experimental material process, a tensile test, a hardness test and chemical analysis tests were conducted. For the tensile test, first of all, steel sheets were cut with a wire erosion machine in 0°, 45° and

90° rolling directions. The arithmetic mean of the results from the hardness and the tensile test is given in Table 1, and the results from the chemical analysis is given in Table 2.

TABLE VII
THE RESULTS OF TENSILE AND HARDNESS TESTS

Maximum Tensile Stress (MPa)	Tensile Stress at Yield (MPa)	Tensile Strain at Maximum Tensile Stress (%)	Young's Modulus (MPa)	Hardness, HB
658.83620	314.131533	20.62258	20830,5069	169.66

TABLE II
THE CHEMICAL COMPOSITION OF EXPERIMENT MATERIAL (% WT)

Material	Zn	Fe	Mn	Cr	Co
DP 600	73.346	25.702	0.515	0.091	0.311

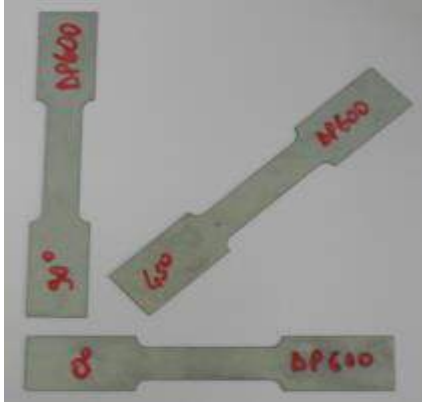


Fig. 2 The prepared specimens for tensile test

between these planes. The angle measurements of DP600 sheet material by CMM is given in Figure 3.



Fig. 3 The springback measurement by CMM

E. Test Parameters

In the experimental studies; die angle, punch radius and holding time are determined as experiment parameters. The values of experiment parameters are given in Table 3. For the experimental studies, every experiment is conducted twice adding up to 90 experiments in total.

TABLE III
THE EXPERIMENTAL STUDY PARAMETERS AND UNITS OF PARAMETERS

Experiment Parameters	The Values of Parameters
Die angle, degree	15, 30, 45, 60 and 75
Punch radius, mm	0, 2 and 4
Holding time, sec.	0, 10 and 20

For the calculation of the press load that is applied in experimental studies Eq.1 was used. In Eq.1 are given as L is press load, l is length of bend, t is work metal thickness, k is a die-opening factor, S is tensile strength of the work metal, and s is width of die opening [15].

$$L = \frac{l \cdot t^2 \cdot k \cdot S}{s} \quad (1)$$

F. The Measurement of Springback

For the measurement of springback Coordinate Measurement Machine (CMM) is used. For the measurement process, in the first stage, the formed experiment materials were sensitively pasted on a sheet without any deformation or spring. In the second stage, a plane was created by placing the probe in three different points on one side of the bent piece. In the same way, another plane is created by placing the probe in three different points on the other side of the bent piece. After this, the springback angles were calculated by measuring the angles

III. EXPERIMENTAL STUDY RESULTS

The results obtained from experimental studies were analysed with regards to the effect of die angle, holding time, and punch radius on springback. The values of springback angles that were obtained from the experimental studies according to experiment parameters are given in Figure 4-6.

In bending operations, compressive stress occurs on the inner surface and tensile stress occurs among the outer surface of the formed piece's bending area. The values of these stresses increase depending on the die stroke [16]. Also, in bending operations, die stroke increases when the angle of bend is increased thus increasing compressive and tensile stress. This increase in the stresses results in the increase of springback angle depending on the die angle. In the experimental studies, it was found that the 15 degree increase in die angle resulted in a mean 0.61 degree increase in springback angle for DP600 sheet material.

The holding process in bending operations limits the shape of the formed piece, decreases the elastic strain and increases the permanent strain [17-18]. The decrease in elastic strain and the increase in permanent increase restrict the piece from returning back to its former shape and decrease springback and spring forward. In the experimental studies, it was observed that the increase of the holding time by 10 seconds for DP600 sheet material resulted in the decrease of springback by mean 0.12 degree.

During the bending operation, springback changes depending on the size of the plastic area. A small punch radius causes all of the bending force to concentrate on a narrow area. In bending operations with a larger punch radius, the force spreads on a larger plastic area. This increase in the size of the plastic area results in the increase of springback [19]. In the experimental studies, it was observed that 2 mm increase in the punch radius resulted in 0.13 degree increase in springback angle.

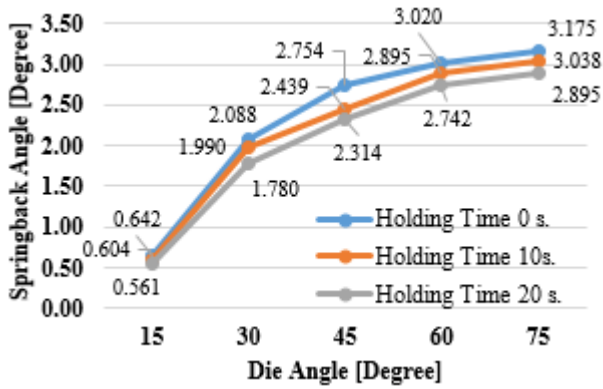


Fig. 4 The relationship of die angle and springback angle for 0 mm punch radius

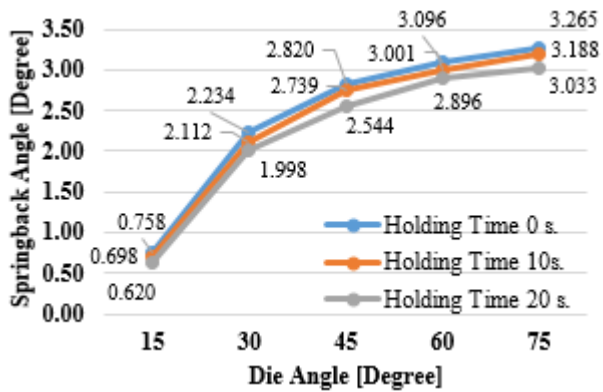


Fig. 5 The relationship of die angle and springback angle for 2 mm punch radius

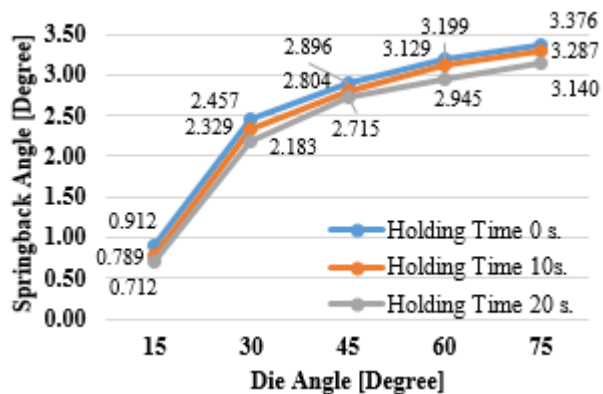


Fig. 6 The relationship of die angle and springback angle for 4 mm punch radius

IV. THE PREDICTION OF SPRINGBACK BY FUZZY LOGIC

In this study, fuzzy logic system is used to estimate the springback for the parameters of the experiments that were not conducted. In the fuzzy logic system; die angle, punch radius and holding time were defined as input variables, and springback was defined as the output variable. While triangular membership functions were used as the fuzzification method,

maximum of centre (CoM) was used as the defuzzification method. The structure of the fuzzy logic system that was constructed is given in Figure 7.

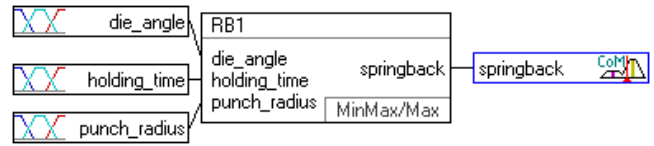


Fig. 7 The structure of fuzzy logic system

While 15, 30, 60 and 75 degrees were used as die angle input variables in the fuzzy logic system, 45 degree die angle values were not included to determine the error ratio of the system. The reliability of the created system was calculated as 98.5%. The reliability rate was obtained by dividing the fuzzy logic estimation result of the 45 degree die which was not included in the system to the result of the experiment. The comparison of each real experiment result in the conditions of 0 second holding time and 0 mm punch radius to the estimation results of fuzzy logic system is given in Figure 8.

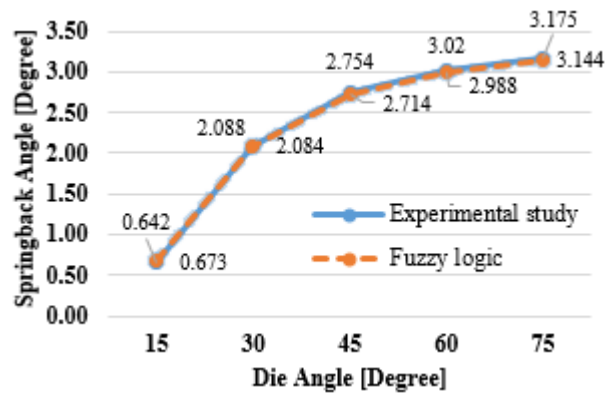


Fig. 8 The comparison of experimental study results and fuzzy results

After determining the reliability of the fuzzy logic system, the estimations were made for the parameters of the experiments that were not conducted. The values from the estimations that were made by the fuzzy logic system for 1 mm punch radius with 5 second holding time, and 3 mm punch radius with 15 second holding time are given in Figure 9.

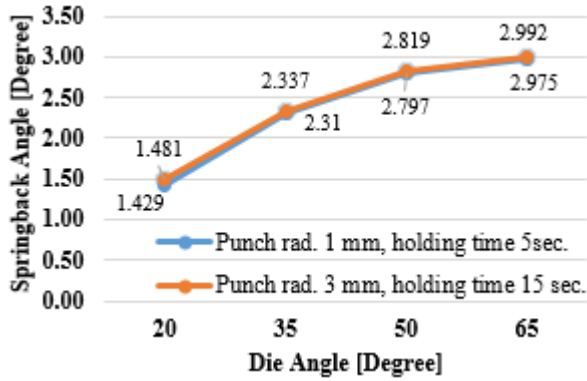


Fig. 9 The springback estimation by fuzzy logic

V. CONCLUSIONS

In the first stage of this study, the springback behaviour of DP600 sheet material which is a type of advanced high strength steel after being bent by V dies was investigated. In the second stage, the springback behaviour was estimated by using fuzzy logic for the parameters of the experiments that were not conducted. The results that were obtained are given below.

- The fact that the estimations that were made by the fuzzy logic system were 98.5% similar to the actual experiment results revealed that fuzzy logic system can be used reliably for estimating the springback.
- It was determined that for DP600 sheet material the 15 degree increase in die angle resulted in a mean 0.61 degree increase in springback angle.
- It was observed that the 10 second increase in holding time decreased the springback angle by mean 0.12 degree.
- It was determined that the 2 mm increase in punch radius increased the springback angle by 0.13 degree.

ACKNOWLEDGMENT

This study was supported by Gazi University Projects of Scientific Investigation Department with 07/2015-12 code numbered project.

REFERENCES

- [1] N. Farabi, D. L. Chen, Y. Zhou, "Microstructure and mechanical properties of laser welded dissimilar DP600/DP980 dual phase steel joints" *Journal of Alloys and Compounds*, vol. 509, pp. 982-989, 2011.
- [2] Eun-Ho Lee, June-Sun Hwang, Chang-Wan Lee, Dong-Yol Yang, Woo-Ho Yang, "A local heating method by near-infrared rays for forming of non-quenchable advanced high-strength steels," *Journal of Materials Processing Technology*, vol. 214, pp. 784-793, 2014.
- [3] M. Tisza, Z. Lukács, "Springback analysis of high strength dual-phase steels," *Procedia Engineering*, vol. 81, pp.975-980, 2014.
- [4] H. Ghadbeigi, C. Pinna, S. Celotto, "Failure mechanisms in DP600 steel: Initiation, evolution and fracture," *Materials Science & Engineering A*, *Materials Science & Engineering A*, vol. 588, pp. 420-431, 2013.
- [5] X. Wei, S. A. Asgari, J. T. Wang, B. F. Rolfe, H. C. Zhu, P. D. Hodgson, "Micromechanical modelling of bending under tension forming behaviour of dual phase steel 600," *Computational Materials Science*, vol. 108, pp. 72-79, 2015.
- [6] F. Oztürk, S. Toros, S. Kılıc, "Tensile and Spring-Back Behavior of DP600 Advanced High Strength Steel at Warm Temperatures," *Journal of Iron And Steel Research, International*, vol. 16(6), pp. 41-46, 2009.
- [7] R. Padmanabhan, J. Sung, H. Lim, M. C. Oliveira, L. F. Menezes, R. H. Wagoner, "Influence of draw restraining force on the springback in advanced high strength steels," *Int J Mater Form*, vol. 1, pp. 177-180, 2008.
- [8] M. Firat, E. Karadeniz, M. Yenice, M. Kaya, "Improving the Accuracy of Stamping Analyses Including Springback Deformations," *JMEPEG*, vol. 22, vol.pp. 332-337, 2013.
- [9] P.A. Eggertsen, K. Mattiasson, "Material modelling for accurate springback prediction", *Int J Mater Form*, vol. 2, pp. 793-796, 2009.
- [10] Y. Aslan, İ. Karaağaç, "V Bükmede geri esneme davranışları", *GU J Sci Part:C*, vol. 2(3), pp. 255-263, 2014.
- [11] S. Toros, A. Polat, F. Ozturk, "Formability and springback characterization of TRIP800 advanced high strength steel," *Materials and Design*, vol. 41, pp. 298-305, 2012.
- [12] X. Xue, J. Liao, G. Vincze, J. Sousa, F. Barlat, J. Gracio, "Modelling and sensitivity analysis of twist springback in deep drawing of dual-phase steel," *Materials and Design*, vol. 90, pp. 204-217, 2016.
- [13] A. Andersson, "Numerical and Experimental Evaluation of Springback in Advanced High Strength Steel," *JMEPEG*, vol. 16, pp. 301-307, 2007.
- [14] H. Lim, M. G. Lee, J. H. Sung, R. H. Wagoner, "Time dependent Springback," *Int J Mater Form*, sup. 1, pp. 157-160, 2008.
- [15] ASM Handbook Committee, "Press Forming of Low-Carbon Steel", *ASM Handbook Volume 14: Forming and Forging*, ASM International, 1996.
- [16] R. Aereens, P. Eyckens, A. V. Bael, J. R. Duflou, "Force prediction for single point incremental forming deduced from experimental and FEM observations," *Int J Adv Manuf Technol*, vol. 46, pp. 969-982, 2010.
- [17] İ. Karaağaç, "The Experimental Investigation of Springback in V-Bending Using the Flexforming Process", *Arab J Sci Eng*, doi:10.1007/s13369-016-2329-6.
- [18] Zong Y. Liu P., Guo B., Shan D., "Springback evaluation in hot V-bending of Ti-6Al-4V alloy sheets", *Int J Adv Manuf Technol*, vol. 76, pp. 577-585, 2015.
- [19] M.M. Buang, S.A. Abdullah, J. Saedon, "Effect of Die and Punch Radius on Springback of Stainless Steel Sheet Metal in The Air V-Die Bending Process", *Journal of Mechanical Engineering and Sciences (JMES)*, vol. 8, pp. 1322-1331, 2015.

Investigation of Heat Recovery and Saving Potential of Hot Stoves in Blast Furnaces

Erhan Kayabaşı*, Fikret Furtun⁺, Mehmet Özkaymak*

*Faculty of Engineering, Department of Mechanical Engineering, Karabuk University, Karabuk, Turkey.

erhankayabasi@karabuk.edu.tr

⁺Kardemir A. Ş. Blast Furnaces Management, Karabük, Turkey.

ffurtun@kardemir.com

Abstract— Blast furnaces are essential departments that consuming the largest energy amount in integrated iron and steel factories. Blast furnaces consist of many vital subsections for survival of iron and steel production. Hot stoves are fundamental auxiliary subsections of blast furnaces consuming fuel and providing hot air into blast furnaces. In this study heat recovery and energy saving potential of hot stoves were investigated and new heat recovery possibilities were recommended. For this purpose, energy production costs per unit energy, specifications of hot stoves construction and fuel components were received from Kardemir A. Ş. blast furnace management. Three heat recovery options were considered in order to determine optimum heat recovery device in terms of energy recovery, saving and investment cost.

Keywords—Blast furnace, hot stove, heat recovery, heat exchanger

I. INTRODUCTION

Over the world almost 33% of the primary energy usage is occupied by production industry. About 20% account of production industry is consists of iron and steel production [1]. Steel industry is one of the production branch involving highest operating temperatures requiring for reduction of iron ore into iron, through the all production industry branches [2]. Blast furnace is extensively used for smelting iron in a continuous

cycle with supplying fuel and metal ore [3]. By a majority, blast furnaces account for 70% of overall iron and steel production and consumes more than 50% of total energy usage in many iron and steel enterprises [1, 4-6]. Most of required energy in blast furnaces is provided by preheated air heated in hot stoves between 900-1350°C by injecting into blast furnaces [4, 7]. Hot stove is a kind of regenerative heat exchanger with a tall and cylindrical structure consisting of refractory matrixes, occupied for supply hot air, which is utilized as an auxiliary equipment. Every blast furnace operates with at least three hot stoves working in a heating and cooling cycle respectively [1, 4, 6, 8]. Hot stoves work together with blast furnace simultaneously and while one of them is heating blast air, other two of them are exposed to self-heating [6]. General arrangement of blast furnace and hot stoves were demonstrated in Figure 1. In conventional iron and steel facilities 10-20% of total energy used in blast furnace is consumed in hot stoves [1, 6]. In addition, energy is lost as waste heat through the flue gas in 250°C from funnel of hot stoves [7]. Hence, there is a great deal about minimizing primary energy source consumption both in hot stoves and blast furnaces such as optimization of fuel mixture, optimization of hot stove system in to provide higher temperature hot blast into blast furnace, preheating fuels and installation of heat recovery units for heating the combustion air delivered into hot stoves [6, 7].

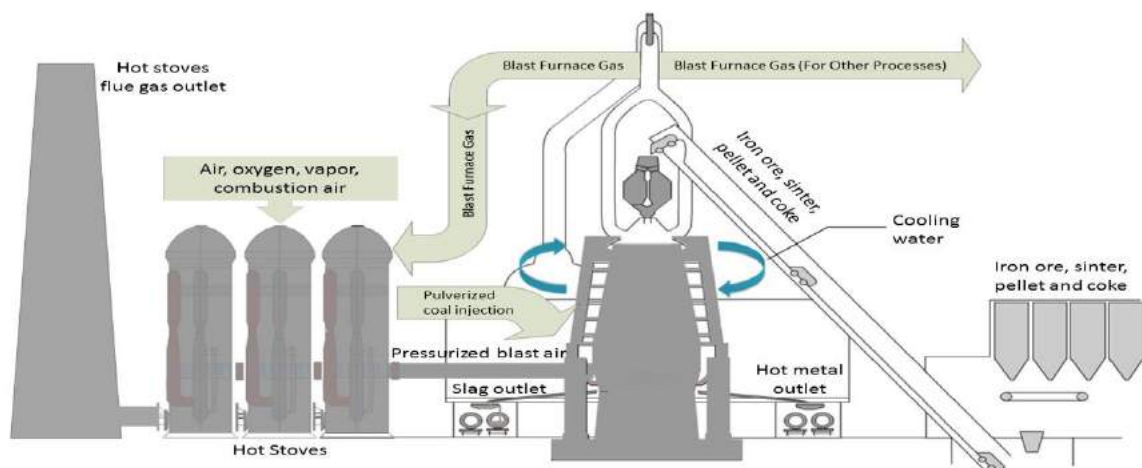


Fig. 1 Flow chart of steel production process.

Heat exchangers are extensively used in several industrial applications including cooling, heating and chemical operations as heat transfer mechanisms [9]. Heat exchangers are applied to recover waste energy from hot flue gas, to cold combustion air for furnaces or hot stoves in iron and steel production industry. In this way, quantity of required fuel for heating decreases and so total efficiency of system enhances [2]. In addition, heat exchanger does not require any energy input while executing heat recovery operation other than investment and maintenance cost. Hence, heat exchangers are used as heat recovery technology developed to reduce fuel consumption, pollutant emissions and operating costs for the facilities using thermal energy [10]. Although, heat exchangers are simple and static devices, selecting correct type and size is a significant issue for specific applications. Furthermore, thermal simulations and economic calculations should be performed for predicting how design and type affect the heat recovery rate, fuel consumption, efficiency of total system, economical contribution and payback period before heat exchanger was built. In this study, proper heat exchanger was designed and simulated for the operating conditions of hot stoves. Optimum heat recovery potential, saving and payback period were investigated for the designed heat exchanger. Results of all calculations and simulations were discussed and different options were evaluated.

II MATERIAL AND METHOD

In iron and steel production process blast furnace and hot stoves are operated simultaneously in order to keep the production continuously. In Kardemir A.Ş. blast furnace department, there exist three hot stoves on operation and one of them is standing on-blast position for providing hot blast into blast furnace and two of them are on-gas position for heating stoves by combusting the fuel. First of all, the technical data, general arrangement of hot stoves and constructional information of funnel were gathered from blast furnace management. Secondly, measurements were performed at funnel of hot stoves in order to inspect components, temperature, velocity and pressure of flue gas. Measurement results were utilized in thermal calculations for predicting heat recovery potential of flue gas. Furthermore, fuel components were received from management to validate flue gas components ratios obtained from measurements by comparing the theoretical combustion results of hot stoves. In thermal calculations the fundamental parameter overall heat transfer coefficient (U) was calculated firstly. After, constructional design was performed according to dimensions obtained from thermal calculations. Also, constructional design was revised considering blast furnace management special demands. Design procedure is given in Figure 2.

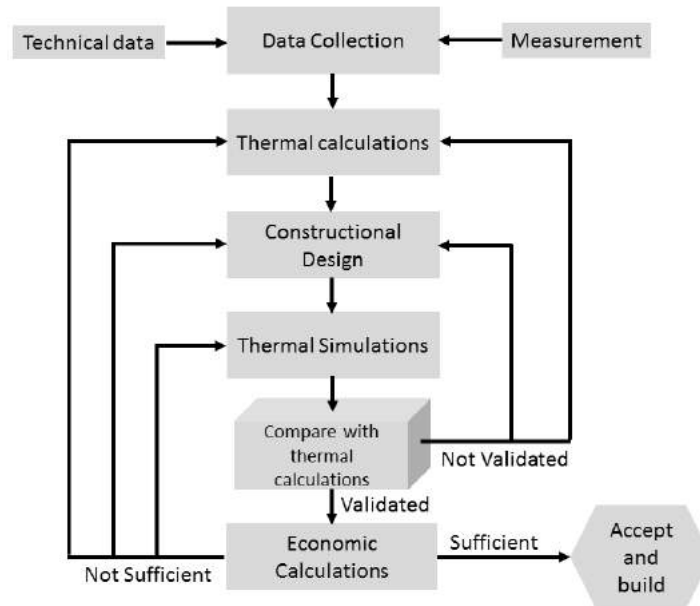


Figure 2. Design procedure of recuperator for hot stoves.

Thermal simulations were performed in Strelow's Static Simulation method based on Effectiveness-Number of Transfer Unit (ϵ -NTU) method. In static simulation recuperators were divided into sub cells and they were considered as a heat exchanger network. Temperature distribution and outlet temperatures of flows were determined without using any iterations, special simulation software and high capacity

computers such as work stations. Relation between inlet and outlet temperatures was given in Equation 1. Paths of flows were described in structure matrix (S) according to selected flow types.

$$\begin{bmatrix} T_h^o \\ T_c^o \end{bmatrix} = \begin{bmatrix} E - \epsilon_h & \epsilon_h \\ \epsilon_c & E - \epsilon_c \end{bmatrix} \cdot \begin{bmatrix} T_h^i \\ T_c^i \end{bmatrix} \quad (1)$$

Inlet temperature distribution through the recuperator for the flows were calculated with Equation 2 [11].

$$\begin{bmatrix} T_h^i \\ T_c^i \end{bmatrix} = \begin{bmatrix} S_{hh} & S_{hc} \\ S_{ch} & S_{cc} \end{bmatrix} \cdot \begin{bmatrix} T_h^o \\ T_c^o \end{bmatrix} + \begin{bmatrix} I_h & 0 \\ 0 & I_c \end{bmatrix} \cdot \begin{bmatrix} T_h^I \\ T_c^I \end{bmatrix} \quad (2)$$

Substituting Equation 2 into Equation 1, Equation 3 was obtained which gives the outlet temperature distribution through the recuperator [11].

$$T^o = (E - \varepsilon \cdot S)^{-1} \cdot \varepsilon \cdot I \cdot T^I \quad (3)$$

In next step of study, economic calculations were performed by considering operating cost, heating cost, and investment cost before and after the recuperator was utilized. Overall saving was calculated with Equation 4.

$$E = T_B Q_R (\kappa_h + \kappa_c) - \kappa_a A_R z \quad (4)$$

Where κ_h is energy production cost, κ_c is cooling cost, T_B is operating duration, Q_R is amount of recovered energy, κ_a is cost of heat transfer surface, A_R is total heat transfer area of heat exchanger, z is depreciation coefficient [12].

III RESULTS AND DISCUSSION

Data required for thermal and economical calculations received from the management of the blast furnace department and measurements were accomplished. After application of a proper recuperator, temperature of flue gas was aimed to decrease from 260°C to 140°C-160°C interval with minimum required A_R . In addition, temperature of combustion air was aimed to increase from 20°C to 180°C - 225°C interval with minimum required A_R . Specifications of the flows desired recuperator were given in Table 1. Firstly, thermal calculations single pass crossflow heat exchanger model was considered. After, three heat exchanger flow model were considered for simulations. Results of thermal calculations were given in Table 2.

Table 2. Flow properties of flue gas and combustion air.

Flow	Parameter	Value	Unit
Flue Gas	Flow rate, [\dot{V}_h]	100 000	[m ³ /h]
	Density, [ρ_h]	0.768	[kg/m ³]
	Heat conduction coefficient, [k_h]	0.0370	[W/mK]
	Specific heat, [$C_{p,h}$]	1.058	[kJ/kgK]
	Inlet temp., [$T_{h,i}$]	260	[°C]
	Desired outlet temp., [$T_{h,o}$]	140-160	[°C]
Combustion Air	Flow rate, [\dot{V}_c]	50 000	[m ³ /h]
	Density, [ρ_c]	0.99	[kg/m ³]
	Heat conduction coefficient, [k_c]	0.03	[W/mK]
	Specific heat, [$C_{p,c}$]	1.009	[kJ/kgK]

Inlet temp., [$T_{c,i}$]	20	[°C]
Desired outlet Temp., [$T_{c,o}$]	180-225	[°C]

Table 1. Results of thermal calculations of single pass crossflow heat exchanger model.

Parameter	Value	Unit
Heat recovery, [\dot{Q}]	2258	[kW]
Hot flow outlet temp.	160	[°C]
Cold flow outlet temp.	182	[°C]
Total heat transfer area, [A_R]	1200	[m ²]
Overall heat transfer coefficient, [U]	24	[W/m ² K]
Effectiveness, [ε]	0.41	-
Pressure Drop, [P]	0.23	[Pa]

First one was single pass crossflow heat exchanger model, second one was single pass hot flow double pass cold flow crossflow heat exchanger model, last one was single pass hot flow three pass cold flow crossflow heat exchanger model. In the simulations, initial parameters were assumed as in single pass crossflow heat exchanger model obtained in thermal calculations step. Results of simulations were summarized in Figure 3, Figures 4 and Figure 5. In first simulation model as seen in Figure 3, results almost validated thermal calculations. Hot fluid and cold fluid outlet temperatures were obtained very close to thermal calculation results.

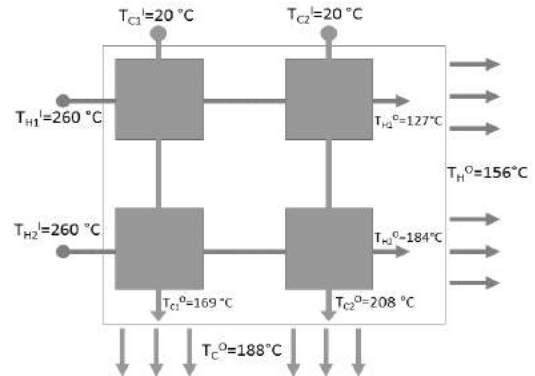


Figure 3. Outlet temperature results of first simulation model.

Second simulation results for single pass hot flow double pass cold flow was represented in Figure 4. According to Figure 4, we can observe the improvements at the outlet temperatures with a minor revision in flow arrangement. Outlet temperature of flue gas is decrease 15°C more than first model. Outlet temperature of cold flow is increase 24°C more than first model.

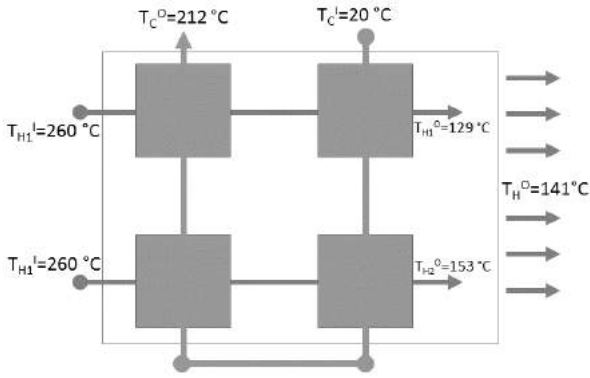


Figure 4. Outlet temperature results of second simulation model.

Third simulation results for single pass hot flow three pass cold flow was represented in Figure 5. According to Figure 5, we can observe the improvements at the outlet temperatures with a minor revision in flow arrangement. Outlet temperature of flue gas decreases 14°C more than second model. Outlet temperature of cold flow increases 10°C more than second model.

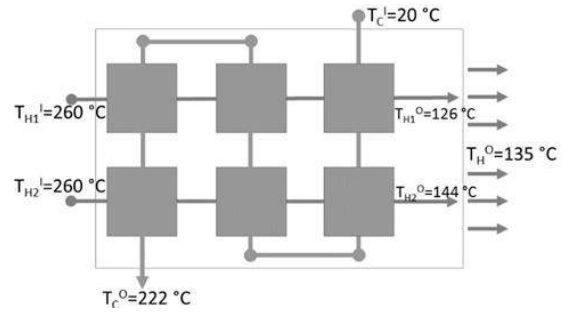


Figure 5. Outlet temperature results of third simulation model.

Furthermore, outlet temperature differences of flue gas and combustion air are observed 21°C and 24°C between third simulation and first simulation model respectively.

According to results of economic calculation given in Table 3, payback period is decreased from 3 years to 2.5 year with increase of heat transfer rate from 2349 kW to 2823 kW. Investment cost is considered constant because heat transfer surfaces are considered identical in all heat exchanger models.

Table 3. Summary of economic calculations.

Simulation Model	Heat Recovery Rate [kW]	Payback Period [Year]	Investment [TL]	Profit [TL/Year]	Expense [TL/Year]	Saving [TL/Year]
Model 1	2349	3	1440 000	473 321	216 000	257 321
Model 2	2688	2.65	1440 000	541 589	216 000	325 589
Model 3	2823	2.5	1440 000	568 896	216 000	352 896

That is to say there is great profit with same heat transfer surface, only changing the flow arrangement of heat exchangers. Also, profit of the facility is increasing due to increase in heat transfer rate. Third simulation model is 16.8% and 4.8% more profitable than first and second simulation model and respectively. However, complexity of heat exchanger structure is increasing in second and third simulation model respectively.

IV. CONCLUSION

In this study three heat recovery options were evaluated and economic calculations were performed. In preparation step of study, technical data belong to hot stoves received from management of blast furnace and flue gas components, flue gas velocity and flue gas temperatures were measured from funnel of hot stoves. Energy of flue gas released in 260°C was desired to be used a seconder energy resource for combustion air heated in hot stoves. Furthermore, not only thermal evaluation but also economical calculations were taken into account in order to determine the best profitable option for the facility. In thermal simulations Strelow’s static simulation model based on ϵ -NTU method was utilized as an easy and effective method. According to thermal simulation results 202°C and 135°C temperature differences can be

realized in combustion air and flue gas outlet temperatures respectively. In economic calculations, total heat recovery rate, payback period, yearly economical profit, investment cost and total saving of the three options were presented in Table 3. Great amount of saving potentials were observed such as 257 321 TL, 325 589 TL, 352 896 TL per year for first, second and third heat exchanger option respectively. Furthermore, thermal contribution of heat recovery in hot stoves, should be investigated in order to how temperature increase in hot stoves affects the molten metal production and energy consumption in blast furnace. This study is expected to be a road map for engineers and researchers studying on heat recovery options of facilities using thermal energy.

V. ACKNOWLEDGEMENT

This project was performed with the co-operation of KARDEMIR Karabük Iron Steel Industry and Trade A.Ş. and Karabük University Faculty of Engineering.

IV. REFERENCES

- [1]. Zetterholm, J., et al., *Model Development of a Blast Furnace Stove*. Energy Procedia, 2015. **75**: p. 1758-1765.
- [2]. McBrien, M., A.C. Serrenho, and J.M. Allwood, *Potential for energy savings by heat recovery in an integrated steel supply chain*. Applied Thermal Engineering, 2016. **103**: p. 592-606.

- [3]. Zeng, J.-s. and C.-h. Gao, *Improvement of identification of blast furnace ironmaking process by outlier detection and missing value imputation*. Journal of Process Control, 2009. **19**(9): p. 1519-1528.
- [4]. R.Pardeshi, P. and B.S.Kothavale, *Energy Management of Stove in Pig-Iron Plant*, in *Second International Conference on Emerging Trends in Engineering*. 2013, IOSR Journal of Mechanical and Civil Engineering. p. 48-51.
- [5]. Liu, X., et al., *Constructural design of a blast furnace iron-making process based on multi-objective optimization*. Energy, 2016. **109**: p. 137-151.
- [6]. Zetterholm, J., et al., *Dynamic modelling for the hot blast stove*. Applied Energy, 2017. **185**: p. 2142-2150.
- [7]. Worrell, E., et al., *Energy Efficiency Improvement and Cost Saving Opportunities for the U.S. Iron and Steel Industry*. 2010, Ernest Orlando Lawrence Berkeley National Laboratory: U.S.A.
- [8]. Rieger, J., C. Weiss, and B. Rummer, *Modelling and control of pollutant formation in blast stoves*. Journal of Cleaner Production, 2015. **88**: p. 254-261.
- [9]. Eiamsa-ard, S., K. Kiatkittipong, and W. Jedsadaratanachai, *Heat transfer enhancement of TiO₂/water nanofluid in a heat exchanger tube equipped with overlapped dual twisted-tapes*. Engineering Science and Technology, an International Journal, 2015. **18**(3): p. 336-350.
- [10]. Johnson, I., W.T. Choate, and A. Davidson, *Waste Heat Recovery: Technology and Opportunities in U.S. Industry*. 2008: U.S.A.
- [11]. Strelow, O., *Eine allgemeine Berechnungsmethode für Wärmerübertragerschaltungen*. Forsch Ingenieurwes. **63**(1997): p. 255-261.
- [12]. Kardos, J., O. Strelow, and R. Walde, *Bewertung und Optimierung des Wärmerückgewinns in Rekuperatorsystemen*. Chemische Technik, 1983. **35**(2): p. 71-74.

Investigation of The Wetting Behaviours of SAC305 and SAC405 Ternary Lead-Free Solder Alloys on Cu Substrate

Hasan ABUT* A. Mustafa ERER⁺ Ziyaddin RECEBLİ*

*Karabuk University, Technology Faculty, Energy Systems Eng. 78100 KARABUK-TURKEY habut78@hotmail.com

⁺Karabuk University, Science Faculty, Physics Department 78100 KARABUK-TURKEY mustafaerer@karabuk.edu.tr

*Karabuk University, Technology Faculty, Energy Systems Eng. 78100 KARABUK-TURKEY zrecebli@karabuk.edu.tr

Abstract: In present study, wetting behaviours of molten Sn-3Ag-0.5Cu (SAC305) and Sn-4Ag-0.5Cu (SAC405) ternary Pb-free solder alloy were investigated at predetermined temperatures (230, 250 and 280 °C) on Cu substrate. The Contact angles of alloys were measured by using of the sessile drop method. The lowest value of contact angle for SAC405 was 41.05° at 280 °C. Microstructures, inter-metallic phases (IMC) of alloys were examined by optic microscope and scanning electron microscope (SEM+EDX), X-ray diffraction (XRD) and differential scanning calorimeter (DSC). The amount of Ag in the molten Pb-free solder alloy reacts with Sn to occur intermetallic compounds (IMCs) on the interface.

Keywords: Contact angle, wetting, IMCs, lead-free solder alloy.

I. INTRODUCTION

As the limitation of lead in industrial fields has been strongly supported because of the environmental protection on trial chamber of water, air and soil [1]. This trend was reinforced in Europe by the RoHS and WEEE directives [2]. Based on the analysis of many binary and ternary alloys systems are considered as potential replacements for lead solders [3]. Therefore, instead of Sn-Pb lead solder alloys utilized by the electronic industry as a solder material, necessary efforts are spent in development of alternative alloys. In available studies, since melting temperature was reported at a point close to the eutectic Sn-Pb alloy (198 °C) and they have low-cost, SAC305 and SAC405 lead-free solder alloys were taken into consideration [4].

With the electronics industry improve to Pb-free soldering, SAC305 and SAC 405 became the alloys of choice based on lowest available melting temperature, near eutectic composition and acceptable to good cyclic fatigue properties. There were early suspicions that, while SAC 305 or SAC405 clearly met many of the specifications for a successful Pb-free solder, as the database of properties grew there would be performance gaps. That has proven to be the case [5,6]. A thin, continuous, and uniform IMC layer is an essential requirement

for good bonding. Without IMCs, the solder/conductor joint is weak because no metallurgical interaction occurs in the bonding, which is disastrous to electronic packaging [7]. One of the characteristics of IMC is the formation of a scallop-type morphology. Scallop-type Cu₆Sn₅ IMCs were formed at SAC305/Cu interfaces [8]. Therefore, in this study, wetting behaviour of ternary lead free solder alloys SAC305 and SAC405 was investigated.

II. MATERIALS AND METHOD

At present, in determination of wetting properties of SAC305 and SAC405 ternary lead free solder alloys, 99.85% pure electrolytic copper substrate were used. the wetting tests made by the Sessile drop technique. By means of this technique, SAC305 and SAC405 ternary lead free solder alloys were dropped on copper substrate at various temperatures of 230 °C, 250 °C and 280 °C. Casio-Pro EX-F1, 600 FPS Model camera employed to capture views of drops at the 5th, 10th, 15th, 30th, 60th, 90th, 120th and 150th seconds and these images were transferred into Corel Draw X5 Software to measure contact angles of each drop from the right and left profiles. As a result of these processes repeated for each temperature, mean angle values were calculated and new diagrams were drawn through the Sigma Plot 12.0 Software. In order to determine melting temperatures of alloys, the DSC analysis were carried out while specimens in maximum 30 mg weight and at 40 °C-300 °C temperature range (5 min.). Standard metallographic processes were carried out for microstructure examinations. Prepared specimens were etched with 100 ml (H₂O), 2ml (HCl), 10 gr (FeCl₃) solution for 45 seconds. The etched specimens were characterized by the scanning electron microscope (SEM+EDS) and X-ray diffraction (XRD).

III. RESULTS AND DISCUSSION

In Figure 1 and 2 are given micro-structure SEM images of SAC305 and SAC405 lead-free solder alloys.

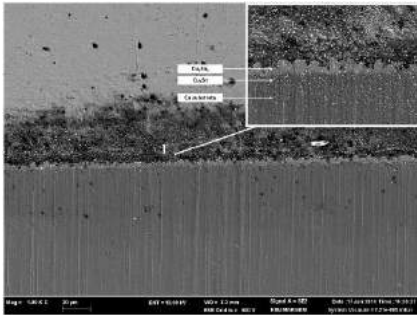


Fig. 1 SEM images of SAC305 lead free solder alloy

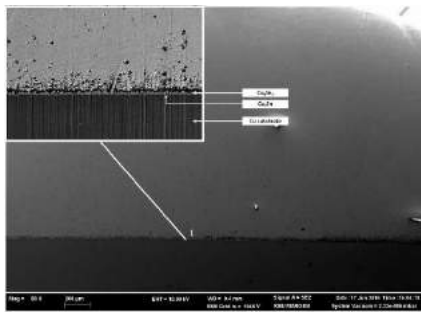


Fig. 2 SEM images of SAC405 lead free solder alloy

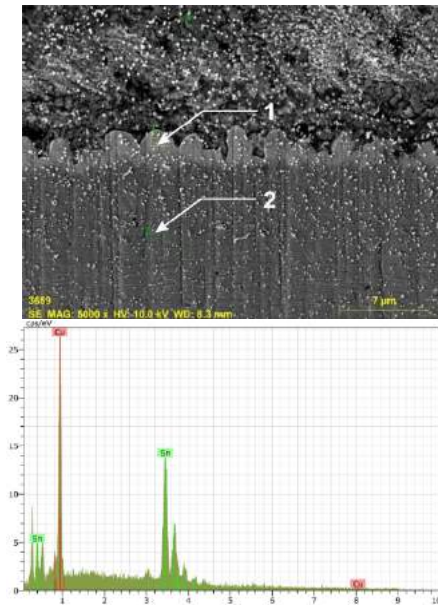


Fig. 3 EDX analysis result of SAC305 solder alloy.

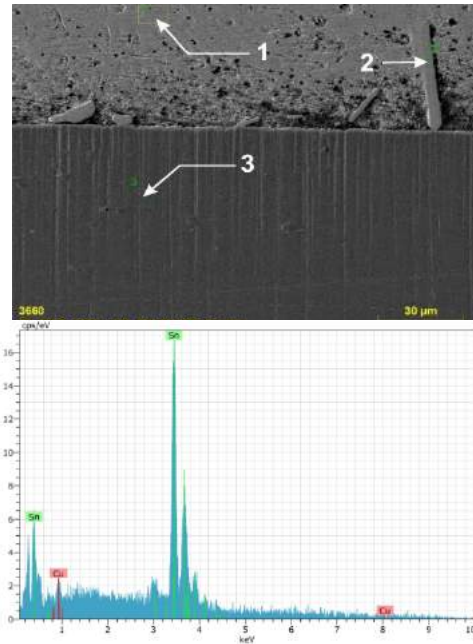


Fig. 4 EDX analysis result of SAC405 solder alloy

From SEM and EDX analyses in Fig. 3 and 4, Cu-Sn IMCs are seen in the Sn-Ag-Cu / Cu interface. Interfacial reactions between the Cu substrate and solder alloys of SAC305 and SAC405 lead to two types of IMCs, Cu_6Sn_5 and Cu_3Sn . While the Cu_6Sn_5 is adjacent to the solder alloys, the Cu_3Sn is adjacent to the Cu substrate. The scallop type Cu_6Sn_5 was formed through the interfacial reactions between Sn-Ag-Cu/Cu systems. The formation of Cu-Sn IMCs is realised by the continuous growth of Cu_6Sn_5 . On the other hand, the formation and growth of Cu_3Sn is realised in the interface of Cu_6Sn_5 and Cu substrate.

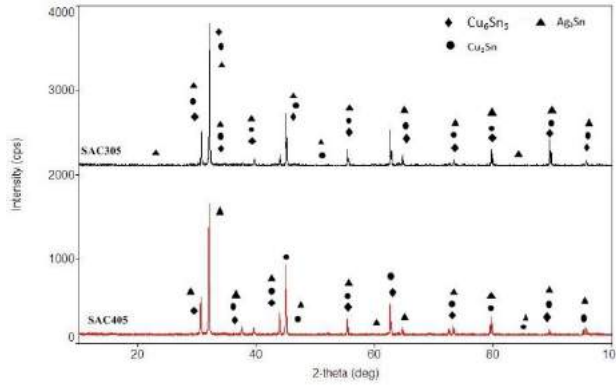


Fig. 5 XRD results of the SAC305 and SAC405 alloys.

In Fig. 5 is given XRD results of the near-eutectic SAC305 and SAC405 alloys. It was determined that Cu_6Sn_5 ,

Cu₃Sn and Ag₃Sn phases were formed in the alloy structure according to the XRD results.

REFERENCES

[1] N.Çağlarırnak, A.Z.Hepçimen, *Effect of Heavy Metal Soil Pollution on Food Chain and Human Health*, <http://www.academicfoodjournal.com/archive/2010/2/31-35.pdf>

[2] RoHS (Restriction of Use of Hazardous Substances),<http://eur-lex.europa.eu/oj/direct-access.html>

[3] Zhang X. R., Yuan Z. F., Zhao H. X., Zang L. K., Li J. Qiang, *Wetting behavior and interfacial characteristic of Sn-Ag-Cu solder alloy on Cu substrate*, (2009).

[4] S.K. Das, A. Sharif, Y.C. Chan, N.B.Wong, W.K.C. J. *Alloy. Compd.* **481**, 167 (2009).

[5] Ranjit S. P., Brian G. L., Raghassudha V., Bawa S., *Drop Shock Reliability of Lead-Free Alloys Effect of Micro-Additives*, Cookson Electronics Assembly Materials Group, (2007).

[6] F. Omaç, D. Ozyurek, M. Erer, *Investigation of the Wetting Properties of Ternary Lead-Free Solder Alloys on Copper Substrate*, Proceedings of the 6th International Congress APMAS 2016, June 1–3, (2016).

[7] Liu M. L. and Ahmad A. M., *Interfacial Reaction of Sn-Ag-Cu Lead-Free Solder Alloy on Cu: A Review*, *Advances in Materials Science and Engineering*, (2013).

[8] J.W. Yoon, B.I. Noh, B.K. Kim, C.C. Shur, and S.B. Jung, *Wettability and interfacial reactions of Sn-Ag-Cu/Cu and SnAg-Ni/Cu solder joints*, *Journal of Alloys and Compounds*, vol. 486, no.1-2, pp.142–147, (2009).

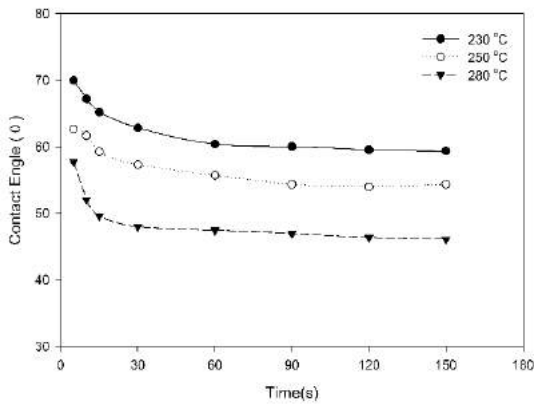


Fig. 7 Wetting results of the SAC405 at various temperature.

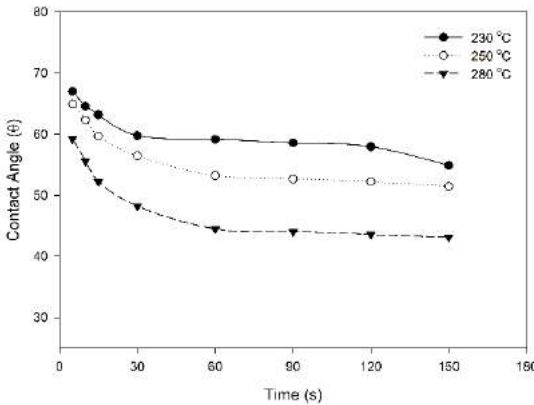


Fig. 7 Wetting results of the SAC405 at various temperature.

According to the contact angle measurement results of SAC305 and SAC405 alloys given in Fig. 6 and Fig. 7 with respect to (230-250-280 °C), it was determined the contact angle varies with time and temperature. There is no change in the contact angle after 60. seconds.

IV. CONCLUSION

The contact angles of SAC305 and SAC 405 alloys were exponentially decreasing over time. The lowest value of ontact angle for SAC405 was 41.05° at 280 °C. As a result of SEM studies, secondary IMC phases were observed in the microstructure. When the EDX analysis of these phases are examined, it is understood that they are Cu₆Sn₅ and Cu₃Sn. It was first determined that the Cu₆Sn₅ phase was formed in the scollap-type and the Cu₃Sn phase was formed later.

Investigation of Physical, Chemical and Metallurgical Properties of Domestic and Imported Pelets

*Neslihan ATALAY and Fatma MEYDANERİ TEZEL **

** Corresponding author: Fatma MEYDANERİ TEZEL*

Speaker: Neslihan ATALAY

Phone: +90 370 433 21 20; Fax: +90 370 433 20 05. E-mail address: fatmameydaneri@karabuk.edu.tr, neslihanatalay12@gmail.com

Department of Metallurgy and Materials Engineering, Faculty of Engineering, Karabük University, 78050, Karabük, Turkey

ABSTRACT

These ores are primarily enriched in order to make low-grade iron ores (> 50% Fe content) available at the blast furnace, which can be fed directly to the blast furnace. The most widely used method of agglomeration after enrichment is pelleting. In this study, the characteristic features of three different pellet types, one domestic and two imported (Ferroexpo and east); chemical, physical and metallurgical properties have been determined. The element and compound analysis were performed with XRF and XRD devices. By using different size of sieves, grain size analysis and moisture were determined before entering the blast furnace. By the Rul (R40) test at 1050 °C, with the mix gas (%40 CO+ 2% H₂ + 58% N₂), the reduction rate of the furnace was measured by difference in height and pressure inside the furnace. The volume increase during reduction was determined by swelling test on 18 pellets at 900 °C. The degradation index of the iron ores reduced by mix gas at 500 °C was determined by the LTD test. The crumbling and dusting indexes of pellets during transport in the plant was measured by the drum test. At the end of the research, it was found out that 3 different pellets provided by KARDEMİR A.Ş. were advantageous, and the changes in mineral ratios changed the technological test results and this effect on the blast furnace reactions.

Keywords: Pelet; blast furnace; low-grade iron ores; agglomeration

Investigation of dynamic strain aging properties of hot work tool steel

Demet TASTEMÜR*, Süleyman GÜNDÜZ*

* Manufacturing Engineering, Karabük University
Karabük, Turkey

{demettastemur, sgunduz}@karabuk.edu.tr

Abstract— Dynamic strain aging behaviour of hot work tool steel (H10) was investigated under as received conditions. Hot tensile testing was carried out at temperatures ranging from room temperature (RT) to 700 °C at a strain rate of $10^{-3}s^{-1}$. The microstructure of the specimens was analyzed in detail by using optical microscopy and scanning electron microscopy (SEM). The results indicated that mechanical properties of H10 tool steel depends on test temperature. Tensile strength and yield strength showed slight decrease with increasing testing temperature to 400°C. Above 400°C these properties become so poor. It was also observed that as the testing temperature increased to 400°C a continuous decrease in elongation was noticed. Further increase in the testing temperature of 500, 600 or 700°C has increased the elongation. It is believed that dynamic strain ageing and high temperature mechanical properties are affected by interaction between dislocation and precipitate particles such as MC (VC), M₆C (Mo₆C) and M₂₃C₆ (Cr₂₃C₆) or solute atoms.

Keywords— Hot work tool steel, Dynamic strain aging, Mechanical properties

I. INTRODUCTION

The steels used for hot forming is a special type of tool steel, made to withstand a combination of heat, pressure and abrasion and has been classified hot work tool steel, AISI type H. All hot-work tool steels are used in a quenched and tempered condition. The most essential properties for these types of steels are high levels of hot strength, ductility, toughness, thermal conductivity, creep strength, temper resistance and also low thermal expansion [1, 2]. Hot work tool steels have a highly alloyed with strong carbide-forming elements such as Cr, V and Mo. These elements play an important role when the tool steels are subjected to high temperatures, since they precipitate as fine alloy carbides, which not only retards the softening but also increases the hardness [3].

Typical microstructures of hot work tool steels are consisted of tempered martensite with high dislocation density and carbide precipitates [4]. These steels with high alloy content and dislocation density can indicate that dynamic strain aging may occur in hot work tool steel. The elastic interaction between the interstitial atoms/precipitates and dislocations in the steel causes the dislocations to be firmly pinned which can lead to occurrence of strain aging.

Strain aging is classified- static strain aging which occurs after plastic deformation of the aging process, and dynamic strain aging which occurs during plastic deformation. The static strain aging leads to the reappearance of the upper yield point and the yield point elongation, while the dynamic strain aging has been shown to result in the inhomogeneous deformation characterized by serrated flow. However, in both cases there is an increase in flow stress and work hardening rate while a decrease in ductility is observed [5]. Dynamic strain ageing may induce negative strain rate sensitivity and may even cause flow limitation in cold and warm areas during plastic deformation. For this reason, effect of the dynamic strain aging on deformation pattern and mechanical properties are important for the correct design of the metal forming process [6]. Several researches have been conducted to study the effect of dynamic strain aging on mechanical properties in various engineering alloys.

In the present study, the occurrence of dynamic strain aging and its effects on microstructure and mechanical properties of H10 hot work tool steel are investigated.

II. EXPERIMENTAL PROCEDURE

AISI H10 type hot work tool steel was chosen to study dynamic strain ageing behaviour in as-received condition. The chemical composition of steel is given in Table 1. Tensile test specimens for dynamic strain ageing were manufactured in accordance with the relevant ASTM standard E8 (30 mm gauge length and 3 mm diameter). Tensile tests were performed using a MTS (100kN Servohydraulic Dynamic Tester) at a strain rate of $10^{-3} s^{-1}$. The test was carried out from room temperature to 700 °C. After each test, stress and strain diagrams were obtained. Values of ultimate tensile stress (UTS), flow stress (0.2%) and elongation (%) were determined. Microstructure and fracture surfaces of the tensile tested specimens were examined by optic and scanning electron microscopy respectively.

TABLE I
CHEMICAL COMPOSITION OF STEEL USED IN RESEARCH

Chemical Composition (% Wt)						
C	Si	Mn	P	S	Cr	Mo
0.31	0.25	0.30	0.017	<0.001	3.19	2.73

III. RESULT AND DISCUSSION

Fig. 1 shows the microstructure of the H10 tool steel samples tested at room temperature, 400 °C and 700 °C. As can be seen, the steel consists of ferrite structure with alloy carbides which were distributed along the grain boundaries after testing at room temperature (Fig 1a). It was observed that carbides are distributed more homogeneously when the testing temperature is increased to 400 °C or 700 °C. These carbides have an important role in increasing high temperature resistance of steels [7]. Tool steel is usually delivered to the user as soft annealed condition. In the soft annealed condition, the carbides are embedded in the matrix.

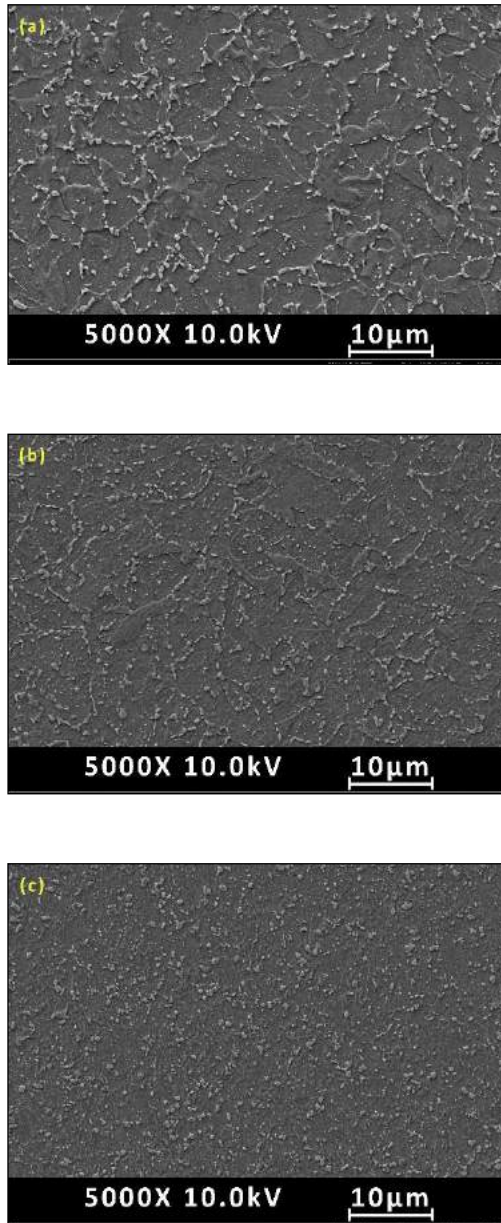


Figure 1. Microstructure of the as received samples tested at (a) room temperature, (b) 400 °C and (c) 700 °C.

Table 2 shows hot tensile test results for H10 tool steel under as received condition, including tensile strength, yield strength and elongation (%). It is noted that the tensile strength and yield strength of H10 tool steel are about 646 MPa and 451 MPa respectively. Increasing test temperature within the range of 100 °C -400 °C causes slight decrease in tensile strength and yield strength to 522 MPa and 408 MPa respectively. Exceeding testing temperature of 400 °C causes a significant decline. It was also observed that as the testing temperature increased to 400 °C a continuous decrease in elongation was noticed. Further increase in the testing temperature of 500, 600 or 700 °C has increased the elongation. It can be concluded that above 400 °C mechanical properties of H10 steel become so poor under as received condition. The results obtained from this study is consistent with the results obtained from Gündüz and Cochrane [8] who investigated the effect of temperature on the ultimate tensile strength of vanadium microalloyed steels under as received, stainless steel cooled and air cooled conditions. They observed rapid decrease in strength from room temperature to 100 °C then slower decrease corresponding to dynamic strain ageing which persists up to 200 °C -400 °C due to interaction between dislocation and solute atoms/precipitate particles.

TABLE II

TENSILE PROPERTIES OF THE H10 STEEL AT VARIOUS TEMPERATURES

Temperature (°C)	Tensile Strength (MPa)	0.2% Yield Strength (MPa)	Elongation (%)
RT	646	451	24,1
100	569	426	22,1
200	548	397	19,5
300	525	388	19,5
400	522	408	17,2
500	468	363	24,3
600	319	313	43,7
700	195	132	57,9

Stress and strain diagrams of H10 tool steel tested between room temperature and 700 °C at a strain rate of 10^{-3} s^{-1} are shown in Fig. 2. Serrated flow, one of the characteristics of dynamic strain ageing, was observed at 400 °C for as received specimens. The serrated flow occurs when the solute atoms move to the dislocations and prevent their motion [9,10-11]. It is now well accepted that serrated yielding exhibited by a material occurs due to interaction between diffusing solute atoms and dislocations [12].

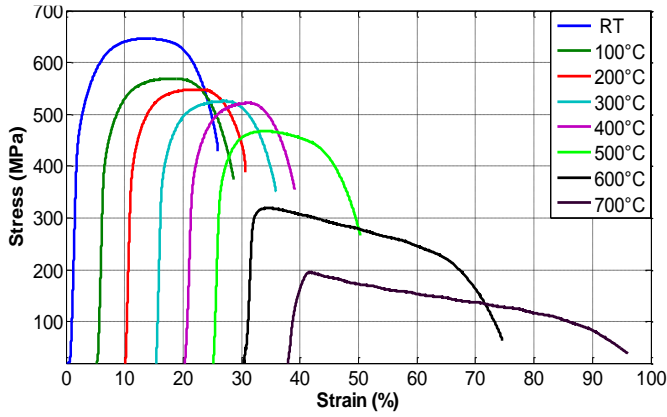


Fig. 2 Tensile stress–strain curves of the H10 steel at different temperatures from RT to 700 °C

Figure 3 shows EDS analysis with the spectrum points 1-5 marked on the microstructure of H10 hot work tool steel tested at 400 °C. Points 1-3 contains Mo and C, point 4 contains Cr and C. The presence of these elements indicates that M_6C (Mo_6C) and $M_{23}C_6$ ($Cr_{23}C_6$) occurred in H10 tool steel and contributed to high temperature resistance between 200 °C -400 °C as suggested by Bahrami et al [13]. Such carbides forming elements may also interfere with the interstitial atoms and cause dynamic strain aging.

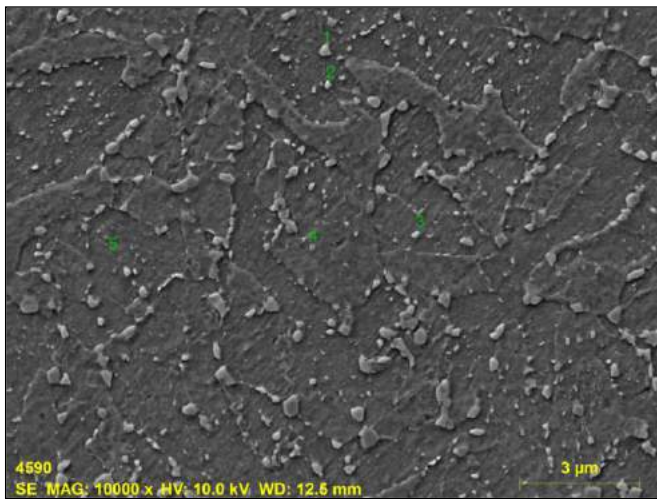


Fig.3 SEM images of H10 tool steel tested at 400°C (a) and corresponding EDS of the indicated points (b)

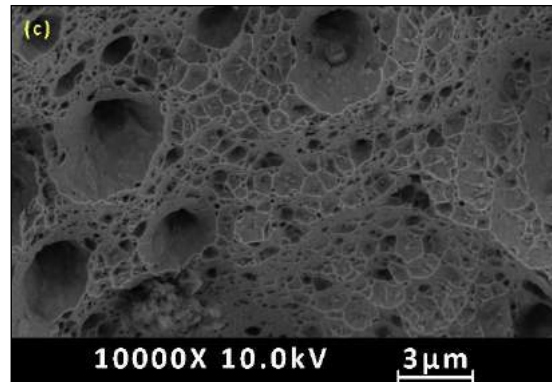
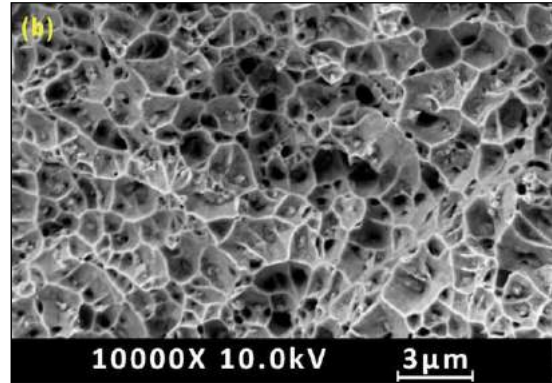
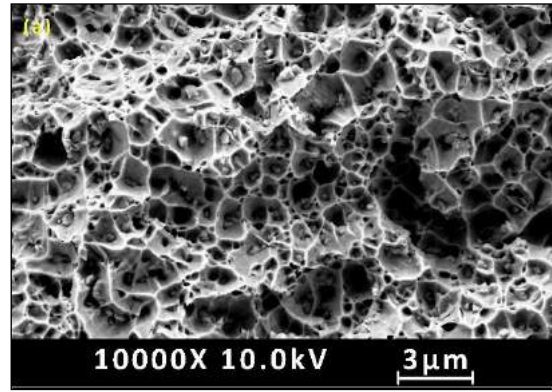


Fig. 4 Fracture surfaces of H10 tool steel tested at (a) room temperature, (b) 400 °C and (c) 700 °C

Figure 4 shows scanning electron fractographs of the H10 tool steel tested at room temperature, 400 °C and 700 °C. It was observed that samples tested at room temperature showed ductile dimple fracture (Fig. 1a). On the other hand, a mixed pattern of dimple and cleavage facets is apparent in the sample tested at 400 °C (Fig. 1b). This is consistent with the elongation results which showed the lowest value after testing at 400 °C. This is due to the interaction between mobile dislocation and solute atoms/precipitate particles [14]. At 700 °C, dimple pattern was observed again on the fracture surface with increasing elongation (Fig. 1c). Sample tested at 700 °C also showed some deep large cusps which may be attributed to removal of precipitate particles through pulling of under heavy tensile loading conditions.

IV. CONCLUSIONS

Dynamic strain ageing behaviors of H10 tool steel were investigated at a strain rate of 10^{-3} s^{-1} in the temperature range of 25-700°C. The following conclusions obtained from present study as follows:

1. Dynamic strain ageing and secondary hardening take place in the H10 tool steel over the temperature range from 25°C to 400°C.
2. In the testing temperature of 25-400°C, H10 tool steel exhibit higher temperature resistance due to interaction between dislocation and solute atoms/precipitate particles. Above 400°C these properties become so poor.
3. Ductile dimple was observed at the testing temperature of 25°C. However, a mixed pattern of dimple and cleavage facets is apparent in the sample tested at 400°C. At 700°C, dimple pattern was observed again on the fracture surface with increasing ductility.

VI. ACKNOWLEDGMENTS

This work was supported by Scientific Research Projects Coordination Unit of Karabük University. Project Number: KBU-BAP-16/2-YL-072

VII. REFERENCES

- [1]. L.J.D. Sully, In: Metals handbook, 9th ed., vol. 15, ASM International, Metals Park, Ohio, 1988, p. 286.
- [2]. J.R. Davis (Ed.), ASM Speciality Handbook, Tool Materials, ASM International, Materials Park, Ohio, 1995, p. 251.
- [3]. Johnny Sjöström, Chromium martensitic hot-work tool steels, Ph. D Thesis, Department of Materials Engineering, Karlstad University, Karlstad-Sweden, 2004.
- [4]. A. Medvedeva, J. Bergström, S. Gunnarsson, and J. Andersson, "High-temperature properties and microstructural stability of hot-work tool steels," *Mater. Sci. Eng. A*, vol. 523, pp. 39–46, 2009.
- [5]. A. K. Sachdev, "Dynamic Strain Aging of Various Steels," *Metall. Trans. A*, vol. 13, pp. 1793–1797, 1982.
- [6]. A. R. Kohandehghan, A. R. Sadeghi, J. M. Akhgar, and S. Serajzadeh, "Investigation into dynamic strain aging behaviour in high carbon steel," *Ironmak. Steelmak.*, vol. 37, no. 2, pp. 155–160, 2010.
- [7]. G.A. Robert, R.A. Gary, Tool Steels, American Society for Metals, 1998.
- [8]. S. Gündüz, R. C. Cochrane, Effect of Dynamic Strain Ageing on Mechanical Properties of Vanadium Microalloyed Steel, *Materials Science and Technology*, Vol:19, No:4, 422-428, 2003.
- [9]. W. Karlsen, M. Ivanchenko, U. Ehrnsten, Y. Yagodzinsky, H. Hanninen, *J. Nucl. Mater.* 395 (2009) 156–161.
- [10]. P. Rodriguez, *Bull. Mater. Sci.* 6 (1984) 653–663.
- [11]. A. Van Den Beukel, *Phys. Status Solidi A* 30 (1975) 197–206.
- [12]. S. Gündüz, Dynamic Strain Ageing Effects in Niobium Microalloyed Steel, *Ironmaking and Steelmaking: Products and Applications*, Vol. 29, No. 5, 341-346, 2002.
- [13]. A. Bahrami, S.H. Mousavi Anijdan, M.A. Golozar, M. Shamsian, N. Varahram, Effects of conventional heat treatment on wear resistance of AISI H13 tool steel, *Wear* 258 (2005) 846–851.
- [14]. W.F. Smith, *Structure and Properties of Engineering Alloys*, McGraw-Hill, New York, 1981.

The Effects of Speed Control with Fuzzy Logic to Surface Roughness in Machining

Kürşat Mustafa KARAOĞLAN*, Metin ZEYVELİ†

TOBB Vocational School, Karabuk University, Karabuk, Turkey
kkaraoglan@karabuk.edu.tr

† *Mechatronics Engineering, Karabuk University, Karabuk, Turkey*
mzeyveli@karabuk.edu.tr

Abstract— Surface roughness is one of the important factors affecting the quality of the material. In this study, speed control with a fuzzy logic (FL) controller was applied to cutting speed which is a cutting parameter to improve surface roughness of 2xxx series aluminium alloy material during machining. The effect of the automatic usage and FL speed control method on the surface roughness of the work piece is compared. For this purpose, experimental works realized at three different cutting speeds (200, 320 and 440 m/min), at three different feed rates (0.05, 0.1, 0.15 mm/rev) and constant cutting depth (0.5 mm). As a result of experimental study, it has been observed that results obtained with the FL speed control is better than results obtained with the automatic usage. Due to the positive contribution of the surface roughness values, the FL speed control method has shown to can be used successfully in machining operations..

Keywords— Fuzzy logic, intelligent control, surface roughness, spindle speed control.

I. INTRODUCTION

The surface roughness results are the main quality characteristics to determine and assess the quality of the product in manufacturing. The quality of surface roughness is a common requirement for the work piece. In this regard, major factors which affects the surface roughness of the product material contains parameters such as cutting speed and cutting depth [1]. It is necessary and important to calculate optimized cut parameters to improve and control the surface roughness values [2]. As in all areas of the industry, it has become an important criterion to use such as Artificial Neural Networks (ANN), Genetic Algorithms (GA), FL and expert systems for the in solving optimization problems with technological developments [3].

Many studies have been carried out to determine the optimum cutting conditions that cause surface roughness. Oktem and his colleagues have presented about GA approach to determine optimum cutting conditions to achieve the minimum surface roughness values. In their study, the Reaction Surface Method (RSM) methodology with analytical model is presented by using parameters such as feed, cutting speed, cutting depth and work piece radius [4]. A similar approach was processed in the work of the Suresh and his colleagues. In this study, a surface roughness prediction model has been

developed using GA with RSM methodology for processing mild steel [5].

Nalbant and colleagues have used the Taguchi Method in the turning to determine optimum cutting parameters in their study. The surface roughness values are optimized by considering cutting edge radius, feed and cut depth parameters. They have presented orthogonal array, signal-to-noise ratio, variance analysis using AISI 1030 steel bar in their work [6]. Barzani and his colleagues have presented to improve the surface roughness with artificial intelligence technique to predict for the processing performance on Al-Si-Cu-Fe cast alloy which has been treated with different dopants in turning. In this study, cutting speed, processing parameters such as feed rate and cutting depth are optimized according to the surface roughness [7]. Kovac and colleagues have presented an approach to modelling and predicting surface roughness by using regression analysis and artificial intelligence methods such as FL in their study [8].

Makadia and his colleagues have experimented to investigate the effect of parameters such as feed rate, tool radius, cutting speed and cutting depth on the surface roughness of the AISI 410 steel. They have developed a mathematical model for predicting these parameters. The effects of these parameters on the surface roughness has been investigated with using RSM in their study [9]. Franci and his colleagues has published about simulation for real-time control of surface roughness in their study. In this study, it is aimed to achieve the desired surface roughness by set the machining parameters and applying a constant shear force. For this purpose they have presented a more efficient method by changing the feeding speed for surface roughness value in real time [10]

In our study has been presented about achieving better surface roughness values by compensating for speed losses by setting the steady cutting rate parameter during machining in real time. For this purpose, experiments were performed using the cutting speed control with FL. The surface roughness results has been obtained with FL are compared with automatic usage results. In the study, Arduino Due 32 bit Cortex M3 ARM microcontroller has been used as microcontroller. Cutting speed control is provided with embedded software designed on the microcontroller. Experimental studies have been realized by using Bohler TCGT 16T308-270 coded cutting tool.

II. MATERIAL AND METHODS

G. Materials

In the study, 600 watt permanent magnet brush a spindle (spindle) motor is used in the CNC system. This engine is a minimum of 150, the maximum is 2500 rev / min can be operated in the range. Cutting speed control has been implemented on the spindle motor with the help of a 220 Volt voltage supply and a highly efficient motor drive. This control was implemented with embedded software on Arduino Due 32 bits Cortex M3 ARM microcontroller with 12 bits ADC resolution capability.

Measurements of the cutting speed of the spindle motor are obtained by converting the pulse values to the frequency value with the magnetic hall effect sensor. 2 pieces of Nema23 type 2.2. Nm stepping motors and drives are used for the movements of the axes (X and Z axis) in the bench system, depending on the design during the turning process. In experimental work on turning, Bohler TCGT 16T308-270 coded cutting tool was used.

H. Method

It is expected to be low cost in terms of investment and operation and ensuring system stability and increasing the performance of the system to the desired level in an industrial process control. In order to realize these conditions, a mathematical modelling is required depending on the structure of the system to be controlled and the dynamic properties [11].

The FL approach, one of the artificial intelligence methods, was first introduced by Lotfi A. Zadeh in 1965. This approach provides the ability to use human-specific data for symbolic expressions rather than numeric expressions and to work with expertise. Computer transmission of verbal expressions is based on a mathematical basis. This mathematical basis is called the fuzzy set theory. FL refers to many levels in the range instead of the Aristotelian ratios [0,1]. Especially, FL control method is very convenient in case when the system is complicated and the analysis can not be done with classical methods and the information is uncertain [12].

In general, the FL system consists individual knowledge rule base, fuzzification unit, inference unit and defuzzification unit [13]. Figure 1. shows a basic block diagram of the FL speed control method.

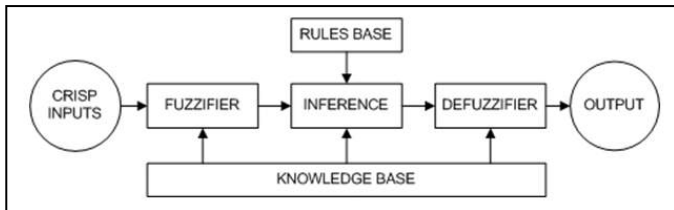


Fig. 1. Basic block diagram of speed control with FL.

In the work performed, triangular membership functions are used because of the computational efficiency in the application. The output value a, b, c of the triangular membership function is obtained by the relations with respect to the rating parameters given in Equation 1.

$$f(a, b, c) = \begin{cases} 0, & x \leq a \\ (x - a)/(b - a), & a < x \leq b \\ (c - x)/(c - b), & b < x \leq c \\ 0, & c < x \end{cases} \quad (1)$$

It is defined speed failure, changes in error, constraint values of verbal variables in fuzzier the correction values of output error in the error, in the universal set with a triangular membership functions. In Figure 2, the FL speed control input and output functions identified as the fuzzier result are given in triangular membership functions.

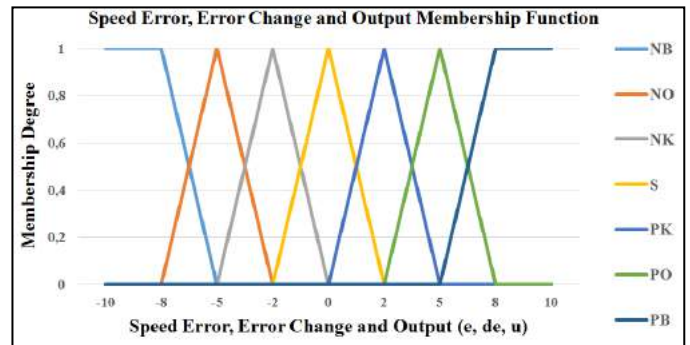


Fig. 2. Membership functions of the FL controller's input and output verbal variables.

Input and output values used in the speed control method with the FL are defined in universal set in the range [-10, + 10]. Table 1 shows that the input and output verbal variables defined for the membership functions in the performed study, as seen in the membership function given in Figure 2. These verbal variables represent analogue values from 0 to 4095 with a resolution of 12 bits.

TABLE VIII
INPUT AND OUTPUT VERBAL VARIABLES FOR MEMBERSHIP FUNCTIONS IN FUZZY SPEED CONTROL METHOD

Verbal Variable	Abbreviation
Negative High	NB
Negative Moderate	NO
Negative Low	NK
Zero	S
Positive Low	PK
Positive Moderate	PO
Positive High	PB

The referenced rule base unit supports the outcome unit to switch to the fuzzification process in the FL method. The rule base contains rules that are determined by experts and which determine the behaviour of the method. The output of the FL

controller is obtained by evaluation of these rules. The table of the FL rule base used in the experiments carried out is given in the Figure 3.

e \ de	NB	NO	NK	S	PK	PO	PB
NB	NB	NO	NO	NK	S	S	PK
NO	NO	NO	NK	S	S	PK	PK
NK	NO	NK	NK	S	PK	PK	PO
S	NK	NK	S	PK	PK	PO	PO
PK	NK	S	PK	PK	PO	PO	PO
PO	S	PK	PK	PO	PO	PO	PO
PB	S	PK	PO	PO	PO	PO	PB

Fig. 3. The rule base table of the FL controller.

It is preferable to apply the Mamdani FL model in all the fuzzy inferences that are performed because it is simple and suited to the system structure. The Mamdani FL model is given in Figure 4. In this model, each rule is operated separately. The fusion set values are obtained from the output values generated by the execution of each rule. Depending on this fusion set values, the defuzzifier process is passed to achieve absolute values..

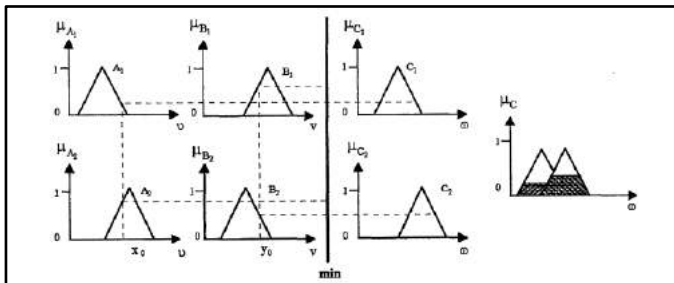


Fig. 4. Max, min theorem of Mamdani FL extraction.

The results that the designer wants to reach with rinsing methods are determined according to the methods recommended by the experts. Among these methods, the weighted average central method is the commonly used defuzzification method [11]. Because of the use of symmetric membership functions, easy compatibility with the systems, prevalence and computational efficiency, the weighted average method is preferred in the process of defuzzification of result set.

A sample graph of the defuzzifier process of the extraction set is given in Figure 5. mathematical expression of the defuzzifier process is presented in Equation 2.

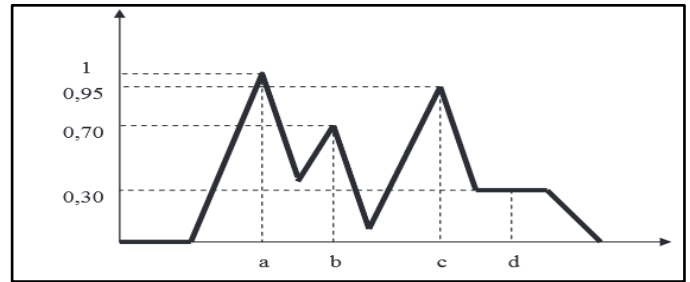


Fig. 5. A graph of the defuzzification with the weighted average method.

$$x = \frac{a * 1.0 + b * 0.70 + c * 0.95 + d * 0.30}{a + b + c + d} \quad (2)$$

III. EXPERIMENTAL STUDIES

The FL speed control method has been tested for cutting speed value, depending on different cutting speeds in the experiments performed. The arithmetic average roughness values were obtained by this control and compared with the average roughness values obtained by automatic usage. The experiments were carried out at three different cutting speeds (200, 320 and 440 m / min) at three different feed values (0.05, 0.1, 0.15 mm / rev) and at constant cutting depth (0,5 mm). TCGT 16T308-270 cutting tool was used in the experiments. As a result of the experiments, the effect of the FL speed control and automatic usage on the surface roughness of the processed material was compared. AA 2XXX series materials have used with dimensions of $\phi 75 \times 100$ mm in experimental studies. Roughness measurements were obtained on each 10 mm processed surface and the arithmetic mean was calculated. The roughness values measured after machining are shown graphically in Fig. 6., Fig. 7. and Fig. 8.

When Figure 6 is examined, the best roughness value obtained by FL speed monitoring is calculated as 1,018 μm , while for automatic use, 1,552 μm is calculated in the experiment carried out at a cutting speed of 200 m / min at a feed rate of 0,05 mm / rev.

According to Fig. 6, the roughness values obtained by FL speed control and automatic use seem to increase with the increase of the speed of progress for a cutting speed of 200 m / min. It can be seen that the inclination of the roughness curves obtained according to the progress value in both processing methods exhibits a parallel structure to one another. According to this graph, the lowest roughness values were 1,552 μm at 0,05 mm / rev feed rate for automatic machining, and 1,018 μm at 0,05 mm / rev feed rate when machined with FL. According to these results, the roughness value obtained with FL gave about 52,42% better than the automatic usage.

During automatic usage, the spindle motor speed can be reduced during the lifting of the spindle due to the material structure and the difficulties caused by cutting conditions. This causes the roughness values of the working surface to be high.

However, on the contrary to this situation, as a result of difficulties in the spindle motor at the moment of lifting the machined bits with the FL, the cycle losses in the spindle speed are eliminated by the instantaneous intervention of the FL controller and the number of spindles is kept constant at the desired value.

The roughness values obtained with FL were also lower than in automatic processing. The roughness values obtained with FL were also lower than in automatic processing.

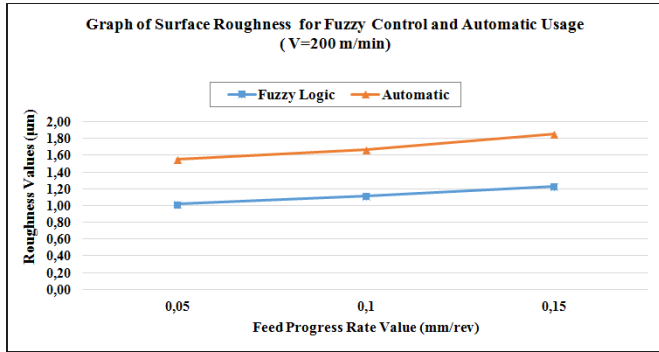


Fig. 6. At the cutting speed of 200 m / min, post-processing arithmetic average surface roughness results of BM speed control and automatic usage.

Figure 7 shows that surface roughness values obtained by FL and automatic machining at a cutting speed of 320 m / min. In this graph, as shown in Fig. 6 in general, the increase in the values of the advance at the cutting speed caused the roughness values to increase.

According to these values, the roughness values obtained with FL are lower than the roughness values obtained by automatic processing. However, in the experiments performed at a cutting speed of 320 m/min, the curve formed by the FL process has a lower slope and the difference between the roughness values formed in the advance values is lower. On the contrary, in the case of automatic processing, there are big differences between roughness values. Another important point is that roughness values obtained at a cutting speed of 320 m/min are lower than the roughness values obtained at a cutting speed of 200 m/min, and between the minimum 0,889 and maximum 1,03 µm.

This is because the roughness values are lower as a result of easier machining at higher cutting speeds. Moreover, due to the increase in cutting speed, the difficulties at the tool-chip interface are reduced, the cutting process is easier and the roughness values in the automatic process are getting lower and the process is getting closer to the FL. According to this graph, the lowest roughness value was formed as 0,889 µm at 0,05 mm/rev progression value in processing with FL. According to these results, the roughness value obtained with the FL is about 16,12% better than the automatic process.

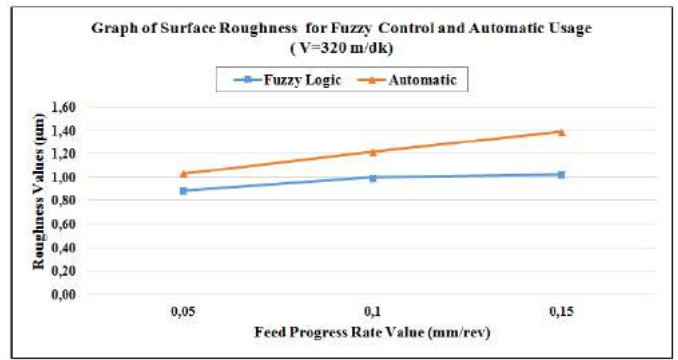


Fig. 7. At the cutting speed of 320 m / min, post-processing arithmetic average surface roughness results of BM speed control and automatic usage.

According to Figure 8., it is seen that the roughness values obtained from the processing tests made with FL in general are lowered as in the above-mentioned cutting speeds. It is clear that the roughness values obtained from this graph and the roughness data obtained at 320 m / min cutting speed show similar values. At this cutting speed, the difference between the lowest and highest roughness values obtained in automatic processing is lower than the differences in the other cutting speeds due to the increase in cutting speed. At a cutting speed of 440 m / min, the lowest roughness value is formed as 0,860 µm at a feed rate of 0,05 mm/rev. According to these results, the roughness value obtained with FL gave about 19,37% better than the automatic usage. According to this graph, we can clearly say that the difference between the lowest progression in FL and automatic processing and the roughness values in the highest progress value decreases with increasing cutting speed.

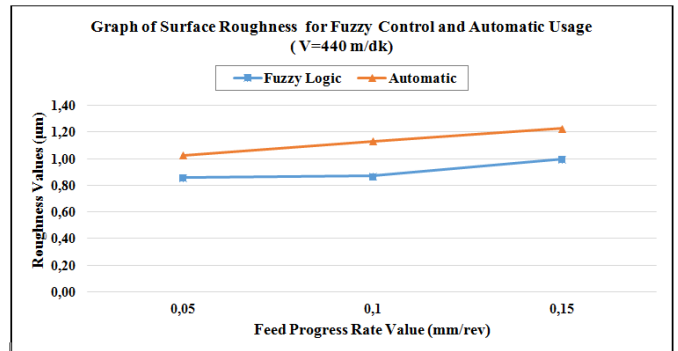


Fig. 8. At the cutting speed of 440 m / min, post-processing arithmetic average surface roughness results of BM speed control and automatic usage.

When the surface roughness graphs are examined, for all feed rate values performed at cutting speeds of 200, 320 and 440 m / min; Roughness values obtained with FL speed control showed better performance than automatic use. The best average roughness results are achieved at the highest cutting speed at 440 m/min. In the experimental work carried out by selecting 440 m/min cutting speed and 0,05 mm/rev feed, surface roughness values of 0,860 µm for FL speed control method and 1,027 µm for automatic usage were measured (Fig.8).

IV. CONCLUSIONS

In this study, experimental works realized at three different cutting speeds (200, 320 and 440 m /min), at three different feed rates (0.05, 0.1, 0.15 mm/rpm) and constant cutting depth (0,5 mm). In the experiments, the surface roughness results of the work pieces were compared of automatic usage with FL speed control depending on cutting speed. As a result of the experimental studies, when the obtained surface roughness values are examined, it is concluded that the speed control with FL at 100% of the works shows better performance than automatic usage. In this context, the positive effect of the FL speed control method on the surface roughness results shows that it can be successfully applied in systems used in machining operations.

REFERENCES

- [1] Factors Affecting Surface Roughness in Finish Turning M.M. Ratnam, Reference Module in Materials Science and Materials Engineering, Comprehensive Materials Finishing, Pages 1–25, (2017).
- [2] Abouelatta, O. B., and J. Madl. "Surface roughness prediction based on cutting parameters and tool vibrations in turning operations." *Journal of materials processing technology* 118.1: 269-277, (2001).
- [3] Benardos, P. G., and G-C. Vosniakos. "Predicting surface roughness in machining: a review." *International journal of machine tools and manufacture* 43.8: 833-844, (2001).
- [4] Öktem, H., T. Erzurumlu, and H. Kurtaran. "Application of response surface methodology in the optimization of cutting conditions for surface roughness." *Journal of Materials Processing Technology* 170.1: 11-16, (2005).
- [5] Suresh, P. V. S., P. Venkateswara Rao, and S. G. Deshmukh. "A genetic algorithmic approach for optimization of surface roughness prediction model." *International Journal of Machine Tools and Manufacture* 42.6: 675-680, (2002).
- [6] Nalbant, M., H. Gökkaya, and G. Sur. "Application of Taguchi method in the optimization of cutting parameters for surface roughness in turning." *Materials & design* 28.4: 1379-1385, (2007).
- [7] Barzani, Mohsen Marani, et al. "Fuzzy logic based model for predicting surface roughness of machined Al-Si-Cu-Fe die casting alloy using different additives-turning." *Measurement* 61: 150-161, (2015).
- [8] Kovac, Pavel, et al. "Application of fuzzy logic and regression analysis for modeling surface roughness in face milling." *Journal of Intelligent manufacturing* 24.4: 755-762, (2013).
- [9] Makadia, Ashvin J., and J. I. Nanavati. "Optimisation of machining parameters for turning operations based on response surface methodology." *Measurement* 46.4: 1521-1529, (2013).
- [10] Čuš, Franci, and Uroš Župerl. "Surface roughness control simulation of turning processes." *Strojniški vestnik-Journal of Mechanical Engineering* 61.4: 245-253, (2015).
- [11] Efe, M. Ö., "Otomatik kontrol sistemleri", Seçkin Yayıncılık A.Ş., Ankara, 18-35 (2012).
- [12] Ç. Elmas, Bulanık Mantık Denetleyiciler, Seçkin Yayıncılık A.Ş., Ankara, 12-38 (2003).
- [13] Soy, H., Yılmaz, E., and Allahverdi, N., "Design of an embedded fuzzy PD controller for thermal comfort applications.", *International Journal of Reasoning-based Intelligent Systems*, 2 (3-4): 293-299, (2010).

Effects of Slag Optimization on Steel Cleanliness in Secondary Metallurgy Process

Emre Alan^{*}, Zafer Çetin^{*}, Kağan Keler^{*}, İlker Ayçiçek⁺

[#]Ereğli Iron and Steel Works, Co. (Erdemir), Zonguldak, Turkey
ealan@erdemir.com.tr

⁺İskenderun Iron and Steel Works, Co. (Isdemir), Hatay, Turkey
iaycicek@isdemir.com.tr

Abstract— Slag plays an important role in steelmaking process by providing an insulation of liquid metal surface, preventing heat losses and removing impurities and inclusions in liquid steel, etc. For these reasons, in order to produce “a cleaner steel” attention should be paid on controlling of chemical and also physical properties of slag in steelmaking process. Initial formation of ladle furnace slag consists of carry-over slag of converter tapping and tapping additions. In this study, effects of different tapping additions to ladle slag conditions and steel cleanliness were investigated. Additionally, Sulphur removal capacities of slags were compared by means of chemical and physical properties with using FactSage Computational Thermochemistry Software and ARL Spark-DAT inclusion analyzer.

Keywords— Steelmaking, steel cleanliness, slag, tapping, secondary metallurgy

I. INTRODUCTION

Steelmaking slags are by-products of smelting and refining processes of liquid steel in high temperatures and they consist of a mixture of various oxides [1]. Slag plays an important role in steelmaking due to it acts as a thermal barrier to prevent heat transfer from liquid steel to the surrounding, protects liquid steel from re-oxidation, also absorbs non-metallic inclusions and provides steel cleanliness [2].

“Steel cleanliness” is one of the major assignments for steel producers. The demand for cleaner steel requires lowering the occurrence of non-metallic inclusions and/or modifying them in order to eliminate their harmful effects. Depending on their quantity, morphology and size distributions, non-metallic inclusions give rise to nozzle clogging in continuous casting process, surface defects in rolling process and adverse effects on mechanical properties and magnetic properties in final product, etc [3]. Non-metallic inclusions may formed in solidified steel as a result of chemical reactions between elements dissolved in steel or derived from external sources such as refractory materials, additions, etc. [4]. Practically, it is not possible in steelmaking conditions to produce steel without any inclusion, thus it is important that to produce a “cleaner steel” with removing non-metallic inclusions as much as possible by applying proper practices.

II. EXPERIMENTAL

In this study, the effects of different tapping addition practices were compared in order to produce a cleaner steel. Heat size of trials were 200 tons.

Initial formation of ladle furnace slag consists of carry-over slag of converter tapping and tapping additions. Carry-over slag contains high amount of FeO content. FeO is a weak oxide and may cause formation of non-metallic inclusions in steelmaking conditions. Additionally, higher amount of FeO in slag reduces desulfurization rate in secondary metallurgy process [5]. Therefore, steelmakers take precautions to minimize carry-over slag amount by using different type of techniques.

TABLE I
COMPARISON OF TAPPING ADDITIONS

Tapping Additions [kg]	Tapping Addition Practice	
	Regular	Trial
Ferro Manganese [H.C]	1550	1550
Ferro Silicomanganese	1500	1700
Calcium Fluorite	100	-
Calcium Aluminate	-	550
Lime	1350	1100
Aluminium [Ingot]	100	350
Aluminium [Ingot]	-	80

Additions of steel deoxidation, alloying and fluxes are usually made in tapping of liquid steel from convertor into ladle. In plant trials, High Carbon FeMn, FeSiMn and Ingot Aluminium were used for steel deoxidation and alloying, Coke was used for pre-deoxidation of liquid steel, Calcium Fluorite (CaF₂), Calcium Aluminate (CaO.Al₂O₃), Lime (CaO) and Pyramid Aluminium were used for slag deoxidation and providing a proper slag condition. Comparison tapping addition amounts according to different practices are listed in Table 1.

III. RESULTS

The impurity capacity in the steelmaking slags is related to the slag basicity, viscosity and oxygen activity of slag. Generally, a creamy liquid formation and a high basicity are required for ladle slags that have high impurity capacity. The addition of CaF₂ to ladle slag increases the solubility of basic

oxides and provides required fluidity in the slag as the slag temperature decreases [6]. To achieve this requirements, CaF₂ was used in regular practice while Calcium Aluminate and higher amount of Al were used in trials.

can rapidly determine non-metallic inclusions in steel and a complete analysis of the inclusions by means of their type, number and distribution [7].

Weaker oxide components in ladle slag like FeO_T and MnO may cause non-metallic inclusion formation by reoxidation in further processes. Additionally, the reduction of FeO_T and MnO from ladle slag is beneficial for preventing yield loss and refractory erosion. Therefore, it is important to obtain a deoxidized slag in initial stages of ladle furnace process. Table 2 shows the comparison of FeO_T and MnO contents of ladle slags after tapping additions. In tapping process, Al addition amount was increased in trials when compared to regular heats and also an amount of extra Al addition was added onto the carry-over slag in order to slag deoxidation.

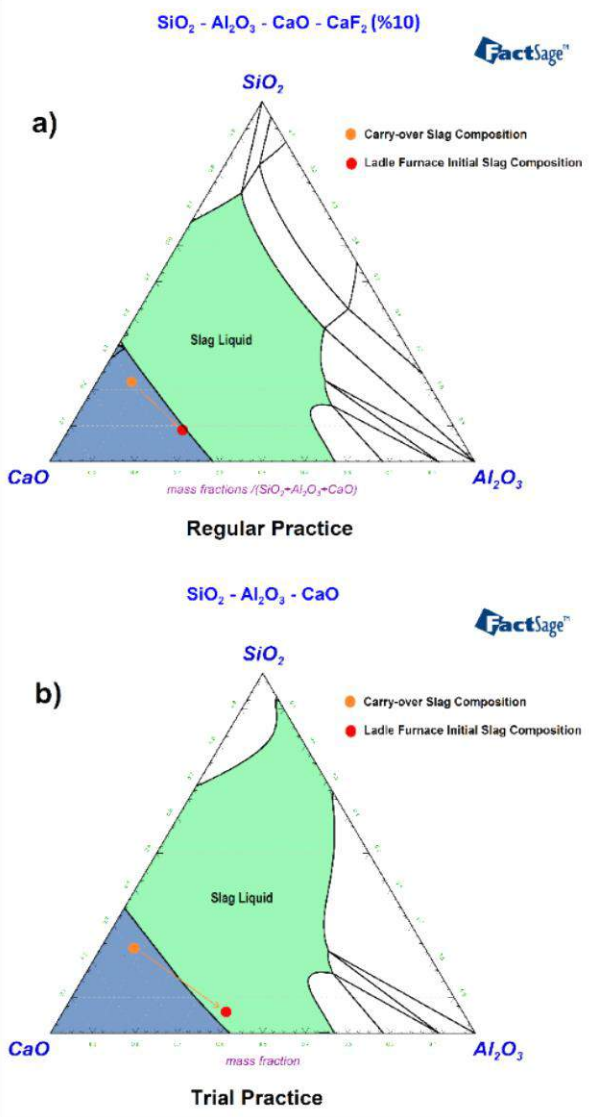


Fig. 1. Ternary phase diagrams of ladle furnace slags; (a) regular and (b) trial heats.

By using FactSage 6.4 computational thermodynamic software, slag compositions of each practices were plotted on ternary phase diagrams. As shown in Fig. 1, after fluxing and deoxidizing additions were made in tapping process, initial ladle slag contains some undissolved lime content in heats with regular practice while slag compositions have no undissolved component in trial heats.

In order to determine steel cleanliness of steel samples that were taken from liquid steel in secondary metallurgy process, investigations were made with using ARL 4460 Optical Emission Spectrometer (OES) equipped with ARL Spark-DAT technique. ARL Spark-DAT is a measurement technique that

TABLE II
COMPARISON OF FeO_T AND MnO CONTENTS OF LADLE SLAGS ACCORDING TO TAPPING ADDITION PRACTICES.

Sample	Component [%]	
	FeO _T	MnO
BOF Slag	20,4	3,8
Regular	1,5	0,8
Trial	0,6	0,1

A ladle slag with a high sulphide capacity should has properties such as high basicity and a high fluidity. Additionally, higher amount of slag is more effective for removal of S in liquid steel [8]. With the increment of slag liquidity in trials, the reduction of FeO_T and MnO contents in ladle furnace slag also helped the S removal from liquid steel in secondary metallurgy process as shown in Fig. 2. Although the S content in liquid steel in converter process was same, a significant reduction was observed in the first steel sample of ladle furnace process in trial heats.

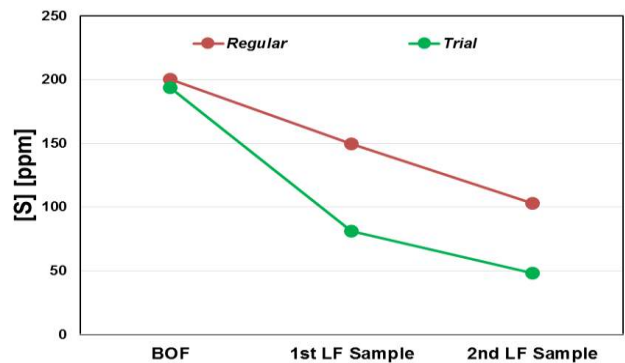


Fig. 2. Ternary phase diagrams of ladle furnace slags; regular (a) and trial heats (b).

The high amount of S in liquid steel before Ca treatment causes to formation of CaS inclusions which have negative effects on nozzle clogging in continuous casting process.

Therefore, removal of S in liquid steel is important for secondary metallurgy process. Amount of CaS inclusions in liquid steel in regular and trial heats according to S content before CaSi wire injection is shown in Fig. 3.

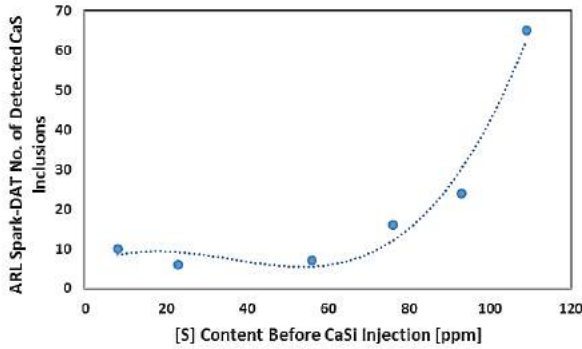


Fig. 3. CaS inclusions in liquid steel according to S content before CaSi wire injection.

Addition of deoxidation and alloying materials depending on the range of steel specification in tapping allows more time to inclusion removal applications in ladle furnace operation. Besides, according to addition amount and impurity content of materials, alloying additions in ladle furnace process may give a rise to non-metallic inclusion ratio in liquid steel. In this case, an additional time is required to provide steel cleanliness in secondary metallurgy process.

TABLE III

COMPARISON OF ADDITIONS IN SECONDARY METALLURGY PROCESS

Tapping Practice	Additions in Secondary Metallurgy Process [kg]				
	Al [wire]	FeMn [H.C.]	Lime	FeSi	Coke
Trial	72	233	320	105	112
Regular	163	375	332	230	115

The total numbers of detected non-metallic inclusions in regular and trial heats were calculated as shown in Fig. 4. The total number of detected non-metallic inclusions in trial heats calculated less than regular heats after secondary metallurgy process.

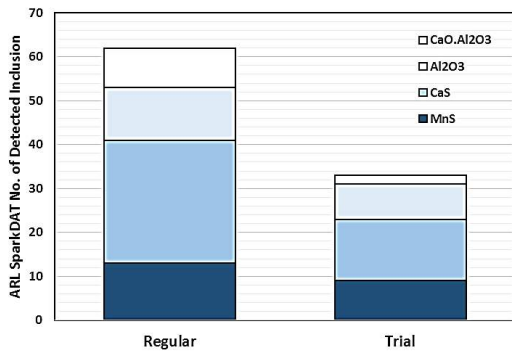


Fig. 4. Comparison of total non-metallic inclusions after secondary metallurgy process.

Steel cleanliness comparison of regular and trial heats is given in Fig. 5. Optical microscopy images showed that steel cleanliness was better in samples of trials heat that were taken from end of secondary metallurgy process than regular heats.

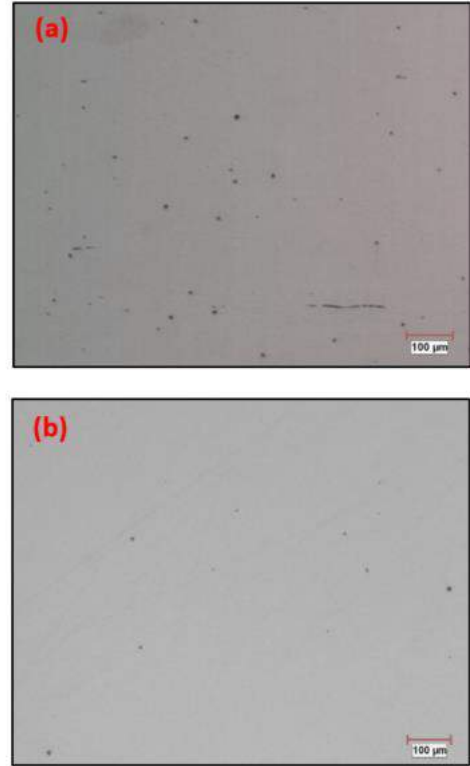


Fig. 5. Optical microscopy images with 100X magnification of samples taken from end of secondary steelmaking process; (a) regular and (b) trial heats.

IV. CONCLUSIONS

In this study, effects of different tapping additions to ladle slag conditions and steel cleanliness were investigated. S removal capacities of slags were compared by means of chemical and physical properties with using FactSage Computational Thermochemistry Software and ARL Spark-DAT inclusion analyzer. In trial heats, increasing of Al₂O₃ content of slag in tapping process provided an increment in fluidity of initial ladle slag by dissolving over-saturated CaO content. Slag deoxidation was applied by adding Al onto slag to obtain lower FeO_t content in initial ladle slag. Therefore, the desulphurization capacity of slag is increased by obtaining a proper slag formation, increasing slag basicity and reducing FeO_t content in trial heats. In addition to slag conditioning parameters, it was observed that the total number of detected non-metallic inclusions were reduced after secondary metallurgy process by reducing the amount of addition materials in secondary metallurgy process by increasing the addition amounts during tapping.

REFERENCES

- [1] K. Morita, "Thermodynamics of Slags", *Treatise on Process Metallurgy*, vol. 1, pp. 587-615, 2013.
- [2] S. C. Koria, "Lecture 4: Slag in steelmaking", Material Science and Engineering IIT, Kanpur.
- [3] E. Alan, Z. Çetin, "Estimation on Non-Metallic Inclusions in Steelmaking Process by Using Computational Thermodynamics Software", in 18th International Metallurgy & Materials Congress, Istanbul, 2016.
- [4] [4] S. Kumar, "Inclusion Control for Clean Steel", MGR (SMS) NINL, 2014.
- [5] Y. Jing-Bo, Y. Shu-Feng, G. Xiang-Zhou, L. Jing-She, "Sulfur Control in Ultra-Low Sulfur Steel Refined by Ladle Furnace-Vacuum Degassing", *Metal Journal*, 2013.
- [6] E. Pretorius, "The Effect of Fluorspar in Steelmaking Slags", 2004.
- [7] [6] G. H. Vlaicu, I. V. Popescu, F. Parsan, N. Pavel, M. Bahrim and I. Bancuta, *Romanian Reports in Physics*, Vol. 62, No. 2, pp. 350-359, 2010
- [8] A. Yang, "A Pre-study of Hot Metal Desulphurization", *Master's Degree Project*, Department of Materials Science and Engineering Royal Institute of Technology, Sweden, 2012

An Example Implementation for the Lowest Reduction of Environmental Effects of Chemical Oriented Disasters: The REACH System

Bora BALUN*, Gazanfer ERBAY⁺,

Ph.D. Student, Anadolu University, Department of Labour Economics and Industrial Relations, Eskisehir, Turkey
borabalun@hotmail.com

⁺Ph.D., Karabuk Provincial Disaster and Emergency Directorate, Karabuk, Turkey
gerbay1966@hotmail.com

Abstract— Modern industrial manufacturing processes and modern societies need to use chemical substances. Chemistry and chemical products are described as the key elements in development of modern societies. In addition, chemical substances are used extensively in almost every stage of industrial production including in the iron and steel industry. Thus, production of chemicals and their usage are getting increased through the worldwide.

Due to transboundary nature of flyaway distribution of chemical substances, in terms of human health and environmental should be required of national and international cooperation. Therefore, there are a lot of applications in field of international collaboration. One of these applications is the REACH System developed by the European Union.

The REACH System is aimed to higher level protection of human health and environmental. Thanks to this system, will have more knowledge about chemical substances and this knowledge will be shared with the society. In this study, developing on chemicals control by the European Union will be discussed through implementation areas of the REACH System. An Erasmus+ project related to field will also briefly presented.

Keywords—Chemical Substances, International Collaboration, The REACH System.

I. INTRODUCTION

Modern production processes are need to chemical substances and it has become an indispensable condition for industrial industries. Chemical substances are important components for agriculture, manufacturing, construction and service sectors besides consumption goods. It is produced at least 400 million tons of chemical substance in every year world, so chemical substances as solid, liquid and gas are in every aspect of our lives.

The chemical substances that products produced by the chemical industry are used in other sectors (70%). At the same time, at the rate of 30% from plastics to paints is directly reaching to consumer (Fig.1.). - According to studies, in sectors in direct relationship with chemical industry is 9% rate of sectors of mining, metal industry, machinery and electricity (Fig.2.).-

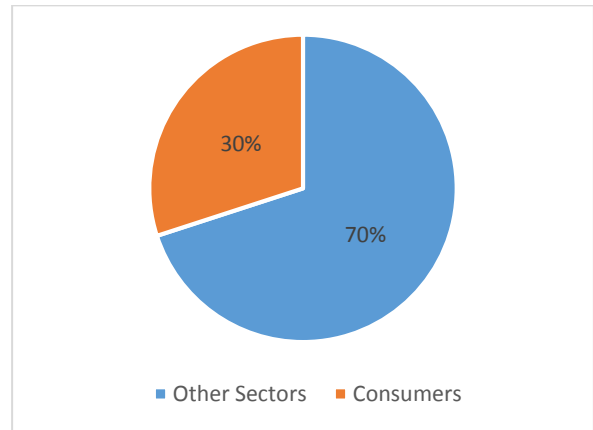


Fig. 1 Used of Chemical Substances (According to the intensity of use) (%)

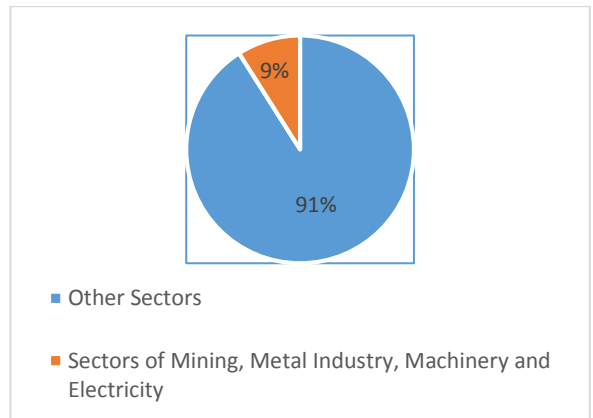


Fig. 2 Used of Chemical Substances (According to Sectors) (%)

There are efficient functions of the chemical substances in terms of modern societies and there are risks caused by production, storage, use and sale for some of them. Major industrial accidents are events which leads to great harm to human life and the natural environment. In addition, they are caused to disorders on economic and social life. For example, due to problems caused by substances with chemical origin has increased in number of technological and natural disasters in

our country and world. As a result of disasters were injured and dead of thousands people (Fig.3-4).

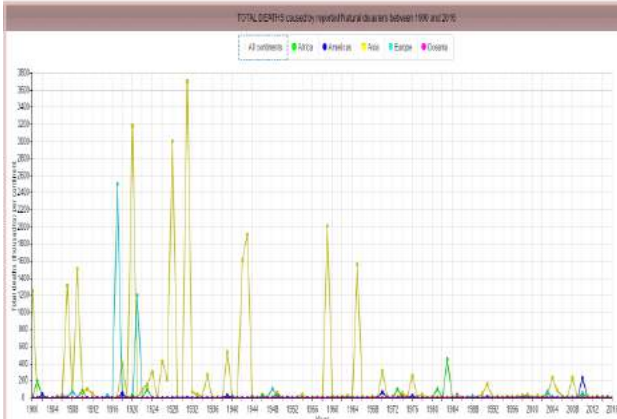


Fig.3. Total Deaths Caused by Natural Disasters [1].

According to official data of The International Disaster Database (EMDAT) was occurred 8351 technological disasters between 1900 and 2016. Number of total deaths in these technological disasters is accounted as 363.505 persons. The total number of injured is accounted as 420.379 persons [2]. These accidents should be also considered in terms of financial losses, workforce losses and psychological traumas. A lot of these losses should be required to reconstruction process with long period.

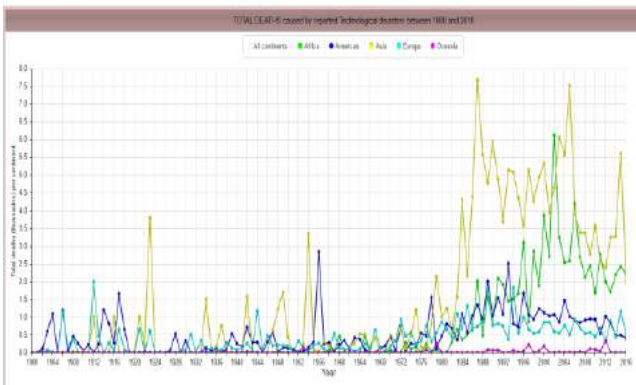


Fig.4. Total Deaths Caused by Technological Disasters [1].

There are three main stakeholders as governments, institutions and communities in industrial accidents. Because of spreading due to winds of toxic releases there is no defined limit within area of influence of accidents with chemical origin. Due to increased in number of chemical accidents is necessary to undertaken in joint studies. In time, related to chemical accidents has started to studies in world and European Union. One of these studies is also REACH.

II. THE REACH SYSTEM

REACH is a regulation developed for examined of environment and health conditions to caused by complex situation of chemical substances in The European Union. REACH is prepared looking at data composed by chemical

substances and it is also encompassing in taken to control communication.

It is a new regulation of the European Union On Registration, Evaluation, Authorisation and Restriction of Chemicals. REACH is abbreviation of Registration, Evaluation, Authorisation and Restriction. REACH was entered into force on June 1, 2007 and it includes a number of the European Union rules and regulations.

It has been established of European Chemical Agency (ECHA) in Helsinki for technical, scientific and administrative management of the regulation [6].

There are 7 basic objectives in REACH System [7]:

1. To protection of human health and the environment,
2. To protection and development of competition power of the EU chemical industry,
3. To protect to unity of the internal market,
4. To raise of transparency,
5. To adapt to international developments,
6. To remove of experiments on animals,
7. To carried out the EU's international obligations under the World Trade Organization (WTO).

A. The REACH Certificate

Priority aims with REACH Certificate is protection of human and environment health. After REACH, some approaches on dangers related to chemical substances, sellers and manufacturers is entered into force.

These approaches can be summarized as follows:

- To create awareness,
- To facilitate of sales of chemical substances in The European Union,
- To create of competitive space,
- To increase of research and development.

Processes with these aims are started with registration to European Chemical Agency (ECHA) for importers and manufacturers, and then are carried out procedures by transmitting of requested data. If are produced and sent to The European Union of chemical substances over one tonne, REACH Certificate should be received.

Sectors in scope of REACH can be summarized as follows:

- Chemical Product Manufacturers,
- Chemical Product Importers,
- Goods Manufacturers Containing Chemical,
- Goods Importers Containing Chemical,
- Dealer of Chemical Goods,
- Sellers of Chemical Goods.

Recorded files in REACH are analysed by the Agency. Application Evaluation Process in REACH can be summarized as follow:

Conformity Assessment: Information of Sending from industry is examined. It will apply by European Chemical Agency in Helsinki. It will happen over the samples obtained from files under registration for interval of each tonnage (at least 5%).

Analysis of File: For substances recorded at a high tonnage level (100 tonne/year) will be proposed an offer regarding to animal experiments by recording owner (for animals required of test). These offers will be examined for avoiding from unnecessary animal experiments.

Analysis of Substances: By authorized of European union members will be applied for substances with harmful qualities. The all files will be examined in terms of suitability.

B. Scope and Exemptions (No Data, No Market!)

A registration package will be supported with a standard set of data about substance. Amount of data is proportional to the quantity of the substance to be produced or offered. If the substance is not recorded, it will not be placed on data about substances. Therefore, these products are not legally produced in European Union or presented to European Union. So, no data, no market! [8].

The list of chemical substances is published via their internet addresses by European Chemical Agency (ECHA) [3]. The lists are identified as a Substance of Very High Concern (SVHC). The lists are always updated by ECHA. The lists should be examined by importers or manufacturers.

Obligation for Substances: By dealer after 28 October 2008, in the European Union for substances in SVHC must be provided to customers to safety data sheet related to these substances.

Obligations for Preparations : After 28 October 2008, for preparations not covered by the Dangerous Preparations Directive https://en.wikipedia.org/wiki/Dangerous_Preparations_Directive - cite note-1 [4] should be provided Safety Data Sheet in case of demand by The European Union manufacturer.

Follows substances are also scope of REACH Certificate which are substances be able to cancers from chemical substances.

- Substances with toxic,
- Substances it can be affected to genetic's structure,
- Persistent pollutants.

These substances are assessed as important at a high level.

REACH is generally applied to all substances in its own state and in the mixture or in the material. Some substances have been specifically excluded. These substances are follows.

- Radioactive substances,
- Substances under customs control,
- Convey of substances,
- Non isolated intermediate products,
- Wastes,
- Some natural harmful substances.

Some substances are prevented with special regulations. These substances are follows.

- Human and veterinary medicines,
- Food and food additives,
- Plant protection products and biocides.

If they are used in certain conditions, there are other substances with more specific measures in REACH.

- Intermediate products with isolated,
- Substances used in research and development (for scientific research and development)

III. APPLICATIONS OUTSIDE THE EUROPEAN UNION

With REACH of firms of export and production from Turkey to European Union there are new responsibilities and obligations [5]. If sent to The European Union to chemical substances over one tonne, these substances should be registered. But, natural persons or legal persons outside The European Union can't register. There are three alternatives in front of natural persons or legal persons to entered to The European Union markets. These alternatives are follows [9].

1. Registration via dealer / agency / branch in The European Union: If there are dealer, branch, agency in The European Union of the companies it these companies can register.

2. Registration via importer in The European Union: Legal liability in terms of product of sent to The European Union is based on importer companies. Related products by importer companies can register to the ECHA.

3. Registration via exclusive agent (Sole Representative): Established in The EU in order to registered to the ECHA is a legal entity. By sole representative as "recorder"; belonging to importer companies should be performed of all obligations.

C. Manufacturers / Importers

If by firms is send or import to The European Union of chemical substances over one tonne every year, of their files with related to these substances should be registered to The

ECHA. The exporters should be registered to The ECHA in order to protect of their place in the markets. If release is designed, the substances within goods are also includes.

D. Downstream Users

For downstream users is covered to the area of almost every business with chemical substance. Companies using chemicals, they are responsible for safe use of chemicals. They are also responsible for transmitted in the supply chain.

E. Other Actors in the Supply Chain (Distributors, Suppliers, etc.)

By sellers are obliged to transmit information to customers, if desired are also obliged to transmit information to suppliers. The exporters from the countries outside the European Union to the European Union can't appoint one representative by distributors.

IV. CONCLUSIONS

- The tasks of the states are generally to creates awareness.
- Registration obligation has been given to firms.
- Responsibility for "Product Safety" has passed from the public to the industry.
- Directives and regulations has been combined after REACH.
- There are occurred special measures for protection of human health and environment.
- There are increased in level of knowledge shared between sectors and the publics.
- There are increased in scientific research and development.
- To follow of substances of used of supplies in the supply chain has been become easier.
- There are discriminations in terms of "Risk" and "Quantity" instead of "Old Product "and" New Product ".

ACKNOWLEDGMENT

The authors would like to thanks their institutions, Karabük Provincial Disaster and Emergency Directorate, Karabük, Turkey. They also express their special appreciation to European Commission, for funding the Erasmus KA2 Project (2015-1-TR01-KA202-021323KA202).

REFERENCES

- [1] The International Disaster Database, http://www.emdat.be/disaster_trends/index.html, Date of access: January 13, 2017.
- [2] The International Disaster Database, http://www.emdat.be/advanced_search/index.html, Date of access: January 13, 2017.
- [3] The European Chemical Agency, <https://echa.europa.eu/candidate-list-table>, Date of access: January 21, 2017.
- [4] Directive 1999/45/EC of the European Parliament and of the Council of 31 May 1999 concerning the approximation of the laws, regulations and

- administrative provisions of the Member States relating to the classification, packaging and labelling of dangerous preparations.
- [5] The European Chemical Agency, "Identify Your Obligations, <https://echa.europa.eu/web/guest/support/guidance-on-reach-and-clp-implementation/identify-your-obligations>, Date of access: February 03, 2017.
 - [6] The European Chemical Agency, "Understanding REACH" <https://echa.europa.eu/regulations/reach/understanding-reach> (Date of Accesses January 02, 2017
 - [7] REACH Regulation (EC) No 1907/2006, Title I, Chapter 1, Article 1.
 - [8] REACH Regulation (EC) No 1907/2006, Title II, Chapter 1, Article 5.
 - [9] REACH Regulation (EC) No 1907/2006, Title II, VI, VII.

Vanadiumboride Coating of a Low Carbon Steel by Plasma Transferred Arc (PTA) Method

Yusuf DONAT¹, Mehmet EROĞLU²

1,2 University of Firat, Faculty of Engineering, Department of Metallurgical and Materials
Engineering, Elazig-Turkey

ydonat@firat.edu.tr, meroglu@firat.edu.tr

ABSTRACT

In this study, a low carbon steel surfaces were coated with vanadium borides using plasma transferred arc (PTA) method. In the plasma arc surface coating method, very high heat occurring by plasma melts the powder on the surface. In the study, ferroboration and ferrovanadium powders were used as a source of boron and vanadium, separately. For vanadium boride, five different amounts of powders were used to obtain coatings having different amounts of VB. After the coating studies, microstructural examination, elemental and X-ray analyses, hardness measurements and abrasive wear tests were performed. From the results, it was seen that hardness and wear resistance of the coatings increased with the increase of VB contents.

Keywords:PTA, Vanadium borides, low carbon steel, surface coating

Boride Coatings on a Low Carbon Steel Using Shielded Metal Arc Welding Electrode With Boron Carbide

Mehmet EROĞLU¹, Yusuf DONAT²

*1,2University of Firat, Faculty of Engineering, Department of Metallurgical and Materials
Engineering, Elazig-Turkey*

meroglu@firat.edu.tr, ydonat@firat.edu.tr

ABSTRACT

In the present study, shielded metal arc welding electrodes containing boroncarbide in the shield were produced for making boride coatings and low-carbon steel plates were surfaced with single-double and triple pass welds. The effects of the boron content on the microstructure and hardness of the coatings were investigated. After deposition, microstructural analyses including metallographic examination, wavelength-dispersive X ray (WDX), X-ray and microhardness measurements of the coatings were evaluated. From the results, it was seen that different boron contents formed primary and eutectic Fe₂B, and consequently had an effect on the hardness of the coating.

Key words: Boroncarbide, Coating, Microstructure, Hardness.

Friction Stir Spot Welding for Different Metals: A Review

Melike ŞAŞMAZ, Hilal KIRIKÇI, Yahya BOZKURT*

melsasmaz@gmail.com,

hilalkirikci@hotmail.com,

*ybozkurt@marmara.edu.tr

Marmara University, Technology Faculty,

Metallurgy and Materials Engineering Department,

34722, Kadıköy- Istanbul, Turkey

Abstract— There have been several problems regarding the welding of materials with advanced and complex structure for the industry during the recent years. Solid state welding methods have been developed to eliminate these problems. One of these is friction stir spot welding (FSSW). FSSW method is derived from of the friction stir welding (FSW) process and this is a new process that has recently received considerable attention from various industry branches. In both methods, the joining mechanism is the same. However, there are several differences as to the application. The tool used for the FSSW process is similar to the that of FSW and the FSSW process consists of three phases of plunging, stirring and retraction. Studies have also indicated that the effect of tool rotation speed, tool penetration and dwell time on lap shear tensile failure load of the joint have great importance for this method.

In this study, how the FSSW method works, the properties of this method, the application of the FSSW method on many different materials have been examined. The results have been reported from the current literature under separate headings.

Keywords— Friction stir spot welding, Welding of dissimilar materials, Aluminium alloys, Mechanical properties, Microstructure.

I. INTRODUCTION

Throughout history, humankind has used self-assemble method in the production of necessary tools and equipment [1]. The problems encountered in the source of thin-section metal materials used in many areas such as the automotive sector, space and aircraft technologies, steel structures, steel product manufacturing, precision equipment manufacturing, electrotechnics, pipe production, machinery sector have provided the development of different types of welding [2]. Today, these methods are still in operation. Considering the materials and alloys developed in our era, it seems that more modern joining methods are needed. Therefore, the development of new and more effective welding methods in recent years has become heavily focused on an area. When the studies are examined, it is seen that it is important not only to merge but also to apply the joining method without affecting the structure and properties of the material [1]. Resistance spot welding, laser spot welding and riveting have been widely used for aluminium alloys sheet assemblies. However, the conventional resistance spot welding has disadvantages such as consumption of tool during joining, large heat distortion, and

poor weld strength in joints; porosity defects cannot be avoided by laser spot welding; riveting will increase the weight of components and the drilling needed will increase the cost. Hence, new spot welding processes are required for joining parts made of aluminium alloys [3].

The friction stir welding process was developed by TWI (Abington, United Kingdom) in 1991 as a novel method for joining aluminum alloys. Since that time, the welding process has been employed in aerospace, rail, automotive, and marine industries for joining aluminum, titanium, magnesium, zinc and copper alloys, steel, and thermoplastics in thicknesses ranging from 1 to 50 mm [4]. FSSW which is a variant of FSW has seen remarkable growth in research, development and applications in recent years [5].

The FSSW method is carried out by immersing two overlapping plates with a shoulder stirrer tip rotating at high speed. In principle, friction is the same as mixing source and there is difference between them in terms of application [6-7]. In the friction welding, the heat released during the friction of two materials ensures that the friction surfaces reach the temperatures near the melting temperature in a short time. Friction surfaces, locally crushing and rubbing stumps suddenly weld and then break apart. As friction continues, high temperatures are reached in a very short time and the parts are eventually welded under the applied stacking force [8]. Fig.1 shows the typical micrographs of the cross-sections of the dissimilar Al alloys [9].

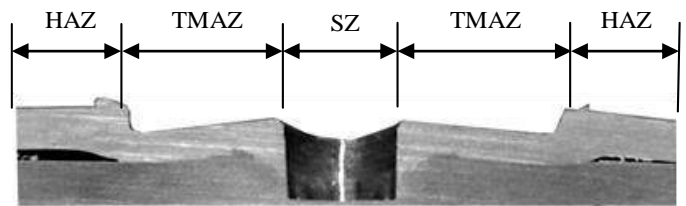


Fig. 1 A typical micrograph of the cross-section of the FSSW [9].

The cross-section of the FSSW joint consists of four regions, which are namely base material (BM), heat affected zone (HAZ), thermo mechanically affected zone (TMAZ) and stir zone (SZ), as also pointed out in Ref. [10].

In this study, how the FSSW method works, the properties of this method, the application of the FSSW method on similar and dissimilar materials have been examined. The results have

been reported from the current literature under separate headings.

II. FSSW PROCESSES

The FSSW processes purely mechanical. It permits an assembly without fusion and presents several advantages, especially for the materials such as aluminum, magnesium, and copper alloys, which are not easily joined with conventional fusion welding method [11]. FSSW was invented by Mazda Motor Corporation in 1993. As shown in Fig. 2, The FSSW process consists of three stages: plunging, stirring, and retracting [3].

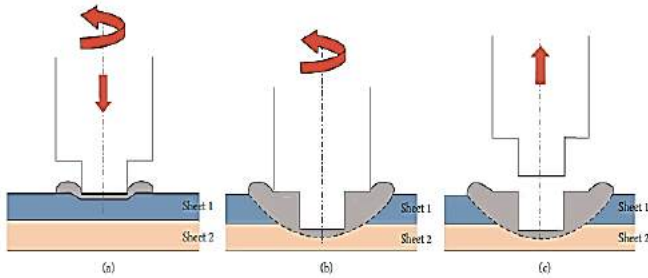


Fig.2 Illustration of the FSSW process: (a) plunging, (b) stirring, and (c) retracting [8].

1. *Plunging*: The joining tool, while rotating, is forced against the workpiece with a specified amount of pressure. This pressure creates frictional heat between the workpiece and the pin on the tip of the tool softening the metal and allowing the pin to plunge into the workpiece. This step ends with the tool's shoulder touching the surface of the upper part [12,13].

2. *Joining*: The pin becomes completely embedded in the workpiece and the press force on the tool is maintained for a given interval even after the shoulder on the outer edge of the tool comes in contact with the work piece (refer to the drawing below for the joining mechanism). There are two kinds of movements of the softening material at the mixing stage. Movement of material softened in axial direction and movement of material softened in the direction of rotation [12,13-15].

3. *Retracting*: The tool and the pin are retract after the joining is completed. When the welding tool is completely moved away from the parts, it is seen that there is a characteristic gap in the center of the welding area [12-15].

The lack of melting in the material during welding will minimize impacts and provide better properties [16]. The simplicity and environmental friendliness of the automotive industry has been a major concern because of the lack of smoke and radiation, the absence of protective gas, dust, wire or electrocution during its application, low investment costs and significant energy savings [12,13,17].

The appearance of the source coming to the scene in the FSSW method is similar to the resistance point source commonly used for the assembly of automobile bodies. But the first car body welding method for mounting electrical resistance spot welding, many lightweight construction

materials, such as aluminum alloys and advanced high strength steels (AHSS) to create problems. Until now, the majority of research and development efforts on the FSSW method have been based on aluminum alloys. However FSSW method of AHSS welding, as well as to the suppliers of the steel requirements and has offered some unique technical excellence for the car users [14]. FSSW for merging with Al, this method is not suitable for any inaccuracies in the high current requirements of the finished weld joint quality. Today, the automotive industry, the use of light alloys instead of conventional steel elements has increased significantly.

III. CURRENT STATUS OF FSSW FOR DISSIMILAR METALS

A. FSSW of Aluminium to Steel

S. Bozzi et. al. [11], joined A6008 aluminum alloy plate of 2.5 mm thickness superimposed to a galvanized steel plate of 2 mm thickness as shown in Fig.3. The nature of the steel used here is specific to the automotive industry. The tool has a diameter of 6 mm. As the tool is 4 mm length, it penetrates completely into the aluminum sheet and partially into the steel sheet. Figures and tables must be centered in the column. Large figures and tables may span across both columns. Any table or figure that takes up more than 1 column width must be positioned either at the top or at the bottom of the page.

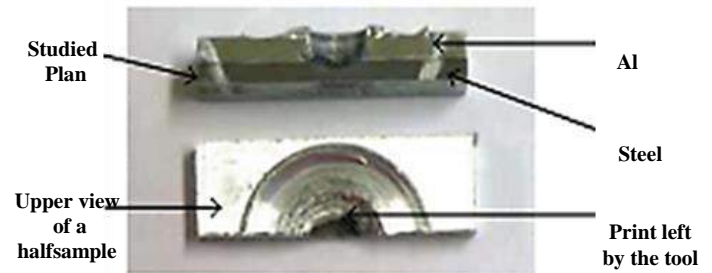


Fig. 3 Photography of a cut sample, which shows the studied plan of the welds [11].

Therefore, the principal welding parameters are the rotation speed of the tool, the effort of welding, and the dwell time, which corresponds to the time during which the tool stays in rotation at the bottom of the weld and the geometry and the material used to machine the FSW tool. This study had the aim to understand the influence of the dwell time on the microstructure around the weld. So, to conclude, an intermediate dwell time value gives a good compromise between a sufficient width of the hanging and limited intermetallic compounds formation, in order to optimize the mechanical resistance.

Chen et al [18], joined 1 mm thick 6111-T4 Al and DC04 low carbon steel sheet. The tool had 11 mm diameter steel shoulder, with a scroll profile to improve the flow of material, and a tapered 3 mm diameter WC 1 mm long probe. The radius of the probes orbital path was 2.5 mm, which produced a swept area of 8 mm diameter on the steel surface. As a result, They produced high quality FSSW between thin Al and steel

automotive sheet within a weld time of 1 second which is a desired goal time by industries.

Sun et al [19], successfully joined the 6061-T6 Al alloy and mild steel plate with a thickness of 1 mm by the flat FSSW method, which contains two steps during the entire welding process. No obvious intermetallic compound layer was observed along the Al/Fe interface after the first and second welding steps. The use of tool with different probe length shows little effect on the weld properties, which can significantly increase the tool life and therefore the manufacturing cost. After welding, the appearances of the all the welds are very similar regardless of the use of different probe length. As a typical example, Fig. 4 shows the appearance of the welds produced by this flat FSSW. After the first step, a keyhole can be observed on the top side of the upper Al alloy sheet, which looks similar to that formed in conventional FSSW processed materials. However, on the bottom surface of the lower steel sheet, a protuberance was formed just below the keyhole due to the flow of the materials into the dent on the back plate. After the second step, the keyhole and the protuberance were completely removed by using a rotating tool without probe. The surfaces on both sides of the weld thus became very smooth. Only a little flash formed around the edge of the stir zone and can be easily removed.

Fig. 5 shows the typical cross-sectional macrostructure of the samples produced with the different rotating tools. After the first step, all the samples show a keyhole on the upper Al alloy sheet and a protuberance on the lower steel sheet. However, the depth of the keyhole becomes larger with the increase of the probe length. As a result, the thickness of the Al alloy sheet beneath the keyhole decreased from 0.76 mm when a 1 mm long probe was used to 0.41 mm when a 1.5 mm long probe was used. However, the shape and thickness of the lower steel sheets are almost equal to each other when different probe lengths were used. After the second step, the macrostructures of the stir zone are quite similar regardless of the different macrostructures formed in the first step. The thickness of the upper Al alloy sheet is almost same for all the samples welded with the different probe lengths in the first step [19].

A study by Tanaka; et. al. [20] provides some performance data regarding FSSW joints between aluminum and steel. For the study a6xxx series aluminum was used with a thickness of 1.0 mm. This was joined to a cold rolled carbon steel sheet with a thickness of 0.7mm. The best result for the described joint was 3.6 kN in lap shear. Although the process has been demonstrated to successfully join aluminum to steel, the joint strengths are not spectacular. This limits the processes applications to those that do not require high strength. A better performing technology for joining aluminum and steel is still desirable, especially for structural applications where strength is a top priority.

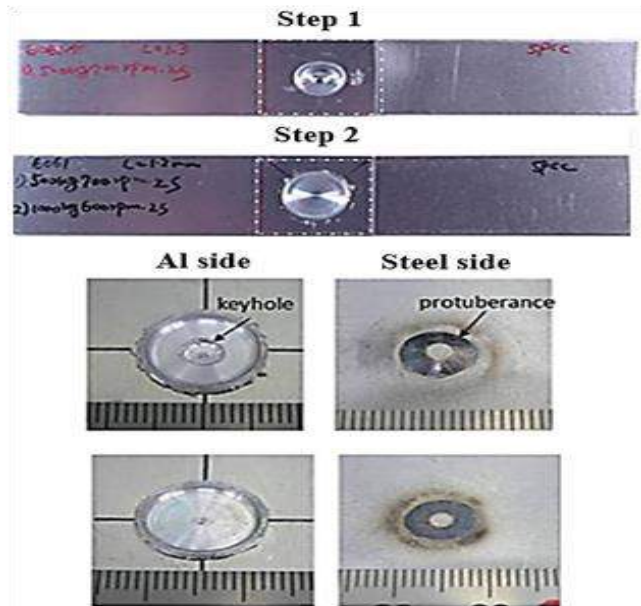


Fig. 4 Appearance of the welds after the first step and the second step [19].

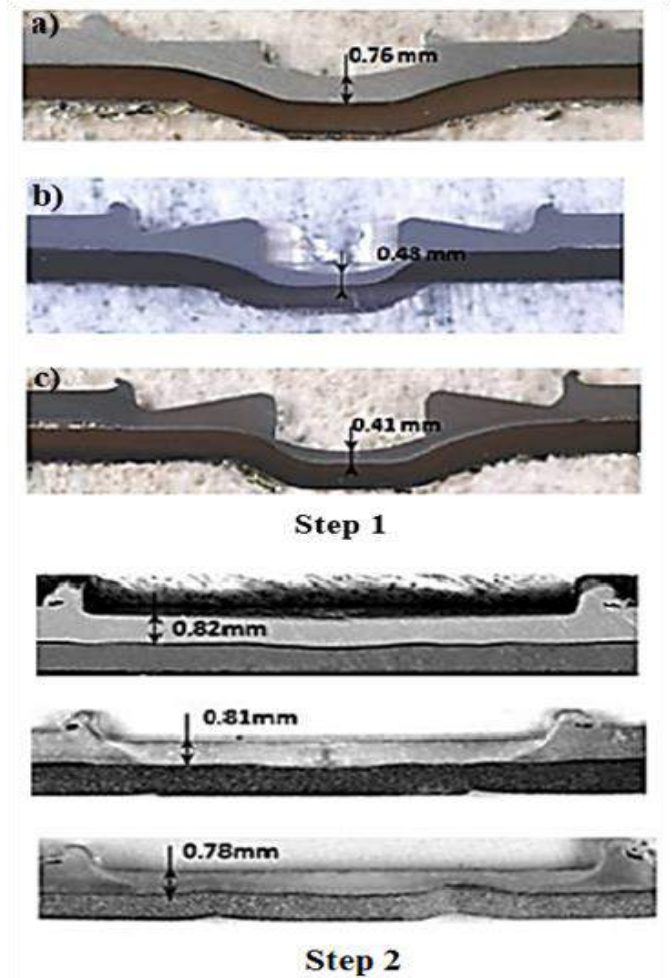


Fig. 5 Cross-sectional macrostructure of the welds after the first and second steps. (a) Probe length = 1.0 mm; (b) probe length = 1.3 mm; (c) probe length = 1.5 mm [19]

B. FSSW of Aluminium Alloys

A. Gerlich et. al. [21], joined the factors determining the temperature, heating rate, microstructure, and strain rate in Al 7075-T6 friction stir spot welds produced using different tool rotational speed settings were investigated. The following conclusions can be drawn from this research. The average crystallite dimensions within the stir zone were negligibly affected when the dwell time increased from 1 to 4 seconds; there was also no evidence of grain growth when Al 7075-T6 spot welds cooled to room temperature. The temperature exceeds the reported solidus temperature of Al 7075-T6 material (475 °C) in spot welds made using tool rotational speeds from 1500 to 3000 rpm. The highest temperature during friction stir spot welding (527 °C) was observed in spot welds made using a tool rotational speed of 3000 rpm and a dwell time of 4 seconds. Transient local melting and tool slippage occur at the contact interface between the periphery of the rotating tool and adjacent material in the stir zone when the cycle time, tool rotational speed, and dwell time produce high heating rates and temperatures during the spot welding operation. In contrast, transient local melting and tool slippage does not occur no matter the dwell time, which is applied when Al 7075-T6 sheet is spot welded using a rotational speed of 1000 rpm.

Huijie Liu et. al. [22], joined the 2A12-T4 aluminum alloy was friction stir spot welded, and the microstructural characteristics and mechanical properties of the joints were investigated. They were used 2A12-T4 aluminum alloy sheets with 3mm thickness as the base material.

Microstructural characteristics and mechanical properties of friction stir spot welded 2A12-T4 aluminum alloy were investigated, and the conclusions can be drawn as follows. The area of complete bonding region at the interface increased with the welding heat input because more interface metals were mixed. A softened microstructural region existed in the joint, and it consisted of SZ, TMAZ, and HAZ. The minimum hardness was located in the TMAZ. The tensile shear failure load of the joint increased with increasing rotation speed from 400 to 1000 rpm.

In study of Patel, V. V. et. al. [23], are performed FSSW of AA5052-H32 and AA6082-T6 dissimilar aluminum alloys at three different tool rotations specifically 1500, 1070, and 765 rpm. The objective of the present investigation to find influence of tool rotational speed on tensile-shear, microstructural, and micro indentation hardness properties of FSSW of dissimilar Al-alloy sheets AA5052 H32 and AA6082-T6. FSSW welds were created of AA5052-H32 and AA6082-T6, with both the aluminum plates being 1.5 mm thick each. After comparing the results for FSSW, it is clear that higher rotational speed was preferred for FSSW. The similar trend can also be seen for micro indentation hardness. To finally conclude, higher rpm FSSW process is superior compared to lower rpm FSSW process, which has been proved on the basis of satisfactory test results.

FSSW was applied to join the 6061-T4 aluminum alloy sheet with 2 mm thickness by Zhikang Shen et. al. [24]. All of the specimens are welded in the center of the overlap area. In this study, the microstructure and mechanical properties of

friction spot welded 6061-T4 aluminum alloy have been investigated and the main conclusions can be made as follows: There exists change of grain size in the width and thickness direction due to the difference in strain rate of the material. Furthermore, material flow model has been built based on the principle of FSSW and the characteristics of the microstructure. The hardness profiles of the welds exhibit a W-shaped appearance and the minimum hardness was measured on the periphery of the pin. Both the tensile/shear and cross-tension strength reached the maximum of 7117.0 N and 4555.4 N, respectively. Three different fracture modes have been observed under both tensile/shear and cross-tension loadings: plug type fracture, shear fracture and plug-shear fracture under tensile/ shear loadings, and plug type fracture (on the upper sheet), nugget debonding and plug type fracture (on the lower sheet) under cross tension loadings.

Fig. 6a and b, reveal the close-up top view and cross section of the weld made at the welding condition of the rotational speed of 1500 rpm and dwell time of 3s. The magnified views of the regions A and B marked in Fig. 6b are revealed in Fig. 6c. As shown in Fig. 6c, the approximate boundary between SZ, TMAZ and HAZ can be easily distinguished (indicated by black solid line). The grains in the regions SZ and TMAZ are much finer than those in BM. The HAZ only experiences a weld thermal cycle, inducing the coarse grains than those in BM, especially in the thickness direction, or more precisely, the grain sizes of HAZ and BM are about 22 and 17 μm , respectively. It is also important to highlight that there exists variations of grain size in the width and thickness directions in the SZ, in other words, the grains in regions C and D are much finer than those in the center (see in Fig. 6c)

As shown in Figs. 7a and b, the appearance of bonding ligament is rather different between the center and edge. More precisely, the bonding ligament presents an inclined zigzag appearance on the edge, whose orientation is in good agreement with that of materials' flow. However, the bonding ligament presents banded structure due to symmetric flow of the materials and the downward force in the joint. The hook diminishes the integrity of the joint because crack can propagate along the hook when the weld is subjected to external loading. As shown in Fig. 7d, the retractable line (indicated by white dotted line) is located at the path through which the sleeve plunges into the upper sheet, and the materials there undergo more plastic deformation compared to those around because of higher linear velocity at the periphery of the sleeve. Hence, the grains are much finer, where the crack initiation is more possible due to the drastic change of microstructure [24].

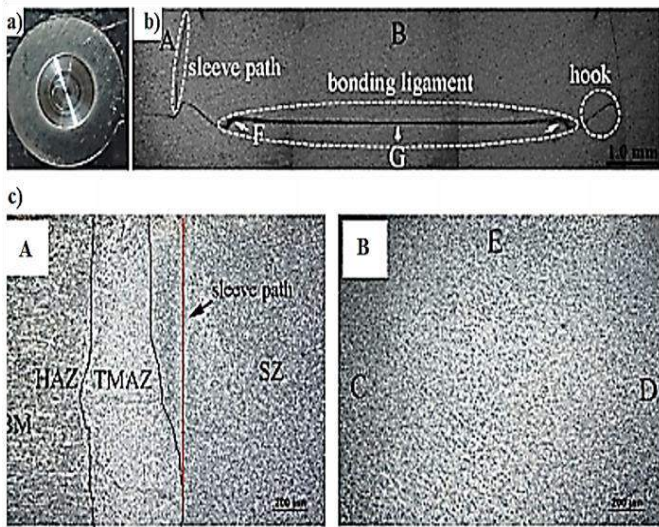


Fig. 6 Macroscopic appearance of and microstructure of FSSW joint made at welding condition of the rotational speed of 1500 rpm and dwell time of 3 s: (a) top view of weld zone, (b) cross section of weld zone and (c) magnified views of the regions A-B marked in b [24].

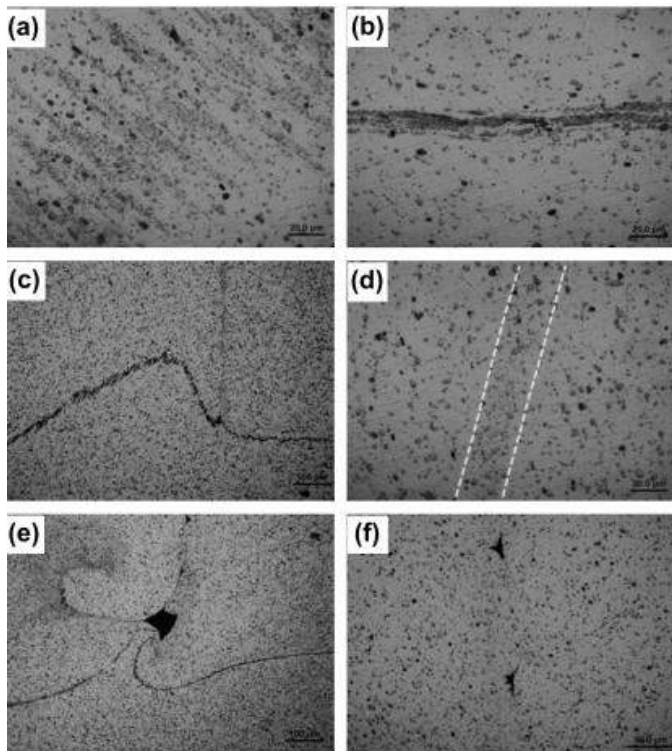


Fig. 7 Characteristics of the defects of the joint: (a) bonding ligament (magnified view of region F in Fig. 4b), (b) bonding ligament (magnified view of region G in Fig. 6 b), (c) hook, (d) retractable line, (e) voids on the hook and (f) voids on e retractable line [24].

M. Kulekci and O. Er [25], joined the AlMg1 aluminum sheets with a thickness of 1.5 mm with optimum welding parameters. Optimum welding parameter levels for these connections; tool plunge depth of 2.6 mm, tool rotational speed of 1500 rpm and dwell time of 10s. As a result of this study, it has been determined that the team diving distance has the most important effect on the point source connection. It has been

observed that the cutting shear strength of the welded joint is also increased in direct proportion to the increase of the tool plunge distance. It has been observed that the welding performance improves in proportion to the increase of the tool plunge distance. However, this definition applies to parameter values in the range of two different tool plunge distances used in the study. When the inter parameter interactions are examined, it is seen that the most important interactions are the interactions between tool plunge distance - welding time and tool turnover time. It has been determined that the effect of welding time on shear force depends on the level of tool plunge distance. However, it has been observed that depending on the level of the source when the effect of the transfer of shearing forces on the cutting tool.

C. FSSW of Aluminium and Copper Alloys

R. Kaçar et. al [8], joined AA5754 aluminum sheet couple using interlayer copper by FSSW. In this study was used 1000 and 1600 rpm tool rotation speed for 3 and 5 second time intervals. FSSW method combined with Al-Cu-Al tensile shear load carrying capacity of the samples was found to increase with increasing tool rotation speed and dwell time. The tensile shear load carrying capacities of a pair of Al-Cu-Al materials joined using a copper interlayer were found to be higher than the Al-Al joints obtained with the same weld parameters without the use of a copper interlayer. Al-Cu-Al bonding has been found to increase the hardness along the aluminum copper interface.

Heideman et al [26], joined between a 1-5 mm 6061 Al-T6 sheet and a 1-5 mm Cu sheet by FSSW. The tools used a threaded pin design using a prehardened H13 tool steel. The shoulder diameter, pin diameter and thread pitch were held constant at 10, 4 and 0-7 mm respectively. The shoulder geometry was concave shaped. They found this results. The rotation speed had the most significant effect on the weld strength, which increases with increasing rotation speed. The average weld strength also increases with increasing pin length. The Cu ring promoted interlocking and bonding between the two sheets. The interface between the Cu ring and the surrounding Al was free from intermetallics.

D. FSSW between Aluminium and Magnesium

Suhddin et al [27] successfully joined Al alloy AA5754 to Mg alloy AZ31. The materials used for welding were 2 mm thick Al alloy AA5754 and Mg alloy AZ31 sheets. The welding parameters included a tool rotational speed of 1900 rpm, a sleeve plunge depth of 1.6 mm, a dwell time of 2 s and a clamping force of 12 kN. In the present study, they measured the thermal cycling behavior during the dissimilar friction spot welding of AA 5754/AZ31. The plastic deformation and high-temperature exposure induced the grain boundary diffusion and the interfacial diffusion, thus local melting occurred. Liquefaction and solidification occurred repeatedly, resulting in a non-equilibrium solidus temperature. During the sleeve retraction period, the "solid-liquid" phase material experienced further diffusion and dynamic recrystallization, resulting in the formation of the fine equiaxed Al17Mg12 grains at the weld center.

Chowdhury et al [28], used FSSW process to join commercial AZ31B-H24 Mg and AA5754 with a thickness of 2 mm. The FSSW tool made from H13 tool steel had diameters of 13 mm for the scrolled shoulder and 5 mm for the left-hand threaded pin. The welding process parameters were: pin length of 2.8 mm, tool rotational speed of 2000 rpm, tool plunge rate of 3 mm/s, tool removal rate of 15 mm/s, shoulder plunge depth of 0.2 mm and dwell time of 2 s. After FSSW the elongated grains in the base Mg alloy became equiaxed as a result of dynamic recrystallization in the SZ of the Mg/Mg similar weld, with partial recrystallization occurring in the TMAZ and HAZ. Both Mg/Mg and Al/Al similar welds had significantly higher lap shear strength and failure energy than the Al/Mg dissimilar weld. While the fatigue life of the Al/Al similar weld was generally higher than that of the Mg/Mg similar weld, both the Al/Al and Mg/Mg similar welds had a much longer fatigue life than the Al/Mg dissimilar weld especially at higher cyclic load levels.

IV. CONCLUSIONS

FSSW welding method developed to solve the problems in FSW has attracted considerable attention. In this study, A literature study on the FSSW method of different metals was performed. These studies have been made around the world and have shown positive results. But, more researches need to be further conducted to fully understand and optimize the FSSW process. FSSW research between Al and Cu is limited. For this reason, it is ocured that they paid no attention about this case. Apart from the tool geometry in the FSSW method, the tool rotational speeds, tool plunge depth, tool tilt angle and dwell time are important parameters and the lap shear tensile load has an important effect. It is expected that if the process is applied efficiently, it can be a technical and economical process compared to the traditional welding processes.

ACKNOWLEDGMENT

The authors are deeply grateful for the financial support of Marmara University Directorate of Health, Culture and Sports.

REFERENCES

[1] H.Kafalı, and N. AY., "Sürtünme Karıştırma Kaynağıyla Birleştirilmiş Havacılık Ve Uzay Yapılarında Kullanılan Al 6013-T6 Alaşımının Mikroyapı ve Mekanik Özelliklerinin İncelenmesi." Journal of Aeronautics & Space Technologies/Havacılık ve Uzay Teknolojileri Dergisi, vol. 7, issue: 2, pp. 85-101, 2014.

[2] Ş. Mert, and S. Mert "Sürtünme karıştırma nokta kaynak yönteminin incelenmesi." İleri Teknoloji Bilimleri Dergisi vol. 2, issue:1, pp. 26-35, 2013.

[3] Yang, X. W., T. Fu, and W. Y. Li. "Friction stir spot welding: a review on joint macro-and microstructure, property, and process modelling." Advances in Materials Science and Engineering, vol.2014, pp.1-11, 2014

[4] Su, P., et al. "Intermixing in dissimilar friction stir spot welds." Metallurgical and materials transactions A vol.38.3 (2007), pp. 584-595.

[5] Patel, Vivek V., et al. "Effect of tool rotation speed on friction stir spot welded AA5052-H32 and AA6082-T6 dissimilar aluminum alloys." Metallography, Microstructure, and Analysis vol.5(2) (2016), pp.142-148.

[6] E. Kalunç, E. Taban, "Otomobil endüstrisinde direnç nokta kaynağına alternatif bir yöntem: Sürtünen elemanla nokta kaynağı", Kaynak

Teknolojisi VI Ulusal Kongresi ve Sergisi, TMMOB, 9-10 Kasım 2007, pp.51-60

[7] N. Kahraman,, B. Yılbaş,, D. Odabaşı, "H 2210 çeliği ile alüminyum sürtünme kaynağı ile işleme ve kaynak parametrelerinin kaynak üzerine etkilerinin deneysel olarak araştırılması", 6. Denizli Malzeme Sempozyumu, Denizli, 1995,

[8] R. Kaçar,, et al. "Al-Cu-Al Malzeme Çiftinin Sürtünme Karıştırma Nokta Kaynak Kabiliyeti." Gazi Üniversitesi Mühendislik-Mimarlık Fakültesi Dergisi vol.26.2 (2011), pp. 1-354-356

[9] Y. Bozkurt, S. Salman, G. Cam, Effect of welding parameters on lap shear tensile properties of dissimilar friction stir spot welded AA 5754-H22/2024-T3 joints, Science and Technology of Welding and Joining, 2013, vol.18 (4), pp. 337-345

[10] H. Badarinarayan,, Q. Yang, and S. Zhu 'Effect of tool geometry on static strength of friction stir spot-welded aluminum alloy', International Journal of Machine Tools and Manufacture, 2009.vol. 49(2), pp. 142-148.

[11] S. Bozzi,, et al. "Mechanical behaviour and microstructure of aluminum-steel sheets joined by FSSW." Texture, Stress, and Microstructure 2008 pp. 2-7-8

[12] Feng, Z., et al. High strength weight reduction materials-friction stir welding and processing of advanced materials. Oak Ridge National Laboratory Report DE-AC05-00OR22725, 2004.

[13] Kawasaki Heavy Industries Ltd., (2006). A new method for light alloy joining - friction spot joining - kawasaki robot, Japan, www.kawasakirobot.com, visit date: 18 March 2006.

[14] Fena, Z., et al. "Friction stir spot welding of advanced high-strength steels: A feasibility study." SAE transactions vol.114.5 (2005) pp. 592-598.

[15] S. Lathabai., M. J. Painter, G. M. D Cantin., and V. K Tyagi., (2006). Friction spot joining of an extruded Al-Mg-Si alloy, Scripta Materialia, vol. 55, pp.899-902.

[16] Kimberley, W., (November 2005). Joining up, Focus Manufacturing, vol.36.

[17] J. Hinrichs,, (2006). Friction Stir Spot Welding, Friction Stir Link Inc.,www.frictionstirlink.com, visit date: 21 March 2006

[18] Chen, Y. C., A. Gholinia, and P. B. Prangnell. "Interface structure and bonding in abrasion circle friction stir spot welding: a novel approach for rapid welding aluminium alloy to steel automotive sheet." Materials Chemistry and Physics 134.1 (2012): pp.459-463.

[19] Sun Y.F., Fujii H., Takaki N., Okitsu Y. "Microstructure and mechanical properties of dissimilar Al alloy/steel joints prepared by a flat spot friction stir welding technique" Materials and Design vol.47 (2013), pp. 350-357.

[20] Tanaka, Koji, Masaki Kumagai, and H.Yoshida. "Dissimilar joining of aluminum alloy and steel sheets by friction stir spot welding." JOURNAL-JAPAN INSTITUTE OF LIGHT METALS vol.56.6 (2006), pp. 317.

[21] A Gerlich,, G. Avramovic-Cingara, and T. H. North. "Stir zone microstructure and strain rate during Al 7075-T6 friction stir spot welding." Metallurgical and Materials Transactions A vol.37.9 (2006), pp. 2773-2786.

[22] Liu, Huijie, et al. "Microstructural characteristics and mechanical properties of friction stir spot welded 2A12-T4 aluminum alloy." Advances in Materials Science and Engineering vol.2013, pp.2-9.

[23] Patel, V. V., Sejani, D. J., Patel, N. J., Vora, J. J., Gadhvi, B. J., Padodara, N. R., & Vamja, C. D. Effect of tool rotation speed on friction stir spot welded AA5052-H32 and AA6082-T6 dissimilar aluminum alloys. Metallography, Microstructure, and Analysis, vol.5(2), (2016). pp. 142-148.

[24] Shen, Zhikang, et al. "Microstructure and mechanical properties of friction spot welded 6061-T4 aluminum alloy." Materials & Design (1980-2015) vol.54 (2014), pp. 766-778.

[25] Külekçi, M. Kemal and E. R. Onur. "Sürtünme Karıştırma Nokta Kaynaklı En Aw-5005 (AlMg1) alüminyum alaşımı için optimum kaynak parametre Seviyelerinin Belirlenmesi." Gazi Üniversitesi Mühendislik-Mimarlık Fakültesi Dergisi vol.27.3 (2012).

[26] R. Heideman., C. Johnson, S. Kou, 'Metallurgical analysis of Al/Cu friction stir spot welding' Science and Technology of Welding and Joining vol.15(7), 2010, pp. 597-604.

- [27] U.F.H Suhuddin., V. Fischer and dos Santos J.F., "The thermal cycle during the dissimilar friction spot welding of aluminum and magnesium alloy" *Scripta Materialia* vol.68 (2013), pp. 87-90.
- [28] S.H Chowdhury., D.L. Chen, S.D Bhole, X. Cao., P. Wanjara., "Lap shear strength and fatigue life of friction stir spot welded AZ31 magnesium and 5754 aluminum alloys" *Materials Science& Engineering A* vol.556, pp. 500-509, 2012.

Effect of Chromium on the Boronizing Behavior of Iron

Mehmet Tarakci*, Yucel Gencer⁺

**Department of Materials Science and Engineering Gebze Technical University
41400 Gebze, Kocaeli, Turkey
mtarakci@gtu.edu.tr (Corresponding author)*

*⁺Department of Materials Science and Engineering Gebze Technical University
41400 Gebze, Kocaeli, Turkey
gencer@gtu.edu.tr*

Abstract— In this study, the boronizing of Fe-Cr binary alloys (2, 4, 8 at. % Cr) was investigated by pack boronizing treatment at 1100°C for 3 hours. Fe-Cr binary alloys were prepared under controlled atmosphere. The characterization of the borided alloys was carried out XRD, SEM, SEM-EDS and Vickers microhardness measurements. The boride layer on the Fe-Cr alloys was composed of Fe₂B phase. The saw tooth morphology changed to a smoother interface layer (coating-substrate), the boride layer thickness decreased while microhardness did not change significantly with chromium content in the Fe-Cr alloys. The Cr-rich precipitates formed in the transition zone and their amount increased with increasing amount of the chromium in the substrates.

Keywords— Fe-Cr alloy, boronizing, iron boride, microhardness, Fe₂B

I. INTRODUCTION

Steels with different chemical compositions were boronized and it was reported that alloying elements is one of the parameters effecting boride layer properties formed on steels by boronising which is a thermochemical process applied ferrous and some non-ferrous metallic materials. In addition to the chemical composition of the substrate, boronising method, temperature and duration of the process were also critical parameters for the boronizing treatment [1-8]. To investigate the effect of the chemical composition of the substrate on the boronizing behavior of Fe based materials, various systematical studies were carried out. For the purpose binary Fe-M Alloys (M=C, Ti, Cu, V, Mn, Ni, Si, W, Mo, Co) were prepared and boronised [5-7, 9-17]. Since, chromium is one of the most important alloying elements in tool steels and stainless steels, binary Fe-Cr Alloys were also boronised to reveal the effect of Cr on the boronizing behavior of steel [9]. However, the studies on Fe-Cr were based on single composition of Cr in the boronised alloys at different temperatures up to 1000 °C and different duration of the process. Brakman et al. have reported that chromium was distributed almost homogenously in the boride layer formed and the boride layer hardness increased with the addition of chromium in the substrate [5].

In this study, a systematical investigation was carried out to reveal the individual effect of different amount of chromium addition into pure iron on formed boride layer properties. For the purpose, firstly, synthetic Fe-Cr alloys with Cr content of 2, 4, 8 at.% were prepared under controlled atmosphere. Then, these Fe-Cr alloys were pack boronised at 1100 °C for 3 h and characterized by XRD, SEM, SEM-EDX and microhardness measurements.

II. EXPERIMENTAL STUDY

The experimental studies on the boronising behavior of synthetically prepared Fe-Cr binary alloys are composed of three basic steps; Preparation of substrates, pack boronising of the substrates and the characterization of the borided Fe-Cr alloys.

A. Preparation of Fe-Cr Alloy Substrates

Fe-Cr binary alloys with 2, 4, 8 at. % Cr were prepared using 99.97% purity Fe and 99.8% purity Cr pieces in an arc melting system under controlled atmosphere. These alloys are named as Fe-2Cr, Fe-4Cr and Fe-8Cr, respectively. Fe-Cr binary alloys produced at sizes of 50 x 10 x 10 mm³ were sliced to be at sizes of 10 x 10 x 5 mm³ samples. These samples were then abraded with silicon carbide (SiC) sand and polished with diamond paste.

B. Pack Boronizing of Fe-Cr Alloys

Polished Fe-Cr binary alloys were buried in the crucible filled with commercial Ekabor 2 boronising powder. In order to prevent the samples from being oxidized during the pack boronising process, the crucible lid was tightly closed by adding antioxidant powder to the crucible. The furnace was heated to 1100 ± 5 °C at a rate of 30 °C / min, and subjected to pack boronising at this temperature for 3 hours after the crucible containing the Fe-Cr samples therein was placed in the furnace. Following the boronising process, the samples were cooled to 300 °C in the furnace at a rate of 100 °C / min and then cooled to room temperature outside the furnace. After removing the borided samples from the crucible, the possible dust residues on the samples were mechanically cleaned.

C. Characterization of Borided Fe-Cr Alloys

XRD phase analysis of the borided Fe-Cr samples was carried out using Bruker D8 X-ray diffractometer with Cu-K α ray scanning angle by selecting the angles between 20° and 100°. The borided samples were analyzed from the surface. The XRD pattern was obtained by using the X'Pert High Score Plus software on the PC. For further XRD phase analysis was carried out after grinding and removing approximately half of the borided layer on Fe-8Cr. Then, the boronized Fe-Cr samples were sliced into two pieces with precision diamond saws and mounted using cold resin so that their cross-sections appeared. The samples were ground and polished so that a cross-section view of these samples was exposed. In order to determine the microhardness values of the coatings, the microhardness change along the thickness of the coating from the coating surface to the substrate was measured by employing Mitutoyo Vickers microhardness tester by application of a 25 g load for 10 seconds. After the optical microscope (OM) examination was performed, more detailed microstructural examination of the cross section of the borided samples were made using Philips XL-30 SEM. Boride layer thickness measurements were made on the obtained SEM micrographs. The chemical analyzes were also performed with SEM equipped with Energy Dispersive Spectrometer (EDS).

III. EXPERIMENTAL RESULTS

A. Coating Thickness

Fig. 1 shows the variation of the boron layer thickness on the surface of boronized Fe-Cr binary alloys depending on the increasing amount of Cr. When the graph is examined, it is seen that the thickness of the coating decreases almost linearly with some scatters by increasing amount of Cr in the substrates. The maximum thickness of the dense boride layer obtained on Fe-2Cr as approximately 180 μm while the minimum thickness formed on Fe-8Cr as approximately 120 μm .

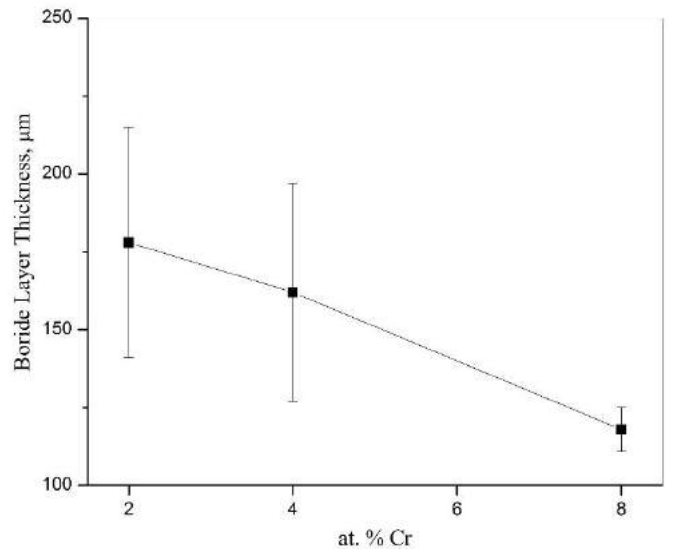
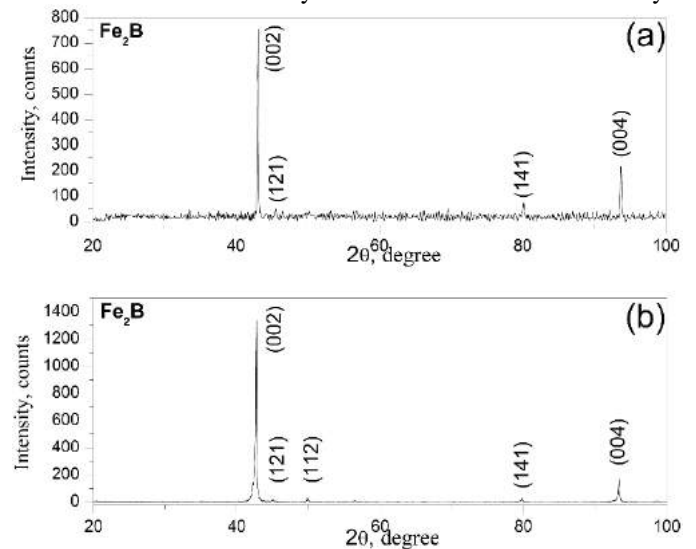


Fig. 1 The change in boride layer thickness with Cr in Fe-Cr alloys

B. Phase Analysis

XRD spectra of the borided Fe-Cr binary alloys from their surfaces are given in Fig. 2. Only Fe₂B phase is formed on the surface of all boronized Fe-Cr alloys and it is understood that this phase are composed of boride crystals having different orientations while it seems there is a preferential growth the Fe₂B crystals, as there is very strong peak from (002) plane. Furthermore, the XRD analyses from the surface of the ground surface of borided Fe-8Cr confirmed that the only phase in the boride layer was Fe₂B. Any phase belongs to Cr-B was not detected by XRD analysis, neither from the outer surface nor from the inside of boride layer formed on borided Fe-Cr alloys.



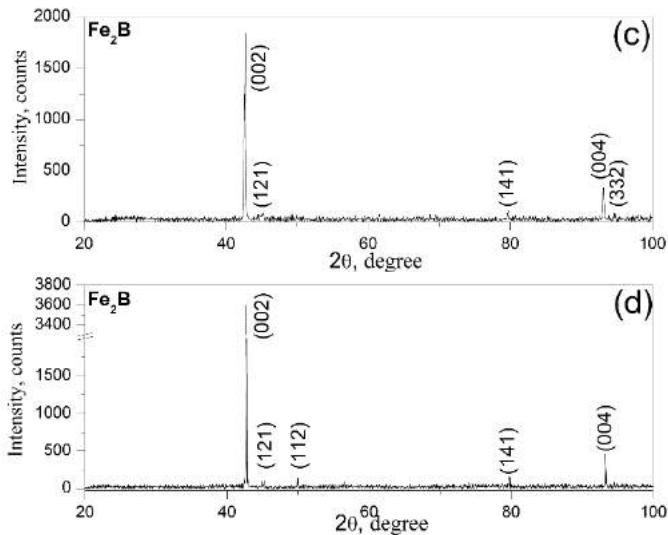


Fig. 2 The surface XRD spectrums of the boride layer on Fe-Cr alloys; (a) Fe-2Cr, (b) Fe-4Cr, (c) Fe-8Cr and (d) Fe-8Cr (ground)

Cross sectional SEM micrographs of borided Fe-Cr alloys having 2, 4 and 8 at. % Cr are given in Fig. 3. When looking at the boride layer formed on the surface of borided Fe-2Cr and Fe-4Cr, it is obvious that the main boride layer (Region I) has a single-color appearance and has saw tooth morphology (Fig. 3a-b). In addition, it is observed that there are pores in the boride layer and the amount of pores in the layer is high especially near the surface. It is evident when the Cr content is increased and the saw tooth morphology is diminished and rather compact boride layer formed on Fe-8Cr. It is also seen from the micrographs that increase in Cr in the substrates resulted in the formation of precipitates (Region II) which grow randomly towards the substrates. Further increase of Cr in the substrates these precipitates form a network like structure. The region (II) with these precipitates is usually called as transition zone.

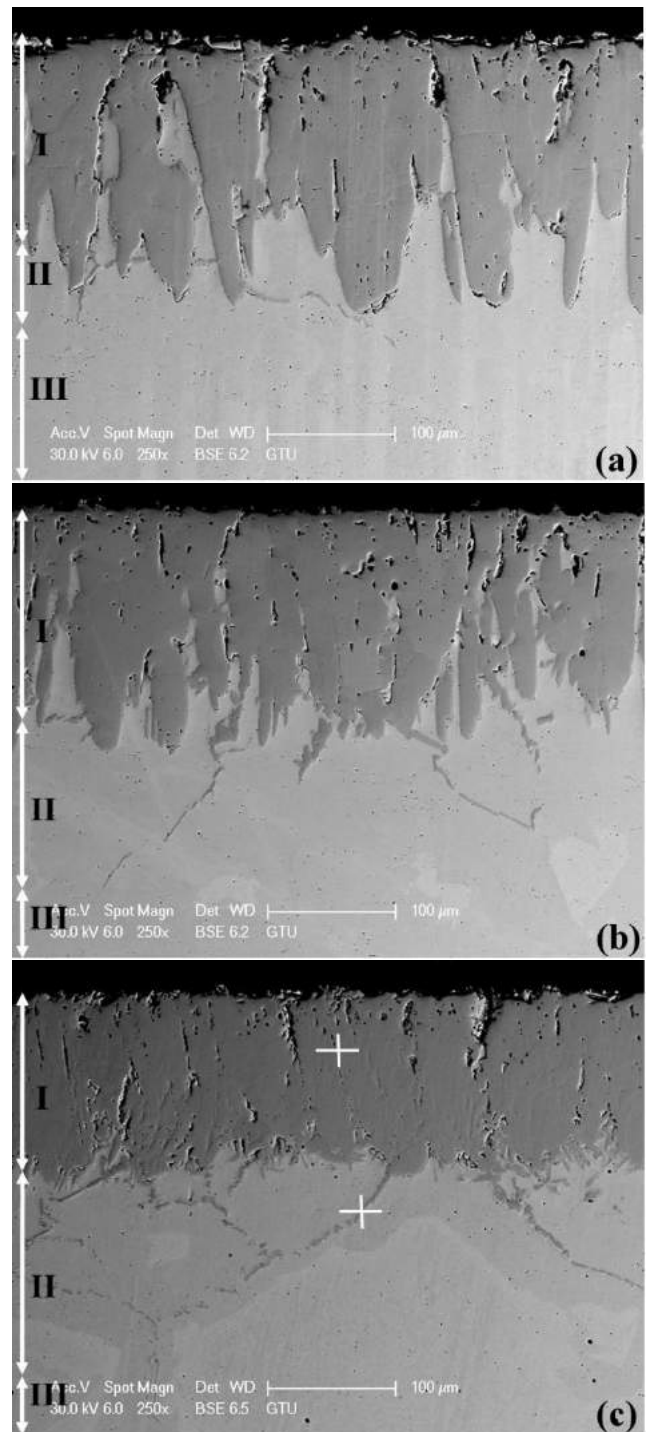


Fig. 3 Cross sectional SEM micrographs of borided Fe-Cr alloys (a) Fe-2Cr, (b) Fe-4Cr, and (c) Fe-8Cr

C. SEM-EDS Analysis

The typical SEM-EDS spectra obtained from the regions marked I (main boride layer) and II (precipitates in the transition zone) on the cross-sectional SEM image of Fe-8Cr in Fig. 3c are given in Fig 4. When the SEM-EDS results of I and II regions (Figs. 4 (a) and (b)) are examined, the presence of the iron, boron and chromium elements is evident. The chromium composition in II regions is relatively higher than that of in

region I. As chromium is evenly distributed along the main boride layer according to SEM-EDS results, only a typical spectra obtained from the main boride layer was given.

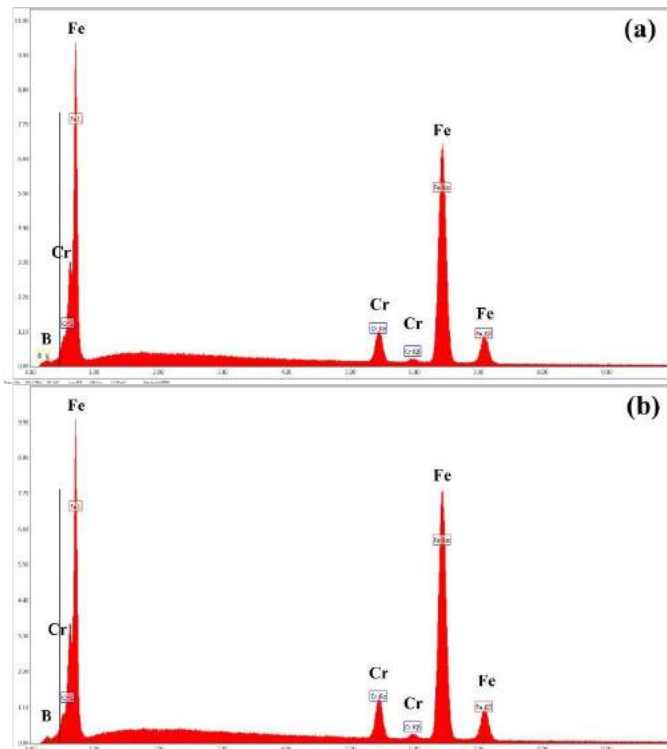


Fig. 4 SEM-EDS spectrum for Fe-8Cr alloy: (a) Area I, and (b) Area II in Fig. 3c

The typical SEM-EDS spectra obtained from the regions marked I (main boride layer) and II (precipitates in the transition zone) on the cross-sectional SEM image of Fe-8Cr in Fig. 3c are given in Fig. 4. When the SEM-EDS results of I and II regions (Figs. 4 (a) and (b)) are examined, the presence of the iron, boron and chromium elements is evident. The chromium composition in II regions is relatively higher than that of in region I. As chromium is evenly distributed along the main boride layer according to SEM-EDS results, only a typical spectra obtained from the main boride layer was given.

D. Microhardness

The change from the substrate to the surface of the boride layer depending on the distance from interface is shown in Fig. 5 for borided Fe-Cr alloys. Boride layer microhardness varies between 1200 HV and 2050 HV, while substrate hardness value varies approximately between 150 HV and 250 HV. It is understood that there is a scattering in the boride layer hardness values and there is no change depending on the amount of Cr in the substrates. For all alloys there is a sudden decrease in microhardness values from the boron layer to the substrate and there is no transition zone in terms of microhardness values.

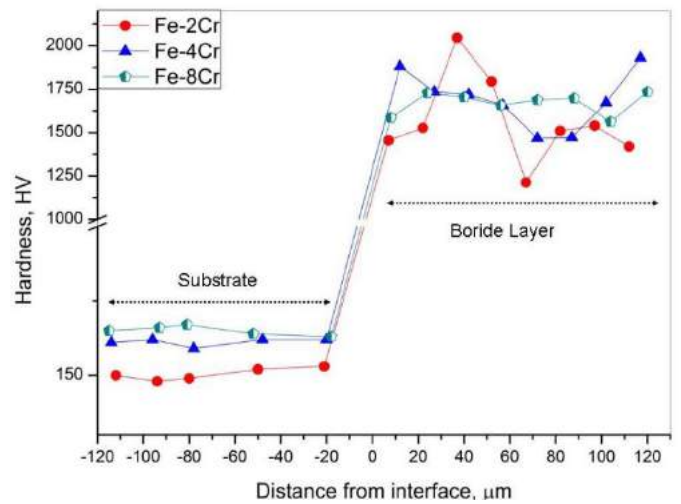


Fig. 5 Microhardness profile from the substrates towards the boride layer surface for the borided Fe-Cr alloys

IV. DISCUSSION

Homemade Fe-Cr binary alloys with 2, 4, 8 at. % Cr were boronized at 1100°C for 3 h and then characterized after boronizing treatment. Highly oriented Fe_2B phase was the main phase constituents of the main boride layer. Usually, Fe_2B and FeB phases are the main constituents of the borided iron base materials though sometimes only Fe_2B phase forms depending on experimental parameters such as boron potential, duration and temperature of the treatment and chemical composition of the substrate [1, 3-7, 9, 12, 13, 17]. Actually, the single phase of Fe_2B formation is preferred, as two-phase (FeB and Fe_2B) boride layer creates crack due to their thermal expansion coefficient difference [11]. The addition of Cr to the substrate did not result in formation of any phase belongs to Cr-B in the boride layer formed on borided Fe-Cr alloys. However, SEM-EDS analysis revealed the presence of evenly distribution of Cr in the layer. This finding is parallel to the results noted by Brakman et al. as they reported that chromium had distributed almost homogeneously in the boride layer with the addition of chromium in the substrate [5]. The increase in Cr in the substrates resulted in the formation of precipitates which grow randomly towards the substrates and additional increase of Cr in the substrates the precipitates form a network like structure in the transition zone. Because, as the enrichment of grain boundaries by Cr element in Fe-Cr alloy resulted in these Cr rich precipitate (Fig. 4) formation with the boron diffusion along the grain boundaries which are fast diffusion paths. It has been determined that the microhardness value of the boride layer remains approximately constant with distance from the interface and the dependence of microhardness value on Cr in the substrate is not significant in this study reported the increase in hardness values [5]. This difference may be attributed to their high Cr content in the substrates used. It should be noted that, the microhardness values of the substrates have significantly changed with the addition and increase of Cr in the substrate. It should be noted that the hardness values of iron borides and CrB are similar though some other Cr-B phases have much higher hardness values [18]. The clear effect

of Cr addition into the substrate was seen on morphology of the boride layer as the saw-tooth morphology changed to compact morphology with the addition and increase of Cr in the substrate. The flattening of the saw tooth morphology along with decrease in boride layer thickness may be attributed to the distribution of Cr in the main boride layer. Although this obstructing effect of Cr is not as significant as some other alloying elements such as Ti, Mo, V, W [7, 13, 16, 17].

V. CONCLUSIONS

In this work, binary Fe-Cr alloys containing atomic 2, 4 and 8 Cr were prepared by arc melting method and these alloys were coated with pack boronizing method at 1100°C for 3 hours. The resulting coatings were characterized and the following results were obtained;

1. The saw-tooth morphology boride layer on the substrate materials changed to compact morphology with the amount of Cr in the substrate.
2. The boride layer is composed of only highly oriented Fe₂B phase.
3. The presence of homogeneously distributed Cr in the boride layer was detected.
4. Thickness of the boride layer decreased almost linearly with the increase of Cr in the substrates.
6. It has been determined that the microhardness value of the boride layer remains approximately constant with distance from the interface and the dependence of microhardness value on Cr in the substrate is not significant.

ACKNOWLEDGMENT

Thanks to Zafer Çağatay Öter, Sezgin Cengiz and Yunus Azaklı for their support in experimental works.

REFERENCES

- [1] M. Kulka, A. Pertek, *The importance of carbon content beneath iron borides after boriding of chromium and nickel-based low-carbon steel*, Appl Surf Sci, 214 (2003) 161-171.
- [2] N. Ueda, T. Mizukoshi, K. Demizu, T. Sone, A. Ikenaga, M. Kawamoto, *Boriding of nickel by the powder-pack method*, Surf Coat Tech, 126 (2000) 25-30.
- [3] I. Campos, G. Ramirez, U. Figueroa, J. Martinez, O. Morales, *Evaluation of boron mobility on the phases FeB, Fe₂B and diffusion zone in AISI 1045 and M2 steels*, Appl Surf Sci, 253 (2007) 3469-3475.
- [4] V. Jain, G. Sundararajan, *Influence of the pack thickness of the boronizing mixture on the boriding of steel*, Surf Coat Tech, 149 (2002) 21-26.
- [5] C.M. Brakman, A.W.J. Gommers, E.J. Mittemeijer, *Boriding of Fe and Fe-C, Fe-Cr, and Fe-Ni Alloys - Boride-Layer Growth-Kinetics*, J Mater Res, 4 (1989) 1354-1370.
- [6] M. Carbuicchio, G. Palombarini, *Effects of Alloying Elements on the Growth of Iron Boride Coatings*, J Mater Sci Lett, 6 (1987) 1147-1149.
- [7] K.O. Gunduz, Y. Gencer, M. Tarakci, A. Calik, *The effect of vanadium on the boronizing properties of pure iron*, Surf Coat Tech, 221 (2013) 104-110.
- [8] P. Juijerm, *Diffusion kinetics of different boronizing processes on martensitic stainless steel AISI 420*, Kovove Mater, 52 (2014) 231-236.

- [9] V.I. Dybkov, *Effect of microstructure on the wear resistance of borided Fe-Cr alloys*, Int J Mater Res, 104 (2013) 617-629.
- [10] M.T. Y. Gencer, *50Fe-50Co Alaşiminin Borlanması Ve Karakterizasyonu*, 16th International Materials Symposium IMSP'2016, Denizli, Turkey, 2016.
- [11] Y. Gencer, *Influence of manganese on pack boriding behaviour of pure iron*, Surf Eng, 27 (2011) 634-638.
- [12] M. Tarakci, Y. Gencer, Y. Azakli, U. Sahinturk, *Surface Modification of Fe-8Si Alloy By Boronizing And Its Characterization*, J Fac Eng Archit Gaz, 28 (2013) 645-655.
- [13] Y. Gencer, M. Tarakci, A. Calik, *Effect of titanium on the boronizing behaviour of pure iron*, Surf Coat Tech, 203 (2008) 9-14.
- [14] S. Cengiz, Y. Gencer, M. Tarakci, Y. Azakli, *Influence Of Copper Amount On The Pack Boronizing Behaviour Of Fe-Cu Binary Alloys*, J Fac Eng Archit Gaz, 30 (2015) 339-349.
- [15] Y. Azakli, K.O. Gunduz, M. Tarakci, Y. Gencer, *A Comparative Study on Boride Layer Morphology of Fe-4Co, Fe-4V and Fe-4W Binary Alloys*, Acta Phys Pol A, 127 (2015) 1326-1330.
- [16] Y. Azakli, S. Cengiz, M. Tarakci, Y. Gencer, *Characterisation of boride layer formed on Fe-Mo binary alloys*, Surf Eng, 32 (2016) 589-595.
- [17] M.T. Y. Azakli, *Microstructural characterisation of borided binary Fe-W alloys*, Surf Eng, DOI <http://dx.doi.org/10.1080/02670844.2016.1263712>(2016).
- [18] M.T. Y. Gencer, *Atomik Olarak Eşit Miktarda Demir Ve Krom İçeren Fe-Cr İkili Alaşımın Borlanması*, 16th International Materials Symposium IMSP'2016, Denizli, Türkiye, 2016, pp. 77.

Characterization of Boride Layer Formed on Fe-Ni Alloys

Naim B. Mackan*, Yucel Gencer⁺

*Department of Materials Science and Engineering Gebze Technical University
41400 Gebze, Kocaeli, Turkey
burackmackan@hotmail.com

⁺Department of Materials Science and Engineering Gebze Technical University
41400 Gebze, Kocaeli, Turkey
gencer@gtu.edu.tr (Corresponding author)

Abstract— In this study, Fe-Ni binary alloys containing 1, 2 and 4 at. % Ni were prepared under controlled atmosphere conditions and then these alloys along with pure Fe were pack boronized at 1100°C for 3 h. The boronised samples were characterized by SEM, SEM-EDS, XRD and microhardness measurements. The boride layer with saw-tooth morphology on the substrate materials changed to compact morphology and the branchy structure around the boride crystals was formed with the increasing amount of Ni in the substrates. The main boride layer was composed of FeB and Fe₂B phases with homogeneously distributed Ni in the main boride layer and accumulation of Ni in the boride layer/substrate was detected for the borided samples. Ni addition was ineffective on microhardness and thickness of boride layer while the thickness decreased with high addition of Ni.

Keywords— Iron-nickel, Fe-Ni alloys, iron boride, boronizing

I. INTRODUCTION

Steels are divided into several groups according to their alloying elements, usage and their prominent properties. Alloying elements are added to steels to provide desirable properties. The harsh conditions such as highly corrosive environment and elevated temperatures decrease the performance of the steels [1-5]. Improving the surface properties of the metallic materials instead of changing their bulk properties is more economical and time saving. Boriding is one of the thermochemical processes to enhance the surface properties of the steels. Boriding process provides the high surface hardness, wear resistance and corrosion resistance of steels [1, 6-13]. Although the effects of alloying elements on the boronizing of steel are recognized, the individual influences of alloying additions on the boronizing mechanism of steel are not totally clear yet although some enlightening studies were reported recently. It was reported that the morphology, growth, phase composition, microhardness and thickness of the boride layer were affected by the alloying elements in the steels [7, 12-16]. However, the alloying elements' individual influence on the boronising of steels is not fully understood due to the presence of other alloying elements. To overcome the complex effect that arose due to the other alloying elements in steels, some systematical studies were carried out to reveal the specific effect of some alloying elements by boriding the binary alloys of Fe-M (M = Cr, Ti, Ni, V, Mn, Si, Mo, Cu, W, Co) [1, 6, 8-

11, 17-24]. Brakman et al. studied the boronising kinetic of Fe-Ni alloys with 4 and 10 wt. % (approx. 3.8 and 9.6 at.%) Nickel has been found to concentrate below the boride layer and it enters the main boride layer and in some instances promotes the precipitation of Ni₃B from the FeB layer [18]. It also segregates strongly to the surface from the underlying zone corresponding to the Fe₂B layer. However, this study was not enough to reveal the effect of Ni on boride layer properties with increasing amount Ni in Fe-Ni alloys [12].

In this study, the effect of increasing Ni addition into Fe-Ni on the boride layer properties was investigated. The materials chosen for this purpose were Fe-Ni alloys with 1, 2 and 4 at.% Ni and pure Fe as control group. The samples were pack boronized at 1100 °C for 3 h. The borided samples were characterized by X-ray diffractometer (XRD), scanning electron microscopy (SEM), energy dispersive spectrometer (EDS) and Vickers microhardness measurement.

II. EXPERIMENTAL

Iron and nickel pieces with 99.9 % purity were obtained from Alfa Easer and mixed to produce Fe-Ni alloys with 1, 2, 4 at. % Ni and named as Fe-1Ni, Fe-2Ni, Fe-4Ni, respectively. These alloys were prepared under atmosphere-controlled furnace. The Fe-Ni alloys were sliced to obtain samples with the dimensions of 10 mm × 10 mm × 3 mm. The samples were ground sequentially using 80–800 grit SiC papers, then polished using alumina sol, with a particle size of 3–1 μm. A control group of pure iron sample with the same dimensions was prepared using the same route of the processes. The samples were placed in an alumina crucible and packed with commercial Ekabor II powders (90% SiC, 5% B₄C and 5% KBF). Deoxidant powder was also added on the Ekabor powder to prevent oxidation. After tight sealing with a lid the crucible was heated up to 1100°C in an electrical box furnace. The boronising process was carried out for 3 hours under atmospheric conditions. Then the samples were cooled to room temperature. Right after the cooling process, the borided samples were ultrasonically cleaned in ethanol and dried with warm air. The borided Fe-Ni alloys and the borided pure iron were characterized by XRD to identify the phases of the boride layer formed on the substrates using X-ray diffractometer (Rigaku D-MAX 2200), with a

CuK α radiation over a 2θ range from 20° to 90° . The borided samples were cut into two pieces using a precision diamond saw. One-half of the samples were mounted into epoxy resin. Then metallographically similar to the substrates preparation to examine the cross section of the boride layers formed. Microhardness measurements of the polished samples from their cross section were made using the microhardness tester (Mitutoyo HM220) using applied load of 30 g for 5 seconds. The formed indents were measured during cross-sectional SEM examinations. Philips XL 30 SEM was employed for surface, cross-sectional microstructure examinations. The chemical composition of the boride layer was analyzed in line and spot modes via SEM-EDS detector. Also the boride layer thicknesses were measured via cross-sectional SEM images.

III. RESULTS

A. XRD Results

The surface XRD analyses showed that the layers formed on boronised Fe–Ni binary alloys and pure Fe contain FeB and Fe₂B phases. It can be seen in Fig. 1 that the peak intensities of the phases varied with Ni content in the samples though their variation is not systematical and the possible diffraction peaks belong to both phases exist in the XRD spectrum.

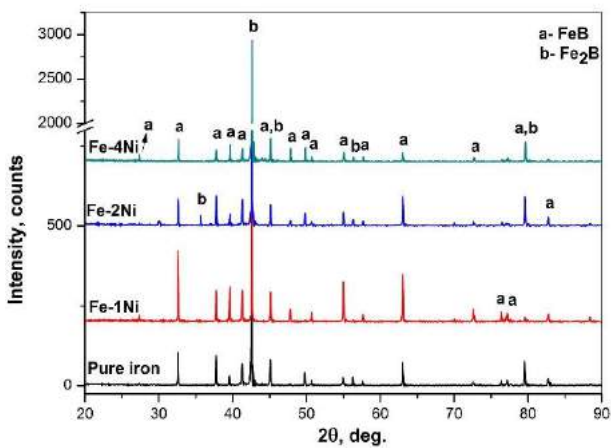


Fig. 1 XRD results of the Fe-Ni alloys and pure Fe

B. SEM and SEM-EDS Analysis Results

Fig. 2 shows cross-sectional SEM images of the borided Fe–Ni alloys and pure iron. The figure illustrates that a well adhered boride layer with saw-tooth morphology was formed on the pure iron and on Fe-Ni alloys with 1 and 2 at. % Ni. The saw-tooth morphology started to change to relatively compact morphology though the main saw-tooth like crystals still apparent with higher content of Ni in Fe–Ni (Fig. 2d). It should be noted that new grown features around the main saw-tooth like crystals are seen also for this borided alloy (Fig 2d). In fact these features are also evident for the alloy with Fe-2Ni. Furthermore, some porosity was observed nearby to the surface of the borided specimens.

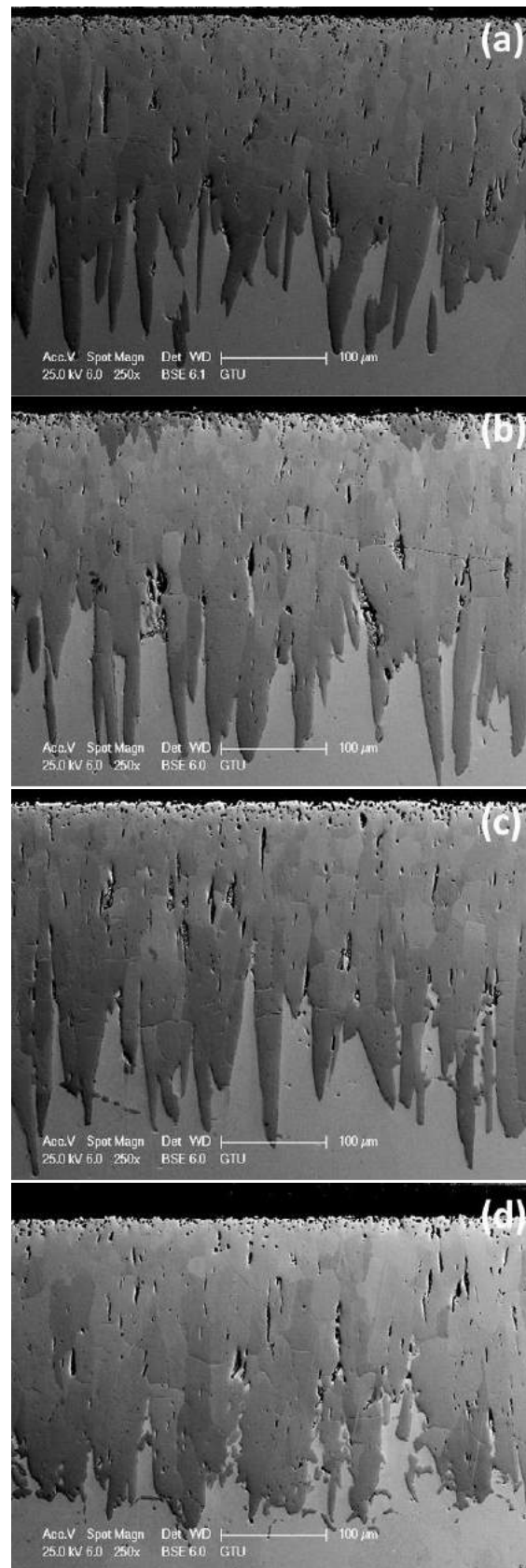


Fig. 2 Cross-sectional SEM images of boronised samples (a) pure Fe, (b) Fe-1Ni, (c) Fe-2Ni, (d) Fe-4Ni

A typical cross-sectional SEM micrograph and corresponding line SEM-EDS result for borided Fe-4Ni alloy are given in Fig. 3. The line SEM-EDS spectrum shows that the change of the constituents of Fe and Ni through the boride layer from the surface to the substrate. The amount of Fe and Ni do not change significantly along the main boride layer. However, the amount of Fe increase in the substrate compared to that of the boride layer though its amount does not change in the substrate. The amount of Ni is almost the same in the main boride layer and substrate. But, the line SEM-EDS spectrum explicitly shows that the amount of Ni increases underlying zone of the boride layer where precipitate formed. Furthermore, Table 1 shows the amount of Fe, Ni and B in different region shown in Fig.3a. The chemical composition of points 1 and 2 is almost the same but point 2 has slightly higher content of Ni while the amount of boron slightly decreased. The amount of Ni is the highest at point 3 and it is almost the same as substrates' content at point 4. Boron was not detected at points 3 and 4.

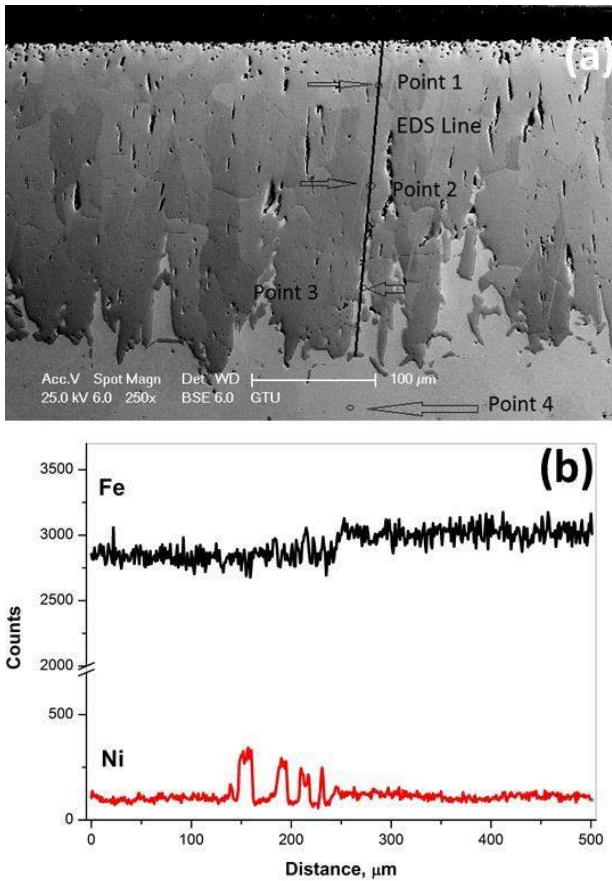


Fig. 3 (a) SEM image of Fe-4Ni alloy shows SEM-EDS line and spots analysis positions and (b) corresponding SEM-EDS spectrum

Table 1 Quantitative SEM-EDS results for the spots shown in Fig 3a

Element	Point 1 (at. %)	Point2 (at. %)	Point3 (at. %)	Point4 (at. %)
Fe	35.26	36.87	90.81	95.89
Ni	1.35	1.51	9.19	4.11
B	63.40	61.62	-	-

C. Boride Layer Thickness and Hardness

The variation of thickness values measured from the cross-sectional SEM images of the coating on borided Fe-Ni alloys and pure Fe with Ni content in the substrate is illustrated in Fig 4. The coating thickness of the borided alloy with 1 at.% Ni alloy is approximately same with that of borided pure iron. Increasing Ni content in Fe-Ni alloys resulted in the boride layer thickness decreases slightly with Fe-2Ni and significantly with Fe-4Ni.

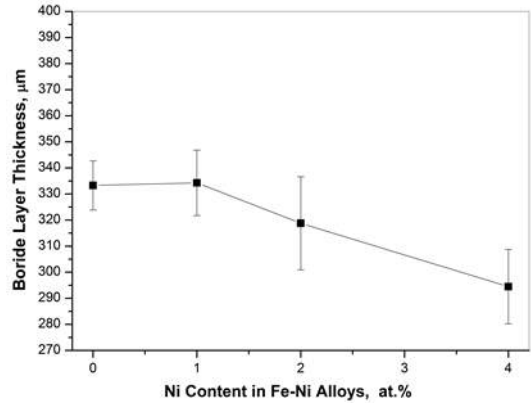


Fig. 4 The change in boride layer thickness with Ni in the borided samples

Fig. 5 shows the change in microhardness values from the coating surface to the substrate for boronised Fe-Ni alloys and pure iron. The microhardness values for the boride layer changes between 1200 HV and 1900 HV without a clear dependence on Ni content while the microhardness values of the substrates are between 150 HV and 200 HV for Fe-Ni alloys and pure iron.

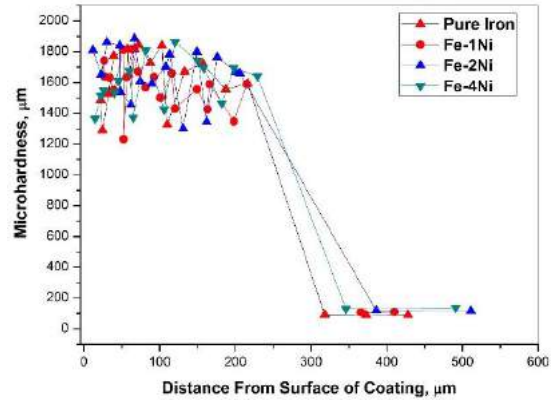


Fig. 5 Change in microhardness values from surface to the substrate for the borided samples

IV. DISCUSSION

This study has revealed that there is a significant effect of Ni addition with increasing amount into Fe-Ni alloys which were borided at 1100°C for 3 h by pack boronising. The coating thickness, chemical constituents of the main boride layer as well as the interface between the boride layer and the substrate was significantly affected with the presence of increasing amount of Ni in Fe-Ni alloys. In the literature, it is reported that the main boride layer is composed of two distinct phases that

can be distinguished from their contrast difference being the outer dark region is FeB and the inner lighter region is Fe₂B for borided ferrous alloys [9, 10, 12]. Although the existence of both phases was evident in the results of XRD but the differentiation of these two iron boride phases was possible only for boride Fe-1Ni alloy. This may be because of FeB did not formed as continuous phase on Fe₂B to be detected from their color which was the case for some similar studies [6, 24]. It should be noted that any Ni-B phase was detected neither in the main boride layer nor in the region between substrate and the main boride layer. This region is usually called as transition zone in other similar studies for borided Fe-M (M=Ti, V, W) alloys [10, 11, 23] if there exist new M-B features or there is gradual microhardness variation. Microhardness measurements in this study showed that there was no gradual decrease in the microhardness values from the surface of the boride layer to the substrate for neither of the Fe-Ni alloys studied. So, there is no clear transition zone for borided Fe-Ni alloy for the composition tested in this study.

The existence of Ni was confirmed by SEM-EDS analyses in point and line modes for the boride coating formed on Fe-Ni alloys. According to detailed SEM-EDS analysis of this study Ni was detected as almost the same in the boride layer and substrate where boron has not diffused. By considering XRD and SEM-EDS results together, it is possible to state that Ni atoms presents in FeB and Fe₂B as solution such as (Fe,Ni)B and/or (Fe,Ni)₂B.

In addition, significant enrichment of Ni in the main boride layer/substrate interface was easily detected by SEM-EDS in line and spot mode analysis. The SEM-EDS analysis in line mode confirmed that the branchy features formed surround the tip of boride crystal or between the boride crystal has the same Ni concentration with the main boride layer itself though in the surrounding area has much higher Ni concentration. Similar results of Ni enrichment were also reported by Brakman et al. who studied the boronising kinetic of Fe-Ni alloys with relatively higher Ni concentration of approx. 3.8 and 9.6 at.% and nickel had been found to concentrate below the boride layer and it entered the main boride layer [18]. This accumulation of Ni resulted in altered saw-tooth morphology to more compact boride layer in borided Fe-Ni alloys with relatively higher Ni in the substrate. This accumulation was also effective on growth mechanism of boride crystals. Because, while the boride crystals grow in saw-tooth morphology for pure iron as well as Fe-Ni alloys with low content of Ni, with the increase of Ni branchy boride crystals formation was evident (Fig. 2d). This branchy growth of the boride crystals may be partly attributed to the accumulation of Ni just in front of the boride crystals which obstructed further growth of boride crystals towards the substrate. Consequently, in addition to flattening of saw-tooth morphology, the thickness of the boride layer reduced with the increase on Ni in the borided substrates.

V. CONCLUSIONS

Fe-Ni binary alloys containing 1, 2 and 4at. % Ni were prepared under controlled atmosphere conditions. The alloys

along with pure Fe were pack boronized at 1100°C for 3 h. The boronised samples were characterized and the following results were extracted;

1. The boride layer with saw-tooth morphology on the substrate materials changed to compact morphology and the branchy structure around the boride crystals was formed with the increasing amount of Ni in the substrates.
2. The main boride layer was composed of FeB and Fe₂B phases with homogeneously distributed Ni in the main boride layer and accumulation of Ni in the boride layer/substrate was evident.
3. The low addition of Ni into the substrate was not effective on the coating thickness of the boride layer while higher addition of Ni decreased the boride layer thickness.
4. Ni addition was ineffective on the microhardness values of the boride layer formed on the samples tested.

ACKNOWLEDGMENT

The authors thank to Sezgin Cengiz and Yunus Azakli for their support in this study.

REFERENCES

- [1] P. Goeuriot, R. Fillit, F. Thevenot, J.H. Driver, H. Bruyas, *The Influence of Alloying Element Additions on the Boriding of Steels*, Mater Sci Eng, 55 (1982) 9-19.
- [2] K.H. Prabhudev, *Handbook of Heat Treatment of Steels*, Mc-Graw-Hill Company, NY, 1992.
- [3] E.C. Hwang, S. Lee, H.C. Lee, *Effects of alloying elements on microstructure and fracture properties of cast high speed steel rolls Part I: Microstructural analysis*, Mat Sci Eng a-Struct, 254 (1998) 282-295.
- [4] B. Liu, Y.F. Zheng, *Effects of alloying elements (Mn, Co, Al, W, Sn, B, C and S) on biodegradability and in vitro biocompatibility of pure iron*, Acta Biomater, 7 (2011) 1407-1420.
- [5] H.E. Townsend, *Effects of alloying elements on the corrosion of steel in industrial atmospheres*, Corrosion, 57 (2001) 497-501.
- [6] Y. Azakli, S. Cengiz, M. Tarakci, Y. Gencer, *Characterisation of boride layer formed on Fe-Mo binary alloys*, Surf Eng, 32 (2016) 589-595.
- [7] I. Campos, G. Ramirez, U. Figueroa, J. Martinez, O. Morales, *Evaluation of boron mobility on the phases FeB, Fe₂B and diffusion zone in AISI 1045 and M2 steels*, Appl Surf Sci, 253 (2007) 3469-3475.
- [8] V.I. Dybkov, *Effect of microstructure on the wear resistance of borided Fe-Cr alloys*, Int J Mater Res, 104 (2013) 617-629.
- [9] Y. Gencer, *Influence of manganese on pack boriding behaviour of pure iron*, Surf Eng, 27 (2011) 634-638.
- [10] Y. Gencer, M. Tarakci, A. Calik, *Effect of titanium on the boronizing behaviour of pure iron*, Surf Coat Tech, 203 (2008) 9-14.
- [11] K.O. Gunduz, Y. Gencer, M. Tarakci, A. Calik, *The effect of vanadium on the boronizing properties of pure iron*, Surf Coat Tech, 221 (2013) 104-110.
- [12] B.P.D. Anil Kumar Sinha, *Boriding (Boronizing)*, ASM Handbook ASM, Metals Park, OH., 1991, pp. 437-447.
- [13] J.B. Jiang, Y. Wang, Q.D. Zhong, Q.Y. Zhou, L. Zhang, *Preparation of Fe₂B boride coating on low-carbon steel surfaces and its evaluation of hardness and corrosion resistance*, Surf Coat Tech, 206 (2011) 473-478.
- [14] V. Jain, G. Sundararajan, *Influence of the pack thickness of the boronizing mixture on the boriding of steel*, Surf Coat Tech, 149 (2002) 21-26.
- [15] P. Juijerm, *Diffusion kinetics of different boronizing processes on martensitic stainless steel AISI 420*, Kovove Mater, 52 (2014) 231-236.
- [16] M. Kulka, A. Pertek, *The importance of carbon content beneath iron borides after boriding of chromium and nickel-based low-carbon steel*, Appl Surf Sci, 214 (2003) 161-171.
- [17] Y. Azakli, K.O. Gunduz, M. Tarakci, Y. Gencer, *A Comparative Study on Boride Layer Morphology of Fe-4Co, Fe-4V and Fe-4W Binary Alloys*, Acta Phys Pol A, 127 (2015) 1326-1330.

- [18] C.M. Brakman, A.W.J. Gommers, E.J. Mittemeijer, *Boriding of Fe and Fe-C, Fe-Cr, and Fe-Ni Alloys - Boride-Layer Growth-Kinetics*, J Mater Res, 4 (1989) 1354-1370.
- [19] M. Carbucicchio, G. Palombarini, *Effects of Alloying Elements on the Growth of Iron Boride Coatings*, J Mater Sci Lett, 6 (1987) 1147-1149.
- [20] S. Cengiz, Y. Gencer, M. Tarakci, Y. Azakli, *Influence Of Copper Amount On The Pack Boronizing Behaviour Of Fe-Cu Binary Alloys*, J Fac Eng Archit Gaz, 30 (2015) 339-349.
- [21] M. Tarakci, Y. Gencer, Y. Azakli, U. Sahinturk, *Surface Modification of Fe-8Si Alloy By Boronizing And Its Characterization*, J Fac Eng Archit Gaz, 28 (2013) 645-655.
- [22] M.T. Y. Gencer, *50Fe-50Co Alaşiminin Borlanması Ve Karakterizasyonu*, 16th International Materials Symposium IMSP'2016, Denizli, Turkey, 2016.
- [23] M.T. Y. Azakli, *Microstructural characterisation of borided binary Fe-W alloys*, Surf Eng, DOI <http://dx.doi.org/10.1080/02670844.2016.1263712>(2016).
- [24] M.T. Y. Gencer, *Atomik Olarak Eşit Miktarda Demir Ve Krom İçeren Fe-Cr İkili Alaşımın Borlanması*, 16th International Materials Symposium IMSP'2016, Denizli, Türkiye, 2016, pp. 77.

Characterization of Biodegradable Fe-Co alloys

Mehmet Tarakci^a, Yunus Azaklia, Sezgin Cengiza, Mehmet Yazicia,^b Yucel Gencera*

*a*Department of Materials Science and Engineering, Gebze Technical University

41400 Gebze, Kocaeli, Turkey

*b*Ondokuz Mayıs University, Departure of Materials Science and Engineering, 55139, Kurupelit, Samsun, Turkey

*e-mail: gencer@gyte.edu.tr (Corresponding Author)

ABSTRACT

The aim of this study is to produce new generation biodegradable iron-based alloys and to investigate their compatibleness for using as transient implantable materials. Produced iron-cobalt alloys were immersed in SBF to simulate the degradation properties in human body. Degradation behavior of the Fe-Co alloys were investigated using both mass loss tests for following the rate of degradation and observed growth of the apatite structure in the simulated body fluid. Also, general characterization methods (XRD, SEM and EDS) were used for investigation of the samples.

Keywords:iron-cobalt, Fe-Co alloys, biodegradable, implant

Effect of Multipass Welding on Microstructural and Mechanical Properties of AISI 2205 Duplex Stainless Steel

Alptekin Kısasöz*, Mustafa Tümer[†], Ahmet Karaaslan*

*Yildiz Technical University, Department of Metallurgical and Materials Engineering
Istanbul Turkey

akisasoz@yildiz.edu.tr, karaas@yildiz.edu.tr

[†]Kocaeli University, Uzunçiftlik Nuh Çimento Vocational School
Kocaeli, Turkey

mustafa.tumer@kocaeli.edu.tr

Abstract— In this study, AISI 2205 types of duplex stainless steels were welded by FCAW (flux cored arc welding) using E2209 T1-1/4 type flux cored filler metal. Joinings welded with different heat input and number of passes were characterized by microstructural analysis and Charpy impact test. Also, ferrite/austenite phase ratios in welded specimens were investigated and variations in microstructural and mechanical properties were compared by ferrite/austenite phase balance. Moreover, effects of microstructural properties on mechanical properties of welded specimens were determined.

Keywords— Duplex stainless steel, Welding, FCAW, Multipass welding, Material characterization

I. INTRODUCTION

Duplex stainless steels (DSSs) are widely used in offshore, piping and nuclear industries owing to their higher mechanical properties and corrosion performance. DSSs have higher mechanical and corrosion properties with dual phase microstructure comprised of ferrite and austenite phases in equal amount. Ferrite enhances the mechanical strength and pitting corrosion resistance and also, austenite enhances the ductility and general corrosion resistance of the DSSs [1-5].

Microstructure properties of the DSS is critical for the formation of the DSSs properties. Intermetallics as nitrides, carbides, σ or χ phases can be formed during the fabrication or usage of DSSs and these intermetallics are detrimental for mechanical and corrosion properties of DSSs. Also, ferrite-austenite fraction is critical for DSSs [6-11].

Welding is generally used in fabrication of DSSs products. In welding of DSSs, variation of ferrite-austenite fraction and formation of intermetallics at the ferrite-ferrite and ferrite-austenite grain boundaries can occur based on the welding method, welding design and heat input. Especially, higher heat input and thermal cycles increase the ferrite fraction in weld seam and cause the formation of intermetallic phases in heat affected zone (HAZ). Therefore, determining the welding parameters and providing decent joining process are critical for welded DSSs [12-16].

In this study, variation of microstructural and mechanical properties of AISI 2205 DSS in multipass welding was studied.

AISI 2205 DSS was welded by E2209 T1-1/4 flux cored wires with various passes. Also, effects of heat input and thermal cycles on mechanical and corrosion properties of DSS were investigated.

II. EXPERIMENTAL

AISI 2205 DSS plates with 400x150x8 mm dimension were joined by E2209 T1-1/4 type flux cored wire in 3 and 7 passes, respectively. The chemical compositions of base material and filler metal are given in Table I.

TABLE I
CHEMICAL COMPOSITIONS OF BASE MATERIAL AND FILLER METAL (WT. %).

	C	Cr	Ni	Mo	Mn
Base Material	0.020	22.560	5.420	2.950	1.290
Filler Material	0.03	22.0	10.0	2.7	0.9
	Si	P	S	N	Fe
Base Material	0.457	0.031	0.014	0.170	Bal.
Filler Material	0.5	-	-	0.12	Bal.

Specimens were joined with V welding groove joining design by FCAW. Welding parameters and V welding groove joining design are shown in Table II and Figure 1, respectively.

TABLE IX
WELDING PARAMETERS

Filler Metal	Current (A)	Voltage (V)	Shielding Gas
E2209 T1-1/4	230	37	%100 CO ₂

Metallographic preparation was performed by grinding, polishing and etching. Water cooled silicon carbide papers of 180, 240, 320, 400, 600, 800, 1000, 1200 and 2000 grit size were used in grinding, respectively. Also, polishing was performed by using 1 μ m diamond paste. Specimens were etched electrochemically with KOH solution. The microstructure of the welded DSSs were determined with light microscopy. Also, ferrite-austenite volume fractions were studied by image analysis.

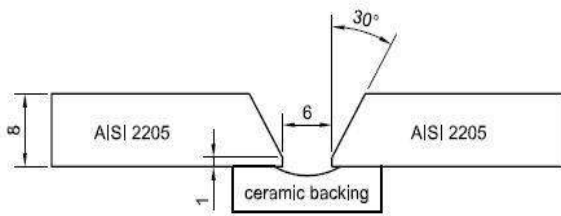


Fig. 1 Joining design.

Effects of the welding process on the mechanical properties of the specimens were investigated with Charpy impact tests at room temperature. Charpy impact tests were carried out according to TS EN ISO 9016:2012 Charpy impact test standard.

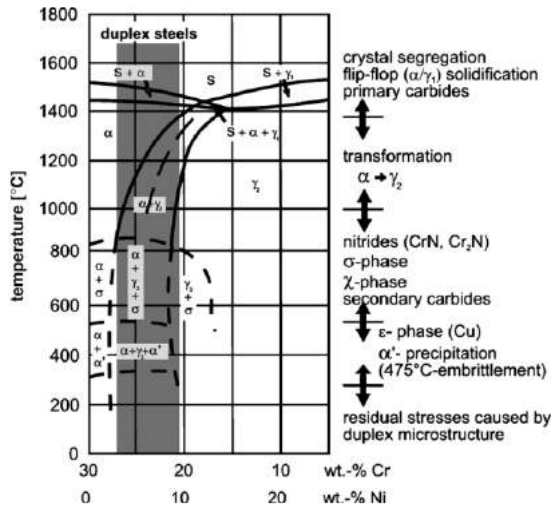


Fig. 2 DSS phase diagram [17].

III. RESULTS AND DISCUSSION

Ferrite phase (δ) forms in liquid metal during the solidification of DSSs. Also below the 1200°C, austenite phase (γ) composes from ferrite and duplex microstructure occurs as shown in Figure 2.

Generally, austenite nucleates at grain boundaries of ferrite and grows into ferrite grain. Moreover, between 950°C and 650°C, eutectoid decomposition of ferrite occurs and intermetallics occur with secondary austenite beside the primary austenite. Also, various microstructural changes happen due to material properties (chemical composition, specimen dimension etc.) and welding parameters (welding method, heat input, thermal cycle etc.) during the welding of DSSs.

Various austenite phase formation can occur during the welding of DSS, especially according to chemical composition, heat input and thermal cycle. Firstly, grain boundary austenite (GBA) nucleate at ferrite grain boundaries due to higher energy level of grain boundaries and GBA grows along the grain boundary. Widmanstätten austenite (WA) forms from GBA and grows with a decent angle. On the other hand, intragranular austenite (IGA) nucleates in regions having higher Ni concentration in ferrite phase which are preferential sites for

austenite nucleation. Moreover, in multipass welding, each pass reheats the previous pass and reheating activates the ferrite-austenite transformation and induces the secondary austenite (SA) formation. SA formation is inevitable in multipass welding [18, 19].

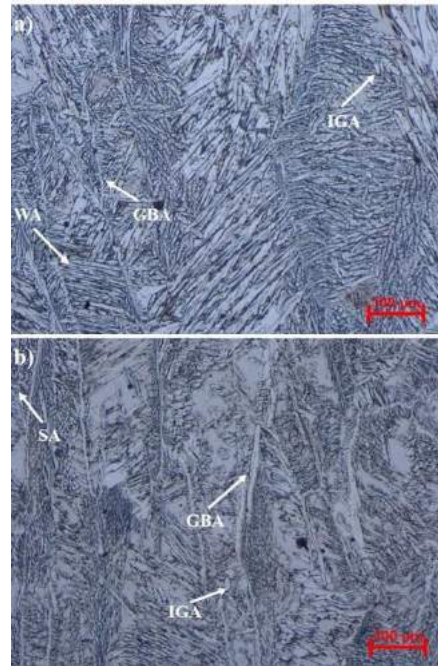


Fig. 3 Weld seam microstructure of FCAW a) welding with 3 passes, b) welding with 7 passes.

Weld seam microstructures of FCAW are seen in Figure 3 for 3 and 7 passes, respectively. GBA, WA, IGA, SA are seen in weld seam microstructures. WA did not occur in high passes and grain sizes for GBA and IA increased in 7 passes welding. Reheating effect and higher heat input of multipass welding caused grain growth for GBA and IGA. Moreover, reheating effect induced more SA formation for 7 passes welding than 3 passes welding. Thus, SA volume fraction is higher for 7 passes welding than 3 passes welding as seen in Figure 3.

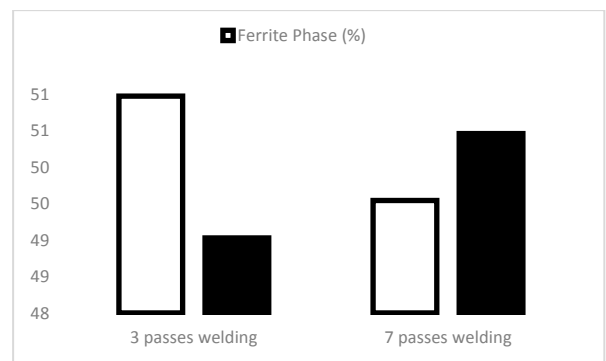


Fig. 4 Volume fraction (%) of ferrite and austenite phases in weld seams for multipass FCAW.

Volume fractions (%) of ferrite austenite phases in weld seams for 3 passes and 7 passes FCAW are seen in Figure 4. Austenite phase volume fractions are 49.03% and 50.46% for 3

passes and 7 passes FCAW, respectively. Image analysis results for the ferrite-austenite ratio in weld seams are compatible with Figure 3. In 7 passes welding, each pass reheated the previous pass as mentioned before and SA formation occurred by ferrite-austenite formation. Hence, increase in number of passes during the FCAW process induced the higher austenite phase ratio as seen in Figure 4. Charpy impact tests were applied according to TS EN ISO 9016:2012 test standard. Also, average impact strength values for 3 passes and 7 passes FCAW were determined as 77.555 ± 3 j/cm² and 60.392 ± 2 j/cm², respectively. Especially grain growth for GBA and IGA in 7 passes FCAW as seen in Figure 3 causes decrease in weld seam impact strength value.

IV. CONCLUSIONS

In this study, FCAW of AISI 2205 DSS with E2209 T1-1/4 type flux cored filler metal was studied. Specimens were welded with different passes (3 passes and 7 passes) and effect of number of passes in FCAW for AISI 2205 DSS alloy were investigated.

Microstructural characterization of welded AISI 2205 DSS specimens were carried out with optical microscopy and image analysis. Formation of various types of austenite phase as GBA, WA, IGA and SA were identified in weld seam of welded specimens. Especially image analysis show that increases in number of passes lead to formation of SA in weld seam.

Impact strength of the welded specimens decreased with increasing number of passes. Also, grain growth in IGA and GBA caused decrease for impact strength values for specimens welded with 7 passes.

REFERENCES

- [1] T.H. Chen and J.R. Yang, "Effects of solution treatment and continuous cooling on σ -phase precipitation in a 2205 duplex stainless steel," *Materials Science and Engineering A*, vol. 311, no. 1–2, pp. 28–41, 2001.
- [2] H. Hwang and Y. Park, "Effects of Heat Treatment on the Phase Ratio and Corrosion Resistance of Duplex Stainless Steel," *Materials Transactions*, vol. 50, no. 6, pp. 1548–1552, 2009.
- [3] J.W. Elmer, T.A. Palmer, and E. D. Specht, "Direct Observations of Sigma Phase Formation in Duplex Stainless Steels Using In-Situ Synchrotron X-Ray Diffraction," *Metallurgical and Materials Transactions A*, vol. 38, pp. 464–475, 2007.
- [4] T. Karahan, H. Ertek Emre, M. Tümer, and R. Kaçar, "Strengthening of AISI 2205 duplex stainless steel by strain ageing," *Materials and Design*, vol. 55, pp. 250–256, 2014.
- [5] A. Kısasöz and A. Karaaslan, "Dubleks Paslanmaz Çeliklerde İkincil Faz Oluşumuna Sıcaklığın ve Sürenin Etkisi," in *4. Isıl İşlem Sempozyumu (4HTS)*, 2013, pp. 22–28.
- [6] A. Kısasöz, S. Gurel, and A. Karaaslan, "Effects of Annealing Time and Cooling Rate on Precipitations in Duplex Stainless Steel," *Metal Science and Heat Treatment*, vol. 57, pp. 8–11, 2016.
- [7] S.M. Dubiel and J. Cieslak, "Sigma-phase in Fe-Cr and Fe-V alloy systems and its physical properties," *Critical Reviews in Solid State and Materials Science*, vol. 36, pp. 191–208, 2011.
- [8] D.M. Escriba, E. Materna-Morris, R.L. Plaut, and A.F. Padilha, "Chi-phase precipitation in a duplex stainless steel," *Materials Characterization*, vol. 60, pp. 1214–1219, 2009.
- [9] C.C. Hsieh and W. Wu, "Overview of Intermetallic Sigma Phase Precipitation in Stainless Steels," *ISRN Metallurgy*, vol. 2012, pp. 1–16, 2012.
- [10] J.A. Jimenez, M. Carsi, and O.A. Ruano, "Characterization of a δ/γ duplex stainless steel," *Journal of Materials Science*, vol. 35, pp. 907–915, 2000.
- [11] J. Michalska and M. Sozańska, "Qualitative and quantitative analysis of σ and χ phases in 2205 duplex stainless steel," *Materials Characterization*, vol. 56, pp. 355–362, 2006.
- [12] Y.S. Sato, T.W. Nelson, C.J. Sterling, R.J. Steel, and C.O. Pettersson, "Microstructure and mechanical properties of friction stir welded SAF 2507 super duplex stainless steel," *Materials Science and Engineering A*, vol. 397, pp. 376–384, 2005.
- [13] P. Sathiya, S. Aravindan, R. Soundararajan, and a. Noorul Haq, "Effect of shielding gases on mechanical and metallurgical properties of duplex stainless-steel welds," *Journal of Materials Science*, vol. 44, pp. 114–121, 2009.
- [14] E. Kaluç and E. Taban, *Paslanmaz Çelikler, Geliştirilen Yeni Türleri ve Kaynak Edilebilirlikleri*. İstanbul: TMMOB, 2007.
- [15] A. Kısasöz and A. Karaaslan, "Finite Element Analysis of 2205 Duplex Stainless Steel Welds," *Materials Testing*, vol. 56, pp. 795–799, 2014.
- [16] I. Alvarez-Armas, "Duplex Stainless Steels: Brief History and Some Recent Alloys," *Recent Patents on Mechanical Engineering*, vol. 1, pp. 51–57, 2008.
- [17] M. Pohl, O. Storz, and T. Glogowski, "Effect of intermetallic precipitations on the properties of duplex stainless steel," *Materials Characterization*, vol. 58, pp. 65–71, 2007.
- [18] S. Geng, J. Sun, L. Guo, and H. Wang, "Evolution of microstructure and corrosion behavior in 2205 duplex stainless steel GTA-welding joint," *Journal of Manufacturing Processes*, vol. 19, pp. 32–37, 2015.
- [19] A.J. Ramirez, "The Relationship between Chromium Nitride and Secondary Austenite Precipitation in Duplex Stainless Steels," *Metallurgical and Materials Transactions A*, vol. 34A, pp. 1575–1597, 2003.

Assessment of Material Selection and Corrosion Performances for Plate Heat Exchangers

Haluk Erdemir, Cem Çakıroğlu, Ahmet Çakır
halukerdemir35@gmail.com Turkey, Dokuz Eylül Üniversitesi
Cem.Cakiroglu@tr.bosch.com Turkey, Bosch Termoteknik Isıtma ve Klima San. Tic. A.Ş.
ahmet.cakir@deu.edu.tr Turkey, Dokuz Eylül Üniversitesi

ABSTRACT

This study was carried out to determine a more economical and reliable stainless steel types for plate heat exchangers without sacrificing their operating efficiencies and performances. In line with this purpose, corrosion behavior of stainless steel types 316L and 304L were studied under the used conditions to evaluate, whether stainless steel type 316L can be replace by the cheaper 304L stainless steel. To start with, the operating and boundary conditions of stainless steel plate heat exchangers was determined. Electrochemical corrosion tests were carried out by considering the types of corrosion such as pitting, crevice and stress corrosion likely to be effective on the named stainless steels under the simulated service conditions and the preselected test parameters associated with the types of corrosion. Studies were carried out to determine the corrosion resistance of materials with accelerated polarization tests. The results of the accelerated corrosion tests were compared with corrosion results obtained by testing the stainless steels at a pilot plant which was designed and manufactured by simulating conditions of use. Accordingly an assessment has been made for the service life of plate heat exchangers produced by the use of the stainless steel types 316L and 304L.

Keywords: Corrosion, stainless steel, plate heat exchangers, pitting corrosion, pit morphology, pit depth, crevice corrosion, 304L, 316L

Hydroformability of Advanced High Strength Steels through FEA

Doğan ACAR*, Ömer Necati CORA⁺

Karadeniz Technical University
Department of Mechanical Engineering, 61080, Trabzon, Turkey
[*dgnacar@ktu.edu.tr](mailto:dgnacar@ktu.edu.tr), [+ oncora@ktu.edu.tr](mailto:oncora@ktu.edu.tr)

Abstract— Hydroforming has been increasingly exploited by automotive industry due to several advantages such as more homogeneous deformation of workpiece, uniform thickness distribution, better surface properties due to lack of forming tool – workpiece contact interaction, etc. Advanced High Strength Steels (AHSS), on the other hand, have unique properties that make them prominent near-future solution in lightweighting, and improved safety efforts for auto industry. Current study, is aimed for investigating the hydroformability of DP 600, DP 800, and TRIP 780 advanced high strength steel (AHSS) grades at room temperature. To this goal, FEA of hydroforming process was modeled in which AHSS sheets were hydroformed into a closed die cavity with a non-axisymmetric geometry. 3D FE model of hydroforming process was established and validated with commercial FEA package Ls-Dyna. Process parameters (e.g. hydroforming pressure, blank holder force, etc.) were optimized using Ls-Opt, an artificial neural network (ANN) based optimization module integrated into Ls-Dyna, to compare the formability of AHSS steels. Thickness reduction (TR) of formed sheets and die cavity filling ratio (CFR) were taken as control parameters. Optimum hydroformability was obtained with the combination of 800 kN blank holder force and 25 MPa hydraulic pressure. Moreover, DP 600 has shown the highest hydroformability when TR and CFR values were compared.

Keywords— Hydroforming, AHSS, FEA, Process Optimization

I. INTRODUCTION

Advanced High Strength Steels (AHSS) are widely used in automotive industry for whom lightweighting, crashworthiness and environmental restrictions are primary challenges. Considering long term fuel economy targets, lightweighting is the prominent target. It was reported that replacement of AHSS instead of mild steel may lead 10-25% reduction in mass [1]. Moreover, it was stated that 10% reduction in vehicle mass results 6-8% decrease in fuel consumption [2]. As it can be seen from Fig. 1, although the formability of AHSS is higher than High Strength Steel (HSS), formability of mild steel is superior to AHSS [3]. Due to its multi-phase structure and phase changes during deformation, AHSS depicts different failure mechanisms [4]. This phenomenon is also a barrier against formability of AHSS. Therefore, application of novel manufacturing processes come front to increase the formability of the AHSS. During last two decades, hydroforming (HF) process has found increased number of applications automotive industry. Parts in tube form as well as sheet blanks can be formed via hydroforming.

Sheet hydroforming (SHF) process is similar to conventional deep drawing except usage of pressurized hydraulic medium in lieu of punch or die [5]. In hydroforming process, workpiece can either be formed with hydraulic fluid or combined effect of hydraulic fluid and movement of punch (hydromechanical effect), as it can be seen in Fig. . Hydroforming has many advantages such as, increase in formability, reduction in die expenditures, forming complex-shaped parts in one step and uniform thickness distribution. Some automotive industry application examples are given in Fig. [6].

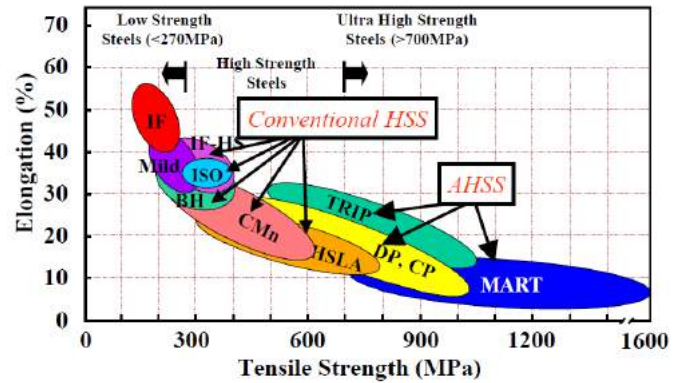


Fig. 1. Total elongation (%EL) vs. ultimate tensile strength (UTS) "Banana Curve" of automotive steels [3]

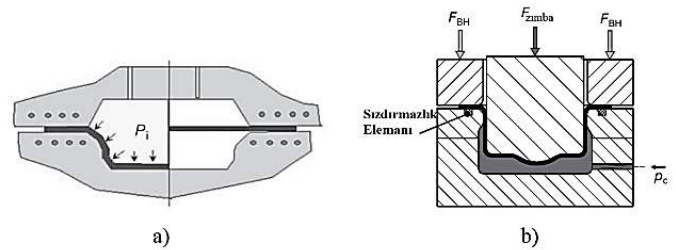


Fig. 2. a) Hydroforming with female die, b) hydromechanical deep drawing [5]

In current study, two different types of AHSS, which are Dual Phase (DP 600, DP 800) and Transformation Induced Plasticity (TRIP 780), are interest of investigation. All three AHSS are formed into a closed die cavity via hydroforming process. Established finite element (FE) model is used to perform optimization analyses. Optimal values of loading parameters, blank holder force (BHF) and hydraulic pressure

(HP), were determined using an artificial neural network optimization model. Moreover, thickness reduction percentage (TR) and cavity filling ratio (CFR) of hydroformed AHSS sheets were used to compare hydroformability performance of AHSS grades.

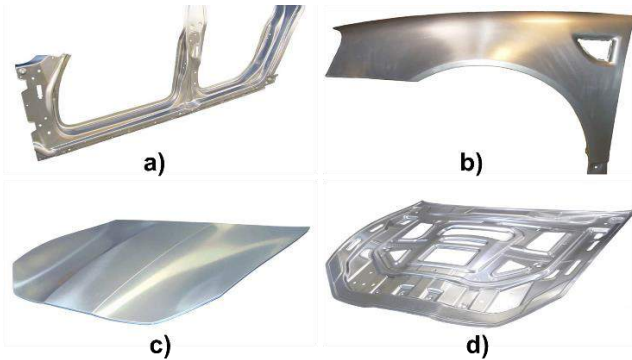


Fig. 3. Sheet metal forming applications in automotive industry, a) body side lower, b) front fender, c) hood outer hydroformed parts, d) hood inner [6]

II. MATERIALS AND EXPERIMENTAL SETUP

A. Experimental Setup

An experimental hydroforming setup used in second author’s previous studies was taken as reference in the current FE and optimization analyses [7]. AHSS steel sheets are clamped between closed-die shown in Fig. and a blank holder. The sheet, is then formed with the aid of hydraulic pressure into die cavity under the clamping force effect. Die and blank holder materials are assumed to be made of AISI 1040 steel as in real experimentation.

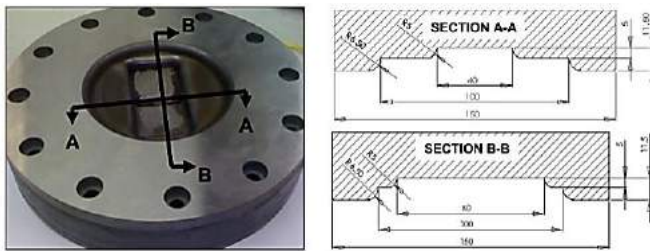


Fig. 4. Closed-die geometry and dimensions taken as reference from [7]

B. Materials

In the analyses, three different types of AHSS which are DP 600 and DP 800 (Dual Phase) steels and TRIP 780 (Transformation Induced Plasticity) steel with 1 mm thickness were investigated. The microstructure of DP steels is composed of ferrite and martensite whereas the microstructure of TRIP steels is a ferrite matrix in which martensite and/or bainite,

austenite are present [8]. All these three AHSS grades are of great interest for automotive industry thanking to their high strength, low weight and higher crash performance feature that found applications including B-pillar, bumper reinforcements, front and rear rails, etc.

Mechanical properties of studied AHSS grades, such as yield stress (YS), ultimate tensile strength (UTS) and percent total elongation (%TE) are given in Table I. Stress-strain curves for those obtained at room temperature and quasi static conditions are depicted in Fig. 5.

TABLE I
MECHANICAL PROPERTIES FOR AHSS GRADES

AHSS	YS (MPa)	UTS (MPa)	TE (%)
DP 600	379	624	23.51
DP 800	448	785	16.80
TRIP 780	505	793	29.4

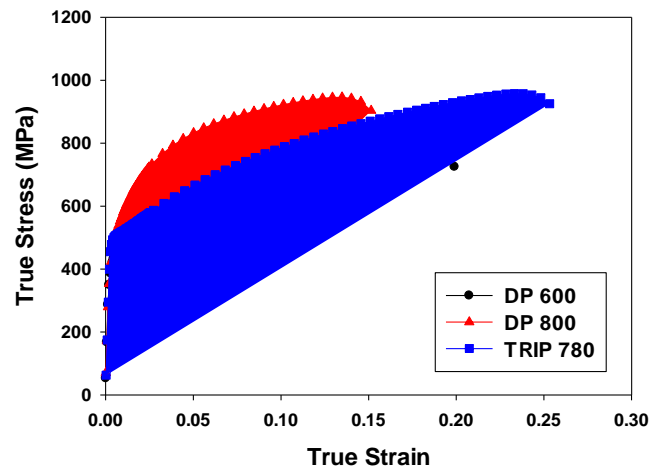


Fig. 5. True stress-true strain curves at room temperature for AHSS grades [9]

III. NUMERICAL STUDIES

C. Finite Element Model of Closed-Die Hydroforming

Finite element mesh discretization of hydroforming was prepared using Hypermesh (Altair Engineering Corp., Troy, MI, USA) while commercial LS-Dyna (LSTC Corp., Livermore, CA, USA) dynamic explicit scheme is used as solver [10]. In order to reduce solution time, a quarter 3D model was established taking advantage of the symmetry of workpiece, and die (Fig.6). Workpiece was modeled as elastic-plastic where die and blank holder were both assumed as rigid. Workpiece was modeled with 1947 quadrilateral shell elements with 5 integration points and Belytscko-Tsay element formulation. Due to high deformation nature of hydroforming, remeshing was activated to acquire numerically stable results. Therefore, number of elements for workpiece was recorded around 5000 at the end of analysis (Fig. 8). Coulomb friction coefficient (μ) was defined as 0.1 between workpiece-die, and workpiece-blank holder contact interfaces [7].

Blank holder force (BHF) and hydraulic pressure (HP) loading values were defined parametrically in the model. All analyses were performed at room temperature. Power_Law_Plasticity (MAT18) was implemented as material model. von Mises stress distribution on hydroformed AHSS (DP 600) at the end of analysis is given in Fig. 7.

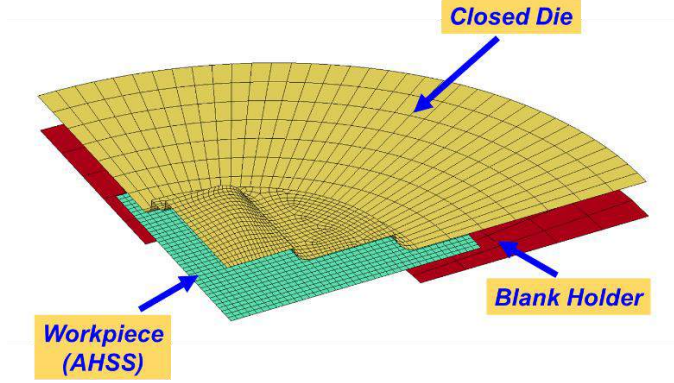


Fig. 2. 3D quarter FE model of closed-die hydroforming process

Flow curves in Fig.5 were used to apply to MAT18 material model. True stress-true strain values, after yield point to ultimate tensile strength value, were used to fit material model parameters K and n values for MAT18. Obtained K and n values are given in Table II.

TABLE II
POWER LAW MATERIAL MODEL (MAT18) COEFFICIENTS FOR AHSS GRADES STUDIED

AHSS Grade	K (MPa)	n
DP 600	989	0.135
DP 800	1298	0.150
TRIP 780	1179	0.165



Fig. 4. Mesh structure after remeshing for hydroformed AHSS sheet

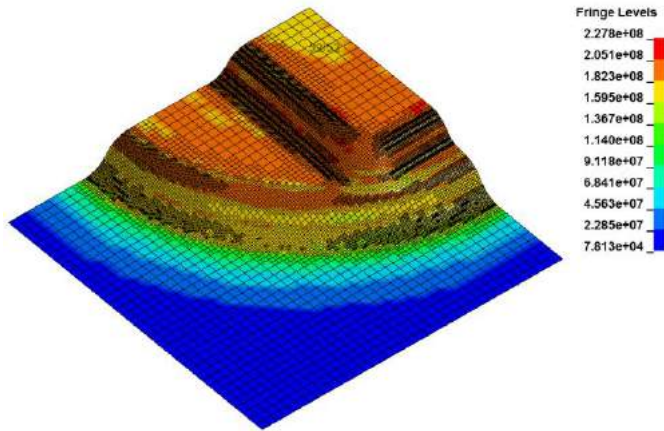


Fig. 3. von Mises stress distribution on hydroformed DP 600 steel

D. Material Model

Establishing FE model with more accurate results requires precise definition of physical and mechanical behavior of investigated workpiece material. Such accuracy can only be achieved by using right and accurate material model. Material model from LS-Dyna material library, which is Power_Law_Plasticity (MAT18) was implemented into FE

IV. OPTIMIZATION STUDIES

Closed-die hydroforming process parameter optimization was performed with neural network based LS-Opt which works compatible with LS-Dyna [11]. Artificial neural network (ANN) is widely used to model nonlinear systems [12]. In this method, several analyses are performed at sampling points. Results extracted from these analyses are used as training data for ANN based model. Finally, one last more analysis is performed using ANN trained with sampling points data to obtain optimum values. Blank holder force and hydraulic pressure were previously defined as parametric in FE model. All parameters are defined as discrete using LS-Opt interface. Three different blank holder force (BHF), namely 800, 1000, 1200 kN, and three different hydraulic pressure (HP) level, 25, 30, 35 MPa, were defined. Other optimization settings used in LS-Opt are given in Table III.

TABLE XII
OPTIMIZATION SETTINGS FOR LS-OPT

Strategy	Sampling Method	Algorithm
Single iteration	Radial Basis Function Network: Space Filling	Global Algorithm Population Size: 100 Number of Generations:250

Radial basis function artificial neural network with space-filling sampling point method was used in optimization. Three optimization runs were performed for three AHSS grades (DP 600, DP 800, TRIP 780). Each run was carried out with 9 sampling point analyses and an additional optimization run. 30 analyses were performed for optimization study, in total.

Thickness reduction was taken as control parameter. The higher degree of thinning without fracture was accepted as better formability. At the end of the optimization, a 3D response surface defining effect of blank holder force and hydraulic pressure on thinning was constructed (Fig. 9). The yellow point in the graph denotes the maximum mean thinning condition. As it can be seen in Fig. 9, optimum value was obtained with the combination of 25 MPa of HP and 800 kN of BHF.

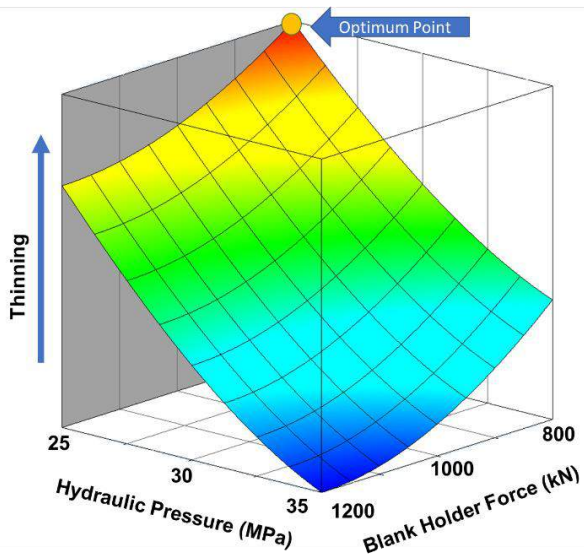


Fig. 5. Thinning change as a function of blank holder force and hydraulic pressure

Thinning comparison between AHSS grades was also performed. Thickness reduction percentage (TR %) was measured along the curvilinear distance on hydroformed workpiece shown on top-right of Fig. 10. Results illustrated for three different AHSS grades were obtained under same BHF and HP conditions, 800 kN and 25 MPa, respectively. Examining Fig. 10, one can easily notice that the highest TR % values achieved with DP 600, and followed by TRIP 780, and DP 800 grades.

Cavity filling ratio (CFR) was also taken as hydroformability evaluation criterion. CFR is calculated with equation given in Fig. 11. The ratio of filled area under the workpiece midsurface line (denoted as Filled Area in Fig. 7) to the area under die face line is equal to CFR. As it can be seen from Fig. 12 within the range examined, both BHF and HP have a slight effect on CFR which can be neglected. Though, increasing HP was increased up to 50 MPa, it was observed CFR value reaches up to 90%. Furthermore, same trend in TR

is observed in CFR. Even though the differences do not seem to be significant, DP 600 achieves the highest CFR when compared to DP 800 and TRIP 780. Similar to thickness reduction results, CFR values for TRIP 780 are higher than that for DP 800. The reason for this result is explained with the flow curves. Since flow curve and yield strength of DP 600 are lower than other AHSS grades, it resembles higher formability.

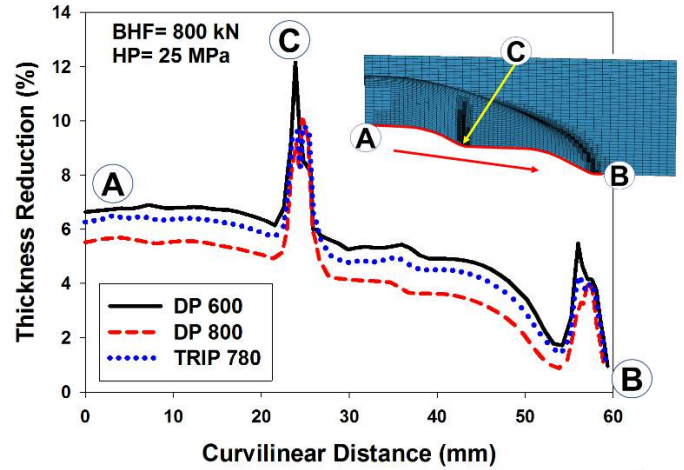


Fig. 6. Thickness reduction comparison for AHSS grades

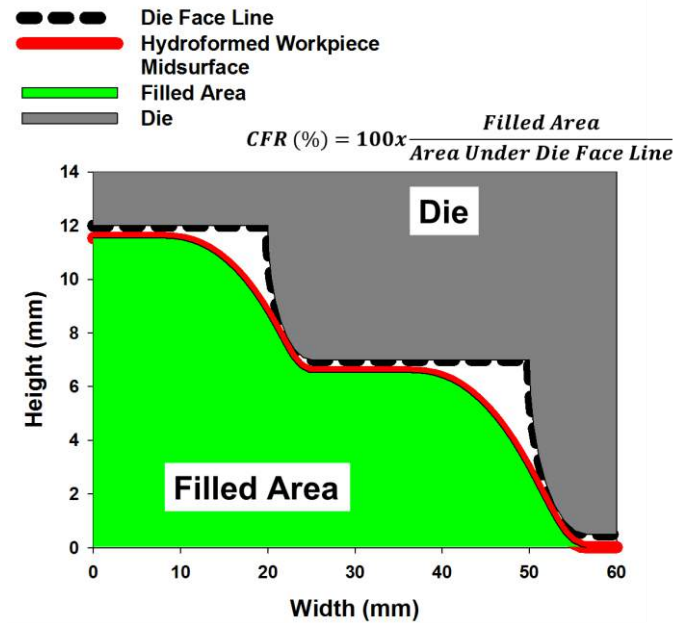


Fig. 7. Cavity Filling Ratio (CFR) calculation

V. CONCLUSION

In this study, hydroformability of three commonly used AHSS grades in automotive industry (DP 600, DP 800 and TRIP 780) was investigated through FEA. A detailed FE model was established. Power-law plasticity was implemented as material model. Moreover, a coupled artificial neural network-FEA based optimization procedure was performed to obtain appropriate blank holder force and hydraulic pressure values to

achieve higher hydroformability. Optimization study resulted in optimal values of blank holder force as 800 kN, and hydraulic pressure of 25 MPa. Additionally, thickness reduction and cavity filling ratio performance of all the three AHSS grades were compared in terms of higher hydroformability. From both thickness reduction and cavity filling ratio point of view, DP 600 has shown the highest formability followed by TRIP 780, and DP 800.

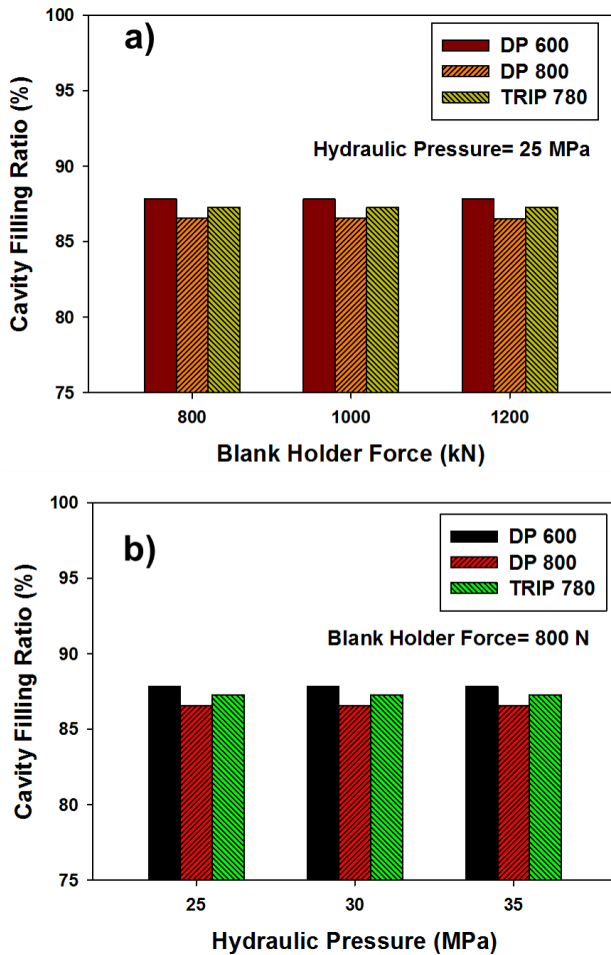


Fig. 8. Effect of BHF and HP on CFR of AHSS grades, a) BHF effect, b) HP effect

REFERENCES

[1] W. F. Powers, "Automotive Materials in the 21st Century," *Advanced Materials and Processes*, vol.157(5), pp. 38-42, 2000.

[2] R.Schultz, "Aluminum for light vehicles—an objective look at the next ten to twenty years," in *Proc. Metal Bulletin International Aluminum Conference*, 1999, September 15, Montreal, Canada.

[3] S. Sadagopan, "Formability characterization of advanced high-strength steels," in *Proc. Great Designs in Steel Seminar*, 2004, Livonia MI.

[4] J. Dykeman, D. Hoydick, T. Linkand, and H. Mitsuji, , "Material property and formability characterization of various types of high strength dual phase steel," SAE Tech. Rep. No. 0148-7191, 2009.

[5] M. Koç, *Hydroforming for Advanced Manufacturing*, 1st ed., M. Koç, Ed. Cambridge England: Woodhead Publishing Ltd., 2008.

[6] (2017) AMINO North America Corp. Sheet Hydroforming Applications website. [Online]. Available: <http://www.aminonac.ca/sheet-hydroforming-parts.asp>.

[7] H. Gedikli, Ö. N. Cora, and M. Koç, "Comparative Investigations on Numerical Modeling for Warm Hydroforming of AA5754-O Aluminum Sheet Alloy," *Materials & Design*, vol. 32(5), pp. 2650-2662, 2011.

[8] A. E. Al-Nasser, "Characterization of sheet materials for stamping and finite element simulation of sheet hydroforming," M. Eng. Thesis, The Ohio State University, Ohio, USA, 2009.

[9] (2017) Steel Market Development Institute website. [Online]. Available: <http://www.autosteel.org/>

[10] J. O. Hallquist, "LS-DYNA Theory Manual," Livermore Software Technology Corporation, Livermore, USA, vol. 3, 2006.

[11] N. Stander, W. Roux, T. Goel, T. Eggleston, and K. Craig, , "LS-OPT User's manual," 2008.

[12] W. Pawlus, K. G. Robbersmyr and H. R. Karimi, "Performance evaluation of feed forward neural networks for modeling a vehicle to pole central collision," in *Recent researches in geography, geology, energy, environment and biomedicine*. WSEAS Press, Corfu Island, pp. 467-472, 2011.

High Performance Copper and Copper Alloys Fabricated by Severe Plastic Deformation

Aslihan GÖKDUMAN¹, Hakan YILMAZER², Ceren GÖDE³, Burak DİKİCİ⁴, Jiri Dvorak⁵, Vaclav SKLENICKA⁵,
Aslı GÜNAY⁶, Adem BAKKALOĞLU², Halil GÖKER⁷

¹ Graduate Student, Department of Metallurgical and Materials Engineering, Yildiz Technical University, Istanbul, Turkey

² Department of Metallurgical and Materials Engineering, Yildiz Technical University, Istanbul, Turkey

³ School of Denizli Vocational Technology, Program of Machine, Pamukkale University, 20100 Denizli, Turkey

⁴ Department of Mechanical Engineering, YüzüncüYıl University, Van, Turkey

⁵ Institute of Physics of Materials, Academy of Science, Brno, The Czech Republic

⁶ Department of Mechanical Engineering, Yildiz Technical University, Istanbul, Turkey

⁷ Er-Bakir Electrolytic Copper Products Inc.

Abstract— Severe plastic deformation (SPD) has gained attention to ultrafine grained (<500 nm) and nano-grained (<100 nm) bulk materials producing. Equal channel angular pressing (ECAP) is the most common SPD process. ECAP has three critical disadvantages such as industrially discontinuity, limited small products, and non-uniform deformation such as gross distortions at the front and back of every billet. In this study, we systematically studied on an alternative approach which ECAP combined with the Conform process, developed for continuous extrusion-forming of metal wires (ECAP-Conform). The as-casted dilute copper alloys have been subjected to ECAP-Conform. The microstructural evaluation and hardness distribution have been investigated before and after ECAP-Conform.

Keywords— Copper and copper alloys, severe plastic deformation, ECAP-Conform

I. INTRODUCTION

In the last decade, the process of severe plastic deformation (SPD) of bulk metallic has been shown to produce ultrafine grained (UFG) structures. Even though the grain size is strictly not in the nanometer range, there has been considerable amount of research work on the structure and properties of materials produced by these methods [1, 2, 3]. Equal channel angular pressing (ECAP) is one of SPD processes suitable for producing ultrafine grained (<500 nm) and nano-grained (<100 nm) bulk materials [4,6]. These materials are characterized by a very fine grain size and a large amount of grain boundary area. The presence of a large amount of grain boundary area results in unusual and extraordinary changes in both mechanical and physical properties [5, 6].

Nevertheless, ECAP has three critical disadvantages. First, and most important, conventional ECAP is a discontinuous process involving a repetitive sequence in which the billet is inserted into the die, pressed through the die, removed and then reinserted to impose an even higher strain. This means that, although ECAP is an effective processing tool for laboratory research, it is labor-intensive and not easily adapted for use in industrial operations. Second, there is a limitation on the total lengths of the billets employed in ECAP because the length is restricted both in order to maintain a critical aspect ratio and as

a consequence of the limitation on the total available displacement of the pressing ram. Third, there is a problem because very significant waste is incurred with ECAP due to the non-uniform deformation and gross distortions that are introduced at the front and back of every billet. For example, detailed hardness measurements were recorded on longitudinal sections of pressed billets of an aluminum alloy and they showed there was an effective length of uniform flow occurring over a distance of ~38 mm for billets having initial lengths of 70 mm [7,8].

An alternative approach is based on the Conform process which was introduced many years ago for the continuous extrusion-forming of metal wires [8-10]. In 1974, Etherington [11, 13] developed an effective process, Conform, for continuous extrusion of metals. The Conform process “coins” the feedstock, in the form of round wires or powders, into the shape of a groove on a rotating wheel. Three sides of the groove move with the wheel, providing frictional driving force, while the groove was covered with a stationary shoe, which confines the feeding stock in the groove. The contact interface between the feeding stock and the shoe results in dragging frictional force. Therefore, the feeding stock will have three of the surfaces driving it forward and one surface dragging it backward, with a net forward driving force. The feeding stock in the groove is stopped by an abutment and extruded through an outlet either in the forward direction or perpendicular to the forward direction [12, 13]. The outlet cross-section is usually in a shape different from the groove because the objective of the Conform is to change the geometry of the feedstock or consolidate the powders, which usually requires only one process pass. The deformation of the feedstock during extrusion is similar to conventional extrusion process [13].

Industrial applications required high performance material and a convenient manufacturing process. Therefore, in this study, we focus on an alternative approach which ECAP combined with the Conform process (ECAP-Conform). This study was carried out to investigate the effects of ECAP-Conform on the microstructure and mechanical properties of the diluted Cu alloys. In this study, Cu-0,18wt%Sn and Cu-0,23wt%Sn alloys was processed by equal channel angular pressing-conform (ECAP-Conform) at 400°C to obtain ultra-fine grained (UFG) structure. Microstructure and mechanical properties of Cu-Sn

(%0.18) and Cu-Sn (%0.23) alloys subjected to 1 and 2 ECAP-Conform passes were compared with unprocessed samples.

II. EXPERIMENTAL

A. MATERIALS

Continuous casting: Cu-Sn alloys were produced at 1100-1200 °C in 20 mm wire rod sizes in a continuous casting furnace (Rautomead) with a graphite pot of 500 kg capacity used for the production of non-ferrous metals. Cu-Sn alloys were produced in two different types of wire rod containing 0.18% and 0.23% by weight (Table 1). Figure 1 shows a schematic view of the continuous casting furnace and process, in which the production of Cu-Sn alloys produced in operation is carried out with a graphite pot. Equipped with high automation technology, many parameters including casting speed and casting temperature can be adjusted precisely in the system. To prevent oxidation of the alloy during processing, the liquid metal surface is covered with special graphite casting dust.

TABLE I
TABLE I CHEMICAL COMPOSITIONS OF CU-0.18WT%SN AND CU-0.23WT%SN ALLOY

Cu-0.18wt%Sn							
Element	Sn	Zn	Pb	P	Mg	Se	Cu
Mass %	0.17	<0.001	<0.001	<0.02	<0.0021	<0.0001	bal.
Cu-0.23wt%Sn							
Element	Sn	Zn	Pb	P	Mg	Se	Cu
Mass %	0.22	<0.001	<0.001	<0.0008	<0.013	<0.0002	bal.

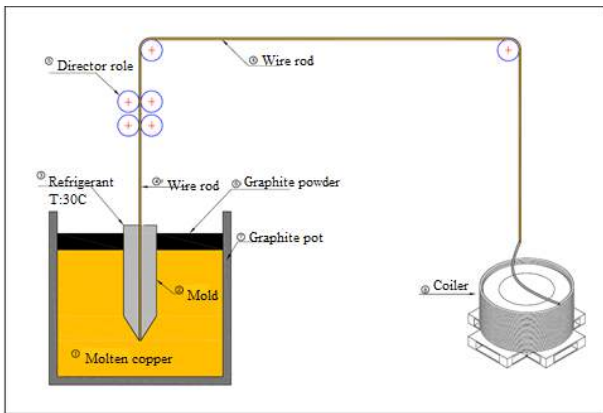


Fig. 1: Upright continuous casting unit with graphite pot

2) Extrusion of Rod:

The TJ400 copper bus bar continuous rotary extrusion line uses $\Phi 20$ mm oxygen-free copper rods which can be simply produces using upward casting technique as the feedstock to manufacture high quality oxygen-free copper bus bar with a sectional area below 2000mm².

Adopting the innovative online scrapless cutting technique, this range of continuous rotary extrusion machine maximizes the feedstock utilization rate, which helps users cut down production cost.

The modular structure of main components and the extrusion die ensures convenient parts replacement, thus minimizing the maintenance cost.

The maximum extruded copper product width is up to 170mm and average production speed of the continuous rotary extrusion line reaches 1100 kg/h.

This continuous rotary extrusion line is originally designed for copper bus bar production. Also, it can be utilized for manufacturing the copper bar, copper rod and other types of extruded copper products that are widely used in the motors, transformers and power distribution cabinets [16].

3) *Equal Channel Angular Pressing – Conform:* In this study, we used TLJ400 Conform machine. At the start the mold is heated up to around 800 °C. The temperature of the copper bar can be as high as 400°C in the mold. Other parameters are as shown in Table III.

TABLE II
OTHER PARAMETERS FOR ECAP-CONFORM

Nominal Diameter of Extrusion Wheel (mm)	400
Rated Speed of Extrusion Whell (rpm)	12.5
Max. Width of Product (mm)	170
Section Area of Product (mm ²)	100-2000
Average Output (kg/h)	1300
Scrap (%)	5-8

B. Material Characterizations

The microstructure of the samples was characterized by Electron Backscattered Diffraction (EBSD). The specimens were subjected to metallurgical sample preparation methods to make the mirror polished. The samples were sanded with sanders numbered 400, 1200, 2500 and 4000 respectively and then mirror polished by electrolytic polishing. There were 250 ml phosphoric acid, 250 ml ethyl alcohol, 50 ml propyl alcohol and 500 ml distilled water in the electrolytic polishing solution. Diffraction-based techniques for localized crystal orientation measurements, such as EBSD, are of central importance today for a characterization of these fine-scale microstructural features [17,18, 19]. The EBSD measurement was performed in a JOEL JSM-7001F Field Emission SEM (at 20 kV accelerate voltage) using the Oxford Instruments HKL Channel 5 Software package. The data obtained by EBSD were analyzed at two values of boundary misorientation (sub grains with $\Delta \geq 2^\circ$ and grains with $\Delta \geq 15^\circ$). Each examined specimen was analyzed in the section denoted XZ. Where axis X is parallel to the last pressing direction and axis Z perpendicular to the bottom of the channel [20,21].

C. Mechanical Hardness Measurement

Mechanical hardness measurements were carried out using a micro Vickers hardness testing. Load was selected 1 kg and

dwel time were 10 s on the sample surface. Measurement locations on the sample surface were shown in Figure 2. Distance between two measurements was 1 mm. The local mechanical hardness distributions were then plotted as [22] graphically.

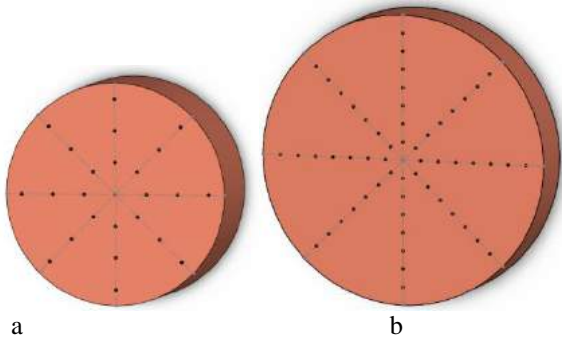


Fig. 2 : Measurement locations on the sample surface a). 8 mm diameter sample by ECAP-Conform through two passes b). 16 mm diameter sample by ECAP-Conform through one

III. RESULT AND DISCUSSION

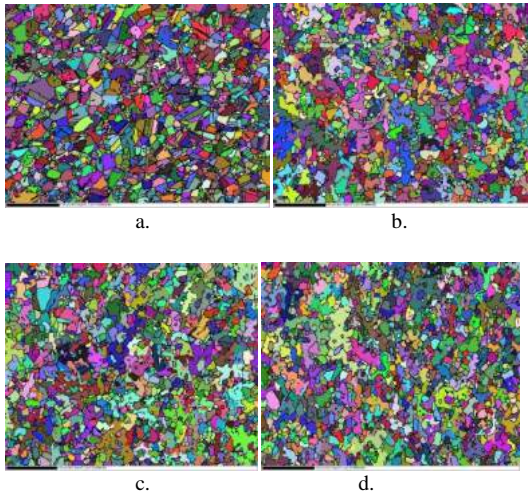


Fig. 3: Microstructure results for the specimen subjected to the ECAP-Conform, for one pass a. Cu-0.18wt%Sn, b. Cu-0.23wt%Sn, and for two pass c. Cu-0.18wt%Sn, d. Cu-0.23wt%Sn

Following processing, it is apparent that the microstructures exhibit two important characteristics on the longitudinal sections. First, the grain size is significantly reduced after ECAP-Conform by comparison with the unprocessed condition. Second, the grains are elongated on these sections and close inspection showed the maximum lengths were aligned approximately along the extrusion axis [8].

As seen from Fig. 3; after one pass, the microstructures are essentially homogeneous. Additionally, significant decrease in grain size was observed, but the grain size of the edge regions was found to be smaller. The specimens average grain sizes of after one ECAP-Conform for Cu-0.18wt%Sn are $\sim 1.3\mu\text{m}$ with twins and $\sim 2.6\mu\text{m}$ without twins and for Cu-0.23wt%Sn are $\sim 1.55\mu\text{m}$ with twins and $\sim 2.25\mu\text{m}$ without twins.

Figure 3c and d shows resultant material microstructures after two ECAP-Conform passes. The average grain sizes after two ECAP-Conform for Cu-0.23wt%Sn are $\sim 1.5\mu\text{m}$ with twins, $\sim 1.9\mu\text{m}$ without twins and for Cu-0.18wt%Sn are $\sim 1.5\mu\text{m}$ with twins, $\sim 2.5\mu\text{m}$ without twins.

Analysis of the textures and grain boundary structures in the damascene lines resulted in another indication that shear stress is important in developing a preponderance of twin boundaries [24].

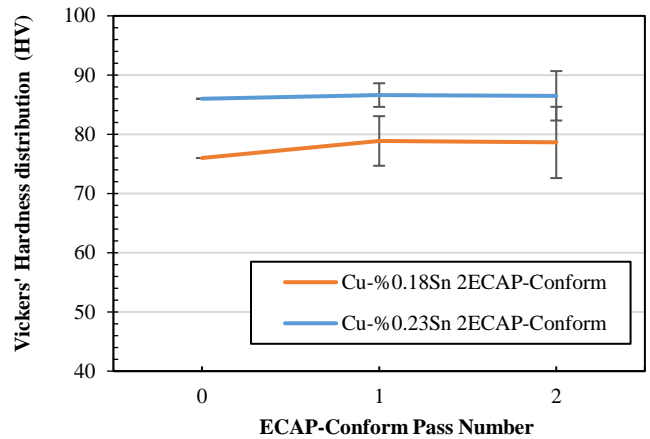
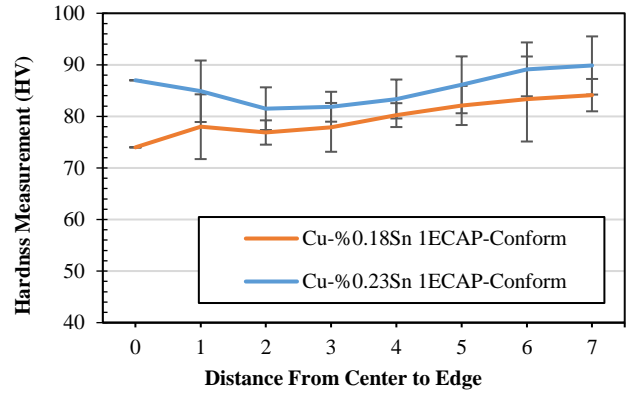


Fig. 4: Mechanical hardness distributions on the surfaces of the specimen subjected to ECA-Conform: a).after one pass forCu-0.18wt%Sn and Cu-0.23wt%Sn and b).two passes forCu-0.18wt%Sn and Cu-0.23wt%Sn

Figure4 shows the mechanical hardness distributions on surface. Apparently, the mechanical hardness distributions are heterogeneous. While we expected the hardness values be higher in the center, we can see that the values at the edge of the sample have higher hardness values. In addition to this we thought specimens after two ECAP-Conform passes would have higher hardness values, but these results show that specimens after one ECAP-Conform pass have higher hardness values.

IV. CONCLUSIONS

This study was carried out to investigate the effects of ECAP-Conform on microstructure and mechanical properties of the diluted Cu alloys. The following results were obtained:

1. It was observed that the samples of after processing by ECAP–Conform through two passes had finer-grained structure and they have $\sim 1.5\mu\text{m}$ with twins $\sim 1.9\mu\text{m}$ without twins grain size.
2. Conclusion of ECAP-Conform process at 400°C , twinning occurrences in microstructure were reported due to the fact that temperature reached material recrystallization temperature.
3. According to measurements of the hardness on surface, the hardest material was Cu-0.23wt%Sn alloy subjected to the ECAP–Conform after two passes. However, the homogeneity we wanted was not observed.
4. The direct effect of the alloying element on the structure could not be observed.

V. ACKNOWLEDGEMENT

This work was supported in part by “The Yildiz Technical University Scientific Research Fund” under contract No. 2016-07-02-YL12.

REFERENCES

- [1] R.Z. Valiev, R.K. Islamgaliev and I.V. Alexandrov: Prog.Mater.Sci. Vol.45 (2002), p.103.
- [2] Y.Z.Zhu, T.G. Langdon, R.S. Mishra, S.L. Semiatin, M.J. Saran and T.C.Lowe (eds): Ultrafine Grained Materials II (TMS, USA, 2002).
- [3] V. Sklenicka, J. Dvorak, M. Svoboda, P. Kral, B. Vlach: Material Science Forum Vol. 482 (2005) 83-88
- [4] R.Z. Valiev, T.G. Langdon, Prog. Mater. Sci. 51 (2006) 881–981.
- [5] R. Daly, S. Zghal, N. Njeh, Phys. Procedia 2 (2009) 677–684.
- [6] EBSD analysis of nano-structured copper processed by ECAP Farideh Salimyanfard, Mohammad Reza Toroghinejad, Fakhreddin Ashrafizadeh, Meysam Jafari, Materials Science and Engineering A (2010), 5348-5355
- [7] Prell M, Xu C, Langdon TG. Mater Sci Eng 2008; A480:449.
- [8] Cheng Xu, Steven Schroeder, Patrick B. Berbon, Terence G. Langdon: Acta Materialia 58 (2010) 1379–1386
- [9] Green D. J Inst Metals 1972;100:295.
- [10] Etherington C. J Eng Ind 1974;96:893.
- [11] C. Etherington, J. Eng. Ind. (August) (1974) 893
- [12] C. Wick, J.T. Benedict, E.F. Veilleux (Eds.), Tool and Manufacturing Engineers Handbook, fourth ed., vol. 2, Society of Manufacturing Engineers, Dearborn, MI, USA, 1983.
- [13] Georgy J. Raab, Ruslan Z. Valiev, Terry C. Lowe, Yuntian T. Zhu, Materials Science and Engineering A 382 (2004) 30–34
- [14] Yang W, Messler R, Felton L. J Electron Mater 1994;23(8):765e72
- [15] Takemoto T, Matsunawa A, Takahashi M. J Mater Sci 1997;32(15):4077e84.
- [16] Changzhou Aibang Machinery & Science Technology co., Ltd.
- [17] F.J. Humphreys, J. Mater. Sci. 36 (2001) 3833-3854
- [18] L. Ilucova, I. Saxl, M. Svoboda, V. Sklenicka, P. Kral, Image anal. Stereol. 26 (2007) 37-43
- [19] V. Sklenicka, J. Dvorak, P. Kral, M. Svoboda, M. Kvapilova, T.G. Langdon, Materials Science and Engineering A 558 (2012) 403-411
- [20] I. Saxl, V. Sklenicka, I. Ilucova, M. Svoboda and P. Kral: Mater. Sci. Forum Vol. 561-565 (2007), p. 813
- [21] P. Kral, J. Dvorak, M. Kvapilova, M. Svoboda, V. Benes, P. Ponizil, O. Sedivy, V. Sklenicka: Mater. Sci. Forum Vols. 667-669 (2011) pp. 235-240
- [22] H. Yilmazer, M. Niinomi, M. Nakai, J. Hieda, Y. Todaka, T. Akahori, T. Miyazaki: Journal of The Mechanical Behaviour of Biomedical Materials 10 (2012) 235–245

High Pressure Torsion Applications on Dilute Copper Alloys

Hasan Köklü¹, Hakan Yılmaz², Ceren GÖDE³, Burak Dikici⁴, Yoshikazu Todaka⁵, Halil Göker⁶

¹ Graduate Student, Department of Metallurgical and Materials Engineering, Yildiz Technical University, Istanbul, Turkey

² Department of Metallurgical and Materials Engineering, Yildiz Technical University, Istanbul, Turkey

³ School of Denizli Vocational Technology, Program of Machine, Pamukkale University, Denizli, Turkey

⁴ Department of Mechanical Engineering, Yüzüncü Yil University, Van, Turkey

⁵ Department of Mechanical Engineering, Toyohashi University of Technology, Toyohashi, Japan

⁶ Er-Bakir Electrolytic Copper Products Inc

Abstract

High-performance Cu alloys are required for the female and male terminal conductors in the power transmission of automobiles. A good longevity-conductivity relation and consequently high mechanical strength and good conductivity are being sought. Recently, severe plastic deformation (SPD) has provided new opportunities in investigations of the unusual mechanical, physical and electrochemical properties by permitting grain refinement to ultrafine-grained (UFG) and/or nano grained (NG) level, especially under (<100 nm). In this study, the some dilute Cu-Sn alloys subjected to high pressure torsion (HPT) processing at various rotation numbers have been studied systematically.

Keywords— Copper alloys, Severe plastic deformation, High-pressure torsion, ultra-fine grain

1. INTRODUCTION

Recently, research and development (R&D) activities are focused on the high-performance Cu and alloys in applications such as female and male conductor terminals, rotor and brush bars, armatures and heavy electrical switches in high-speed trains. The most important handicap in increasing the speed of today's fast trains is due to the inadequate mechanical performance of the catenary line. In summary, the required properties for this wire are conductivity and high strength above. However, both high mechanical performance and good conductivity are often difficult to find for the Cu and its alloys. Despite its excellent conductivity, the strength of pure Cu (~100 MPa) is not sufficient for such applications.

In recent years, "Severe Plastic Deformation" (SPD) methods have attracted the attention of researchers because of their ability to develop extraordinary mechanical, physical and electrochemical properties in bulk materials. Unlike conventional plastic deformations, the spreading of material during the deformation is prevented and the pre-process and post-process shapes remain the same and excessive shear deformation occurs in the material without permitting dimensional change. Considerable interest has developed over the last decade in the processing materials through the application of SPD in order to achieve grain sizes at ultrafine grained (UFG) (< 500 nm) and nanograined (NG) (<100nm) level [1–3]. The extraordinary properties exhibited by the SPD methods are indicative of the promise of these methods. However, because of the limited sample size that it has, only some processes have been able to pass serial production. The

inadequacy of conventional methods on the Cu and Cu alloys required the application of SPD methods.

Although several SPD techniques are available, the most promising procedure appears to be the high-pressure torsion (HPT) [4,5]. Experiments have shown that HPT is especially effective in producing extremely small grain sizes when compared with other SPD processing techniques. [6–8] The HPT process is known as the SPD method, which aims to reduce the grain size under pressure of the sample by applying rotational motion with the press to the disk-like sample placed between the two opposing anvils. One of the anvils used in the HPT process when moving effect on the movement and rotation presses the sample, and the other is trying to prevent the flow of the sample became constant during operation. At this point, the grains in the sample move from the middle to the edge of the sample, and at the same time, it shrinks. If there is no loss of material out of the sample being treated between the anvils and the sample thickness remains constant, the shear strain is calculated as:

$$\gamma=2\pi Nr/t \quad (1.1)$$

Where γ is the shear strain, N is number of rotations, r is the distance between the center of the disc and the edge, and t is the thickness of the sample. If we think that there is a loss of material between the two molds and a change in the thickness of the sample, it is possible to mention an alternative connection. Compared to other SPD methods, the true stress ϵ can be calculated as:

$$\epsilon=\gamma/\sqrt{3} \quad (1.2)$$

This is a coefficient, and according to two different theories, this value changes to 2 (Tresca theory) or $\sqrt{3}$ (Mises theory). Figure 2 shows the coin-shaped specimen before and after HPT processing.

High-pressure during SPD significantly affects the development of the grain structure and consequently enables the production of bulk materials composed of ultrafine or/and nanostructured grains. Among the SPD techniques, HPT processing is an especially attractive procedure because, by comparison with ECAP, it leads both to smaller grains and to a higher fraction of high-angle grain boundaries. [9]

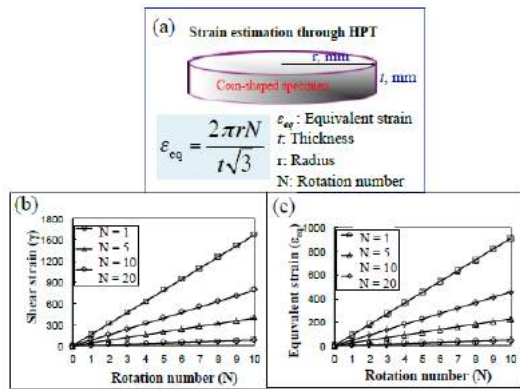


Fig. 1. (a) Principle of estimating strain on coin-shaped specimen, and change in (b) shear strain (γ) and (c) equivalent strain (ϵ_{eq}) calculated by Eq (1.1) and Eq (1.2).

UFG / NG materials are filled with dislocation cells consisting of grain and lower grain boundaries and high density oriented dislocations and exhibit a unique thermodynamically unstable microstructure. Despite having an excessive deformation with SPD, due to the microstructure obtained, the materials exhibit extraordinary properties with improved ductility and fatigue behavior together with high strength and hardness. Therefore, in this study, the diluted Cu-Sn alloys was processed by HPT processing for various rotation numbers. The microstructural evaluation and hardness distributions of the Cu-Sn alloys subjected to the HPT processing was investigated systematically.

II. EXPERIMENTAL PROCEDURES

2.1. Materials

In our study, the Cu-Sn alloys were produced at 1100-1200°C in a continuous casting furnace (Rautomead) with a graphite pot of 500 kg capacity in 20 mm wire rod sizes. Equipped with high automation technology, many parameters including casting speed and casting temperature can be adjusted precisely in the system. To prevent oxidation of the alloy during processing, the liquid metal surface is covered with special graphite casting dust. And then, the Cu bars were cut as some coin-shaped specimens with a diameter of 20 mm and a thickness of 1 mm for HPT processing.

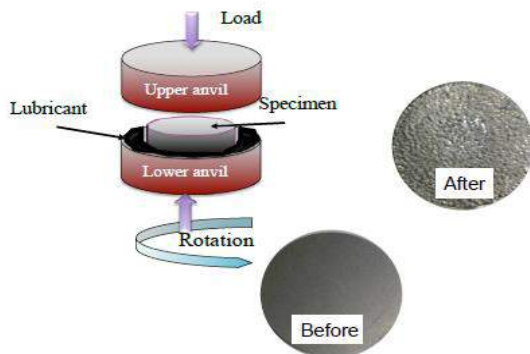


Fig 2. An illustration of HPT processing and the coin-shaped specimens before and after HPT processing [9].

The Cu-Sn coin-shaped specimens were subjected to High pressure torsion (HPT) (Fig. 2) at rotation numbers (N) of 1, 5, and 10 with 0.5 rpm under 2.5 GPa pressure in air at room temperature.

2.2. Material Characterization

The microstructure of each sample was examined using an optical microscope (OM), X-ray diffractometer, Scanning electron microscopy and Transmission electron microscopy. The observation was carried out at a half radius, r_h , position, $r = r_h = 5$ mm, of each specimen. The specimens for OM observation were wet polished using water-proof emery papers of up to #2400 and were then buff polished to obtain the mirror surface using a diamond suspension (1 μ m). Subsequently, they were etched.

TEM observation was performed with an increasing voltage of 200 kV after TEM sample preparation. The specimens for the XRD analysis were wet polished using water-proof emery papers of up to #2400.[10] The phase constitution of each specimen was analyzed at r_h position by XRD using a Cu-K α radiation tube with a voltage of 40 kV and a current of 40 mA

2.3. Hardness Measurement

Hardness measurements were made using a Vickers microhardness tester. Hardness measurements were applied to a section of the coin specimen by applying a load of 500 grams on the surface with a waiting period of 10 seconds. The measurements on the surface of the sample were made at 1 mm intervals between measurement positions along the radial and rotational directions. The local Vickers' hardness radial distributions were then plotted.

III. RESULT AND DISCUSSION

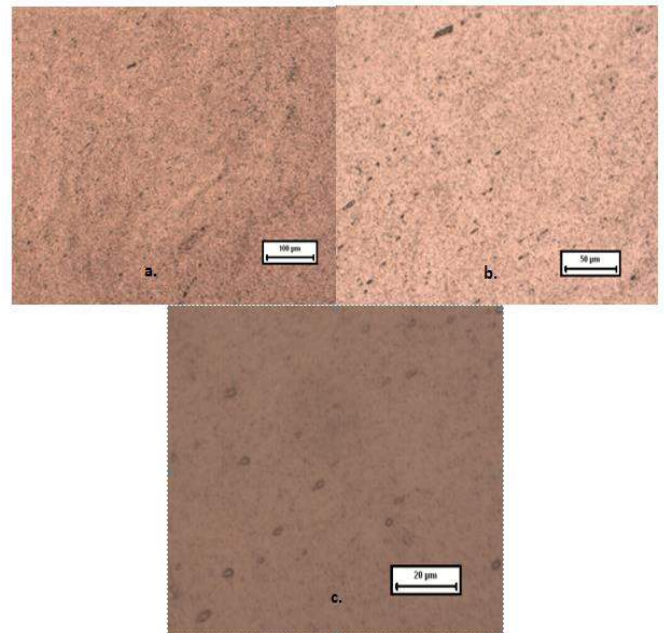


Fig 3. The optical micrographs of the Cu-Sn alloys subjected to HPT processing at N=1, a. 100x, b. 200x, c. 500x.

The microstructures of as-caste Cu-Sn alloys composed of coarse grains with a clear grain boundary. The grains of the pure Cu show elongated morphology from center to edge of bar related to solidification. At earlier stage of the HPT processing, The microstructure of the Cu-Sn HPT specimen at $N = 1$ shows deformation flow lines. Kurzydowski et al. also report such similar microstructure for the pure copper subjected to a conventional plastic deformation [10]. On the other hand, the microstructure of the copper alloys subjected to HPT processing at $N > 1$ clearly exhibit an ultrafine grained structure in Fig. 4. As the amount of excessive plastic deformation applied, that is, the number of rotations, is increased, finer granules are formed and the number of grains is gradually increasing. Increasing the rotation numbers, the grain size decreased, obviously. The HPT specimens show homogeneous microstructure at $N \leq 5$.

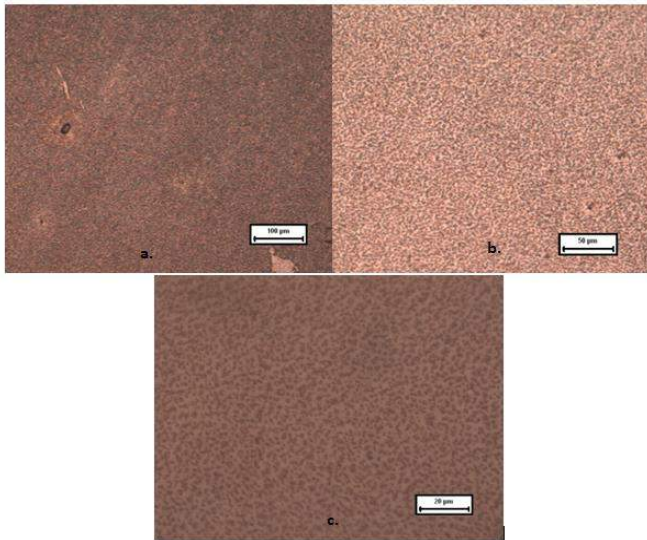


Fig 4. The optical micrographs of the Cu-Sn alloys subjected to HPT processing at $N = 10$, a. 100x, b. 200x, c. 500x

Fig. 5 gives the hardness value of as casted the Cu-Sn alloys subjected to HPT processing at $N = 1, 5$, and 10 . Fig. 5 clearly shows that as the number of rotations increases, the hardness values increase. Also, the hardness values at the center of the sample are lower at lower rotation numbers ($N < 5$). The hardness increases from the center to the edge in the coin-shaped HPT specimens because of the anisotropic grain refinement and dislocation accumulation as a result of variation in ϵ_{eq} with position [11,12]. The Cu-Sn alloys subjected to HPT processing show homogeneous radially distributed hardness value at the Cu-Sn alloys at $N \leq 5$.

As seen in Fig. 5, the hardness values are clearly increased as N increases. However, these increase values are not homogeneous at $N=1$. At lower rotations, the hardness values change more and a certain homogeneity is not achieved. The hardness increases from the center to the edge in the coin-shaped HPT specimens because of the anisotropic grain refinement and dislocation accumulation as a result of variation in ϵ_{eq} with position [11,12]. The hardness values and the

homogeneity increase as the number of high rotations increases. It is clearly seen that the hardness values are very close to each other and the hardness values are very little in the case of $N= 5$ and 10 . Thus, we can see in Figure 5 that a certain homogeneity is achieved as the number of rotations increases. These results provide clear evidence for the achievement of a homogeneous microstructure in the Cu-Sn HPT specimens with increasing N .

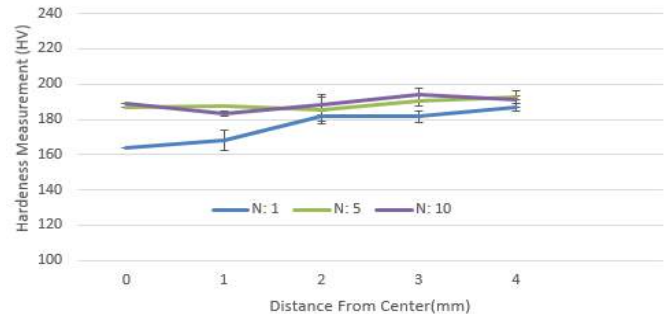


Fig 5. Graph of Hardness measurement results of the Cu-Sn alloys subjected to HPT processing at rotation numbers ($N:1, N:5, N:10$).

In addition, we can see that the hardness values increase clearly from the center of the sample to the edges. In this case, we can say that the HPT process is more effective at the edges of the sample and that higher hardness values can be achieved at the edges of the sample. Similar results have been obtained when working with M. Das and G. Das on 6063 aluminum alloys. [13] This confirms the results of our work. Thus, we can say that the HPT process increases the hardness values at the edges of the sample more than the center.

As a result, the hardness values of the Cu-Sn alloys subjected to HPT processing at different rotation numbers increase as the number of rotations increases and homogeneous hardness values are reached at higher rotation counts. In addition, the hardness values increase from the center of the specimen towards the edges and reach the highest values near the edges of the specimen.

IV. CONCLUSIONS

This study was carried out to investigate the effects of HPT on microstructure and mechanical properties of material. The following results were obtained:

1. Fine grain microstructures were obtained for Cu and Cu alloys subjected to HPT processing.
2. The microstructure of the HPT processed Cu alloys exhibited homogeneity at the higher the number of $N \leq 5$.
3. The hardness values of Cu-Sn alloys subjected to HPT processing increase as N increases. The hardness values increase from the center to the edges of the HPT specimen at $N < 5$.
4. The hardness values reached to homogeneous distribution at $N \leq 5$.

V. ACKNOWLEDGEMENT

This work was supported in part by “The Yildiz Technical University Scientific Research Fund” under contract No. 2016-07-02-YL11. The HPT process was carried out in the Department of Mechanical Engineering at Toyohashi University of Technology.

REFERENCES

- [1] R.Z. Valiev, R.K. Islamgaliev, I.V. Alexandrov, Prog. Mater. Sci. 45 (2000) 103–189.
- [2] R.Z. Valiev, T.G. Langdon, Prog. Mater. Sci. 51 (2006) 881–981.
- [3] R.Z. Valiev, Y. Estrin, Z. Horita, T.G. Langdon, M.J. Zehetbauer, Y.T. Zhu, JOM 58(4) (2006) 33–39.
- [4] N.A. Smirnova, V.I. Levit, V.I. Pilyugin, R.I. Kuznetsov, L.S. Davydova, V.A. Sazonova, Fiz. Met. Metalloved. 68 (1986) 1170–1177.
- [5] T. Hebesberger, H.P. Stuwe, A. Vorhauer, F. Wetscher, R. Pippan, Acta Mater. 53 (2005) 393-402.
- [6] Z. Horita, D.J. Smith, M. Furukawa, M. Nemoto, R.Z. Valiev, T.G. Langdon, J. Mater. Res. 11 (1996) 1880–1890.
- [7] V. Stolyarov, R.Z. Valiev, in: M.J. Zehetbauer, R.Z. Valiev (Eds.), Nanomaterials by Severe Plastic Deformation, Wiley–VCH, Weinheim, Germany, (2004), pp. 125–130.
- [8] C. Rentenberger, T. Waitz, H.P. Karnthaler, Mater. Sci. Eng. A462 (2007) 283–288.
- [9] H. Yilmazer., Improvement of Mechanical Biocompatibility of Biomedical β -Type Titanium Alloys Through High Pressure Torsion (2012)
- [10] K. J. Kurzydowski, H. Garbacz and M. Richert Effect of Severe Plastic Deformation on Microstructure and Mechanical Properties of Al and Cu, Poland. (2004)
- [11] A.P. Zhilyaev, K. Oh-ishi, T.G. Langdon, T.R. McNelley, Mater. Sci. Eng., A 410–411 (2005) 277–280.
- [12] Y. Ito, Z. Horita, Mater. Sci. Eng., A 503 (2009) 32–36.
- [13] M. Das, G. Das, M. Ghosh, M. Wegner, V. Rajnikant, S. G. Chowdhury T.K. Pal, Microstructures and Mechanical Properties Of HPT Processed 6063 Al Alloy (2012).

Energy Saving in Industrial Annealing Furnaces Through an Organic Rankine Cycle System Application

Fatma ÇANKA KILIÇ¹, Mehmet Önder SERT², Muharrem EYİDOĞAN², Durmuş KAYA², Necmi Cemal ÖZDEMİR³

¹Department of Electrical and Energy, Air Conditioning and Refrigeration Technology, Kocaeli Vocational School, Kocaeli University, Mahmutpasa Mah. Mahmutpasa Cad. No: 151, 41140 Kullar/Basiskele/Kocaeli, Turkey.

²Department of Energy Systems Engineering, Faculty of Technology, Kocaeli University, 41380 Umuttepe, Kocaeli, Turkey.

³Department of Electrical Engineering, Faculty of Engineering, Kocaeli University, 41380 Umuttepe, Kocaeli, Turkey.

fatmacanka@hotmail.com, mehmetondersert@hotmail.com, muharrem_eyidogan@hotmail.com, durmuskaya@hotmail.com, necmi.ozdemir41@hotmail.com

Abstract— In this study, an energy efficiency study has been carried out in a natural gas-fired rolling mill annealing furnace of an industrial establishment. In this context, temperature and flue gas measurements were realized while operating the furnace at the operating conditions and waste heat potential was calculated by using these data. In the calculations waste heat potential was determined as 3,630.31 kW. The electricity generation through an Organic Rankine Cycle system has also been determined by using the waste heat potential.

Keywords: Rolling mill annealing furnace, energy efficiency, energy saving, waste heat recovery, Organic Rankine Cycle

1. INTRODUCTION

The efficient use of energy is one of the issues emphasized both in our country and in the world greatly. Energy production and use has many environmental impacts such as air pollution, greenhouse effect and ecosystem effects on the Earth [1]. From an industrial point of view, efficiency-enhancing studies provide significant energy savings amount in the fuel economy, efficient use of resources and environmental pollution reductions [2,3].

As a result of the energy audits in different sectors, it can be seen that between 95% of industrial plants and industrial enterprises energy saving amounts can reach the level of 5% to 40%. What is even more striking is that it is possible to achieve a minimum of 10% energy savings by implementing measures with no or little investment in industrial plants and industrial enterprises. This ratio demonstrates the importance of energy saving in any direction [4].

The iron and steel sector is one of the most energy consuming sectors and accounts for 5% of the world's total energy consumption [5]. With 27-33%

share of the production costs of the sector, the energy costs have the largest slice in the sector, which is the main reason for energy saving studies in this regard. Increasing energy efficiency is possible by determining the locations and quantities of heat losses. Furnaces, especially annealing furnaces operating at high temperatures, are systems that must be operated as efficiently as possible in terms of pollution that caused by exhaust gases, given to the environment, either in terms of fuel consumption or in industrial enterprises [6].

Rankine cycle is one of the most widely used methods of transforming thermal energy into power in high capacities. The nuclear power plants and coal power plants can be given as examples. The main equipment of steam power cycles can be listed as condenser, pump, boiler, turbine and working fluid. In the conventional Rankine cycle, water is used as a working fluid.

Advantages of using water as a working fluid in the Rankine cycle are;

- Very good thermal/chemical stability,
- Very low viscosity (low pumping work),
- Good energy carrying ability (having high evaporation ability and specific heat),
- It is non-poisonous, non-flammable and does not harm the environment,
- It is cheap and abundant in nature.

In addition to these advantages, problems encountered when using water as a working fluid [7];

- To prevent condensation during expansion, hot steam must be produced in the steam turbine,
- Risk of corrosion in turbine blades,
- Working with high pressure in the evaporator,
- It requires complex and expensive turbines to be used in the process.

Due to the reasons mentioned above, water is more suitable for high temperature applications and large central systems. In small and medium scale power cycles, problems that are encountered with water use can be partially reduced by the use of appropriate fluid. These fluids have a higher molecular weight than water and a low critical temperature and they are called organic fluids and they are used in steam cycles called "organic Rankine cycle (ORC)". The energy sources used in the Organic Rankine Cycle system and the Organic Rankine Cycle system is given in Figure 1.1 [8]. An organic Rankine cycle has some advantages over conventional steam cycles as;

- Less heat is needed during the evaporation period,
- Evaporation takes place at low pressure and low temperature,
- The expansion process is finished in the steam zone, so there is no need to over-heat it. This reduces the risk of wear on the turbine blades.

- Low temperature difference between evaporation and condensation means less pressure drop during expansion. For this reason, simple single stage turbines are used for the expansion.

The substances listed for the organic Rankine cycle are listed below;

- Hydrocarbons (HC)
- Hydrofluorocarbons (HFC)
- Hydrochlorofluorocarbons (HCFC)
- Chlorofluorocarbons (CFC)
- Perfluorocarbons (PFC)
- Siloxanes
- Alcohols
- Aldehydes
- Ethers
- Hydrofluoroethers (HFE)
- Amines
- Inorganic fluids

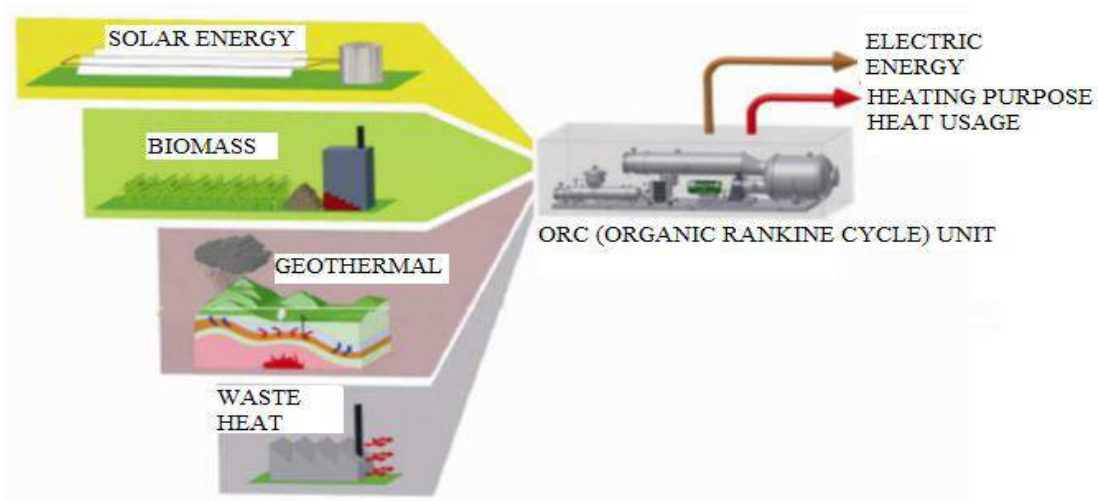


Figure 1. Schematic illustration of the energy sources used in the Organic Rankine Cycle system.

The fluid used in the Organic Rankine Cycle plays a crucial role in determining the performance of the system and the economy of the power plant [9]. For this reason, a lot of studies have been carried out in the literature to have a good flow in different heat recovery applications and the properties that should be existed in good flow are listed below [10-16].

- Zero or positive slope saturation curve (isentropic or dry liquids),
- High evaporation latent heat,
- High density (liquid/vapor phase),
- High specific heat,
- Appropriate critical parameters (temperature, pressure),

- Acceptable condensation and evaporation pressure (> 1 bar and <25 bar),
- Proper heat transfer properties (low viscosity, high thermal conductivity),
- Proper thermal and chemical stability (stability at high temperatures),
- Compatibility with materials (no corrosive effect),
- High thermodynamic performance (high energy/exergy),
- Good safety characteristics (non-toxic and non-flammable),
- Low environmental impact,
- Low cost and easy availability.

Despite the fact that Organic Rankine Cycle systems have been explored since 1880's, they have not been as prevalent as everyday use. The increasing use of fossil fuels has developed a concern for the future and also, the environmental pressures altogether have caused the use of low temperature heat sources in power generation systems. Organic Rankine Cycle systems make it possible to generate electricity from a variety of energy sources, such as solar energy, geothermal energy, biomass, and flue gas waste heat, as it allows for low temperature operations. Organic Rankine Cycle systems are tested and used in many places by USA, Canada, Italy, Austria, Germany, Netherlands, Switzerland and other countries [17-19].

In this study, detailed measurements of energy efficiency were performed in a natural furnace annealing furnace of an industrial corporation, the results of measurements and calculations have been made by using the data obtained from the company. In this direction, the energy saving opportunities and the repayment periods have been determined.

2. MEASUREMENTS AND CALCULATIONS

Waste heat is the unusable heat that is released during the combustion process or any chemical reaction/thermal process and it is directly discharged to the atmosphere. Industrial energy-intensive processes, internal combustion engines and mechanical equipment introduce high amounts of waste heat into the environment [20-22]. Waste heat does not only have a high level of exergy, but it also releases pollutant emissions in abundance, such as carbon dioxide (CO₂), nitrogen oxides (NO_x) and sulfur oxides (SO_x). Some developed countries, while evaluating their waste heat, reduce their energy imports while reducing their emissions. Many energy recovery technologies have been developed to recover waste heat. These are; heat exchangers (recuperators, regenerators, air preheaters, economizers, heat pipes, waste heat boilers, etc.), heat pumps, absorption/adsorption cooling machines and heat-electricity converters in

different types. Waste heat power generation can be achieved using thermodynamic cycles [23]. These are can be listed as; steam Rankine cycle, organic Rankine cycle, Kalina cycle, Gaswami cycle and Trans-critical/supercritical cycles or thermionic, thermoelectric and piezo-electric equipment, which are direct conversion systems [24]. Although thermodynamic power cycles are currently in use, direct conversion systems are still in the development process.

In general, convectional steam cycles operate at medium and high temperatures, but they are not economical in small-scale systems or at low temperatures [25]. At low and moderate temperatures, organic Rankine cycles and Kalina cycles are advantageous because they have a more complex structure.

Heat transfer from the hot heat sink to the power converter takes place in two ways; (1) the flue gas/process heat and the working fluid are transferring the heat in the same heat exchanger or (2) the thermal oil is used as the working fluid to assure the system against the ignition risk of the organic fluid. The equipment selection of the Organic Rankine Cycle system depends primarily on the temperature of the heat source and the amount of desired power [26].

Organic Rankine Cycle technology has been developed to save fuel and protect the environment in the processes where waste heat is present. Organic Rankine cycles have the ability to convert unused waste heat at low temperatures to electric energy which is so important in energy engineering and in various academic and industrial studies. Many aspects of the Organic Rankine Cycle have been explored, but often the researches have focused on the optimal design of the working fluid and the cycle [27-34].

The following measurements have been carried out for the calculation of the waste heat potential of the annealing furnace;

-Flue gas temperature and ambient temperature:

$$T_{\text{flue gas}} = 433,1^{\circ}\text{C} \text{ and } T_{\text{ambient}} = 30^{\circ}\text{C}$$

-Dynamic pressure of the flue gas

$$P_{\text{dynamic flue gas}} = 0,13 \text{ hPa}$$

-Flue gas analysis

Results of the flue gas analysis

$$\text{O}_2 = \%6,5 \quad \text{CO}_2 = \%6,54 \quad \text{N}_2 = \%71,83 \quad \text{Ar} = \%0,18$$

$$\text{H}_2\text{O} = \%14,27$$

A flue gas analyzer is used for flue gas measurement and a pitot tube is used for dynamic pressure measurement.

The natural gas value is taken from the SCADA screen. The diameter of the chimney was measured by using a meter.

$$Q_{\text{natural gas}} = 2.397 \text{ Nm}^3/\text{h} \text{ and } d_{\text{chimney (flue)}} = 2,22 \text{ m}$$

The following calculations were carried out as a result of these measurements;

-The velocity of the flue gas

$$J_{\text{flue gas}} = \frac{\sqrt{(574,2 * T_{\text{flue gas}}) + (156842,77)}}{\sqrt{100910}} * \sqrt{(P_{\text{dynamic}} * 100)} \quad (1)$$

$$J_{\text{flue gas}} = \frac{\sqrt{(574,2 * 433,1) + (156842,77)}}{\sqrt{100910}} * \sqrt{(0,13 * 100)}$$

$$J_{\text{flue gas}} = 7,23 \text{ m/s}$$

-Volumetric flow rate of the flue gas

$$V_{\text{flue gas}} = J_{\text{flue gas}} * A_{\text{flue}} * 3600 \quad (2)$$

$$V_{\text{flue gas}} = 7,23 \text{ m/s} * \left(\frac{\pi * d^2}{4}\right) * 3600$$

$$V_{\text{flue gas}} = 7,23 \text{ m/s} * 3,87 \text{ m}^2 * 3600$$

$$V_{\text{flue gas}} = 100.728,36 \text{ m}^3/\text{h}$$

-The density and heating temperature of the flue gas

Flue gas density and flue gas specific heat are calculated by using the measurement values.

The flue gas density was 0,4838 kg/m³ and the specific heat was 1,1505 kJ/kg.K

-The flue gas mass flow rate:

$$Q_{\text{flue gas}} \text{ (kg/h)} = V_{\text{flue gas}} \text{ (m}^3/\text{h)} * \rho_{\text{flue gas}} \text{ (kg/m}^3) \quad (3)$$

$$Q_{\text{flue gas}} \text{ (kg/h)} = 100.728,36 \text{ m}^3/\text{h} * 0,4838 \text{ kg/m}^3$$

$$Q_{\text{flue gas}} = 48.732,38 \text{ kg/h}$$

-Waste Heat Amount

Waste Heat Amount= (Flue gas flow rate*The temperature difference*Specific Heat) /3600 (4)

$$Q_{\text{waste heat}} = (48.732,38 \text{ kg/h} * (433,1-200) \text{ }^\circ\text{C} * 1,1505 \text{ kJ/kg.K}) / 3600$$

$$Q_{\text{waste heat}} = 3.630,31 \text{ kW}$$

The electric energy that can be obtained is calculated after the amount of waste heat is determined and thus, the feasibility study for the production of electricity has been carried out by using the Organic Rankine Cycle system.

3. THE CALCULATION RESULTS AND RECOMMENDATIONS

The flue gas measurement values that used in the calculations are given in Table 1.

Table 1- Flue Gas Measurements

Equipment	Flue Gas Measurements				Natural Gas Flow Rate	The diameter of the Flue	Velocity
	Flue Gas Temperature	O ₂	CO ₂	CO			
	°C	%	%	ppm			
Annealing furnace flue cold charge	433,10	6,50	6,54	-	2.397,00	2,22	7,23

The calculations for the flue gas and the savings potentials that have been realized by using Table 1 values are given in Table 2 and Table 3.

Table 2- Calculation of flue gas measurements.

Equipment	Flow Rate	Density	Specific Heat	Flow Rate	Heat Exchanger Input Temperature	Heat Exchanger Output Temperature	Amount of Waste Heat	Electricity to be obtained*
	m ³ /h	kg/m ³	kJ/kg.K	kg/h	°C	°C	kW	kW
Annealing furnace flue cold charge	100.728,36	0,4838	1,1505	48.732,38	433,10	200	3.630,31	580,85



800 kW biomass ORC Turboden plant for Teleriscaldamento Varna-Bressanone. Varna – Bolzano, Italy - 2008

Figure 2. Schematic illustration of Organic Rankine Cycle device.

Table 3- The Calculation of Savings Potential.

Waste Heat Amount	Electricity to be obtained*	Working Hour	Energy Earning	Electricity Unit Cost **	Financial Savings	Investment Cost	Simple Payback Period
kW	kW	h/year	kWh/year	Turkish Liras /kWh	Turkish Liras/year	Turkish Liras	year
3.630,31	580,85	2.800	1.626.378,88	0,2681	436.032,18	3.540.790	8,12

Waste heat potential has been calculated as 3.630,31 kW.

The efficiency of the Organic Rankine Cycle system was assumed to be 16%.

-Power to be achieved = Amount of waste heat * System efficiency (5)

$$Q_{\text{electric}} = 3.630,31 \text{ kW} * 0,16$$

$$Q_{\text{electric}} = 580,85 \text{ kW}$$

-Working hours of annealing furnace 2.800 h/year

-Energy gain=Electrical Power* Working hours (6)

$$Q_{\text{energy}} = 580,85 \text{ kW} * 2.800 \text{ h/year}$$

$$Q_{\text{energy}} = 1.626.378,88 \text{ kWh/year}$$

-Electrical unit cost was calculated by using the last electricity bill of the company which was 0,2681 Turkish Liras/kWh.

-Financial savings = Energy gain*Electric unit cost (7)

$$Q_{\text{financial gain}} = 1.626.378,88 \text{ kWh/year} * 0,2681 \text{ Turkish Liras/kWh}$$

$$Q_{\text{financial gain}} = 436.032,18 \text{ Turkish Liras/year}$$

-The investment cost of the Organic Rankine Cycle system is 3.540.790,00 Turkish Liras.

-Investment payback period = Investment cost/Financial gain (8)

$$\text{Simple payback period (SPP)} = (3.540.790,00 \text{ TL}) / (436.032,18 \text{ TL/year}) = 8,12 \text{ year}$$

4. CONCLUSION

In this study, the measurements were taken to determine the energy efficiency and energy saving potentials in the annealing furnace of an industrial enterprise. From the data obtained from the measurements, the waste heat of the annealing furnace was determined as an important heat source potential. It is possible to reduce the electricity

consumption costs of the plant by generating electricity by using the determined waste heat in the annealing furnace through the Organic Rankine Cycle system which will operate with the efficiency of 16%.

It is anticipated that energy savings of the plant will be 1,626,378.88 kWh/year by providing the specific application. The financial value of this savings is to be 436.032,18 Turkish Liras/year and the investment

cost of the Organic Rankine Cycle system is to be 3.540.790,00 Turkish Liras. The simple payback period for the project is to be 8,12 years. Since the working period of the annealing furnace is 2800 hours/year, the investment cannot be accepted as feasible. It has been determined that the investment can only be feasible when the annealing furnace is working at full capacity for 8,000 hours per year.

REFERENCES

- McAllister, S., Chen, J. ve Fernandez-Pello, A. C., "Thermodynamics of Combustion", Fundamentals of Combustion Processes, 1st Edition, Springer, USA, 18-20, 2011.
- Terzi, U.K. ve Baykal, R., "Efficient and effective use of energy: a case study of Tofas", Environmental Research, Engineering and Management, Cilt 1, No 55, 29-33, 2011.
- Simsek, B., Simsek, E.H. ve Altunok, T., "Empirical and Statistical Modeling of Heat Loss from Surface of a Cement Rotary Kiln System", Journal of the Faculty of Engineering and Architecture of Gazi University, Cilt 28, No 1, 59-66, 2013.
- Ünlü, O., "Sanayiye Enerji Tasarrufu Çalışmalarının Önemi ve Buhar Sistemleri ile İlgili Uygulama Örnekleri", IX. Ulusal Tesisat Mühendisliği Kongresi ve Sergisi Bildirileri, 2009.
- Xu, C. ve Cang, D., "A Brief Overview of Low CO₂ Emission Technologies for Iron and Steel Making", Journal of Iron and Steel Research, International, Cilt 17, No 3, 1-7, 2010.
- Eyidoğan, M., Kaya, D., Dursun, Ş., Taylan, O., "Endüstriyel Tav Fırınlarında Enerji Tasarrufu ve Emisyon Azaltma Fırsatları", Gazi Üniversitesi Mühendislik ve Mimarlık Fakültesi Dergisi, Cilt 29, No 4, 735-743, 2014.
- Wali, E., "Optimum working fluids for solar powered Rankine cycle cooling of buildings", Solar Energy, 25 (3): 235-241, 1980.
- Eyidoğan, M., "Organik Rankine Çevrimli Güç Üretim Sisteminin Enerji ve Ekserji Analizi", Doktora Tezi, Karabük Üniversitesi Fen Bilimleri Enstitüsü, 2014.
- Tchanche, B. F., Quoilin, S., Declaye, S., Papadakis, G. and Lemort, V., "Economic optimization of small scale organic Rankine cycles". 23rd International Conference on Efficiency, Cost, Optimization, Simulation and Environmental Impact of Energy Systems (ECOS), Lausanne, Switzerland, 1-10, 2010.
- Papadopoulos, A. I., Stijepovic, M. and Linke, P., "On the systematic design and selection of optimal working fluids for organic Rankine cycles", Applied Thermal Engineering, 30 (6-7): 760-769, 2010.
- Badr, O., Probert, S. D. and O'Callaghan, P. W., "Selecting a working fluid for a Rankine cycle engine", Applied Energy, 21 (1): 1-42, 1985.
- Maizza, V. and Maizza, A., "Unconventional working fluids in organic Rankine cycles for waste energy recovery systems", Applied Thermal Engineering, 21 (3): 381-390, 2001.
- Chen, H., Goswami, D. Y. and Stefanakos, E. K., "A review of thermodynamic cycles and working fluids for the conversion of low-grade heat", Renewable and Sustainable Energy Reviews, 14 (9): 3059-3067, 2010.
- Tchanche, B. F., Papadakis, G., Lambrinos, G. and Frangoudakis, A., "Fluid selection for a low-temperature solar organic Rankine cycle", Applied Thermal Engineering, 29 (11-12): 2468-2476, 2009.
- Wali, E., "Working fluids for solar Rankine-cycle cooling systems", Energy, 5 (7): 631-639, 1980.
- Hung, T. C., Shai, T. Y. and Wang, S. K., "A review of organic Rankine cycles (ORCs) for the recovery of low-grade waste heat", Energy, 22 (7): 661-667, 1997.
- Internet: Total references, "Turboden references" <http://www.turboden.eu/en/references/references-searchpdf.php?country=all&application=all&power=all>, 2013.
- Internet: Reference selection "Tri-o-gen references" <http://www.triogen.nl/references/reference-overview>, 2013.
- Internet: Global project map "Ormat Inc" <http://www.ormat.com/global-project>, 2013.
- Bonilla, J. J., Blanco, J. M., Lopez, L. and Sala, J. M., "Technological recovery potential of waste heat in the industry of the Basque Country", Applied Thermal Engineering, 17 (3): 283-288, 1997.
- Latour, S. R., Menningmann, J. G. and Blanney, B. L., "Waste heat recovery potential in selected industries", (EPA), 30 (7): 1-6, 1982.
- Quoilin, S. and Lemort, V., "Technological and economical survey of organic Rankine cycle systems", 5th European Conference on Economics and Management of Energy in Industry, Algarve-Portugal, 4-5, 2009.
- Galanis, N., Cayer, E., Roy, P., Denis, E. S. and Desilets, M., "Electricity generation from low temperature sources", Journal of Applied Fluid Mechanics, 2 (2): 55-67, 2009.
- BCS Inc. "Waste heat recovery: technologies and opportunities in U.S. industry", US Dept. of Energy (DOE), USA, 25-29, 2008.
- Bohl, R., "Waste heat recovery from existing simple cycle gas turbine plants - a case study", 18th Symposium on Industrial Application of Gas Turbines (IAGT), Banff, Alberta, Canada, 1-14, 2009.
- Quoilin, S., Declaye, S. and Lemort, V., "Expansion machine and fluid selection for the organic Rankine cycle", 7th International Conference on Heat Transfer, Fluid Mechanics and Thermodynamics (HEFAT), Antalya, Turkey, 1-7, 2010.
- Maizza, V. and Maizza, A., "Unconventional working fluids in organic Rankine cycles for waste energy recovery systems", Applied Thermal Engineering, 21 (3): 381-390, 2001.
- Chen, H., Goswami, D. Y. and Stefanakos, E. K., "A review of thermodynamic cycles and working fluids for the conversion of low-grade heat", Renewable and Sustainable Energy Reviews, 14 (9): 3059-3067, 2010.
- Hung, T. C., Shai, T. Y. and Wang, S. K., "A review of organic Rankine cycles (ORCs) for the recovery of low-grade waste heat", Energy, 22 (7): 661-667, 1997.
- Chacartegui, R., Sanchez, D., Munoz, J. M. and Sanchez, T., "Alternative ORC bottoming cycles FOR combined cycle power plants", Applied Energy, 86 (10): 2162-2170, 2009.
- Angelino, G. and Colonna di Paliano, P., "Multicomponent working fluids for organic Rankine cycles (ORCs)", Energy, 23 (6): 449-463, 1998.
- Chen, H., Yogi Goswami, D., Rahman, M. M. and Stefanakos, E. K., "Energetic and exergetic analysis of CO₂-and R32-based transcritical Rankine cycles for low-grade heat conversion", Applied Energy, 88 (8): 2802-2808, 2011.
- Lai, N. A., Wendland, M. and Fischer, J., "Working fluids for high-temperature organic Rankine cycles", Energy, 36 (1): 199-211, 2011.
- Cayer, E., Galanis, N., Desilets, M., Nesreddine, H. and Roy, P., "Analysis of a carbon dioxide transcritical power cycle using a low temperature source", Applied Energy, 86 (7-8): 1055-1063, 2008.

X-Ray Radiography of P460 Steel Welded By Submerged Arc Welding

Ugur Caligulu*, Mustafa Turkmen⁺, Ebru Tufanoglu*, Sermin Ozan*

*Firat University, Technology Faculty, Metallurgy and Materials Eng. Depart., 23119 Elazig-Turkey

⁺Kocaeli University, Hereke Vocational School, Metallurgy Department, Kocaeli-Turkey

ucaligulu@firat.edu.tr,

mustafa.turkmen@kocaeli.edu.tr

ebrutufanoglu@gmail.com,

serozan@firat.edu.tr

Abstract— In this study, the results of joining of P460 steel combined with a submerged arc welding (SAW) weld by X-Ray radiographic test were investigated. P460 material pairs were welded at different welding speed and ampere values using the submerged arc welding method. These welded samples are; Notch impact test, microhardness measurement, X-ray diffraction method and radiography tests were examined. Microstructural changes occurring in the weld zone of weld parameters after welding; by optical microscopy and EDS analysis were investigated. As a result of the experiments, it has been found that the P460 steel show the ability to weld sufficiently strong by the submerged welding method.

Keywords— P460, Notch Impact Test, Submerged Arc Welding, X-Ray Radiographic Test.

I. INTRODUCTION

Pressure vessels are defined as vessels closed to atmosphere made by joining spherical, cylindrical or conical shaped volumes used in the production, transportation, and storage of industrial gases in 0.490.105, Pa 0.5 ato and higher pressure (air, oxygen, nitrogen, argon, hydrogen gas), fuel gases (natural gas, acetylene gas, desulphurized coke gas) and steam. P460 steel material is mainly used in the manufacture of bridges, tankers, pipe fittings, and pressure vessels (CO₂ and LPG tanks etc.) [1-2].

The submerged arc welding method is an automatic welding method, and the performance and success of the process depend entirely on the preference of the optimum welding parameters. The submerged arc welding method is a widely used welding method in today's industry due to its advantages such as superior performance in welding of materials with thick section, high metal accumulation capacity, smooth welding seam forms, high penetration depth, labor, energy, time saving and high welding speed [3].

It is possible to have and document x-ray films of all kinds of welding seams, casting, forged pieces and almost all materials with X-ray tubes and Gamma-Ray isotopes. Penetrating short-length radiation waves are used in radiography method.

Fault detections are carried out by virtue of the density differences in the material to be controlled. The beam sent onto the material is generally reflected on the film. Due to the structural defects/discontinuities in the material, different images are generated in the projections of the beams absorbed in different amounts. In reality, the image reflected on the film is a shadow image created by the beam passing through the material. Radiographic tests are usually performed in accordance with EN1435 or EN12517 standards [4].

Gur et al. [4], investigated the results of joining by X-Ray radiographic test in AISI304-Ramor 500 steel pairs joined with Plasma Transfer Arc (PTA) welding. As a result of the tests, they determined that AISI304-Ramor 500 steel pairs showed a sufficiently strong weldability with PTA welding method. In their study Taskin et al. [5], performed X-Ray radiographic tests of AISI 430 and 304 stainless steels with AISI 1010 low-carbon steels welded by CO₂ Laser beam welding (LBW). The result of the radiographic tests indicated that as heat input increased, the widths of the deep penetration increased in all samples. On the contrary, it was found that with increasing welding speeds, the widths of the deep penetration decreased.

Caligulu et al. [6], investigated X-ray radiographic tests of friction-welded AISI 4340-AISI 2205 steels. The result of the radiographic tests indicated that the friction pressure, the forging pressure, the amount of flash increased with increasing the rotation speed in all samples. On the other hand, as the friction time increased, the amount of flash decreased. In the other study; radiographic test of friction welded AISI 1010-Copper alloys was investigated. The result of the radiographic tests indicated that as rotation speed, friction pressure, and forging pressure increased, the amount of flash increased in all samples [7].

Dikbas et al. [8], examined X-Ray radiographic test of Ti6Al4V alloys welded by using Plasma Transfer Arc welding (PTA). After the process, the radiographic tests of the welded joints were examined by X-Ray diffraction. The result of the radiographic tests revealed that with increasing welding rate, the widths of the deep penetration

increased in all samples. On the other hand, as welding speeds increased, the widths of the deep penetration decreased. Kahraman et al. [9], investigated the effect of electrode extension distance on metallurgical and mechanical properties of low carbon steel joints welded with submerged arc welding. OP 139 flux and OE S1 welding wire were used to weld steel parts by using three electrode extension distances. It was found that electrode extension distance affected the hardness and changed the microstructure of weld metal. It was observed that increasing electrode extension distance reduced the hardness of weld metal and HAZ. Tensile tests showed that rupture occurred in the base metal of all samples.

Turkmen et al. [10], investigated the effect of normalization process on microstructure and mechanical properties of microalloyed steels joined by using submerged arc welding. It was observed that depending on the normalization process, the tensile and hardness values of the steels decreased but the % elongation increased. The normalization heat treatment causes the elimination of the hard phases such as martensite forming during the welding and the properties gained by thermomechanical processes during the production of microalloyed steels and the decrease of the strength value. In their study, Ada et al. [11], determined that roll sheet materials that were produced for natural gas and oil pipelines by different steel producers, had the same carbon equivalent and X52 and X65 quality were turned into pipe. These materials were joined by using submerged arc welding method. Microstructure and mechanical properties of weld samples taken from joined pipes were investigated.

Karabulut et al. [12], conducted a study on effect of the tempering process on mechanical properties of microalloyed steels welded by using the submerged welding method. As a result, they determined that while the welded joints made by using microalloyed steel material showed lower hardness, yield, and tensile strength after the tempering, the % elongation increased. Kupeli et al. [13], investigated the weldability of 304 (UNS30400) type austenitic stainless steels with a low carbon non-alloy steels for the submerged arc welding method. Different welding parameters were used for determination of the optimum welding conditions. By using copper base, double-sided submerged arc welding method, 309L submerged arc welding wire and different welding powders, quality joints were obtained.

In the study of Kaya et al. [14], a large part of the ship used in the manufacture of Grade A ship plates having three different thicknesses was joined by using submerged arc welding method. In the study of Akay et al. [15], low alloyed, fine grained, high strength X60, X65 and X70 steels used in petroleum and natural gas pipeline were joined by

Submerged Arc Welding using different type of welding fluxes. As the macrostructure images were analyzed, there were not any cracking, tears, holes, melting / lack of penetration, and slag residues and burning grooves were observed in the weld zone.

In this study, X-ray radiographic test and notch impact test of P460 pressure vessels joined by using submerged welding method were examined.

II. EXPERIMENTAL STUDY

In this study, P460 steel with chemical properties given in Table I and mechanical characteristics given in Table II was joined at 450-500, 475-525, 500-550, 525-575, 550-600A welding power, and 17 and 20 cm/min welding speed by using submerged arc welding method. Table III shows the welding parameters of the submerged welding process.

TABLE I
CHEMICAL COMPOSITIONS OF EXPERIMENTAL MATERIALS

Materials	C	Si	Mn	P	S	Cu	Ni	Mo
P460	0.20	0.60	1.10	0.02	0.005	0.70	0.8	0.1
Gedik S2 wire	0.12	0.10	1.00	-	-	<0.3	-	0.5
ESAB 10.62	0.10	0.4	1.60	0.01	0.007	-	-	0.5

TABLE II
MECHANICAL PROPERTIES OF EXPERIMENTAL MATERIALS

Materials	Yield Strength (MPa)	Tensile Strength (MPa)	% Elongation (min)	Notch Impact Strength (J)	
				- 20 °C	+ 20 °C
P460	450	570	17	35	27
Gedik S2 wire	490	600	26	90	60
ESAB 10.62	450	515	32	-	-

TABLE III
WELDING PARAMETERS

Sample No	Ampere (A)	Voltage (Volt)	Welding speed (cm/min)
S1	450	30-32	17
	500	30-32	20
S2	475	30-32	17
	525	30-32	20
S3	500	30-32	17
	550	30-32	20
S4	525	30-32	17
	575	30-32	20
S5	550	30-32	17
	600	30-32	20

Optical, EDS, and XRD analyzes were performed to determine the structural change in the joining zone of the welded joints. In order to determine the notch impact strengths of the welded joints, the samples proper in accordance with TS 269/75 EN 10 045-1: 1990 standard were prepared on CNC machine and lathe. Notch impact tests were performed in the INSTRON WOLPERT PW30 notch impact device which has a capacity of applying impact of 150 joules. In addition, micro-hardness scanning was performed on both sides of the welded joints. Fracture surfaces were analyzed by SEM after notch impact and damage processes were determined. X-radiographic tests were carried out in accordance with EN ISO 17636-1 standard in such a way to cover the welding seam and HAZ of sample pairs joined by using the submerged welding method. A schematic diagram of the working principle of the submerged arc welding machine with deep penetration and X-ray tester, a non-destructive examination method was given.

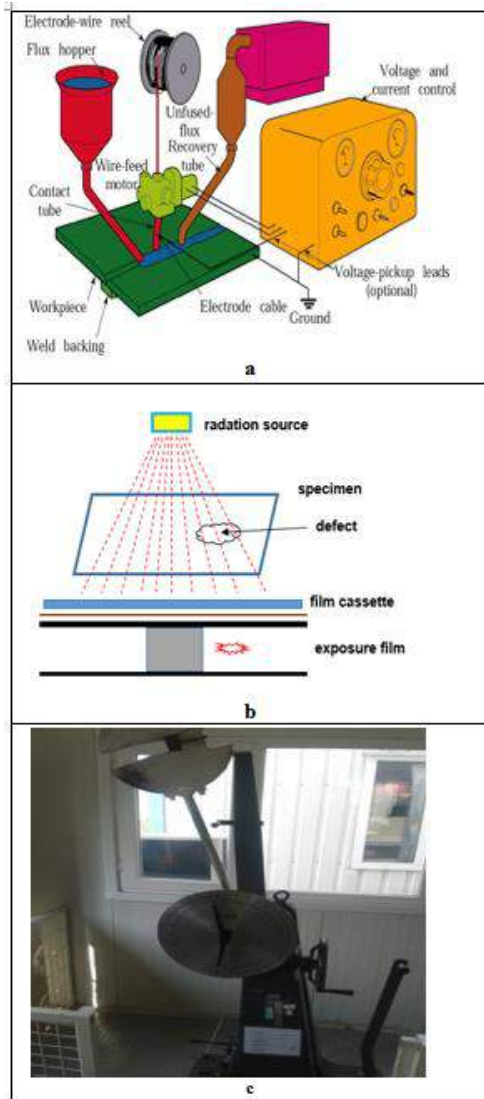


Figure 1. Working principle of (a) submerged arc welding, (b) radiography test and (c) notch impact test

As the X-ray device, Balto Spot type x-ray device with 300 KV capacity was used. Radiation process was performed by placing the film cartridges and samples in a suitable way. Radiation process (having x-ray) was made in the rooms whose protection is strengthened with lead sheets. Developed films were controlled in a PICO-VIEW P-35 brand light device.

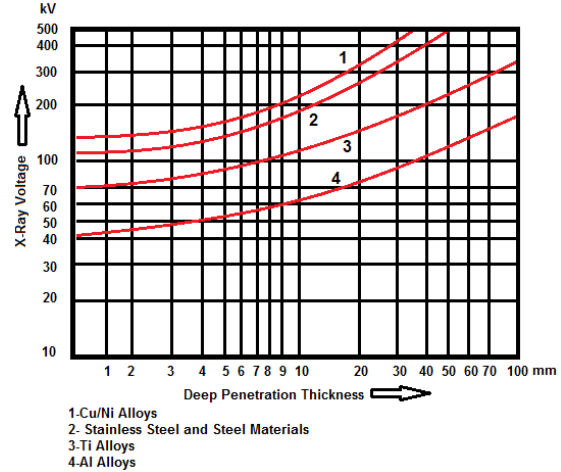


Figure 2. Deep penetration thickness of materials in dependence of X-Ray voltage up to 500 kV [4].

X-ray and notch impact test examinations were carried out to control the strength and penetration of the welding seam of the joined steel pairs. X-ray test standards were applied perpendicular to the welding seam, as shown in Figure 3, including welding seam and the heat affected zone according to TS5127 and EN 1435 standards.

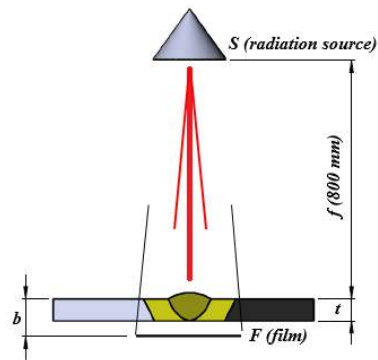


Figure 3. Test preparation for plane wall and one Wall [4]

Table IV shows the parameters used in the X-ray examination process.

TABLE IV
X-RAY RADIOGRAHY PARAMETERS

Test Standard	EN ISO 17636-1
Ray Source	X-RAY
Penetrometer	10 FE EN
Film Type	KODAK T200
Energy	150Kv- 2,4 mA
Film Focus Distance	800 mm
Exposure Time	1min. 10 sec
Inspection Scope	Welding, ITAB
Bath Method	Automatical

III. EXPERIMENTAL RESULTS

A. Examination of Fracture Surfaces and EDS Analyses of Welded Samples

The elemental transitions in the P460 materials used in the tests were calculated with the obtained EDS analysis. As a result of this analysis, it was determined that elemental transition, which was the highest in %, occurred in Fe and C elements. When the fracture surface and SEM images of the material were examined, it was observed that the ductile fracture mechanism occurred. The elements and rates determined in the EDS analyses are given below (Table V).

TABLE V
EDS ANALYSIS RESULTS

Elements	Weight %	Atomic %
C	24.90	60.57
Si	0.27	0.28
Mn	1.25	0.67
Fe	73.33	38.36
Ni	0.24	0.12
Totals	100.00	100.00

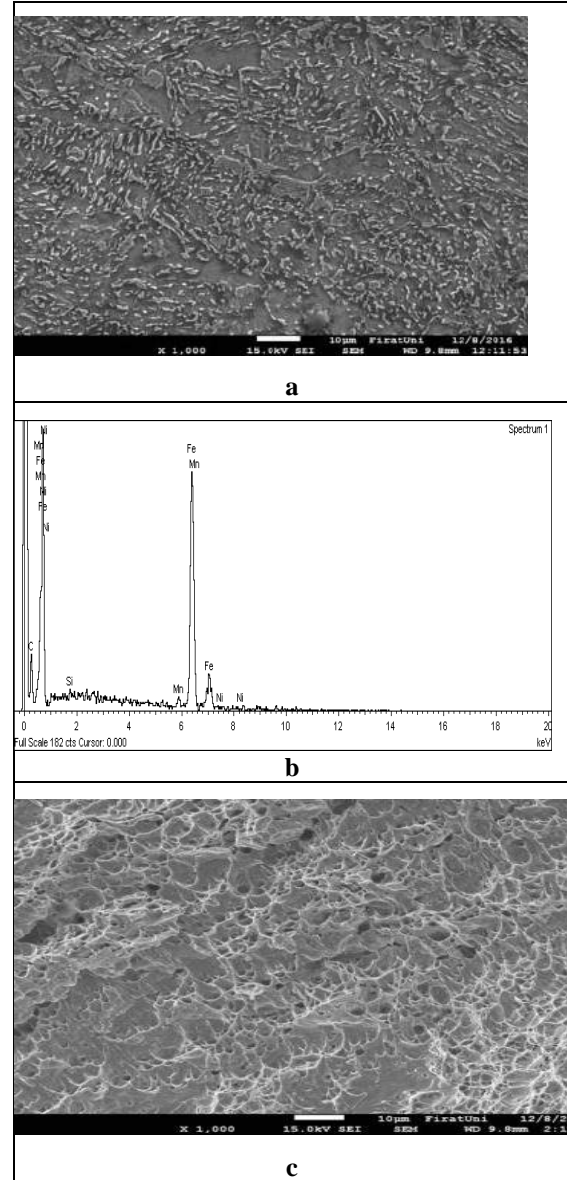


Figure 4. P460 steel a) SEM image b) EDS graphic c) Fracture surface image (500-550 ampere values)

B. Examination of Notch Impact Test Results of Welded Samples

In order to determine the notch impact strengths of the welded joints, samples in the dimensions of 10x10x55 mm were prepared at CNC machine and lathe according to TS 269/75 EN 10 045-1:1990 standard. Notch impact tests were carried out at -20°C, 0°C, and +20°C in the INSTRON WOLPERT PW30 notch impact device with capability of applying an impact of 150 joules.

When the joints of P460 samples made with 17-20 cm/min feed rate at S1 450-500, S2 475-525, S3 500-550, S4 525-575, S5 550-600 ampere values were examined in terms of notch impact test, it was observed that the notch impact strength varied depending on the increasing ampere value (Table VI).

As a result of the impact test, the highest values were observed in samples at 17-20 cm/min welding speed, +20°C and 450-500, 475-525, 500-550 ampere values; whereas, the lowest value was observed as a result of the impact test performed at 550-600 ampere value, 17-20 cm/min welding speed and -20°C. Notch impact energy of base material measured as 35 at -20°C and 27 at -20°C was lower compared to welded samples. The test made at 500-550 A was found to have higher notch impact strength than the others. Even though it was closer to the notch impact strength of the base material at 550-600 A, it was observed to be more unsuccessful compared to the other ampere values (Figure 6).

TABLE VI
NOTCH IMPACT TEST RESULTS OF WELDING SAMPLES
(S1 450-500, S2 475-525, S3 500-550, S4 525-575, S5 550-600
AMPERE VALUES).

NOTCH IMPACT TEST RESULTS (Joule)					
°C	S1- P460	S2- P460	S3- P460	S4- P460	S5- P460
1 (-20)	62	58	63	64	38
2 (-20)	54	88	80	58	54
3 0	91	88	97	91	45
4 0	61	80	92	99	40
5 (+20)	115	115	115	110	54
6 (+20)	95	109	111	102	57

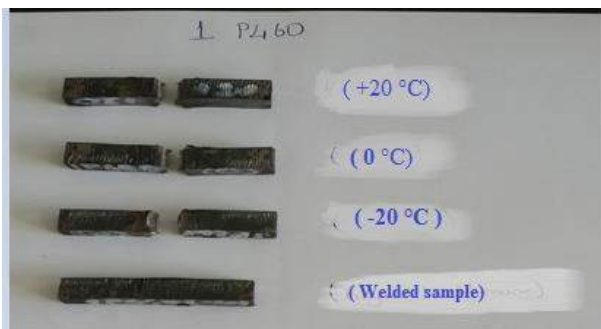


Figure 6. Macro images after notch impact test of P460 steels

C. Examination of X-ray Radiography

Test Results of Welded Samples

The result of the radiographic tests indicated that with increasing heat input, the widths of the deep penetration weld metal also increased. On the contrary, with increasing welding speeds, the widths of the deep penetration weld metals decreased [5].

It was clear that there were no crack and void in the weld interface. From the microstructural observations, it was found that the microstructures formed in the interface zone during or after SAW processes and there were three distinct zones across the samples identified. In all samples, the original structure was preserved in the undeformed region [6]. The flash obtained was symmetric, which indicated plastic deformation on both [7]. Figure 7

shows the radiographic test images of all the samples. The experimental results indicated that P460 steel could be joined by using sub-merged welding method [6].

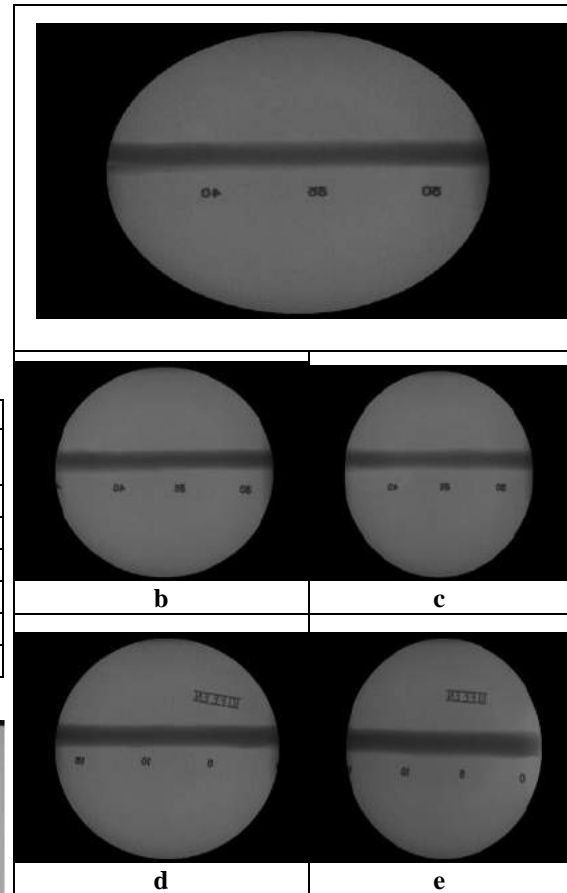


Figure 7. The radiography images of S1 sample a) 450 500A b) 475-525 A c)500-550A d) 525-575 A e) 550-600 A

D. Examination of XRD Analysis Results

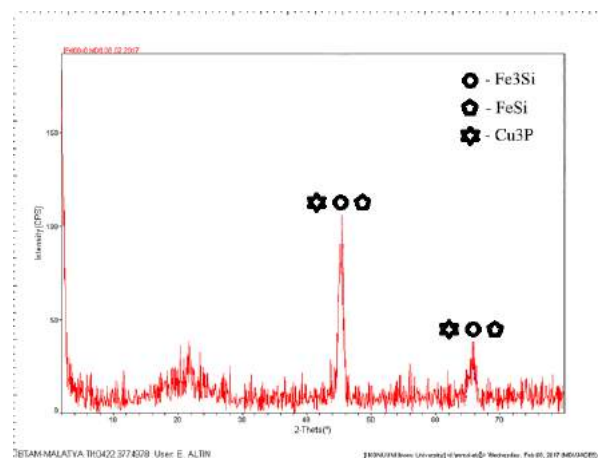


Figure 8. The result of XRD analysis of S3 sample

After XRD analysis, Fe₃Si, FeSi and Cu₃P phases were determined in the structure of P460 steel (Figure 8).

IV. CONCLUSIONS

P460 materials were successfully joined by using the submerged welding method. The elemental transitions in the P460 materials used in the experiments were calculated with the EDS analysis. As a result of this analysis, it was determined that elemental transition, which was the highest in %, occurred in Fe and C elements. When the fracture surface and SEM images of the material were examined, it was observed that the ductile fracture mechanism occurred.

In terms of notch impact, notch impact energy of the base material was determined to be lower than the welded samples. As a result of the impact test, the highest value was observed in samples at 17-20 cm/min welding speed, +20 °C and 450-500, 475-525, 500-550 ampere values (115 Joule); whereas, the lowest value was observed as a result of the impact test performed at 550-600 ampere values and 17-20 cm/min welding speed at the temperature of -20 °C (38 Joule).

The result of the radiographic tests indicated that with increasing heat input, the widths of the deep penetration weld metal also increased. On the other hand, with increasing welding speeds, the widths of the deep penetration weld metals decreased. It was obvious that there were no crack and void in the weld interface. From the microstructural observations, it was found that the microstructures formed in the interface zone during or after SAW processes and there are three distinct zones across the samples identified. In all samples, the original structure was preserved in the undeformed region. After XRD analysis, Fe₃Si, FeSi and Cu₃P phases were determined in the structure of P460 steel structure.

ACKNOWLEDGMENT

The study was supported by the Firat University Research Project Committee (Project No: TEKF.16.27).

REFERENCES

[1] E. Kimsesiz, E. Cayir, N. Reis, V. Gemici, U. Erdonmez, C. Karakus, M. Torlakoglu, "Periodic Test and Control System of Pressure Vessels", III. National Hydraulic Pneumatic Congress and Exhibition, pp. 353-361.
 [2] TMMOB Chamber of Mechanical Engineers, Periodical Control Engineer Manual-II Pressure Vessels, p.79, 2001.
 [3] H., Ada, S., Aksoz, A., Ozer, I., Candan, "Investigation of Metallurgical and Mechanical Properties of Welded Region of API 5L X80 Steel Merged by Submerged Arc Welding Method", ICAT 2016 International Conference on Advances Technology and Science, Konya,309, 2016.
 [4] A.K. Gur, N. Yigiturk, T. Yildiz, "Examination Of Welding Characteristics Of AISI304-Ramor 500 Steel Couples Welded By

Plasma Transferred Arc Welding" SYLWAN, Vol, 160(11), pp. 212-225, 2016.
 [5] M. Taskin, U. Caligulu, M. Turkmen, "X-Ray Tests of AISI 430 and 304 Stainless Steels and AISI 1010 Low Carbon Steel Welded by CO₂ Laser Beam Welding", MP-Materials Testing-Materials and Components Technology and Application, 53 (11-12), pp.741-747, 2011.
 [6] U. Caligulu, M. Yalcinoz, M. Turkmen and S. Mercan, "X-Ray Radiography of AISI 4340-2205 Steels Welded By Friction Welding", Materiali in Tehnologije, MTAEC9-50(1), pp. 39-45, 2016.
 [7] U. Caligulu, M. Acik, M. Turkmen, A.K. Gur, "Radiography Test of AISI 1010-Copper Alloys Welded by Friction Welding", SYLWAN, vol, 160(4), pp. 468-479, 2013.
 [8] H. Dikbas, U. Caligulu, M. Taskin, M. Turkmen, "X-Ray Radiography of Ti6Al4V Welded by Plasma Tungsten Arc (PTA) Welding", Mp- Materials Testing-Materials and Components Technology and Application, pp. 197-202, 2013.
 [9] N. Kahraman, "Investigation of Effect on the Microstructure and Mechanical Properties of Free Wire Length in Low Carbon Steels Welded with Submerged Arc Welding", G.U. Journal of Science, 18(3), pp. 473-480, 2005.
 [10] M. Turkmen, H.,Karabulut, M.A. Erden, S. Gunduz, "The Effect on the Microstructure and Mechanical Properties of Normalization Process in Microalloyed Steel Welded with Submerged Welding Method", 4th International Exhibition of Welding Technology Conference and Exhibition, pp.793-801, 2016.
 [11] H., Ada, S., Aksoz, T., Findik, C., Cetinkaya, M., Gulsun, "Investigation of Microstructure and Mechanical Properties of Petroleum and Natural Gas Pipes Welded with Submerged Welding Method", Polytechnic Journal, 19 (3), pp. 275-282, 2016.
 [12] H. Karabulut, M. Turkmen, "Effect of Tempering Process on Microstructure and Mechanical Properties of Microalloyed Steels Joined by Submerged Arc Welding", Dicle University Eng. Faculty, Journal of Eng-Arthitect, 7(3), pp. 587-594, 2016.
 [13] G. Kupeli, N. Tekin, H.O.,Gulsoy, S. Salman, [The Weldability with Submerged Welding Method of Stainless Steel and Low Carbon Unalloyed Steels](#), 6th International Advanced Technologies Symposium (IATS'11), 2011.
 [14] Y. Kaya, N. Kahraman, A. Durgutlu, B. Gulenc, "Investigation of the Mechanical Properties of Different Thickness of the Grade A Ship Plates Joined by Submerged Arc Welding", e-Journal of New World Sciences Academy Volume: 5, Number: 2, Article Number: 1A0088, 2010.
 [15] A.A. Akay, Y. Kaya, N. Kahraman, "The evaluation of welding zone of X60, X65 and X70 steels welded by sub-merged welding method", Karaelmas Science and Engineering Journal 3 (2), pp. 34-42, 2013.

An effect of stress relief annealing on the resistance spot welded TRIP steel joint

Hayriye ERTEK EMRE*, Ramazan KAÇAR*

#Karabuk University, Manufacturing Engineering Department, KARABUK/TURKEY

hayriyeertek@karabuk.edu.tr

rkacar@karabuk.edu.tr

Abstract— In the present study, the commercially available TRIP800 steel having 1.5 mm thickness was joined with resistance spot welding method by using optimum welding parameters which is assessed with developed weld lobe diagram. A group of samples were post weld heat treated (stress relief annealing treatment) at the temperature of 600°C for 30 minutes. The effect of stress relief annealing treatment on the tensile shear load bearing capacity, energy absorption, hardness and microstructure of weldment was investigated so, the relation with microstructure-mechanical properties was determined. The other group of samples was tested as welded condition for sake of comparison. Conclusively, it is believed that stress relief annealing treatment applied for resistance spot welded TRIP800 weldment did not affect to the constituent phases and failure mode of tensile test sample. However, the hardness decreased in the weld nugget and HAZ. Meanwhile, the tensile shear load bearing capacity and energy absorption of weldment affected negatively.

Keywords— TRIP800 steel, Resistance spot weld, Stress relief annealing, Energy absorption, Tensile shear test

I. INTRODUCTION

Traditional Advanced High Strength Steels (AHSSs) in vehicles can be grouped into dual phase (DP), transformation induced plasticity (TRIP), and complex phase (CP) steel grades [1]. TRIP steel is dominated by a ferrite matrix with retained austenite, bainite, and martensite as dispersed phases, offering excellent mechanical properties due to the transformation of retained austenite into martensite during plastic straining [2–4].

Among the methods used in the automotive industry, resistance spot welding is also an important method for advanced robotic applications. Evaluating the mechanical properties of resistance spot welded joints in TRIP steels is critical in automotive industry [5]. TRIP steels show the transformation of retained austenite into martensite during plastic straining. The effect of electrode force may be cause the plastic deformation in the weld area during the resistance spot welding. The weld nugget and HAZ exhibits martensitic transformation in associate with heat input following rapid cooling and chemical composition of steels [6]. The harder and brittle phases formed in weldment can cause stress and cracking. Because of this, there post weld heat treatment (stress relief annealing treatment) should be applied for TRIP joints. Heat treatment is an operation that is both time consuming and costly. It can affect the strength and toughness of a welded joint,

its corrosion resistance and the level of residual stress but it is also a mandatory operation specified in many application codes and standards. In addition, it is an essential variable in welding procedure qualification specifications [7].

Hilditch et al. [8] performed heat treatments at 300, 400, 500 and 650 °C temperature for resistance spot welded TRIP steels. They reported that tempering of the spot welded samples either below or above the temper embrittlement range resulted in a significant increase in overload weld strength from the as-received TRIP condition and the weld hardness decreased with increasing annealing temperature. Cretteur et al [9] also studied about the improvement of weldability of TRIP steels by use of in-situ pre- and post-heat treatments. They reported that mechanical properties of the weldment significantly improved due to applied heat treatments.

The extensive literature survey revealed that there has been limited research about stress relief annealing heat treatment applied for resistance spot welded TRIP steels. For this purpose; as-welded and stress-relief annealed TRIP800 steels weldment behaviour under the static load were investigated in this study. The effects of welding parameters including; welding current and welding time on tensile shear load bearing capacity, elongation, and energy absorption and failure mode were investigated. The microstructure evaluation and hardness measurements were also carried out on the welded samples.

II. MATERIALS AND EXPERIMENTAL METHODS

A. Material and Welding Procedure

The thickness of TRIP800 steel used in this study was 1.5 mm. Its chemical composition is given in Table 1 and the dimensions of tensile shear specimen are shown in Fig. 1.

TABLE XI
THE CHEMICAL COMPOSITION OF THE TRIP800 STEEL (% WEIGHT).

Base Metal	C	Si	Mn	P	S	Cr	Mo	Al	Fe
TRIP800	0.02	1.66	1.69	0.015	0.0002	0.006	0.011	0.43	bal

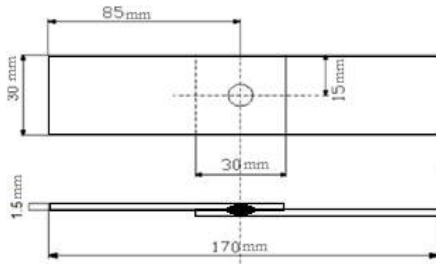


Fig. 9 The tensile shear test sample dimension

A timer and current controlled resistance spot welding machine having a power capacity of 60 kVA and pneumatic application mechanisms with a single lever was used for experiments. The electrode force was continuously measured and controlled at fixed 6 kN force during the experiments. Test samples were joined by using optimum welding parameters which is assessed with developed weld lobe diagram which is published elsewhere [10]. The right limit of used weld lobe diagram was drawn according to 80 and 100 % of maximum strength, while the left limit of weld lobe was established according to indentation depth equal to about 25% of sheet thickness. Therefore, the welding time was applied as 0.3, 0.4 and 0.5 s (15, 20, 25 cycles). Clamping and holding times were kept constant as 15 cycles in all series. The used welding current was 7 and 8 kA. Spherical tip F16 type electrodes (CuCrZr) having a 5.5 mm tip diameter were used. TRIP800 steel weld assembly was joined by constant electrode force by changing welding current and time. Five couples were welded for each condition.

B. Experimental Details

A group of samples was post weld heat treated (stress relief annealing treatment) at the temperature of 600°C for 30 minutes in the furnace. The other group of samples was tested as welded condition for sake of comparison. In order to prevent confusing, stress relief heat treated welded sample is abbreviated “SRHT” while welded sample is named as-received and abbreviated as “AR” hereafter. Since, the AR and SRHT weldment have been joined same welding parameters, the weld nugget size inevitably formed similar size as expected therefore the weld nugget geometry including nugget diameter, nugget height and electrode indentation depth did not compare in this study.

In order to eliminate experimental error, a set of four AR and SRHT samples were subjected to tensile shear test for determining their joint strength. One set of AR and SRHT samples were subjected to microstructure evolution and hardness measurement. The tensile shear test was performed at a crosshead speed of 5mm/min by using Shimadzu universal tensile testing machine. The energy absorption of welded sample was calculated by Shimadzu universal tensile test machine program considering the area under the force-strain curve. The standard deviation (SD) was calculated and the stability of the process was estimated by determining the coefficient K_p [11]:

$$K_p = \frac{F_{max} - F_{min}}{\bar{F}}$$

where F_{max} and F_{min} are maximum and minimum tensile shear load values in the series, respectively. \bar{F} is the mean value in the series.

The tensile shear load bearing capacity was measured as the peak load reached during the test, while the energy absorbed by the welded joint was calculated as the area under the load-displacement curve up to the peak load [12]:

$$\text{Absorbed energy} = \int_0^{X_{max}} F dx = \sum_{i=1}^N F(i)[X(i) - X(i-1)]$$

where F is the load, X is the displacement, X_{max} is the displacement at the peak load, i is the sample datum (20 Hz sampling frequency), and N is the sample datum relative to the peak load.

The failure modes were evaluated from the tensile shear tested AR and SRHT samples. A schematic of the failure modes and fracture paths are shown in Fig. 2. The fracture surface of the tested specimen was also investigated by scanning electron microscope (SEM). Three distinct failure modes were observed: interfacial failure (IF) in which fracture propagates through the fusion zone (mode A), PF in which failure occurs by the effect of the withdrawal of weld nugget from single sheet (mode C, D), and partial interfacial mode (PIF) in which the fracture first propagates in the fusion zone (FZ) and then it is diverted into through thickness (mode B) [13-15].

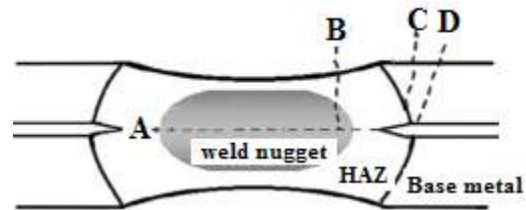


Fig. 2 Schematic of a spot weld cross section with typical tensile shear failure modes

The AR and SRHT samples were cut in a plane perpendicular to the penetration axis and prepared for metallographic examination on the cross sections of penetrations. Microstructure in different zones (weld nugget, heat-affected zone (HAZ), and base metal) was analyzed by using optic microscopy. The samples were etched for 5 s with 2 % nital to identify the microstructure. The Le pera’s solution was also applied for etching to evaluation of structure. In this method, samples were etched for 15 s with 4 % picral and then 25 s with 1 % aqueous solution of sodium meta-bisulfate. The fracture surface of test sample was examined by using Zeiss Ultra Plus type SEM microscope.

III. RESULTS AND DISCUSSIONS

The effect of stress relief annealing treatment on the tensile shear load bearing capacity, energy absorption, hardness and microstructure of AR and SRHT weldment was investigated.

C. Tensile Shear Results

The behavior of AR and SRHT weldments under the static load was determined by tensile shear test. The representative mean tensile shear load bearing capacity-elongation curves of the AR and SRHT weldments are shown in Fig. 3 and Fig. 4 respectively. The mean of tensile shear load bearing capacity, elongation and fracture mode of tested all samples are also summarized in Table 1 a and b.

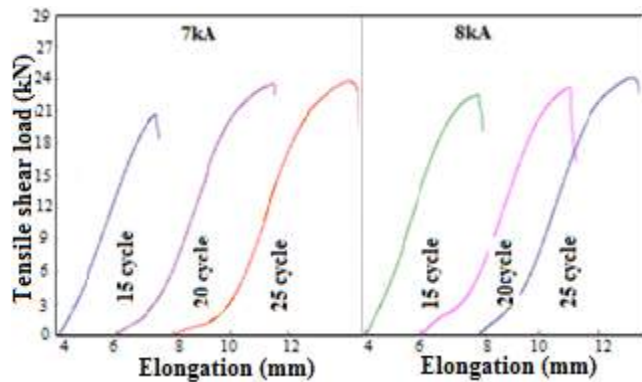


Fig. 3. Tensile shear test results of resistance spot welded AR samples

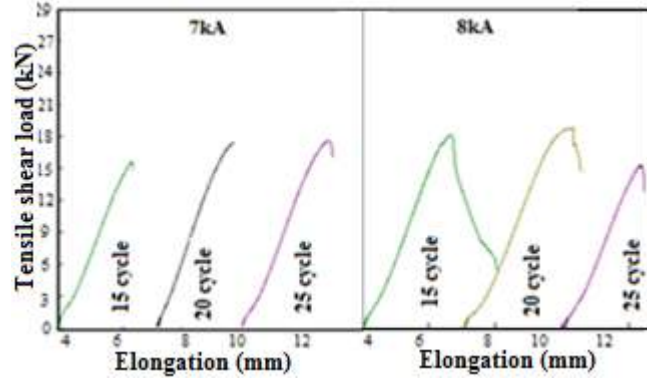


Fig.4. Tensile shear test results of resistance spot welded SRHT samples

TABLE II
TENSILE SHEAR TEST RESULTS OF RESISTANCE SPOT WELDED TRIP800
SAMPLES. A) AR, B) SRHT

Welding parameters	Fmax (kN)	Fmin (kN)	F̄ (kN)	Elongation (mm)	Absorbed Energy (J)	Kp
15cycle-7kA	23	16.3	20.6	4.32	45,2	0,33
20cycle-7kA	27.1	23	23.6	4.35	60	0,08
25cycle-7kA	29.5	19.1	23.8	4.5	66,6	0,3
15cycle-8kA	23.6	20.7	22.4	4.35	47,5	0,12
20cycle-8kA	26.6	21.9	24.7	5.32	85	0,19
25cycle-8kA	27.4	20.6	24.5	5.44	80	0,28

(a)

Welding parameters	Fmax (kN)	Fmin (kN)	F̄ (kN)	Elongation (mm)	Absorbed Energy (J)	Kp
15cycle-7kA	16.3	15.2	15.7	2.3	19,6	0,18
20cycle-7kA	18.2	16.6	17.4	2.3	20	0,4
25cycle-7kA	18.7	16.9	18.0	2.8	28,6	0,27
15cycle-8kA	19.5	17.3	18.3	2.8	30,8	0,26
20cycle-8kA	20.7	16.7	18.5	3.3	38	0,31
25cycle-8kA	17.1	12.0	15.2	2.3	34	0,32

(b)

As seen in Fig. 3, Fig. 4 and Table II, tensile shear load bearing capacity of samples increased with rising welding current and welding time, except for SRHT weldment that was joined at 8kA welding current and 25 cycles welding time. However, the tensile shear load bearing capacity and elongation of SRHT weldment considerably decreased due to stress relief annealing heat treatment which caused tempering effect of brittle phases like martensite in the structure. And also, it's caused decreasing on the absorbed energy for SRHT samples. Conversely, it was reported that tempering of the spot welded samples either below or above the temper embrittlement range resulted in a significant increase in overload weld strength from the as-received TRIP condition [8]. The maximum stability coefficient of Kp is found to be lower than 0.4, stating that the reproducibility of experiments in the range of acceptable level. It was reported that the stability coefficient, Kp, should be in the range of 0.3–0.45 [11,16].

The maximum tensile shear load bearing capacity was found 24.75 kN for AR weldment that was joined with 8kA welding current and 20 cycles welding time for (Table 1a). However, the tensile load bearing capacity of SRHT weldment was determined 18.5 kN for same welding parameter due to the stress relief annealing (Table 1 b). The load bearing capacity decreased 6.25 kN because of annealing at 600 °C for 30 minutes. It is believed that the temperature range within times which stress relief took place causes tempering of those regions in the weld nugget and HAZ's where hard martensitic structures may have formed. The fracture surfaces of AR and SRHT tensile shear samples are shown in Figure 5 and Figure 6, respectively.

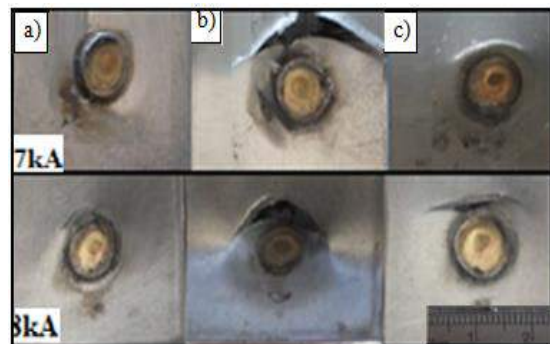


Fig.5. Fracture surfaces AR samples joined with various welding time a) 15 cycles, b) 20 cycles, c) 25 cycles

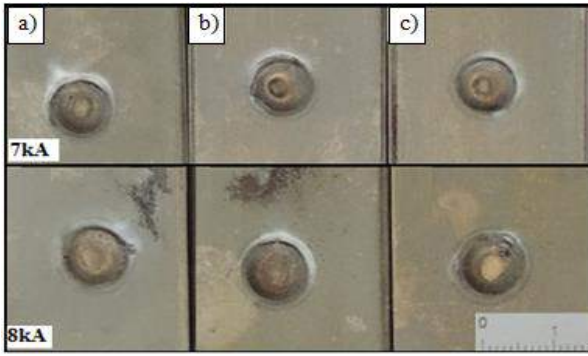


Fig.6. Fracture surfaces SRHT weldment joined with various welding time a) 15 cycles, b) 20 cycles, c) 25 cycles

Although, a few samples failed partial interfacial fracture mode, most of the joints failed predominantly pullout failure mode. Since the TRIP800 steels has been joined with determined good weldable range, AR and SRHT tensile shear test samples almost failed with pullout failure (PF) mode as expected due to obtained acceptable joint quality. So, the desired pullout fracture mode of the SRHT samples did not affected from heat treatment because of having acceptable weld nugget diameter.

The Figure 7 and Figure 8 show various failure modes in tensile shear test sample for AR and SRHT weldment respectively.

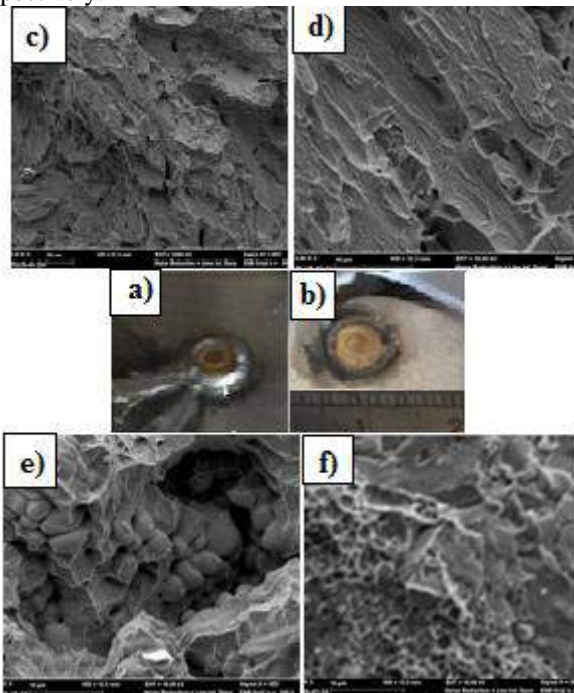


Fig.7. Fracture images of AR weldment a,c,d) Partial interfacial fracture 15 cycles, b,e,f) Pullout fracture

As seen in Fig.7 and 8 a, c and d, the brittle fracture surface morphology of the weld nugget through the HAZ, indicated partial interfacial fracture mode where the failure began in assemblies.

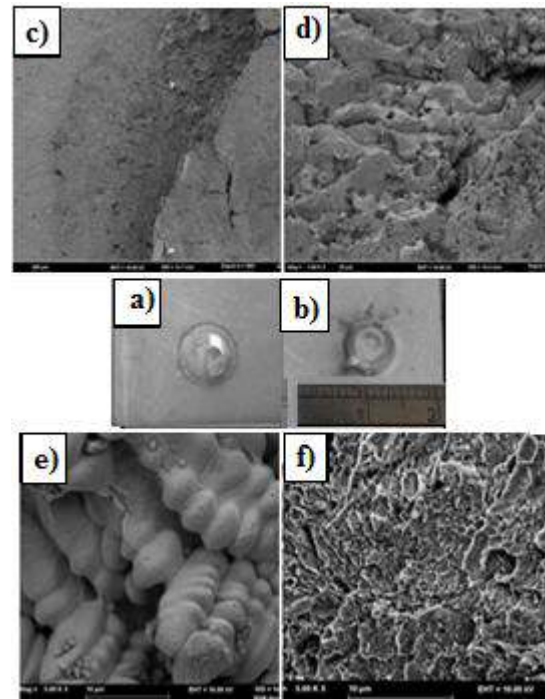
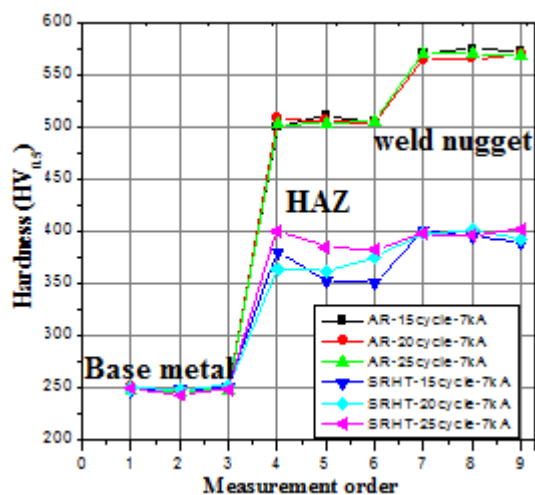


Fig.8. Fracture images of SRHT weldment a,c,d) Partial interfacial fracture 15 cycles, b,e,f) Pullout fracture

It is thought that the stress relief annealing is responsible for removing residual stress and lower hardness in the weld nugget and HAZ due to the elimination of this tough phase tension. It is believed that the crack propagation begin coarse grain having low hardness due to relieving tension of hard phases in the HAZ in associate with annealing The pullout fractures (PF) mode formed from the base metal or mainly from the HAZ through base metal, in semi-brittle, semi-ductile and dendritic form (Fig. 7 and 8 b ,e, f).

D. Hardness Measurement

The hardness measurement was carried out in AR and SRHT weldment and results are shown in Fig.9.



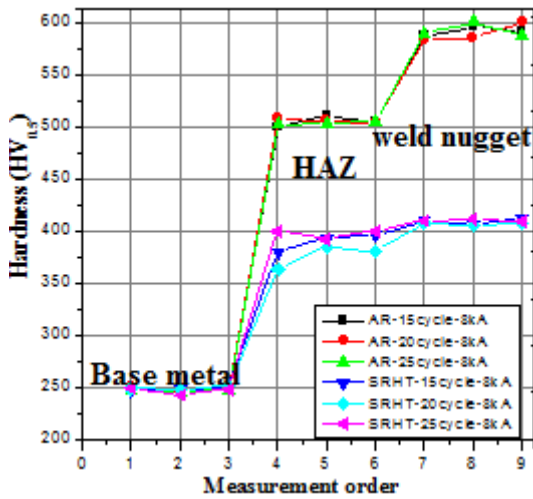


Fig. 9. Hardness results of AR and SRHT weldments

It was determined that the hardness of the both weldments increased from the base material through weld nugget due to martensitic transformation in associated with weld thermal cycle. However, the hardness of the SRHT weldment was found lower than AR weldment due to tempering effect of the annealing and removal of residual stress. For example, the hardness in the AR and SRHT base metal was measured approximately 250 HV and 245 HV respectively. It is thought that the 5 HV hardness difference comes from tempering of effect martensite phase in the TRIP800 steel and removal of residual stresses. It was found that hardness in weld nugget and HAZ of AR weldment altered 560-600 HV and 500-510 HV respectively. The weld nugget and HAZ hardness in SRHT weldment also measured 400-420 HV and 350-400 HV respectively. The hardness in weld nugget and HAZ of the SRHT weldment was found approximately 170 HV and 130 HV lower than those of AR weldment due to tempering effect of the annealing on the formed hard phases and removal of residual stress caused by weld thermal cycle.

E. Microstructure Evaluation

Fig. 10 a-c and Fig. 11 a-c show microstructure of AR and SRHT weldment, respectively. As seen in Fig. 11 and Fig. 12, the AR and SRHT weldment consist of three distinct zones including; weld nugget, HAZ, and base metal regions.

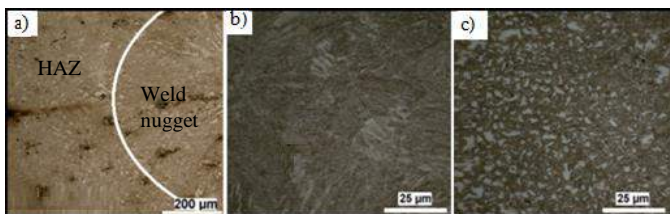


Fig. 100. The microstructure of AR weldment joined with 8 kA welding current for 20 cycles welding time a) transition from weld nugget to HAZ, b) weld nugget, c) HAZ.

The microstructure of AR weld nugget is decorated with martensite phase due to its high cooling rate (Fig. 10 b). The microstructures of base metal consist of ferrite, bainite, and retained austenite phases (Fig. 10 c). The structure of the HAZ transformed to predominantly martensite with small areas of ferrite, lathy bainite, and retained austenite, depending on the ultimate temperature reached and cooling rate (Fig. 10 a).

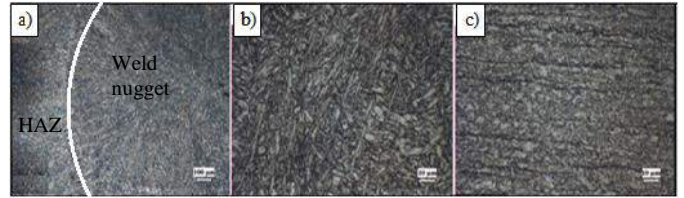
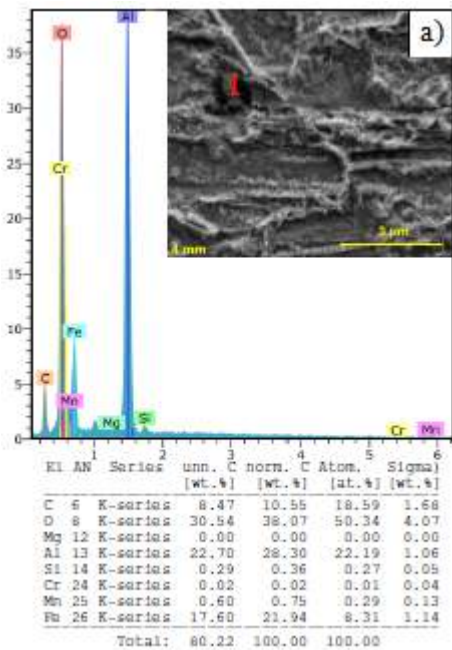


Fig. 111. The microstructure of SRHT weldment joined with 8 kA welding current for 20 cycles welding time a) transition from weld nugget to HAZ, b) weld nugget, c) HAZ.

As seen in Fig 11 a-c, results imply that the stress relief heat treatment which leads to tempering effect on formed hard phases such as martensite in base metal, nugget and HAZ region, did not changed the microstructure of the SRHT weldment. In the case of annealing SRHT weldment, sufficient diffusion occurs in the precipitated solid crystals so the in homogeneity of the alloying elements and distortion in crystal system within the base metal, weld nugget and HAZ produces recovery.

In addition, AR and SRHT samples were analyzed by SEM and point EDS analyzes were performed. The result indicates that inclusions could be mixture of aluminum (Figure 12 a) and the silicon inclusion (Figure 12 b) were detected in the HAZ.



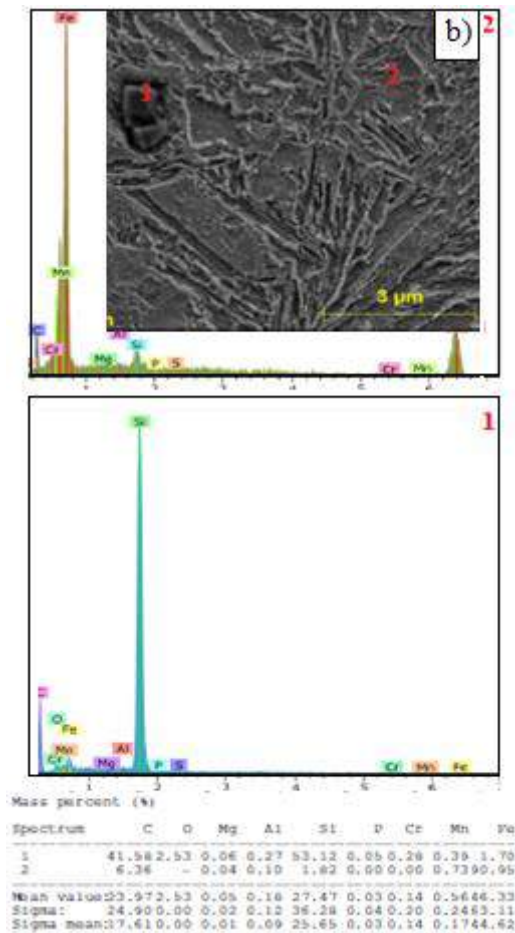


Fig. 122. EDS analysis of SRHT weldment joined with 8 kA welding current, 20 cycles welding time, a) aluminum oxide inclusion; b) silicon oxide inclusion (number 1) and weld nugget (number 2).

In TRIP steels, due to the strong affinity for oxygen, the added Al and Si readily form oxides during welding, while leaving the weld pool depleted of these elements [17, 18]. It is also known that the reaction between the dissolved alloying elements in the weld pool with the available oxygen, nitrogen, and carbon forms nonmetallic inclusions [18]. Similar oxide inclusions were observed in GTA welded high-Al and high-Si TRIP steels [18].

IV. CONCLUSIONS AND SUGGESTION

The present experimental study results provide valuable information for stress relief heat treatment for obtaining acceptable shear strength in resistance spot welded TRIP800 steel couple. As a result of this work, the summary of results and some suggestions are given below:

- The tensile shear load bearing capacity and energy absorption of SRHT weldment considerably decreased because of annealing at 600 °C for 30 minutes.
- The hardness in weld nugget and HAZ of the SRHT weldment was found approximately 170 HV and 130 HV lower than those of AR weldment due to tempering effect of the annealing on the formed hard phases and removal of residual stress caused by weld thermal cycle.

- The microstructure of weld nugget is decorated with martensite phase. The microstructure of base metal consists of ferrite, bainite, and retained austenite phases. The structure of the HAZ transformed to predominantly martensite with small areas of ferrite, lath bainite, and retained austenite, depending on the ultimate temperature reached and cooling rate.
- The stress relief heat treatment which leads to tempering effect on formed hard phases such as martensite in base metal, nugget and HAZ region, did not changed the microstructure of the SRHT weldment.

REFERENCES

- [1] Spena P.R., Maddis, M.D., Lombardi F. and Rossini M., "Investigation on Resistance Spot Welding of TWIP Steel Sheets", *Steel Research Int.* vol. 86, 12, pp. 1480-1489, 2015.
- [2] World Auto Steel. Available online: <http://www.worldautosteel.org/Projects/AHSS-Guidelines.aspx> (accessed on 13 April 2010).
- [3] Lacroix, G., Pardoën, T. and Jacques, P.J. "The fracture toughness of TRIP-assisted multiphase steels". *Acta Mater.*, vol. 56, pp. 3900–3913, 2008.
- [4] Brauser, S., Pepke, L.A., Weber, G. and Rethmeier, M. "Deformation behaviour of spot-welded high strength steels for automotive applications". *Mater. Sci. Eng. A*, vol. 527, pp. 7099–7108, 2010.
- [5] Khan, M.I., Kuntz, M.L. and Zhou, Y. "Effects of weld microstructure on static and impact performance of resistance spot welded joints in advanced high strength steels". *Sci Technol Weld Join.* vol. 13, pp. 294–304, 2008.
- [6] Emre H.E. and Kaçar, R. "Resistance spot weldability of galvanize coated and uncoated TRIP steels" *Metals*, vol. 6, 299, pp. 1-10, 2016.
- [7] <http://www.twi-global.com/technical-knowledge/job-knowledge/heat-treatment-of-welded-joints-part-1-114/> Heat treatment of welded joints
- [8] Hilditch, T.B., Speer, J.G. and Matlock, D.K. "Effect of susceptibility to interfacial fracture on fatigue properties of spot-welded high strength sheet steel" *Materials & Design* vol. 28, 10, pp. 2566–2576, 2007.
- [9] Cretteur, L., Koruk, A.I. and Tosal-Martínez, L., "Improvement of weldability of TRIP steels by use of in-situ pre- and post-heat treatments" *Steel Research Int.*, vol. 73, 6-7, pp. 314–319, 2002.
- [10] Emre H.E. and Kaçar R. "Development of weld lobe for resistance spot-welded TRIP800 steel and evaluation of fracture mode of its weldment" *Int J Adv Manuf Technol* vol. 83, pp.1737–1747, 2016
- [11] Isayev, A.P. and Terekhov, A.A. "Mechanical properties of resistance spot welded joints in zinc-plated TRIP steel". *Weld Int.* vol. 28, pp. 324–328, 2014.
- [12] Spena, P.R., Maddis M.D., D'Antonio G., and Lombardi, F., "Weldability and monitoring of resistance spot welding of Q&P and TRIP steels", *Metals*, vol. 6, 270, pp.1-15, 2016
- [13] Lin, P.C., Lin, S.H. and Pan, J. "Modeling of failure near spot welds in lap-shear specimens based on a plane stress rigid inclusion analysis", *Eng Fract Mech.* vol. 73, pp. 2229–2249, 2006.
- [14] Orlov, B.D. *Technology and equipment for resistance welding*. Mashinostroenie, Moscow, 1986.
- [15] Chao, Y.J. "Failure mode of spot welds: interfacial versus pullout". *Technol. Weld Join.* vol. 8, pp. 133–137, 2003.
- [16] Ma, C., Chen, D.L., Bhole, S.D., Boudreau, G., Lee, A. and Biro, E. "Microstructure and fracture characteristics of spot-welded DP600 steel". *Mater Sci Eng A*, vol. 485, pp. 334–346, 2008.
- [17] Grajcar, A., Rozanski, M., Stano, S., and Kowalski, A. "Microstructure characterization of laser-welded Nb-microalloyed silicon-aluminum TRIP steel". *Journal of Materials Engineering and Performance* vol. 23, 9, pp. 3400-3406, 2014.
- [18] Amirthalingam, M., Hermans, M.J.M., and Richardson, I.M. "Microstructural development during welding of silicon and aluminum based transformation induced plasticity steels — Inclusion and elemental partitioning analysis" *Metall. Mater. Trans. A* vol. 40, 4, pp. 901- 909, 2009.

An Investigation of Resistance Spot Weldability of DP600/TRIP800 Dissimilar Steel Couple

Khaled Omer H. Marwan*, Ramazan KAÇAR*, Hayriye ERTEK EMRE*

#Karabuk University, Manufacturing Engineering Department, KARABUK/TURKEY

k_gewa@yahoo.com, hayriyeertek@karabuk.edu.tr

ramazankacar@karabuk.edu.tr

Abstract— In this study, the resistance spot weldability of DP600 and TRIP800 dissimilar steels, which are used preferentially in automotive industry due to their high strength and good ductility, was investigated in detail with using different electrode force. The tensile shear load bearing capacity, cross tension strength, energy absorption, weld nugget size, the hardness profile of weldment was determined and the metallographic evaluation was also carried out on the cross section of weldment. Thus, the relationship between mechanical properties and microstructure has been confirmed. It was found that electrode force is one of the most important welding parameters which affect to the nugget geometry and mechanical properties of dissimilar steel weldment.

Keywords— DP600/TRIP800 dissimilar steel, Resistance spot welding, Mechanical properties, Microstructure

I. INTRODUCTION

The new generations advanced high strength steels (AHSSs) are more and more employed to fabricate car body components for vehicle chassis and passenger compartment because of the automotive industry is increasingly pay attention to environmental sustainability, to reduce fuel economy, and to improve safety requirements (i.e. crashworthiness) [1-3]. The most common steel grades of AHSS steels family are dual phase (DP) steels and transformation induced plasticity (TRIP) steels, which are widely used in the automotive industry.

TRIP steels have high strength combined with good uniform elongation due to hard and soft composite structure given by its various microstructural constituents like ferrite, bainite, martensite, and retained austenite [4-6]. TRIP steel is commonly alloyed with Mn, Si, or Al to suppress cementite formation by forcing more carbon into retained austenite as both Si and Al are insoluble in cementite [7,8]. DP steel contains 5–20% hard martensite phase in a soft ferrite matrix and is mainly utilized as reinforcing parts in a white body and automotive industry [9,10].

Resistance spot welding (RSW) is the favored process for joining AHSS sheets, although their mechanical and welding properties are very different from low carbon steel sheets [11-13]. The automotive industry uses steel sheets of various thicknesses, coating and composition for many components of an automobile body in-white. Arumugam and Nor [14] reported that panel spring housing assembly is an automobile body component which is made of a combination of two dissimilar

steel sheets with different thicknesses. Marashi et al. reported that the resistance spot welding of dissimilar steels can be more complex than similar welding due to different thermal cycle experienced with each metal [15]. Hernandez et al. [16] investigated the influence of microstructure and weld size on the mechanical behaviour of dissimilar DP600-DP780 and DP600-TRIP780 spot weldments and they found that as compared to the DP600 similar weldment, the pull-out failure mode was activated when DP600 was joined with dissimilar DP780 and TRIP780 steels. Wei et al. [17] investigated similar and dissimilar combinations of DP1000 and TRIP980 steels while Pouranvari and Marashi [18] investigated the mechanical performance of dual-phase DP600, DP780, and DP980 grade steels. They reported that the softening of the heat affected zone plays an important role in the mechanical properties of weldment. Sun et al. [19] concluded that the weld failure mode has a significant influence on both load bearing capacity and the energy absorption capability of DP800-TRIP800 weldment.

The extensive literature survey revealed that there are sufficient amount of research about resistance spot weldability of AHSS. However, it has not been faced study about effect of electrode force on the weld nugget geometry and mechanical properties of DP600/TRIP800 dissimilar steel spot weldment. For this purpose, the DP600/TRIP800 dissimilar steel was combined with various electrode force (4, 5 and 6 kN) at 7 kA constant welding current and 20 cycles constant welding duration. The mechanical properties of DP600/TRIP800 dissimilar steel joints, including failure type, load bearing capacity and the energy absorption capability were determined by using a universal tensile test machine. The failure behavior of tensile shear and cross tension test samples was evaluated. In addition, the weld nugget size was determined and metallographic evaluation was carried out on the cross section of weldment.

II. EXPERIMENTAL STUDY

The chemical composition and mechanical properties of DP600 and TRIP800 steel in 1.5 mm thickness is reported in Table 1.

TABLE I
CHEMICAL COMPOSITION AND MECHANICAL PROPERTIES OF THE BASE METALS (% WEIGHT).

	C	Si	Mn	Cr	Mo	Al	Fe	Yield Strength (MPa)	UTS (MPa)	Elongation (%)
DP600	0.1	0.18	1.6	0.34	0.09	0.05	Bal.	418	580	19
TRIP800	0.21	1.68	1.65	0.016	0.014	0.36	Bal.	510	800	21

Test samples were spot welded in a pneumatic spot welding machine with 60 kVA capacity in 50Hz electrical circuit. Spherical tip electrodes (CuCrZr) having 5.5 mm diameter were used. The welding parameters applied in experiment are given in Table II. Optimum welding time and welding current was determined by pre-experimental studies.

TABLE II
WELDING PARAMETERS FOR DP600/TRIP 800 DISSIMILAR STEELS COUPLE

Electrode force (kN)	Welding time (cycle)	Welding current (kA)	Hold time (cycle)	Squeeze time (cycle)	Clamping time (cycle)
4	20	7	15	25	15
5					
6					

Note: 1cycle= 0.02 s

A group of DP600/TRIP800 steel couple having dimension of 1.5 x 30 x 100 mm³ were adjoined for tensile shear test sample with given welding parameters in Table 2. Other group of DP600/TRIP800 steel couple having dimension of 1.5 x 50 x 150 mm³ were welded for cross tension test sample with same welding parameters in the wooden molding. The welded samples were subjected to tensile shear tests and cross tension test as seen in Figure 1.

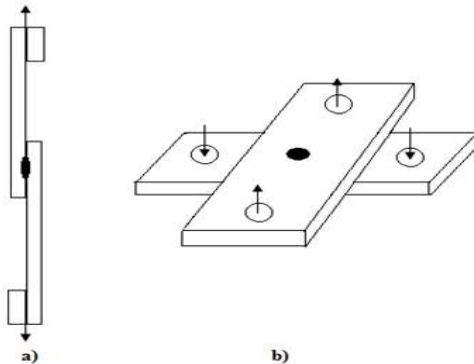


Fig. 1 Schematics of a) Tensile shear test samples, b) Cross tension test samples

The assessment of dissimilar sheet position on the joining of weldment was determined by preliminary experiment. For this purpose, a set of samples in which DP600 steel positioned underside, while TRIP800 steel sheet faced upside of the wooden mould were joined in selected welding parameters. Another set of samples in which the DP600 steel positioned upside, while TRIP800 steel sheet faced underside of the wooden mould were joined in same welding parameters. All

welded samples were carried out tensile shear test and results were compared with each other. Tensile tests results indicate that the couple which was joined at TRIP800 steel sheet faced underside position gave higher tensile shear load bearing capacity. Therefore, dissimilar steel couple welded TRIP800 steel sheet faced underside position for tensile shear and cross tension test samples during the experiment. Five test samples were prepared and then tested for each of the weld variable by using Shimadzu testing machine. Samples were tested with a crosshead speed of 10 mm/min. The tensile shear strength was measured as the peak load reached during the test, while the energy absorbed by the welded joint was calculated as the area under the load-displacement curve up to the peak load [20].

$$\text{Absorbed energy} = \int_0^{X_{max}} F dx = \sum_{i=1}^N F(i)[X(i) - X(i-1)]$$

where F is the load, X is the displacement, Xmax is the displacement at the peak load, i is the sample datum (20 Hz sampling frequency), and N is the sample datum relative to the peak load.

The vickers microhardness measurement on the diagonal of weld cross section in which involving weld nugget, heat affected zone (HAZ) and base metal was carried out with a load of 500 g. The transverse section of the weldment was prepared by standard metallographic procedure. The samples were etched for 5 s with 2 % nital for evaluating microstructure. The microstructural examination of sample was carried out by using a Nikon Optical DIC microscope and Zeiss Ultra Plus type scanning electron microscope (SEM). In addition, the fracture surfaces of tensile shear test samples were examined by using SEM. The nugget diameter is also measured on the metallographic samples.

III. RESULTS

A. Microstructure Evaluation

Fig. 2, Fig. 3 and Fig. 4 shows the microstructures of DP600/TRIP800 weldments, which were joined with various electrode force of 4 kN, 5 kN and 6 kN at 7kA welding current for 20 cycles welding time respectively. During the joining process, DP600/TRIP800 dissimilar steel weldment underwent different thermal cycles due to their different chemical, physical and mechanical properties. As seen in Figure 2-4 TRIP800 steel contains retained austenite and bainite phases in ferrite matrix while, DP600 steel consist of certain amount martensite phases in ferrite matrix. As seen in the cross section of the DP600/TRIP800 spot weldment, there are some weld defects like as voids, cracks and some inclusions across the weld nugget and HAZ. The amount of inclusions and martensite volume fraction was increased with increasing electrode force. The weld nugget was decorated fully martensite phase because of the temperature exceeds Ac₃ so it is completely austenitised and then rapid cooling rate encourages the martensite transformation at this region [21-23]. The martensite volume fraction increased as the location moves towards the weld nugget as a result of the increasing heating

followed by rapid cooling, which resulted in increment for hardness [24].

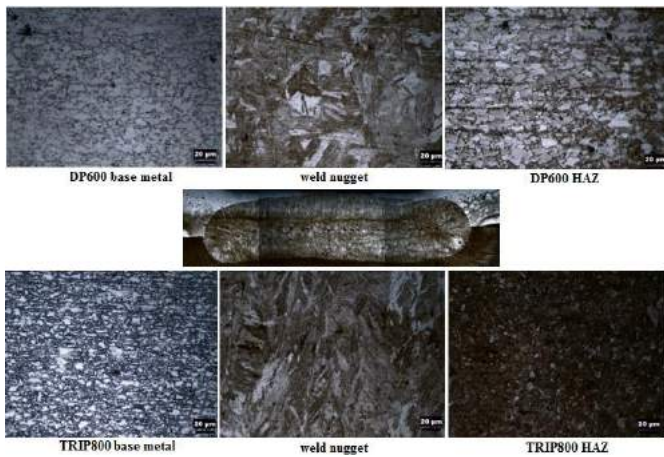


Fig. 2 DP600/TRIP800 weldment joined with 4 kN electrode force at 7kA welding current for 20 cycles welding time

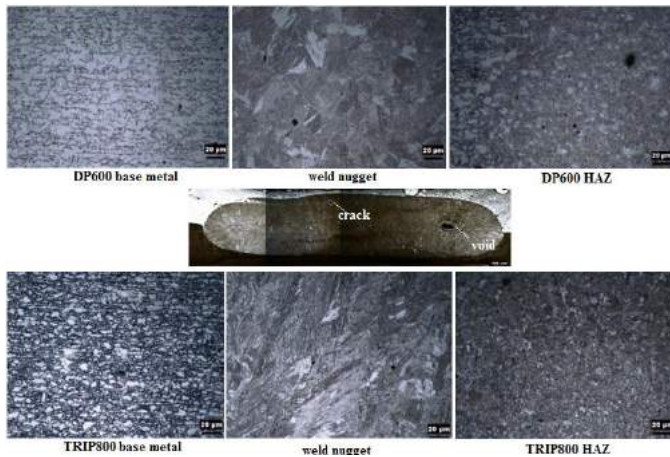


Fig. 3 DP600/TRIP800 weldment joined with 5 kN electrode force at 7kA welding current for 20 cycles welding time

Fig. 2-4 clearly shows HAZ region in DP600 steel side of weldment that exhibits martensitic and ferritic microstructure. As compare to the DP600 base metal, the martensite volume fraction increased because of temperature reached between A_{c1} and A_{c3} range in HAZ region during welding so, it is partially austenitised and then transformed martensite associate with cooling regime [21-23]. Owing to the subsequent rapid cooling, the carbon rich austenite transforms to the martensite phase and ferrite remains the same in the structure [21,25]. The microstructure decorated predominantly martensite side by weld nugget. The HAZ region in TRIP800 steel base metal towards to the weld nugget has a little amount retained austenite and bainite with ferrite as well as martensite phases. The microstructure side by weld nugget was also decorated predominantly martensite phases.

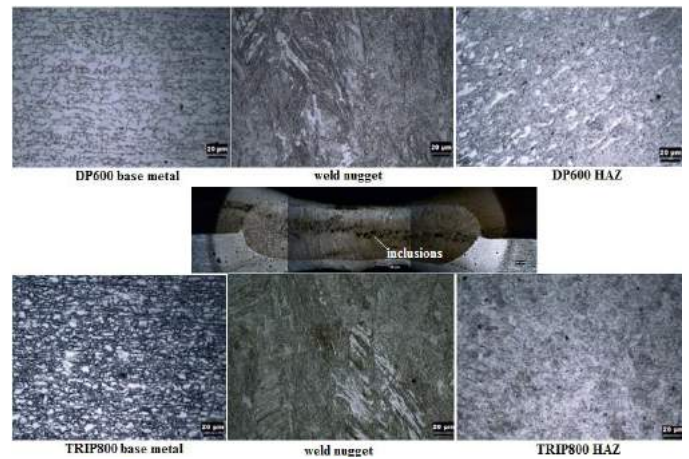
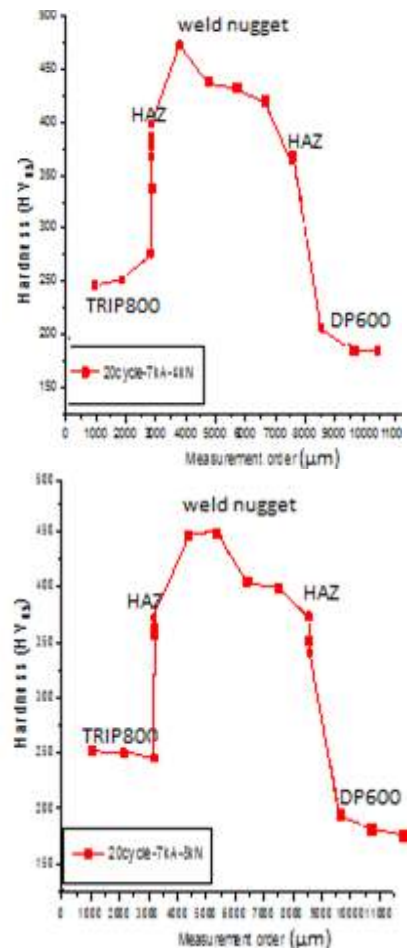


Fig. 4 DP600/TRIP800 weldment joined with 6 kN electrode force at 7kA welding current for 20 cycles welding time

B. Hardness Results

The hardness profiles for DP600/TRIP800 weldments that were joined with 4 kN, 5 kN and 6 kN electrode forces at a constant welding current and duration are shown in Fig 5.



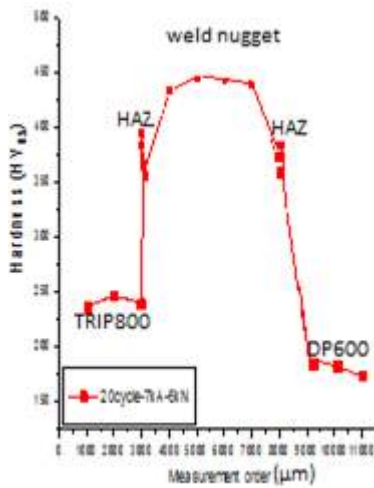


Fig. 5 Hardness profile of DP600/TRIP800 weldments joined with 4 kN, 5 kN and 6 kN electrode forces at a constant welding current and duration

As seen in Figure 5, the hardness values increased from the both base metals towards to HAZ and weld nugget in DP600/TRIP800 weldments. The weld nugget hardness values shifted between 400 HV_{0.5} and 460 HV_{0.5} for 4 kN and 5 kN electrode force. It was notify that the considerable increment in hardness has found in TRIP800 steel side of weld nugget due to high amount of martensitic transformation during welding. It is believed that TRIP800 steel side of weldment severely affected from plastic deformation. However, hardness values of the weld nugget in both steel side of weldment that joined with 6 kN electrode force, found close to each other. This may be attributed to the severely plastic deformation because of high electrode force, which causes more martensitic transformation for both TRIP800 and DP600 side of the weld nugget.

C. Tensile shear and cross tension strength of weldment

The tensile shear and cross tension strength associate with various electrode force and energy absorption is shown graphically in Figure 6 a and b respectively.

An increment in the electrode force from 4 kN to 5kN caused increasing tensile shear load bearing capacity, cross tension strength and absorbed energy of the dissimilar steel weldments due to enlargement in the nugget diameter. Conversely, the considerable diminish in the strength and absorbed energy of weldment was determined by increasing electrode force from 5 kN to 6 kN. It is reported that two main factors are responsible for the reduction in the spot strength as the clamping force is increased: (i) higher clamping forces reduce the heat input and, in turn, the nugget size; (ii) the indentation of the electrode tips on the sheet surfaces induces high stress concentrations in the regions around the weld nugget [26-28]. It is believed that the decrease in the absorbed energy could be second main factor.

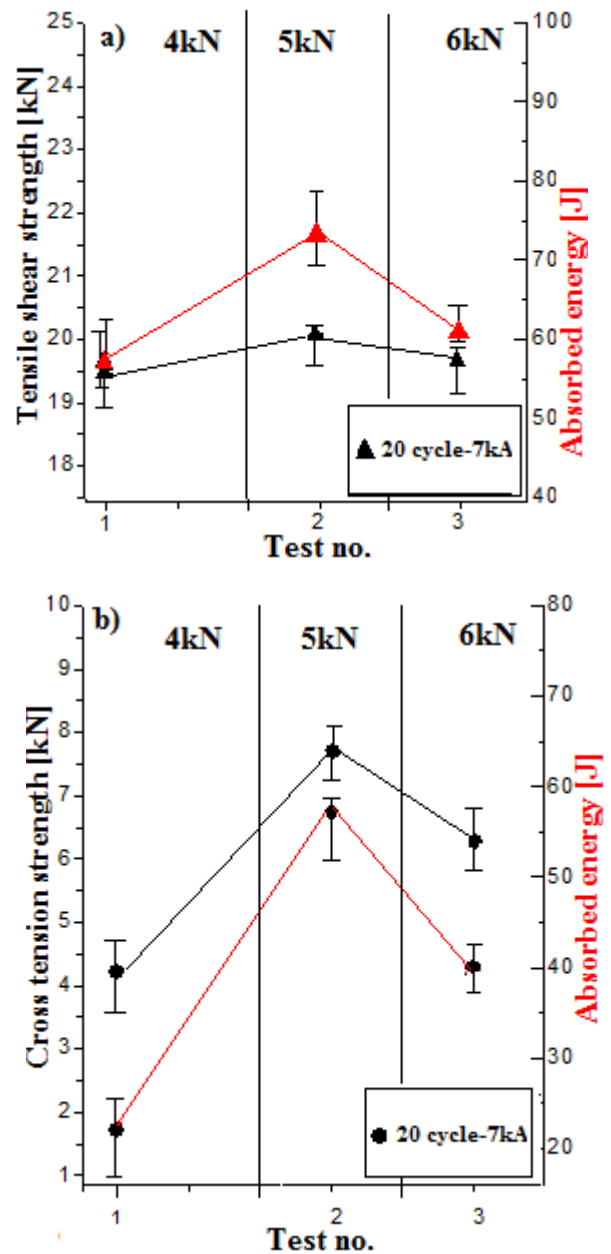


Fig. 6 a) The tensile shear b) The cross tension strength associate with various electrode force and energy absorption

The effect of weld nugget diameter associate with electrode force on tensile shear and cross tension strength of weldment was investigated and result shown graphically in Figure 7.

The common norm for the average nugget diameter is that it should be equal to or larger than $4\sqrt{t}$ (t defined as material thickness in mm). However, according to Sun et al., AHSS spot welds with a weld nugget size of $4\sqrt{t}$ cannot produce nugget with a pullout failure mode for both DP800 and TRIP800 spot welds under lap shear loading [19]. Kumar Pal and Bhowmick [29] showed that the average weld nugget diameter should be equal to or larger than $4\sqrt{t}$ for nugget pull out failure mode in dual phase steels for sheet thickness less than 1.5 mm. For this reason, the $4.5\sqrt{t}$ is sufficient for AHSS steels. In this study, the resistance spot welded DP600/TRIP800 dissimilar joints

supplies the acceptable weld nugget diameter (upper than $4.5\sqrt{t}$ ($=5.51$ mm)) for selected welding parameters.

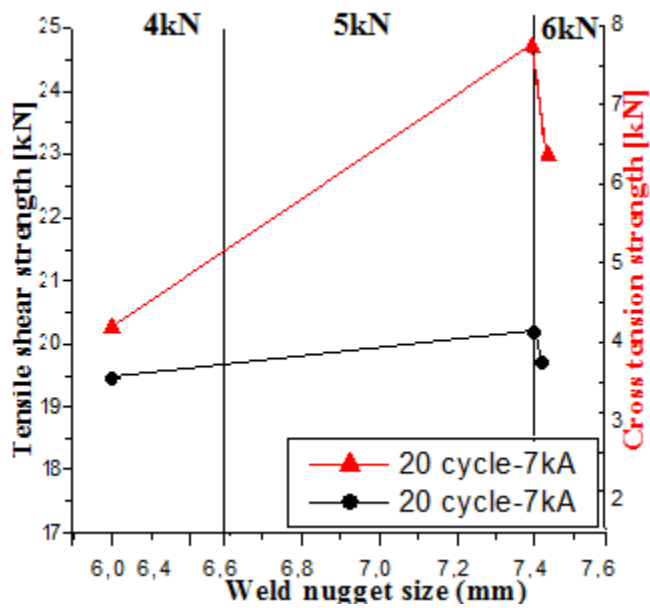


Fig. 7 Effect of nugget diameter associate with electrode force on the tensile shear and the cross tension strength

As seen in Figure 7, the strength of weldment influenced from weld nugget diameter associate with electrode forces. The strengths increased with increment in nugget diameter from 6 mm to 7.4 mm but it started to diminish over the 7.4 mm weld nugget diameter due to metal expulsion. The high electrode force higher than 5 kN and electrode indentation is responsible for decreasing strength that seems sharper in samples which tested with cross tension test.

The weld nugget diameter associate with electrode force and failure mode of the tensile shear and cross tension test samples was investigated. Failure modes of tensile shear test samples and cross tension test samples are shown in Figure 8 a and b respectively.

As seen in Figure 8 a and b, all tested samples failed from the TRIP800 side as pullout failure (PF) mode. Crack propagation in pullout failure mode, the fracture occurred at the edge of the nugget button or in the HAZ. It was reported that the failure mode can significantly affect strength and energy absorption capacity of resistance spot weldments [30]. Generally, the PF mode is the preferred failure mode due to higher plastic deformation and energy absorption associated with it [31-33]. Since, the welding parameters including electrode force, weld current and duration used in this study formed acceptable weld nugget diameter, d_n , $4.5\sqrt{t}$ ($=5.51$ mm), the resistance spot welded DP600/TRIP800 dissimilar joints failed with desired pullout failure (PF) mode.

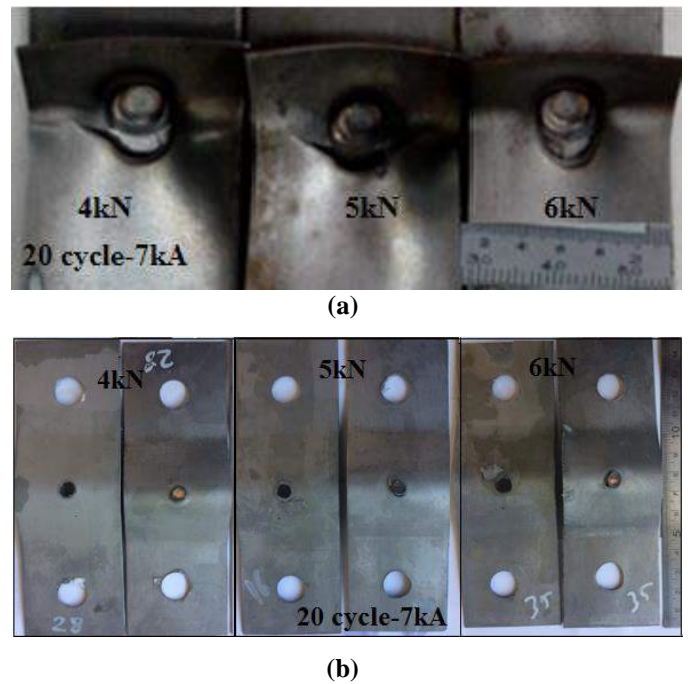


Fig. 8 Pullout failure modes of a) tensile shear b) cross tension test samples

In addition, the ductile and semi-ductile/brittle fracture characteristics of PF mode in spot welded DP600/TRIP800 dissimilar steel couple is shown in Figure 9 a-d. The cleavage facets covering the fracture surface indicate brittle fracture while dimples on the surface refer to ductile fracture.

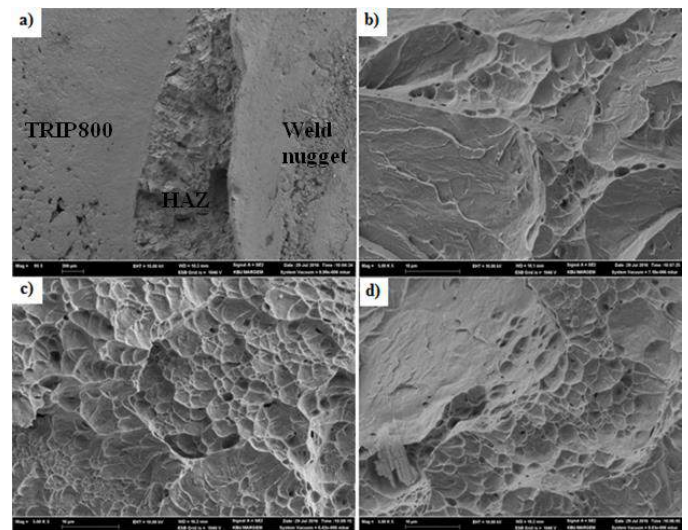


Fig. 9 The fracture characteristics of PF mode in spot-welded DP600/TRIP800 dissimilar steel couple a) fracture surface at low magnification, b,c,d) fracture surface at high magnification

IV. CONCLUSIONS

The summary of results and some suggestions are given below:

- For obtaining higher strength in resistance spot welding of DP600/TRIP800 dissimilar steel, the TRIP800 steel sheet have to be faced underside position during the joining.
- As compare to base metals microstructure, the martensite volume fraction in weld nugget increased due to weld thermal cycle, and the microstructure is transformed fully martensite associate with high cooling regime and chemical compositions of steels.
- The weld nugget hardness values shifted between 400 HV_{0.5} and 460 HV_{0.5} for 4 kN and 5 kN electrode force. It was notify that the considerable increment in hardness has found in TRIP800 steel side of weld nugget. However, hardness values of the weld nugget in both steel side of weldment that joined with 6kN electrode force, found close to each other.
- The maximum weld tensile shear and cross tension strength was obtained in the weldment that was joined with 5 kN electrode force at 7 kA welding current for 20 cycles welding duration.
- The strength and energy absorption influenced from weld nugget diameter associate with electrode force. The strengths and energy absorption increased with increasing electrode force from 4 kN to 5 kN due to enlargement of weld nugget diameter, However, the strengths and energy absorption significantly decreased for upper than 5 kN electrode force due to expulsion and high electrode indentation.
- The resistance spot welded DP600/TRIP800 dissimilar joints failed with desired pullout failure (PF) mode for all welding parameters which provide acceptable weld nugget diameter, $4.5\sqrt{t}$ (=5.51 mm).

REFERENCES

- [1] Májlinger, K., Kalácska, E. and Spena, P. R., "Gas metal arc welding of dissimilar AHSS sheets", *Materials & Design*, vol. 109 pp. 615–621, 2016.
- [2] Hernandez, B., Okita, V.H.H. and Zhou Y., "Second pulse current in resistance spot welded TRIP steel-Effects on the microstructure and mechanical behavior", *Welding Journal* vol. 91, pp. 278- 285, 2012.
- [3] Ma, C., Chen, D.L., Bhole, S.D., Boudreau, G., Lee, A. and Biro, E., "Microstructure and fracture characteristics of spot-welded DP600 steel", *Mater Sci Eng A*. vol. 485, pp. 334–346, 2008.
- [4] Zaeferrer, S., Ohlert, J. and Bleck, W., "A study of microstructure, transformation mechanisms and correlation between microstructure and mechanical properties of low alloyed TRIP steel", *Acta Mater*, vol. 52, pp. 2765–2778, 2004.
- [5] Jacques, P.J., "Transformation-induced plasticity for high strength formable steels", *Curr Opin Solid State Mater Sci*, vol. 8, pp.259–265, 2004.
- [6] Ertek Emre H. and Kaçar, R., "Development of weld lobe for resistance spot-welded TRIP800steel and evaluation of fracture mode of its weldment", *Int J Adv Manuf Technol* vol. 83, pp. 1737–1747, 2016.
- [7] Nayak, S.S., Baltazar Hernandez, V.H., Okita Y. and Zhou Y., "Microstructure-hardness relationship in the fusion zone of TRIP steel welds", *Mater Sci Eng A*, vol. 551, pp.73–812012
- [8] De Cooman, B.C., "Structure-properties relationship in TRIP steels containing carbide-free bainite", *Curr. Opinion Solid State, Mater Sci*, vol. 8, pp.285–303, 2004.
- [9] Zhang, C.W. and Raabge, D., "Interaction between recrystallization and phase transformation during intercritical annealing cold-rolled dual-phase steel: a cellular automation model", *Acta Mater*, vol. 61, 14, pp. 5504- 5517, 2013.
- [10] Ramazani, A., Mukherjee, K., Abdurakhmanov, A., Prahil, U., Schleser, M., Reisgen, U. and Bleck, W., "Micro-macro-characterization and modeling of mechanical properties of gas metal arc welded (GMAW) DP600 steel", *Materials Science and Engineering: A*, vol. 589, pp. 1-14, 2013.
- [11] Lee, W., Chung, K.H, Kim, D., Kim, J., Kim, C., Okamoto, K., Wagoner, R.H. and Chung, K., "Experimental and numerical study on formability of friction stir welded TWB sheets based on hemispherical dome stretch tests", *Int J Plast*, vol. 25, pp. 1626–1654, 2009.
- [12] Kim, J.H., Sung, J.H., Piao, K. and Wagoner, R.H., "The shear fracture of dual-phase steel", *Int J Plast*, vol. 27, pp. 1658–1676, 2011.
- [13] Noh, W., Kim, W., Yang, X., Kang, M, Lee, M.G. and Chung K., "Simple and effective failure analysis of dissimilar resistance spot welded advanced high strength steel sheet", *International Journal of Mechanical Sciences*, vol. 121, pp.76–89, 2017.
- [14] Arumugam, M. Nor, "Spot welding parameter optimization to improve weld characteristics for dissimilar metals", *International Journal of Scientific & Technology Research*, vol. 4, pp. 75-80, 2015.
- [15] Marashi, P., Pouranvari, M., Amirabdollahian, S., Abedi, A. and Goodarzi, M., "Microstructure and failure behavior of dissimilar resistance spot welds between low carbon galvanized and austenitic stainless steels", *Materials Science and Engineering A*, vol. 480, pp. 175–180, 2008.
- [16] Hernandez, B.V., Kuntz, M., Khan, M. and Zhou, Y., "Influence of microstructure and weld size on the mechanical behavior of dissimilar AHSS resistance spot welds", *Sci Technol Weld Joint*, vol. 13, pp. 769–776, 2008.
- [17] Wei, S.T., Lv, D., Liu, R.D., Lin, L., Xu, R.J., Guo, J.Y. and Wang, K.Q. "Similar and dissimilar resistance spot welding of advanced high strength steels: welding and heat treatment procedures, structure and mechanical properties", *Sci Technol Weld Join*, vol. 19, pp. 427–435, 2014.
- [18] Pouranvari, M., Marashi, S.P.H., "Key factors influencing mechanical performance of dual phase steel resistance spot welds", *Sci. Technol. Weld. Join*. Vol. 15, pp.149–155, 2010.
- [19] Sun, X., Stephens, E.V. and Khaleel, M.A. "Effects of fusion zone size and failure mode on peak load and energy absorption of advanced high strength steel spot welds under lap shear loading conditions", *Eng Fail Anal.*, vol. 15, pp. 356–367, 2008.
- [20] Spena, P.R., Maddis M.D., D'Antonio G., and Lombardi, F., "Weldability and monitoring of resistance spot welding of Q&P and TRIP steels", *Metals*, vol. 6, 270, pp.1-15, 2016
- [21] Khan, M.I., Kuntz, M.L., Biro, E. and Zhou, Y. 2008. "Microstructure and mechanical properties of resistance spot welded advanced high strength steels". *Materials Transactions*, 49 (7): 1629-s to 1637-s.
- [22] Kou, S. 2003. *Welding Metallurgy*, 2nd Ed., Hoboken, NJ, J. Wiley & Sons.
- [23] Zhang, H. and Senkara J. *Resistance Welding: Fundamentals and Applications*, Boca Raton, FL, CRC Group, 2006.
- [24] Safanama, D.S., Marashi, S.P.H. and Pouranvari, M. "Similar and dissimilar resistance spot welding of martensitic advanced high strength steel and low carbon steel: metallurgical characteristics and failure mode transition", *Science and Technology of Welding and Joining*, vol. 17 (4), pp. 288-294, 2012.
- [25] Isayev, A.P., Terekhov, A.A. "Mechanical properties of resistance spot welded joints in zinc-plated TRIP steel", *Welding International*, vol. 28 (4), pp. 324-328, 2014.
- [26] Spena, P.R., Maddis, M.D., Lombardi F. and Rossini, M., "Investigation on resistance spot welding of TWIP steel sheets", *Steel Research Int.*, vol. 86, pp. 1480–1489, 2015.

- [27] Chao, Y.J. "Failure modes of spot welds: Interfacial versus pullout", *Sci. Technol. Weld. Join.* vol. 8, pp.133–137, 2003.
- [28] Biro, E., Cretteur, L. and Dupuy, T., "Higher than expected strengths from dissimilar configuration advanced high strength steel spot welds", *In Proceedings of the Sheet Metal Welding Conference XV*, Livonia, MI, USA, 2–5 October 2012.
- [29] Kumar Pal, T. and Bhowmick, K., "Resistance spot welding characteristics and high cycle fatigue behavior of DP 780 steel sheets", *J Mater Eng Perform*, vol. 21, pp. 280–285, 2012.
- [30] Pouranvari, M., Marashi, P., Goodarzi, M. and Abedi A., "An analytical model predicting failure mode of resistance spot welds" *Metal, Hradec nad Moravici* -pp. 1-7, 2008.
- [31] Jacques, P.J. "Transformation-induced plasticity for high strength formable steels", *Curr Opinion Solid State Mater Sci* vol. 8, pp. 259–265, 2004.
- [32] De Cooman, B.C., "Structure–properties relationship in TRIP steels containing carbide-free bainite", *Curr Opinion Solid State Mater Sci* vol. 8, pp. 285–303, 2004.
- [33] Shi, G. and Westgate, S.A., "Techniques for improving the weldability of TRIP steel using resistance spot welding", *1st International Conference Super-High*, vol. 16, pp. 9–14, 2004.

Effect of Homogenization Heat Treatment on Microstructure, Hardness and Toughness Properties of G18NiCrMo3-6 Steel

Funda Gül KOÇ^{a*}, Mustafa ÇÖL^a, Sevim SÜNNETÇİ^b

^a Kocaeli University, Department of Metallurgy and Material Engineering, Kocaeli, Turkey
funda.demircan@kocaeli.edu.tr, mcol@kocaeli.edu.tr

^b Burçelik Bursa Steel Casting Industry, Bursa, Turkey
sevimsunnetci@gmail.com

Abstract — G18NiCrMo3-6 steel is widely used in mining industries, offshore platforms equipments, machine parts due to its high strength and toughness properties.

In this study, the effect of homogenization treatment on the microstructure, hardness and toughness of G18NiCrMo3-6 steel was investigated. For this purpose, a group of specimens were applied homogenization heat treatment at 1150 °C for 3 hours. All specimens were austenitized at 950 °C for 2 hours, quenched in polymer solution at room temperature and then tempered at 500 °C, 620 °C, 650 °C for 1 hour. Charpy V notch impact test was performed to determine the toughness properties of the specimens. Fracture surfaces were investigated by scanning electron microscope (SEM). Microstructures of the specimens were investigated by using light microscope to determine the effect of heat treatment conditions. Changes of the material hardness due to different heat treatment conditions were obtained with hardness measurements.

Keywords — G18NiCrMo3-6, homogenization, microstructure, hardness, toughness

I. INTRODUCTION

G18NiCrMo3-6 steel is extensively used in applications where fatigue resistance, high strength and toughness properties are required, such as mining industries, offshore platforms equipments, and machine parts [1,2].

Casting is a solidification process [3]. During solidification of liquid metals, redistribution of solutes occurs between liquid and solid phases leading to non-uniformity of composition [4]. Two types of segregation can be observed in as-cast structure; microsegregation and macrosegregation. Microsegregation occurs on microscopic scale within the dendritic arm spacing and macrosegregation involves non-uniformity of composition over macroscopic or large areas in as-cast structure [4,5]. Segregation can lead to lower mechanical properties and inhomogeneous microstructure due to local compositional changes [6].

In order to eliminate the segregation and achieve the desired mechanical properties, homogenization, austenitization

followed by quenching and tempering at subcritical temperatures are applied respectively [7-9].

In this study, the effect of homogenization heat treatment on microstructure, hardness and toughness of G18NiCrMo3-6 steel was studied. For this purpose, changes of microstructure properties, hardness and toughness of the specimens in different heat treatment conditions were investigated.

II. EXPERIMENTAL PROCEDURE

In this study, the investigated material was melted in a high frequency induction furnace and was formed by casting into the sand mould. The chemical composition of the cast material was measured by optical emission spectrometry and is shown in Table 1.

Table 1. Chemical composition of cast material (wt.%)

C	Si	Mn	Cr	Ni	Mo	P	S	Fe
0.1	0.5	1.0	0.6	0.8	0.4	0.0	0.0	Balanc
9	2	1	9	8	5	1	1	e

The formation of austenite during continuous heating analyzed by a Netzsch dilatometer with specimen dimension of 5 mm in diameter and 25 mm length. For this purpose, specimen was heated to 1000°C for 1 hour and cooled to room temperature at 10 K/min. According to dilatometer curve, Ac₁ and Ac₃ were determined about 737 °C and 885 °C respectively.

The specimens were cut from cast material and divided into two groups before the heat treatment (Group A and B). Homogenization heat treatment was performed at 1150 °C for 3 hours to group A specimen. After then all specimens were austenitized at 950 °C for 2 hours and quenched in polymer solution at room temperature. Three different temperatures (500, 620, and 650°C) were selected for tempering of the quenched samples. Table 2 shows the heat treatment conditions applied to the specimens.

Table 2. Heat treatment conditions of the specimens

Specimen Code	Heat Treatment	Specimen Code	Heat Treatment
A0	1150 °C/3h+950 °C/2h	B0	950 °C/2h
A1	1150 °C/3h+950 °C/2h+500 °C/1h	B1	950 °C/2h+500 °C/1h
A2	1150 °C/3h+950 °C/2h+620 °C/1h	B2	950 °C/2h+620 °C/1h
A3	1150 °C/3h+950 °C/2h+650 °C/1h	B3	950 °C/2h+650 °C/1h

specimens were prepared with usual manner for metallographic investigations with a final polishing carried out using 3 μm diamond. The specimens were etched for 20s in 3% nital to reveal the microstructures clearly. Olympus light microscope was used for the microstructural investigations.

Hardness tests were performed using a Future-Tech Vickers hardness tester under 10 kg load, 10 seconds of loading duration and five measurements were made on each sample to obtain an average value.

Charpy V notch impact tests were carried out at room temperature to understand the effect of heat treatments on toughness of samples. The size of specimens was 10 x 10 x 50 mm. Fracture surfaces of the samples after impact tests were investigated using scanning electron microscopy.

III. RESULTS AND DISCUSSION

Microstructural Investigations

Figure 1 shows microstructure of the cast specimen. It can be clearly seen that segregation in the microstructure of the cast specimen. Carbon segregation that formed during solidification, leads to non-uniform microstructure in the cast material [9].



Fig. 1 Microstructure of the cast specimen

Microstructures of the quenched specimens are given in Figure 2. It was observed that microstructure was coarser and segregation could not be eliminating completely with homogenization treatment. The microstructures consist of bainite and some martensite. Figure 3 shows microstructures of the specimens tempered at different temperatures. As seen

from Figure 3, martensite tetragonal structure is decomposed by tempering and microstructure is completely consisting of bainite.

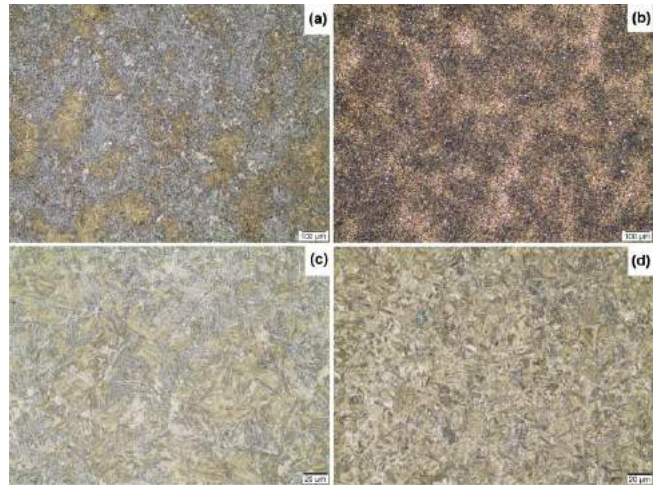


Fig. 2 Microstructures of the quenched specimens a-c) A0, b-d) B0

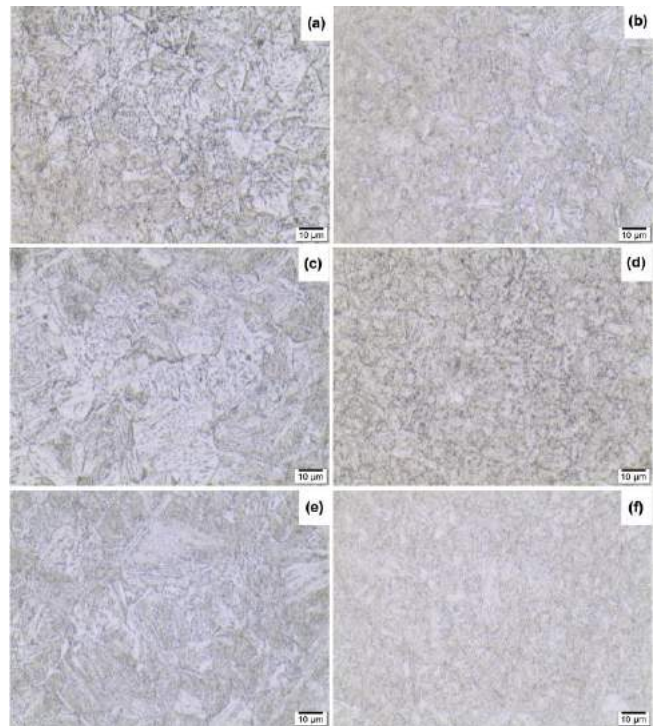


Fig. 3 Microstructures of tempered specimens a) A1, b) B1, c) A2, d) B2, e) A3, f) B3

Hardness Measurements

Hardness tests were performed to determine the effect of homogenization heat treatment and tempering temperature on the hardness of specimens. The hardness of the cast sample was 203 HV. The hardness values of A0 and B0 specimens were

measured as 347 and 423 HV respectively. Hardness of group A specimens is lower as a result of grain coarsening due to homogenization heat treatment. It can be seen from Figure 4, hardness decreases with increasing tempering temperature.

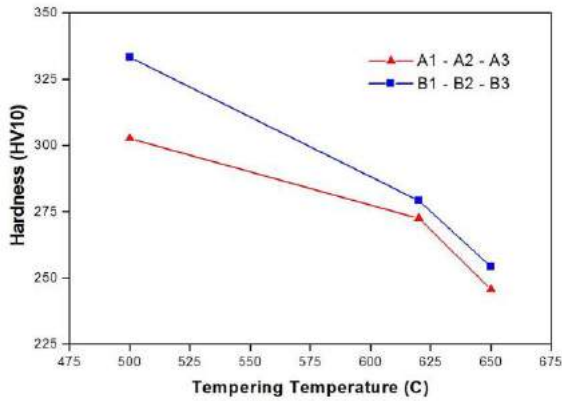


Fig. 4 Effect of heat treatments on the hardness of specimens

Toughness and Fractography

Charpy V notch impact tests were carried out to understand the effect of heat treatment conditions on toughness of materials. The impact energy of the cast sample was 48 Joule. The impact energy of the A0 and B0 specimens were measured as 30 and 22 joule respectively. The changes in the toughness of tempered specimens were given in Figure 5. As seen from Figure 5, material toughness properties increase as the tempering temperature increases. When comparing the toughness of tempered specimens, it is clearly seen that homogenization heat treatment caused an increase on toughness at low tempering temperature (500 °C) especially.

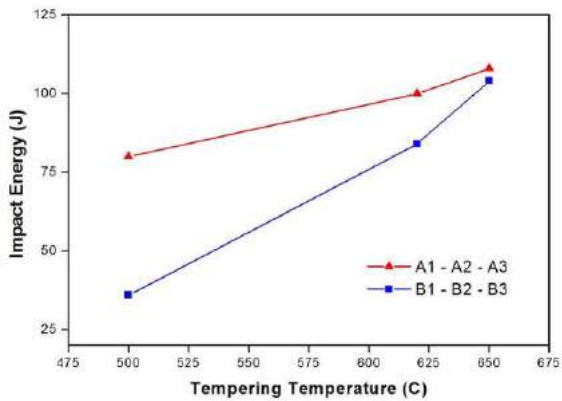


Fig. 5 Effect of heat treatment conditions on toughness of specimens

Fractured surfaces of the different heat treated specimens were investigated by using SEM to determine fracture morphology. As seen from Figure 6, while cast specimen exhibits ductile fracture, fracture morphology is remarkably changed after homogenization and quenching treatment. Fracture morphology of the B1 specimen is which is tempered at 500 °C is more brittle than A1 specimen. It was observed that

fracture morphology of high temperature (620 °C and 650 °C) tempered specimens were more ductile as a result of high toughness properties.

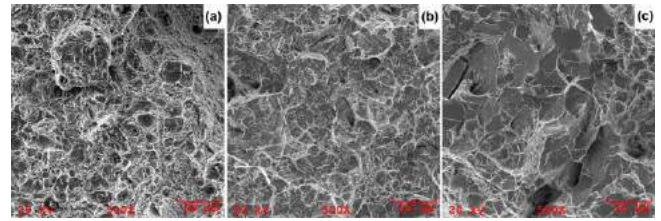


Fig. 6 Fracture surfaces of a) cast sample, b) A0, c) B0

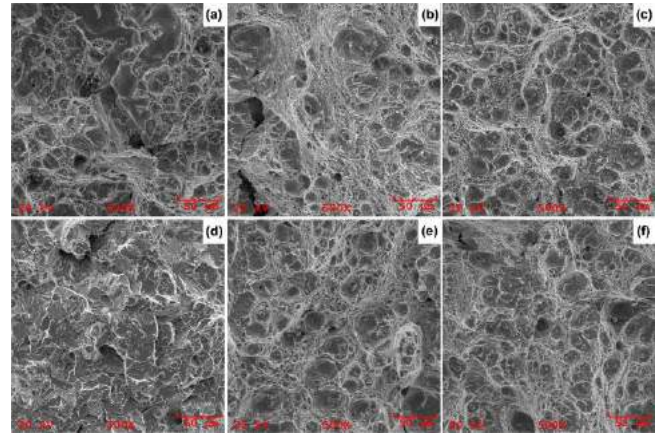


Fig. 7 Fracture surfaces of a) A1 b) A2, c) A3, d) B1, e) B2, f) B3

IV. CONCLUSIONS

In this study, the obtained results can be summarized in the following:

- Homogenization heat treatment causes coarse and more uniform microstructure but it is necessary to increase the heat treatment time to eliminate the segregation completely.
- The hardness of the homogenization heat treated specimens is lower due to coarse grain structure.
- The results of the impact test of the specimens were in good agreement with the material hardness.
- Homogenization heat treatment has an important effect on toughness of the specimens at low tempering temperature especially. Toughness of the material increase with homogenization heat treatment and tempering.

REFERENCES

[1] S. Lim, J. Mun, T. Kim, C. Kang, Development of low temperature high strength integral steel casting for offshore construction by casting process engineering, *International Journal of Naval Architecture and Ocean Engineering*, vol. 6, pp. 922-934, 2014.

- [2] P. Tao, H. Yu, Y. Fan, Y. Fu, Effects of cooling method after intercritical heat treatment on microstructural characteristics and mechanical properties of as-cast high-strength low-alloy steel, *Materials and Design*, vol. 54, pp. 914-923, 2014
- [3] J. Zhao, Z. Jiang, C. S. Lee, Enhancing impact fracture toughness and tensile properties of a microalloyed cast steel by hot forging and post-forging heat treatment processes, *Materials and Design*, vol. 47, pp. 227-233, 2013.
- [4] S. K. Choudhary, S. Ganguly, A. Sengupta, V. Sharma, Solidification morphology and segregation in continuously cast steel slab, *Journal of Materials Processing Technology*, vol. 243, pp. 312-321, 2017.
- [5] M. G. Lage, A. L. V. C. Silva, Evaluating segregation in HSLA steels using computational thermodynamics, *Journal of Materials Research and Technology*, vol. 4, pp. 353-358, 2015.
- [6] M. Bitterlin, A. Loucif, N. Charbonnier, M. Jahazi, L. P. L. Boire, J. B. Morin, Cracking mechanisms in large size ingots of high nickel content low alloyed steel, *Engineering Failure Analysis*, vol. 68, pp. 122-131, 2016.
- [7] H. Najafi, J. Rassizadehghani, S. Asgari, As-cast mechanical properties of vanadium/niobium microalloyed steels, *Materials Science and Engineering A*, vol. 486, pp. 1-7, 2008.
- [8] M. Çöl, F. G. Koç, Effect of homogenization heat treatment on toughness and wear resistance of plastic mold steel, *Materials Testing*, vol. 57, pp. 942-946, 2015.
- [9] J. Zhao, J. H. Lee, Y. W. Kim, Z. Jiang, C. S. Lee, Enhancing mechanical properties of low-carbon microalloyed cast steel by controlled heat treatment, *Materials Science and Engineering A*, vol. 559, pp. 427-435, 2013.

Evaluation of Energy Saving Potential in Industrial Furnaces Used In Iron-Steel Sector

*Şaban PUSAT**, *İsmail EKMEKÇİ†*, *Hasan Hüseyin ERDEM#*

* *Yildiz Technical University, Mechanical Engineering Department, Beşiktaş, İstanbul, Turkey, spusat@yildiz.edu.tr*

† *İstanbul Commerce University, Faculty of Architecture and Design, Küçükyalı, İstanbul, Turkey, iekmekci@ticaret.edu.tr*

Yildiz Technical University, Mechanical Engineering Department, Beşiktaş, İstanbul, Turkey, herdem@yildiz.edu.tr

ABSTRACT

Iron and steel sector is one of the most energy intense sector in the world, and industrial furnaces used in this sector have high importance in terms of energy efficiency. Industrial furnaces should be investigated carefully to be able to decrease the production costs. For this aim, firstly, the heat and mass flows through the furnace should be established. Then, waste heat sources should be revealed. Finally, the potential of waste heat recovery should be determined. In this study with a general point of view, waste heat recovery potential of industrial furnaces used in iron-steel sector was evaluated by setting heat and mass balances. The necessary calculations were done to introduce the waste heat recovery potential for the chimney which is one of the most important zone such equipment. In addition, effects of different process parameters (fuel consumption, yearly working hours, flue gas temperature and flue gas oxygen rate) on energy recovery potential were evaluated. Our main conclusion is that energy saving potentials are promising for the furnaces used in iron-steel sector. Furthermore, all the parameters considered in this study are significant in terms of energy efficiency potential.

Keywords: Iron-steel sector; industrial furnace; waste heat recovery; energy efficiency

Joining GR2 and GR5 Titanium Alloys with Diffusion Bonding Method Using Copper Interlayer

Haluk KEJANLI*, Nida KATI⁺, Uğur ÇALIGÜLÜ⁺

*Dicle University, Faculty of Engineering, Department of Machine Engineering, Diyarbakır,

⁺Fırat University, Faculty of Technology, Department of Metallurgy and Material Engineering, Elazığ

halukkejanli@gmail.com

nkati@firat.edu.tr

ugurcaligulu@gmail.com

Abstract— In this study, GR2 and GR5 alloys among Ti alloys which have increasingly more usage areas in the metal-material industry were joined by diffusion welding method using a copper interlayer. The diffusion temperature was selected as a variable parameter during the diffusion welding process and the effects of the welding temperature on the joint quality were examined. Diffusion welds were made by applying a pressure of 5 MPa at 950 and 980 °C to the samples prepared in Ø12 x 12 mm dimensions in specially prepared diffusion welding apparatus and sending argon gas with a purity of 99.9% at a flow rate of 5 lt/min into a furnace with silicon carbide rod. Welding process was carried out to the experimental samples for 55 minutes. The samples were kept in the furnace until the furnace's temperature decreased to 250 °C and then they were kept to cool down at room temperature. Microstructure analyses were then performed by using an optical microscope and microhardness analysis was performed on each sample. As a result of the study, it was found that as the temperature of diffusion welding increased, the better welded joints were obtained in the samples and their microhardness values also increased.

Keywords— Ti alloys, Diffusion bonding, microstructure, microhardness.

I. INTRODUCTION

Titanium alloy finds wide applications in spacecraft and aircraft industries [1], [2]. As titanium alloy is chemically reactive, it is very difficult to be welded. Titanium alloys can easily pick up nitrogen and oxygen from the atmosphere [3], [4]. Diffusion bonding is a solid state welding process that produces the coalescence of the faying surfaces, by the application of pressure at elevated temperature. The process does not involve the macroscopic deformation or relative motion of the work pieces. In diffusion bonding, high quality joints can be achieved without post weld machining [5]. Better bonding quality in diffusion bonding can be obtained by inserting an interlayer between the materials to be joined [6]. Both similar and dissimilar materials are joined by diffusion bonding [7], [8][9].

Accordingly, some researchers employed interlayers such as Ni [8], Ag [10] and Cu [7], [11] to alleviate residual stress concentration and adjust chemical changes across the

joint zone. In the mentioned works, solid state diffusion was the main mechanism in bonding process while in liquid state diffusion bonding, presence of melted interlayer in the joint zone leads to high diffusion of the elements at the interface and uniformity of chemical composition across the joint [12]. Formation of melted interlayer in the joint zone may require the bonding temperature rises above the β transus temperature in Ti alloy. This can cause main changes in the physical and mechanical properties of the base metal [13].

Diffusion bonded joints of commercially pure titanium (CP Ti) to 304 austenitic stainless steel over the temperature range of 850–950 °C for 1 h under 3 MPa uniaxial pressure were studied. Reaction products formed due to diffusion were identified. Diffusional behavior of Ti, Cr, Ni and Fe has been studied. Room temperature tensile strength of the transition joints was evaluated [14]. Dissimilar titanium/steel metals were successfully joined by diffusion bonding process using copper as interlayer. Joints were successfully established at 850 °C and joints were not successful below bonding temperature of 800 °C [15]. Electrolytic copper rods were bonded to Ti–6Al–4V rods at 875 °C and 890 °C. It was observed that bonding was not successful at bonding temperature of 900 °C [14]. In this work, construction of diffusion bonding windows for Ti–6Al–4V and AISI 304 stainless steel with silver as an interlayer was carried out and the details were presented. Generally, the levels of the temperature selected for diffusion bonding are in the range of 0.6–0.8 T_m , where T_m is the melting temperature [14]. From the previous literature and experiments conducted in our laboratory, important process parameters were chosen to bond the specimen [9]. The bonding characteristic and shear strength of Ti-17 titanium alloy at different bonding time were investigated. The shear strength of bond increased with increasing bonding time and the highest shear strength of 887.4 MPa was achieved at a holding time of 60 min. The contribution of plastic deformation on the void closure and the increase of shear strength was significant even though the time of plastic deformation was short [16]. The microstructures and mechanical properties of Ti–6Al–4V/Cu–10Sn bronze diffusion bonded joint were

studied via scanning electron microscopy (SEM) and energy dispersive spectrometry (EDS). Diffusion bonding of Ti-6Al-4V to Cu-10Sn bronze was investigated at various holding time. It was identified that the bonding had high shear strength up to 102 MPa for the joints bonded at bonding temperature of 830 °C, bonding pressure of 10 MPa and bonding time of 15 min. Shear test results show that the fracture took place between the reaction layer and the Cu-10Sn bronze substrate, and the shear strength was strongly related to the formation of Cu-Ti-Sn intermetallic compounds [9], [17].

The liquid state diffusion bonding mechanism of stainless steel 316 to Ti-6Al-4V using pure Cu interlayer has been investigated at 1100 °C for 60 min bonding time. The microstructure of joint zone was analysed in detail by scanning electron microscope and energy dispersive spectroscopy. The results showed that increasing the interlayer thickness led to the extension of diffusion zone and the increase of final joint width. The maximum shear strength of 284 MPa was obtained for the bond made with 50 μm thick interlayer while with an increase in interlayer thickness, the shear strength values decreased to 145 MPa that could be attributed to formation of brittle intermetallics such as Cu₂Ti and CuTi at the interface [13].

In this study, GR2 and GR5 Titanium alloys were joined by diffusion welding method using copper interlayer. The effect of copper interlayer investigated on Titanium alloys.

II. EXPERIMENTAL STUDY

GR2 and GR5 Ti alloys having dimensions of Ø12 x 12 mm were used in this study. Table I and Table II show the chemical compositions of these alloys.

Table I. Chemical composition of GR 2 alloy

Ti %	Fe %	O %	N %	C %	H %
99,3 - 99,6	0,2 - 0,3	0,12 - 0,25	0,03	0,08	0,013

Table II. Chemical composition of GR 5 alloy

Ti %	Al %	V %	H %	Fe %
88, 74 - 91	5,5 - 6,75	3,5 - 4,5	0,015	0,25

Welding samples prepared in Ø12x12 mm were polished with 1000 mesh sandpaper before diffusion welding and ultrasonically cleaned in acetone. The samples were then made ready for diffusion welding as shown in Fig. 1 Diffusion welding processes were carried out by sending argon gas with purity of 99.9% at the flow rate of 5 lt / min into the furnace with silicon carbide rod. Experiments were performed at the diffusion weld apparatus shown in Fig. 2 The experimental

samples were welded by using the Cu interlayer at 950 and 980 °C for 55 minutes by applying 5 MP pressure. Table III shows the parameters used in the welding process.

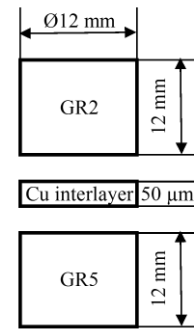


Fig. 1 Schematic illustration of the sample prepared for the diffusion welding

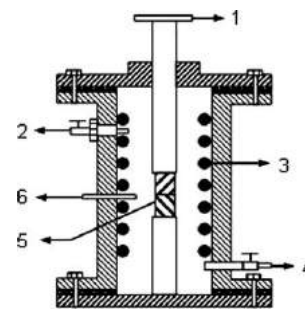


Fig. 2 Schematic illustration of diffusion bonding apparatus [18],

1-Load, 2-Argon Outlet, 3-Heat Coil, 4-Argon Inlet, 5-Specimens, 6-Thermocouple

The samples were kept in the furnace until the furnace's temperature decreased to 250 °C and they were kept to cool down at the room temperature.

Table III. The parameters used in diffusion welding process

Sample	S1	S2
Bonding Pressure (MPa)	5	5
Bonding Temperature (°C)	950	980
Holding Time (min.)	55	55

After the diffusion welding process, the welded samples were cut perpendicular to the surface of the intermediate layer and the surface to be measured was sandpapered under water with 100-150-600-800-1000-1200 grit SiC abrasive. The surfaces of

the polished samples were washed with alcohol and then dried. The samples made ready for microscopic examination were microscopically examined after being etched with Kroll's reagent. EDS and X-ray analyses were performed on sample S2. Microhardness measurements of the samples were then carried out at 50 μm intervals under a load of 50 g with the help of a Leica MHF-10 device (0.05 HV) in order to observe the changes in hardness at the welding interface. Fig. 3 shows the points of microhardness measurements.

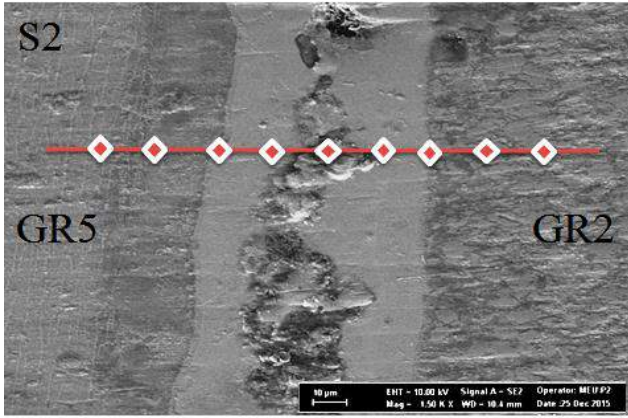


Fig. 3 Microhardness measurement points

In order to determine the joint strength of the samples after the welding, lap-shear tests were carried out in accordance with ASTM D-3165-07 standards in the specially prepared lap-shear apparatus shown in Fig. 4. Shear stresses of the welded joints whose lap-shear tests were performed at room temperature in 2mm/min velocity were calculated according to the obtained data.

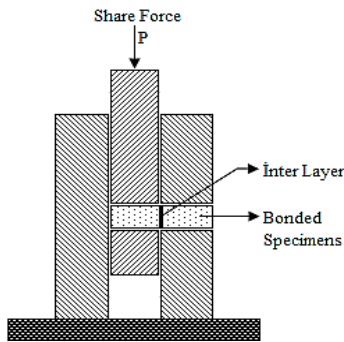


Fig. 4 Schematic illustration of shear strength testing apparatus [19].

I. RESULTS AND DISCUSSION

A. Microstructure results

GR2 and GR5 Titanium alloys were successfully joined via diffusion welding method by using the copper interlayer. Fig. 5 shows microstructure images of samples S1 and S2. When these images were examined, Cu interlayer, diffusion zone and

GR2 and GR5 materials can be clearly observed. A less thinning was observed due to diffusion deficiency in the 50 μm thick interlayer of sample S1, where welding pressure of 5 MPa, welding temperature of 950°C, and welding time of 55 min were used, compared to sample S2. In sample S2 made at 980°C welding temperature, the interlayer was seen to get thinner more compared to sample S1 depending on the increased diffusion. This indicated that copper diffusion to the base material was more at 980°C, and formed a transition zone near the junction points.

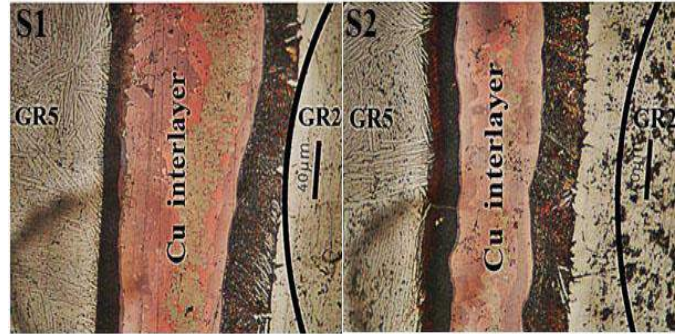


Fig. 5 Microstructure photographs of samples S1 and S2

In order to observe the element concentration in the welding interface, EDS analysis was performed on the sample S2. While Fig. 6 shows the points of the EDS analysis, Fig. 7 shows the element contents at these points. As a result of the performed analysis, Al, Ti, V, Fe and Cu elements were determined to diffuse mutually. It was observed that the elements which were mutually best diffused were Ti and Cu.

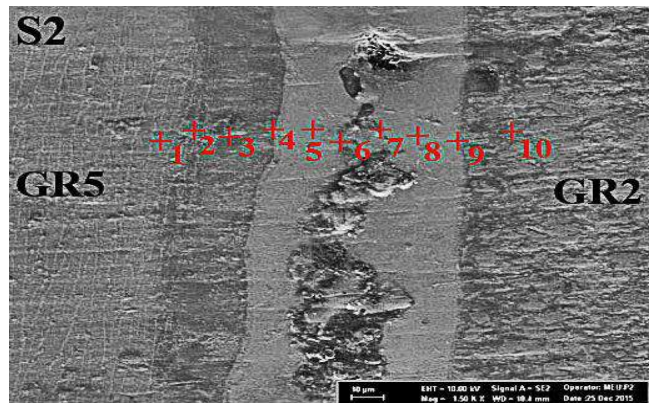


Fig. 6 Points of the EDS analysis

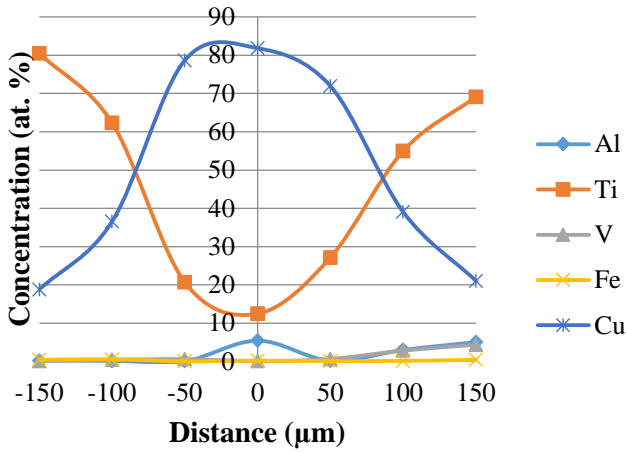


Fig. 7 Element distribution of EDS analysis

XRD analysis was performed on the sample S2 to determine the phases that may occur in the welding interface. Table IV shows the results of the XRD analysis. When the table was examined, it was observed that Ti element formed various compounds with Cu element.

Table IV. Element contents and phases of S2 sample

No	Element	Al	Ti	V	Fe	Cu	Total	Possible Phase
1		0,21	80,48	0,12	0,40	18,79	100,00	Ti ₁₆ Cu ₃
2		0,13	62,33	0,44	0,56	36,54	100,00	Ti ₄₃ Cu ₁₉ Ti ₅₂ Cu ₂₃
3		0,07	20,68	0,57	0,00	78,68	100,00	Cu ₅₅ Ti ₁₉
4		5,42	12,45	0,09	0,20	81,84	100,00	Cu ₁₀ Ti ₃
5		0,18	27,15	0,64	0,07	71,97	100,00	Cu ₂ Ti Cu ₄ Ti ₂ Cu ₆ Ti ₃
6		2,99	54,99	2,82	0,14	39,07	100,00	Ti ₁₁₃₄₈ Cu ₆₀₇₅ Al ₁₀₉₅ V ₅₄₇ Fe ₂₃
7		5,03	69,16	4,34	0,42	21,05	100,00	Ti ₃₁ Cu ₇ Al ₄ V ₂

B. Microhardness results

Fig. 8 shows the microhardness results of samples S1 and S2. When this graph was examined, it was observed that the hardness increased when getting close to the interlayer zone from base material in both samples and the hardness reached to the values close to the base material when moving away from the weld zone. When the microhardness results of samples S1 and S2 were compared, the hardness value increased when the temperature at sample S2 increased and maximum hardness values was measured as 512.16 HV. It was thought that this increase was associated with the intermetallic phases formed by the Cu and Ti elements at the interface depending on the diffusion.

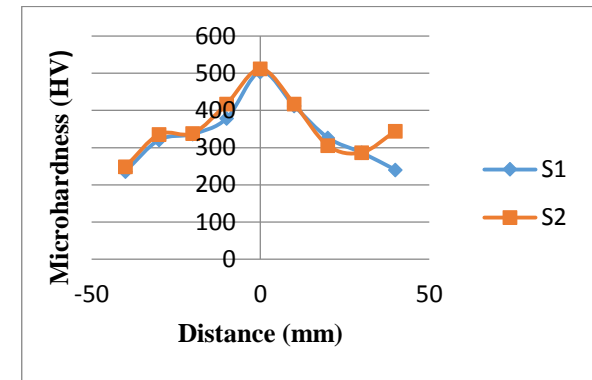


Fig. 8 Microhardness results of samples S1 and S2.

C. Lap-shear test results

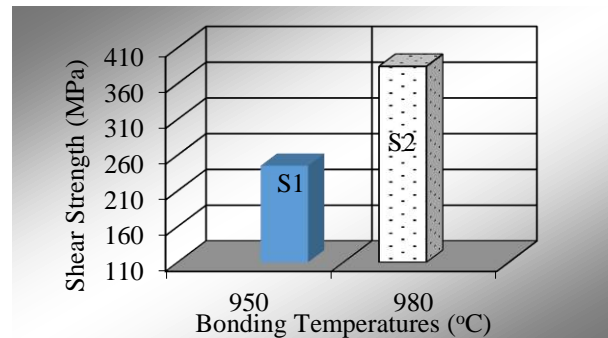


Fig. 9 The lap-shear strength of the S1 and S2 sample

Fig. 9 shows results of the lap-shear test made in samples S1 and S2. When these results were examined, it was found that while the lowest lap-shear strength was measured as 245 MPa at sample S1, the highest lap-shear strength was measured as 384 MPa at sample S2. Copper interlayer was observed to form a stronger bond depending on the increased temperature. This is an expected result of the high lap-shear strength values due to the effect of the compounds occurring in the structure in the joints made at high temperatures.

II. CONCLUSIONS

A successful joint was achieved under 5 MPa uniaxial pressure in argon gas atmosphere at 950-980°C temperature interval by using 50 µm thick copper interlayer and applying solid state diffusion process to GR2 and GR5 titanium materials.

The EDS analyses show that Cu interlayer was a little more diffusive to GR5 material than GR2 material.

When higher test temperatures and pressures were applied, a wavy deformation pattern occurred at both interfaces which affected the bonding strength of the interface.

As a result of XRD analysis, it was observed that Ti₁₆Cu₃, Ti₄₃Cu₁₉, Ti₅₂Cu₂₃, Cu₅₅Ti₁₉, Cu₁₀Ti₃, Cu₂Ti, Cu₄Ti₂, Cu₆Ti₃, Ti₁₁₃₄₈Cu₆₀₇₅Al₁₀₉₅V₅₄₇Fe₂₃, and Ti₃₁Cu₇Al₄V₂ phases formed in the zone affected from the diffusion and in the interlayer with increasing joining temperature.

These phases formed different mixtures in diffusion interfaces. The scope of these phase mixtures caused mutual diffusion coefficient in Cu to be strengthened due to the lower operating temperatures and the increase in the joining temperature and increased interdiffusion coefficient.

Microhardness peaks of the joined samples occurred in the intermediate region, the highest hardness was measured as 512.16 HV, and the hardness values on both side decreased gradually as moving away from the interface. This is because the Cu interlayer effect decreased as we move away from the interface.

Both the hardness values and the lap-shear strength depend on the intermetallic compounds formed at the interface. In the microscopic and EDS analysis of the cross-sections, diffusion of copper in the reaction zone led to an increase in mechanical resistance. The highest shear strength was measured as 384 MPa in the sample S2 joined at 980°C. It was assumed that the shear strength increased with increasing process temperature was associated with flowability of the copper and yield strength of the base material

REFERENCES

- [1] T. Vigraman, D. Ravindran, and R. Narayanasamy, "Effect of phase transformation and intermetallic compounds on the microstructure and tensile strength properties of diffusion-bonded joints between Ti-6Al-4V and AISI 304L," *Materials and Design*, vol. 36, pp. 714–727, 2012.
- [2] M. Balasubramanian, V. Jayabalan, and V. Balasubramanian, "Developing mathematical models to predict tensile properties of pulsed current gas tungsten arc welded Ti-6Al-4V alloy," *Materials and Design*, vol. 29, no. 1, pp. 92–97, 2008.
- [3] N. Kahraman, B. Gulenc, and F. Findik, "Corrosion and mechanical-microstructural aspects of dissimilar joints of Ti-6Al-4V and Al plates," *International Journal of Impact Engineering*, vol. 34, no. 8, pp. 1423–1432, 2007.
- [4] Z. Sun, I. Annergren, D. Pan, and T. . Mai, "Effect of laser surface remelting on the corrosion behavior of commercially pure titanium sheet," *Materials Science and Engineering: A*, vol. 345, no. 1, pp. 293–300, 2003.
- [5] A. M. Kliauga, D. Travessa, and M. Ferrante, "Al₂O₃/Ti interlayer/AISI 304 diffusion bonded joint: Microstructural characterization of the two interfaces," *Materials Characterization*, vol. 46, no. 1, pp. 65–74, 2001.
- [6] M. Ghosh and S. Chatterjee, "Effect of interface microstructure on the bond strength of the diffusion welded joints between titanium and stainless steel," *Materials Characterization*, vol. 54, no. 4–5, pp. 327–337, 2005.
- [7] S. Kundu, M. Ghosh, A. Laik, K. Bhanumurthy, G. B. Kale, and S. Chatterjee, "Diffusion bonding of commercially pure titanium to 304 stainless steel using copper interlayer," *Materials Science and Engineering A*, vol. 407, no. 1–2, pp. 154–160, 2005.
- [8] S. Kundu and S. Chatterjee, "Interfacial microstructure and mechanical properties of diffusion-bonded titanium-stainless steel joints using a nickel interlayer," *Materials Science and Engineering A*, vol. 425, no. 1–2, pp. 107–113, 2006.
- [9] M. Balasubramanian, "Development of processing windows for diffusion bonding of Ti-6Al-4V titanium alloy and 304 stainless steel with silver as intermediate layer," *Transactions of Nonferrous Metals Society of China (English Edition)*, vol. 25, no. 9, pp. 2932–2938, 2015.
- [10] P. Li, J. Li, J. Xiong, F. Zhang, and S. H. Raza, "Diffusion bonding titanium to stainless steel using Nb/Cu/Ni multi-interlayer," *Materials Characterization*, vol. 68, pp. 82–87, 2012.
- [11] A. Elrefaey, L. Wojarski, and W. Tillmann, "Preliminary investigation on brazing performance of Ti/Ti and Ti/steel joints using copper film deposited by PVD technique," *Journal of Materials Engineering and Performance*, vol. 21, no. 5, pp. 696–700, 2012.
- [12] G. O. Cook and C. D. Sorensen, "Overview of transient liquid phase and partial transient liquid phase bonding," *Journal of Materials Science*, vol. 46, no. 16, pp. 5305–5323, 2011.
- [13] S. Zakipour, M. Samavatian, A. Halvae, A. Amadeh, and A. Khodabandeh, "The effect of interlayer thickness on liquid state diffusion bonding behavior of dissimilar stainless steel 316/Ti-6Al-4V system," *Materials Letters*, vol. 142, pp. 168–171, 2015.
- [14] M. Ghosh and S. Chatterjee, "Diffusion bonded transition joints of titanium to stainless steel with improved properties," *Materials Science and Engineering A*, vol. 358, no. 1–2, pp. 152–158, 2003.
- [15] A. Elrefaey and W. Tillmann, "Solid state diffusion bonding of titanium to steel using a copper base alloy as interlayer," *Journal of Materials Processing Technology*, vol. 209, no. 5, pp. 2746–2752, 2009.
- [16] H. Li, C. Zhang, H. Bin Liu, and M. Q. Li, "Bonding interface characteristic and shear strength of diffusion bonded Ti-17 titanium alloy," *Transactions of Nonferrous Metals Society of China (English Edition)*, vol. 25, no. 1, pp. 80–87, 2015.
- [17] H. Zhao, J. Cao, and J. C. Feng, "Microstructure and mechanical properties of Ti6Al4V/Cu-10Sn bronze diffusion-bonded joint," *Transactions of Nonferrous Metals Society of China (English Edition)*, vol. 19, no. SUPPL. 2, 2009.
- [18] Aydın, M., TR2002 02710 U Patented Diffusion Bonding Machine, Department of Machine Engineering, Faculty of Engineering, University of Dumlupinar, Kütahya, Turkey.
- [19] Taskin, M., Kejanli, H. and Caligulu, U., "The Effect on The Connecting Characteristic of Welding Temperatures on The Joining With The Diffusion Bonding Using Ni And Cu Interlayer of Ni-Ti-Cu Composites Manufactured By Powder Metallurgy Method", *e- Journal of New World Sciences Academy*, 3(4), 556-568, 2008.

An Integrated Process Design for Magnesium Alloy Part Manufacturing in Turkey

Ali Serdar Vanli, Anil Akdogan

Yildiz Technical University, Mechanical Engineering Department, Istanbul, Turkey
 svanli@yildiz.edu.tr, nomak@yildiz.edu.tr

Abstract— As the known lightest structural metal, Magnesium (Mg) has attracted interests for automotive, electronics and aircraft industries. There is a common usage at industrial applications of Mg alloys because of their distinguishing performance characteristics. However, there almost isn't an integrated mass production line at the industrial scale in Turkey which can supply high density and strong mechanical property Mg products due to the lack of experience and knowledge in this subject. Unfortunately, Turkey deliberately avoid to manufacture Mg alloy parts thus can only use them by importing. Honestly, there is an integrated mass production system including a dosing furnace, a molten metal transfer system, a gas mixing unit, a die heating-cooling device, and a cold chamber die casting machine for Mg alloys mass production in Yildiz Technical University, Mechanical Engineering Department, Die Casting Laboratory. Today, it is possible to get acceptable mechanical and metallurgical propertied, high density parts by considering the three basic production steps i.e. melting, dosing, and casting precisely.

Keywords— Magnesium alloys, die casting, mass production, process parameters, high mechanical properties.

I. INTRODUCTION

As the iron and steel industry supplies input to almost all manufacturing sectors, it plays an important role in the industrialization and development of Turkey [1]. Besides them, our country is still needs to develop using its own underground treasures about light metals. One of them is magnesium which is about two-thirds lighter than steel and one-third lighter than aluminium. This weight advantage makes Mg-alloy parts very attractive for many industries. These light products have good deformation properties, giving the products good impact, as well as fatigue resistance. The alloys also display fine machinability and good thermal and electrical conductivity. Die casting of Mg alloys has been the fastest grown up and the most globally developed section in the Mg industry (Fig. 1). Production of the Mg alloy parts with pressure die casting process has huge economic benefits which cannot be presented by any other product systems [2].

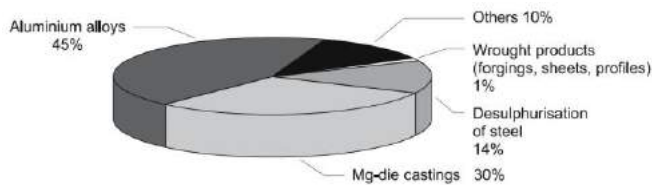


Fig. 1 Mg alloys usage areas [3].

Die casting of Mg alloys is an ideal process for high capacity production conditions because of its appropriateness for automation systems. Although high-pressure die casting is a very precision process; there are many effective factors on product quality and also mechanical properties. These factors consist of, but not limited, the casting part design and die construction besides the various process parameters. There are three basic production steps in die casting process need to be considered precisely and carefully to get high mechanical and metallurgical propertied, low porosity included parts. These steps are melting, dosing, and casting processes, respectively. Due to the lack of experience and knowledge in each step, especially in the melting process, unfortunately our casting industry deliberately avoids to manufacture Mg alloy parts, thus can only use them by importing [4]. However, fortunately there is an integrated mass production line including a dosing furnace, a molten metal transfer system, a gas mixing unit, a die heating-cooling device, and a cold chamber die casting machine for Mg alloy parts mass production in Yildiz Technical University, Mechanical Engineering Department, Die Casting Laboratory since 2013. This system serves primarily to the scientific works and education in the subject area in our country and abroad and to the industry, as well.

II. MG ALLOY PART MANUFACTURING STEPS

Although high pressure die casting (HPDC) is a very precision process; there are lots of factors which are negatively effective on the product quality and mechanical properties of the products [5]. There are four different kinds of commercial Mg-alloy series for HPDC process systems. These are Mg-Al-Zn (AZ) series, Mg-Al-Mn (AM) series, Mg-Al-Si (AS) series and newly developed Mg-Al-RE (AE) series [6]. General properties of the commercial die-cast Mg alloys are given in Table 1. Three basic production steps in the die casting method namely melting, dosing, and casting processes are needed a detail examination in magnesium alloy parts production [4].

At first, it is necessary to solve the critical problem which is magnesium's reaction affinity with the oxygen in the air during the melting process. Many methods have been investigated to reduce the oxidizing and burning of Mg melt in the air, such as flux covering, alloying by reducing elements, fluxless gas protection methods etc. Among these methods, protection by Sulphur hexafluoride (SF₆) gas mixture is currently considered as an effective solution to protect Mg alloy melts from oxidization during melting. It is essential to prevent the reaction of magnesium with the oxygen in the air. Currently, this is mainly accomplished with SF₆ gas. The Mg metal

production and casting industry have been using SF₆ as a cover gas to prevent the violent oxidation of molten Mg in the presence of air. It is a colorless, non-toxic, and non-flammable gas. However, alternative protective gas mixing solutions are now under investigation at all over the world since SF₆ is a potential greenhouse gas [7]. The industry adopted the use of SF₆ to replace Sulphur dioxide (SO₂), which is toxic and requires careful handling in order to supply worker's safety [8].

TABLE I
COMMERCIAL MG ALLOY PROPERTIES [6]

	Al	Mn	Zn	Other	Yield Strength	Tensile Strength	Elongation	Hardness
					(N/mm ²)	(N/mm ²)	(%)	HB
AE42	4.0	0.2	---	2.5 RE	145	230	11	60
AM20	2.1	0.4	---	---	90	210	20	45
AM50	4.9	0.4	---	---	110	200	10	58
AM60	6.0	0.4	---	---	130	220	8	62
AS21	2.2	0.2	---	1.0 Si	120	230	12	55
AS41	4.2	0.2	---	1.0 Si	140	210	6	60
AZ91	9.0	0.2	0.7	---	150	230	7	63

Nowadays, concerning the protection mechanism of HFC-134a gas for the Mg alloy melt, some researchers have reported that it provides excellent protection for molten Mg. It is considered against SF₆. The thermal stability of HFC-134a is inferior at high temperatures, so that it could give up fluorine easily to protect the melt compared with SF₆ [9-11]. The most effective recommended gas mix units in vol. % in literature are given in Table 2.

TABLE XII
RECOMMENDED GAS MIX FOR MG PROTECTION [12]

Melting Temperature (°C)	Recommended Gas Mix (vol. %)
650 - 700	N ₂ % 100+ 0.25%SF ₆
650 - 700	75% air + 25%CO ₂ + 0.25%SF ₆
700 - 750	50% air + 50%CO ₂ + 0.30%SF ₆
650 - 700	N ₂ % 100+ 0.30%HFC-134a
650 - 700	N ₂ % 100+ 1%SO ₂
700 - 750	N ₂ % 100+ 2%SO ₂

Secondly, there are some new alternative ways at the dosing step. Considering today's developed production technologies, gas pressured metal dosing systems and some hi-tech methods like Vacural process are not preferred commonly due to their high costs. In addition, manual transfer systems appear to be one of the insufficient solutions as they are useless for automation. On the other hand, melting pump dosing system

with its integrated transfer tube is an economical and useful solution with its low cost for automation in the mass production environment [13,14].

Finally, the die casting process has been favored for its unique ability to transform the molten Mg into an accurately dimensioned form in the shortest possible time in Mg part production industry. But the wrong selection of the process parameters for the casting operation can cause defective and low mechanical propertied casting products even they have perfect design features. Therefore, die casting parameters can be identified as the most important factors that are effective on the product quality. For the better mechanical properties, low porosity content and perfect features; the optimum process parameters should be determined for each alloy. The process parameters are casting and die temperatures, filling time of the die, plunger and gate velocities, injection and intensification pressures with protective gas mixing rate [12].

III. HIGH PRESSURE DIE CASTING

A typical die casting cycle for cold chamber process is given in Figure 2. Normally this process is an efficient and economical solution for part manufacturing. Initially, liquid metal is metered into a shot sleeve (a), which is then immediately pushed (b) through a runner system by a plunger (c) into a die cavity (d) under high pressure according to the machine capability and the requirements. High pressure is applied on the alloy during solidification. After the solidification process, the die opens (e) and the casting part is ejected by the ejectors (f). Conventional die casting is utilized to produce many products in the current global market [15].

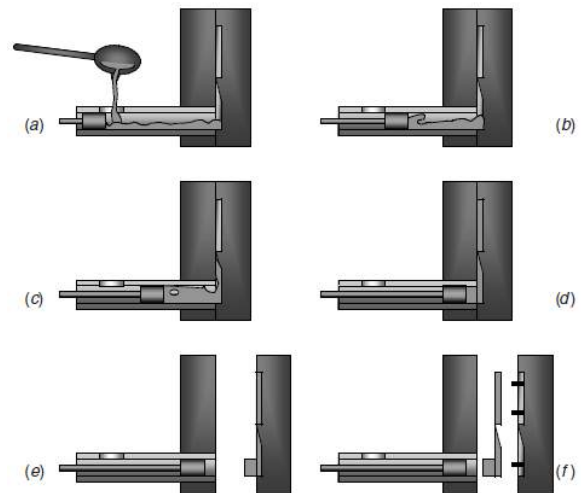


Fig. 2 Casting cycle for cold chamber die casting [15].

Unfortunately, conventional die casting has a major limitation that is preventing its use on a broader scale. High-pressure die-casting process often leads to formation of significant amount of defect formation in the Mg-alloy castings. A common and well known defect in the conventional

die casting process is porosity. Micro-porosity, macro-segregation and other casting defects adversely affect the fracture of the cast Mg-alloys related with mechanical properties. Therefore, a systematic study of the correlations between important process parameters of the high-pressure die-casting and the defect generation in the Mg alloys involve considerable practical interest [15,16].

The molten metal temperature, filling ratio of the shot sleeve, filling time of the cavity, piston velocity in the first and the second phases, gate velocity at the second phase, intensification pressure of the third phase, runner cross-sections, die temperature, venting area, casting geometry, protective gas concentration, and die and plunger lubrication conditions are some of the most important parameters that affect the porosity, segregation and mechanical properties in HPDC of the Mg alloy casting parts [5,12].

IV. AN INTEGRATED PROCESS DESIGN

An integrated mass production line for Mg alloy part manufacturing was established at Yildiz Technical University, Mechanical Engineering Department, Die Casting Laboratory, in 2013. This system includes a dosing furnace, a molten metal transfer system, a gas mixing unit, a die heating-cooling device, and a cold chamber die casting machine. The detailed layout plan of the integrated serial production line, which is formed by assembling all the components and has the capability of being the first mass production line established in this capacity and competence in our country, is given in Figure 3. This system serves primarily to the scientific works in our country (one doctorate, two masters and many under graduation thesis up to now) in the subject area and to the industry, as well.

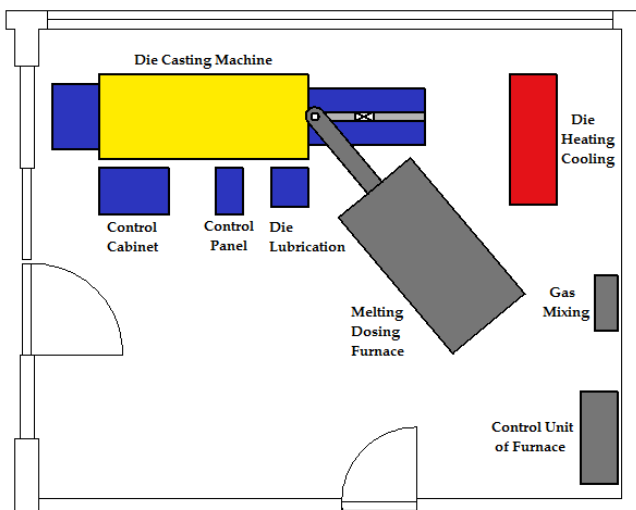


Fig. 3 Detailed layout plan of the integrated serial production line

The selected Metal Pres, MP100 type, Turkey, cold chamber HPDC machine size (1000 kN locking force) is basically determined by the shot volume and the projection area of the casting product including the designed gating system

(Fig. 4) considering the maximum pressure during the intensification phase [12]. The casting part manufactured as a tensile test sample according to ASTM B557M-10, and the mold material is selected as the X40CrMoV5-1 hot work tool steel and hardened between 46-48 HRC.

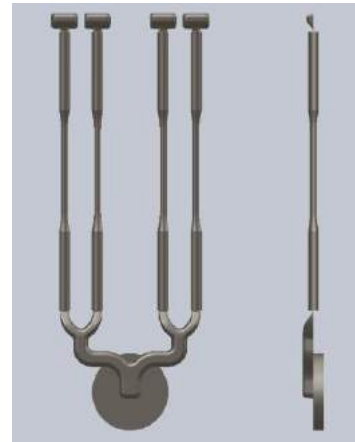


Fig. 4 Die-cast product with gating system [12]

Since melting pump dosing system with its integrated transfer tube is an economical and useful solution with low costs for automation in the mass production environment, the Authors used it at die casting laboratory as illustrated in Figure 5. Resistance furnace is one of the most preferable furnace types due to its low setting up and operating costs in industrial scale, Meltec GmbH, MDF-200C, Austria, magnesium dosing furnace is used. The maximum melting temperature ability is 700 °C. Protective gas mixing is preferred as N₂-SF₆ mix in the system while the N₂ is need to be %99.9 purity for proper operations.

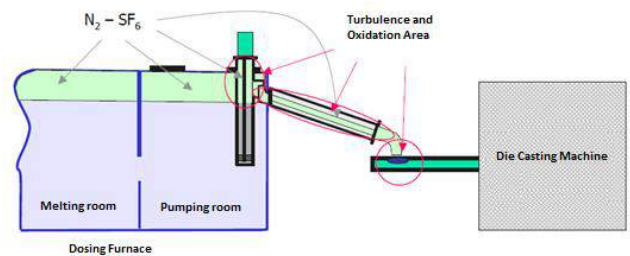


Fig. 5 Melting pump dosing system [17]

Quality factors for the parts consists of, but not limited, high mechanical properties, low porosity content, accurately dimensioned form and perfect surface features. The most effective factors on part quality are the various process parameters with the die design and the part construction. Since, the process parameters are one of the most important factors; the Authors have been conducted works on determining the optimum process parameters. These parameters are casting and die temperatures, filling time of the cavity, plunger and gate velocities, injection and intensification pressures with protective gas mixing rate. The most effectives of them were gathered and analyzed in a detailed manner of the part quality

and casting defects for AZ91 Mg alloy. Chemical composition of the used AZ91 Mg alloy is given in Table 3.

TABLE XIII
CHEMICAL COMPOSITION OF AZ91 MG ALLOY

Element	Mg	Al	Zn	Mn	Fe	Cu	Ni	Cr	Ti	V	W	Si
%	89.830	9.077	0.682	0.180	0.026	0.002	0.004	0.009	0.033	0.018	0.009	0.014
±	0.303	0.297	0.013	0.014	0.006	0.001	0.002	0.003	0.008	0.005	0.003	0.009

V. RESULTS

The findings that are obtained from the results of the all studies made by the Authors are as follows;

Injection and intensification pressures values should be raised as much as possible. Raising the pressure decreases the amount of porosity in the part and increases the density. Mechanical properties of low porosity and high density parts are better. The specific pressure range applied to the cold chamber casting of magnesium alloys is 50-120 MPa. The maximum value for the intensification pressure must not exceed 150 MPa.

The casting temperature should be kept as low as possible. As the temperature of the liquid metal increases, the rate of gas solubility in the metal increases. These gases (especially hydrogen gas), which dissolve in the metal during melting, can't go out of the part parallel to the rate of dissolution in the solidification process, which leads to the formation of gas porosity. Accepted casting range is 30-90 °C above the liquidus curve. If the part is not too complicated, the casting temperature can be chosen at 30-40 °C above the melting point. The mold temperatures affect the formation of solidification. Low mold temperatures are responsible for the creation of different solidification layers, increasing the amount of shrinkage and hot tears. For mold temperatures, 250±15 °C is regarded as the optimum temperature range.

The gate velocity should be chosen at the lowest values to fill the mold before solidification. A range of 30-50 m/s is recommended for gate velocity. In very thin sections, the velocity values can rarely reach up to 100 m/s. If the thickness exceeds 5 mm, it can be reduced below 30 m/s. The reduction of the velocity below 30 m/s leads to an increase in the amount of porosity resulting from shrinkage; velocity values above 50 m/s cause an increase in the gas porosity due to the entrapped gases in the mold cavity. In addition, the wear of the mold increases at high speeds, and due to the turbulent flow, wave and swirl traces are formed on the part surface.

VI. CONCLUSIONS

Production of the Mg alloy parts with HPDC process has a huge economic benefit which can't be presented by any other

production system. Although HPDC is a very precision process; there are lots of factors which are negatively effective on the quality and mechanical properties of the products.

The mentioned process parameters have vital effects on strength properties and defect formation, as well. The right choice of process parameters means the correct production of the part. Therefore, it is important to pay attention to the important points in the selection of the process parameters in order to make defect-free casting parts in a cold chamber high pressure die casting production line.

ACKNOWLEDGEMENT

This research has been supported by Science, Industry and Technology Ministry of Republic of Turkey project numbered 00961.STZ.2011-2 and by Yıldız Technical University, Coordination of Scientific Research Projects numbered 2015-06-01-GEP02.

REFERENCES

- [1] Economy Ministry of Republic of Turkey, *Iron and Steel Industry in Turkey*, Ankara, 2014.
- [2] H. Sönmez, A. Akdoğan ve A.S. Vanlı, "Magnezyum Alaşımları Yüksek Kalitede Basınçlı Dökülüyor", *Metalik Dergisi*, Sayı 21: pp. 28-31, Ağustos 2013.
- [3] H.E. Friedrich and B.L. Mordike, *Magnesium Technology: Metallurgy, Design Data, Applications*, 1st ed., Berlin, Germany: Springer-Verlag, 2006.
- [4] A.S. Vanlı, A. Akdoğan ve H. Sönmez, "Magnezyum Alaşımı Parça İmalatı İçin Soğuk Kamaralı Basınçlı Döküm Makinası ve İmalat Prosesinin Tasarımı", *Bildiriler Kitabı MATIT'13*, 2013, MMO Yayın No: E/2013/6078: 372-378.
- [5] A.S. Vanlı, A. Akdoğan and H. Sonmez, "Investigation the Effects of Process Parameters on Product Quality in Cold Chamber High Pressure Die Casting of Magnesium Alloys", in *Proc. IJAS'10*, 2010, vol. 3(9), pp. 320-325.
- [6] ASM Specialty Handbook, *Magnesium and Magnesium Alloys*, 2nd ed., ASM International Handbook Committee, Ohio, USA, 1999.
- [7] A.S. Vanlı, "Investigation of the Protective Atmospheres Used for Melting Process of High Pressure Die Casting Magnesium Alloys", *Academic Journal of Science*, vol. 1(3), pp. 109-120, 2012.
- [8] M.J.F. Gandara, Recent Growing Demand for Magnesium in the automotive Industry, *Materials and Technology*, vol. 45(6), pp. 633-637, 2011.
- [9] J.R. Liu, H.K. Chen, L. Zhao, and W.D. Huang, "Oxidation Behavior of Molten Magnesium and AZ91D Magnesium alloy in 1,1,1,2-tetrafluoroethane/air Atmospheres", *Corrosion Science*, vol. 51(1), pp. 129-134, 2009.
- [10] H. Chen, J. Liu, and W. Huang, "The Protective Surface Film Formed on Molten ZK60 Magnesium Alloy in 1,1,1,2-tetrafluoroethane/air Atmospheres", *Corrosion Science*, vol. 52(11), pp. 3639-3645, 2010.
- [11] W. Ha and Y.J. Kim, "Effects of Cover Gases on Melt Protection of Mg Alloys", *Journal of Alloys and Compounds*, vol. 422, pp. 208-213, 2006.
- [12] A.S. Vanlı, "Optimization of the Process Parameters Effective on the Product Quality in Die Casting of Magnesium Alloys", PhD. Thesis, Yıldız Technical University, Graduate School of Applied and Natural Sciences, Department of Mechanical Engineering, Turkey, Istanbul, Nov. 2013.
- [13] A.S. Vanlı, "Investigation of Different Mass Production Lines Used for High Pressure Die Casting of Magnesium Alloy Products" in *Proc. IJAS'11*, 2011, vol. 4(19), pp.269-275.
- [14] B. Andresen, *Die Casting Engineering: A Hydraulic, Thermal, and Mechanical Process*, 1st ed., New York: USA, Marcel Dekker, 2005.
- [15] E.J. Vinarcik, *High Integrity Die Casting Processes*, 1st ed., New Jersey: USA, John Wiley & Sons Inc., 2003.

- [16] H. Kaufmann and P.J. Uggowitzer, *Metallurgy and Processing of High-Integrity Light Metal Pressure Castings*, 1st ed., Berlin, Germany, Fachverlag Scihele & Schön GmbH, 2007.
- [17] M. Demirci, A.S. Vanlı, A. Akdoğan ve H. Sönmez, "Magnezyum Alaşımlarının Ergitme Prosesinde Koruyucu Gaz Atmosferlerinin Kullanımı", *MakinaTek Dergisi*, Sayı 200, pp. 280-286, Haziran 2014.

Electricity Generation With Organic Rankine Cycle From Waste Gases

EmreCAN ERCAN, Cabir KÜÇÜK, Durmuş KAYA

Department of Energy Systems Engineering, Kocaeli University Umuttepe Campus 41380, Kocaeli/TURKEY

emreercan36@gmail.com , cabirkucuk61@gmail.com , durmuskaya@hotmail.com

Abstract—Organic rankine cycle (ORC), special fluids are used which can evaporate at relatively low temperature instead of water as the vehicle fluid. In this way it is possible to produce electricity from waste heat sources at low temperatures.

In this study, it was investigated that the required thermal energy for the ORC was achieved by burning gases in a combustion chamber (Flare) in a low-emission hot water boiler. The electricity generated at the end of the cycle is theoretically calculated. The main components of the system are the boiler, turbine, and cooling unit has been examined. Cost, feasibility and emission analyzes of the system are made; according to TURKEY and USA conditions, the repayment period and internal rate of return are calculated. As a result of the application, it is seen that electricity production can be done at 76,5 kWe power from 118 Nm³/h waste gas.

Author keywords: Electric production, organic rankine cycle, flare gas, energy efficiency, emission reduction

1. INTRODUCTION

Flare chimney systems in industrial industries are a place where waste gases are removed and the pressure is reduced. So it is one of the places where significant losses occur. Two of the major problems caused by exhaust gases from the blades are environmental and economic problems.

Waste gases are released to the atmosphere from many places such as factories, vehicles, garbage storage areas. The air is largely composed of oxygen and nitrogen gases. Waste gases released into the air, clinging to oxygen makes it dysfunctional. Causes air pollution. The deterioration of the oxygen / nitrogen ratio in the air over time results in the perforation of the ozone layer.

Depletion of the ozone layer can be considered a disaster for the world. The direct sunlight reaching the Earth is one of the main problems and brings with it many problems. Ecosystems are totally destroyed, cancerous cells are exploding rapidly, and perhaps it is impossible to live like the planets on the world. The release of waste gases into the atmosphere may be the end of the world.

According to the report of the International Energy Agency, it is stated that CO₂ emissions from energy production will increase by 49% in 2030 compared to 2005 and that many countries will face high energy prices in medium and long term. It can save fuel while increasing the efficiency in terms of business enterprises in the industrial sector, efficient use of resources and can make an important contribution to the reduction of environmental pollution[1].

2. WHAT IS THE FLARE ?

Industry Chimney systems used in the industry are a place where waste gases are removed and the pressure is reduced. So it is one of the places where significant losses occur. At flare is reducing the harmful effects of waste gases produced in industrial processes. Thus, the atmosphere directly prevents the escape of waste gases. Since industrial gases cause bad effects on the acid rain, industrial gases are burned to reduce this effect. For this reason, every kind of industry (steel, petroleum production facilities, etc.) industry uses these types of flare chimneys.

2.1. Characteristics Of Flare Gases

The content of the burned wastes gases in the flue are given in Table-1 and Table-2

Table-1 Chemical content and quantity of wastes gases [2]

FLARE FUEL GAS		
Gas Type	%	(m ³ /h)
Carbon Dioxide	0,8568	1,01
Ethane	19	22,42
Hexanes Plus	1,1164	1,32
Izobutan	1,0991	1,3
Izopentane	0,5983	0,7
Metan	61,7027	72,8
n-Butane	3,1861	3,74
Nitrogen	2,0724	2,45
n-Pentane	0,885	1,05
Propan	9,5551	11,22
Total	100	118

Table-2 Flare gas heat and flow rate [2]

FLARE FUEL GAS	
HHV (kcal/Nm ³)	15580
LHV (kcal/Nm ³)	14500
Flow (m ³ /h)	118
Flow (m ³ /day)	2832

3. ORGANIC RANKINE CYCLE (ORC)

Organic Rankine Cycle (ORC) is a widely used energy production system with a high ability to generate electricity. The working principle is to convert the thermal energy of the turbo-generator to mechanical energy first, then to an electric generator by means of an electric generator. Compared with the conventional steam turbine; The ORC system evaporates an organic liquid that is higher than the molecular weight of water vapor and thus leads to slower speed of rotation and less pressures on metal parts. After warming up with hot welds (thermal oil, hot water, hot steam, etc.) and evaporating the organic liquid with a suitable exchanger system, by the ORC system mechanically transforms by expanding it in the turbine. It turns it into electric energy with the help of generator. Then, in the closed circuit, the steam is cooled by a liquid or gas, condensed and pumped back to the regenerator to close the circuit and start the cycle again. Figure 1 shows the operation diagram of the system [3].

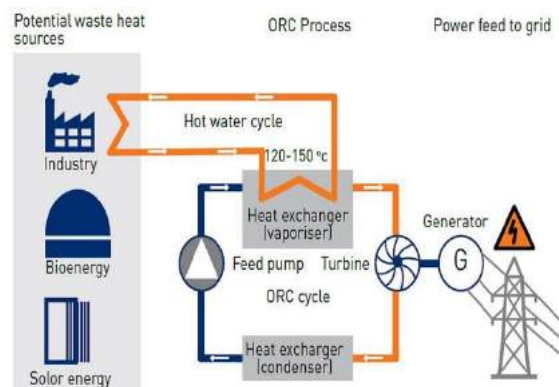


Fig.-1 General Operation Scheme of ORC System

3.1. Main Application Technologies

ORC technology is used in many application areas. The main areas of application are explained below[4].

Geothermal: Generally used in the field of hybrid flash & binary solutions using water-based sources.

Biomass: Biomass is used in the field of electricity generation and cogeneration.

Industrial Processes: Used in the field of waste heat recovery in energy-consuming processes (eg cement, glass, steel production) and the oil & gas sector.

Piston Engine and Gas Turbines: It is used in combination with piston engine and gas turbine which increase efficiency and reduce fuel consumption.

Energy From Waste: Used in the field of heat recovery from waste to power plants.

Solar Energy: Used in the field of electricity generation for solar energy applications connected to medium-high degree solar collectors.

4. WORKING PRINCIPLES AND PURPOSES OF THE SYSTEM

The application uses flue gas to burn the low-emission hot water boiler and then provides the ORC with the thermal units required to generate power. The objectives of this project are to reduce waste gases, generate power for on-site processes, increase efficiency, increase energy efficiency, reduce the environmental impact of the flames and create a more favorable public perception of the flue gas and waste processing plants in the industrial industry. The overall objective is to describe and demonstrate a gas-using technology for the beneficial use of flue gases (electricity generation). Electricity will reduce the operating costs by converting the waste gases into electricity with low emission, and minimize the environmental impact will be. The operating principle of the system is shown below. (Figure-2)

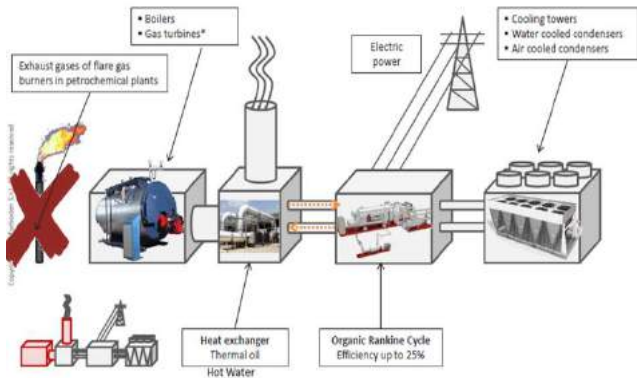


Fig.-2 System Operation Diagram[5]

5. MAIN EQUIPMENT OF THE SYSTEM

The system in general consists of three main equipment and the other specified equipment.

5.1. ORC Turbine

The ORC type used in the system is an imported product (origin: USA) manufactured by ELECTRATHERM Company. (Figure-3) Up to 110 kWe of power produces electricity. R245fa is used as working fluid. The study data belonging to the ORC turbine are given in Table-3 and the performance graph is given in Figure-4.



Fig.-3 Electratherm Series 6500 ORC Turbine [6]

6500-FL Specifications

- Dimensions: 12 x 2.4 x 2.9 m
- Weight: 14,515 kg / 32,000 lbs
- Turnkey inc. liquid loop radiator, all piping/pumps, no concrete foundation required, minimal engineering
- Manufacturer's Suggested Retail Price: \$409,159

Table-3 ORC Turbine Working Data [6]

Hot Water Input Parameters	Hot water input temp range	°F	170 - 252
		[°C]	[77 - 122]
	Thermal input range	MMBTU/hr	1.2 - 5.4
		[kWth]	[330 - 1600]
Flow rate range		gpm	100 - 350
		[l/s]	[6.4 - 22.1]
Water Cooled Condensing Parameters	Cooling water input temp range	°F	40 - 150
		[°C]	[4 - 65]
	Heat rejected to cooling water range	MMBTU/hr	1.1 - 5.1
		[kWth]	[320 - 1500]
Cooling water flow rate		gpm	325
		[l/s]	[<22.1]
Liquid Loop Radiator (LLR)*	LLR approach to ambient air temp	°F	25
		[°C]	[14]
*6500-FL Only	Heat rejected to LLR	MMBTU/hr	1.1 - 5.1
		[kWth]	[320 - 1500]

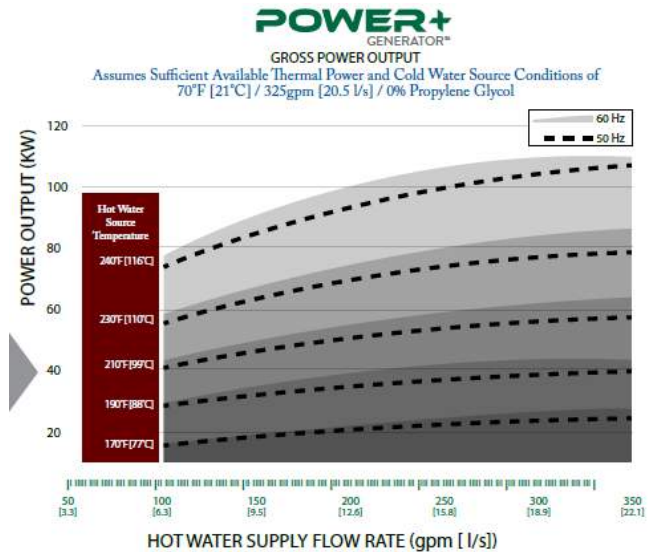


Fig.-4 ORC Turbine Performance Chart [6]

5.2. Hot Water Boiler

The boiler used in the system is an imported product (Origin: USA) which is manufactured by Cleaver Brooks Company[7]. (Figure-5)

Capacity: 2,000,000 kcal / hr

Boiler Type: Steam (15-250 psi) and Hot Water (30-125 psi)

Emission Value: <30 ppm NOx



Fig.-5 CBR 250 HP Hot Water Boiler

5.3 Cooling Tower

The cooling tower used in ORC turbines consists of two types of systems. These systems are air cooling and water cooling systems. The system used in this project is the water cooling system. A sample showing the system is given in figure-6. Cooling system characteristics are listed in Table-3[6].



Fig.-6 ORC Turbine Water Cooling Unit

5.4 Other Equipments

Some of the important equipment used in the system are listed below;

- Pipelines
- Vans
- Connection equipments (Electricity and Water)
- Pumps

6. MEASUREMENT AND CALCULATION METHODS

In this study, the emission values of the waste gas directly burned in the flue gas and the hot water boiler used in the operation of the system were calculated. The values of NO_x, CO, VOC gases forming the main emission are taken into consideration. In addition, the electric energy generated by the burned-out hot water and the ORC turbine is theoretically calculated.

6.1. Flare Emission Calculation Method

Emission factors from the US EPA emission factor certificate (AP-42) were used to determine NO_x, CO and VOC emissions. Values are given in Table-4.

Flare Emission Factors		
Toplam VOC (lb/MMBtu)	CO (lb/MMBtu)	NO _x (lb/MMBtu)
0,140	0,370	0,068

Table-4 Emission Factors for Flare Flue (AP-42)[8]

Flare gas emission values are calculated by the following formula.

$$\text{Fuel Gas HHV (1655.93 Btu/scf)} \times \text{Flowrate (_____scfh)} \times \text{MM/1,000,000} \times \text{Emission Factor (lb pollutant/MMBtu)} = \text{(.....lb/hr)} \quad (1)$$

*1 lb/hr = 0.4535 kg/hr *1 Btu/scf = 9,41 kcal/Nm³
 * 1SCFH = 0.02832 Nm³/Hr

6.2. Boiler Emission Calculation

Model specific emission factors for boiler emission calculations Power 250 Hp Calculated from Cleaver Brooks® boiler operator manual using the following formula. (Table 5)..

$$\text{Flowrate (_____scf/hr or scfh)} \times \text{MM/1,000,000} \times \text{Emission Factor (lb pollutant/MMscf)} = \text{lb pollutant/hr} \quad (2)$$

EMISSION FACTORS		
	AP-42 Table 1-4.2	Cleaver Brooks
	lb/MMscf	lb/MMscf ¹
CO	84.00	58.17
NO _x	50.00	50.89
VOC	5.50	14.54

¹Conversion to lb/MMscf based on fuel gas HHV of 1655.93 Btu/scf

Table-5 Emission Factors for Boiler [9]

6.3. Theoretical Power Calculations

Thermal Power (Nominal Thermal Power): It is the actual power value that is obtained by multiplying the amount of fuel burned at the unit time with the fuel lower heat value at a combustion plant. KW, MW units. It is calculated by the following formula;

Thermal Power: At unit time fuel consumption ($Nm^3/saat$) \times Alt isıl değeri ($kcal/Nm^3$) \times 4,18 $kJ/kcal \times h/3600s = \dots kw$ (3)
 *4,18 kJ: 1 kcal *1 hour (h): 3600 s

After calculating the thermal power, the gross electric power generated by the ORC turbine is calculated by the following formula.

The gross electric power (kW): Thermal Power (kW) \times Boiler Efficiency (%) \times ORC Electrical Efficiency (%) (4)

7. EMISSION AND THEORETICAL POWER VALUES

7.1. Flare Emission Values

The daily total emission values were calculated using equation number (1) (Table 6).

Flare Emissions		
Waste Gas	lb/hr	kg/hr
CO	61,269	27,57105
NOx	11,26	5,067
VOC	23,18	10,431

Table-6 Flare Emission Values

7.2. Boiler Emission Values

The daily total emission values were calculated using equation number (2) (Table 7).

Boiler Emissions		
Waste Gas	CBR 250HP Boiler	
	lb/hr	kg/hr
CO	5,817	2,61765
NOx	5,089	2,29005
VOC	1,454	0,6543

Table-7 Boiler Emission Values

7.3. Comparison of Emission Values

The emission values at the end of the project and the percentage of the initial are given in Table 8 as a comparative example.

Emission Comparison Table			
Waste Gas	Flare	Boiler	of Flare (%)
CO	27,57105	2,61765	9,49
NOx	5,067	2,29005	45,19
VOC	10,431	0,6543	6,08

Table-8 Comparison of Emission Values

7.4. Theoretical Power Values

Theoretical power values obtained by ORC Turbine are calculated by using the equation (3) and (4) (Table-9).

Project Name		Energy Production From Flare Gases		
Capacity		105,8	kWe	
YERİMLİ	Gross Power	106	kWe/h	
	H. Exchanger Efficiency	95	%	
	Boiler Efficiency	80	%	
	ORC Efficiency	7	%	
Yakıt Gizi	Fuel Gaz	Flow (Nm^3/h)	Low Heating Value ($kcal/Nm^3$)	Therm. Pow. ($kWth$)
		118	14500	1990

Table-9 ORC Turbine Theoretical Power Values

ORC Input Values		
Hot Water Input Temp.	122	C
Hot Water Flow	22	l/s
Hot Water Thermal Power	1500	kWth
Cold Water Input Temp.	26	C
Cold Water Flow	20,5	l/s
Electric frequency	50	Hz

Table-10 ORC Turbine Input Values

ORC Average Estimated Outputs		
Gross Power Output	103	kWe
ORC Pump Power	-10	kWe
Net Power Output	93	kWe
Cooling System Power (Pump + Fan)	-16,5	kWe
Net Power Output From System	76,5	kWe
Thermal Power at Turbine Inlet	1289	kWth
Remaining Thermal Power	211	kWth
Thermal Power Rejected to Cooler	1175	kWth
Hot Water Exit Temperature	108	C
Cold Water Exit Temperature	40	C

Table-11 ORC Turbine Estimated Output Values

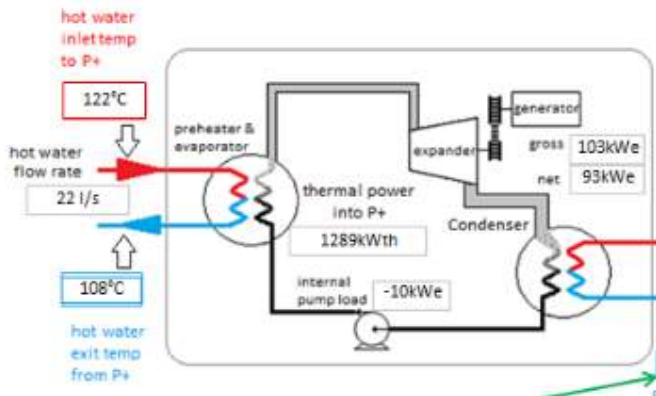


Fig.-7 ORC Turbine Power Rating Schematic Display

8. COST AND FEASIBILITY ANALYSIS

Calculations have been made for Turkey and USA conditions.

8.1. Project Analysis (TURKEY)

The project cost analysis and feasibility established under Turkish conditions are given in Table-12.

COST AND FEASIBILITY(TURKEY)	
6000 Series Power+Generator	\$410.000,00
Water Plumbing	\$10.000,00
Electrical Components and Hookup	\$10.000,00
Sitework and Footings For P+	\$5.000,00
Boller (Outside ET Scope Of Supply)	\$200.000,00
Commissioning and Startup Of P+	\$10.000,00
Shipping Power+Generator	\$8.000,00
Estimated Total Capital Expenditure (CapEx)	\$653.000,00
Total Value Of Power/kWh	\$0,08
Percentage Of Uptime Hours (100% max/8760 hrs)	(%) 97
Estimated Net Power Output in kWe	76,5
Average Total Net Power Output in kWe	76,5
Annual Value Of Power Produced By P+	\$52.000,00
AVG Annual P+ O&M Expense Based on \$ 0,013/kWh	\$8.319,00
Simple Paybeck in Years	14,94
Projected Lifetime	20
Estimated % Annual Increase in \$/kWh	(%) 0,00
Projected Lifetime Net Revenue	\$1.040.000,00
Total Cost/kWh Over Lifetime	\$0,063
IRR For Proceted Lifetime	(%) 5
Net Present Value Of Investment Over 20 Years	\$1.040.000,00

Table-12 Turkey Project Cost Analysis and Feasibility

8.2. Project Analysis (USA)

The project cost analysis and feasibility established under ABD conditions are given in Table-13.

COST AND FEASIBILITY(USA)	
6000 Series Power+Generator	\$410.000,00
Water Plumbing	\$10.000,00
Electrical Components and Hookup	\$10.000,00
Sitework and Footings For P+	\$5.000,00
Boller (Outside ET Scope Of Supply)	\$200.000,00
Commissioning and Startup Of P+	\$10.000,00
Shipping Power+Generator	\$8.000,00
Estimated Total Capital Expenditure (CapEx)	\$653.000,00
Total Value Of Power/kWh	\$0,21
Percentage Of Uptime Hours (100% max/8760 hrs)	(%) 97
Estimated Net Power Output in kWe	76,5
Average Total Net Power Output in kWe	76,5
Annual Value Of Power Produced By P+	\$136.508,00
AVG Annual P+ O&M Expense Based on \$ 0,013/kWh	\$8.319,00
Simple Paybeck in Years	4,99
Projected Lifetime	20
Estimated % Annual Increase in \$/kWh	(%) 0,00
Projected Lifetime Net Revenue	\$1.910.767,00
Total Cost/kWh Over Lifetime	\$0,063
IRR For Proceted Lifetime	(%) 19,18
Net Present Value Of Investment Over 20 Years	\$1.910.767,00

Tablo-13 ABD Project Cost Analysis and Feasibility

9. CONCLUSIONS AND RECOMMENDATIONS

As a result of this work, it was seen that there were solutions to environmental and economic problems which are the two main problems caused by the gases emitted from the flue gas. Flue gas emission calculations made before and after at the project are compared in Table-8. As a result of this comparison, it is seen that the decrease in emission values is considerably high. Also at the end of this project by contributing to with ORC turbine will be used in energy costs, the company produced 76.5 kW electrical power will be to achieve additional earnings. But in our country, the cost of installation is very high because we do not have or enough grants and domestic equipment manufacturing facilities given to such projects in our country. So the return period of the project corresponds to a very long time.

ABBREVIATIONS

- ORC: Organic Rankine Cycle
- HHV: High Heating Value
- LHV: Low Heating Value
- VOC: Volatile Organic Compound

REFERENCES

1. IEA, "Global Energy Trends", World Energy Outlook 2007 Edition, International Energy Agency, 73-75, 2007.
2. HESS Corporation - Fuel Analyses, Raw Gas and Fuel Gas, 8/27/2015
3. Duvia A., Tavolo S., "Application Of Orc Units In The Pellet Production Field: Technical-Economic Considerations And

Overview Of The Operational Results Of An Orc Plant In The Industry Installed In Mudau (Germany)", 2008

4. Turboden ORC Product Catalog
5. Turboden ORC, Heat Recovery: Oil & Gas Presentation – 2016
<http://www.turboden.eu/en/downloads/downloads.php?categoria=presentations>
6. Electratherm Product Catalog: Series 6500 FL
7. Cleaver Brooks®, Model CBR 125-800 HP Boilers Operators Manual
8. US EPA AP-42, Chapter 13.5 Industrial Flares
9. US EPA AP-42, Chapter 1.4 External Combustion Sources

Feeder Design Optimization for Aluminum Sand Casting

Mustafa ERCAN*, Erdal KARADENİZ⁺, Murat ÇOLAK*

*Sakarya University, Engineering Faculty, Department of Mechanical Engineering, 54187 Sakarya, Turkey
mustafaercan1986@gmail.com

*Sakarya University, Engineering Faculty, Department of Mechanical Engineering, 54187 Sakarya, Turkey
erdalk@sakarya.edu.tr

*Bayburt University, Engineering Faculty, Department of Mechanical Engineering, 69000 Bayburt, Turkey
mcolak@bayburt.edu.tr

Abstract— The gating and riser system (feeder) design play very important role for improving casting quality. Many defects such as tensile void, porosity and segregation in products produced by casting methods may be detected. The porosity is the one of the defects most frequently encountered in casting. Porosity formation cause costly scrap loss and limits the use of cast parts in applications requiring high sealing. The amount of porosity is closely related to sand casting process parameters. A considerable reduction in porosity formation can be obtained using riser design optimization technique in the sand casting process. The design of feeder requires knowledge and experience. Therefore, hot spot formation, solidification period, feeder sprue and volume are important criteria. However, these may be not enough to produce high quality castings, and the importance of simulation techniques increases. The aim of this study is to make a feeder design optimisation for a cast part produced from Etial 160 aluminium alloy by sand mould casting method. In this study, gating and riser design, module criteria, feeder volume and size were investigated by SOLIDCast casting simulation program. The real and simulated casting values were compared with each other in the light of macro and micro-porosity results.

Keywords— Feeder design, Casting simulation, Aluminium casting, Porosity, Sand casting.

I. INTRODUCTION

Casting is a widely used manufacturing method because metal parts can be produced very economically and complex shapes can be obtained with very little processing. A successful casting process can be accomplished by designing the hardware system required to select the casting process and then to enter all regions of the molten metal piece ([1]).

In the casting process, the molten metal in the mold cavity must be fed with molten metal to compensate for the draw, since it is reduced in volume during solidification. If it can not be fed, drawback voids and porosity flaws can occur as a result of the volume of the molten metal shrinking. Nutrients are used to compensate for defects that occur as a result of volume shrinkage during solidification ([1], [5]). The position, number, shape, and dimensions of the feeder in the model design for a casting process are important variables to be determined ([1], [2]). Implementation of the trial and error method in the

development of the feed system requires a lot of time, cost and labor. Feeder design is very important in order to obtain a solid casting. For this reason, even nowadays, many foundry engineers carry out their nutritional designs and dimensions in the light of their own experiences ([2], [3]).

Feeder shape and size design, hot spot, solidification time (Module), feed path, feeder volume and Naval Research Lab. (NRL) are used. These criteria may be inadequate for producing cast parts at high quality and simulation techniques are also used for optimum feeder design ([1], [3]- [7]). [18]

One feature of molten aluminum that concerns the nutrient design in casting is the ability to easily extract hydrogen from refractors containing atmospheres or moisture, resulting in very low solubility of hydrogen in solid aluminum, thereby causing micro- or macro-porosity when hydrogen gas is thrown away when the alloy is solidified [6]. In addition, the feeder design for aluminum alloys has different challenges compared to heavy metals ([1], [6]).

Due to the differences between the feeder size specification criteria and the values suggested by the simulation software, in this study, molding design studies were carried out to avoid macro and micro porosity on a sample piece. For the purpose of helping to choose between the techniques, a casting part made of Etial 160 Aluminum alloy produced by sand mold casting method has been investigated with feeder design criteria and simulation techniques. In feeder design studies, module criterion, feeder volume criterion and SOLIDCast casting simulation software were used. The nutrient sizes obtained from the criteria and proposed by the simulation program were compared with the optimum nutrient size values obtained from the simulation studies. The most appropriate result is obtained from simulation studies.

II. EXPERIMENTAL STUDIES

Experimental studies have been carried out on the basis of the desired fuel tank cover which has high sealing properties produced by Etial-160 Aluminum alloy sand casting method. The sand mold was prepared with 90-110 AFS grain size sand,

4 wt. % bentonite, 6 wt. % water and wet mold sand obtained by mixing it in a mixer. The chemical composition of the Etial-160 Aluminum alloy used as the test material were given in Table I.

TABLE I. ETİAL 160 ALUMINUM ALLOY CHEMICAL COMPOSITION (% WT.)

Si	Fe	Cu	Mn	Mg	Zn	Al
8,62	0,824	3,091	0,2248	0,2804	0,9	Rest

In Figure 1, a cross-sectional image and a photograph showing the result of the production are presented. As a result of the insufficient feeder usage, the fuel tank cover part photo, which is produced, contains porosity as seen in Figure 1.b. This result is a defect for the part and causes the part to be separated. For this reason, the proper nutritional design for the part to be investigated is important for the production of robust and quality parts.

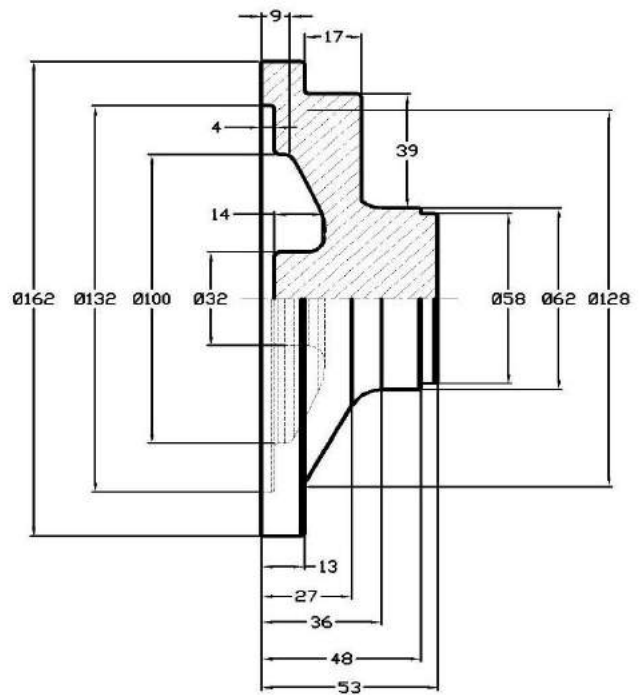
Some criteria are used in nutritional design. Among these, the most commonly used solidification time (module) criterion. The module criterion provides small feeder size values due to the track geometry being examined. For this reason, it is recommended that nutritional volume criterion be evaluated together with its results. Therefore, in the scope of the study, nominal criterion and feeder volume criterion and feeder size calculations have been used.

[20]

Solidification Time (Module) Criteria: In casting mold design, the progress of the solidification towards the feeders and the ending in the feeders is called oriented solidification, and the feeders must solidify slightly later than the hot spots of the cast to provide this criterion. In coarse castings, the solidification time of a given section can be calculated by the Chvorinov approach, which is proportional to the volume surface area of that section ([8]). According to this;

$$t = k (V / A)^2$$

Where t is the time constant of solidification in minutes, V is the volume of the casting, A is the surface area of the die casting contacted with the die, and k is the constant of the equation which varies according to the casting alloy and the die material.



a)



b)

Figure 1. Fuel tank cover a) technical drawing, b) fault seen in red circle

(V / A) factor is called "module" (M) and it must be larger than the cast module of the feeder in a suitable design. Accordingly, the feeder must solidify later than the nearest hot spot to it. This criterion is usually expressed by the following equation ([5], [8]- [11]).

$$(V / A)_{\text{feeder}} > (V / A)_{\text{casting}}$$

When calculating the feeder size, the casters require the solidifier to have a longer solidification time than the solidification of the casting piece. With this in mind;

$$\text{Feeder Modular } (M_{\text{feeder}}) = 1.2 \times (M_{\text{casting}})$$

1.2 is the safety factor.

Nutritional Requirement (Volume) Criteria: Except for some cases, all cast alloys shrink by about 2-7 % in volume

during cooling and solidification. This shrinkage, which is called volumetric shrinkage, naturally leads to a certain gap in the last hardened areas of the cast parts (hot spots). Feeders have a specific feed capacity and this capacity has to be limited to a certain volume limit. This limit, which can be expressed by the following relation, should not be smaller than this volume since a limiter will determine the minimum amount of metal that a feeder should have for a casting.

$$V_b = \alpha V_d / \varepsilon - \alpha$$

Where V_d is the volume of the casting part when a single feeder is used, the volume of the part to be connected to the feeder if more than one feeder is to be used, the volumetric draw ratio of the casting alloy α is ε , and ε is the volumetric draw ratio of the casting alloy, Is the feed metal that can be consumed as a percentage of the total volume, and expresses "feeder efficiency" ([5], [9]- [11]).

[21]

As a nutritious volume criterion in the literature:

$$W_{\text{cast}} = (C / 100) \times (W_{\text{feeder}} \times 100 / S)$$

Equation is also proposed. In this equation, W represents the feed weight, W feed weight,% draw ratio of C alloy, and the total feed metal volume ratio of the liquid metal to feed the cast part in the S feeder. C value is recommended as 16% in sand mold casting applications. An S-scale table is chosen and given as 8% for aluminum alloys ([3]).

The feeder position is considered suitable as a top feeder when considering the shape of the part. Feeder height / feeder diameter dimensioning ratio 1/1 was accepted for initial evaluations. The dimensional adjustment is deemed appropriate because the diameter of the region to which the feeder is to be positioned is 58 mm. The results obtained were again 50 mm in diameter, and the dimensional calculations were applied again.

Computer Aided Casting Design Studies: Molding design for an ideal casting can only be achieved by satisfying all the criteria given above. Casting parts with complicated geometry and different cross-sectional thicknesses require very difficult and intensive engineering knowledge and skill. But by the influence of rapid developments in computer technology, modeling of casting processes; Micro and macro structures can be predicted by casting simulation programs ([12], [13]).

Casting is a multi-stage process and includes all the processes from 2D drawing to determining the design of the optimum casting part. If we examine these processes in turn;

- Making Technical Drawing as a three-dimensional (3D) solid model
- Determination of properties of materials and casting components
- Test casting to determine the module and hot spots of the solid model

- Feeder calculations
- Mold designing
- Analysis of the molding design in the simulation program
- Examination of the results
- Overhaul and redesign in mold design if necessary
- It is possible to specify the optimum design and report the results ([14]).

Since the simulation is a process that can be repeated, the desired changes are tried and studies continue until the optimum result is reached. Since all processes are done on computer, modeling, molding and melting costs are eliminated. [22]

III. EXPERIMENTAL RESULTS AND DISCUSSION

The weight, volume and surface area values of the fuel tank lid used in the experimental works are given in Table II.

TABLE II.
TEST PIECE WEIGHT, VOLUME AND SURFACE AREA VALUES

Weiht, gr	Volume, mm ³	Surface area, mm ²
926,72	335757,71	58288,82

The module criterion with feeder height / feeder diameter sizing ratio of 1/1 acceptance and both feeder volume criterion results are given in Table 3. Volume 1 was obtained from the equation $V_b = \alpha V_d / \varepsilon - \alpha$, Volume 2 $W_{\text{cast}} = (C / 100) \times (W_{\text{feeder}} \times 100 / S)$.

TABLE III.
RESULTS OF FEEDER SIZES CALCULATED BY CRITERIA

Criteria	H (mm)	D (mm)	Hregulated (mm)	Dregulated (mm)
Modul	41,472	41,472	-	-
Volume 1	75,33	75,33	171	50
Volume 2	59,80	59,80	85,50	50

When the results in Table 3 are examined, it is clear that there is a huge difference between the results obtained using the criteria. However, both the module criterion and the volume criterion are evaluated together, and depending on the geometry of the part, the criterion is preferred in terms of the use of the feeder if the criterion required by the criterion is greater. When considering the track examined, the nutrient usage determined as the volume criterion will be appropriate when the module criterion results are small. Volume 1 results are quite large, and the maximum 3/1 ratio for the H / D ratio is also exceeded.

In this study, the models were made with SolidCast casting simulation program. The program is a software that solves the three-dimensional casting-mold geometry with the help of cubic meshes and the finite difference method according to the given boundary conditions. The software performs the cooling model with the help of heat transfer formulas. As the first step

in mold design with casting simulation programs, modeling of the relevant part without connecting the feeder and runner is the process of determining the hot spots. Depending on the size of the hot spot determined afterwards, the feeder sizes required in the casting simulation software can be determined depending on the desired boundary conditions. This will lead to the design of molds according to the number of feeders required and the required feeder sizes. In the SolidCast casting simulation program, the equivalent alloy of Etial 160 alloy was selected as the casting alloy material and the casting temperature was set at 720 °C and the solidification temperature was set at 537 °C. Figure 2 shows the modeling endpoint hot spot and location of the part.

As seen in Fig. 2, when the model is solidified in this way, it is seen that there is only one hot zone in the 0,7069 cm modulus in the middle bosom. For this reason, it is deemed appropriate to carry out the molding design and casting studies by putting 1 feeder on the relevant region. Within the program, the feeder design wizard module specifies the feeder dimensions required to feed the corresponding region. It is possible to design according to different boundary conditions for the feeder account required in the feeder design wizard. When choosing the most economical and effective feeder design choice according to the parameter $h = 2d$, the feeder with 42.27 mm diameter and 84.54 mm height has been selected by the program. Simulation studies have been carried out and it has been found that the feeder sizes are sufficient for macro porosity and only for microporosity (Fig. 3).

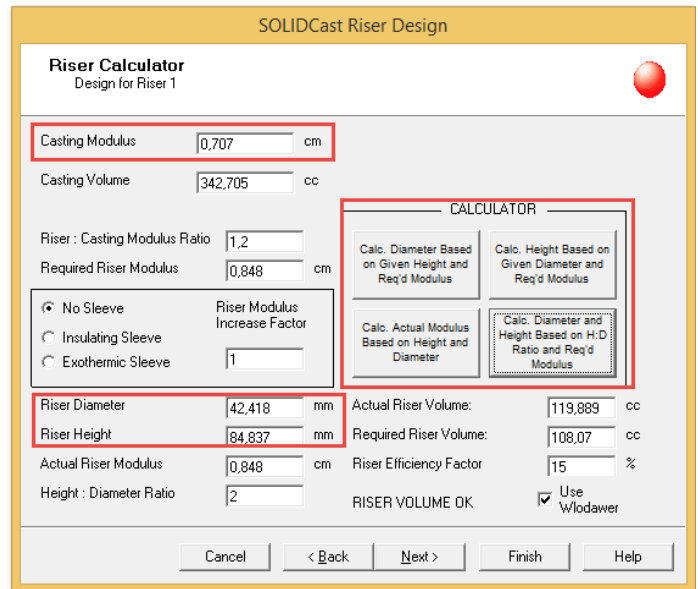


Figure 2. a) Hot spot formed in SolidCast modeling result in casting, b) Feeder design wizard calculation screen image

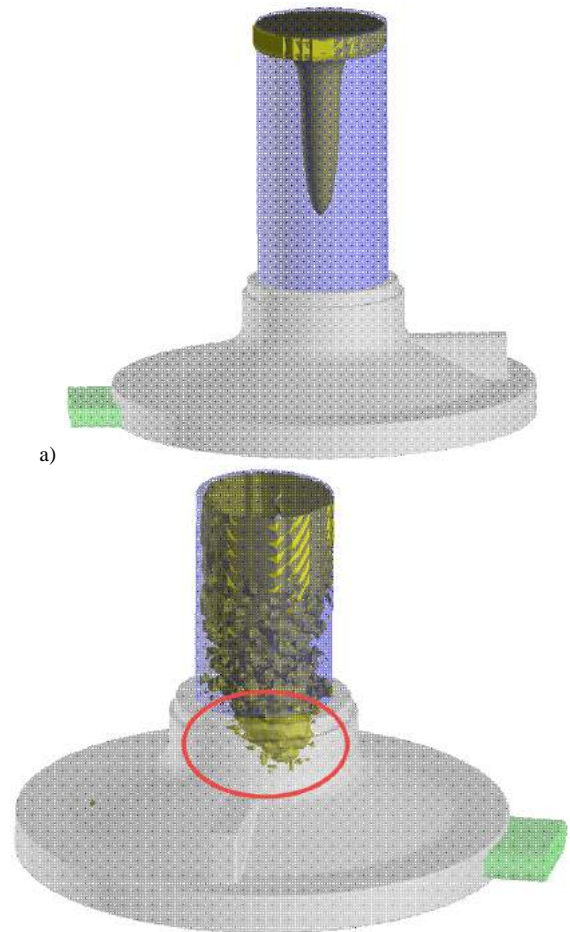
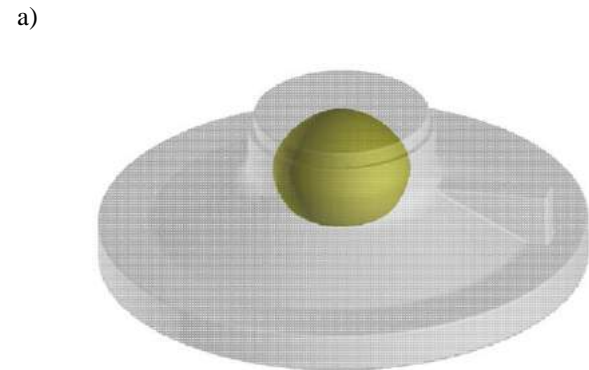


Figure 3. Simulation results of the molding design with Design-1 (42 mm diameter and 84 mm height feeder) a) macro porosity, b) microporosity condition

In the context of this study, it is necessary to take into account the microporosity results in this part design, since the parts to be designed are very desirable to have high sealing properties. For this reason, the simulation has been progressively continued with the enlargement of the feeder sizes, so that the micro pore on the part is lifted out of the way. In such cases the ultimate design and optimum results have been achieved, as the height / diameter ratio is 2, as the feeder neck elevation solution may be the solution to remove the micro-tile from the part. Accordingly, it was determined that the feeder with a diameter of 50 mm and a height of 100 mm would be sufficient. In Figure 4, modeling studies are presented with a solid model image of the molding design which is deemed appropriate.

Figure 4 shows the molding design and components used in the model. Since there is no region of very thin sections associated with the filling of the part and the casting has to be solidified after completion of the filling of the parts of the runway, only the runway entry is specified in the models and the work is done in this way. If there is a risk associated with the filling, or if fluid flow modeling is desired, it is possible to draw the modeling of the roadway into the molding design and make it in the FlowCast filling simulation program of the model. However, this work focuses on solidification modeling depending on part geometry and requirements.

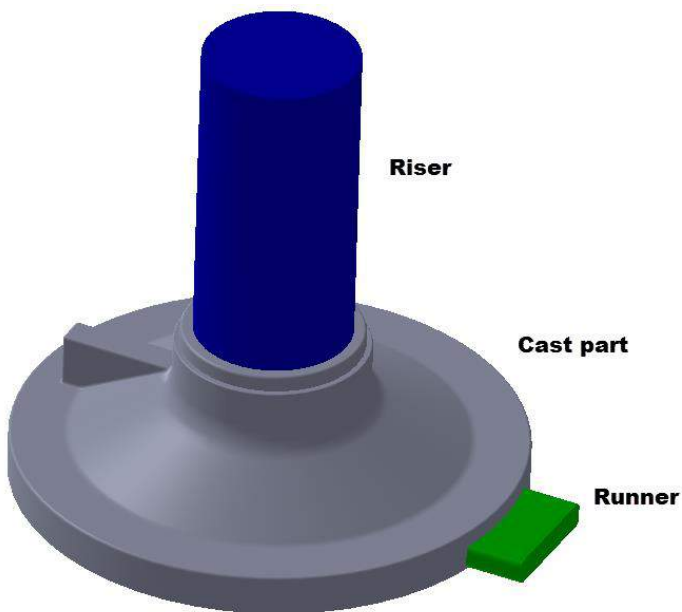


Figure 4. Molding design suitable for modeling program

In the casting model, granular separation is known as a basic process from the modeling process steps, and the selected dimension is important in terms of process accuracy. For this reason, the granules are separated by at least 3 from the thinnest section of the casting piece. Figure 5 shows the screen images taken from the SolidCast program during the meshing process for model and die.

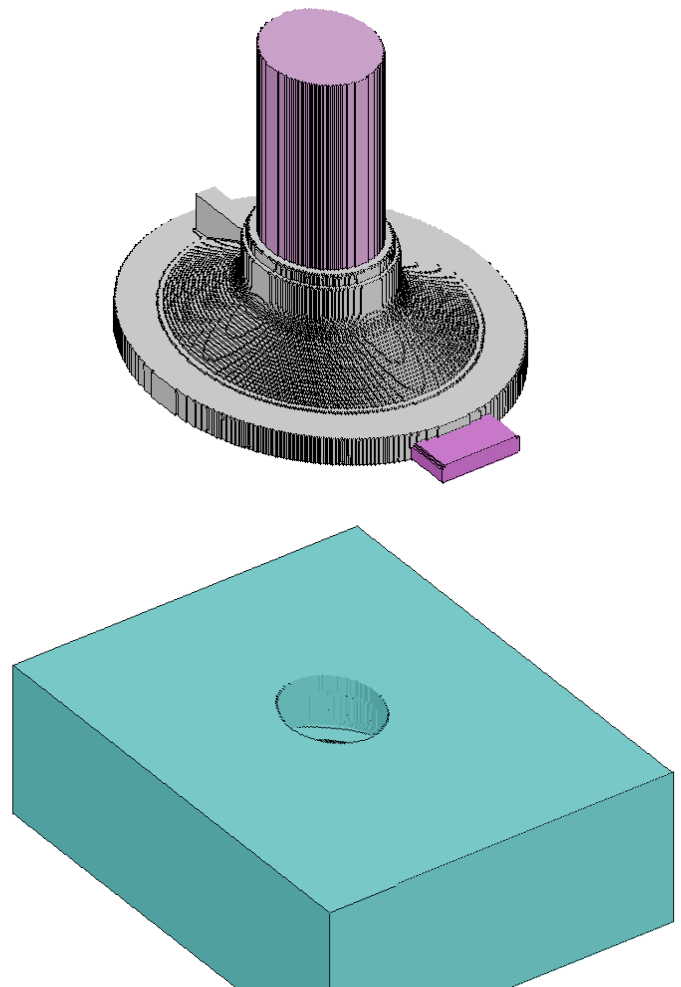


Figure 5. Modeling program image in mold and model granularity

Simulation has been started after separating the particles. After completion of the modeling process, the results are examined for the suitability of the parts and the robustness of the design. In general, to ensure that the casting is considered to be solid, there should be no risk of macro and micro porosity on the casting, and the solidification must be solidified in the last feeders oriented towards the feeders. Once the suitability of the design is determined in this way, many different results can be evaluated in the program depending on the desire. Figure 6.a shows macro-pore analysis, Figure 6.b shows micropore traction, Figure 7 shows solid-dispersion image.

The macro porosity given in Figure 6.a has been investigated with 99.8 % sensitivity considering the sealing properties of the resulting image part. As can be seen from the images obtained, it is understood that the molding design is appropriate and does not involve any drawbacks in terms of macro and micro. It is seen that all the risky nutrients that may occur in molding design are found. The macro porosity image (Fig. 6. b) shows that the microporosity results are only the size that the feeder can tolerate, as long as the feeder size is large,

and the risk of microporosity is high when the smaller feeder is used.

TABLE IV.
CRITERIA FOR FEEDER OPTIMIZATION AND FEEDER

Criteria	H (mm)	ØD (mm)	Volume (mm ³)	Explanati on
Module	41,47	41,47	28006,71	Macro and micro pore available
Volume 1	171,00	50,00	335757,71	Design suitable
Volume 2	85,50	50,00	167878,85	micro pore available
Simulation Design 1	84,54	42,27	118636,03	micro pore available
End Simulation Design	100,00	50,00	196349,54	Design suitable

the edges of the mold and the solidification of the entire mold ended in 7.21 minutes. From the color scale given on the figure, the blue stain marks the first solidified regions, while the yellow stain shows the last solidified regions. Accordingly, it has been determined that the orientation of the solidification is desired and that the final feeders are terminated starting from the edges of the pieces. It is understood that there is no risk situation in the casting part since the last solidification takes place in the feeders. According to these results, no error is detected on the part, so it is understood that the design can pass through the production as it is.

In the study, the module criterion, the volume criterion and the results of the nutrient sizes obtained by the simulation software for the nutrient-optimized part are given in Table IV.

IV. DIMENSIONS CALCULATED FROM SOFTWARE

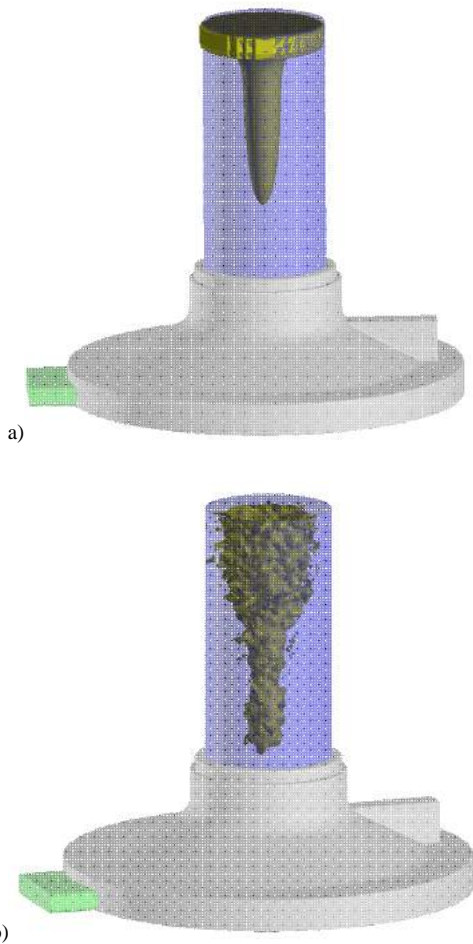


Figure 6. a) Macroporozity, b) Microporozity retraction analysis results image

The solidification analysis of the molding design in Figure 7 shows that the solidification first started at 0.66 minutes on

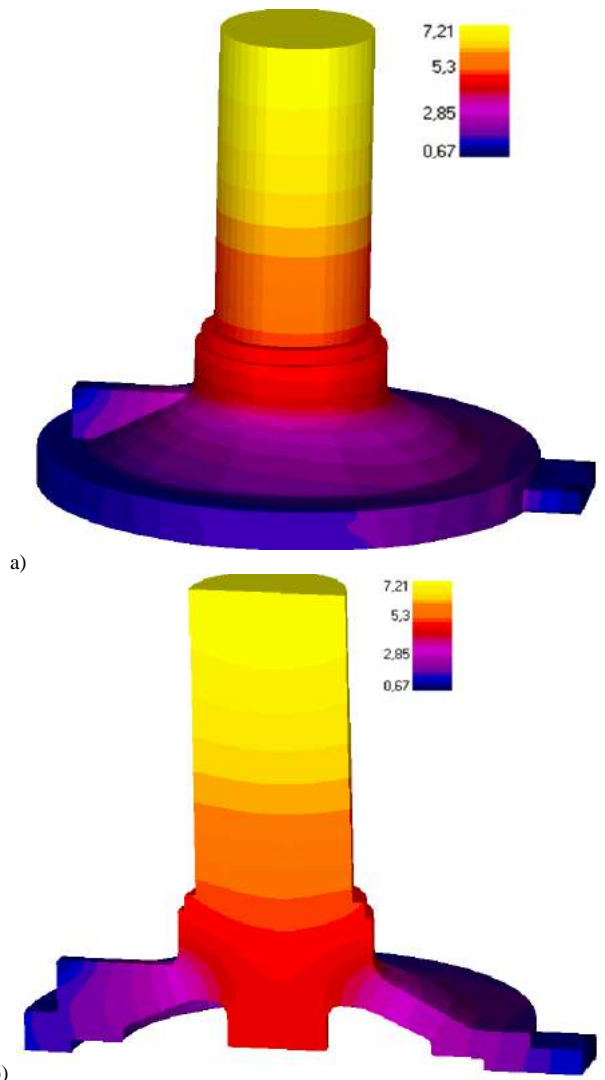


Figure 7. a) Solidification distribution analysis, b) Solidification distribution analysis section view

As can be seen from the results given in Table 4, it is possible to produce nutrients of the specified sizes and no macro- and micro-pore risk at the end of the volume 1 criterion and the gradual final simulation designs. When we compare the values for feeder optimization, it is determined that the feeder calculated by modeling is 41.52% smaller than the calculation method using the Volume-1 criterion. According to volume 2 and the most economical design made by the model, the micro pore pulls the risk while the part does not contain macro pore risk in the case of nutrient use. However, in the sample used in the work, it is not desirable in the micro-pores due to the high leak-tightness expectations. For this reason, it is not possible to produce solid parts with desired characteristics with the nutrients calculated with these criteria and module criterion. It can be considered that conventional calculation methods can be used in parts where micro-pore formation can be neglected. In this case, however, as shown in Table 4, it is observed that the nutrient sizes determined by the Simulation Design-1 method are 29.24 % smaller than the nutrients determined according to the Volume 2 criterion. Since module criterion and volume criterion are evaluated jointly based on part geometry, they have not been considered in evaluations because volume criterion must be used in situations where smaller feeders are required than module criteria. As a result, the use of modeling programs in terms of accuracy and economy is very important in terms of nutritional optimization.

V. GENERAL RESULTS

The results obtained from the experimental and modeling studies in the study of the design and production of the Etial 160 aluminum alloy and the tank lid piece with a sand casting method are summarized as follows:

- Hot spot formation occurs at the center of the part depending on the part geometry.
- Classical engineering methods and computer aided casting simulation have been used for necessary feeder calculations for the solid part design to produce solid parts.
- When modeling results are examined, it is observed that they are compatible with actual casting results. According to this result, it can be said that the molding design for the castings to be made with the alloy Etial 160 can be optimally and safely optimized by the calculation and modeling techniques used in this study.
- Casting simulation program for the macro and micro pore-free feeder design for the sample has been observed to be able to design a molding with 41.52 % more economical feeder than the conventional calculation methods.
- It has been observed that for casting simulation program for feeder design that does not contain only macro pore for the sample, molding design with 29.24 % more economical feeder can be realized compared to the conventional calculation methods.
- It can be said that the molding design for the castings to be made with Etial 160 alloy can be optimized with the calculation and modeling techniques used in this study correctly and safely.
- Depending on the part geometry, it is not possible to produce solid parts which are always desired with the feeders

determined by classical engineering calculations (volume and module criterion). It can be considered that conventional calculation methods can be used in parts where micro-pore formation can be neglected. However, it is understood that simulation software is more advantageous when economy is taken into consideration.

REFERENCES

- [1] Guleyupoglu S., Casting Process Design Guidelines, AFS Transactions, 83, 869-876, 1997.
- [2] Tavakoli R., Davami P., Automatic optimal feeder design in steel casting process, Computer Methods in Applied Mechanical Engineering, 197, 921– 932, 2008
- [3] Candeğer K. C., Dökümde besleyiciler ve ekzotermik besleyici malzemeler, Metaluji, 126, 5-12, 2001
- [4] Nimbalkar S. L., Dalu R. S., Minimization of Gas Porosity through Casting Simulation Tool for Sand Casting, International Journal for Scientific Research & Development| Vol. 2, 11, 2015
- [5] Kayıkcı R., Akar N., Farklı Kesit Kalınlıklarına Sahip Büyük Hacimli Bir Çelik Dökümünün Simülasyon Teknikleriyle Tasarlanması, Politeknik Dergisi, 10-4, 214-2274, 2007
- [6] Cupido L.H., Żak P.L., Simulation of Casting Technologies for Al-Si-Cu Plate Casting, Archives of Foundry Engineering, 13, 3, 11-14, 2013
- [7] Manjabacas M.C., Miguel-Eguía V., A comparison between traditional criteria and FEM analysis results for gravity casting feeding and risering systems, American Institute of Physics, The 4th. Manufacturing Engineering Society International Conference MESIC 2011, 751-760
- [8] Chvorinov N., Theory of Solidification of Castings, Giesserei, 27, 177-225, 1940
- [9] Kayıkcı R., Büyük kütleli bir çelik parçanın dökümünde klasik ve bilgisayar destekli mühendislik yöntemlerinin karşılaştırılması, Journal of The Faculty of Engineering and Architecture of Gazi University, 23, 2, 2008.
- [10] Arda İ. ve Kayıkcı R., Döküm simülasyonu nedir? Ne değildir?, Metal Dünyası, Mart 2006.
- [11] Franssman H., Hızlı ve Doğru Yolluk ve Besleyici Dizaynı için Döküm Simülasyon Programlarının Pratik Kullanımı, Metal Dünyası, 164, 30-31, 2007
- [12] <http://www.finitesolutions.com/> (Ocak 2017)
- [13] Çolak, M. ve Kayıkcı, R. Döküm Simülasyon Programları Üzerine Genel Bir Değerlendirme, Metal Dünyası, Sayı 190, Mart 2009.
- [14] M.Çolak, S.Şirin, SolidCast Döküm Simülasyon Programıyla Kalıplama Tasarımının İşlem Basamakları, Metal Dünyası, Sayı 202, Mart 2010.

Barkhausen Noise as a Magnetic Nondestructive Testing Technique

Oğuz KOÇAR

oguz.kocar@beun.edu.tr

Mechatronics Engineering, Bulent Ecevit University

Incivez, Zonguldak, Turkey

ABSTRACT

There are many destructive and non-destructive tests for detecting microstructural changes and faults in steel parts. The term “non-destructive testing” (NDT) is used for material testing methods that can be applied without harming the material. NDT can be applied to materials, parts, assemblies or structures. One of the non-destructive evaluation methods is Barkhausen Noise (BN) that is magnetic based and is used mainly in the automotive and aviation industry. Barkhausen noise (BN) measurement is an electromagnetic testing method that is suitable for ferromagnetic materials. Ferromagnetic materials are made up of small magnetic domains which are separated by domain walls and orientated in different direction. As a result of the external magnetic field applied, domains will turn to the direction of magnetization, moving the domain walls which will cause jumps of magnetic flux density. These jumps are called Magnetic Barkhausen Noise (MBN). MBN is sensitive to different material properties such as microstructure, composition, residual stress and hardness. This paper focus on describing an improved Non-Destructive Testing methodology based on the analysis of BN. It also explains the relationship between material properties and BN profile. Also, it is aimed to introduce applications and test equipments of BN.

Keywords: Barkhausen Noise (BN), Material Properties, BN Applications, BN Experimental Setup and BN Signal

Thermal Stability and Phase Transformation of Nanocrystalline Stainless Steels Prepared By Mechanical Alloying

Hakan Kotan, Ahmet B. BATIBAY

Konya Necmettin Erbakan University

hkotan@konya.edu.tr

ABSTRACT

Nanocrystalline stainless steels with solute additions are synthesized using high energy mechanical alloying. Microstructural evolutions as a function of alloy compositions and annealing temperatures are investigated using focused ion beam microscopy, transmission electron microscopy and in-situ and ex-situ X-ray diffraction techniques. The dependence of hardness on the microstructure is utilized to study the mechanical changes. The relative importance of composition and solute additions in various temperature ranges are discussed with respect to grain growth and phase stability. The research reported in this work was supported by TUBITAK under Grant number 114M214. The authors wish to thank TUBITAK for the support.

Keywords: Stainless steels, phase transformation, grain growth, mechanical alloying

Investigation of Nanocrystalline Stainless Steels As A Function Of Milling Time

Ahmet BURCIN, Hasan KOTAN
Konya Necmettin Erbakan University
hkotan@konya.edu.tr

ABSTRACT

Fe – 18Cr – 8Ni (at.%) stainless steels from elemental powders were synthesized by high energy mechanical alloying in a Spex™ 8000D Mixer/Mill. In order to investigate the alloying and transformation kinetics, milling time was ranged up to 30 hours at room temperature. The resultant powders were investigated as a function of milling time by x-ray diffraction (XRD), thermogravimetric analysis (TGA) and scanning electron microscope (SEM). The primary results have shown that the high energy milling induced martensitic transformation due to the severe plastic deformation as the martensite-to-austenite phase ratio was observed to increase with increasing milling time. The dependence of hardness on the microstructure was utilized to investigate the mechanical properties of synthesized powders. The research reported in this work was supported by TUBITAK under grant number 114M214.

Keywords: Stainless Steels, Mechanical alloying, Phase Transformation

Economic Crises in Turkey and In the World and Their Effects on Iron and Steel Market

Nazmi Sarıkaya^a, Ahmet Gürbüz^b

^a Kardemir Karabük Iron & Steel Industry, Production Planning Department, Karabük
nsarikaya@kardemir.com

^b Karabük University, Balıklar Kayası Region, 78050 Karabük
agurbuz@karabuk.edu.tr

Abstract

Iron and steel production and consumption values are the most important indicators which demonstrate development and industrial growth of countries. In our study, world iron and steel sector production capacities and development of steel production values are examined by years. During this period, except global crisis times, iron and steel capacities and production values' constantly increasement are observed. Growth rates and iron and steel production values are compared, during economic crisis where world and our country are affected. In the last part of our study, a regression model of salable billet and ribbed bar steel prices was set up to estimate with using independent variables such as the global and Turkey liquid steel production, world and Turkey% growth rates. Except negative effects of economic crisis' on sector's development; low capacity usage rates due excess supply over demand, raw material procurement price fluctuations, China's iron and steel sector developments, decreasing other producers' competition ability due to imports from China to all over world and protective tax regulations on behalf of protection of local producers, create uncertainty to development and future of sector.

Keywords: Steel, Steel production in crisis period, world economic crisis

1. INTRODUCTION

The iron and steel sector has the locomotive sector attribute to the country's economy and industrialization. When the relationship between developments in the iron and steel industry and the development process is examined, iron and steel products play an important role in the development of the iron and steel sub-sectors of the economy. This sector's primarily importance is due to the input of all industrial sectors. The iron and steel industry has contributed to especially construction materials and the production of all kinds of automotive, ship, aircraft, railway and wagon vehicles, as well as all the machinery, equipment and articles that may come to mind (Ministry, 2012).

When the supply-demand balance in world iron-steel production and consumption is examined, it is observed that production capacities are over steel consumption in each period. The development of world liquid steel production capacity between 2000 and 2017 is shown in Figure 1 (<http://www.oecd.org/sti/ind/steelcapacity.htm>, 2017).

Despite the current ettireme global steel production capacity and weak market conditions, the production capacity is expected to grow even in 2015-2017. It is expected that the

capacity of the OECD area will remain roughly unchanged and several new projects will be balanced by capacity closures. It is predicted that most of the increase in the capacity of the world will take place in regions with net steel importers. As a result of numerous investment projects around the world, it is estimated that by 2017, world steel production capacity will be 2.42 billion tonnes per year, and that non-OECD economies will account for about 72.4% of the total capacity in 2017 (<http://www.oecd.org/sti/ind/steelcapacity.htm>, 2017).

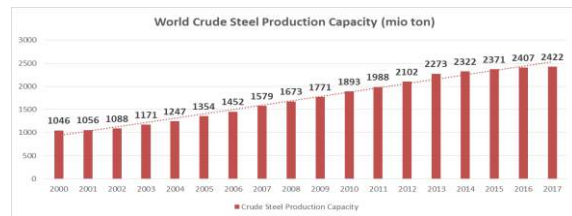


Figure 1. World crude steel production capacity

The capacity increase in the Chinese iron and steel production sector has shown a significant improvement and accounts for 48.3% of the global steel production capacity by 2016, despite the fact that the world steel production capacity has been on an increasing trend by years. Figure 2 shows the comparative development of the world and China's crude steel production capacities (Yayan, 2016).

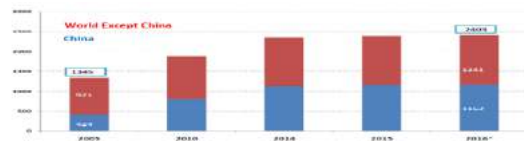


Figure 2. World - China steel capacity development

Turkey's iron and steel production capacity increasement has shown a rapid growth between 2005 and 2011, and stagnation between 2012 and 2016. Figure 3 shows the development of Turkey's crude steel production capacity (Yayan, 2016).



Figure 3. Turkey's crude steel capacity development

While the sector has a capacity utilization rate reaching 86% before the 2008 global financial crisis, capacity utilization rates in the sector have fallen below 70% in recent years due to high installed capacity quantities. Global capacity utilization rates in the world iron and steel industry are shown in Figure 4 by years (Turgut, 2016).

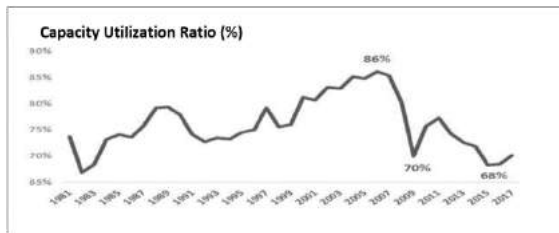


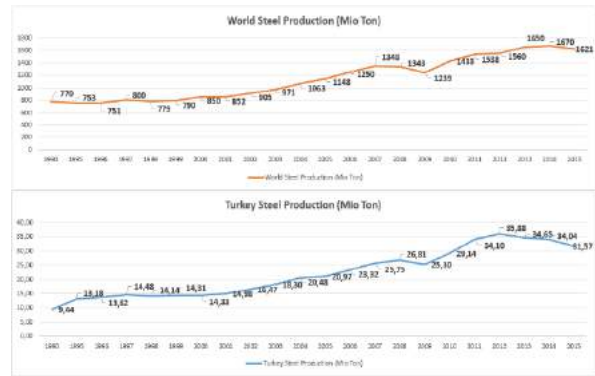
Figure 4. Global capacity utilization rates

II. WORLD AND TURKEY STEEL PRODUCTION DEVELOPMENT

Global steel production has increased over the last 10 years. While production in 2005 was 1.1 billion tons, by 2015, an increase of 41.4% to 1.6 billion tons, an increase of 475 million metric tons over the past ten years. Following the global financial crisis, global production has returned rapidly in 2010 with a dip in 2009. In 2014, global production reached a record level of 1.67 billion tons. Weak global steel demand in 2015 led to a slight contraction in world crude steel production, down 2.8% from 2014. The World Steel Association estimates that production may remain stable at current levels in the near future, taking into account stagnant steel demand levels between 2016 and 2017. The growth rates of crude steel production in the last 10 years have reinforced that production may be upward in the future. It's been only three years since 2006 with negative growth rates. As the global financial crisis experienced in 2008 and 2009 affected the steel industry, growth rates decreased by -0.3% and -7.8% respectively. As steel demand is weak, crude steel production shrank by -2.8% in 2015. The growth rate of the majority of the years that have experienced positive growth in steel demand, has exceeded % 5. The growth rate in 2010 reached the highest level with 15.7% (International Trade Administration, 2016).

Steel production in Turkey showed a steady increase with an average of 8.8% between 2001-2007. The effects of the global crisis experienced in 2008 were reflected in Turkey as well, with a contraction of 5.6% in 2009 in the sector against 4.1% growth in 2008. Figure 5 shows the steel production

quantities in the world and in Turkey as of years (World Steel Association) (World Steel Association).



A. 1994 Mexican Crisis

The Mexican crisis of 1994-1995 emerged in an environment where macroeconomic stability was relatively favored. For example, in Mexico there were no major budget deficits seen in other countries and the inflation rate was low. However, factors such as the rapid increase in loans opened in the private sector, the continuation of the exchange rate policy, the increase in the international interest rates, especially the interest rates in the US, and the uncertainties due to political murders have weakened the confidence in the Mexican economy. After the Mexican government's decision to expand the exchange rate band by 15% on December 20, 1994, pesos began to depreciate much more quickly than expected, after international reserves had dissolved in the two days by \$ 5 billion, it was thought that this would not be enough and the peso was left to fluctuate on December 22. This has caused interest rates to escalate and accelerated the deterioration of banks' portfolios. International investors have begun to withdraw their funds quickly and in panic and have caused a crisis (Sargedik, 2008).

When the indicators are examined such as country growth rates, liquid steel production quantities and % increase in liquid steel production, during the crisis period, 2 years before the crisis period and 2 years period after the crisis, especially in 1995, while the country's economy contracted by 5.76%, the steel production volume increased by 18%. Figure 6. shows the growth rate of Mexico, % growth of liquid steel production and % World Growth rates between 1992 and 2015. Figure 7 shows liquid steel production and annual growth rates in the crisis years of 1994 and 2008. Figure 8 also compares the growth rate of Mexican average liquid steel production, average annual growth rate and average world annual growth rate for the period 1993-2015 (World Steel Association) (The World Bank).

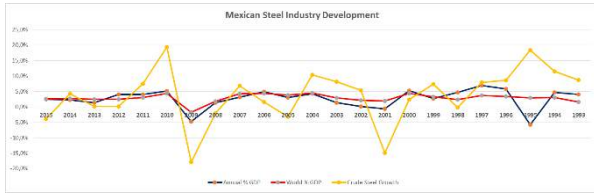


Figure 6. Mexican steel industry development by years

Mexican	2010	2009	2008	2007	2006	1996	1995	1994	1993	1992
Annual % GDP	5,11%	-4,70%	1,40%	3,20%	4,94%	5,87%	-5,76%	4,73%	4,06%	3,63%
World % GDP	4,37%	-1,70%	1,84%	4,32%	4,38%	3,33%	2,96%	3,03%	1,65%	1,79%
Crude Steel Growth	19,4%	-17,9%	-2,1%	6,8%	1,6%	8,6%	18,4%	11,5%	8,7%	
Crude Steel Production (ton)	16.870	14.132	17.209	17.573	16.447	13.196	12.147	10.260	9.199	8.459

Figure 7. Mexican steel industry development during crisis period

Mexican	Average % (1993-2015)
Annual % GDP	2,65%
World % GDP	2,90%
Crude Steel Growth	3,77%
World Av.Steel Growth	3,82%

Figure 8. Mexican steel industry and growth rate development

B. 1997 Asian Financial Crisis

The crises that lived in the 1990s are called Secondary Generation Crises. Even if there is no significant imbalance in the economy, it is a consequence of the speculators speculative attacks and in case of not to take the necessary precautions against foreign currency by the authorized bodies (İlhan, 2007).

The most important financial event of the 1990s is the financial crisis in Southeast Asia that affects all world economies. The financial crisis that began in February 1997 and spread to regional economies and the world with the devaluation of Thailand's currency "Baht" on 2 July is seen as an important economic event in various aspects. The unpredictability of such a crisis has led to the resurgence of both the problem of management and control of the international financial system and the speculative capital movements that played an important role in the crisis, as the absence of any problems in the real economies of the frustrated countries (İlhan, 2007).

Although the South Asian crisis began in Thailand, it spread to Malaysia, Indonesia, Singapore and the Philippines, also known as "Asean-5". The South Asian Crisis has caused the economies in the affected countries to shrink, the collapse of stock exchanges, the increase of unemployment, the rapid fall of the international area credit flow, the bankruptcy of companies and banks, the rapid increase of interest rates at national and international markets and the decrease of trade volume at international level (İlhan, 2007).

Figure 9 shows the development of Asian region iron and steel production, the development of Chinese iron and steel production, and the development of iron and steel production in the world (World Steel Association). As can be seen in

Figure 10, it is observed that the Chinese iron and steel industry has achieved an average growth rate of 10.79% per year between 1993 and 2015, above the world average (3.82%) of iron and steel production growth (World Steel Association) (The World Bank).

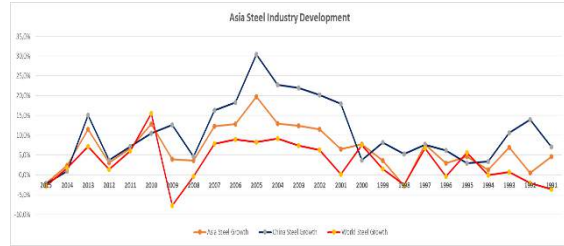


Figure 9. Asia steel industry development by years

Region	Average % (1993-2015)
Asia Steel Growth	7,04%
China Steel Growth	10,79%
World Steel Growth	3,82%

Figure 10. Asia steel industry and growth rate developments

C. 1998 Russian Financial Crisis

We can list the causes of the Russian crisis in the following articles in general (Sarigedik, 2008) :

- Extensive budget deficits, excessive exposure of firms to currency risk,
- The repayment period for foreign loans is the weight of short-term debts that expire within one year,
- Inadequacy of infrastructure and supervision legislation in finance and banking sectors,
- Non-payment of salaries and wages due to loss of budget discipline and increase in debts due to social payments,
- The interest burden of repayment of debts,
- Increased mutual debt between institutions and bankruptcy of many institutions in the real sector,
- World prices of raw materials, particularly oil and gas, fall in the world,
- Ruble to be indexed and artificially overvalued in US dollars,
- Finding outdated industrial and agricultural businesses,
- The failure to establish a strong legal system demanded by the free market economy,
- Problems in the fields of investment, company establishment, work place etc,
- Inadequate security system in the economic field,
- Bribery and corruption,
- Dominant monopoly and oligopoly companies in the market,
- Inadequate entrepreneur class,

- The lack of support from the Russian administration to solve these structural problems and to make reforms necessary for wider market operation,
- The low level of foreign exchange reserves, the speculation of the stock market that does not reflect the real situation of the economy,
- The absence of any government program to increase economic growth and industrial production,
- External causes (Asian crisis, falling oil prices, etc.).

Figure 11 shows the development of the Russian steel industry, the economic growth rate of the country, and world economic growth rates. Figure 12 shows the realization of the same parameters during the crisis period, Figure 13 shows the average Russian liquid steel production growth, average annual % growth rate and world average annual growth rates between 1993 and 2015 (World Steel Association) (The World Bank). It is observed that the Russian steel industry has been in a steady contraction for two years before the 1998 crisis but a very rapid increase in production has been observed after the crisis.

It is observed that the Russian steel industry has grown by an average of 0.60% between 1993 and 2015, falling behind the world average steel production growth rate (3.82%) in the same period.



Figure 11. Russian steel industry developments by years

Russia	2010	2009	2008	2007	2006	2000	1999	1998	1997	1996
Annual % GDP	4,50%	-7,82%	5,25%	8,54%	8,15%	10,00%	6,40%	-5,30%	1,40%	-3,60%
World % GDP	4,37%	-1,70%	1,84%	4,32%	4,38%	4,34%	3,31%	2,43%	3,75%	3,33%
Crude Steel Growth	11,5%	-12,4%	-5,4%	2,2%	7,1%	14,8%	17,5%	-9,6%	-1,5%	-4,5%

Figure 12. Russian steel industry developments during crisis period

Russia	Average % (1993-2015)
Annual % GDP	1,69%
World % GDP	2,90%
Crude Steel Growth	0,60%
World Av. Steel Growth	3,82%

Figure 13. Russian steel industry and growth rate development

D. 1999 Argentina Crisis

The main reasons for the Argentine crisis are; overvalued exchange rate, "Peso's situation where the price has been equalized to dollar for 10 years, reduces the competitive power in exports, devaluation expectation, unreduced public spendings, decline in tax revenues and record unemployment

rates at 17%. The Asian financial crisis of 1997 was also a reflection on Latin America countries and Argentina was less affected than its neighbors. With the announcement of Russia's postponement of debt in 1998 and Brazil's entry into the balance-of-payments crisis and its devaluation in 1999, Argentina entered a crisis (Sarigedik, 2008).

Figure 14 shows the evolution of the Argentine steel industry, the economic growth rate of the country and the world economic growth rates, Figure 15 shows the same parameters during the crisis period, Figure 16 shows the average annual liquid steel production growth, % Growth rate, and world average annual growth rates between 1993-2015 (World Steel Association) (The World Bank). Before the 1999 crisis, while steel production growth was declining, an increase of 17.8% was achieved in the year after the crisis period. However, this increase has seen a contraction of 8.2 % in 2001. During the 2008 global crisis, a 27.6% contraction was experienced in the sector especially in 2009, and a production increase of 28% was achieved in 2010. Between 1993 and 2015, Argentina's iron and steel production grew by 3.40% each year, close to the world average of 3.82%.



Argentina	2010	2009	2008	2007	2006	2001	2000	1999	1998	1997
Annual % GDP	10,35%	-6,01%	4,09%	9,02%	8,14%	-4,41%	-0,79%	-3,39%	3,85%	8,11%
World % GDP	4,37%	-1,70%	1,84%	4,32%	4,38%	1,98%	4,34%	3,31%	2,43%	3,75%
Crude Steel Growth	28,0%	-27,6%	2,9%	-2,6%	2,8%	-8,2%	17,8%	-9,9%	1,1%	2,3%

Figure 15. Argentina steel industry developments during crisis Period

Argentina	Average % (1993-2015)
Annual % GDP	2,89%
World % GDP	2,90%
Crude Steel Growth	3,40%
World Av. Steel Growth	3,82%

Figure 16. Argentina steel development, annual growth rate and world growth rate changes

E. 2008 Global Economic Crisis

The world economy has grown rapidly since 2005. In addition to growth, trade volume has expanded, inflation has historically gone down to the lowest levels, interest rates have fallen and liquidity opportunities have increased. However, the fluctuations that began in the financial markets due to the difficulties in the repayment of risky housing loans extended to low-income-level savings holders in the US in the summer of 2007, have deepened into a global financial crisis since November 2008 (Darican, 2015).

Figure 17 shows the world steel industry growth and economic growth rates, Figure 18 shows the same parameters during the 2008 crisis period and world liquid steel production, Figure 19 shows the world average liquid steel production growth and world average growth rate between 1993 and 2015 (World Steel Association) (The World Bank). As can be seen in Figure 17, world steel production has grown and shrunk considerably between 1994-2001. The sector, which showed a slower growth between 2002-2007, suffered a severe contraction with its effect in the global financial crisis in 2008-2009. As can be seen in Figure 19, the sector grew an average of 3.82% per year between 1993 and 2015.

2000. With this IMF supported program, it is aimed to reduce inflation rapidly, to control public deficits and to restructure financial sector. However, the fact that the program is based on the exchange rate and the rigidity created by the earlier announcement of the exchange rate basket in line with the inflation target in this framework, as well as the inadequacy of the international conjuncture and delays in structural reform, the economy has faced serious problems since November 2000. In spite of the problems experienced in November 2000, as a result of the efforts to maintain the "Program to Fight Inflation Based on Rate", the economy faced a severe financial crisis in February 2001 and the program being abandoned (Yükseler, 2009).

3) 2008 Global Crisis – Impact on Turkey: 2008 was a year in which the economic crisis continued to intensify in Turkey as well as in the world as a whole. The decline in the pre-crisis growth rate is due to the failure of the global crisis to channel credit channels based on the international banking system to Turkey And capital inflows and decreases in external demand and parallel to the decline in capital inflows and external demand, it has turned into a recession from the last quarter of 2008 and In 2009, except for financial institutions, almost all sectors experienced serious contraction. The direct impact of this contraction in the economy in terms of working life has been on employment and Turkey has been faced with the transformation of the real economy crisis in 2008 into the employment crisis (Darican, 2015).

Figure 20 shows the growth rates of the Turkish steel industry, the economic growth rate of the country and the world economic growth rates, Figure 21 shows the results of the same parameters during the crisis period, Figure 22 shows average liquid steel production growth, annual% growth rate and world% annual growth rate between 1993 and 2015 (World Steel Association) (The World Bank). In the 1994 economic crisis, it achieved an average growth rate of 3.89% in 1995 and 1996, even if it was slightly below the previous year's growth in iron and steel production. In the crisis period of 2001, the sector continued its growth in a serious way. It is observed that after experiencing a period of contraction in the global financial crisis period of 2008, it has regained a serious growth rate again in 2010. Between 1993 and 2015, the Turkish iron and steel industry grew by 3.17% year on year and reached a bigger growth rate than average growth rate of world liquid steel which the rate of 3.82%,



World	2010	2009	2008	2007	2006
World % GDP	4,37%	-1,70%	1,84%	4,32%	4,38%
Crude Steel Growth	15,52%	-7,77%	-0,39%	7,88%	8,90%
Crude Steel Production (ton)	1.405.421	1.216.568	1.319.069	1.324.207	1.227.461

Figure 18. World steel industry developments during crisis period

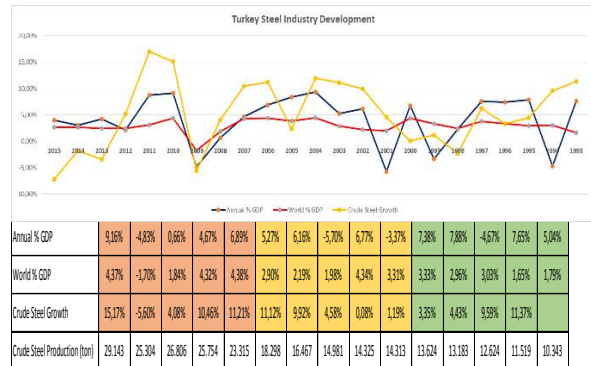
World	Average % (1993-2015)
World % GDP	2,90%
Crude Steel Growth	3,82%

Figure 19. World steel growth and annual growth rates changes

F. Crisis Periods in Turkey

1) 1994 Crisis: Following the liberation of capital movements in 1989, in the 1990s, domestic and foreign fluctuations were encountered in the economy, accompanied by mismatches in macroeconomic policies and political instabilities. Comprehensive economic arrangements were made in 1994 during the 1990s. These decisions, also known as the "April 5 Decisions", aim to narrow the public deficit and increase the economic competitiveness. These decisions have helped to narrow the public deficit and solve the real wage-real exchange problem and have severely limited the negative effects of the customs union agreement with the EU on the economy. However, "April 5 resolutions" did not succeed in solving the chronic inflation - high interest problem in the economy and regulating the financial sector (Yükseler, 2009).

2) 2001 Crisis: In order to solve the problem of chronic inflation and high interest in the economy, the "Currencies-Based Inflationary Fight Program" was put into effect in early



Annual % GDP	9,16%	-4,83%	0,66%	4,67%	6,89%	5,27%	6,16%	-5,70%	6,77%	-3,37%	7,38%	7,88%	-4,67%	7,65%	5,04%
World % GDP	4,37%	-1,70%	1,84%	4,32%	4,38%	2,90%	2,19%	1,98%	4,34%	3,31%	3,33%	2,96%	3,03%	1,65%	1,79%
Crude Steel Growth	15,17%	-5,60%	4,08%	10,46%	11,21%	11,12%	9,92%	4,58%	0,08%	1,19%	3,35%	4,43%	9,59%	11,37%	
Crude Steel Production (ton)	29.148	25.304	26.806	25.754	23.315	18.288	16.467	14.981	14.325	14.313	13.624	13.183	12.624	11.519	10.343

Figure 21 Turkey steel industry developments during crisis period

Turkey	Average % (1993-2015)
Annual % GDP	4,07%
World % GDP	2,90%
Crude Steel Growth	5,17%
World Av.Steel Growth	3,82%

Figure 22. Turkey steel development, annual growth rate and world growth rate changes

IV. IRON & STEEL PRICES IN TURKEY AND CRISIS PERIODS' IMPACT ON STEEL PRICES

Annual average billet and ribbed bar FOB Turkey prices between 1995 and 2016 are shown in Figure 23 on a dollar / t basis (Metal Bulletin). Before the 2001 crisis, it was observed that average prices of steel prices declined by around 15% per year in 1998-1999, and prices rose rapidly until 2004 after the crisis. While there was a steady increase in the prices until the global crisis of 2008, except for 2005 and 2006, it was observed that the prices had fallen by 49% in 2009 due to the effect of the crisis

Despite the recovery in prices in the aftermath of the crisis in 2010 and 2011, the listed reasons such as the surplus capacity on the demand side in the iron and steel sector, the developments in the Chinese iron and steel sector and steel trade to all over the world from China, caused the prices to regress regularly between 2012 and 2014 and finally in 2015 about 27%.

Years	Billet FOB Turkey (USD/t)	Billet FOB Turkey (% Change)	Ribbed Bar FOB Türkiye (USD/t)	Ribbed Bar FOB Türkiye (% Change)
2016	362	-3,0%	395	-3,3%
2015	374	-27,1%	408	-26,7%
2014	512	-4,6%	557	-6,3%
2013	537	-8,5%	594	-6,1%
2012	588	-9,7%	633	-8,6%
2011	651	20,4%	693	19,8%
2010	540	31,6%	578	23,3%
2009	411	-49,1%	469	-48,8%
2008	807	54,7%	916	56,6%
2007	522	48,2%	585	19,4%
2006	352	0,2%	490	18,7%
2005	351	-5,8%	413	-7,2%
2004	373	51,8%	445	60,4%
2003	246	27,6%	277	28,0%
2002	193	13,6%	217	8,2%
2001	170	-4,1%	200	-3,8%
2000	177	6,5%	208	5,9%
1999	166	-15,1%	196	-14,5%
1998	195	-15,9%	230	-15,0%
1997	232	1,9%	270	1,8%
1996	228	0,3%	265	-2,7%
1995	228		273	

Figure 23. 1995-2015 Billet and ribbed bar FOB Turkey price changes

A regression analysis study was conducted in order to measure the effects of Turkey's liquid steel production, world liquid steel production, world annual growth rate and Turkey's annual% growth rates on Turkish steel prices in the 21-year period (1995-2015) of billet and ribbed bar prices.

As can be seen in Figure 24, we can formulate our regression model to be used in estimating billet prices as follows:

$$* \text{Billet Sales Price } (\$) = -13,84 -178,97*World \text{ Annual Growth}(\%) - 0,211*World \text{ Crude Steel Production}(\text{Mio ton}) +$$

$$279,94*Turkey \text{ Annual Growth}(\%) + 27,39*Turkey \text{ Crude Steel Production}(\text{Mio Ton})$$

Model	Unstandardized Coefficients		Standardized Coefficients		95,0% Confidence Interval for B		Correlations			Collinearity Statistics	
	B	Std. Error	Beta	Lower Bound	Upper Bound	Zero-order	Partial	Part	Tolerance	VF	
(Constant)	-13,848	128,742		-286,769	259,073						
worldgrowth	-178,974	2766,038	-0,013	-6042,712	5684,765	-0,1	-0,016	-0,009	0,423	2,366	
worldcrudesteel	-0,211	0,453	-0,375	-1,172	0,749	0,816	-0,116	-0,062	0,028	36,224	
Turkeygrowth	279,949	797,942	0,068	-1411,613	1971,51	0,072	0,087	0,047	0,47	2,127	
Turkeycrudesteel	27,397	18,47	1,206	-11,758	66,553	0,841	0,348	0,198	0,027	37,085	

a. Dependent Variable: billet

Figure 24. Billet FOB Turkey price movements regression analysis

As can be seen in Figure 25, the effect of the independent variables forming the regression model on billet prices can be explained as 84.5%.

Model	R	R Square	Adjusted R Square	Std. Error of the Estimate	Change Statistics				Durbin-Watson	
					R Square Change	F Change	df1	df2		Sig. F Change
1	.845 ^a	0,715	0,643	109,72506	0,715	10,019	4	16	0	1,283

a. Predictors: (Constant), worldgrowth,worldcrudesteel,Turkeygrowth,Turkeycrudesteel

b. Dependent Variable: billet

Figure 25. Billet FOB Turkey price movement regression analysis table

As can be seen in Figure 26, we can formulate our regression model to be used in the estimation of ribbed bar prices as follows:

$$* \text{Ribbed Bar Sale Price } (\$) = -13,299 - 297,79*World \text{ Annual Growth}(\%) - 0,072*World \text{ Crude Steel Production}(\text{Mio ton}) + 346,05*Turkey \text{ Annual Growth}(\%) + 22,63*Turkey \text{ Crude Steel Production}(\text{Mio Ton})$$

Model	Unstandardized Coefficients		Standardized Coefficients		95,0% Confidence Interval for B		Correlations			Collinearity Statistics	
	B	Std. Error	Beta	Lower Bound	Upper Bound	Zero-order	Partial	Part	Tolerance	VF	
(Constant)	-13,299	150,155		-331,613	305,015						
worldgrowth	-297,798	3226,093	-0,021	-7136,811	6541,214	-0,083	-0,023	-0,013	0,423	2,366	
worldcrudesteel	-0,072	0,529	-0,118	-1,192	1,049	0,796	-0,034	-0,02	0,028	36,224	
Turkeygrowth	346,051	930,658	0,078	-1626,856	2318,959	0,08	0,093	0,054	0,47	2,127	
Turkeycrudesteel	22,638	21,542	0,925	-23,03	68,305	0,813	0,254	0,152	0,027	37,085	

a. Dependent Variable: ribbed bar

Figure 26. Ribbed Bar FOB Turkey price movements regression analysis

As seen in Figure 27, the effect of the independent variables forming the regression model on the ribbed bar prices is calculated as 81.6%

Model	R	R Square	Adjusted R Square	Std. Error of the Estimate	Change Statistics				Durbin-Watson	
					R Square Change	F Change	df1	df2		Sig. F Change
1	.816 ^a	0,666	0,582	127,97495	0,666	7,971	4	16	0,001	1,177

a. Predictors: (Constant), worldgrowth,worldcrudesteel,Turkeygrowth,Turkeycrudesteel

b. Dependent Variable: ribbed bar

Figure 27. Ribbed Bar FOB Turkey price movement regression analysis table

V. CONCLUSION

The production of iron and steel products, which is the basic input of the industry, is one of the important indicators showing the development levels of the countries. Economic crises at global scale and/ or regional level, affect directly growth indicators of countries/regions, which also negatively affects the production of iron and steel products. As can be seen

in our study, production quantities of iron and steel products affected in parallel with the economic crises, can show a significant increase after crisis periods. However, in addition to the negative effects of the deep economic crises on the sector, it is also observed that many different parameters such as the production levels and/or prices fluctuates impact negatively to the sector.

China's iron and steel production policies (continuous increase in production volume and state incentives/protections), iron and steel product exports from China to all over the world, iron and steel production/consumption balance in countries' own domestic markets, the increased protectionism customs procedures, increased regional warfare and/ or instability are creating significant uncertainties about the future of the industry. The most fundamental way to convert all these uncertainties to the advantages, which are also influential in our country, is to switch idle production capacities and old production technologies to the production of value-added steel products.

REFERENCES

- Darican, M. F. (2015). Ekonomik Krizler ve Türkiye. *Istanbul Aydin University Magazine (İAÜD)*, 39-46.
- <http://www.oecd.org/sti/ind/steelcapacity.htm>. (2017).
<http://www.oecd.org/sti/ind/steelcapacity.htm> adresinden alındı
- İlhan, E. (2007). 1997 Güney Asya Finansal Krizi ve Güney Asya Ülkelerinde Emeklilik Sistemi Reformları: Türkiye ve Güney Asya Ülkeleri Bireysel Emeklilik Sistemlerinin Karşılaştırılması. *8th International Congress of Asian and North African Studies (ICANAS 38)*. Ankara, Türkiye: Atatürk Kültür, Dil ve Tarih Yüksek Kurumu.
- International Trade Administration. (2016). *Global Steel Report*. U.S. Department of Commerce.
- M. o. (2012). Iron-Steel, Iron-Steel Goods, Sector Reports. s. 0.
- Metal Bulletin. (tarih yok). *American Metal Market*. 02 20, 2017 tarihinde <https://www.metalbulletin.com/price-book.html> adresinden alındı
- Sarıgedik, İ. (2008). 1994-2001 Krizlerine Genel Bakış. Ankara: Ankara University, Social Sciences Institute, Department of Business Administration, Semester Project without Thesis.
- The World Bank. (tarih yok). *World Development Indicators*. 02 20, 2017 tarihinde <http://databank.worldbank.org> adresinden alındı
- Turgut, B. (2016). Steel Sector Impressions. *11. Turkish Steel Market Conference*. İstanbul: SteelOrbis.
- World Steel Association. (tarih yok). *Steel Statistical Yearbook*. 02 20, 2017 tarihinde <https://www.worldsteel.org/steel-by-topic/statistics/steel-statistical-yearbook-.html> adresinden alındı
- World Steel Association. (tarih yok). *World Steel in Figures 2016*. 02 20, 2017 tarihinde www.worldsteel.org adresinden alındı
- Yükseler, Z. (2009, Temmuz). *Economic Developments and Balance Adjustment in Crisis Periods in Turkey*.
- Yayan, D. (2016). Situation of Turkish Steel Industry. *11. Turkish Steel Market Conference*. İstanbul: SteelOrbis.

A Method for Assessment of Rust Preventive Oil on Galvanized Steel

Özgür KARAKAŞ^{a*}, Erdogan KANCA^b, Faruk CAVDAR^c, Alper AKÜN^a, İbrahim GÖÇER^a

^aMMK Metalurji San. Tic. ve Liman İşlt. A.Ş. Dortyol, Hatay, Turkey, okarakas@mmkturkey.com.tr

^bMechanical Engineering Department, Iskenderun Technical University, Hatay, Turkey, kancaerdogan@gmail.com

^cDepartment of Machinery, Iskenderun Technical University, Hatay, Turkey, cavdarf@gmail.com

Abstract— This paper proposes a new method for the assessment of performance of protective oil on galvanized and skin passed sheets. 11 different protective oil products were applied (1 g/m²) to hot dip galvanized and skin passed 66 sheet samples and subjected to Neutral Salt Spray Fog Testing (NSSFT) with 5% NaCl solution. Amount of white rust on the samples has been determined at 2, 6, 9 and 24 hours. Test results showed that application of NSSFT test for 9 hours gives best deterministic results.

Keywords— Carbon steel, Zinc, White Rust, Atmospheric corrosion, RPO, Rust Preventive Oil

I. INTRODUCTION

Protecting galvanized sheets from corrosion is very important in all usage areas of them, whether used as bare or painted [1]. Continuous layer of zinc forms a barrier against the effects of the atmosphere and cathodically protects the steel phase. However, usually white rust forms on continuous layer of zinc and causes deformations. It advances with time and formation of red rust begins on the surface after a while.

It is known that corrosion resistance of galvanized sheet changes, depend on the chemical composition of the coating layer. A galvanized coating including 5% Al and 0.1% Mg which increases corrosion resistance significantly have been developed by Yasuhide et al. They have demonstrated that corrosion resistance increased when Al percentage increased in the coating [2]. Prosek et al. have ranged corrosion resistance of some coating composition as; HDG (Zn-0.25% Al) < Zn-Al-Mg < Zn-Al-Mg-Si < Galfan (Zn-Al%5) < Zn-Mg [3].

Chemical composition of galvanized sheets depends mostly on the chemical composition of the liquid zinc in the zinc pot that, the sheet is dipped into. In Zinc-Iron alloy coated sheet (ZF) manufacturing, strip comes out of the zinc pot with a coating of 99% zinc content and subsequent annealing increases iron content to 8 % - 12 % in the coating. By this process the percentage of iron in the coating might increase to a total of 8 to 12% through Fe-Zn phases. While percentage of Al is approximately 5% in the layers of Zinc-Aluminium alloy coated sheets (ZA), Al is 55% and Si is 1.6% in the ones with Aluminium-Zinc alloy coated sheets (AZ) and Al is around 8%

and Si is around 11% in the ones with Aluminium-Silicium alloy coated sheets (AS) [4]. In addition to aluminium and Silicium, copper, tin, lead and nickel are the other widely used elements in coating alloys [5].

If galvanized sheet was designed to be painted, surface is roughened between 0.6 and 1.3 µm (Ra) by means of skin pass procedure in order to improve adhesion of paint coat to the galvanized sheet surface. After the sheet dipped into liquid zinc, it is taken out of the bath, excess zinc on the sheet's surface is scraped into the pot with air knives immediately and cooled in the cooling tower at a certain speed. This procedure creates a continuous coat of solid zinc with homogenous characteristics on the surface of the sheet. Then the sheet passed through skin pass rolls with roughened surfaces under pressure. This procedure spoils the smoothness of the surface of the coating, increases surface area to increase adhesion of paint, but it decreases the corrosion resistance of the zinc coating [6].

White rust forms easily on skin passed sheet due to increased surface area and its deformation. It forms a loose intermediate layer between the paint film and galvanized surface and this loose layer causes paint not to adhere to the sheets. Moreover, white rust on galvanized surface under paint film may cause some other problems such as cracking, roughening, and peeling off the paint film during shaping of the painted sheet [7].

During storage and shipment process, surface of the skin passed sheet is coated with corrosion protective oil up to 1 g/m² in order to prevent the white rust formation. Electrostatic lubricants are usually used for this process. These specially designed oils are hydrophobic materials which can form a perfect bound with zinc. They are easy cleanable in alkali cleaning units.

There are several protective oils to protect galvanised sheets available in the market. Therefore, it is imperative for the galvanized sheet manufacturers to decide the most suitable oil for their application in order to avoid customer complaints regarding white rust formation.

Although Neutral Salt Spray Fog Testing (NSSFT) method is weak for the simulation of natural corrosion due to the complexity and dynamic conditions of nature compared to NSSFT conditions [8], it is one of the most preferred methods due to providing fast results, monitoring development of corrosion visually and offering standard data. On the other hand, any study to provide a method for choosing corrosion protective oil for the best protection of galvanized sheet from rust formation has not been detected during literature survey.

This study examines the formation of white rust on surface of galvanized sheets when forced into corrosion with Neutral Salt Spray Fog (NSSF) and the effects of protective oil on corrosion resistance. In addition, this study proposes an evaluating method for choosing the correct protective oil for galvanized sheets.

II. EXPERIMENTAL STUDIES

A. Materials

Tests were conducted on samples cut from DX51D+Z grade steel sheet galvanized by hot dip method. Chemical compositions of used sheet, zinc pot and zinc coating are given in Table 1 to 3 respectively. Zinc coating thickness of the samples used in the study was 100 g/m².

Table 1

CHEMICAL COMPOSITION OF THE STEEL SHEET IN WEIGHT (%)

C	0.045
Si	0.024
Mc	0.234
P	0.011
S	0.005

Table 2

CHEMICAL COMPOSITION OF ZINC COATING IN WEIGHT (%)

Al	0.52153
Cd	0.00009
Sb	0.00004
Pb	0.00153

Table 3

CHEMICAL COMPOSITION OF ZINC POT IN WEIGHT (%)

Al	0.21135
Fe	0.01634
Cd	0.00009
Sb	0.00004
Pb	0.00151

Performance of 11 different mineral based protective oil samples from 6 different manufacturers were assessed in this study. Each oil product contains corrosion inhibitors and oil additives which the type and quantities of these agents are not

declared by the companies. Considering the principles of secrecy, manufacturing companies of oils were coded with capital letters and the protective oils, manufactured by these companies were coded with numbers. Data regarding these oil products are presented in Table 4.

Table 4

PROPERTIES OF OIL PRODUCTS USED IN THE STUDY

Manufacturing Company Code	Product Code	Density @20 °C (g/ml)	Flashpoint (°C)	Kinematic Viscosity @40 °C (mm ² /s)
A	A1	0,89	165	19,5
	A2	0,89	165	19,5
B	B1	0,86	198	42
C	C1	0,88	201	34
	C2	0,88	198	36
D	D1	0,91	196	60
	D2	0,89	214	36
E	E1	0,87	190	24
	E2	0,87	180	26

B. Devices and Equipment

Chemical analysis of the galvanized sheets was performed with Thermo Fisher brand optical emission spectrometer and composition of the zinc coating was analysed with Varian brand ICP-OES 710-ES axial spectrometer. Hommel Wave Werke System was used to measure the roughness of the surfaces of the sheets. Corrosion conditions for the study were provided by Sheen brand, FMC 1000 FogMaster model Cyclic Corrosion Cabinet. DJH MonoZoom Optical Microscope x50 was used for capturing images. Photographs were taken using Sony brand DSC-W530 model digital camera

C. Chemicals

In order to create the NSSFT medium in the corrosion cabin, 5% neutral brine solution was prepared with NaCl with analytic purity (Merck katalog No. 1.06404.9050) and ultra-pure water with a conductivity less than 0.1 µS/cm. HCl with analytic purity (Merck katalog No. 1.00317.2501) was used for dissolving zinc coating and some other tests.

D. Test and Assessment Method

Tests were performed on 11 different protective oil products, manufactured by 6 different manufacturers. These 11 products comprise approximately 95% of the total protective oil brands used for galvanized sheet sector. Totally 66 sheet samples are used considering the general applications and optimum application amount of electrostatic oilers. Amount of oiling was determined as 1 g/m².

Protective oil applied on panels manually and amount of oil on samples was determined by weighting precisely. Average oil

amount for all panels held in 8% positive deviation because it is impossible to get perfect amount. Realized oil amounts on each sample are presented on Table 5.

Table 5

AMOUNT OF WHITE RUST ON 1 G/M² PROTECTIVE OIL APPLIED GALVANIZED SHEETS

Test No	Protective Oil		Realized Amount RPO (g/m ²)	White Rust Amount (%)			
	Company code	Product Code		at 2 Hours	at 6 Hours	at 9 Hours	at 24 Hours
1	A	A 1	1.06	3	20	30	100
2	A	A 1	1.50	5	40	70	100
3	A	A 1	1.36	0	15	50	100
4	A	A 1	1.43	3	28	60	100
5	A	A 1	1.06	3	20	30	100
6	A	A 1	1.16	5	15	30	100
7	A	A 1	1.16	5	30	70	100
8	A	A 1	1.05	0	55	65	100
9	A	A 1	0.95	0	65	85	100
10	A	A 1	1.03	0	60	95	100
11	A	A 1	0.96	0	70	95	100
12	A	A 2	0.99	0	20	50	100
13	A	A 2	1.10	0	25	40	100
14	A	A 2	0.91	0	20	60	100
15	A	A 2	1.01	0	15	50	100
16	B	B1	0.98	0	0	10	60
17	B	B1	1.36	2	5	15	100
18	B	B1	1.06	0	3	15	100
19	B	B1	1.20	0	4	10	100
20	B	B1	1.00	5	20	60	100
21	B	B1	1.13	0	4	13	100
22	B	B1	1.36	2	5	15	100
23	B	B1	1.13	0	4	13	100
24	C	C1	1.10	3 2	48	82	98
25	C	C2	1.20	2 8	50	83	100
26	D	D 1	0.89	0	0	11	100
27	D	D 1	1.20	4	15	20	100
28	D	D 1	1.36	1	8	15	100
29	D	D 1	1.31	0	3	10	100

30	D	D 1	1.10	1	6	13	100
31	D	D 1	1.20	4	15	20	100
32	D	D 1	1.21	1	6	13	100
33	D	D 1	0.96	5	9	18	100
34	D	D 2	1.02	0	5	16	80
35	D	D 2	0.90	0	1	5	100
36	D	D 2	1.06	1	5	10	100
37	D	D 2	1.13	1	5	20	100
38	D	D 2	1.10	1	5	15	100
39	D	D 2	0.90	0	1	5	100
40	D	D 2	1.10	1	5	15	100
41	D	D 2	1.03	0	3	8	100
42	E	E1	1.31	1	4	10	95
43	E	E1	1.13	0	5	20	100
44	E	E1	1.10	0	15	40	100
45	E	E1	1.12	0	10	30	100
46	E	E1	1.25	1	4	10	95
47	E	E1	1.12	0	10	30	100
48	E	E1	1.06	0	35	85	100
49	E	E2	1.12	2	58	95	100
50	E	E2	0.98	3	75	100	100
51	F	F1	1.02	0	1	6	90
52	F	F1	1.06	1	5	13	90
53	F	F1	1.06	1	3	10	100
54	F	F1	1.13	0	1	7	100
55	F	F1	1.10	1	2	8	100
56	F	F1	1.06	1	5	10	90
57	F	F1	1.10	1	2	11	100
58	F	F1	0.96	0	3	12	100
59	F	F2	1.00	7	15	53	100
60	F	F2	1.20	2 5	30	35	100
61	F	F2	1.00	1 0	15	15	100
62	F	F2	0.83	1 5	35	80	100
63	F	F2	0.92	1 3	25	48	100
64	F	F2	1.20	2 5	30	35	100
65	F	F2	0.92	1 3	25	48	100
66	F	F2	1.06	2 5	65	85	100

1: Preparation of the Test Panels and Conditions of Neutral Salt Spray Fog Test (NSSFT) Cabin: Test samples with 150 mm x 200 mm dimensions were prepared and their surfaces were examined. Sample surfaces were controlled and the samples having surface defect were weeded out in order to eliminate the effect caused by improper samples.

Edges of the cut samples would be subjected to faster corrosion because of anodic reaction in neutral salt spray fog conditions. Therefore, edges of the samples were taped to isolate them. After applying the protective oil, the samples were placed in the cabin with an angle of 15° to vertical axis during all tests. Neutral brine solution with a 5% saturation was prepared with NaCl with analytic purity and ultra-pure water (conductivity <math><0.1 \mu\text{S}/\text{cm}</math>).

Fog density was determined by placing a volumetric measure with a funnel with 80 cm² surface area in the cabin. The air pressure is set for a fog density to get accumulation of 1-2 ml solution per hour on average and this pressure value was used for all tests. Thus, a standard corrosive medium was created by homogenising the fog density for all samples. The cabin was kept at constant 35 °C temperature and 100% relative humidity during all tests.

2: *Assessment of Neutral Salt Spray Fog Test: (NSSFT) samples by using the template method:* In order to assess the amount of corrosion, images of sample surfaces were taken from 20 cm distance by means of a high resolution digital camera. Then a grid with 100 equal boxes is placed on each image on computer. The number of boxes containing corrosion yields percentage of corrosion. Whether a box was full of corrosion or only a small part of it had corrosion, the box was considered as corroded. Results are disclosed as % white rust and % red rust. Considering that red rust forms after white rust, boxes with red rust (even if there was not any white rust seen) were counted as boxes with white rust. However, only the boxes with red rust are counted to get percentage of red rust. Thus, percentage of red rust cannot be more than white rust in template method. Fig. 1 to 3 show some samples, forced into corrosion in NSSFT cabin and assessed by the template method.

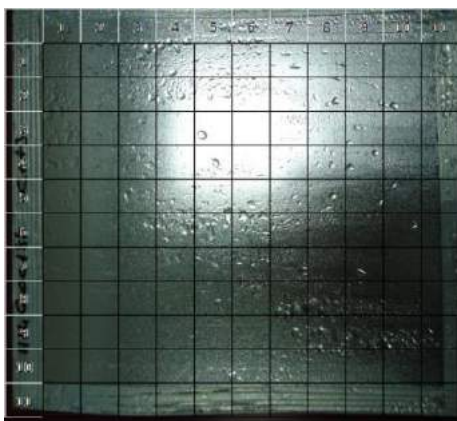


Fig. 6 White Rust = 0%, Red Rust = 0%

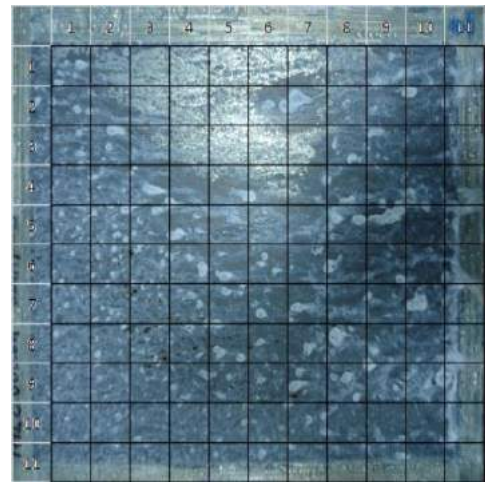


Fig. 7 White Rust = 100%, Red Rust = 0%

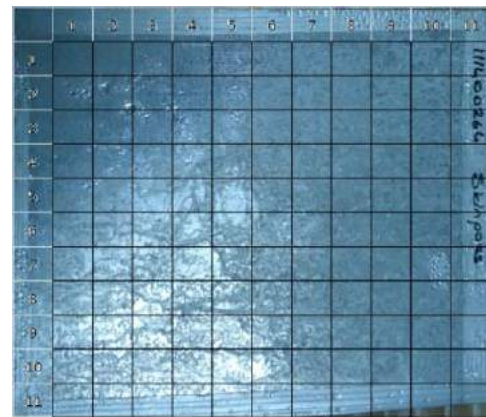


Fig. 3 White Rust = %100, Red Rust = 14%

III. RESULTS

E. Corrosion status of sheets, on which protective oil was not used

In order to determine the status of specimens without protective oil samples with skin pass without oil (blind) were forced into corrosion in the NSSFT cabin up to 24 hours. As seen in Fig. 4, observed white rust amount is 100% at 2 hours and red rust amount is 34% at 24 hours on blind panels.

F. Determining the protective performances from corrosion of protective oils

After application of 1 g/m² oil on a total of 66 samples, using 11 different protective oils, samples were forced into corrosion in NSSFT cabin. Formations of white rust in 2, 6, 9 and 24 hours were assessed and findings are provided in Table 6.

To get 95% reliability, extreme values belonging to each oil samples, which are highlighted on Table 3, were determined by Q test and eliminated. This has caused C1, C2, and E2 data to

be out of table completely. Average and standard deviation values for remaining oil products are listed in Table 6.

When Table 6 is examined, it is seen that standard deviations in average white rust amounts were low at the end of the first 2 hours and therefore 2 hours did not offer optimum data for an assessment. Furthermore, surface of many panels were completely covered with white rust in 24 hours and amount of corrosion reached 100% white rust or became very close to this value at the end of 24 hours. Such as the data at the end of 2 hours, the data at the end of 24 hours are devoid of providing significant differences for a distinctive assessment.

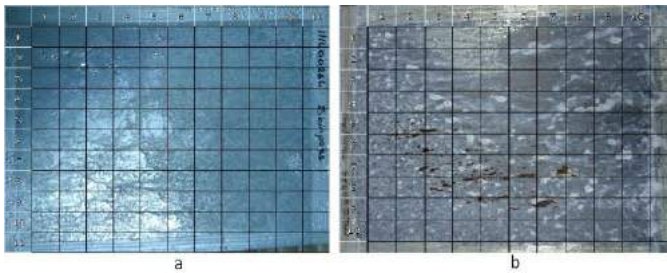


Fig. 4 When blind samples were forced into corrosion in the NSSFT cabin, 100% white rust and 0% red rust was observed in 2 hours (a) and 100% white rust and 34% red rust was observed in 24 hours (b).

Data at 6th and 9th hours yield higher standard deviation in comparison to the data at 2nd and 24th hours and the average white rust formation percentage at 6th and 9th hours comprise more suitable distinctiveness amounts in terms of visual distinctiveness.

It can be seen that 9th hour data offer both higher amount of average white rust data and have relatively higher standard deviations when the most suitable one among 6th and 9th hour data are examined to determine the protective performance of the oil. So, application of NSSFT for 9 hours can be suggested for the most distinctive determination of performance of protective oil products on galvanized and skin passed sheets.

According to Table 6 data, the oil with the highest performance for protection of galvanized sheets against white rust is F1 oil means the 1st oil of the manufacturer F.

Table 6

AVERAGE CORROSION AMOUNTS AND STANDARD DEVIATIONS FOR PROTECTIVE OILS

Product Code	Realized Amount of Oil (g/m ²)		White Rust Amount							
			at 2 hours		at 6 hours		at 9 hours		at 24 hours	
	Average	Std Dev.	Average	Std Dev.	Average	Std Dev.	Average	Std Dev.	Average	Std Dev.

A1	1.15	0.22	1.79	2.38	49.64	17.14	77.14	14.39	100.00	0.00
A2	1.00	0.08	0.00	0.00	20.00	4.08	50.00	8.16	100.00	0.00
B1	1.17	0.14	0.57	0.98	3.43	1.69	12.86	2.25	94.29	15
D1	1.17	0.19	0.40	0.42	4.40	3.03	12.20	1.89	100.00	12
D2	1.03	0.09	0.50	0.53	3.75	1.83	11.75	5.55	97.50	7.07
E1	1.17	0.09	0.33	0.52	8.00	4.43	23.33	12.11	98.33	2.58
F1	1.06	0.05	0.50	0.46	2.75	1.58	9.63	2.45	96.25	5.18
F2	1.04	0.13	15.33	0.76	23.33	6.83	38.83	13.77	100.00	0.00

IV. CONCLUSION

Protective oil is used to prevent white rust formation on galvanized sheet. Choosing the protective oil with the highest performance has critical importance for galvanized sheet manufacturers to overcome problems related to white rust formation. A method for comparing corrosion protective oil on galvanized and skin passed sheet suggested as:

- 1) Approximately 1 g/m² protective oil might be applied on the samples
- 2) The samples should be kept in NSSFT cabin with 5% brine NaCl solution hold at 35 °C temperature and 100% relative humidity for 9 hours.
- 3) Formation of white rust might be assessed and compared using template method mentioned in section 2.4.2.

ACKNOWLEDGMENT

This study was supported by MMK Metalurji San. Tic. ve Liman İřlt. A.ř. The authors would like to thank for supplying the sheet and oil product samples and utilisation of laboratories.

REFERENCES

- [1] Jandel L.T.// La Metallurgia Italiana. 2012. V. 1. P. 17.
- [2] Morimoto Y., Honda K., Nishimura K. ET AL./ Technical Report. Excellent Corrosion – resistant Zn-Al-Mg-Si Alloy Hot-dip Galvanized Steel Sheet Super Dyma. Nippon Steel. 2003. No. 87. P. 24.
- [3] Prosek T., Persson D., Stoulij J. et al.// Corrosion Science. 2014. V. 86. P. 231.
- [4] DIN Deutsches Institut für Normung/ Standard. Continuously hot-dip coated steel flat products – Technical delivery conditions. 2009. Berlin. Beuth Verlag GmbH. 2009. 41 PP.
- [5] Vourlias G., Pistofidis N., Stergioudis G. et al.// Crystal Research and Technology. 2004. V. 39. P. 23.
- [6] Riener C.K., Preis K., Achammer E., Angeli G./ 8th International Conference on Zinc and Zinc Alloy. Coated Steel Sheet Nano Characterisation of the Surface of HDG Zn-Al-Mg Coated Steel Sheets. Genova. 2011.
- [7] Gordon L. N./ Paint and Coating Testing Manual. ASTM International, 1995, P. 516.
- [8] ASTM International./ Standard. ASTM B117-11. Materials, Standard Practice for Operating Salt Spray (Fog) Apparatus. West Conshohocken PA. 1985.

Interlaboratory Proficiency of Tensile Test for Reinforcing Steel Related to ISO 6892-1

Alper INCESU, Betül USTA*

Karabük University, Iron and Steel Institute, 78050, Karabük, TÜRKİYE
alperincesu@karabuk.edu.tr , betulusta@karabuk.edu.tr

Abstract— The accuracy and reliability of the tests and analyses applied by the laboratories are audited and recorded in accordance with ISO 17025 standard. The proficiency test stipulated by the standard are also an indication of how well the applied laboratory method has been applied by the laboratory concerned. In this study, calculations and the results of calculations related to the performance evaluations for proficiency test organized with the participation of different laboratories in accordance with ISO 6892-1: Tensile Test Standard in Metallic Materials at Room Temperature. The Z-scores of the laboratories were calculated as a result of deviations from the test machine and the expert, regardless of the similar feature specimens of reinforcing steel sent to all participants.

Keywords— proficiency test, tensile test, reinforced steel

I. INTRODUCTION

Engineering materials are deformed under force because they are not rigid and show shape and size changes. Mechanical tests are performed to understand the material properties. The most important of these is the "tensile test".

The purpose of the tensile is determined elastic and plastic behaviour of materials under static load. For this purpose, circular or rectangular test piece that have dimensions in accordance with the standards are connected to the tensile testing machine then axial and variable forces are applied. The tensile test machine mainly comprises: Consists of two jaws connected by the test piece which can move up and down with respect to each other and units measuring these two sizes. By moving one of the jaws at constant speed, a tensile force is applied to the test piece in variable amounts, and the corresponding elongation is recorded.

Main parameters that are reported as a result of tensile test are; yield strength ($R_{p0.2}$) in N/mm^2 (MPa) , tensile strength (R_m) in N/mm^2 (MPa) and percent elongation at break in (A). When these parameters are not properly detected, it becomes the main cause of many mechanical failures. To avoid such problems, accurate tensile test performances of products is therefore very important. To be able to perform a "correct" tensile test the designer needs reliable material data.

However, reliable tensile test data is hard to get, there are so many sources that affect the results. Therefore quality assurance activities for tensile testing are important. One such quality assurance activity is proficiency test. Proficiency test help the laboratories to improve their performance as well as to give the customers information about how reliable tensile test data are [1]. According to ISO 17025 standard testing

laboratories should have quality control procedure. Participation in proficiency test or proficiency-testing is one of the quality control procedures that testing laboratories supposed to adopt [2].

Proficiency test is an external way of assuring quality control among laboratories. It allows the participants to detect unsuspected errors and deficiencies in their methodology [3]. Beside this, it has benefits for identification of proficiency differences and education of participating laboratories based on the outcomes of such test. Such a quality assurances need is not only essential for laboratories and their customers but also for other interested parties, such as regulators, laboratory accreditation bodies and other organizations that specify requirements for laboratories [4].

In this study, methodology, calculations and results of an proficiency testing for tensile test of reinforcing steel related to ISO 6892-1 [5] that organized by Karabuk University Iron and Steel Institute MARGEM Laboratories was reported.

II. TECHNICAL PROTOCOL

First of all, the technical protocol was prepared and it was sent to all participant laboratories. It includes the preparation of the test samples, distribution of them to the laboratories, time table for the tests, test reports and test requirements [6].

III. PARTICIPANTS

Nine different test laboratories have participated to this proficiency testing in Turkey. All laboratories declared to provide all special requirements of tensile test during measurements.

IV. EXPERIMENTAL

The participants received information about the test specimens (without material data) together with the following instructions:

- Tensile test will be performed related to ISO 6892-1 standard: Metallic materials - Tensile testing - Part 1: Method of test at room temperature [5].
- All participants get three identical S420 quality reinforced steel with a nominal diameter of 12 mm and length of 450 ± 20 mm.
- Test length of the specimens was taken as 60 mm.

- Yield strength ($R_{p0,2}$) in N/mm^2 (MPa) , tensile strength (R_m) in N/mm^2 (MPa) and percent elongation at break in (A_{60}) will be reported for all specimens, respectively.

V. RESULTS

Reports of the completed tests by each laboratory were sent to the organizer laboratory which is Karabuk University Iron and Steel Institute MARGEM Laboratories. MARGEM evaluated all test reports according to ISO/IEC 17043 standard [4]. Depending on the privacy contract, the names of the participants will only be expressed in codes. In given figures and tables, each laboratory is represented with a letter as A, B, C, D, E, F, G, H and I. Average values of results of all laboratories were taken as reference values.

The results of the three samples to which each participant was sent, the average values and the standard deviations of the participants own experiments, together with the average values and the standard deviations, are shown in Table 1, Table 2 and Table 3 for yield strength, tensile strength and percent elongation at break [7].

Participants were found to have consistent results in the samples they tested when looking at standard deviations from their experiments, $R_{p0,2}$ for yield strength, R_m for tensile strength, and A for code percent elongation at break.

TABLE I
DISTRIBUTION RANGES OF YIELD STRENGTHS ($R_{p0,2}$) FOR THE PARTICIPANT LABORATORIES [7]

Participant Laboratory Codes	Result 1	Result 2	Result 3	Mean Value	Standard Deviation
	MPa				
A	479,0	483,0	490,0	484,0	5,57
B	491,0	498,0	495,0	494,7	3,51
C	508,4	494,1	510,7	504,4	8,99
D	486,0	479,0	514,0	493,0	18,52
E	476,4	485,4	467,9	476,6	8,75
F	478,1	471,2	474,1	474,5	3,48
G	485,0	488,0	484,0	485,7	2,08
H	483,3	482,0	481,2	482,2	1,08
I	495,0	490,0	488,0	491,0	3,61
	General Mean Value			487,3	
	General Standard Deviation			9,44	

TABLE II
DISTRIBUTION RANGES OF TENSILE STRENGTHS (R_m) FOR THE PARTICIPANT LABORATORIES [7]

Participant Laboratory Codes	Result 1	Result 2	Result 3	Mean Value	Standard Deviation
	MPa				
A	638,0	626,0	640,0	634,7	7,57
B	653,0	657,0	683,0	664,3	16,29
C	652,5	641,8	657,5	650,6	8,02
D	636,0	636,0	671,0	647,7	20,21
E	625,8	640,5	644,7	637,0	9,92
F	636,8	637,8	641,7	638,7	2,58
G	627,0	649,0	650,0	642,0	13,00
H	634,7	631,0	631,1	632,3	2,15
I	651,0	652,0	655,0	652,7	2,08
	General Mean Value			644,4	
	General Standard Deviation			10,30	

TABLE III
DISTRIBUTION RANGES OF PERCENT ELONGATION AT BREAK (A_{60}) FOR THE PARTICIPANT LABORATORIES [7]

Participant Laboratory Codes	Result 1	Result 2	Result 3	Mean Value	Standard Deviation
	%				
A	27,1	27,4	28,0	27,5	0,46
B	20,9	20,8	20,1	20,6	0,44
C	30,3	29,3	27,3	29,0	1,53
D	28,5	30,0	29,3	29,3	0,75
E	27,0	26,0	26,0	26,3	0,58
F	13,9	12,9	13,5	13,4	0,50
G	22,0	20,0	20,0	20,7	1,15
H	30,0	28,0	28,0	28,7	1,11
I	21,3	24,2	22,9	22,8	1,45
	General Mean Value			24,2	
	General Standard Deviation			5,33	

The Z-score measures the deviation of the result of each laboratory from the “true” value, by test with a reference standard deviation and is given by the formula:

$$Z=(x-X)/S \quad \text{Equation 1.}$$

Where;

x : mean value of the results of the participant laboratory
 X: value assumed to be true (it employed the mean of the results of all participants, after excluding the outlier values.)

S: standard deviation of the mean of the results, after exclusion of the stragglers and/or outliers values

Criteria for performance evaluation should be established after taking into account whether the performance measure involves certain features. The features of Z-scores for performance evaluation are the following [4];

- $|Z| \leq 2$ indicates “satisfactory” performance
- $2 < |Z| < 3$ indicates “questionable” performance
- $|Z| \geq 3$ indicates “unsatisfactory” performance

The Z-scores that express the performances of the participants for yield strength, tensile strength and percent elongation at break were given on Table 4, together. Also Z-scores were graphically expressed in Figure 1, Figure 2 and Figure 3, separately for $R_{p0,2}$, R_m and A_{60} .

TABLE IV
CALCULATED Z-SCORES OF ALL PARTICIPANTS FOR ALL TENSILE TEST RESULTS [7]

Participant Laboratory Codes	$R_{p0,2}$	R_m	A_{60}
A	-0,35	-0,95	0,61
B	0,78	1,93	-0,68
C	1,81	0,60	0,89
D	0,60	0,31	0,94
E	-1,14	-0,72	0,39
F	-1,36	-0,55	-2,03
G	-0,18	-0,24	-0,67
H	-0,55	-1,18	0,83
I	0,39	0,80	-0,27

For Z-score of yield strength, all participant laboratories had $|Z| \leq 2$. So, no laboratories need to check their test systems. For Z-score of tensile strength, also all participants had $|Z| \leq 2$. So, their results are gratifying. At last, for Z-score of percent elongation at break one participant had $2 < |Z| < 3$. This laboratory was F. Thus this laboratory should need to questionable their results and then check their test procedure and test systems top to bottom.

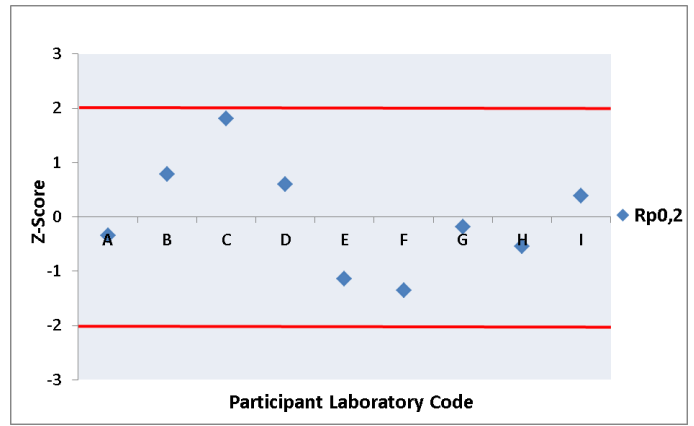


Fig. 1 Z-Score Distribution of Participant Laboratories for Yield Strength ($R_{p0,2}$)

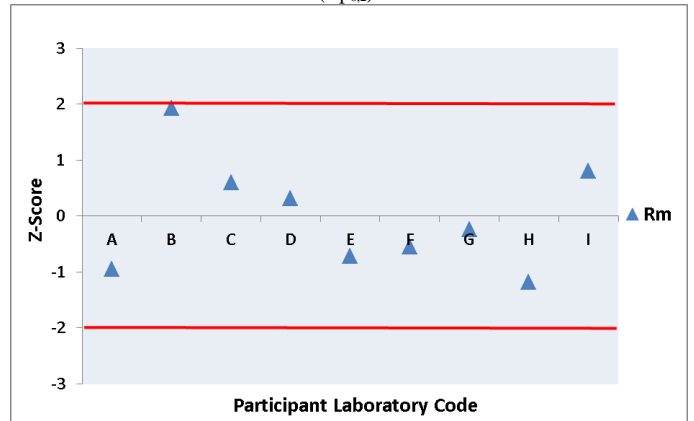


Fig. 2 Z-Score Distribution of Participant Laboratories for Tensile Strength (R_m)

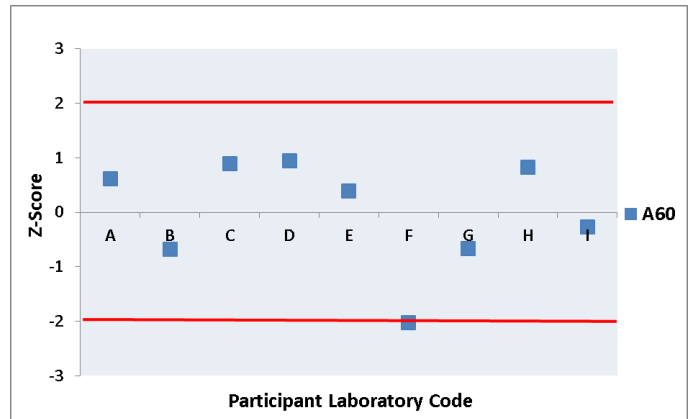


Fig. 3 Z-Score Distribution of Participant Laboratories for Percent Elongation at break (A_{60})

VI. CONCLUSION

Nine (9) different laboratories have participated in to the proficiency test of tensile test for yield strength, tensile strength and elongation at break of S420 reinforced steel. Karabuk University Iron and Steel Institute MARGEM Laboratories has organized Proficiency test in 2016. Initially, technical protocol and test samples were prepared and sent to the participant laboratories. Test measurements carried out in accordance with technical protocol. After each laboratory completed all tests, the test reports were sent to MARGEM. All test reports were

evaluated by MARGEM according to ISO 17043 standard. All participants were successful except for a laboratory (F) outside a parameter (A_{60}). In order to verify testing capability of the test laboratories, the proficiency tests are very important for assessment of the tensile test measurement capabilities of all laboratories and it should be repeated periodically.

REFERENCES

- [1] Inter-laboratory test of fatigue test with evaluation of the participating laboratories calculations of measurement uncertainty (Nordtest-project 1591-02), Thomas Svensson Magnus Holmgren, Klas Johansson and Erland Johnson, 2003
- [2] EN ISO 17025 General requirements for the competence of testing and calibration laboratories, 2005
- [3] Proficiency Test of Analytical Results a Measure of Quality Control, Conceição Fonseca, Dra. Rosário Amaral and Rui Lucas of CTCV – Technological Centre of Ceramic and Glass – Coimbra – Portugal, vol:14 No:1
- [4] EN ISO/IEC 17043, Conformity assessment - General requirements for proficiency testing, 2010
- [5] ISO 6892-1, Metallic materials - Tensile testing - Part 1: Method of test at room temperature, 2009
- [6] Usta , B., Incesu, A., Turan, M. E., Proficiency Test Tests Technical Protocol, 2016
- [7] Usta , B., Incesu, A., Turan, M. E., Proficiency Test Tests Final Report, 2016

The Wear Performance of Tool Steel (AISI M2) Coated with TiAlN by DC Reactive Magnetron Sputtering Technique

Şengül Danışman^{1*}, Oğuzhan Bendeş², Soner Savaş³

¹Erciyes University, Faculty of Engineering,

Department of Mechanical Engineering, Kayseri, Turkey

sdanisman@erciyes.edu.tr (*correspondingauthor)

²TEMSAN, Turkish Electromechanics Industry,

Department of Technology Development, Ankara, Turkey

oguzhan.bendes@temsan.gov.tr

³Erciyes University, Faculty of Engineering,

Department of Material Science and Engineering, Kayseri, Turkey

ssavas@erciyes.edu.tr

Abstract— In this study, TiAlN coating obtained by using the magnetron sputtering method was deposited on M2 tool steel samples using selected parameters (0, -100V and -200V bias voltages and 0.3 mtorr, 0.6 mtorr, 1.2 mtorr pressures). The characterization was done and wear properties of the coatings were investigated. The distance between the target and the coating was kept constant during the operation. Hardening and nitriding processes were applied to the base material. The coating characteristics of hardened and hardened + nitrided samples, surface properties and wear behaviors were compared. The best results for the coating characteristics were determined. It was found that the hardened + nitrided of AISI M2 samples with high nitrogen pressure (0.3 mtorr) gave the best wear resistance which resulted in a decreased coefficient of friction and a reduction in wear rates.

Keywords— Magnetron sputtering method, TiAlN, M2 steel, Wear, Coatings characteristics

I. INTRODUCTION

Wear is one of the most important problems in manufacturing industry. The behavior of friction and wear characteristics is as important as other mechanical and chemical characteristics in cutting tools. The most important cause of wear is friction due to surfaces moving against each other. Friction is caused when surfaces are moved relative to each other or two surfaces are forced to move in spite of resistance to movement. The main factors to increase wear are pressure, sliding rate, coefficient of friction, surface morphology, modulus of elasticity, strength of material, resistance of fatigue and corrosion.

Surface coatings provide wear and corrosion resistance, design flexibility and many features for materials and as a result have found many application sectors in industry in general, and in the manufacturing industry in particular [1]. They have been increasingly in demand by this industry in recent years due to their properties to reduce loads (mechanical, thermal, etc.), ensure longer operating life, reduce weight and friction, and

increase corrosion resistance in tools [2]. Studies on this issue have revealed that friction and wear characteristics are optimized by applying surface and coating methods but the use of classic coating methods suffer from problems of adhesion. However, PVD methods have a lower processing temperature and good substrate and bond strength and, as a result, PVD methods are preferred to classic coating methods [3]. The PVD process can be applied at temperatures lower than 250 °C. For the purpose of this study, a hard ceramic coating (TiAlN) was performed on selected AISI M2 samples which were used in different tools so as to obtain a low friction coefficient, to achieve good wear advantage and to increase performance.

II. COATING METHOD

The PVD (Physical Vapor Deposition) method is mainly based on sputtering and evaporation in the materials under vacuum and involves the removal of atomized material from the substrate surface after the bombardment of its surface layer by ions or atoms. In general the PVD method has two processes: sputtering and evaporation. Sputtering is basically the removal of atomized material from a solid by energetic bombardment of its surface layer which is dependent on the exchange of momentum. The high energy particles used are usually those of a heavy inert or reactive gas (argon, the most commonly used inert gas) or the coating material forms a positive ion. The sputtering material is thrown in an atomic state from the coating material which is called the target. The base material is placed in front of the target to interrupt the flow of sputtered atoms [1]. Fig. 1 shows the principle of the DC sputtering method. Magnetron sputtering is a coating technique that is used to produce thin films with magnets placed behind the target in order to limit the plasma; also, the film layer has different properties and is achieved by changing the deposition

parameter and target (coating material supply) configurations. The magnetron sputtering method was used in this study.

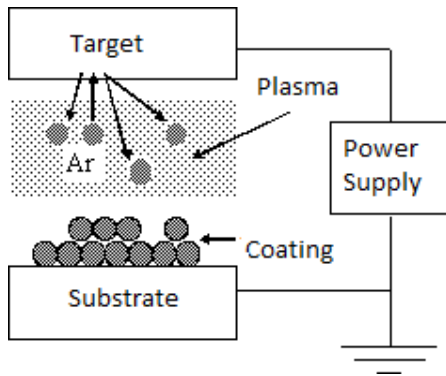


Fig. 1 Principle of the DC sputtering method

III. EXPERIMENTAL STUDY

A. Sample Preparation

The samples were prepared from the base material AISI M2 (DIN S 6-5-2) whose chemical composition is shown in Table I. They were 21 mm in height and had a diameter of 8 mm. Some of the samples were hardened and others were hardened + nitrided before coating. The plasma nitriding parameters are given in Table II. Before being placed in the vacuum chamber, the samples were mechanically polished and ultrasonically cleaned in alcohol and also in acetone for 10 minutes each, and then dried. The samples were coated with TiAlN by using the PVD- magnetron sputtering method. The distance between the target and the coating was kept constant (11 cm) during the coating process. The TiAlN coatings were produced at different nitrogen (N₂) pressures (0.3, 0.6, 1.2 mtorr) and bias voltages (0, -100, -200 V) by using a TiAl compound target (atomic Ti 50%-Al 50%). Then all the coated samples were examined for their structural, mechanical and tribological properties and the coating parameters were investigated as to the effect of coating properties.

The coating adhesion characteristics were measured with a CSEM scratch tester and a multi-pass sliding wear system, "Rugosimeter Wear Profile Measurement Device" was used to examine wear behavior. The coatings obtained with different parameters were examined by comparing their tribological and mechanical properties and comments were made. The cross – sections of nitrided AISI M2 steel samples were examined and the diffusion and white layer thickness (69.32 and 3.44 μm respectively) were also determined by SEM as shown in Fig. 2. The hardness of the diffusion layer was measured from the surface of the sample after removal of the white layer by a Struers microhardness device under load of 100 g. The measurement result shows that the hardness of the diffusion layer for AISI M2 is approximately 1440 HV. The results obtained are summarized in Table III and in Table IV.

The coating process applied to AISI M2 and the silicon wafer was conducted as follows: A pressure of 5 mtorr (~25 sccm) and target power of 4500 W were used for about 5 minutes to clean the target (with dimensions of 645 mm x 110 mm x 10 mm). The samples were then cleaned by dc sputtering for about 25 minutes using a pressure of 5 mtorr, a target power of 150 W and voltage of -750 V of the base material.

TABLE I
CHEMICAL COMPOSITION OF MATERIAL USED IN EXPERIMENTAL STUDY

Elem. (%)	C	Si	P	Co	Mn
M2 Steel	0.92	0.31	0.03	0.83	0.27
Ni	Cr	Mo	V	W	Fe
0.29	3.88	4.66	1.66	5.87	Bal.

TABLE II
PARAMETERS OF PLASMA NITRIDING PROCESS

Time (hr.)	Temp. (°C)	N ₂ /H ₂ ratio	Pressure (Pa)
10	500	4/1	200

TABLE III
HARDNESS OF SAMPLES BEFORE AND AFTER HARDENING AND THE ROUGHNESS AFTER POLISHING

Mat.	Hardn. before hardening (Base material)	Hardness after hardening	Roughness R _a (μm)	
			Hardn.	Hard. + Nitrided
M2	252 HV	794,8 HV	0.05	0.14

TABLE IV
CHARACTERISTICS OF THE SAMPLES AFTER PLASMA NITRIDING

Mat.	Thickness of diffusion layer (μm)	Thick. of white layer (μm)	Hard. of diffusion layer (HV)	Hardness of base mate. (HV)
M2	69.32	3.44	1440	794.8

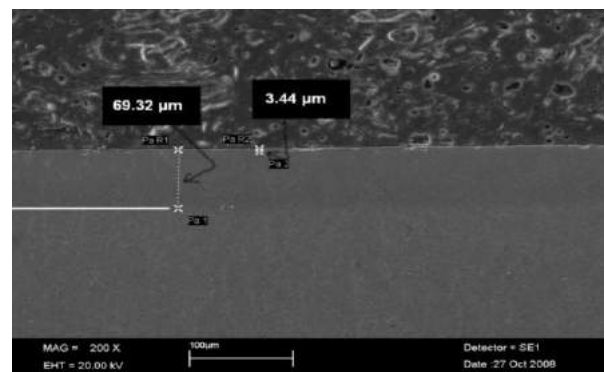


Fig. 2 Cross-sectional SEM image of plasma nitriding of AISI M2 steel

First of all, the TiAl coating was applied at a target power of 4000 W and 15 sccm argon flows for 30 seconds and then the TiAlN coating was applied using a target power of 4000 W and argon + N₂ atmosphere in the coating process. Different N₂ pressures and bias voltages were chosen as coating process parameters. The coating process was repeated for 0.3, 0.6 and 1.2 mtorr nitrogen pressures and 0, (-) 100 and (-) 200 V bias voltages. The total operating (Ar+N₂ pressure) pressures were, respectively, 1.8, 2.1 and 2.7 mtorr. The distance between the samples and the target was 11 cm using a stainless steel holder which was fixed in front of the TiAl target during the coating process. The coating parameters for the AISI M2 base material are summarized in Table V.

TABLE V
COATING PARAMETERS FOR AISI M2 BASE MATERIAL

Coa. No	Bias Voltage (V)	N ₂ Pressure (mtorr)	TiAl Target Power (W)	TiAl Coating Time (sec.)	TiAlN Coating Time (min.)
1		0.3			
2	0	0.6	4000	30	45
3		1.2			
4		0.3			
5	100	0.6	4000	30	45
6		1.2			
7		0.3			
8	200	0.6	4000	30	45
9		1.2			

B. Wear Tests

The wear tests of the AISI M2 samples coated with TiAlN were performed on a CSEM – Revetest scratch tester and used multi-pass sliding wear tests. Al₂O₃ ceramic balls with a diameter of 3.175 mm and a hardness of 1365 HV were used as wearing part in the wear tests. The normal force, F_N was kept at a constant rate (15N), and a sliding distance of 2 mm for the table feed rate control was provided by the computer. In similar studies in the literature, when the scratch tester is used for multi-pass sliding wear testing, the appropriate load range is selected depending on the coating adhesion resistance[4-6]. For this reason, the wear load value is selected as 15 N.

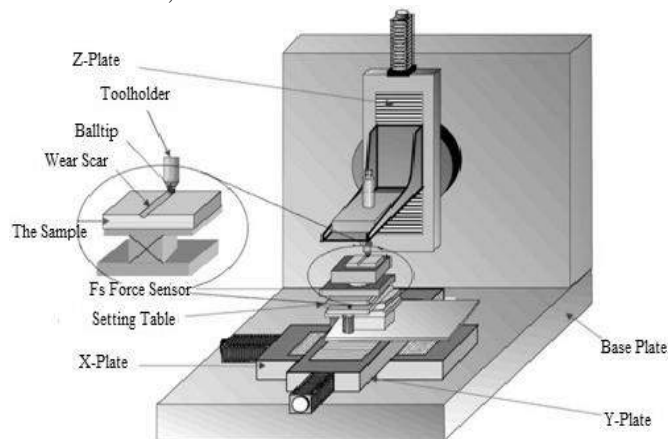


Fig. 3 Schematic diagram of the wear device

Friction force (F_s) depending on sliding distance was recorded simultaneously. A schematic diagram of the device is given in Fig. 3.

The normal force depending on sliding rate and sliding distance was selected. After the full movement of the ball on the sample (Fig. 4a) was completed, the tip automatically returned to the starting point and then the second cycle started again by computer control. This cycle continued until the number 100 was reached. The trajectory of the wear element is shown in Fig. 4b. The results of the wear test obtained the wear volumes of the samples from profilometer measurements which were used to calculate wear rate as a measure of wear.

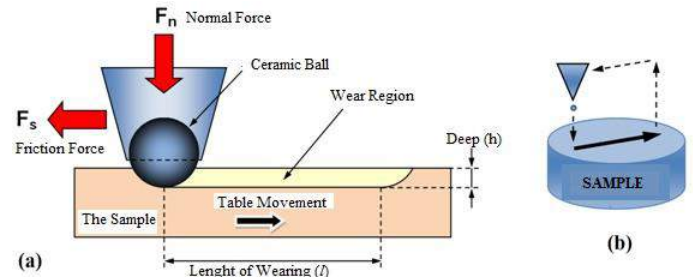


Fig. 4 a) The geometry of the contact and forces of wear element-samples used in wear tests, b) the trajectory of the wear element

III. EXPERIMENTAL RESULTS AND DISCUSSION

The coating thickness of the samples was determined by examining the SEM images of the silicon wafers. The deposition rate of the samples was calculated in terms of nm/min taking into account 45.5 minutes of coating time(the thickness of metallic coating was added to the total of the coating thickness). In addition the CSEM Calotest coating device measured the samples, thickness and approximately verified them. The thickness of the coatings and deposition rates are summarized in Fig. 5.

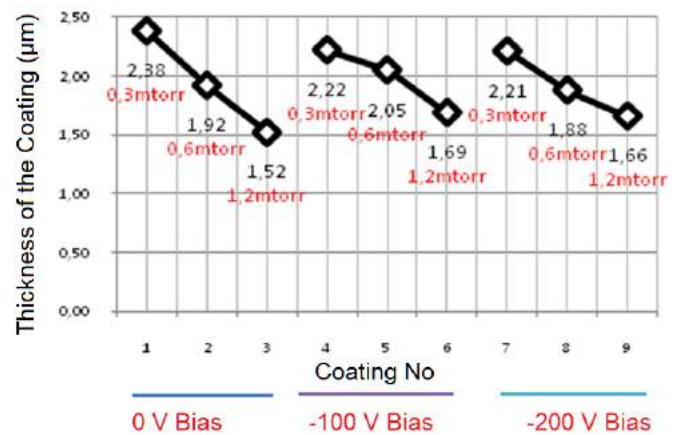


Fig. 5 Thickness of TiAlN coatings deposited on silicon wafers

The silicon wafer cross-sectional SEM images of the coatings (0V, -100V, -200 V bias voltages) are shown in Fig. 6. The thickness of the coatings is very stable and has a relatively columnar structure which can be seen on the images. The coating parameters are given according to deposition rate change in Fig.7 which shows a decrease in nitrogen pressure as the deposition rate increased.

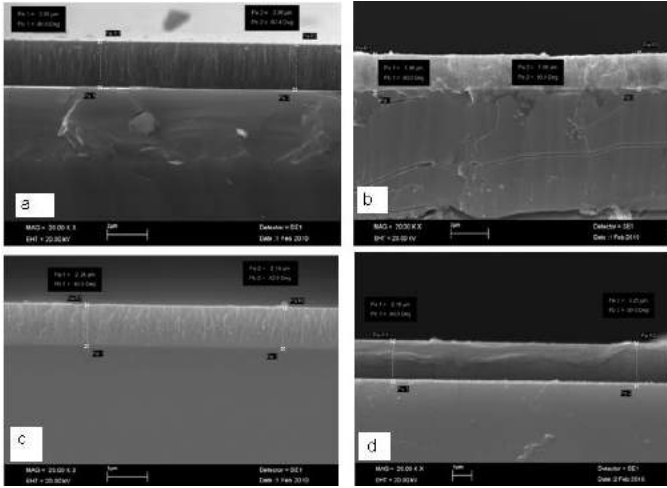


Fig. 6 (a) Sample no 1 (0V, 0.3 mtorr) cross-sectional view, (b) sample no 2 (0V, 0.6 mtorr) cross-sectional view, (c) sample no 4 (-100V, 0.3 mtorr) cross-sectional view, (d) sample no 7 (-200V, 0.6 mtorr) cross-sectional view

This result is also consistent with that found by Wuhrer et al [7]. They reported that the deposition rate of the coatings decreased at high nitrogen pressure. The poisoning of the magnetron targets, and reducing the number and kinetic energy of the species approaching the substrate caused, besides grain structure are the more coarser than at low nitrogen pressures. On the other hand, the bias voltage applied to the samples can be an important parameter and closely affects film density, particle size and morphology [8]. Tanaka et al. were pointed out that TiAlN coatings deposited by reactive magnetron sputtering at zero bias voltage were associated with an open porous columnar structure resulting in inferior hardness [9]. Hakansson et al. however reported that as the bias voltage increased, this open porous columnar structure was suppressed with a substantial hardness enhancement [10]. The thickness of the coating was not affected by change in bias voltage in this study.

The hardnesses of deposited TiAlN coatings on silicon wafers were measured in accordance with the Oliver –Pharr method by a CSEM nano-hardness tester using a square-based diamond Vickers tip. Increasing the coating hardness with bias voltage at different pressure values (0.3, 0.6, 1.2 mtorr) did not result in further changes. This result is similar to the hardness results of nitride coatings in another study which showed that a significant change cannot be achieved by increasing the applied bias voltage on a base material [11]. Also, in the literature [12], it was found that hardness could be improved in samples with a high percentage of nitrogen as was seen in this study. In addition, the graphs in Fig. 7 and Fig. 8 show that the hardness

of the samples is comparably lower which have higher Al% ratio (number of 1 and 7). It is noted that the current hardness values of the TiAlN films on Si wafer slides are lower than those depositions on steel substrates due to substrate effects [8].

Scratch tests for the AISI M2 samples were subjected to test strength of 150 N (duration 1 min.), for a distance of 15 mm by the CSEM Revetest scratch tester. The Rockwell C type, which has a 200 μm radius tip and a 120° angle conical diamond tip, was used in the tests. A load application rate of 100 N/min and a scratch rate of 10 mm/min were used. The appropriate emission graph can be obtained by changing acoustic emission intensity between 0-1.2. The results for the critical load (Lc) of the base material according to different pressure values at different bias voltages are shown in Fig. 9. In general, the results of the samples showed that the critical load (Lc) values of the nitrided samples were higher. This result shows that coating bonded to the base material with better adhesion in the nitrided samples of the base material. Increasing surface roughness for better adhesion force and increasing the strength of the base material to prevent deformation resulted in the increased adhesion of the coating layer by the nitriding process.

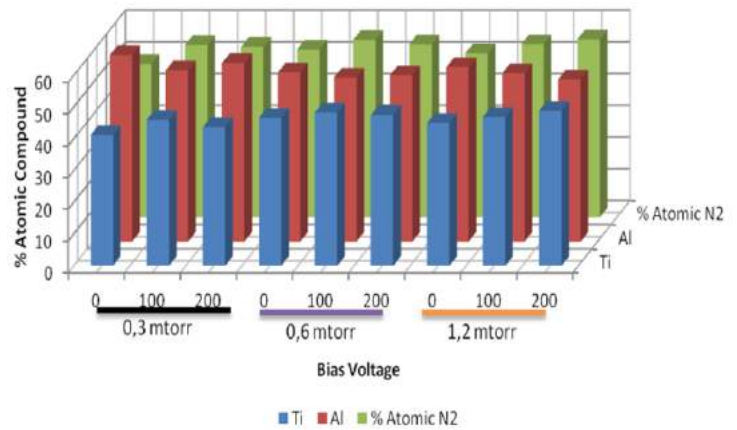


Fig. 7 Graph of Al / Ti ratio changes depending on coating parameters

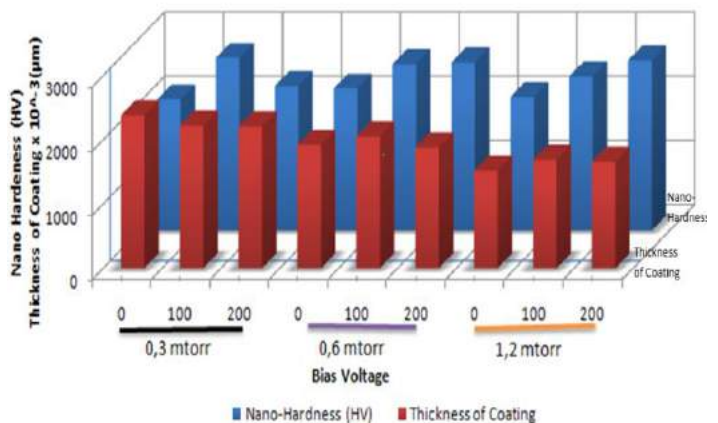


Fig. 8 Graph of TiAlN coatings' nano-hardness and coating thickness

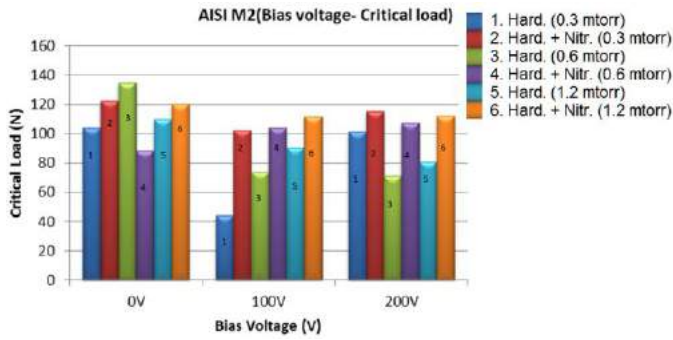


Fig. 9 Result of scratch test of AISI M2 base material according to different pressure values at different bias voltages

A. Results of Wear Test

Wear tests for AISI M2 samples with TiAlN coatings were performed at room temperature (20-22 °C) and in dry conditions using the following parameters; 15 N normal loads, 10 mm/min sliding rate and sliding distance of 2 mm. Determination of the number of cycles to 100 defined with pre-test and force of friction change should remain constant as a criterion. The L8 experimental design was used for evaluating wear tests. Wear rates were calculated by the formulation in equation 4.1. Where V_w is the volume of wear (mm^3), F_n is normal force (15 N) and a is the total sliding distance ($0.002 m \times 100 \text{ cycles} = 0.2 m$).

$$Wear\ Rate\ (mm^3/Nm) = \frac{Wear\ Volume\ (mm^3)}{Contact\ Energy\ (Nm)} = \frac{vV_w}{F_n a} \quad (1)$$

According to the results of wear testing, it was found that TiAlN coating reduces the coefficient of friction in samples subjected to hardening applications. Hardened + nitride +TiAlN coated samples had a higher coefficient of friction (at 1.2 mtorr, 0 V and -200V, $\mu=0.55-0.65$) as shown in Fig.10a. The reason for this was the high surface roughness of the nitrided base material with a column structure [13, 14]. It is very important for the surface of a coating to be as smooth as possible to reduce contact stress with the rough surface of the base material. It was determined that nitrided samples had a low wear rate despite having a high coefficient of friction and were followed by the hardened samples. The lowest wear rate achieved in the coating process using hardened + nitrided AISI M2 steels was with a bias voltage of 0 V and pressure of 0.3 mtorr. This result was also proportional to the hardness of the samples.

The best results in terms of wear were found by considering the base materials, hardness, and strength and coating adhesion results by the depositing of TiAlN on the AISI M2 material at a bias voltage of 0V and pressure of 0.3 mtorr, as shown in Fig. 10b. The coating thickness of the samples (Fig.5) directly affects wear resistance. The samples with a high coating thickness showed better wear resistance [15, 16]. The adhesion between the TiAlN and the hardened+nitrided samples, as seen in Fig. 9, suggesting that the wear resistance was dominantly affected by adhesion, and load bearing capacity of the nitrided layer was great. Trace images obtained from TiAlN coated

samples and wear test results of abrasive wear sphere shown in Fig. 11. Depending on the direction of wear is observed adhering on the edge sections (Fig. 11a-b) also on the abrasive wear sphere occurring of the wear region and adhered coating particles (Fig. 11c). Oxidation and breakage of the coating was observed on the edge section with increased of plastic deformation during the wear (Fig. 11d).

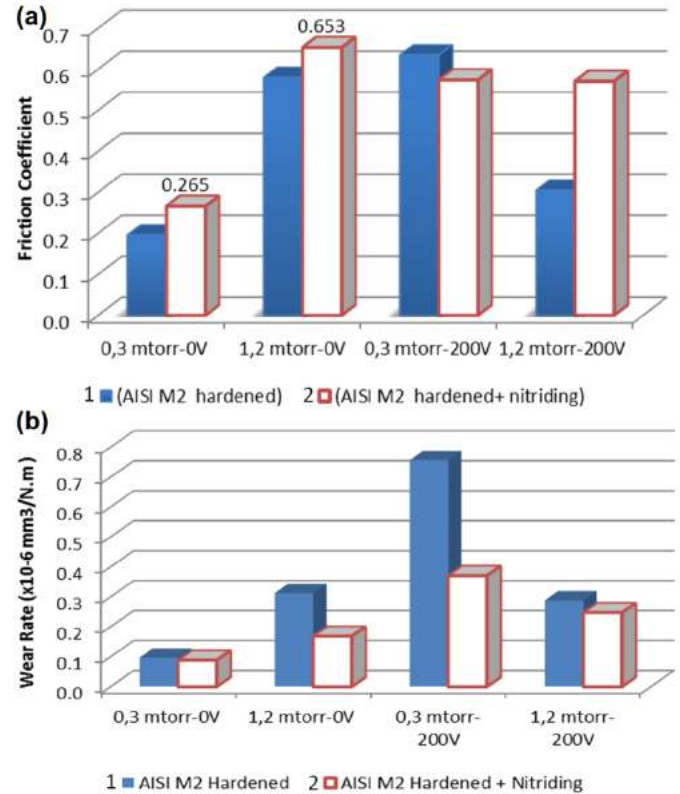


Fig 10.a) The friction coefficient values and b) wear rates obtained from wear test results for TiAlN-coated samples (cycles: 100)

In the wear tests, a three-factor two-level ($2^3=8$ runs) full factorial experimental design was applied. Three factors, involving in the bias voltage, nitrogen pressure and pretreatment type of the base material, were selected to characterize TiAlN coatings. For each factor, two levels were chosen to cover the experimental region. MINITAB® Release 14 statistical software was used to analyze the experimental data in order to measure the effect of various factors and interactions on wear properties using “the smaller the better” situation. The factors and the values corresponding to their levels used in this study are listed in Table VI.

The normal probability plot of the effects and the interaction plot for wear rates are given in Fig. 12a and b, respectively. In general it was found that the effect values of the plotted L8-normal probability graphic are low for wear rate but it was determined that the most effective parameters for AISI M2 were A (bias voltage), and then parameter C (pre-treatment). Nitriding is more effective than hardening treatment for samples.

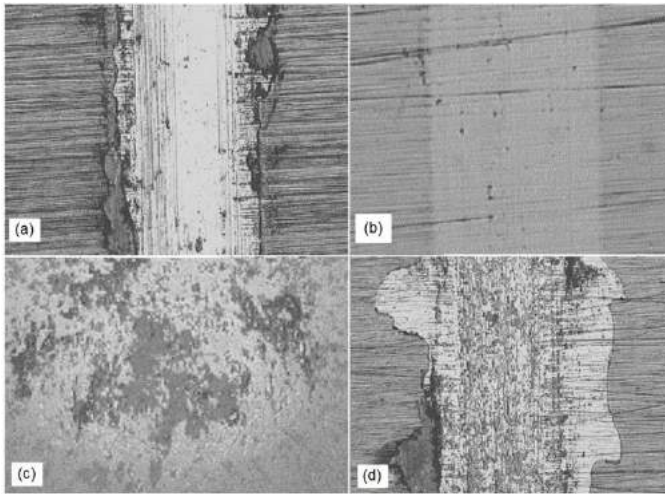


Fig. 11 Trace images obtained from TiAlN coated samples and wear test results of abrasive wear sphere

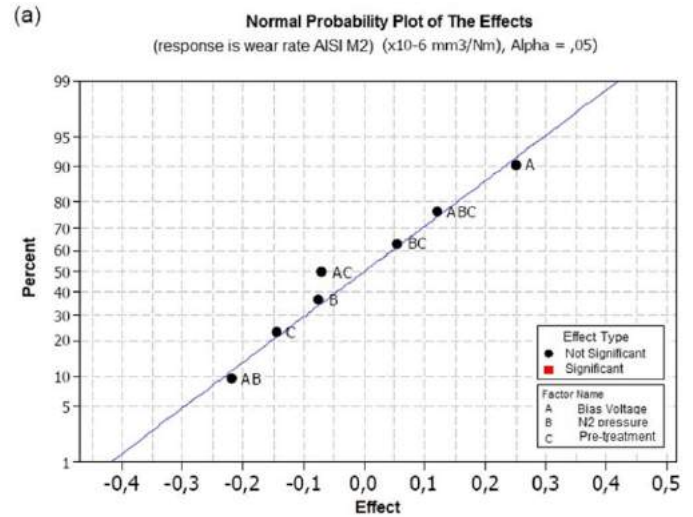
TABLE VI
THE L8 FACTORS AND THE VALUES CORRESPONDING TO THEIR LEVELS

Factors		Levels	
		-1	+1
A	Biasvoltage (-V)	0	200
B	N ₂ pressure (mtorr)	0.3	1.2
C	Pretreatment of thebasematerial	a	b

a-Hardened b-nitrided+hardened

The wear resistance of the base material was improved by increasing the load carrying capacity of the pretreatment effect. The effect of the pretreatment differed according to the samples. Interaction of the bias voltage with the pretreatment of AISI M2 steel was higher than nitrogen pressure, as shown in Fig. 12b. Interaction of the parameters with each other was not clearly determined but in particular, the AC and AB interactions (bias voltage - pretreatment and nitrogen pressure-pretreatment) were observed to be in the forefront. The lowest wear rate was achieved at a bias voltage of -0V in the hardened + nitriding base material. These results show that taking into account the effect of hardening, bias voltage should be chosen according to the appropriate process. However, according to the results obtained for the TiAlN coating deposited on the AISI M2 base material for bias voltage it was understood that the wear rates of the coating were lower in nitrided samples and at a high nitrogen pressure (0.3 mtorr). As a result, it was found that the hardening + nitriding process of AISI M2 with high nitrogen pressure(0.3 mtorr) gave the best wear resistance.

Hardness, thickness of coating and roughness were tested on silicon wafers. It was determined that on samples deposited of more Al % ratio has lower nano-hardness. Aluminum Nitride has grainand hexagonal lattice structure because of increasing ratio of Al % is increased brittleness of the coating.



(b) Interaction Plot (data means) for Wear rate AISI M2 (x 10-6 mm3/Nm)

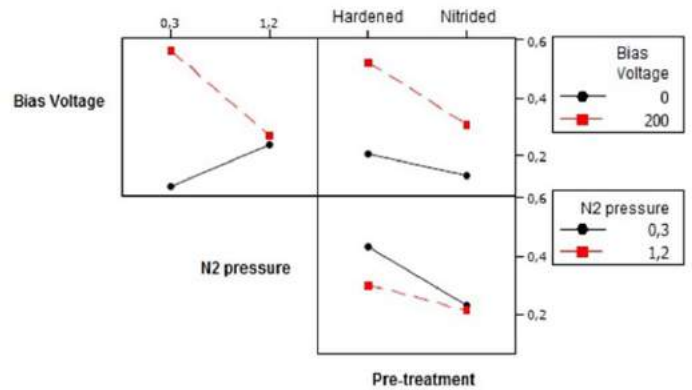


Fig. 12 Obtained with Minitab-14 program, the wear rates for a) L8-normal probability graph, b) interaction charts

It was observed that bias voltage did not significantly change the value of the surface roughness. However the roughness of nitrided samples was higher than that of the hardened samples. Also, nitriding caused an increase in the critical load value. The material surface strength was increased by increased hardness thereby base material surface deformation can be avoided even with increased load. The adhesion strength of samples increased with increasing roughness in the nitrided samples which also increased the critical load value. Bias voltage did not have a clear effect on the adhesion strength of the coating deposited on the AISI M2 base material. The adhesion resistance of the samples is important for the hardness of the base material and coating thickness (> 2 μm). Coating thickness was observed to be an effective parameter for wear rate. Despite the friction coefficient increase with increasing roughness in the nitrided samples, wear performance was increasingly influenced by the increase in surface hardness. The wear properties of the coating deposited on the samples were affected by the interaction of the surface properties, bias voltage and pressure.

IV. CONCLUSIONS

Developing technology and difficulties of competitiveness have forced the manufacturing industry to focus on the use or development of longer life tools. Environmental impacts, production costs etc. should be kept in mind during the design process. Longlife and performance is especially important for tools used in the manufacture of these parts. In this study, the AISI M2 steel material was selected because of its use in this field. TiAlN coating was deposited on AISI M2 base material at bias voltages of 0V, -100V, -200 V and nitrogen pressures of 0.3 mtorr, 0.6 mtorr, and 1.2 mtorr. Wear tests were performed at room temperature and in dry conditions. The effect of deposition parameters on wear rate were investigated using L8(2³) experimental design. The optimum process parameters were determined by the statistical evaluation of the data. It was found that the hardening + nitriding process of AISI M2 with high nitrogen pressure (0.3mtorr) gave the best wear resistance which resulted in a decreased coefficient of friction and a reduction in wear rates.

ACKNOWLEDGEMENTS

The authors would like to thank the Scientific Research Units at Erciyes University for their contribution and support (Project No: FBY 09-854).

REFERENCES

- [1] Danışman Ş., Savaş S., Işık G., Bendeş O., Özbekler A., "Uçak Türbin Kanatlarında Kullanılan Erozyon ve Korozyon Dirençli Sert Seramik Kaplamalar", HASEM'08, Kayseri VIII. Havacılık Sempozyumu, Erciyes Üniv., Kayseri, 41-47, (2008).
- [2] Grzesik, W., Zalisz, Z., Nieslony, P., Friction and Wear Testing of Multilayer Coatings on Carbide Substrates for Dry Machining Applications, Surface and Coatings Technology, 155, 37-45, 2002.
- [3] Ceschini L., Lanzoni E., Martini C., Prandstraller D. and Sambogna G., "Comparison of Dry Sliding Friction and Wear of Ti6Al4V Alloy Treated by Plasma Electrolytic Oxidation and PVD Coating", Wear, Vol. 264, pp. 86-95, (2008).
- [4] Mezlini S., et al., "Effect of Indenter Geometry and Relationship Between Abrasive Wear and Hardness in Early Stage of Repetitive Sliding", Wear, 260, 412-421, (2006).
- [5] Efeoğlu I., "Co-sputtered Mo:S:C:Ti:B Based Coating for Tribological Applications", Surface and Coatings Technology, 200, 1724-1730, (2005).
- [6] Lau K.H., Li K.Y., "Correlation between Adhesion and Wear Behaviour of Commercial Carbon Based Coatings", Tribology International, 39, 115-123, (2006).
- [7] Wuhrer R., Yeung W.Y., "Effect of Target-Substrate Working Distance on Magnetron Sputter Deposition of Nanostructured Titanium Aluminium Nitride Coatings", Scripta Materialia, 49, 199-205, (2003).
- [8] Wuhrer R., Kim S., Yeung W.Y., "Effect of Nitrogen Partial Pressure on the Surface Morphology and Properties of Reactive DC Magnetron Sputtered Titanium Aluminium Nitride Coatings", Scripta Materialia, 37, 1163-1168, (1997).
- [9] Tanaka Y., Gür T.M., Kelly M., Hagstrom S.B., Ikeda T., "Structure and properties of (Ti1-xAlx)N films prepared by reactive sputtering" Thin Solid Films, 228, 1-2, 238-241, (1993).
- [10] Håkansson G., Sundgren J.E., McIntyre D., Greene J.E., Münz W.D., "Microstructure and physical properties of polycrystalline metastable Ti0.5Al0.5N alloys grown by d.c. magnetron sputter deposition", Thin Solid Films, 153, 1-3, 55-65, (1987).
- [11] Barshilia H.C., Yogesh K., Rajam K.S. "Deposition of TiAlN coatings using reactive bipolar-pulsed direct current unbalanced magnetron sputtering", Vacuum, 83, 427-434, (2009).
- [12] Fossati A., Borgioli F., Galvanetto E., Bacci T., "Glow-discharge nitriding of AISI 316L austenitic stainless steel: influence of treatment time", Surface and Coatings Tech., 200, Issue 11, 3511-3517, (2006).
- [13] Yetim A.F., "Biyomalzeme Olarak Kullanılan AISI 316L Paslanmaz Çelik ve Ti6Al4V Alaşımının Plazma ile Nitritleme Davranışı, Ti-DLC İnce Film Kaplama ile Karşılaştırılması", Phd Thesis, Atatürk University Graduate School of Natural and Applied Sciences, 62-63 (2009).
- [14] Luo K., Hovsepian P.Eh., Lewis D.B., Münz W.D., Kok Y.N., Kokrem et al., "Tribological properties of unbalanced magnetron sputtered nano-scale multilayer coatings TiAlN/VN and TiAlCrYN deposited on plasma nitrided steels", Surface and Coatings Technology, 193, 39-45 (2005).
- [15] De Las Heras E., Egidi DA., Corengia P., Gonzalez-Santamaria D., Garcia-Luis A., Brizuela M., "Duplex surface treatment of an AISI 316L stainless steel: microstructure and tribological behavior". Surf Coat Technol, 202, 2945-54, (2008).
- [16] Wolfgang T., Vogli E., Momeni S., "Mechanical and tribological properties of Ti/TiAlN duplex coatings on high and low alloy tool steels", Vacuum, 84, 387-392, (2010).

The Changes in ISO 6892-1:2016 Metallic Materials Tensile Testing Standard

Bülent Aydemir*

* TUBITAK UME, Tubitak gebze yerleşkesi, Gebze/Kocaeli/TURKEY, bulent.aydemir@tubitak.gov.tr

Abstract— Today, as the current standard tensile test for metallic materials ISO 6892-1 standard are used. The English version of the standard in 2009 and the Turkish version in 2011 were published. The English version was renewed in 2016. In this study, we aimed to summarize the major changes made in this standard. In this way, it is aimed to be transmitted detailed and accurate information for related person.

Keywords— ISO 6892-1, Tensile test, Metallic materials

I. INTRODUCTION

Along with the developing technology, tensile testing practice and calculation differences in results bring about changes in standards. When you search at the changes in the standard of tensile testing in metallic materials in our country; TS 138 EN 10002-1(1996, 2004) and TS EN ISO 6892-1(2011) are published. The English version of the standard is published in ISO 6892-1(2009), and it is published as TS EN ISO 6892-1(2011) by the Turkish standard TSE. In 2016, ISO 6892-1(2016) was revised and published, but Turkish has not been published yet [1-3].

In the metal industry, at room temperature, the tensile test standard comes out against ISO 6892-1(2016) and ASTM E8/8M(2016). ASTM standards are used in America, whereas, ISO standards are used in Europe. Japanese Industrial Standards (JIS) and GBT (Chinese Standards) in Asia have adopted the ISO 6892-1 standard.

The tensile test for metallic materials at ISO 6892-1 ambient temperatures is a very detailed standard. This standard describes the method to be applied in the experiment, the calculations used, the results to be reported, as well as the equipment to be used for the test. The changes in this standard are likely to affect everyone in the metal industry.

This study has highlighted important changes between the ISO 6892-1(2016) standard and the previous ISO 6892-1(2009) standard [1,2]. On this study, it is aimed to give detailed and accurate information to the persons who are related to the emphasis of differences of this standard which is used in metal industry.

II. THE CHANGES OF ISO 6892-1:2016

Its summary is given below those changes between 2016 to 2009 version of ISO 6892-1 tensile testing method of test at room temperature of metallic materials

A. New terms and definitions

The 2016 version of standard is added the following term and definitions.

Item 3.12 computer-controlled tensile testing machine: machine for which the control and monitoring of the test, the measurements, and the data processing are undertaken by computer.

Item 3.13 modulus of elasticity (E): quotient of change of stress ΔR and change of percentage extension Δe in the range of evaluation, multiplied by 100 %.

$$E = \frac{\Delta R}{\Delta e} \cdot 100\%$$

Item 3.14 default value: lower or upper value for stress respectively strain which is used for the description of the range where the modulus of elasticity is calculated

Item 3.15 coefficient of correlation (R^2): additional result of the linear regression which describes the quality of the stress-strain curve in the evaluation range

Item 3.16 standard deviation of the slope (S_m): additional result of the linear regression which describes the difference of the stress values from the best fit line for the given extension values in the evaluation range

Item 3.17 relative standard deviation of the slope ($S_{m(rel)}$): quotient of the standard deviation of the slope and the slope in the evaluation range, multiplied by 100 %.

$$S_{m(rel)} = \frac{S_m}{E} \cdot 100\%$$

The symbols of item 4 in the standard are added the new term defined in item 3 [1,3].

B. The changes in test speeds

Test speeds or test rates in heading 10.3 of ISO 6892-1:2016 standard have been changed and the speeds are explained in more detail as Method A1, A2 and B, respectively. The extension speed of the method in the 2009 version of the ISO 6892-1 standard was defined as two methods in the 2016 version. It is expressed as Method A1 (Closed loop strain control) and Method A2 (Open loop strain control).

Closed loop strain control, method A1, is the strain rate control based on the feedback of the data obtained from the instrument's extensometer. The application for this method is given by the tolerances of the required 4 step speed standard. The standard speed steps are schematically shown in figure 1 [5-7]. The other method, Method A2, open loop strain control,

involves the control of the estimated strain rate over the parallel length, ($\dot{\epsilon}_{Lc}$), which is achieved by using the crosshead separation speed (v_c) calculated by multiplying the required strain rate by the parallel length. For a better understanding of this, we can give an example as follows. For a sample with a parallel length of 80 mm, the required crosshead speed (for the 2nd and 4th range velocities given in figure 1) should be:

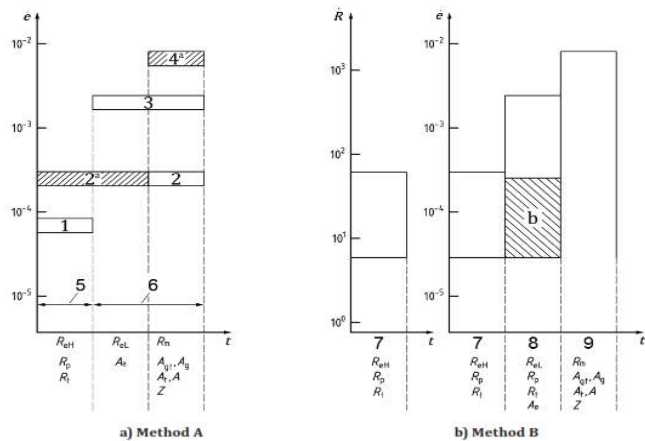
$$v_c = L_c \cdot \dot{\epsilon}_{Lc}$$

- Range 2: (0.00025 mm/mm/s)
0.00025 mm/mm/s X 80 mm = 0.02 mm/s (or 1.2 mm/min)
- Range 4: (0.0067 mm/mm/s)
0.0067 mm/mm/s X 80 mm = 0.536 mm/s (or 32.16 mm/min)

Stress rate control is defined in Method B as standard. This definition doesn't change from the previous version. The tensile stress rate (\dot{R}) varies according to the modulus of elasticity of the material being applied. These values are given in Table 1 below.

Table 3 — Stress rate

Modulus of elasticity of the material <i>E</i> MPa	Stress rate \dot{R} MPa s ⁻¹	
	min.	max.
<150 000	2	20
≥150 000	6	60



- Key**
- $\dot{\epsilon}$ strain rate, in s⁻¹
 - \dot{R} stress rate, in MPa.s⁻¹
 - t* time
 - 1 range 1: $\dot{\epsilon} = 0,000\ 07\ s^{-1}$, with a relative tolerance of $\pm 20\ \%$
 - 2 range 2: $\dot{\epsilon} = 0,000\ 25\ s^{-1}$, with a relative tolerance of $\pm 20\ \%$
 - 3 range 3: $\dot{\epsilon} = 0,002\ s^{-1}$, with a relative tolerance of $\pm 20\ \%$
 - 4 range 4: $\dot{\epsilon} = 0,006\ 7\ s^{-1}$, with a relative tolerance of $\pm 20\ \%$ (0,4 min⁻¹, with a relative tolerance of $\pm 20\ \%$)
 - 5 control mode: Extensometer control or crosshead control
 - 6 control mode: Crosshead control
 - 7 elastic range of the test
 - 8 plastic range for the determination of $R_{eL}, R_{p}, R_{t}, A_e$
 - 9 maximum strain rate for the determination of $R_{m}, A_{gt}, A_b, A_t, A, Z$
 - a Recommended.
 - b Expanded range to lower rates, if testing machine is not capable of measuring or controlling the strain rate (see 10.3.3.2.5).

NOTE 1 Symbols refer to Table 1.
NOTE 2 Strain rate in the elastic range for method B is calculated from stress rate using a Young's modulus of 210 000 MPa (steel).

Fig. 1. Recommended speed ranges according to ISO 6892-1: 2016 standard

In the 2016 version of the standard, the recommended speed values in Figure 1 are detailed. Speed steps 1,2,3,4,5 for method A1; 5.6 speed steps for method A2; For the method B, 7 speed stages can be used.

C. Other changes

The 8th heading of the standard was changed to the "Marking the original gauge length" in the 2009 version, while the "Original gauge length and extensometer gauge length" was changed in the 2016 version. In addition to, the headings of choice of the original gauge length, marking the original gauge length and choice of the extensometer gauge length have been added.

Appendix G, as a new part of the standard, is added specifies the determination of the modulus of elasticity. In the 2016 version, the names of the other suffixes have changed due to the addition of Annex G chapter, but the sections remained the same.

Important information is given in Annex G. For example, it is stated that the material testing machine has class 1 or better class according to ISO 7500-1 standard. The extensometer system is required to have class 0.5 or better class according to ISO 9513 standard. It is defined that the sample sizes are measured with a calibrated device with better accuracy than $\pm 0.5\ \%$. It has also been disclosed that it is important that the material testing machine is made according to ASTM E1012 or ISO 23788 in the measurement of the alignment.

In addition, when determining the minimum data sampling frequency (*f*), the following formula is proposed:

$$f = \frac{N \cdot E \cdot \dot{\epsilon}}{R_2 - R_1}$$

Where *N* is the number of measured values, *E* is the elastic modulus, $\dot{\epsilon}$ is the test speed, and *R*₁, and *R*₂ are the tensile values that the data sampling frequency is determined. For example, if *R*₁ = 10 MPa, *R*₂ = 50 MPa for steel, and the test speed is 0.00007 s⁻¹, the data sampling frequency shall be greater than 18 Hz.

Furthermore, methods of calculating elastic modulus and calculation of elastic modulus uncertainty are described in detail.

Apart from these, the bibliography has increased 41 to 58 by the additional resources given in the Annex G section [1, 3].

III. THE EFFECTS OF TENSILE TEST SPEEDS (RATES) CHANGES

Testing laboratories should plan to use either Method A1 or Method A2 according to ISO 6892-1. The method A1 and Method A2 provide better test applications and more comparable results. For this reason, it is important to provide Method A1 when purchasing a new tester or improving your existing machine, and increasing the efficiency of controlling the tester, based on the extensometer feedback (Fig. 2). Alternatively, if your current testing machine can not apply Method A1, using it at a fixed crosshead speed according to Method A2 will provide minimal change in results and increase comparability [5-7].

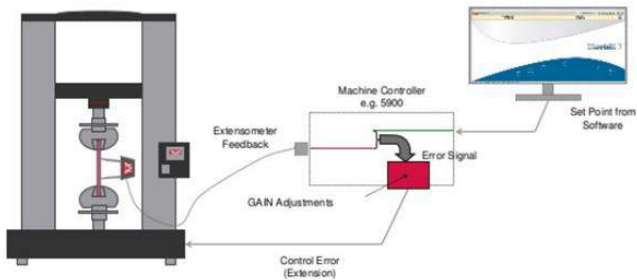


Fig. 2. Graphic representation of extensometer feedback loop of method A1

The advantage of the methods A1 and A2 is to reduce the uncertainty of the measurement results of the test results by reducing the test speeds by minimizing the moment when the parameters sensitive to strain rate are determined. Figure 3 graphically shows the test speeds according to methods A1 and A2 and the test parameters that these speeds affect [5].

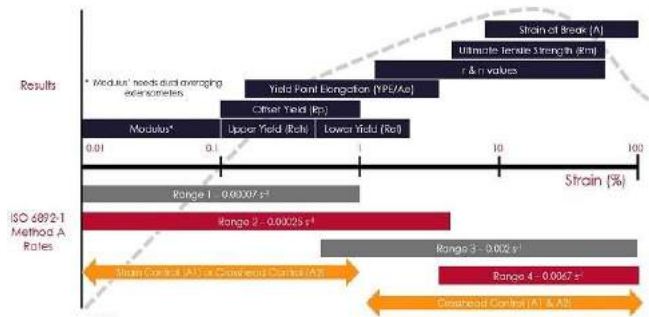


Fig. 3. ISO6892-1: 2016 Graphic representation of the required test results with the speeds of method A1 and A2

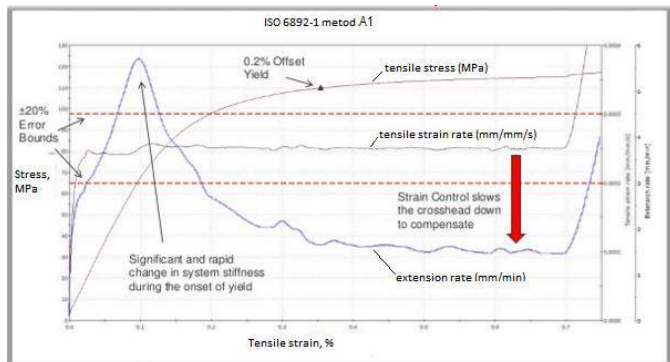


Fig. 4. Stress-strain graphic of Method A1 and its speeds chancing

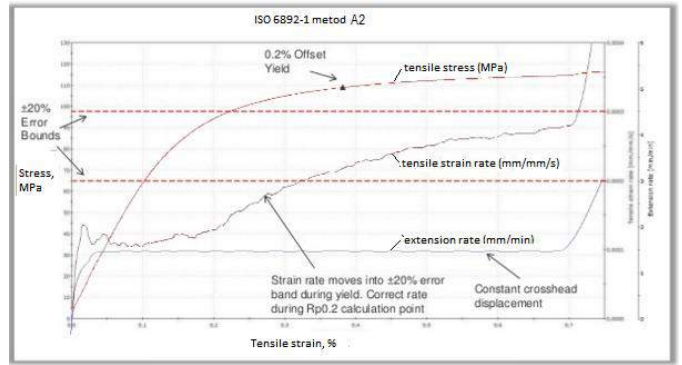


Fig. 5. Stress-strain graphic of Method A2 and its speeds chancing

The test chart of the method according to ISO 6892-1 and the closed loop strain control (method A1) is given in figure 4. In here, the horizontal axis strain (%) shows the vertical axis stress (MPa) value. The strain rate (mm / mm / min) graph is shown by the dashed line between $\pm 20\%$ tape lines. The crosshead speed is marked with a large arrow in the graph. The test chart for the same sample according to ISO 6892-1 method A2 and the estimated strain (crosshead speed) control is given in figure 5. In here, it is seen that the strain rate (mm / mm / min) graph is inserted between $\pm 20\%$ band lines after more strain than figure 4.

Method B stretch rate control has the advantage that it is a simpler control method and can be used in most test machines. However, the disadvantages of the test period extension (fig. 6) are that additional calculations are required for the rigidity of the machine and that different results can be obtained from the machine if the machine is not set. During method B testing, there are many sources of uncertainty and error. Most metallic materials are sensitive to stress ratio; so, the mechanical properties vary depending on the test speed.

Stiffness varies according to each machine, and is an effective parameter on the test results. Figure 6 gives the stress-percent strain graph for two machines with different stiffness. For two test rigs, one rigid and the other less rigid, the results are the same on the average at the same test speed when testing the same material. To further exaggerate this situation, if the very rigid system is much faster and the less rigid system is tested slower, a difference of more than 10 % can be obtained between the results obtained from the same material [3,5-9].

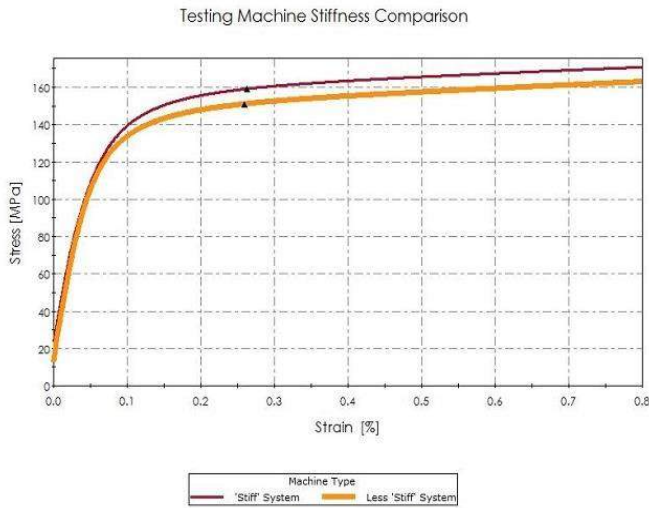


Fig. 6. Test Machine Rigidity Comparison - two tests were performed with the same material and at the same crosshead speed but with two different machines

In the figure given in Figure 7, the test time is given for the aluminium sample according to different test speeds. As can be seen, the test carried out in method A1 according to ISO 6892-1 in the closed loop strain control provides a time saving of 35 % compared to the method A2 and method B control [3, 5-7].

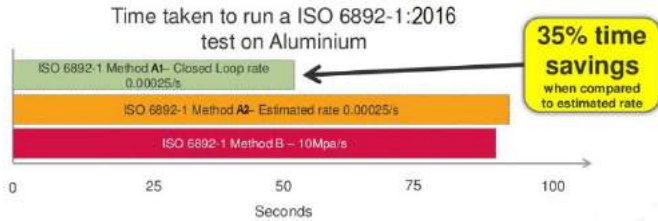


Fig. 7. Comparison of test times for aluminium samples at different speeds

IV. CONCLUSIONS

In this study, significant changes were summarized between the ISO 6892-1 (2016) standard and the previous ISO 6892-1 (2009) standard. In this respect, it is aimed to help the understanding of this standard which is used in many testing laboratory in this sector. In addition, the results of the most important of these changes on the tensile test speed selection are summarized.

For the purpose of using methods A1 and A2 in ISO 6892-1, the explanation is as follows: "It is intended to reduce the measurement uncertainty associated with the change in the test speed and the test results at which the speed-sensitive parameters A1 and A2 are to be determined." In addition, - it is desirable to document the shape of the curve in the test speed and to document the speed of the test. In addition, the similarity of test speeds in the reproducibility and reproducibility of the yield strength results is also important.

A summary table of the test speed methods defined in ISO 6892-1 is given in Table 2 [5]. Inhere the control types and the feedback sources for the control are given for different methods. Time-to-install time was measured as the test time, and the reproducibility values of the test results were given as comparability. Different test speeds are the most important affect test time. The aim is that Method A1 provides this for accurate and reproducible results in the shortest test run.

Table 2. Summary table of test speed methods defined in ISO 6892-1 standard

ISO 6892-1:2016			
Method	Method A1	Method A2	Method B
Control Type	Strain control	Crosshead control	Stress control
Feedback source	Extensometer	Displacement	Loadcell
Setup time	Low	Medium/High	Low/Medium
Test speed	Fast	Slow	Medium
Comparability	High	High	Low/Medium

REFERENCES

- [1] ISO 6892-1, (2016), Metallic materials -- Tensile testing -- Part 1: Method of test at room temperature
- [2] ISO 6892-1, (2009), Metallic materials -- Tensile testing -- Part 1: Method of test at room temperature
- [3] B. Aydemir, *ISO 6892-1:2016 Metalik Malzemelerin Çekme Deneyi Standardındaki Değişiklikler ve Etkileri*, 2017, Metal Dünyası, Sayı:283, S.68-72
- [4] B. Aydemir, *Metalik Malzemelerin Çekme Deneyi Standardı EN ISO 6892-1'in Getirdiği Değişiklikler*, 2013, Makine Teknolojileri Elektronik Dergisi Cilt: 10, No: 3, 2013 (61-70)
- [5] <http://www.instron.com.tr/tr-tr/testing-solutions/by-material/metals/tension/iso-6892-12016>
- [6] Understanding the New ISO 6892-1:2016 and the Most Notable Changes: An Interview with Matthew Spiret, <http://www.azom.com/article.aspx?ArticleID=13017>
- [7] Updates to metals standards 2015, www.instron.com
- [8] B. Aydemir, H. Taşcan, C. Camyurdu, *Çekme deneyinde farklı uzama ölçme yöntemlerinin etkilerinin incelenmesi*, 2015, Metal Dünyası, Sayı 266, S.44-50, İstanbul
- [9] B. Aydemir, *Malzeme Deneylerinde (Çekme deneyi) Ölçüm Belirsizliğinin Hesaplanması Eğitim Dokümanı - G2KV-110, 2015, G2KV-110, Nisan 2015, TÜBİTAK UME*

Formaton of Triangle Shaped TiB₂ Borides in Coated Surface Produced by GTAW

Mehmet YAZ,[#] Serdar Osman YILMAZ,⁺ Zülküf BALALAN^{*}

Firat Universty

myaz@firat.edu.tr

Bingol Universty

zbalalan@bingol.edu.tr

Namik Kemal Universty

oyilmaz@nku.edu.tr

Abstract

In this investigation, a gas tungsten arc welding (GTAW) is used as a high energy density beam to form a coated surface over 0.15% C carbon steel with FeB, FeTi and graphite powders. The microstructure, microhardness and dry-sliding wear behavior of the composite coating were investigated by using optical micrograph (OM), X-ray diffraction (XRD), scanning electron micrograph (SEM), energy dispersive X-ray analysis (EDS), microhardness tester and adhesive wear tester. A lot of types of carbide and borides were formed. The shape of the graphite present in the FeB-FeTi-C composite TIG welding coatings is various from sheet-like to triangle. Within the wear test conditions used in the present research, on Fe₂B coated samples wear was essentially oxidative until the failure of the coating.

Keywords: FeB, FeTi, adhesive wear, GTAW, coating

I. INTRODUCTION

Instead of improving surface properties of materials to improve has been used different techniques. TIG welding process is a good source of high-quality welding and operation is used when needed. TIG method, high-intensity laser and thermal spray methods with original coatings and material provided significant improvements in the production [1-2]. TIG welding method with application of coatings made easy and similar methods, that reveals the superiority of cheap [3]. Surface properties of the resulting microstructure development of corrosion and abrasion resistance According to conventional surface treatment techniques resulting is much better [4, 5]. TIG method is some species of alloying technique; in principle, have the appropriate composition alloy dust or powder is applied to the surface of the substrate material of arc temperature influence melt down, coating is a solid form method. Melting, both in the main material and and an additional metal or takes place at the same time in the compound [3]. Surface properties of the resulting microstructure development of corrosion and abrasion resistance

are much better than those obtained by conventional surface treatment techniques [4, 5]. In principle, have the appropriate composition alloy dust or powder is applied to the surface of the substrate material of arc temperature influence melt down, coating is a solid form method. Melting takes place at both of the main material and an additional metal at the same time. Solidification occurs quickly, hence concentration of the coated surface and base metal differs. Base metal and coating material differs in property by creating solid solution or compound in connect to each other combinations [6-7]. The rate of solidification is very high during this coating process. Advantages of similar techniques, well microstructure by rapid cooling, high hardness and increased wear resistance. In this technique, Fe, Cr, Co and Ni based alloys are used for coating various conventional base materials [8].

Tools and the quality of life of the mold and are important factors in production. Especially in complex and large mass production using different techniques for many years in the service life of and abrasion resistance of visibly made many research to improve. Research is enough as a result of thermal processes and the implementation of better quality materials and to increase the durability of surface coating and modification of the development of the different methods is provided. Surface layers, resulting in a different way in use other physical and chemical properties, crystal lattices, with material microstructure and chemical variety from properties [9, 10].

Iron-based matrix composites due to a combination of high mechanical strength they have a wide place application. Interface reaction and avoid interface compatibility improved, high-performance composites to produce the important techniques. Ceramic particle reinforced metal matrix composites new techniques for the of production [11, 12].

AISI 1018 steel can be developed using the technique of boron on the plates is GTAW. The elevation of boron content causes a small amount of ferrite-primary Fe₂B, Fe₂B and boride eutectic a hypo eutectic microstructure of high allows relaying hypo eutectic [13].

Boron reinforced metal matrix composites (MMC) compared to the matrix alloys wear properties and they indicate significantly rising of mechanical strength and generally soft matrix applied to the load distribution from the reinforcement phase and compression of pressure with the transmission and high stress resistance have the to quality. On the other hand, metal matrix composites compared with the matrix low malleability and fracture toughness in the second degree is trouble and the particulate reinforced usually is expensive, cost of final production is also rising due to expensive production processes. Surface modification technology, with inexpensive coarse materials with high for bearance and fracture toughness is an alternative solution that combines the superior features of an MMC surface layer. In the recent past, composite layers Fe-B-Cr triple phase system applicable CrB and Cr₂B Particles or Fe-B applicable with binary phase system Fe₂B and FeB on the surface of the steel [14].

Development situation of hard surface coating alloys more efficient than on one hand Fe-Cr-C or Fe-C-B systems of content, on the other hand there are more expensive tungsten carbide reinforced synthetic multiphase composites. Therefore, niobium, boron and carbon in its composition, titanium and molybdenum complex Fe-based alloys with the best matrix properties and significant progress has been achieved by attaining wear resistance according to different depositions of abrasion-resistant hard phases [15-17]. Fe-C-X (X=Cr, Mn, W, Mo, Ni, B vs.) alloys, excellent applicant for surfaces with high wear resistance and hard surface coating materials. Laser alloyed Fe-C-X The microstructural characterization of the coating depends on the chromium concentration, out of place ferrite matrix M₇C₃ carbides or twinned austenite needles and completely martensite phase formation [18,19].

In this study, a gas tungsten welding method (TIG), AISI1018 surface of steel FeB, FeTi and used as high energy density beams for coating with graphite powders phase transformations on coated

surfaces are optical microscopy (OM) and scanning electron microscopes (SEM) X-rays and EDS analysis were combined studied systematically.

Purpose of the study is characterising sliding wear behaviors of coated surfaces by FeB, FeTi, FeW and graphite powders and to improve the friction coefficient and abrasion based on the basic specification by using an adhesive abrasion equipment.

II. EXPERIMENT METHOD

FeB, FeTi, FeW and mixtures of graphite powders as coating material used. 100x50x10 mm is used as low carbon steel material base material. Chemical analysis of base plate material 0.15% C, 0.22% Si, 0.76% Mn, 0.034% P, 0.05% S, 0.12% Cr 0.03% Mo, 0.10% Ni ve 0.52% Cu content of elementers. FeB, FeTi, FeW and chemical analysis of graphite are given in table 1. FeB, FeTi, FeW and graphite powders are given in table 2. FeB, FeTi, FeW and mean values of graphite particles are as small as 50 µm. In order to obtain a homogeneous mixture of particles was mixed up with a mixer for about 1 hour. The resulting mixture was treated with sodium silicate (Na₂SiO₃) made into with paste. 3 mm depth to the surface of the base material 16 mm wide milling cutter opened, The obtained paste was filled in this channel tightly and air desiccated at room temperature. The experimental conditions are given in table 3. As a melting electrode %2 ThO₂ tungsten is used and the diameter of the nozzle is 11 mm. Microstructural effects of process parameters are purposed. Argon gas was used as protective gas during the process. The coatings obtained for the metallographic examination of the samples were cut perpendicularly to prepare samples with dimensions of 10x10x10 mm and the surfaces of the samples were polished with 80 mesh to 1200 mesh abrasive. 3 µm diamond pie was used for final polishing. After the final polishing, the sample surfaces were etched with a mixture of 100 ml of HCl, 1 g of picric acid and 100 ml of ethyl alcohol. Microstructure photographs were taken with an optical microscope of the etching samples. EDS analyzes were taken by scanning with scanning electron microscope (SEM). Analyzed with X-ray (XRD) to determine the carbides formed on the coating surface. The microhardness of the resulting coatings was measured with a Leica Q550 device starting at the coating surface and at a load of 50 g toward the transitionzone.

Table 1. Chemical analysis of reinforcement materials (wt%)

	Al	Ti	FeW	Si	%S	Fe	Cr	B	C	%P
FeB	0.5			2.5	0.05	Bal.		18.1	0.5	0.025
FeTi	4	75		0.5	0.03	Bal.				0.03
FeW			80	0.5		Bal.	0.5			0.04
Graphite									99.9	

Table 2. Coating materials used for mixing ratios (wt%)

Sample No	FeB (%)	FeTi (%)	FeW(%)	C (%)
S1	90	5	2	3
S2	80	10	2	8
S3	70	15	2	13

Table 3. Gas tungsten welding method of process parameters

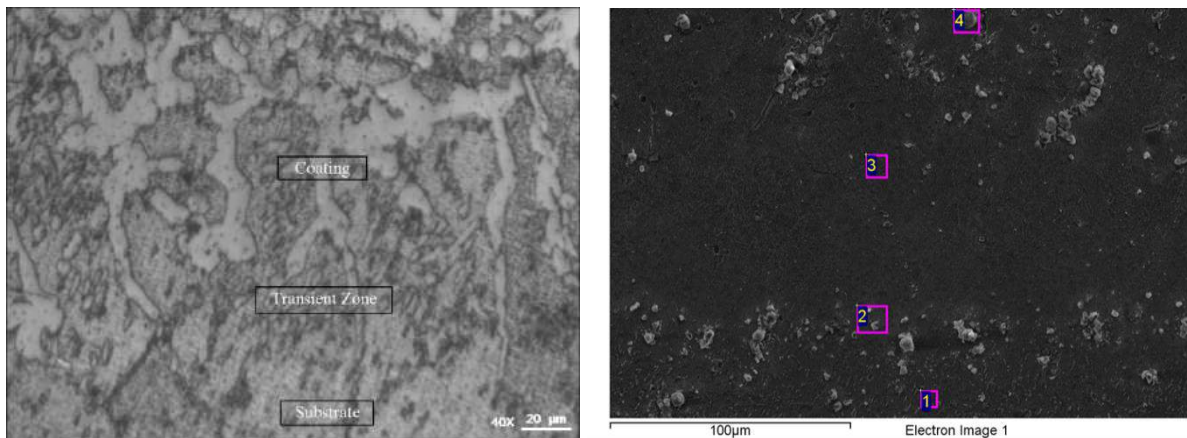
Current	120-140 A
Welding speed	10 cm/min.
Protective gas	Ar-99.9%
Shielding gas flow rate	14 l/min.
Nonconsumable electrode	W-2%Th
Electrode diameter	2.4 mm

III. RESULT AND DISCUSSION

3.1 Microstructure Analysis

Microstructures on coated surfaces were not homogeneous throughout the coating. The coated surface area is shown in the optical microstructure photograph of the S1 sample shown in figure 1a and as can be seen in the SEM photograph shown in figure 1b, it can be avowable that it can be divided into bases. Boron, carbon, titanium in the coating area three samples used at the rates given in table 2. The distribution of boron and carbides along the cross section was investigated by using boron and carbon together. The transitional zone immediately adjacent to the base material was formed on an eutectic microstructure consisting of an eutectic structure with sorbitic perlite base [15, 16]. There is a texture of carbide and boron in the coating area. When the cross section of the coating area from the

outer surface to the base material is examined, the ratio of square and triangle shaped TiC and Ti₂B boron is increased. In the microstructure, triangle and square physical shapes of titanium borides were observed in the eutectic matrix. Figure 1b shows the locations of the EDS analyzes from the three regions. According to EDS analyzes, An eutectic structure with carbides of Fe₃ (BC) in the first region was found (Figure 1b). Furthermore, the analyzes showed that the hard phase in the second region, Fe₇C₃ (Figure 1b) And the phase in the third region is a structure of "Fe₂B + TiB₂" consisting of boron and carbide. When the EDS analysis data and the XRD results were evaluated together, the results obtained from the EDS analyzes were confirmed. The results of the EDS analyzes from the regions shown in figure 1b are given in table 4.



a)

Fig. 1. Transition zone microstructure of photos S1; a) OM b) SEM

b)

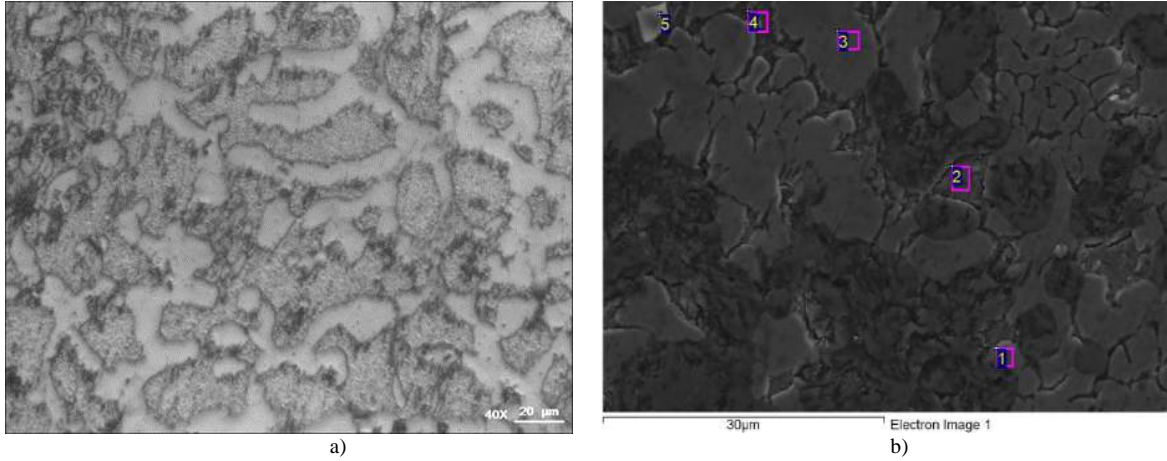


Fig. 2. Microstructure photographs taken from the middle regions of the coating at S1; a) OM b) SEM

Table 4 gives the analysis from the transition zone of the S1 sample. As you can see, the concentration of titanium in the transition zone is limited. The hard phases in the structure are iron carbide and boron.

Table 4. EDS analyse results of S1 taken from the structure given in Figure 1b

	Elements wt %									
	B	C	Al	Si	Mn	Fe	Ti	W	Cu	O
Point1	0.69	7.15		0.29	0.74	84.00	--	0.07	1.91	5.15
Point2	0.63	6.39		0.30	0.67	86.84		0.14	2.06	2.97
Point3	-	6.58	0.26	0.26	0.62	82.91	0.75	0.21	2.55	5.86
Point4	1.12	10.87	0.29	0.21	0.67	64.86	1.83	0.29	1.22	18.49

The middle sections of the coverage area of table 5 were examined. Titanium carbides and titanium borides formed in the structure. EDS analysis are insufficient to give definite rates in the detection of

boron and carbon elements these results, when evaluated together with XRD analyzes, TiC, Ti₂B, Fe₃C₂ and Fe₂B hard phases were formed.

Table 5. EDS analyse results of S1 taken from the structure given in Figure 2b

	Elements wt %									
	B	C	Si	Al	Mn	Fe	Ti	W	O	
Point1	4.28	8.56	0.24	0.97	0.38	55.29	20.73	1.58	7.49	
Point2	1.02	4.77	0.84	1.36	0.47	73.86	15.29	1.98	--	
Point3	2.04	5.00	0.88	0.73	--	60.36	29.03	1.96	--	
Point4	--	2.32	1.91	0.83	--	67.87	24.10	2.98	--	
Point5	--	2.31	1.44	0.88	--	68.45	23.60	2.80	--	

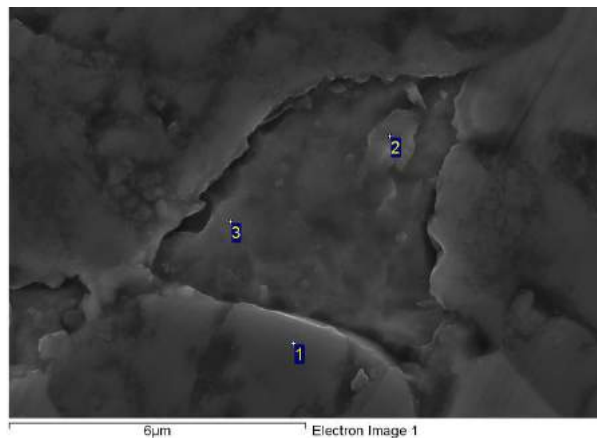


Fig. 3. Microstructure photograph taken from the middle regions of the coating at S1; SEM X10000

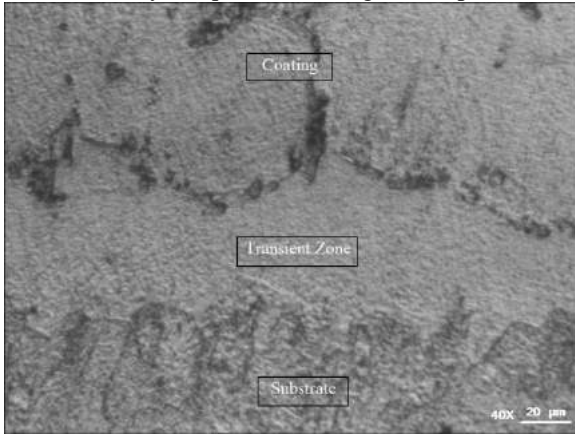
Table 6. EDS analyse results of S1 taken from the structure given in Figure 3

	Elements wt %							
	B	C	Si	Al	Mn	Fe	Ti	W
Point1	--	4.51	0.82	1.41	0.47	76.40	13.90	1.97
Point2	--	4.14	1.00	1.25	--	73.90	17.09	2.10
Point3	1.52	4.02	0.98	1.24	--	82.91	18.57	2.42

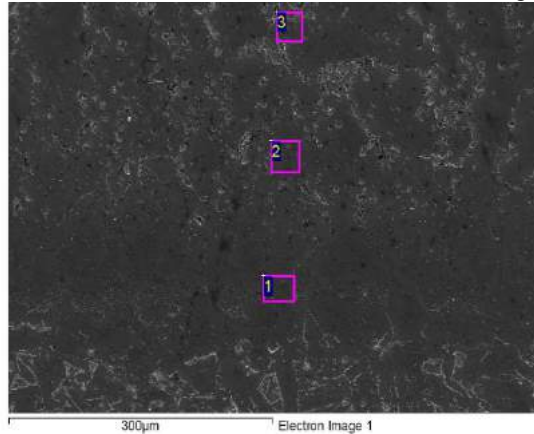
The X10000 expansion SEM photograph taken in the middle regions of the S1 sample is shown in figure 3. The presence of TiC's is evident from the EDS analysis shown in table 6.

The transition zone microstructure and SEM images of sample S2 are shown in figure 4. Similar microstructure photographs were seen in S1 and S2. Three different microstructure zones are seen. The eutectic structure is hard to the transition zone, But the density of square and triangular shaped TiC's

increases towards the surface of the coating (Figure 4a, 4b). From the SEM and EDS analysis, it can be assumed that the hard phases are TiC and Fe₅C₂ and the structure of the transition region in sample 2 is an eutectic phase mixture (Figure 4). From the EDS analysis, it can be said that Ti and C atoms are diffused to the substrate material (Table 7). The microstructure photographs taken from the second zone (middle of the coating) are given in figure 5 and the EDS analysis are given in table 8. It can be said that the Fe₂B borides are clustered in this region.



a)

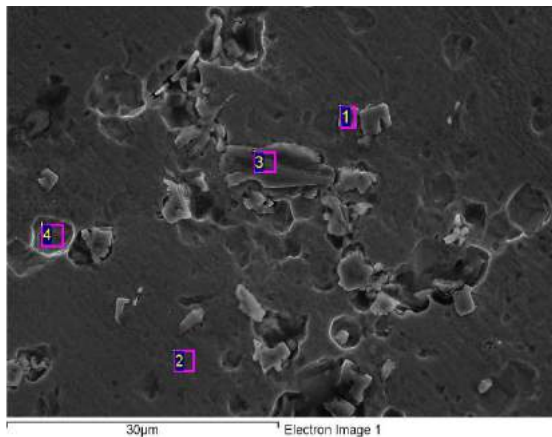


b)

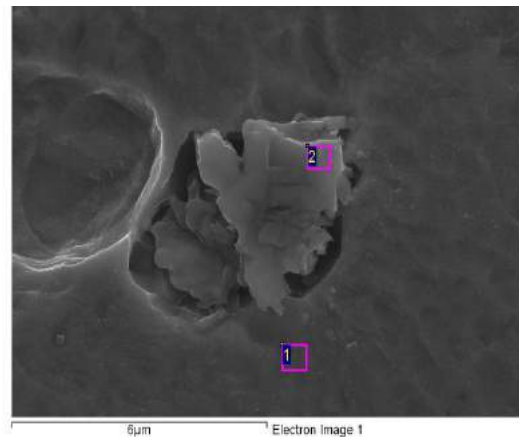
Fig. 4. Microstructure photographs taken from the transition areas of the coating at S2; a) OM b) SEM

Table 7. EDS analysis of the transition region of the S2 sample taken from the microstructure photograph given in Fig. 4b

	Elements wt %								
	B	C	Si	Mn	Fe	Ti	O	W	Cu
Point1	--	2.84	0.25	0.59	90.10	0.68	3.10	--	2.45
Point2	--	2.49	0.42	0.64	92.33	1.31	--	--	2.82
Point3	--	6.76	0.27	0.53	80.12	7.72	--	2.40	2.20



a)



b)

Fig. 5. SEM microstructure photographs of the middle region of S2 a) Central region b) Central region X10000

Table 8. EDS analysis of the S2 sample taken from the microstructure photograph given in Figure 5a

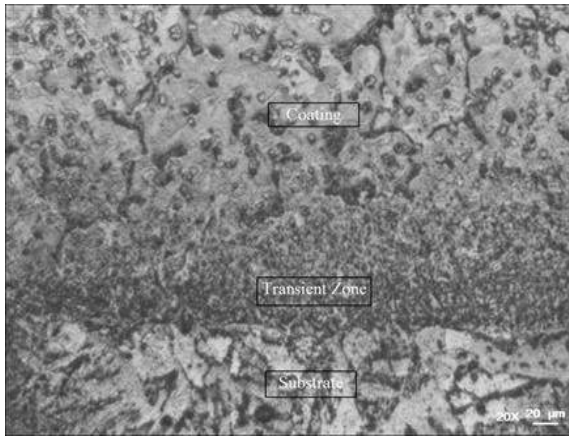
	Elements wt %							
	B	C	Si	Mn	Fe	Ti	W	Cu
Point1	--	1.95	0.43	0.56	92.98	0.93	0.75	2.40
Point2	19.09	--	0.15	0.51	64.66	11.34	2.52	1.72
Point3	--	1.94	0.40	0.58	92.75	1.19	0.80	2.34
Point4	--	1.74	0.43	0.68	92.88	1.01	0.94	2.34

Table 9. EDS analysis taken from the microstructure photograph of the S2 sample given in 5b

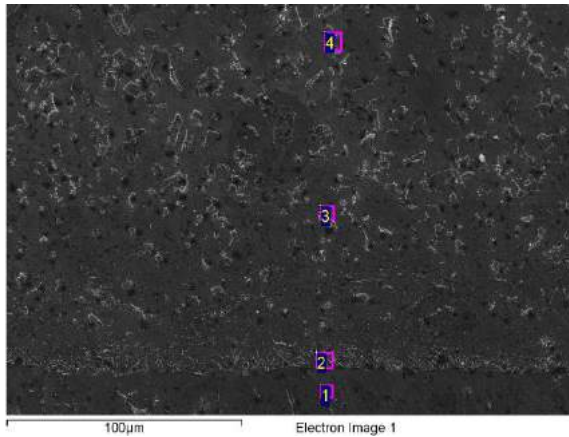
	Elements wt %							
	B	C	Si	Mn	Fe	Ti	W	Cu
Point1	8.24	31.52	0.11	0.31	50.30	6.47	2.01	1.04
Point2	1.03	5.26	0.12	0.53	67.24	18.90	5.47	1.46

Microstructure photographs of the Fe_5C_2 , B_4C , FeB , TiC hard phase mixtures on S3 are given in figure 6. The EDS analysis values from this microstructure photograph are given in table 7. The microstructure of the sample S2 at the interface of the matrix and boride plates is shown in figure 7a. At higher temperature it can be seen that the eutectic

mixture melts the liquid alloy along grain boundaries. During the rapid cooling from high temperature, these melted zones remained and land formed within the eutectic [19]. On the other side, a completely eutectic microstructure is seen in the middle part of the coating (Figure 7b).



a)



b)

Fig. 6. Photographs of the transition zone of S3 a) OM b) SEM

EDS analysis from the center of the S3 sample and microstructure photographs support eutectic (Figure 7a). In addition, it is seen that the EDS analyzed at point 1 diffuses the C atom to the base material, but not the B and Ti atoms (Fig. 7b). The density of

boron atoms increases from the edge of the substrate material to the center of the coating. However, the density of C shows a balanced distribution towards the surface, the Ti density increases from the center of the coating to the surface (Table 10).

Table 10. EDS analysis taken from the microstructure photograph from the transition zone of the sample S3 in Figure 6b

	Elements wt %								
	B	C	Si	Al	Mn	Fe	Ti	W	Cu
Point1	--	2.85	0.37	--	0.73	94.82	--	--	1.22
Point2	--	3.59	0.50	0.40	0.54	92.49	0.40	0.85	1.24
Point3	--	3.10	0.62	0.43	0.63	90.74	1.33	1.32	1.47
Point4	--	3.12	0.72	0.40	0.70	89.69	1.97	--	3.03

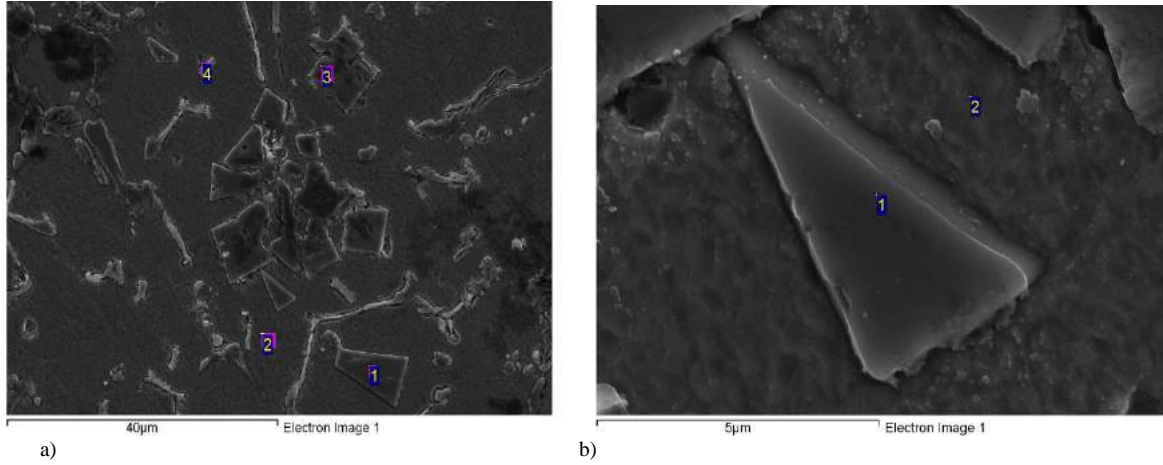


Fig. 7. SEM microstructure S3; a) Central region b) X12000

Table 11. EDS analysis taken from the microstructure photograph of sample S3 in Figure 7a

	Elements wt %							
	B	C	Si	Al	Mn	Fe	Ti	W
Point1	3.18	18.02	0.26		0.81	23.62	38.26	16.92
Point2	--	4.48	0.54	0.49	0.54	87.14	3.98	2.49
Point3	21.05	9.07	0.05	0.22	--	40.50	21.84	6.92
Point4	--	6.84	0.47	0.43	--	75.74	10.93	5.18

Table 12. The EDS analyzes taken from the microstructure photograph (X12000) of the sample S3 of Figure 7b

	Elements wt %							
	B	C	Si	Al	Mn	Fe	Ti	W
Point1		2.48	0.51	0.53	0.38	87.79	5.77	2.53
Point2	0.14	13.03	0.19	0.37	0.40	55.73	22.64	7.49

3.2 XRD Analysis

The microstructure of the sample S3 at the interface of the matrix and the boron layers is shown in figure 7a. At higher temperature it can be seen that the eutectic mixture melts the liquid alloy along grain boundaries. During the rapid cooling from high temperature, these melted zones remained and land formed within the eutectic [19]. On the other hand, the X12000 extension SEM photograph taken from the center of the coating shows triangular TiC (Figure 7b).

X-ray results show a wide variety of carbide types depending on the content of boron, titanium,

tungsten and carbon. XRD results of sample 1 (Figure 8). In the structure of the coating TiB_2 , Fe_2B , WB_4 , Ti_3B_4 , B_2W , B_8C , TiB_{12} , $FeWB$, WB , Fe_7C_3 , Fe_3W_3C , indicate that there are phases. The XRD results of the S2 sample (Figure 9) show WB_4 , WB , Fe_7C_3 , Fe_3W_3C phases (Figure 10). X-ray as a result of analysis of sample S3, WB_4 , Ti_3B_4 , B_8C , TiB_{12} , $FeWB$, WB , Fe_7C_3 , Fe_3W_3C in addition to the phases Fe_5C_2 , B_4C , FeB , TiC , $B_{13}C_2$, Fe_2C phases were seen (Figure 10).

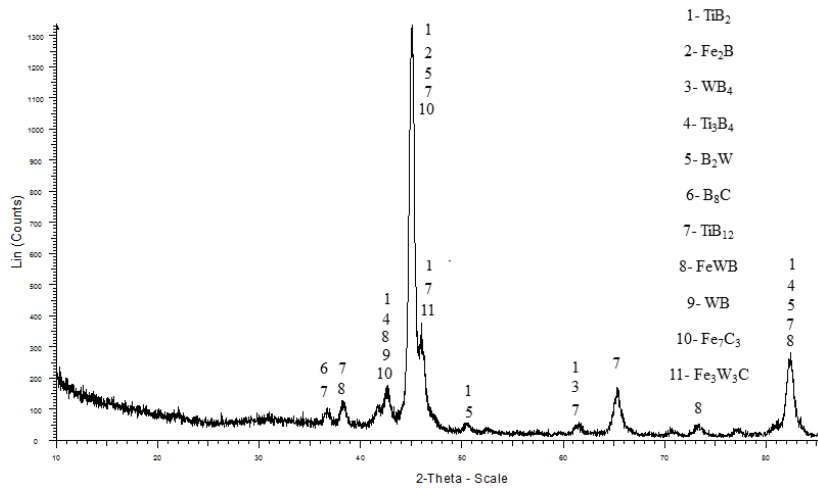


Fig. 8. XRD results of S1

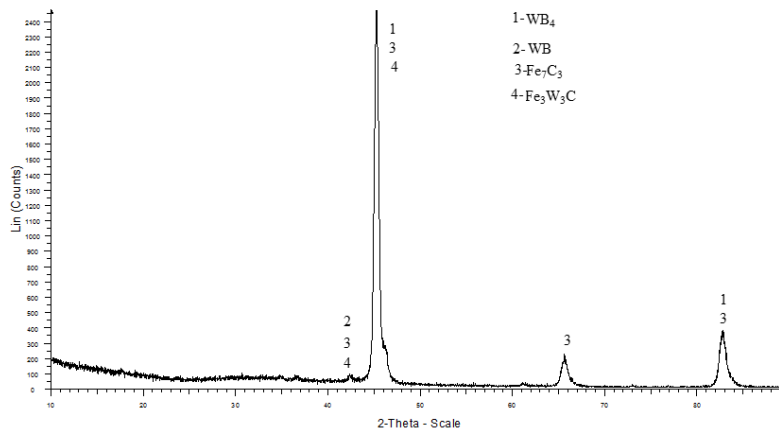


Fig. 9. XRD results of S2

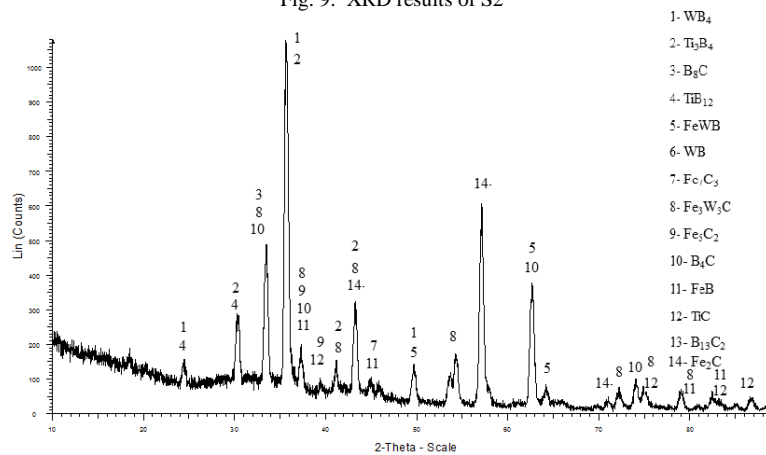


Fig. 10. XRD results of S3

3.3 Microhardness

The microhardness values measured at the depth of 3500 μm from the coating surface are given in figure 11. Hardness values of S1 sample rate varies from 688 Hv to 1354 Hv. The hardness values measured from the coverage area of the S2 sample are between 710 Hv and 1045 Hv and the upper value is lower than S1 and the lower value is higher

than S1. The microhardness values measured at S3 are between 860 and 2440 Hv. The lowest hardness value was seen on sample S2, as seen in Figure 11 the S3 has a very high hardness value on the sample compared to the others. From the XRD graph of high hardness value S3 sample it is tied to hard carbides in a very large amount. Compared with hardness values of coatings, may be associated with a decrease in the content of low hardness value boron in the

transition zone due to low boron, titanium and tungsten content in the transition zone milder phases were produced compared to the phases in the coating zone. This large reduction in the transition zone can be considered as an advantage of the good diffusivity of the boride layer to the substrate material [13,20]. The microhardness values in the heat-affected zone

of the substrate material range from 270 Hv to 350 Hv and decrease 265 Hv as it moves towards the base material and ultimately to the original hardness values of the base plate material. In general, microhardness values are consistent with the literature [13].

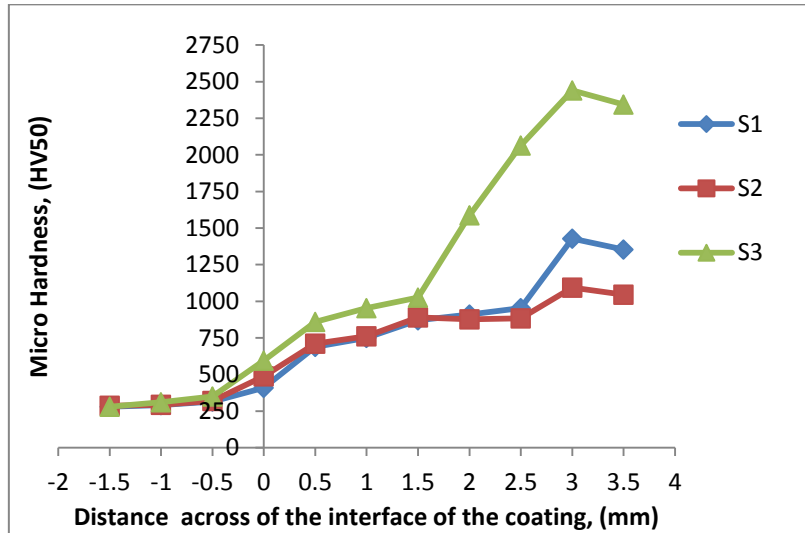


Fig. 11. Microhardness

3.4 Wear

The abrasion rates of the samples were investigated as weight loss against the road under 170 N load (Figure 12). The results show that the weight loss is up to 500 meters raising. Increased wear path indicates weight loss is falling. The minimum amount of wear was observed in S3, that

it contains high FeB, FeTi, FeW and C the number of boron, titanium, wolfram and carbon-bonded carbides formed by these elements. Generally, in all three samples, the amount of abrasion followed a horizontal course with a decrease of 500 m due to the formation of graphite sheets.

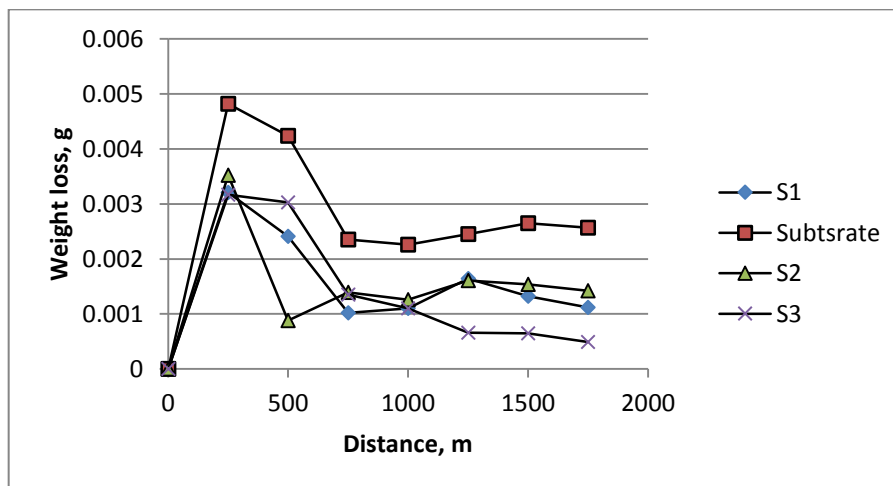


Fig. 12. Wear graphics

IV. CONCLUSIONS

The main metallurgical reaction occurred between FeB, FeTi, FeW and C during coating of FeB-FeTi-FeW-C mixed powders. The metallurgical reaction between these quartets is only limited in the transition region.

Many types of carbides and borides have been formed. TiB₂, Fe₂B, WB₄, Ti₃B₄, B₂W, B₈C, TiB₁₂, FeWB, WB, Fe₇C₃, Fe₃W₃C phase formed on the coating surface. XRD results of sample S₂ are seen WB₄, WB, Fe₇C₃, Fe₃W₃C phases. X-ray analysis of sample S₃ result, WB₄, Ti₃B₄, B₈C, TiB₁₂, FeWB, WB, Fe₇C₃, Fe₃W₃C in addition to the phases were seen Fe₅C₂, B₄C, FeB, TiC, B₁₃C₂, Fe₂C. Although the FeW ratio is kept constant at 2% in all three samples, various and important wolfram carbides are formed.

On the basis of the experimental results it can be concluded the graphite obtained from the GTAW

process was used for the surface alloying elements together with the fact that the carbon steel can improve the wear resistance [21]. Since the addition of carbon increases from 3% to 13%, the addition of graphite leads to the formation of graphite sheets, so the amount of wear is gradually reduced. As a result of the wear test used in this study, the least amount of wear was observed in S₃, high FeB, FeTi, FeW and C and the formation of a large number of boron, titanium, wolfram and carbon-bonded carbides formed by these elements.

ACKNOWLEDGEMENT

The authors wishes to thank Firat University Scientific Reserch Pprojects Unit. This work was supported by FUBAP (Project No: 1809)

REFERENCES

- [1] S. Buytoz, M. Ulutan, M. M. Yildirim, "Dry sliding wear behavior of TIG welding clad WC composite coatings", *Applied Surface Science*, Vol. 252, Iss. 5, pp. 1313-1323, 2005.
- [2] E. Gemelli, A. Gallerie, F. C. T. Kopp, N. H. A. Camargo, "Improved surface properties of D2 steel by laser surface alloying", *Journal of Materials Science*, Vol. 40, pp.5649–5653, 2005.
- [3] I.R. Pashby, S. Barnes, B.G. Bryden, "Surface hardening of steel using a high power diode laser", *Journal of Materials Processing Technology*, Vol. 139, pp. 585–588, 2003.
- [4] M. M. Yildirim, S. Buytoz, M. Ulutan, "Microstructural Changes to SiC Coated Metallic Surfaces Produced by the TIG Welding Process on a 45Mn5 Steel", *Prakt. Metallogr.*, Vol. 44 (2), 59-69, 2007.
- [5] X. Wu and G. Chen, "Nonequilibrium microstructures and their evolution in a Fe–Cr–W–Ni–C laser clad coating", *Materials Science and Engineering*, A270, pp. 183–189, (1999).
- [6] J. Khedkar, A.S. Khanna, K.M. Gupt, "Tribological behaviour of plasma and laser coated steels", *Wear*, Vol.205, pp.220-227, 1997.
- [7] M.H. Korkut, O. Yılmaz, S. Buytoz, "Effect of aging on the microstructure and toughness of the interface zone of a gas tungsten arc (GTA) synthesized Fe–Cr–Si–Mo–C coated low carbon steel", *Surface and Coatings Technology*, Vol.157, pp. 5–13, 2002.
- [8] S.O. Yılmaz, Wear behavior of gas tungsten arc deposited FeCrC, FeCrSi, and WCo coatings on AISI-1018 steel, *Surface and Coatings Technology*, 194 (2005)175–83.
- [9] B. Matijević, and M. Stupnišek, Novelty in diffusion coating technology, *Materials and Manufacturing Processes*, 24 (2009) 887–893.
- [10] H. Fujita and T. Arai, Carbide coatings in molten Borax bath- growth mechanism of layer, Properties and Application, *Proceedings of the 4th Int. Congress of IFHT*. Berlin, 1985, 1109–1124.
- [11] Z.Y. Ma, S.C. Tjong, L. Gen. In-situ Ti–TiB metal–matrix composite prepared by a reactive pressing process, *Scripta Materialia*;42(4)(2000)367–73.
- [12] S.O. Yılmaz, M.Ozenbas, M. Yaz., Synthesis of TiB₂-reinforced iron-based composite, *Coating, Tribology International* 42 (2009) 1220–1229
- [13] L. Bourithis, S. Papaefthymiou, G. D. Papadimitriou, Plasma transferred arc boriding of a low carbon steel: microstructure and wear properties, *Applied Surface Science*, Volume 200, 1-4(2002) 203-218
- [14] M. Darabara, G.D. Papadimitriou, L. Bourithis, Production of Fe–B–TiB₂ metal matrix composites on steel surface, *Surface & Coatings Technology* 201 (2006) 3518–3523
- [15] M.F. Buchely, J.C. Gutierrez, L.M. Leon, A. Toro, The effect of microstructure on abrasive wear of hardfacing alloys, *Wear* 259 (2005) 52–61.
- [16] H. Berns, Microstructural properties of wear resistant alloys, *Wear* 181(1995) 271–279.
- [17] M. Kirchgabner, E. Badisch, F. Franek, Behaviour of iron-based hardfacing alloys under abrasion and impact, *Wear* 265 (2008) 772–779
- [18] Xiaolei Wu, Guanguan Chen, *Material Science and Engineering*, A 270 (1999) 183.
- [19] L. Zhang, B. Liu, H. Yu, D. Sun, Rapidly solidified non-equilibrium microstructure and phase transformation of plasma cladding Fe-based alloy coating *Surface & Coatings Technology* 201 (2007) 5931–5936
- [20] M. Eroglu, Boride coatings on steel using shielded metal arc welding electrode: Microstructure and hardness, *Surface & Coatings Technology* 203 (2009) 2229–2235
- [21] M. Yaz, In situ formation of square shaped Fe₂B borides in coated surface produced by GTAW, *JOAM*, 15(2013) 1037 – 1046.

Analysis of Accredited Laboratories in the Steel Sector in Turkey

Murat KAVRUK*, Bülent AYDEMİR⁺

[#]TSE, TSE Çayırova Kampüsü, Çayırova /Kocaeli/TURKEY, mkavruk@tse.org.tr

⁺TUBITAK UME, Tubitak Gebze Yerleşkesi, Gebze/Kocaeli/TURKEY, bulent.aydemir@tubitak.gov.tr

Abstract—As a conformity assessment activity, testing is a crucial step in iron and steel industry. The characteristics and quality of the material are determined by the test. Manufacturers who manufacture in the sector and manufacturers who buy products make the acceptance of the material according to the results of the test. The reliability of test results is ensured through accreditation. In this study, the scope of the accredited laboratories in Turkey serving the iron and steel industry has been examined in detail. These results are compared with the same sector-based laboratories that are accredited in Germany. As a result, proposals have been made for future plans of test laboratories serving the iron and steel industry.

Keywords— Accreditation, Test laboratory, Iron and Steel industry, Scope

I. IRON & STEEL SECTOR

Due to their vast usage areas, Iron and Steel (will be mentioned as I&S) such as; construction, automotive, machinery, transportation or home appliances, even the slightest growth in other industries, can increase growth in the I&S sector as shown in Fig.1.

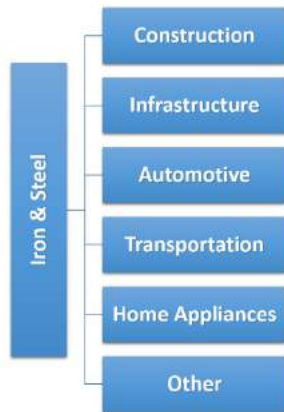


Fig. 1. Main effective sectors of I&S industry

In 2011 and 2012, I&S sector in Turkey had shown a significant growth pattern being the fastest country to increase its steel production. Based on this trend, Deloitte and Emerging Market Insights had forecasted a continuous expansion in Turkey for the following 5 years [1]. However, the reality of the market cannot be more deviated. Turkish steel production showed a drop in 2013-2015 resulting the third country to have largest decline in the world and loss of position in the world's

largest steelmaking countries list and dropped to 9th rank from 8th [2].

“Since Chinese, Russian and Ukrainian steelmakers and exporters became more active both in Turkish market and Turkey’s export markets with lower prices, Turkish steelmakers had difficulty in entering the main export markets where those competitors increased their existence. Turkey’s steel products export/import ratio declined from 126 % to 95 %. As a result, despite having more than 19 million tonne (steel production) capacity, Turkey became a net steel importer for the first time in 15 years” [2].

A. 2023 Goals & Projection of Turkey

Policy of Turkish Steel Industry has been revised in 10th Development Plan (2014-2018) as focusing on increasing competitiveness in export via R&D and innovation activities by:

“In the basic metals industry, sustainable and secure procurement of inputs will be ensured. Diversification in products that bear higher value-added and are imported will be ensured by increasing their weight in domestic production” [3].

In accordance with the development plan, Investment Support and Promotion Agency of Turkey states that “Turkey’s iron-steel export goal for 2023 is \$ 55 billion, securing a 4 % share of the global iron-steel market and growing annually 7.4 % on average. Turkey aims to reach 85 million tonne year capacity and 70 million tonne/year production.” [4].

The 2023 export goals for the sub-sectors of iron and steel can be summarized as follows:

Long product	\$ 23.6 billion
Flat product	\$ 15.7 billion
By products	\$ 3.9 billion
Pipe	\$ 7.9 billion
Construction parts	\$ 3.9 billion

In addition to these expectations, four million of vehicle production annually is projected in 2023, three million of it aimed for export. Thus, the sector will need a vast supply of finished steel products which will also catalyze the trading and conformity assessment of I&S industry [4].

B. I&S Sector Similarities and Differences Between Germany and Turkey

Germany has been chosen for laboratory competence comparison due to some reasons based on their respective market and conformity assessment data. According to the World Steel association, Germany and Turkey have world crude steel production percentage of 3 % and 2 % respectively

[5]. And also, the driving forces of I&S market is similar in Germany like automotive, engineering and residential construction sectors as key customer industries. Germany is the world's second-largest steel importer as Turkey is a net steel importing country. The steel industry in Germany roughly 1.40 % of German GDP (Gross Domestic Product) [6]. This is higher than the percentage of sector in Turkey (1.10 %) but similar with the 2023 Projection (1.35 %). GDP percentage of I&S industry in Turkey is 1.08 % in 2012, and has a positive correlation with total GDP increase with 1.35 % expectations in 2023 [7]. For the sake of generalization 1.10 % of GDP percentage is used in this study.

The top 5 source countries for Germany's steel imports represented 63 % of the total steel import volume in order of Belgium, Italy, Netherland, France and Austria [8]. In addition to geographic advantage, it can be arguably stated that, ability to choose, trade, test and inspect of quality steel products makes these countries, capacity to produce quality steel, top steel exporters to Germany. Deutsche Bank Research clearly and officially clarify same threat of China-originated imports as a near future problem (in case of increase in quality), not a real-time problem as in the case of Turkey.

According to the report, it is mainly the quality of steel, which is a conformity assessment issue, which determines the import. "Even though most of the rising volume of steel from China does not (yet) come directly to Germany, and often does not match the quality of the steel produced in Germany, the Chinese output and exports still have an overall impact on German producers. Firstly, if the steel is of similar quality (which is not yet usually the case) and is offered in third-party markets in which German producers are also active; this has a negative impact on German sales in terms of volume and/or price. Secondly, steelmakers from other countries that are also suffering from China's export boom are now increasingly attempting to resolve their problems by penetrating the German market, which is attractive because of its relatively high volume consumption. Thirdly, it is becoming tougher than before to sell German metal products in Chinese markets because of the rise in domestic supply in China. The adverse impact on metalworking companies is naturally also felt in turn by domestic steel producers in Germany [9]. Addition of information about top 10 countries that Germany exports steel (9 EU countries plus USA), it is clear that trading of high quality I&S products is key factor in gaining advantage in this sector.

II. CONFORMITY ASSESSMENT IN I&S SECTOR

Mentioning of quality has a direct correlation with quality assurance and conformity assessment activities. Fig. 2 is graphing Conformity Assessment Cycle (CAC). With some shortcuts or substitution of other steps, this cycle is applicable to all sector or activity accommodating conformity assessment in its context and lifecycle.



Fig. 2 Conformity assessment cycle (CAC)

When we started to analyze I&S sector for conformity assessment in order to shed light to the comparison of sectors in Germany and Turkey, we have come up with the fact that; testing can be used as a reference point for comparison. Since the I&S is a world-wide well established sector, standards and metrology are universal issues and calibration is a consequence of the devices used in the sector. However; for the development, trading and quality determination of products in I&S sector, testing, certification and inspection are crucial steps. Thus in this research, accredited testing laboratories and testing methods are to be analysed at the level of methods.

There are more than 20 certifications that can be applicable to I&S industry, nearly half of them containing testing necessities in its context. Some of them are listed below.

- Ship Plate Manufacturing Approval Certificate - Lloyd's Register
- CE Certificate of Structural Steel
- CE Certificate for Pressure Vessels (DIN EN 10028)
- RINA Normal and High Strength Construction Steel Manufacturing Approval Certificate
- Approval Certificate for Ship Plate Factory - BV
- TS 9016 Product Compliance Certificate
- TS 9914 - Steel Billets, Square Crossed Product Compliance Certificate

Rest of this paper focuses on the accredited laboratories and methods in Turkey related with I&S industry and comparison of this data with Germany.

III. ANALYSIS OF LABORATORY CAPABILITIES

As a result of a project conducted in Turkish Standards Institution (TSE), a high correlation was observed between GDP and number of accredited laboratories for a particular country [10] and same approach was proved to be applied for sector-specific analysis for accredited laboratories in food sector [11]. Based on the GDP and number of accredited laboratories of 20 countries with different geographic, economic and industrial status given in Table 1, highly positive correlation of $0.9 < r = 9.906 < 1$ was observed.

GDP of country ~ number of accredited laboratories

From this information, a coefficient of accredited laboratories (k_K) is proposed with a value of:

$k_k: 0,97 \times 10^{-9}$

This coefficient can be used to predict the projected volume of accredited laboratories on average founded on GDP of a country. These findings will be used at end of the analysis. Although validity of this derived number as a coefficient is at its infancy, for conformity assessment sector, it is pioneer step towards sector prediction and trend analysis.

TABLE XIV
GDP AND ACCREDITED LABORATORY DATA OF COUNTRIES

Country	Accredited Labs.	GDP 2015 (\$ million)	Proportion of Lab. and GDP ($\times 10^9$)
Germany	2.706	3.852.556	0,70
Italy	1.498	2.144.338	0,70
Belgium	1.459	533.383	2,74
Mexico	740	1.282.715	0,58
Turkey	713	799.535	0,89
Czechia	638	205.523	3,10
Malaysia	565	326.933	1,73
Switzerland	520	68.543	7,59
Portugal	500	229.584	2,18
South Africa	493	349.817	1,41
Croatia	383	57.223	6,69
Singapore	318	307.872	1,03
Egypt	247	286.538	0,86
Norway	128	499.817	0,25
Bosn.& Herz.	63	18.344	3,43
Macedonia	60	11.324	5,30
Sri Lanka	59	74.941	0,79
Slovakia	25	99.790	0,25
Algeria	21	214.063	0,10
Uzbekistan	13	72.744	0,18

C. Accredited Laboratories and Methods of Turkey in I&S Sector

The analysis of TÜRKAK Accredited Laboratory Database of 2015 [12], about the test methods related with the I&S sector shows us that, there are 86 scope from 27 different accredited bodies having 30 distinctly identified laboratories (as branches). For instance, Turkish Standards Institution has one accredited body (AB-0001-T) having 20 distinct laboratory units (in terms of TÜRKAK audition units) in 9 cities and more than 1.500 scopes. Since the body represents legal entity and laboratory represents the scope of service given to costumers, the number and characteristics of laboratories has been used in the study.

Fig. 3 shows the distribution of major steel production sites (indicated as shades of red with respect to number of industry) and main steel-intensive sectors (indicated as blue cylinders being sized according to the number of industry) in Turkey [13], [14]. As seen in the map, the industry is concentrated in the west region of Turkey, in accordance with most of other sectors. However, the spatial correlation of steel production and utilization sites are highest in Izmir, Hatay and Kocaeli.

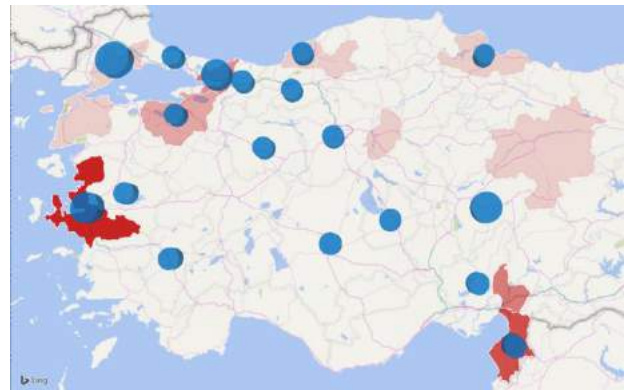


Fig. 3. Distribution of major steel production industry in Turkey

The accredited laboratory service locations are shown in Fig. 4 as shades of red indicates the distribution and concentration of accredited laboratories in I&S sector, blue cylinders represent the number of scopes in particular area indicating majority of the accredited scope of Turkey. Istanbul, Kocaeli and Ankara share the majority of the scopes due to private (in Istanbul) and public (in Ankara and Kocaeli) laboratory concentration [13], [14].

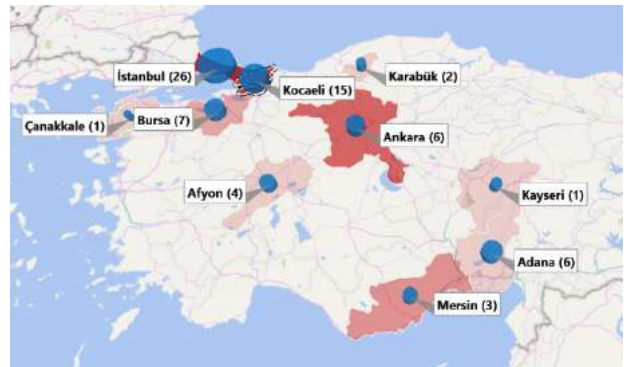


Fig. 4. Distribution of accredited laboratory service locations in Turkey

In the Fig. 5, the distribution of bodies, laboratories and scopes are shown in terms of legal institution type. Although the numbers of private laboratories are seen higher then public laboratories, number of scope per accredited body represents a higher value of 5.3 than private sector of 2.8 as seen in Fig. 6. From these findings, we can state that, in terms of giving service of international validity, public laboratories are still comprehensive capacity.

The scope of these laboratories can be further analysed in terms of base-standard for accreditation. The term “base-standard” is proposed for the first time in this study in order to identify the root of laboratory activity. For example, although a product standard like TS 708 is a national standard, at its base, there are method standards like ISO 15630-1 which are international.

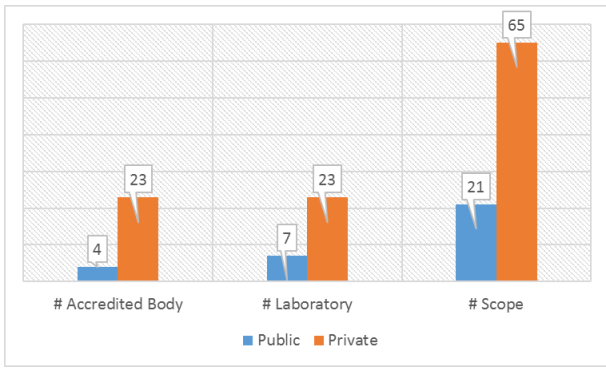


Fig. 5. Distribution of accredited laboratory according to institution type in Turkey

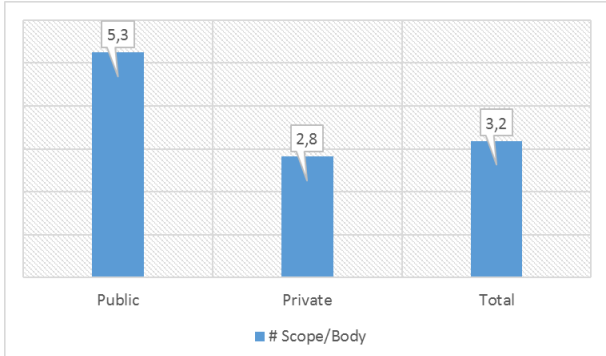


Fig. 6. Changing scope/body ratio according to institution type in Turkey

From this perspective, in I&S sector, the accredited scope of laboratories in Turkey is shown in Fig. 7. 85 % of scopes are international and American standards, which have high validity in market, and only 5 % of the scope is at national level. This gives us the conclusion that, accredited laboratories in Turkey have completed their integration at the international in terms of their focusing area. The issue of the extensiveness and efficacy of these scopes are topic of another research and with current data available; it is out of the scope of this research.

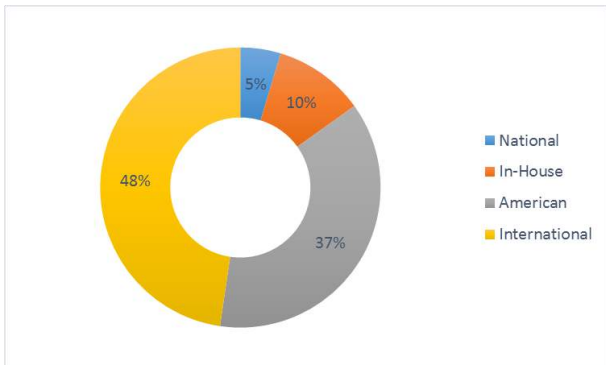


Fig. 7. The origin of standard method of the accredited scope of laboratories in Turkey

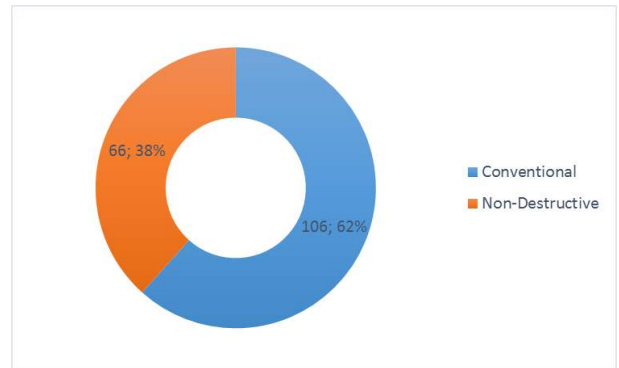


Fig. 8. Changing scope/body ratio according to institution type in Turkey

When the scopes of accreditation in I&S sector is diffracted further into units of standards, a different figure emerges. There are in total 172 occurrences of standard code in I&S accreditation scope having 84 unique standards/in-house methods shown in Table 2. If we divide the laboratory service as conventional and non-destructive, the percentage in Fig. 8 will appear. Since NDT standards are highly subdivided into sub-activities (like different international standards for measurement and interpretation), the number of occurrences of standards related with NDT are significant. Relatively comprehensive scopes of NDT laboratories also contribute to these results.

Half of these standard occurrences are categorised under 20 different standards. National standards and in-house methods will be excluded for comparison with accreditation scopes of Germany.

TABLE XV
MAJOR STANDARD TYPES AND OCCURRENCES IN SCOPES FOR TURKEY

Standard	Occurrences in TURKAK Database	Standard Type
ISO 6892-1	11	method
TS 708	11	product
ISO 15630-1	10	method
ASTM E 415	10	method
In-House	9	method
ASTM E 1086	7	method
ISO 17635	6	method
ISO 5817	6	method
KTA 3401.1	5	method
KTA 3401.3	5	method
KTA 3401.4	4	method
ASTM E 3	2	method
ASTM E 45	2	method
EN 13674-1	2	product
ASTM E 381	2	method
ISO 2597-1	2	method
ISO 4968	2	method
EN 13261	2	product
ASTM A255	2	method
ISO 14284	2	method
TS 12655	2	product
ASTM E 1077	2	method
ASTM E 1019	2	method

The general distribution in number of occurrences of the standards is shown in Fig. 9. There are nearly 60 standards occurred only once in the whole scope, while only a small amount of standards are repetitive in the scope. Although this graph is insufficient to reach a conclusion, distribution of the standards frequency having left-hand side peak can arguably state a developing laboratory sector in I&S industry in terms of accreditation; since, there are many standards scattered in one or two laboratories and/or scopes, while small but apparent number of standards are becoming common in laboratories and peak frequency number are nearly 1/3 of total number of laboratories.

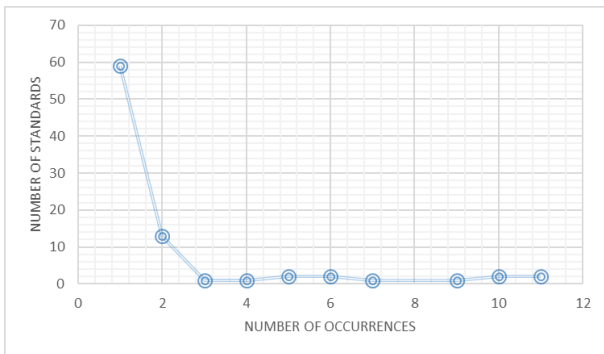


Fig.9. Occurrence graphics of standards

D. Comparison of Accredited Laboratory Capability between Turkey and Germany

As a second stage of the analysis in accredited laboratories of I&S sector, the international standards identified in national accredited laboratory database of TÜRKAK and have been investigated in DAkkS, national accreditation body for Germany. Table 3 summarizes the comparison between the number of laboratories in Turkey and Germany having the corresponding standard in its accreditation scopes.

When the Table 3 is drawn in a graph, following Fig. 10 can be observed. For nearly all of the standards mentioned, there are more accredited scopes of laboratory in Germany. This trend is especially evident in ISO 6892-1 (Metallic materials - Tensile testing - Part 1: Method of test at room temperature), ISO 17635 (Non-destructive testing of welds -- General rules for metallic materials) and ISO 5817 (Welding - Fusion-welded joints in steel, nickel, titanium and their alloys (beam welding excluded) - Quality levels for imperfections) consequently.

Since industrial sector comprises 30 % of the total GDP of Germany, accreditation about tensile strength and welding can be associable for the quantitative competence of the country. However, it is very crucial to note that, a NDT (non-destructive testing) method is also higher accreditation ratio in Germany which is also related with welding. A similar difference in number and scopes of NDT has been observed in other methods as the data is not shown.

TABLE III
COMPARE MAJOR STANDARD TYPES AND SCOPES FOR TURKEY AND GERMANY

Standard	Labs in Turkey	Labs in Germany
ISO 6892-1	5	145
ISO 15630-1	5	20
ASTM E 415	7	10
ASTM E 1086	2	4
ISO 17635	2	44
ISO 5817	2	30
KTA 3401.1	2	2
KTA 3401.3	2	4
KTA 3401.4	2	5
ASTM E 3	1	4
ASTM E 45	1	16
EN 13674-1	1	0
ASTM E 381	1	4
ISO 2597-1	1	2
ISO 4968	1	16
EN 13261	1	4
ASTM A255	1	9
ISO 14284	1	1
ASTM E 1077	1	4
Total	39	324

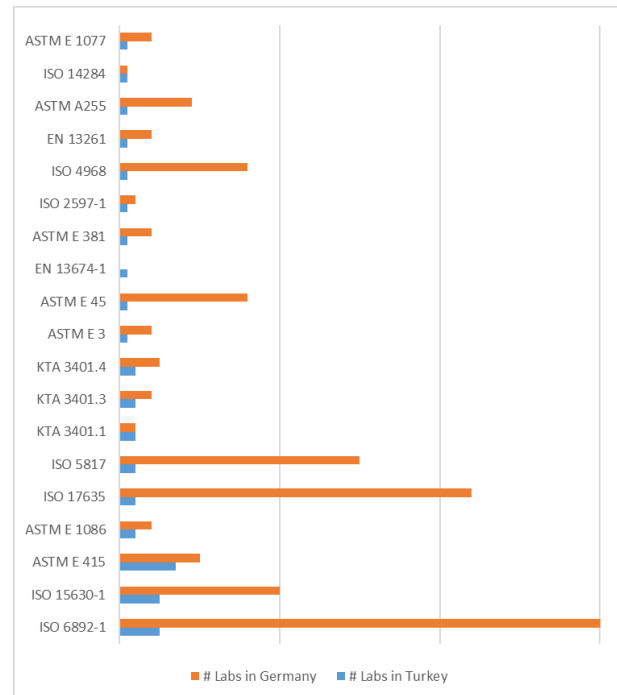


Fig. 10. The compare on standard method and the accredited scope of laboratories in Turkey and Germany

At the last stage of our analysis, number of accredited laboratories in I&S sector was compared based on GDP % and k_K . The following numbers appear to be interpreted.

Table 4 gives us the summarized comparison of laboratories between Turkey and Germany. Coefficient of accredited bodies (k_K), being derived from GDP and number of accredited bodies of 20 different countries, allows us to execute a $Lab_{DER-total}$ (number of predicted/derived accredited laboratory in

particular country) and Lab_{DER-I&S} (number of predicted/derived accredited body in I&S sector). Although the apparent number of laboratories (Lab_{APP}) is similar to derived for Turkey with a fair 10 % margin, the scenario is much deviated in Germany maybe due to high number of accredited laboratories and corresponding trade volume in Belgium.

TABLE IV
THE SUMMARIZED COMPARISON OF LABORATORY BETWEEN TURKEY AND GERMANY

Country	Lab _{APP} - total	Lab _{DER} - total	Lab _{APP} - I&S	Lab _{DER} - I&S
Turkey	713	776	27	9
Germany	2707	3737	194	52

However, the situation is reversed in accredited laboratories in I&S sector. Since I&S sector is a basis for most of other sectors, this vertical relationship in industry can also be expected in conformity assessment and laboratory sectors. Thus, in the beginning of the study, higher Lab_{DER-I&S} was expected in both countries. After data mining numbers appeared, it has been concluded that the I&S laboratory competence of Germany is higher as Lab_{APP-I&S} of Germany gives a higher ratio in against both total apparent laboratories (7.2 % of Germany to 3.8 % of Turkey) and derived/expected accredited body (373 % of Germany to 300 % of Turkey).

IV. CONCLUSIONS

As a pioneering and correlative study in laboratory-based and method-based accredited scope analysis, this research has come up with some quantitative data that can be further analysed. Accredited laboratory scopes of Turkey and Germany in I&S sector have been focused as a representative study for both evaluating the laboratory competence comparison and correlation of these values with the GDP and industrial scale of the sector itself.

Accredited laboratory spatial distribution and overlapping with producing and utilizing I&S industry in Turkey have been emerged for the first time with this research. In addition, by implementing a finding of a previous study, analysis with a coefficient for accredited laboratories has given us the competence of Turkey and Germany. Based on the proposing a correlation with GDP and analyzing method-based accredited scopes: two important findings were emerged. Firstly, non-destructive methods are more common in Germany and not only independent laboratories, but also the institutes and laboratories of firms have also accredited scopes. Secondly, percentage of accredited laboratories of Germany reveals a stronger vertical connection of laboratories between I&S sector and steel utilizing industries resulting a positive deviation from what the coefficient had predicted.

In this paper, we proposed some methods for analyzing laboratory database of countries in spatial and sector-oriented distribution. Although there are some parameters unable to be integrated in the analysis such as; in-house methods, national standards, scope-based data of Germany and skipped standards, this research revealed preliminary findings that can be applied

to other sectors. The literature does not contain such analysis of sector-based laboratories. Thus, in terms of conformity assessment sector and its implications to other industries, the findings and proposals of this paper have the potential to become tools of prediction and forecasting.

REFERENCES

- [1] Deloitte, "The Iron and Steel Industry in Turkey," Investment Support and Promotion Agency of Turkey, Ankara, 8, 2013.
- [2] Turkish Steel Producers Association. (2015) Turkish Steel Industry in 2015. [Online]. Available: <http://www.dcu.org.tr/en/page.asp?id=30>
- [3] Y. Ocal, "Innovation in the Steel Sector: Turkish Steel Industry," Republic of Turkey Ministry of Development, Ankara, 5, 2015.
- [4] Deloitte, "The Iron and Steel Industry in Turkey," Investment Support and Promotion Agency of Turkey, Ankara, 39, 2013.
- [5] World Steel Association, "World Steel in Figures 2015," World Steel Association, Brussels, 9, 2015.
- [6] S. Fenton. (2016) German economy minister says EU should protect steel sector. [Online]. Available: <http://www.reuters.com/article/europe-steel-gabriel-idUSL5N17P3RB>
- [7] Deloitte, "The Iron and Steel Industry in Turkey," Investment Support and Promotion Agency of Turkey, Ankara, 11, 2013.
- [8] International Trade Administration, "Steel Imports Report: Germany," Department of Commerce, Washington, 4, 2016.
- [9] J. Auer, "German Steel Set to Benefit from Global Growth," Deutsche Bank Research, Frankfurt, 7, 2016.
- [10] B. Nasır, S. Alia, E. Çakıl, L. Ekşi, "Dünya Akredite Laboratuvarcılık Sektörü İncelemesi", *TSE Standard Ekonomik ve Teknik Dergi*, vol. 638, pp. 38-41, Jan. 2016.
- [11] M. Kavruk, "İslam Ülkelerindeki Helal Gıda Laboratuvarları ve Uygunluk Değerlendirme Faaliyetlerinin Araştırılması," Tur. thesis, Turkish Standards Institution, Ankara, Turkey, In Press.
- [12] (2015) TURKAK website. [Online]. Available: www.turkak.org.tr/
- [13] Turkish Steel Association. (2016) Steel Map of Turkey. [Online]. Available: <http://www.dcu.org.tr/en/page.asp?id=12>
- [14] Deloitte, "The Iron and Steel Industry in Turkey," Investment Support and Promotion Agency of Turkey, Ankara, 21, 2013.

Comparison of Various Critical Plane Approaches Under Proportional and Non-Proportional Multiaxial Stress States

Tuğçe Leblebici, Emin Sünbuloğlu, S. Ergün Bozdağ

Faculty of Mechanical Engineering, Istanbul Technical University, Istanbul, Turkey
leblebicitu@itu.edu.tr, sunbuloglu@itu.edu.tr, bozdager@itu.edu.tr

Abstract—The investigation of the fatigue behaviour of metals under non-proportional multi-axial stress states is an important problem to minimize design-induced errors and improve structural durability, especially for cast and light-weight sheet-metal structures. Various approaches that can be used in fatigue analyses make use of stress states, strain states and strain energy densities to obtain an endurance limit value, a fracture plane estimate, S-N curve and/or a combination of these. Thus, the determination of the possible initial cracking plane and an estimation of crack initiation is an important step in fatigue analysis of structural design, especially under multiaxial stress states based on theories that are stress-based where the method of critical planes is the most commonly applied. Such methods seek for the orientation of fracture plane by using different parameters based on the assumed input parameters. The purpose of this research is to identify and compare critical plane orientations using various stress approaches to critical plane methods. The determination of several parameters in different stress based critical plane search is indicated. Furthermore, critical planes are found for different stress states with using pre-assumed material properties from available test data. Based on the outcomes, a method of better versatility and ease of application is proposed among the methods investigated for practical applications of fatigue analysis.

Keywords— multiaxial stress, critical plane, fatigue analysis, non-proportional loading, multiaxial fatigue

I. INTRODUCTION

Under multiaxial cyclic loading, some changes such as crack initiation and propagation occur in the material microstructure. It is quite difficult to observe these structural changes from external surfaces. Therefore, analytical calculations are developed and a number of experiments are conducted to examine the material behaviour and determine the fatigue life.

Wöhler made first fatigue experiments on the wagon axles and used the S N diagrams for fatigue life of material. Different approaches are adopted with the developing technology and multiple formulas are used. The critical plane approach, which is defined as the maximum damage plane, is widely used. Critical plane definitions are formulated analytically in different forms. Fatigue life is also calculated afterwards by taking advantage of this approach [1].

Under non proportional loading conditions, it is necessary to determine the most appropriate analytical approach matching the experiments. Although there are various critical plane approaches under multi-axial stress state, studies on the

comparison of these critical plane definitions are yet insufficient. Therefore, in this study different critical plane definitions are made and the results are evaluated.

II. A BRIEF REVIEW OF VARIOUS CRITICAL PLANE APPROACHES UNDER PROPORTIONAL AND NON-PROPORTIONAL MULTIAXIAL STRESS STATES

Findley, McDiarmid and Matake evaluated the effect of alternating shear stress and normal stress fracture plane using Nishihara test results in combination of torsion and bending cases [2]. The definition of the critical plane is made by the different linear combinations of these two stress components and the specified material parameters. On the other hand Carpinter, Macha and Spognali calculated weighted mean principal directions [3]. Using these calculations, the critical plane is expressed as a nonlinear combination of maximum normal stress and the shear stress amplitude.

Different from these criteria, Dang Van and Papadopoulos carry on studies related to material mesoscopic behaviour. Dang Van studied indicate fatigue failure plane and definition of the plane compare with biaxial stress criteria [4]. Then Papadopoulos define generalized shear stress amplitude (T_a) [5]. Using the spherical coordinate system with the help of the unit vectors in the material plane. Papadopoulos search for T_a values for fully reversed torsion and fully reversed bending case. In addition to this T_a value, required material parameters are calculated from the S N diagrams and the maximum hydrostatic pressure value is used to determine the fatigue life limit.

In this paper, Findley, Matake, McDiarmid, Carpinteri, Papadopoulos and Dietmann stress based critical plane approaches, which are defined as combinations of shear stress and normal stress, are examined in detail. In addition to the fully reversed torsion and fully reversed bending conditions, Papadopoulos and Findley critical plane directions are found and evaluated for different stress states.

A. The Findley Formulation

Findley investigated the effects of mean stress and alternating on the orientation of the critical shear plane. The material parameter k has different values for brittle and ductile materials. According to this approach, the critical plane is

defined as maximum value of the linear combination of these stresses [6].

Findley's critical plane can be formulated by normal stress and shear stress amplitude [7].

$$\tau_a + k \sigma_{max} = f$$

$$k = \frac{2 \frac{\sigma_{af}}{\tau_{af}}}{2 \sqrt{\frac{\sigma_{af}}{\tau_{af}} - 1}}, f = \sqrt{\frac{\sigma_{af}^2}{4(\frac{\sigma_{af}}{\tau_{af}} - 1)}}$$

Where τ_a shear stress amplitude, k and f are material constants and σ_{max} is maximum normal stress value [2].

B. McDiarmid Formulation

Firstly McDiarmid obtains the maximum shear stress value determining the critical fatigue plane. Then the fatigue limit is determined by defining the shear stress, the maximum normal stress and the material parameters in non-proportional fatigue loadings [8].

McDiarmid fatigue limit can be defined as follows:

$$\tau_a + \frac{\tau_{af}}{2\sigma_u} \sigma_{max} \leq \tau_{af}$$

For the formula above, τ_{af} and σ_u denote, respectively, shear stress fatigue limit and ultimate tensile strength of materials [2].

C. Mataka Formulation

Mataka also expresses the critical plane equation linearly taking into account the influence of material parameters. In this approach, when the critical plane position is determined the maximum shear stress value and maximum normal stress value are used [9].

Mataka critical plane orientation can be computed as follows:

$$\tau_a + \mu \sigma_{max} \leq \tau_{af}$$

$$\mu = \frac{2\tau_{af}}{\sigma_{af}} - 1$$

Where μ is material parameter [2].

D. Papadopoulos Formulation

In contrast to other critical plane theory Papadopoulos criteria is based on mesoscopic approach. Under multiaxial stress condition, Papadopoulos describes failure material plane by unit vectors. Position of maximum generalised shear stress plane is investigated. This plane is defined as critical plane.

Fatigue failure criterion formulated below is based on generalised shear stress amplitude [5].

Fatigue limit criterion can be described by combination of maximum stress and maximum Ta value which is equal to [10];

$$\max(T_a) + \alpha_{\infty} \sigma \leq \gamma_{\infty}$$

Error index can be written as:

$$I = \frac{\text{left hand side} - \text{right hand side}}{\text{right hand side}} (\%)$$

E. Carpinteri, Spognali and Macha Formulation

Weight functions of principal stress are computed from ϕ , θ , θ Euler angles [3]. Carpinteri, Spognali and Macha determine maximum fracture plane by various weight functions [11]. They determine the fracture plane directions taking these weight functions into consideration and compare the test results with the analytical calculations. According to the comparison results, the optimal weight function is determined.

The weighted means of Euler angles are obtained from following equations [11]:

$$\phi = \frac{1}{W} \sum_{t_1}^{t_N} \phi(t)W(t)$$

$$\theta = \frac{1}{W} \sum_{t_1}^{t_N} \theta(t)W(t)$$

$$\theta = \frac{1}{W} \sum_{t_1}^{t_N} \theta(t)W(t)$$

The easiest weight function formulation is the arithmetic average of these angles. The authors propose that the most effective one as Weight VI in

Weight VI

$$W_k = 0 \quad \text{if } \sigma_{1k} < a \sigma_{af}$$

$$\left(\frac{\sigma_{1k}}{a \sigma_{af}}\right)^{m_{\sigma}} \quad \text{if } \sigma_{1k} \geq a \sigma_{af}$$

$$(k=1, \dots, N)$$

$$(0 < a \leq 1)$$

where σ_1, σ_{af} , m_{σ} and a are maximum principal stress, fatigue strength limit under sinusoidal tension-compression, exponential constant and constant coefficient respectively [11].

F. Dietmann Formulation

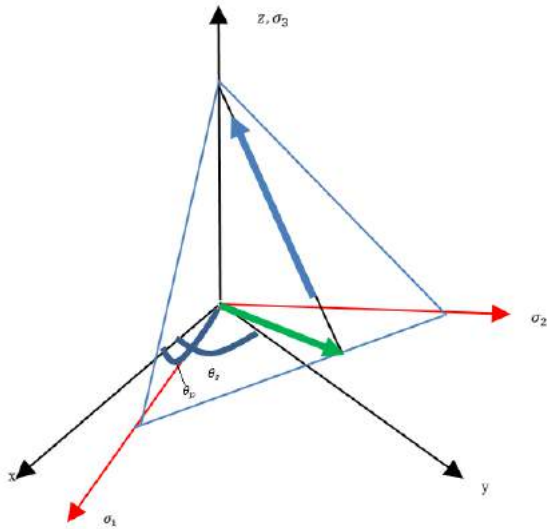


Fig. 1 Position of the x-y plane

Dietmann reveals Modified Octahedral Shear Stress Theory while determining the critical plane position. According to Dietmann theory, xy plane is defined as biaxial loading plane.

The principal stress direction is determined in xy plane. The angle of maximum shear stress vector with x axis is found by taking advantage of principal direction value. It is assumed that for this stress condition, the octahedral plane also rotates around the z axis by a fixed value. The critical plane position is thus determined by taking the projection of the shear stress vector in the xy plane onto the fixed z axis [12].

III. Comparison of Available Results from Authors

Papadopoulos et al. define several critical plane approaches and compare critical planes error for different materials under out of phase bending and torsion [10]. In addition to this study, four critical plane angles are calculated and compare with each other. As shown in Table 1 Findley, Mataka and McDiarmid critical planes with linear formulas have similar values while Papadopoulos cannot calculate a specific critical plane angle.

The experimental values in the Table 3 are taken from multiaxial fatigue study of Carpinteri and Spognali. They examine also different material plane orientations and calculate error estimation [2]. As noted in Table 2, the critical plane is defined for different stress states with hard steel properties in present research. The critical plane angle is determined for each bending and torsion stress combination.

IV. A Systematic Comparison of Various Approaches under Various Biaxial Stress States

Biaxial stress state including two normal stresses are investigated to determine the optimal critical plane approach. In Carpinteri et al. study, Rotlev's experimental data are used and calculate critical plane angle by defining the weight functions [3]. Fatigue limits are determined taking into account the properties of 0.35% C steel. In addition to this, Papadopoulos, Dietman et al. and linear critical plane theories such as Findley, Mc Diarmid and Mataka critical plane angles are obtained. As seen in Table 3, critical plane angles have different values according to these six critical plane approaches.

Table 16 Comparison of Experimental and Theoretical Critical Plane Angles

Test No	1	2	3	4	5	6	7	8	9	10
Sxx,a	138,0	140,4	145,7	150,2	245,3	249,7	252,4	258,0	299,1	304,5
Sxx,m	0	0	0	0	0	0	0	0	0	0
Sxy,a	167,1	169,9	176,3	181,7	122,7	124,9	126,2	129,0	62,8	63,9
Sxy,m	0	0	0	0	0	0	0	0	0	0
Phase	0	30	60	90	0	30	60	90	0	90
Mataka Error	1,8	2,8	8,5	11,8	3,6	5,4	3,3	-1,4	2,6	-1,4
Mataka Critical Plane Angle	100	100	95	90	113	112	110	90	35	45-135
McDiarmid Critical Plane Angle	100	100	95	0-90	23	23	110	90	35	45-135
McDiarmid Error	-2,5	-2,3	1,1	3,2	-2,8	-4,6	-7,7	-15,9	-6,3	-10,7
Findley Error	0,9	1,5	5,6	8,8	4	4,4	1,3	-3,5	1,7	-1,9
Findley critical Plane Angle	95	95	95	90	*	*	105	90	40	50-130
Papadopoulos Critical Plane Angle	0 70:90 160:180	0	0-90	0	*	*	0-90	0-90	*	0 30:90 115:180
Papadopoulos error	-2,3	-1,0	2,6	6,3	1,5	3,1	4,2	6,7	0,9	2,7

Papadopoulos et al data are used in calculations [10]

Table 17 Comparison of Experimental and Theoretical Critical Plane Angles

Test No	1	2	3	4	5	6	7	8	9	10	11
Syy-A	327,7	308,0	255,1	141,9	255,1	142,0	255,1	147,2	308,0	264,9	152,5
Syy-Phase	-	-	-	-	-	-	-	-	-	-	-
Sxy-M	-	-	-	-	-	-	-	-	-	-	-
Sxy-A	0,0	63,9	127,5	171,3	127,5	171,2	127,5	177,6	63,9	132,4	184,2
Sxy-Phase	0	0	0	0	30	30	60	60	90	90	90
Exp. Angle (°)	0,0	12,0	22,0	34,0	16,0	32,0	8,0	22,0	0,0	0,0	28,0
Dietmann et al. Critical Plane Angle	0,0	124,0	112,5	101,5	130,0	164,0	0-90	0-90	0-45-90	0-45-90	0-45-90
Carpinteri Angle for weight I	0	0	1	1	0	1	0	0	0	0	0
Carpinteri Angle for weight II	0	0	0	0	0	0	0	0	0	0	0
Carpinteri Angle for weight III	34	34	34	25	30	25	39	26	34	43	34
Carpinteri Angle for weight V	12	12	11	8	11	7	11	6	12	12	8
Carpinteri Angle for weight VI	101	19	97	32	23	167	157	43	102	86	37
Carpinteri Angle for weight VII	0,0	0,1	0,2	0,1	0,1	0,1	0,1	0,1	0,0	0,0	0,0
Papadopoulos Error	4,2	3,8	5,5	0,2	5,2	-0,2	5,2	3,5	3,8	9,5	7,8
Papadopoulos Critical Plane	*	*	0:45 90:135	0:20 90:110	0-90	0-90	0-90	0-90	0-90	0-90	0-90
McDiarmid Error	-5,1	-3,6	1,0	-0,6	-2,7	-3,0	-14,0	-4,0	-10,0	-19,0	5,0
McDiarmid Critical Plane	45,0	35,0	22,5	11,0	22,0	11,0	20,0	7,0	45,0	45,0	90,0
Matake Error	4,2	3,6	8,6	2,4	7,7	-0,2	-8,0	3,2	-0,3	-8,9	-6,1
Matake Critical Plane Angle	45	125	112	10	112	10	20	5	45-135	45-435	0
Findley Error	4,1	4,6	8,2	3,5	6,6	2,3	2,4	6,4	-0,8	-0,9	10,3
Findley Critical Plane Angle	50-130	40-140	30	95	105	95	105	95	90-130	90	5

Carpinteri and Spagnoli data are used in calculations [2]

Table 18 Comparison of Experimental and Theoretical Critical Plane Angles under Various Biaxial Stress States

Test No	1	2	3	4	5	6
Sxx-A	227,6	233,5	171,7	121,6	6,9	155
Sxx-M	0	52	-24,5	11,8	0	79,5
Sxx-Phase	0	0	0	0	0	0
Syy-A	1,96	191,3	228,6	156	224,6	118,7
Syy-M	0	41,2	-11,8	-7,8	-2,9	0
Syy-Phase	-	-	-	-	180	180
Sxy-M	-	-	-	-	-	-
Sxy-A	-	-	-	-	-	-
Sxy-Phase	-	-	-	-	-	-
Exp. Angle (°)	0	0	90	90	90	0
Findley	0	45-135	50-130	45-135	50-130	40-140
McDiarmid	45-135	135	45	135	135	135
Matake	45-135	135	45	135	135	135
Carpiteri weight I	0,0	0	0	0	0	0
Carpiteri weight II	0	0	0	0	0	0
Carpiteri weight III	15	24	0	15	26	56
Carpiteri weight IV	15	24	15	15	26	73
Carpiteri weight V	6	6	15	1	10	19
Carpiteri weight VI	169	161	3	165	*	*
Carpiteri weight VII	0	0	29	0	0	0
Papadopoulos	*	*	*	*	45-135	45-135
Dietmann	45-135	135	45-135	45-135	150	45-135

Carpinteri et al. data are used in calculations[3]

V. CONCLUSIONS

In the present studies, biaxial stress states are investigated using Rotvel's experiment data [13]. For each experimental data, Macha, Carpinteri, Spagnoli try to determine critical plane positions [3]. In addition to Carpinteri & Spagnoli studies, the different critical plane approaches described above are compared for biaxial loading cases. Critical plane angles are obtained for Findley, Mataka and McDiarmid critical plane approximations. It is clear that these angles have similar values for each biaxial stress state. Dietmann obtains values similar to the numerical values of the linear critical plane theory for this stress state. Dietmann critical plane angles are compatible with linear critical plane approaches angles such as Findley, McDiarmid and Mataka. On the other hand, according to the Papadopoulos critical plane formulation, although the material fatigue life can be calculated, critical plane angle is not determined. Macha defines many weight functions methods which are rendered critical plane directions. Carpinteri also benefits from weight functions and defines the critical plane position with the help of Euler angles. It is more convenient to define these angles and directions for multi-axial stress states. According to this approach, an axis is regarded as a constant when the critical plane angle is calculated for biaxial stress states. However the calculated directions also take different values depending on the fact that the Mohr's circle is differently expressed under the variable stress state. In plane approach, the definition of critical plane is not the same and shows variability. Therefore, critical plane angle values cannot be specifically found according to the Carpinteri critical plane formulation. The comparison of critical plane angles are shown in Table 1-2.

In conclusion, each critical plane criterion examined is suitable for specific stress state. However, it is difficult to calculate and compare critical plane angles accurately for the same stress situations. It is assumed that the stress values change on a single plane for 2D stress state. However, this specified plane may not include critical plane. Also it should be considered strictly that the chosen criteria can handle such complex situations without any unexpected requirements.

VI. REFERENCES

- [1] A. Karolczuk, E. Macha, "A review of critical plane orientations in multiaxial fatigue failure criteria of metallic materials.", *Int. J. Fract.* 134:267-304, 2005.
- [2] A. Carpinteri, and A. Spagnoli, "Multiaxial high-cycle fatigue criterion for hard metals." *International Journal of Fatigue* 23, 135-145, 2001.
- [3] A. Carpinteri, E. Macha, R. Brighenti, and A. Spagnoli, "Expected principal stress directions under multiaxial random loading. Part II: Numerical simulation and experimental assessment through the weight function method." *International Journal of Fatigue* 21, 89-96, 1999.
- [4] K. Dang Van, G. Cailletaud, J.F Flavenot, A. Le Douaron and H.P. Lieurade, "Criterion for high cycle fatigue failure under multiaxial loading. In *Biaxial and Multiaxial Fatigue* (edited by Brown, M. and Miller, K.J.). *Mechanical Engineering Publications*, London, pp. 459-478. (1989).
- [5] I. V. Papadopoulos. "Long life fatigue under multiaxial loading." *International Journal of Fatigue*, 23, 831-849. 2001.
- [6] W.N. Findley. "A theory for the effect of mean stress on fatigue of metals under combined torsion and axial load or bending." *Journal of Engineering for Industry*, pp. 301-306, Nov. 1959.
- [7] D. Socie, "Critical Plane Approaches for Multiaxial Fatigue Damage Assessment," *Advances in Multiaxial Fatigue*, ASTM STP 1191, D. L. McDowell and R. Ellis, Eds., American Society for Testing and Materials, Philadelphia, pp. 7-36, 1993.
- [8] DL. McDiarmid, "A general criterion for high cycle multiaxial fatigue failure." *Fatigue and Fracture of Engineering Materials and Structures*, 14: 429-453, 1990.
- [9] T. Mataka, "An explanation on fatigue limit under combined stress." *Bulletin of the The Japan Society of Mechanical Engineers* 20, 257-263, 1977.
- [10] I. V. Papadopoulos, P. Davoli, C. Gorla, M. Flippini, A. Bernasconi: "A comparative study of multiaxial high-cycle fatigue criteria for metals." *International Journal of Fatigue* Vol.19, pp. 219-235, 1997.
- [11] E. Macha, "Simulation investigations of the position of fatigue fracture plane in materials with biaxial loads." *Material Wissenschaft und Werkstofftechnik*, 20, pp. 132-136 and 153-163, 1989.
- [12] H. Dietmann, T. Bhongbhibhat and A. Schmid, "Multiaxial Fatigue Behaviour of Steels under In-Phase and Out-Of-Phase Loading, Including Different Wave Forms and Frequencies." In: K. Kussmaul, D. McDiarmid and D. Socie (Eds.) - *Fatigue Under Biaxial and Multiaxial Loading*. Mechanical Engineering Publications, London, pp. 449-469, 1976.
- [13] F. Rotvel, "Biaxial fatigue tests with zero mean stresses using tabular specimens," *Int. J. Mech. Sci.*, vol. 12, 7, pp. 597-613, 1970.

An Investigation on Cutting Behavior of CoNiAl Shape Memory Alloy by Abrasive Water Jet

Mehmet DEMİR¹, Erdoğan KANCA¹, Mustafa Serdar KARAKAŞ², Murat YILDIZ¹, Ali GÜNEN³, Ersan KIRAR⁴, M. Mustafa ERŞEN⁵

¹Mechanical Engineering, Faculty of Engineering and Natural Sciences, Iskenderun Technical University, Hatay, Turkey

² Metallurgical and Materials Engineering, Faculty of Engineering, Cankaya University, Ankara, Turkey

³ Metallurgical and Materials Engineering, Faculty of Technology, Iskenderun Technical University, Hatay, Turkey

⁴ Machinery and Metal Technology, Şanlıurfa Technical Sciences vocational School, Harran University, Şanlıurfa, Turkey.

⁵ MMK Metallurgy, Industry, Trade and Port Co., Dortyol, Hatay

Corresponding author: ali.gunen@iste.edu.tr

Abstract— Machining of many polycrystalline shape memory alloys CoNiAl (SMA) has been considerably a new phenomenon. CoNiAl alloys should be made available for final use after being formed, without loss of their shape memory properties. In this study, the effect of cutting parameters on kerf width and dimension tolerance of the Co based Shape Memory Alloy (SMA) have been investigated on the Abrasive Water Jet (AWJ) machine. After the cutting process, kerf width of the samples were investigated. The experimental results showed that water pressure, traverse speed and abrasive flow rate have a great effect on kerf width and dimension tolerance.

Keywords— Shape memory alloy, CoNiAl, Machinability, AWJ, Kerf Width

I. INTRODUCTION

Today, cutting with abrasive water jet (AWJ) has become an important manufacturing method in order to produce high quality products in the current strong competitive environment in the market. In this cutting method, abrasive powders are added to the water sprayed from a thin nozzle at high speed. Sprayed water and dust mixture will wear the material and perform the cutting process [1]. The main advantage of cutting by AWJ is that it is easy to cut hard materials such as glass, steel, ceramics, stone, composites, etc. with low tolerances [2]. In addition, since there is no region affected by heat (HAZ), thermal stresses do not occur and changes in internal structure are not observed [1].

Recently, researchers have done a lot of study on AWJ such as revealing the mechanics of its cutting techniques [1], [3]-[7], improving its cutting quality [9]-[14], optimization [15]-[18], modeling [19]-[23] and comparing it to the other cutting methods [1], [24], [25]. The effective parameters for cutting by AWJ can be addressed as the thickness of cut material, feed rate, distance and angle between nozzle and material, particle size, amount and type of abrasive dust, water pressure and nozzle diameters. The things customers expect from their purchase are a good surface quality and dimensional accuracy. For this reason, in recent times, researchers have attempted to

determine optimal values for removing or at least reducing the surface roughness and to completely take out the material geometry the materials need to be worked on using the variables that are previously mentioned. For this purpose, optimum working conditions should be determined if a good surface roughness, material geometry and dimensional tolerances are to be achieved in cutting a new material by using AWJ. It has also been observed that different parameters for each material give the intended results.

In the literature research, no study about cutting of CoNiAl shape memory alloys with AWJ was found. The shape memory alloys are smart materials that can be returned to their actual shape and size by a suitable heat treatment. Their basic characteristics are that they have two different shapes or crystal structures above and below the critical conversion temperature. The material is cooled in austenite phase and it transforms to the martensite phases, then the deformed material remembers its first shape when reheated to pass through the austenite phase. This is called the shape memory feature [26]-[30].

In this study, the feed rate in abrasive water jet, the amount of abrasive dust and the effects of cutting parameters on cutting geometry in the CoNiAl shape memory alloys, kerf width and dimensional tolerance were investigated.

II. EXPERIMENTAL STUDIES AND PROCEDURES

The areas of utilization of CoNiAl alloy shape memory materials can be grouped under four main headings. These can be grouped as medical industry and technology, space and aviation industry, automotive industry and other applications. Especially, It is preferred as a performance enhancer in springs, turbine engines, robotic tools and air conditioning industry.

Ferromagnetic Co₄₃Ni₄₁Al₁₀Si₃Ag₂ alloys and Co₄₄Ni₄₀Al₇Cu₅Si₄ alloys were produced in a vacuum induction furnace under argon atmosphere. First, the Co and Ni elements in the zirconia-based crucible were melted, secondly, alloying elements (Al, Cu, Si, Ag etc.) in the alloy additive

section were added and finally the ceramic mold was poured. Casting temperature was kept constant between 1600-1700 °C and Argon pressure was about 200 Torr. Melting was repeated 3 times under vacuum and argon atmosphere to ensure homogeneity in alloy. 11 mm diameter and 100 mm size samples were produced at TÜBİTAK MAM. Then the chemical analyses of the produced samples were made on Thermo Jarrell ASH-BAIRD Corp. DV-6S 3063A brand spectral analyzer. The results obtained are given in Table 1.

TABLE I
Chemical Analysis of CoNiAl

Element	Weight (%)	Atomic (%)
Al	11.04	20.49
Si	4.13	7.36
Co	44.24	37.58
Ni	40.16	34.24
Zn	0.42	0.33

The crystallographic phase analysis of the alloy was generated by using the X-ray diffraction readings. To do it, a PC controlled RIGAKU RADB DMAX-III X-ray diffractometer with CuK α radiation which had 1.54056 Å wavelength and 2 θ has been used (Fig. 1).

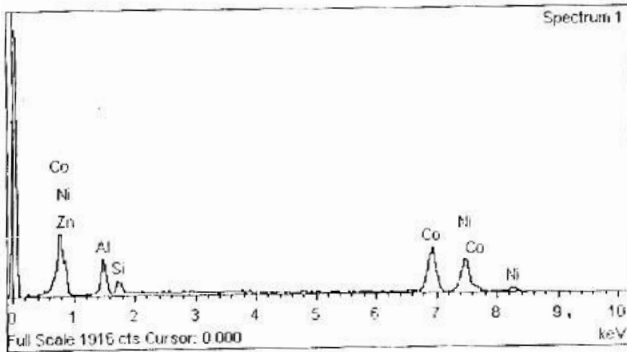


Fig.1 Crystallographic phase analysis of CoNiAl alloy

Shape memory alloys with highly complex mechanisms in their formation may be affected by mechanical and thermal strains during the shaping phase and may lose their properties. It has been predicted that the cutting method by AWJ is the most appropriate method to cut the material property without losing it.

The main characteristics of the abrasive waterjet cutter are given in Table 2. The samples of CoNiAl shape memory alloy were cut by using Ct-S-Standart Series portal EXP AWJ.

The variations for CoNiAl alloy material getting cut by using AWJ have been characterized by the water pressure (3000, 3200, 3400 bar), abrasive flow rate (300, 340, 380 g/min) and traverse speed (45, 60, 75 mm/min). The other variations were unchanged for the experiments. After the cutting processes were done, the effects of the parameters have been investigated on the kerf width of the samples.

TABLE II
Main properties of water jet cutter

Machine Model	Ct-S-Standart Series portal EXP
Standoff distance (mm)	2
Nozzle diameter (mm)	1
Water consumption (lt/m)	3,8
Abrasive mesh size	80/garnet
Nozzle angle (degree)	90

III. RESULTS AND DISCUSSIONS

The kerf width is an important factor in deciding the rating of quality for the AWJ process. Also the kerf width is a critical output for archiving the eventual product and dimensional accuracy for the materials when cut by using AWJ. The kerf width measurements were conducted by using an optic microscope on 5 different points for the every sample, delicately. The first of those points was where the water jet touched the target material for the first time. 1.5 mm was considered as the first kerf width value (Point A1). Then 3 more measurements were taken with every 3 mm distance between them (A2, A3, A4). Finally, the last point was the exiting point of the water jet.

In total 27 experiments were conducted. Variations and the results were acquired are shown in Table 3. The Schematic presentation and cross section image of the material can be seen in Fig. 2.

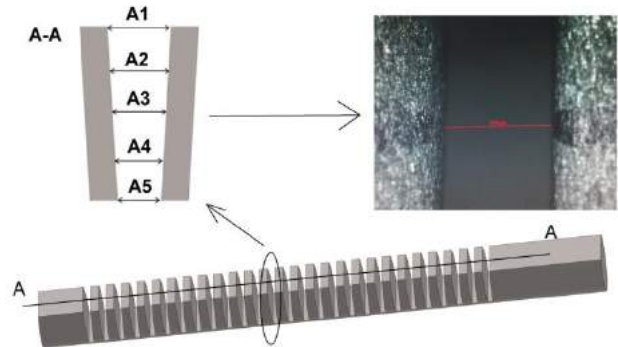


Fig. 2 Schematic presentation and cross section image

The medium values for experiment parameters have been generated when their effects on the kerf width were regarded and put into the graphs (Fig 4,5,6). Interpretations were done considering the mean kerf width values (Fig. 3).

TABLE III
Variations and Results

Number	Water Pressure (bar)	Abrasive Flow Rate (g/min)	Traverse Speed (mm/min)	Kerf Width (μm)				
				A1	A2	A3	A4	A5
1	3200	300	45	1500	1332	1060	911	638
2	3200	300	60	1500	1351	1012	931	535
3	3200	300	75	1500	1270	915	827	570
4	3200	340	45	1500	1331	1073	911	651
5	3200	340	60	1500	1313	999	840	521
6	3200	340	75	1500	1296	928	821	376
7	3200	380	45	1500	1335	1080	895	679
8	3200	380	60	1500	1328	1018	873	586
9	3200	380	75	1500	1319	954	847	589
10	3400	300	45	1500	1331	1054	937	735
11	3400	300	60	1500	1283	976	911	554
12	3400	300	75	1500	1295	950	876	550
13	3400	340	45	1500	1318	1044	902	721
14	3400	340	60	1500	1360	1008	963	599
15	3400	340	75	1500	1151	957	905	525
16	3400	380	45	1500	1347	1076	953	722
17	3400	380	60	1500	1337	1038	934	593
18	3400	380	75	1500	1260	1005	876	499
19	3600	300	45	1500	1289	1065	937	651
20	3600	300	60	1500	1276	970	886	579
21	3600	300	75	1500	1237	950	892	454
22	3600	340	45	1500	1208	1076	944	711
23	3600	340	60	1500	1267	1025	902	609
24	3600	340	75	1500	1244	1002	895	518
25	3600	380	45	1500	1292	1089	863	709
26	3600	380	60	1500	1253	1048	937	676
27	3600	380	75	1500	1205	980	868	608

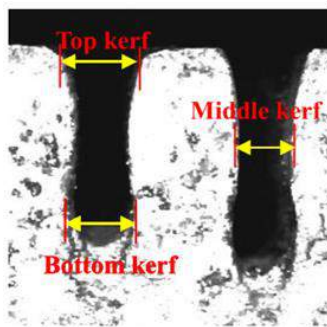


Fig. 3 Geometry of micro-channel [31]

A. Effect of the Traverse Speed

The relationship between traverse speed and the kerf width is presented in Fig. 4. Usually it can be expected to see a narrowing in the kerf width if there is an increase in traverse speed. It can be seen in Fig. 4. That there is decrease in the kerf width when traverse speed is increased, in a linear fashion, as expected. At the traverse speed of 45 mm/min, the width is closer to the exiting width from the nozzle as it can be inferred from the fig. As for the reason, it can be said that a relatively faster cross (Traverse) speed has less time to touch the cutting area and thus move less material than usual. In turn this causes the kerf width to be narrow.

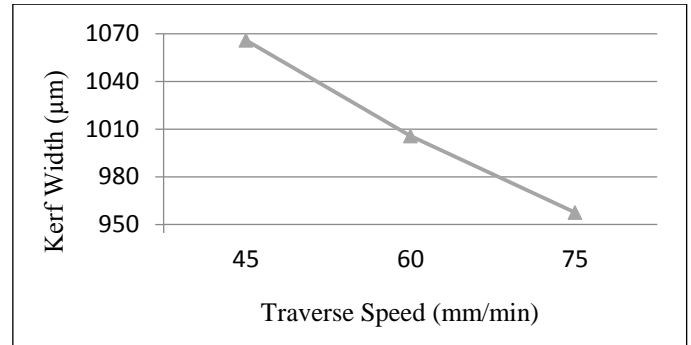


Fig. 4 Effect of traverse speed on the kerf width

However, the connection between the kerf width and the traverse speed can be pretty complex. The previously mentioned linear relationship might not be seen with the constant increasing of the traverse speed [21]. The three different variant that were considered in this study, the traverse speed was the most influential one among them.

B. Effect of the Abrasive Flow Rate

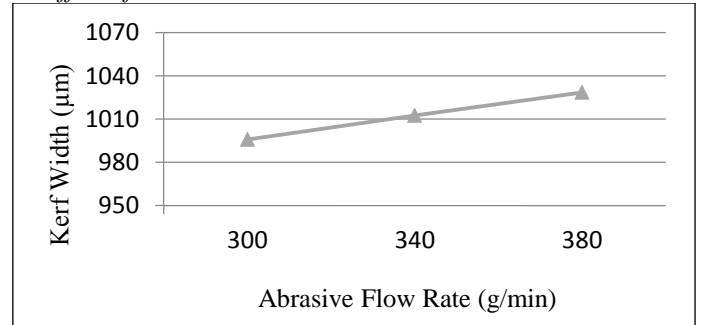


Fig. 5 Effect of abrasive flow rate on the kerf width

The relationship between the kerf width and abrasive flow rate is shown in Fig. 3. Increasing the abrasive flow rate caused the kerf width get wider as well. The most optimum width rates were obtained at the medium values of 380 g/min. Still, even though it wasn't observed in this study, other similar studies showed that the kerf width doesn't necessarily get wider even if the abrasive flow rate is increased, all the time. It can get narrow after passing the critical value as well. [13, 21]. If the amount of the abrasive dust in water is increased it will mean more abrasive dust reaches to the sample that is being cut

so the slit will be wider. However not all of the abrasive dust can reach the material as some of them just go through the slit with the flow of water so it can't be expected the kerf width will still get wider after the critical threshold is passed even if the amount of abrasive dust is increased. Though, it is still an important parameter for the kerf width.

C. Effect of the Water Pressure

The relationship between kerf width and the water pressure is shown in Fig. 6. It is observed that the kerf width is get wider by increasing the water pressure. The most optimum width rates were obtained at 3600 bar pressure. The abrasive dust in the water flow gains high levels of speed and energy when the water pressure is increased so this can explain the reason for the kerf width getting wider by increasing the water pressure. The abrasive dust can remove more material from the samples if they have more energy. The data that were obtained in this study is in coherent with the data that were provided in the previous studies. [21, 27, 29]. As was the case with the abrasive flow rate, there is a critical water pressure value as well and in case of passing that value, the efficiency might decrease. [21, 23]. The three different variants that were considered in this study, the water pressure was the least influential one among them.

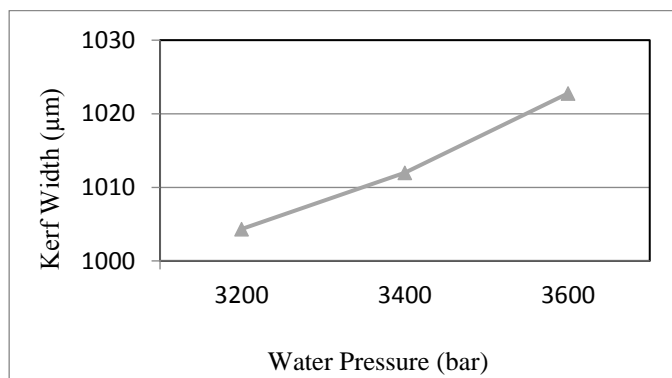


Fig 6 Effect of water pressure on the kerf width

CONCLUSIONS

The results that were obtained is presented as the following:

- The traverse speed was the most influential one on shape memory alloys CoNiAl getting cut by using AWJ, the among the parameters that were considered in this study.
- Increasing the abrasive flow rate causes the kerf width to get wider.
- Increasing the water pressure causes the abrasive dust to have more energy and speed thus a wider kerf width but the water pressure was the least influential one among the parameters that were considered in this study.
- The process of shape memory alloys CoNiAl getting cut by using AWJ still allows for the material to sustain its smart material abilities so the AWJ is recommended for this kind of tasks.

REFERENCES

- [1] L. Ohlsson, "The Theory and Practice of Abrasive Water Jet Cutting," Doctoral Thesis, Luleå University of Technology, Malaysia, Feb. 1995.
- [2] M. Rajyalakshmi and P. S. Babu, "Abrasive Water Jet Machining - A Review on Current Development," *Int. J. Sci. Technol. Eng.*, vol. 2, no. 12, pp. 428–434, 2016.
- [3] R. H. M. Jafar, V. Hadavi, J. K. Spelt, and M. Papini, "Dust reduction in abrasive jet micro-machining using liquid films," *Powder Technol.*, vol. 301, pp. 1270–1274, 2016.
- [4] F. Kartal, "A review of the current state of abrasive water-jet turning machining method," *Int. J. Adv. Manuf. Technol.*, pp. 495–505, 2016.
- [5] F. Mendi and M. K. Kulekci, "İmalatta su jeti uygulamalarının değerlendirilmesi," *Pamukkale Üniversitesi Mühendislik Bilim. Derg.*, vol. 5, pp. 1067–1075, 1999.
- [6] A. Akkurt, "Su jeti ile kesme sistemleri ve uygulama alanlarının değerlendirilmesi," *Politek. Derg.*, vol. 7, pp. 129–139, 2004.
- [7] H. Orbanic and M. Junkar, "Analysis of striation formation mechanism in abrasive water jet cutting," *Wear*, vol. 265, no. 5–6, pp. 821–830, 2008.
- [8] J. Folkes, "Waterjet-An innovative tool for manufacturing," *J. Mater. Process. Technol.*, vol. 209, no. 20, pp. 6181–6189, 2009.
- [9] A. Akkurt, M. K. Kulekci, U. Seker, and F. Ercan, "Effect of feed rate on surface roughness in abrasive waterjet cutting applications," *J. Mater. Process. Technol.*, vol. 147, no. 3, pp. 389–396, 2004.
- [10] B. Hajdarevic, A. Cekic, M. Mehmedovic, and A. Djelmic, "Experimental Study on Surface Roughness in Abrasive Water Jet Cutting," *Procedia Eng.*, vol. 100, pp. 394–399, 2015.
- [11] M. Duspara, T. Palatinuš, I. Samardžić, D. Marić, V. Starčević, and A. Stoić, "Influence of abrasive feeding and cutting direction on the surface roughness," *Procedia Eng.*, vol. 149, no. June, pp. 48–55, 2016.
- [12] F. Kartal, Z. Yerlikaya, and H. Gokkaya, "Effects of machining parameters on surface roughness and macro surface characteristics when the machining of Al-6082 T6 alloy using AWJT," *Meas. J. Int. Meas. Confed.*, vol. 95, pp. 216–222, 2017.
- [13] J. Wang, T. Kuriyagawa, and C. Z. Huang, "An Experimental Study to Enhance the Cutting Performance in Abrasive Waterjet Machining," *Mach. Sci. Technol.*, vol. 7, no. 2, pp. 191–207, 2003.
- [14] L. M. Hlaváč *et al.*, "Experimental method for the investigation of the abrasive water jet cutting quality," *J. Mater. Process. Technol.*, vol. 209, no. 20, pp. 6190–6195, 2009.
- [15] A. Akkurt, "AISI 1030 çeliğinin aşındırıcılı su jeti ile kesilmesinde yüzey pürüzlülüğünün ve kesme önu geometrisinin incelenmesi," *Pamukkale Üniversitesi Mühendislik Bilim. Derg.*, vol. 15, pp. 1–11, 2009.
- [16] P. Löschner, K. Jarosz, and P. Nieslony, "Investigation of the effect of cutting speed on surface quality in abrasive water jet cutting of 316L stainless steel," *Procedia Eng.*, vol. 149, no. June, pp. 276–282, 2016.
- [17] D. S. Reddy, A. S. Kumar, and M. S. Rao, "Parametric Optimization of Abrasive Water Jet Machining of Inconel 800H Using Taguchi Methodology," *Univers. J. Mech. Eng.*, vol. 2, no. 5, pp. 158–162, 2014.
- [18] N. Yuvaraj and M. P. Kumar, "Surface integrity studies on abrasive water jet cutting of AISI D2 steel," *Mater. Manuf. Process.*, vol. 32, no. 2, pp. 162–170, 2017.
- [19] M. Kök, E. Kanca, and Ö. Eyercioğlu, "Prediction of surface roughness in abrasive waterjet machining of particle reinforced MMCs using genetic expression programming," *Int. J. Adv. Manuf. Technol.*, vol. 55, no. 9–12, pp. 955–968, 2011.
- [20] Z. Cojbasic *et al.*, "Surface roughness prediction by extreme learning machine constructed with abrasive water jet," *Precis. Eng.*, vol. 43, pp. 86–92, 2016.
- [21] I. Karakurt, G. Aydin, and K. Aydiner, "A machinability study of granite using abrasive waterjet cutting technology," *Gazi Univ. J. Sci.*, vol. 24, no. 1, pp. 143–151, 2011.
- [22] H. Gärdek and O. Boubker, "A State of the Art Report and Comparison with Conventional Methods of Abrasive Waterjet Machining Technology Gärdek Harald," p. 43, 2015.

- [23] R. T. Deam, E. Lemma, and D. H. Ahmed, "Modelling of the abrasive water jet cutting process," *Wear*, vol. 257, no. 9–10, pp. 877–891, 2004.
- [24] H. Gärdek and O. Boubker, "A State of the Art Report and Comparison with Conventional Methods of Abrasive Waterjet Machining Technology Gärdek Harald," p. 43, 2015.
- [25] P. U. Shinde and T. Z. Quazi, "Composite Materials -Abrasive Water Jet Machining," vol. 6, no. 12, 2015.
- [26] K. Enami, and S. Nenno, "Memory effect in Ni-36.8 At. Pct Al martensite," *Metal. Trans.* vol 5, p.1487-1490, 1971.
- [27] G. F. Xu, Z. M. Yin, F. H. Luo, S. Z. Muo and K. Oikawa, "Martensitic and magnetic transformation of Co₄₁Ni₃₂Al₂₄Sb₃ and Co₄₁Ni₃₂Al₂₇ alloys," *Transactions of Nonferrous Metals Society of China*, vol 16, p.776-782, 2006.
- [28] W. Maziarz, "Structure changes of Co-Ni-Al ferromagnetic shape memory alloys after vacuum annealing and hot rolling," *Journal of Alloys and Compounds*, vol 448, p.223-226, 2008.
- [29] J. Liu, J.G. Li, "Magnetic Force Microscopy Observations of Co–Ni–Ga and Co–Ni–Al Alloys With Two-Phase Structures," *Scripta Materialia*, vol 55, p.755–758, 2006.
- [30] A. Ç. Akis, M. Eskil, and E. Sevval, "Farklı Etkiler Altında Şekil Hatırlamalı CoNiAl Alaşımlarının Martensitik Dönüşüm Sıcaklıklarındaki Değişimler" *Journal of New World Sciences Academy*, vol 6, 2001.
- [31] D. Patel, P. Tandon, "Optimization of Kerf Surface and Material Removal Rate Using Abrasive Water-Slurry Jet Machining Setup," *Adv. Manuf* Vol 2B, p.1-9, 2013.

Application of Different Coating Methods to External Cooling Roller and Characterization of Applied Coatings

Ali GÜNEN¹, Erdoğan KANCA², Mustafa Serdar KARAKAŞ³, Vahdettin KOÇ⁴, Mustafa Sabri GÖK⁵
Ahmet ÇÜRÜK¹, Mehmet DEMİR²

¹ Metallurgical and Materials Engineering, Faculty of Technology, Iskenderun Technical University, Hatay, Turkey

² Mechanical Engineering, Faculty of Engineering and Natural Sciences, Iskenderun Technical University, Hatay, Turkey

³ Metallurgical and Materials Engineering, Faculty of Engineering, Cankaya University, Ankara, Turkey

⁴ Mechanical and Metal Technology, Vocational school of Technical Sciences Adiyaman University, Adiyaman, Turkey

⁵ Mechanical Engineering, Faculty of Engineering, Bartın University, Bartın, Turkey

Corresponding author: mehmet.demir@iste.edu.tr

Abstract— Rolling has an important place in iron and steel industry due to the advantages such as production speed, continuity and easy to process applications. Roll materials must be resistant to high heat temperature conditions, high breaking resistance, good surface quality, proper hardness, good wear resistance and thermal shocks. However, producing an alloy material with all of these features together will be very costly. Instead of producing a roll material having all of these properties, it is more economical and practical approach to provide these characteristics by surface modification. In this study, External cooling rollers (ECR) coated by different four techniques which, Flame spray, boriding, titanizing and borotitanizing. After the coating process, the thickness of the coating layer, hardness, and layer structures examined by optic microscope, scanning electron microscope, micro hardness, and X-ray analyses. A wide range of coating thicknesses and microhardness values obtained depending on coating technique. The highest microhardness obtained in the titanized sample, but the lowest coating thickness. The obtained hardness values were 3 times higher than those in the current application. The cost of rolling will be reduced by increase in ECR tool life.

Keywords— External cooling roller, STKM 13a, Flame spray, Thermochemical processes, Coating, Microstructure.

I. INTRODUCTION

A. Rolling Mills and Rolls

The process of plastically deforming a material (hot or cold) by passing it between rolls with compressive forces is known as rolling. If deformation is carried out at temperatures above the recrystallization temperature the process is known as hot rolling. Hot rolling has its place in the steel industry as a field wherein new techniques are developed and improvements in quality are constantly made, inasmuch as competition carries on and profit margins are reduced [1-2]. Therefore, for many applications, steel strips need to have preferably less thickness

and higher strength with low surface roughness. Since rolls can have great influence on these properties, it is crucial to improve upon their mechanical properties such as surface roughness, wear resistance, toughness and thermal fatigue.

External cooling roller are a series of rolls where the material leaving the hot rolling mill is cooled to obtain the desired mechanical properties and conveyed to coil winding (Fig. 1). The numbers of rolls in the cooling bed of a rolling plant depend on the production speed as well as the thickness of the steel sheet. Aside from the rolls, there are also waterjets located underneath and in between the rolls of the cooling bed to provide cooling for the passing material. There are also waterjets directly beneath the rolls to cool the rolls. The rolls can be internally or externally cooled. The main purpose of internally cooled rollers is the measurement of the surface quality, thickness and width of the sheet. To obtain accurate readings from the electronic measuring equipment, no water should be present.



Fig. 1 The appearance of the external cooling rollers

Compressive forces are applied to the cooling beds during the rolling operation. The main reason for these forces is the tight coiling forces necessary for the sheet which is coiled as it is rolled. If coiled without enough tightening, the interior of the sheet expands and bulges out making further processing difficult. To obtain tight coiling, some tension must exist between the rolls and the coiling equipment but should be limited such that the sheet is not damaged. This will cause compressive forces on the rolls and this compressive force will increase wear rates. When the tail end of the sheet leaves the last roll of the cooling bed, it is pulled in tension through what are called pinch rolls which enable proper winding in the coiler. In the case of any malfunction in the rolling system, the broken or failed sheets enter the cooling system. In the case where the failed sheet locks up the mechanical system, the sheet must be removed from the rolling system as quickly as possible. Such events may cause the failed sheets to enter the cooling bed, damaging the rolls. The removal of failed material from the cooling bed also requires mechanical and electromagnetic equipment. High loads, specialized welding torches and impact blows to the mechanical systems are likely to occur at this stage.

Cooling beds are engine-actuated and since reducers are not used (to enable variable rpm values) they operate at high speeds. But because the thickness of the materials also changes, the rpm values of the rolls also change. For low energy consumption the rolls also need to be lightweight. To decrease the weight of the rolls, they are manufactured hollow and only contain load bearing

supports. To prevent seepage of water, both stationary and moving components have to have very low clearance values. There are both advantages and disadvantages to this. If adhesive forces are weakened in preexisting coatings on the surface of the roll due to impact and high temperatures (such as in the case of plasma or HVOF coatings) the roller is affected and the low clearance regions rub against each other and obstruct the movement of the rolls. In addition, leading ends of thick products cause the products to hit each and every roll during conveying. During cooling the leading end hardens. These impacts can cause failures on the surfaces of the coatings (delamination and spalling in plasma spray coatings). These failures not only affect the rolls. The following pinch rolls are also affected in that surface blisters or markings are formed on the surface of the product. This is highly undesirable for mass-production companies. When multiple rolls are used, troubleshooting also becomes difficult. Failure identification studies also result in production losses.

The cooling bed starts at the end of the rolling regime about 30 m beyond the rolling mill. The reason for this is the thickness and surface quality inspections that are necessary before cooling. The rolls operating in this intermediate stage are subjected to temperatures of 880-950 °C due to heat transfer from the steel product. Furthermore, the surface scale that forms here cannot be removed due to the absence of water and this scale damages any existing coatings on the counter facing rolls. The scale also tends to spread towards the ends of the rolls, and often reaches the bearings, interferes with moving components and causes premature failures which also lead to production losses. As mentioned earlier, the sheet exits the rolling mill at high temperatures and the smallest flaw that forms at the surface affects the final product. For all of the reasons stated above, any improvements achieved in extending the lifespan of cooling beds are of great importance.

B. Surface Modification

Nowadays, a wide variety of surface modification processes are available as options for protecting metal surfaces from the effects of external environments, reducing the effects of abrasion, friction corrosion and fatigue to which they are

exposed to during their use. One of the easiest and most economical ways to improve the mechanical properties of the material surface is surface hardening. Diffusion treatments can be used to form nitrides, carbides or borides on the surface of materials to make their surfaces harder, stronger and more resistant to wear. Since these treatments usually have very little on the core, high toughness and high energy absorption under dynamic loads can be maintained. Thermal spray coatings, chemical vapor deposition, physical vapor deposition, boriding and thermoreactive diffusion (TRD) methods are among the most widely used surface hardening processes. All of these methods have advantages (and disadvantages) over each other. TiBCN (multi-phase) type coatings have been obtained by the above-mentioned methods excluding boriding and TRD methods are discussed in the literature review section. Although installation costs for boriding and TRD methods are lower compared to the other methods mentioned above, virtually no studies on such coatings prepared by these thermochemical methods exist.

When it comes to thermochemical methods, boriding and TRD methods are among the first that come to mind. Boronizing is a surface hardening process, can be simply defined as diffusion of boron into a metal surface. Boronized steels are characterized by high surface hardness and high wear resistance. For this reason, studies on the boride layers obtained in boronized materials are mostly focused on hardness, abrasion and corrosion [3]. An important feature of the boride coating is its high hardness and its ability to protect the surface even at temperatures approaching 900-1000 °C. The boride coating can offer superior resistance to corrosion and wear without losing its tribological properties at high temperatures [5]. In the coming years, processes by which coatings are produced with the use of nanosized boriding powders, a new technology, may allow mechanical properties to be achieved in much shorter time and greatly increase the importance of these processes [6-7].

Thermo - reactive diffusion is a technique which forms hard and wear resistant layers of carbides, nitrides and carbonitrides on the surfaces of steel. This technique was first developed by Toyota in Japan in the 1970s, and was successful in enhancing

the life of tool steels by 2 to 20 times. According to this technique, strong carbide and nitriding elements such as V, Nb, Ti, Ta, and Cr added to a borax salt bath combine with carbon and nitrogen on the contacting steel surface to form metallic carbides, nitrides and carbonitride layers on the surfaces. Realization of this method in a solid medium rather than in a liquid medium has also been called pack cementation [8-12].

The pack cementation described here is a thermochemical process. However, it is slightly different from conventional thermochemical processes. In the coating process, carbon and nitrogen in the steel substrate combine with the strong carbide- and nitride-forming refractory transition metals such as titanium, vanadium, niobium, tantalum, chromium, molybdenum or tungsten at high temperatures (800-1250 °C) creating a highly adherent coating on top of the base metal. Contrary to conventional methods, the coating layer grows on the surface of the substrate. There is a distinct boundary between the substrate material and the covering layer. However, since the process is carried out at elevated temperatures, the diffusion of carbide forming elements into the base metal is concerned. This forms a metallurgically bonded structure [10].

The pack cementation described is unlike conventional surface hardening methods. In conventional surface hardening methods, carbon and nitrogen are diffused into the surface to harden the surface of the substrate material. Although the pack carburizing process is similar to the conventional diffusion, in this process the coating grows outwards from the surface of the substrate material. The formation of coatings in the form of carbides, nitrides and carbonitrides on the substrate material include certain steps which include the dissolution of carbide- and nitride-forming elements in borax, the reactions between these soluble elements and the carbon and nitrogen in the material, and the deposition of carbide and nitride-containing layers on the surface. Coating layer thicknesses achieved comparable to that achieved using chemical vapor deposition (CVD) or physical vapor deposition (PVD) techniques that require high installation costs are possible with this method [13].

When previous studies in the literature are examined, Shan et al. [14] carburized and subsequently vanadium-niobized AISI H13 steel using TRD. They found that processes which increase the concentration of interstitials on the surface such as carburizing In the conclusion, it has been reported that processes such as carburizing or nitriding prior to the TRD process allow coating layers of greater thickness to be achieved. Chicco et al. [15] reported that complex vanadium carbonitride coatings can be obtained in a process where nitriding or nitrocarburizing prior to TRD processes allow the formation of thicker multicomponent coatings in the TRD vanadium process while uniform single-layer coatings were obtained in single TD processes. They also noted that the highest hardness values were obtained for coatings containing carbon. Sen et al. [16] borided the surface of AISI M2 steel using a liquid boriding method at 1000 °C for 2 hours, and subsequently applied a TRD treatment for 1 to 4 hours. They found that the resulting coating layer was smooth, compact and homogeneous, and reported 2700 HV hardness for the niobium boride layer with thickness values ranging between 0.97 µm to 3.25 µm depending on processing time. Similar results should be expected for hard carbides instead of nitrides [17] or for other boride-forming transition elements. The aim of the present study is to obtain in the wide range of coatings on the surface using 4 different coating methods in combination with a borotitanizing treatment (a two-step thermochemical treatment), forming coatings containing a transition zone, carbides, nitrides and carbonitrides with hardness decreasing from the surface to the substrate, boron and nitride layer, and to compare the thicknesses of the coatings to flame sprayed coatings. Therefore flame spraying, boronizing, titanizing and borotitanizing treatments are used in this study.

STKM-13a	0.9	0.25	0.35	0.04	0.04	Balance
----------	-----	------	------	------	------	---------

The samples cuttings in appropriate sizes were coated by FS, boronizing, titanizing and borotitanizing processes. Metco 15F, EKaboron 2 and blend powder (45% ferro-titanium, 45% Al₂O₃ and 10% NH₄Cl) were used as cotiang powder in the flame spray, boronizing, titanizing and borotitanizing processes, respectively.

Flame spraying was carried out using a Metco type 5P spray gun. The processes parameters of FS selected as spray distances 200 mm, powder feed rate/ Pressure 10 kg/h, flow rate/pressure 0.90 C₂H₂ m³/h and O₂ flow rate/Presure 1.8 m³/h. The boriding and titanizing process was carried out at 1000 °C for 5 hours. The borotitanizing (boriding and subsequent titanium diffusion stages) were carried out at 1000 °C for 5 h, and at 1000 °C for 2 h, respectively. The samples to be applied FS grit blasted with Al₂O₃ and the others were grounded with 1200 grit SiC for to obtaining appropriate coating.

Metallography, microhardness and XRD specimens of 10 × 10 × 5 mm size were extracted from each of the coated 60 × 60 × 5 mm specimens. The metallography specimens were sectioned and cold mounted. The specimens were then grinded using 400, 600, 800, 1000 and 1200 grit abrasive papers and polished with 3 µm alumina paste followed by 1 µm diamond paste. After polishing the specimens were etched with a solution consisting of %3 nital for 3 minutes to reveal microstructural details.

Optical studies were carried out using a Nikon MA-200 metal microscope equipped with Clemex image analysis software. Scanning electron microscopy (SEM) studies were performed with a JEOL JSM-5600 scanning electron microscope equipped with Energy Dispersive Spectroscopy (EDS) capability, at 25 kV accelerating voltage. Microhardness measurements of the layers were recorded utilizing a Highwood HWMMT-X3 hardness tester using 50 gf 15-s dwell time. The thicknesses of the coatings were determined by a Clemex digital thickness measurement instrument attached to a Nikon MA-200 optical microscope. Values of the thickness and hardness reported were

II. EXPERIMENTAL STUDIES

STKM-13a was used as the base material, with specimens the size of 60 × 60 × 5 mm obtained from ECR. The chemical composition of the base material in mass percent is given in Table1.

TABLE 1
CHEMICAL COMPOSITION OF STKM-13A STEEL.

Material	Mn	C	Si	P	S	Fe
----------	----	---	----	---	---	----

the averages of ten and five measurements, respectively. X-ray diffraction (XRD) analyses were carried out using a computer-controlled Bruker AXS D8 Advance Diffractometer with Cu K α radiation ($\lambda_{Cu} = 0.1540 \text{ nm}$) and 2θ angles ranging from 0° to 90° .

III. RESULT AND DISCUSSIONS

A. Microstructural Characterization

Layer thicknesses and micro hardness values as measured from the coating cross-section, are given in Table 2. It can be seen that from table 2 the hardness measurements for all coatings produced by four different coating process range from 850-2462 HV0.05. This is significantly higher than the hardness of bare substrate, measuring $<130 \text{ HV0.05}$. It was found that the hardness of the thermo-chemical processes were higher than the FS process. Such high hardness is expected to be favorable for wear resistance applications. The highest micro hardness obtained in ferro titanium powder carried out by titanizing and the lowest in 15F deposited by FS method. This can be attributed to the microstructure and phase formation of the hard phases, such as TiC. In addition the thickness of coatings measured between a wide range of $3.36 - 1306 \mu\text{m}$. The coating obtained by the FS method is considerably higher than the thermal coatings in the literature [10, 18-20]. On the other hand thick boron layers were obtained according to alloyed steel [3, 4, 7]. As the low content of carbon contributed to easier diffuse of boron to inner, but low content of carbon reduced the TiC formation in titanizing process. However, contrary to the literature, the TiC layer was formed although the C ratio of the samples was wt 0.25% [17, 21]. Surface roughness Ra and Rz measured as $0.4 - 3.15 \mu\text{m}$ and $1.3 - 14.90$, respectively. Surface roughness values increased with increase of coating thickness.

TABLE 3
PROPERTIES OF COATINGS USED IN THIS STUDY

Coating Named	Coating process	Thickness (μm)	Micro-hardness (HV)	Ra	Rz
1	FS	1306	850.53	3.15	14,90
2	Boronizing	244.7	1416.6	1.08	3.25
3	Borotitanizing	261.2	2387.6	2.21	6.65
4	Titanizing	3.36	2462.2	0.4	1.3

Figure 2 shows the OM image of the coatings produced by different four coating processes.

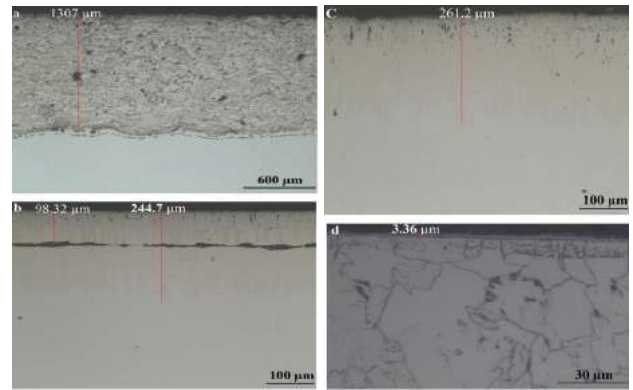


Fig. 2 OM images of a)FS coated b) boronized c) borotitanized d) titanized of STKM 13a steel.

The coatings named 2, 3, 4 appears to be fully dense, but the 1 FS coating showing oxides, cracks and porosity with in the some regions. This is crucial for coatings which have to operate under tribo-corrosion conditions. As cracks and porosities are the starting points of corrosion (Fig. 3). With the onset of corrosion the coating loses its function and spall off from surface [22]. In this case wear resistance of the coating decreases.



Fig. 3 Appearance of corrosion beginning in ECR.

In order to examine the distribution of the elements on surface in the FS layer and verify the formation of TiC layer EDS mapping and EDS X-ray microanalyses were made (Fig. 4). Fig. 4a shows the distribution of the elements Al, Cr, Ni, Mn in the surface. It can be seen from Fig. 4a content of the regions considered as oxides were found to be Al, Cr and O. In the other parts of the FS coating, generally homogeneous distribution was observed.

On the other hand the EDS spectrum from the topmost layer Fig. 4b, the point marked as Spectrum 4 indicates high concentrations of Ti and C (63.4 wt.% Ti and 23.6 wt.% C), which is close to the composition of TiC. The points from the underlying layer, marked as Spectrum 3, Spectrum 2, and Spectrum 1 are contain very small quantities of Ti. The concentrations for Fe increase with increasing depth, while Ti and C decrease. Since the boron and borotitanium layers were clearly visible with an optical microscope, it was not necessary to obtain EDS from these regions.

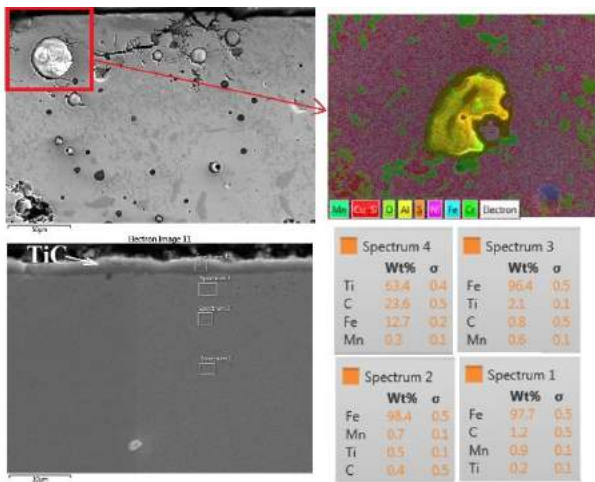


Fig. 4 SEM and EDS analyses of a)FS coated b) titanized samples

Figure 5 shows the XRD analysis of samples coated by FS, boronizing, borotitanizing and titanizing. In the sample coated by FS Cr₂B, Cr₂₃C₆, FeNi₃ and NiCr phases were detected. It can be said that boron (B) and iron (Fe) are effective in the phase formation (Gunen, 2016). In the boronized sample, dual phase formation (FeB+Fe₂B) phases were detected in accordance with the literature [3, 4, 7] as well as minor amount of MnB. The boro titanized samples. TiB₂ phase was obtained in addition to the phases obtained in the boronizing step. TiC and FeTi₂ phase was obtained in the sample which was subjected to only titanizing treatment. Briefly, it appeared different phases in the samples depending on coating process and the chemical composition of the powders used as coating agents.

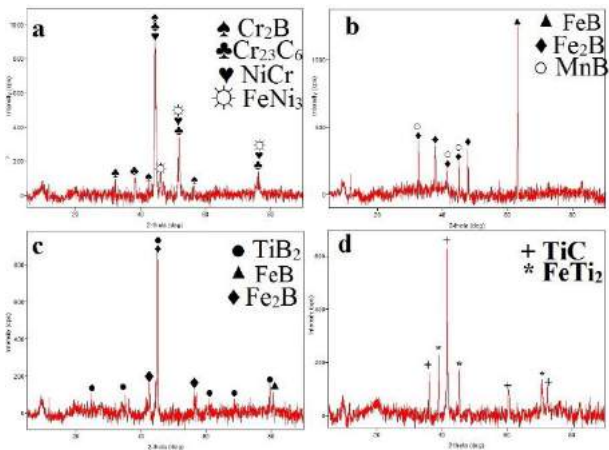


Figure 5. XRD analysis of the samples which coated by a) FS b) boronizing c) borotitanizing d) titanizing process.

IV. CONCLUSION

In this study, ECR STKM 13a steel samples were subjected to different four kind of coating processes. The effects of the different treatment on microstructure, micro-hardness and phase formation were investigated. Main results can be summarized as:

- Flame spray, boronizing, borotitanizing and titanizing treatments were successfully applied the STKM 13a steel.
- The morphology of coating was in the acceptable range. However, some cracks, oxides and porosity formations were found in the FS coatings.
- Coating thicknesses and hardness values were obtained over a wide range depending on the coating method.
- Increase in coating thicknesses result in increase in surface roughness values.
- The obtained phases are based on the chemical composition of used powder and consistent with the literature.
- It is thought that the wide range of coating layers and hardness values will result in the different wear resistance. Therefore, it is important that determining of corrosion and wear resistance of ECR according to the working conditions.

REFERENCES

- Aran A., Demirkol M., Plastic Forming Technology, ITU. Faculty of Mechanical Engineering 1994.
- Kayali E.S., Ensari C., Principles and Applications of Metal Forming, İstanbul, 1st edition 1986.
- Şen, Ş., Özbek, I., Sen, U., ve Bindal, C., Mechanical Behavior of Borides Formed On Borided Cold Work Tool Steel, , Surface And Coat. Technol. Vol. 135, 173-177, 2001.
- Ulutan, M., Yildirim, M.M., Celik, O.N., Buytoz, S., "Tribological properties of borided AISI 4140 steel with the powder pack-boriding method," Tribol. Let., 38, pp. 231-36, 2010.
- Karamış, M.B, Nair, F, Selçuk, B. Tribological Properties of Borided Materials, 6th Denizli Materials Symposium Proceedings Book pp:446-454, 1995.
- Gunen, A., Kurt, B., Orhan, N., Kanca, E., "The investigation of corrosion behavior of borided AISI 304 austenitic stainless steel with nanoboron powder," Protection of Metals and Physical Chemistry of Surface, 50, (1), pp. 106–112, 2014.
- Gunen, A., Gok, M.S., Erdogan, A., Kurt, B., Orhan, N., Investigation Of Mikro-Abrasion Wear Behavior Of Boronized Stainless Steel with Nanoboron Powder, Tribology Transactions, Volume: 56; Issue:3 pp. 400-409, 2013.
- Naiming LIN, Faqin XIE, Tao ZHONG, Xiangqing WU, Wei TIAN. Influence of adding various rare earths on microstructures and corrosion resistance of chromizing coatings prepared via pack cementation on P110 steel. Journal of Rare Earths, Volume 28, Pp. 301-304, 2010.
- Tsipas, S.A., Omar, H., Perez, F.H., Tsipas, D.N., Boroaluminide coatings on ferritic–martensitic steel deposited by low-temperature pack cementation. Surface and Coatings Technology, V: 202, I: 14, 15, Pp 3263–3271, 2008.
- Chaliampalias, D., Vourlias, G., Pavlidou, E., Skolianos, S., Chrissafis, K., Stergioudis, G., Comparative examination of the microstructure and high temperature oxidation performance of NiCrBSi flame sprayed and pack cementation coatings. Applied Surface Science, V: 255, I: 6, pp. 3605-3612, 2009.
- Zhou, Y., Chen, H. Zhang, H., Wang, Y., Oxidation of Al₂O₃-dispersion chromizing coating by pack-cementation at 800 °C. Transactions of Nonferrous Metals Society of China, V:18, I: 3, pp 598-602, 2008.
- Pang, Q., Wu, G.H., Sun, D.L., Xiu, Z.Y., Jiang, L.T., A dual-layer Ce–Cr/Al oxidation resistant coating for 3D open-cell nickel based foams by

- [a two-step pack cementation](#). Materials Science and Engineering: A, V: 568, pp. 228-238, 2013.
- [13] Arai, T., Moriyama, S., Growth behavior of vanadium carbide coatings on steel substrates by a salt bath immersion coating process, *Thin Solid Films*, V:249, I:1, 54–61, 1994.
- [14] Shan, Z. J., Pang, Z. G., Luo, F. Q., Wei, F. D., Kinetics of V(N,C) and Nb(N, C) coatings produced by V–Nb–RE deposition technique, *Surf. Coat. Technol.* 206, pp. 4322–4327, 2012.
- [15] Chicco, B., Borbidge, W.E., Summerville, E., Experimental study of vanadium carbide and carbonitride coatings, *Materials Science and Engineering*, A266, pp. 62–72,1999.
- [16] Sen, U., Pazarlıoğlu, S. S., Sen, S., Niobium boride coating on AISI M2 steel by boro niobizing treatment, *Mater. Lett.* 62, pp. 2444–2446, 2008.
- [17] Arai, T., Fujita, H., Sugimoto, Y., Ohta, Y., Diffusion carbide coatings formed in molten borax systems, *J. Mater. Eng.*, 9(2), pp.183–189, 1987.
- [18] Richert, M.W., Mikułowski, B., Pałka, P., Hotłoś, A., Malgorzata P.N., "The Effect of Chemical Composition and Thermal Sprayed Method on the Chromium and Tungsten Carbides Coatings Microstructure," *Journal of Surface Engineered Materials and Advanced Technology*, 3, 1-5. DOI: 10.4236/jsemat.2013.31001, 2013.
- [19] Bolelli, G., Lusvarghi, L., Giovanardi, R., A Comparison Between the Corrosion Resistances of Some HVOF-Sprayed Metal Alloy Coatings, *Surface & Coatings Technology* 202, pp. 4793–4809. doi:10.1016/j.surfcoat.2008.04.056, 2008.
- [20] Dorfman, M., Clayton, C.R., Herman, H., The Cavitation Behavior Of Rolled And Sintered Flame-Sprayed Active Coatings, *Thin Solid Films*, V:73 I:1 pp.80-85 1980.
- [21] Kurt, B., Sinoplu, O., Carboga, C., and Demirel, B., The Investigation and Growth Kinetics of TiC Coatings on AISI D3 Steel Produced by Thermo-Reactive Diffusion Technique. *Practical Metallography: Vol. 51, No. 2*, pp. 95-106, 2014.
- [22] Pileggi, R., Mario Tului M., Stocchi, D., Lionetti S., "Tribo-corrosion behaviour of chromium carbide based coatings deposited by HVOF." *Surface & Coatings Technology* 268, pp. 247–251. doi:10.1016/j.surfcoat.2014.10.007, 2015.

Determining the Corrosion Behaviour of EN 1.4462 Duplex Stainless Steel in FeCl₃ Media for Various Solution Treatment Conditions

Alptekin Kısasöz*, Ahmet Karaaslan*

*Yildiz Technical University, Department of Metallurgical and Materials Engineering
Istanbul, Turkey
akisasoz@yildiz.edu.tr
karaas@yildiz.edu.tr

Abstract— Duplex stainless steels (DSSs) have both higher mechanical properties and corrosion resistance in the cause of austenitic and ferritic microstructure. DSSs, generally have equal amount of austenite and ferrite phases. Solution heat treatment is applied to DSSs for providing homogenous microstructure, composing desired austenite-ferrite phase fraction and resolving intermetallic phases. After the solution treatment, mechanical properties and corrosion resistance of DSSs can be alter, especially with changes in austenite-ferrite phase ratio. In this study, effect of solution treatment conditions on corrosion behaviour of EN 1.4462 was investigated. Solution treatments were applied at 1100°C and 1150°C for 2 hours and 8 hours. Corrosion test was applied in FeCl₃ (10% wt.) media for solution treated specimens. Corrosion properties of the specimens were determined with weight loss and also, microstructural characterization was carried out by optical microscopy analysis.

Keywords— Duplex stainless steel, Heat treatment, Corrosion, EN 1.4462 alloy, Secondary phases

I. INTRODUCTION

Duplex stainless steels (DSSs) have improved mechanical properties and corrosion resistance owing to duplex microstructure consisting ferrite and austenite phases. DSSs are widely used in piping, storage tanks, offshore and nuclear power plants for these advanced properties [1-4].

DSSs solidify as ferrite phase and duplex microstructure are formed with solution heat treatments applied between 1000°C–1200°C range. Also, 950°C–650°C range is critical both for production and usage of DSSs and requires high attention to protect improved mechanical properties and corrosion resistance of DSSs. Ferrite-austenite eutectoid transformation occurs at 950°C–650°C temperature range and secondary phases like σ , χ , carbides and nitrides form and these secondary phases have detrimental effects on mechanical and corrosion properties of DSSs. Especially, σ and χ phases are critical for DSSs [5-7].

σ and χ phases nucleate at ferrite-ferrite and ferrite-austenite grain boundaries. σ phase has great amount of Cr and for this reason, σ phase grow into ferrite grain. Mechanical properties and corrosion resistance of DSSs decrease with formation of σ and χ phases [8, 9].

In solution treatment of DSSs, obtaining the decent ferrite-austenite phase volume fractions is critical besides hindering

the formation of secondary phases. Desired mechanical properties and corrosion resistance of DSSs are obtained with proper ferrite-austenite phase volume fractions. Especially, solution treatment conditions are significant for proper ferrite-austenite ratio. Therefore, determining the decent solution treatment temperature, time and cooling condition is critical for successful solution treatment process [10, 11].

In this study, effects of solution treatment process parameters on properties of EN 1.4462 DSS were studied. Also, variation of corrosion behaviour of EN 1.4462 DSS with various solution treatment conditions were investigated in FeCl₃ (10% wt.) media.

II. EXPERIMENTAL

EN 1.4462 DSS specimens were used for experimental studies with 10x10x5 mm dimension. The chemical compositions of EN 1.4462 alloy was given in Table I.

TABLE XIX
CHEMICAL COMPOSITIONS OF EN 1.4462 ALLOY (WT. %).

EN 1.4462 Alloy	C	Cr	Ni	Mo	Mn
	0.020	22.560	5.420	2.950	1.290
	Si	P	S	N	Fe
0.457	0.031	0.014	0.170	Bal.	

The solution heat treatment was applied at 1100°C and 1150°C for 2 and 8 hours, respectively. 4 and 10 h with cooling in the furnace or in air. Metallographic preparation was performed by grinding, polishing and etching. Water cooled silicon carbide papers of 180, 240, 320, 400, 600, 800, 1000, 1200 and 2000 grit size were used in grinding, respectively. Also, polishing was performed by using 1 μ m diamond paste. Specimens were etched electrochemically with KOH solution. Microstructural characterizations were carried out by optical microscopy and image analysis. Moreover, corrosion properties were investigated in FeCl₃ (10% wt.) media for 23 hours. Also, corrosion resistance of the specimens was determined with weight loss measurements.

III. RESULTS AND DISCUSSION

Microstructural analysis were studied with optical microscopy as seen in Figure 1. Secondary phases did not occur

for air cooled specimens both annealed at 1100 °C and 1150 °C. Because of the small size of experimental specimens (10x10x5 mm), air cooling induced quenched effect and 950 °C – 650 °C temperature range was passed with rapid cooling. Moreover, furnace cooling induced slow cooling conditions at 950 °C – 650 °C temperature range and intermetallics occurred for furnace cooled specimens as seen in Figure 1b.

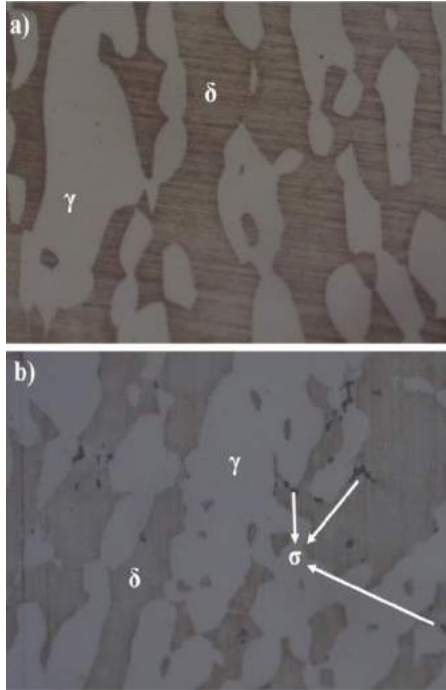


Fig. 1 Microstructures of annealed specimens; a) 2 hours annealed at 1100 °C and air cooled, b) 2 hours annealed at 1100 °C and furnace cooled

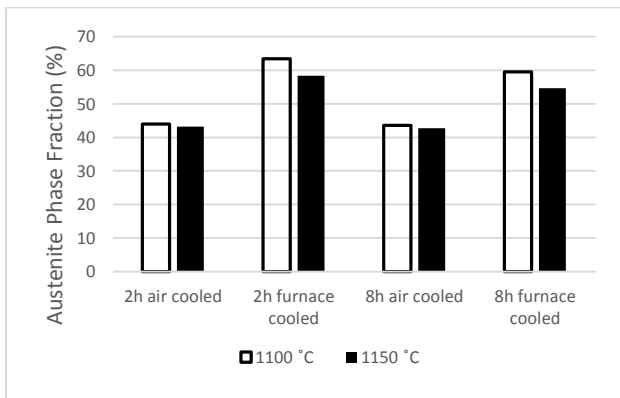


Fig. 2 Austenite phase fractions (%) of annealed specimens

Austenite phase fractions of annealed specimens are seen in Figure 2. Austenite phase fractions of the annealed specimens decreased at elevated solution treatment temperatures. Austenite-ferrite transformation occurred and also, ferrite phase in DSSs became more stable with increasing heat treatment temperature. Thus, ferrite phase ratio increased and austenite phase ratio decreased at elevated temperatures. Moreover, austenite transformed to ferrite with increasing solution treatment time at constant temperature. Simply,

increasing solution treatment temperature was more effective than increasing solution treatment for obtaining more stable ferrite phase and higher ferrite phase fraction. Moreover, furnace cooled specimens have higher austenite fractions than air cooled specimens and also, formation of secondary phases was seen for furnace cooled specimens. Specimens had lower cooling rates in furnace cooling conditions and secondary phases occurred and austenite phase fraction increased with ferrite-austenite eutectoid transformation during cooling after solution treatment.

TABLE XX
WEIGHT LOSS/UNIT AREA VALUES (MG/MM²)

Solution Treatment Time	Cooling Condition	Solution Treatment Temperature	
		1100 °C	1150 °C
		Weight Loss (mg/mm ²)	
2 hours	Air Cooling	0.0772	0.1116
8 hours	Furnace Cooling	0.0838	0.1734
2 hours	Air Cooling	0.0807	0.1297
8 hours	Furnace Cooling	0.0905	0.2110

Weight loss/unit area values are seen in Table II. Specimens annealed at 1150°C have higher corrosion rates than specimens annealed at 1100°C. Ferrite phase enhance the mechanical properties of DSSs and austenite phase enhance the general corrosion resistance of DSSs. Thus, corrosion resistance of the specimens decreased with increasing solution treatment temperature. Also, existence of secondary phases in DSSs has detrimental effect on corrosion properties. Furnace cooled specimens had lower corrosion resistance because of formation of secondary phases as seen in Figure 1.

IV. CONCLUSIONS

In this study, effect of solution treatment conditions on corrosion behaviour of EN 1.4462 was investigated. Solution treatments were applied at 1100°C and 1150°C for 2 hours and 8 hours. Corrosion test was applied in FeCl₃ (10% wt.) media for solution treated specimens.

Secondary phases did not occur for air cooled specimens both annealed at 1100°C and 1150°C. Moreover, furnace cooling induced slow cooling conditions at 950°C–650°C temperature range and intermetallics occurred for furnace cooled specimens.

Austenite phase fractions of the annealed specimens decreased at elevated solution treatment temperatures. Moreover, austenite transformed to ferrite with increasing solution treatment time at constant temperature. Simply, increasing solution treatment temperature was more effective than increasing solution treatment for obtaining more stable ferrite phase and higher ferrite phase fraction.

Corrosion resistance of the specimens decreased with increasing solution treatment temperature. Furnace cooled

specimens had lower corrosion resistance because of formation of secondary phases.

REFERENCES

- [1] I. Alvarez-Armas, "Duplex Stainless Steels: Brief History and Some Recent Alloys," *Recent Patents on Mechanical Engineering*, vol. 1, pp. 51–57, 2008.
- [2] R. Badji, M. Bouabdallah, B. Bacroix, C. Kahloun, K. Bettahar, and N. Kherrouba, "Effect of solution treatment temperature on the precipitation kinetic of σ -phase in 2205 duplex stainless steel welds," *Materials Science and Engineering A*, vol. 496, pp. 447–454, 2008.
- [3] A. Kisasoz, S. Gurel, and A. Karaaslan, "Effects of Annealing Time and Cooling Rate on Precipitations in Duplex Stainless Steel," *Metal Science and Heat Treatment*, vol. 57, pp. 544–547, 2016.
- [4] K.H. Lo, C.H. Shek, and J.K.L. Lai, "Recent developments in stainless steels," *Materials Science and Engineering R: Reports*, vol. 65, pp. 39–104, 2009.
- [5] Y.J. Kim, L.S. Chumbley, and B. Gleeson, "Determination of isothermal transformation diagrams for sigma-phase formation in cast duplex stainless steels CD3MN and CD3MWCuN," *Metallurgical and Materials Transactions A*, vol. 35, pp. 3377–3386, 2004.
- [6] A. Kisasöz and A. Karaaslan, "Dubleks Paslanmaz Çeliklerde Oluşan Yüksek Sıcaklık Fazlarına Genel Bir Bakış," *Metallurji*, vol. 162, pp. 57–61, 2012.
- [7] S.M. Dubiel and J. Cieslak, "Sigma-phase in Fe-Cr and Fe-V alloy systems and its physical properties," *Critical Reviews in Solid State and Materials Science*, vol. 36, pp. 191–208, 2011.
- [8] C.C. Hsieh and W. Wu, "Overview of Intermetallic Sigma Phase Precipitation in Stainless Steels," *ISRN Metallurgy*, vol. 2012, pp. 1–16, 2012.
- [9] J. Michalska and M. Sozańska, "Qualitative and quantitative analysis of σ and χ phases in 2205 duplex stainless steel," *Materials Characterization*, vol. 56, pp. 355–362, 2006.
- [10] M. Pohl and O. Storz, "Sigma-phase in duplex-stainless steels," *Zeitschrift für Metallkunde*, vol. 95, no. 7, pp. 631–638, 2004.
- [11] L. Duprez, B. C. De Cooman, and N. Akdut, "Redistribution of the substitutional elements during σ and χ phase formation in a duplex stainless steel," *Steel Research*, vol. 72, no. 8, pp. 311–316.

Comparison of Energy Absorbing Members for Passenger Coaches

Ramazan ÖZMEN*, Tuncer TOPRAK⁺

*Karabuk University Engineering Faculty, Karabük, TURKEY,
ramazanozmen@karabuk.edu.tr

⁺İstanbul Technical University Engineering Faculty, İstanbul TURKEY

Abstract— In order to prevent fatalities and injuries in the accidents occurred in railway transportation, crash zones were developed at the front and back ends of the coaches. These crash zones are aimed to absorb the kinetic energy in a controlled manner and protect the health of the passenger and the structure of occupied areas in the coach. The primary energy absorber is one of the most important components of the system and is able to absorb an impact energy of about 1.3MJ. In this study, deformation behaviours of tube like structures with square and circular cross sections under the axial impact load were investigated by means of finite element analysis. The investigated tube like structures are the same size and weight and have five different wall thicknesses. At the end of the study, the performances of square and circular sections were compared in terms of energy absorption capacities and average deformation forces.

Keywords— Impact, Energy absorption, Finite element analysis, Tube deformation

I. INTRODUCTION

In order to prevent tragic events such as accidental death and injury in railway transport, collision zones have been developed in front and rear of the car to damp the collision energy. By means of these collision zones, the kinetic energy is consumed during the accident in a controlled manner to preserve the integrity of the passengers and the occupied areas, thereby reducing undesirable situations such as injury and death [1, 2]. In order to absorb collision energy, thin-walled tube-like structures are commonly used as energy absorbing members in vehicles such as cars, planes and trains etc. The static and dynamic axial impact behaviors of these members with various cross sections (circular, rectangular etc.) were investigated by means of several experimental and theoretical studies and the theoretical expressions were presented according to the cross sectional properties [3].

The primary energy absorber is one of the most important member in the passenger wagon that is designed for the collapse of collision energy (Figure 1). The existing primary energy absorber is consisting of two tube like structures in the form of square cross section. Holes are drilled on the member to improve energy absorption capability and the two members are joined to each other using welded intermediate diaphragm like members [4].

Axial impact behavior and energy absorption capabilities of thin-walled tubes depend on many factors such as member geometry [5], material properties [6], applied boundary conditions [7], impact velocity [8] and forming history [9]. These studies have revealed that the hardening characteristics and strain rate sensitivity of the material are significant influences on the collision behavior of the energy absorber [6]. On the other hand, it was stated that the stress-strain relationship of the material has an important place in the

numerical simulation of the collision events in which the large deformations occurs[10].

In some studies, aluminum foams and honeycomb structures were placed inside the energy absorber to increase the energy absorption capability of the member [11]. Trigger structures like holes and groves have been utilized to ensure a controlled deformation and to increase energy absorption. One of the most important features of this trigger mechanism is to reduce the initial peak force generated during the impact [12].

In this study, the deformation behaviors of tube like structures have been using in passenger coaches as energy absorbing members with flat square and cylindrical cross sections were investigated by means of finite element analysis method.

As a result of the study, the axial deformation of square and circular sections with the same weight and length and different wall thicknesses were evaluated in terms of the parameters given from the studies about deformation of the members subjected to axial impact load.



Figure 8 Primary energy absorbing member for passenger cars [4]

II. MATERIAL and METHOD

A. Material Model

High-strength low alloy (HSLA) or micro alloyed steels present a yield strength of 340–420 MPa and ultimate tensile strength of 410–510 MPa, while their uniform elongation ranges between 10 and 25%. As a result, HSLA steels usually require 25–30% more power to form because of their higher strength and toughness, for example compared to carbon steels [13]. Thus, these steels are commonly used in trucks, construction equipment, off-highway vehicles, mining equipment, and heavy-duty vehicles for constructing chassis components, buckets and grader blades [14]. In the light of this knowledge, the HSLA 350 steel was chosen as material in the axial collision analysis of the energy dissipation elements using in the passenger car.

The main criterion in the design of members is that the member weights are the same. For this reason, the weight of the square member with a thickness of 6 mm is taken as the reference member weight.

In order to achieve the same weight value, the cross section of the member is increased as the thickness is decreased, and the member cross section is decreased as the thickness is increased. Accordingly, the member sizes used in the analysis are given in Table 1.

In the analysis, the speed and mass values of the impacting wall, which was modeled for the axial deformation of the structure in the form of the tube, were taken from the tests applied to the existing energy absorbing member used in passenger coaches [15].

A comparison was made between the analysis results and the theoretical equations revealed by the experimental studies of the deformation of the thin-walled tubes. The method and material properties used during modeling are given below.

TABLE I

Member dimensions used in analysis

Thickness	Square Edge A (mm)	Cylinder Radius R (mm)
8	114.3	70.7
7	130.6	80.8
6	152.4	94.3
5	182.9	113.1
4	228.6	141.4

In the axial collision analysis of the energy absorbing members made of HSLA 350 material, stress strain diagrams of the material were used depending on the strain rate. The stress-strain diagram of the HSLA-350 high strength steel, depending on the deformation rate, is given in Figure 2.

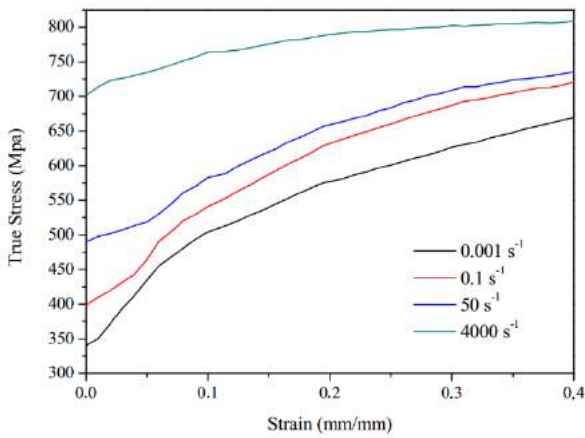


Figure 9 Stress-strain diagram of HSLA-350 steel depending on strain rate [6]

In LS-DYNA these stress-strain values were defined using the Type-24 material model. This material model is defined as a piecewise linear isotropic elastic-plastic material model. In Type-24 material model, the effect of strain rate is achieved by Cowper-Symonds equation. In this equation the yield stress is multiplied by the factor given below [16].

$$\sigma_d = \sigma_y \left[1 + \left(\frac{\dot{\epsilon}}{D} \right)^{1/p} \right]$$

where;

σ_d : Dynamic yield stress,

σ_y : yield stress,

$\dot{\epsilon}$: Deformation rate,

D ve p are Cowper-Symonds material constants.

B. Finite Element Model

In this study the deformation behaviors of thin-walled tubes under axial load were examined by the software of LS-DYNA. When describing the boundary conditions in the finite element model, existing installation conditions were taken into account. Under existing conditions, one end of one energy absorbing member free and the other is welded to the frame of the CEM (Crash Energy Management) system (Fig. 1). For this reason, all the degrees of freedom of the base nodes of the modeled member were restricted and no boundary conditions were applied to the ceiling nodes. The impacting body was modeled with a rigid plate with a mass of 2500 kg and a velocity of 21 m/s. The finite element model of the energy absorbing member used in the analyses is given in Fig. 3.

The automatic contact option was used to prevent the folding surfaces from penetrating into each other during deformation, and the friction coefficient was taken as 0.25 for dynamic and static friction conditions. In addition, the friction coefficient for the friction between the moving rigid plate and the tube was also taken as 0.25. Belytscho-Tsay shell elements with six degrees of freedom for each node and five integration points along the thickness was chosen for meshing the tube because of frequently used element type in the collision analysis for giving short solution times and approximate value assignments [10]. When, the experimental results are compared with the finite element analysis in the collision tests in terms of the calculation efficiency, the shape of the deformed member, and the force-displacement graphs, the best collision results were obtained when the member mesh size used in the analysis was twice the thickness [36]. Consequently, the mesh size in the analyses was chosen to be about twice the thickness value used for each member.

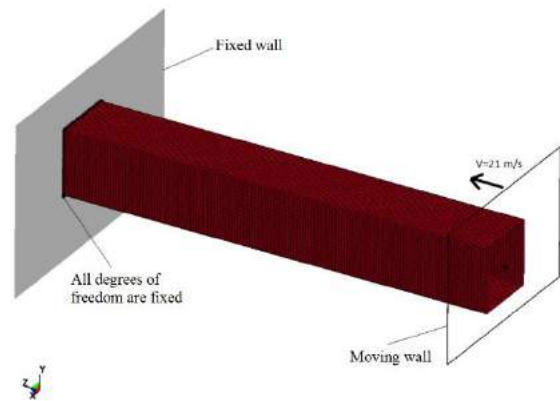


Figure 10 Finite element model of the member

III. RESULTS AND DISCUSSION

In this section, axial deformation behaviors of tube-like structures with cylindrical and square cross-section under dynamic loading conditions were investigated. The average force values obtained from the analysis of the energy absorbing members with five different wall thicknesses were compared with the theoretical expressions given by Abramowicz and Jones [3] for the dynamic axial deformation modes of the thin-walled square and cylindrical members.

The symmetric axial deformation expression given by Abramowicz and Jones [3] was used to compare the average deformation force of a square cross-section tube, since the general deformation behavior of the square cross-sectional tube was in symmetrical deformation mode. This expression is given by;

$$\frac{P_m^d}{M_0} = 52.22 \left\{ 1 + \left(0.33 \frac{V}{cD} \right)^{1/p} \right\} \left(\frac{c}{h} \right)^{1/3}$$

Where, $M_0 = \sigma_0 h^2 / 4$ fully plastic moment, V: impact velocity, c: edge length of the energy absorber, D and p Cowper Symonds constants.

The deformation mode of the circular cross-section tube, which started symmetrically at the beginning, was observed to continue to form lobes at later stages of the analysis. For this reason, the non-axisymmetric deformation behavior given by Abramowicz and Jones was used to compare the average deformation force for the circular section tube.

The average deformation force comparison was made according to the formation of the two lobes and coefficients A_{3N} , A_{4N} and A_{5N} were taken as coefficients in case of two lobes.

$$\frac{P_m^d}{M_0} = \left\{ A_{3N} \left(\frac{2R}{h} \right)^{1/2} + A_{4N} \right\} \left[1 + \left\{ \frac{A_{5N} V (h/2R)^{1/2}}{DR} \right\}^{1/p} \right]$$

The average deformation force of square and circular cross-section tubes obtained by the theoretical expressions and finite element analysis is given comparatively in Fig. 4

It can be seen from the Figure 4 that the average force values obtained from the finite element analysis of the circular and square cross-section tubes are close to theoretically calculated forces.

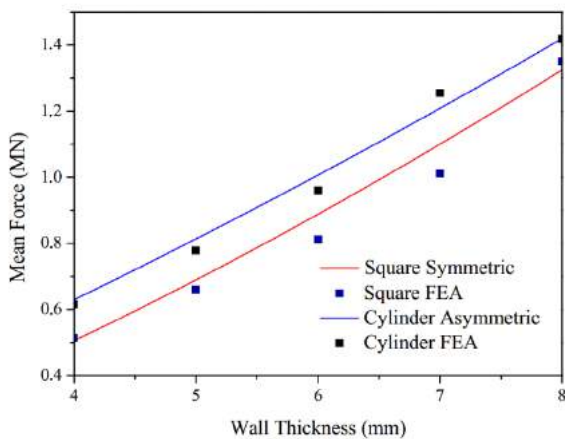


Figure 11 Comparison of mean deformation forces

Figure 5 shows the deformation patterns of square cross-section tubes with wall thicknesses of 4, 6 and 8 mm and also Figure 6 shows deformation patterns of circular cross-section tubes with wall thicknesses of 4, 6 and 8 mm. When the deformation behavior of the member with a square cross-section under the axial impact load is examined (Fig. 5), it is seen that the deformation first occurs at the side of the impacting wall. For all thicknesses the deformation of the square member was determined to be extensional mode at the beginning and after continued as symmetrical mode. Therefore, in the mean force comparison theoretically given relation for the symmetric deformation mode was used. In the deformation behavior of a member with a circular cross-section under the axial impact load (Figure 6), the deformation first occurred in the form of ring mode on the side of the impacting wall and later continued in the form of non-axisymmetric deformation mode.

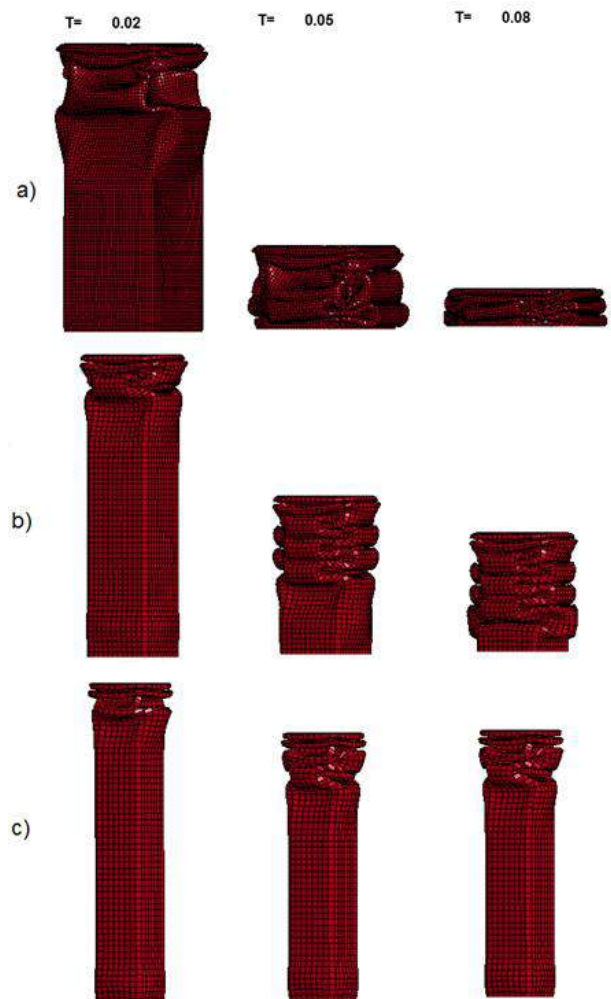


Figure 12 Deformation states of square cross section members with respect to time; a) 4 mm, b) 6 mm, c) 8 mm

Since the material and member properties were perfectly defined and imperfections were ignored in the finite element

analysis, the deformation patterns in the studied members were realized in these modes. In the real case, the deformation patterns may be different from the analysis due to defects in the material and the member. Gümruk and Karadeniz [9] studied the deformation behavior of the flat profile under axial load by defining the plastic deformations, residual stresses and thickness differences as defects resulting from the forming of the flat profile in the finite element analysis. In their work, they stated that the residual effects from the forming history of the member affects the collision behavior of the energy absorber.

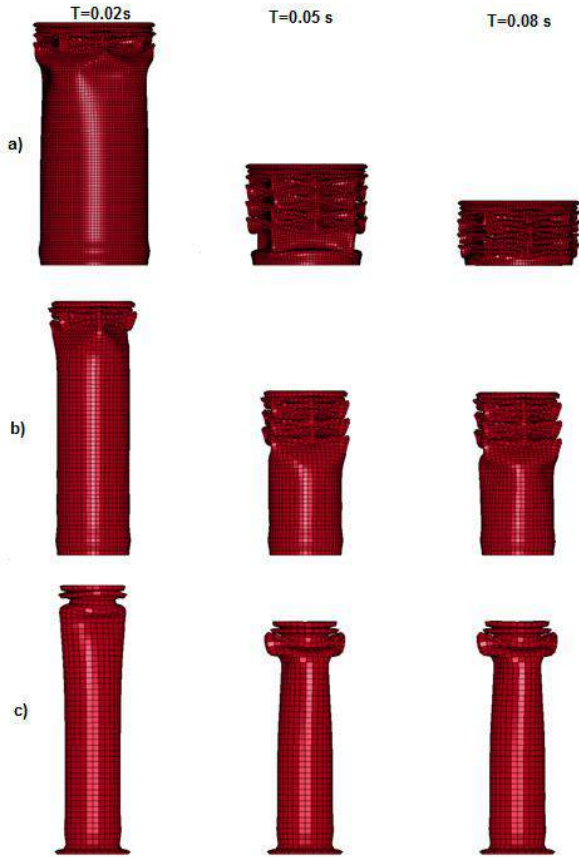


Figure 13 Deformation states of cylindrical cross section members with respect to time; a) 4 mm, b) 6 mm, c) 8 mm

For square and circular cross-section members, rigid wall force-displacement graph is given in Figure 7, the mean force-displacement graph is given in Figure 8, and the absorbed energy-displacement graph is given in Figure 9.

It is seen from Figure 7 that; the local maximum and minimum force values are comprised during the formation of the folds in the axial deformation of the square and circular section members. In the formation of the first fold the rigid wall force value reaches its maximum and then decreases suddenly. During the formation of the second and subsequent folds, the force fluctuates between the local maximum and minimum values.

Al Galib and Limam [17] emphasized this situation that, the initial force required to form the first fold of the member should be high because there is no deformation at the beginning of the

tube. When the formation of the first fold, deformations occur in the member and that these deformations reduce the subsequent peak forces.

If the member has the capability to absorb the current impact energy, the force value reaches zero at the rigid wall force-displacement graph. Otherwise, the member loses its energy absorbing ability and starts to behave like a rigid body.

When the rigid plate wall force - displacement graph is examined (Fig. 7), it is seen that the rigid wall force increases again towards the end of the analysis due to the loss of energy absorbing ability of members with 4 mm thickness.

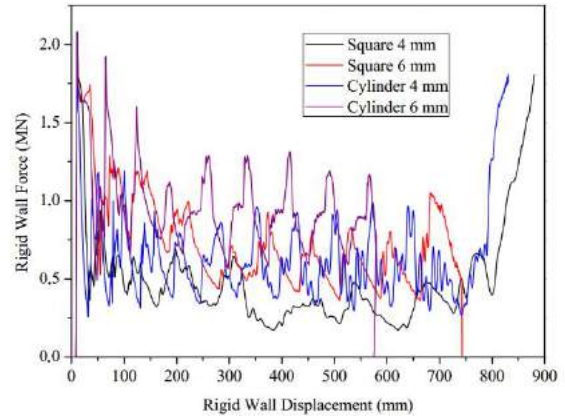


Figure 14 Rigid wall force-displacement graph of square and circular cross-section members

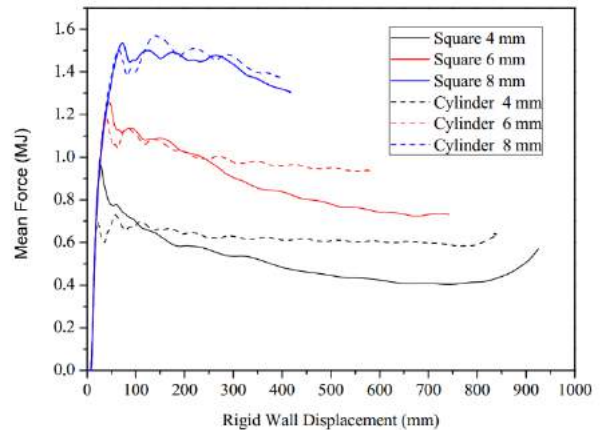


Figure 15 Mean force-displacement graph of square and circular cross-section elements.

According to the average deformation force-rigid plate displacement graph (Fig. 8), it is seen that the average deformation force increases as the thickness increases because a rigid structure is obtained at the same member weight. Though the weight is the same, the member becomes more rigid as the thickness increases. In this graph, when a comparison is made between members having circular and square cross-sections, it is seen that the average force values of circular cross-section members with the same thickness value are higher than those with square cross-section members. This is because the cross-sectional area of the circular cross-section member is

higher than that of square cross-section members with the same wall thicknesses.

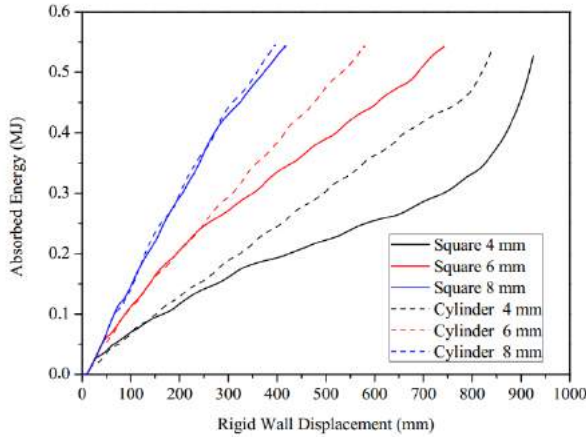


Figure 16 Absorbed energy-displacement graph of square and circular cross-section elements.

According to the absorbed energy-rigid plate displacement graph (Fig. 9), the initial impact energy can be absorbed at the shorter deformation length, despite the decrease in cross section as the thickness increases. When a comparison is made between the square and the circular cross-section members per this graph, it is seen that the circular cross-section member has a higher energy damping ability than the square cross-section member with the same wall thickness.

Crush force efficiency (AE), total efficiency (TE), deformation capacity (DC) are parameters that is used to compare the performance of energy absorbers. The deformation capacity D_C is defined as division of the actual deformation d to the original length l of the crushed member. The crush force efficiency A_E of the absorber is defined as the ratio between the average crush force F_{avg} and maximum crush force F_{max} both calculated in the interval $(0, d)$. It may be considered as optimum properties of the energy absorber when the division of the absorbed total energy to the maximum force F_{max} achieves a maximal value and this property defined as the total efficiency T_E [11].

The obtained performance parameter values from the analysis for the comparison of axial deformations of square and circular sections are given in Fig. 10.

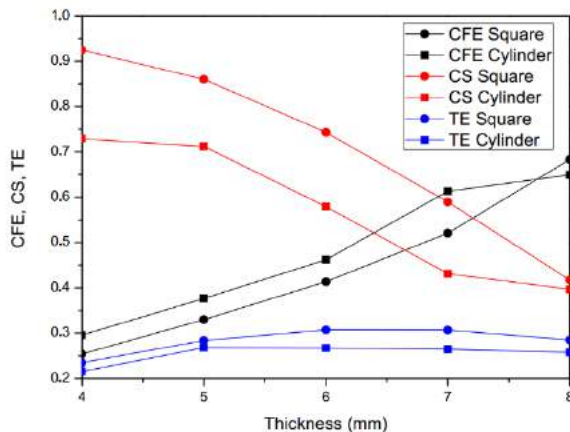


Figure 17 Calculated performance parameters of axial deformations of square and circular sections

As it is seen from the absorbed energy vs. rigid wall displacement graph (Fig. 9), the energy absorption capacity of the circular cross-section members is higher than that of the square cross-section members, which results in a higher collision force efficiency for the circular members. However, when comparing the total deformation efficiencies given in Fig. 10, it is seen that the total efficiency of the square cross-section members are better than the circular cross-section members with the same thickness.

IV. CONCLUSIONS

In this study, the deformation behaviors of the elements with circular and square cross sections were investigated under the impact force acting on the existing primary energy absorbing member.

In the study, deformation performances were compared with the condition that the weight and length of the square and circular section elements were the same. As a result of comparison, it was found that the average deformation forces and energy absorbing performances of circular cross-section members with the same wall thickness were higher than those of square cross-section members. It has been found that even though the thicknesses are the same, it is caused by the area of the circular cross sectional members higher than the square ones. However, when the total deformation efficiencies were compared, it was determined that the total deformation efficiencies of the square section members are higher than the circular ones.

REFERENCES

- [1] K. Jacobsen, D. Tyrell, and B. Perlman, "Impact Tests of Crash Energy Management Passenger Rail Cars: Analysis and Structural Measurements," in *ASME 2004 International Mechanical Engineering Congress and Exposition*, 2004, pp. 97–105.
- [2] E. Martinez, DavidTyrell, R. Rancatore, R. Stringfellow, and G. Amar, "A crush zone design for an existing passenger rail cab car," in *Proceedings of 2005 ASME International Mechanical Engineering Congress & Exposition*, 2004, pp. 85–94.
- [3] W. Abramowicz and N. Jones, "Dynamic progressive buckling of circular and square tubes," *Int. J. Impact Eng.*, vol. 4, no. 4, pp. 243–270, 1986.
- [4] G. Mayville, R. A., Rancatore, R. J., Stringfellow, R. G., Amar, "Repair of Budd Pioneer Coach Car Crush Zones," Cambridge, MA, 2007.
- [5] A. A. Nia and J. H. Hamedani, "Comparative analysis of energy absorption and deformations of thin walled tubes with various section geometries," *Thin-Walled Struct.*, vol. 48, no. 12, pp. 946–954, 2010.
- [6] S. Simunovic, J. Shaw, and G. a Aramayo, "Material Modeling Effects on Impact Deformation of Ultralight Steel Auto Body," *SAE Tech. Pap.*, no. 724, 2000.
- [7] A. Tasdemirci, "The effect of tube end constraining on the axial crushing behavior of an aluminum tube," *Mater. Des.*, vol. 29, no. 10, pp. 1992–2001, 2008.
- [8] M. Langseth, O. S. Hopperstad, and T. Berstad, "Crashworthiness of aluminium extrusions: validation of numerical simulation, effect of mass ratio and impact velocity," *Int. J. Impact Eng.*, vol. 22, no. 9–10, pp. 829–854, 1999.
- [9] R. Gümruk and S. Karadeniz, "The influences of the residual forming data on the quasi-static axial crash response of a top-hat

- section,” *Int. J. Mech. Sci.*, vol. 51, no. 5, pp. 350–362, 2009.
- [10] R. Gümrük and S. Karadeniz, “A numerical study of the influence of bump type triggers on the axial crushing of top hat thin-walled sections,” *Thin-Walled Struct.*, vol. 46, no. 10, pp. 1094–1106, 2008.
- [11] A. G. Hanssen, M. Langseth, and O. S. Hopperstad, “Static and dynamic crushing of circular aluminium extrusions with aluminium foam filler,” *Int. J. Impact Eng.*, vol. 24, no. 5, pp. 475–507, 2000.
- [12] G. Chen, X. M. Chen, and M. F. Shi, “Experimental and Numerical Studies of Crash Trigger Sensitivity in Frontal Impact,” *SAE Tech. Pap.*, no. 724, 2005.
- [13] D. A. Skobir, “High-strength low-alloy (HSLA) steels,” *Mater. Technol.*, vol. 45, no. 4, pp. 295–301, 2011.
- [14] J. Patel, C. Klinkenberg, and K. Hulka, “Hot rolled HSLA strip steels for automotive and construction applications,” *Niobium Sci. Technol.*, no. Grade 100, pp. 647–674, 2001.
- [15] R. Mayville, A. D. Little, K. Johnson, and P. Engineering, “The Development of a Rail Passenger Coach Car Crush Zone,” in *Proceedings of the 2003 IEEE/ASME Joint Rail Conference*, 2003, pp. 1–8.
- [16] J. O. Hallquist, *LS-DYNA users manual*. Livermore, California: Livermore Software Technology Corporation, 1998.
- [17] D. Al Galib and A. Limam, “Experimental and numerical investigation of static and dynamic axial crushing of circular aluminum tubes,” *Thin-Walled Struct.*, vol. 42, no. 8, pp. 1103–1137, 2004.

Importance of Force Measurements and Their Traceability in Steel Industry

Haldun DİZDAR, Bülent AYDEMİR, Cemal VATAN

TÜBİTAK Ulusal Metroloji Enstitüsü, Gebze-Kocaeli, Türkiye

haldun.dizdar@tubitak.gov.tr, bulent.aydemir@tubitak.gov.tr, cemal.vatan@tubitak.gov.tr

Abstract— In iron and steel industry, force measurements play an important role in areas such as pressing, rolling and extrusion, both in process control and in development of reproducible similar products and quality. In order to obtain accurate and reliable measurement results, it is needed to perform traceable calibrations of devices used in measurements. Calibration of devices should be performed according to ISO, ASTM, and TS standards. Using inappropriate equipment will result in production losses and cost increases that will be reflected in product quality. For this reason, calibrated devices should be used in measurements; also these devices should have acceptable range of deviation. In this study, usage area of force measurements in iron and steel industry and importance of certifying performed measurements have been examined.

Keywords— Force measurements, calibration, traceability, iron and steel industry

I. INTRODUCTION

Manufacturers of steels need to pass compliance standards before shipping and selling their product. Measurement and testing are necessary for ensuring a safe, high quality steel material. These actions will keep end consumer satisfied and dramatically reduce chance of failure in the field.

Specifically in iron and steel industry, these force measurements play an important role in areas such as pressing, rolling and extrusion, both in process control and in development of reproducible similar products and quality.

Depending on the area of need, force measurements can range from 1 N (Newton) up to 10 MN (10 million Newtons). Force measurements are measured either directly by means of sensors (force transducers, load cells, dynamometers etc.) or indirectly by means of sensors called strain gauges attached to mechanical system.

In order to obtain accurate and reliable measurement results from force measuring devices used in production and tests in steel industry, these devices should have traceability to international force standards and their calibrations are required. In this study, usage area of force measurements in iron and steel industry and importance of certifying performed measurements have been examined.

II. FORCE MEASUREMENT APPLICATIONS

Force measurement systems are widely used in many areas of the industry such as mechanical engineering, aviation

industry, power generation industry, construction industry, security engineering, testing of products and materials. In particular, common applications of force measurement fields are listed below as examples:

- Determination of rolling process machine forces in steel industry,
- Optimum and controlled application of pressing forces on metal plate and sheet material,
- Material testing machines used in mechanical tests applied to initial production and control of subsequent operations of products,
- Mechanical testing of steel materials and construction products used in construction and bridging industries,
- Applying forces that will tension the paper, plastic film and laminate coils,
- Cutting forces on metal plate and sheet material
- Determination of hook and rope forces to be anchored to ship and tankers,
- Overload control in towers and overhead cranes and elevators,
- Determining the forces that the truck wheels apply on the paved road in traffic,
- Measuring the forces coming to the tower legs on the offshore oil platforms,
- Forces applied to adjust the cable tension during cable,
- Forces applied in underwater pipe laying.

In these examples, particularly for steel industry force measurement applications are discussed in details below.

1. Importance of Forces in Rolling Process

Both in terms of product quality and operational safety measuring the forces applied by rollers for metal rolling is very important. Figure 1 shows the construction of roller mill bearing, which is connected to force measuring device.

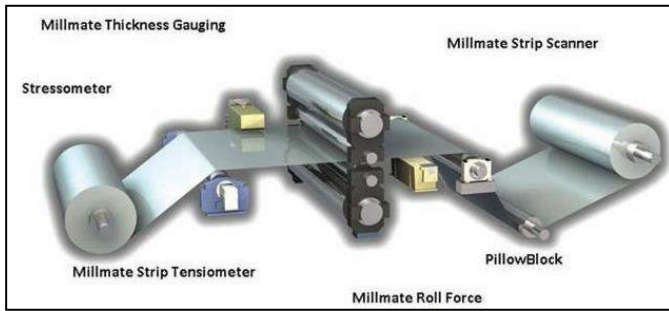


Figure 1. Roller mill shaft connected force measurement system

For carrying out hot or cold rolling process in rolls, traceable forces should be implemented in a correct and controlled manner. This allows quality of product and similar products to be reproduced later with same properties.

2. Importance of Forces in Metal Sheet Forming

In metal sheet forming and pressing process, determination of optimum forces during shaping corresponding to controlled application force is crucial for product quality, undamaged production and low energy usage (Fig. 2).

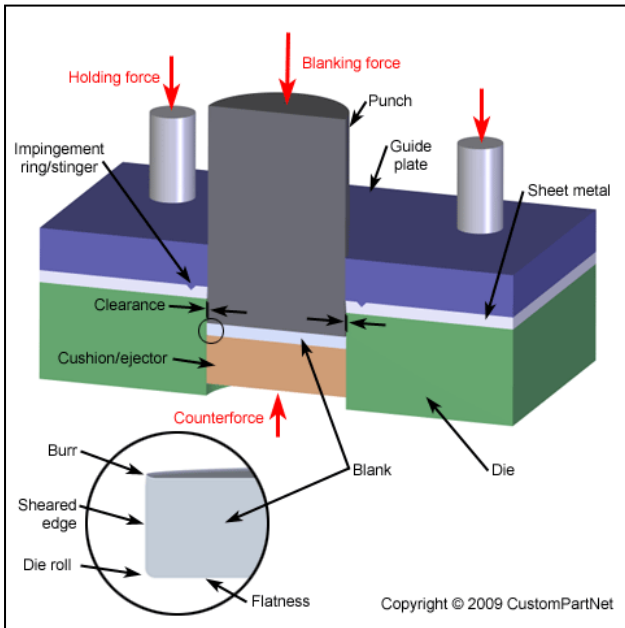


Figure 2. Schematic representation of metal sheet forming and pressing process

Recently, process control has become a very important factor in ensuring quality rather than post-production quality control in all manufactured products. The only way to achieve this is to determine accuracy of measuring and test equipment used in process before, during and after production. From design stage to production stage utilizing correct materials with well-known mechanical properties ensures in all process development and manufacture of economical and more reliable products.

3. Importance of Forces in Hot and Cold Forging

In order to ensure parts specified characteristics, durability and rigidity in terms of application, required by automotive industry, especially hot and cold forging forces in iron and steel industry, have great importance (Fig. 3, 4). It is essence that application of force in a controlled manner is to provide desired mechanical properties, to avoid overloads and to apply same forces determined for similar products.

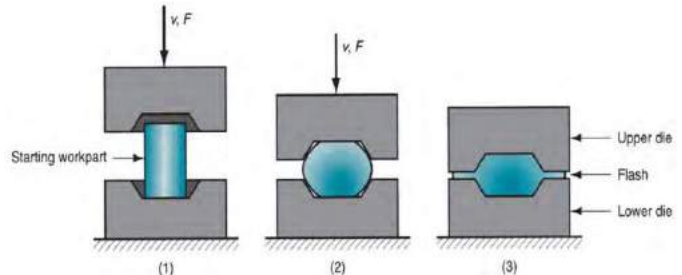


Figure 3. Schematic representation of hot forging forces

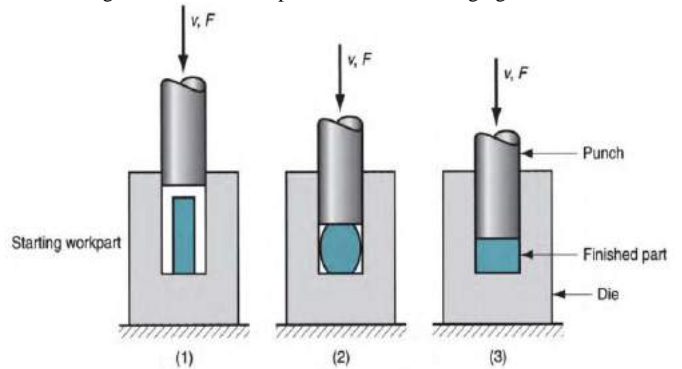


Figure 4. Schematic representation of cold forging and pressing process

4. Importance of Forces in Mechanical Tests

There are a lot of mechanical tests in steel industry. Mechanical test methods are tension, bending, hardness, impact according to ASTM A370 on definitions for mechanical testing of steel products. Force effect in these mechanical tests is briefly explained below.

ISO 6892-1 and ASTM E8 standards provide data on the strength and ductility of steel under uniaxial tensile forces. The tensile strength of steel is essentially its ability to withstand tensile loads without failure. On the other hand, ductility, measures a material's ability to deform under tensile stresses. This is an important factor in metal forming processes since brittle metals are more likely to rupture. Within this framework, determination and improvement of accuracy of tensile testing machines, which are used, will directly reflect quality of product.

Technicians who conduct tensile testing of steels measure a number of mechanical properties to determine the material's quality. Table 1 shows in change on tensile strength of structural steels concerning to steel type. When data in table are analysed, tensile strength values of St 50 steel are ranging from 470 MPa to 610 MPa, while St 52 steel values have the tensile strength values in between 490 MPa and 630 MPa.

TABLE XXI
TENSILE STRENGTH VALUES OF GENERAL STRUCTURAL STEELS

Structural Steel (DIN)	Tensile Strength (MPa) (3 mm ≤ Diameter ≤ 100 mm)
St 33	290-510
St 37	340-470
St 44	410-560
St 50	470-610
St 52	490-630

A difference of about 4% between these two steels changes classification and name of structural steel. When these steels are tested for classification, large deviation of force in tensile testing machine will cause a fault in classification. This will lead to errors both in manufacturing process and in quality of product. Calibration of tensile testing machines and determination of its accuracy are important in this respect. It is common for steel materials according to international standards; material testing machines have at least 1% of force deviation and uncertainty (Fig.5a). hardness testing machines have also at least 1% of force deviation according to standards (Fig.5b). In the notch impact test, the change of the impact force of the hammer is the important parameters affecting the measurements (Fig.5c).



Fig.5a. Material testing machine

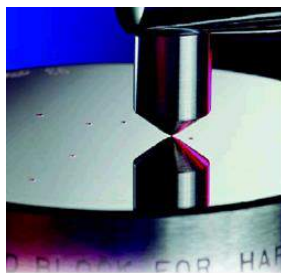


Fig.5b. Hardness test machine



Fig.5c. Notch impact test machine

III. CERTIFICATION OF FORCE

In steel industry, mechanical test measurement devices are used in various applications. These devices and force they apply, how accurate or uncertain, are carried out by metrology institutes in country, concerning to international unit system (SI). TÜBİTAK National Metrology Institute (UME) is responsible organization for calibrating first level of force measuring devices in our country and ensuring its integration into international system. In Force Laboratory, which is located in TÜBİTAK-UME, is realized the calibration of force measuring devices by using five different capacity force standard machines in range of 0.5 N to 3 MN corresponding to standards (ISO 376, ASTM E74, ISO 7500-1) for international validity and acceptance. In this way, dissemination the unit of force “Newton (N)” from national standards to industrial applications which is given in Fig.6. Thus, all force measurements performed in our country are provided with traceability to international standards and therefore international measurement system.

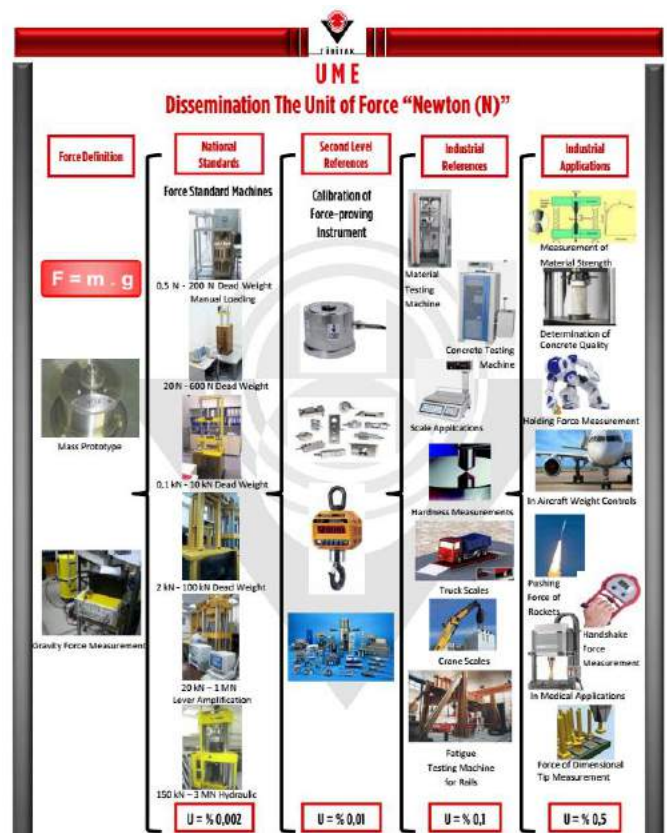


Figure 6. Dissemination of the unit of force “Newton (N)”

IV. CONCLUSIONS

Accurate and reliable measurement is very important for product quality, producing safe, reducing energy consumption in steel industry. Adding, it is important to produce same products repeatedly according to the order and offering acceptable products in international markets. Therefore, measurements, especially force, realized in the iron and steel

industry must be ensured traceability within the metrology system.

In this study, some examples of force measurement application in steel industry are discussed. In order to obtain accurate and reliable measurement results, it is needed to perform traceable calibrations of devices used in mechanical test and application of force measurements. We have summarized importance of force measurements and its effect in steel industry.

REFERENCES

- [1] Aydemir, B., Dizdar, H., Vatan, C. Genel Kuvvet Metrolojisi Eğitim Dökümanı, G2KV-010, TÜBİTAK UME, 2017
- [2] Aydemir, B., Dizdar, H., Vatan, C. Tek Eksenli Statik Malzeme Test Makinalarının Kuvvet Kalibrasyonu Eğitim Dökümanı G2KV-020, TÜBİTAK UME, 2016
- [3] EURAMET-cg-04.01 Uncertainty of Force Measurements, March 2010
- [4] EURAMET-cg-04, Kalibrasyon Rehberi, "Kuvvet Ölçümlerinde Belirsizlik" Dizdar, H., Aydemir, B., Vatan, C. 2015
- [5] EN ISO 376, Metallic Materials - Calibration of Force-Proving Instruments Used for the Verification of The Uniaxial Testing Machine, 2011
- [6] ASTM E74, Standard Practice of Calibration of Force-Measuring Instruments for Verifying the Force Indication of Testing Machines, 2013
- [7] EN ISO 7500 -1, Metallic Materials — Calibration and Verification of Static Uniaxial Testing Machines, 2015
- [8] Meganewton Seviyesindeki Kuvvetlerin Çelik Endüstrisinde Uygulama Alanları ve İzlenebilirlik İhtiyacı, Metal Dünyası Dergisi Sayı: 263, Mayıs 2015
- [9] Hasçelik Teknik Katalog 2016
- [10] <http://www.admet.com/why-tensile-testing-is-imperative-for-metals-manufacturers>

Interlaboratory Comparisons of Charpy Impact Test for S275JR steel according to ISO 148-1

Betul USTA, Alper INCESU

*Karabük University, Iron and Steel Institute, 78050, Karabük, TÜRKİYE
betulusta@karabuk.edu.tr, alperincesu@karabuk.edu.tr*

Abstract- Evaluation of the performance of the laboratories for specific tests and monitoring laboratory performance, laboratories need to participate interlaboratory comparisons. As a means of quality assurance such an external quality control studies have an importance for laboratory accreditation. In this study, charpy impact test samples were prepared related to ISO 148-1 from S275JR quality steel and randomly sent to participant laboratories. Each samples were tested according to ISO 148-1: Charpy pendulum impact test standard in metallic materials at room temperature by each participant. Test results of laboratories were collected and performance of laboratories were determined by statistical method offered by ISO 13528:2015 standard.

Keywords: Charpy Impact Test, Interlaboratory Comparisons, ISO 148-1 Standart

A Research on Business Satisfaction Levels of Occupational Health and Safety Specialists in Occupational Health and Safety Practice

Volkan SANCI, Abdullah KARAKAYA

Karabük University, Iron and Steel Institute, 78050, Karabük, TÜRKİYE
volkansanci@gmail.com, akarakaya@karabuk.edu.tr

Abstract -High technology based production with the advent of industrialization has created some new issues. Foremost among them is the occupational health and safety. The facts that the business environment is particularly unsafe and puts health at risk have increased the importance of health and safety in work places. Measures in regards to work safety in the iron and steel sector are at the forefront of the issues that must be prioritized. It is crucial that job satisfaction levels of occupational health and safety specialists, who not only have good knowledge of both the workplace and the production process but also can determine, along with best safety measures, hazards related to the nature of work and production tools, are high so that they can work effectively and efficiently. Considering this facts a field study was done in order to measure job satisfaction levels of health and safety specialists working in the Black Sea Region. The data obtained from the questionnaire with 379 samples was evaluated with factor analysis and then, it was analysed to see if there is variation by applying nonparametric Mann-Whitney U ve Kruskal-Wallis H tests. As a result of the analysis, it was found that job satisfaction levels of occupational health and safety specialists did not vary in respect to age, sex and OHG (Occupational Health Safety) certificate but varied in respect to occupational experience.

Keywords: Occupational health and Safety, Health and safety specialist, Job satisfaction

Mechanical Characterization of Thin Sheet Metals for Suspension System Forming Design

Alimurtaza RUTCİ¹, Tuğba ALBAY², Mehmet Okan GÖRTAN³
¹Teknorot Otomotiv Ürünleri A.Ş., alimurtaza.rutci@teknorot.com
²Teknorot Otomotiv Ürünleri A.Ş., tugba.ablay@teknorot.com
³Hacettepe University, okangortan@hacettepe.edu.tr

Abstract- Suspension system is an important part of vehicles that manages the motion of the wheels in relation to body. The motion between wheel and chassis is provided with control arms. Control arm is one of the most crucial components which is usually made of either steel or aluminium. Various processes are used in the manufacturing of steel control arms. Due to its cost-effectiveness in mass production, sheet metal forming process is preferred for the manufacturing of control arm. Sheet metal control arms have considerable advantages in terms of weight and cost to their forged counterparts. The aim of study is to characterize thin sheet metals which are used in control arm manufacturing. For sheet material, the ability of sheet metal to be formed into a desired shape without failure such as necking and wrinkling is often called as its formability. To investigate the formability, it is crucial to describe the behaviour of the sheet metal in a precise way and express properties in a mathematical form. Moreover, it is also important to be able to select appropriate tests to define materials behaviour. In the current study, most suitable mechanical, metallurgical and chemical properties are examined for suspension system forming design.

Keywords: Sheet Metal, Forming, Design, Characterization

A Forecasting Analysis of Exports of Rail and Rail Equipments in Turkey by Grey Prediction and Exponential Smoothing

Ahmet Ziyaeddin BULUM¹, Muharrem DÜĞENCİ², Mümtaz İPEK³, Halil İbrahim DEMİR⁴

¹Karabuk University, ahmetbulum@karabuk.edu.tr

²Karabuk University, mdugenci@karabuk.edu.tr

³Sakarya University, ipek@sakarya.edu.tr

⁴Sakarya University, hidemir@sakarya.edu.tr

Abstract- Prices are falling in the world iron and steel industry due to China's high production capacity. This leads manufacturers to produce high-yielding products with less amount of production. Rail and rail equipment is one of the increasingly being produced iron and steel product in our country in recent years. In this study, by analyzing export data of rail and rail equipment (including wagon wheel) of Turkey, a forecasting for the years 2016-2020 has been made with the aim of guiding producers and giving an idea about exporting of these products. Grey prediction method and Holt's exponential smoothing technique were used for forecasting and the results were compared.

Keywords: Forecasting, Railway, Export, Grey Prediction, Exponential, Smoothing

An Investigation of the Influence of Keyhole Laser Welding Parameters on Weld Bead Shape and Integrity

Ömer Ekinci*, John Francis⁺, Zülküf Balalan*

[#] Faculty of Engineering and Architecture, Department of Mechanical Engineering, Bingöl University, Turkey
oekinci@bingol.edu.tr

⁺ School of Mechanical, Aerospace and Civil Engineering, The University of Manchester, United Kingdom
John.Francis@manchester.ac.uk

^{*} Faculty of Engineering and Architecture, Department of Mechanical Engineering, Bingöl University, Turkey
zbalalan@bingol.edu.tr

Abstract— The purpose in this study was to investigate the effects of keyhole laser welding parameters (laser beam power, laser welding speed, and heat input) on weld bead shape and integrity such as fusion zone and heat affected zone. Hence, butt-joint keyhole laser welding practices were conducted on S700 steel plates thickness of 13 mm by applying various laser beam power and welding speed with a 16 kW Ytterbium fibre laser and using pure argon as shielding gas in the Mechanical Engineering Laboratory of The University of Machester. The weld cross-sections were examined under an optical microscope and widths of fusion zone, coarse grained heat affected zone and intercritical heat affected zone were measured and also defects that occurred during welding were determined based on laser beam power and welding speed. As a result, effects of laser beam power and laser welding speed on fusion zone width and heat affected zone width were plotted and results were compared with previous studies published.

Keywords— Keyhole laser welding, fusion zone, heat affected zone, defects

I. INTRODUCTION

Welding with lasers has been an important joining method in industry due to the fact that laser welding enables some significant advantages over the other commonly used welding methods, for instance, laser welding can provide high power density, high penetration weld beads, high welding speeds, narrow weld beads and keyhole mode weldings [1]. Nowadays, fiber laser welding is a favorite bonding process amongst others laser welding techniques in industry and wavelength of fiber laser is ten times less than that widely used CO₂-lasers have, which leads to a higher laser energy absorption by the treated metal [2,3]. High strength low alloy (HSLA) steels have been widely utilized for years in many different applications because they have a strong and tough structure. For instance, HSLA steels are utilized in structural components, pressure vessels and fluid transportation pipes, in shipbuilding, offshore construction, automotive applications, and lifting and handling equipment [4,5]. In general, Gas tungsten arc welding (GTAW), gas metal arc welding (GMAW), submerged arc welding (SAW) and resistance spot welding (RSW) are used for welding HSLA steels in industry [6-11]. Although welding

HSLA steels by these conventional welding methods meet the demands, welding efficiency of these conventional welding methods is very low because they have a low penetration depth. Also, these conventional welding methods can generate a great quantity of heat input in workpieces [12], which causes major residual stresses and distortions in the welded workpieces. In the meantime, heat affected zone (HAZ) in fusion-welded HSLA steels becomes soft when they are subjected to thermal cycles, which causes mechanical properties of fusion-welded joints to deteriorate and also it has been determined that heat affected zone (HAZ) is getting larger when heat input increases in welding workpieces [13]. As a result, new advanced welding technics are required to attain welds with narrow heat affected zones and high mechanical properties. Laser welding is good at welding HSLA steels. Moreover, laser welding has a high welding efficiency, high power density and can produce high penetration welds with narrow heat affected zones through low heat inputs [14,15].

In this study, in order to determine laser welding ability, 16 kW Ytterbium Fibre Laser was used for butt welding of 13 mm thick S700 HSLA steel plates so as to determine effect of laser welding power and welding speed on fusion zone (FZ), heat affected zone (HAZ) and weld quality.

II. MATERIAL AND EXPERIMENTAL PROCEDURE

16 kW Ytterbium fiber laser with a focus length of 400 mm was used for keyhole fiber laser butt welding of 13 mm thick S700 HSLA steel plates. Chemical composition of S700 HSLA steel plates in weight percent was shown in Table I. S700 steel has a minimum yield strength of 700 MPa and it has been produced recently by Tata Steel to be used in production of heavy lifting equipment [16]. Keyhole fiber laser welding operation consisted of several steps. In the first step, oxidation layer on the front side and back side of S700 steel plates was removed by a sand blaster operation and then surfaces of the plates were cleaned via ethanol. Later, keyhole fiber laser single pass autogenous (without using filler material) butt welding operation was performed as shown in Fig. 1. Pure argon was used as shielding gas and it was provided through a nozzle and hose. While front side of the weld zone was shielded by a

shielding gas nozzle, back side of the weld zone was shielded by a shielding gas hose as indicated in Fig. 1. For butt-joint welding of 13 mm thick plates, laser power - welding speed (11.5 kW-49.62 cm/min and 13 kW-72 cm/min) were applied. After the keyhole fiber laser butt welding operations of 13 mm thick S700 steel plates were completed, cross sections of the welds were prepared by using labotom disk cutter machine and then polished by several different emery papers. Subsequently, the polished cross sections were etched by nital ethyl alcohol to reveal fusion zone and heat affected zone. Finally, in order to evaluate fusion zone and heat affected zone, widths of fusion zones, widths of coarse grained and intercritical heat affected zones were measured by using an optical microscope.

Table I Chemical composition of S700 steel plate

Material	Elements (mass %)												
	C	Si	Mn	P	S	Cr	Mo	Al	Nb	V	B	Ti	Fe
S700	0.066	0.107	1.55	0.01	0.003	0.499	0.239	0.07	0.04	0.051	0.002	0.002	Bal

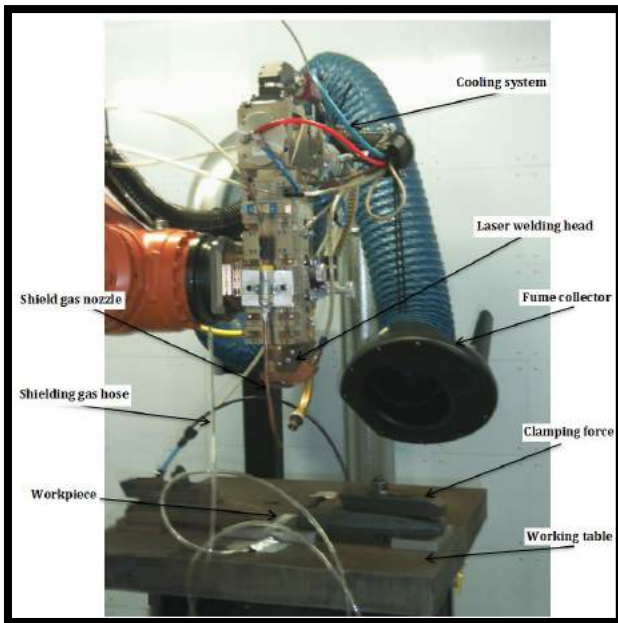


Fig. 1 Experimental set-up for the keyhole fiber laser welding

III. RESULTS AND DISCUSSION

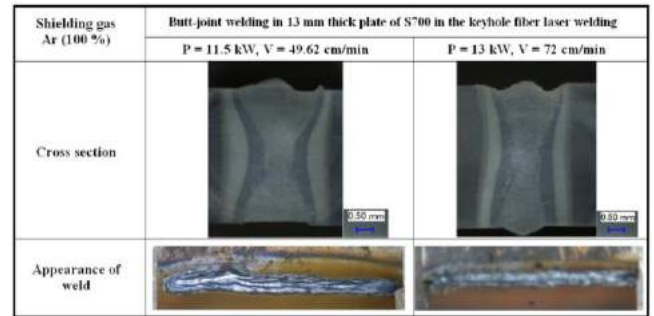


Fig. 2 Effect of laser power and welding speed on the weld bead formation

As it is seen in Fig. 2, shape of fusion zone and heat affected zone (weld bead cross-section appearance) changed when both laser power and welding speed were increased. Width of fusion zone decreased from 4.77 mm to 3.706 mm when laser welding speed was increased from 49.62 cm/min to 72 cm/min, even though laser power was also increased from 11.5 kW to 13 kW as shown in Table II and Fig. 3. The reason for this decrease in width of fusion zone is because heat input to the workpieces decreased from 13905.68 J/cm to 10833.33 J/cm illustrated in Table III. Heat input was found by dividing laser power into laser welding speed (laser power / laser welding speed).

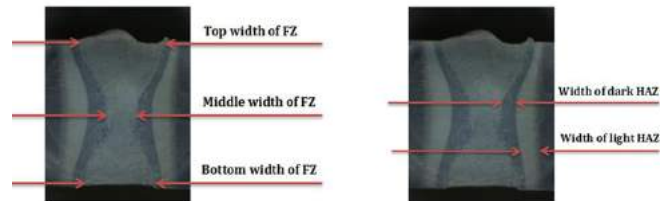


Fig. 3 Measuring width of fusion zone and heat affected zone

- FZ:** Fusion Zone
- HAZ:** Heat Affected Zone
- Dark HAZ:** Coarse Grained Heat Affected Zone
- Light HAZ:** Intercritical Fusion Zone

Widths of light HAZ (intercritical HAZ) are wider than widths of dark HAZ (coarse grained HAZ) in both laser welding conditions as presented in Table II.

Table II Dimensions of fusion and heat affected zones for different laser power and laser welding speed

Shielding gas Ar (100 %)	Dimensions of butt joint weld in 13 mm thick plate of S700					
	Top width of FZ	Middle width of FZ	Bottom Width of FZ	Average width of FZ	Average width of dark HAZ	Average Width of light HAZ
Laser power = 11.5 kW Welding speed = 49.62 cm/min	6.64 mm	2.13 mm	5.54 mm	4.77 mm	1.013 mm	1.5 mm
Laser power = 13 kW Welding speed = 72 cm/min	5.54 mm	1.95 mm	3.63 mm	3.706 mm	0.69 mm	1.189 mm

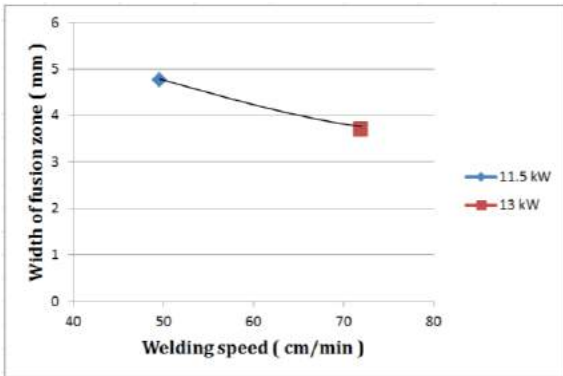


Fig. 3 Effect of combination of laser power and welding speed on width of fusion zone

Table III Effect of heat input on fusion zone and heat affected zone

Laser power (kW)	Welding speed (cm/min)	Heat input (J/cm)	Average width of FZ (mm)	Average width of dark HAZ (mm)	Average Width of light HAZ (mm)
11.5	49.62	13905.68	4.77	1.013	1.5
13	72	10833.33	3.706	0.69	1.189

In a previous published study, Cao, X. et al [17] performed keyhole laser welding of cast WE43 alloy by applying various laser power values for a constant laser welding speed of 33 mm/s and a focused diameter of 0.25 mm using CO₂ laser. They established effect of laser power on width of weld bead as shown in Fig. 4. It can be seen from Fig. 4 that width of weld bead increases with increasing laser power.

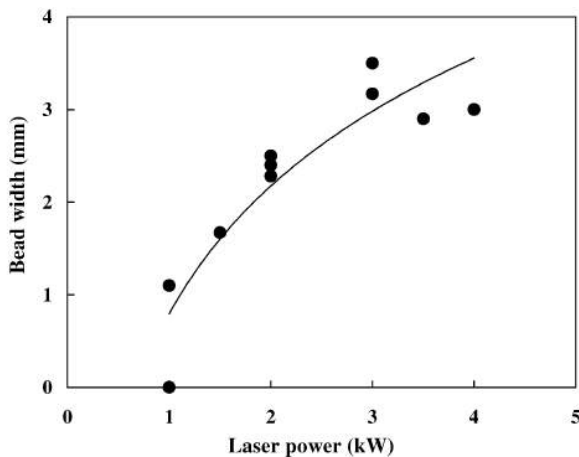


Fig. 4 Effect of laser power on weld bead width [17]

Cao, X. et al [17] also found effect of welding speed on weld bead width as presented in Fig. 5. From Fig. 5, it is clear that weld bead width decreases with increasing laser welding speed.

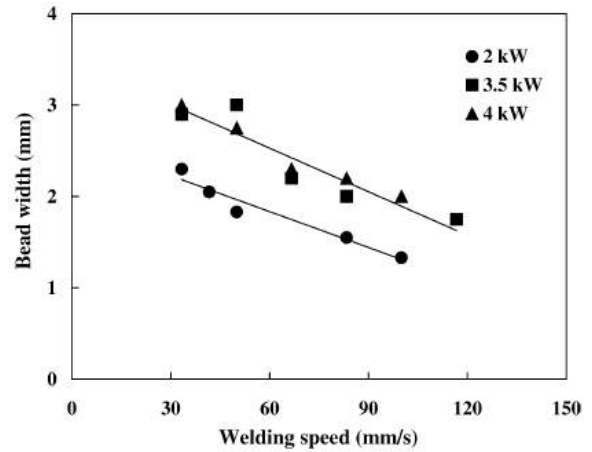


Fig. 5 Effect of welding speed on weld bead width [17]

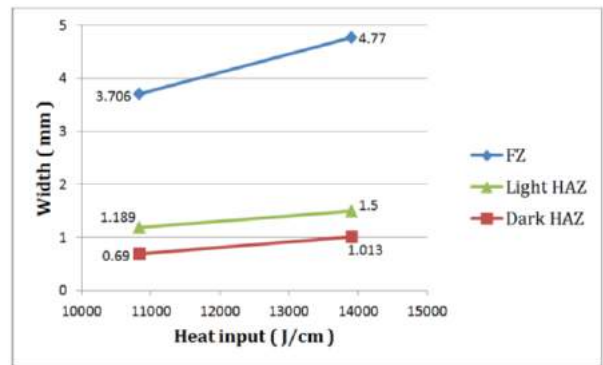


Fig. 6 Effect of heat input on width of FZ, coarse grained HAZ and intercritical HAZ

It can be seen from Fig. 6 that width of FZ, coarse grained HAZ and intercritical HAZ went up when heat input rose. Therefore, based on Fig. 6, it can be said that width of FZ, coarse grained HAZ and intercritical HAZ are directly proportionate to heat input. Grajcar, A. et al [18] determined effect of heat input on weld width and heat affected zone width as presented in Fig. 7. It is evident from Fig. 7 that when heat input increases, weld width and heat affected zone width rise. In addition, it is seen from Fig. 7 that weld width and heat affected zone width are in direct proportion to heat input.

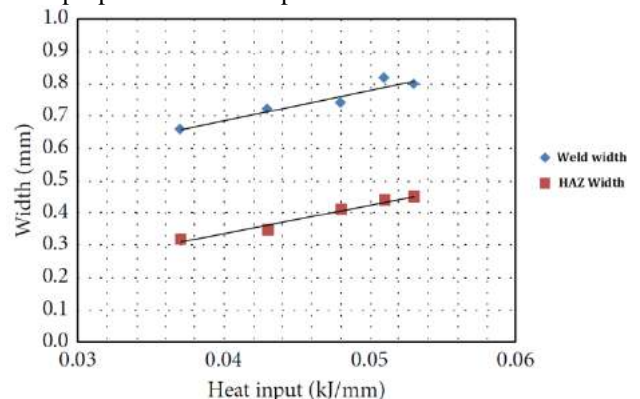


Fig. 7 Effect of heat input on weld width and HAZ width [18]

In this experimental keyhole fiber laser welding study, several defects were observed at higher laser welding speed of 72 cm/min, for example spatter particles took place on the top of plates and some porosity were observed on fusion zone.

IV. CONCLUSIONS

In this study, keyhole fiber laser single pass autogenous (without using filler material) butt welding of 13 mm S700 steel plates was successfully carried out. Some conclusions were presented as the following.

1. At higher fiber laser welding power of 13 kW and welding speed of 72 cm/min, narrower fusion zone width and heat affected zone width were obtained. However, spatter particles on plates and some porosity on fusion zone occurred.

2. For a constant laser welding speed, width of fusion zone and heat affected zone increased when increasing laser power. On the other hand, for a constant laser power, width of fusion zone and heat affected zone decreased when increasing laser welding speed.

3. Heat input is the dividing of laser power into laser welding speed (laser power / laser welding speed). width of fusion zone and heat affected zone are directly proportional with heat input which means that when heat input increases, weld bead and heat affected zone increase. When heat input decreases, weld bead and heat affected zone decrease.

4. As heat input was increased from 10.833 kJ/cm to 13.9 kJ/cm, width of fusion zone increased from 1.189 mm to 1.5 mm.

5. At high laser powers, good laser weld beads can be acquired with high laser welding speeds.

6. In order to achieve desired welds, it is necessary to choose proper laser welding parameters.

ACKNOWLEDGMENT

The author thank Dr John Francis for his support and encouragement and also thank Zülküf Balalan and Anıl İmak for their useful beneficial ideas and comments.

REFERENCES

[1] W. M. Steen, *Laser Material processing*, Springer, London, 1991.
 [2] M. Van Dijk (2003) Welding heat exchangers Industrial Laser Solutions;No11[Online].Available:http://www.industrialasers.com/articles/2003/11/welding-heat-exchangers.html
 [3] C .Yao, B .Xu, X. Zhang, J. Huang, J. Fu and Y. Wu. "Interface microstructure and mechanical properties of laser welding copper–steel dissimilar joint". *Opt Lasers Eng* 2009;47:807–14.
 [4] Onˆoro JRC, Fatigue Behaviour of Laser Welds of High-Strength Low-Alloy Steels. *Journal of Materials Processing Technology* 68:68–70, 1997.
 [5] W. Yan, L. Zhu, W. Sha, Y-Y. Shan, K .Yang, Change of Tensile Behavior of a High-Strength Low-Alloy Steel With Tempering Temperature. *Materials Science and Engineering A* 517:369–374, 2009.

[6] Shen S, Oguocha INA, Yannacopoulos S. Effect of heat input on weld bead geometry of submerged arc welded ASTM A709 Grade 50 steel joints. *Journal of Materials Processing Technology*. 2012;212:286-94.
 [7] M. Goodarzi, SPH Marashi and M. Pouranvari, Dependence of overload performance on weld attributes for resistance spot welded galvanized low carbon steel. *Journal of Materials Processing Technology*. 2009;209:4379-84.
 [8] S. Moeinifar, AH Kokabi, and HRM Hosseini, Effect of tandem submerged arc welding process and parameters of Gleeble simulator thermal cycles on properties of the intercritically reheated heat affected zone. *Materials & Design*. 2011;32:869-76.
 [9] IK Lee, CL Chung, YT Lee and YT Chien, Effect of thermal refining on mechanical properties of annealed SAE 4130 by multilayer GTAW, *Journal of Iron and Steel Research, International*. 2012;19:71-8.
 [10] P. Yayla, E. Kaluc and K. Ural, Effects of welding processes on the mechanical properties of HY 80 steel weldments, *Materials & Design*. 2007;28:1898-906.
 [11] T. Mohandas, Reddy G Madhusudan and B. Satish Kumar, Heat-affected zone softening in high-strength low-alloy steels, *Journal of Materials Processing Technology*. 1999;88:284-94.
 [12] S. Moeinifar, AH Kokabi and HRM Hosseini, Role of tandem submerged arc welding thermal cycles on properties of the heat affected zone in X80 microalloyed pipe line steel, *Journal of Materials Processing Technology*. 2011;211:368-75.
 [13] Reddy G Madhusudhan and T. Mohandas, Ballistic performance of high-strength low-alloy steel weldments, *Journal of Materials Processing Technology*. 1996;57:23-30.
 [14] H. Bley, L. Weyand and A. Luft, An alternative approach for the cost-efficient laser welding of Zinc-coated sheet metal, *CIRP Annals - Manufacturing Technology*. 2007;56:17-20.
 [15] Z. Li and G. Fontana, Autogenous laser welding of stainless steel to free-cutting steel for the manufacture of hydraulic valves, *Journal of Materials Processing Technology*. 1998;74:174-82.
 [16] W. Guo, "Laser Welding of High Strength Steels," Doctorial thesis, Univ. of Manchester, School of Mechanical, Aerospace and Civil Engineering, Manchester, UK, Dec. 2015.
 [17] X. Cao, M. Jahazi, J. P. Immarigeon and W. Wallace, A Review of Laser Welding Techniques For Magnesium Alloys. *Journal of Materials Processing Technology*, 171(2), pp.188-204, 2006.
 [18] A. Grajcar, M. Rˆozański, S. Stano, A. Kowalski and B. Grzegorzcyk, Effect of Heat Input on Microstructure and Hardness Distribution of Laser Welded Si-Al TRIP-Type Steel. *Advances in Materials Science and Engineering*, Hindawi Publishing Corporation, Gliwice, Poland, 2014.

The Investigation of Tribological Properties of Thermal Aged CuAl10Fe Alloys

Zülküf BALALAN*, Furkan SARSILMAZ,# Anıl İMAK*, Niyazi ÖZDEMİR#, Ömer EKİNCİ*

Faculty of Engineering and Architecture, Department of Mechanical Engineering, Bingöl University, Turkey
zbalalan@bingol.edu.tr

+ Faculty of Technology, Department of Mechatronics Engineering, Firat University, Turkey
f.sarsilmaz@firat.edu.tr

+ Faculty of Technology, Department of Metallurgical and Materials Engineering, Firat University, Turkey
nozdemir@firat.edu.tr

* Faculty of Engineering and Architecture, Department of Mechanical Engineering, Bingöl University, Turkey
aimak@.bingol.edu.tr

* Faculty of Engineering and Architecture, Department of Mechanical Engineering, Bingöl University, Turkey
oekinci@bingol.edu.tr

Abstract— In this work, thermal cycles were applied to samples of CuAl10Fe aluminum bronze alloy which are commonly used in marine hardware, shipping and journal bearings. The samples were maintained in heat treatment furnace at 950 °C (for 30 minutes) and cooled after than subjected to aging process by storing in heat treatment furnace (at 100 °C and 150 °C) for different times (8, 10 and 12 hours). Therefore, aged samples of the data on microhardness and wear resistance values were compared to non-aged base sample depending on the microstructural transformation. As a consequence of this, there is an important increasing at aged samples of microhardness and wear resistance values when comparing with non-aged base sample.

Keywords— Al bronze, Wear, Microhardness

I. INTRODUCTION

Today, as the manufacturing industry increases the production capacity of non-ferrous metal alloys every year, the demand for copper and its alloys in these alloys is also increasing [1]. Copper alloys are among the most common metals found in the industry. Pure copper can be added together with elements such as aluminum, nickel, iron, lead, manganese, cobalt, silicon, silver, tin, beryllium and zirconium in a single combination of these elements. It is possible to improve the mechanical, chemical and physical properties of these alloying elements depending on the processing conditions with the pure copper admixture [2]. These alloys are used in many tribological applications due to their excellent wear and lubrication properties as well as their superior heat and electrical conductivity properties [1,2]. One of the most common uses of copper alloys found in the iron and steel industry is bronze alloys, which are often preferred as bearing materials [3]. The most common bedding materials are made of aluminum bronze, which is made of aluminum and copper together. In these alloys, there are iron, nickel silicon and

manganese elements beside the main alloy element aluminum element. Aluminum

bronzes containing 2-4% iron in particular reduce the temperature of the eutectoid conversion point, while mechanical properties can be improved by up to 3% addition of nickel [4]. CuAl10Fe alloys, for example, which are often used by the industry, are examples of this. Bearings made from these materials have high impact and abrasion resistance. These alloys maintain their strength at elevated temperatures and are preferred over high load and low speed applications, where it is good to lubricate in equipment bearings operating above 250 °C [5-7] Furthermore, an important feature of this alloy compared to other Al bronzes is that it prevents the formation of unwanted secondary compound phases during cooling in the internal structure with nickel and iron admixtures. On the other hand, precipitation hardening (aging) can increase the corrosion and abrasion resistance in addition to the mechanical properties such as maximum hardness, strength and toughness, while increasing the strength with the addition of alloy element additives to copper alloys [7,8].

For this reason, in our work, it is aimed to determine and compare the possible performance of the existing alloy considering the widespread use of CuAl10Fe aluminum bronze in the industry. Aluminum bronzes including Al, Fe, Mn and Ni elements exhibit high hardness properties. However, mechanical properties also have a certain life span. It is possible to increase these lifetimes by improving the wear resistance. For this reason, artificial aging heat treatments were applied at various temperatures in order to improve the wearability of the CuAl10Fe alloy and microstructure, mechanical properties and wear properties of the alloy were investigated for this purpose.

II. EXPERIMENTAL STUDIES

In the experimental work, CuAl10Fe aluminum bronze with chemical content in Table I is commercially available. No heat treatment has been applied to the aluminum bronze alloys used in the experimental work. These alloys were cut at 20 mm diameter and 8 mm height and their surfaces were cleaned before aging and polished with diamond paste by metallography and polished with acid solution. The basic microstructure photographs of the pre-aging samples were determined by electron microscopy on the base sample. Subsequently, the samples were heated to 950 °C for 30 minutes and then rapidly cooled to room temperature. Then, the samples 6 and 7 (8-10-12 hours) at the temperature (100 and 150 °C) given in Table II were subjected to thermal cycling under argon gas in the heat treatment furnace. The following table shows the waiting time and temperature values of the samples subjected to the aging process (Table II). All artificial aging processes are carried out in a temperature and time controlled heat treatment furnace (Protherm). The parameters for the selected aging process in the experimental study were selected by examining and interpreting the data obtained from the literature [6-8]. Mechanical hardness tests and wear tests were applied to these samples subjected to aging treatment. The hardness and wear test specimens used in the test were selected from samples taken at different aging times and prepared in accordance with the standards. At least three samples were selected for each different aging period and the mean values were obtained by performing relevant tests/experiments on these samples. For microhardness testing of samples with different aging parameters, the surfaces are first cleaned and polished by sanding with 120-1200 grit sandpaper [9]. Then, 6 different points were measured at equal intervals of 1 mm on the surface of the samples and hardness test graphics were obtained. Microhardness tests were carried out with a Vickers MHT 10 type microhardness tester under a load of 5 gr and a waiting time of 10 seconds.

The abrasion tests were carried out at room temperature using an adhesive of the pin ten disk type tester according to the dry environment conditions. Cylindrical geometry samples with a diameter of 10 mm and a length of 40 mm were used in the experiments. In the experiment, discs of SAE 1050 steel were used as abrasive counterparts. Table III shows the chemical content of SAE 1050 steel abrasive. The abrasive disc is manufactured in a lathe with a width of 100mm and a thickness of 5mm and then the surfaces are ground. The surfaces of the samples were sanded with 1200 grit sandpaper, both contact surfaces were cleaned with acetone and dried. The abrasion tests were carried out at a constant speed of 190 rpm in the lathe and on the test specimens with a total wear distance of 500 m, 30 N, 60 N loads were applied respectively and the test specimens were disassembled at the end of each 50 m wear path, Weight loss was detected with the help of an electronic scales with cleaned and 10^{-4} sensitivity. In addition, the modifications of the worn surfaces of the samples were

examined by SEM and surface photographs were taken. Typical wear rates (W_a) were calculated by determining the weight losses (ΔG) of the specimens after the wear operations.

$$W_a = \frac{\Delta G}{dMs} = (\text{m}^3/\text{Nm})$$

Here; W_a is the wear rate, ΔG is the weight loss (gr), s is the shear distance, M is the load applied, and d is the density of the material [10].

Table I Chemical composition of test materials

Material	Alloying Elements,% Weight				
	Al	Fe	Mn	Ni	Cu
CuAl10Fe	8-11	2-4	1	3	Remaining

Table II Thermal Cycles Applied to CuAl10Fe Alloy

Sample No	Aging Temperature	Aging Time
N1	150	8
N2	150	10
N3	150	12
N4	100	8
N5	100	10
N6	100	12

Table III. Chemical components of the shaft of SAE 1050 steel mile

Material	Alloying Elements,% Weight					
	C	Si	Mn	P	S	Fe
SAE 1050	0,51	0,25	0,75	0,04	0,05	Remaining

III. EXAMINATION OF EXPERIMENTAL STUDIES

3.1 Microstructure Investigations

Fe is added in 1-4% to reduce the grain structure of industrial aluminum bronzes and to increase hardness and strength. In these materials containing 8-10% Al, heat treatment is not possible if there is no 3-5% Ni in the composition.[4]. For this reason, nickel-aluminum alloys have a special place in aluminum bronzes. These materials have α and β phases depending on the heat treatment applied in the microstructure. However, the β -phase transformation at 565 °C is converted to the $\alpha + \gamma_2$ structure by slow cooling from the heat treatment temperature, and this structure continues until room temperature. It is not desirable in Al bronzes if the γ_2 phase is a crunchy and brittle phase. To prevent β phase, the alloy is heated to above the eutectoid temperature and very rapid cooling is applied at this temperature [4,5]. Thus, phase transformation is prevented and the alloy structure maintains itself as α and β until room temperature. For this reason, especially in our work for CuAl10Fe bronzes, fast cooling was applied in the first stage aging processes. The SEM photograph of the CuAl10Fe alloy, which is not aged in the following way, shows that the alloy is in a very fine-grained structure.

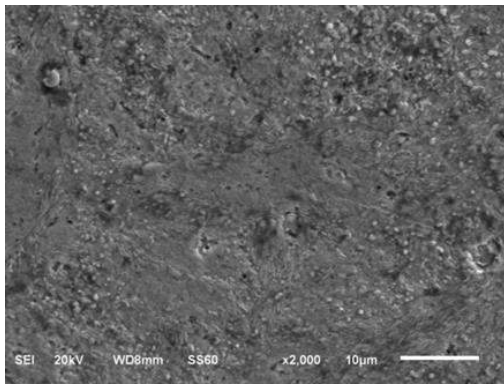


Fig. 1 SEM microstructure photograph of base CuAl10Fe alloy with no aging

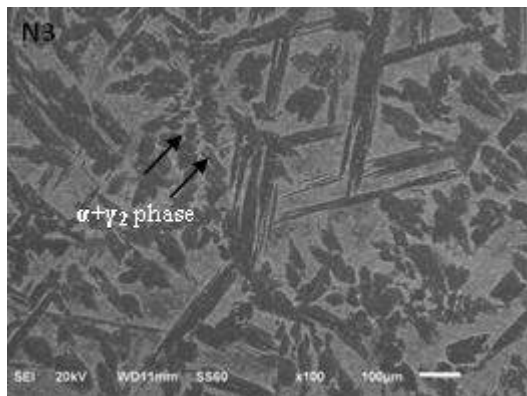
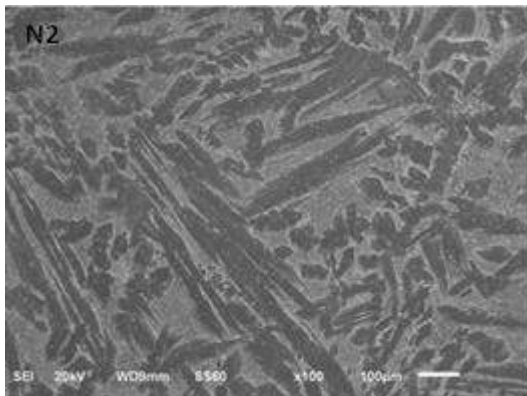
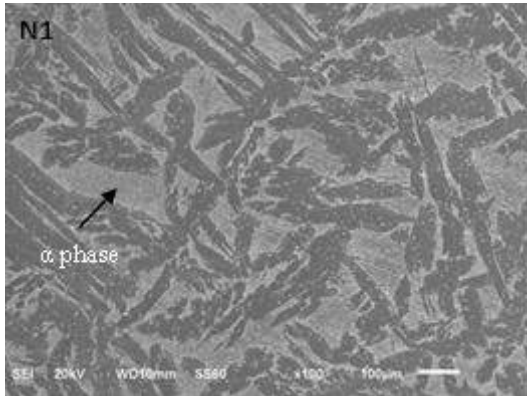


Fig. 2 SEM microstructure photograph of sample N1, N2 and N3 aged at 150 °C

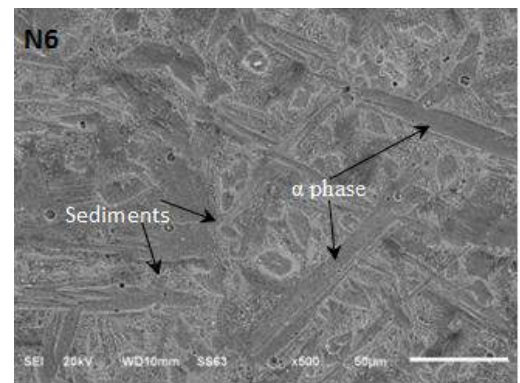
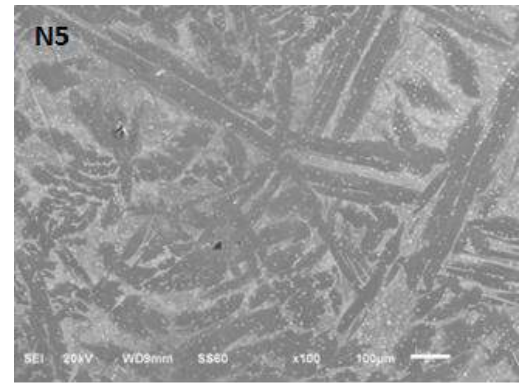
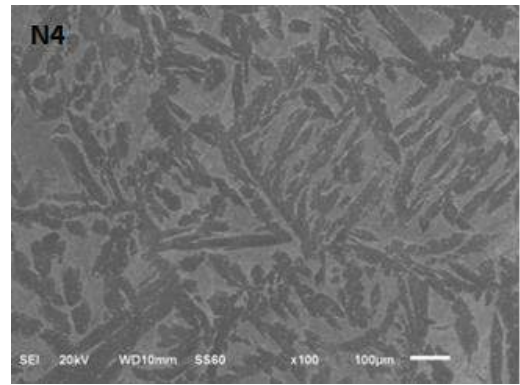


Fig. 3 SEM microstructure photograph of sample N4, N5 and N6 aged at 100 °C

The microstructural transformations in the samples after aging are given in Figure 2 and 3, respectively. Compared to the non-aging sample, all the images show the remnants of the martensite transformation due to the Fe content in the alpha phase, which is left over from the rapid cooling process. This is thought to be due to the fact that the martensite in rod form in α phase is not able to convert to the more spherical $\alpha + \beta$ phase because of the insufficient aging temperature. However, the existence of $\alpha + \gamma_2$ -phase structures in the shape of a small island, which is separated from the martensite rods and exhibits sedimentation characteristics, appears in the microstructure. When the aging temperature of the samples was examined, it was found that there was no obvious difference in structural transformation between 100 °C and 150 °C, but when the waiting times were evaluated in their own temperature group, the grain sizes and sedimentation amounts were observed to change visually during the 12 hour waiting period.

3.2 Wear and Microhardness Investigations

In the abrasion tests, the wear quantities of each sample were examined for two different loads and six different aging conditions. Wear rates (Wa) due to weight loss in the loads and samples applied to each sliding bed sample are shown in Fig. 4, with respect to the raw material without aging and the samples subjected to aging.

It was observed that as the weight of all the samples increased, the weight loss increased. Generally, it was determined that the highest weight loss occurred at N6 sample aged under 60 N load and 12 °C at 100 °C. Material loss under different aging conditions of each sample increases linearly with the applied load increasing. The increase in the temperature of the bed due to the effects of high dry environment working conditions reduces the load carrying capacity of the bed. Due to the effect of temperature and pressure, the amount of material broken off from the sample contact surfaces caused high weight losses. For this reason, it is clear that the selection of appropriate pressure and load values in sliding bearings is an important factor.

As can be seen in Figure 4, two different aging temperatures, compared with each other, showed that wear-weight losses and wear rates of samples aged at 150 °C decreased slightly compared to aged samples at 100 °C, whereas microhardness values increased. However, according to the base material, it is easily noticed that the aging effect significantly reduces the microhardness values by reducing the weight losses (Figure 5). In addition, the mass loss in the samples increases with the increase of all three aging times of 8, 10 and 12 hours. This can be said to have a negative effect on the general strength character of the material during the temperatures above the 8 hour aging time. In the samples kept at the same temperature, Fig. 5 shows that the aging times increase and the microhardness values also decrease. The amounts of wear loss and microhardness measurements obtained at this stage support each other.

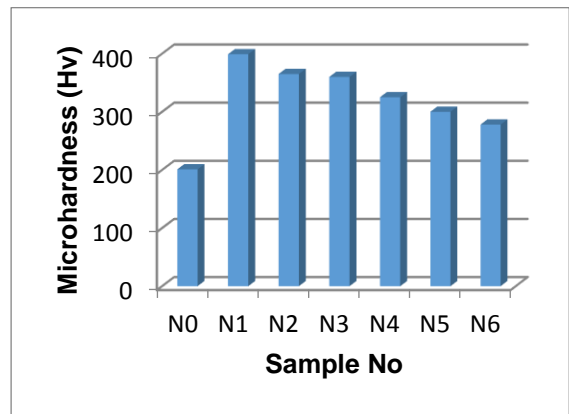


Fig. 5 Microhardness values of the samples

SEM images of wear surface photographs of all samples are given in Fig. 6 and Fig. 7, respectively. From the SEM images of the specimens resulting from the wear test under different test parameters (aging time, temperature and load), abrasion scratches can be clearly seen at different depths on the friction surfaces. In Figure 6, it was observed that the depth of wear lines increased compared to the other specimens, especially in N0, where no aging was applied. This is thought to be a consequence of the change in wear rate values obtained from the samples. In addition, when the wear surfaces of all samples are compared, it is seen from the photographs that the abrasion surface lines are more deeply deeper at 150 °C and less debris, parallel to wear data and microhardness data. This is especially the case at 150 °C and at low waiting times it can be said that the samples subjected to abrasion are less affected by the impact on the shaft and therefore the shaft is less abraded.

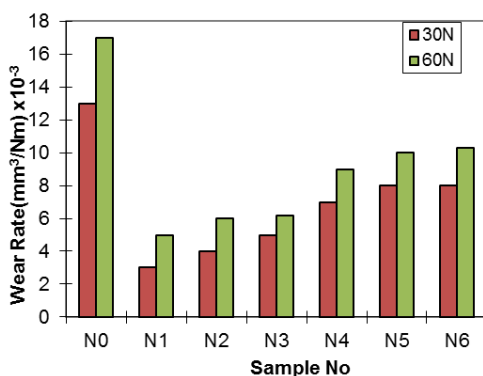
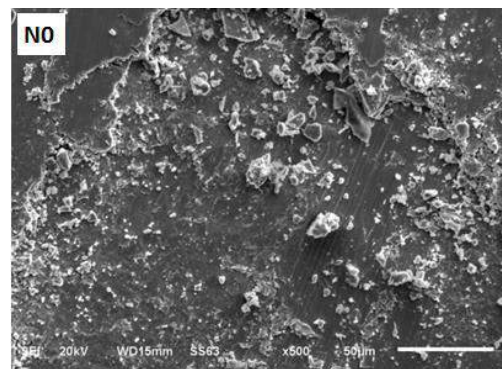


Fig. 4 Thermal cycle after-wear rates applied to the samples (Wa)



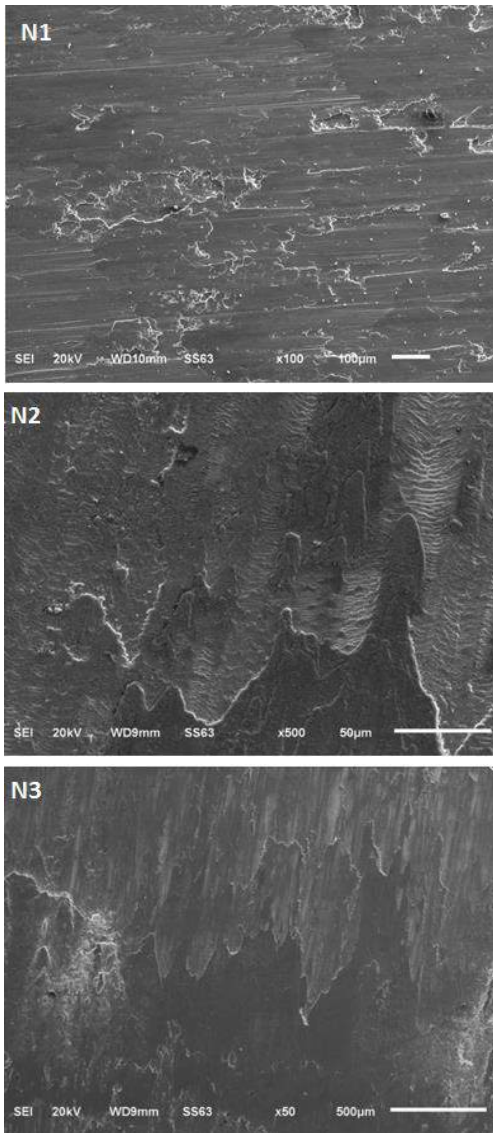


Fig. 6 Wear surface SEM images of samples with no aging (N0) and with aging at 150 °C (N1, N2 and N3)

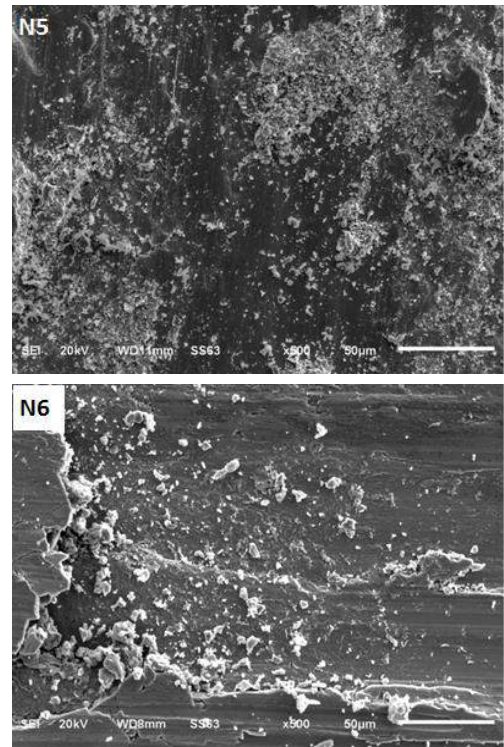
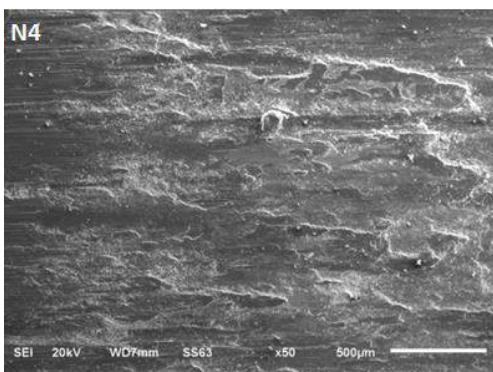


Fig. 7 Wear surface SEM images of samples aged at 100 °C (N4, N5 and N6)

IV. CONCLUSIONS

The microstructure and mechanical wear properties of the CuAl10Fe alloy under different aging conditions have been investigated and compared as a result of all experiments. The following conclusions have been reached regarding the wear characteristics of sliding bearings as well as the results obtained.

1.) In CuAl10Fe alloys with and without aging, it was determined that as the applied load increased, the weight losses increased and the wear rates increased accordingly. The highest wear rate value was determined as 10.2% at N6, which was aged at 12 ° C for 10 hours at 100 ° C except for the sample without aging.

2.) The aging procedures under two different temperatures were compared with each other, and it was determined that the samples aged at 100 ° C were subjected to more mass loss than the samples aged at 150 ° C. At 150 ° C, the precipitation of intermetallic compounds by the transformation of the beta phase leads to an increase in internal strength. On the other hand, overly long waiting times have been found to reduce the amount of precipitate in the inner layer, which does not provide the desired hardness and wear resistance of the aging process. For this reason, the highest microhardness values were obtained at N1 of 390 Hv.

3.) From the SEM images obtained as a result of the abrasion test of the samples, the marks of abrasion at different depths on the friction surfaces were clearly determined. It has been determined that the depth of wear lines increases in NO sample without aging compared to other samples. It is clearly understood that the depth of wear trace increases in parallel with the increase of the wear rates of the samples. This is thought to be a result of the change in the wear rate values obtained from the samples. The amounts of wear loss, microhardness measurement results and wear trace depth obtained at this stage are mutually supportive.

REFERENCES

- [1] Ünlü B. S., Köksal N. S., Atik E., Meriç C. 2005 "Investigation of tribological properties of CuSn10 bearing material "Pamukkale University Journal of Engineering Sciences, 11 (1), pp. 41-45.
- [2] Özçelik S. 2007, "Experimental Investigation of Wear Properties of Cu and Fe Based t / m Bearing Materials" M.Sc. Thesis, Selcuk University Institute of Science and Technology, Konya
- [3] Atik, E., Ünlü, B., S., Meriç, C. 2001. "Design of Radial Sliding Bearing Experiment Device", Machine Materials and Technology (MAMTEK) Symposium, S. 98-103, Manisa.
- [4] Ünal M. 1999, "Effect of Different Solidification Rates on Microstructure and Mechanical Properties of Aluminum Bronze Da" Gazi University Institute of Natural and Applied Sciences, Ankara
- [5] Koçak T.Ü., Yanar H., Pürçek G., Birol F. "Comparison of a nickel aluminum bronze (CuAl10Ni5Fe4) and tin bronze (CuSn11) in terms of friction and abrasion properties" 2nd International Iron and Steel Symposium (IISS'15), 1-3 Nisan 2014, Karabük, Türkiye.
- [6] Thossatheppitak. B, Suranuntchai. S, Uthaisangsuk. V, Manonukul. A, Mugsuntisuk. P, Microstructure evolution of nickel aluminum bronze alloy during compression at elevated temperatures, Advanced Materials research, vol. 893, 365-370. 2014
- [7] H. Ping, H.F. Lopez, Athermal ϵ Martensite in a Co–Cr–Mo Alloy: Grain Size Effects, Materials Letters, 39 (1999) pp. 249–253.
- [8] Paulo, Davim, J. 2000. "An Experimental Study of the Tribological Behaviour of the Brass/Steel Pair", Materials Processing Technology, pp: 273-277.
- [9] Varol, R. 2001. "Wear Properties of Cu and Fe Based T / M Bearing Materials", DEÜ Müh. The faculty. Science and Eng. Magazine, Cilt 3, Sayı 1, s. 81-90.
- [10] Özdemir N., Sarsilmaz F., Orhan N. (2008) "The Effect of Cementite Size and Morphology on the Abrasive Wear Behavior of UHC Steel" Journal of Tribology, ASME 130: pp. 021602.1-021602.5

Investigation of Gas Pressure Effect on Powder Characterization of Al-12Si Alloy Produced by Gas Atomization Method

Mehmet Akkaş*, Tayfun Çetin⁺, Atakan Oğuz Ocak⁺, Kamal Mohamed Em Akra⁺, Mustafa Boz⁺

*Kastamonu University, Cide Rifat Ilgaz Vocational High School, Kastamonu, Turkey,

[*mehmetakkas@kastamonu.edu.tr](mailto:mehmetakkas@kastamonu.edu.tr)

⁺Karabuk University, Faculty of Technology, Department of Manufacturing Engineering, Karabuk, Turkey, ,

[+tayfuncetin@outlook.com](mailto:tayfuncetin@outlook.com) [+aocak@karabuk.edu.tr](mailto:aocak@karabuk.edu.tr) [+kamalakra55@gmail.com](mailto:kamalakra55@gmail.com) [+mboz@karabuk.edu.tr](mailto:mboz@karabuk.edu.tr)

Abstract— In this study, the effects of different gas pressures on the shape and size of Al-12Si alloy powder produced by gas atomization method are investigated experimentally. Experiments were carried out at the Gas Atomization Unit, which was redesigned at Karabuk University Faculty of Technology Department of Manufacturing Engineering. Experiments were carried out at a stable temperature of 770 °C, at a nozzle diameter of 2 mm and by applying 6 different gas pressures (5-10-15-20-30-35 bar). Argon gas was used to atomize the melt. In order to determine the size and shape of Al₁₂Si powders produced, scanning electron microscope (SEM) images and powder size analysis were performed by [screen analysis](#) method. As a result of the analysis, it was determined that the increase of the gas pressure caused the powder size to decrease and the powder shape to change from the ligament and the dripping structure to the spheroidal. It has been observed that the thinnest powders produced are in the gas pressure of 35 bar and the usually of the powders is complex.

Keywords: Gas atomization, Al-12Si alloy powder, nozzle, gas pressure

I. INTRODUCTION

Powder metallurgy was developed as an alternative method for manufacturing methods like casting, forging, forming and machining. Powder production made by powder metallurgy is done by four different methods. These methods are; mechanical methods, chemical methods, electrolysis method and atomization method. Among those methods, gas atomization method is the most frequent used process to obtain thin and spherical powders. Atomization is defined as breaking apart of molten metal into miniscule fragments made by high-pressured gases or mechanical methods[1,2]. Atomization process is divided into four different methods those are water atomization, gas atomization, centrifugal atomization and vacuum atomization. However, the fact that %60 percent of metallic and non-metallic powders are produced by this method, that makes gas atomization superior over other methods. At the gas atomization process, gases such as air, nitrogen, argon and helium can be used to break up the liquid metal flow [3,4].

Powder production of every material which can be molten is possible by gas atomisation process [5,6].

Parameters such as type of gas, gas pressure, nozzle diameter and melting point are useable for the metal powders produced by gas atomization method. Due to the increase of gas pressure values, temperature and viscosity of molten metal decreases which enables the powder to be produced in smaller sizes [7,8].

The most important properties that define the ease of use of Al-Si alloys in industrial applications are mechanical, corrosion and pourable properties. All of those properties are determined by chemical composition and microstructure of alloys [9].

In this study, Al-12Si alloy, which is used generally in the automotive and aerospace industries and which is particularly produced by means of casting, is produced by powder atomization method. As seen on Figure 1., the eutectic point in the aluminum-silicium phase diagram corresponds to 12.6% Si weight percentage. Production of Al-12Si alloy , which is below the eutectic point, is preferred in order to have high powder strenght and to form dendritic powders.

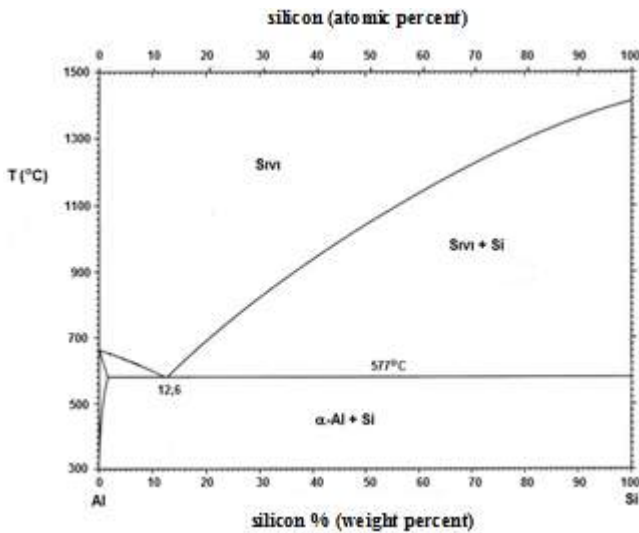


Figure 1. Al-Si phase diagram

liquid metal and the powders produced. The melting process was carried out in graphite melting pot which locates inside the furnace. A graphite plug was used to control the flow of molten metal in the melting pot. For the powder production parameters, closely matched and circular rounded nozzles are used. The nozzle is placed on a nozzle holder inside the oven.

Atomization tower is made from stainless steel. The powders are collected in the powder collection area at the bottom of the atomization tower. There are two cyclones for the removal of the gas from the atomisation tower and the retention of fine powders. During the atomization process, 3 tubes filled with argon gas were connected to the gas ramp to prevent the gas pressure changing and fluctuating. Melting process was carried out in the graphite melting pot placed in the furnace. The temperature of the molten Al-12Si alloy is measured by means of two thermocouples, which are immersed in the graphite melting pot and located outside the pot.

Experiments were carried out at 770 ° C constant temperature, 2 mm nozzle diameter and 6 different gas pressures (5, 10, 15, 20, 30 and 35 Bar). Argon gas is used as atomizing gas.

II. EXPERIMENTAL STUDIES

Experimental studies were carried out at the Gas Atomization Unit at Manufacturing Engineering Department of Karabük University Technology Faculty. The Gas Atomization Unit, shown in Figure 2, consists of five basic parts. These parts can be defined as; 1.Melting furnace, 2.Atomization tower, 3.Nozzle, 4.Powder collecting compartment, 5.Gas pressure ramp.



Figure 2. Karabük University Gas Atomization Unit

The melting furnace is manufactured to be able to heat up to approximately 1200 °C. Gas inlet and outlet units are installed on the sides of the furnace to prevent oxidation of the

Powder production parameters are given in Table I. In addition to the melting temperature and the diameter of the nozzle, the gas pressure is also known to have an important influence on the size and shape of powders at gas atomization technique. Production parameters were selected for this purpose.

TABLE I
POWDER PRODUCTION PARAMETERS

	Gas Pressure (Bar)	Melting Point (°C)	Nozzle Diameter (mm)
S1	5	770	2
S2	10		
S3	15		
S4	20		
S5	30		
S6	35		

Powder particle size distributions were made by sieve method which is the easiest and most widely used analysis method. The size analysis of the powders was done by vibratory sieve analyzer. The sieve analyzer is given in Figure 3. The device can measure powder sizes between 45-1000 µm. The size of Al-12Si alloy powders was determined by using sieves in 8 hole sizes of 45 µm, 63 µm, 90 µm, 125 µm, 250 µm, 500 µm, 710 µm and 1000 µm, respectively.



Figure 3. Sieve Analyzer

SEM images of the produced Al-12Si alloy powders were obtained from the Carl Zeiss Ultra Plus Gemini Fesem brand device at the Karabük University Iron and Steel Institute Materials Research and Development Center (MARGEM) Laboratory. The particle size distribution of the powders was determined with the sieve analyzer located in Engineering Manufacturing Engineering Laboratory of Karabük University.

III. EXPERIMENTAL RESULTS AND DISCUSSION

The weight percentages of Al-12Si powders produced by different gas pressures are given in Table 2. It has been determined that the proportion of small sized powders increases with the increase of the gas pressure given in this table. It has been found that no powder is produced below 63 μm at the 5 bar gas pressure and 2 mm nozzle diameter given by the S1 code parameters and powders are generally produced between 125 and 710 μm sizes. It is seen that no powders are produced bigger than 500 μm diameter with S6 code with the parameters of 35 bar gas press and nozzle diameter of 2 mm, and the most intense powders occur within the powders less than 45 μm . When these results are evaluated, it can be reported that the powder size decreases by the increasing gas pressure.

TABLE II
% WEIGHT PROPORTIONS OF AL-12SI ALLOY POWDERS

	-710 +500 μm	-500 +250 μm	-250 +125 μm	-125 +90 μm	-90 +63 μm	-63 +45 μm	-45 μm
S1	40,486	33,131	15,061	7,209	4,111	0	0
S2	10,264	36,435	33,837	11,019	5,506	1,778	1,157
S3	5,915	25,299	33,824	15,946	11,248	4,569	3,195
S4	2,516	15,277	34,17	20,01	16,494	5,984	5,546
S5	0	8,298	21,068	21,747	26,039	11,886	10,959
S6	0	5,592	15,176	16,275	21,592	19,008	22,355

Frequency densities of Al-12Si powders produced with different gas pressures related to powder size ranges are given in Figure 4. Frequency densities are; % Weight values divided by sieve interval value. The result is seen on Figure 4 that by increasing gas pressure, the percentages of powders up to 125 μm are increased and the proportion of coarse powders increases after 125 μm . Also; from the SEM images of the powders produced in Figure 5, it is clearly seen that the powder size has decreased due to the increase of the gas pressure.

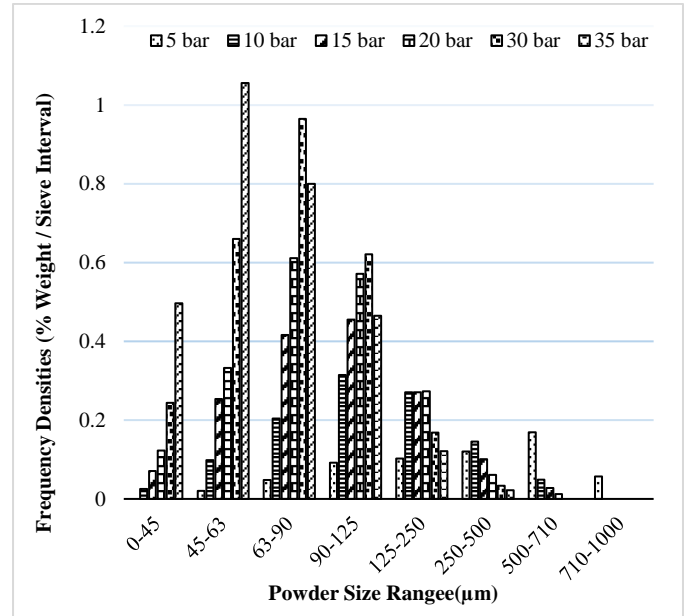


Figure 4. Frequency densities of Al-12Si powders that produced with different gas pressure values related to powder size ranges.

The Al-12Si alloy powders produced are generally ligamentous, droplet and spherical, as shown in Figure 5. It has been observed that even though the shapes of the powders are ligamentous and droplet under the low gas pressure, their shapes are becoming spherical under the higher gas pressures. Oğuz and Öztürk [3,4] published similar results in their studies on atomization. In addition, Klar et al. [10] studied the effects of gas pressure and surface tension on the shape of the powder, and found that the force acting on the globalization of a liquid droplet were surface stresses.

In powder production studies, it was observed that small particulate powders saturate on large particulate powders. Fischmeister and his colleagues found that the saturation occurred in the final stage when small particles of powder collided with large powder particles that had not yet completed the solidification process during atomization. [11th]. On the other hand, Clyne and colleagues have emphasized in a similar study that the difference between the solidification times of powders formed at large and small sizes and the acceleration of different droplets at different rates by the effect of atomization gas lead to the process of saturation [12]. In Aller and Losada's work, they found that the powder was formed by the partially coating by the droplet or completely coating of droplet by the powder [13].

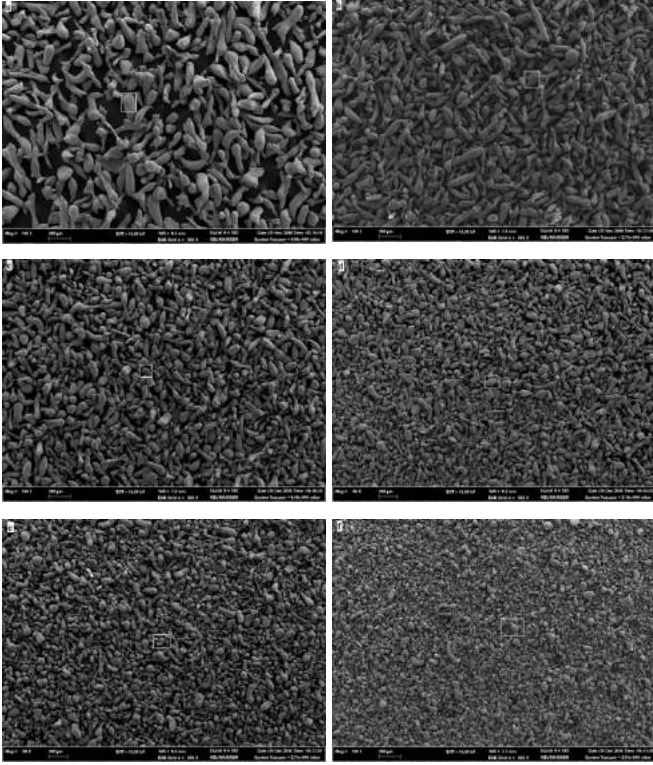


Figure 5. SEM images of Al₁₂Si alloy powders . a) 5 bars b) 10 bars c) 15 bars d) 20 bars e) 30 bars f) 35 bars

Figure 6 shows that Al-12Si powders have dendritic and cellular-dendritic microstructure in images taken at 15000 magnifications from the surface of powders produced at different gas pressures by scanning electron microscopy (SEM). Looking at the surface images, the dendritic image changed from spherical dendritic to complex dendritic due to increased gas pressure. It is also seen that the increase with the gas pressure the structure becomes cellular dendritic. No information was found in the literature in this regard. However, it has been directly determined that the increasing gas pressure changes the morphology of the powder noticeably and that the surface morphology influences the powder shape.

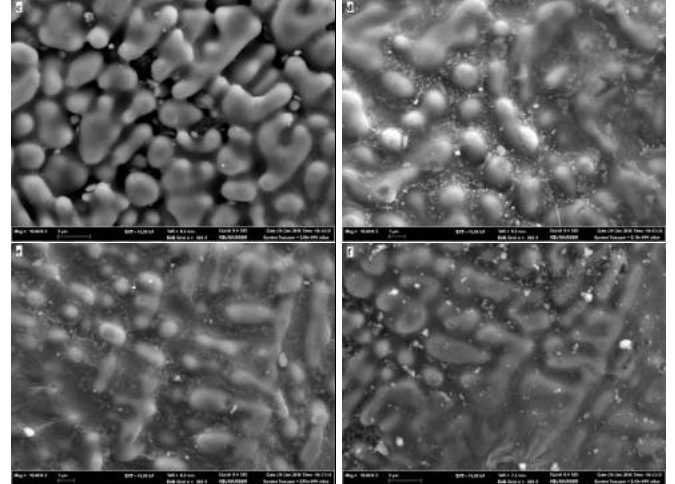
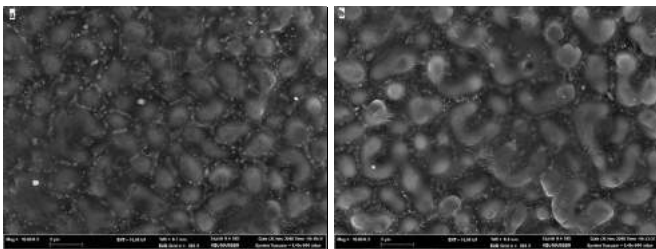


Figure 6. SEM images of Al₁₂Si alloy powders (x15000 magnification). a) 5 bars b) 10 bars c) 15 bars d) 20 bars e) 30 bars f) 35 bars

IV. RESULTS

The following results were obtained for Al-12Si powder produced by the gas atomization method.

- ✓ The powder production by the gas atomization method was carried out in the Gas Atomization Unit, and powders with different shapes and sizes were obtained. The smallest powder size was obtained at a gas pressure of 35 bar.
- ✓ It has been determined that the size of the powder is reduced due to the increase of the gas pressure.
- ✓ As the gas pressure increased, the size of the powder decreased and the shape of the powder changed from the ligament and the droplet structure to the global one.

ACKNOWLEDGEMENT

This work was supported by Scientific Research Projects Coordination Unit of Karabük University. Project Number: KBÜ-BAP-15/2-DR-001

REFERENCES

- [1] Rajan T P D, Jayakumar E, and Pai B C, *Trans Indian Inst Met* **65** (6) (2012) 531.
- [2] Wang, Y., Li, HT. & Fan, Z. *Trans Indian Inst Met* (2012) 65: 653.
- [3] Oğuz, Ş; Öztürk, Z; Uzun, E; Kurt, A; Boz, M. Gaz atomizasyonu yöntemi ile kalay tozu üretiminde gaz basıncının toz boyutu ve şekline etkisi. 6th International Advanced Technologies Symposium (IATS'11), 2011, 565-568.

- [4] Öztürk, Z; Aslan H; Uzun E; Boz, M. Gaz Atomizasyon Yöntemi ile Al 2024 Tozu Üretimi ve Karakterizasyonu, 7. th International Powder Metallurgy Conference, 24-28 Haziran, 2014.
- [5] German, R.M., 1994, Powder metallurgy science, 2nd edition, Metal Powder Industries Federation, USA.
- [6] Lawley, A., 1992, Atomization: The production of metal powders, Metal Powder Industries Federation, Princeton, New Jersey, USA
- [7] Aydın, M. ve Ünal, R., “Laval tipi yeni bir nozul tasarımı ile metal tozu üretimi ve üretim değişkenlerinin etkisinin incelenmesi”, Makine Teknolojileri Elektronik Dergisi, (1): 69-76 (2007).
- [8] Uslan, İ. ve Küçükarslan S., “Kalay tozu üretimine gaz atomizasyonu parametrelerinin etkisinin incelenmesi” Gazi Üniv. Müh. Mim. Fak. Der., Cilt 25, No (1): 1-8 (2010).
- [9] Zolotarevsky, V.S., Belov, N.A., Glazoff, M.V., 2007. Casting Aluminum Alloys, Elsevier, Amsterdam, Holland.
- [10] Klar, E., and Fesko, J.W., 1984, Production of metal powders, Metals Handbook, 9th ed. Vol. 7, Powder Metallurgy, 25 – 51, Ohio.
- [11] Fischmeister, H.F., Ozerskii, A.D., and Olsson, L., 1982, Solidification structure of gas atomized high speed steel powders, Powder Metallurgy, 25(1), 1 – 9.
- [12] Clyne, T.W., Ricks, R.A., and Goodhew, P.J., 1984 – 85, The production of rapidly – solidified aluminium powder by ultrasonic gas atomization. Part I: Heat and fluid flow, Int.J. Rapid solidification, 1, 59 – 80.
- [13] Aller, A.J., and Losada, A., 1985, Characteristics of atomized powders, Powder Metallurgy Int., 21(5), 15 –19.

Affecting Factors on Gloss Value for Galvanized Cold Rolled Sheets

Özgür KARAKAŞ^{a*}, Erdogan KANCA^b, İbrahim GÖÇER^a, Alper AKÜN^a, Erkan PÜGE^a, Güzin Müge LÜLE^a, Ali DOĞAN^a, Ahmet ÖZDEMİR^a

^aMMK Metalurji San. Tic. ve Liman İstl. A.Ş. Dörtyol, Hatay, Turkey, okarakas@mmkturkey.com.tr

^bMechanical Engineering Department, Iskenderun Technical University, Hatay, Turkey,kancaerdogan@gmail.com

Abstract— Flat steel products are coated with zinc to ensure decorative requirements and prevent the steel from corrosion. Galvanized cold rolled (GCR) sheets has three main characteristics for decorative requirements, these are metallic effect, spangle and gloss. High gloss value is one of effective parameter on the customer demand.

In order to define influencing factors on gloss value, GCR sheet samples, with different dimensions and produced with different parameters, had been taken. Influencing factors such as zinc coating mass, sheet thickness, chemical composition of zinc coating, line speed were investigated under constant zinc pot metallurgy conditions.

This study finds out increase in strip thickness and Al% content of zinc coating leads to increase in gloss value, increase in coating mass leads to decrease in gloss value and gloss-line speed data gives a Gaussian curve where the gloss value reaches a maximum magnitude at about 100 m/min.

Keywords: Galvanized Cold Rolled, Gloss, Zinc, GCR, Zinc Pot, Coating Mass.

I. INTRODUCTION

Galvanization is the process of applying zinc coating on steel to prevent corrosion. In addition to corrosion inhibition effect, zinc coating gives aesthetic metallic surface to steel. This metallic surface is also used to meet decorative requirements and has become a customer request over the years for applications like roofing, culvert pipes, panels, building sidewall panels, flashing doors etc. There are three different decorative expectations; metallic effect, spangle and shine. Metallic effect is come from zinc color in any case. As the Zn coating on a steel sheet solidifies, dendritic crystals grow around a core of solidified Zn, and in some cases, a flower-like pattern called “spangle” forms on the surface of the galvanized sheet. [1]. Shine is the ability of light reflection through galvanized surface [2]. The appearance of the coating (matte grey, shiny, spangled) does nothing to change the corrosion protection of the zinc coating [3].

There are two different production types according to application of zinc to steel surface. One is hot dip galvanizing which structural steel pieces are dipped into a molten zinc bath, held there until the temperature of the steel equilibrates with that of the bath and cooled down. The second is continuous hot dip galvanizing which is applicable to strip and where strip passes through a zinc bath as continuous.

Continuously galvanised steel sheets are defined in EN 10346-Continuously hot-dip coated steel flat products –

Technical delivery conditions, but shine or gloss is not a specified characteristic of the product in this standard [4]. Also there is no quantitative specification to evaluate the appearance of galvanized sheet. Only, International standard ISO 14713-2:2009 divides coating characteristics into two groups relating to steel chemical composition: 1) Coating has a shiny appearance with a finer texture. Coating structure includes outer zinc layer. 2) Coating has a darker appearance with a coarser texture [5]. Whereas shine is a requested property for galvanised sheet by consumers in the market.

For example, shinier galvanized sheets are preferable for the producer of panels according to MMK Metalurji customer request analyse [6]. Because, it is known that “Consumers focus increasingly on the visual appearance of product features and often evaluate the product quality and performance based on this [7].

For some constructions the visual homogeneity is important. However, the ones, which are composed of galvanized sheet with different thickness and coating mass, have shine difference between parts of the body. Fig. 1 shows a silo which has dull and shiny parts on the body.



Fig.1 A Silo with dull and shiny parts

In batch hot dip galvanizing, it is known how to make shine or dull appearance by the help of studies about this issue. In batch galvanizing, shiny surface is directly related to free zinc layer and this layer depends on steel chemistries (with a typical

levels of silicon, phosphorus, manganese & carbon), zinc bath chemistries, cooling time and withdrawal speed [8].

However, study, about shine property of continuous galvanized sheet, had not been found during literature research. On the other hand, parameters of production may change shine of surface relatively like Fig.3. This difference between two images on galvanized surfaces is a significant visual variation which is big enough to effect customer's aesthetic expectations.

Although the human eye is still the most capable instrument, automated gloss measurement is needed for quantitative and reliable quality control in industrial settings [9]. Under this article's test and assessment method title, determination of the best proximate evaluation method is discussed.

In this study, gloss change of continuously galvanized steel surface was examined according to parameters like line speed, strip thickness, coating thickness and Al% content of coating.

II. EXPERIMENTAL STUDIES

C. Materials

DX51D+Z grade steel sheets samples were used in the study produced by MMK Metalurji hot dip galvanizing line. Mechanical and chemical specifications of DX51D steel grade are given in Table 1 and Table 2 respectively.

TABLE 1
DX51D STEEL GRADE MECHANICAL SPECIFICATIONS

Tensile Strength (N/mm ²)	Elongation (%) Min.
270 - 500	22

TABLE 2
DX51D STEEL GRADE CHEMICAL SPECIFICATIONS (MAX.)

C%	Si%	Mn%	P%	S%	Al%
0,18	0,50	1,20	0,12	0,045	0,030

D. Devices and Equipment

Sheet samples used in the study were prepared with hydraulic punch press which has 75 mm x 75 mm cut dimension. AND brand GR200 model precision scales (0,0001g precision) were used for weighing samples. Samples thickness had been measured with Horex brand IP54 model thickness gauge. Composition of the zinc coating was analysed with Varian brand ICP-OES 710-ES axial spectrometer. Gloss values were measured at 20 ° with BYK TRI-glossmaster device Fig. 2.



Fig. 2 Glossmaster™ Gloss Meter

E. Chemicals

Analytical Grade %36,5-38 HCl (Sigma-Aldrich brand) and %99 Hexamethylenetetramine (Merck brand) as an inhibitor were used in order to solubilise zinc coating from samples. Mutli-element Standard Solution IV (Merck brand) was used to create a method with ICP-OES 710-ES axial spectrometer.

F. Test and Assessment Method

Shine property measurement method and optical properties of different surfaces are widely studied especially by the glossmeter manufacturers from beginning of 20th century up to now.

Hunter R. S., in 1937 described six different kinds of gloss: (1) specular gloss, (2) sheen, (3) contrast gloss, (4) absence-of-bloom gloss, (5) distinctness-of-reflected-image gloss, (6) absence of-surface-texture gloss. He indicated that both metallic and nonmetallic surfaces exhibit specular reflectance [10].

Linke B., in 2016 investigated the gloss measuring systems of different surfaces and also metallic surfaces for determination of quality defects on metal surfaces by gloss measurements. For her purpose she used specular glossmeters with the angels 60° and 20° [11]

In the technical catalogue of glossmeter suppliers it is indicated that gloss measurement is available at 20° angle for the metallic surfaces which have mirror effects [12, 13]

Considering studies above, 20° and 60° gloss measurements are done and the most compatible angle with human eye is decided. The photo on the left gives 97 GU at 60° and 207 GU at 20° and the one on the right which is shinier gives 116 GU at 60° and 423 GU at 20°. 20° angle is decided to use because of its distinctiveness even for small shine differences for human eye Fig. 3.



Fig. 3 A photo of a dull and a shiny galvanize samples

The dimensions of related galvanized steel test specimens were 75 mm x 75 mm. Minimum 5 test specimens had been prepared for each parameter. Gloss values were calculated as an average of 3 different points' measurement values by glossmaster device on each test specimen in accordance with EN 13523-2. Zinc coating mass analyses were done in accordance with EN 10346.

Thicknesses of test specimens were measured with calliper gage. Zinc pot metallurgy and coating compositions were analysed by in ICP-OES (inductively coupled plasma optical emission spectrometry) device in accordance with TS EN ISO 3815-2 [14].

Influencing factors such as zinc coating mass, sheet thickness, chemical composition of zinc coating, line speed were investigated under constant zinc pot metallurgy conditions Table 3.

TABLE 3
ZINC POT METALLURGY OF MMK METALURJI

%Al	%Cd	%Fe	%Pb	%Sb
0,22-0,25	0,003	0,0400	0,0200	0,0040

1) *Effects of Zinc Coating Mass on Gloss Value:* In this part, effect of zinc coating mass on gloss value was investigated with test specimens which have constant thickness 1.00 mm and variable zinc coating mass range between 80 – 300 gr/m² (Total Number of Samples: 25).

2) *Effects of Sheet Thickness on Gloss Value:* Effect of strip thickness on gloss value was studied under constant coating mass 100 g/m² (Total Number of Samples : 50)

3) *Effects of Al% concentration of Zinc Coating on Gloss Value:* Al% concentration of samples with different strip thickness and coating mass were analysed and gloss value of each sample is recorded. (Total Number of Samples: 29)

4) *Effects of Line Speed on Gloss Value:* In this part, effects of line Speed value was investigated on 36 test specimens which are randomly collected from HDG line products. The gloss values are measured and recorded.

III. RESULTS

1) *Effects of Zinc Coating Mass on Gloss Value:* Gloss value decreases by increasing coating mass as shown in table 4 and Fig. 4.

TABLE 4
GLOSS VALUES OF DIFFERENT COATING MASS

Coating Mass (g/m ²)	Average Gloss @20°	Sample Number
80	441	5
100	355	5
140	262	5
275	171	5
300	127	5

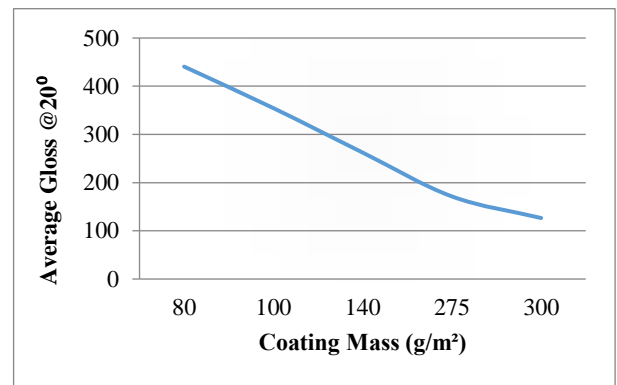


Fig. 4 Average Gloss – Coating Mass Graph

2) *Effects of Sheet Thickness on Gloss Value:* Increasing coil thickness results an increase at gloss value as shown in Table 5 and Fig 5.

TABLE 5
GLOSS VALUES OF DIFFERENT THICKNESSES

Thickness	Average Gloss @20°	Sample Number
0,43	249	5
0,50	222	5
0,60	288	5
0,80	332	5
1,00	261	5
1,20	447	5
1,35	467	5
1,40	384	5
1,90	530	5
2,00	467	5

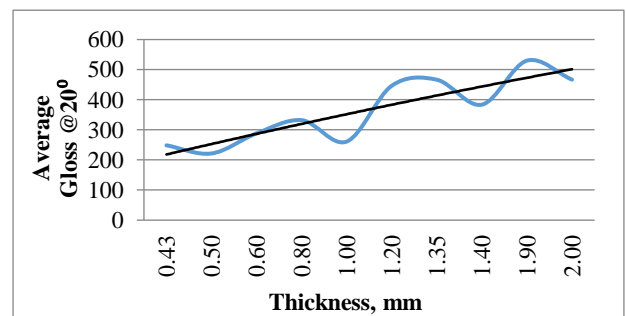


Fig. 5 Average Gloss – Sheet Thickness Graph

3) *Effects of Al% concentration of Zinc Coating on Gloss Value:* Increasing Al% content in the coating causes an increase on gloss value. The data regarding the effect is given in Table 6 and the graph in Fig. 6.

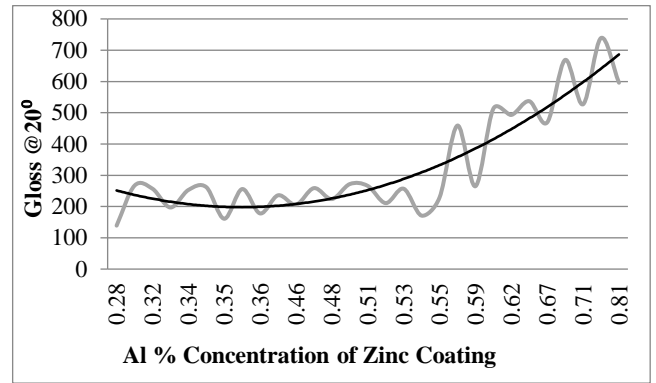


Fig. 6 Gloss – Al% Concentration of Zinc Coating Graph

TABLE 6

GLOSS VALUES OF DIFFERENT AL % CONCENTRATION OF COATING

Al % Conc. of Coating Mass	Gloss @20°
0,28	139
0,31	267
0,32	257
0,33	197
0,34	253
0,35	262
0,35	161
0,36	256
0,36	178
0,41	236
0,46	206
0,48	259
0,48	224
0,50	272
0,51	266
0,52	211
0,53	257
0,53	171
0,55	229
0,56	459
0,59	265
0,61	513
0,62	493
0,64	537
0,67	469
0,69	669
0,71	527
0,73	739
0,81	596

4) *Effects of Line Speed on Gloss Value:* Line speed vs gloss values gives a Gaussian curve where gloss value increases up to a top magnitude at about 100 m/min and decreases then by increasing line speed, see, Table 7, Fig. 7.

TABLE 7

AVERAGE GLOSS VALUES OF GALVANISED SHEETS PRODUCED AT DIFFERENT LINE SPEEDS

Average Gloss @20°	Line Speed (m/min)
210	55
336	77
529	99
288	134
253	180

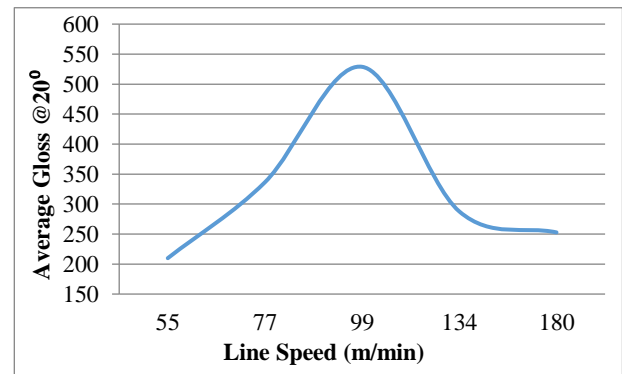


Fig.7 Average Gloss – Line Speed Graph

IV. CONCLUSIONS

This study finds out that gloss value increases by increasing sheet thickness, increasing Al% in the zinc coating and

decreasing coating mass. Also, line speed value is effective on gloss. The gloss of the galvanised sheet increases up to a certain line speed value like 100 m/min and tends to decrease on the line speeds bigger than 100 m/min.

Gloss is one of the leading decorative property on customer demand but unfortunately it depends on the customer order characteristics like sheet thickness, coating mass etc. which determines the line speed and Al% concentration of the coating during the galvanised sheet production.

According to the results of this study, in a conventional continuous hot dip galvanising line with the capacity 30 to 180 m/min line speed, 70 to 600 g/m² coating mass and 0,25 to 3 mm strip thickness, the most glossy (shiny) product can be obtained with the production parameters between 90 to 110 m/min line speed, 70 to 80 g/m² coating mass and 0,95 to 1,24 mm strip thickness.

ACKNOWLEDGEMENTS

This study was supported by MMK Metalurji San. Tic. ve Liman İřlt. A.ř. The authors would like to thank MMK Metalurji CEO Mr Denis Kvasov for providing opportunity for this study.

REFERENCES

- [1] Tobiyama Y., Abotani K., 2004, Hot-Dip Galvanized Steel Sheet with Excellent Surface Quality for Automotive Outer Panels, JFE TECHNICAL REPORT, No.4
- [2] Koleske J. V., Paint and Coating Testing Manual, 2nd edition 2008, ASTM International
- [3] STEEL INTERCHANGE, AISC's Steel Solutions, 2003
- [4] EN 10346 Continuously hot-dip coated steel flat products – Technical delivery conditions
- [5] S. Sepper, 2011 Methods for evaluating the appearance of hot dip galvanized coatings, Agronomy Research Biosystem Engineering Special Issue 1, 229-236
- [6] MMK Metalurji Customer Request Analyse Report, 2016
- [7] Du, P. and MacDonald, E. F., "Eye-Tracking Data Predicts Importance of Product Features and Saliency of Size Change," Proc. ASME 2013 International Design Engineering Technical Conferences and Computers and Information in Engineering Conference.
- [8] The Basics of Hot Dip Galvanized Steel, Galvanizers Association of Australia, 2012
- [9] Kigle-Boeckler, G., 1995, "Measurement of Gloss and Reflection Properties of Surfaces," Metal Finishing(May 1995), pp. 28 - 31.
- [10] Hunter R. S., 1937, National Bureau of Standards, Research Paper Rp958, Part of Journal of Research of the :National Bureau of Standards, Volume 18, Washington, USA
- [11] Linke B., Das J., 2016, Aesthetics and Gloss of Ground Surfaces: A Review on Measurement and Generation, Journal of Manufacturing Science and Engineering, 138(6)
- [12] Gloss Measurement, Introduction, BYK-Gardner GmbH http://www.byk.com/fileadmin/byk/support/instruments/theory/appearance/en/Intro_Gloss.pdf
- [13] Technical catalog of Sheen Instruments, Tri-GLOSSmaster (260), <http://www.sheeninstruments.com/sites/sheeninstruments.com/files/SHE14a-Tri-Glossmaster.pdf>
- [14] TS EN ISO 3815-2 Zinc and zinc alloys - Part 2: Analysis by inductively coupled plasma optical emission spectrometry.

Development of High Value Alloys without Critical Raw Materials through High Entropy Alloys

Hakan YILMAZER¹, Burak DIKICI²

¹ Department of Metallurgy and Materials Engineering, Yıldız Technical University, yilmazerh@gmail.com

² Yüzüncü Yıl Üniversitesi, burakdikici@gmail.com

ABSTRACT

Abstract- Niobium (Nb) and Chromium (Cr), being crucial alloying elements in the high value alloys such as the High Strength Low Alloys (HSLA) and Stainless Steels, especially Austenitic Stainless Steels (AUST.SS), have been identified and classified as critical raw materials (CRM). The potential of not producing these high value alloys has an adverse effect on the EU and Turkish economy due to the fact that Nb and Cr. Therefore, it is necessary to develop a new generation of structural alloys that will be free from CRM elements and exhibiting superior performance. However, it is difficult to develop such proposed high performance alloys by conventional alloying, which are formed around a dominant element like iron in the steel. The High Entropy Alloying, an innovative approach introduced in the last decade, is the alloying using the alloying elements at equiatomic or near equiatomic percentage, consequently the presence of the high mixing enthalpy positioned the alloying elements within the same phase crystal lattice system. As alternatives to HSLA and AUST.SS alloys, the novel structural alloys can be designed and developed by means of HEA approach and gain to industries. The purpose of the study is the designing and developing novel structural alloys as an HSLA and AUST.SS) using innovative High Entropy Alloying (HEA) approach. The proposed High Entropy Structural Alloys (HESA) in this project will be manufactured through the conventional melting and thermomechanical processing. The HESA alloy groups, which will have key roles in many important industrial applications, are aimed at exhibiting superior mechanical properties and corrosion values and meeting the industrial and economic conditions of production.

Keywords- Alloy Development, Critical raw materials, High Value Alloys, High Entropy Alloy Design

Change in Chloride Content of Regenerated Red Iron Oxide Particles in Accordance with Particle Sizes

Özgür KARAKAŞ^{a*}, Erdogan KANCA^b, İbrahim GÖÇER^a, Alper AKÜN^a, Erkan Püğe^a, Güzin Müge LÜLE^a,
Tuğçe TUNÇBİLEK TOP^a

^aMMK Metalurji San. Tic. ve Liman İşt. A.Ş. Doryol, Hatay, Turkey, okarakas@mmkturkey.com.tr

^bMechanical Engineering Departmen, Iskenderun Technical University, Hatay, Turkey kancaerdogan@gmail.com

Abstract — Red iron oxide which is produced by regeneration of waste hydrochloric acid from steel pickling line contains chloride. Chloride has negative effects on industrial productions which use red iron oxide as a raw material.

This paper asserts red iron oxide particles have different chloride content according to their particle size. Regenerated red iron oxide was sampled from different production batches and these samples were grouped according to their particle size with sieving them from 1 mm to 75 µm. Sieved red iron oxide samples were analysed with spectrophotometer to determine chloride content.

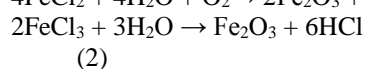
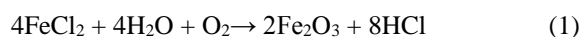
The study found out that chloride content slightly increased by increasing particle size up to 710 µm, after that size chloride content was drastically increased, such that, removing particles bigger than 1 mm from the iron oxide provides a 11,97 % reduction of the total chloride content and causes only 0,27 % loss from the total material.

Keywords: Regeneration Red Iron Oxide; Chloride; Particle Size, Steel Pickling, Hematite.

I. INTRODUCTION

Pickling plants are production lines where the oxide layer on hot rolled coils is cleaned in acid baths. In this line, the oxidized surfaces of the coils are cleaned and prepared for further processes. During pickling process, used acid is contaminated with iron chloride. This waste acid is regenerated in acid regeneration plant (ARP) in order to re-use.

In ARP, waste acid is regenerated to remove iron and this reaction is given in formula (1) and (2) [1]



Oxygen and evaporated water convert metal chlorides into oxides and HCl. The solid particles (Fe_2O_3) will fall down to the lower cone of the reactor in the form of powder and are discharged through a rotary valve which keeps gases inside of the reactor separated from the outside atmosphere [2, 3].

As explained above; metal oxide product decomposes completely into red $\alpha\text{-Fe}_2\text{O}_3$ powders. The recovery of $\alpha\text{-Fe}_2\text{O}_3$ is not only economic demand, but also an environmental necessity [4]. Although this metal oxide is defined as waste, it is semi-finished or by-product for some sectors directly or indirectly. Over the years, intensive R&D activities have led to enhancements in physical and chemical properties of iron oxides. These products are increasingly finding wide applications across various industries such as use of iron oxide

in water treatment & purification and in chemical processing as catalyst are anticipated to offer new opportunities of growth of value-added iron oxide products [5]. In additionally, spray roasted iron oxides have been used on an industrial scale for the production of soft and hard ferrites on an industrial scale at steel mills in Japan, USA and Europe since the year 1964 [6].

One of the negative characteristic of red iron oxide powder is its chloride content for the mentioned industrial usage. Reducing the chloride content in regenerated iron oxides by an economical procedure, without significantly changing the ferric oxide quality is believed to be one of the most critical issues for the development of regenerated iron oxides as commercially useful raw materials [7].

Kohno (1992) reported how some of characteristic of spray roasted iron oxide can be controlled by the operation of the HCl regeneration roaster. Such properties as particle size, oxide diameter, pressed compact density and chloride content can be improved by selection of conditions in the ARP [8].

Ruthner M. J. (2014), explained washed iron oxides exhibiting total chloride levels in the order of 600 ppm Cl^- are available. Further washing results in Cl^- levels of 300 ppm and an additional thermal treatment, by means of a short treatment within a vertical un-obstructed furnace, yields iron oxides with < 20 ppm Cl^- [9].

Itoh S. (1976) explained that red iron oxide particles are formed around droplets of acid as spherical shell during the regeneration of waste acid [10] (Fig. 1).

II. EXPERIMENTAL STUDIES

G. Materials

Iron oxides, used in this study are produced by pickling line of MMK Metalurji & Liman İşletmeciliği A.Ş. Technical data sheet of Iron oxides is given in Table-1.

TABLE-1
RED IRON OXIDE TECHNICAL DATA SHEET

Iron Oxide is the product of Acid Regeneration Plant	No	Property	Value
	1	Fe ₂ O ₃	Min 98,5
	2	MnO	0,2 (± 0,10)
	3	SiO ₂	Max 0,15
	4	Al ₂ O ₃	Max 0,08
	5	TiO ₂	< 0,03
	6	Cr ₂ O ₃	< 0,05
	7	Na ₂ O	< 0,04
	8	K ₂ O	< 0,01
	9	CaO	< 0,01
	10	MgO	< 0,01
	11	P ₂ O ₅	< 0,02
	12	SO ₃	< 0,01
	13	LOI	0,95
	14	Chloride %	< 0,5
	15	Bulk Density, g/cm ³	< 0,5
	16	Moisture @ 105°C, %	< 1
17	pH @ 10% Suspension	3 (± 0,5)	

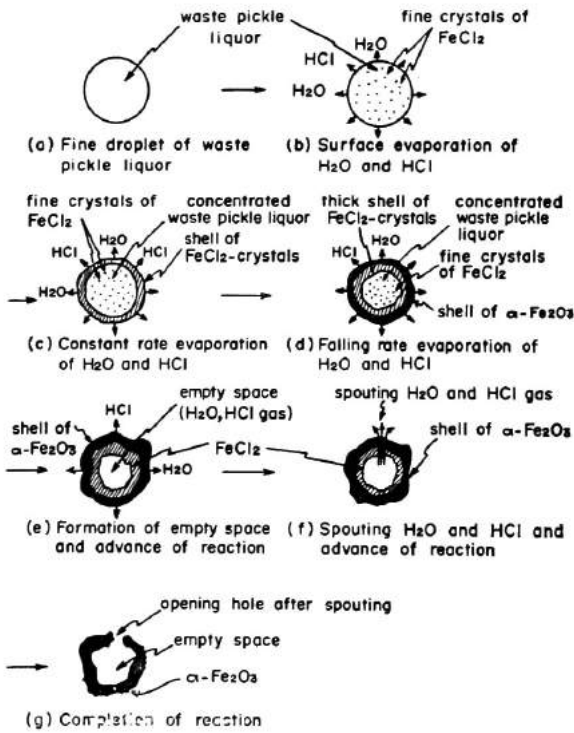


Fig. 1 Formation scheme of granulated roaster hematite from droplet of waste acid

Red iron oxide analysed under SEM and their images had been taken (Fig. 2). According to images, particle structure of iron oxides is a mixture of cracked and uncracked spheres where uncracked particles are bigger and may keep more chloride than the cracked ones. This study is based on mentioned theory and aims to prove it.

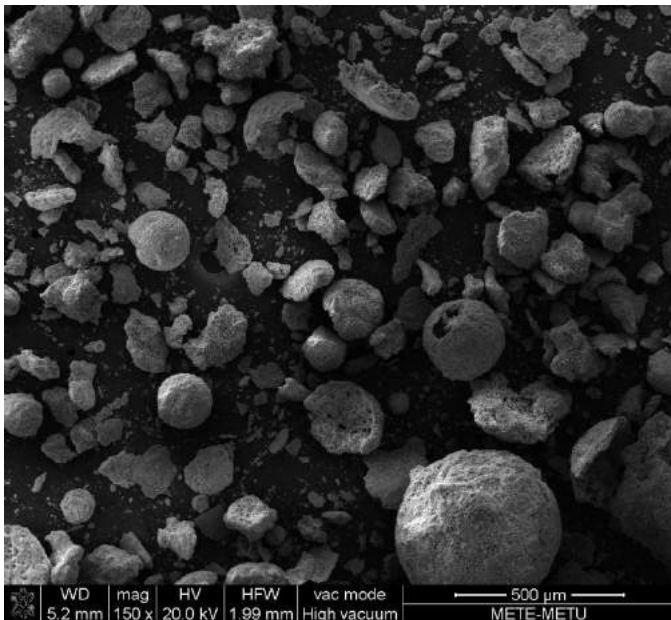


Fig. 2 SEM Image of Red Iron Oxide

H. Devices and equipment

Iron oxide was sieved with Fritsch brand sieves + 1 mm, + 710 µm, + 500 µm, + 250 µm, + 150 µm, + 100 µm, + 75 µm.[13] AND brand GR200 model precision scales (0,0001g precision) were used for weighing samples. Iso lob brand filters and DR 5000 Brand spectrophotometer were used for chloride analyses. Elektro-Mag 30x45 Brand heating plate was used to heat.

I. Chemicals

Merck Brand Analytical grade 99,5% NaCl, 99% Ammonium iron (III) sulphate dodecahydrate ((NH₃)Fe(SO₄)₃.12H₂O, 99% Mercury (II) c (Hg(SCN)₂), 65% Nitric Acid (HNO₃) and SIGMA- ALDIRICH brand 99,8% Ethanol (C₂H₅OH) was used to prepare solutions. Ultra high pure water, which was produced with MES 08 brand device was used.

J. Test and Assessment Method

Samples were prepared according to TS ISO 11648-2 [11]. Iron oxide samples, taken from different production batches, were sieved with +1mm / +710 µm / +500 µm / +250 µm / 150 µm / +100 µm and +75 µm sieves and each amount of iron oxide, refuse of sieve, were weighed. The sieving process was carried out using the FRITSCH brand screens in FRITSCH

sieving machine which conformed with TS ISO 3310-1 [12] that's shown in Fig. 3.



Fig. 3 Fritsch Sieves

According to sieve size, chloride content of each batch was analysed. To analyse chloride content, 1,000 g iron oxide was heated in 100 ml water, after boiling point, mixture is cooled down and filtered with membrane filter. Chloride content of iron oxide was analysed with spectrophotometer under method of 0-1-2-5-10-15-20-30 mg/L calibration graph and 455 nm wave length. Chloride content measured in Hach DR 5000 Spectrophotometer which shown in Fig. 4.



Fig. 4 Hach DR 5000 Spectrophotometer

III. RESULTS

Percentage of sieve fraction and chloride content are given in Table-2 for the iron oxides from 12 different batches and sieved between +1mm, -75 μ m.

TABLE -2

PARTICLE SIZE DISTRIBUTION AND CHLORIDE CONTENT

No	Sample Date	Batch No	Sieve Size	Quantity %	Cl ⁻ % Content
1	22.07/2016	16RIO2107B003	+ 1 mm	0.17	20.37
			+710 µm	2.20	0.99
			+500 µm	10.80	0.45
			+250 µm	15.00	0.33
			+150 µm	27.33	0.32
			+100 µm	20.67	0.27
			+75 µm	19.66	0.30
			-75 µm	4.17	0.25
2	02/08/2016	16RIO0208B001	+ 1 mm	0.17	14.90
			+710 µm	2.40	0.46
			+500 µm	11.60	0.31
			+250 µm	23.00	0.27
			+150 µm	27.50	0.28
			+100 µm	16.17	0.24
			+75 µm	14.00	0.33
			-75 µm	5.16	0.30
3	05/08/2016	16RIO0508B002	+ 1 mm	0.50	17.80
			+710 µm	7.00	0.81
			+500 µm	14.00	0.38
			+250 µm	36.50	0.24
			+150 µm	20.50	0.20
			+100 µm	9.83	0.18
			+75 µm	7.17	0.22
			-75 µm	4.50	0.25
4	10/08/2016	16RIO1008B008	+ 1 mm	1.00	18.93
			+710 µm	7.90	1.02
			+500 µm	24.10	0.30
			+250 µm	51.83	0.23
			+150 µm	7.33	0.22
			+100 µm	3.17	0.21
			+75 µm	2.00	0.24
			-75 µm	2.67	0.35
5	02/09/2016	16RIO0209B005	+ 1 mm	0.17	15.48
			+710 µm	4.70	0.43
			+500 µm	15.30	0.21
			+250 µm	36.83	0.19
			+150 µm	19.00	0.19
			+100 µm	11.33	0.18
			+75 µm	6.84	0.19
			-75 µm	5.83	0.20
6	05/09/2016	16RIO0509B005	+ 1 mm	0.17	12.93
			+710 µm	5.80	0.49
			+500 µm	13.20	0.18
			+250 µm	38.33	0.10
			+150 µm	20.00	0.11
			+100 µm	10.67	0.10
			+75 µm	6.67	0.08
			-75 µm	5.16	0.08

No	Sample Date	Batch No	Sieve Size	Quantity %	Cl ⁻ % Content
7	06/10/2016	16RIO0610B006	+ 1 mm	0.16	14.86
			+710 µm	1.80	0.87
			+500 µm	13.00	0.22
			+250 µm	47.30	0.13
			+150 µm	23.64	0.15
			+100 µm	6.50	0.14
			+75 µm	4.30	0.19
			-75 µm	3.30	0.23
8	07/10/2016	16RIO0710B005	+ 1 mm	0.05	18.92
			+710 µm	3.95	1.43
			+500 µm	19.17	0.31
			+250 µm	47.33	0.25
			+150 µm	19.00	0.27
			+100 µm	5.00	0.33
			+75 µm	3.33	0.44
			-75 µm	2.17	0.49
9	11/10/2016	16RIO1110B006	+ 1 mm	0.17	25.63
			+710 µm	9.16	2.93
			+500 µm	15.17	0.45
			+250 µm	34.50	0.24
			+150 µm	21.50	0.29
			+100 µm	10.00	0.31
			+75 µm	3.83	0.40
			-75 µm	5.67	0.52
10	26/10/2016	16RIO2610B008	+ 1 mm	0.35	16.80
			+710 µm	8.50	1.33
			+500 µm	15.67	0.49
			+250 µm	48.15	0.24
			+150 µm	16.83	0.28
			+100 µm	5.17	0.30
			+75 µm	2.50	0.35
			-75 µm	2.83	0.43
11	09/11/2016	16RIO0811B008	+ 1 mm	0.01	17.18
			+710 µm	3.63	0.70
			+500 µm	10.03	0.40
			+250 µm	40.00	0.20
			+150 µm	26.67	0.21
			+100 µm	8.50	0.27
			+75 µm	5.50	0.37
			-75 µm	5.66	0.56
12	10/02/2017	17RIO1002B007	+ 1 mm	0.33	31.02
			+710 µm	10.00	9.75
			+500 µm	4.83	1.52
			+250 µm	20.83	0.61
			+150 µm	24.50	0.56
			+100 µm	12.50	0.52
			+75 µm	10.84	0.57
			-75 µm	16.17	0.83

For 12 batches, average percentage of sieve fraction and chloride content is given in Table-3.

TABLE 3

AVERAGE PARTICLE SIZE DISTRIBUTION AND CHLORIDE CONTENT

Sieve Size	% Quantity	% Cl ⁻
+ 1 mm	0,27	18,74
+710 μm	5,59	1,77
+500 μm	13,91	0,44
+250 μm	36,63	0,25
+150 μm	21,15	0,26
+100 μm	9,96	0,25
+75 μm	7,22	0,31
-75 μm	5,27	0,37

According to the data given in Table-3, red iron oxide particles' sizes give a Gaussian distribution graphic, Fig. 5.

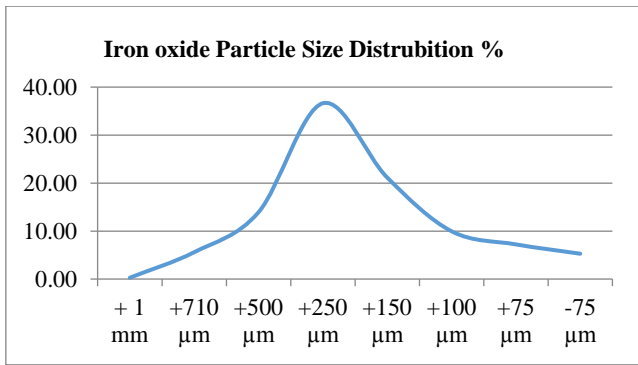


Fig. 5 Iron Oxide Particle Size Distribution %

Also particles bigger than 1 mm have highest chloride content. Chloride content decrease with the decreasing particle size, but gains a tendency to increase for the particles with a size smaller than 100 μm, Fig. 6.

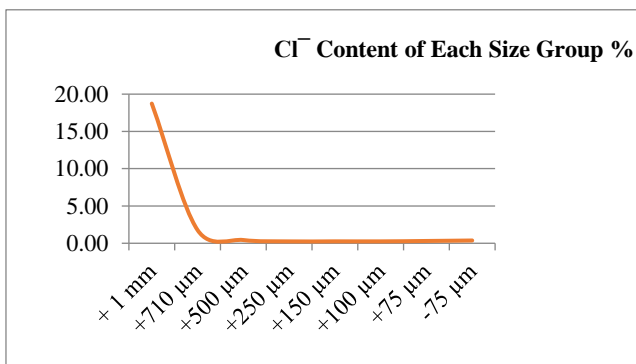


Fig. 6 Chloride Content of Each Size Group

Cl⁻ quantity for each size is given at Table 4. Total Cl⁻ in the sieved red iron oxide is 0,424 and it is the sum of the Cl⁻

quantity coming from each size. Cl⁻ % quantity for each size is calculated. For example for +1 mm size, Cl⁻ % Quantity = $0,51/0,424 \times 100 = 11,97$. Means, 0,27% of total red iron oxide particle size is bigger than 1 mm and the Cl⁻ in this size group is 11,97% of the total Cl⁻.

TABLE 4

CHLORIDE QUANTITY FOR EACH SIZE

Sieve Size	Quantity %	Cl ⁻ % Content	Cl ⁻ Quantity for Each Size	Cl ⁻ % Quantity for Each Size
+ 1 mm	0,27	18,74	0,051	11,97
+710 μm	5,59	1,77	0,099	23,29
+500 μm	13,91	0,44	0,060	14,27
+250 μm	36,63	0,25	0,092	21,82
+150 μm	21,15	0,26	0,054	12,80
+100 μm	9,96	0,25	0,025	5,97
+75 μm	7,22	0,31	0,022	5,22
-75 μm	5,27	0,37	0,020	4,655
Total:			0,424	100,000

IV. CONCLUSIONS

The chloride contamination in the red iron oxide produced by pickling process waste hydrochloric acid regeneration is one of the most refusing factors for the further sectors which use it as a raw material. This study finds out that the bigger particles contain the higher chloride.

By removing particles bigger than 1 mm from the iron oxide provides a 11,97 % reduction on the total chloride content and causes only 0,27 % loss from the total material.

ACKNOWLEDGEMENTS

This study was supported by MMK Metalurji San. Tic. ve Liman İřlt. A.ř. The authors would like to thank MMK Metalurji CEO Mr Denis Kvasov for providing opportunity for this study.

REFERENCES

- [1] Mmk Turkey Acid Regeneration Plant Main Data, DANIELI TRAINING CENTER, DANIELI & C SPA.
- [2] Fouad N. E., Ismail H. M., Recovery of red iron oxide pigmentry powders from chemically modified steel pickling chemical waste, Journal Of Materials Science Letters 17 (1998)
- [3] Ismail H. M., Zaki M. I., Hussein G. A. M. and Magar M. N., Powder Technology. 63 (1990) 87
- [4] Devi A., Singhal A. and Gupta R., A Review on spent pickling liquor, Civil Engineering Department, Birla Institute of Technology & Science, International Journal Of Environmental Sciences Volume 4, No 3, 2013
- [5] Iron Oxide Market; Paints and Coating to Surface as New Avenue for Iron Oxide Producer and Support Demand for the same over the Forecast Period: Global Industry Analysis and Opportunity Assessment, 2015 – 2025
- [6] Goldman A, Modern Ferrite Technology 2nd Edition, 2005
- [7] US00597547A, 1997, Reduction Of Residual Chloride In Iron Oxides, Inventor: Hamilton, Jr. David M., Assignee: Shell Oil Company

- [8] Goldman A., Handbook of Modern Ferromagnetic Materials, Springer Science+Business Media, LLC, 1st Edition, 1999
- [9] Ruthner M. J., 2014, Desired Development Aspects for Spray Roasted Iron Oxides Predominantly for the Production of Ferrites, J. Jpn. Soc. Powder Powder Metallurgy Vol. 61 Supplement, No. S1
- [10] Itoh S., Endo I., Maki K., Kosaka A., 1976. "Ferric oxide produced by spray roasting of HCl pickling liquor", Tetsu-to-Hagane, 62(8), 1035-1044
- [11] TS ISO 11648-2, Statistical aspects of sampling from bulk materials - Part 2: Sampling of particulate materials
- [12] TS ISO 3310-1 Test sieves - Technical requirements and testing - Part 1: Test sieves of metal wire cloth

Removal and Absorption of Ammonia by an Air stripping Process using Water-Spraying Aero-Column Reactor

Fuat Ozyonar^{a*}, Bunyamin Karagozoglu^a, Mehmet Kobya^b

^aCumhuriyet University, Department of Environmental Engineering, 58140, Sivas, Turkey
fozyonar@cumhuriyet.edu.tr

^aCumhuriyet University, Department of Environmental Engineering, 58140, Sivas, Turkey
bkaragoz@cumhuriyet.edu.tr

^bGebze Institute of Technology, Department of Environmental Engineering, 41400, Kocaeli, Turkey
kobya@cumhuriyet.edu.tr

Abstract— Air stripping process for removal of ammonia is a commonly used process for the pretreatment of wastewater. In this study, removal and absorption of ammonia from coke wastewater by an air stripping reactor was investigated. Air stripping of ammonia from wastewater was performed a water-spraying aero-column reactor. Scaling and fouling on the packing surface in paced towers are not two major problem in this process. During the experiments, ammonia was stripped with air in a semi-batch system and absorbed in sulphuric acid solution. Effects of various operating parameters such as initial pH, stripping time, air flow and liquid flow on ammonia removal with air stripping process were examined. The mass transfer coefficient for air stripping process was calculated for different operation condition. Increment in the mass transfer coefficient was observed with increasing pH level and air flow rate. The highest value of mass transfer coefficient was 0.452 h^{-1} , obtained at initial pH 12, air flow 12 L/min and liquid flow 2.5 mL/min. In these condition, removal efficiency of ammonia (at 10 h stripping time) was obtained as 100%. Approximately 92-95% of ammonia in the absorption unit was recovered as ammonia sulphate.

Keywords: Removal of ammonia, absorption of ammonia, air stripping, coke wastewater, water spraying aero-column

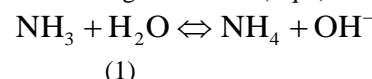
I. Introduction

The coke wastewater is a toxic industrial wastewater in many steel production facilities. Coking wastewater is produced from coal coking, coal gas purification and by-product recovery processes of coking. The coke wastewater has a lot of hazardous organic and inorganic pollutants and most of them toxic, mutative and carcinogenic, for example ammonium, sulfate, cyanide, thiocyanate, phenolic compounds and polynuclear aromatic hydrocarbons [1-4]. Among the pollutants, ammonia is a major concern and high levels of ammonia are commonly presented in coke wastewater [5-9]. The accumulation of ammonia in discharge water results in eutrophication and reduction of oxygen because of nitrification [10]. In addition, ammonia is widely toxic and unfeasible biological treatment [11]. So, ammonia must be treated from coke wastewater before it discharges into aquatic media. The ammonia can be removed or decomposed by several methods such as air stripping [12-14], biological nitrification-denitrification [15,16], breakpoint chlorination [17], struvite precipitation [17,20],

membrane separation [10], catalytic liquid-phase oxidation [11], and selective ion exchange [21].

Stripping and Absorption

Stripping and spray ponds are physical operations used to remove ammonia from wastewaters. In order to the ammonia to be stripped from a wastewater it must be in the dissolved gas form (NH_3), which requires a pH of about 10.8 or greater [22]. The ammonia gas is in equilibrium with the ammonium ions as given below (Eq 1)



As the pH is increased, the equilibrium shifts more to be left. The percent ammonia in the gas from at 25 °C is as follows [22],

$$\text{NH}_3 \text{ (percent)} = \frac{100}{1 + 1.75 \times 10^{+9} [\text{H}^+]} \quad (2)$$

Where H^+ : hydrogen ion concentration, At 25°C and pH 10.8, 97.3% of ammonia will be in the form of ammonia gas molecules dissolved in water. Ammonia equilibrium in aqueous solution is pH dependent and The ionization constant of ammonia (pK_a) is also temperature dependent according to Eq. 3.

$$\text{pK}_a = 0.09018 + \frac{2729.92}{T} \quad (3)$$

Where T is the temperature in degrees Kelvin (°K) .

Stripping and absorption processes for removal of ammonia are effective only if the stripping conditions are well optimized. Ammonia is very soluble in water. So, High air flow rates can be effective more than low in the stripping process. In the case of absorption, solubility of ammonia is an advantage only if the pH is low [13].

The air stripping process of ammonia has been successfully applied in pre-treating coke wastewater. Moreover, ammonia removed by air stripping can be

reabsorbed to acid absorption solution. If sulphuric acid is used as an absorber, ammonium sulphate slurry formed can be potentially used for fertilizer production. So, air stripping is an effective method for the removal of ammonia from wastewater. There are various air stripping systems such as packed tower [24, 25], bubble aeration [24], water-sparged aeroclone [26] and micro-fabricated stripping column [27]. Air stripping is usually operated in a packed tower because it can provide a larger mass transfer area [25,13]. However, air stripping in packed tower generally occurs to scaling and fouling on packing due to reaction between CO₂ in air and some metal ions in water [26]. Other air stripping system is bubble aeration, used for removal of gas contaminants without packing. This kind of air stripping process has a number of advantages which does not require any construction, is a simple and is generally inexpensive [24]. Another study, some new gas-liquid contactors were used for the gas-liquid operation that have obtained high mass rate, are without packing [25]. In this study, the air stripping designed gas-liquid contactor, water-spraying aero-column reactor without packing, was developed.

A literature survey has shown that the above mentioned studies, which investigated removal and absorption of ammonia, are a few studies. For example, Basakçılardan-Kabakçı(2007), recovered ammonia as ammonia sulphate (92%) from urine. Bonmati and Floats (2003) absorbed ammonia in sulphuric acid to recover ammonia from pig slurry. At 80 °C and high initial pH 11.5, complement of ammonia was removed.

In this study, water spaying aero-column reactors as air stripping process was applied to removal of ammonia from coke wastewaters containing for high concentrations of ammonia. The removal efficiency of ammonia was investigated for effects of initial pH, stripping time, air flow and liquid flow (semi-batch condition). Moreover, mass transfer coefficients of air stripping process were calculated.

II. Methods

The raw coke wastewater was collected from a coking plant in Turkey producing approximately 600 m³ of wastewater per day. The characterization of the raw coke wastewater at Table I has been shown.

A. Water Spaying Aero-Column Reactors Experimental Setup and Mass Transfer

A plexiglass column was used for air stripping as water spaying Aero-column (50 cm height x 5 cm internal diameter) under semi-batch. Spraying the wastewater into the column is provided by an atomizer and the pump. In the experimental setup and the absorption unit at Figure 1 is shown. The connection tube was used to transmit the ammonia-air gaseous mixture from stripper to absorber unit. The air-ammonia gaseous mixture from stripper was bubbled through 0.5 M H₂SO₄ solution (98%). All runs were performed at constant temperature (25 °C). The efficiency of ammonia removal, η is defined according to (Eq.4).

$$\eta = \frac{(C_{in} - C_t)}{C_{in}} \times 100 \quad (4)$$

TABLE I

Characterization of the coke wastewater

Parameter	Average Concentration
pH	10.5
Conductivity (mS/cm)	12.6
COD (mg/L)	6250
TOC (mg/L)	2200
Phenols (mg/L)	1400
NH ₃ ⁻ (mg/ L)	2500
CN ⁻ (mg/L)	210
SCN ⁻ (mg/L)	420
S ²⁻ (mg/L)	1.4
SO ₃ (mg/L)	45

where C_{in} and C_t are the ammonia concentrations (mg/L) in the suspension at the beginning and at any time (h).

For an air stripping system, the mass transfer rate of volatile ammonia from wastewater in a batch stripping unit was derived [28] and shown as follows:

$$-\ln \left(\frac{C_{A_t}}{C_{A_0}} \right) = \frac{Q_G H_A}{V_L} \left[1 - \exp \left(- \frac{K_L a V_L}{H_A Q_G} \right) \right] t \quad (5)$$

where C_{At} and C_{A0} are the liquid phase concentrations (g/m³) of ammonia at any time and at the beginning; H_A is the dimensionless Henry's constant; K_L is the overall liquid mass transfer coefficient (m/min); a is the interface area per unit volume of liquid (m²/m³); V_L is the total volume of liquid (L), Q_G is the gas flow rate (L/min) and t is the stripping time (min). When K_LaV_L/H_AQ_G << 1, Eq. (5) predicts as the exit stripping gas was far from saturation.

In this study, ammonia is an easily soluble gas and the exit stripping gas is possibly far from saturation, so the calculation of the mass transfer coefficient of ammonia removal was tentatively made according to Eq.(6).

$$-\ln \frac{C_{A_t}}{C_{A_0}} = K_L a t \quad (6)$$

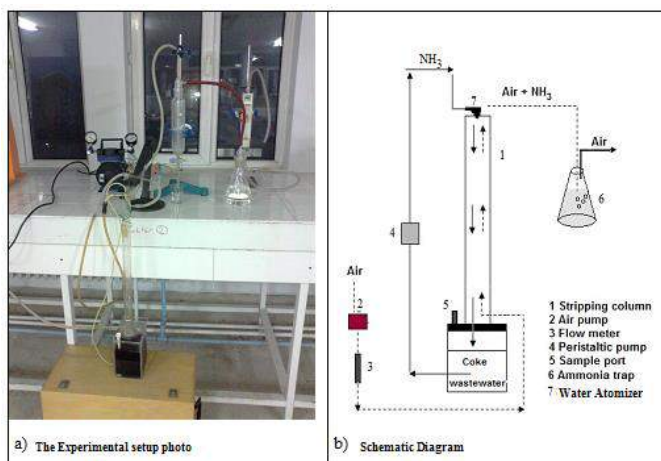


Fig. 1. A schematic representation of used processes ammonia removal from coke wastewater.

B. Analytical Procedures

Determinations of ammonia, pH, conductivity, COD, TOC, phenols, CN^- , SCN^- , S^{2-} , SO_3 were carried out by standard analysis methods [29]. Concentrations of COD, CN^- , SCN^- , phenols were determined by using a single beam spectrophotometer (UV-VIS, Chebios, Italy). TOC of the samples were analysed by using TOC analyser (Apollo 9000, Tekmar-Dohrmann, USA) Turbidity was measured by turbidity meter (Micro TPI, HF scientific, USA). pH and conductivity of samples were measured by a pH meter (C931, Consort, Belgium) and conductivity meter (340i, WTW, USA), respectively. pH adjustments were done by NaOH or H_2SO_4 (Merck).

III. Results and Discussion

In this study, efficiency of ammonia removal from coke wastewater by air stripping depends on several operating parameters such as initial pH, air flow, stripping time and liquid flow.

A. Effect of initial pH on ammonia removal

The Effect of the initial pH on the air stripping efficiency of ammonia is shown in Fig. 2. The initial pH was adjusted using NaOH. Initial pH values were varied in the range of 9.6-13. Experiments were conducted at 10 L/min air flow, water flow 5 mL/min and 24 h stripping time. The removal of ammonia increased significantly with raising the pH level as dependent stripping time. When the initial pH is 9.6, percent removal of ammonia is 41,1% at 10 h stripping time. Raising the pH value from 10 to 13 at the same stripping time (10 h) the removal of ammonia from 52.7% to 97.8 % was increased. But there wasn't much difference in removal of ammonia between pH 12 and 13. This result was expected hoped, since the ammonia concentration in wastewater at pH12 was almost equal to the concentration at pH 13. The removal of all ammonia was obtained at pH 12 and 13 h stripping time.

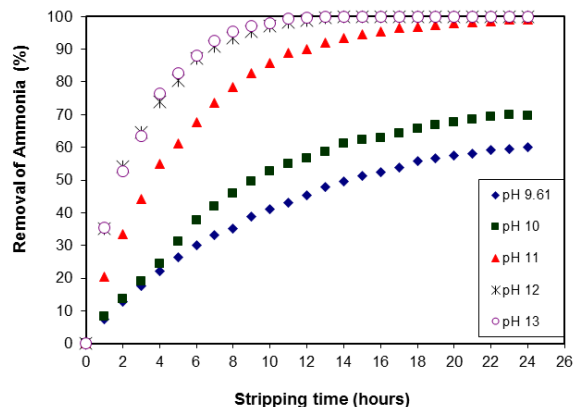


Fig. 2. Effect of initial pH on removal of ammonia in packed tower air stripping (Air flow of 10 L/min, Liquid flow of 5 mL/min, stripping time of 24 h).

The change of the mass transfer coefficients under different initial pH and stripping time can be calculated using Eq. 5, i.e plotting $-\ln(C_t/C_i)$, stripping time, t , making a linear regression between $-\ln(C_t/C_i)$, and stripping time can get the mass transfer coefficients, K_{La} , shown in Fig. 3, with a very good relative coefficient ($R^2= 0.9912 - 0.991$). It clearly indicates that initial pH has very effect on the mass transfer coefficients.

When the initial pH increases from 9.6 to 13, the mass transfer coefficient has been calculated as 0.0523 h^{-1} and 0.376 h^{-1} .

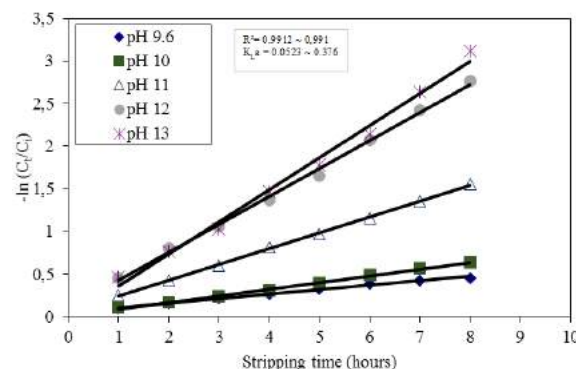


Fig. 3. Effect of initial pH on the mass transfer coefficient in the air stripping (air flow of 10 L/min, liquid flow of 5 mL/min, stripping time of 24 h).

B. Effect of air flow on removal ammonia

The effect of air flow on air stripping efficiency and on the mass transfer coefficient of ammonia removal are shown in Figs 4 and 5. The air stripping experiments were carried out using various air flows (8-12 L/min). When the air flow from 8 L/min to 12 L/min was increased, ammonia removal efficiency increased. For 10 L/min and 12 L/min air flows, there wasn't much difference with result. When the air flow was 10 L/min, ammonia concentrations at 8 h and 13 h stripping time were 140 mg/L and 0 mg/L, respectively.

By increasing the air flow could be decreased the mass transfer resistance in the gas film side. When the air flow rate increases, the mass transfer coefficient increases (from 0.286 to 0.416). The mass transfer coefficient at air flow 10 l/min was calculated as 0.376 h⁻¹.

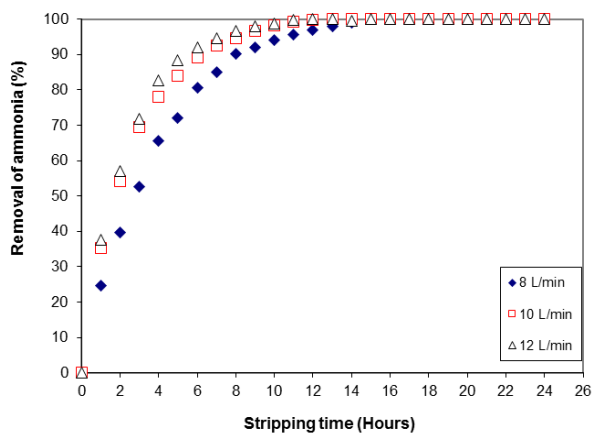


Fig. 4. Effect of air flow on removal of ammonia in the air stripping (Initial pH 12, Liquid flow of 5 mL/min, stripping time of 24 h).

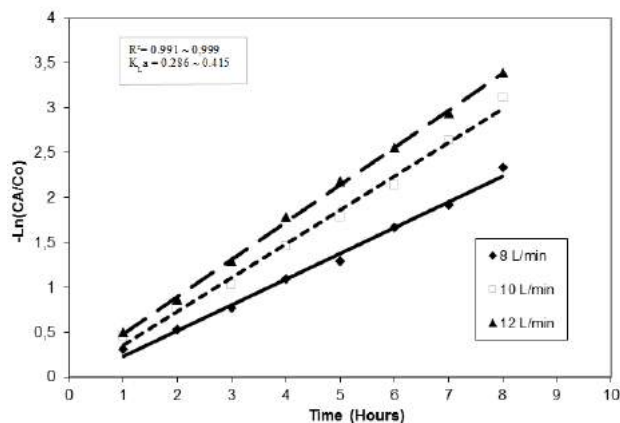


Fig. 5. Effect of air flow on the mass transfer coefficient in the air stripping (initial pH 12, liquid flow of 5 mL/min, stripping time of 24 h).

C. Effect of liquid flow on removal ammonia

Another important operation parameter is liquid flow. Because the liquid flow changes to the air to liquid ratio. Effect of liquid flow on removal efficiency of ammonia was investigated (Figure 6). Another studies, the air to liquid ratio amounted to approximately 30:1 [12], while in others studies, the values of the ratio were approximately 3000:1 [30] and 2000:1 [31]. For the purpose, effects of liquid flow on removal of ammonia varied from 2.5 to 10 ml/min (air to liquid rate, from 4000:1 to 1000:1) were applied. The effect of liquid flow is not significant down to the 10 ml/min. As seen Fig. 7, when the liquid flows decreased, the mass transfer coefficients do not an important change. The effect of liquid flow is less significant at high liquid flow rates with the mass transfer coefficient between 0.355 h⁻¹ and 0.452 h⁻¹.

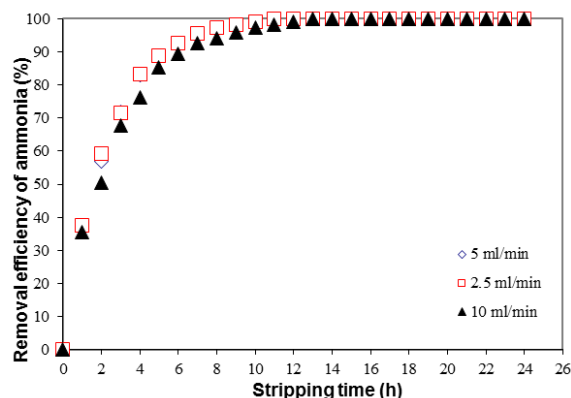


Fig. 6. Effect of liquid flow on removal of ammonia in the air stripping (initial pH 12, air flow of 12 L/min, stripping time of 24 h).

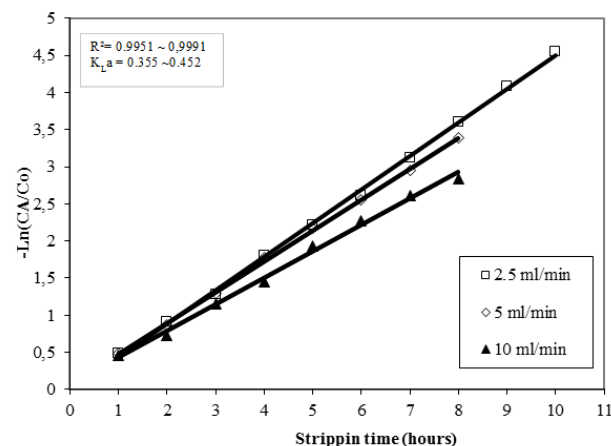


Fig. 7. Effect of liquid flow on the mass transfer coefficient in the air stripping (initial pH 12, air flow of 12 L/min, Stripping time of 24 h).

D. Absorption of ammonia

As can be seen Fig 1, air changed with ammonia and volatile organic matter were bubbled into a strong acid solution, one ammonia trap was used. The resultant ammonia sulphate solution was evaporated to dryness to crystallize ammonium sulphate. Crystallized ammonia sulphate is shown in Fig. 7. Beside, FT-IR results were more reliable if the crystals were assessed in terms of impurity. The patterns were compared with standard ammonium sulphate FT-IR spectrum (Fig. 8). Although the sample showed the same patterns with standard ammonium spectra, the wastewater has contains volatile organic matter. So this organic matter have been transferred to the ammonia-salt obtained in the absorption process. After air stripping process, in terms of pollutant concentrations of the wastewater decreased between 3% and 5%.



Fig. 7. Picture of crystallized ammonium sulphate samples.

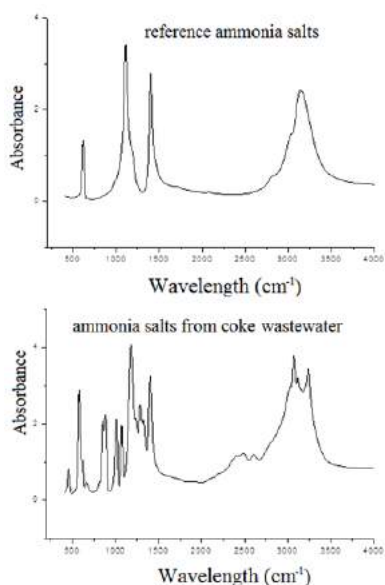


Figure.8 FT-IR spectra of reference ammonia salts and ammonia salts from coke wastewater.

IV. CONCLUSIONS

The air stripping process was successfully used to remove ammonia from coke wastewater. Traditionally, as air stripping processes are used to stripping tanks or packed towers. In these processes, scaling and fouling on a packing surface in packed tower and lower stripping efficiency in tanks are the major problems. The results of the experiments indicated that air stripping and absorption by water spraying aero-column reactor were efficient for removing. The pH level has one of the the most important effect on the ammonia removal efficiency and if the air flow rises used during stripping the removal of ammonia can increase. The optimum operation parameters in removal of ammonia by air stripping process were initial pH of 12, air flow of 10 L/min, liquid flow of 2.5 mL/min and stripping time of 10 h. Under these conditions, residual ammonia concentration and mass transfer coefficient was 0 mg/L and 0.452 min⁻¹, respectively, Moreover, averagely 92-95% of ammonia in the absorption process using acid solution at trap was recovered as ammonia sulphate.

REFERENCES

- [1] Y. Hong-Duck, C. Young-Ok, and Lee. Sang-III, "Effect of Ferrous Ion Coagulation on Biological Ammonium Nitrogen Removal in Treating Coke Wastewater," *Environmental Enniner Science*, vol. 26, 12, pp. 1739-1746, 2009.
- [2] M. Zhang, J.H. Tay, T. Qian, and X.S. Gu, "Coke plant wastewater treatment by fixed biofilm systems for COD and NH₃-N removal," *Water Res.* vol. 32, pp. 519-527,1998.
- [3] M.S. Kumar, A.N. Vaidya, N. Shivaraman, and A.S. Bal, "Performance evaluation of a full-scale coke oven wastewater treatment plant in an integrated steel plant," *Indian J. Environ. Health*, vol. 45, pp. 29-38, 2003.
- [4] Y. Li, G.W. Gu, J.F. Zhao, H.Q. Yu, Y.L. Qin, and Y.Z. Peng, "Treatment of coke-plant wastewater by biofilm systems for removal of organic compounds and nitrogen," *Chemosphere*, vol. 52, pp. 997-1005, 2003.
- [5] Y.M. Kim, D. Park, D.S. Lee, and J.M. Park, "Instability of biological nitrogen removal in a cokes wastewater treatment facility during summer," *J Hazard. Mater.* vol. 141, pp. 27-32, 2007.
- [6] S. Chakraborty, and H. Veeramani, "Effect of HRT and recycle ratio on removal of cyanide, phenol, thiocyanate and ammonia in an anaerobic-anoxic-aerobic continuous system," *Process Biochem.* vol. 41, pp. 96-105, 2006.
- [7] G.M. Wong-Chong, "Retrofitting LTV coke plant waste water treatment system to comply with pretreatment discharge limits," *Iron Steel Eng.* vol.71, pp. 26-28, 1994.
- [8] Y.S. Jeong, and J.S. Chung, "Simultaneous removal of COD, thiocyanate, cyanide and nitrogen from coal process wastewater using fluidized biofilm process," *Process Biochem.* vol. 41, pp. 1141-1147, 2006.
- [9] Q.I. Rong, Y. Kun, and ZX, Yu "Treatment of coke plant wastewater by SND fixed biofilm hybrid system," *J. Environ. Sci.* vol. 19, pp. 153-159, 2007.
- [10] X.Y. Tan, S.P. Tan, W.K. Teo, and K. Li, "Polyvinylidene fluoride (PVDF) hollow fibre membranes for ammonia removal from water," *J.Membr. Sci.* vol. 271, pp. 59-68, 2006.
- [11] C.M. Hung, J.C. Lou, and C.H. Lin, "Removal of ammonia solutions used in catalytic wet oxidation processes," *Chemosphere* vol. 52, pp. 989-995, 2003.
- [12] A. Bonmati, and X. Floatats, "Air stripping of ammonia from pig slurry: characterization and feasibility as a pre- or post-treatment to mesophilic anaerobic digestion," *Waste Manage.* vol. 23, pp. 261-272, 2003.
- [13] S. Basakcildan-kabakci, A.N. Ipekoglu, and I. Talinli, "Recovery of ammonia from human urine by stripping and absorption," *Environ. Eng. Sci.* vol. 24, (5), pp. 615-624, 2007.
- [14] I. Ozturk, M. Altinbas, I. Koyuncu, O. Arikan, and C. Gomec-Yangin, "Advanced physical-chemical treatment experiences on young municipal landfill leachates," *Waste Manage.* vol. 23, pp. 441-446, 2003.
- [15] B. Calli, B. Mertoglu, and B. Inanc, "Landfill leachates management in Istanbul: applications and alternatives," *Chemosphere.* vol. 59, pp. 819-829, 2005.
- [16] M.J. Dempsey, K.C. Lannigan, and R.J. Minall, "Particulate-biofilm, expanded-bed technology for high-rate, low-cost wastewater treatment: nitrification," *Water Res.* vol. 39, pp. 965-974. 2005.
- [17] Prasad, B. and Singh, G., Removal of Ammonia from wastewater with special emphasis on coke-oven effluents, *Environ. Protec. Eng.* Vol. 16, 39, 1990.
- [18] S.I. Lee, S.Y. Weon, C.W. Lee, and B. Koopman, "Removal of nitrogen and phosphate from wastewater by the addition of bittern," *Chemosphere.* vol. 51, pp. 265-271, 2003.
- [19] S. Uludag-Demirer, G.N. Demirer, and S. Chen, "Ammonia removal from anaerobically digested dairy manure by struvite precipitation," *Process Biochem.* vol. 40, pp. 3667-3674, 2005.
- [20] P. Rensburg, E.V. Musvoto, M.C. Wentzel, and G.A. Ekama, "Modelling multiple mineral precipitation in anaerobic digester liquor," *Water Res.* vol. 37, pp. 3087-3097, 2003.

- [21] T.C. Jorgensen, and L.R. Weatherley, "Ammonia removal from wastewater by ion exchange in the presence of organic contaminants," *Water Res.* vol. 37, pp.1723–1728, 2003.
- [22] T.D. Reynolds, and R.A. Richards, "Unit Opretaions and Processes in Environmental Engineering," *PWS puslishing Company*, New York.
- [23] P.H. Liao, A. Chen, and K.V. Lo, "Removal of Nitrogen from Swine Manure Wastewaters by Ammonia Stripping," *Bioresource Technology.* vol. 54, pp. 17-20, 1995.
- [24] Y. Djebbar, and R.M. Naraitz, "Improved Onda correlations for mass transfer in packed towers," *Water Sci. Technol.* vol. 38, (6), pp. 295–302, 1998.
- [25] X. Quan, F. Wang, Q. Zhao, T. Zhao, and J. Xiang, "Air Stripping of Ammonia in a water-sparged aerocyclone reactor," *Journal of Hazardous Materials*, vol. 170, pp. 983-988, 2009.
- [26] Cypes, S.H. and Engstrom, J.R., Analysis of a toluene stripping process: a comparasion between a microfabricated stripping column and a conventional packed tower, *Chemical Engineering Journal*, Vol. 101, 49-56, 2004.
- [27] S.H. Cypes, and J.R. Engstrom, "Analysis of a toluene stripping process: a comparasion between a microfabricated stripping column and a conventional packed tower," *Chemical Engineering Journal*, vol. 101, pp. 49-56, 2004.
- [28] Y. Wu, Q. Li, and F. Li, "Desulfurization in the gas-continuous impinging stream gas-liquid reactor," *Chem. Eng. Sci.* vol. 62, pp.1814–1824, 2007.
- [29] APHA, Standart Methods for examination of water and wastewater. American Water Work Association. New York. 1992.
- [30] K.W. Pi, Z. Li, D.J. Wan, and L.X. Gao, "Pre-treatment of municipal landfill lechate by a combined process," *Process Saf. Environ. Prot.* vol 87, pp. 191-196.
- [31] S. Gustin, and R.M. Logar, "Effect of pH, temperature and air flow rate on the continuous ammonia stripping of the anaerobic digestion effluent," *Proces. Saf. Environ. Protec.* vol. 89, pp. 61-66, 2011.

An Observation on Natural Weathering Effect on Colour and Gloss Properties of PPG Coils Based on Dörtyol/Hatay/Turkey Region Compared With Florida

Özgür KARAKAŞ^{a*}, Tuğçe TOP^a, Erdogan KANCA^b, Hatice Arslan^a, Hazar Çelik^c, Fahri Akça^a and Güzin Müge Lüle^a

^aMMK Metalurji San. Tic. ve Liman İstl. A.Ş. Dörtyol, Hatay, Turkey, okarakas@mmkturkey.com.tr

^bMechanical Engineering Department ,Iskenderun Technical University, Hatay, Turkey kancaerdogan@gmail.com

^cTosyalı Toyo Çelik A.Ş., Osmaniye, Turkey, celikhazar@gmail.com

Abstract- Pre-painted galvanized (PPG) steel coils, comparing to galvanized coils, have better corrosion resistance and fascinating decorative properties with their color alternatives and glossy appearance. Color of PPG coils, during service period, by the effect of environmental conditions, fades and their surface lose their glossy appearance. This study investigated the color and gloss stability of PPG steel sheet samples, painted with 14 different colors and 3 different paint type. 23 parallel samples were exposed to natural environmental conditions during 2 years at two different locations, Florida/USA and Dörtyol/Hatay/Turkey. For natural tests, environmental meteorological parameters such as temperature, humidity, rain and various weather conditions are recorded monthly. This study shows the effect of natural environment of Dörtyol/Hatay/Turkey location and the regions similar meteorological conditions like Dörtyol/Hatay/Turkey on color and gloss of PPG coils.

Keywords: Natural Weathering, Gloss, Color, Pre-painted Galvanize, PPG, Dörtyol, Hatay, Turkey, Florida

I. INTRODUCTION

Pre-painted galvanized steel sheet (PPG) is a hot dip zinc coated steel, painted before forming, also known as pre-painted galvanized iron, pre-coated steel, coil coated steel, colour coated steel etc. Pre-painted steel sheet offers users a unique combination of advantages: the strength of steel, the corrosion resistance of coating and the beauty and additional corrosion protection of paint. Along with that flexibility of the coil coating process makes it possible to offer a wide range of finished surfaces (smooth, wrinkled, textured, orange peel effect etc.), which can be obtained in various levels of colours (saturated, metallic) and shining (matt, glossy).

In terms of lifespan performance, the demands on PPGs are much the same as on any other metal coating, to look good and to continue for the life of the product, while protecting the metal substrate. All of these properties are available in PPGs, but of course, improved performance will come at a cost, so it is important to specify a product which meets the requirements which are important in a given application without over-specifying an expensive product [1]. However, to achieve

desired lifespan it should be known environmental conditions which Pre-painted galvanized steel sheet product will be exposed in the service.

There are some test methods, used both by PPG producers and paint manufacturers around the world where surface properties are determined to be resistant to environmental conditions. These test methods are separated as natural and laboratory weathering. For natural weathering there are locations all around the world which are accepted as standard location because of their extreme weather conditions.[2] The extremely sunny, humid, and warm climate has been proven especially useful for certain types of testing including: Colour change, fading, and gloss loss, mechanical strength loss and physical deterioration, accelerated corrosion testing [3]. Manufacturers also take into account secondary effects (gases, pollution, acid rain, and blowing dust) and different climatic conditions (as a result different latitude, weather patterns, topographical and geographical features) because they do rather unique environments such as North America, Europe, India, Asia, Australia.

In Brazil, there is a different study about colour changes and gloss factor which shows the importance of testing the materials at many different sites, because each location has its particular set of influencing factors. The three natural weathering sites were geographically near but they presented rural, marine and urban atmospheres, which resulted in great differences in the exposure results [4]. Another study reveals the performance and durability of 11 industrial coating systems for two and a half years at five weathering sites in the industrial belt of Shuaiba Area, Kuwait in the Arabian Gulf. Experience has shown that under conditions like those in Kuwaiti industrial areas, degradation of coatings has tended to be faster than in the Western countries for which most of these coating systems were developed [5].

Because of different effect of locations on PPG performance, a study was done to define performance of PPG products of MMK Metalurji in the region where it locates. To have a comparison, Florida was chosen as benchmark location, because Florida is the internationally recognized benchmark location for outdoor exposure testing and has more specimens

on test than any other outdoor weathering facility in the world. (Site latitude 25° 27' North and longitude 80° 20' west).

As a result of study, performance of PPG products was observed in the region Dörtyol/Hatay/Turkey where performance of PPG products in Florida/USA is reference.

II. EXPERIMENTAL STUDIES

K. Materials

The samples which were used in this study had been produced by MMK Metalurji in hot deep galvanized line. Specifications of samples are given respectively, thickness range between 0.40 - 0.70 mm, coated with 100g/m² zinc and passivated, pre-treated with Cr⁶⁺, under coated with 5µm yellow undercoating (consisting of chromate) [SP(CR)], coated with 20 µm top coating paint. 3 different top coating paints with different RAL codes were used, these are polyester (SP), polyvinylidene fluoride (PVDF) and wrinkle polyester (SP-WR). The specimens used in the study were prepared by dimensioning them in the size of 15 * 20 cm from the same coil.

L. Devices and Equipment

Sizing of the samples made with Kanca brand 3BR4 300 model hand scissors.

The paint coating thicknesses of the sheets used in the work were measured with Erichsen Paint Borer 518S destructive thickness gauge and the gloss measurements at 60 ° with BYK TRI-GlossMaster device as shown Fig.1 and Fig 2.

Colour measurements of the painted sheets were made by X-Rite Color i7 colour spectrophotometer. The equipment is shown in Fig 3.



Fig.1 Erichsen Paint Borer 518S



Fig.2 BYK TRI-GlossMaster



Fig.3 X-Rite Color i7 Colour Spectrophotometer

M. Test and Assessment Method

For natural weathering test, the upper and lower parts of the samples were insulated with a waterproof tape. All the colour and brightness measurements were applied on those insulated panels. After that, samples were placed southwestwardly on a stand with 45° angle in the factory site of MMK Metalurji in Dörtyol/Hatay/Turkey. Fig.5

The stand is painted with a special paint type for painting ships to eliminate the effect of stand's corrosion on samples.

The colour and brightness values of painted panels were measured at South Florida and MMK Metalurji Dörtyol locations every 3 month periods. Before colour and gloss measurements were taken, the samples were washed with warm water (with detergent) and soft sponge without scratching the surfaces and then rinsed with pure water.

The samples were dried at room temperature and then measurements were taken. After the measurements were taken, the waterproof tapes of the samples were renewed and the stand was replaced for further testing.

Colour measurements are made in accordance with EN 13523-3 [6] standard with X-Rite Color i7 colour measuring device.

The gloss measurements were made at 60° with the BYK TRI-glossMaster device according to EN 13523-2 [7]

1. South Florida

Florida is located in Miami, the only tropical region of the United States, located on the southern of Florida with 25 ° 27' northern latitudes and 80° 20' east longitude. All season of the year in South Florida, temperatures are high. The tropical monsoon climate is dominant in the region, so the summer season is hot and humid, and the winter season is warm and dry. The average temperature in summer from 28 to 30 °C, while temperatures vary from 16 to 20 °C in winter. The rainy season is between June and October. Also, hurricanes happen in this period from time to time. Moisture increases with summer. Fig 4.



Fig.4 MMK Metalurji samples at natural weathering test area in Florida

Florida is an internationally recognized benchmark location for natural weathering test. Florida tropical weathering test is not only realistic test, but also accelerated test. Because in one year, insolation of Florida is equivalent to several years of anywhere insolation. The weather condition of Florida site is high intensity sunshine, annual high UV and high temperatures throughout the year, heavy rainfall and very high humidity.

2. MMK Metalurji Dörtyol/ Hatay/ Turkey

MMK Metalurji is located in Dörtyol at 36° 49' northern latitudes and 36° 13' east longitude, the southernmost in Turkey. Natural weathering stand location is 1 km away from sea and 38 m high from sea level in MMK Metalurji Dörtyol site.

Weather condition is typical Mediterranean climate, the summers are hot and dry, and the winters are warm and rainy.

There is snowfall for a few days. Annual range of temperature is between -6 °C and + 43 °C. The annual rainfall ranges from 562.2-1216.3 mm. The maximum rainfall falls in the winter, the lowest rainfall is seen in the summer. Fig 5



Fig.5 MMK Metalurji samples at natural weathering test area in Dörtyol/Hatay/Turkey

III. RESULTS

The PPG samples were exposed to natural environment for 24 months at South Florida and Dörtyol locations. The meteorological conditions data were recorded during this period and yearly averages were calculated.

Yearly temperature average values for South Florida and Dörtyol are 24.5 °C and 21.2 °C respectively. Monthly temperature distribution graphs are given at Fig 6.

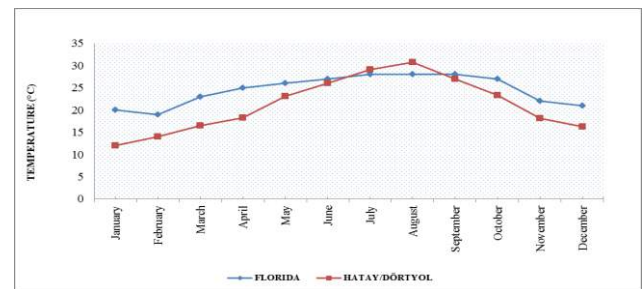


Fig 6. Yearly Temperature Distribution Graphs

Yearly rainfall average for South Florida and Dörtyol are 68.7 mm and 79.3 mm respectively. Monthly rainfall distribution graphs are given at Fig 7.

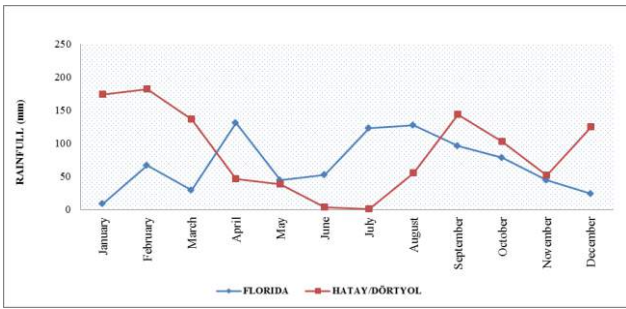


Fig 7. Yearly Rainfall Distribution Graphs

Yearly humidity average for South Florida and Dörtiyol are 78.0 % and 59.9 % respectively. Monthly rainfall distribution graphs are given at Fig 8

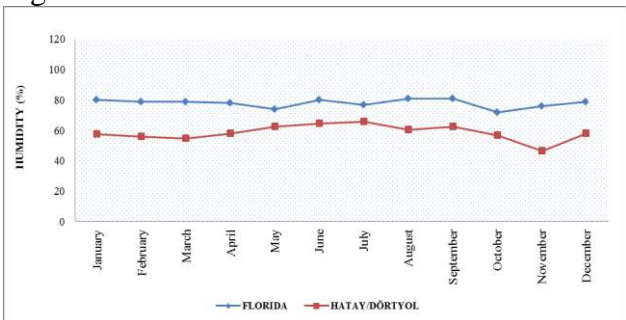


Fig 8. Yearly Humidity Distribution Graphs

Colour deviation and change on gloss value as protection% are recorded. The protection% values are calculated with the formula: 24th month gloss measurement value / initial gloss measurement value x 100. These data is given at Table 1

TABLE 1

COLOR DEVIATION AND GLOSS CHANGE % VALUES AFTER 24 MONTHS

COLOR	PAINT TYPE	GLOSS TYPE	MMK DÖRTYOL (COLOR DEVIATION, ΔE)	MMK DÖRTYOL GLOSS (% PROTECTION)	FLORIDA (COLOR DEVIATION, ΔE)	FLORIDA GLOSS (% PROTECTION)
MP 1014	SP	SEMIGLOSS	1,64	71,0	2,58	43,8
RAL 3004	SP	SEMIGLOSS	2,26	50,0	1,27	15,2
RAL 3004	SP	SEMIGLOSS	2,31	51,5	1,7	18,8
MP 3005	SP	SEMIGLOSS	0,82	61,3	0,99	32,3
RAL 3009	SP	SEMIGLOSS	0,65	27,0	1,31	8,3
RAL 3009	SP	SEMIGLOSS	0,81	29,4	0,84	8,8
MP 5005	SP	SEMIGLOSS	2,81	75,0	2,5	50,0
RAL 5010	SP	SEMIGLOSS	1,05	73,5	1,37	55,9
MP 6005	SP	SEMIGLOSS	1,4	66,7	1,58	38,9
RAL 6020	SP WR	MATT	0,76	100,0	0,65	75,0
MP 8017	SP	SEMIGLOSS	1,12	46,7	0,77	19,4
RAL 9002	SP	SEMIGLOSS	1,47	81,5	0,8	51,7
RAL 9002	SP	SEMIGLOSS	1,76	79,3	0,43	50,0
RAL 9002	SP	SEMIGLOSS	2,55	70,6	1,15	31,4
RAL 9002	SP	SEMIGLOSS	2,98	75,0	1,74	40,6
RAL 9002	SP	SEMIGLOSS	2,42	85,4	1,2	48,7
RAL 9002	PVDF	SEMIGLOSS	0,61	84,4	0,21	97,2
RAL 9002	PVDF	SEMIGLOSS	0,63	88,9	0,16	103,7
MP 9003	SP	SEMIGLOSS	5,48	44,8	3,49	28,6
RAL 9003	SP	HIGHGLOSS	2,77	87,9	1,4	82,6
RAL 9006	SP	SEMIGLOSS	0,62	88,2	0,54	63,9
RAL 9010	SP	SEMIGLOSS	4,73	56,5	2,68	34,8
RAL 9016	SP	SEMIGLOSS	2,09	76,3	1,57	52,6

According to the data given in Table 1, gloss protection % values in Dörtiyol is higher than that in South Florida except RAL 9002 PVDF type painted PPGs. The gloss protection% values according to the paint type and colours are given in Fig 9.

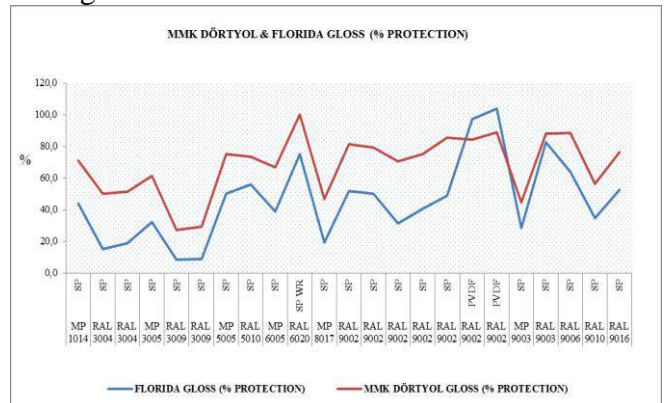


Fig 9. Gloss protection% Graphs according to the paint type and colours

For white colour tones (Ral 9002, 9003 and 9016) colour change quantity in Dörtiyol location is higher than that in South Florida and for the rest colours more or less the colour change quantities are the same. The colour change values according to the colours are given in Fig 10.

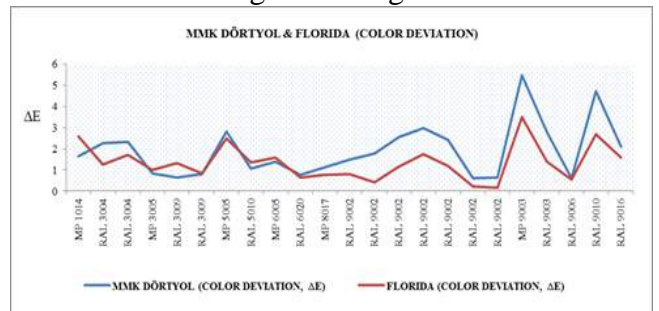


Fig 10. Colour Change Graph

IV. CONCLUSIONS

This study investigated that South Florida Location is more aggressive on reduction of gloss than Dörtyol Location for polyester type painted PPGs. Color deviation in Dörtyol location is higher than that in South Florida for white colour tones but for the rest colour tones there is not any significant difference on colour deviation.

V. ACKNOWLEDGMENT

This study was supported by MMK Metalurji San. Tic. ve Liman İşlt. A.Ş. The authors would like to thank MMK Metalurji CEO Mr Denis Kvasov for providing opportunity for this study.

VI. REFERENCES

- [1] Choosing the Right Prepainted Metal Product, ECCA, Technical paper ,2010
- [2] Koleske J. V., Paint and Coating Testing Manual, 40th Edition, 2008
- [3] (2017) The Q-Lab Florida Outdoor Exposure Testing website. [Online]. Available: www.q-lab.com
- [4] Comparative Evaluation Between Accelerated and Outdoor Ageing of Brazilian Paints - Part one
- [5] Performance of Coating Systems in Industrial Atmosphere on the Arabian Gulf
- [6] EN 13523-3 Coil coated metals-Test Methods-Part 3: Color difference-Instrumental comparison
- [7] EN 13523-2 Coil coated metals - Test methods - Part 2: Gloss

Investigation of Sheet Metal Forming Process Based on Finite Element Simulation

Alimurtaza RUTCI*, Fatih KACMAZ⁺

*Teknorot Automotive Product Industry, Research-Development Center, Düzce –Turkey
alimurtaza.rutci@teknorot.com

⁺Teknorot Automotive Product Industry, Research-Development Center, Düzce –Turkey
fatih.kacmaz@teknorot.com

Abstract — Most of vehicle chassis components are produced by forming process in conventional method. Die design and production of robust tooling demand comprehensive knowledge and experience for sheet metal forming. Nowadays, simulation technology and software tools support sheet metal forming, tooling design, and process design. This study showed that the finite element simulation help to die designer to predict failure which is excessive thinning, wrinkling, shear fracture etc. for tooling and process design. In this study, sheet metal wishbone analysed with forming simulations software. Simulations showed that excessive thinning zone occurred. Also, undesired tearing was observed rubber bush assembly section. According to simulation result, tool design modified at an early stage before prototype sheet metal wishbone had been produced. The final die design was created more die step and wishbone shape has changed. With simulations result, defects have been identified and prevented earlier. Development time and costs are reduced whereby finite element simulations. Also, all of these operations help enhance product quality. Finite element methods will gradually replace manual trial-and-error design iteration.

Keywords — sheet metal, wishbone, forming, simulations, finite element method

I. INTRODUCTION

In general, automotive industries use various manufacturing method to produce a vehicle. Sheet metal forming is one of the most important manufacturing processes for mass production, especially in the automotive industries. Because this type of forming process is cost effective for large quantity production.

Design engineers often takes trial-and-error measures to find acceptable tooling and process that is inefficient and expensive for robust tooling. Within development of computer simulation technology and software tools, design engineers achieve produce quality parts more efficiently and with less prototype cost. Also there are so many advantages to use finite element method. With this technology, design engineers take a technical information about process and parts before had been produced. These technical informations enhance to understand mechanics and physics in metal forming.

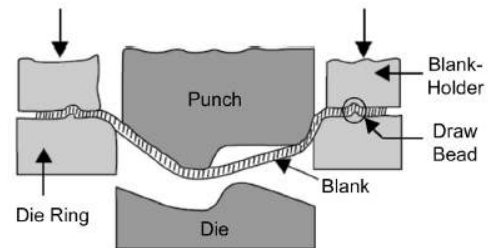


Fig.18 Schematic Illustration of a Deep Drawing Process

N. Deep Drawing Forming Process

The deep drawing (draw forming) is one of the oldest and most widely used sheet forming processes. As shown in Fig.1, this process typically requires a punch, a die, and a blank holder as forming tools (the so-called tooling). During a drawing operation, the blank holder or binder clamps the blank over the binder surface of the die, while the punch moves toward the blank and squeezes it into the shaped die, forcing the material to deform plastically according to the geometry of the die cavity.

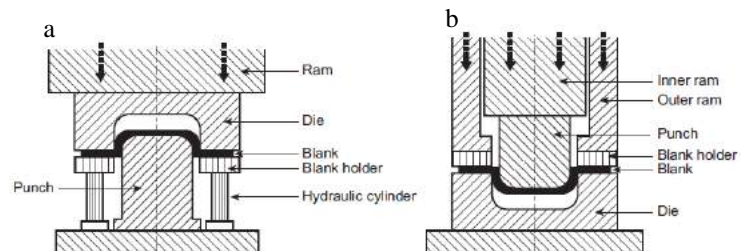


Fig.19 Single Action Draw (a) & Double Action Draw (b)

Draw processes can be categorized based on the number of rams that can be operated independently of each other on the forming equipment. In a single-action draw operation, the female die is often the moving tool, and the blank holder force is provided by hydraulic cylinders as depicted in Fig.2a or a die cushion mechanism. The pressure of the cylinders needs to be adjusted during the process to control the force applied to the blank through the blank holder. For double-action draw as shown in Fig.2b the outer and inner rams, which can be controlled independently, are used to drive the blank holder and the male punch, respectively. In both types, the blank holder

force is a crucial parameter that controls the material flow and prevents excessive forming defects, especially wrinkling, in drawing.

II. MATERIALS AND METHODS

In metal forming, two types of deformation has been occurred. Elastic deformation is always the initial phase of loading, in which the material will change shape as load is applied. However, when the load is removed, the material returns to its original shape. In other words, elastic deformation is a change in shape of a material at low stress that is recoverable after the stress is removed. When the stress is sufficient to permanently deform the metal, it is called plastic deformation. The stress-strain relationship in the elastic-plastic state is nonlinear because phenomena such as irreversible dislocation motions are the basis of plastic deformations.

O. Modelling of Materials

In finite element simulations method, modelling of materials is very important. To modelling materials of sheet metal forming process we use tensile test sample as shown Fig3.

In this study we use DD13 (ERD 6224) and S355MC (ERD 4936) to simulate deep drawing processes.



Fig.20 Tensile Test Samples (a)

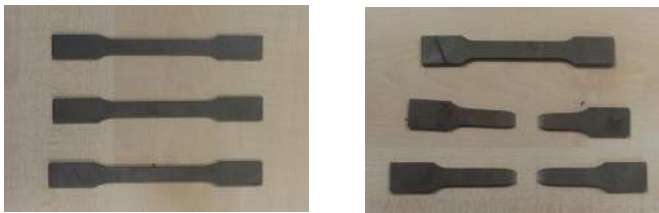


Fig.21 Tensile Test Samples (b) & (c)

I. Strain-Stress Curve

The relationship between the stress and strain that a particular material displays is known as that particular material's stress-strain curve.

It is unique for each material and is found by recording the amount of deformation (strain) at distinct intervals of tensile or compressive loading (stress).

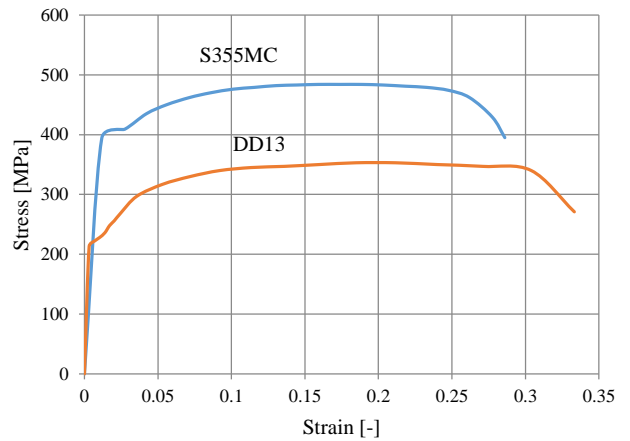


Fig.22 Stress - Strain Curve of DD13 & S355MC

II. Flow Curve

Flow curve used to describe the true stress-strain curve, except for the elastic regime. Flow stress curves are very important in design of metal forming processes, since they describe material behavior during deformation.

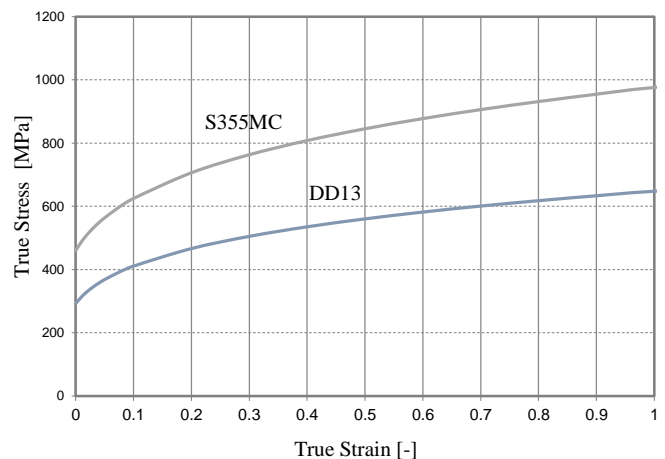


Fig.23 Flow Curve of DD13 & S355MC

III. Material Anisotropy

Anisotropy is the property of being directionally dependent, which implies different properties in different directions, as opposed to isotropy. It can be defined as a difference, when measured along different axes, in a material's physical or mechanical properties. Most materials exhibit anisotropic behavior. Metals and alloys tend to be more isotropic, though they can sometimes exhibit significant anisotropic behaviour. This is especially important in processes such as deep-drawing. When simulating sheet metal forming processes, the anisotropy coefficients are denoted (r_0 , r_{45} , r_{90}). Definition of the

anisotropy, R , in terms of width and thickness strains in a tensile-test specimen cut from a rolled sheet shown in Fig.3[8]. The specimen can be cut in different directions with respect to the length, or rolling direction, of the sheet.

$$R = \frac{\epsilon_w}{\epsilon_t}$$

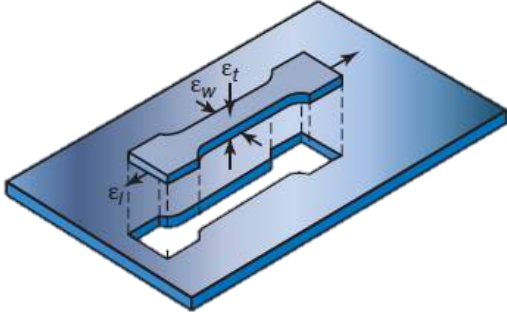


Fig.24 Definition of the Anisotropy

i) Normal anisotropy

The condition is all in plane direction as equivalent with only the thickness direction different called normal anisotropy.

$$\bar{R} = \frac{R_0 + 2R_{45} + R_{90}}{4}$$

ii) Planar anisotropy

The variation of anisotropy coefficients within the sheet plane known as the coefficient of planar anisotropy.

$$\Delta R = \frac{R_0 - 2R_{45} + R_{90}}{2}$$

Material	DD13 (ERD 6224)			S355MC (ERD 4936)		
	R ₀	R ₄₅	R ₉₀	R ₀	R ₄₅	R ₉₀
Material Anisotropy, R	0.715	0.948	0.836	0.654	1.067	1.143
Normal Anisotropy, R _n	0.86			0.98		
Planar Anisotropy, R _p	-0.17			-0.17		

Table-I Anisotropy Coefficient of DD13 & S355MC

IV. Forming Limit Diagram

For numerous materials the critical area between the domains has been detected both by means of laboratory tests and by forming of industrial components. These measurements were conducted for various materials. The excellent correlation of the results was a proof that the forming limits in sheet metal forming can be evaluated very well by determining the forming limit diagram.

P. Modelling of Components

The digital model of the product is created in a CAD system according to original part. For finite element analysis we use 3D cad design. Fig.7 show us a original sheet metal control arm and Fig.8 show us a 3D cad design.

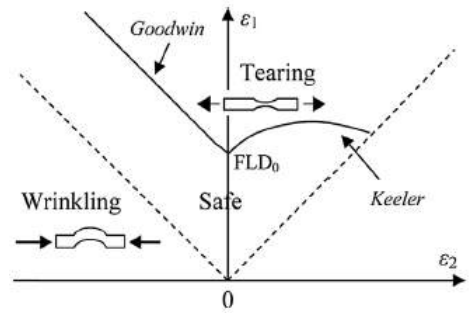


Fig.25 A Schematic Forming Limit Diagram

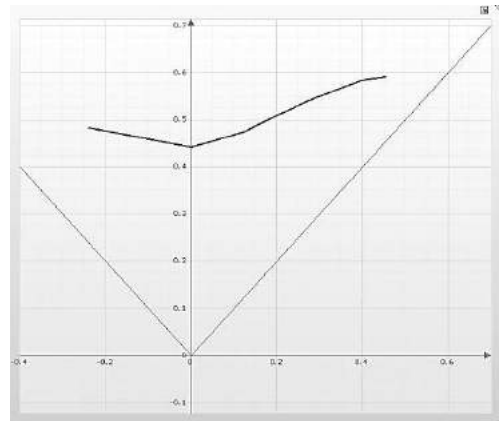


Fig.26 DD13 Material Forming Limit Diagram

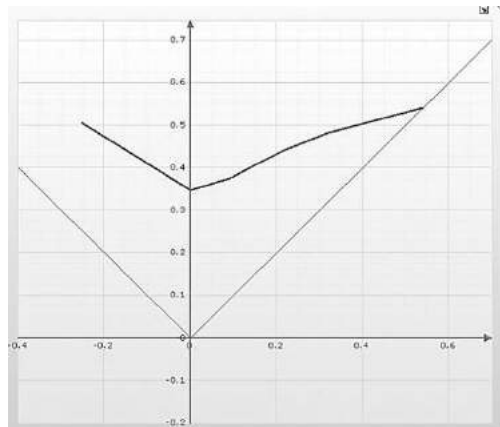


Fig.27 S355MC Material Forming Limit Diagram



Fig.28 Sheet Metal Control Arm – Original Part

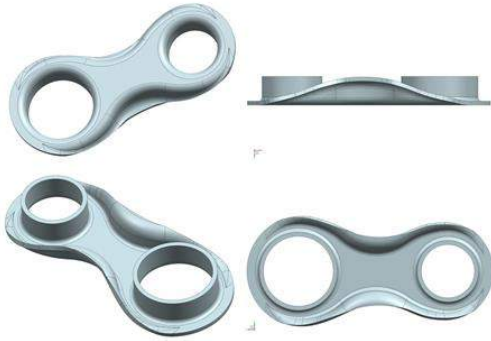


Fig.12 Sheet Metal Control Arm – 3D Cad Design

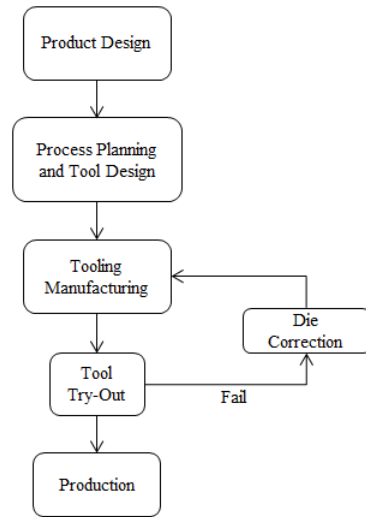


Fig.13 Flowchart of Conventional Process

7) Simulation-Based Process Planning And Tooling Design Process

Using forming simulation to bring more knowledge to help engineers understand the physics and mechanics of the metal forming process.

One-step simulation is primarily used to quickly assess part formability and estimate the blank outline in the early stage of the forming process design. According to result of one-step formability study, if there is a failed situation part has been redesigned small changes.

Incremental forming simulation allows the accurate modeling of sheet forming processes. The forming process is divided into steps or increments, and the problem is solved incrementally through time. Within each step or increment, the positions, velocities, accelerations, and forces are calculated at the nodal points in the blank. Within each blank element, stresses and strains can be evaluated from nodal displacements.

When a formed part is removed from the die, the material has a tendency to partially return to its original shape on the release of the forming forces. This elastic shape change, or springback, is caused by the elastic recovery of the material and uneven stress distribution after forming.

With simulations result, defects have been identified and prevented earlier. Development time and costs are reduced whereby finite element simulations.

Q. Tooling and Process Design

Tooling and process design is an important part of any product's manufacturing process. Within development of computer simulation technology and software tools, tooling and process planning engineers achieve produce quality parts more efficiently and with less prototype cost. Also there are so many advantages to use finite element method. With this technology, engineers use simulation based process instead of conventional design process.

6) Process Planning and Tooling Design Process

In conventional process, parts design according to original part. After that process planning and tooling designs within 3D cad parts. Before final prototype, tooling manufacturing and tool try out section design.

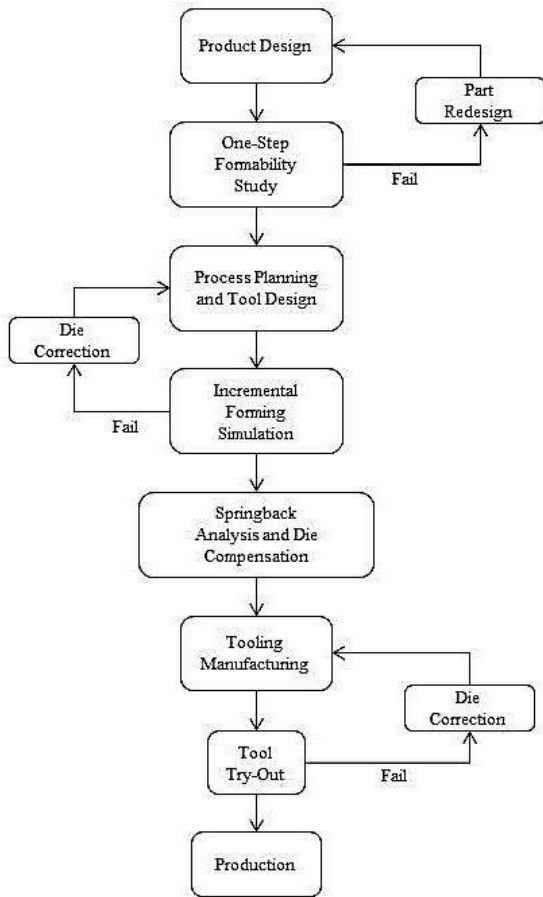


Fig.14 Flowchart of Simulation Based Process

8) Tooling Components

a. Pre-Forming

In this step we prepared to part for hole cutting without excessive thickness.

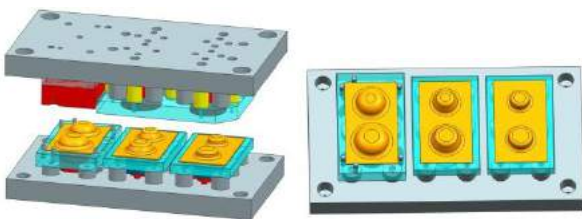


Fig.29 Pre-Forming Tool

b. Hole Cutting

In this step, our aim is to create a hole which is used for bush housing.

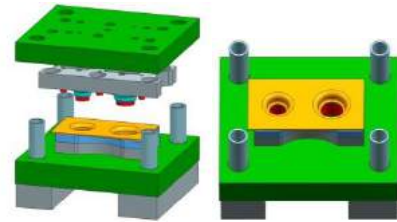


Fig.30 Hole Cutting Tool

c. Edge Forming

In this tooling step, we prepared bush region to shrink fit process.

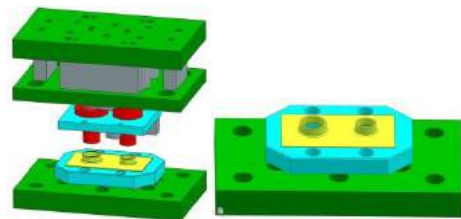


Fig.17 Edge Forming Tool

d. Blank Cutting

Blanking is very important process for part because of final design shape. In this step, we cut the part to prepare final forming process.

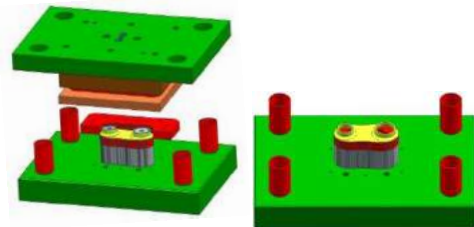


Fig.18 Blank Cutting Tool

e. Final Forming

With final forming step, we create the design according to original data.

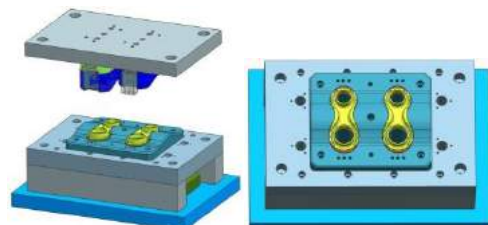


Fig.19 Final Forming Tool

III. EXPERIMENTAL & NUMERIC STUDY

Designs have been tested both numerically and experimentally. Before simulation based tooling process design, there were some defect and failure by trial-and-error method. It is difficult to get out these defect and failure at this situation. In addition to these it is very hard to get back to revise tooling. Development time and costs are too long without FEM.

With finite element simulations process, defects have been identified and prevented earlier. Development time and costs (material, machine and labor) are reduced whereby finite element simulations. Also, all of these operations help enhance product quality and reduced development time.

A. Experimental Study

The following failure modes have occurred when the tooling design have been tested. According to defects and failures many revision and design changes have been made numerous times.

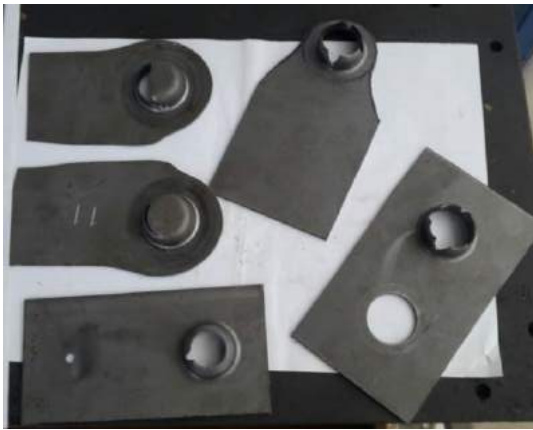


Fig.20 Failure Modes

Errors have occurred with edge forming and hole cutting process as shown Fig.15. To solve these problems tooling planning and design redesign lots of time.



Fig.31 Failure Modes

B. Numeric Study

Within development of simulation technology and computer, numerical study start to increase. Numeric studies help engineers understand the physics and mechanics of the metal forming process. Computer simulations shows promise in realistically simulating. According to simulation result, tool design modified at an early stage before prototype sheet metal wishbone had been produced.

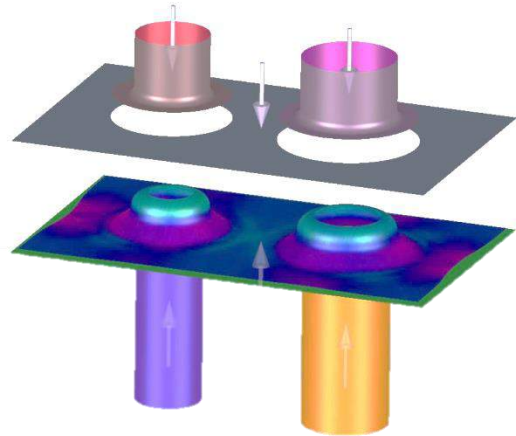


Fig.22 3D Tooling Simulation

Simulation set up for the sheet metal wishbone study As shown in Fig.16, this study illustrates the use of simulation software to learn the causes of the excessive thinning and possible solutions in process parameters to take away thinning.

Tools are required to form the part; namely the die, the punch, the binder and blank. We start to create a new forming simulation with final shape. Autoform convert to final shape to shell model. Material has been assigned according to material test results. And if the other parameters are available, the analysis run. According to analysis result product approval given or not.



Fig.23 Simulation Steps and Final Part

Tooling designs are preliminarily simulated. After computer aided simulations, results supported with experimental study.

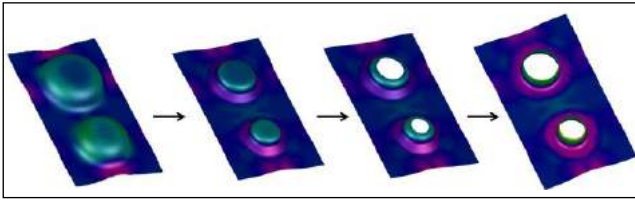


Fig.24 Simulation Based Tool Design

According to computer aided analysis and experimental study result, design engineers approved the tooling plan and process. And part manufacturing has been started.

As illustrated Fig.19 the formed part is acceptable for use in front suspension system after e-coating process.

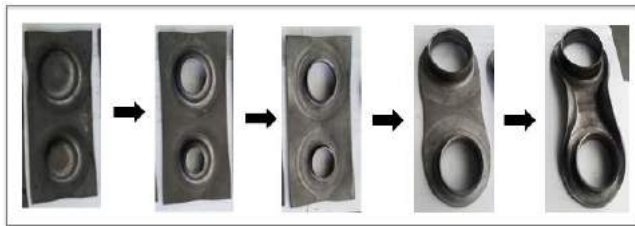


Fig.25 Part Manufacturing With Tooling

IV. RESULTS AND DISCUSSIONS

With simulations result, defects have been identified and prevented earlier. This results enables us to redesign for get out of failure. Visualizing the sheet metal part deformation greatly improve our understanding of the mechanics and physics in sheet metal forming. With simulation based process planning and tooling design reduce labor and material cost.

In the figures below, we show the some result and output parameters. Even caveats and action are also listed below.

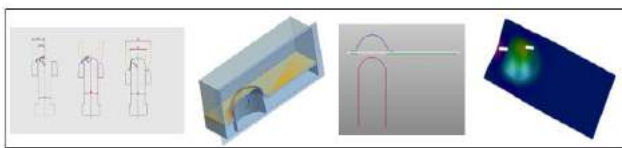


Fig.32 Excessive Thinning Problems Stage

Excessive thinning occurred. Dome radius and part diameter has been optimized.

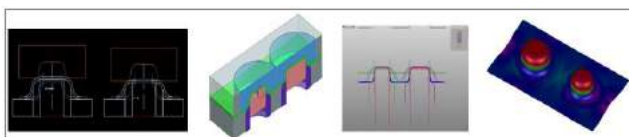


Fig.33 Tearing Problems Stage

Tearing was observed rubber bush housing region. Some splits may be correctable via process adjustment (i.e. different blank outline, holding condition, multi-stage forming)

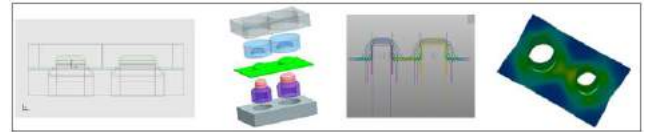


Fig.34 Optimized and Correct Design

With the incremental forming result has shown. Other defect or failure parameters have optimized.

V. CONCLUSION

Simulation technology and software tools offer engineers an effective alternative to achieve tooling design and a process that can produce quality parts more efficiently and with less cost.

There are enormously advantages to using simulation technology and software tools to support sheet metal forming, tooling planning and process design. Simulation technology and software help reduce prototype parts development time, improve product quality, and reduce costs. Above all, the biggest advantage is that the simulation offers engineers visualizations of the blank deformation during the forming process with a display of engineering information like residual stress, strain, thickness distribution, and so on. Finite element methods will gradually replace manual trial-and-error design iteration.

ACKNOWLEDGMENT

These study was supported by Teknorot Automotive A.S R&D Center. We thank our colleagues from R&D Center who provided insight and expertise of this paper.

REFERENCES

- [1] Manufacturing Processes for Engineering Materials, 5th ed. Kalpakjian Schmid © 2008, Pearson Education
- [2] <https://www.nde-ed.org/AboutNDT/aboutndt.htm>
- [3] Metal Forming and the Finite-Element Method, Kobayashi, S., Oh, S., Altan, T., Oxford University Press
- [4] Sheet Metal Forming Processes, Dorel Banabic © Springer-Verlag Berlin Heidelberg 2010
- [5] Autoform User Manual and Training Note
- [6] Teknorot Automotive R&D Center Design Guide

Investigation of Weldability of DP 1000-DP 1000 Steel Using Electron Beam Welding

Cihangir Tevfik SEZGİN*, Fatih HAYAT⁺

[#]Kastamonu University Cide MYO Cide/Kastamonu,

Turkey

ctsezgin@kastamonu.edu.tr

⁺Metallurgy and Materials Engineering, Karabük University

Turkey

fhayat@karabuk.edu.tr

Abstract— In this study, weldability of DP 1000-DP 1000 steel with electron beam welding method was investigated. Consisted of microstructure after welding was investigated with microscopy and SEM. Microstructure properties was investigated such as tensile strength and microhardness. Average of fusion zone microhardness was found as 284 HV. Average tensile strength was found as 656 MPa and elongation was found 3%.

Keywords— DP 1000, electron beam welding, microstructure, weldability, mechanical properties

I. INTRODUCTION

Dual phase steel (DP) is one of the high strength low alloy steel (HSLA). It includes two major phase which are martensite and ferrite. It is named due to combination of these two phases [1]. It uses widespread in automotive industry cause of high elongation level and strength. Besides that, it also provides high crash performance, less fuel consumption, less amount of pollution [2-7]. In this combination of two phases, martensite contributes with high strength and ferrite matrix provides good elongation that can produce a good combination of strength and ductility for applications which require good formability. During manufacturing of automotive components, welding is the mostly used joining operation [8]. Generally laser welding, resistance spot welding, metal inert gas welding, metal active gas welding are using for welding method in automotive industry. But electron beam welding (EBW) is rarely used in automotive industry. Because it is not fast like laser welding or resistance spot welding. Furthermore its initial investment cost is too expensive according to other welding machines.

EBW process is used in a variety of industries. But it is generally used in aerospace industry. EBW is one of the best fusion welding processes which provides good mechanical and metallurgical properties in comparison to other welding processes. EBW has advantages such as high power density, weldability of refractory and weldability of high melting point metal like tantalum and wolfram, low heat input, high penetration, very low or not distortion, high depth penetration (about 200 mm depth), narrow heat effect zone (HAZ) [9-12].

None studies was found study about DP 1000-DP 1000 butt joint welding using electron beam welding in literature.

In this study, microstructure and mechanical properties such as tensile strength, microhardness was investigated. Microhardness and microstructure of fusion zone, HAZ and base metal (BM) were compared. Additionally microstructure was observed with scanning electron microscope (SEM). Fracture surface of DP 1000- DP 1000 joint was observed with SEM.

II. EXPERIMENTAL METHODS

The chemical composition of BM is shown in Table 1. Thickness of DP 1000 steel is 1 mm. The mechanical properties of weldless DP 1000 steel is shown in Table 2. These properties was taken from producing company. Trading name is Docol 1000. Optimisation of weld parameters is very important in welding process to achieve a sound weld quality with uniform microstructure and excellent mechanical properties of weld joints. Metallurgical and mechanical properties characterisation of welded joints is related with welding parameters. So in this study, parameter of EBW except current was stable. Penetration wasn't gotten at 15 and 20 mA. Parameter of EBW is shown in Table 3.

Welded sample was shown in Figure 1. Sample was cut with wire erosion. Because cutting process temperature is low. So heating couldn't change microstructure and mechanical properties. 3 samples were used for tensile test for getting average tensile strength and elongation ratio. The samples were ground using grinding papers of 240-400-600-800-1200-2000-3000 mesh and polished with diamond paste of 3 µm in size. The polished surfaces were then etched chemically with 2% nital and 98% methanol solution. It was kept 12 seconds in solution.

Microhardness test was carried out under 200 gr. load. It is Vickers. Distance Between two microhardness points was 0,4 mm. Microhardness test was measured from 15 point. Tensile test was carried out at 60 tons tensile test machine. Tensile test sample drawing was shown in Figure 2. "R" means rest in Table 1. TS EN ISO 6892 standard was used for sample dimension.

TABLE XXII
CHEMICAL COMPOSITIN OF DP 1000 (WEIGHTH %)

C	Si	Mn	Al	Mo	Ni	Nb	V	Fe
0,15	0,5	1,5	0,05	0,01	0,03	0,02	0,01	R

TABLE II
MECHANICAL PROPERTIES OF DP 1000

Yield Strength (MPa)	Tensile Strength (MPa)	Elongation (%)
797	1081	8

TABLE III
PARAMETERS OF EBW

Focus (mA)	510
Voltage (KV)	40
Current (mA)	25
Speed of mirror (mm/min)	200
Pressure (vacuum) (torr)	10 ⁻⁴

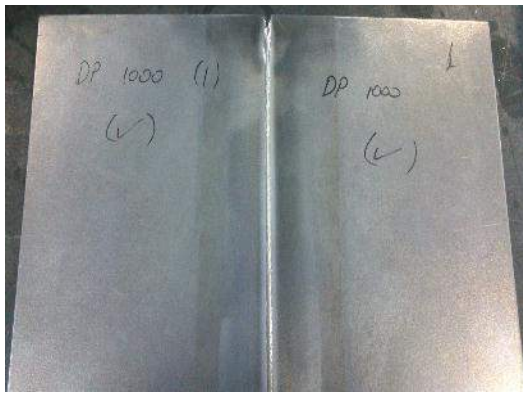


Fig. 1 Welded sample with EBW

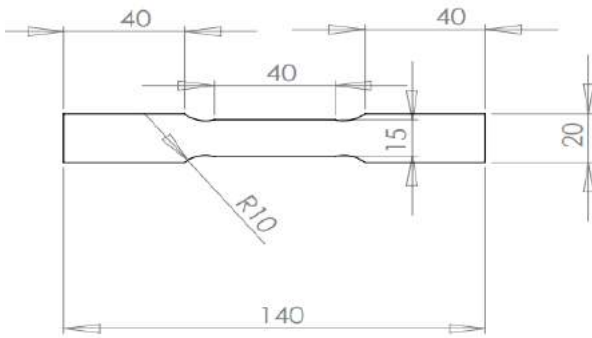


Fig. 2 Schematic of tensile test sample

III.RESULT AND DISCUSSION

A. Microstructure

In the fusion zone there is martensite more than ferrite. It is shown in Figure 3. In the fusion zone, the peak temperature is above the melting point. As expected by the high level presence of martensite microstructure. So it causes to increase hardness at fusion zone. In HAZ, ferrite and martensite is seen (Figure 4). At base metal, ferrite is more than martensite. It was shown in Figure 5. Orange surface is ferrite and black surface is martensite.

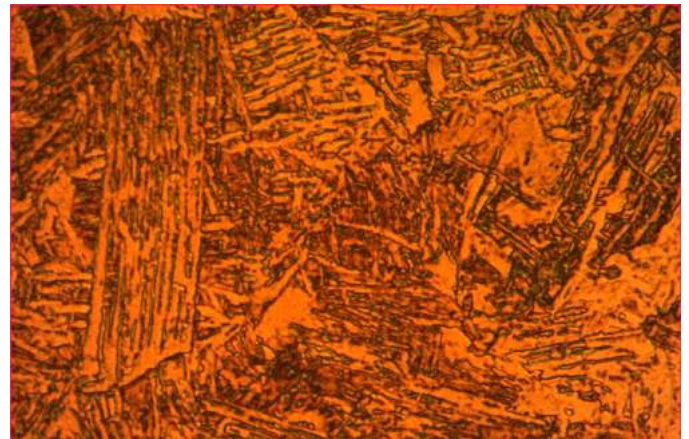


Fig. 3 Fusion zone of DP 1000-DP 1000

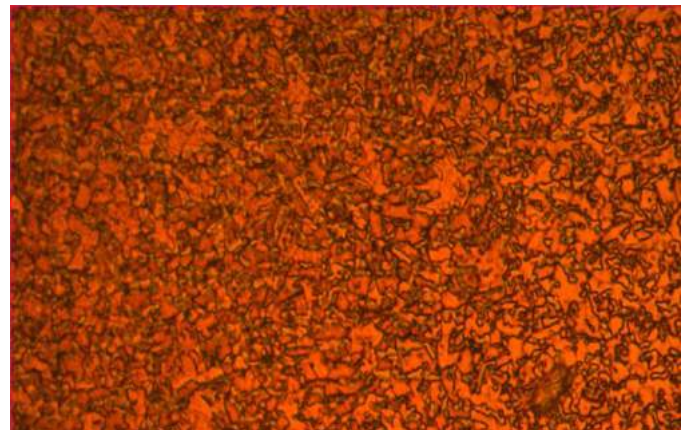


Fig. 4 HAZ of DP 1000-DP 1000

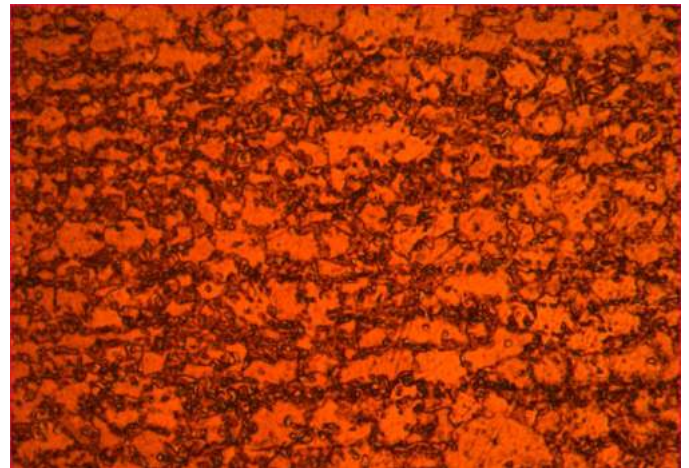


Fig. 5 Base metal

In the base metal, ferrite as black surface and martensite like island above the main surface was shown in Figure 6. F symbolizes ferrite and M symbolizes martensite.

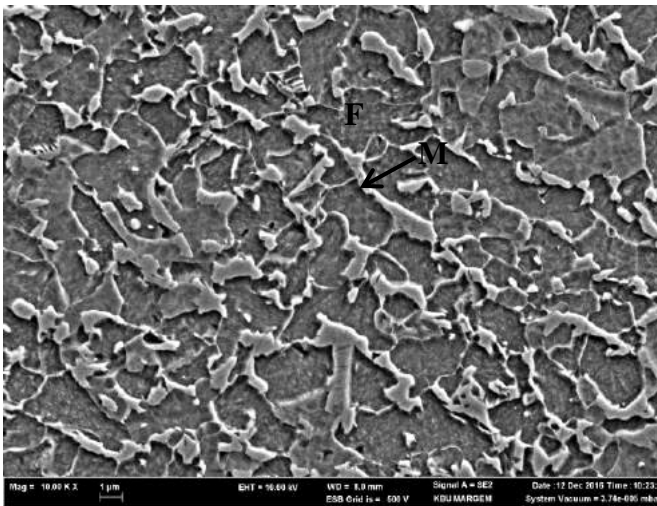


Fig. 6 SEM analysis of base metal

In fusion zone, martensite is shown like needle in Figure 7.

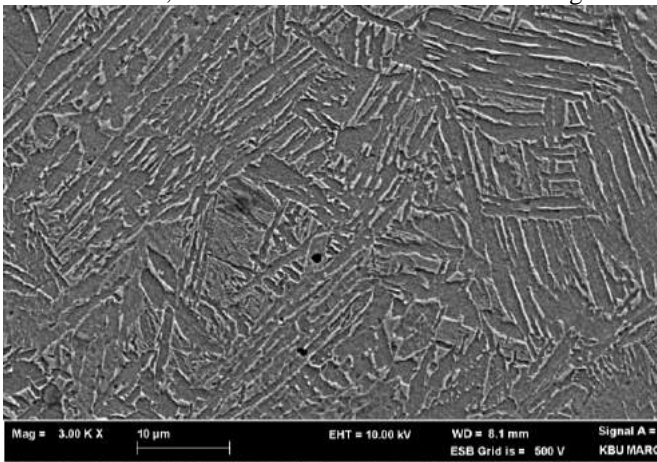


Fig.7 SEM analysis of fusion zone

B. Mechanical Properties

Table IV shows the tensile strength and elongation of DP 1000 –DP 1000 EBW joint samples.

Percentage elongation decreased with welding process. Base metal percentage elongation was 8% although welding joint percentage elongation was 3% . Average tensile strength of welded joint was 656 MPa. Another study about DP 980 laser welding was shown that tensile strength of welding joint was 985,2 MPa [13]. In our study tensile strength value is lower than base metal strength value. Waiting for opening vacuum cabin door may cause decreasing amount of martensite. Because temperature was very high and samples couldn't contact with air for cooling. DP 1000 stayed in vacuum cabin during welding. A few seconds -approximately 15 seconds- needs for opening vacuum cabin door.

Table V shows the hardness of EBW DP 1000 steel joints. It was clear from Vickers hardness measurements that DP 1000 joint fusion zone had higher hardness than HAZ and base metal . Presence of martensite increases hardness of fusion zone. Average hardness of fusion zone is 284 HV_{0.2}. Hardness of HAZ is higher than base metal.

TABLE IV
RESULT OF TENSILE TEST

Sample Number	% Elongation	Tensile Strength (MPa)
1	3	653
2	3	658
3	3	657

All samples were broken from HAZ. Figure 8 shows failure surface.

TABLE V
RESULT OF MICROHARDNESS TEST (HV 0.2)

Base Metal	224
	235
HAZ	220
	257
	270
Fusion Zone	291
	289
	240
	280
	320
	304
HAZ	255
	213
	229
Base Metal	219

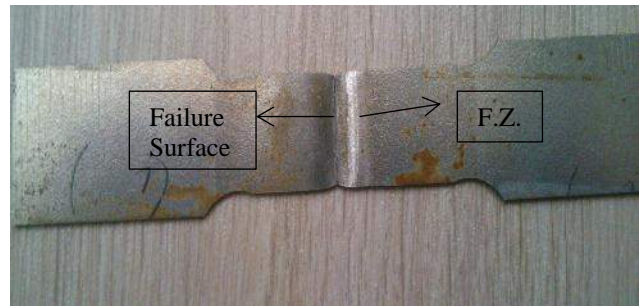


Fig.8 Failed sample of welded joint

IV.CONCLUSIONS

- ✓ Microhardness result shows the highest hardness was observed in fusion zone . Average of fusion zone is 284 HV.
- ✓ Elongation of EBW DP 1000 joint sample is lower than original material.
- ✓ Percentage elongation of base metal was 8% while welded joint percentage elongation was 3%.
- ✓ Tensile strength of joint sample is lower than original material. Base metal tensile strength was 1081 MPa while welded joint tensile strength was 656 MPa. Cause of decreasing of tensile strength value was supposed due to the fact that sample waited little more than normal welding time in vacuum cabinet.

ACKNOWLEDGMENT

This work was supported by Scientific Research Projects Coordination Unit of Karabük University. Project number: KBÜ-BAP-16/2-DS-086

REFERENCES

- [1] F. Hayat, "Masif ve özlü kaynak telleri ile birleştirilen çift fazlı çeliklerin mekanik ve mikroyapı özellikleri", Doctoral Thesis, Sakarya University, Sakarya, Turkey June 2009.
- [2] H. Ashrafi, M. Shamanian, R. Emadi, N. Saeidi, "A novel and simple technique for development of dual phase steels with excellent ductility", Materials Science & Engineering A vol. 680, 197-202, 2017.
- [3] N. Ormsuptave, V. Uthaisangsuk, "Modeling of bake-hardening effect for fine grain bainite-aided dual phase steel", Materials and Design, vol.118, 314-329, Jan. 2017.
- [4] B. Anbarlooie, H. Hosseini-Toudeshky, J., Kadkhodapour, "High cycle fatigue micromechanical behavior of dual phase steel: Damage initiation, propagation and final failure", Mechanics of Materials, vol.106, 8-19, Jan. 2017.
- [5] A.Ghatei Kalashami, A. Kermanpur, E. Ghassemali, A. Najafizadeh, Y. Mazaheri, "The effect of Nb on texture evolutions of the ultrafine-grained dual phase steel fabricated by cold rolling and intercritical annealing", Journals of Alloys and Compounds vol. 694, 1026-1035, Oct.2016
- [6] B. Demir, "Çift fazlı çelik üretimi, çift fazlı çeliklerde martenzit hacim oranı ve morfolojisinin çekme özellikleri üzerine etkisi", Master thesis Gazi University Ankara, Turkey 1997.
- [7] R. Pradhan,, "Continuous Annealing Steel", ASM Metal Handbook Heat Treating Volume 4, U.S.A. The Materials Information Company, 135-160, 1993.
- [8] D. Dong,, Y. Liu, Y. Yang, J. Li, M. Ma, T. Jiang, "Microstructure and dynamic tensile behavior of DP600 dual phase steel joint by laser welding", Materials Science & Engineering A, vol.594, 17-25, 2014.
- [9] G. Zhang , X. Yang , X. He, J. Li , H." Enhancement of mechanical properties and failure mechanism of electronbeam welded 300M ultrahigh strength steel joints" Materials and Design vol. 45, 56-66, 2013
- [10] S.S. Nayak, V.H. Baltazar Hernandez, Y. Okita, Y. Zhou., "Microstructure-hardness relationship in the fusion zone of TRIP steel welds", Materials Science & Engineering A, vol. 551, 73-81, May 2012.
- [11] J. Wang , L. Yang, M. Sun, T. Liu, H. Li, "A study of the softening mechanisms of laser-welded DP1000 steel butt joints", Materials and Design vol. 97, 118-125 Feb. 2016.
- [12] N. Kahraman, B. Gülenç, *Modern Kaynak Teknolojisi*, 2nd. Ed, Ankara, Turkey, Epa-Mat, 2013.

Aging of A356 aluminum billets produced by semi-solid metal processing

Ridvan Gecu¹, Serhat Acar¹, Alptekin Kisasoz¹, Kerem Altug Guler¹, Ahmet Karaaslan¹

**Yildiz Technical University*

Yildiz Technical University, Department of Metallurgical and Materials Engineering, Istanbul, Turkey

gecur@yildiz.edu.tr, seacar@yildiz.edu.tr, akisasoz@yildiz.edu.tr, kguler@yildiz.edu.tr, karaas@yildiz.edu.tr

Abstract— The effects of artificial aging on A356 aluminum billets were investigated. Low superheat casting (LSC) was performed in order to prepare appropriate samples by equiaxed grains formation instead of dendrites for further semi-solid metal process. Specimens were cast at 635°C in LSC technique and non-dendritic grains were obtained. Produced billets were reheated at 595°C where both solid and liquid phases of the alloy coexist. Samples were held in this semi-solid region for varied times followed by quenching. After reheating step, specimens were solution treated, water-cooled and artificial aged. The microstructural evaluation and related hardness changing of reheated billets were examined by image analyser assisted light optical microscopy and Brinell hardness measurements. Aging process leads to attain relatively uniform microstructure with newly formed precipitates which provide increase in hardness considerably.

Keywords— Semi-solid metal processing, low superheat casting, aging, aluminum, A356 alloy

I. INTRODUCTION

Aluminum and its alloys have been gained very significant importance in past decades for automotive, construction and aerospace industries due to their excellent specific mechanical properties and good corrosion resistance to increase fuel efficiency by constructing lightweight structures [1, 2]. In order to manufacture these alloys with desired properties, microstructure should be homogenous, non-dendritic and non-porous. In favour of obtaining non-dendritic feedstock, semi-solid metal (SSM) forming techniques are preferable rather than conventional production routes [3]. These non-dendritic SSM starting materials can be attained by different methods like agitating liquid state methods such as magnetohydrodynamic stirring process [4], non-agitating liquid state methods such as addition of grain refiners [5] and gas atomized spray forming [6] or solid state processes like stress induced melt activated (SIMA) process [7] and recrystallization and partial melting (RAP) [8] process.

Low superheat casting (LSC) process is low cost and environment friendly method for producing feedstock materials with spheroidized microstructure concomitantly thixotropic features for SSM forming techniques [9]. This process does not need any external force and requires low time per cycle, therefore becomes much practical among the other alternative processes [9, 10]. Along this procedure, material is superheated

and solidified at slightly above the liquidus temperature and reheating step after solidification provides equiaxed non-dendritic microstructure [11].

T6 heat treatment is another way to control microstructure and improve mechanical strength by precipitation hardening mechanism in solid state [12, 13]. This process consists of solution treatment, quenching and artificial aging steps. Solution treatment with optimum conditions also involves homogenization of α -Al phase and spheroidisation of Si particles without grain coarsening [14].

In this study, hypoeutectic A356 aluminum alloy was chosen owing to its relatively high volume of Al-Si eutectic and wide solidification range. Billets produced by LSC were reheated at semi-solid state, quenched and T6-treated. As-cast, reheated and T6-treated microstructures and related Brinell hardness measurements of A356 alloy were researched.

II. EXPERIMENTAL

1000 g A356 casting alloy was melted in a resistance furnace. Chemical composition of A356 alloy was given in Table 1. Molten alloy was cast into a permanent mould and billets were manufactured via LSC method. LSC temperature was chosen as 635°C which is slightly above the liquidus temperature of subjected alloy. Billets were sliced into cylindrical pieces with the dimensions of 40 mm diameter and 40 mm height. One as-cast specimen was kept as a reference for further processes and others were reheated for 20, 40, 60 and 80 min at 595°C that both liquid and solid phases of alloy coexist. After reheating, samples were quenched and subjected to subsequent T6 heat treatment process. Solution treatment and artificial aging were performed at 535°C for 4 h and 180°C for 4 h, respectively. Sample surfaces were grinded, polished and etched for microstructural analysis. 0.5% HF solution was used as an etchant and micrographs were taken with Nikon Eclipse MA100 light optical microscope. Brinell hardness measurements of quenched, solution treated and aged specimens were carried out via universal test device with 62.5 kg load and 2.5 mm tip diameter.

Table 1. Chemical composition of A356 alloy (wt.%)

Si	Fe	Cu	Mn	Mg	Zn	Ti	Al
7.29	0.14	0.01	0.03	0.35	0.01	0.12	Bal.

III. RESULTS AND DISCUSSION

SSM methods are performed to prevent dendritic structure which is naturally formed by conventional casting methods. LSC technique is a kind of SSM technique to produce billets with equiaxed formation. Reheating after LSC provides spheroidizing of equiaxed grains. The micrographs of as-cast and reheated samples that produced by LSC were given in Fig. 1. α -Al (white region), eutectic (dark gray region) and polyhedral Si (bluish particles) phases were observed. A356 is a hypoeutectic Al-Si alloy which flows sufficiently. Thus, LSC method was successfully implemented to samples without any pouring problem. Non-dendritic spherical α -Al phase encircled by Al-Si eutectic structure was obtained in as-cast specimen that can be seen in Fig. 1(a). LSC process recomposed the α -Al phase by suppressing dendritic growth. According to Fig. 1(b) and 1(c), reheating changed as-cast structure with eutectic deterioration. Polyhedral Si formation was initiated by released Si from eutectic structure at 20 min reheated sample. For 40 min reheated sample, eutectic structure was completely transformed into polyhedral Si and the amount of polyhedral Si particles was increased due to relatively higher reheating time. Partial remelting of eutectic may be the reason of this situation. Spheroidization of α -Al and coarsening of polyhedral Si particles were observed at 60 min reheated sample (Fig. 1(d)). Contrary to other samples, for 80 min reheated one, eutectic was completely remelted and solidified as similar to as-cast microstructure, except α -Al coarsening. It can be seen in Fig. 1(d) and 1(e), some eutectic particles with rounded geometry were formed inside α -Al due to the grain growth and the coalescence of α -Al. As a consequence, eutectic was entrapped there.

T6 heat treatment was conducted on reheated samples to enhance mechanical properties. T6 heat treatment includes solution treatment and artificial aging steps. The micrographs of solution treated samples were given in Fig. 2. Solution treatment caused much more uniform distribution of eutectic than non-treated samples. Compact eutectic structure was transformed into sparse distribution. With increasing reheating time, some amount of Si particles were dissolved in α -Al phase while the rest of them was coalesced with each other during solution treatment.

Specimens were artificially aged at 180°C for 4 hours after solution treatment. Aged micrographs of A356 alloys were shown in Fig. 3. It can be obviously seen that α -Al grains were grown after aging. New smaller precipitates were obtained inside α -Al and especially for 60 and 80 min reheated samples, entrapped eutectic was broken down due to the heat exposure for a long time. Refinement of eutectic distribution was preserved same as in solution treated form.

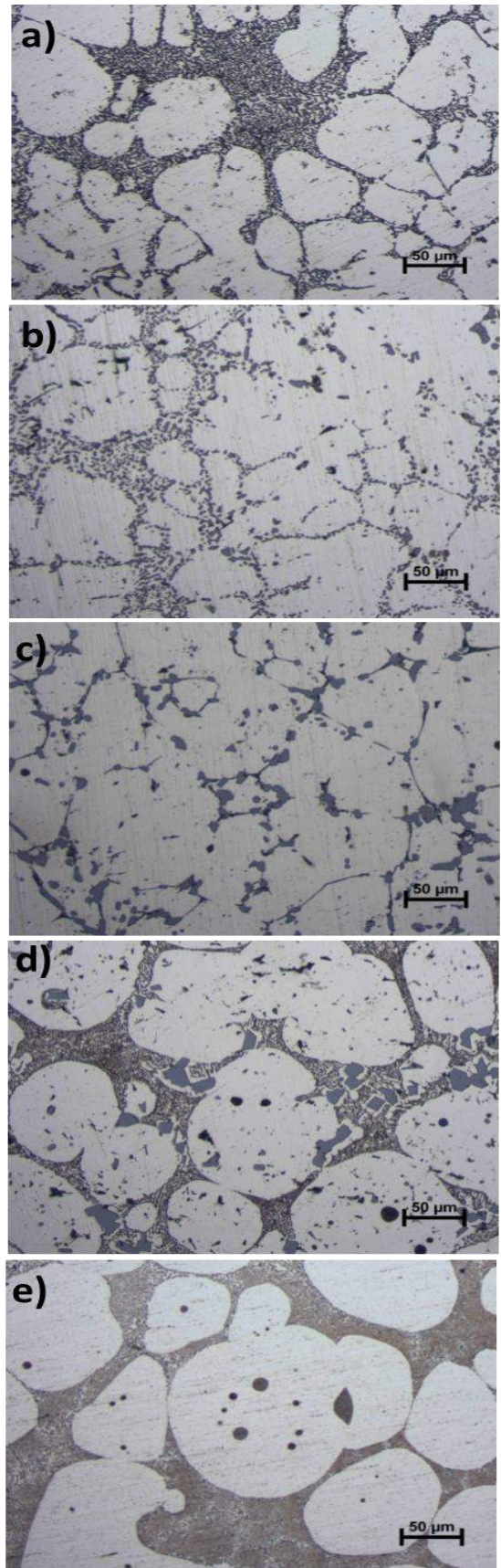


Figure 1. Micrographs of (a) as-cast, (b) 20 min reheated, (c) 40 min reheated, (d) 60 min reheated, (e) 80 min reheated samples

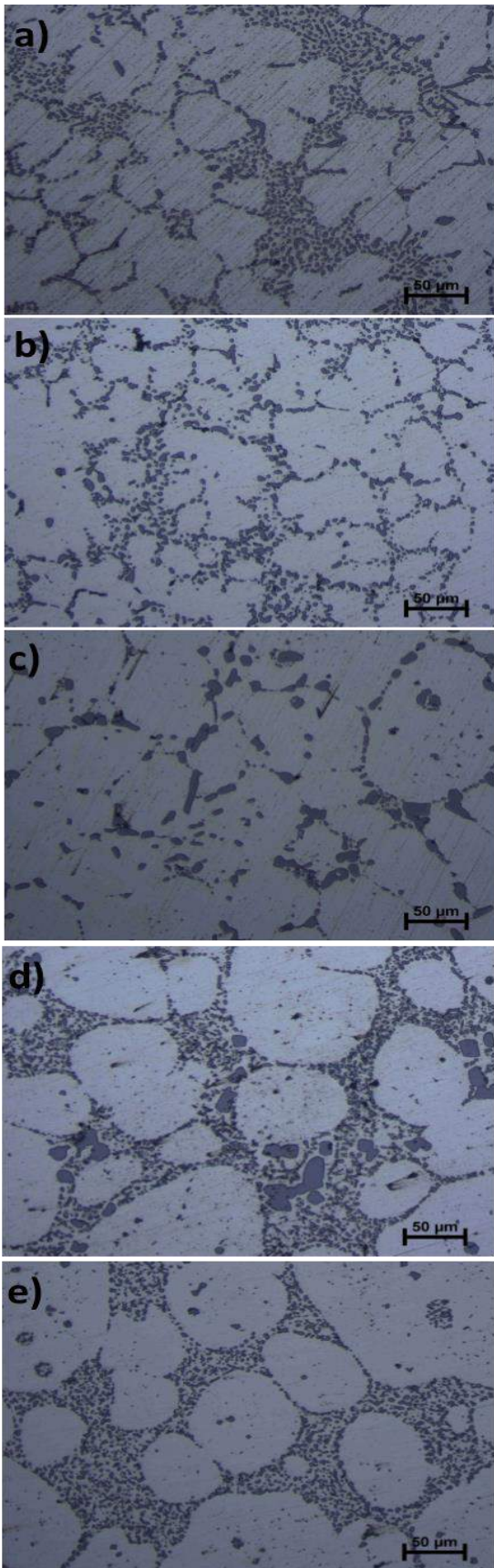


Figure 2. Micrographs of solution treated (a) as-cast, (b) 20 min reheated, (c) 40 min reheated, (d) 60 min reheated, (e) 80 min reheated samples

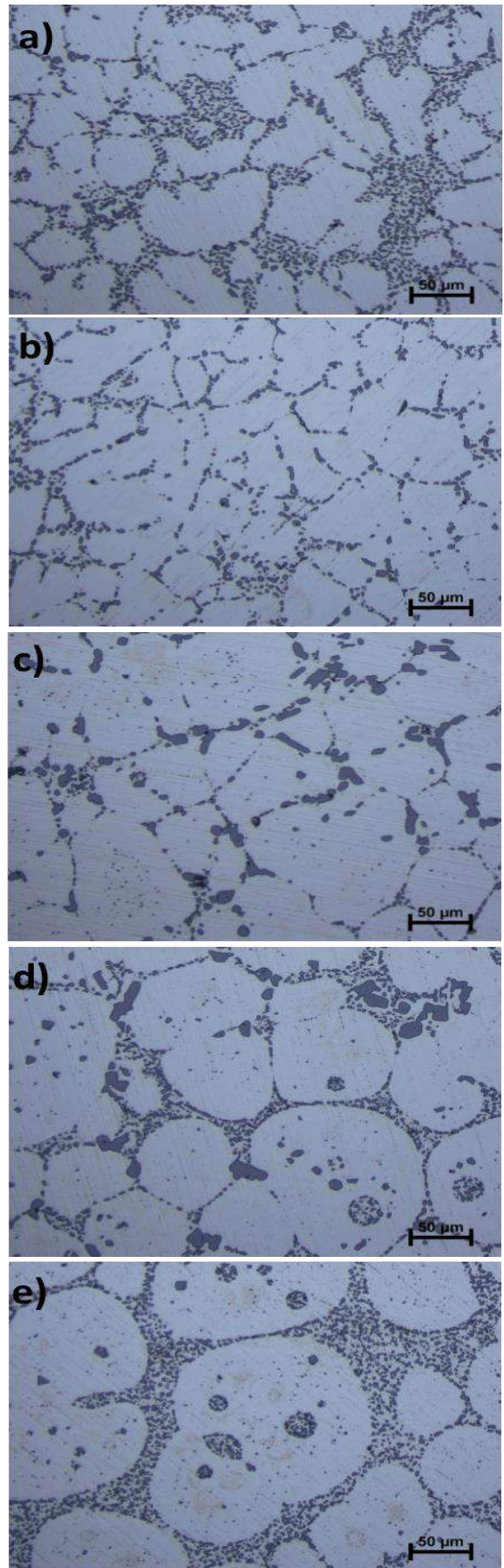
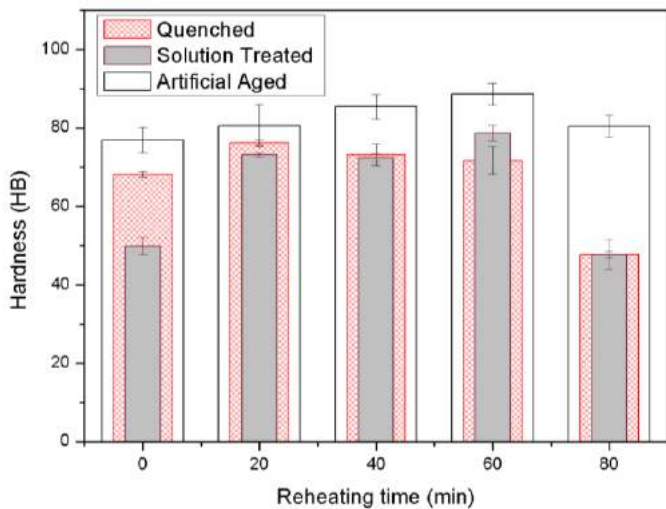


Figure 3. Micrographs of artificial aged (a) as-cast, (b) 20 min reheated, (c) 40 min reheated, (d) 60 min reheated, (e) 80 min reheated samples

Brinell hardness measurement was carried out after microstructural investigations. The results of hardness tests were shown in Fig. 4. For reheated A356 samples, hardness values were varied from ~68 HB to ~76 HB except 80 min reheated one which has 47 HB hardness. This dramatical decrease was resulted from the coarsening of α -Al grains. 20, 40 and 60 min reheated samples had higher hardness than as-cast specimen due to existence of polyhedral Si particles in microstructure.

After solution treatment, the hardness of as-cast sample was significantly decreased while 20 and 40 min reheated samples were decreased slightly. A considerable increase in 60 min reheated sample was obtained. Only 80 min reheated sample preserved its former hardness. This hardness variation can be explained by distinctness of released Si amount from eutectic and α -Al grain growth rate between samples.

Hardness values were increased after artificial aging for all samples. The most dramatic increase occurred in 80 min reheated specimen. However, its hardness was obtained less than it should be. 80 min reheating caused grain growth at first and grains were continued to grow during heat treatment process owing to heat input. Hardness values were affected by this excessive grain growth. Newly formed precipitates along grain boundaries and inside α -Al may be responsible to the increase in hardness after aging for all samples. It can be concluded that 4 hour-treatment was suitable to improve mechanical features for A356 alloy that produced by SSM technique.



IV. CONCLUSIONS

A356 aluminum billets were successfully manufactured by LSC process without any pouring problem. LSC rearranged α -Al formation by preventing dendritic growth. Accordingly,

spherical α -Al grains were formed. Reheating samples at semi-solid state caused to alteration of microstructure with eutectic deterioration. Released Si atoms from eutectic initiated polyhedral Si formation at grain boundaries and the amount of polyhedral Si was increased with increasing reheating time, except 80 min reheated sample which solidified as similar to as-cast structure because of complete remelting of eutectic during reheating. Solution treatment provided sparse distribution of eutectic instead of compact distribution. After artificial aging, refinement of eutectic was preserved and newly formed precipitates were obtained inside α -Al and along grain boundaries. Aging provided improvement of hardness values of non-treated samples.

REFERENCES

- [1] J. Hirsch, "Recent development in aluminium for automotive applications", *Trans. Nonferrous Met. Soc. China*, vol. 24(7), pp. 1995–2002, 2014.
- [2] T. Dursun and C. Soutis, "Recent developments in advanced aircraft aluminium alloys", *Mater. Des.*, vol. 56, pp. 862–871, 2014.
- [3] D. H. Kirkwood, "Semi-solid metal processing.", *J. Japan Inst. Light Met.*, vol. 45, pp. 346–354, 1994.
- [4] B. A. Sivak, V. G. Grachev, V. M. Parshin, A. D. Chertov, S. V. Zarubin, V. G. Fisenko, and A. A. Solov'ev, "MHD processes in the electromagnetic stirring of liquid metal in continuous section and bloom casters", *Metallurgist*, vol. 53, pp. 469–481, 2009.
- [5] B. S. Murty, S. A. Kori, and M. Chakraborty, "Grain refinement of aluminium and its alloys by heterogeneous nucleation and alloying", *Int. Mater. Rev.*, vol. 47, pp. 3–29, 2002.
- [6] G. S. E. Antipas, "Review of gas atomisation and spray forming phenomenology", *Powder Metallurgy*, vol. 56, pp. 317–330, 2013.
- [7] E. Tzimas and A. Zavaliangos, "A comparative characterization of near-equiaxed microstructures as produced by spray casting, magnetohydrodynamic casting and the stress induced, melt activated process", *Mater. Sci. Eng. A*, vol. 289, pp. 217–227, 2000.
- [8] M. Margarido and M. H. Robert, "Production of rheocast slurries by partial melting through alternative thermomechanical treatments", *J. Brazilian Soc. Mech. Sci. Eng.*, vol. 25, pp. 207–214, 2003.
- [9] T. S. Mahmoud, E. Y. El-Kady, H. M. Zakaria, A. El-Awady, and M. F. El-Sherbiny, "Optimization of the low superheat casting process parameters for producing of thixotropic A356 alloy feedstock", *Mater. Sci. An Indian J.*, vol. 14, pp. 246–254, 2016.
- [10] H. Guo, X. Yang, and B. Hu, "Rheocasting of a356 alloy by low superheat pouring with a shearing field", *Acta Metall. Sin.*, vol. 19, pp. 328–334, 2006.
- [11] W. W. Mullins and R. F. Sekerka, "Morphological Stability of a Particle Growing by Diffusion or Heat Flow", *J. Appl. Phys.*, vol. 34, pp. 323–329, 1963.
- [12] T. A. Costa, M. Dias, L. G. Gomes, O. L. Rocha, and A. Garcia, "Effect of solution time in T6 heat treatment on microstructure and hardness of a directionally solidified Al–Si–Cu alloy", *J. Alloys Compd.*, vol. 683, pp. 485–494, 2016.
- [13] M. Zhu, Z. Jian, G. Yang, and Y. Zhou, "Effects of T6 heat treatment on the microstructure, tensile properties, and fracture behavior of the modified A356 alloys", *Mater. Des.*, vol. 36, pp. 243–249, 2012.
- [14] D. L. Zhang, L. H. Zheng, and D. H. StJohn, "Effect of a short solution treatment time on microstructure and mechanical properties of modified Al–7wt.%Si–0.3wt.%Mg alloy", *J. Light Met.*, vol. 2, pp. 27–36, 2002.

Industrialization and Cancer Risks

Kasım YILMAZ*, Işıl Işık ANDSOY⁺

*Karabuk University, TOBB, Technical Science
Occupational College, Karabuk, TURKEY
kasimyilmaz@karabuk.edu.tr

⁺Karabuk University, Faculty of Health Sciences,
Karabuk, TURKEY
isilandsoy@gmail.com

Abstract- Cancer is one of the most important health problems today, due to high incidence of mortality. Approximately 7.6 million people die from cancer every year in the world and the cancer incidence increases over time. Beside life style-related factors, environmental factors affect cancer development. According to the World Health Organization, new chemical substances are synthesized every year without adequate investigation about their toxicity. Among industrial workers, an increase has been observed in bladder and other organ cancers, especially lung cancer. Studies find increased incidence of lung cancer among workers in iron mines, steel foundries and industries in which workers are exposed to iron oxides such as the iron and steel industry. Most studies state the exposure to metal fumes, crystalline silica dust and pyrolysis products emitted under heat, particularly polycyclic aromatic hydrocarbons (PAHs) used in iron and steel industry cause cancer. There are also some studies which state that there is no clear relationship between the risk of cancer and the industrialism. In this review, the relationship between industrialization and cancer risk is discussed in the light of current literature.

Keywords- Industrialization, Cancer, Relations Between Industrialization and Cancer

I. INTRODUCTION

Cancer is one of the most important health problems of our time due to its' high incidence and mortality rates. About 7.6 million people die from cancer every year in the world, and the rate of cancer cases increases rapidly [1]. The World Health Organization estimates the pathogenesis as occupational or environmental factors for 80% of total cancer cases. Each year many new chemical substances with possible toxic effects are synthesized without adequate examination process. Many hazardous chemicals are released into the environment during industrial processes and may threaten employees' health around the workplace [1-5].

II. CANCER RISKS

Environmental factors play an important role in addition to lifestyle-related factors in cancer development. In parallel with rapid developing technology, increasing exposure to environmental carcinogens is a factor that increases the cancer incidence. Air pollution as leading environmental factor causes respiratory and heart diseases. In terms of substances that cause cancer, World Health Organization (WHO) classifies air pollution in the same category with tobacco smoke, UV radiation and plutonium. The substances causing air pollution also cause mutation in the cells leading to cancer[3-12]. WHO has indicated that air pollutants cause primarily lung cancer, bladder and other organ cancers. WHO also reported 223,000

air-pollutant caused lung cancer patients died in 2010 around the world [1], [2]. In countries such as China and East Asia countries where experienced rapid industrializational progress, it is stated that the air pollution-related cancer death rates are higher. For our country, there couldn't be found enough data about air pollution related cancer cases.

Industrialization also enhanced cancer risk. The British physician Percival Pott's study about scrotum cancer among chimney sweepers in 1775 is between the first examples of reseachs in this field. Approximately 4-5% of cancer in humans originates from the effects of industrial factors. Today, studies on potential risk factors for cancer are being conducted intensively [5-10].

International Agency for Research on Cancer (IARC), a subsidiary of the World Health Organization states the substances used in the industry which cause cancer in human. IARC classifies harmful factors according to the properties of cancer-cause factors of chemicals, compounds and industrial processes in five groups [10-12]:

Group 1: Carcinogen in humans

Group 2A: Probably carcinogen in humans

2B: Possibly carcinogen in humans

Group 3: Not carcinogen in humans

Group 4: Probably no carcinogenic effects in humans

There are about 30 chemicals or physical factors in Group 1 and about 60 chemicals and factors in each of Group 2-A and Group 2-B, totally 150 chemicals, physical and biological factors all of which certainly or probably may cause cancer. Among these substances and factors most well knowns and frequently encountered ones are as follows:

a. Asbestos: It is formed in nature and composed of fibrous minerals. This substance was proven to cause lung cancer in the 1950s. In the industry white, blue and brown asbestos species have been used for various purposes.

b. Heavy metals and dusts: Arsenic, chromium, nickel and cadmium are the major carcinogenic metals. Lung, skin, bladder and liver cancers are observed at people who were exposed to arsenic in their occupational environment as in fur manufacturing, metallurgy, agricultural activities where pesticides used like viticulture. Lung and nasal sinus cancers are encountered at people who are exposed to chromium and its compounds in their work environment. Similar results are observed for people who are exposed to nickel.

In iron and steel industry, a considerable amount of fugitive dust is generated during manufacturing processes. Particularly polycyclic aromatic hydrocarbons (PAHs) emissions occur during coke production, sintering, casting, cooling and steel production processes. Also in this industry exposure to silica

dust, iron dust, cement dust, welding dust, coal dust, high temperature, wood dust, grinding dust, sulphate and sulfur provokes adverse effects in human health.

c. Polycyclic aromatic hydrocarbons (PAHs):PAHs are generated as the result of incomplete combustion of organic materials. Since they are present in very different compounds and compositions, their risks are difficult to be completely determined. In industrial processes where PAHs generated like aluminum production, gas production, coke production, foundry and tar distillation, increased risk of lung, skin and bladder cancers are observed at people exposed to PAHs[9-15].

It is reported that exposure to pyrolysis products emitted during heating the mold binders and seeds like metal steam, crystalline silica dust and polycyclic aromatic hydrocarbons (PAHs) cause cancer. It is also emphasized that exposure to radon in iron mines, diesel exhaust fumes and cigarette smoking are other important factors that increase this risk[11-15].

d. Benzene: It is a frequently used chemical in processing of many petroleum products, chemicals and solvents, and also intensively used in shoes and rubber industry. Benzene causes plague anemia and leukemia.

e. Aromatic amines: Amino benzene (aniline) is the simplest substance in the group of aromatic amines obtained by amine (NH₂) attachment to the benzene molecule. In this group there are also substances other than aniline such as benzidine, alpha and beta naphthyl amine. These materials are widely used in the paint industry and in tire manufacturing.

f. Benzo(a)pyrene and Benzo(a)anthracene: Soot and tar generated by the combustion of coal, wood or petroleum products and tobacco smoke contain these substances. They are generally used in asphalt road construction and roof insulation. They cause cancer through contact. Vapor inhalation of those leads to lung cancer.

g. Chrome: It is used in leather industry, chrome plating and stainless steel making processes. It causes lung cancer.

h. Vinyl chloride: It is used in plastic industry. It causes liver cancer[9-11].

It is expressed that exposure to radon and diesel exhaust fumes in iron mines and tobacco smoke are also factors that increase cancer risk. It is emphasized that unless protective applications used in working environment in iron and steel industry and foundries, workers health problems including primarily cancer will increase[10],[11-16].

Although there are studies which show that there is no clear relationship between cancer risk and industrialism[3],[4-19], there are a number of studies that points that industrialization as caused an increase in exposure to carcinogens [1], [16-18].

III. CONCLUSIONS

Despite the uncertainties, many chemicals and physical factors, in paralel with industrialization, may cause cancer because of their mutagenic or promoting properties and carcinogenic effects. In this context, it is important to take urgent action plans to raise social awareness and to prevent cancer in our country.

REFERENCES

- [1] [http://www.who.int/gho/publications/world_health_statistics/2016/dashboard /en/](http://www.who.int/gho/publications/world_health_statistics/2016/dashboard/en/) accessed date: 12.02.2017
- [2] IARC Monographs on the Evaluation of Carcinogenic Risks to Humans, Volume 82, Some drinking water disinfectants and contaminants, including arsenic. Lyon, France: International Agency for Research on Cancer , 2014.
- [3] T.C. Sağlık Bakanlığı, Türkiye Halk Sağlığı Kurumu, Kanser Daire Başkanlığı. <http://kanser.gov.tr/kanser.html>, Erişim: 07.01.2017.
- [4] Ivanov, I.D, Straif, K. Prevention of Occupational Cancers. The Global Occupational Health Network. GOHNET Newsletter. World Health Organisation, 2006, issue: 11.
- [5] Steenland, K., Burnett, C., Lalic, N., Ward, E., Hurrell, J (2003). Dying for work: The magnitude US mortality from selected causes of death associated with occupation. *Am J Ind Med*; 43(5): 461-82.
- [6] Tanır F. Sanayileşme ve kansinöjenler,17.Ulusal Halk Sağlığı Kongresi Kitabı, 2014, Edirne, p.134-140.
- [7] Keskin Ö, Aksoy S. Occupation related cancers, *Hacettepe Tıp Dergisi* 2011; 42:173-179.
- [8] Clapp RW, Howe GK, Jacobs MM. Environmental and occupational causes of cancer: A call to act on what we know. *Biomedicine and Pharmacotherapy* 2007; 61, 631-639.
- [9] Siemiatycki J, Richardson L, Straif K, Latreille B, Lakhani R, Campbell S et al. Listing occupational carcinogens. *Environmental Health Perspectives* 2004; 112(15):1447.
- [10] Boffetta P. Epidemiology of environmental and occupational cancer. *Oncogene* 2004; 23, 6392-6403.
- [11] Turgut NH, Kara H. Heavy Metals and Cancer Risk, *Türkiye Klinikleri J Vet Sci Pharmacol Toxicol-Special Topics* 2016;2(3):1-7
- [12] Siemiatycki J, Richardson L, Straif K. Listing occupational carcinogens. *Environ Health Perspect* 2004; 112:1447-59.
- [13] Bilir N. Mesleki kanserler, Bilir N, Yıldız AN (editörler). İş sağlığı ve güvenliği. Ankara: Hacettepe Üniversitesi Yayını, 2004: 235-43.
- [14] Alver E, Demirci A, Özçimdir M. Polycyclic Aromatic Hydrocarbons and their Effects on Health, *MAKÜ FEBED* 2012; 3(1): 45-52.
- [15] Zhang, J.L.G., Li, X.D., Qi, S.H., Liu, G.Q., Peng, X.Z. Source seasonality of polycyclic aromatic hydrocarbons (PAHs) in subtropical city,Guangzhou, South China. *Science of the Total Environment* 2006;355, 145-155.
- [16] Hoshuyama, T., Pan, G., Tanaka, C., Feng, Y., Liu, T., Liu, L., ... & Takahashi, K. "Mortality of iron-steel workers in Anshanl China: A retrospective cohort study. *International journal of occupational and environmental health*", 12(3), 193-202. (2006).
- [17] Tsai, J. H., Lin, K. H., Chen, C. Y., Ding, J. Y., Choa, C. G., & Chiang, H. L. "Chemical constituents in particulate emissions from an integrated iron and steel facility. *Journal of Hazardous Materials*", 147(1), 111-119. (2007).
- [18] Khaparde, V. V., Bhanarkar, A. D., Majumdar, D., & Rao, C. C. "Characterization of polycyclic aromatic hydrocarbons in fugitive PM 10 emissions from an integrated iron and steel plant. *Science of the Total Environment*", 562, 155-163. (2016).
- [19] Bourgard, E., Wild, P., Courcot, B., Diss, M., Ettlinger, J., Goutet, P., & Rohn-Janssens, M. P. "Lung cancer mortality and iron oxide exposure in a French steel-producing factory". *Occupational and environmental medicine*. (2008).

Safe Behaviour Change to Release of OHS Culture in the Iron and Steel Sector

Cumhur KOCAMAN¹, Ulus Kürşat ŞERİFOĞLU¹, Erdoğan KANCA², Ali GÜNEN³

¹ Iskenderun Iron and Steel Co., Iskenderun, Hatay

² Mechanical Engineering, Faculty of Engineering and Natural Sciences, Iskenderun Technical University, Hatay, Turkey

³ Metallurgical and Materials Engineering, Faculty of Technology, Iskenderun Technical University, Hatay, Turkey

Corresponding author: ali.gunen@iste.edu.tr

Abstract - A key factor in ensuring sustainable occupational health and safety culture is an established occupational health and safety culture. Occupational health and safety culture is the whole set of behaviours feeling all over the organization in terms of approach, perception, behaviour, commitment.

Proactive, that is to say, "the accident without seeing the missing and healing" approach. In order to establish a proactive environment approach, the concept should be supported by national / internationally accepted practices and specific methods. Various materials can be used at this stage. For example; trying to make determinations about unsafe behaviors and / or situations with (more) eyes at a certain point in the organization. In this way, many employees wearing OHS glasses are provided and serious improvements can be made.

Another case study is the study of the reports of the insufficiently cheap unsafe conditions and behaviors, which are termed "near miss".

It is the last point where employees are warning each other about insecure approaches and work, that safety behavior is not a "natural drive", but that every employee wakes up each other. In this regard, the bradley curve suggests that a proactive and sustainable OHS approach can achieve the "0" accident target, stimulating each other as a living organism composed of cells. It has been observed that the OHS culture was placed in the organization by various applications mentioned above.

Keywords - Health and safety, safety culture, proactive behaviour

I. INTRODUCTION

OHS culture is a key factor in ensuring sustainable OHS culture. In this context, the concepts of OHS culture, OHS climate concepts, which are thought to be the sub-layers of OHS culture, are antagonistic. The use of OHS culture and OSH climate concepts is documented after the major disasters in the International Atomic Energy Agency (IAEA) and the Organization for Economic Co-operation and Development (OECD), nuclear power plant Chernobyl. [1]

OHS culture or Safety culture is the whole set of behaviours-perceptions affecting every part of the organization, feeling all over the organization, approach, perception, behaviour, commitment. [2]

The concept of OHS climate is a little different from culture, and it is a sign of ensuring the parity between the practices of the undertakings and the practices of the organization in its safety approach. To put it more clearly, how the concept of safety undertaken in the organization is perceived by field workers. For example; If you are declared

that you need to use Personal Protective Equipment (Safety Belt) with high work and if large and small insecure approaches are then violated by subordinate and / or mid-level managers to complete the job on site, then the concept of safety climate understood by employees is understood.

Factors affecting OHS climate include; The importance of OHS trainings, the impact of OHS on work, the implementation of OHS commitments in the field, managerial factors, the approach of top management, Many critical factors are emerging.

Many instruments can be used so that the significance and emphasis of the OHS concept can be felt not only by the top management, but also throughout the organization. One of these instruments is Proactive, which means "seeing and healing without an accident". In order to establish the proactive OSH approach, the concept should be supported by national / internationally accepted practices and specific methods. Various materials can be used at this stage. For example; Attempting to make inspections about unsafe behaviors and / or situations with (more) eyes at a certain point in the organization. In this way, many employees wearing OHS glasses are provided and serious improvements can be made.

Another case study is the study of the reports of the "unfinished" unsafe conditions and behaviours, which are described as "runaway" and which are described as "cheaper drowning", "salvation".

Reporting these inexpensive and accident-free events that are described as "survivors" and providing the necessary improvements will provide the organization with free learning and correction and will be a stepping stone to the accident-free production.

Establishment, use and dissemination of such OHS instruments will primarily affect the "climate" in the organization. Occupations of OHS will gradually be traced to these changes. Random field detections, in molar conversations, the difference between old and new perception will be seen.

In a certain matter, even a certain time is needed to talk about the existence of a cult, and the footprints of change are called "climate". Organizations, through their commitments, practices and approaches, will primarily impact on the "climate" and create "Organizational OHS Culture" through stable practices and systematic approaches.

The traces of the formation of the OHS culture are striking with their approach and safe practices. In Random Field Controls, observing safe behavior of employees performing

certain tasks is another indication of approaching desired results.

It is the last point where employees are warning each other about insecure approaches and activities, not the "natural distinct" of safe behavior, but the desire of every employee to wage each other.

"Zero Accident" target is an accidental objective in the work of the employees working in the OHS approach. Only an administrative / managerial measure and a written instructional approach will help achieve the desired goal. The Bradley curve suggests that a personal, proactive and sustainable OHS approach can achieve the "0" accident target by warning the entire organization that it is not enough to reach the "0" accident target on a personal basis.

In the iron and steel sector, OHS culture is spread and safe behavior is exhibited; The importance of companies' approach and priorities, the importance of OHS systematics, the involvement of employees in proactive OSH approach, and the effective use of intracompany communication facilities.

A. Previous Works

It is possible to get the desired accident rate rates in the organizations, to make safe production and to provide OHS culture. OHS culture is the whole of perceptions, approaches and behaviors that are felt individually and as a group from top to bottom in every aspect of the organization. Formation, session and propagation takes time.

In addition to this concept, the concept of safety climate is also included. Safety climate is concerned with what employees perceive and feel from all of the OSH activities that are mentioned. The climate is influenced in the future, while the cultures have a characteristic from the past [3];

Continuous development phase (Level 5) means that the targets are now "0". In this phase, all work accidents are being followed up, being examined and no major work accidents are experienced. It is important to take the necessary measures to ensure the commitment, participation and continuity of the management during the formation and development of all these phases. For the development of OHS culture, it is a must to achieve harmony and harmony between all these levels.

Another study in the formation of OHS culture is given below [4];

Reactive approach from the pathological approach, computational approach from the reactive approach, proactive approach from the computational approach, generative (productive) approach from the proactive approach, that is, high reliability approach is similar to the same parameters in the transition phase. In the pathological approach part, management blames the employees for the occurrence of work accidents. The management department does not hold itself responsible at this stage. In the reactive category, recurring accidents are continuing and although OHS is an important issue, sufficient results can not be obtained. In the computational approach, quantitative risk assessment techniques are used and management uses these data for decision making / calculation. Individuals are not exactly part of the OHS system. In the proactive category, OHS has been the subject of management and first level managers. Despite reaching the desired OHS data, unexpected accidents occur. In the generative (category) category, OHS is fully committed to every part of the organization. The organization is always involved in the prevention of potential workplace accidents. Consistent approach and accountability in OHS provide the accessibility to the desired approach.

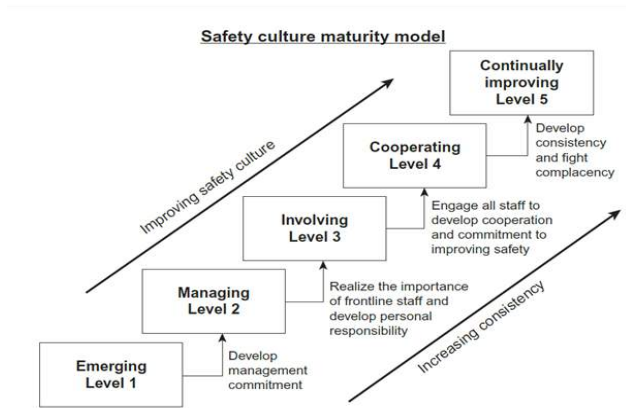


Figure-1; Safety Culture Maturity Model

In the given example, the part indicated as the initial stage (Level 1) for the development of OHS culture is the safety approach and the consciousness of weakness. The OSH support is the weakest. The managerial stage (Level 2) is the support of management but the predominantly reactive approach is proactive approach. In the part defined as the participation phase (Level 3), there is a decrease in the accidents but it is the approach to the improvement and improvement of the employees due to participation in the first part of the managerial stage. In the case of co-operation (Level 4), employees have begun to grasp the importance of the OSH approach. First-tier managers are making more effort to develop the OHS approach.

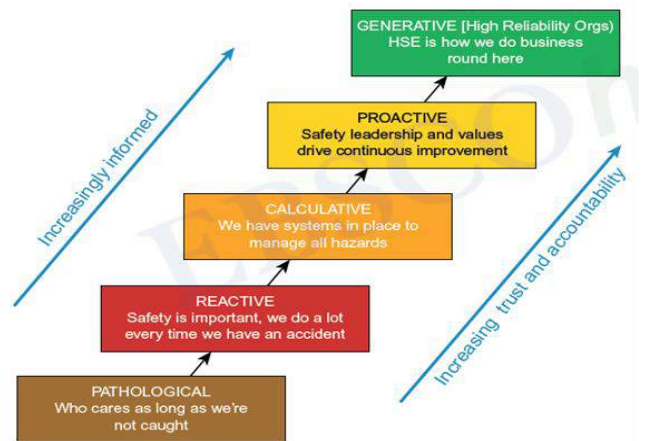


Figure-2; Hearts & Minds Emniyet Kültürü Modu



Figure-3; DuPont Safety model

In order to achieve excellence in the OHS approach, the system consists of 22 elements in four dimensions: culture, activity, work and technology. In the DuPont system [5], it is stated that both the OHS leadership and Operational Excellence must be carried out together for the 22-element approach. In addition to the management's commitment to achieve the "0" accident target, the importance of culture, technology, facilities and employee-based factors is emphasized. In the Bradley curve on DuPont's OHS approach to culture exchange for excellence, the OSG issue has been delegated to the manager of Occupational Health and Safety in the reactive category.

Management's true sense of approach, participation and employee perception are insufficient. In the dependent category, the rule and procedural approach began to gain weight, with a small positive increase in management commitment. OHS trainings have increased. In the independent category, the OHS approach has gradually begun to internalize. Habits, work techniques have begun to improve. In the interdependent phase, employees have started to alert each other to safe approaches and work and have made it part of the work of the OHS issue culture [6];

- Providing clear and clear communication for the development of the OHS Approach, asking employees questions about the OHS dimension,
- To be flexible and flexible towards new and changing situation
- Vigilance / alertness against urgent / unwanted situations

There are various measures in the assessment of companies' OHS approach, including weak, good or world-class companies. Preliminary and post-visual indicators also play a role in the observation of OHS culture. A good OHS culture can be assessed by data showing reduced job accidents, increased profitability due to reduced accidents, compliance with standards and procedures, and a multitude of good practices. In the weak OSH culture, backward indicators that measure the increase in work accident data come to the forefront. Interviews with employees, field trips, analysis with questions, etc. Methods can be used to analyse the organization's OSH culture. Cultural change requires behaviour and change of mentality.

The framework for the characterization of the safety culture developed by the International Atomic Energy Agency (IAEA) is given below [6];



Figure-5; International Atomic Energy Agency Safety Culture Characteristics

In this developed approach; In the formation of a strong OHS culture; It is stated that integration of OSH into all activities, OSH approach is open to continuous learning, OSH approach is accountable, OSH expresses clear and open value for organization, and leadership in OSH approach should be expressed clearly. In the formation of strong OHS culture, it is important that the OHS priority, starting from the top of the organization to the bottom, actually spreads.

Glendon & Stanton 2000 assessed the levels of OHS culture as follows [8];



Figure-4; DuPont Bradley Curve, Cultural Change

Characteristics of good OHS culture [7];

- Commitment to the development of safe behaviors and approaches at all levels of the organization,

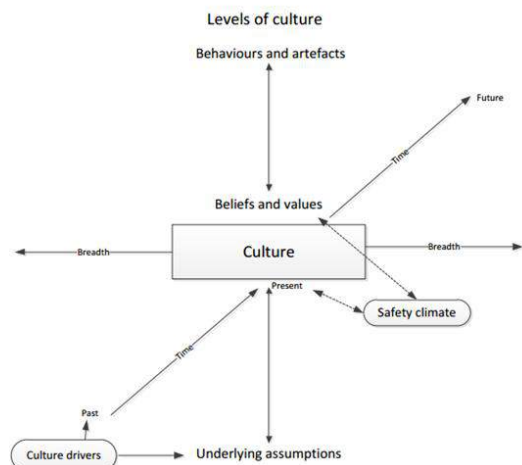


Figure-6; Levels of Culture, Glandon & Stanton

It is shared that the time is needed for the formation of the safety culture in the past, the safety climate under the safety culture, the values that are mutually influenced by the default values, and the behaviour and values affect each other in the formation of the safety culture.

The International Atomic Energy Agency emphasizes that the culture of safety culture organization must be a strong and sustainable process, that all activities should be the spotlight. Safety culture is the individual and collective behaviour of the organization.

Cooper's [9] interactive interaction model was assessed on an organization - employee - job basis. It was stated that employees' safety perception can be determined by psychometric measures, and how they interact with organizational and job-based factors.

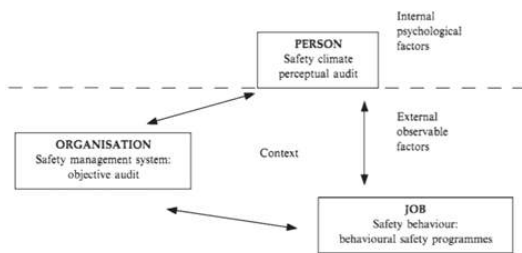


Figure-7; Interactive OSH Culture, Cooper

The graph below shows the relationship between the frequency of accidents for the US Department of Transportation and the safety climate for the million miles [10];

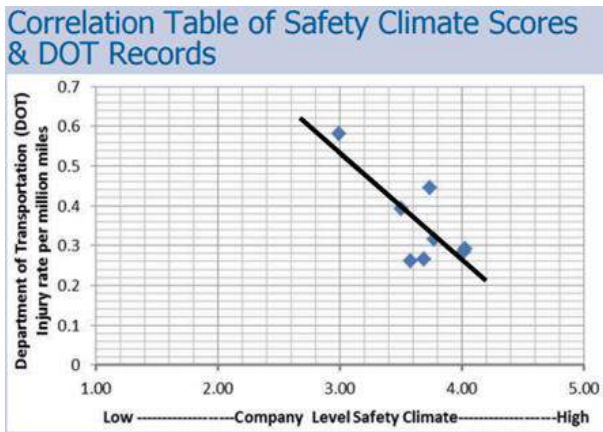


Figure-8; Correlation table of Safety Climate Scores & DOT Records

It is seen that the frequency of accidents after the development of safety climate is decreased.

For example, the World Steel Association has identified some principles of how the OHS approach should be on an individual and organizational basis, as companies that account for about 80% of the iron and steel production in the world are members. These principles are;

1. All injuries and work-related illness can and must be prevented.
2. Management is responsible and accountable for safety and Health performance.
3. Employee engagement and training is essential.
4. Working safely is a condition of employment.

5. Excellence in safety and Health supports excellent business results.
6. Safety and Health must be integrated in all business management processes.

As can be seen from these principles, items numbered 2-5-6 are actually the subject of the OHS leadership and the work done in this regard. The concept of safety leadership and "role model" is crucial for the establishment of an organizational approach and the provision of permanent behavioural change as well as the change of safety climate in the formation of safety culture.

The role of leadership is crucial in providing safety culture. In relation to the subject below, the approach indicated in the leadership guide in OECD high-risk industries is shown below [11];



Figure-11; OECD Leadership and Cultural Approach Model

In order to achieve the desired approach according to this approach, it is necessary to follow the activities of the OHS with the knowledge and competent employee factor in the engineering and Operational basis, under the roof of the leadership and culture, to perform the necessary actions, to develop the risk consciousness.

The OHS approach, which is laid by the executives of the organization and CEO, is an important indicator of the continuity of the approach. Integrating strategic objectives related to short, medium and long term OHS to all organizational systems (finance, human resources, purchasing, marketing, procurement etc.) will show the importance and importance of your leadership in OHS approach. The follow-up of this entire ISG approach on every managerial level and integrated systems will be an example of good safety leadership approach. Otherwise, the formation of the desired safety culture will not occur. It is imperative that the organization's safety commitment is reflected from the top to the bottom in all levels, it must be felt, measured and followed in all units and processes. The quality and continuity of this OHS approach is one of the important parameters in ensuring the realization of positive safety culture.

II. RESULT AND DISCUSSIONS

Some of the systematic methods used in Iskenderun Iron and Steel Co. in the ISG approach and discussed below;

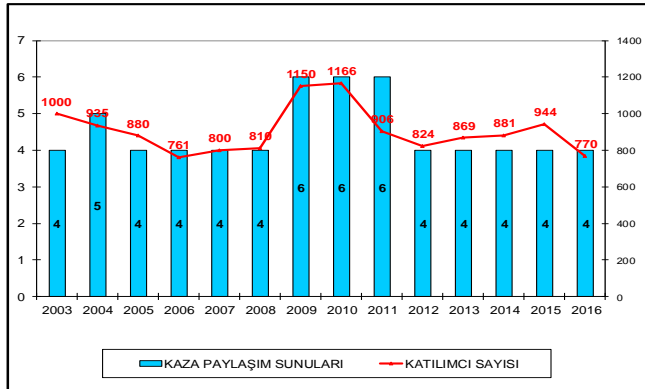
- Accident Sharing Presentations
- Safety Tours (Informed / Unannounced Safety Tours)
- 5S Cleaning and Layout Applications
- PPE (Personal Protective Equipment Commission)
- Reporting of Near Miss Events
- Reflex Measurements
- Reaction / Reactivity Questionnaire Applications
- Behaviour Oriented Safety Management Works On Blast Furnaces Dept.
- Individual Behaviour Based Development- Observation Project on Steel Making Plant Directorate

A. Accident Sharing Presentations

The job accidents that can be taken in the places of work and the accidents that happened to the accident are presented as presentations and the same type of job accident and the lectures are taken from the events of the ramen to share these work accidents with the employees so that they will not be lived again. Some photos are shared from accident sharing presentations below [12] ;



In the accident sharing presentations where Blue and White collar employees participate widely, job accidents and incidents that are determined to be beneficial and necessary to be shared by evaluation are evaluated and shared with the employees. With this method, the inclusion of large-scale participation and the management's OHS approach also come to the forefront



İsdemir Accident Sharing Presentations Datas Graphic

Since the commencement of the systematic implementation of the accident sharing submissions, 63 meetings were held with 12,696 employees.

E. Safety Tours (Informed / Unannounced Safety Tours)

The informed security tours are carried out with the participation of the related and other employees in order to determine the open areas for improvement in terms of Occupational Health and Safety at the work places and to remove the unsafe conditions by eliminating the determined deficiencies and spreading the safety consciousness to the floor.

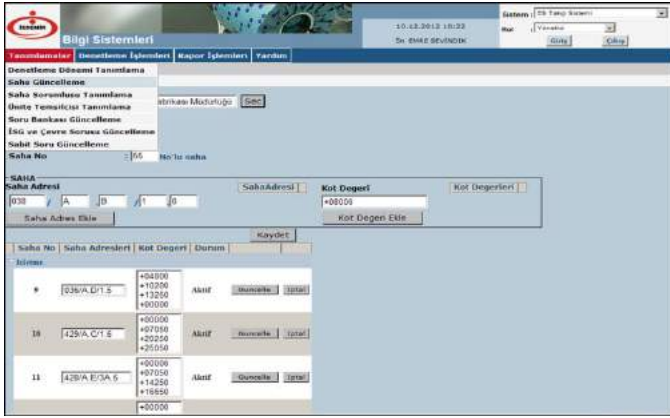
Photographs from informed / unannounced security tours conducted with the participation of unit administrators and employees are given below. (Source; İsdemir Occ.Safety Dept.)



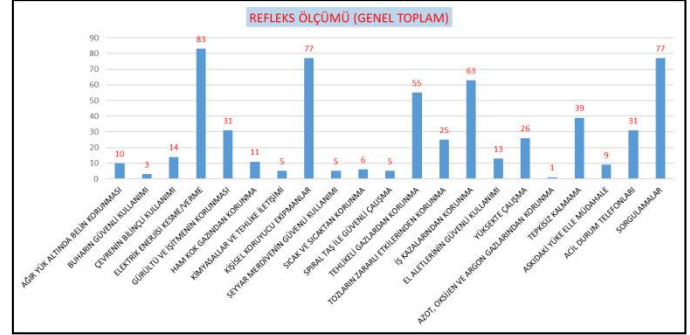
Identification / determination of the field to be audited and the questions that can be asked at the first stage of making informed / unannounced security tours. In the second stage, a short briefing is given to the scene before the inspection phase, to declare what the purpose is and to declare that it is assembled to form a safe working environment. In the third phase, work accidents, potentially dangerous events, Monitoring over the data, monitoring awareness and requirements for possible emergencies, fire protection systems, possibility of chemical substance release, etc. Issues need to be examined. In the fourth stage, detailed field technical tour is coming. At this stage, the general field layout and layouts, outlets, electrical cables, danger zones, stairwells, work equipment, etc. All safety issues should be assessed. The fifth stage is the phase of detection and evaluation of findings. The sixth and final stage is to follow the improvement activities related to the identified issues [13]

F. 5S cleanliness & orderness systematic

In the 5S system, which is established in order to provide order and discipline by increasing the participation and motivation of the employees with work security, environment, productivity, machine performance and workplace; 5S Field Sign Standard, White Label, Red Label, Flag Standards, İsdemir Sign and Colour Standards, Colour Codes According to Flow Through Pipelines, İsdemir Factory Site Colour Codes, Site and Road Lines are standardized in all units. The software system created in İsdemir is used to evaluate the parcels that are plotted with the determined legal / special audit questions and then the continuity is ensured periodically according to years and periods. Below is a screenshot of the software and control pages created for İsdemir.



important to know and apply the employees. Some graphs are given from some studies related to the following studies [14]



B. PPE (Personal Protective Equipment Commission)

İsdemir has a Protective Material Commission to detect protective materials suitable for working conditions, to conduct research in this subject, to prepare technical specifications of protective materials, to make them available for purchase, and to make necessary improvements by following them while using them. For example; to prevent accidents by workers working with liquid steel, liquid metal spill resistant special work clothes and other heat / oil resistant protectors (face shields, harnesses, etc.) are used.

C. Reporting of Near Miss Events

A "Report on Near Miss" will be issued to identify and record events that are not affecting employees, damage to equipment, but could cause injury or damage in case of repetition. For the İSDEMİR personnel who will not enter the computer environment, Near Miss Event Form was arranged and 30 pieces of Near Miss Box and Panels were created. (Example: Isdemir Near Miss software and datas)

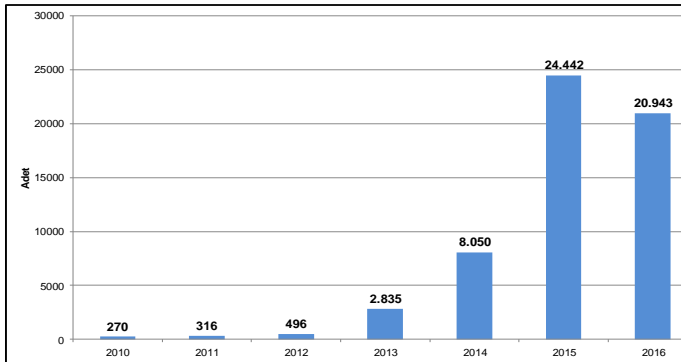


Figure-12; İsdemir Ramak Kaldı Raporlama Verileri Grafiği Örneği

In the above chart, the data of Isdemir related to the data of the near miss events which contributed to the studies of the development of general OSH by encouraging the reporting of the unemployment is shared.

D. Reflex Measurements

In addition, specific OHS practices were also implemented for the units. Reflex measurement studies are also one of them. In reflex measurement studies, it is tried to measure the reflexes that are shown against the workings and observations performed on the areas in relation to the safety issues which are

Behaviour Oriented Safety Management Works On Blast Furnaces Dept.;

Within the context of the Behavioural Oriented Safety Management trainings conducted within the framework of the following subjects, it is aimed to improve the effectiveness of trainings given to employees (16 modules) on field applications.

- Protection from Harmful Effects of Dust
- Hot and Temperature Protection
- Protection from Hazardous Gases
- Heavy Load Lifting and Protection
- Protection from Occupational Injuries
- Chemicals and Hazard Communication
- Personal Protective Equipment
- Protection of noise and hearing capacity
- Protection from Raw Coke Gas
- Protection from Nitrogen, Oxygen and Argon Gases
- Safely working with grinding machine
- Safely usage of Mobile Ladder
- Awareness of the Environment
- Safely Use of Hand Tools
- Safely Use of Steam
- Energy Safety (LOTO)

These studies are important in terms of the development and improvement of the OHS approach of the employees and they are useful instruments used to reduce work accidents.

Individual Behaviour Based Development- Observation Project on Steel Making Plant;

Within the scope of improvement of employee behavior and improvement of OHS approach, "Individual Behavior Focused Development-Observation" project was initiated as a pilot unit in İskenderun Iron and Steel Factory (İSDEMİR) within the scope of Steelmaking Plant Directorate and employees were aimed to develop safety consciousness, increase awareness and reduce work accidents.

The "Individual Behaviour Based Development-Observation" project, which started in September 2014 after the action phase and continued to develop itself, has been supported by top management applied on the Steel Making Plant, Continuous Casting Dept. and Wire Rod Mill.

At the beginning of the work being done, if any unsafe condition does not arise, the unsafe behaviour is tried to be photographed. Employees who act as observers in the project are required to photograph absolutely unsafe behaviour if possible. On this page, there is the compilation and examination of visual donations about what is unsafe behaviour. At the same time, photographs of employees who demonstrate safe behaviour are also photographed and shared.

However, the danger level of the activity carried out, the continuity of the operation and the safety always require photography. Can not withdraw.

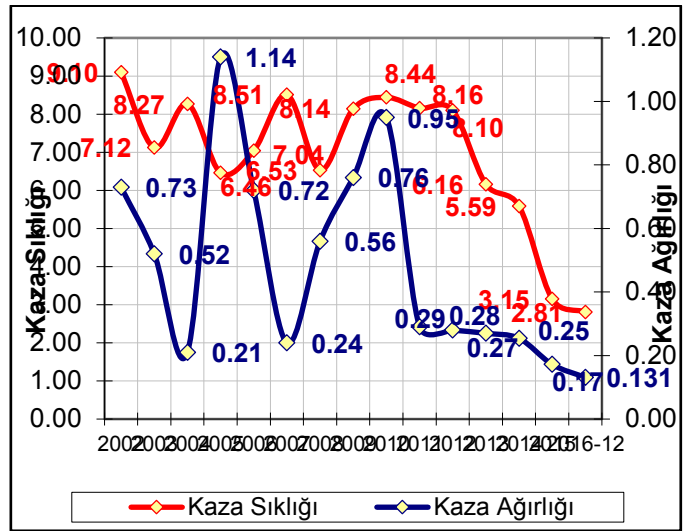
At the beginning of the work, on the business scene, a small team of misdemeanors has been passed on to detect unethical behavior.

On the other hand, an increase in unsafe behaviour determinations in the practice of on-the-job practices to create a safe behavioural change, more control of the eye, and an easier manoeuvring of the observer profile and the observer's ability to use the safety climate and the employee's perception will change faster and more. For this reason, "Observation card" was created with the evaluation of the field activities, field activities and business accidents of the Steel Making Plant in the "Individual Behaviour Focused Development-Monitoring" project initiated as a pilot application in the Steelworks Directorate. In the document identified as "Safety Behaviour Monitoring / Control Card", employee, place, date, observer information exhibiting erroneous behaviour are defined. It is the highest priority objective that the results of the trainings carried out reflect on the behaviours of the people. The main objective of the "Individual Behaviour-focused Development-Observation" project is to improve the perception of the employee to ensure a permanent safe behavioural change.

G. Evaluation of Data

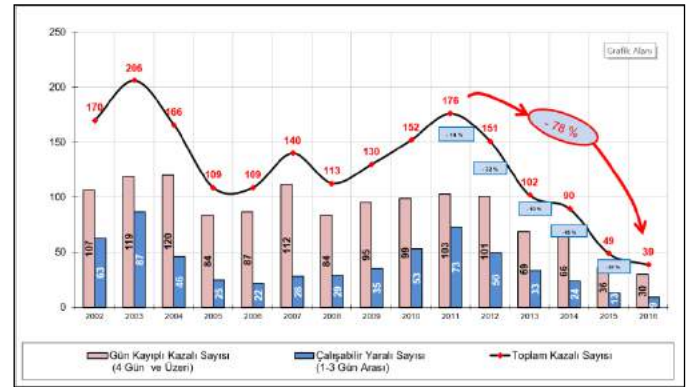
Assessment of the sample work accident data and OHS targets of the related companies (Isdemir is taken as an example for Çukurova Region) and changes of understanding about the employees' proactive OHS approach will be shared. Comparisons of work done for behaviour change with accident results, to see and evaluate statistical trends.

As a result of these safety applications, Isdemir Occupational injuries data has reached the following values. Accident frequency values decreased by about 70% compared to the values of the last five years. Accident frequency (LTIFR) is currently at 2.16.

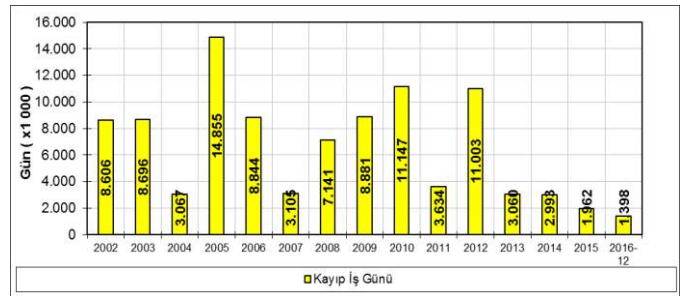


2002-2016 Lost time injury-lost day frequency rates

In the chart below, day-loss accident data are shared. The declining trend in lost day accident data has been shown.

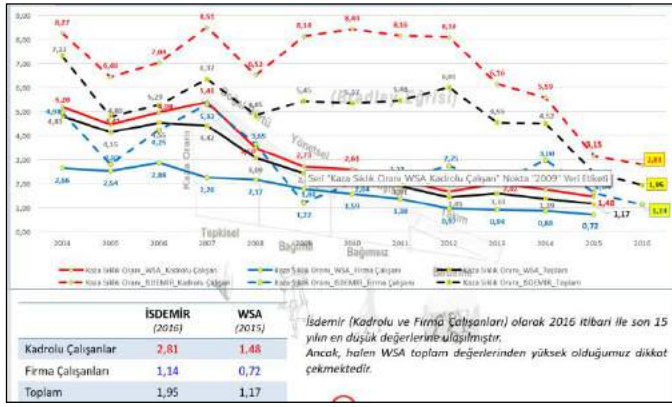


Day-Loss-Workable Casualty Accidents for 2002-2016 Years



Day Losses Resulting from 2002-2016 Accidents

In the above chart, the data on the loss of labour power that is experienced as a result of live accidents are shared.



Isdemir-WSA Accident frequency comparison chart between 2004 and 2016 [15]

III. CONCLUSION

In order to ensure safe behaviour change in the iron and steel sector, the organization is integrated into every step of the safety culture organization, the sense of perception and sense of this integration, the visible support of the management and administrators in this context and the stability are the most important parameters. In addition, it is important to use various proactive and reactive safety instruments to provide the desired results, as well as various field applications, OHS systematics (safety tours, exercises, field observations and behaviour observations, OHS meetings, etc.), analysis of occupational accidents, hazard / risk assessments among other things. In addition to all these, the sustainability of the entire safety approach is an indispensable condition, and the accident plays an important role in reducing the frequency and weight data.

REFERENCES

- [1] Measuring safety climate: identifying the common features, R. Flin, K. Mearns, P. O'Connor, R. Bryden, safety science, volume 34, Issues 1-3, February 2000, page 177-192
- [2] Improvement factors in common among organizations making large improvement in OHS Performance: Results of an exploratory case study, Safety Science 86 (2016), 211-227
- [3] HSE SCMM, Fleiming 2001, Sam Mannan, Lees' Process Safety Essentials, 23.01.2017, Çukurova University,
- [4] Hearts and Minds safety culture mode. Energy Institute, Shelle&P, <http://publishing.energyinst.org/heartsandminds/culture>
- [5] <http://www.rimbach.com/scripts/Article/IHN/Number.idc?Number=113>
- [6] DuPont Bradley Curve, <http://www.dupont.com/products-and-services/consulting-services-process-technologies/articles/bradley-curve-infographic.html>
- [7] <http://www-ns.iaea.org/tech-areas/operational-safety/safety-culture-home.asp>
- [8] http://csq.org.au/csq/media/Common/publications/ACA_HealthandSafety_Report_August_2014.pdf
- [9] M.D.Cooper Ph.D., Towards a model of safety culture, Safety Science, http://www.behavioral-safety.com/articles/Towards_a_model_of_safety_culture.pdf
- [10] http://www.asse.org/assets/1/7/F1_0117.pdf, Professional Safety dergisi, Ocak 2017 Sayısı, Sayfa 31

- [11] OECD Guidance for Senior Leaders in High Hazard Industries, <http://www.oecd.org/chemicalsafety/corporategovernance/ceforprocesssafety.htm>
- [12] İsdemir Occupational Safety Dept., 2016 Annual Activity Presentation Datas,
- [13] Journal of American Society of Safety Engineers, 6 step to proper Auditing, Tips form David Regelbrugge, Senior Manager at Environ.
- [14] İsdemir OHS activities data.
- [15] World Steel Association (WSA) safety statistics

2D Modelling of Residual Stresses in Hard Turning of AISI 4140 Steel

Mehmet Erdi KORKMAZ^{1*}, Nafiz YAŞAR², Mustafa GÜNAY³

^{1*} Karabük University Engineering Faculty, Karabük/TURKEY, merdikorkmaz@karabuk.edu.tr

² Karabük University Karabük TOBB Vocational High School, Karabük/TURKEY, nafizyasar@karabuk.edu.tr

³ Karabük University Engineering Faculty, Karabük/TURKEY, mgunay@karabuk.edu.tr

Abstract— The residual stresses induced by any machining process affects fatigue life, corrosion crack resistance and part distortion. Therefore, residual stresses should be predicted better and the cutting parameters should be arranged for minimum value. This paper presents a 2D finite element analysis (FEA) on residual stresses during hard turning of AISI 4140 steel with HSS tools. The cutting parameters are chosen as feed rate and cutting speed with three levels and constant depth of cut. In simulation after the cutting process is finished, both the chip and tool are removed and the workpiece can thermo-mechanically relax. The average of three extraction points on eight different depths of machined surface for residual stresses is calculated for better results. FEA results showed that both tangential and axial residual stresses act as tensile in the depths near the surface until about 75 µm while they act as compressive stress after the depth of 75 µm until about 300 µm. Also, increasing cutting speed has decreasing effect on tensile residual stresses while increasing effect on compressive residual stresses.

Keywords— Hard turning, AISI H13, Finite element method, Residual Stress

I. INTRODUCTION

Manufacturing of hardened steel parts known as hard turning with high accuracy and surface quality is commonly replaced by grinding because of the comparatively high cost and setup time of the grinding process. Flexibility and positive ecological effects are other advantages of dry hard machining [1]. Surface integrity of components affects their service life and dimensional stability, so it is extremely important to control the final surface state of parts after hard machining. Among the properties commonly enclosed in the surface integrity of a component, the most relevant are residual stresses, roughness, hardness and microstructure followed by cutting temperature and forces. Particularly, residual stresses play a key role in the service life of components, because they add up to the external stresses acting over the part during service, leading to a real stress higher than the applied stress, and therefore the fatigue resistance of the component is reduced, leading to possible premature failure of the components during its service life [2]. Therefore, a lot of machining studies have been performed in order to control the residual stresses which determine the fatigue life. Navas et al. [1] studied the effects of cutting speed, feed, tool nose radius, geometry of the tool chip breaker and coating of the cutting tool on the final surface stress state and cutting temperature in AISI 4340 steel.

In all cases surface tensile residual stresses have been measured, tending to be more or less tensile (and consequently

more or less detrimental to the service life of the machined component) depending on the cutting conditions and the characteristics of the cutting tool. The authors stated that when feed increases, residual stresses tend to be more tensile due to an increase in cutting temperature with feed, and also surface roughness increases. Therefore, surface integrity of the part deteriorates with the increase in cutting feed. Also, maximum stresses are located near cutting direction, approaching this direction slightly as cutting speed and feed increase. Smith et al. [3] investigated the relationship between fatigue life and surface integrity of hard turned AISI 52100 steel (60–62 HRC) characterized via residual stress measurements with five distinct surface conditions, namely, hard turned with continuous white layer, hard turned with no white layer, ground, and super finished hard turned and ground specimens. The results suggested that the effect of residual stress on fatigue life is more significant than the effect of white layer. For the hard-turned surfaces, the fatigue life is found to be directly proportional to both the surface compressive residual stress and the maximum compressive residual stress. Jafarian et al. [4] estimated and optimized the effect of machining parameters including cutting speed, depth of cut and feed rate on induced tensile residual stresses measured by X-ray Diffraction (XRD) method in the finish/semi-finish turning process of Inconel718. Then, the experimental results were introduced to the intelligent systems including Artificial Neural Network (ANN) and Genetic Algorithm (GA) to estimate residual stress at the various machining parameters and optimize the process. It was shown that, implemented efficient intelligent techniques in this paper are remarkably appropriate for machining of Inconel718.

Residual stresses occur on workpiece materials during all machining processes. The material may unintentionally bend, twist or have micro-macro crack due to these stresses. Both time and cost wasting are faced because of decreasing product quality. Therefore, these residual stresses should be measured and minimized. There are two methods in industry named as destructive (stress tests, crash tests and hardness tests) and non-destructive testing (X-ray diffraction, neutron irradiation, etc). However, making a selection between them is very difficult because destructive testing method is tedious and non-destructive testing is very expensive. There can be a lot of time and material saving if machining processes including residual stresses were performed and supported with finite element modeling which predicts and controls the machining characteristics. Thus, many finite element modeling studies have been performed with this purpose. Abboud et al. [5]

developed a finite element model of orthogonal cutting using DEFORM-2D in order to build a predictive tool for machining-induced residual stresses in titanium alloy Ti-6Al-4V. A full factorial orthogonal cutting experiment is conducted using sharp tools to investigate the effect of feed rate (f) and cutting speed (v) on residual stresses under finish-turning conditions. The results show that experimental and finite element modeling results are compatible for forces, temperatures and residual stresses. It was also observed that residual stresses become more compressive with increasing feed rate and less compressive with increasing edge radius or cutting speed. Ratchev et al. [6] presented a finite element model with ABAQUS 2D for prediction of turning induced residual stresses of Ti6Al4V alloy in two cutting depths (100 and 500 μm). Dynamic thermo-mechanical FE analysis using explicit integration is performed. The workpiece is modelled as an isotropic thermal-elastic-plastic model using the Johnson-Cook constitutive equation. The near-surface residual stresses are predicted and compared with experimentally measured results. It can be seen from results that the measured and the predicted stresses are compressive near the machined surface and the predicted stresses from FEM are in very good agreement with the experimentally measured stresses in the minimum and maximum principal directions for both depths of cut (100 and 500 μm). Stenberg and Proudian [7] presented a thermo-mechanical numerical simulation of the machining operation to obtain the impacts of parameters on residual stresses and compare these stresses to measurements of a machined axis. The simulations were performed with the software package DEFORM which has a remeshing function that, for practical reasons, is necessary when forming chips. The large deformations will make the FE-analysis to costly otherwise. The simulation results showed that the residual stresses are however a bit hard to extract since the re-mesh function moved the nodes around and thereby adding extra work in the post processing phase. Therefore, 2-D simulations were used instead of 3-D simulations because of relatively low on calculation time. Özel and Ulutan [8] presented experimental investigations and finite element simulations on turning of Ti-6Al-4V titanium alloy and IN100 nickel based alloy with uncoated and TiAlN coated tools. Face turning of Ti-6Al-4V and IN100 using uncoated tools with various edge radii and TiAlN coated carbide tools was conducted; and residual stresses were measured in radial and circumferential directions using X-ray diffraction technique. The authors stated that predicted residual stresses are influenced by the tool micro-geometry as they become more compressive with increased edge radius but more tensile at the surface when coated. The results also showed that the experimental results are compatible with FEM results. Korkmaz and Günay [9] studied finite element modelling of tool stresses in hard turning of AISI L2 steel. Authors stated that crater wear which is the most common damage type in hard turning may occur at the chamfered zone of tool-nose due to very small cutting area. Because, chamfered tool geometry causes negative rake angle and increase cutting forces, thus high cutting stresses occurred on tool-chip contact area.

This study presents a 2D finite element analysis (FEA) on residual stresses during hard turning of AISI 4140 steel with HSS tools.

II. MATERIAL AND METHOD

The aim of this study was to investigate the effects of cutting parameters on residual stresses in high precision hard turning of AISI 4140 steel with HSS tools. The finite element analyses were performed with Advantedge software with 2D orthogonal turning instead of 3D turning due to low calculation time. The following cutting conditions were used for the experiments: feed rate (f) of 0.09, 0.18 and 0.27 mm/rev and cutting speed (V) of 50.2, 100.4 and 141.4 m/min with constant cutting depth (a) of 0.1 mm.

II.I. Work piece material

The workpiece material has the following chemical composition: 0.4% C, 0.25% Si, 0.85% Mn, 0.95% Cr, 0.2% Mo, 0.04% S, 0.035% P and the balance is Fe. The workpiece was hardened to 55±1 HRC by means of heat treatment by quenching in a vacuum atmosphere. The Johnson-Cook model [10] widely-used material model for machining simulations is given in Eq. 1. This material model is particularly suited to model high strain rate deformation of metals. It is generally used in adiabatic transient dynamic analysis. The hardening is a particular type of isotropic hardening in which the yield stress σ^0 is assumed as [11]:

$$\sigma^0 = (A + B(\epsilon^p)^n) \left(1 + C \log \left(\frac{\dot{\epsilon}^p}{\dot{\epsilon}_0} \right) \right) \left(1 - \left(\frac{T - T_r}{T_m - T_r} \right)^m \right) \quad (1)$$

In equation (1), material parameters obtained from mechanical tests that are A , B , C , n and m are yield stress below room temperature, strain hardening, strain rate constant, strain hardening constant and thermal softening constant, respectively. The other parameters ϵ^p , $\dot{\epsilon}^p$, $\dot{\epsilon}_0$, T_r , T_m and T are equivalent plastic strain, plastic strain rate, reference strain rate, room temperature, melting temperature and reference temperature, respectively. Also, $\dot{\epsilon}_0$ and C are usually measured at or below the reference temperature. The Johnson-Cook parameters and other material parameters for AISI 4140 steel was given in Table 1 and Table 2, respectively [12].

TABLE I

Johnson-Cook parameters for the AISI 4140 steel material

A (MPa)	B(MPa)	C	n	m	T _r (°C)	T _m (°C)	ε ₀
595	580	0.023	0.133	1.03	27	1550	1

TABLE II

The other material parameters for the work piece (AISI 4140)

Density (g/cm ³)	Poisson ratio	Young's Modulus (GPa)	Thermal Conductivity (W/m.K)	Specific Heat (J/kg°C)	Thermal Expansion (10 ⁻⁶ °C)
7.8	0.3	210	46.6	477	11.9

II.II. Cutting Tool

HSS tool steel (18 X 200) manufactured by BÖHLER have been used as cutting tools in 2D orthogonal analyses. The tool has a rake angle (γ)= 15° and clearance angle (α)= 15° with the edge radius (r) of 0.02 mm because edge radius is used instead of tool nose radius in 2D orthogonal turning (Fig. 1). The material parameters for HSS cutting tool was given in Table 3.

TABLE III

The material parameters for cutting tool (HSS)

Density (g/cm ³)	Poisson ratio	Young's Modulus (GPa)	Thermal Conductivity (W/m.K)	Specific Heat (J/kg°C)	Thermal Expansion (10 ⁻⁶ °C)
8.00	0.3	210	25	460	6.8

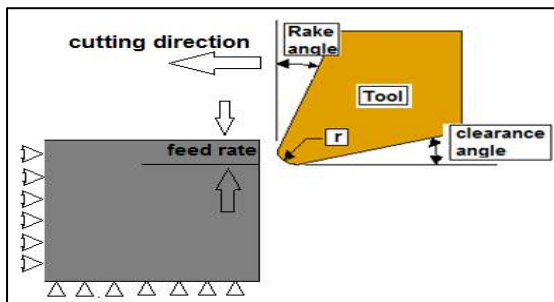


Fig. 1 2D model of cutting tool

II.III. Finite Element Simulations

The finite element analyses of residual stresses were performed with Advantedge software depending on finite element method. Advantedge uses an Arbitrary Lagrangian solver and it has adaptive remeshing function to provide more accurate results although it takes more time. The first stage of simulation is to determine the workpiece length (3 mm) and height (1 mm) with workpiece material. The second stage is determining the tool parameters (rake angle, clearance angle and edge radius) with tool material. The final stage is to enter required simulation parameters such as feed rate, depth of cut, length of cut and cutting speed after meshing parameters and coefficient of friction is adjusted.

The interface between tool and work piece was modelled with a standard Coulomb friction which is assumed as 0.5. The meshing parameters were used as 0.1 mm and 0.02 mm for maximum and minimum element size, respectively. After these assumptions, a verification simulation was done with parameters used by Hadad [13]. The finite element model was then verified due to the difference between cutting forces in experiment and simulation is less than %5. The cutting parameters chosen for these finite element analyses were given in Table 4.

TABLE IV

Cutting parameters

Levels	1	2	3
Feed rate (mm/rev)	0.09	0.18	0.27
Cutting speed (m/min)	50.2	100.4	141.4
Depth of cut (mm)	0.1		
Coefficient of friction	0.5		

The workpiece was cut off 1mm in analyses of residual stresses. After the cutting process is finished, both the chip and tool are removed and the workpiece is allowed to thermo-mechanically relax. The residual stresses were obtained from three extraction levels (%20, %50 and %80) of workpiece starting point. The average of these values then calculated for more accurate results. The eight depth of workpiece were considered for residual stress analyses. The simulation model and cutting scheme were shown in Fig. 2.

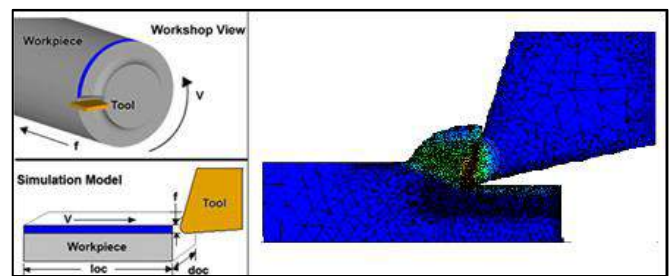


Fig. 2 2D simulation model

III. RESULTS AND DISCUSSION

Only 2D simulation was performed in this study instead of 3D simulation due to low calculation of time. As shown from Fig 3-5, the eight depth of workpiece were considered for residual stress analyses. The residual stresses were obtained from three extraction levels (%20, %50 and %80) of workpiece starting point and then average of these values calculated for more accurate results.

The influences of cutting parameters (feed rate and cutting speed) on residual stresses were assessed by means of the figures. In general, Fig. 3-5 display similar tendency. Both tangential and axial residual stresses act as tensile in the depths near the surface until about 75 μm while they act as compressive stress after the depth of 75 μm until about 300 μm without considering the change of feed rate and cutting speed.

The tensile residual stresses in feed rate of 0.09 mm/rev decrease with increasing cutting speed for tangential direction according to Fig.3. However, the compressive residual stresses increase with increasing feed rate. The tangential tensile residual stress decrease about %6.6 and %19.2 when the cutting speed increase from 50.2 to 100.4 and 100.4 to 141.4 m/min, respectively in 20 μm depth from workpiece surface. The tangential compressive residual stresses increase about %18 and %17 when the cutting speed increase from 50.2 to 100.4 and 100.4 to 141.4 m/min, respectively in 100 μm depth from workpiece surface. The axial residual stresses have not an important change for all feed rate with increasing cutting speed except for the surface in depth of 5 μm.

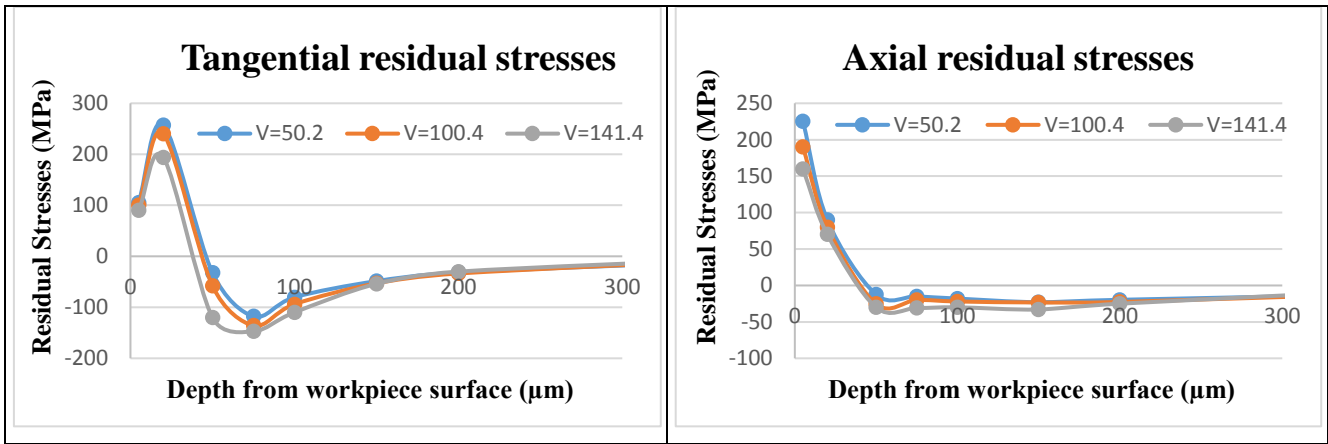


Fig. 3 Residual stresses for $f=0.09$ mm/rev

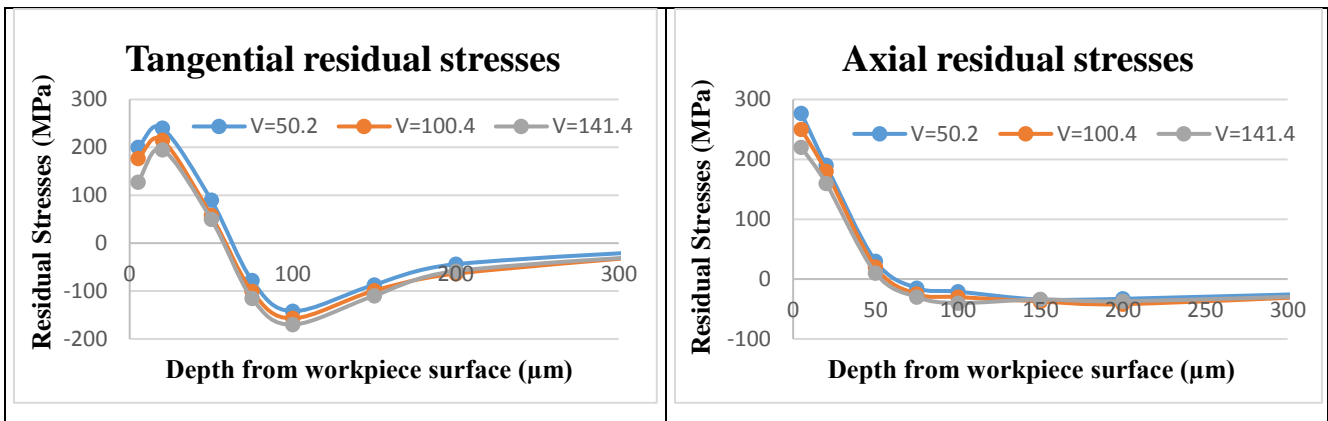


Fig. 4. Residual stresses for $f=0.18$ mm/rev

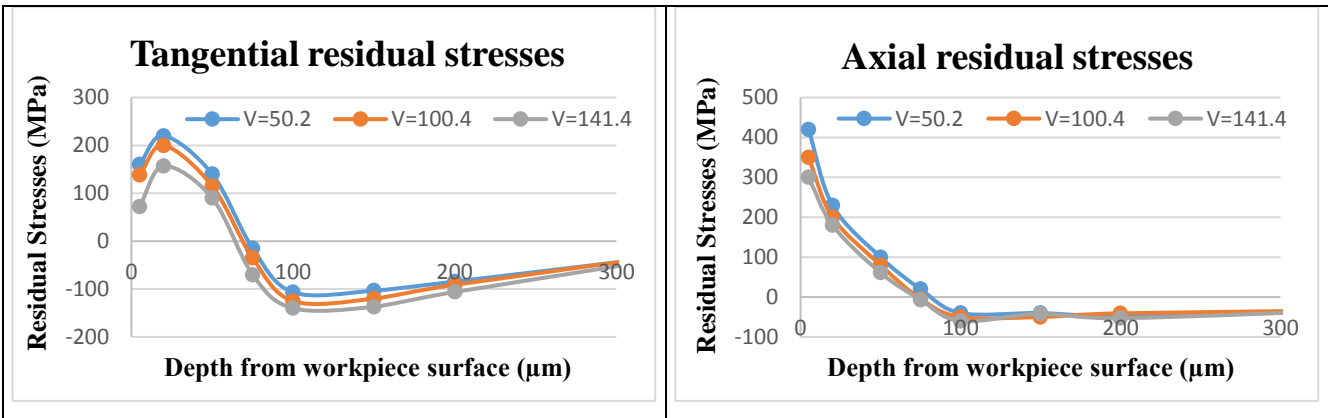


Fig. 5. Residual stresses for $f=0.27$ mm/rev

Fig. 4 acts similar tendency like Fig. 3. The tangential tensile residual stress decrease about %10.4 and %9.3 when the cutting speed increase from 50.2 to 100.4 and 100.4 to 141.4 m/min, respectively in 20 μm depth from workpiece surface. The tangential compressive residual stresses increase about %42.9 and %33.3 when the cutting speed increase from 50.2 to 100.4 and 100.4 to 141.4 m/min, respectively in 100 μm depth from workpiece surface.

The tangential tensile residual stress decrease about %9.1 and %21.7 when the cutting speed increase from 50.2 to 100.4 and 100.4 to 141.4 m/min, respectively in 20 μm depth from workpiece surface. The tangential compressive residual stresses increase about %52 and %23 when the cutting speed increase from 50.2 to 100.4 and 100.4 to 141.4 m/min, respectively in 100 μm depth from workpiece surface.

The cutting speed has a little change on residual stresses when examining Fig. 3-5. The tangential compressive residual

stresses increase about %25.6 and %20.3 when the cutting speed increase from 150 to 200 and 200 to 250 m/min, respectively. The axial residual stresses decrease about average %10 and %20 when the feed rate increase from 0.09 to 0.18 and 0.18 to 0.27 mm/rev, respectively.

IV. CONCLUSION

In this study, the effects of cutting parameters on residual stresses on tool-chip interface have been analyzed with finite element method in hard machining of AISI 4140 steel workpieces with 55±1 HRC hardness using HSS tools. 2D orthogonal cutting has been used instead of 3D cutting due to low calculation of time in finite element analyses. The following conclusions are drawn from this study:

Both tangential and axial residual stresses act as tensile in the depths near the surface until about 75 µm while they act as compressive stress after the depth of 75 µm until about 300 µm without considering the change of feed rate and cutting speed.

The tensile residual stresses decrease with increasing cutting speed while the compressive residual stresses increase with increasing cutting speed for tangential direction. The axial residual stresses have not an important change for all feed rate with increasing cutting speed except for the surface in depth of 5 µm.

The highest tangential tensile residual stress was obtained with feed rate of 0.09 mm/rev and cutting speed of 50.2 m/min. However, the highest axial tensile residual stress was obtained with feed rate of 0.27 mm/rev and cutting speed of 50.2 m/min. Thus, if the workpiece is generally used as a tangentially compressive part in industry, lower feed rate with lower cutting speed should be used during machining of it. But, the workpiece is used as a axially tensile part in industry, higher feed rate with lower cutting speed should be used.

References

- [1] H.K. Tonshoff, C. Arend, R.B. Amor, Cutting of hardened steel, *CIRP Annals- Manufacturing Technologies* 49 (2), 547–566, 2000.
- [2] G.K. Dosbaeva, M.A. El Hakim, M.A. Shalaby, J.E. Krzanowski, S.C. Veldhuis, Cutting temperature effect on PCBN and CVD coated carbide tools in hard turning of D2 tool steel, *International Journal of Refractory Metals and Hard Materials*, 50, 1–8, 2015.
- [3] Stephen Smith, Shreyes N. Melkote, Edgar Lara-Curzio, Thomas R. Watkins, Larry Allard, Laura Riester, Effect of surface integrity of hard turned AISI 52100 steel on fatigue performance, *Materials Science and Engineering A* 459, 337–346, 2007.
- [4] Farshid Jafarian, Hossein Amirabadi, Javad Sadri, Experimental measurement and optimization of tensile residual stress in turning process of Inconel718 superalloy, *Measurement* 63, 1-10, 2015.
- [5] E. Abboud, B. Shi, H. Attia, V. Thomson, Y. Mebrahtu, Finite element-based modeling of machining-induced residual stresses in Ti-6Al-4V under finish turning conditions, *Procedia CIRP* 8, 63-68, 2013.
- [6] S.M. Ratchev, S.M. Afazov, A.A. Becker, S. Liu, Mathematical modelling and integration of micro-scale residual stresses into axisymmetric FE models of Ti6Al4V alloy in turning, *CIRP Journal of Manufacturing Science and Technology* 4, 80–89, 2011.
- [7] N. Stenberg, J. Proudian, Numerical modelling of turning to find residual stresses, *Procedia CIRP* 8, 258-264, 2013.
- [8] T. Özel, D. Ulutan, Prediction of machining induced residual stresses in turning of titanium and nickel based alloys with experiments and finite element simulations, *CIRP Annals – Manufacturing Technology* 61, 547–550, 2012.
- [9] M.E. Korkmaz, M. Günay, Finite Element Modeling of Tool Stresses in Hard Turning of AISI L2 Steel: Prediction by ANN, *International Journal of Modern Engineering Research*, 6 (11), 30-40, 2016.
- [10] M.E. Korkmaz, N. Yaşar, M. Günay, Finite Element Modeling of Residual Stresses and Cutting Temperature in Hard Turning, International Conference on Engineering and Natural Sciences, Bosnia and Herzegovina, 2016.
- [11] A. Dorogoy and D. Rittel, Determination of the Johnson–Cook Material Parameters Using the SCS Specimen, *Experimental Mechanics* 49, 881–885, 2009.
- [12] M. Agmell, A. Ahadi, J.E. Stahl, The Link Between Plasticity Parameters and Process Parameters in Orthogonal Cutting, *Procedia CIRP*, 8, 224 – 229, 2013.
- [13] M. Hadad, B. Sadeghi, Minimum quantity lubrication-MQL turning of AISI 4140 steel alloy, *Journal of Cleaner Production* 54, 332-343, 2013.

MODELLING OF ROUND ROLLING PROCESS BY USING FINITE ELEMENT METHOD

Emre EROL¹, Mehmet Erdi KORKMAZ^{2*}, Mustafa GÜNAY³

¹ KARDEMİR A.Ş, Karabük/TURKEY, eerol@kardemir.com

^{2*} Karabük University Engineering Faculty, Karabük/TURKEY, merdikorkmaz@karabuk.edu.tr

³ Karabük University Engineering Faculty, Karabük/TURKEY, mgunay@karabuk.edu.tr

Abstract— Machining parameters for manufacturing methods can be optimized based on the finite element method using numerical simulation software. In this study, the simulation of the hot rolling process was performed for plain round bar producing. Rolling simulations were done in DEFORM-3D software and the hot rolling process was analyzed with three different rolling temperatures and rotation speed of rolls. In the results of numerical analysis, diameter and circularity tolerances have been measured for the product. The outputs of the finite element simulation were evaluated to determine the effects of rolling parameters on size quality of round bar product. The analysis of variance (ANOVA) with %95 confidence level was performed in order to determine the effect level of rolling parameters. It was determined that the rounded product geometry is out of diameter and circularity tolerances by increasing the rolling temperature and the rotational speed.

Keywords— Hot rolling, Round bar, Finite element method, DEFORM, Optimization

I. INTRODUCTION

Rolling is the process of reducing the thickness or changing the cross-section of a long workpiece by compressive forces applied through a set rolls. Rolling is classified according to the temperature of the metal rolled. If the temperature of the metal is above its recrystallization temperature, then the process is known as hot rolling. During this phase, the coarse-grained, brittle and porous structure of the ingot or the continuously cast metal is broken down into a wrought structure, having a finer grain size and enhanced properties. If the temperature of the metal is below its recrystallization temperature, the process is known as cold rolling [1]. Rolling is one of the most important and most efficient forming processes to obtain higher quality products in the modern manufacturing. Many important parameters, such as deformation ratio, rolling temperature, cooling condition, rolling speed, etc., depend on thermo-mechanical behavior and display great influence on the improvement of product quality in rolling process [2]. The accuracy of shape mills products (round bars, square, etc.) is determined by the deviation of the actual size of the cross-section bandwidth compared to the nominal values. The main dimensions of products shape mills are the height and width of the finished product and the weight of current one meter. For round bars also determines the circularity, as the difference in the horizontal and vertical diameter, and for the square bars determines the difference in diagonals. Production of rolled

products in the field below zero deviation tolerances is a growing interest of customers [3].

In traditional rolling process, it is necessary to carry out experiments that need trial method with high machinery costs and loss of production. Currently, to prevent such disadvantageous factors, many new technologies are carried out to design and optimize the manufacturing process of products. Therefore, many finite element modeling (FEM) studies have been performed with this purpose. Kumar and Kodli [4] studied on reducing or minimizing the defects of rolling process with finite element modelling. The analysis has been carried out for different temperatures. Hot rolling process helps in reduced residual stresses at high temperature and helps in formation of smooth granular structure of product. FEM results showed that the residual stresses decrease as the temperature goes on increasing correspondingly. Szota et. al [5] performed on numerical modelling of the round bar rolling process, while considering the wear of the passes depending on their shape. Authors presented a methodology for the determination of the quantitative wear of rolls based on the results of computer simulations for a selected oval pass during rolling of round bars. The results showed that it was possible to determine the roll wear factor that enables the calculation of the quantitative wear of the rolls during the round bar hot rolling process with satisfactory accuracy on the basis of the performed experimental tests and theoretical computations. Çavdar et. al [6] modelled rolling pass designs of four production plant producing rebar and performed simulation of the production processes by means of commercial finite elements software. Used pass designs have been compared with respect to production rate and forming energy as a result of analysis. It was observed that variations of pass design effect considerably forming energy and time. Milenin et. al [7] proposed a mathematical model of the multi-pass rolling. The problem of non-isothermal metal forming during multi-pass rolling in grooved rolls was solved with using of the FEM. The rheological model was developed on the base of the dislocation theory of plastic deformation to take into account the changes of plastic properties of the rolled metal during its deformation in a roll gap as well as in the time between passes. The results showed that the developed mathematical model and the computer program can be applied to multi-pass rolling in industrial conditions. Aksenov et. al [8] considered an application of finite element simulation to the problem of roll pass design for round bar rolling. Two roll pass sequences were

II. MATERIAL AND METHOD

developed by analytical methods and then optimized using 2.5D FEM. The first one was a classical oval-round roll pass design. The second one was a combination of flat rolls and round roll passes. The results indicated that both considered roll pass designs are similar in terms of force and energy characteristics, as well as in terms of the final temperature and microstructure distributions. However, the advantage of the flat-round pass sequence lies in its far lower requirements for the necessary length of the working part of the roll. Riljak [9] firstly applied a FE program for coupled thermomechanical simulations of wire-rod rolling in order to predict material behavior of an AISI 302 stainless steel at high strain rates generated during wire-rod rolling. Then, the evolution of temperature, strain rate and flow stress was predicted in the first four rolling passes of a wire block. Secondly, an alternative approach to simulation of shape rolling was evaluated. The approach was applied in both 2D and fully 3D FE analyses. The comparison results showed that the simplified approach can predict roll forces and roll torques with a fair accuracy, but the predicted area reductions are a bit underestimated. The reasons for the deviations between the simplified approach and the 3D FEM will be discussed. Bagheripoor and Bisadi [10] performed a precision analysis of the roll force and roll torque and their instabilities during the rolling process. In doing so, a coupling multi-variable simulation model for hot strip rolling was built using non-linear thermo-viscoplastic FEM. Fluctuations of roll force and torque about the steady-state operating point were derived and the effects of main process parameters such as rolling speed and strip reduction on these instabilities were investigated. The results showed that the rolling force and torque values are not stable in the steady-state region and fluctuate around the average value. These fluctuations were increased in higher thickness reduction amounts that can be caused by contact condition changes. Motallebi [11] simulated the hot rolling process of a strip with commercial DEFORM 2D. The roll was assumed to be rigid and for the deformable aluminum strip, the thermo-elastoplastic analysis, through 2D sequential transient thermal and incremental lagrangian analyses, was carried out. This way the effect of different process parameters such as initial thickness of the strip, rolling speed and roll diameter, thickness reduction was studied. The results indicated that temperature of the strip, during rolling process, depends on several parameters such as interface heat transfer coefficient, rolling speed, and the amount of thickness reduction.

In the literature review, the numerical simulation by FEM was used in universal rolling process. Then, the theory of universal rolling method was developed and improved. In this study, the simulation of the hot rolling process was performed by DEFORM 3D software for thick round bar producing. The effects of rotational speed of roller and rolling temperature on product geometry were evaluated based on diameter and circularity tolerance.

II.I. Material and Equipment

In this study, final rolling process of round semi-finished product made by rolling of AISI 1045 steel was analyzed via simulation software. The chemical composition of workpiece is as %0.42-0.50 C, % 0.40 Si, %0.50-0.80 Mn, %0.035 P, %0.03 S and balance of Fe. The effects of some rolling parameters related to final rolling pass were evaluated on product quality in production of this material which is known as thick round industrially. Rolling simulations depending on finite element method were performed for three different levels of rolling parameters named as rotational speed of roller (Nm) and rolling temperature (Tm). The simulations performed by DEFORM 3D were conducted according to parameters in Table I.

TABLE I

Rolling parameters

Parameter	Rotational speed (Nm), rpm	Rolling temperature (Tm), °C
Value	55, 65, 75	850, 950, 1050

In rolling industry, there are some accepted standards for dimension qualities for semi-finished product. For thick round rolled semi-finished product ($\varnothing 200$ mm), the size and shape tolerances of the first quality products prescribed by the relevant sector companies are ± 2.5 mm (diameter) and ± 3.75 mm (circularity) respectively [12]. In addition, the size controls of the semi-finished product are made on hot material. The product measurements from the rolling process change due to the shrinkage varying depending on the material cooling. Therefore, the quality grade of final product geometry is evaluated by multiplying the material cooling coefficient ($k = 0.987$).

II.II. Finite Element Analysis

The finite element model used in the rolling simulations was created for finish rolling operation. In this regard, the procedure applied in the simulation processes in Deform 3D software and the finite element model were given in detail below. AISI 1045 material with an oval shape of 1 m length is accepted as a semi-finished product, dimensions used in material model and finite element mesh structure were given in Figure 1.

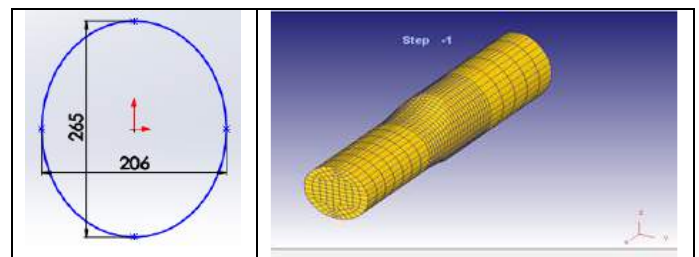


Fig.1 Semi-finish product dimensions and mesh structure

In the rolling simulations, the rollers were considered to be rigid and the Johnson-Cook material model was used for AISI 1045 material (Eqn. 1). In equation (1), material parameters

obtained from mechanical tests that are A , B , C , n and m are yield stress below room temperature, strain hardening, strain rate constant, strain hardening constant and thermal softening constant, respectively. The other parameters ε^p , $\dot{\varepsilon}^p$, $\dot{\varepsilon}_0$, T_r , T_m and T are equivalent plastic strain, plastic strain rate, reference strain rate, room temperature, melting temperature and reference temperature, respectively. Also, $\dot{\varepsilon}_0$ and C are usually measured at or below the reference temperature. The Johnson-Cook parameters for rolling material was given in Table 2.

$$\sigma^0 = (A + B(\varepsilon^p)^n) \left(1 + C \log \left(\frac{\dot{\varepsilon}^p}{\dot{\varepsilon}_0} \right) \right) \left(1 - \left(\frac{T - T_r}{T_m - T_r} \right)^m \right) \quad (1)$$

TABLE II

Johnson-Cook parameters for AISI 1045 [13].

A	B	n	C	m	Tr (°C)	Tm (°C)
105,84	198,61	0,331	0,085	0,52	25	1500

In finite element modelling, a dual roller set was used and the AISI 4340 steel material model was defined as the roll material so that it is compatible with the actual rolling process. Furthermore, the heat transfer simulation module between materials and rollers was chosen in finite element model. The caliber values entered as finish pass for the oval material and the air gap between the rolls (1 mm) in order to create a first quality Ø200 thick round material as a result of the simulation were shown in Figure 2. In addition, upper and lower roller temperatures were assumed to be 50 °C.

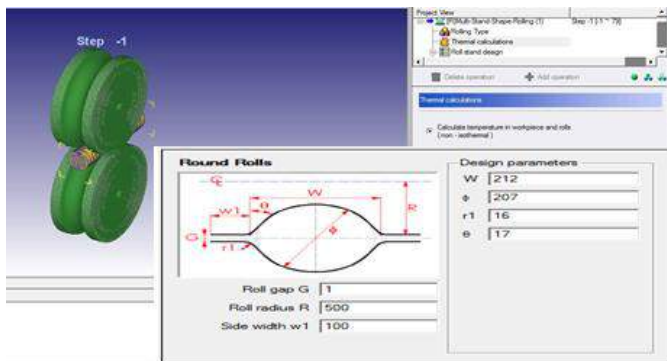


Fig. 2 Roller calibrated design and display of oval material

The caliber applied in the modelling of the rolling simulation corresponds to the 8th pass from furnace in rolling in the workshop environment. The furnace temperature is assumed to be 1250 °C, and considering that the material in real rolling loses 50 °C in each pass [14], a temperature loss of approximately 400 °C may occur up to the simulated caliber. For this reason, 850-1050 °C range is used as rolling temperature or workpiece temperature in simulations. Rolling simulations were performed in 200 steps for each rolling parameter. The deformation and reduction steps that occur in each step can be recorded in the program at 0.001 second level.

III. RESULT AND DISCUSSION

Rolling simulations for thick round were carried out with a total of 9 finite element analyses using three different temperatures and speeds. In order to evaluate the quality of the round semi-finished product, firstly the diameter and circularity values obtained as a result of 200 steps were measured. The diameter values were determined by measuring the width (W) as parallel to the X-axis and the height (H) over the Y-axis from the front surface of the round product formed as a result of the simulation (Figure 3). Similarly, the circularity tolerance was determined by measuring from two points at an angle of 45 ° from the front surface of the product, with the maximum value (O1) and the minimum value (O2). Then, the measured values were multiplied by the cooling coefficient (k) of the material and the actual diameter and circularity tolerances were calculated (Table III).

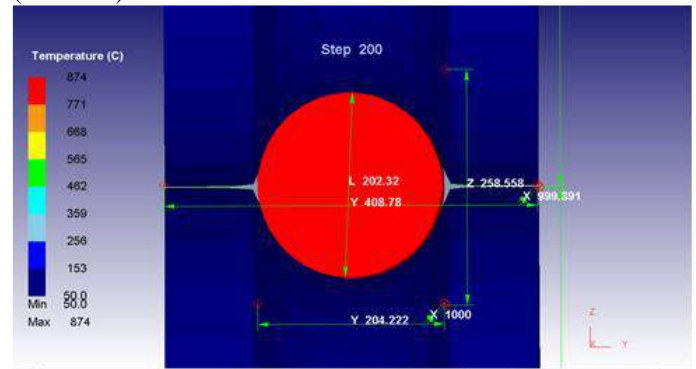


Fig. 3 Measurement of diameter in simulations

TABLE III

Diameter and circularity results according to rolling parameters

Exp. No	Parameters		Diameter		Circularity	
	Nm	Tm	W	H	O1	O2
1	55	850	201.24	199.72	199.22	199.12
2	65	850	201.57	199.69	199.50	199.39
3	75	850	201.83	199.66	199.61	199.49
4	55	950	201.89	199.68	199.82	198.74
5	65	950	202.23	199.66	199.59	198.84
6	75	950	202.56	199.63	199.02	198.75
7	55	1050	202.51	199.73	198.85	198.63
8	65	1050	202.63	199.47	198.70	198.54
9	75	1050	203.03	199.55	198.91	198.75

When determining the quality class in round rolling products, firstly the diameter tolerance is evaluated and it is known that the products which are not tolerated cannot reach to the first level class without considering the circularity tolerances. If the diameter is within the value tolerance, the

quality class of the thick round rolling product is determined by taking the difference between the largest diameter value (W) and the smallest circularity value (O2). In this regard, Figure 4 was plotted in order to see the tolerance deviations that occur according to the diameters and circularity measurements obtained in the rolling simulations.

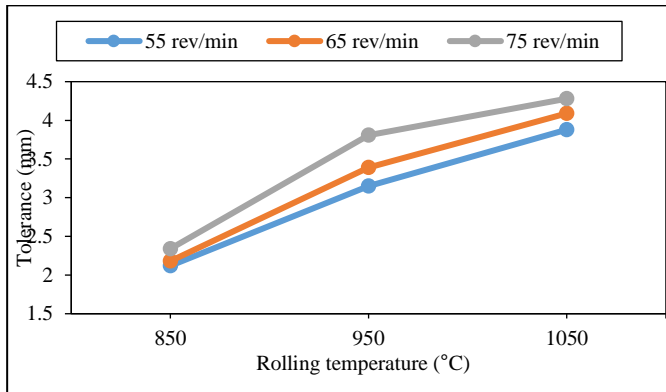


Fig. 4 Circularity tolerance changes according to rolling parameters

Figure 4 shows the change in the rolling temperature with respect to the tolerance of the rounded product depending on the rotational speed of rollers. When the graph is examined, it is seen that the product geometry has moved away from circularity tolerance with the increase in temperature. It was determined that the tolerance value increase with increasing the rotational speed and the maximum tolerance is obtained at 75 rev/min and 1050 °C. As can be seen from Table IV, the products obtained as a result of the first 5 rolling simulations are within diameter tolerance and evaluated according to circularity tolerance. As a result of these evaluations, it was determined that products obtained at 850 °C at all cycles and at 950 °C at low and middle speeds are 1st level. The maximum diameter value was stayed out of tolerance (± 2.5) in the last experiment for 950 °C and all experiments for 1050 °C. For this reason, it can be said that the round products obtained from these experiments take place in the second quality irrespective of the circularity tolerances. Bagheripoor and Bisadi stated that as the rolling speed increases, the fluctuations in the rolling force and torque values will increase. If the fluctuating in rolling force and torque are considered to affect the thermal-mechanical formations that can occur in the material, the deformation behavior (strain, strain rate, stress distribution, etc.) of the material can be examined at high temperature and speed to understand the deviation from circularity.

Finite element model results showed that round products could be obtained within the circular tolerance specified in the standard and at the same time it was determined that the rolling parameters affected the results at different levels. For this purpose, variance analysis (ANOVA) was performed at 95% confidence level to determine the effect of rolling parameters on circularity (TABLE II). Here, P values indicating importance level of each parameter and degrees of freedom (DF), sum of squares (SS), mean squares (MS) and F ratios are shown. The significance level of the variables is determined by considering the P value in the ANOVA table. In addition,

Percentage Contribution Ratio (PCR) on the circularity tolerance of each variable was calculated and given in the ANOVA table. When TABLE II was examined, material temperature was found as the most important parameter on circularity tolerance with PCR of 94.29% in results of rolling simulation. Rotational speed of rollers was determined as second important parameter on circularity with PCR of 4.81%.

TABLE IV
ANOVA results for circularity tolerance

Parameters	DF	SS	MS	F ratio	P value	PCR (%)
Nm	2	0.27682	0.13841	10.58	0.025	4.81
Tm	2	5.42736	2.71368	207.50	0.000	94.29
Error	4	0.05231	0.01308			0.90
Total	8	5.75649				

IV. CONCLUSION

In this study, rolling simulations were carried out in a commercial program by creating a finite element model for a round bar of hot rolled product. As a result of the finite element analysis, the diameter and circularity measured on the round product were analyzed and the obtained results were summarized below.

It was determined that the round product geometry is out of diameter and circularity tolerances by increasing the rolling temperature and the rotational speed. According to ANOVA results, the most important parameter on product quality is rolling temperature in hot rolling. In this regard, it has been determined that the optimum rolling temperature and speed for the first grade products as a result of hot rolling, depending on the applied simulation conditions, are 850-950 °C and 55 rev/min, respectively. Here, the final element method can be applied for the optimization of the hot rolling process, taking into consideration other parameters as well as the rolling temperature and rotational speed.

References

- [1] S. Kalpakjian, S.R. Schmid, K.S.V. Sekar, Manufacturing Engineering and Technology, Pearson Education, Singapore, 2014.
- [2] S.Y. Yuan, L.W. Zhang, S.L. Liao, G.D. Jiang, Y.S. Yu, M. Qi, Simulation of deformation and temperature in multi-pass continuous rolling by three-dimensional FEM, *Journal of Materials Processing Technology*, 209, 2760-2766, 2009.
- [3] Giacomini L. Go long - go strong, *Metals and Mining*, 2, 34-35, 2007.
- [4] S. Kumar, B. S. Kodli, A Study on Thermo-Mechanical Analysis of Hot Rolling & Estimation of Residual Stresses by using FEM. *IOSR Journal of Mechanical and Civil Engineering*, 9 (3), 26-34. 2013.
- [5] P. Szota, S. Mróz, A. Stefanik, H. Dyja, Numerical Modelling of the Working Rolls Wear During Rods Rolling Process. *Archives of Metallurgy and Materials*, 56 (2), 495-501, 2011.
- [6] F. Çavdar, E. Kanca, M. Yaşar, A. Günen, İ. Kalleci, M. Demir, Modeling of Rough Rolling Process by Using Finite Element Method, *2. International Iron & Steel Symposium*, 2015.
- [7] A.A. Milenin, H. Dyja, S. Mróz, Simulation of metal forming during multi-pass rolling of shape bars, *Journal of Materials Processing Technology*, 153-154, 108-114, 2004.

- [8] S. A. Aksenov, E. N. Chumachenko, I. V. Logashina, T. Kubina, Numerical Simulation in Roll Pass Design for Bar Rolling, *Metalurgija*, 54 (1), 75-78, 2015.
- [9] S. Riljak, Numerical Simulation of Shape Rolling, *Royal Institute of Technology School of Industrial Engineering and Management Material Science and Engineering*, MSc Thesis, Sweden, 2006.
- [10] M. Bagheripoor and H. Bisadi, An investigation on the roll force and torque fluctuations during hot strip rolling process, *Production & Manufacturing Research*, 2(1), 128-141, 2014.
- [11] S.R. Motallebi, Investigation of Influence Parameters on the Hot Rolling Process Using Finite Element Method, *2nd International Conference on Engineering Optimization*, Portugal, 2010.
- [12] TS EN 10060, Genel Kullanım Amaçları İçin Sıcak Haddelenmiş Yuvarlak Kesitli Çelik Çubuklar-Boyutlar, Şekil Ve Boyut Toleransları, 2005.
- [13] M.Çakırcalı, C. Kılıçaslan, M. Güden, B. Yardımoğlu, V. Shchukin, V. Petronko, Çapraz kama haddeleme işleminin Sonlu Elemanlar Simülasyonu ve Parametrik Çalışması, *MMO Mühendis ve Makina Dergisi*, 51, 608, 2010.
- [14] İ. Koçali, Haddeleme Tekniğinin Esasları I, *Türkiye Demir ve Çelik İşletmeleri Eğitim Yayınları*, 1985.

Synthesis, characterization and tribological studies of Chromium-Nano diamond composite coating

N. Zoghipour*, E. Salamci*, R. Unal*, N. Gidikova**, R. Valov**, V. Petkov**

MSc. Student - Assi. Prof. - Prof. - Phd. Chem. Eng. - MSc. Chem. Eng. - Phd. Chem. Eng.

*Gazi University, Engineering Faculty, Mechanical Engineering Department, 06570, Ankara, Turkey

** Institute of Metal Science, Equipment and Technologies 67 Shipchenski prohod Blvd 1574 Sofia, Bulgaria

nima.zoghipour@gmail.com, esalamci@gazi.edu.tr, runal@gazi.edu.tr

gidikova@ims.bas.bg, radoslav.valov@gmail.com, vladimirpe2@yahoo.com

Mechanical Engineering Department, Gazi University
Maltepe, Ankara, Turkey

Abstract—Nano composite coatings are a new forms of materials containing hard phase particles to enhance the hardness and wear resistance, among which diamond in terms of feasibility and cost, is the best combination for chromium. In this study, electrolytic coating of pure chromium and Cr-ND (nano diamond) composite coatings were applied on pre-alloy metal powder metallurgy specimens. The effects of the ND particles on tribological behavior of the chromium coatings were investigated. Characterization tests were carried out using an optical microscope, SEM, EDS, XRD and AFM. The dry sliding wear behavior of the specimens was carried out using pin on plate configuration. The hardness and wear resistance of the Cr-ND coated samples were compared with pure chromium coated and non-coated specimens. The results demonstrated that the embedding of the ND particles in the chromium matrix led to a significant improvement on the hardness and wear behavior of the Cr-ND coatings than pure chromium coatings and non-coated specimens.

Keywords—Nano Composite, electrolytic coating, tribology, SEM (scanning electron microscope), EDS (Energy-dispersive X-ray spectroscopy), XRD (X-ray diffraction), AFM (Atomic Force Microscope)

I. INTRODUCTION

Being a precise method, PM has the capability of forming parts with near net shape and complex geometries in acceptable dimensional precision with no need for machining. The mentioned characteristics of PM makes it irresistible in aerospace, mining, automotive and weaponry industries. However, certain problems are arisen in the powder metallurgy parts when they contain pre-existing porosity and voids associated with property degradation [1, 12]. The existence of porosities results in large decreases in both strength and ductility. Porous substrates show less resistance to corrosive agents, reduced mechanical properties, and deleteriously influenced density, electrical properties and diffusion characteristics [1, 2, 12]. To avoid the problems mentioned above, industries are highly inclined to make bigger demands for improved performance. Therefore, it seems that the development of near- perfect surface coatings with higher wear and corrosion resistance is imperative [1, 2]. One useful technique to produce nano composites by deposition of

dispersed nano particles (metallic, non-metallic or polymeric) in the matrix solution to fulfil the uniformity of the external layer of a part is electrolytic coating [2, 6]. Diamond, the frequently studied and applied [5, 13] for its high hardness, good oxidation resistance, chemical stability and wear resistance [12], is a common particulate material to be used for reinforcement in the field of composite coating. The type, shape, size and properties of particles affect the final properties of the composite coatings. So far, most studies have been concentrated on the micro sized particles. However, the application of nano particles is quite a new field for their mechanical, magnetical and optical properties.

Juneghani et. al [8] coated AISI 1020 with pure Cr and Cr-SiC nano composite. They reported that the hardness value of the nanocomposite coating is higher than that of pure chromium coating and with the increasing amount of SiC added to the solution, the hardness value of the coating and the corrosion resistance have improved. Yousefpour et al. [7] studied the wear and corrosion behavior of Ck 75 steel Coated with TiO₂, Al₂O₃ and SiO₂ particles reinforced chromium matrix and reported an increase in wear, corrosion resistance and microhardness. Gidikova et al. [5] coated the carbon steel C45 with electrochemical nano diamond reinforced chromium in acid solution of CrO₃ and they found evolution in the hardness values by increasing nano diamond particle concentration. Isakov et al. [13], studied the surface properties of nano diamond reinforced chromium on stainless steel. The main goal of this study was to investigate the influences of ND particles on the surface morphology, phase structure, grain and crystal sizes, hardness, wear resistance within a chromium matrix on a sintered pre-alloy powder substrate.

II. EXPERIMENTAL PROCEDURES

R. Press and sintering:

The pre-alloy metal powder, supplied by the Toz Metal A. Ş. with the chemical properties as in Table 1 was pressed at 550 MPa in a biaxial die into 31.7×12.7×7.9 mm. The sintering of pressed specimens took place at 1120 °C for 25 minutes in %0.6

carbon potential atmosphere ($\text{CH}_4+\text{C}_3\text{H}_8$) where the total sintering process time was 150 minutes.

TABLE XXIII
THE CHEMICAL PROPERTIES OF THE USED METAL POWDER

Composition	wt. %
AHC.100.29	96.8
Cu	1.5
Graphite F10	0.2
Graphite KS44	0.2
MnS	0.5
Lube E	0.8

S. Deposition of Chromium and Chromium-Nanodiamond coatings

A reduction in H_2 at 950°C for 45 minutes followed by degreasing in 1.2 dichloroethane solution for 10 minutes were done on the specimen to perish the oxide layer on the surface prior to the coating. The galvanic electrodeposition bath based on the Hull-Cell method was taken advantage of to do the chromium and the nano diamond coatings. Lead was used to be anode, and the distance between anode and cathode was 50-60 mm.

TABLE XXIV
ELECTRODEPOSITION BATH COMPOSITION AND PARAMETERS [4]

Electrodeposition bath composition and parameters	Value
CrO_3	220 g/l
H_2SO_4	2.2 g/l
ND concentration	0 and 25
Current density	45 A/dm ²
Temperature	50° C
Stirring rate	100 rpm
pH	5.5-5.8
Average ND size	6 nm

T. Characterization of the materials

The densities of the sintered and coated specimens were calculated with Archimedes principle. The porosity percent, coating thickness of the coated and non-coated specimens were calculated from the average value of the taken pictures of the cross section by optical microscope using ImageJ software.

U. Microstructure and surface morphology tests

The surface morphologies of electrodeposited Cr-ND composite coatings were investigated using scanning electron microscope (SEM). The chemical composition of coatings analysed by Energy-dispersive X-ray spectroscopy (EDS) and X-ray diffraction (XRD). The grain and crystal size of the coating were calculated using Intercept method and Scherrer formula.

V. Hardness tests

The macro hardness tests of the sintered specimens were carried out using 100 Kg. The micro hardness of coatings and non-coated samples was measured using Vickers diamond indenter by a load of 50 g for a loading time of 15 sec. The average of ten repeated measurements has been reported.

W. Wear tests

The dry wear tests of the non-coated and Cr-ND coated specimens were carried out in pin on plate configuration under 1.4 MPa, 20 mm/s at room temperature. The weight loss of the specimens was calculated at 10, 40 and 90 meters of sliding distance after ultrasonic cleaning for 10 minutes in distilled water. The surface roughness and their distribution have been measured before and after every sliding.

III. RESULTS AND DISCUSSION

The sintered specimens' density was measured at 6.90 g/cm^3 . The total porosity rate of the non-coated samples was %11.751 where the average surface porosity rate was %10.870. Due to the low melting point of copper, increased porosity was brought about during the sintering process [12]. Fig. 1a and b are representative of the microstructures of sintered specimens prior to and following the coating process by chromium.

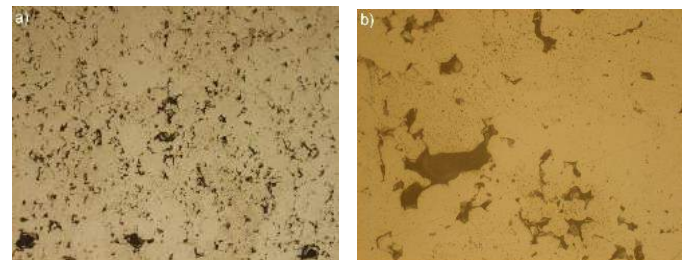


Fig. 13 The surface porosities of the samples before coating; a)100X, b)500X

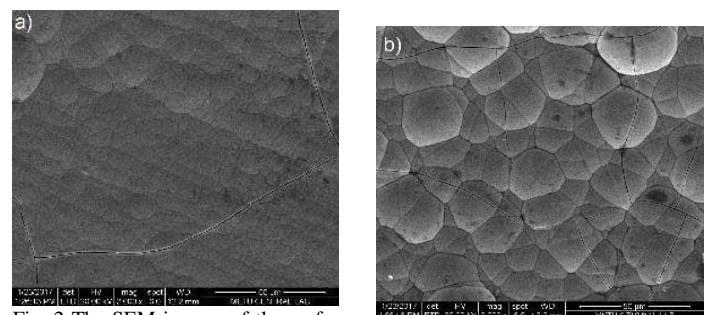


Fig. 2 The SEM images of the surfaces of the coated samples, a) Cr-ND, b) Pure Cr

Fig. 2 a and b demonstrate the microstructures of coated specimens. The average grain size of the Cr-ND coating was calculated $14.28\ \mu\text{m}$, however this value was $39.68\ \mu\text{m}$ for pure Cr. The average thickness of the pure chromium and Cr-ND coated samples were 17,26 and 19,02 μm , respectively. It is worth noting that the chromium yield noticeably increased [5, 13] to %1.55 by enhancing the ND particles in the bath for the $25\ \text{g.l}^{-1}$ concentration while this value was %1.13 for the pure

chromium. The more ND particles in the bath are, the higher the chromium yield becomes. This behavior is justified by the incorporation of the nano particles into the metal coating according to the Guglielmi model [6, 7]. The Guglielmi Model is mainly a two-step process [3, 4]. Initially, the particles approach the cathode and are weakly absorbed onto the cathode surface. The ion cloud surrounds the weakly bound particles. In the second stage, the particles leave the ion cloud surrounding them due to the chemical reaction and are absorbed more strongly on the cathodic surface. Additionally, the increase in particle concentration in the electrolyte also increases the absorption on the cathode surface, according to the two-step model. As a result, there is an increase in the coating's particle content.

The average macro hardness of the sintered parts was 56.38 HRB. Fig 3 shows the average micro hardness values of the specimens.

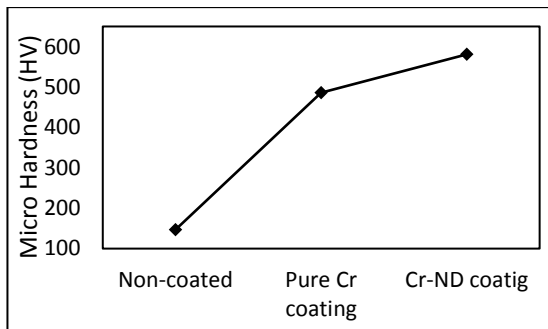


Fig. 3 The average micro hardness of the specimens

The mechanisms for the strengthening of metals and alloys can be explained as follows: a) Strain hardening b) Grain-boundary strengthening and grain-size reduction c) Dispersion strengthening d) Dilute atoms and solid solution strengthening e) Crystal orientation (f) precipitation hardening.

Thus, when considering nano composite coatings, hardness is achieved through mechanisms b and c. The equation below describes grain size reduction and grain boundary strengthening from the Hall-Petch contribution to strengthening.

$$\sigma_y = \sigma_0 + kd^{1/2}$$

where σ_y is the yield stress, σ_0 a friction stress, d the average grain size in diameter and k is a constant [8]. In grain-boundary strengthening, the grain boundaries act as pinning points impeding further dislocation propagation. Since the lattice structure of adjacent grains differs in orientation, it requires more energy for a dislocation to change directions and move into the adjacent grain. The grain boundary is also much more disordered than inside the grain, which also prevents the dislocations from moving in a continuous slip plane. Impeding this dislocation movement will hinder the onset of plasticity and hence increase the yield strength of the material. The dispersion strengthening by Orowan mechanism suggests the yield stress of an alloy/composite containing a dispersion of fine particles is determined by the shear stress required to force

a dislocation line between two particles separated by a distance $2r$ [9]. The dislocation line between the particles turn into a semicircle. The resulting semicircle can be calculated by:

$$r = \frac{D-d}{2}; \sigma_y = \frac{Gb}{r}; \tau_0 = \frac{Gb}{2r}$$

where G shear modulus of the matrix, b the Burger's vector of the dislocation and τ_0 the shear stress required to move dislocation between the blocks in the microstructure obstacles (Cr-ND), D the distance between the centres of two particles and d refers to the diameter of a particle.

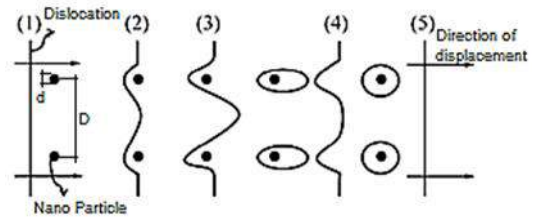


Fig. 4 Schematic view of Orowan dispersion hardening mechanism [8]

In Fig. 4. line 1 exhibits a straight dislocation line approaching two particles separated by a distance $2r$. The line began to bend in the 2nd, the critical bend in the 3rd. Dislocation, without reduction in the radius of the curve, it can be carried forward until it encounters the oppositely marked dislocation. Dislocations in opposite directions in the 4th grade meet each other and destroy each other. Then to continue the original dislocation movement free [9].

For pure chromium G and b are supposed 115 GPa and 0.2884 nm respectively [8]. Restriction occurs in the growth of the chromium grains, crystals and the plastic deformation of the matrix under a loading by way of grain size reduction, dispersive strengthening and crystal orientation effects, and the hardness of Cr-ND composite coatings enhances due to the distribution of ND particles in the Cr matrix. The contribution from the dispersion strengthening is largely due to the uniform distribution of ND particles in the coatings in the case of nanocomposite coatings. Such particles possess a fine grain size. The inclusion of nano diamond particles activates the hardening mechanism of the second phase barrier. When the material flow is hindered by distributed hard nanometer diamond particles as a barrier to dislocation movement, the plastic deformation of the depositions would be more difficult. The hardness would also be improved by achieving a better distribution of nanometer particles within the chromium deposition matrix. Results are confirmed by the SEM and XRD analysis.

The electro-deposited Cr-ND coating is composed of a solid solution in a mono-phase matrix, as confirmed by the XRD pattern shown in Fig. 5. The peaks corresponding to the [111] peaks of nano diamond in the coatings are shown in the graphs, implying that the nano diamond particles have been embedded in the chromium matrix.

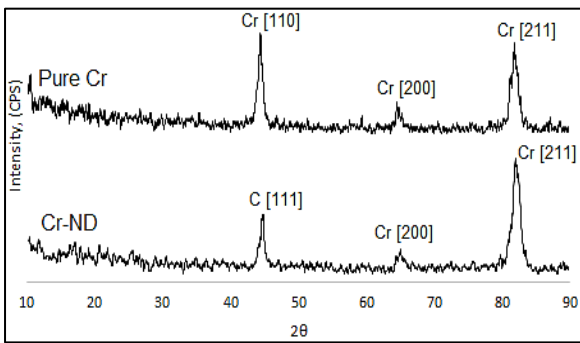


Fig. 5 The XRD pattern of pure Cr and Cr-ND coatings

Diffraction lines are exhibited by pure chromium deposit [110], [200] and [211]. The intensity of the diffraction peaks of the chromium in the nano composite coating is lower and the peak width is broader than that of the pure chromium coating. The peak of Cr [200] in pure Cr is sharper and higher than that of the Cr-ND coating. With respect to the peak of pure chromium, the Cr [200] and [211] peaks occurring at 2θ angle of the samples differed somewhat in the Bragg angle. The fact that the lattice distance of chromium is restricted by the incorporated ND particles is due to the physical effect of the composite coating process. No diffraction peaks of any unexpected substance arose due to chemical reactions, as demonstrated in the graphs. The crystal sizes of the chromium have decreased with the incorporation of ND particles in chromium with respect to pure chromium coating [6, 10, 11].

The EDS analyses expressed the composition of the electrodeposited Cr-ND coating in which the weight percent of Cr is 84.94 wt.% and that of ND is 5.05 wt.% from EDS as shown in Fig. 6.

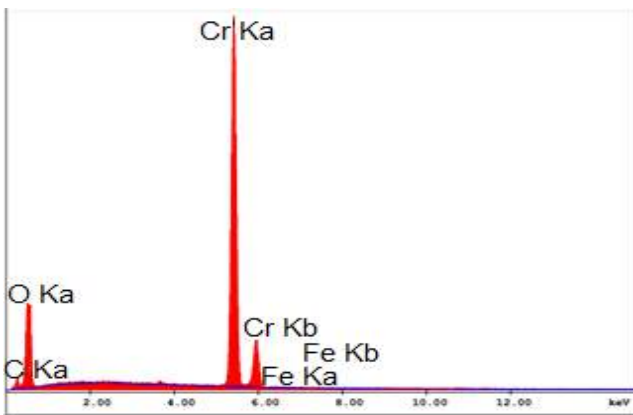


Fig. 6 The EDS graph of Cr-ND coating

Fig 7. shows the mass loss during wear test, Fig 8. shows the total mass loss and wear rate. It is found that the Cr-ND composite coating shows higher wear resistance than the pure chromium coating. The influences of ND particles in the amendment of the tribological properties of Cr-ND composite coatings is due to the incorporation of the ball-shaped and ultra-hard ND particles in the coatings refined grain sizes [8, 9]. The increase microhardness of Cr-ND composite coatings can improve the wear resistance remarkably.

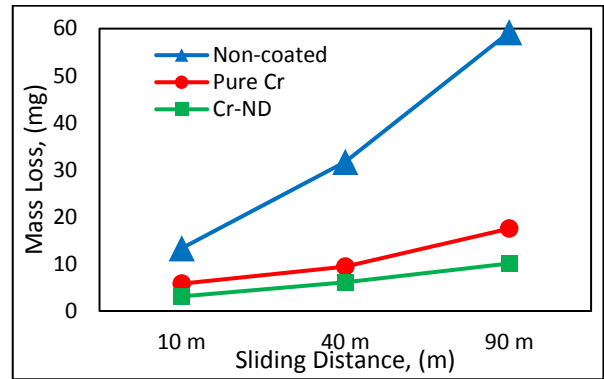


Fig. 7 The mass loss during wear test

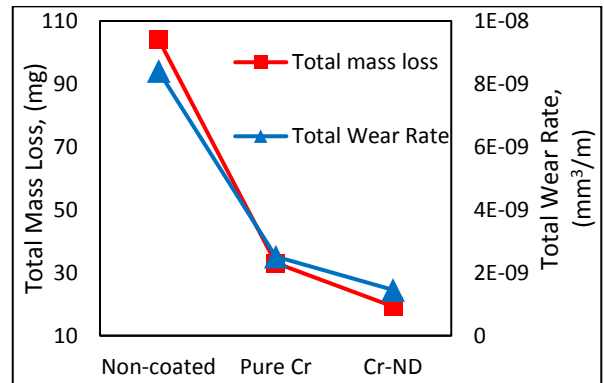


Fig. 8 The total mass loss and wear rate

Fig 9. shows the average surface roughness and its distribution during the wear tests of the specimens. With increasing the sliding distance, the surface roughness and its distribution of the non-coated specimen increases, whereas these the opposite is valid for the Cr and Cr-ND coated specimens. The increasing surface roughness and its distribution of the non-coated specimen can be attributed to the adhesive and abrasive wear [14].

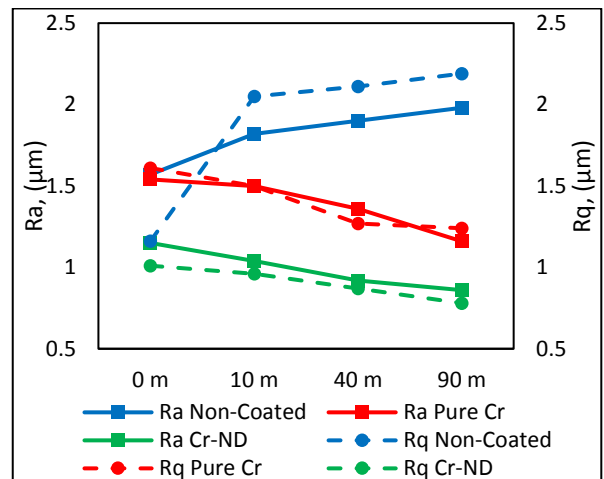


Fig. 9 The surface roughness and its distribution during wear test

Fig. 10, Fig. 11 and Fig. 12 demonstrate the worn surfaces of the non-coated, pure Cr and Cr-ND coating. The parallel lines on the surface are indicative of abrasive wear. Adhesive

wear is also noticeable on the non-coated specimen as well as abrasive wear.

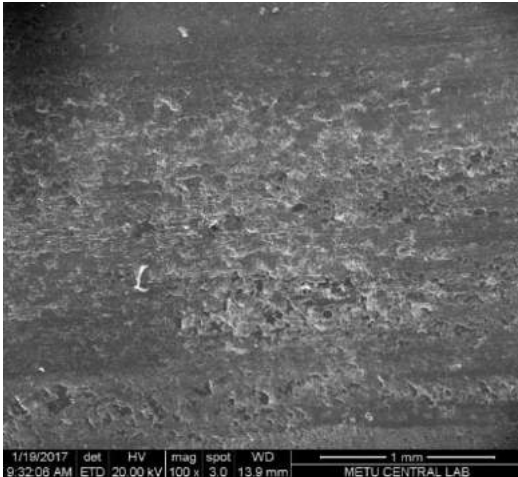


Fig 10. The SEM image of the worn Non-coated sample

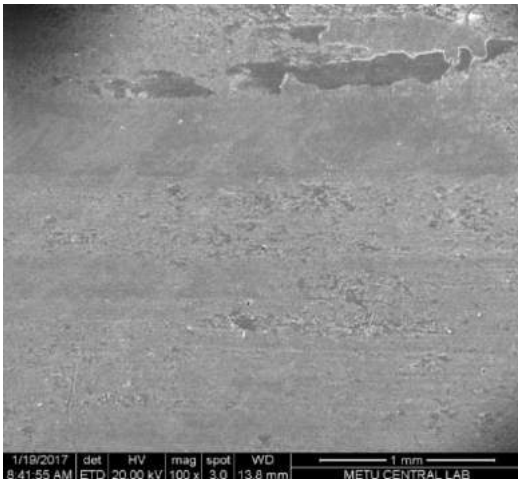


Fig 11. The SEM image of the worn pure Cr coated sample

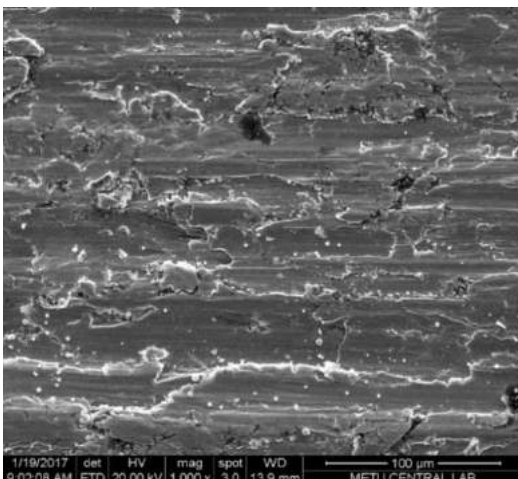


Fig 12. The SEM image of the worn Cr-ND coated sample

The 3D surface topography of the surfaces was taken from a $1 \times 1 \mu\text{m}^2$ area by AFM of the samples. The 3-D surface

topography of the Cr-ND coating is shown Fig. The R_a surface roughness, RMS surface roughness distribution values were calculated. The surface roughness and its distribution values of Cr-ND are less than both pure Cr and non-coated surfaces. This can be attributed to the contribution of ND particles which created a more compact and smoother surface.

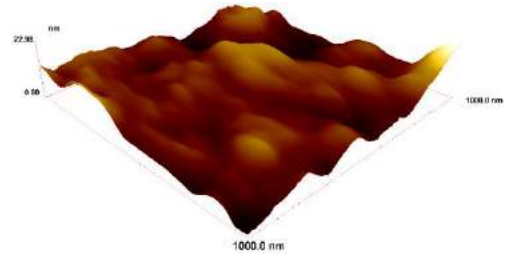


Fig 11. The AFM image of the Cr-ND coated sample

TABLE III

THE 3D SURFACE TOPOGRAPHY RESULTS OF THE SPECIMENS

Sample	R_a (nm)	RMS (nm)
Non-coated	5.04	6.62
Pure Cr	2.86	3.81
Cr-ND	2.12	2.65

IV. CONCLUSIONS

X-ray diffraction analyses performed a successful mono phase nanocomposite coating process on pre-alloy metal powder substrates by electrolytic coating process.

The incorporation of ND particles during electrochemical deposition of chromium enhances of the chromium yield and the thickness of the coating.

The embedding of ND particles in the chromium matrix resulted in a layer with smaller crystallite and grain sizes and more compact and smoother surface than those of pure Cr deposits.

It could be observed from the SEM micrographs of the worn sample surfaces in the dry wear tests that abrasion was the main wear mechanism. Furthermore, a little adhesion occurred on the worn surface of the substrate, especially on the non-coated samples.

The embedding of ND particles in the chromium matrix enhances the hardness, wear behavior.

ACKNOWLEDGMENT

The authors acknowledge with thanks the financial supports granted by TÜBİTAK to the project no. 214M098, and Toz Metal A. Ş. for providing the metal powders. The specimens were produced in the framework of the bilateral cooperation between Gazi University and Bulgarian Academy of Sciences (BAS). We also thank Mr. Pouya Zoghipour (Phd Student of Mechanical Engineering-Middle East

Technical University) for assisting us in preparing the paper.

REFERENCES

- [1] Leisner P, Leu RC, Moller P. Electroplating of porous PM compacts. *Powder Metall* 1997; 40:207–10.
- [2] Gabe DR., Corrosion protection of sintered metal parts. *Powder Metall* 1977; 20:227–31.
- [3] Z. Zeng, L. Wang, A. Liang, J. Zhang, “Tribological and electrochemical behavior of thick Cr–C alloy coatings electrodeposited in trivalent chromium bath as an alternative to conventional Cr coatings”, *Electrochim Acta* 52 (2006) 1366–1373.
- [4] Mandich, N. and Dennis, J., Codeposition of nanodiamonds with chromium, *Metal Finishing*, 99 (6),117-119, 2001.
- [5] Gidikova N., Cias A., Petkov V., Madej M., Sulowski M., and Valov R., “Wear resistant chromium coatings modified with diamond nanoparticles”, *Archives of Metallurgy and Materials*, 59 (4), 1513-1516, 2014.
- [6] Abdel Aal A., “Hard and corrosion resistant nanocomposite coating for Al alloy”, *Material Science and Engineering A*, 2008, 474:181-187.
- [7] Yousefpour M., Rahimi A., “Characterization and selection of optimal parameters to achieve the best tribological performance of the electrodeposited cr nanocomposite coating”, *Materials & Design*, 54, 382- 389, 2014.
- [8] Juneghani M. A., Farzam M., and Zohdirad, H., “Wear and corrosion resistance and electroplating characteristics of electrodeposited Cr–SiC nanocomposite coatings”, *Transactions of Nonferrous Metals Society of China*, 23 (7), 1993-2001, 2013.
- [9] DIETER G E. *Mechanical metallurgy [M]*. 3rd ed. London: McGraw-Hill, 1988.
- [10] P. Gyftou, E.A. Pavlatou, N. Spyrellis, “Effect of pulse electrodeposition parameters on the properties of Ni/nano-SiC composites”, *Applied Surface Science*, 254 (2008) 5910–5916.
- [11] Hui Xu, Zhi Yanga, Meng-Ke Lia, Yan-Li Shia, Yi Huang, Hu-Lin Li, “Synthesis and properties of electroless Ni–P–Nanometer Diamond composite coatings”, *Surface & Coatings Technology*, 191 (2005) 161–165.
- [12] M. Etaat, M. Emamy, M. Ghambari, E. Fadaei, “Surface treatment and nickel plating of iron powder metallurgy parts for corrosion protection”, *Materials and Design*, 30 (2009) 3560–3565.
- [13] V. P. Isakov, A. I. Lyamkin, D. N. Nikitin, A. S. Shalimova, and A. V. Solntsev, “Structure and Properties of Chromium–Nanodiamond Composite Electrochemical Coatings”, *ISSN 2070.2051, Protection of Metals and Physical Chemistry of Surfaces*, 2010, Vol. 46, No. 5, pp. 578–581.
- [14] Koji Kato, Koshi Adachi, *Wear Mechanisms*, Chapter 7, Tohoku University, 2001 CRS press by LLC.

Use of Steel Slag in Rubble-Mound Marine Structures

V.Ş. Özgür Kırca[#], Baran Çağlar⁺, Taylan Bağcı^{*}, Evren Kılıcı[#], M. Sedat Kabdaşlı[#]

[#]Istanbul Technical University, Dept. of Civil Eng., Maslak 34469 Istanbul, Turkey
{kircave, ekilci, kabdaslis}@itu.edu.tr

⁺ERDEMİR Mühendislik A.Ş., Ardıç S., No:6 Ataşehir 34746 Istanbul, Turkey
bcaglar@erdemir.com.tr

[#]Doğuş University, Dept. of Civil Eng., Acıbadem Kadıköy, 34722 Istanbul, Turkey
tbagci@dogus.edu.tr

Abstract— The slag from the steel industry has been utilized for a variety of purposes ranging from road construction, cement production and fill material. The usability of steel slag is economically important since vast amount of steel slag is produced as a by-product of steel industry. For each usage type of steel slag, proper tests and analyses must be performed in order to ensure that the material exhibits the necessary performance and reconciles with environmental codes of practice. In this study, the steel slag from Erdemir and İsdemir (two major steel production facilities in Turkey) has been tested by means of physical modelling in the Hydraulic Laboratory of Istanbul Technical University for determination of their suitability to be used in rubble-mound marine structures. Results indicated that steel slag can be a viable alternative as a core material in marine structures; given it is high grain density and shear strength. With these positive results, it turns out the use of steel slag in core of rubble-mound structure is likely to contribute the effective usage of the material and constitutes an innegligible recycling opportunity.

Keywords— Steel slag, Rubble-mound marine structures, Core material, By-product

I. INTRODUCTION

One of the most important and vastly produced by-product of steel industry is slag. Generally, slag can be classified with respect to the production process of steel; such as the blast-furnace slag, electric-arc furnace slag, basic oxygen steel-making furnace slag etc. The slag from the steel industry has been utilized for a variety of purposes ranging from road construction, cement production and marine engineering application (as a core or fill material). The usability of steel slag bears a very significant importance from economical point of view since this material is an inevitable by-product of steel industry all over the world. For each usage type of steel slag, proper tests and analyses must be performed in order to ensure that the material exhibits the necessary performance in terms of mechanical and chemical characteristics as well as reconciliation with environmental codes of practice.

Although the characteristics of steel slag is not standard and may vary from facility to facility, the same process followed for steel production causes the steel slag to exhibit similar chemical and mineral compositions ([1]). At the production stage, steel slag generally constitutes 42%-55% CaO and 12%-

15% SiO₂, rest of it including other materials. The most important mechanical criterion for the steel slag to be used in civil engineering processes is its volumetric stability associated with free CaO and MgO. When reacted with water, these minerals turn into hydroxides and cause volume expansion and loss of mechanical strength of the material. If steel slag undergoes *aging* process (stored in open air for months to years or any other advanced aging process such as steam curing, etc.), it releases the CaO and MgO it constituted and gains its volumetric stability.

The use of steel slag in marine structures as a fill or core material is not very common although there are a few application examples, such as the South Star project breakwater in Taiwan ([2]), Hammond Marina breakwater in Lake Michigan USA ([3]) and Osaka Harbour and Airport in Japan ([4]). Since rubble-mound marine structures (such as breakwaters or dikes) require massive amounts of core fills, usage of steel slag is a very important opportunity for utilising it as a by-product. In Hammond Marina for example, 60000 tons of slag was used for the breakwater core.

On the other hand, there are some stringent characteristics desired for materials to be used in rubble-mound marine structures, where hydrodynamic forces due to waves and currents are very effective as well as chemically aggressive seawater. As compilation of usage opportunities, [5] mentions the usage of steel slag in road construction and embankments, as well as dams, dikes, stabilisation of river beds and river banks. Additionally, [6] regulates the properties of the steel slag to be used as an additive in the concrete mix-design of armour units for coastal protection. Yet, there is no particularly defined clear-cut criteria for steel slag to be used in rubble-mound structures as fill or core material.

For the particular usage of steel slag in marine structures as a fill or core material, the most important mechanical characteristics can be listed as specific mass, grain size distribution, porosity, shear strength, resistance to impact and crushing, water absorption ratio and volume expansion or swelling ([1]; [5]). As mentioned above, aging is the key process to improve the mechanical characteristics of the steel slag as well as reducing the environmental risk since harmful

release of lime can be diminished or prevented by means of aging.

The primary purpose of this study is to investigate the usability of steel slag as a core or fill material in rubble-mound marine structures given the possible benefits of such a utilisation. Accordingly, steel slag from two major steel production facilities in Turkey (Erdemir and Isdemir) has been tested by means of physical modelling in the Hydraulic Laboratory of Istanbul Technical University (ITU) for determination of their suitability to be used as core material in coastal defence structures. Within this scope, two different physical modelling strategies were practiced: (1) Scaled physical modelling of general structure stability and (2) full-scale physical modelling of core under oscillatory pressure gradients.

The first of these two approaches involved wave flume tests, in which a scaled breakwater model was subjected to irregular wave attack. The second modelling technique was employed particularly to simulate the full-scale behaviour and performance of the core material under oscillatory pressure gradients since such behaviours cannot be simulated in small scale flume tests. The two models constituted a complementary source of information on the performance of core material. Once the usability of the steel slag as a core or fill material in rubble-mound structures is confirmed, an estimation analysis has been carried out to assess how much steel slag can feasibly be utilised as core material and what may be the economical outcome of this utilisation.

II. EXPERIMENTAL SETUP AND PROCEDURE

In this chapter, the details of the experiments along with the material properties, setup, instrumentation and procedure will be presented.

X. Material Characteristics

As stated above, steel slag samples from two different production facilities were used in the experiments. Both of the steel slag samples sent to ITU were chosen among the slag mounds which already had gone through at least 18 months of aging process in the open air. This was preferred in order to limit the release of lime in water and assure the volumetric stability of the material.

When analysed, it was seen that these two samples exhibited essentially the same mechanical characteristics (with very

slight difference). In order to study the effect of grain size distribution, different grain size compositions were chosen from these two samples. The Isdemir slag sample was sieved such that only large grains ($d > 5$ mm) was used in the tests, whereas the Erdemir slag sample was not sieved so that it included the very fine grains (down to silt size of 0.05 mm). The material characteristics of the two steel slag samples are summarised in Table I. As can be followed from this table, the specific mass as well as shear strength of the steel slag are higher than the common fill material (i.e. quartz sand). These two mechanical characteristics are particularly important for the stability under hydrodynamic loading.

TABLE XXV
MECHANICAL CHARACTERISTICS OF STEEL SLAG SAMPLES USED IN THE EXPERIMENTS

Parameter	Unit	Erdemir Sample	Isdemir Sample
Specific mass, ρ_s	g/cm ³	3.42	3.40
Median grain size, d_{50}	mm	0.7	15.0
Geometric standard deviation, σ_g	--	3.0	1.8
Volume expansion, $\Delta V/V$	%	< 3	< 3
Internal friction angle, ϕ'	°	40	42
Porosity, n	--	0.38	0.41

Y. The Wave Flume Experiments

Wave flume experiments were conducted in the 26 m long, 1 m wide and 1 m deep irregular wave flume of ITU Hydraulics Laboratory. For testing the Erdemir and Isdemir steel slag samples as core material, two different breakwater models were constructed as shown in Fig. 1 and Fig. 2 which are called ER and ID models, respectively. The geometric scales of the breakwater models were 1/48 and 1/35 for ER and IS experiments, respectively.

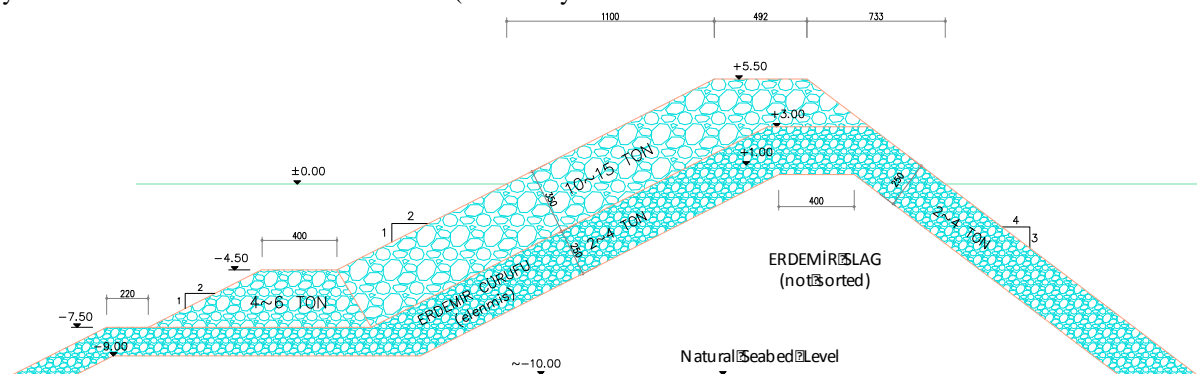


Fig. 14 The ER breakwater model with core made of steel slag from Erdemir facility. Given are prototype dimensions in m, model was scaled to 1/48.

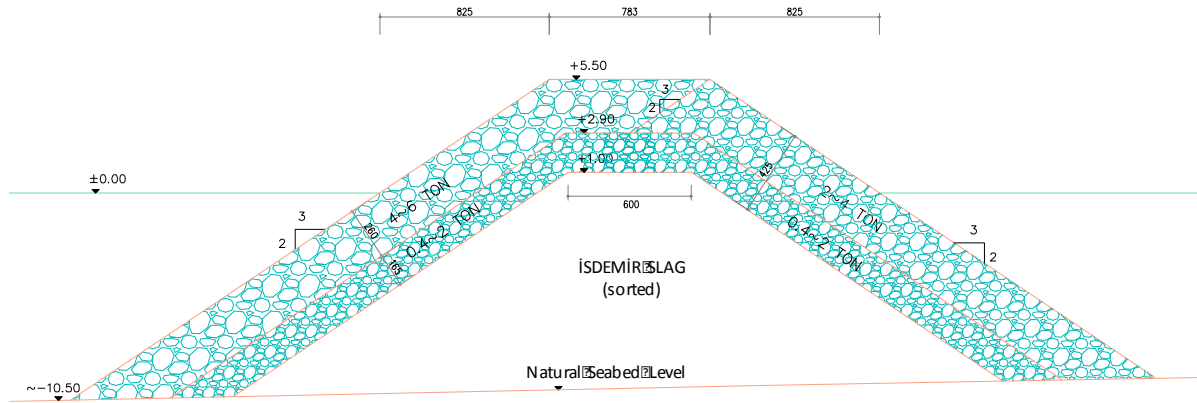


Fig. 15 The IS breakwater model with core made of steel slag from İsdemir facility. Given are prototype dimensions in m, model was scaled to 1/35.

Generally speaking, ER model reflects the design of a typical breakwater in Black Sea, whereas IS model represents the breakwater lay-out in the East Mediterranean. The wave conditions simulated by the two breakwater models are presented in Table II. Pierson-Moskowitz type wave spectra were generated with 30 minutes long wave time series (approximately 1400 waves). Wave heights were measured by three resistance type wave probes and spectral decomposition technique was used for decomposing incident and reflected waves ([7]). The overall stability of the breakwaters were observed after each tests by comparing the after-the-test photographs of the armour layer as well as the breakwater toe. No repair was conducted in between the tests, such that the damage of the armour layer (as % of units dislocated) were measured in a cumulative manner. A snapshot of the models during tests is shown in Fig.3, whereas a sample after-the-test photo is shown in Fig. 4



Fig. 17 A sample after-the-test photo that shows the damage on the armour layer due to wave attack.

TABLE XXVI

THE WAVE CHARACTERISTICS APPLIED IN THE WAVE FLUME EXPERIMENTS

Parameter	ER-1	ER-2	ER-3	IS-1	IS-2	IS-3
Significant wave height, H_s	4.60	4.80	5.20	3.35	3.85	4.05
Maximum wave height, H_{max}	7.50	7.65	8.00	6.30	7.10	7.25
Spectral peak wave period, T_p	9.6	9.8	10.0	8.8	9.1	9.3



Fig. 16 A snapshot from the wave flume experiments tests during the IS-2 model run.

Z. Oscillatory Pressure Gradient Experiments

Although the scaled physical models in the wave flume can give some insightful results about the performance of the steel slag as a core material, it is generally not possible to simulate the entire physics of hydraulic processes related to the instability of core material, especially the flow through porous media under oscillatory pressure gradients. Therefore, as a second experimental campaign, a full-scale (i.e. large scale) physical model was set in ITU Hydraulics Laboratory, by which the sloped face of the material was exposed to oscillatory pressure gradients with the same magnitudes and time scales as in the prototype. For this purpose, a novel experimental apparatus was designed and constructed, as sketched in Fig. 5. This apparatus comprised a cylindrical chamber of diameter $D = 30$ cm and height $l = 100$ cm with a filter at the bottom. The chamber can be inclined up to $\alpha = 30^\circ$ with reference to the vertical for simulating the face slope. Once the material sample was placed in the chamber, it was exposed to oscillatory pressure gradients driven by means of a water column moved up and down via a pneumatic piston.

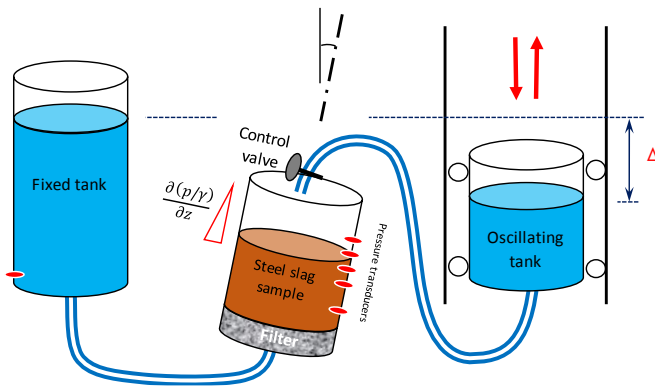


Fig. 18 Sketch of the oscillatory pressure gradient apparatus.

In addition to the two steel slag samples, medium-coarse size quartz sand ($d_{50}=0.7$ mm, $\sigma_g=2$, $\rho_s=2.65$ g/cm³) was also tested with the same apparatus in order to compare the behaviour of the steel slag with the regular fill material for the rubble-mound breakwaters. Dynamic pressure gradients were measured by means of five pressure transducers that were installed on the testing chamber with intervals 5 to 8 cm. Together with the pressure measurements, video recording was performed particularly close to the surface of the steel slag sample. Observations were focused on seeing any possible failures; heaving, boiling, piping, etc. Therefore, the pressure gradient timeseries and the video recordings were synchronized.

More than 50 tests were performed with the two steel slag samples from Erdemir and İsdemir facility, whereas 20 tests were conducted for the sand in these tests the oscillations of the tank ranged from ± 15 cm to ± 65 cm with periods of 8 to 12 s. In those tests, three different inclination angles of the chamber (i.e. face slope) was used; 0°, 18°, 34°.

III. RESULTS AND DISCUSSIONS

AA. Results of Flume Experiments

As shown in Table II, the breakwater models were subjected to three different wave series, which start from relatively moderate sea to rougher sea states. Moreover, these wave series were deliberately selected slightly larger than the design wave characteristics of the modelled sections, so that the influence of armour damage on the behaviour of core material (i.e. steel slag) could be observed. Table III summarises the results of the wave flume tests in terms of armour layer damage, reflection coefficient and overall stability state of the structure after each wave series attack.

As can be seen from the Table III, although the first wave series has the smallest wave height in ER tests, the damage is highest among the three tests conducted. Furthermore, the damage gets even less for the highest wave series. The reason is the initial settlement of the blocks after the construction of the model. The ER model has a mild foreshore slope (1v:2h), which renders the effective dissipation of the waves and hence resulting a stable structure. In parallel to this, the reflection coefficients are relatively low. On the other hand, the IS model

has a steep foreshore slope (3v:4h) that resulted with poor incident energy dissipation. Reflection coefficients as well as the armour damage ratios are high.

TABLE XXVII
SUMMARY OF THE WAVE FLUME EXPERIMENT RESULTS

Test	H_s (m)	T_p (s)	K_R	Damage	Remark
ER-1	4.60	9.6	0.36	6%	Slight initial settlement, slight toe damage, no serious damage, armour stable, core stable
ER-2	4.80	9.8	0.36	4%	No significant settlement, a few armour units displaced, armour stable, core stable
ER-3	5.20	10.0	0.28	3%	Slight settlement, a few armour units dislocated, slight toe damage, armour stable, core stable
IS-1	3.35	8.8	0.52	7%	Slight initial settlement, no serious damage, armour stable, core stable
IS-2	3.85	9.1	0.48	28%	Significant settlement, serious damage at the foreshore, armour hardly stable, core stable
IS-3	4.05	9.3	0.46	> 30%	General settlement, extensive foreshore damage, filter exposed, armour do not function, core stable

Although the armour layer became unstable from in IS experiments, meaning that too many armour blocks are displaced or dislocated for the structure to properly function, the core was still intact as well as the filter. This is mostly owing to the grain size distribution of the steel slag used in the IS tests, which does not include any fines ($d > 5$ mm). Furthermore, the specific mass and the shear strength of the steel slags seems to have contributed to the overall stability of the breakwater. Although the filter was exposed here and there, the structure remained intact.

On the other hand, the waves were not strong enough to destroy the armour layer in the ER experiments. Although the grain size distribution of the breakwater model core included silt-size fines (down to 0.05 mm), this was not seen to have an adverse effect on the stability of the breakwater, provided that the armour layer kept functioning. Had the armour layer of the ER model breakwater been damaged as much as the IS experiments, it had not been possible for the breakwater to keep its integrity.

BB. Results of the Full-Scale Oscillatory Pressure Gradient Experiments

As stated above, it was envisaged that the novel experimental apparatus that is designed for the simulation of the core behaviour under oscillatory pressure gradients would give a much more detailed description of the performance of steel slag as a core material in rubble-mound marine structures. The reason is that it is not

possible to simulate the flow through porous medium and the intergranular forces in small-scale flume experiments, in which the primary purpose is usually to test the performance of the armour layer of the structure rather than a particular stability analysis of the core.

To describe the effect of hydrodynamic forces (being the waves and currents) in the marine environment on a protected slope of material, Fig. 6 is schematised. Since the slope is protected with a revetment or an armour layer, the tangential forces induced by the moving water would be limited. In fact, there might still be some amount of turbulence intruded in between the armour blocks and reached the slope surface, but in this specific case the shear stresses are assumed to be fully diminished by the armour and only the normal forces (or the pressure forces) are expected to be effective. Let a parcel of material is taken as the shaded control volume. This material would resist the pressure induced uplift force F_u by its submerged weight W' and the frictional stress F_s at the lateral interface. The thickness of this parcel is Δz and the surface-projected area is ΔA .

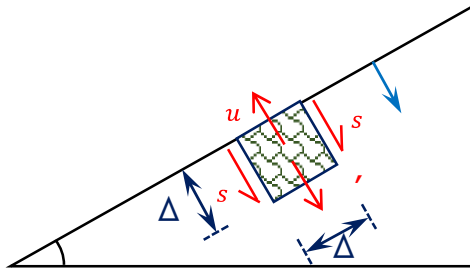


Fig. 19 Schematic description of the hydrodynamic loading on a protected slope in the marine environment.

By use of the force balance equation and steady-state assumption, one can show that the critical pressure gradient (hydraulic slope) to cause this material parcel to move upwards and to be sucked into the flow is:

$$\frac{\partial(p/\gamma)}{\partial z} \geq (s - 1) (1 - n) \cos \alpha + \frac{F_s}{\Delta A \Delta z \gamma} \quad (1)$$

in which $s = \rho_s/\rho_w$ is the specific gravity of the material grains, n is the porosity of the material and γ is the specific weight of water. This equation is also known as the piping criterion and was previously defined by other researchers in slightly different forms ([8]). It should also be noted that the stability of the breakwater core against pressure gradient forces has recently been investigated experimentally by other researchers, albeit in the context of wave flume experiments ([9]-[10]).

On the other hand, for an unsteady pressure gradient (oscillating in the case of waves, run-up and run-down one after the other), the inertia terms kick in which makes the picture a lot more complicated. In such a situation, one of the best

strategies to follow is the full-scale physical modelling, with which the schematic picture given by Fig. 6 can be reproduced. For the values given in Table I and neglecting the friction term (F_s), the critical pressure gradient to cause piping on a flat surface becomes approximately $\frac{\partial(p/\gamma)}{\partial z} \geq 1.4$. On the other hand, the same number for quartz sand with identical porosity would be at the order of $\frac{\partial(p/\gamma)}{\partial z} \geq 1.1$. Thus, one can generally say that steel slag has an advantage over quartz sand in terms of piping resistance given its higher specific mass.

In order to compare regular quartz sand, sieved steel slag (İsdemir sample) and not sieved steel slag (Erdemir sample), three figures are presented, Fig. 7, 8 and 9, respectively. In these figures the orange curve shows the pressure gradient on the surface of the material, whereas red and blue curves give the pressure gradient at 3.5 and 15 cm down below the surface. Comparing those three figures, the sieved steel slag, which does not include grains finer than 5 mm, has performed much better from the other two tested materials. Although the face slope was very steep and the amplitude of the oscillations were high, the pressure gradient generated across the surface remained very limited. This is basically associated with the high permeability of the material. The pores within the grains let the water flow through and the upward directed force becomes very limited. In addition to this, the heavy grain density and high intergranular friction are additional stabilizing forces for the material. Quartz sand went through piping failure for an amplitude of 50 cm for zero inclination. On the other hand, not sieved steels lag (which includes fines down to 0.05 mm) went through piping when the inclination is 18° and oscillation amplitude is 15 cm.

These results suggest that hydraulic conductivity (permeability) of the material plays a major role on its performance as a core material. For steel slag to be used in the core layers of rubble-mound marine structures (such as breakwaters) one of the most important criterion comes out to be the grains size distribution (i.e. the ratio of fines in the grain composition). The comparison of steels slag with quartz material shows that steel slag is advantageous with its high specific mass and intergranular friction. Yet, it should be born in mind that the steel slag used in the structures must be undergone the aging process so that the volumetric stability of the material is maintained.

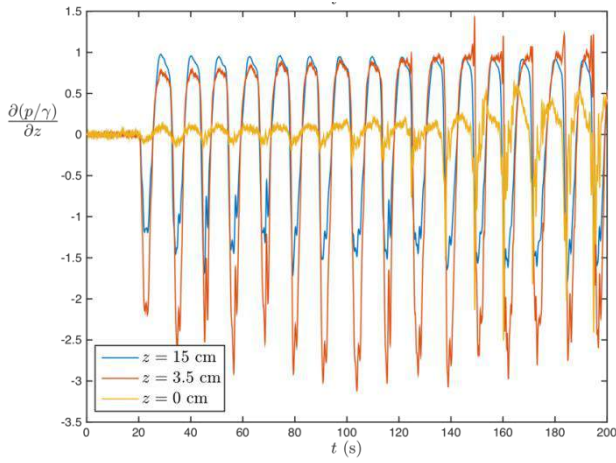


Fig. 20 Pressure gradient time series of quartz sand sample with model parameters $\alpha = 0^\circ$, $\Delta H = 50$ cm, $T = 12$ s, $\left(\frac{\partial(p/\gamma)}{\partial z}\right)_{max} = 1.0$, piping observed.

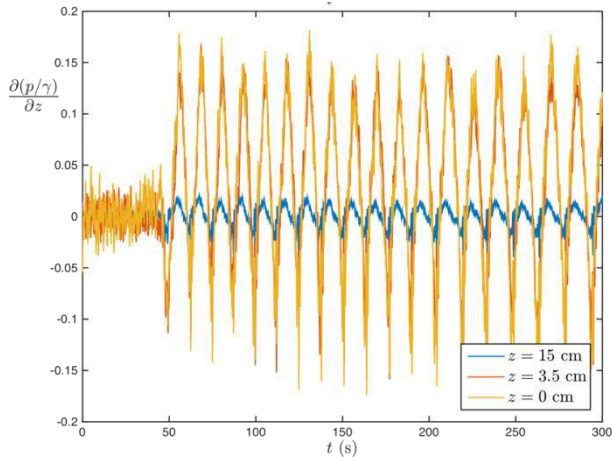


Fig. 21 Pressure gradient time series of sieved steel slag sample from İsdemir (no fines) with model parameters $\alpha = 34^\circ$, $\Delta H = 65$ cm, $T = 12$ s, $\left(\frac{\partial(p/\gamma)}{\partial z}\right)_{max} = 0.17$, piping NOT observed.

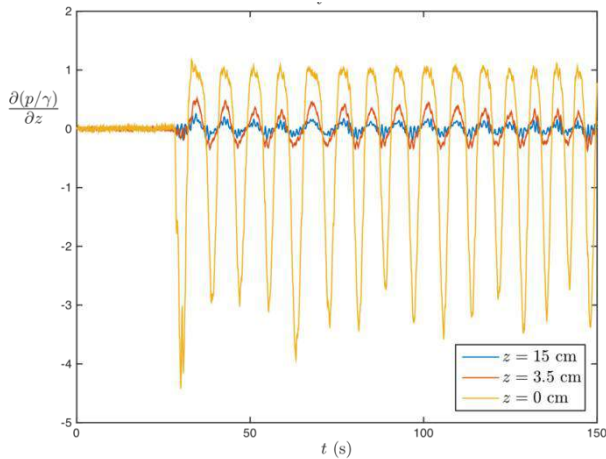


Fig. 22 Pressure gradient time series of not-sieved steel slag sample from Erdemir (including fines) with model parameters $\alpha = 18^\circ$, $\Delta H = 15$ cm, $T = 12$ s, $\left(\frac{\partial(p/\gamma)}{\partial z}\right)_{max} = 1.1$, piping observed at the limit.

IV. REMARKS ON PRACTICAL APPLICATION

Since steel slag is an inevitable by-product of the steel industry, proper utilisation of this material is of utmost importance from the economic, environmental and sustainability points of view. By applying proper treatment and sorting processes on steel slag, the material may be rendered to a viable alternative to be used in the core fills of rubble-mound marine structures. The utilisation ratio of steel slag is European countries is at the order of 68%. The raw steel production of Turkey was reported to be over 50 million tons in 2014 ([11]), which is one of the major export item of the country. The utilisation ratio of steel slag in Turkey is less than 40%.

When it comes to hydraulic structures, especially rubble-mound structures, electric-arc furnace slag has been utilised for quite a long time all over the world ([11]). The present study showed that steel slag can also be a viable material for the core fills of rubble-mound structures, provided that the aging process and grains size sorting is properly organised. In the design of marine structures the core materials are usually desired to have no finer material than the medium-fine sand size (0.3-0.5 mm). This size of material would likely to constitute more than half of the steel slag produced regular. Another alternative may be mixing the steel slag with quarry run and use this mixture as the core material. By this way, the stability of the quarry run would be modified.

Considering that roughly 500000-1000000 tons of core material is needed in the marine construction sector of Turkey, this suggested usage of steel slag would definitely contribute to the increasing of utilisation ratio of steel slag in Turkey.

V. CONCLUSIONS

In this study, the use of steel slag as a core material in rubble-mound structures are investigated by means of physical modelling experiments. For these, two steel slag samples from to different facility (Erdemir and İsdemir) were tested in ITU Hydraulics Laboratory. The experiments included both the classical wave flume tests and full scale oscillatory pressure gradient tests. The following conclusions are drawn:

- When used in the core layer of scaled breakwater models, steel slag exhibited a good performance in terms of overall breakwater stability under storm waves.
- The sieved steel slag performed much superior compared to not-sieved steel slag (which included fines). Fine material (such as fine sand and silt) are undesirable in within the composition of core layers of marine structures.
- The oscillatory pressure gradient experimental apparatus is a novel setup specifically designed to test the applicability of steel slag in the core of rubble-mound structures under the hydrodynamic forcing due to currents and waves. In this device, three different materials were tested: two steel slag samples and regular quartz sand. Results indicated that when the fines are excluded, steel slag can be used very effectively in the core layer and exhibits a remarkable resistance to the upward directed

oscillatory pressure gradients (i.e. wave run-up and run-down).

- On the other hand, if the material is not sorted (or sieved) and includes fines, the efficiency of the core under hydrodynamic loading significantly reduces due to decreased permeability and intergranular resistance.
- The volumetric stability of steel slag is another important criterion that should be born in mind for usage in marine structures. If the material did not undergo a proper aging process, the release of lime and magnesium monoxide may not only jeopardize the structural stability, but also constitutes an environmental threat.
- Proper utilisation of steel slag is of utmost importance from the economic, environmental and sustainability points of views. So far, there are many examples where electric-arc furnace slag is used in marine and hydraulic structures. Steel slag seems to be a potential material for such as usage. If utilised, a very important added value would be obtained. Pilot applications for such usage is suggested for the sake of full-scale applicability of such a utilisation.

ACKNOWLEDGMENT

The support of ERDEMİR Group for the implementation of this study is gratefully acknowledged.

REFERENCES

- [1] Motz, H., and J. Geiseler. "Products of steel slags an opportunity to save natural resources." *Waste Management* 21.3 (2001): 285-293.
- [2] Abraham, Dulcy M., Miao-Hui Joanne Yeh, and Daniel W. Halpin. "Modeling and simulation of breakwater construction." *Simulation Conference Proceedings*, 1995. Winter. IEEE, 1995.
- [3] NSA: National Slag Association Brochure of "Construction Material of Choice", 2006. <http://www.nationalslag.org>.
- [4] NMD: Nippon Magnetic Dressing Ltd. Corporate Presentation on "Utilisation of Steel Slag" (in Turkish), 2015.
- [5] CIRIA: Construction Industry Research, Information Association, Civieltechnisch Centrum Uitvoering Research en Regelgeving (Netherlands), & Centre d'études maritimes et fluviales (France). (2007). *The Rock Manual: The use of rock in hydraulic engineering* (Vol. 683). Ciria.
- [6] BSEN 13383-1:2013 - Armourstone. Specification (last issued in 2013).
- [7] Kirca, V.S.Ö. and Kbdasli, M.S.. "Reduction of non-breaking wave loads on caisson type breakwaters using a modified perforated configuration." *Ocean Engineering* 36.17 (2009): 1316-1331.
- [8] Sumer, B. Mutlu, and Jørgen Fredsøe. *The mechanics of scour in the marine environment*. World Scientific, 2002.
- [9] Jensen, Bjarne, Erik Damgaard Christensen, and B. Mutlu Sumer. "Pressure-induced forces and shear stresses on rubble mound breakwater armour layers in regular waves." *Coastal Engineering* 91 (2014): 60-75.
- [10] Jensen, Bjarne, et al. "Flow and Turbulence at Rubble-Mound Breakwater Armor Layers under Solitary Wave." *Journal of Waterway, Port, Coastal, and Ocean Engineering* 141.6 (2015): 04015006..
- [11] TCUD: Turkish Association of Steel Producers. "A report on Steel Slag in Turkey" (in Turkish), 2015, <http://www.dcu.org.tr/>

An Experimental Study on Effects of Laser Welding Speed and Laser Power on Weld Bead Shape and Heat Affected Zone in Keyhole Laser Welding

Ömer Ekinci*, John Francis⁺, Anıl İmak* Zülküf Balalan*

[#] Faculty of Engineering and Architecture, Department of Mechanical Engineering, Bingöl University, Turkey
oekinci@bingol.edu.tr

⁺ School of Mechanical, Aerospace and Civil Engineering, The University of Manchester, United Kingdom
John.Francis@manchester.ac.uk

⁺ Faculty of Engineering and Architecture, Department of Mechanical Engineering, Bingöl University, Turkey
aimak@bingol.edu.tr

*Faculty of Engineering and Architecture, Department of Mechanical Engineering, Bingöl University, Turkey
zbalalan@bingol.edu.tr

Abstract— In this study, many operations carried out by traversing laser beam on 6 mm thick S960 steel plates for various laser welding speeds and powers in order to determine influence of welding speed and power on penetration, shape of fusion zone and heat affected zone. A 16 kW Ytterbium fibre laser and pure argon as shielding gas were used in this experimental study. Data was evaluated and compared with some previous studies. Furthermore, an empirical formula between heat input and weld bead width was developed from results.

Keywords— laser welding, S960 steel, fusion zone, heat affected zone

I. INTRODUCTION

High strength low alloy (HSLA) steels have a strong and tough structure, hence they have been commonly exploited for years in a wide range of applications, for instance, in structural components, pressure vessels and fluid transportation pipes, in shipbuilding, offshore construction, automotive applications, and lifting and handling equipments [1,2]. HSLA steels allow lighter and thinner components to be used and lower construction costs without losing structural strength [3]. S960 steel is one of the high strength low alloy (HSLA) steel and has a minimum yield strength of 960 MPa. This S960 steel is usually used in production of heavy lifting equipment and recently produced by Tata Steel [4]. Fiber laser welding has been drawing attention lately because of the advantages that fiber laser provide such as high power, high beam quality, flexible optical fibre beam delivery, and high energy efficiency. In addition, these advantages allow to generate deep penetration welds even at high welding speeds and also small heat affected zone, narrow weld width, low distortion can be attained by laser welding [5,6]. Laser weld shape and integrity are created by laser welding parameters such as laser power, laser welding speed, shielding gas, focal point position, workpiece position accuracy because heat input is determined by combining these parameters [7]. Therefore, in order to obtain a good weld, it is important to choose correct laser

welding parameters [8]. The purpose of this work was to find out the influence of laser power, laser welding speed and laser heat input on weld bead fusion zone and heat affected zone for fiber laser bead on welding of 6 mm thick S960 steel plates. Size of fusion and heat affected zones were measured through an optical microscope.

II. MATERIAL AND EXPERIMENTAL PROCEDURE

6 mm thick S960 steel plates were used as workpieces and its chemical composition in weight percent was shown in Table I. Keyhole fiber laser bead on plate single pass autogenous welding (without filler material) process was composed of several operations. Before starting to weld the plates, oxidation layer of the plates on the front side and back side was removed by a sand blaster operation and then surfaces of the plates were cleaned by ethanol. Subsequently, S960 steel plate was clamped on the working table via a vise. After settings, keyhole fiber laser bead on plate single pass autogenous weldings (without filler material) were performed at laser power-welding speed (4kW-90cm/min. , 5kW-105cm/min. , 6kW-120cm/min. , 6kW-150cm/min.). Pure argon was supplied as shielding gas and it was provided through a nozzle and hose. While front side of the weld zone was shielded by a shielding gas nozzle, back side of the weld zone was shielded by a shielding gas hose. A 16 kW Ytterbium Fiber Laser was utilised with a focus length of 400 mm. After the keyhole fiber laser bead on plate welding trials of 6mm plates were completed, cross sections of the welds were prepared by using labotom disk cutter machine and then polished by emery papers. Later, the polished weld cross sections were etched by nital ethyl alcohol to reveal the microstructure. Finally, in order to evaluate welding bead characteristics, weld cross sections were observed and the width of fusion zone, coarse grained zone and intercritical heat affected zone were measured for each trial by using an optical microscope.

Table I Chemical composition of S960 steel plate

Material	Elements (mass %)													
	C	Si	Mn	P	S	Al	Cr	Mo	B	Ti	Nb	V	N	Fe
S960	0.094	0.108	1.59	0.011	0.002	0.038	0.50	0.26	0.0025	0.027	0.04	0.047	0.0052	Bal

III. RESULTS AND DISCUSSION

Shielding gas Ar (100 %)	Bead-on-plate welding of 6 mm thick plate of S960 in the keyhole fiber laser welding			
	Laser power			
	4 kW	5 kW	6 kW	6 kW
Cross section				
Welding speed	90 cm/min	105 cm/min	120 cm/min	150 cm/min

Fig. 1 Variation in the weld cross-section as a function of laser power and welding speed in the keyhole fiber laser bead on plate single pass autogenous welding of 6 mm thick S960 steel plates

Fig. 1 shows the cross sections of fiber laser bead on plate welds of 6 mm thick S960 steel plates. It can be seen that the shape of weld cross section had changed with increasing the laser power and welding speed. Hence, it was observed that when welding at power of 4 kW and welding speed of 90 cm/min, excessive weld metal took place at the weld bead root as indicated in Fig. 1. However, it disappeared as the laser power and welding speed were enhanced. Formation of excessive weld metal at the weld bead root could be because of lower welding speed. John C. Ion [9] asserts that excess weld metal appears in autogenous welds in response to four conditions which are inadequate welding speed, contraction of the plates, excess shielding gas pressure and longitudinal flow in the weld bead. Another important aspect was that undercut defect occurred at the top of the weld as illustrated Fig. 1 at higher laser power and welding speed (6 kW with 120 cm/min. and 6 kW with 150 cm/min.) The reason for these undercut formations was most likely due to the high welding speed. Also, John C. Ion [9] states that undercut occurs because of high welding speed and suggests that undercuts can be prevented by reducing the welding speed besides John C. Ion [9] claims that undercut defect does not significantly reduce the static strength of the joint, but it can degrade fatigue properties by acting as a site for crack initiation.

3.1 Influence of Laser Power and Welding Speed on Width of Fusion Zone and Heat Affected Zone

widths of fusion zones, coarse grained heat affected zones and intercritical heat affected zones increased when both the laser power and laser welding speed were simultaneously increased, laser power from 4kW to 6kW and laser welding speed from 90cm/min to 120cm/min. However, when laser power was kept constant at 6kW and then laser welding speed was increased from 120cm/min to 150cm/min, width of fusion zone, coarse grained heat affected zone and intercritical heat affected zone decreased as illustrated in Table II.

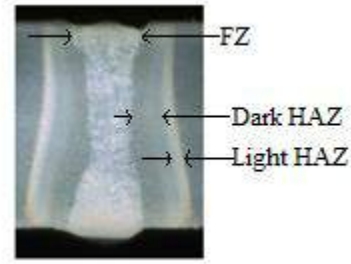


Fig. 2 Fusion zone, coarse grained heat affected zone and intercritical heat affected zone

- FZ:** Fusion Zone
- HAZ:** Heat Affected Zone
- Dark HAZ:** Coarse grained heat affected zone
- Light HAZ:** Intercritical heat affected zone

Table II Average width of fusion zone (FZ), coarse grained heat affected zone (dark HAZ) and intercritical heat affected zone (light HAZ) versus laser power and laser welding speed

Shielding gas Ar (100 %)	Dimensions of bead-on-plate weld on 6 mm thick plate of S960					
	Top width of FZ	Middle width of FZ	Bottom Width of FZ	Average width of FZ	Average width of dark HAZ	Average Width of light HAZ
Laser power = 4 kW Welding speed = 90 cm/min	1.733 mm	1.020 mm	1.187 mm	1.313 mm	0.460 mm	0.22 mm
Laser power = 5 kW Welding speed = 105 cm/min	1.585 mm	0.847 mm	1.617 mm	1.35 mm	0.682 mm	0.238 mm
Laser power = 6 kW Welding speed = 120 cm/min	1.367 mm	0.968 mm	1.739 mm	1.358 mm	0.752 mm	0.308 mm
Laser power = 6 kW Welding speed = 150 cm/min	1.258 mm	0.86 mm	1.437 mm	1.185 mm	0.553 mm	0.203 mm

when laser power was kept constant at 6kW and then laser welding speed was increased from 120cm/min to 150cm/min, width of fusion zone decreased from 1.358mm to 1.185mm as shown in Fig 3. As a result, it can be said that width of fusion zone, coarse grained heat affected zone and intercritical heat affected zone increase with increasing laser power for a constant laser welding speed, but they decrease with increasing laser welding speed for a constant laser power.

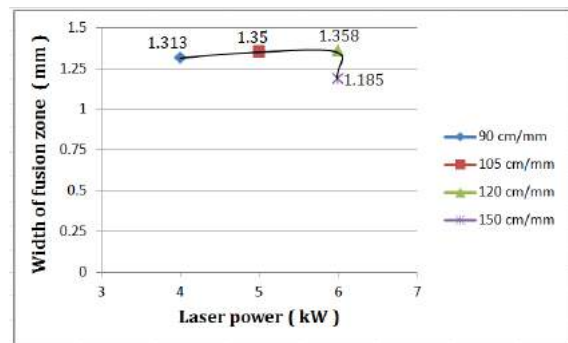


Fig. 3 Effect of combination of laser power and laser welding speed on width of fusion zone

Cao, X. et al [10] conducted a study on keyhole laser welding of cast WE43 alloy at a constant laser welding speed of 33 mm/s for various laser power values and a focused diameter of 0.25 mm using CO₂ laser. They determined the effect of laser power on weld bead width as shown in Fig 4. It can be seen

from Fig 4 that as laser power was enhanced, weld bead width also enhanced.

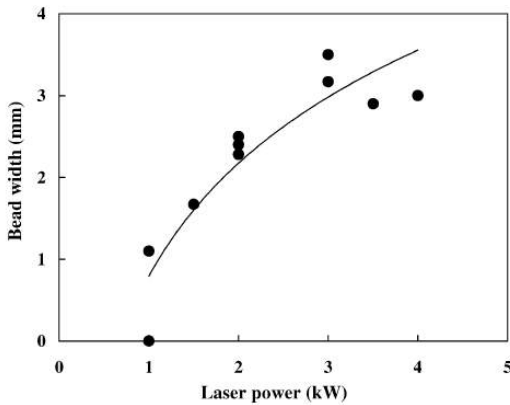


Fig. 4 Effect of laser power on weld bead width [10]

Cao, X. et al [10] determined laser welding speed as well presented in Fig. 5. From Fig. 5, it is evident that weld bead width decreased with rising laser welding speed.

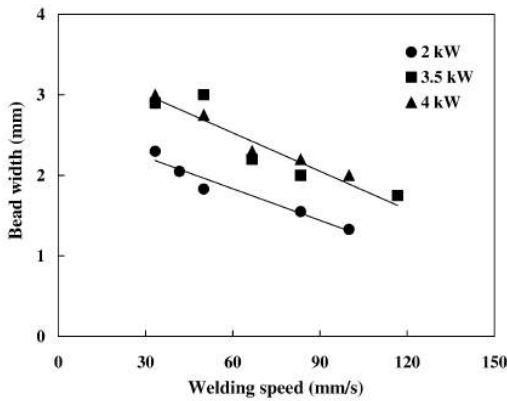


Fig. 5 Effect of laser welding speed on weld bead width [10]

INFLUENCE OF LASER HEAT INPUT ON WIDTH OF FUSION ZONE AND HEAT AFFECTED ZONE

Heat input was considered as below equation

$$\text{Heat input} = \text{laser power} / \text{laser welding speed}$$

Table II Influence of heat input on width of fusion zone (FZ), Coarse grained heat affected zone (dark HAZ) and intercritical heat affected zone (light HAZ) for various laser power and laser welding speed values.

Laser power (kW)	Welding speed (cm/min)	Heat input (J/cm)	Average width of FZ (mm)	Average width of dark HAZ (mm)	Average Width of light HAZ (mm)
4	90	2666.67	1.313	0.460	0.22
5	105	2857.14	1.35	0.682	0.238
6	120	3000	1.358	0.752	0.308
6	150	2400	1.185	0.553	0.203

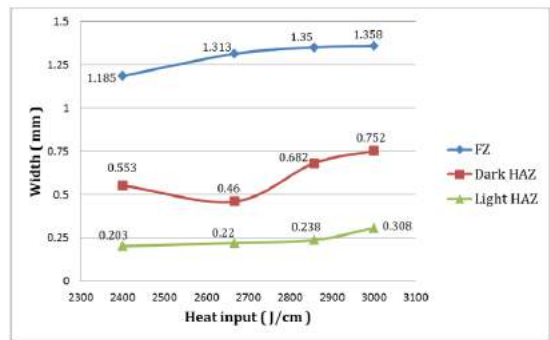


Fig. 6 Heat input versus width of fusion zone (FZ), Coarse grained heat affected zone (dark HAZ) and intercritical heat affected zone (light HAZ)

Fig 6 illustrates that width of fusion zone (FZ), Coarse grained heat affected zone (dark HAZ) and intercritical heat affected zone (light HAZ) went up as heat input to plates was raised. Therefore, based on Fig 6, it can be said that weld bead width and heat affected zone width is directly proportional with laser heat input. Grajcar, A. et al [11] also determined effect of heat input on weld bead width and heat affected zone width as shown in Fig. 7. It is seen from Fig. 7 that when heat input increases, weld bead width and heat affected zone width go up in direct proportion to heat input.

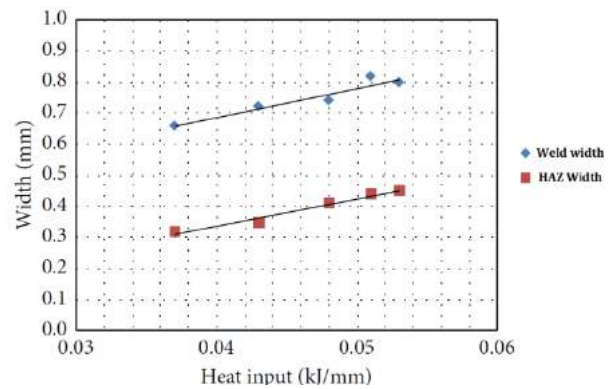


Fig. 7 Effect of heat input on the weld width and HAZ width [11]

As a result, a formula between heat input and weld bead width for Keyhole fiber laser bead on plate single pass autogenous welding of High strength low alloy steels can be proposed since width of weld bead and heat affected zone is directly proportionate to heat input.

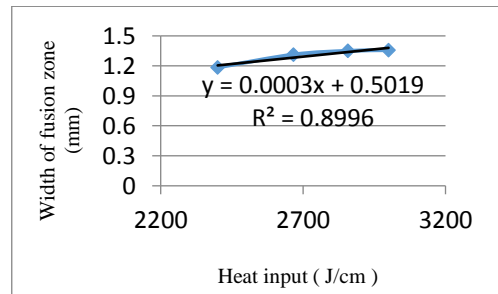


Fig. 8 Relationship between heat input and fusion zone width

Based on experimental data, $y = 0.0003x + 0.5019$ formula was created from Fig. 8. Here, y is fusion zone width, on the other hand x is heat input (laser power / laser welding speed). The coefficient determination, $R^2 = 0.8996$ from the trendline in Fig. 8. The coefficient determination is nearly 90%, it is close to 100% and it seems fine.

Table III Model design

Variables	Code	Unit
Laser power	LP	kW
Welding speed	S	cm/min
Focused position	F	mm
Fusion zone width	W_{fz}	mm
Heat input	$LP*60000/S$	J/cm

Mathematical model developed for fusion zone width

$$W_{fz} = 0.0003 * \left(\frac{LP * 1000 * 60}{s} \right) + 0.5019$$

IV. CONCLUSIONS

In this study, Keyhole fiber laser bead on plate single pass autogenous welding (without filler material) of 6 mm S960 steel plates was successfully carried out. some conclusions were drawn as the following.

1. It was determined that heat input is in direct proportion to width of weld bead and heat affected zone in this study and other studies published before, which means when heat input rises, width of weld bead and heat affected zone becomes larger.

2. Bigger laser powers lead to Bigger widths of weld bead, and heat affected zone while higher laser welding speeds lead to smaller widths of weld bead, and heat affected zone.

3. Higher laser powers enabled higher welding speeds to be available.

4. It is important to select correct welding parameters to avoid welding defects and so to obtain good quality welds.

ACKNOWLEDGMENT

I thank my my supervisor Dr. John Francis for his support and encouragement and also I thank Zülküf Balalan and Anıl İmak for their useful beneficial ideas and comments.

REFERENCES

- [1] On'oro JRC, Fatigue Behaviour of Laser Welds of High-Strength Low-Alloy Steels. Journal of Materials Processing Technology 68:68–70, 1997.
- [2] W. Yan, L. Zhu, W. Sha, Y-Y. Shan, K .Yang, Change of Tensile Behavior of a High-Strength Low-Alloy Steel With Tempering Temperature. Materials Science and Engineering A 517:369–374, 2009.
- [3] K. Takasawa, R. Ikeda, N. Ishikawa, R. Ishigaki, Effects of Grain Size and Dislocation Density on the Susceptibility to High-Pressure Hydrogen Environment Embrittlement of High-Strength Low-Alloy Steels. International Journal of Hydrogen Energy 37:2669–2675, 2012.
- [4] W. Guo, "Laser Welding of High Strength Steels," Doctorial thesis, Univ. of Manchester, School of Mechanical, Aerospace and Civil Engineering, Manchester, UK, Dec. 2015.
- [5] L. Li, R. Eghlio, S. Marimuthu, Laser Net Shape Welding. CIRP Annals –Manufacturing Technology 60:223–226, 2011.
- [6] M. Schmidt, A. Otto, C. Ka'geler, Analysis of YAG Laser Lap-Welding of Zinc Coated Steel Sheets. CIRP Annals – Manufacturing Technology 57:213–216, 2008.
- [7] C. Dawes, Laser welding, Abington Publishing, New York, NY, 1992.
- [8] Q. Huang, J. Hagstroem, H. Skoog and G. Kullberg, Effect of laser parameter variation on sheet metal welding, Inter. J. for the joining of Materials, Vol. 3, No. 3, pp. 79-88, Sep. 1991.
- [9] J. C. Ion, Laser processing of engineering materials: principles, procedure and industrial application, Elsevier Butterworth-Heinemann, Oxford, UK, 2005.
- [10] X. Cao, M. Jahazi, J. P. Immarigeon and W. Wallace, A Review of Laser Welding Techniques For Magnesium Alloys. Journal of Materials Processing Technology, 171(2), pp.188-204, 2006.
- [11] A. Grajcar, M. Rózański, S. Stano, A. Kowalski and B. Grzegorzcyk, Effect of Heat Input on Microstructure and Hardness Distribution of Laser Welded Si-Al TRIP-Type Steel. Advances in Materials Science and Engineering, Hindawi Publishing Corporation, Gliwice, Poland, 2014.

Effect of Reduction Rate in Formability of Titanium + Niobium Alloyed Steel

M. Mustafa ERŞEN¹, Erdoğan KANCA², Ali GÜNEN³, Murat YILDIZ², Mehmet DEMİR²,
Bülent KURT⁴ Mustafa Sabri GÖK⁵

¹MMK Metallurgy, Industry, Trade and Port Co., Dortyol, Hatay

²Mechanical Engineering, Faculty of Engineering and Natural Sciences, Iskenderun Technical University, Hatay, Turkey

³Metallurgical and Materials Engineering, Faculty of Technology, Iskenderun Technical University, Hatay, Turkey

⁴Materials Engineering, Faculty of Engineering and Architecture, Nevşehir Hacı Bektaş_i Veli University, Nevşehir, Turkey

⁵Mechanical Engineering, Faculty of Engineering, Bartın University, Bartın, Turkey

Corresponding author: ali.gunen@iste.edu.tr

Abstract- Titanium (Ti) + Niobium (Ni) doped Interstitial Free (IF) steel grades (Ti + Nb IF steel) are widely used in steel industries because of their good formability properties. In this study, the effect of cold rolling reduction rate on the microstructure and mechanical properties of IF steel was investigated in details. The samples subjected to cold rolling with various reduction rates ranging from 40% to 80% at constant annealed temperature. The changes in microstructure were examined with optical microscope. Mechanical properties such as cupping values, anisotropy values (r) yield strength, tensile strength and elongation, were examined by Erichson and tensile test. The results affects the microstructural evolution and carbide precipitations significantly, in turn altering the mechanical properties. Increasing amount of cold rolling reduction rate resulted for an increase in the cupping values, anisotropy values, yield strength and elongation, whereas it led to a decrease in tensile strength. As a result of this trial experiment it can be said that reduction rate has a great effect on mechanical and microstructure properties of Ti+Nb doped IF steel. clearly demonstrated that the reduction rate of cold rolling.

Keywords: IF steel Reduction rate, Mechanical properties, Microstructure

I. Introduction

A new generation of steels has been developed along with advances in technology for the iron and steel industry and thus significant gains such as strength and lightness have been achieved. One of these gains is undoubtedly the introduction of IF steels to the steel market. IF steels have a total C+N content that is usually less than 50 ppm and contain micro alloy additions of Ti or/and Nb [1-3]. These steels are one of the most important products used in the construction of DX54 in the flat steel industry.

IF steels are the most preferred steels by automotive and

white goods manufacturers due to their high formability, deep drawability and good weldability properties [4]. They have extremely high formability characteristics under the forming presses. Interstitials (C and N atoms) adversely affects formability characteristics of steel. Therefore elimination of these elements is a must. This problem (C and N) can be solved through a careful supervision of the steel making process by adding of Ti and/or Nb to get them interact with N and C to form precipitates. This process is the first to determine grain size and homogeneity. They also serve as grain refiners and hardeners by forming carbide, nitrides or carbon-nitrides in the microstructure [2].

All the process parameters from steel casting to cold rolling process affects the mechanical properties of IF steels. Especially the mechanical properties of IF steels are largely depended on the finishing temperature, the cooling temperature and the reduction ratio [1] as these parameters effect the size of the precipitates and the grain size of hot rolled steel product. On the other hand, the “ r ” value is the most important parameter in determining formability of the steel. Therefore, the “ r ” value must always be considered during the production development stages.

Many various methods are applied to meet customer expectations and improve the mechanical properties while keeping costs at a minimum. Small process changes can offer more economically produced, high yield products with different mechanical properties that can respond the demands of the consumer. Reduction rate is one of the important factor in the cold rolling process. In a reversible cold rolling process, the first-pass reduction rate determines the mechanical properties of the material.

Cold rolling, applied when the material's temperature is below its recrystallization temperature, can improve the microstructures and mechanical properties of low carbon steels by refining the grain size and increasing the dislocation density, thus causing the strain hardening. Furthermore, the structure of grain boundaries, which

differs transport mechanisms, may be affected by the cold rolling parameters such as reduction rate and annealing conditions. Thus, thermo-mechanical processing, cold rolling and inter-critical annealing treatment are most suitable in terms of industrial processing to change the mechanical properties of the material [5].

Considering the studies in the literature, a number of authors have found that the hot rolled grain size [36] and cold rolling reduction ratio have a significant effect on the r value and elongations in some steels [6-9]. Whereas Osawa et al. found that increase in cold reduction results lower elongations and strain hardening exponent, higher yield and tensile strengths values at cold reductions ranging from 65 % to 80 % for continuously annealed Ti-IF steel [10]. For this purpose, the influence of cold rolling reduction rate on mechanical as well as microstructure properties of IF steel (Ti + Nb alloy), which are suitable for low-strength cold-rolling process and used in DX54 construction according to DIN EN 10346 standard, was investigated in this study.

II. Materials and Methods

A. Materials

DX 54 grade hot rolled Ti+Nb doped IF steel sheet with a thickness of 2 mm was the material used in this study. The chemical composition and mechanical properties of as-received hot rolled sheets of used IF steel are given in Table 1 and Table 2, respectively.

Table 1. The chemical composition of used IF steel

%C	%Si	%Mn	%P	%S	%AL	%Ti	%Nb	%Al
0	0,01	0,09	0	0,01	0,04	0,05	0,03	0,1

Table 2. Mechanical properties of used IF steel as-received hot rolled sheets

Yield	Tensile	Elongation
Strength (N/mm ²)	Strength (N/mm ²)	(%)
165	285	39,6
168	290	40
162	280	40,8
172	288	41,3
164	299	40,5

The yield strength, tensile strength and elongation of the as-received material were in the range of 164-172 MPa, 280-299 MPa and 39.6% -41.3%, respectively.

B. Cold Rolling and Galvanizing Process

The as-received hot rolled sheets were cold rolled with different five reduction rates such as 40%, 55%, 65%, 75% and 80%. Some properties of the samples subjected to cold rolling process are given in Table 3.

Table 3. Some values of the samples before and after cold rolling process

Before cold rolling			After cold rolling	
Thickness	Width	Reduction ratio	Thickness	Width
(mm)	(mm)	%	(mm)	(mm)
2	1205	40	1,2	1204
2	1205	55	0,9	1204
2	1205	65	0,7	1203
2	1205	75	0,5	1202
2	1205	80	0,4	1202

The tensile test specimens were extracted both from the as-received and cold-rolled sheets while referencing to the rolling direction. Yield strength, ultimate tensile strength and elongation values of all the extracted specimens are determined according to EN 10002 / 10025 by using a tensile test equipment. Tensile tests were carried out at room temperature at a cross-head speed of 5 mm/min using Zwick / Roll Z250.

The as-received hot rolled sheets were cold rolled with different reduction rates and dipped into molten zinc bath of 460 °C. Afterwards, the wet film thickness on the surface was reduced with the help of the stripping rollers and the desired amount of Cr⁶⁺ was left on the surface of the sheet and then they were baked. The furnace annealing temperatures were kept constant at 840 °C for 20 second in order to better analyze the effect of reduction ratio on the mechanical properties of the galvanized finished product.

For metallographic examinations the samples were cut and cross-sectional surfaces were cold mounted. The mounted specimens were then ground using 240, 320, 400, 600, 800, 1000 and 1200 grit abrasive papers and polished with 3 µm alumina paste followed by 1 µm diamond paste. After polishing, the specimens were etched with a solution of 2 percent nital and 98 percent water to reveal the microstructures. Detailed microstructural investigations were carried out on the prepared specimens using a Nikon MA200 metal microscope equipped with 3D Clemex image analysis software.

III. Results and Discussion

a. Mechanical Properties

Tensile testing allows to obtain many mechanical values of materials such as, yield strength tensile strength, elongation at fracture and anisotropy coefficients. In addition, in order to determine the effect of cold rolling ratio on deep

drawability, Cupping (Erichson) test applied on all of the samples.

The anisotropy values (r) obtained according to different reduction ratios are given in Fig. 1

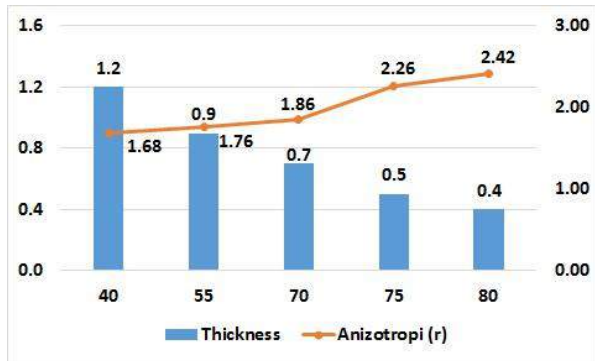


Figure 1. Change of anisotropy values (r) according to applied reduction rate ratios.

Increasing the reduction ratio resulted in an increase in anisotropy values (r). Fukuda [11] explained the effect of cold rolling reduction on the development of r values and he said that the high r values are associated with the formation of beneficial recrystallization textures that are produced after hot deformation, coiling, cold rolling and annealing. Tokunaga and Yamada [12] argued that the best r value could be achieved with a 90% reduction rate. However, this ratio is impractical due to the limitations of hot rolled gauge and cold rolling mill power. Therefore, they obtained the best values with 80% reduction ratio. Also in our study the best value was obtained at the 80% reduction ratio.

The Cupping values obtained in samples prepared by applying different reduction ratios are given in Fig. 2.

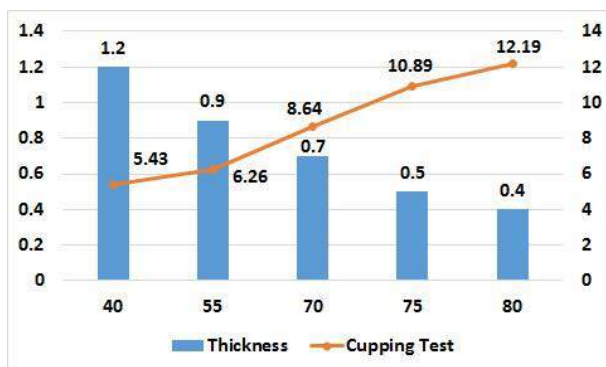


Figure 2. Change of cupping values according to applied reduction rate ratios

The cupping values were risen by increasing the reduction ratios since the deep drawability depends on anisotropy values. In the literature, it is stated that the addition of Ti

and Nb increases the deep drawability properties of IF steels [2,3,8]. Since these elements tend to bond to C and N elements in the structure and prevent precipitations events.

The mechanical properties of the samples cold rolled by different reduction ratio are given in Table 3.

Table 3. Some mechanical properties of Ti+Nb doped IF steel samples after cold rolling process

Variation of thickness	Yield Strength (N/mm ²)	Tensile Strength (N/mm ²)	Elongation (%)
1,2	204	280	40,3
0,9	192	282	42,4
0,7	196	286	41,3
0,5	189	276	42,6
0,4	170	265	43

Table 3 shows that the yield strength and elongation values tend to increase while the tensile strengths decrease by increasing reduction ratio.

b. Microstructure

The optical micrographs of the Ti+Nb doped IF steel specimens for the as-received (hot-rolled) condition as well as the cold-rolled states for which different reduction rates applied, are given from Figure 3 to Figure 8.

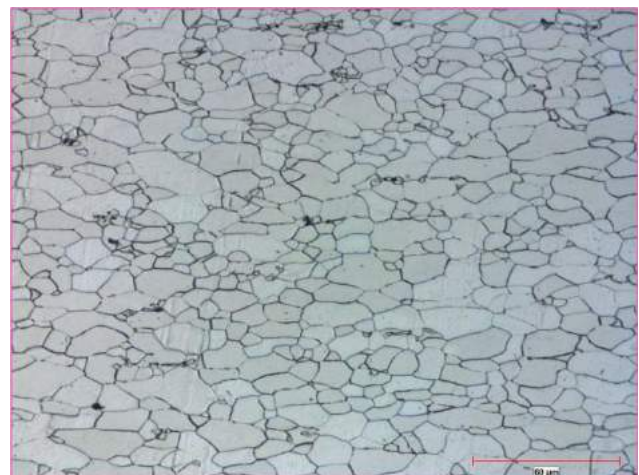


Figure 3. The optical micrograph showing the microstructure of as-received (hot-rolled) Ti+Nb doped IF steel.

It can be seen that from Figure 1 that the grain boundaries have been etched clearly and the microstructure typically consists of ferrite grains with differently sized grain morphologies. The size and shape of the grains are

inhomogeneous and some precipitations have been observed at the grain boundary lines (Figure 1). The dark regions in these micrographs are carbide participations.

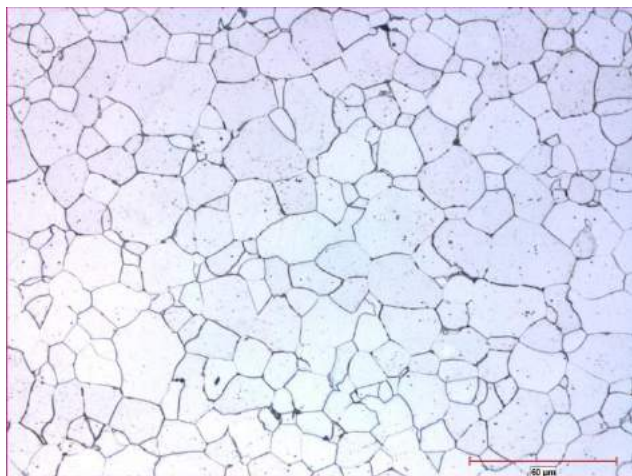


Figure 4. Optical micrographs of cold rolled IF steel samples with %80 reduction rate.

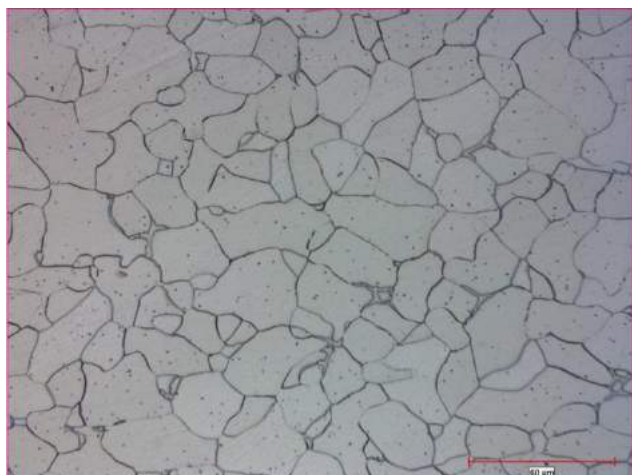


Figure 5. Optical micrographs of cold rolled IF steel samples with %75 reduction rate.

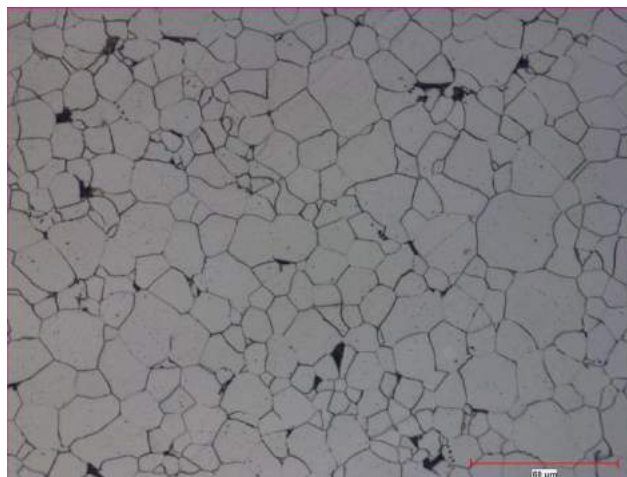


Figure 6. Optical micrographs of cold rolled IF steel samples with %65 reduction rate.

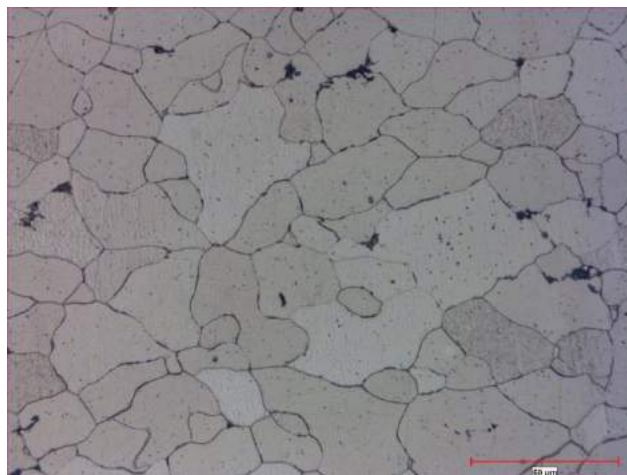


Figure 7. Optical micrographs of cold rolled IF steel samples with %55 reduction rate.

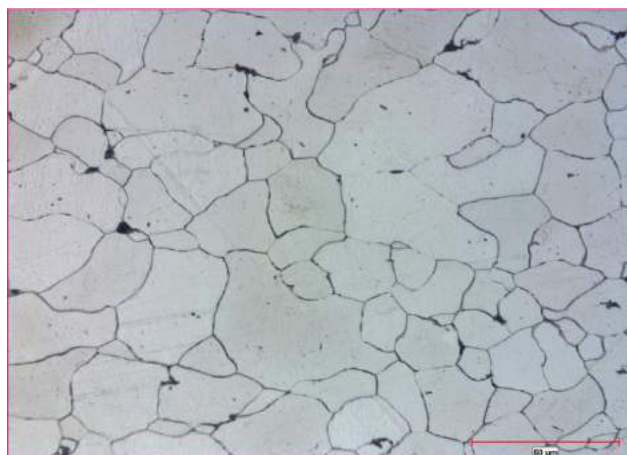


Figure 8. Optical micrographs of cold rolled IF steel samples with %40 reduction rate.

When the microstructure images of cold rolled samples considered, it can be seen that there is a tendency for the grain size getting smaller with an increasing reduction ratio for constant annealing temperature. Among the cold rolled Ti+Nb doped IF steel samples, one of them which was cold rolled 75% had no precipitation appeared on grain size microstructure. Many researchers have determined by using EDS analysis that these precipitations, which originate from Ti and Nb based alloying elements, are composed of Ti (C-N), TiN, (TiNb)C, Ti₄C₂S₂, TiS, and TiC [3,7,13,14].

As shown in Figure 3 that the tearing event did not occur at 75% and 80% reduction ratio. Precipitates give a rise to tearing by lowering the deep drawability properties. The result of this research showed that: High reduction rates can prevent tearing.

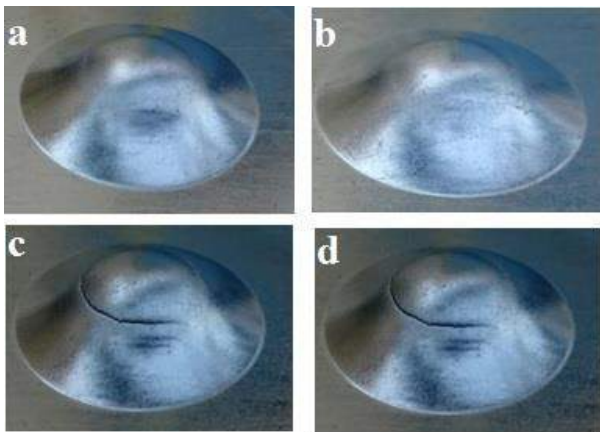


Figure 9. Surface appearance of samples which cold rolled by a) 80% b) 75% c) 65% d) 40% reduction ratio.

V. RESULT

In this study, DX54 type Ti+Nb doped IF plates were subjected to cold rolling with the different reduction ratios. The influence of the reduction rate on microstructure and mechanical properties were investigated. The following results were derived from the present study:

- 1- The applied reduction rate affected the microstructure and mechanical properties of IF steel.
- 2- The increase in cold rolling reduction rate resulted in a decrease in grain size and precipitations.
- 3- An increase in the reduction ratio generally resulted in increase in yield strength and the elongation, but decrease in tensile strength.
- 4- Both cupping and anisotropy values were risen with increasing the reduction ratio. The highest cupping and anisotropy values (r) were achieved at the 80% reduction ratio with the values of 2.42 and 12.19 respectively.

- 5- Tearing of IF steels can be eliminated by applying high reduction ratios.

References

- [1] Hoile, S., Processing and properties of mild interstitial free steels, *Materials Science and Technology* Volume: 16 Issue: 10 Pp. 1079-1093 Published: Oct 2000.
- [2] Carabajar S., Merlin J., Massardier V and Chabanet S., Precipitation evolution during the annealing of an interstitial free steel, *Materials Science and Engineering Proceedings A281*, pp. 132-142, 2000.
- [3] Yascan D. A., Optimization of alloying elements and process parameters for extra deep drawability property of cold rolled automotive steels, Istanbul Technical University Institute of Science and Technology, Master's thesis, 2007 Istanbul.
- [4] Humane, M.M., Minz, R.K., Peshwe, D.R., Paretkar, R.K., Effect of two step cold rolling continuous annealing on microstructures, textures and mechanical properties in IF and IF-HS steel sheets, *Transactions of the Indian Institute of Metals*, Volume: 63, Issue: 1, Pages: 21-30, Published: FEB 2010.
- [5] Karmakar, A., Ghosh, M., Chakrabarti, D., Cold-rolling and inter-critical annealing of low-carbon steel: Effect of initial microstructure and heating-rate. *Mater. Sci. Eng. A* 564, 389–399. doi:10.1016/j.msea.2012.11.109, 2013.
- [6] Ray R.K., Jonas J.J., and Hook F.J., Cold rolling and annealing textures in low carbon and extra low carbon steels, *International Materials Reviews.*, 39, (4), 129-172. 1994.
- [7] Tsunoyama, K., et al. "Hot-& Cold-rolled Sheet Steels ed. by R." Pradhan and G. Kudkovsky,(MetSoc, 1988) pp 155-164, 1988.
- [8] Ghosh, Pampa, Chiradeep Ghosh, and R. K. Ray. "Precipitation in interstitial free high strength steels." *ISIJ international* 49.7, 1080-1086, 2009.
- [9] Banerjee, Kulkum. *Physical metallurgy and drawability of extra deep drawing and interstitial free steels*. INTECH Open Access Publisher, 2012.
- [10] Osawa, K., Satoh, S., Obara, T., Katoh, T., Abe, H., Tsunoyama, K., Recrystallization behavior of extra low c cold rolled sheet steels during continuous annealing. *Metall. Vac. Degassed Steel Prod.* 181 – 196, 1990.
- [11] Fukuda, N., Progress of rolling technologies in Japan, proceedings of International conference on steel rolling, V:1 Iron and Steel Institute of Japan, pp.1-26 1980.
- [12] Tokunaga Y. and Yamada M., Method for the production of a cold rolled steel sheet having super deep drawability, US Patent 4, 504-326, 1985.
- [13] Hashimoto O., Satoh S., Irie T., and Ohashi N., 1982. Proc. Int. Conf. on Advances in physical metallurgy and applications of steel, Book 284, 95-104; Warrendale, PA, TMD.
- [14] Katoh H., Takechi H., Takahashi N., and Abe M., 1985 in Technology of continuously annealed cold-rolled sheet steel, (ed.R.Pradhan), 37-60; Warrendale PA, AIME.
- [15] Sumit, G., Suhrit, M., Thermomechanical processing of low carbon Nb-Ti stabilized microalloyed steel: Microstructure and mechanical properties, *Materials Science&Engineering A* 646, 218–233, 2015.

The Development of a Decision Support System for Iron and Steel Industry in Turkey

Turgut Ozseven¹, Muharrem Dugenci², Filiz Ersoz² Halil Ibrahim Demir³

Gaziosmanpasa University, Tokat, Turkey
Email: turgutozseven@gmail.com

Karabuk University/ Industrial Engineering Department, Karabuk, Turkey
Email: { mdugenci , fersoz }@karabuk.edu.tr

Sakarya University/ Industrial Engineering Department, Sakarya, Turkey
Email: hidemir@sakarya.edu.tr

Abstract-Since ancient times Iron and Steel Industry has great importance in the community development and in the development of various industries. Especially in developing countries, iron and steel sector has pioneered to continuing other sectors. Iron and steel sector which is an important sector for Turkey and the World has an important place in the industrialization in the global economy and the country's economy. This study is performed to develop a decision support system for the iron and steel industry for the managers of the iron and steel sector business, associations and institutions. Solving the problems arising from supply-demand imbalance of iron and steel products, Closing directions of uncovering the balance of payments deficit, Uncertainty in the imports and exports estimates, Developing a database for the institutions and organizations for the needs, profiles and projections, Creating long term strategies and the idea of development of close cooperation between industry and university are the major driving forces of this study.

Effect on The Formation of Boride Layer of Increasing Amount of Niobium in Pure Iron

¹Tanju TEKER, ²S. Osman YILMAZ, ³Eyyüp Murat KARAKURT

^{1*,3}Adıyaman University, Faculty of Engineering, Department of Metallurgical and Materials Engineering, 02040 Adıyaman, Turkey.

²Namık Kemal University, Faculty of Engineering, Department of Mechanical Engineering, 59500, Çorlu, Tekirdağ, Turkey.

tteker@adiyaman.edu.tr, osyilmaz@nku.edu.tr, ekarakurt@adiyaman.edu.tr

Abstract—In this study; Fe-1Nb and Fe-10Nb (at.%) binary alloys were boronized at 950 °C for 3 hours. Effect on the formation of boride layer of increasing amount of niobium in pure iron was experimentally investigated. Microstructural changes occurring on the surfaces of the samples after boronizing process were examined by optical microscope (OM), and microhardness and boride layer thickness were measured separately for each sample. Typical sawtooth morphologies were observed on the surface coatings. As a result, hardnesses of boron layers obtained from the surface of the samples were much higher than base metal. In addition, it was found that boride layer thickness was decreased with increasing niobium content in pure iron.

Keywords—Boronizing, Binary alloy, Pure iron, Niobium, Boride layer.

I. INTRODUCTION

Boronizing is the process of forming a boron layer by diffusion of boron atoms on the surface of the base metal at high temperature. Today, boronizing is applied not only to metals but also to ceramic materials [1]. Boron coating is also known as the diffusion of boron atoms, which will form a compound on the surface [2]. That process can be applied to well-surface cleaned materials between 650 and 1200 °C temperature for 1-10 hours in various media such as solid, paste, liquid, gas, etc. With recent economic developments, new techniques such as plasma boronizing and fluidized bed boronizing are used besides thermochemical boronizing methods in gas environment. In addition, non-thermochemical physical vapor deposition (PVD), chemical vapor depositions (CVD), plasma spray and ion deposition methods can be used for boronizing [3-5]. While boronizing process increases the rupture and yield strengths of the iron based materials by % 10-20 and the fatigue strength by % 25 and corrosion fatigue life by % 200, it reduces the plasticity properties. Furthermore, it increased hardness, wear and corrosion resistance on the surfaces of metals and alloys, at the same time; it is used to protect these properties at high temperatures and to increase erosion resistance[6-9].

Boronizing process is industrially applied to iron-based alloys. Recently, boron coated parts are also used in various application areas. It provides a significant increase in the

lifetime of the machine elements and improvements in the life of the work tools [10].

In this study, effect on the formation of boride layer of increasing amount of niobium in pure iron was experimentally investigated. Microhardness test and boride layer thickness measurements were analyzed.

II. MATERIALS AND METHODS

99.97 pure iron and 99.98 pure niobium (wt.%) metals supplied commercially available were prepared in the arc melter as Fe-1Nb and Fe-10Nb (at.%) with dimensions of 80 × 10 × 10 mm. Elemental analyses of the samples were then made by using a spectrometer device in order to determine the accuracy of the element fractions contained in the binary alloys. Test samples manually were cut into slices by Microtest cutter device. Before boronizing process, surfaces of samples were grinded by 80-1200 mesh SiC grinding paper and then, polished by 1-3 μm diamond paste.

Ekabor II powder was subjected to drying for 1 day at 100 °C by using oven drying method to remove the moisture content of the powder. As shown in the following schematic diagram (Figure1), samples were placed in the pot.

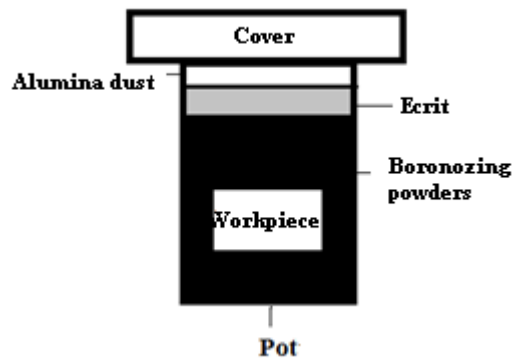


Fig. 1. Arrangement of the samples in the pot.

Samples were subjected to boronizing treatment at 950 °C for 3 hours by using a digitally controlled Protherm furnace device. The boronized samples were cut in the middle by Brillant 210 precision cutting machine to determine cross sectional characterization. Then, crosssectional surfaces of the boronized samples were grinded by 80-1200 mesh SiC grinding paper and polished by 1-3 μm diamond paste again. The samples were etched with a solution having 98 alcohol + 2HNO₃ (wt.%) at 3-5 sec. Structural changes in the crosssectional surfaces were analyzed by using LEICA optical microscope device (OM). Microhardness measurements were performed with the HV scale of hardness under 25 gr loads by QNESS Q10 test device. Furthermore, the boride layer thicknesses were measured for each sample by scaling of photographs taken with an optical microscope.

III. EXPERIMENTAL RESULTS

1. Chemical Analysis of Base Material

Before boronizing process, the chemical compositions of base metals prepared in the arc melter were given in Table 1.

Table 1. Chemical compositions of base metals (wt.%).

Substrate Materials (at.%)	Chemical Compositions (wt.%)							
	Fe	Nb	C	Mn	Si	Ti	Cr	Ni
Fe-1Nb	96.56	0.370	0.02	0.07	0.02	0,02	0,01 0	0.037
Fe-10Nb	80.00	>6.0	0.04	0.19	0.13	0.10	0,02 4	0.035

The percentages by weight of Fe-Nb binary alloys were calculated as Fe-1.6Nb and Fe-15Nb (wt.%) respectively. In this context, it is possible to say that results obtained from the spectrometer device are consistent with the chemical compositions of Fe-Nb binary alloys.

2. Microstructure Analysis

As shown in Fig. 2, the cross-sectional surfaces of samples were given respectively. When the microstructure photographs of the crosssectional surfaces were examined, it was seen that boron layers were formed on the surfaces of Fe-1Nb and Fe-10Nb (at.%) binary alloys.

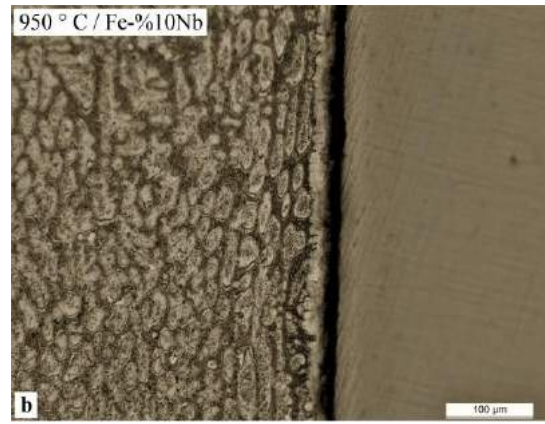
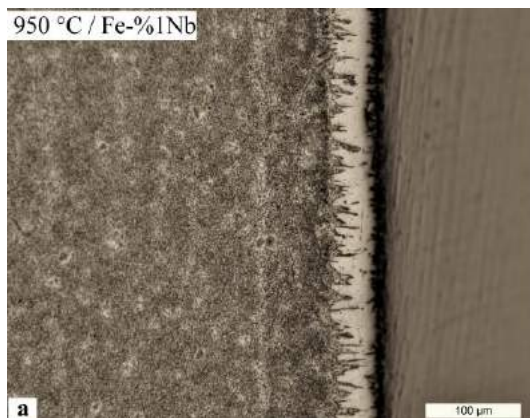


Fig. 2. Optical images of samples boronized at 950 °C.

The typical sawtooth morphologies were seen in all samples. As indicated in the literature, the diffusion rate is higher in preferential directions. Therefore, boron layers are diffused more rapidly to the surface of the base metal in some regions, while they are diffused more slowly to the surface of the base metal.

Depending on the increased amount of niobium, the appearance of sawtooth morphology was suppressed at the Fe-10Nb (at.%) and obstacle (precipitate phase) tried to flatten the sawtooth morphology. Boron crystals of the second phase prevent diffusion, since diffusion rate of boron atom get changed in this second phase.

3. Microhardness Test Analysis

Microhardness graphics of boronized samples were given in Fig. 3. When the hardness profiles were analyzed, it was observed that a similar hardness distribution occurred in all samples. While this distribution was the maximum on the surface of the samples, it decreased in the base metal. The highest hardness value obtained in the boron layers was measured for Fe-1Nb and Fe-10Nb (at.%) binary alloys as 1780 and 1695 HV respectively.

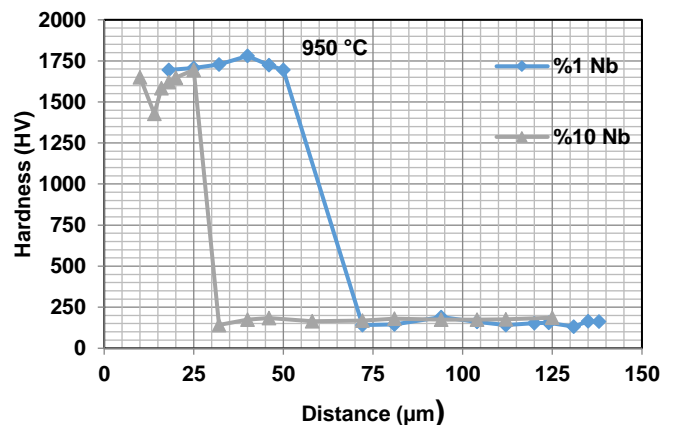


Fig. 3. Microhardness graphs for Fe-1Nb and Fe-10Nb (at.%) binary alloys boronized at 950 °C.

Accordingly, the boronized samples have higher hardness values than base material. Because, it is considered that Fe₂B and FeB phases were formed in the surface coatings. Fe₂B and

FeB layers, composed of iron-boron compound, are ceramic characteristics and have a hard and brittle structure. However, FeB phase structure is harder and more brittle than Fe₂B. Therefore, the different zones of the coating have different hardness values.

4. Boride Layer Thickness Analysis

The boride layer thicknesses were shown in Fig. 4. Accordingly, there was a decrease depending on the increased amount of niobium in the boride layer thicknesses of Fe-10Nb (at.%). The reason for this is the obstacles, different density planes and the amount of different voids in the atoms cause the diffusion rate to decrease. Furthermore, this is directly related to the dissolution or un-dissolution of the alloying element atoms in the boron phase and also to the tight planes, lattice vacancy rate and direction of this structure.

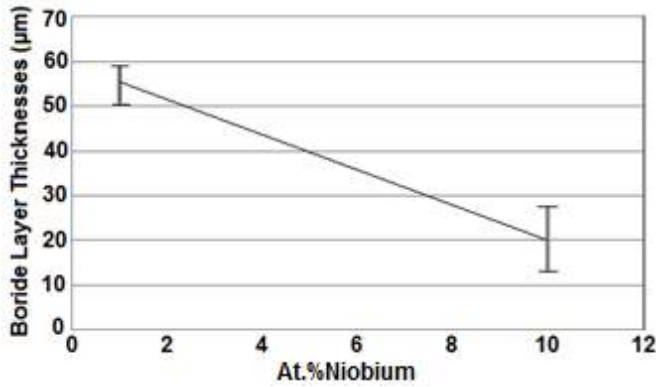


Fig. 4. The boride layer thicknesses for Fe-1Nb and Fe-10Nb (at.%) binary alloys boronized at 950 °C.

IV. CONCLUSIONS

In this study, Fe-1Nb and Fe-10Nb (at.%) binary alloys were boronized at 950 °C for 3 hours. Effect on the formation of boride layer of increasing amount of niobium in pure iron was experimentally investigated. According to analysis results, the following facts were obtained.

- 1) The typical sawtooth morphologies were seen in all samples. However, the increased amount of niobium suppressed the appearance of sawtooth structure at the Fe-10Nb (at.%)
- 2) The boronized samples have higher hardness values than base material.
- 3) There was a decrease depending on the increased amount of niobium in the boride layer thicknesses of Fe-10Nb (at.%) binary alloy.

ACKNOWLEDGEMENT

This study supported with the Project no. MÜFMAP/2015-007 by Adiyaman University, Scientific Researches Unit. The authors present endless thanks to Adiyaman University, Scientific Researches Unit provided financial support.

REFERENCES

- [1] A.K. Sinha, "Boriding (boronizing)", ASM Handbook of Heat Treating, vol. 4, ASM International, Materials Park, OH, pp. 437-47, 1991.
- [2] W. Fichtl, "Boronizing and its Practical Applications", Mater. in Eng., vol. 2, pp. 276-286, 1981.
- [3] Th. Lampe, S. Eisenberg, E. Rodriguez Cabeo, "Plasma surface engineering in the automotive industry-trends and future perspectives", Surf. Coat. Technol., vol. 174-175, 1-7, 2003.
- [4] Y. Gencer, "Influence of manganese on pack boriding behaviour of pure iron", Surf. Eng., vol. 27, pp. 634-638, 2011.
- [5] K.H. Habig, "Wear protection of steels by boriding, vanadizing, nitriding, carburising, and hardening", Mater. Eng., vol. 2, 83-92, 1980.
- [6] M. Tarakçı, Y. Gencer, Y. Azaklı and U. Şahintürk, "Surface modification of Fe-8Si alloy by boronizing and its characterization", J. Fac. Eng. Archit. Gaz., vol. 28, pp. 645-655, 2013.
- [7] S. O. Yılmaz, T. Teker, S. Karataş, Wear behavior of iron boride coating on AISI 4140, Prot. Met. Phys. Chem. of Surf., vol. 52, pp. 119-127, 2016.
- [8] P. Geoeuriot, R. Fillet, F. Thevenot, J.H. Driver, H. Bruyas, "The influence of alloying element additions on the boriding of steels", Mater.Sci. and Eng., vol. 55, pp. 9-19, 1982.
- [9] M. Blazon, B. Stanojevic, V. Veljkovic, "Effect of alloying elements on the formation of boride layer on steel", Scripta Met., vol. 19, pp. 1153-1156, 1975.
- [10] A. Çalık, A. Özsoy, "Termal Çevrimli Borlama İşleminin Ç1010 Çeliği Üzerine Etkileri", 11. Uluslararası Metalurji ve Malzeme Kongresi, pp. 187-194, 2002.

Relation Between Microstructure and Hardness in HARDOX 450+FeW Based Composite Coating Fabricated by Plasma Transferred Arc Cladding

Tanju TEKER¹, Eyyüp Murat KARAKURT²

^{1,2}University of Adiyaman, Faculty of Engineering, Department of Metallurgy and Materials Engineering, 02040, Adiyaman, Turkey.

tteker@adiyaman.edu.tr, ekarakurt@adiyaman.edu.tr

Abstract— In this study, Hardox 450 reinforced and FeW based metal matrix composites (MMC) were combined on AISI 1020 steel substrate by using plasma transferred arc welding (PTAW) process. The new created coated surfaces were examined by using optic microscopy (OM), energy dispersive spectrometry (EDS) and microhardness tests. The microstructure studies of the superficial layers of the coating revealed presence of a mixture of the dendritic phase structure of ferrite (α). The results show that; the change of hardness and the size of dendrites formed on the coated surfaces changed by the variation of the processing parameters. Hardox 450 + 10 wt.%FeW composite coating was the most appropriate combination in terms of hardness performance.

Keywords— PTAW, Hardox 450, FeW, Surface Coating.

I. INTRODUCTION

Surface cladding has been used for a long time to improve the wear resistance of materials. Various studies have addressed properties of clad layers and used them under suitable conditions. Such research has considered the cladding process, the material of the substrate, the composition of the cladding materials, and the microstructure of the clad layer. It is well known that the performance of wear resistant surface depends on the physical and mechanical properties and also, on the beneficial phenomena that could be happened in service especially the variation of hardness and structure [1,2]

Hardfacing coating methods using high energy density sources such as the plasma transferred arc welding (PTAW) process and laser cladding have been widely applied commercially in order to enhance the wear and corrosion resistance of the surfaces [3,4]. Among the deposition techniques, PTAW process is one of the most promising processes because of its higher deposition rate and lower heat input and especially for the wide applicability of materials. Hardfacing alloys obtained by PTAW process are of much interest in science and technology due to its good surface finish and higher wear resistance at elevated temperature [5,6].

Improving the wear resistance of surfaces on existing industrial parts, devices, and machines by providing a hard protective surface layer is the basis for hardfacing. This approach of applying advanced protective metallurgically bonded thick coatings, results in the development of relatively low cost high performance material systems since often a relatively low cost substrate can be used with an advanced hardfacing coating [7]. PTAW is a hardfacing technique which is a high energy welding process where inert argon gas is used for the arc plasma supply, for powder transport, and for shielding of the molten material. PTAW welds generally produce a high quality deposit offering precision weld deposits with minimal dilution (typically less than 10%) or deformation of the base material [8-9].

The advantages of hardfacing are many, including the ability to rebuild and restore worn out parts with significant cost savings. The use of plasma transferred arc technique for deposition of high-performance coatings has been attempted by many researchers. Gurumoorthy et al. [10] have reported the microstructural evolution and wear behaviour of plasma transferred arc surfaced Ni-based hardfacing alloy deposits on a stainless steel substrates.

In this study, Hardox 450 + FeW alloyed on the AISI 1020 steel surface by the plasma transferred arc (PTA) method and its surface properties have been changed; the effects of carbide, nitride and the other phases, which are formed on the microstructure, on hardness of the material were researched.

II. MATERIAL AND METHOD

In the present study, the chemical components of the AISI 1020 steel in the dimensions of 100x20x10 mm has a canal with a depth of 1.5 mm used as substrate materials and the Hardox 450 and FeW powders used as the coating material are given in Table 1. The rates of the coating materials used in the experiments are given in Table 2 and the production parameters of the coating process carried out by using Thermal Dynamics PS 3000 branded PTA welding machine are given in Table 3.

Table 1. The chemical components of alloy and substrate materials used in experiments (wt.%).

Materials	Fe	C	Cr	Ni	Si	Mn	P
AISI 1020	Bal.	0.20	-	0.08	0.22	0.57	0.01
Hardox 450	Bal.	0.26	1.40	1.50	0.70	1.60	0.01
FeW	Bal.	-	-	-	-	-	20

Table 2. Rates of coating materials used in experiments (wt.%).

Sample	wt. %		
	S1.1	S2.1	S2.2
FeW	-	5	10
Hardox 450	100	95	90

Table 3. The production parameters of the coating process.

Coat size (mm)	100
Current (A)	140
Heat Input (J)	20.208
Electrode	%2 thorium tungsten electrode
Shielding Gas	% 99.9 Argon
Shielding Gas Flow Rate (l/min.)	25
Plasma Gas Flow Rate (l/min.)	0.8
Electrode Diameter (mm)	3.2
Welding Speed (m/min.)	0.01

For metallographic examinations; samples manually were cut into slices by Struers Accutom cutter device. Surfaces of samples were grinded by 200-1200 mesh SiC grinding paper and then, polished by 1-3 μm diamond paste. Afterward, the samples were etched with a solution having %98 alcohol+ %2HNO₃ at 3-5 sec. Microstructure photographs of the etched samples were analyzed by LEICA DM750 optical microscope device. X-ray energy distribution spectrometry was used for EDS analyzes. Microhardness measurements were performed with HV scale of hardness under 100 g loads for 5 sec. at 0.5 mm intervals by QNESS Q10 test device in order to determine the hardness change in the junction.

III. THE EXPERIMENTAL RESULTS

1. The Macro and Microstructure Results

The macrosurface image is given in Figure 1, which belongs to the S1.1 coating sample obtained during the surface modification process of Hardox450+FeW coating alloy materials- which have been alloyed to the surface of the AISI 1020 steel by using the 130 Ampere of current density, the 0.8 l/min of plasma gas flow rate, the 0.01 m/min of welding speed and the argon shielding gas made by using PTAW method. When the macrosurface photos of the experimental samples are examined, it has been detected that the fusion happened pretty good, that the coating layer has a smooth appearance, that no pores and cracks emerged as a result of rapid cooling on the coating layer and the stitch structure has a smooth crater structure, that the welding craters emerged at the starting and ending points of the coating layer.



Fig. 1. The macrosurface image of the sample S1.1.

Hardox 450 coating alloy material, which we regard as reference, has been alloyed to the surface of the AISI 1020 steel by using the 130 Ampere of current density, the 0.8 l/min of plasma gas flow rate, the 0.01 m/min of welding speed and the argon shielding gas and by using PTAW method, and the optical surface photo, which has been taken from the interface of alloy material after the surface modification process made, is given in Figure 2. When the optical surface photo of the S1.1 sample is examined, Hardox 450 based coating of sample S1.1 in Fig. 1 showed that ferrite and pearlite established in the microstructure. It was shown that the sample can be divided into three regions; clad layer, heat affected zone (HAZ) and substrate. During PTA cladding the severity of thermal excursions experienced by the sample varied from region to region, resulting in these three distinct regions.

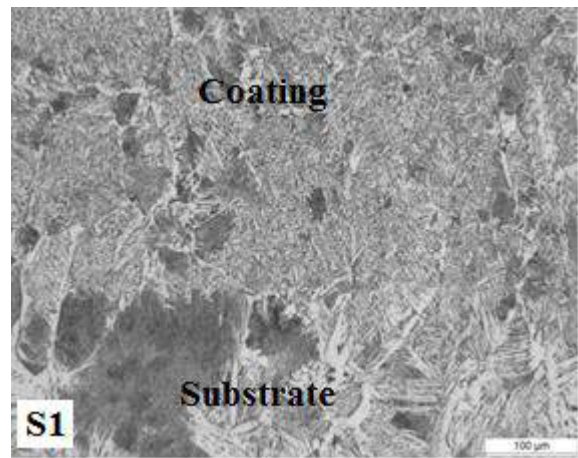
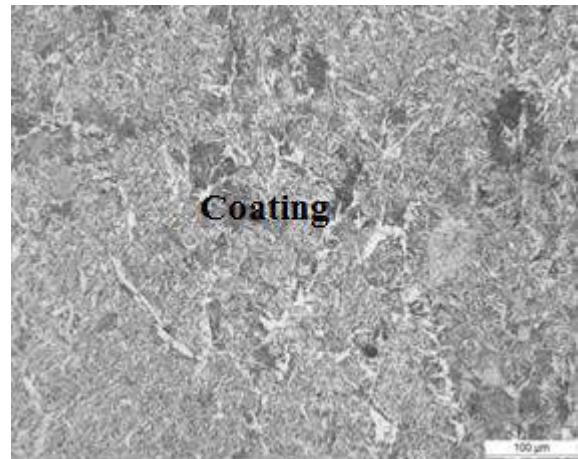


Fig. 2. The optical photo of sample S1.1, a) Coating layer, b) General view.

Hardox 450 coating alloy material, which we regard as reference, and 5% of FeW have been alloyed to the surface of the AISI 1020 steel by using the 130 Ampere of current density, the 0.8 l/min of plasma gas flow rate, the 0.01 m/min of welding pace and the argon shielding gas and by using PTAW method, and the optical surface photo, which has been taken from the interface of alloy material after the surface modification process made, is given in Figure 3. When the optical surface

photo of the S2.1 sample is examined, the alloy has the light-colored second-phase regions which are in the shape of long line resembling a dendritic structure and are varied from region to region. It is seen in the structure that the grains are directed axially and are monitored clearly, and that their lengths are in the same dimensions. Due to the fact that the powder amount is low, the amount of energy corresponding to unit weight increased and accordingly the fusion and dissolution occurred at much higher levels. While the primary dendrite arms were formed completely, the fact that the main metal coated was cold blocked the apparent formation of secondary dendrite arms and the transition of metal atoms among the layers remained limited as a result of rapid cooling.

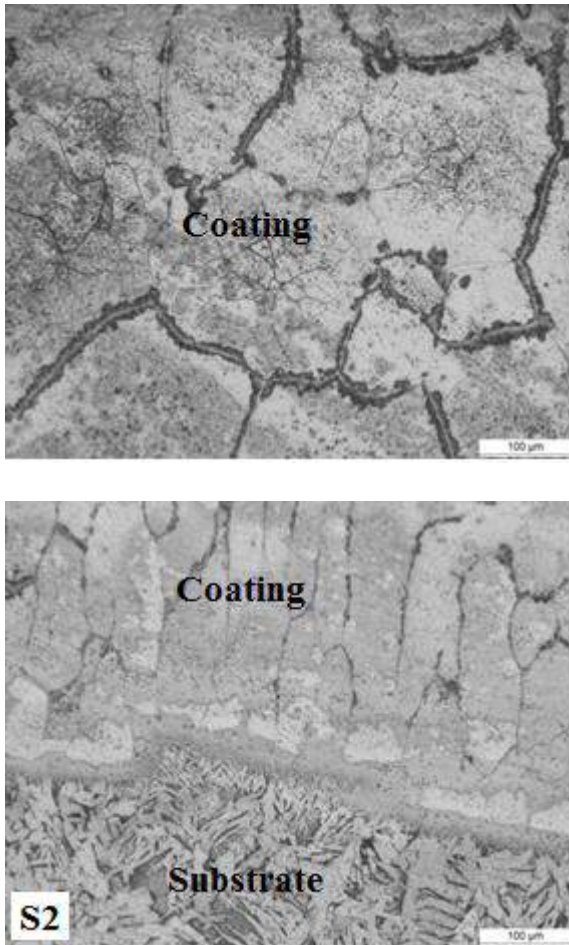


Fig. 3. The optical photo of sample S2.1, a) Coating layer, b) General view.

10% of FeW addition has been alloyed by using the 130 Ampere of current density, the 0.6 l/min of plasma gas flow rate, the 0.01 m/min of welding speed and the argon shielding gas and by using PTAW method, and the optical surface photo, which has been taken from the interface of alloy material after the surface modification process made, is given in Figure 4. When the optical surface photo of the S2.2 sample is examined, it is seen that the dendritic structure disappeared on microstructure images and the carbides are formed within the

grain, in addition to grain boundary carbides. While the partial increase occurred in matrix and eutectic structure, the carbon rate in matrix and eutectic structure was decreased apparently, along with the increasing FeW rate. The reason of this change has been attributed to the carbon shrinkage from the structure due to the formation of FeW and CrC carbides within the grain in the structure. This result is supported by the tungsten change in matrix and eutectic structure.

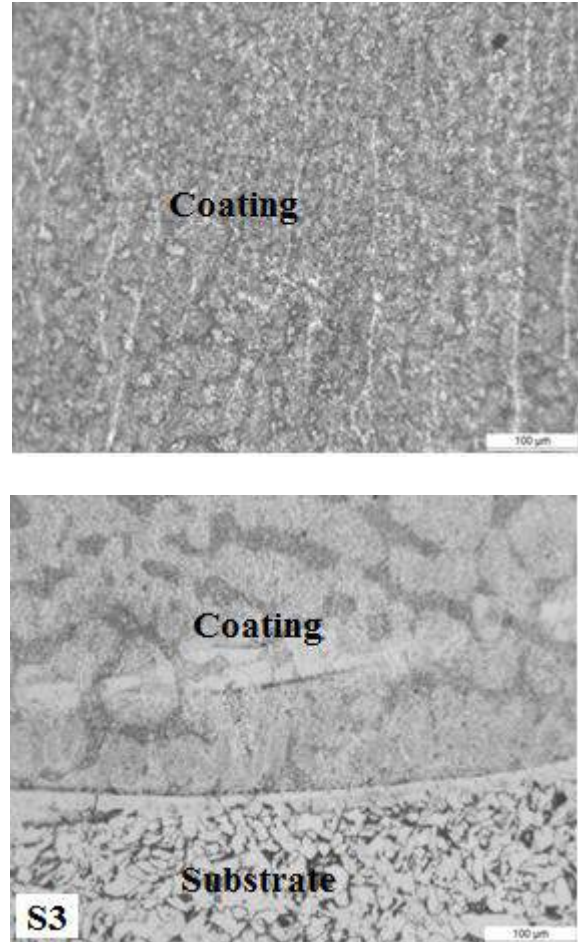


Fig. 4. The optical photo of sample S2.2 a) Coating layer, b) General view.

Figure 5. shows SEM photo of EDS analysis points of sample S2.2. EDS analysis results of sample S2.2 are given in Table 4. When EDS analysis results of this alloy are examined, the elements 66.10%Fe, 4.28%W, 29.38%C, 0.13%Cr and 0.20%Si were detected in the 1st region; 58.43%Fe, 7.32%W, 33.37%C, 0.24%Mn, 0.15%Cr, 0.50%Si were detected in the 2nd region; 69.23%Fe, 3.43%W, 26.86%C, 0.39%Mn, 0.09%Cr were detected in the 3rd region; 82.07%Fe, 7.27%W, 10.06%C, 0.32%Mn, 0.24%Cr, 0.05%Si were detected in the 4th region; 70.89%Fe, 13.83%W, 13.70%C, 0.36%Mn, 0.29%Cr, 0.93%Si were detected in the 5th region. When EDS analysis results are evaluated, we can say that the elements of W, Cr and C passed from the coating material to the coated base material AISI 1020, and the elements of Fe, C passed from the base material to the coating material by the diffusion.

Moreover, the 4th and 5th regions consisted of W, Si, C, Fe, Mn and Cr, which are the elements of the coating material.

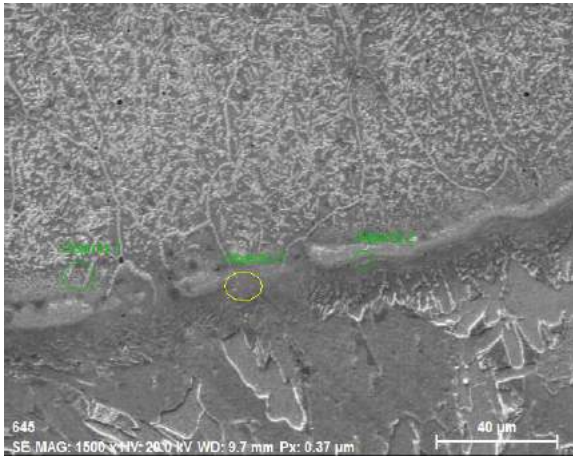


Fig. 5. SEM micrographs of transition region EDS analysis points of S2.2 sample.

Table 4. EDS analysis results of sample S2.2.

Sample No	Analysis Points	Elementer (wt.%)					
		Fe	W	C	Mn	Cr	Si
S2.2	1. Point	66.1	4.28	29.3	-	0.13	0.2
	2. Point	58.4	7.32	33.3	0.24	0.15	0.50
	3. Point	69.2	3.43	26.8	0.39	0.09	-
	4. Point	82.0	7.27	10.0	0.32	0.24	0.05
	5. Point	70.8	13.83	13.7	0.36	0.29	0.93

2. Microhardness Test Results

Microhardness graphic of test samples is given in Figure 6. When the microhardness graphic is examined; it has been seen that positive increase occurred in the coating hardness of samples based on the increasing reinforcement rate. In hardness measurements made starting from the main material through the coating layer; it was detected that, based on the increasing diffusion effect and amount of hard compounds as the main material approached the coating layer, the hardness increased rapidly, that the increase of hardness continued within intermediate and coating layers and eventually that it reached the highest hardness value on the surface.

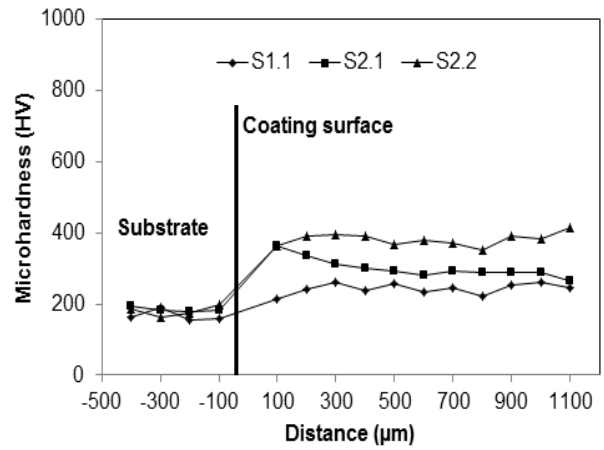


Fig. 6. Microhardness test graphics of test samples.

IV. CONCLUSIONS

In this study, Hardox 450 reinforced and FeW based metal matrix composites (MMC) were alloyed on AISI 1020 steel substrate using plasma transferred arc welding (PTAW) process. Following results were obtained.

- 1) Optical analyses demonstrated that a crack-free and nonporous microstructure formed in these coatings obtained with all production parameters.
- 2) It is seen that the dendritic structure disappears based on the increasing amount of powder and the carbides are formed within the grain, in addition to grain boundary carbides.
- 3) It was seen that the microhardness increase was on the upper region of the coating layers, on all the coatings. In parallel with the increasing amount of powder, the microhardness was also observed to increase based on the formation of hard compounds.
- 4) It was detected that the elements of W, Cr and C passed from the coating material to the coated base material AISI 1020, and the elements of Fe, C passed from the base material to the coating material by the diffusion.

ACKNOWLEDGEMENT

This study supported with the Project no. MÜFYL/2016-001 by Adıyaman University, Scientific Researches Unit. The authors present endless thanks to Adıyaman University, Scientific Researches Unit provided financial support.

REFERENCES

- [1] I. Radu, D.Y. Li, R. Llewellyn, "Tribological behaviour of Stellite 21 modified with yttrium," *Wear*, vol. 257, pp. 1154-1166, 2004.
- [2] D.H.E. Persson, S. Jacobson, "Effect of temperature on friction and galling of laser processed Norem 02 and Stellite 21," *Wear*, vol. 255, pp. 498-503, 2003.
- [3] E. Bourithis, A. Tazedakis, G. Papadimitriou, "A study on the surface treatment of "Calmax" tool steel by plasma

- transferred arc (PTA) process,” *J. Mater. Process. Technol.*, vol. 128, pp. 169-177, 2002.
- [4] A. Conde, I. Garcia, J.J.D. Damborenea, “Pitting corrosion of 304 stainless steel after laser surface melting in argon and nitrogen atmospheres,” *Corros. Sci.*, vol. 43, pp. 817-828, 2001.
- [5] A.S.C.M. D’Oliveira, R.S.C. Paredes, R.L.C. Santos, “Pulsed current plasma transferred arc hardfacing,” *J. Mater. Process. Technol.*, vol. 171, pp. 167-174, 2006.
- [6] A. Gatto, E. Bassoli, M. Fornari, “Plasma transferred arc deposition of powdered high performances alloys: process parameters optimization as a function of alloy and geometrical configuration,” *Surf. Coat. Technol.*, vol. 187, pp. 265-271, 2004.
- [7] Q.Y. Hou, J.S. Gao, F. Zhou, “Microstructure and wear characteristic of cobalt-based alloy deposited by plasma transferred arc weld surfacing,” *Surf. Coat. Technol.*, vol. 194, pp. 238-243, 2005.
- [9] H. Qingyu, H. Zhenyi, G. Jiasheng, “Effects of Y203 on the microstructure and wear resistance of cobalt-based alloy coatings deposited by plasma transferred arc process,” *Rare Metals*, vol. 26, pp. 103-109, 2007.
- [10] A. Klimpel, L.A. Dobrzański, A. Lisiecki, D. Janicki, “The study of the technology of laser and plasma surfacing of engine valves face made of X40CrSiMo10-2 steel using cobalt-based powders,” *J. Mater. Process. Technol.*, vol. 175, pp. 251-256, 2006.
- [11] K. Gurumoorthy, M. Kamaraj, K. Prasad Rao, A. Sambasiva Rao, S. Venugopal, “Microstructural aspects of plasma transferred arc surfaced Ni-based hardfacing alloy,” *Mater. Sci. Eng. A.*, vol. 456, pp. 11-19, 2007

Effect of Heat Treatment Parameters Applied to AA7075 Alloy on Corrosion Behavior

*Gökhan ÖZER, Ahmet KARAASLAN
Yildiz Technical University, Istanbul, TURKEY
ozergokhan@gmail.com, karaas@yildiz.edu.tr*

Abstract- The AA7075 alloy has a wide range of applications due to its high strength and light weight. The T6 heat treatment applied to the AA7075 alloy increases the strength of the alloy but its corrosion properties remain poor. T73 heat treatment to increase the corrosion sensitivity reduces the strength of the alloy. A special heat treatment applied to the AA7075 alloy improves the corrosion and mechanical properties of the alloy at the same time. In this study, the effects of special heat treatment parameters applied to AA7075 alloy on alloy strength and corrosion were investigated.

Keywords: AA7075, Heat Treatment, Corrosion

Comparison of the Mechanical Properties of Different Quality Austenitic Stainless Steels after Wire Drawing

¹Ekrem ALTUNCU, ²Yılmaz YILDIRIM

¹Sakarya University, Tech. Fac. Dept. Metallurgy and Materials Eng., Sakarya 54187 Turkey, altuncu@sakarya.edu.tr

²Guney Celik, R&D Center, Adana Turkey, guneycelik@guneycelik.com.tr

Abstract— Stainless steels are primarily utilized on account of their high corrosion resistance. However, the scope of excellent mechanical properties offered by the various classifications and grades within the family of stainless steel render them extremely versatile materials. Austenitic stainless steel wires are widely used in industrial applications and have a rapidly growing demand. With the wire drawing process, the mechanical properties change considerably after the diameter reduction process. In this study, the mechanical properties of austenitic stainless steels (304, 309 and 316L) were compared in three different qualities. As a result of experimental studies, the highest mechanical properties were observed in 304 and 309 series stainless steels, respectively. There is an effect on the phase transformation as well as the rate of cold deformation in the increase of mechanical properties.

Keywords— Stainless Steel, Wire Drawing, Mechanical Properties

I. INTRODUCTION

Austenitic stainless steels such as AISI-304L, AISI 316L and AISI 309S are an extremely important commercial alloys due to its excellent corrosion resistance, high strength, good ductility and toughness. The common feature of these three alloys is that they have lower carbon content.

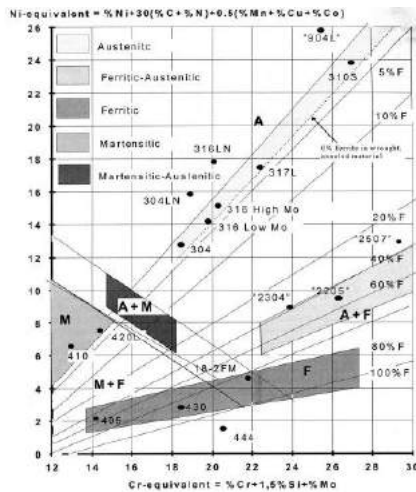


Fig.1: Schaeffler-Delongs diagram, predicting the phase structure for different alloys and chemical compositions in stainless steels

Industrial use of long products such as stainless steel-based rod and wire is rapidly increasing. They are especially used for welding wires, sieve wires, medical wires, resistance wires and cutting wires. The wire rod diameter can be reduced from 6mm

to 1mm or less, especially with the wire drawing process. The mechanical properties of the drawn wires change with the diameter reduction. The ASTM A580 standard describes the mechanical properties for such stainless steels. During the diameter reduction, increase in tensile and yield strength, decrease in elongation ratio are expected. Metallurgical and microstructural events that cause this increase are affecting wire drawability. However, it is structurally metastable and undergoes a partial phase transformation when subjected to sufficient stress or strain. Mechanically induced martensite transformation and transformation-induced plasticity are important phenomena for precise understanding of the deformation behaviour of metastable steels. The effects of martensite phase transformation on the mechanical strength response of the material were of particular interest in this study [1-7].

II. EXPERIMENTS

The aim of this part is to completely analyse mechanical properties by measuring the applied stress and the transformation of microstructure. In this way, in the first step, the drawing experiments are presented. In the second step, the mechanical properties and microstructural transformation are described for each quality of stainless steel wires. The chemical analysis, initial tensile properties and hardness for each quality of stainless steel wire rods are given in Table 1, Table 2 and Table 3, respectively. The hardness testing was done in two directions 90 degrees to each other.

Table 1: Chemical Analysis of Stainless Steel Wire rods

Quality	C	Si	Mn	P	S	Ni	Cr	Mo
304L	0,026	0,45	1,88	0,025	0,004	8,01	18,7	-
309S	0,063	0,53	1,95	0,028	0,003	12,1	22,5	-
316L	0,022	0,39	1,44	0,043	0,001	11,5	16,1	2,0


Table 2: Initial Tensile Properties of Stainless Steel Wire rods (6mm)

Quality	Yield Strength (MPa)	Tensile Strength (MPa)	Elongation (%)
304L	345,33	639,89	42,11
309S	379,56	672,36	38,99
316L	284,79	579,91	42,11

Table 3: Initial Hardness Properties of Stainless Steel Wire rods (6mm)

Quality	Average Hardness (Hv)	
	X Directions	Y Directions

304L	197	185
309S	194	209
316L	199	205



II.I. Drawing Experiments

The wire drawing is a metalworking process used to reduce the cross-section of a wire by pulling the wire through a single, or series of, drawing die(s) (Fig 2). The studied wire drawing process consists of 8 passes, with the section area reduction varies from 26% (the first pass) to 11%. The final wire diameter after 8 drawing passes is 3.00 mm. The drawing speed was about 6 m/s. The strategy is a possible highest decrease in reduction ratio. Die geometries and angles were determined from industrial experiments. The pressure PCD and W wire drawing dies are used in this studies.

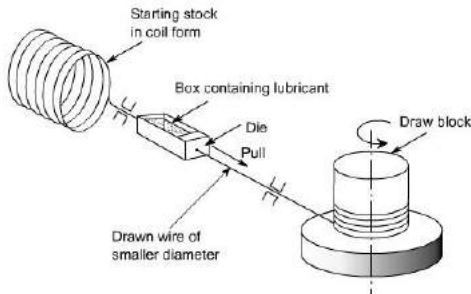


Fig.2: Schematically wire drawing process

Before drawing, all calculations about reduction for each pass by dies are made. The wires are coated with lubricant and feed to wire drawing die (Fig 3).



Fig. 3: The wire is passing on the first drawing head

III. RESULTS AND DISCUSSIONS :

III.I. Mechanical Properties of Wires

The tensile strength which gives indication of the materials, such as its hardness is a good measure of the material brittle nature as the degree of drawn deformation increases. The wire tensile strength and microhardness properties for each quality stainless steel are measured by

universal tensile testing machine and Vickers hardness testing machine after and before wire drawing process and results are given as in Fig 4 and 5 respectively. Hardness of both specimens was measured using the Vickers microhardness method on the longitudinal and cross sections of polished samples. Deformation caused grain hardening of the stainless steel studied affecting its mechanical properties by increasing its tensile/ yield stress, hardness and by reducing its ductility. The different tensile strengths obtained for the low carbon stainless steel at different degrees of cold-drawn deformation. The highest degree of hardness and the tensile stress increase in 304L type stainless steel was observed after 8th head.

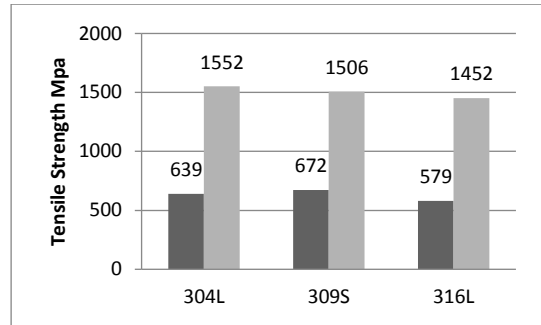


Fig. 4: Initial and final tensile properties for wires (dark: initial, bright: final head after wire drawing)

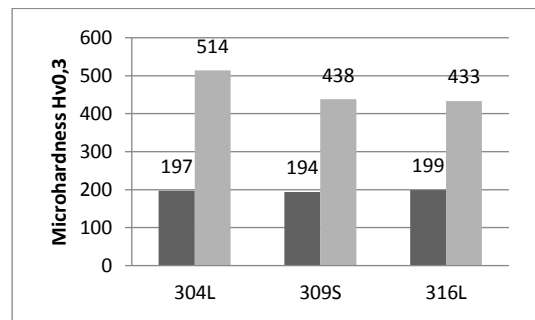


Fig. 5: Initial and final hardness testing results (dark: initial, bright: final head after drawing)

III.II. Microstructure of the Stainless Steel Wires

The microstructural transformations in the stainless steel wires from beginning to end of wire drawing process for each quality is examined in Sakarya University Laboratories by using Scanning Electron Microscope (SEM) and Guney Celik A.S. R&D Laboratories by Optical Microscope (OM). The results are given for each quality with Figure 6 and 7. Figure 6 shows the microstructures of the initial section(a) and after final head wire drawing section (b) of stainless steel wires. Grains are fine and uniform, and the grain boundary is not clear. The martensite phase can be observed when enlarged to about 200 times. It is observed that the organization is elongated a grain along drawing direction and the boundaries is not easy to be identified. This is not only because its appearance changed when the wire was drawing strain, but also the inside grain

became tensile deformation. The grain boundary became destruction and phase transformation occurred. Under this experimental condition, martensitic transformation was induced due to the deformation caused by the cold drawing of stainless steel wire. The resulting martensite was α' phase, the substructure is dislocations and twins.

In Figure 7. During cold-work crystalline defects like dislocations and porosity increase with the degree of deformation and it may decrease the mechanical properties. Microstructural investigations showed that cold deformation causes significant microstructural modifications in these stainless steels, mainly hardening.

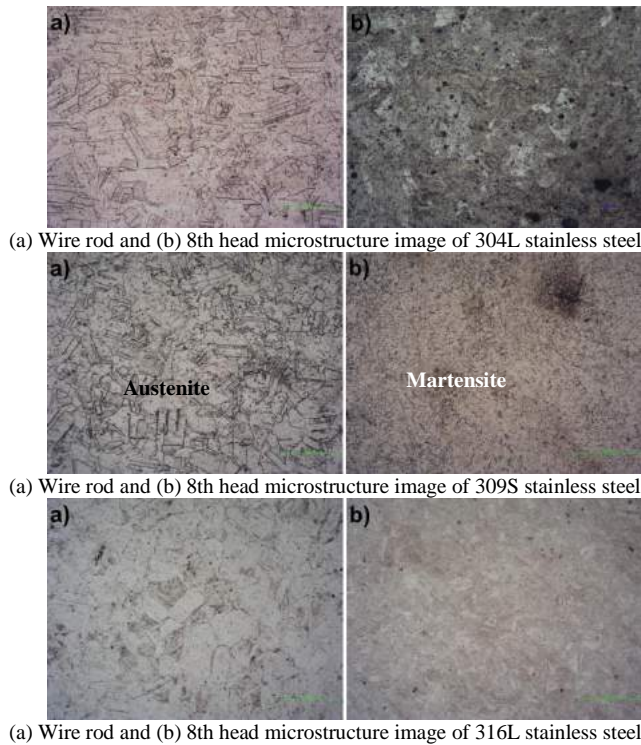


Fig 6. Optical Microscope images of different quality stainless steel wires a. initial wire rod b.after final head.

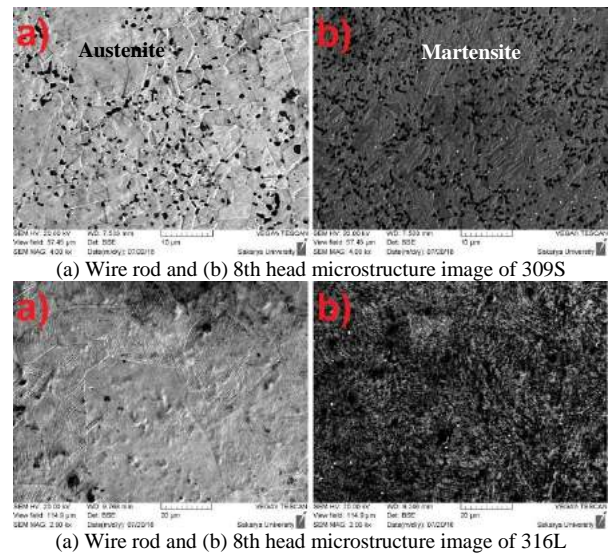


Fig.7. Stainless steel wire SEM micrographs a. before b. after wire drawing.

III.II. Phase Transformation Mechanism

Dislocation slip, mechanical twinning and martensite transformation co-existed during the deformation of 304L, 316L and 309S in the present study (Fig.8). Dislocations are the main carriers of plastic deformation in crystalline materials, and they may or may not travel across grains depending on the nature of interfaces. At all strain levels, dislocation slip is noted to be the dominant deformation mechanism. The dislocation concentration in the grain interiors continues to increase with increasing plastic strain, giving rise to various types of intra granular dislocation-dislocation interaction processes associated with the glide of extended dislocations on different slip systems. Dislocation activity is a precursor of twinning, and subsequently twinning proceeds as an energetically favourable rearrangement of partial dislocations (SFs). In fcc metals, SFs and twins can be formed from the dissociation of a screw dislocation or a 60° dislocation. It is believed that SFs can act as a precursor for the nucleation of α' -martensite, which has an hcp structure. In fact, the fcc and hcp structures are closely related due to their close-packed nature.

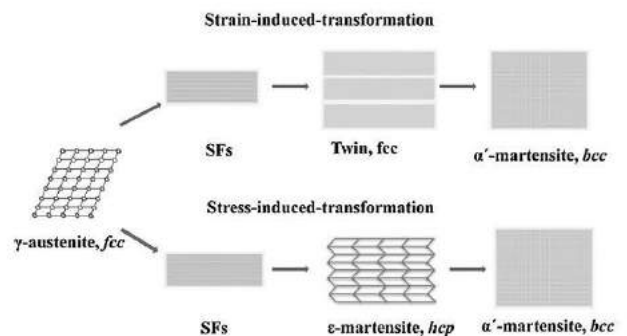


Fig. 8: Schematic illustration of deformation process for the austenitic stainless steel wires

IV. CONCLUSIONS

For the studied austenitic 304L, 316L and 309S type stainless steel wires, the following conclusions can be given:

- The microstructures of these stainless steels were correlated with their mechanical properties. This study is of particular importance due to the integrated industrial project that will use these type stainless steels in the different applications as sieving, weld rod, wire rope and resistance wires.
- The increase in tensile strength is mostly 316L quality and the minimum increase is 309S quality.
- The hardness increase was highest in 304L quality and the minimum increase was in 316L quality.
- The highest degree of hardness and the tensile stress increase in 304L type stainless steel was observed after 8th head.
- Microstructures represent a) austenitic (before wire drawing) and b) martensitic structures (after wire drawing)
- The amount of strain-induced martensite is related to the drawing strain.
- With the deformation applied in the wire drawing process, SFs and martensites are formed.
- When deformation increased, the density of martensite further increases but that of twin abruptly decreases with increasing strain. And the increment of induced martensite causes the drop of twin density.
- The loss of twin relationship across their boundaries due to crystal rotations of the austenitic lattice is also responsible for the decrease of twin density before fracture.

- [6] Hedayati, A.; Najafizadeh, A.; Kermanpur, A.; Forouzan, F. The effect of cold rolling regime on microstructure and mechanical properties of AISI 304L stainless steel. *J. Mater. Process. Tech.* 2010, 210, 1017–1022.
- [7] A. Kurc. , Z. Stoklosa, “The effect of ($\gamma \rightarrow \alpha'$) phase transformation on microstructure and properties of austenitic Cr-Ni steels,” in *Archives Materials Science and Engineering* of paper 85-94, Feb. 2010.
- [8] Luoping Xu, Meitang Shi, Guangjie Shao. The Influences of Heat Treatment and Cold Deformation on microstructure and properties of 18-8 austenitic stainless steel. *Shanghai Metal*, 1993, 15(5): 18-22.

ACKNOWLEDGMENT

This project supported by The Scientific And Technological Research Council Of Turkey; **Tubitak 1501-3150405** numbered project. The authors gratefully acknowledge the experimental support of the University of Sakarya for this research through the project.

REFERENCES

- [1] ASM Internationals, *Stainless Steels for Design Engineers* 2008.
- [2] ASTM A580 / A580M - 16 Standard Specification for Stainless Steel Wire.
- [3] M. Domoinkova, M. Peter and M. Roman, “The Effect of Cold Work on the Sensitization of Austenitic Stainless Steels,” *MTAEC* 9, Vol. 41, No. 3, 2007, pp. 131-134.
- [4] S. J. Pawlak and H. J. Krzton, “Cold Worked High Alloy Ultra-High Strength Steels with Aged Martensite Structure,” *Journal of Achievement in Materials and Engineering*, Vol. 36, No. 1, 2009, pp. 18-24.
- [5] V. Tsakiris, D.V. Edmonds, “Martensite and deformation twinning in austenitic steels, *Materials Science and Engineering* A273–275 (1999) 430–436.

Effect of Boron Addition on Microstructure and Corrosion Properties of CrMo Steels

C. Carboga^{a*}, B. Kurt^a, B. Demirel^b, Y. Sun^c, H. Ahlatci^c, E. Cevik^c

^a*Nevsehir University, Faculty of Engineering and Architecture, Metallurgy and Material Engineering Department, Nevsehir, Turkey.*

^b*Erciyes University, Faculty of Engineering and Architecture, Material Science and Material Engineering Department, Kayseri, Turkey.*

^c*Karabuk University, Faculty of Engineering and Architecture, Metallurgy and Material Engineering Department, Karabuk, Turkey.*

Abstract— In this study, the effect of boron addition at different ratios (2-38 ppm) on the microstructure and corrosion properties of Cr-Mo steels was investigated. Square cross-sections of the boron containing steels obtained at different ratios measuring 40×40 mm were rolled in three passes, and a deformation of totally 200-300 percent was obtained. The rolled specimens were examined by optical microscopy and corrosion test. Electrochemical potentiodynamic polarisation measurements were taken to evaluate corrosion behaviours of the examined steels. Analysing the potentiodynamic corrosion test results applied to the CrMo steels containing boron at different ratios, it is seen that there has been increase at the corrosion rates when the boron amounts are low.

Keywords— Cr-Mo steels, Boron addition, microstructure characterization, corrosion behaviour.

Experimental Investigation on the Usability of Granulated Furnace Slag in Biogas Purification Processes

Mustafa KARAGÖZ^a, Nuri TUNÇ^b, Burak ÇİFTÇİ^a, İsmail EKMEKÇİ^c, Emrah DENİZ^d

^aTOBB Tech. Sciences Vocational School, Karabuk University, Turkey

{mustafakaragoz, burakciftci}@karabuk.edu.tr

^bGraduate School of Natural & Applied Sciences, Department of Mechanical Engineering, Karabuk University, Turkey.
tunckar.nt@gmail.com

^cFaculty of Engineering and Design, Istanbul Commerce University, Turkey
iekmekci@ticaret.edu.tr

^dFaculty of Engineering, Department of Mechanical Engineering, Karabuk University, Turkey
edeniz@karabuk.edu.tr

Abstract— In our day, due to the both depletion of the reserves and the significant environmental problems of fossil based fuels, efforts to improve and smooth use of alternative energy sources have gained momentum. The work on alternative energy sources is mainly focused on the solar, wind and biogas fields and studies have been carried out and being continued to carry out to develop new systems and application methods in order to develop these resources. Biogas, one of the alternative energy sources, is a gas which is obtained by deterioration of biological wastes in a anaerobic environment. The pollutants in the biogas can decrease the lower heat value of the fuel and also cause corrosion and rust in the equipment and components used. Therefore, before using the biogas, it is necessary to remove contaminants in it. In this performed study, biogas has been produced from animal waste by co-fermentation method. In order to purify the pollutant gases in the produced biogas content, the effect of granular slag (an iron steel plant waste) in H₂S removal from the biogas, has been experimentally investigated for different flow rates. As a result of the experiments, it was determined that the 198 ppm H₂S value of the biogas measured before entering the purification tower with slag material was purified with a ratio of 76,8% and decreased to 46 ppm without methane loss.

Keywords— Biogas, Slag, Waste, H₂S, Purification.

I. INTRODUCTION

Global energy demand is rapidly increasing with technological improvements, and about 88% of this demand is met by fossil fuels, which is the main energy source [1]. Due to increasing greenhouse gas emissions and energy security problems in parallel with increased energy consumption, many countries are choosing to supply their energy needs from alternative energy sources such as renewable and nuclear energy [2].

Biogas, one of the alternative energy sources, is at the forefront of both the generation of energy and the potential to produce high quality natural fertilizers by eliminating waste [3-6]. The biogas is produced by anaerobic digestion of organic matter which is a mixture of approximately 55-70% CH₄, 30-

45% CO₂ and a small amount of NH₃ (80-100 ppm), H₂S (1000-3000 ppm) and hydrocarbons (<100 ppm) [7].

The biogas which is produced from decomposition of animal wastes in the anaerobic environment should not be released directly to the atmosphere due to its ingredient of high amount CH₄ that is a greenhouse gas. Instead, heat energy can be obtained by direct combustion, as well as obtaining electrical and mechanical power of being used as fuel in internal combustion engines. However, in order to use biogas as fuel, purification process is required. In order to use the CH₄ of biogas efficiently both as a fuel for internal combustion engines and for domestic heating as well as for cooking, it is necessary to purify the pollutant gases contained in the biogas. Purification is aimed at removing the H₂S, CO₂, moisture and other gas components that do not enter the combustion reaction in the biogas, enriching the CH₄ content and increasing the thermal value of the biogas. The most common biogas purification processes are given in Table 1.

TABLE I
Biogas Purification Processes

	Purification Process
1	Water and Polyethylene Glycol Brushing
2	Chemical Absorption
3	Pressure Swing Adsorption
4	Separation by Membrane
5	Biological Filter
6	Cryogenic Separation
7	Physical Absorption
8	Purification by Hydrate Formation
9	In-situ CH ₄ Enrichment

Once the biogas is obtained, it can be used as fuel in internal combustion engines or in the form of heat energy. However, since the presence of H₂S in the biogas has a detrimental and toxic effect on many equipment, purification process is required [8]. Adsorption with activated carbon is one of the most suitable methods for purifying H₂S in biogas. However, due to the high operating costs, it is encouraged to search for

low-cost alternative absorbers using industrial materials such as natural materials (wood, peat, coal, lignite, etc.) as well as industrial / agricultural / household wastes or by-products such as slag, fine ash, pulp, red mud [9-14].

Özekmekci et al. (2015), in their work; H₂S retention capacities of zeolites were investigated. In experimental and theoretical studies, they found approximately the same results for the predicted sorption selectivity for different zeolites in removing H₂S from biogas, the best value is found in the range of 4.5-10 for faujasite known as 13X and the lowest value is found in the range of 1.8-2.7 for the zeolites known as 4A and 5A. Zeolites have been reported to have a high H₂S retention capacity with the change of metal oxide to metal oxide [15]. Rakmak and his colleagues, in their studies; used Fe⁺³ added MgO catalyst to purify H₂S from biogas. The absorption column containing the water adsorbent is operated with reverse flow mode to absorb H₂S from the biogas. The synthesized catalyst was filled into the column according to continue H₂S dissolution in the aqueous adsorbent fluid and allowed to regenerate the system by introducing air flow. As a result of their experiments; The optimum state was found to be 72% of the maximum H₂S removal efficiency without a loss of CH₄, a liquid / gas ratio of 0.6, a biogas flow rate of 1 L / min. and 10 parts catalyst in a double packed column system [16]. Liu and colleagues in their study; aimed to capture SO₂ and removing H₂S from biogas by coating TiO₂ on the inexpensive and natural zeolite surface by ultrasonic-calcination with TiO₂ / zeolite which is an efficient hybrid adsorbent / photocatalytic compound. 5-TiO₂ / Zeolite (0.013 mmol / g) showed the highest H₂S purification ratio when compared to zeolite (0.05 mmol / g) and TiO₂ (0.07 mmol / g), and the lowest SO₂ emission was achieved when compared to humid TiO₂ [17]. Lestari et al. studied SFS in which the sulphur oxidizing bacteria were attached as biofilms, in a packed bed reactor in order to remove H₂S and the results were evaluated. The obtained results indicate that H₂S can be reduced from 142.48 ppm to 4.06 ppm (97.15% removal efficiency) at a biogas flow rate of 8550 g m⁻³ h⁻¹, corresponding to a residence time of 4 hours for a biofilter-attached isolate with a height of 80 cm and an internal diameter of 8 cm) [18].

Although there are many studies in the literature to purify biogas, there is no experimental study in which granule slag (iron-steel production process waste), is used for this purpose. In the first stage of the study, biogas was produced by co-fermentation method and in the second stage, the purification rates of H₂S in the biogas were determined by passing the biogas through the purification unit which includes granulated slag.

II. MATERIAL AND METHOD

Experimental study was carried out in the laboratory of Karabük University, Biogas Research Center. The granulated slag used in the works was obtained from the Karabük Iron-Steel Factory, the EDX analysis values of Karabük University Institute of Iron and Steel are shown in Table 2, and the one

hundred and five hundred fold magnified SEM images of the internal structure are shown in Fig. 1.

TABLE II
Element content of granulated slag produced in the plant
Karabük Iron Steel Factory.

Element	Mass Ratio (%)
C	8,72
O	35,24
Al	0,70
Si	2,20
P	1,51
S	0,64
K	0,22
Ca	37,69
Mn	4,20
Fe	8,88

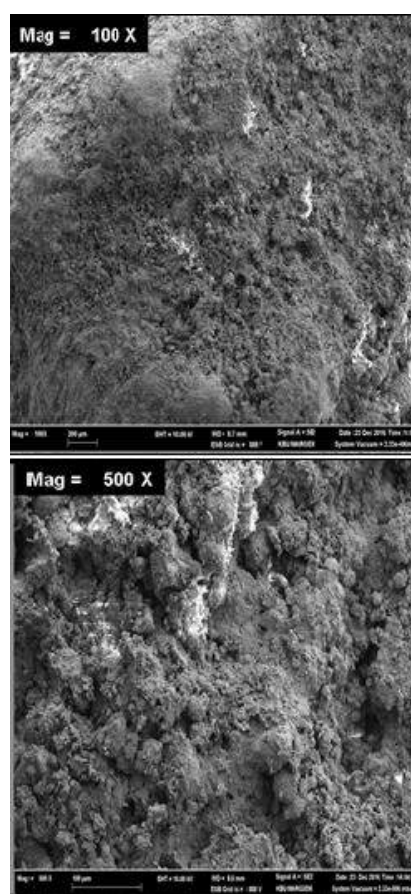


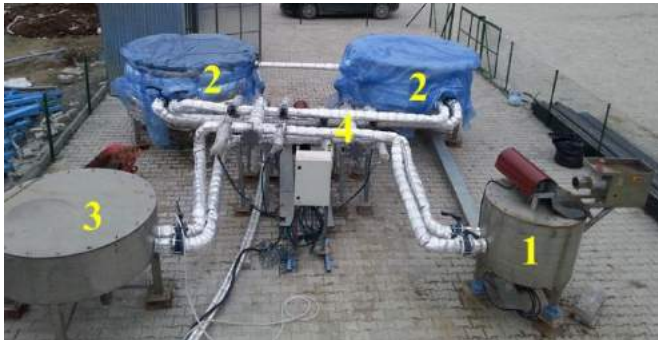
Fig. 1. SEM images of granulated slag.

Granulated slag which is procured and preliminary investigated, is passed through a 6-10 mm sieve and classified as below the sieve and above the sieve, then subjected to washing process to remove dust and other contaminants in it. Afterwards, it was laid flat and left to dry as shown in Fig. 2. The dried granulated slag was made ready to be placed in the purification tower to be used in the experiments.



Fig. 2. Preparation of granulated slag.

In the course of biogas production, about 150 kg of substrate per day (35% water by mass, 17% by volume of whey, 40% by cattle feedstock and 8% by chicken stew) are prepared at the front tank and sent to fermenter via a lobed pump. Biogas production was carried out by subjecting the substrate to anaerobic fermentation at a constant temperature of 37 °C in the fermenter. The image of the main components of the biogas production system is shown in Fig. 3.



1 Front Tank 2 Fermenters
3 Last Tank 4 Raw material transfer system

Fig. 3. The main elements of the biogas production system.

Various experimental instruments and equipments were used in experimental studies. A digital stopwatch was used to measure the duration of the experiments, it was runned at the beginning of the experiment and stopped at the end of the experiment. First, the biogas was drawn from the tank with a blower fan and to run through the purification tower again with a blower fan. Biogas was passed through the gas flow meter and the flow rate was fixed with the flow regulator before purification tower. The experiment is started when the flow rate is fixed. The gases in the biogas were measured with a GA 5000 biogas analyser before purification tower and recorded down. After passing through the biogas purification tower, it was remeasured with the analyser and recorded down. The gas leaving the purification tower is stored in the sample container. Fig. 4 shows the equipment used in the test system for different pressures at constant pressure and the flow chart of the purification process of the biogas.



1 Soft tank 4 Gas flow meter 7 Biogas analyzer
2 Blower fan 5 Digital stopwatch 8 Purification tower
3 Flow regulator 6 Sample valve 9 Sample Container

Fig.4. H₂S removal system for constant pressure

In the experimental system, the gas pressure was kept constant, the produced biogas was passed through the granulated slag placed in the purification tower at flow rates of 3 lt / min, 6 lt / min and 9 lt / min and the H₂S purification rates of the materials were examined. The H₂S purification efficiency of the system used is determined by the measured H₂S input and output values as shown in Equation 1 [16].

$$\% \text{ H}_2\text{S Purification} = \frac{\text{H}_2\text{S Input} - \text{H}_2\text{S Output}}{\text{H}_2\text{S Input}} \times 100 \quad (1)$$

In the given equation;

% H₂S Purification : Percentage of H₂S purification efficiency,

H₂S input : H₂S value of the biogas measured before entering purification tower,

H₂S output : Gives the measured H₂S value at the exit of the purification tower.

III. RESULTS AND DISCUSSIONS

In the first phase of the study, the amount of biogas produced by the co-fermentation method on a pilot-scale biogas system varied and the average amount of biogas produced was 1.6 m³ and the amount of CH₄ increased up to 71%. Different H₂S purification rates were obtained from the purification column of the produced biogas by passing through granulated slag (6-10 mm) at constant pressure and at variable flow rates of 3 lt / min, 6 lt / min and 9 lt / min. The results of the experiments performed are given in Table 3.

It has been found that the H₂S purification rate is increased by increasing the flow rate of the gas passing through the slag material. The purification rates for flow rates 3 – 6 - 9 L / min were 71%, 74% and 77%, respectively. In parallel with the increase in the flow rate, the C₂O purification rate has also increased. C₂O purification rates for flow rates of 3, 6 and 9 L / min were respectively 8%, 12% and 14%.

TABLE III
Different flow rates results for slag material.

Flow Rate			
3 L/min.			
Compound	Input (ppm)	Output (ppm)	Change (%)
CH ₄	15,5	15,5	0
C ₂ O	9,0	8,3	8
O ₂	15,2	14,6	4
H ₂ S	49	14	71
Flow Rate			
6 L/min.			
Compound	Input (ppm)	Output (ppm)	Change (%)
CH ₄	25,7	25,7	0
C ₂ O	16,1	14,2	12
O ₂	11,9	13,1	-10
H ₂ S	116	30	74
Flow Rate			
9 L/min.			
Compound	Input (ppm)	Output (ppm)	Change (%)
CH ₄	36,2	35,1	3
C ₂ O	23,6	20,2	14
O ₂	8,2	9,9	-21
H ₂ S	198	46	77

The obtained H₂S purification data shows that granulated slag material can be used particularly efficiently in pre-purification processes of biogas, and will prolong the lifetimes of other purification units used in biogas systems and reduce the cost of H₂S purification considerably. The obtained data show that a new field of application is being developed for the granulated slag material which is abundantly found in iron and steel plants. In addition, granule slag, which is a problem of disposal and storage, has also been shown to provide added value.

In new studies on biogas purification in the light of experimental and theoretical studies;

- Alternative methods should be developed and supplemented by experimental studies in order to purify the biogas and increase the CH₄ ratios by removing contaminants in the contents.
- The purification performance must be determined by detecting new wastes or natural materials with suitable properties that can be used to purify H₂S.

ACKNOWLEDGMENT

This study is funded by the Karabük University Scientific Research Projects Unit (project number: KBÜ-BAP-16/1-YL-103).

REFERENCES

- [1] World Energy Outlook, *International Energy Agency*, Paris, Part A 2: 65-78 (2006).
- [2] European parliament and council. "Directive 2009/28/EC on the promotion of the use of energy from renewable sources". *Official Journal of the European Communities*, vol. L 283/33; (2009).
- [3] European Parliament and Council. "Report from the commission to the council and the European Parliament on sustainability requirements for the use of solid and gaseous biomass sources in electricity, heating and cooling", *European Parliament and Council* (2010).

- [4] S.R. Wan Alwi, J.J. Klemes, and P.S. Varbanov, "Cleaner energy planning, management and technologies: Perspectives of supply-demand side and end-of-pipe management", *Journal of Cleaner Production*, 136:1-13 (2016).
- [5] H. Von Blottnitz, and M. Curran, "A review of assessments conducted on bio-ethanol as a transportation fuel from a net energy, greenhouse gas, and environmental life cycle perspective", *J Clean Prod*, 15: 607–19 (2007).
- [6] M. Karagöz, "Hayvansal Atıkların Kofermantasyonu ile Biyogaz Üretimi", Doktora Tezi, *Karabük Üniversitesi Fen Bilimleri Enstitüsü*, 15-80, (2016).
- [7] J. Xuan, M. Leung, D. Leung, and M. Ni, "A review of biomass-derived fuel processors for fuel cell systems" *Renew. Sustain. Energy Rev.*, 13: 1301–1313 (2009).
- [8] L.C. Lúa, N.M. Nor, K.T. Leeb, and A.R. Mohamed, "Selection of better synthesis route of CeO₂/NaOH/PSAC for hydrogen sulphide removal from biogas", *Journal of Environmental Chemical Engineering*, 3:1522–1529 (2015).
- [9] A. Mitomo, T. Sato, N. Kobayashi, S. Hatano, Y. Itaya, and S. Mori, "Adsorption removal of hydrogen sulfide by activated coke produced from wood pellet in the recycle system of biomass", *J. Chem. Eng. Jpn.*, 36: 1050–1056 (2003).
- [10] A. Ros, M.A. Lillo-Ródenas, E. Fuente, M.A. Montes-Morán, M.J. Martín, and A. Linares-Solano, "High surface area materials prepared from sewage sludge-based precursors", *Chemosphere*, 65: 132–140 (2006).
- [11] N. Gil-Lalaguna, J.L. Sánchez, M.B. Murillo, G. Gea, Use of sewage sludge combustion ash and gasification ash for high-temperature desulphurization of different gas streams, *Fuel*, 141: 99–108 (2015).
- [12] N.M. Nor, L.L. Chung, L.K. Teong, and A.R. Mohamed, "Synthesis of activated carbon from lignocellulosic biomass and its applications in air pollution control a review", *J. Environ. Chem. Eng.*, 1: 658–666 (2013).
- [13] J.M. Dias, M.C.M. Alvim-Ferraz, M.F. Almeida, J. Rivera-Utrilla, and M. Sánchez-Polo, "Waste materials for activated carbon preparation and its use in aqueous-phase treatment: a review", *J. Environ. Manag.*, 85: 833–846 (2007).
- [14] G. Xu, X. Yang, and L. Spinosa, "Development of sludge-based adsorbents: preparation, characterization, utilization and its feasibility assessment", *J. Environ. Manag.*, 151: 221–232 (2015).
- [15] M. Ozekmekci, G. Salkic, and M.F. Fellah, "Use of Zeolites for the removal of H₂S: A mini-review", *Fuel Processing Technology*, 139: 49–60 (2015).
- [16] N. Rakmak, W. Wiyaratn, and J. Chungsiriporn, "Removal of H₂S from Biogas by Iron (Fe³⁺) doped MgO on Ceramic Honeycomb Catalyst Using Double Packed Columns System", *Engineering Journal*, 14: 1-15 (2010).
- [17] C. Liu, R. Zhang, S. Wei, J. Wang, Y. Liu, M. Li, and R. Liu, "Selective Removal of H₂S from Biogas Using a Regenerable Hybrid TiO₂/Zeolite Composite", *Fuel*, 157: 183-190 (2015).
- [18] R.A.S. Lestari, W.B. Sediawan, S. Syamsiah, and J.A. Teixeira, "Hydrogen sulfide removal from biogas using salak fruit seeds packed bed reactor with sulfur oxidizing bacteria as biofilm", *Journal of Environmental Chemical Engineering*, 4: 2370-2377 (2016).

The Investigation of the Effect of Tempcore Process on Structural Form and Mechanical Properties of the Hot Rolled Steel NPU and Equal Angle Type of Profiles

Tuna Tok*, Aytac Bulut*, Gamze Ay*, Engin Tan⁺

**Kar-demir Rolling Industry Trade Ltd. Co. R&D Center
İzmir, Turkey*

tuna@kar-demir.com.tr, aytacbulutt@gmail.com, gamze.ay@kar-demir.com.tr

*⁺Pamukkale University, Faculty of Technology, Department of Materials Science and Engineering
Denizli, Turkey
etan@pau.edu.tr*

Abstract- In hot rolling which is one of the plastic forming, the operation called “Tempcore Process” provides to obtain different microstructures from the surface to the core by quenching before the cooling platform where the conventional cooling is performed in steel profiles come out of the finish workbench which is the last stage of rolling. The purpose of this process is to obtain a martensitic structure up to a certain thickness from the surface of the profiles to the center and tempering the martensite with the effect of high temperature in the core. Thus, a hard and tough product is manufactured. However, it is ensured that the linearity of the product is maintained at the platform exit. In this study, the Tempcore Process was carried out NPU and Equal Angle type profiles of S275JR quality steel produced in Kar-demir Rolling Industry Trade Ltd. Co. and the effects of this process on the structural form and mechanical properties of the profiles were investigated. In this context, pre- and post-Tempcore Process, hardness measurements, tensile and impact tests were applied and the results were assessed comparatively.

Keywords: Tempcore Process, Hot Rolling, NPU and Equal Angle Type of Profiles, Martensitic Structure, Quenching.

Analysis and Optimization of Rolling Parameters in Steel Profile Hot Rolling Process

Didem Kilic*, Metehan Bacaksiz*,Orhan Akyol*, Engin Tan⁺

**Kar-demir Rolling Industry Trade Ltd. Co. R&D Center
Izmir, Turkey*

didem.kilic@kar-demir.com.tr, metehan.bacaksiz@kar-demir.com.tr, orhan.akyol@kar-demir.com.tr

*⁺Pamukkale University, Faculty of Technology, Department of Materials Science and Engineering
Denizli, Turkey
etan@pau.edu.tr*

Abstract- Process control for optimizing factors such as product quality, energy and cost becomes increasingly important in industry. In this study, the analysis and optimization of the rolling parameters were carried out in steel profile hot rolling process applied in Kar-demir Rolling Industry Trade Ltd. Co. which execute R&D and production activities in the rolling industry. In this context, the analysis of the rolling parameters such as roll position, force, moment, temperature, thickness and crushing amount belonging to rolling mechanics were carried out based on the empirical models widely used in the hot rolling process. As the result of the study, optimum roll positioning and crushing amount calculations are proposed to minimize energy and time cost.

Keywords: Steel profile, Hot rolling, Roll position, Crushing, Optimization.

Pure Bending Fatigue Behaviors Of 80 C Steel Cord Filaments

Hüseyin KOYMATCIK*, Hayrettin AHLATCI+, Yunus TUREN+, Yavuz SUN+, Sait ÖZCELİK+,

*Kardemir A.Ş.Karabuk
hkoymatcik@kardemir.com

+Karabuk University Metallurgy and Materials Science Engineering Depart Karabuk
hahlatci@karabuk.edu.tr, yturen@karabuk.edu.tr, ysun@karabuk.edu.tr

Abstract— In this work we measure and estimate, experimentally and numerically, approximate fatigue strengths of steel filaments of 0.25 mm diameter with 80% C by the pure bending test method. All fatigue tests have been realized at room temperature and at a frequency of 10 Hz via a custom manufactured pure bending tester of which the fully reserved strain value, $R = \epsilon_{min}/\epsilon_{max}$, is -1 . The applied value of cyclic deformation, ϵ , has been chosen from the range 0.46-1.07. The plots of S-N (Strain–Cycle) curves are based on high fatigue cycle (HFC) lives that are greater than or equal to 10^6 cycles.

fine grinding with sandpapers of 1000 and 3000 grit sizes, they have been polished with diamond abrasives.

Table 1: Chemical and mechanical properties

Grade Code	Chemical Composition					Tensile Strength* N/mm2
	%C	%Mn	%Si	%P	%S	
	Avg.	Avg.	Avg.	Max.	Max.	
0.25 HT-80 C	0.43	0.3	0.15	0.2	0.15	3149.11

*Manufacturer's data.

Keywords— Steel Cord, Fatigue, Pure Bending, Tire Cord

I. INTRODUCTION

Sensitive fatigue life estimation in the design of structures subject to variable load conditions is critical when human life is particularly at stake. As steel cord filaments are the most important building blocks of a tire, their fatigue life values exhibit parallels with the life time of the tire. Thus, a tire with a high fatigue strength meets the needs such as long life, better fuel economy, and in particular safety. Tire cord filaments are being produced in diameters varying from 0.15 to 0.40 mm and production of tire cords are carried out by meshing certain amount of filaments together. Changes in the intensities of force and/or deformation of a tire cord sustaining repeated loads in addition to road conditions such as obstacles and speed bumps exhibit variability when a tire is in motion. Accurate estimation of fatigue properties of cord steel during its service is of vital importance because of this variable repeated loading[1-8].

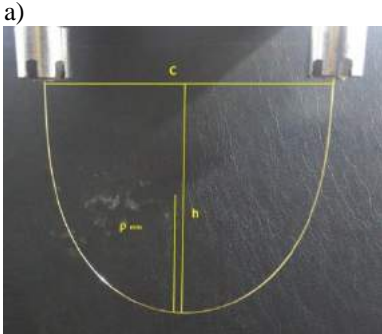
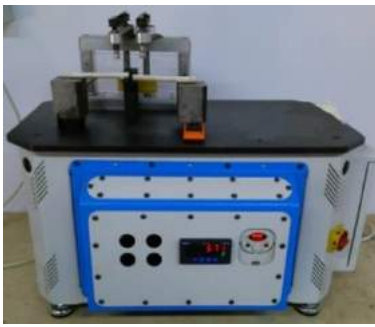
II. EXPERIMENTAL

Steel cord filaments with carbon contents of 0.80% which are procured from Bekaert have been employed in this work. Their chemical compositions and mechanical properties are given in Table 1. The number 0.25 in the material codes of Table 1 indicates the filament diameter and the letters T, N, H, S, and U stand for Tensile, Normal, High, Super, and Ultra, respectively.

Samples of 4 different qualities as given in Table 1 have been taken into Bakelite, positioned longitudinally and vertically to the axis of drawing, for metallographic examination and after a

Inspections of inclusion on the sample surfaces fine grinded and polished and microstructure examination of the sample surfaces following an etching via 4% nital have been carried out with a Carl Zeiss Ultra Plus Gemini Fesem SEM device. Five sound hardness measurements for each sample fine grinded and polished longitudinally and vertically have been taken via a QNESS Q10 brand microhardness tester employing a diamond square pyramidal tip with an apex angle of 136° by applying a 3 kg of load, for 15 s. In this work, pure bending fatigue tests of the steel cord filaments have been realized via a fatigue tester, as exhibited in Figure 1, which is designed and produced to apply ASTM E2948-14 standard test method. Cord samples of certain length are curved via special clamps so that they do not sustain plastic deformations and are tested on the fatigue tester as seen in Figure 1b.

Fatigue tests of the filaments in accordance with ASTM E2948-14 standard, are performed at room temperature and ambient air, at deformation ratio of $R=-1$ via an application of repeated unit elastic deformation. Steel cord filament is bended in such a way that the elastic deformation region faces inside as shown in Figure 1b and the total length and the bending radius have been calculated as a function of the distance C between the clamps [10,11].



a)
b)
Figure 1: (a) Pure bending fatigue tester designed and produced for this work and (b) actual sample installed in chucks

$$\rho_{\min} = 0,417C \quad (1)$$

$$L = 2,19C \quad (2)$$

Unit deformation ε amount under elastic bending is found through Equation 3. where d represents cord diameter[11].

$$\% \varepsilon = \left[\frac{(d/2)}{\rho_{\min}} \right] \times 100 \quad (3)$$

III. RESULT AND DISCUSSION

Figure 2 exhibits microstructures of the 0.25 HT-80 C filament at high magnification.

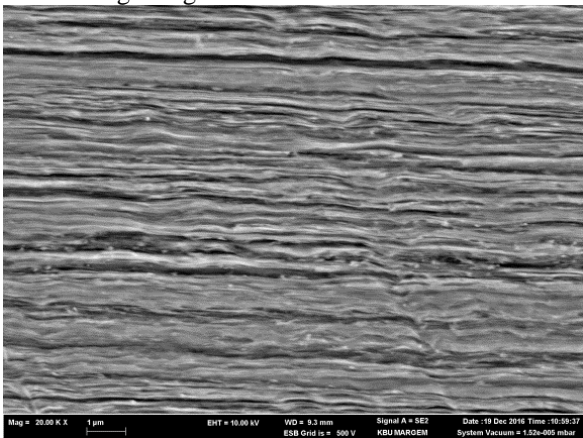


Figure 2: SEM images of the examined filament.

HV₃ hardness values for the steel cord filaments, as ascertained at their longitudinally and vertically polished surfaces, are given in Figure 3.

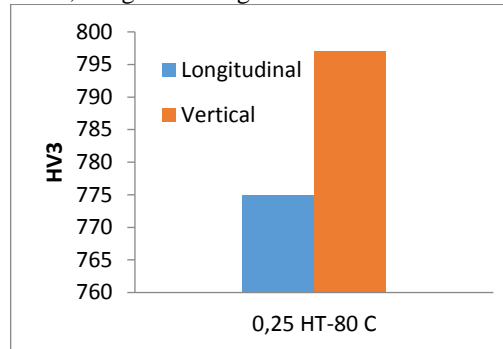


Figure 3: HV₃ hardness values of the examined filament.

S-N curves for filaments of 4 different qualities which have been inspected in this work are exhibited in Figure 4. S-N curves are plotted on a logarithmic scale as damage realized at a particular strain value versus number of cycles (fatigue life) or unit deformations (fatigue limits) that made 10⁶ cycles. The fatigue deformation limit of the 0.25 HT-80 C filament is 0.39. the hardness survey of the 0.25 HT-80 C filament is 775 HV₃.

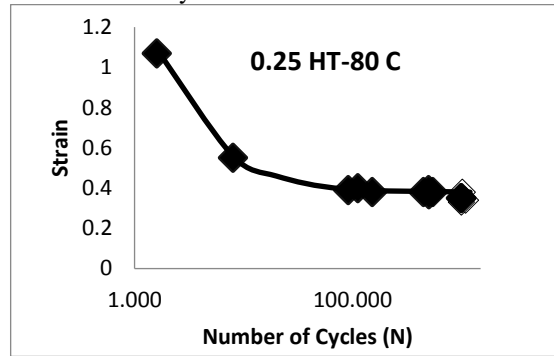
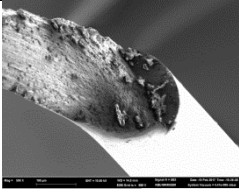
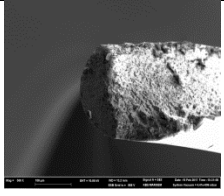


Figure 4: Strain (%)–cycle curves of the examined filament.

Finally, Figure 5 has demonstrated that the final crack of filaments occurs among the pearlite fibers.

Wire	Fatigue	Matching surfaces of the fractured filament	
0.25 HT-	1,07		

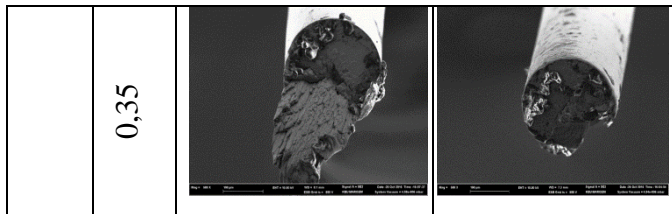


Figure 5: SEM images of the 0.25 HT-80 C filament after fatigue testing.

IV. CONCLUSIONS

In the present study, the fatigue resistance has been investigated for the tire cord filament drawn up to 0.25 mm diameter. The fractured surfaces obtained after the fatigue test are divided into two as angled and flat regions. Widen the flat region leads to the increase in the fatigue deformation limit values.

V. ACKNOWLEDGMENTS

The authors would like to express thanks to Bekaert İzmit Steel Cord Industry and Trade Inc. Technology department and Karabuk University Coordination of Scientific Research Projects (BAP) Project code coded as KBÜ-BAP-1512-DR-023 for supplying steel wires and supporting this work financially.

VI. REFERENCES

- [1] Bekaert Steel Cord Catalogue , Steel cord for Tire Reinforcement, NV Bekaert S. A., Belgium, 2016
- [2] R. Kruzel, M. Suliga, The effect of multiple bending of wire on the residual stresses of high carbon steel wires, *Metalurgija*, 52 (2013) 1, 93-95.
- [3] M. Suliga, R. Kruzel, T. Garstka, J. Gazdowicz, The Influence Of Drawing Speed On Structure Changes In High Carbon Steel Wires, *Metalurgija* 54 (2015) 1, 161-164.
- [4] Shikha Gupta , Alan R. Peltonb , Jason D. Weavera , Xiao-Yan Gongc , Srinidhi Nagarajaa,n, High compressive pre-strains reduce the bending fatigue life of nitinol wire, *Journal of the Mechanical Behavior of Biomedical Materials* Volume 44, April 2015, Pages 96–108
- [5] S. Wang, D. Zhang, K. Chen, L. Xua, S. Gea, Corrosion fatigue behaviors of steel wires used in coalmine, *Materials & Design* Volume 53, January 2014, Pages 58–64
- [6] Wei, O. A. Olatunbosun, The effects of tyre material and structure properties on relaxation length using finite element method, *Materials & Design* Volume 102, 15 July 2016, Pages 14–20
- [7] Y.S. Yanga,J.G. Baec,C.G. Parka, Improvement of the bending fatigue resistance of the hyper-eutectoid steel wires used for tire cords by a post-processing annealing, *Materials Science and Engineering: A*Volume 488, Issues 1–2, 15 August 2008, Pages 554–561
- [8] R. Kruzel, M. Suliga, The effect of multiple bending of wire on the residual stresses of high carbon steel wires, *Metalurgija*, 52 (2013) 1, 93-95.

Measurement Uncertainty Calculation for Charpy Impact Test of S275JR Quality Steel

Alper INCESU*, Betül USTA

Karabük University, Iron and Steel Institute, 78050, Karabük, TÜRKİYE
alperincesu@karabuk.edu.tr , betulusta@karabuk.edu.tr

Abstract— Commercial material producers should accurately know their products performances in service conditions. Test and analyze techniques are very important instruments to understand mechanical, chemical, physical etc. properties of the products. However during the application of these test and analyses some parameters affect the accuracy of results. Calculation of measurement uncertainty is important to put a tolerance value to the results of test and analyses related to these parameters. During the calculation of measurement uncertainty man (personal), machine, material etc. parameters should be clearly and objectively defined and uncertainty that comes from these parameters should be put on to the total uncertainty calculation. In this study, measurement uncertainty for Charpy impact test at room temperature related to EN ISO 148-1 of commercial S275JR quality steel is used at building applications as plate like flat materials was calculated. Parameters that effects the uncertainty calculations were clearly defined and results were reported related to these parameters.

Keywords— measurement uncertainty, Charpy impact test, S275JR quality steel

I. INTRODUCTION

Mechanical and metallurgical testing for continues production and quality control processes are very important to understand performance of materials under service conditions. From ore to final product many characteristics must be monitored to obtain material with free or acceptable defects. Using the adequate instrument and equipment characterizations of such material can be made.

Among the mechanical characterization test Charpy impact test is used to determine the mechanical properties of materials that work under conditions that can cause brittle fracture. The aim of the impact test in general is to determine the amount of energy and ductile-brittle transition temperature required to break the metallic materials under dynamic forces.

Charpy impact test consists of breaking a notched test piece with a single blow from a swinging pendulum, under the some determined conditions. The notch in the test piece has specified geometry and is located in the middle between two supports, opposite to the location which is struck in the test. The energy absorbed in the impact test is determined [1].

When reporting the result of a measurement of test and analysis, it is obligatory that some quantitative indication of the quality of the result be given so that those who use it can assess its reliability. Without such an indication, measurement results cannot be compared, either among themselves or with reference

values given in a specification or standard. It is therefore necessary that there be a readily implemented, easily understood, and generally accepted procedure for characterizing the quality of a result of a measurement, that is, for evaluating and expressing its uncertainty [2-5].

Laboratories operating under ISO/IEC 17025 accreditation and related systems are accordingly required to evaluate measurement uncertainty for measurement and test results and report the uncertainty where relevant. Taking into account all uncertainty components which are of importance in the given situation is obligatory when reporting the measurement uncertainty. [6].

In this study, measurement uncertainty for Charpy impact test at room temperature related to EN ISO 148-1 of commercial S275JR quality steel is used at building applications as plate like flat materials was calculated. Parameters that effects the uncertainty calculations; man (personal), machine and material were clearly defined and results were reported related to these parameters.

II. MATERIAL

Structural steel is a standard construction material, made from specific grades of steel and formed in a range of industry standard cross-sectional shapes. Structural steel grades are designed with specific chemical compositions and mechanical properties formulated for particular applications.

In Europe, Structural Steel must comply with the European Standard EN 10025 a Governed by the ECIS (European Committee for Iron and Steel Standardization) a subset of CEN (European Committee for Standardization).

There are many examples of European grades of structural steel such as; S195, S235, S275JR, S355, S420, S460 etc. Denotation of structural steel can be explained by the followings;

S – denotes the fact that it is Structural Steel

235 – denotes the minimum yield strength of the steel

J2 / K2 / JR / JO – denoted the material toughness in relation to the Charpy impact or 'V' notch test methodology.

Structural steels are used in many ways and their application can be diverse. They are particularly useful because they offer the unique combination of good welding properties with guaranteed strengths. Structural Steel is an extremely adaptable

product and is often favoured by the engineer trying to maximize strength or structure while minimizing its weight.

Some application areas of structural steels are; High Rise Buildings / Skyscrapers, Houses, Factories, Offices, Shopping Malls, Train Tracks, Road Barriers and Bridges [7].

S275JR is a general purpose steel used in construction and building industry. It has a very low carbon steel for easy machining. Chemical composition of S275JR steel was given in Table 1.

TABLE I
CHEMICAL COMPOSITION OF S275JR STEEL [7]

C	Si	Mn	P	S	N
% max					
0,25	0,05	1,60	0,05	0,05	0,014

Also some approximate mechanical properties of S275JR steel were given in Table 2.

TABLE II
SOME MECHANICAL PROPERTIES OF S275JR STEEL [8]

Mechanical Property	Value
Yield Strength (N/mm ²)	> 275
Tensile Strength (N/mm ²)	410 - 560
Elongation (%)	> 23
Impact Strength at +20 °C (J)	> 27
Brinell Hardness (HB)	122 - 162

Identical prepared S275JR steel was used for the calculation of measurement uncertainty of Charpy Impact Test that conducted on Zwick/Roell RKP 450 Motorized Impact Test Machine. Temperature of environment was stable at 23 ± 5 °C.

III. UNCERTAINTY ANALYSIS

No matter what are the sources of your uncertainties, there are two approaches to estimating them: 'Type A' and 'Type B' evaluations. In most measurement situations, uncertainty evaluations of both types are needed. Type A evaluations - uncertainty estimates using statistics (usually from repeated readings) Type B evaluations - uncertainty estimates from any other information.

Information from past experience of the measurements, from calibration certificates, manufacturer's specifications, from calculations, from published information, and from common sense. There is a temptation to think of 'Type A' as 'random' and 'Type B' as 'systematic', but this is not necessarily true [9]. In this study, Type B used for calculation of measurement uncertainty.

To specify the calculation of measurement uncertainty fish bone diagram is helpful. The main sources of measurement uncertainty are indicated as arrows and other factors influencing these sources of uncertainty are also shown in the form of small arrows. Three main source of measurement

uncertainty are man (personal), machine and material. Figure 1 shows all the sources and factors influencing these sources of measurement for Charpy impact test. Environmental temperature should be in a range of 23±5 °C, moisture also should be constant. For this study environmental conditions measured as desired values.

Measurement unit for Charpy impact test is Joule. So, units of all uncertainties comes from the sources must be in a unit of Joule. The values from the sources of uncertainty are converted into relative values and finally converted to the unit of measure to ensure accountability.

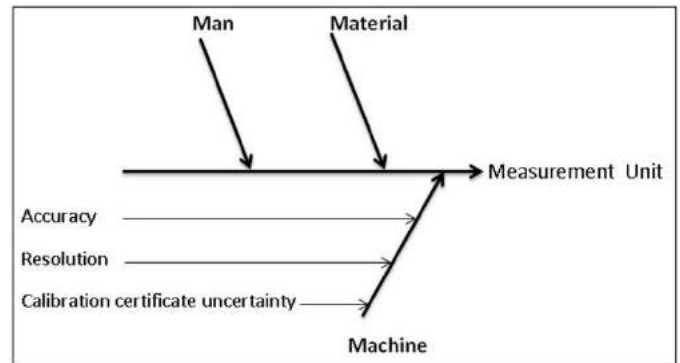


Fig. 1 Fish bone diagram for measurement uncertainty calculation

To calculate the uncertainty comes from the operator (man) repeatability analysis should be done. Basic method is two operator conduct ten identical test individually, then standard deviation of this repeatability tests are calculated. Standard deviations are assumed as normal distribution, so uncertainty from the repeatability is added to the total uncertainty as equation 1. For this study uncertainty of repeatability for two operator is 1,9 Joules. To convert the uncertainty of repeatability to unitless u_{Rep} divided to average value of repeatability tests. It is 27 joules.

$$u_{Rep} = \frac{\delta_{Rep}}{\sqrt{n}} \quad \text{Equation 1.} \quad [10]$$

u_{Rep} = uncertainty of repeatability
 δ_{Rep} = standard deviation of repeatability study
 n= individually conducted test number for repeatability study

Reference materials are used to calculate uncertainty comes from the material. For Charpy impact test reference materials are available at different breaking energy levels. Normal distribution is also valid for this uncertainty source. Three reference samples were broken and their standard deviation is added to the total uncertainty as equation 2. Reference materials has 124 Joules impact energy and standard deviation of three samples was 1,2 Joules.

$$u_{Ref} = \frac{\delta_{Ref}}{\sqrt{n}} \quad \text{Equation 2. [10]}$$

u_{Ref} = uncertainty of reference material
 δ_{Ref} = standard deviation of broken reference materials

n= Number of conducted reference materials

Uncertainty of machine composed of 3 sub sources. These are accuracy, resolution and calibration certificate uncertainty. Material testing machines are calibrated according to ISO 148-2:2008 - Metallic materials - Charpy pendulum impact test - Part 2: Verification of testing machines [11]. Calibration class of testing machine must be 0,5. This mean is < 0,5 the accuracy of the device. The maximum fault tolerance is considered to be 2 times the accuracy of the test machine. So, it is assumed as 1 % for Charpy impact test. Accuracy uncertainty assumed as rectangular distribution. So, uncertainty of accuracy is calculated related to equation 3.

$$u_{acc} = \frac{U_{acc}}{\sqrt{3}} \quad \text{Equation 3.[10]}$$

U_{acc} = (Maximum fault tolerance) x (reference materials value)
 u_{acc} = uncertainty of accuracy

Resolution of the testing machine is 0,1 Joule. Also rectangular distribution is valid, so uncertainty of resolution is calculated related to equation 4.

$$u_{res} = \frac{d}{\sqrt{3}} \quad \text{Equation 4.[10]}$$

d= Resolution of testing machine
 u_{res} = uncertainty of resolution

Calibration certificate uncertainty is given as $k = 2$ and 95 % confidence interval. It joined to the total measurement uncertainty related to the equation 5 with an assumption of normal distribution. Calibration certificate uncertainty was 1 %.

$$u_{cal} = \frac{U_{cal}}{2} \quad \text{Equation 5.[10]}$$

U_{cal} = (Calibration certificate uncertainty) x (reference material value)
 u_{cal} = uncertainty of calibration certificate

To convert the uncertainty of repeatability to unitless u_{Ref} , u_{acc} , u_{res} and u_{cal} divided to reference sample breaking energy value. It was 124 joules.

Relative total uncertainty is calculated related to equation 6.

$$u_{tot-rel} = \sqrt{u_{rep-rel}^2 + u_{ref-rel}^2 + u_{acc-rel}^2 + u_{res-rel}^2 + u_{cal-rel}^2}$$

Equation 6.[10]

Relative expanded uncertainty $k = 2$, 95 % confidence interval is reported related to equation 7.

$$U_{rel} = u_{tot-rel} \times k \quad \text{Equation 7.[10]}$$

IV. RESULTS

Results of the uncertainty analysis of Charpy Impact Test for S275JR steel alloy are given in Table 3. All uncertainty sources defined with their symbols on the table. Using equations from (1) to (7) measurement uncertainties of the test results commercial S275JR quality steel are calculated.

Value of measurement uncertainty for this material under these conditions is reported as $27 \pm 1,31$ Joule.

TABLE III
 RESULTS OF THE UNCERTAINTY ANALYSIS OF CHARPY IMPACT TEST FOR S275JR STEEL ALLOY

Sources of Uncertainty				Partial uncertainties			
Definition	Symbol	Estimated value	Unit	Uncertainty	Unit	Distribution Type	
Man (Personal)	U_{Rep}	27	Joule	1,9	Joule	Normal	
Material	U_{Ref}	124	Joule	1,2	Joule	Normal	
Machine	Accuracy	u_{acc}	124	Joule	1,0	%	Rectangular
	Resolution	u_{res}	124	Joule	0,1	Joule	Rectangular
	Calibration Certificate	u_{cal}	124	Joule	1,0	%	Normal
RESULT	27 Joule ± 1,31 Joule			Standard Uncertainty (relative), u_{rel}		0,0243	
				Expanded Uncertainty (relative), U_{rel}		0,0486	
				k=2, 95 % Confidence interval			

V. CONCLUSION

Measurement uncertainty is very important issue to report the results of test and analyses. Every measurement includes uncertainty. So, for all conducted test and analyses sources of uncertainty should be determined and measurement uncertainty must be calculated. In order to quantify the uncertainty all the factors that could influence the results must be considered. In this work, sources of measurement uncertainty were determined; man (personal), material, machine and measurement uncertainty of Charpy impact test for S275JR quality steel was calculated.

REFERENCES

- [1] Metallic materials - Charpy pendulum impact test - Part 1: Test method (ISO 148-1:2009)

- [2] Evaluation of measurement data — Guide to the expression of uncertainty in measurement, JCGM 100:2008
- [3] M. Bazil and C. Papadopoulos, Application of Probabilistic Uncertainty Methods (Monte Carlo Simulation) in Flow Measurement Uncertainty Estimation, *Flow Measurement International Conference*, 2011
- [4] T. M. Adams, A2LA Guide for Estimation of Measurement Uncertainty in Testing, July 2002, Guidance, G104
- [5] *EA guidelines on the expression of uncertainty in quantitative testing*, EA-4/16 G:2003
- [6] *General requirements for the competence of testing and calibration laboratories* EN ISO/IEC 17025, 2005
- [7] N. Gilbert *Structural Steel - S235, S275, S355 Chemical Composition, Mechanical Properties and Common Application*, AZO Materials, 2012.
- [8] *EN 10025-2:2004 – Hot rolled products for structural steel, 2004*
- [9] Stephanie Bell, *A Beginner's Guide to Uncertainty of Measurement*, 1999
- [10] BIPM, IEC, IFCC, ISO, IUPAC, IUPAP, OIML. *International Vocabulary of Basic and General Terms in Metrology* Second Edition. International Organization for Standardization, Geneva, 1993.
- [11] *ISO 148-2:2008 - Metallic materials - Charpy pendulum impact test - Part 2: Verification of testing machines*, 2008

Effect of Grain Boundary Characteristics on the Impact Properties of Thermomechanically Rolled API X70 Pipeline Steels

Semih Engün^a, Servet Turan^b, Orhan Uzun^a, Oğuz Gündüz^c

[#]Bülent Ecevit University Department of Metallurgical and Materials Engineering, Zonguldak, 67100, TURKEY

^bAnadolu University Department of Materials Science and Engineering, Eskişehir, 26555, TURKEY

^cEreğli Iron & Steel Works Co., Zonguldak, 67330, TURKEY

semihengun@beun.edu.tr (corresponding author)

Abstract— A quantitative grain boundary analysis and impact properties of thermomechanically rolled X70 pipeline steels were conducted. Three different X70 samples that were coiled at different temperatures were characterized by SEM-EBSD technique. Number of low angle and coincidence site lattice (CSL) grain boundaries were quantified. Tensile and impact properties were measured and related by low angle grain boundaries (LAGB) and CSL boundaries. The results showed that, tensile and impact properties are varying with these boundary types. While yield and tensile strength increases by increasing LAGB and $\Sigma 3$ boundaries, impact properties i.e Charpy and drop weight tear (DWTT) energies are generally in a decreasing trend. Moreover, it was observed that grain size due to higher Ti/N rate is a more effective mechanism for Charpy energy than the grain boundary type.

Keywords— Pipeline, Steel, EBSD, CSL, Charpy

I. INTRODUCTION

World's crude oil and natural gas is transported from long distance reservoirs to refineries or end users. Therefore, high-pressure resistant pipelines and minimised wall thickness are required [1, 2]

Type and amount of grain boundaries play significant role on the structure-property relationship of X70 pipeline steels. During grain growth, they encounter each other and misorientation occurs between two grains. This is called grain boundary [3]. If the misorientation angle is lower than 15° , it is called low angle grain boundary (LAGB). However, as crystals rotate more, misorientation angle gets higher and regular structure of grain boundaries starts to break down. This grain boundary is called high angle grain boundary (HAGB) [4]. Since these types of boundaries have high energy, they need less activation energy in order to move, so HAGB are more irregular and mobile than LAGB.

Nevertheless, it was seen that every HAGB is not mobile in the case of each lattice at the two sides of grain boundaries intersects each other. Those special boundaries are called

coincidence site lattice (CSL). For this reason CSL boundary has low energy even though they are HAGB. On the other hand, while some Σ boundaries are truly special, the others are not different than the random HAGB [5, 6].

While LAGB, $\Sigma 11$, $\Sigma 13$ and $\Sigma 5$ type CSL boundaries are crack resistant, random and HAGBs are inclined to crack propagation. However CSL boundaries beyond $\Sigma 13$ are not effective for arresting inter granular stress corrosion crack (IGSCC) [7]. There is an excellent linear relationship between type and structure of grain boundary and fracture behaviour in boron-free Ni3Al. Ductility increases with the fraction of LAGB and low Σ boundaries ($\Sigma 1$, $\Sigma 3$) [8]. According to several studies in the literature, samples that have more $\Sigma 3$ fraction has the highest fracture strength [5, 9-11]. In HSLA steels, thermomechanical rolling stimulates the beneficial occurrence of $\Sigma 3$ and $\Sigma 11$ and prevents the formation of $\Sigma 5$, $\Sigma 7$ and $\Sigma 9$ boundaries [12].

Although grain boundary types and fractions were presented in many studies, there is no clear quantitative criteria for these fractions and mechanical properties; specifically Charpy Impact and DWTT properties.

The goal of the present work is to identify the structure-property relationship in thermomechanically rolled API X70 pipeline steel by classifying and quantifying grain boundary types. This was achieved by EBSD technique; which provides very credible data for distinguishing types and amount of grain boundaries in steels beside phase and texture analysis by using crystallographic information [13].

In accordance with this purpose tensile and impact properties (Charpy and DWTT) were sorted according to grain boundary type and density. Moreover, the effect of thermomechanical rolling parameters on the generation of those constituents and their relationship with impact properties were discussed.

II. EXPERIMENTAL PROCEDURE

Three different API X70 samples, produced by Ereğli Iron and Steel Works Company with the composition given in Table I, were coiled at different temperatures. Samples were thermomechanically rolled at the temperatures given in Table II.

composition, rolling and coiling temperature.

For EBSD mapping, the transverse cross sections of the rolled steels were first mechanically polished with standard metallographic procedure. Mechanical polishing was finished by colloidal silica. After sample was thinned about 300 µm and punched at a 3 mm diameter, electropolishing was applied by digitally controlled automatic electropolisher for TEM samples (Struers Tenupol-5). Samples were etched by a 5% nital solution for optical microscope investigation.

The EBSD measurements were carried out in a field emission type SEM (Zeiss Supra 50-VP) equipped with Oxford Instruments HKL system for collecting and analysing of EBSD data. Patterns were obtained under the 25 kV accelerating voltage, with 17.5 mm working distance and 120 µm aperture size.

Table XXVIII: Chemical composition of the X70 steel (wt%)

	Fe	C	Si	P	Ti	N	Mn	Ni	Nb	Mo
x	97,6	0,08	0,15	0,01	0,008	0,004	1,6	0,2	0,09	0,24
y	97,1	0,07	0,17	0,02	0,02	0,005	1,6	0,2	0,09	0,24
z	97,1	0,07	0,16	0,01	0,01	0,007	1,6	0	0,09	0,18

Table XXIX: Thermomechanical processing conditions

Sample	Rolling Temperature (°C)	Coiling Temperature (°C)	Temperature Difference (°C)
x	898	479	419
y	875	462	413
z	816	514	302

III. RESULTS AND DISCUSSIONS

Figure 1 shows optical micrographs of x, y and z steels. It can be seen from the image that while white regions consist of acicular ferrite, dark regions are bainite and perlite. Particularly in sample y in which Ti/N rate is 4.2 % grains are larger and sheaved. According to Wang [14], when the Ti/N rate exceeds 3.2%, prior austenite grains start to grow and grain refining function of Ti reverse. On the other hand, sample z has smaller and more equiaxed grains than others because of having more Al and V.

Role of the grain boundary characteristics on the impact properties in X70 were examined in three specimens rolled and coiled at different temperatures. The investigations showed that types of grain boundaries in X70 are varied depending on the

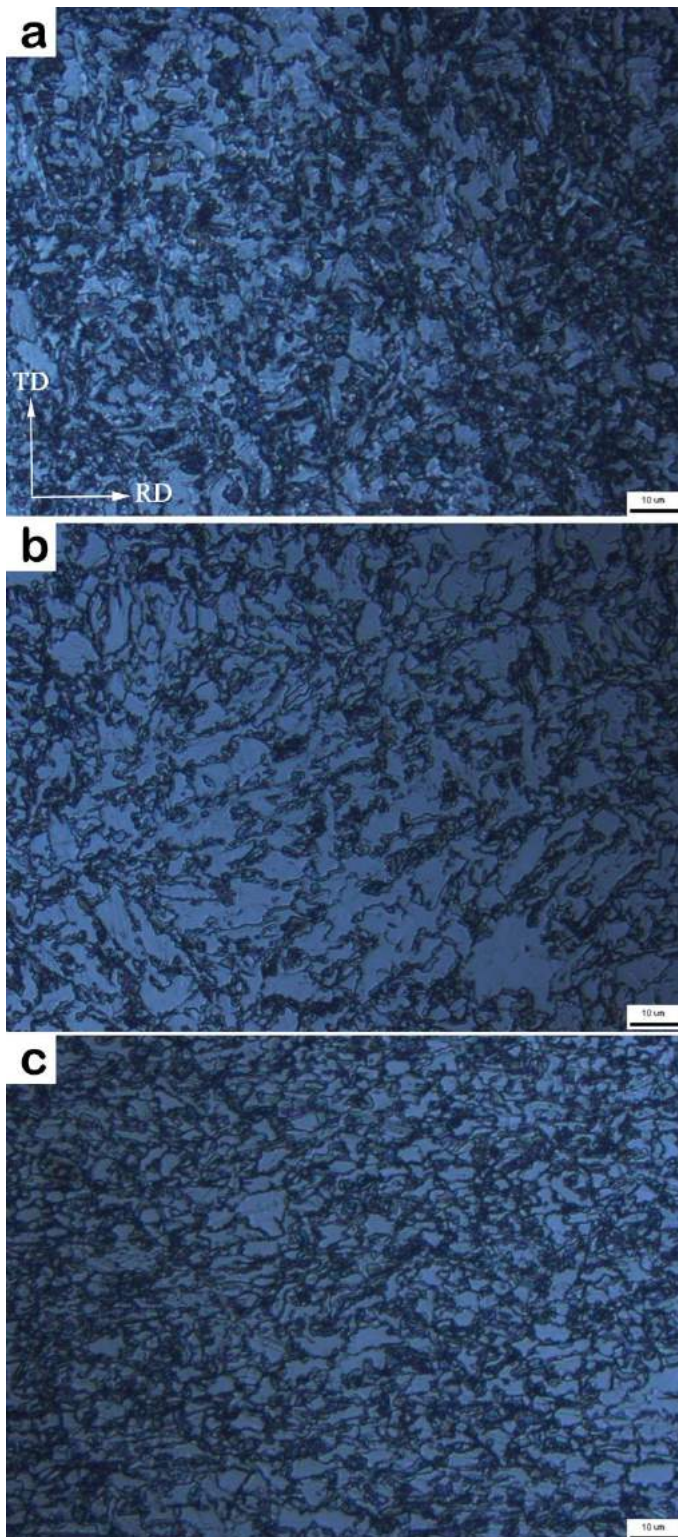


Figure 35: Optical micrographs of the (a) steel x, (b) steel y and (c) with different thermomechanical conditions (500x).

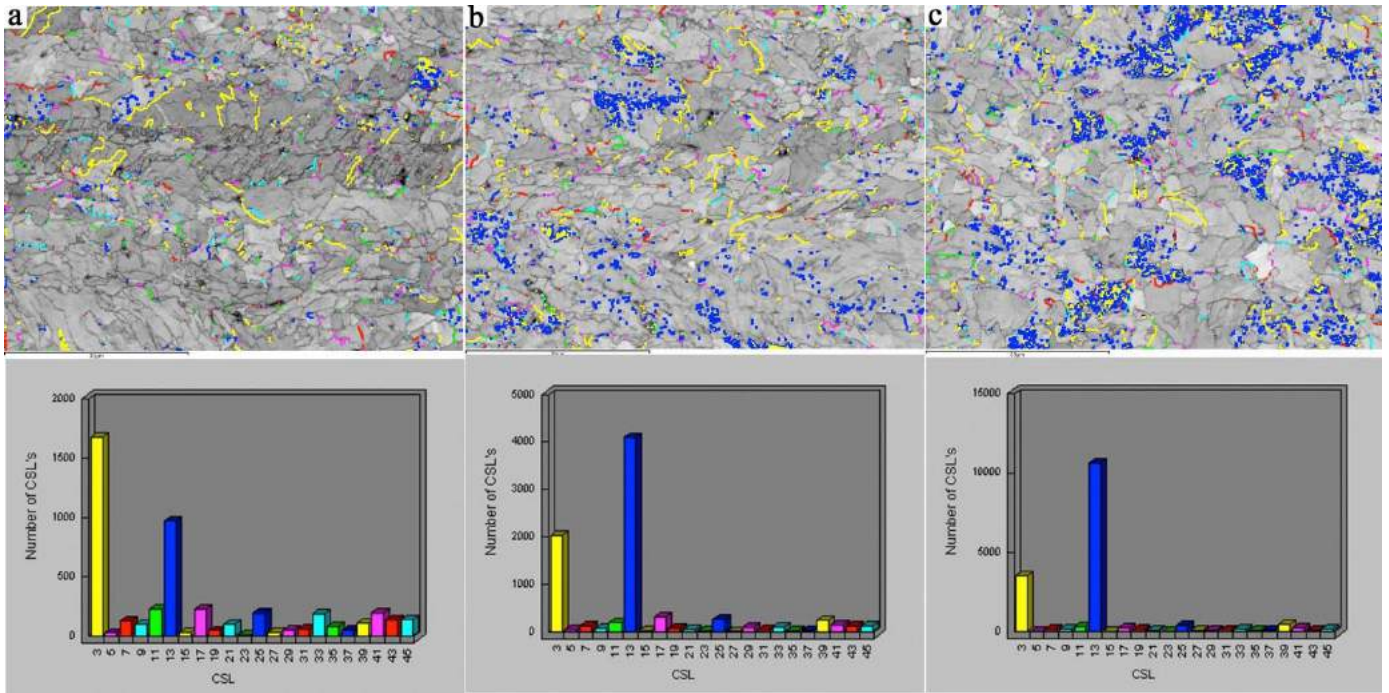


Figure 36: Number and distribution of CSL boundaries on the pattern quality map (a) steel x, (b) steel y

Table III shows distribution of LAGB and CSL boundary fraction of X70 samples. Starting from this point, it was seen that sample x which has the highest temperature difference also has the highest fraction of LAGB and $\Sigma 3$ while it has the lowest $\Sigma 13$ density. Number and distribution of CSL boundaries were shown in Figure 2. Obviously, $\Sigma 3$ and $\Sigma 13$ boundary types seem to be the most dominant CSL boundaries. Furthermore, number of $\Sigma 13$ boundaries seem to be more than the $\Sigma 3$ boundaries except sample x.

Table XXX: Distribution of grain boundary characteristics in X70

Direction	Sample	LAGB < 15° (%)	CSL	
			$\Sigma 3$ (%)	$\Sigma 13$ (%)
TD	x _t	65,28	35,64	20,75
	y _t	57,8	24,97	50,2
	z _t	51,65	20,97	63,24

Table IV shows mechanical properties of x, y and z steels. It is seen that while yield and tensile strengths decreased in x, y and z samples respectively, DWTT increased. However, Charpy energy behaved differently according to DWTT. An abrupt drop in the Charpy energy of sample y was observed. This anomalous behavior can be explained by being higher Ti/N ratio of this sample than 3.20 % [14]. Since prior austenite grains are larger due to the higher Ti/N ratio, Charpy impact energy became the lowest in the sample y.

Table XXXI: Mechanical properties of X70 samples

Sample	Yield Strength (kg/mm ²)	Tensile Strength (kg/mm ²)	Charpy Energy (J) (-20 °C)	DWTT Energy (%) (-20J)
x	64.7	75.8	190	24
y	62.5	73.9	65	30
z	54.7	67	299	94

Figure 3 and Figure 4 shows variation of yield and tensile strengths with grain boundary character distribution respectively. It can be said that as the volume fraction of LAGB and $\Sigma 3$ increased, yield and tensile strengths increased. However, $\Sigma 13$ boundaries show reverse effect to the strength in comparison with LAGB and $\Sigma 3$ grain boundaries.

According to the Figure 5, sample z, which has the highest $\Sigma 13$ ratio, is the most crack resistant sample. However, sample y is the most crack inclined sample contrary to expectations. This abrupt decrease in the Charpy energy due to the larger prior austenite grain size shows that type and distribution of the grain boundary character is not a more dominant factor than the grain size in order to determine Charpy impact energy.

It is seen from Figure 6 DWTT shows an increase by decreasing LAGB and $\Sigma 3$; and increasing $\Sigma 13$ type grain boundaries.

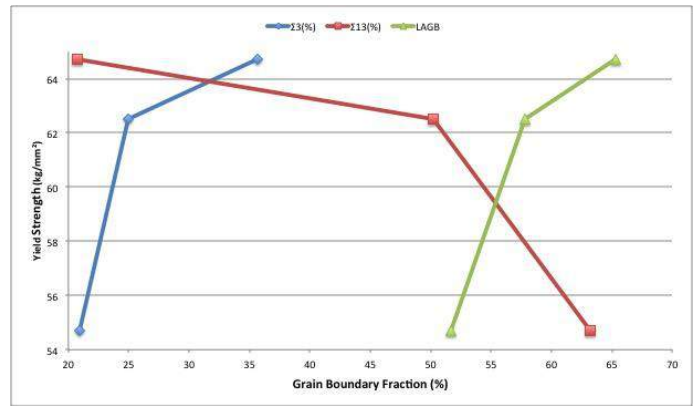


Figure 37: Grain boundary fraction and yield strength of X70 samples.

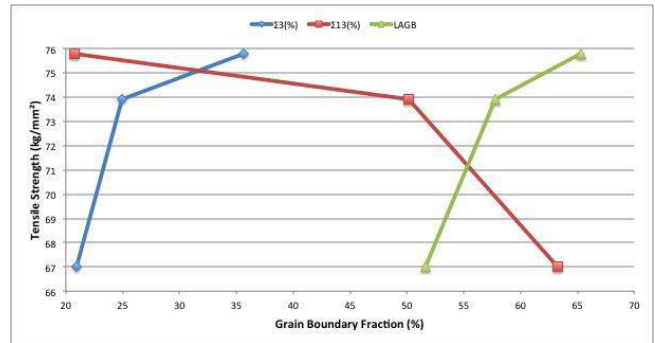


Figure 38: Grain boundary fraction and tensile strength of X70 samples

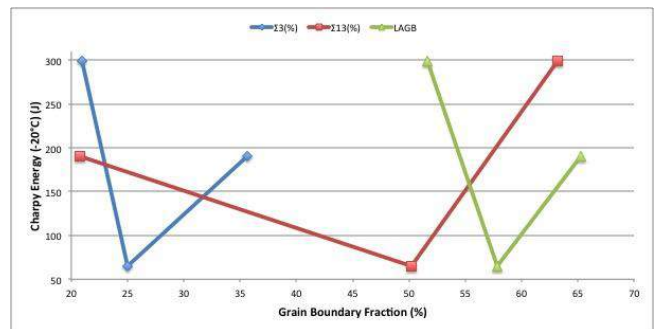


Figure 39: Grain boundary fraction and Charpy energy of X70 samples.

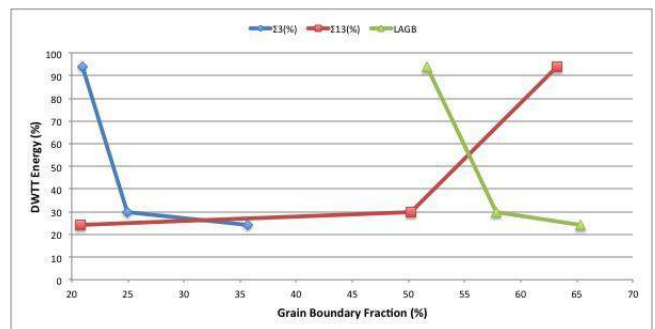


Figure 40: Grain boundary fraction and Charpy energy of X70 samples.

IV. CONCLUSION

Grain boundary distribution characteristics depending on three different cooling temperatures in API grade X70

pipeline steel was gained by using EBSD technique. This was achieved by determining grain boundary characteristics and fractions on the basis of orientation measurements via automated EBSD scan. Fraction of LAGB, $\Sigma 3$ and $\Sigma 13$ grain boundaries was calculated and related with rolling and coiling temperatures. Furthermore, the effect of those fractions on the tensile and impact properties was discussed.

The outcomes of this study can be summed up as follows:

(1) Acicular ferrite, bainite and perlite were observed in microstructure. Since sample y having the higher cooling ratio has % 4.2 Ti/N ratio, it has larger grains and sheaved morphology,

(2) It is seen that the grain boundary character distribution plays a significant role on the mechanical properties. Increases in LAGB and $\Sigma 3$ boundaries have been found to increase yield and tensile strength, while increases in $\Sigma 13$ boundaries have been observed to improve impact properties.

(3) Although grain boundary characteristics and quantity determine the tensile and impact properties of the X70 pipeline steel, grain size due to the higher Ti/N ratio appears to be a more dominant factor for Charpy impact properties.

Acknowledgement

The authors gratefully acknowledge Anadolu University Scientific Research Projects Commission for the financial support by under the contract number: 1404F233.

References:

- [1] Qi, L. and Yang, L. and Niu, J. and Feng, Y. and Zhang, J, *Advances in Materials Science and Engineering*, 2010.
- [2] Tekin, E, "API Standardı Petrol ve Doğalgaz Boruları Çeliklerine Genel Bir Bakış", Metalurji Mühendisleri Odası, Tech Rep. 23-41, 2012.
- [3] W.D, Callister, *Materials Science and Engineering An Introduction*, 8th ed., John Wiley and Sons, Inc., 2007.
- [4] Abbaschian R, *Physical Metallurgy Principles*, Cengage Learning., 2009
- [5] Arafın, M.A. and Szpunar, JA, "Modeling of grain boundary character reconstruction and predicting intergranular fracture susceptibility of textured and random polycrystalline materials," *Computational Materials Science*, vol. 50, pp. 656-665, Dec. 2010.
- [6] Gertsman, V.Y. and S.M. Bruemmer, "Study of grain boundary character along intergranular stress corrosion crack paths in austenitic alloys," *Acta Materialia*, vol.49, pp.1589-1598, May.2001.
- [7] Arafın, M.A. and J.A. Szpunar, *A new understanding of intergranular stress corrosion cracking resistance of pipeline steel through grain boundary character and crystallographic texture studies* *Corrosion Science*, vol. 51(2009) pp.119-128, Jan. 2009.
- [8] Watanabe, T, *Materials Science and Engineering: A, The impact of grain boundary character distribution on fracture in polycrystals*, vol. 17, pp.639-49, Jan. 1994.
- [9] Ikeda, K, *Journal of the Japan Institute of Metals*, 63(199) 179-186.
- [10] Kurishita, H, *Nippon Kinzoku Gakkaisi*, 47 (1983) 546-554.
- [11] Tanaka, T, *Nippon Kinzoku Gakkaisi/ Journal of the Japan Institute of Metals*, "Misorientation dependence of fracture stress and grain boundary energy in molybdenum with $\langle 110 \rangle$ symmetric tilt-boundaries" vol. 58, pp. 382-389, Apr. 1994
- [12] De Castro, *Materials Research*, "Effects of thermomechanical treatment on the occurrence of coincident site lattice boundaries in high strength low alloy steel" vol.16, pp.1350-1354, Aug. 2013.

[13] Schwartz, A.J, *Electron Backscatter Diffraction in Materials Science*. 2000: Springer.

[14] Wang, S. C., *Journal of Materials Science "The effect of titanium and nitrogen contents on the austenite grain coarsening temperature"*, vol. 24(1), pp. 105-109, Dec. 1987.

Electrostatic Powder Coating Plant Conveyor System and Energy Efficiency

Demet Taskan^{*1}, Ahmet Serhan Hergul¹, Volkan Coban¹, Durmus Kaya¹

¹Kocaeli University, Faculty of Technology, Energy Systems Engineering Department
Kocaeli University, Umuttepe Campus, 41380, Kocaeli/TURKEY

^{*}demettaskan90@gmail.com

Abstract— In recent years, Turkey' energy consumption has increased with the increasing rate parallel to the growth rate. For this reason, the importance of efficient use of energy has become more and more remarkable every day. In this study, the potential of ability to the work by the control and automation of the electrostatic powder coating system in a sample operation is increased. In addition, efficiency has been ensured in terms of natural gas consumption and electricity consumption. In terms of the coating operation, the amount of dye consumed per unit m² has been reduced and the operating costs have been reduced. In this context, surface cleaning, drying, dyeing and curing steps in the electrostatic powder coating cabinets in the drying cabinets have been transferred to the conveyor system. For electricity and natural gas consumption, the cost of energy consumption per m² is calculated to produce unit work for energy efficiency. Feasibility studies were made for the facility and the system was installed. The simple payback period is calculated and the increase in the total efficiency of the system and the increase in capacity are presented.

Keywords— Energy efficiency, energy saving, electrostatic powder coating, drying, curing

I. INTRODUCTION

Due to technological developments and increased energy demand, the efficient use of energy has gained importance in recent years. Businesses need to plan expense items well due to increased production costs and competitive conditions. In this respect, companies' competitiveness will rise and production capacities will increase as well as their business potentials. Due to the diminishing energy intensity of unit-work production of energy-efficient companies, the export potential is rising both nationally and internationally.

When the level of development and growth rate of our country is taken into consideration, energy consumption also increases rapidly. The increase in energy consumption in the studies that are being done triggers economic growth, but it also has a negative effect on the current account deficit due to our dependency on the energy source [1,2].

Increasing energy demand in our country necessitates studies for efficient use of energy. When considered on the sectoral

basis, energy is used intensely in many industrial sectors such as chemistry, automotive, plastic, food, cement, ceramics, iron and steel. Energy saving rates are determined in various studies [3]. In addition to energy costs, imports of raw materials used in the production sector hold an important place among the expense items of the enterprises to be supplied from abroad. In this study, the transition from manual application to automation application of the electrostatic powder coating plant is examined.

Electrostatic powder coating technology is mostly applied on metal surfaces. The material which is resistant to corrosion on this side is becomes a tough material against extreme environmental conditions [4]. The coating process increases the resistance of materials to corrosive ambient conditions, high temperature, humidity and acidic environments. Through the method used, the application time of the coating is shortened while the coating yield is increased.

Shah et al. in their work performed drying using fine and coarse dust particles and they used the Navier-Stokes equations to analysis the coating quality and the efficient use of the dye. They have revealed the superiority of finely ground powder grains. The properties of the surface are also important in terms of making the coating process healthy. Surface cleaning solutions developed for this purpose are also used for pretreatment [5]. Cazaux has done an analysis to determine the critical thickness for electrostatic powder coating in his work. It has been made inspections about the electric field and the effects of the dielectric field for the insulating subsurface [6]. Electrostatic powder coating technology is also frequently used in the drug industry. Because of the coating technology which can be applied without solvent, negative effects on drug and users are minimised [7,8].

In this study, the savings potentials that can be put forward by adding control and automation systems of the electrostatic powder coating system were calculated and the system's payback period was revealed. Savings have been calculated in terms of electricity and natural gas consumption, the increase

in the potential for doing business has been determined and the savings in dye raw materials have been revealed.

II. SYSTEM DESCRIPTION

Electrostatic powder coating technology is a concept accepted in the 1930s and 1940s [9]. Electrostatic powder coating is a solvent-free surface coating method. Electrostatic powder coating is a coating method applied by spraying method using special paint guns in powder coating booths. The negatively charged dye particles that come out at the moment of spraying from the paint gun are called electrostatic powder coating by the Korona method to adhere to the surface of a very well grounded material by loading under very low current and very low voltage direct current such as 0,6-0,8mA.

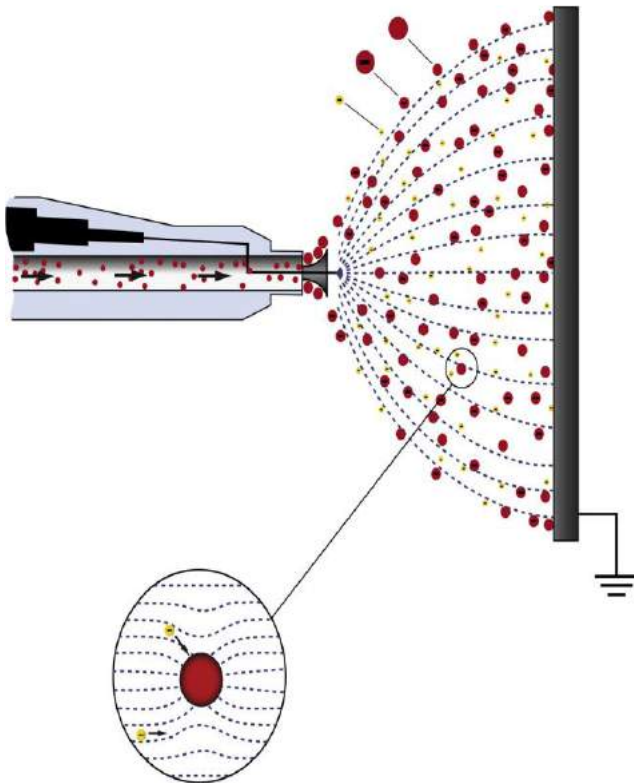


Figure 1: Electrostatic powder coating process and corona effect [10]

Electrostatic powder coating also paints all metal surfaces and therefore the area of use is very wide. For this reason, the system in an electrostatic powder coating operation was automated. In addition to the quality of the product after the automation application, production speed and energy savings have been examined. The basic components in the electrostatic powder coating plant and the results obtained in the first stage with the revision system are as follows.

A. Surface Cleaning Line

In the previous method, the pre-painted zone is prepared by cleaning the surface of the material with dirt, rust and oil by manually wiping it together with certain solvents which are suitable for the surface cleanliness by the employees. In the present case, a pretreatment is started with a special chemical in the spray line, which is a nanotechnology product, and rinsing is then carried out with tap water in the rinsing line. In this way, the dirt on the surface of the material is purified from the dirt, rust and oil before coating.

B. Drying Furnace

In the first application, it is expected that the products which have been cleaned surface are dried outdoors. For this reason, the drying process continues for a longer period. In order to make dry the wet surface of the cleaned products before the electrostatic powder coating, the drying process is completed by waiting for 3 minutes at 80-150 ° C in the drying furnace.



Figure 2: Drying process of the cleaned materials

C. Electrostatic Powder Coating Application

In the conventional application, electrostatic powder coating is applied by spraying technique together with a manual gun. In this application, about 60-70% of the material surface is adhered with powder dye, and powder dye which does not adhere to the material surface is spilled and becomes waste dye. Along with the installed system, electrostatic powder coat is applied in a versatile manner with automatic guns using spray technique. Dye which does not adhere to the surface of the

material is spilled, but powder coated by using the cyclone type powder coating application cabinet is recycled and used.

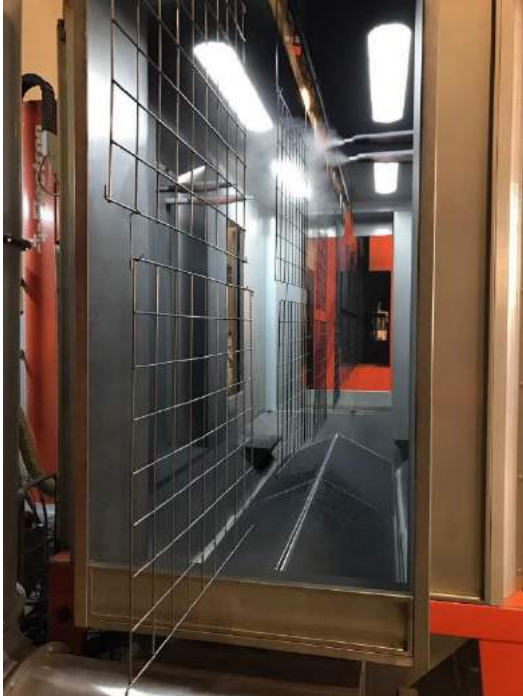


Figure 3: Electrostatic powder coating application stage

On the other hand, approximately half of the approximately 30% powder dye which does not adhere to the part compared to the manual application in the powder coating cabinet accumulates in the underside of the vibrating cyclone and half in the cabinet floor. The dye which accumulates on the cabin floor is automatically pumped to the cyclone by the pneumatic system. Powder dyes deposited in swept paint reservoir and under cyclone reservoir are transferred back to the system with automatic painting center.

Thus, very small dye particles are sent at the rate of 3-4% in the filter group. After applying this method, the yield is 95% by using cyclone, whereas in the other method, the yield with the previous method is around 60-70% due to the dust particles falling. Cyclone type powder painting application cabinet is preferred because of the higher powder coating efficiency with the automation application [11].

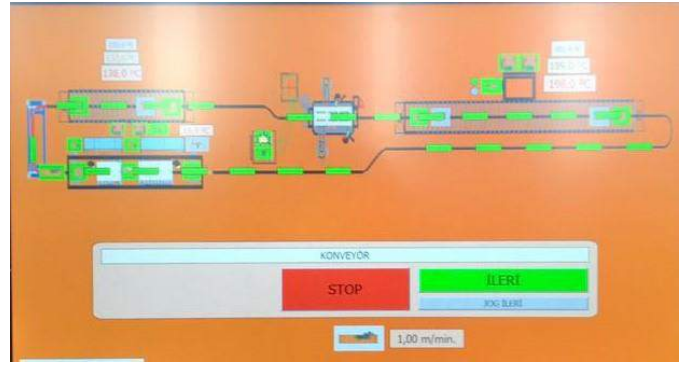


Figure 4: Workflow in the main panel

D. Curing Process

The products which are coated in manual application are heated for 10 minutes at 160-200 °C in the furnace by hanging the curing furnace by hand. With automation application, powder coated products are cured. At this stage, the products are exposed to a temperature of 160-200 °C for 10 minutes given in the application properties of the dyes. The electrostatic powder coated dye melts to form a smooth surface and then cures. At the end of this period, the products are removed from the furnace and the coating process is completed.

III. RESULTS AND DISCUSSION

The following table shows the amount of the dye consumption, energy consumption that has been spent as a result of previous applications and also increases of the facility' production potential.

As can be seen in the table, electricity consumption is decreased to 0,108 kWh/m² which means that 2.77 times less consumption is achieved. The daily work capacity increased 10 times. Beside that in terms of natural gas consumption 2,66 times less gas consumption is achieved.

Table 1: Comparison table of the both application

	Previous Application	Automation Application
Workpiece Velocity	0,167 m ² /min	1,66 m ² /min
Total Daily Work Value	75 m ² /day	750 m ² /day
Electricity Consumption	22,5 kWh/h	81 kWh/h
Natural Gas Consumption	232 kWh/h	872 kWh/h

Total Energy Consumption	254,5 kWh/h	953 kWh/h
Electricity Consumption per m ²	0,3 kWh/m ²	0,108 kWh/m ²
Natural Gas Consumption per m ²	3,093 kWh/m ²	1,162 kWh/m ²
Total Energy Consumption per m ²	3,393 kWh	1,27 kWh
Energy Savings Per Year	-	11.920.896 kWh
Dye Consumption Per m ²	0,178 kg/m ²	0,125 kg/m ²

With reference to the energy consumed to produce the same workpiece, 10.842.624 kWh of natural gas saving per year has been achieved. With the same approach, 1.078.272 kWh saving is achieved for electricity consumption. Given natural gas and electricity prices, 975.836 ₺ natural gas and 334.264 ₺ electricity prices have been saved to produce the same quantity of workpieces. As a result, annual energy savings of 11.920.896 kWh is achieved per year. The financial value of saving is realised as 1.310.100 ₺ per year.

IV. CONCLUSIONS

Due to technological developments and increased energy demand, the efficient use of energy has gained importance in recent years. In the work done, analyses were made about the transformation of the electrostatic powder coating system to the automation in an industrial firm. In terms of the coating operation, the amount of dye consumed per unit m² has been reduced and also operating costs have been reduced. The total decrease in the amount spent to dye the same workpiece is about 12,5 tonnes per year. The savings obtained from the dye reach 148,500 ₺ per year. Given the total investment cost of the plant, the entire system has a payback period of 8 months.

REFERENCES

- [1] Rüstem Yanar, Gül den Kerimoğlu, Türkiye’de Enerji Tüketimi, Ekonomik Büyüme ve Cari Açık İlişkisi, Ekonomi Bilimleri Dergisi, 3(2), 2011, 191-201.
- [2] Fatma Fehime AYDIN, Enerji Tüketimi ve Ekonomik Büyüme, Erciyes Üniversitesi İktisadi ve İdari Bilimler Fakültesi Dergisi, 35, 2010, 317-340.
- [3] Ağış Ö., Kojenerasyonun Dünü, Bugünü ve Geleceği, Energyworld Dergisi, 24, 2013, 66-68.
- [4] Wicks, Z.W., Jones, F.N., Pappas, S.P., Wicks, D.A., 2007. Organic Coatings: Science and Technology, Wiley-Interscience, Hoboken, N.J, 3rd ed.

- [5] U. Shah, C. Zhang, J. Zhu, Comparison of electrostatic fine powder coating and coarse powder coating by numerical simulations, Journal of Electrostatics 64,2006, 345–354.
- [6] Jacques Cazaux, Critical thicknesses of electrostatic powder coatings from inside, Journal of Electrostatics 65, 2007, 764–774.
- [7] Qingliang Yang, Yingliang Ma, Jesse Zhu, Applying a novel electrostatic dry powder coating technology to pellets, European Journal of Pharmaceutics and Biopharmaceutics 97, 2015, 118–124.
- [8] Leena Kumari Prasad, Justin S. LaFontaine, Justin M. Keen, Robert O. Williams III, James W. McGinity, Influence of process parameters on the preparation of pharmaceutical films by electrostatic powder deposition, International Journal of Pharmaceutics 515, 2016, 94–103.
- [9] G.S.P. Castle, Industrial applications of electrostatics:the past, present and future, Journal of Electrostatics, 51(52), 2001, 1-7.
- [10] Leena Kumari Prasad, James W. McGinity, Robert O. Williams III, Electrostatic powder coating: Principles and pharmaceutical applications, International Journal of Pharmaceutics, 505, 2016, 289–302.
- [11] Demir Raf Company, Sprayer Washing Machine, Technical Document, 060-2015, 2016.

Determination of Phase Equilibria in High Alloy White Cast Irons

Öncü AKYILDIZ*, Duygu CANDEMİR

*Faculty of Engineering, Department of Metallurgical and Materials Engineering, Hitit University, TR-19030, Çorum/TURKEY

oncuakyildiz@hitit.edu.tr, duygukorsacilar@hitit.edu.tr

ABSTRACT

White cast irons are hypoeutectic alloys in which the carbon remains dissolved in the iron carbide phase, called cementite, without decomposing into graphite during solidification. Because of the hard cementite phase, they preferred in high abrasion resistance required applications. In order to improve further the wear resistance they are alloyed with strong carbide forming elements (W, Mn, Mo, S, Cr, V, Mg, etc.). There is a strong relationship between the mechanical properties of alloys and the internal structure they possess. In order to reveal the effect of the internal structure, the diagrams showing the phase equilibria of the material should be known. Today, various software programs are used to make thermodynamic calculations relevant to phase equilibria. In this study, using the Materials Calculator software program, it is aimed to simulate the pseudo binary phase diagrams (i.e. isoplethal maps) where the molar fractions of alloying elements other than carbon are fixed. In order to check the accuracy of the constructed diagrams, the casted samples with determined compositions will be analyzed by differential scanning calorimetry (DSC) and the theoretical and experimental data will be compared. The diagrams for changing the type and amount of the alloying addition will be examined and the effects of changing the amount and distribution of carbides with increasing carbon content and temperature will be discussed to improve the wear resistance.

Keywords: White Cast Iron, Phase Equilibria, Computational Thermodynamics.

An Investigation of the Optimum Insert Diameter/Molding Diameter Ratio by Inserted Powder Injection Molding

Oğuz Yılmaz^{1a}, Kamran Samet^{1b}, Harun Koçak^{2c}, Çetin Karataş^{1d},

¹Gazi University, Faculty of Technology, Manufacturing Engineering, Ankara, TURKEY

²Selçuk University, Machine and Metal Technology School of Higher Education Faculty of Technology, Konya, TURKEY

^aoguz.yilmaz2@gazi.edu.tr, ^bkamran.samet@gazi.edu.tr, ^charunkocak@selcuk.edu.tr, ^dcetink@gazi.edu.tr

Abstract— Inserted powder injection molding (IPIM) is developed to produce a larger volume parts in powder injection molding (PIM). In this method, the injection process is carried out on the part called insert. Since the injection volume gets smaller, the debinding time decreases. However, the insert diameter/the molding diameter ratio (D_i/D_m) is the important parameter in that method. There could occur crack in the injection side unless the ratio determines properly. In this study, the insert and injection's materials is high speed steel (HSS) and WC-%9Co feedstock, respectively. Different amount of expansion occurs since the materials have different thermal expansion coefficients. This difference causes a thermal stress in the connection surface. If the resulting thermal stress exceeds the compressing strength of the material in the injection side, then thermal cracks occur. Mathematical calculations have been carried out to determine the optimum ratio of D_i/D_m . In order to validate the calculations, finite element analysis was performed by ANSYS software. Theoretical results were supported with experimental studies. The risk of cracking in the injection side increases as the ratio of D_i/D_m increases. As a result of the study, the optimum ratio of D_i/D_m was determined as 0.45 for the part produced by PIM.

Keywords— Powder Injection Molding, Thermal cracking, Expansion, Thermal Analysis, Finite Elements

V. INTRODUCTION

Inserted powder injection molding (IPIM) is a method which is metal or ceramic powder based feedstock injection on insert [1]. Produced part thickness by powder injection molding (PIM) is limited to 10 mm. This reason for this limitation is difficulty in debinding that as the part thickness increases parts manufacturing time and cost of production rises [2, 3]. The thickness of the injected side decreases with IPIM. Debinding is possible for larger volume parts thanks to thickness reduction. The first advantage of IPIM is to shorten the duration the debinding process and the second advantage of IPIM is to reduce cost due to the use of less feedstock [4].

The part produced using IPIM occurs as a result of combining two materials. At this point, it is important to select materials which have thermal expansion coefficient close to each other in the injection side [5], for, permanent deformation

and cracks may occur in the sintering stage if insert expands more than the injection side. The thermal expansion is a crucial thermo-physical property of materials, which can be quantitatively described by the thermal expansion coefficient, for many industrial applications pertinent to dimensional stability and is a key issue for defect control, performance prediction and optimization of technologies [6].

When the same material is used for the insert and the injection region, the thermal expansion difference does not occur. Therefore, in the manufacturing process, insert dimension does not affect crack formation for the same materials [4]. If the insert and injection sides are different materials, thermal expansion difference causes thermal stresses between the connection surface at the pre-sintering stage. When these stresses reach the strength of the material in injection side, cracks occur in the injection side. The cause of crack formation is tensile and compressive stresses which occur as a result of thermal stresses in the material. Consequently, thermal expansion is significant in the parts produced through the combination of different materials [7-9]. If insert dimensions are important, continuity of the stress distribution can be ensured with creating layered structures to avoid the cracking [10].

When insert dimensions are important, continuity of the stress distribution is ensured with creating layered structures and then cracking can be prevented. Another way to prevent cracking due to thermal stresses is to accurately determine the ratio of insert diameter/molding diameter (D_i/D_m).

In this study, the ratio of D_i/D_m effect was investigated with injecting the WC-%9Co feedstock onto HSS. The thermal stresses in the connection surface of the designed specimens were determined using ANSYS software and mathematical calculations. Then experimental studies were carried out by IPIM method. As a result of the theoretical and experimental studies, the optimum diameter ratio was determined as 0.45.

VI. MATERIAL AND METHOD

In this study, the thermal stresses at the connection surfaces were investigated for the D_i/D_m ratios of 0.4, 0.45, 0.5, 0.6, 0.7 and 0.8. A three-dimensional model of the design part using the SolidWorks software was created. The ANSYS software was used for stress analysis at the connection surface. The developed three-dimensional model was transferred to the ANSYS software and analyzed by finite elements method. The chemical composition of feedstock and insert used are given in Table I and Table II.

TABLE I

CHEMICAL COMPOSITION OF FEEDSTOCK (WC-%9Co)

Element	C	Co	Cr	Fe
Wt. %	5,54	8,97	0,01	0,01
Element	Mo	Ni	O	W
Wt. %	0,01	0,01	0,05	Bal

TABLE II

CHEMICAL COMPOSITION OF INSERT

Element	C	Si	Cr	Mo
Wt. %	0,90	0,25	4,10	5,00
Element	Mn	V	W	
Wt. %	0,30	1,80	6,40	

CC. Mathematical Model

The sample design to be produced by IPIM is shown in Fig. 1. According to this design, the part consists of two different materials. The difference in the thermal expansion coefficients will cause stresses in the connection surface with an increase in temperature. Changing in the D_i/D_m ratio changes the stress occurring at connection surface.

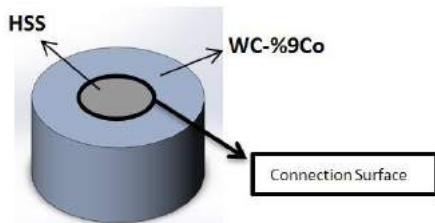


Fig. 1 Designed sample and displaying of the connection surface

The diameter of the mold cavity (D_m), 20 mm, was fixed. However, the diameter of the insert (D_i) was changed. The emerging diameter ratios (D_i/D_m) were calculated.

The thermal stress in the connection surface was calculated by the superposition method. Accordingly, the mathematical model is likened to the rod model which is between the two fixed supports (Fig. 2).

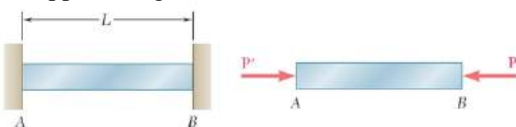


Fig. 2 Modelling of the designed geometry [11]

In the first situation, there is no deformation and stress, but if the temperature of the rod increases as many ΔT as, the fixed supports will not allow any extension. Because the deformation is blocked by the supports, P and P' occur which are equal and opposite forces on the supports of the rod. Thus, a stress occurs on the rod.

The thermal stress occurring in the contact surface due to the ΔT temperature change is calculated using (1):

$$\sigma = P/A = -E \alpha \Delta T \tag{1}$$

σ = Stress (MPa) E = Young's modulus (GPa)

ΔT = Temperature difference ($^{\circ}C$) A = Cross-sectional area of the rod (mm^2)

L = The length of the rod (mm) α = Thermal expansion coefficient ($1/^{\circ}C$)

This model is adapted to the created geometry. The insert and injection side will expand as the temperature increases and the insert will apply force to the injection side. On the other hand, the injection side creates an equal and opposite force as a response which emerge by expansion. The stresses were calculated by dividing the emerging force by the connection surface.

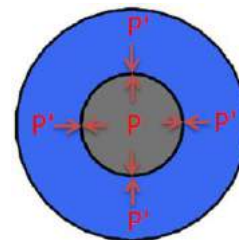


Fig. 3 Internal forces in the connection surface occurring with temperature

DD. Finite Elements

The stress analysis in the connection surface was performed using the finite element method using ANSYS software. Insert material of the modelled sample was high speed steel (HSS) and material of injection side was WC-% 9Co based. The material properties of the insert and injection side were entered to the program. The connection conditions between the insert and injection were determined and the mesh structure was established (Fig. 4). The number of elements and nodes was shown in Table III.

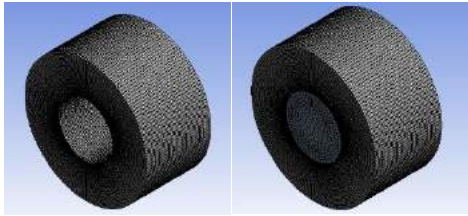


Fig. 4 The mesh structure of the modelled sample in the ANSYS software

Table III
THE NUMBER OF ELEMENTS AND NODES

Number of Elements	Number of Nodes
256,000	1,062,720

EE. Experimental

The IPIM process basically consists of three steps: feedstock injection into the mold, debinding and sintering. HSS inserts which have different diameter ratios were placed in the mold cavity before the injection process. Then WC-% 9Co based feedstock was injected onto the insert. As a result of the injection process, the circumference of the insert material was molded with WC-% 9Co-based feedstock.

The specimens were molded using the Arburg Allrounder 220S/250-60 injection molding machine. Fig. 5 shows the parts produced by the IPIM method which have different diameter ratios.



Fig. 5 Samples which have outer diameter of 20 mm and D_i/D_m ratio of 0.6, 0.7 and 0.8

The chemical debinding process was applied to the samples which were molded by the ITEK method. This process was carried out in ethanol environment, at 60 °C temperature for 48 hours. Sintering was carried out in the GSL-1500X sintering furnace at different temperatures in the mixed gas atmosphere (5% H_2 + 95% N_2).

VII. RESULTS

The thermal stresses at the connection surface were under temperature influence for the part that includes two different materials by IPIM. Thermal crack observation was done for the parts which have different D_i/D_m ratios. The outside diameters of the part were kept constant, and the diameters of the inserts were changed to 8, 9, 10, 12, 14 and 16 mm. D_i/D_m ratios were obtained 0.4, 0.45, 0.5, 0.6, 0.7 and 0.8, respectively. The results were obtained for part which completed injection and

debinding process using the temperature values of 100, 150, 200, 250, 300 °C. The stresses were analyzed for these temperatures by finite element analysis using the ANSYS software. The analyses were supported with mathematical model and experimental studies.

FF. Determination of Cracking Temperature

The cracking temperatures were determined after the chemical debinding process. Therefore, the samples having 0.6 D_i/D_m ratio were tested in 1340, 1300, 1250, 1200, 600, 300 and 250 °C. The obtained results are given in Fig. 6. According to the experiments at temperatures between 1300 and 1340 °C, in addition to cracking of the injection side, steel melted. Sintering was done at the temperatures of 1200 and 1250 °C and the injection side reached its actual density. However, cracking was continued. Sintering cannot be carried out at 600 and 300 °C. Feedstock remained at brown density and cracking continued.

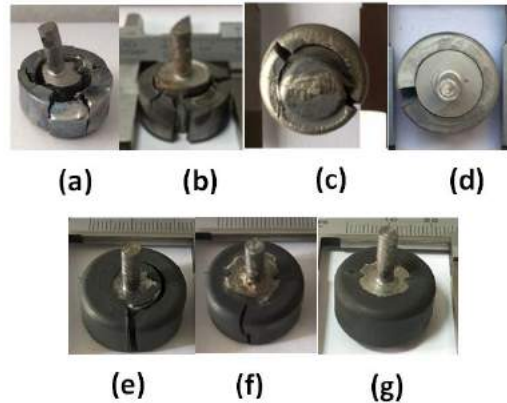


Fig. 6 Specimens at: a) 1340 b) 1300 c) 1250 d) 1200 e) 600 f) 300 g) 250 °C

As a result of the experiments which have different temperatures, cracking was prevented at 250°C. According to the result of the analysis, critical temperature was taken at 250 °C.

GG. Determination of Thermal Expansion Coefficients

The thermal expansion coefficient is necessary to calculate the values of the thermal stress. The thermal expansion coefficients of feedstock and steel must be determined. The thermal expansion coefficient of HSS was determined from the data of the company supplied steel. However, thermal expansion coefficient of the feedstock is not constant due to the feedstocks' binders. The thermal expansion coefficient of the material can be determined by dilatometer (size change) analysis [12, 13]. Therefore, dilatometer analysis was performed based on sintering parameters.

According to the result of the analysis, expansion occurred between 0-800 °C and then the size of the used sample shrunk when temperature was increasing. The expansion was carried out between 0-800 °C because polymer based binders did not

remove. After the debinding process, liquid phase sintering started and the sample size shrunk (Fig. 7).

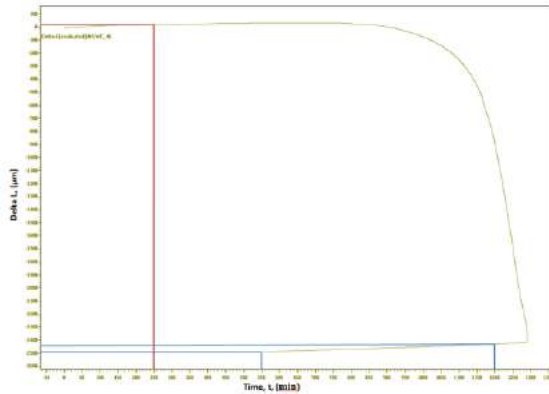


Fig. 7 Dimensional change according to the measured temperature in the dilatometer analysis of the produced samples from the WC-% 9Co feedstock

The thermal expansion coefficient of the feedstock was calculated from the graph obtained as a result of the dilatometer analysis (Fig. 7). The thermal expansion coefficient until 250 °C was determined and used for the analysis. The thermal expansion coefficient of the WC-% 9Co feedstock between 0-250 °C was calculated using (2). In this equation, the initial size of the sample was L, length changed along with temperature is ΔL and temperature difference was ΔT.

$$L \alpha \Delta T = \Delta L \implies \alpha = \frac{\Delta L}{\Delta T L} = \frac{0.018}{250 \times 14.1} = 5.1 \times 10^{-6} \frac{1}{^{\circ}\text{C}} \quad (2)$$

The coefficient was found as $5.1 \times 10^{-6} 1/ (^{\circ}\text{C})$.

HH. Determination of The Strength

Another required parameter for the analysis is the determination of the strength of the injection side. At this point, it was accepted that the value of strength was not change with temperature. The required strength value for the analysis was feedstock of strength at brown part (non-sintered) situation because the cracking occurs at 250 °C. As a result of the literature review, the strength value of the brown part feedstock could not be reached.

Tensile test was performed to clarify the strength of brown part WC-%9Co feedstock. However, the useful data cannot be obtained since the strength of brown part is low. Topuz at al. could not find the strength of brown part [14]. The fact that the material is ceramics based and has a brown part density was caused to fail.

Not having been found through experiments, the strength value was obtained as a result of theoretical calculations. According to Hook Law (3);

$$E = \frac{\sigma}{\epsilon} \implies \sigma = E \epsilon \quad (3)$$

Young's modulus (E) and strain (ε) values must be known for the determination of strength [15]. As a result of literature review, these values were found (Table IV).

TABLE IV
YOUNG'S MODULUS AND STRAIN VALUES OF FEEDSTOCK

Young's modulus (GPa)	70	[16]
Strain (mm/mm)	0.0008	[17]

There are studies on the determination of the Young's modulus of the WC-Co feedstock in the literature. However, they were carried out when the material had full density. Teppernegg at al. studied Young's modulus detection for WC-Co hard metal materials which have different Co percentages. Young's modulus was obtained 580 GPa for 8% Co and 560 GPa for 10.5% Co [18]. Since the cracking temperature was 250 °C in the current study, the injection side had not been sintered yet. Topuz at al. tested the mechanical properties of the parts produced by powder metallurgy before and after sintering process. Significant differences were observed between the strength values for before and after sintering process. This indicates that the Young's Modulus value (70 GPa) taken from the literature was acceptable.

If (4) was solved according to these data;

$$\sigma = E \epsilon = 70 \times 0.0008 = 56 \text{ MPa} \quad (4)$$

The rupture strength of the brown part feedstock was determined to 56 MPa. Stress-strain diagram of feedstock result, ceramic-based feedstock obtained from literature has been established (Fig. 8). Yield point is not observed since the feedstock used is ceramics based.

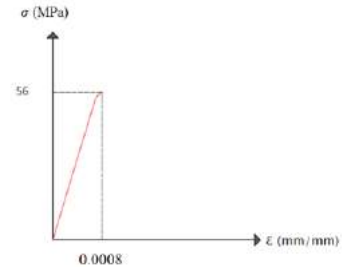


Fig. 8 Stress-strain curves found a result of the approaches

The material properties found as a result of the calculations were entered into ANSYS software (Table 5). The properties of the HSS were taken from the supplier's data.

TABLE V
PROPERTIES OF FEEDSTOCK AND INSERT

	α (10 ⁻⁶ /°C)	E (GPa)	σ (MPa)	Referances
HSS	11,7	217	750	[19]
WC-%9Co	5,1	70	56	[20]

II. Experimental and Theoretical Results

Thermal stresses on connection surface were found by the theoretical calculation before the experimental studies. Equation (1) gives the stress for a single material. The stress occurring in the connection surface due to the expansion of two different materials can be calculated if this model is adapted to Fig 3. Therefore, the force to be generated in the contact zone is denoted by P, then the strain of steel (insert),

$$\delta_s = -\frac{P L_s}{A_s E_s} + L_s \alpha_s (\Delta T) \implies \epsilon_s = -\frac{P}{A_s E_s} + \alpha_s (\Delta T) \quad (5)$$

The strain of injection side,

$$\delta_i = \frac{P L_i}{A_i E_i} + L_i \alpha_i (\Delta T) \implies \epsilon_i = \frac{P}{A_i E_i} + \alpha_i (\Delta T) \quad (6)$$

Expressing that the total deformation must be zero, then

$$\epsilon_s = \epsilon_i \quad (7)$$

$$-\frac{P}{A_s E_s} + \alpha_s (\Delta T) = \frac{P}{A_i E_i} + \alpha_i (\Delta T)$$

$$\left(\frac{1}{A_s E_s} + \frac{1}{A_i E_i}\right) P = (\alpha_s - \alpha_i) (\Delta T) \quad (8)$$

Here, A_s and A_i value can be expressed with respect to diameter ratio by:

$$A_s = \frac{\pi}{4} d_d^2 \quad (9)$$

$$A_i = \frac{\pi}{4} (d_d^2 - d_i^2) \quad (10)$$

The P force generated in connection surface can determine using Equation 8. The stresses generated by P force in the insert side and injection side can be calculated as follows:

$$\sigma_s = \frac{P}{A_s}, \quad \sigma_i = \frac{P}{A_i} \quad (11)$$

δ_s = Deformation or displacement of steel (insert) due to the temperature change (mm)

δ_i = Deformation or displacement of injection side due to the temperature change (mm)

L_s = Length or diameter of steel (mm)

L_i = Length or diameter of insert (mm)

A_s = Area of insert (mm²)

A_i = Area of injection side (mm²)

E_s = Young modulus of steel (GPa)

E_i = Young modulus of WC-%9Co (GPa)

ϵ_s = Strain of insert

ϵ_i = Strain of injection side

α_s = Thermal expansion of steel (1/°C)

α_i = Thermal expansion of WC-%9Co (1/°C)

P = Force applied to injection side and insert (N)

d_d = Outer diameter (mm)

d_i = Inner diameter (mm)

σ_s = Stress in steel (MPa)

σ_i = Stress in injection side (MPa)

Stress values in injection side obtained using (11) are shown in Table 6. The maximum stress was obtained at the maximum value of D_i/D_m ratio. As the thickness of the injection side increased, the stress was reduced.

TABLE VI
STRESS IN INJECTION SIDE FOR DIFFERENT THE D_i/D_m RATIOS

D_i/D_m (%)	40	45	50
Stress (MPa)	40,60631	48,26285	55,78698
D_i/D_m (%)	60	70	80
Stress (MPa)	70,00316	82,71224	93,76031

Considering that the strength of injection side was 56 MPa, crack formation was expected when the D_i/D_m ratio was greater than the 0.5. However, the mathematical calculation was not enough to accurate interpretation. It was necessary to confirm with experimental studies.

In addition to the mathematical calculations finite element analysis was performed using ANSYS software. The material properties of HSS and WC-%9Co feedstock was inputted into ANSYS. In the next step, the mesh structure was generated (Fig. 4). For thermal analysis, 15 °C and 250 °C were inputted into ANSYS as an initial temperature and final temperature, respectively.

The experimental studies were carried out 1200 °C to see whether the sintered part was cracking or not. The results of the analysis and experimental studies are compared below:

1) $D_i/D_m = 0.8$: The sample having a steel diameter of 9.6 mm and an molding diameter of 12 mm was designed in ANSYS software and then analysis was carried out in condition specified earlier. Accordingly, the maximum stress occurred at connection (Fig. 9). According to ANSYS result, the maximum

stress was 93.976 MPa and it occurred at connection surface as previous study [21].

As a result of the mathematical calculations, this value was obtained as 93.76031 MPa. When the theoretical results were compared with the strength of injection side which is 56 MPa, the sample with a ratio of 0.8 D_i/D_m was predicted to crack. The experimental studies support these results. ANSYS result and sintered part having 0.8 D_i/D_m ratio are shown in Fig. 9. The cracks were formed during the debinding stage because the stress in injection side was higher than the strength of brown part feedstock. The broken pieces were sintered due to elevated temperature. However, since the desired joining cannot be achieved a ratio of 0.8 D_i/D_m was not suitable for this material pair.

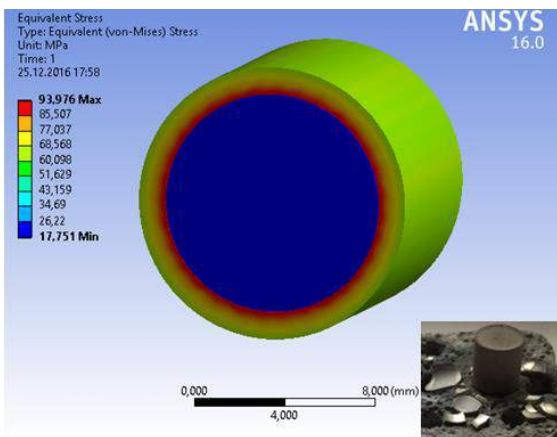


Fig. 9 ANSYS resultant stresses and sintering test result for $D_i/D_m = 0.8$

2) $D_i/D_m = 0.7$: Fig. 10 shows the experimental and ANSYS results for the sample having a steel diameter of 14 mm. According to the mathematical calculation, the maximum stress at the connection surface was 82.71224 MPa and the ANSYS result is 83.6 MPa. When the theoretical results are compared with the brown part strength of feedstock (56 MPa) the sample with a 0.7 D_i/D_m ratio can be predicted to crack. Fig. 10 shows the cracked part, similar to the case with a 0.8 D_i/D_m ratio. However, the stress occurred at connection surface is lower. Although the stress is lower, as stress in injection side is higher than the strength of brown part feedstock, the crack formation continued. The theoretical results were supported by experimental studies. The part which has 0.7 D_i/D_m ratio is not suitable for this material pair since the desired joining cannot be achieved.

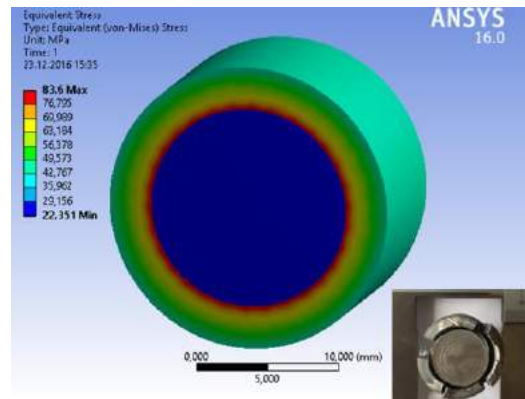


Fig. 10 ANSYS resultant stresses and sintering test result for $D_i/D_m = 0.7$

3) $D_i/D_m = 0.6$: Fig. 11 shows the experimental and ANSYS results for the sample having a steel diameter of 12 mm. According to the mathematical calculation, the maximum stress at the connection surface is 70.00316 MPa while the ANSYS result is 69.412 MPa. The difference between mathematical calculation and analysis results may be due to the mesh structure. However, the difference is negligible.

The sample with a ratio of 0.6 D_i/D_m can be predicted to crack when theoretical results and the brown part strength are compared. It can be seen in Fig. 11 that crack formation continues, and when compared with higher D_i/D_m results, it has lower stress value at the connection surface. However, since it was still higher than the strength of brown part WC-%9Co feedstock, a crack was formed in injection side. Accordingly, the ratio of 0.6 D_i/D_m is not suitable for this material pair. Additionally, the injection side was partially preserved its integrity. This was a physical sign that there was stress reduction at the connection surface.

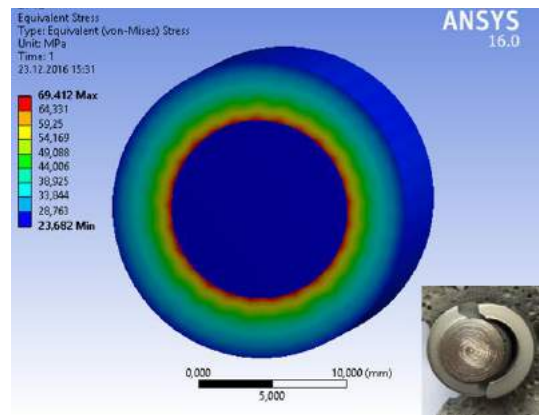


Fig. 11 ANSYS resultant stresses and sintering test result for $D_i/D_m = 0.6$

4) $D_i/D_m = 0.5$: Fig. 12 shows the experimental and ANSYS results for the sample having a steel diameter of 10 mm. The resulting stresses found in the mathematical calculations and ANSYS result were 55.78698 and 55.651 MPa, respectively. These values are close to brown part feedstock strength. Although the theoretical calculations result is lower than the brown part feedstock strength, since values are close to each

other, it may not be correct to make a clear interpretation that the injection part will not crack.

Two different results emerged at the end of the sintering experiment. Some of the samples with the same ratio of D_i/D_m were cracked, while some of them did not crack (Fig. 12). Accordingly, it can be stated that the critical D_i/D_m ratio is 0.5 for this material pair. As the smaller D_i/D_m ratios will have the lower stress, the probability of cracking will be lower.

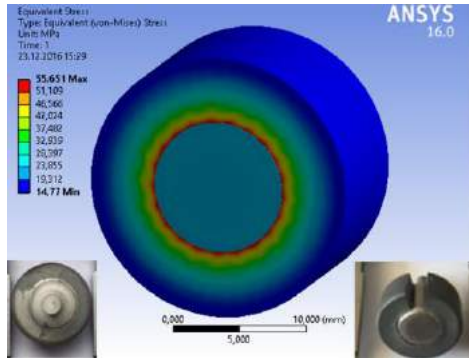


Fig. 12 ANSYS resultant stresses and sintering test results for $D_i/D_m = 0.5$

5) $D_i/D_m = 0.45$: The experimental and ANSYS results for the sample having a steel diameter of 9 mm is shown in Fig. 13. The maximum stress occurring at connection surface is 48.2628 MPa according to mathematical calculation and it was obtained as 48.797 MPa at the end of ANSYS analysis. These values are lower than the brown part strength of feedstock, 56 MPa. Therefore, crack formation in injection side was not expected during sintering. After the sintering experiment, it was clear that the experimental studies supported the theoretical results and cracking was not observed as shown in Fig. 13. The sample preserved its appearance after the injection. These results agree with the theoretical result and the sample having D_i/D_m ratio was produced without cracking.

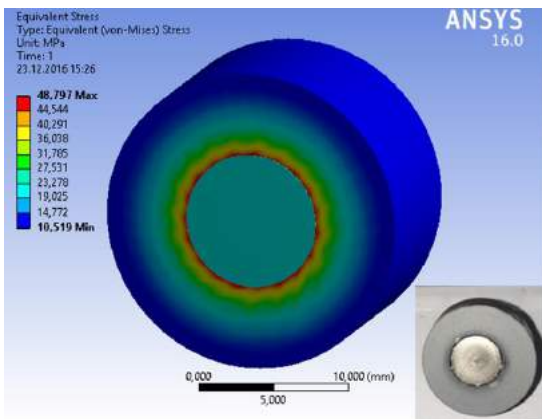


Fig. 13 ANSYS resultant stresses and sintering test result for $D_i/D_m = 0.45$

6) $D_i/D_m = 0.4$: Fig. 14 shows the experimental and ANSYS results for the sample having a steel diameter of 8 mm. The

mathematical calculation and ANSYS analysis result are 40.60631 MPa and 40.67 MPa, respectively. These values are lower than the strength of brown part feedstock and it is expected that the cracking of injection side will not observe. The result of sintering experiment is shown in Fig. 14. It can be seen that there is no crack formation.

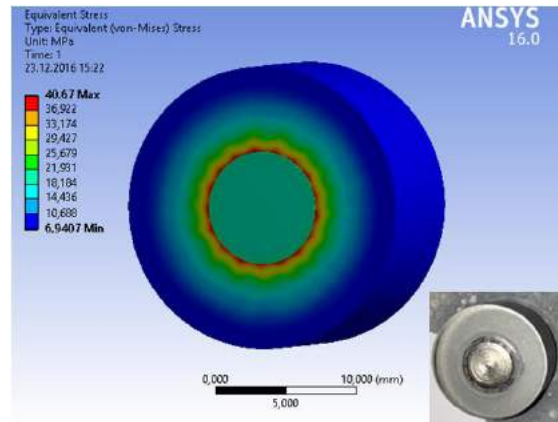


Fig. 14 ANSYS resultant stresses and sintering test result for $D_i/D_m = 0.4$

Although cracking was not observed, the stress occurring at the connection surface was lower than the higher D_i/D_m ratio. The stress at the connection surface influences the force needed to join the materials.

It is aimed to generate the diffusion bonding between steel, HSS, and feedstock, WC-%9Co in these experiments. There are three parameters affecting the diffusion bonding. These are temperature, pressure and holding time [22]. Since the temperature and time are constant, the variable parameter is pressure. A higher pressure provides a stronger connection. Accordingly, while the D_i/D_m ratio is determining the pressure should be high as possible to get a better connection. The maximum stress was obtained in the case of 0.8 D_i/D_m ratio. However, there was a crack at injection side. Although the maximum stress was obtained in the case of 0.5 D_i/D_m ratio, without cracking at injection side, there was a cracking possibility. Besides, the maximum stress at connection surface for the sample having 0.4 D_i/D_m ratio lower than the sample having 0.45 D_i/D_m ratio. Correspondingly, the optimum D_i/D_m ratio was determined as 0.45.

The mathematical calculation results, ANSYS results and brown part strength of WC-%9Co feedstock are compared in Fig. 15. The stress at connection surface increased with increasing D_i/D_m ratio. The mathematical results and ANSYS results are close to each other. 0.5 D_i/D_m ratio is the critical ratio for WC-%9Co feedstock and HSS pairs. If the D_i/D_m ratio exceeds 0.5 it may predict that the injection side will crack since the stress occurring at the connection surface was higher than the strength of brown part feedstock.

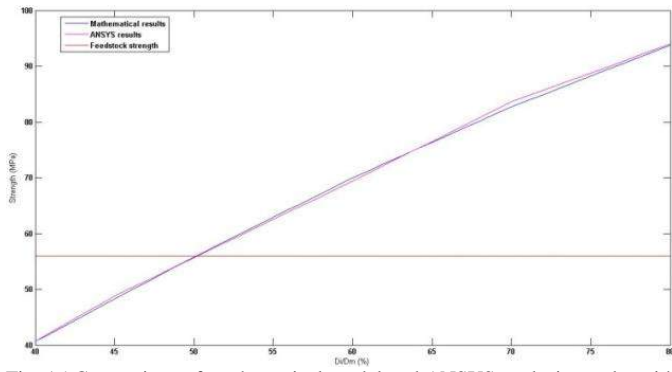


Fig. 15 Comparison of mathematical model and ANSYS analysis results with material strength

VIII. CONCLUSIONS

Expansions of different materials at different ratios develop thermal stress at connection surface. The study provides a new solution for joining the two different materials by inserted powder injection molding (IPIM). In this study, the optimum insert diameter/mold diameter (D_i/D_m) ratio was identified using WC-%9Co feedstock and HSS by IPIM. The study presented the practical solution for the probable cracking problem occurring at injection side in sintering process. The optimum D_i/D_m ratio can be obtained without performing any experimental studies. According to different materials and geometries the optimum D_i/D_m ratio can determine theoretically, and then the part can be produced without cracking. Thus, the production time will save and production cost will be reduced in IPIM method.

The stresses at connection surface were analyzed with mathematical model and finite element analysis (by ANSYS software) then, the results were compared with experimental studies. Accordingly, the results were listed below:

- The ANSYS and the mathematical model results were close to each other and these results were tested with experimental studies.
- The connection surface stress increases with increasing the D_i/D_m ratio. The maximum stress, 93.76031 MPa, was obtained for the sample having 0.8 D_i/D_m ratio and the minimum stress, 40.60631 MPa, was obtained when the D_i/D_m ratio was 0.4.

- 0.5 is the critical D_i/D_m ratio, and for the D_i/D_m ratio of 0.4 and 0.45 the cracking was not observed.
- In diffusion bonding mechanisms as the pressure at the connection surface increases, the bonding strength increases. The samples having 0.45 D_i/D_m ratio have the maximum connection surface strength among the non-cracking parts. Consequently, D_i/D_m ratio of 0.45 is the optimum ratio for the WC-%9Co feedstock and HSS pair.

Acknowledgment

The authors would like to thank Scientific and Technological Research Council of Turkey and Gazi University Research Funds for their support for this project under contract 115M437 and 07/2016-21, respectively.

References

- [1] R. M. German, Powder injection molding. Cambridge Univ Press, 1990.
- [2] W. Liu, X. Yang, Z. Xie, C. Jia, and L. Wang, "Novel fabrication of injection-moulded ceramic parts with large section via partially water-debinding method," *Journal of the European Ceramic Society*, vol. 32, no. 10, pp. 2187-2191, 2012.
- [3] D. F. Heaney, Handbook of metal injection molding. Elsevier, 2012.
- [4] A. Safarian, M. Subaşı, and Ç. Karataş, "Reducing debinding time in thick components fabricated by powder injection molding: Paper presented at "7th International Powder Metallurgy Conference and Exhibition"(TPM-7), 24–28 June 2014, Gazi University, Ankara, Turkey," *International Journal of Materials Research*, vol. 106, no. 5, pp. 527-531, 2015.
- [5] M. Schaub, J. Schwiegerling, E. Fest, R. H. Shepard, and A. Symmons, *Molded Optics: Design and Manufacture*. CRC press, 2016.
- [6] S. Choi, H. Cho, and S. Kumai, "Influence of precipitation on the coefficient of thermal expansion of Al-Si-Mg-Cu-(Ti) alloys," *Journal of Alloys and Compounds*, vol. 655, pp. 6-10, 2016.
- [7] M. Briffaut, F. Benboudjema, J. M. Torrenti, and G. Nahas, "A thermal active restrained shrinkage ring test to study the early age concrete behaviour of massive structures," *Cement and Concrete Research*, vol. 41, no. 1, pp. 56-63, 2011.
- [8] M. Briffaut, F. Benboudjema, J. M. Torrenti, and G. Nahas, "Numerical analysis of the thermal active restrained shrinkage ring test to study the early age

- behavior of massive concrete structures," *Engineering Structures*, vol. 33, no. 4, pp. 1390-1401, 2011.
- [9] W. Dong, X. Zhou, Z. Wu, and G. Kastiukas, "Effects of specimen size on assessment of shrinkage cracking of concrete via elliptical rings: Thin vs. thick," *Computers & Structures*, vol. 174, pp. 66-78, 2016.
- [10] Ç. Ersan, "Fonksiyonel derecelendirilmiş disklerde termal gerilme analizi," Pamukkale Üniversitesi Fen Bilimleri Enstitüsü, 2008.
- [11] F. P. Beer, R. Johnston, J. Dewolf, and D. Mazurek, "Mechanics of Materials, McGraw-Hill," New York, pp. 150-233, 1981.
- [12] T. Barron, J. Collins, and G. White, "Thermal expansion of solids at low temperatures," *Advances in Physics*, vol. 29, no. 4, pp. 609-730, 1980.
- [13] A. Safarian, M. Subaşı, and Ç. Karataş, "The effect of sintering parameters on diffusion bonding of 316L stainless steel in inserted metal injection molding," *The International Journal of Advanced Manufacturing Technology*, pp. 1-9, 2016.
- [14] A. Topuz, H. Mollaoğlu, and Ş. Baykal, "Sinterlenmiş ve sinterlenmemiş toz metalurjik parçaların ultrasonik yöntemiyle karakterizasyonu," 3rd International Non-Destructive Testing Symposium and Exhibition, 2008.
- [15] T. Teppernegg et al., "High temperature mechanical properties of WC-Co hard metals," *International Journal of Refractory Metals and Hard Materials*, vol. 56, pp. 139-144, 2016.
- [16] S. Kalpakjian, *Manufacturing engineering and technology*. Pearson Education India, 2001.
- [17] M. Properties. Available: http://www-materials.eng.cam.ac.uk/mpsite/interactive_charts/str ength-ductility/basic.html
- [18] N. Novikov, V. Bondarenko, and V. Golovchan, "High-temperature mechanical properties of WC-Co hard metals (Review)," *Journal of Superhard Materials*, vol. 29, no. 5, pp. 261-280, 2007.
- [19] O. B. S. Catalog. Available: <http://www.osmanli-bohler.com/upload/pdf/S600DE.pdf>
- [20] S. Kalpakjian and S. Schmid, "Manufacturing Processes for Engineering Materials-5th Edition," agenda, vol. 12, p. 1, 2014.
- [21] F. Sen, Y. Pekbey, and O. Saymana, "Elastic-plastic stress analysis of a thermoplastic composite disc under parabolic temperature distribution," 2007.
- [22] N. F. Kazakov, *Diffusion bonding of materials*. Elsevier, 2013.

Nano-sized Iron Oxide Production and Characterization by Arc Discharge Method

Safa POLAT[#], Tugay ÜSTÜN⁺, Ahmet AVCI⁺

[#]Department of Mechanical Engineering, Faculty of Engineering, Karabuk University, TR-78050, Karabuk, Turkey
safapolat@karabuk.edu.tr

⁺Department of Mechanical Engineering, Faculty of Engineering, Selcuk University, TR-42100, Konya, Turkey
tugayu@hotmail.com, aavci@karabuk.edu.tr

ABSTRACT

Iron oxide nanoparticles have been reported to be widely used in many biological applications such as magnetic resonance imaging, anticancer agents, contrast enhancement, tissue repair, and detoxification of biological fluids. The nanoscale size of the iron oxide particles synthesized for use in such applications gives them super magnetic properties. Arc discharge method is one of the simplest methods to be used in nanoparticle production in terms of both feasibility and efficient results. Therefore, arc discharge method has been used in the synthesis of iron oxide nanoparticles for use in such applications. In this method, which simply consists of an anode, cathode and a power source, tungsten electrodes were used to obtain iron oxide nanoparticles. The cathode was drilled and filled with iron powder. The synthesis was carried out in deionize water under 50A DC current and 30V. The synthesized powders were characterized by fourier transform infrared spectroscopy (FTIR), transmission electron microscope (TEM), scanning electron microscope (SEM) electron dispersive X-ray analysis (EDX).

Keywords: Arc-discharge, iron oxide, nanoparticle

Enhanced Synthesis and Functionalization of Boron Nitride Nanoplates

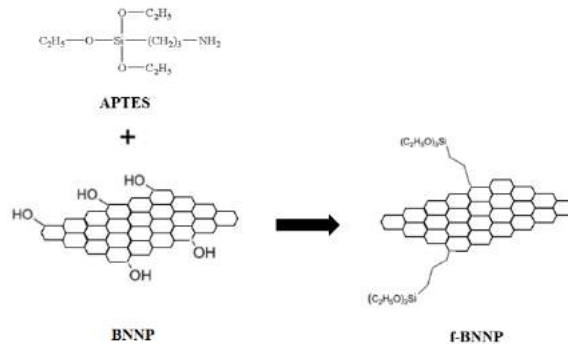
Tugay ÜSTÜN⁺, Safa POLAT[#], Ahmet AVCI⁺

[#]Department of Mechanical Engineering, Faculty of Engineering, Karabuk University, TR-78050, Karabuk, Turkey
safapolat@karabuk.edu.tr

⁺Department of Mechanical Engineering, Faculty of Engineering, Selcuk University, TR-42100, Konya, Turkey
tugayu@hotmail.com, aavci@karabuk.edu.tr

ABSTRACT

Boron nitride (BN) utilizes a wide range of industrial applications (e.g. ceramic composites, lubricants, surface coatings, etc.) because of its low density, high thermal conductivity and superb oxidation resistance [1-4]. For this reason, BN nanoplates were synthesized by arc discharge method. Tungsten electrodes were used as both anode and cathode. The cathode were drilled and filled with boron nitride powder. The synthesis was done under liquid nitrogen environment under 50A DC current and 30V. The synthesized boron nitride nanoparticles with nanoplate morphology have a diameter ~250 nm with thickness ~50 nm. After BNNP had been synthesized, it was functionalized. Firstly, BNNP which were fabricated by arc discharge oxidized with H₂SO₄ solution. Subsequently, oxidized BNNP added (3-Aminopropyl) triethoxysilane (APTES) solution and dried at 100 °C for 2 h. As a result, functional BNNP was characterized by FT-IR and SEM.



Scheme1. Schematic of the reaction between BNNP and APTES.

Keywords: Arc discharge Boron nitride nanoparticle

Modeling of Three-Dimensional Fracture Problems Using FCPAS

M.F. Yaren, A.O. Ayhan*

Sakarya University

Department of Mechanical Engineering, Sakarya University, 54187, Sakarya, Turkey

myaren@sakarya.edu.tr

*ayhan@sakarya.edu.tr

Abstract— In this study, three dimensional crack propagation analyses are performed for a low carbon alloyed steel 16MnR, which has very common usage in the industry especially in pressurized structures. Fatigue crack initiation and crack growth are among widely seen damages in pressure vessels. To avoid damage caused by these types of defects, fracture mechanics analysis is the most common approach. A specified method, enriched finite element method, is used for fracture analysis. The steps of crack growth analysis by using Fracture and Crack Propagation Analysis System (FCPAS) are explained. Material properties are obtained from literature and results are compared with references. The obtained results are in agreement with the literature.

Keywords— Fracture, crack growth, 16MnR, FCPAS.

I. INTRODUCTION

Cracks can be seen on many engineering structures and catastrophic failures can occur as a consequence of a crack growth. Many components like axles, gears, blades and pressure vessels work under cyclic loading which may cause fatigue crack growth.

Fracture analysis programs are used for the assessment of the present condition and for the estimation of crack propagation life. Numerous studies have been conducted over the last two decades to develop three-dimensional crack propagation simulations using numerical techniques and tools for fracture analysis. FRANC3D [1], ZENCRACK [2], ADAPCRACK3D [3], BEASY™ [4] are some of the software that can perform three-dimensional fracture and crack propagation analyses. FRANC3D software uses the boundary element method and the others use the finite element method. The enriched finite element method has also been an attractive method for performing three-dimensional fracture analysis, since it doesn't require any special mesh near the crack. FCPAS [5] is a software which employs enriched finite element formulation. Three-dimensional fracture mechanics problems such as interfacial cracks [7], mixed mode fracture [8], functionally graded materials [9], and multiple cracks [10] have been solved correctly using FCPAS.

The 16MnR low carbon alloy steel is generally used as pressure vessel materials. In the literature there are studies on crack propagation in 16MnR materials [11, 12, 13, 14]. Constant amplitude and overload effect are investigated, a

modified Wheeler model is proposed to estimate crack growth life. According to chemical and mechanical test results by Gao, 16MnR steel is similar to ASME SA302B, St52-3 in Germany and JIS SM490A [11]. Crack growth in 16MnR is investigated by Xiaogui Wang [15]. To determine the effects of stress ratio on the fatigue crack growth, several tests were carried out for different stress ratios and results were compared with the numerical study.

In the current paper, modeling procedures of FCPAS are explained and a crack growth application in a steel structure is performed. Specifically, surface crack on the 16MnR is analyzed and crack fronts are predicted and compared with Ref. [13]. This allows another application and validation of FCPAS for steel structures.

II. MATERIALS AND METHOD

In this section, details of fracture analysis procedure in FCPAS are explained. First, finite element models, boundary conditions and loads are described. In the second section, details of validation model which is obtained from literature are presented.

JJ. Fracture Analysis with FCPAS

The finite element model is created using ANSYS™ [16]. The lists containing the finite element model information are taken from ANSYS and fracture analyses are performed using FCPAS. The enriched finite element technique, which contains crack tip singularity in element formulation, is used in FCPAS. Enriched elements are used around the crack tip and stress intensity factors (SIF) are calculated automatically during solution phase. There are another type of elements, called transition elements, which are located between enriched elements and regular finite elements. Further information about enriched elements can be found in Ref [5, 6].

In Fig. 1, fracture and crack growth analysis procedure is given. Modeling and meshing are done in ANSYS. Then, boundary conditions are applied on nodes and/or element surfaces. Nodes and elements on the crack front are selected and saved as a list. Then, boundary conditions lists; (displacement, force, pressure etc.) and all elements and nodes lists are saved. Using these lists, GEO file is created by a sub preprocessing program in FCPAS. GEO file contains all

information, including loads and boundary conditions and crack definition, about the finite element model. SIFs along the crack front are calculated by FCPAS according to crack definition included in GEO file.

SIFs are compared with the values of threshold and fracture toughness. If SIFs exceed the threshold value, crack grows and when the fracture toughness is reached, fracture occurs.

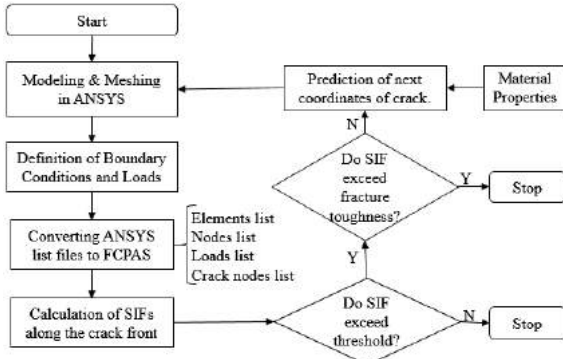


Fig. 1 Process map for FCPAS

Crack propagation analysis is done incrementally by FCPAS. Accurate calculation of SIFs is important to predict the next crack front. As is known from the Paris-Erdogan equation [17], besides SIFs, material properties are also influential for crack propagation. Paris-Erdogan equation is given below as Eqn. 1.

$$\frac{da}{dN} = C(\Delta K)^n \quad 1$$

KK. Details of Validation Model

A model from the literature has been used to confirm the procedure discussed in the previous section. Tu ST has done a crack growth experiment on 16MnR [13]. In 2016, his results are evaluated by Wen J.F. and crack fronts are obtained using ZENCRACK [2].

A surface crack growth on a plate is investigated by Tu ST. The width, length and thickness dimensions of the plate are respectively 89.5x350x7 mm. The crack is in the middle of the plate. So there are two symmetry planes. Initial crack depth a_0 is 3,19 mm and its length $2c_0$ is 6,94 mm. Cyclic loading between 140 kN and 0 kN was applied for crack propagation. Detailed dimensions of the plate can be seen in Fig. 2.

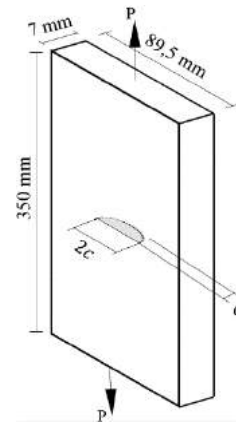


Fig. 2 Schematic view of surface crack model

Elastic modulus and constants for Paris-Erdogan Equation are given in Table 1 for 16MnR low carbon alloyed steel [13].

TABLE XXXII
MATERIAL PROPERTIES FOR 16MNR [13]

Elastic Modulus	Paris-Erdogan Constant, C	Paris-Erdogan Constant, n
209 GPa	$7,3 \times 10^{-15}$	3,42

Finite element model is created and meshed in ANSYS. A view of crack front is given in Fig. 4. Element size on crack front is set as one percent of crack depth, a. Details of mesh view can be seen from Fig. 3 and 4.

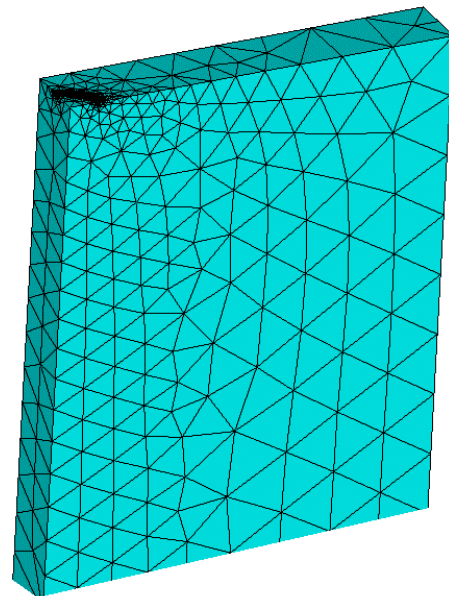


Fig. 3 Finite element fracture model

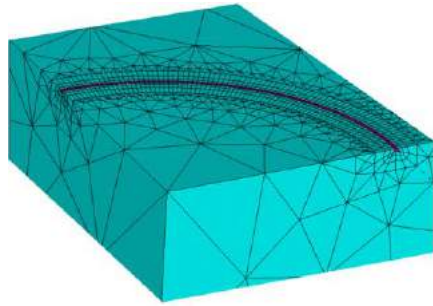


Fig. 4 Close-up view of crack region

As can be seen from Fig. 2, the plate has two symmetry planes, so a quasi-model is used. Thus, a smaller finite element model is created.

III. RESULTS

In this section, results from the analyses are presented. Crack fronts are given and compared with results in the literature [13, 18].

LL. Fracture Analysis Results

In Fig. 5, crack fronts are presented. An experimental view is taken from Ref. [13]. Tu St. applied overload to mark crack fronts in experiment. After the test, specimen is heated to obtain more visible marks. In Ref. [18], fracture analyses are done and crack fronts are predicted. The black continuous line in Fig.5, shows the crack fronts in the Ref. [18]. The red dashed lines are the crack fronts obtained as a result of FCPAS analyses.

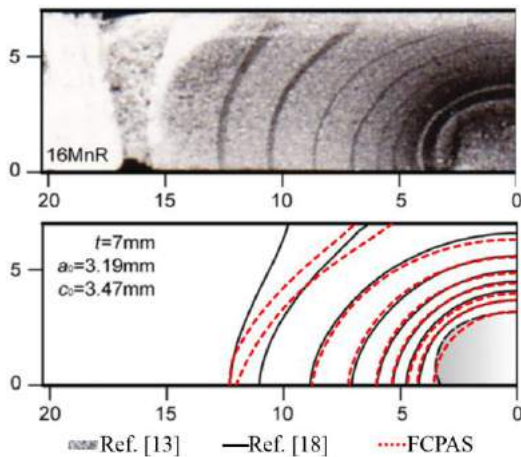


Fig. 5 Comparisons of crack fronts

Using the same data in Fig. 5, variation of the crack aspect ratio of the crack depth along the plate thickness is shown in Fig. 6. This comparison also shows good agreement between FCPAS results and those from the literature in terms of experiment and numerical analyses.

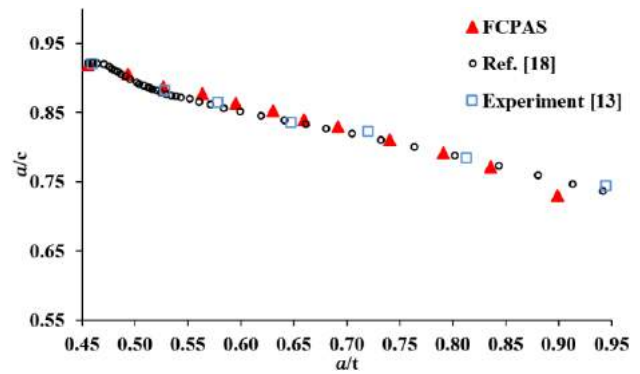


Fig. 6 Variation of aspect ratio with crack depth

It can be seen in Fig. 5-6, crack fronts are very close to the marks taken from the experiment. Predictions are the equal with experimental study until the crack depth reaches the plate thickness. Due to modeling the difficulties, it is not preferred to model the crack front on the corner point.

IV. CONCLUSIONS

In this study, fracture analysis process in FCPAS is explained and applied to a steel structure. A model obtained from the literature is considered and obtained results are compared in terms of crack profiles and aspect ratios. Comparisons showed very good agreement.

V. ACKNOWLEDGEMENT

The financial support by The Scientific and Technological Research Council of Turkey (TUBITAK) under Project Number: 113M407 for this study is gratefully acknowledged.

VI. REFERENCES

- [1] Carter BJ, Wawrzynek PA, Ingraffea AR. Automated 3-D crack growth simulation. *Int. J. Numer. Methods Eng.* 2000; 47:229-53.
- [2] ZENCRACK, Zentech Int. "Tool for 3D fracture mechanics simulation." (2012).
- [3] Schöllmann, M., M. Fulland, and H. A. Richard. "Development of a new software for adaptive crack growth simulations in 3D structures." *Engineering Fracture Mechanics* 70.2 (2003): 249-268.
- [4] BEASY™. Fatigue and crack growth software. <http://www.beasy.com>.
- [5] Ayhan, Ali O. "Simulation of three-dimensional fatigue crack propagation using enriched finite elements." *Computers & Structures* 89.9 (2011): 801-812.
- [6] Ayhan, A. O., and H. F. Nied. "Stress intensity factors for three-dimensional surface cracks using enriched finite elements." *International Journal for Numerical Methods in Engineering* 54.6 (2002): 899-921.
- [7] Ayhan, Ali O., and Herman F. Nied. "Finite element analysis of interface cracking in semiconductor packages." *IEEE Transactions on Components and Packaging Technologies* 22.4 (1999): 503-511.
- [8] Ayhan, Ali O. "Mixed mode stress intensity factors for deflected and inclined corner cracks in finite-thickness plates." *International Journal of Fatigue* 29.2 (2007): 305-317.
- [9] Ayhan, Ali O. "Stress intensity factors for three-dimensional cracks in functionally graded materials using enriched finite elements." *International Journal of Solids and Structures* 44.25 (2007): 8579-8599.
- [10] Dündar, H., and A. O. Ayhan. "Multiple and non-planar crack propagation analyses in thin structures using FCPAS." *Frattura ed Integrità Strutturale* 35 (2016): 360.
- [11] Jiang, Yanyao, et al. "Multiaxial Fatigue of 16MnR Steel." *ASME 2006 Pressure Vessels and Piping/ICPVT-11 Conference*. American Society of Mechanical Engineers, 2006.

- [12] Wang, Xiaogui, et al. "An experimental study of the crack growth behavior of 16MnR pressure vessel steel." *Journal of Pressure Vessel Technology* 131.2 (2009): 021402.
- [13] Tu ST (1988) A Study of Effect of Irregular Crack Like Defects on the Engineering Structural Integrity [Ph.D Thesis]. Nanjing Institute of Chemical Technology, Nanjing, China..
- [14] Shen, Shi-Ming, and Zhi-Li Feng. "Fatigue growth behaviour for a corner crack at a vessel/nozzle junction." *International journal of pressure vessels and piping* 68.3 (1996): 319-324.
- [15] Wang, Xiaogui, et al. "Fatigue crack initiation and growth of 16MnR steel with stress ratio effects." *International Journal of Fatigue* 35.1 (2012): 10-15.
- [16] ANSYS. Version 12.0. Ansys Inc., Canonsburg, PA, USA; 2009.
- [17] Paris, Paul C., Mario P. Gomez, and William E. Anderson. "A rational analytic theory of fatigue." *The trend in engineering* 13.1 (1961): 9-14.
- [18] Wen, Jian-Feng, et al. "A combination rule for multiple surface cracks based on fatigue crack growth life." (2016).

Investigation of Strain Hardening in AISI 430 Ferritic Stainless

Gökhan Arıcı*, Mustafa Acarer⁺, Mesut Uyaner*

* Selcuk University, Metallurgy-Materials Engineering Department, Konya-TURKEY arici@selcuk.edu.tr, muyaner@selcuk.edu.tr

+ Selcuk University, Metallurgy-Materials Engineering Department, Konya-TURKEY macarer@selcuk.edu.tr

ABSTRACT

AISI 430 ferritic stainless steel have almost same mechanical and microstructural properties and corrosion resistance as austenitic stainless steels. In addition, these steels are as cheap as austenitic stainless steel. On the other hand, they lose their strength and toughness at high temperatures. Nowadays, demand to those steels has been increasing due to their convenient properties. AISI 430 ferritic steels are widely used in construction sector, automotive industry and food industry.

The aim of usage of strain aging is driving a strengthening mechanism to increase mechanical properties of AISI 430 stainless steels. This mechanism is based on the principle of increasing dislocations are locked by themselves or carbon and nitrogen atoms after cold deformation. After strain aging, tensile strength and yield strength increase but ductility decreases. Strength and elongation of samples change by altering heat treatment temperature and amount of deformation. The influence of quantity of pre-strain and aging temperature to yield strength, tensile strength and tensile elongation, on AISI 430 stainless steels samples was studied. Identical samples first are pre-strained in tension to a uniform elongation of 5%, 10% and 15% and then aged at 150 °C, 200 °C and 250 °C for 15 minutes, separately. After pre-strained aging process the mechanical properties of final products are compared with untreated AISI 430 steel. It was observed that yield and tensile strength of samples increased with increasing quantity of pre-strain for the same aging temperatures. Also, all heat-treated samples have higher strength than untreated samples. For %5 pre-strained conditions, yield and tensile strength slightly decreased and after then increased by increasing temperature from 150 °C to 200 °C and from 200 °C to 250 °C, respectively. Breaking strength increased by increasing aging temperature for %5 pre-strained. For %10 pre-strained condition, specimens have maximum tensile, yield and breaking strength values for aged temperature of 200 °C. For %15 pre-strained conditions, yield, tensile and breaking strength values are highest at 200 °C. Breaking elongation of samples decreased by increasing pre-strain rates for all temperatures. Breaking elongation of samples is minimum for %10 pre-strain rate at constant aging temperatures.

Keywords: AISI 430, Strain hardening, Aging, Strength.

Estimation of Strength Properties in Concrete Steel Bars by Multiple Regression Method

Fuat ŞİMŞİR*, Hande VURŞAN⁺

*Karabuk University, Balıklarkayası Region, 78050
Karabuk, Turkey
fuatsimsir@karabuk.edu.tr

⁺Kardemir Karabuk Iron Steel Industry Trade and Company INC., Production Planning Department
Karabuk, Turkey
hvursan@kardemir.com

Abstract— Concrete steel bars used in the construction sector are produced according to Turkish Standard, “TS 708 Steel for The Reinforcement of Concrete- Reinforcing Steel”. Suppliers, produce concrete steels using the Tempcore system that provide the desired properties by developing processes for high safety and low cost. The tempcore system is a process of giving a certain amount of water to the surface of the concrete steel bar coming from the finish rolling mill. In our study, our purpose is estimating the mechanical physics properties of the concrete steel bar produced by the tempcore system which is most common method with multiple linear regression. Generating to elements of chemical composition which are carbon, manganese and silica, also parameters (water discharge, size etc.) affecting the strength in the rolling process were determined as “independent variables”. “The Yield Strength” and “Tensile Strength” as a dependent variable is estimated by the Multiple Linear Regression Method.

As a result of the study, it is aimed to reduce the amount of scrap product that is erroneous and/or to be released to the waste by preventing the production faults by predicting which yield values of the input variables such as water flow will yielded in the chemical composition.

Keywords— Concrete steel bar, strenght prooprties, multiple regression

I. INTRODUCTION

It has to be used as a quality concrete and reinforced concrete equipment that can survive for a year, produced with certain standards.

Concrete steel bars; Are flat, ribbed or profiled steel rods with circular cross section and used as concrete accessories in reinforced concrete structures. Straight-surface steel bars are also flat with no adherence enhancing ribs or profiles. On the other hand, ribbed and profiled steel rods have transverse, longitudinal or inclined recesses and protrusions, which increase the surface clamping on the surface [1].

The physical and mechanical properties of the steel and the chemical composition must be within the standard ranges.

The most common method used in the production of high strength reinforced concrete steels is the Tempcore method. The most important property of this process is to increase the ductility, ductility and weldability of hot-rolled concrete steel

bars without lowering the C and Mn ratios and without the addition of alloy elements. Briefly, the Tempcore process, hot rolled and still hot rod, is termed as an accelerated watering event that moment of leaves the last roll pass [2].

In the literature research, studies using various estimation techniques for different types of problem types have been examined.

Başıyigit et al. In the studies, radiation armor thicknesses of concrete were estimated by artificial neural networks and multiple regression methods. To determine the concrete armor thickness value, the multiple regression equation was set up with n values representing the radiation intensity (MeV), the tenth layer thicknesses, and the negative algorithm of the transmission percentages. There was a high correlation between the predicted concrete armor thickness variations in the 95% confidence interval [3].

According to the Yüksek, in the estimation of air pollution, the use of artificial neural networks, fuzzy neural networks and multiple regression methods can produce more positive results which using all together at the same time. When the ineffective variables of the model are determined with multiple regression and after being eliminated, fuzzy neural networks are trained with fewer variables which is more successful results may occur [4].

Okutkan, A study has been conducted on some companies in Istanbul Stock Exchange aiming to estimate stock prices with artificial neural networks and multiple regression methods. Multiple regression is examined in two cases. In both cases, the "share price" was determined as the dependent variable. It has been observed that estimates are consistent in both cases, which are arranged according to investors' decision variables [5].

Akmercan; Households are estimated by using parametric and nonparametric regression method, taking necessary consumption expenditures as dependent variable and comparing these two methods. The nonparametric regression analysis was more comprehensive, but the results of both regression analyzes were consistent [6].

Apronti et al. this study developed two efficient, cost effective and easy to use models for predicting traffic volumes on low volume roads in Wyoming. The first regression model

II. PROBLEM STUDIED

is a linear regression model that utilized pavement type, access to highways, predominant land use types, and population to estimate traffic volume. The second model is a logistic regression model that identified the level of traffic on roads using five thresholds or levels. The logistic regression model is verified by estimating traffic volume thresholds and determining the percentage of roads that were accurately classified as belonging to the given thresholds. It estimates the traffic volume as accurate and cost-effective in two models [7].

Braun et al. Have investigated how climate change will affect buildings' energy consumption. Although many studies have investigated energy consumption in offices and homes, this study investigates how supermarkets in the north of England will affect energy consumption. For this, future energy consumption is predicted by multi-regression model [8].

Fan et al. The strength of the sintering drum will be strengthened and the model to be predicted will be made using ANN and Regression. The mixture water, fuel ratio, sintering speed and sintering drum strength are selected as the output parameters hereby. To develop system software by mix programming way of both Visual C++ and Matlab, then to provide a user-friendly interface, by adopting which, we can optimize the moisture content and fuel ratio and improve the sintering drum strength [9].

Tolon and Tosunoğlu estimated the consumer satisfaction survey in their study with ANN and Regression methods. Both methods gave close results. It has been seen in research that the most important reasons for customer service negatively affect satisfaction is the lack of serviceability to the house and that sales promotion activities are not being carried out effectively. Other variable sets affect the positive direction [10].

Akkus et al. defense and aeronautical industries absorb the energy absorbed aluminum honeycomb structures used in the material absorbed force values are measured. Low velocity impact behaviors of honeycomb composites were investigated experimentally and the force values obtained were modeled and predicted by multiple regression method [11].

Güngör set up a multi-linear regression model with meteorology and air quality daily data observed during the October-March winter months of 2007-2012 due to the increase in air pollution in the province of Isparta. Three models have been set up to estimate the 2011-2012 winter season. The first and third models that best estimate the SO₂ and amount of particulate matter, these models are best estimate in the other models [12].

Şener is generated regression model for electric charge estimation in Ankara metropolitan area. TEİAŞ's 6-year work data are used to peak (instantaneous maximum value) power values, the energy values consumed in the days of the peak. Estimates were made using the regression model for future years by taking advantage of TEİAŞ data [13].

The purpose of our study; The prediction of the strength values of ribbed bar also known as the concrete steel bar (rebar), produced by the Tempcore system according to the chemical composition values.

In the study; The yield and tensile strengths of the ribbed bar produced in S 420 quality are estimated by multiple regression model.

The process flow chart is as follows.

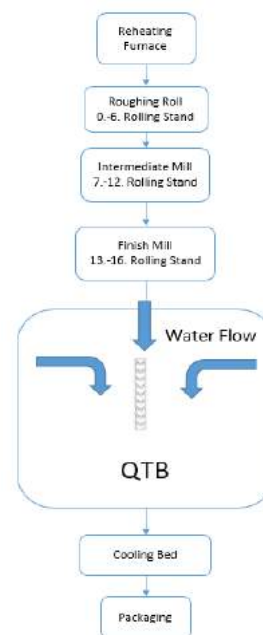


Figure 41 Continuous Rolling Mill Flow Chart

The process starts with annealing the billets defined as semi-finished products in the rolling reheating furnace. After a total of 17 rolling stands, it becomes final product as ribbed bar. The billets charged to the reheating furnace are grade S420. This quality is a steel quality that is within the chemical composition range of TS 708 standard.

This chemical composition such as C, Mn, and Si are in primarily affect the yield, tensile strength values we are aiming to estimate.

An increase in yield stress can be achieved by increasing the combination of carbon and manganese [14].

Another limitation which affects yield, tensile strength is the water flow in the QTB line. QTB (Quenched and Tempered Bar); is a way to improve mechanical properties in the ribbed bar industry. The QTB basic rationale is to provide water to the hot rolled ribbed bar immediately after the production line, and then to temper the internal heat. Within this logic, it is possible to produce ribbed bar without the use of alloy elements and with low carbon, manganese rates and desired properties. This, in turn, means the desired properties and low cost material.

In other words, the Tempcore process is based on the principle that the steel surface is hardened by quenching. When this process is applied, an increase of yield strength of 150 to 230 MPa is obtained depending on the cooling density [2].

III. REGRESSION

Regression analysis is called a multiple regression analysis model in which a dependent variable and several independent variables are involved. In multiple regression analysis, the independent variables are trying to explain the change in the dependent variable at the same time. It is similar to simple regression analysis in terms of calculation and interpretation.

A. Multiple Regression Methods

- Enter Method
- Forward Selection Method
- Backward Elimination Method
- Stepwise Selection Method

The most commonly used method is the Enter method. Then the stepwise method is used [15].

IV. IMPLEMENTATION

Two different models of the same arguments for yield and tensile values were set up. For this reason, the missing values are cleared from the data sets in order to set up the correct model. Frequency analysis was performed to obtain information about the independent variable values used in the yield and tensile tests. Finally, a multiple regression analysis was used to establish the predictive model while performing correlation analysis to examine the relationship between values. Analyzes were done with IBM SPSS Statistics. All results will be explained in the following subsections.

A. Frequency Analysis Results

The minimum, maximum and mean values of the variables used in the tests are summarized in table 1.

TABLE 33. DESCRIPTIVE STATISTICS

	N	Minimum	Maximum	Mean
Carbon	135	,31	,41	,3457
Manganese	135	,59	,73	,6445
Silica	135	,13	,29	,1866
Sulfur	135	,02	,05	,0359
Size	135	140,00	180,00	153,9259
Water Flow	135	210,00	290,00	255,6296
Yield	135	470,00	538,00	499,1852
Tensile	135	599,00	684,00	634,7852

As shown as Table 1, the lowest yield rate is 470 and the highest yield rate is 538 N/mm². For tensile tests, the lowest rate is 599 while the highest tensile rate is 684 N/mm² dr.

Ribbed bar sizes used in tests range from 14 to 18. The water flow used in the rolling mill is in the range of 210-290.

B. Correlation Analysis Results

Correlation analysis was performed with Pearson Correlation values to determine whether there was a relationship between the yield and tensile tests and the independent variables. The coefficients obtained in Table 2 and Table 3 can be observed.

TABLE 34 CORRELATIONS FOR YIELD RATES

	Yield	C	Mn	Si	S	Size	WF
Yield	1	0,092	0,655	-0,49	-0,91	0,658	0,639
Carbon	0,092	1	0,005	0,121	0,1	0,307	-0,09
Manganese	0,655	0,005	1	-0,18	-0,65	0,277	0,391
Silica	-0,49	0,121	-0,18	1	0,475	-0,39	-0,42
Sulfur	-0,91	0,1	-0,65	0,475	1	-0,6	-0,72
Size	0,658	0,307	0,277	-0,39	-0,6	1	0,748
Water Flow (WF)	0,639	-0,09	0,391	-0,42	-0,72	0,748	1

TABLE 35. CORRELATIONS FOR TENSILE RATES

	Ten.	C	Mn	Si	S	Size	WF
Tensile	1	0,076	0,717	0,436	0,922	0,604	0,658
Carbon	0,076	1	0,005	0,121	0,1	0,307	0,091
Mn	0,717	0,005	1	-0,18	0,653	0,277	0,391
Silica	0,436	0,121	-0,18	1	0,475	0,386	-0,42
Sulfur	0,922	0,1	0,653	0,475	1	0,604	0,715
Size	0,604	0,307	0,277	0,386	0,604	1	0,748
Water Flow	0,658	0,091	0,391	-0,42	0,715	0,748	1

When the tables were examined, the following results were obtained.

- There is a relationship between manganese, size, water discharge which are independent variables and yield values in the positive direction and in the medium force relation.
- There is a strong and negative relationship between sulfur and yield values. As the amount of sulfur increases, the yield of the product decreases.
- Sulfur also affects the draw in the opposite direction and the strong direction while the other is the variable mangan that affects the positive direction.

- Other variables are size and water flow affected medium positive direction for tensile tests.

It has been decided to establish a multiple regression model with all the independent variables that we have found to be influencing in a strong or moderate quantity for yield and tensile tests according to the correlation analysis.

C. Regression Models

In the regression analysis, we used the multiple regression model, the enter method, to determine whether all the variables affected the yield and tensile values at the same time.

The results of the analysis for this model are given in Tables 4, 5, 6, 7, Appendix-1 and Appendix-2.

TABLE 36. MODEL SUMMARY FOR YIELD RATES

Model	R	R Square	Adjusted R Square	Std. Error of the Estimate	Durbin-Watson
1	,939 ^a	0,881	0,875	16,00177	0,88

a. Predictors: (Constant), Size, Carbon, Manganese, Silica, Sulfur, Size

b. Dependent Variable: Yield

V. As can be seen from the model summary, the equation explains that 88.1% is carbon, manganese, silica, sulfur, size and water flow of the model.

TABLE 37. ANOVA TABLE

Model		Sum of Squares	df	Mean Square	F	Sig.
1	Regression	242784,3	6	40464,045	158,028	,000 ^b
	Residual	32775,27	128	256,057		
	Total	275559,5	134			

a. Dependent Variable: Yield

b. Predictors: (Constant), Size, Carbon, Manganese, Silica, Sulfur, Size

The Anova chart is statistically significant for sig <0,05.

The equation of our model according to the table in Appendix-1 is as follows.

$$Y_{YIELD} = 356,797 + (254,985 * (Carbon)) + (169,633 * (Manganese)) + (-134,643 * (Silica)) + (0,410 * (Size)) + (-1243,518 * (Sulfur)) + (-0,190 * (Water Flow))$$

According to the table in Appendix-1, the VIF values that should satisfy the multiple regression conditions should be less

than 10 and the Tolerance values should be larger than 0,05. Our table also provides the conditions for both values. There is no perfect linear relationship between forecast variables.

In a second model, it was created using the same arguments for tensile rates with Enter Method.

TABLE 38. MODEL SUMMARY FOR TENSILE RATES

Model	R	R Square	Adjusted R Square	Std. Error of the Estimate	Durbin-Watson
1	,948 ^a	0,899	0,894	18,855	0,672

a. Predictors: (Constant), Water Flow, Carbon, Manganese, Silica, Sulfur, Size

b. Dependent Variable: Tensile

VI. As can be seen from the model summary, 89.9% of the tensile rates is explained by the variables included in the model.

TABLE 39. ANOVA TABLE FOR TENSILE RATES

Model		Sum of Squares	df	Mean Square	F	Sig.
1	Regression	404649,7	6	67441,62	189,703	,000 ^b
	Residual	45505,42	128	355,511		
	Total	450155,1	134			

a. Dependent Variable: Tensile

b. Predictors: (Constant), Water Flow, C, Mn, Si, S, Size

The Anova table is statistically significant as the sig value is less than 0,05.

According to the table in Appendix-2, the equation of our model is as follows.

$$Y_{Tensile} = 333,056 + (470,284 * (Carbon)) + (306,815 * (Manganese)) + (-75,126 * (Silica)) + (-1600,707 * (Sulfur)) + (-0,18 * (Size)) + (0,061 * (Water Flow))$$

According to the table in Appendix-2, the VIF values that should satisfy the multiple regression conditions should be less than 10 and the Tolerance values should be larger than 0,05. Both values provide the conditions as seen on the Appendix-2. There is no perfect linear relationship between forecast variables.

VII. CONCLUSION

In both models, the carbon element appears to be the variable with the highest coefficient value.

The carbon equivalent value is given in the chemical composition and weldability part of TS 708 standard [16]:

$$Ceq = C + Mn/6 + (Cr + Mo + V)/5 + (Ni + Cu)/15$$

In this formula, the elements that can be used as carbon equivalent are shown. The proportion of the manganese element, which may be carbon equivalent, indicates the formation of manganese as the other element that will act as carbon.

In our study, we see that the second element which affects the strength values after carbon (C) is manganese (Mn).

According to expert opinion, it is known that the value of the water flow values in the rolling mill is important for the yield strength. It is also seen that water flow is effective as a correlation coefficient of model effect in our study. In our future studies, we will also investigate the effect of variables on yield and tensile rates by different methods.

It is aimed to develop a useful model by comparing the obtained results with these study results

VIII. REFERENCE

- [1] S. T. Yıldırım, «BETON ÇELİK ÇUBUKLARININ ISI ETKİLERİNE KARŞI MEKANİKSEL VE KİMYASAL YÖNDEN ANALİZİ İLE EKONOMİK DURUMUN ARAŞTIRILMASI,» Fırat University, Graduate School of Natural and Applied Sciences, Elazığ, 1996.
- [2] O. Çelik, «TEPCORE ISIL İŞLEMİ UYGULANMIŞ NERVÜRLÜ BETONERME ÇELİĞİNİN MANYETİK REZONANS YORULMA DAVRANIŞININ İNCELENMESİ,» Karabük University, Graduate School of Natural and Applied Sciences, Karabük, 2015.
- [3] C. Başyigit, A. Kaçar Akkaş ve N. M. Kurtarıcı, «Betonların Radyasyon Zırh Kalınlıklarının Yapay Sinir Ağları ve Çoklu Regresyon Metotları ile Tahmini,» Süleyman Demirel University, Graduate School of Natural and Applied Sciences Magazine ,16-1(2012), 77-81, Isparta, 2012.
- [4] A. G. Yüksek, «HAVA KİRLİLİĞİ TAHMİNİNDE ÇOKLU REGRESYON ANALİZİ VE YAPAY SİNİR AĞLARI YÖNTEMİNİN KARŞILAŞTIRILMASI,» Cumhuriyet University, Sivas, 2007.
- [5] C. Okutkan, «Borsa İstanbul Şirketlerinin Hisse Senedi Getirilerinin Yapay Sinir Ağları Ve Çoklu Regresyon Yöntemleri Kullanarak Analizi,» Kocaeli University, Graduate School of Natural and Applied Sciences, Kocaeli, 2014.
- [6] T. Akmercan, «Hanehalkı Tüketim Harcamalarının Parametrik Olmayan Regresyon Yöntemi İle Tahmini: Türkiye Örneği,» Dumlupınar University, Social Sciences Institute, Kütahya, 2016.
- [7] D. Apronti, K. Ksaibatı, K. Gerow ve J. J. Hepner, «Estimating Traffic Volume On Wyoming Low Volume Roads Using Linear And Logistic Regression Methods,» Journal of Traffic and Transportation Engineering, Wyoming, 2016.
- [8] M. Braun, H. Altan ve S. Beck, «Using Regression Analysis To Predict The Future Energy Consumption Of A Supermarket in The UK,» Applied Energy, Sheffield, İngiltere, 2014.
- [9] X.-h. Fan, Y. Li ve X.-l. Chen, «Prediction of Iron Ore Sintering Characters on the Basis of Regression Analysis and Artificial Neural Network,» Energy Procedia, Changsha, China, 2012.
- [10] M. Tolon ve N. Güneri Tosunoğlu, «Tüketici Tatmini Verilerinin Analizi: Yapay Sinir Ağları Ve Regresyon Analizi Karşılaştırması,» Gazi University, Faculty of Economic and Administrative Sciences Magazine, Ankara, 2008.
- [11] H. Akkuş, H. Düzcükoğlu ve Ö. S. Şahin, «Alüminyum Bal Peteği Yapılarında Darbe Mukavemeti Tahmini İçin Regresyon Modeli Oluşturulması,» Erzincan University, Graduate School of Natural and Applied Sciences, Erzincan, 2016.
- [12] A. Güngör, «Isparta İlindeki Atmosferde Bulunan Kükürtdioksit (So2) Ve Partikül Madde (Pm) Konsantrasyonunun Çoklu Doğrusal Regresyon Yöntemi İle Modellenmesi,» Süleyman Demirel University, Graduate School of Natural and Applied Sciences, Isparta, 2013.
- [13] F. Şener, «Yük Tahmin Yöntemleri ve Ankara Merkez Metropol Alan İçin Regresyon Analizi Yöntemi Kullanılarak Uygulanması,» Gazi University, Graduate School of Natural and Applied Sciences, Ankara, 2005.
- [14] K. M. Tankut, «TEPCORE PROSESİ İLE ÜRETİLEN DÜŞÜK ALAŞIMLI NERVÜRLÜ BETON ÇELİKLERİNİN KARAKTERİSTİĞİ,» İstanbul Technical University, Graduate School of Natural and Applied Sciences , İstanbul, 1995.
- [15] F. Gültekin, «Regresyon Analizi,» [Çevrimiçi]. Available: <http://w3.balikesir.edu.tr/~bsentuna/wp-content/uploads/2013/03/Regresyon-Analizi.pdf>. [Erişildi: Şubat 2017].
- [16] TSE, «TS 708 Çelik Betonarme için- Donatı Çeliği,» [Çevrimiçi]. Available: http://www.mdcdemir.com.tr/upl/TS_708.pdf. [Erişildi: Ocak 2017].
- [17] M. T. Badem, «Beton Çeliklerinin Mekanik Özellikleri ve Denizli'de Kullanılan Beton Çelikleri,» Pamukkale University, Graduate School of Natural and Applied Sciences, Denizli, 2001.

APPENDIX-1

Model		Unstandardized Coefficients		Standardized Coefficients	t	Sig.	95,0% Confidence Interval for B		Correlations			Collinearity Statistics	
		B	Std. Error	Beta			Lower Bound	Upper Bound	Zero-order	Partial	Part	Tolerance	VIF
	Carbon	254,985	88,115	,113	2,894	,004	80,634	429,336	,092	,248	,088	,613	1,631
	Manganese	169,633	52,789	,136	3,213	,002	65,181	274,086	,655	,273	,098	,516	1,939
	Silica	-134,643	49,783	-,097	-2,705	,008	-233,148	-36,138	-,489	-,233	-,082	,722	1,386
	Sulfur	-1243,518	95,295	-,767	-13,049	,000	-1432,075	-1054,960	-,909	-,756	-,398	,269	3,720
	Size	,410	,135	,180	3,035	,003	,143	,677	,658	,259	,093	,264	3,788
	Water Flow	-,190	,086	-,128	-2,206	,029	-,360	-,020	,639	-,191	-,067	,278	3,603

a. Dependent Variable: Yield

APPENDIX-2

Model		Unstandardized Coefficients		Standardized Coefficients	t	Sig.	95,0% Confidence Interval for B		Correlations			Collinearity Statistics	
		B	Std. Error	Beta			Lower Bound	Upper Bound	Zero-order	Partial	Part	Tolerance	VIF
	Carbon	470,284	103,827	,163	4,530	,000	264,845	675,724	,076	,372	,127	,613	1,631
	Manganese	306,815	62,202	,193	4,933	,000	183,738	429,893	,717	,400	,139	,516	1,939
	Silica	-75,126	58,660	-,042	-1,281	,203	-191,196	40,943	-,436	-,112	-,036	,722	1,386
	Sulfur	-1600,707	112,287	-,773	-14,256	,000	-1822,885	-1378,528	-,922	-,783	-,401	,269	3,720
	Size	-,018	,159	-,006	-,115	,909	-,333	,297	,604	-,010	-,003	,264	3,788
	Water Flow	,061	,101	,032	,604	,547	-,139	,262	,658	,053	,017	,278	3,603

a. Dependent Variable: Tensile

Energy Saving by Using Blast Furnace Top Pressure Recovery Turbine (TRT) System

Selçuk KUŞOĞLU^a, Cuma KARAKUŞ^b, Ali GENÇOĞLU^c, Ali Salim AKYOL^d

^aİSDEMİR Iron and Steel CO., Iskenderun/Hatay, Turkey, E-mail: skusoglu@isdemir.com.tr

^bDepartment of Mech. Engineering, ISTE University, Iskenderun/Hatay, Turkey, E-mail: cuma.karakus@iste.edu.tr

^cİSDEMİR Iron and Steel CO., Iskenderun/Hatay, Turkey, E-mail: agencoglu@isdemir.com.tr

^dİSDEMİR Iron and Steel CO., Iskenderun/Hatay, Turkey, E-mail: asakyol@isdemir.com.tr

Abstract

Many industries in the world and the iron and steel sector have focused on energy saving in order to stay in the industry and remain competitive in competition. Energy saving is an important way to increase predictable gains and to reduce dependence on cost and energy resources. Economically, increase of energy productivity is more attractive than investing for putting into use extra new energy sources. Blast Furnace Top Pressure Recovery Turbine System (TRT) which is taking advantage of pressure difference of Blast Furnace Gas by converting mechanical energy to electrical energy which is tool of energy saving and using at iron and steel industry in Brasil, China, Germany, Italy and South Korea and also begin to used in our country recently.

Since the industry and iron and steel sector uses 15% of the world's energy demands, energy saving in these sectors is of great importance. The Turkish iron and steel industry, which has recovered faster than the developed countries in the global crisis, has become the 9th largest producer of crude steel sector in the world and the 2nd big producer in the Europe.

In this study, it was investigated importance of TRT system around the world, returns to sector, the technological advantages and numerical statistics of the countries having the TRT system. It was carried out feasibility study during the installation time and calculated installation and operation costs, total costs and pay-off period about TRT system of a sample factory.

Key Words: Energy, Blast Furnace, Blast Furnace Gas, Energy Recovery, TRT Systems

I. INTRODUCTION

Nowadays, energy has become an important phenomenon for human life and all countries. In addition, Turkey which is one of the developing countries, with the increasing level of economy, welfare and population, industrial energy demand also causes increase of energy supply. The ever-increasing energy prices have become a major cost factor in terms of constant fluctuations and high energy costs. This situation increases needs of energy saving in the iron and steel industry, which has 15% of the world's energy demands.

Energy efficiency is more significant way than investments to supply new energy sources and reducing dependence on cost and energy sources. For this purpose, instead of making expensive investments to produce the energy, it is possible to get energy faster and cheaper by energy saving methods. Because of effecting competition effort, the world countries have to develop more innovative, environmentally friendly and energy-efficient products in sectors of iron and steel, building and transportation.

Carbone dioxide(CO₂) emission reductions are not important only in the energy supply sectors but also is important on the energy efficiency works to adapt the post-Kyoto regimes. According to the Kyoto protocol, member countries are wanted to reduce carbon emissions to 1990 carbon emission levels.

Top Pressure Recovery Turbine (TRT) system is one of the energy saving method such as the using of high efficiency lighting systems to reduce the specific energy consumption, the use of high efficiency motors, the design of high efficiency cooling systems, the construction of line insulations, system insulations, the waste heat systems and the continuous monitoring of the system parameters via PLC.

Junichiro et al. (2007) assessed the potential for reducing CO₂ emissions and the minimum costs of technological facilities in the world iron and steel sector in their works. As an estimation, energy efficiency will increase by 15% in 2030. They concluded that the TRT system, the construction of new generation coke ovens, oxygen gas recovery facilities and coke dry quenching plants have played a major role in achieving energy efficiency in the steel industry.

Guo and Fu (2009) stated that by using the TRT system, up to 30% of the energy consumption can be recovered in the BF. At the end of 2007, 49 units of TRT systems have been established with a volume of 2.000 m³ BF in China and and it was planned to continue the establishment of the TRT system for all BFs which has a big volume up to 2030.

Wu and Yang (2011) signed that the TRT systems used to recover 20% of BF's energy consumption by TRT system and can be installed in every BF with a volume greater than 1.000 m³.

Kuşoğlu et al., (2014) have done a feasibility study about cost of the installation of the TRT systems. They stated that the total costs related to the operation and the return period of the investment.

Cai et al. (2016) informed that the TRT systems are one of the most valuable energy recovery systems in the iron and steel sector and 30% of the energy consumption can be recovered by the rotating generator connected to the turbine system.

In this study, the importance of the TRT systems in the world, the returns to the plants gained by the installation and statistics analysis and technological advantages of the TRT system have been examined. The technical and financial analyses were carried out the feasibility studies for the construction of the BF system for a sample plant and the approximate installation and operating costs of the investment, the total cost and the pay back period were calculated.

A. Energy Saving Applications and the Role of the TRT System over the World

The share of energy sources in energy demand in 2035 is given in Figure 1. The resources of electricity generation and primary energy supplies significant developments and changes have occurred between 1990 and 2016. According to these developments, the world countries are making scenarios to supply with future demands in energy field. The International Energy Agency (IEA) is making scenarios by considering the global climate change, the diminishing use of resources, the energy efficiency improvements in technology, the economic and social conditions. In this framework, in the New Energy Policy and the 450 Scenarios, excepted the current policies, current trend of the world primary energy supply and the consuming rate of resources will change.



Figure 1. The share of energy sources in energy demand in 2035 (IEA, 2011).

According to International Energy Agency (IEA) data, it is predicted that in 2035 the coal usage rate will be nearly 30% and the proportion of other renewable resources will be nearly

2,6%, depending on the current policy. Looking at the 450 scenario, it is predicted that the coal utilization rate will decrease to 15% and the proportion of other renewable resources will increase to 8%.

The TRT systems are widely used in the iron and steel industry as Brasil, Italy, China, Japan, South Korea, Germany and Turkey. While all of the integrated iron and steel plants in Japan and Korea have the TRT system in operation, there are 560 pieces of TRT system being used in China (Anonymous, 2013). In our country, two TRT systems, named the 3rd and the 4th BF, which are belong to Iskenderun iron and steel factory in 2016, have been taken into operation.

B. Energy Saving Applications and the role of the TRT System in Turkey

The amount of produced, imported and consumed energy in Turkey is given in Figure 2 on the basis of million TOE Turkey has started a rapid growth process in iron and steel industry since 2001 and Turkey's crude steel production capacity has increased 70% from 17.7 million tonnes to 29.7 million tonnes between 2000 and 2008. In the same period, the production capacity of electric arc furnaces increased by 91% from 13.6 million tons to 26.1 million tons. At the same time the capacity of integrated plants increased by 30% to 11.5 million tons in 2016. In Turkey, the energy production was 25.1 MTOE in 1990 and it increased by 19.9% to 30.1 MTOE in 2000. The estimated production in 2020 is expected to be 79.3 MTOE with an increase of 163.5%.

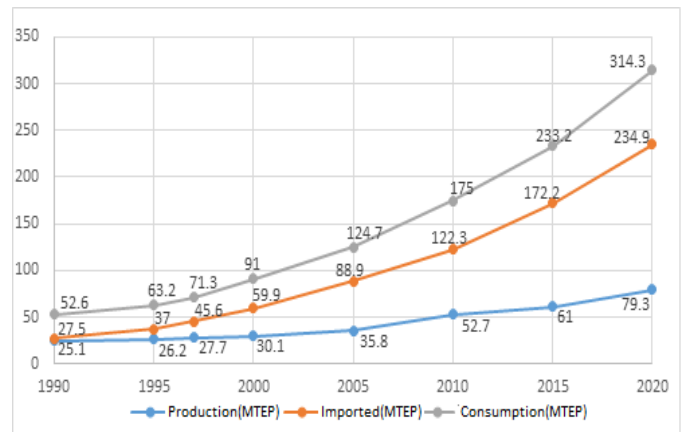


Figure 2. The amount of energy consumed, imported and consumed in Turkey-million TOE (As of 1990, including estimates for 2000-2020).

Iskenderun Iron-Steel Plants, one of the three integrated iron and steel plants in Turkey (Iskenderun, Ereğli and Karabük Iron and Steel Plants), entered the privatization process in February 2002 and has started to increase production capacities with energy saving works at the same time. The production capacity has been continuously increased while the energy consumption has been reduced. In 2001, the specific energy consumption, which was around 8.000 Mcal/t-pig iron, fell below 5.000 Mcal/t-pig iron in 2011, and this value remained around 4.700 Mcal/t-pig iron in 2016. As a result of the energy conservation efforts, Ereğli iron and steel factory

has saved specific energy consumption by 44.5% since 1982 and Iskenderun iron and steel factory has saved 38.5% since 2001.

The amount of saved energy for energy conservation projects from 2002 to 2012 in Iskenderun Iron and Steel factory such as a BF, coke batteries, sinter plants, lime kilns, rolling mill, hot rolling mill, power plant, air separation and turbo blower plants are given in Table 1. As can be seen from the Table 1, while the maximum energy saving investment amount was applied in 2003, the minimum energy saving investment amount was applied in 2010.

Table 1. Iskenderun Iron and Steel factory energy saving values by years (Anonymous, 2013)

Year	Quantity of Improvement	Amount of Energy Saving
2002	2	14.557 TEFO*/year
2003	1	12.937.988TEFO*/year
2004	4	141.070 TEFO*/year
2005	5	47.419 TEFO*/year
2006	5	81.446 TEFO*/year
2007	3	45.560 TEFO*/year
2008	3	69.530 TEFO*/year
2009	1	27.559 TEFO*/year
2010	1	529 TEFO*/year
2011	1	1.447 TEFO*/year
2012	1	11.427 TEFO*/year

In the iron and steel sector in Turkey, two TRT systems were installed 3rd and 4th BFs in Iskenderun Iron-Steel plants which have four BFs in total with 5.250.000 tons/year liquid iron production capacity. In addition, the installation of TRT system for 2nd BF is in feasibility stage. One piece TRT system was installed in Karabük Iron-Steel plants which have five BFs in total with a capacity of 2.500.000 tons/year pig iron production. Two piece TRT systems were installed, named as 1st and 2nd BFs which is planned to be established and commissioned in 2017 in Ereğli Iron and Steel plants with a total production capacity of 4.000.000 tons pig iron/year with two BFs. The electricity production capacity is about 20 MW for two TRT systems which were commissioned in 2016 in Iskenderun iron and steel factories. In Ereğli Iron-Steel factories for two TRT systems electricity production capacity is about 16 MW which will be commissioned in 2017. In Karabük iron and steel factories one TRT system electricity production capacity is about 7 MW which will be commissioned in 2017.

II. TRT SYSTEM AND APPLICATION IN IRON AND STEEL PRODUCING SECTOR

The TRT system is a turbo-generator system which convert BF gas kinetic energy to electrical energy without spending any

additional fuel, instead of decreasing pressure with expanding method. Direction of the gas is rotated to axial flow by guide vane and enter cascade. The gas is continuously expanded through the flow channel that consists of stator blade and rotor blade, its pressure and temperature are reduced stage by stage and converted to kinetic energy that drives the generator by driving the rotor. The outlet gas is expanded through diffuser to increase its back pressure and set value and then discharged through discharge volute casing. Finally, the gas enters the septum valve through outlet goggle valve and outlet butterfly valve.

The installation steps of the TRT system are shown below:

- I. Production capacity of BF
- II. Air flow of Turbo-Blower
- III. Determine capacity of turbine
- IV. Pre-project preparing
- V. Receive tender and determine supplier
- VI. Making detailed projects (electric, mechanic, construction), calculating investment cost and pay back
 - Economical feasibility
 - Technical feasibility
 - Organizational feasibility and time-chart
- VII. Investigation financial selections for investment.
- VIII. Application

While determining needs of TRT System application:

1. Last one or two year's hourly, daily and monthly electricity energy consumption
2. BF production capacities
3. Air flow and technical specifications of Turbo-Blowers air that BF needs
4. Technical specification and cleaning capacity of gas cleaning system of BF
5. Dust content of dirty and clean BF gas
6. Temperature of dirty and clean BF gas
7. Line pressure of inlet and outlet of gas cleaning system
8. Moisture content of gas etc technical specifications have to study well

When checking on the articles I, II and III, the TRT System capacity depends on production capacity of BF, air flow of turbo blower generally. Air flow capacity of turbo blower and also BF gas flow capacity can be determined according to BF pig iron production capacity. The BF gas is occurred by reduction of pig iron and coke after this process the occurred gas is transferred to gas cleaning system then to the TRT system by handling pipelines. The capacity of turbine is determined according to the BF gas flow rate, clean gas temperature, turbine inlet pressure, outlet gas pressure, dust content and the other technical specifications. There are two different alternative TRT systems named as dry type and wet type.

The dry type TRT system which can be seen in Figure 3 is used only for BFs that have dry type gas cleaning system. There is no water using for de-dusting. In comparison with wet

type, dry type method is characterized by less resistance loss of gas and low temperature drop. In this way, generated power recovery of TRT system could be increased by 25-45% of Turbo-Blower energy consumption. On dry type TRT, turbine inlet gas temperature is approximately 240 °C, and needs less water and electric to work than wet type TRT.

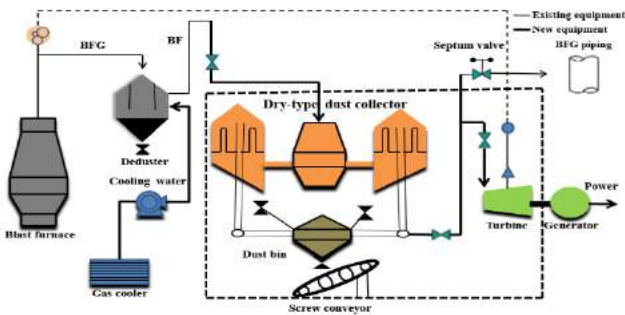


Figure 3. The Dry Type Top Pressure Recovery Turbine (Anonymous, 2008)

The wet type TRT system which can be seen in Figure 4 is used for wet type gas cleaning system in BFs. Since BF gas has a certain amount of dust, either Venturi tube or Bisch-off dust catcher is selected to clean the BF gas, and wet de-dusting treatment is used for wet type TRT system. Energy saving rate is approximately 30%. After cleaning and cooling operations the turbine inlet gas temperature is 55 °C. The top pressure of BF keeps by throttle valves that are set up in parallel with TRT system while the TRT system is out of service.

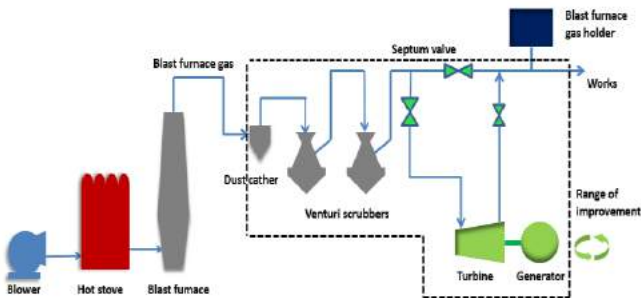


Figure 4. The Wet Type TRT System (Anonymous, 2008)

TRT photos are taken for BFs which have different capacity around the World are shown in Figure 5, Figure 6 and Figure 7.



Figure 5. The TRT that is installed for a BF with a volume of 2500 m³ (Anonymous, 2003)



Figure 6. The TRT that is installed for a BF with a volume of 380 m³ (Anonymous, 2009)



Figure 7. Generator Application for two BF with a volume of 2x450 m³ (Anonymous, 2010)

The TRT systems components are given below as can be seen in Figure 8:

1. Turbine stator-rotor system
2. Generator system
3. Lubrication system
4. Power oil system
5. Nitrogen sealing system
6. Cooling and washing water system
7. Large scale valves and pipes system
8. HV and LV power distribution system

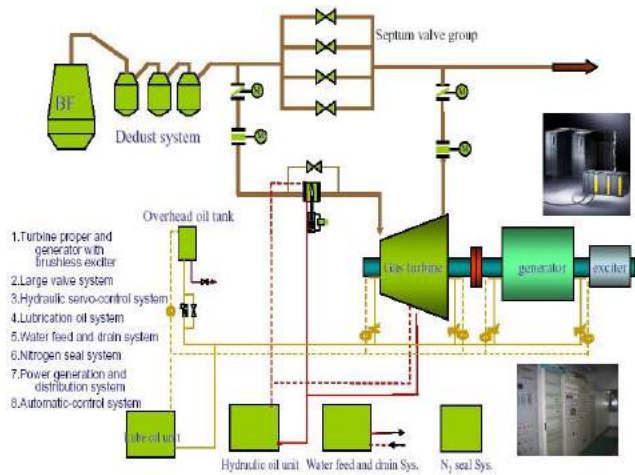


Figure 8. The TRT System Flow Chart (Anonymous, 2010)

III. THE TRT SYSTEM TECHNICAL DATA INVESTIGATION AND CALCULATIONS

The TRT system performance consideration is shown in Table 2. As can be seen from the Table 2, the minimum, average and maximum output turbine power are given according to the minimum, average and maximum process conditions of a sample BF.

The below data is gained from a sample iron and steel factory yearly operation conditions. The detail reports about these data are shown below:

Table 2. The TRT system performance consideration (Anonymous, 2014)

No	Parameters	Unit	Min.	Design	Max.
1	Turbine Inlet Flow Rate	Nm ³ /h	200.000	250.000	300.000
2	Turbine Inlet Gas Pressure	bar (gage)	0,8	1,2	2
3	Turbine Inlet Gas Temperature	°C	35	50	70
5	Turbine Outlet Gas Pressure	bar (gage)	0,07	0,08	0,1
6	Atmosphere Pressure	kPa	----	103,3	-----
8	Turbine Output Power	kW	3,61	5,1	8

- Turbine inlet gas flow:** The BF gas gained during the BF liquid iron produce, follows the gas cleaning way for cooling and cleaning. The gas which pass through the turbine per hour is named as turbine inlet gas flow.
- Turbine inlet gas pressure:** The BF needs suitable pressure with the purpose of reduction liquid iron. BF gas leaves the BF and enters the TRT system to generate gas pressure.
- Turbine inlet gas temperature:** The temperature of the BF gas which is cleaned and cooled by gas cleaning system at

inlet side of the turbine. Turbine inlet gas temperature is one of the important point that effects the turbine efficiency.

- Relative humidity ratio at turbine inlet:** The ratio of the water vapor contained by the BF gas to the water vapor capacity can hold on current situation pressure and temperature value.
- Turbine outlet gas pressure:** The gas pressure of BF gas on turbine outlet point. The turbine outlet pipeline is connected to the main BF gas pipeline and must be nearly equal to the pressure of the main BF gas pipeline pressure.
- Atmosphere pressure:** The atmosphere pressure is determined according to the place of turbine for system calculations.
- Dust content of BF gas on turbine inlet:** The dust content of BF gas that comes from gas cleaning system to the TRT.
- Turbine output power:** Turbine output power is generated by converting the kinetic energy of BF gas to electrical energy by generator.
- Turbine rotation speed:** The rotation speed of turbine rotor while the gas passing through the turbine. The rotation speed of rotor have to be constant while the TRT system on work.

The TRT generator output power has been calculated according to the top pressure, main gas collector pressure, dirty gas temperature, clean gas temperature values are taken during the liquid iron producing from a sample BF.

The BF system monthly averaged process data for 2014 is given at Table 3. As can be seen from the table, the maximum production during the year was made in January and the minimum production was made in July. That was not experienced an unplanned stand on January and BF producing was realised on maximum level. But in July, an unplanned stand was experienced during six days and the TRT couldn't generate the electric because of the standing.

Table 3. The BF system monthly averaged process data on 2014.

2014	The BF System			
	The Top Pressure (bar)	The Main Collector Pressure (bar)	The Dirty Gas (°C)	The Clean gas (°C)
January	1.6	0.0761	85	34
February	1.6	0.076	88	35
March	1.6	0.0765	86	34
April	1.5	0.0761	90	33
May	1.6	0.0762	87	33
June	1.6	0.0764	72	33
July	1.3	0.076	84	35
August	1.6	0.0757	103	37
September	1.5	0.0757	96	34
October	1.6	0.0760	106	34
November	1.5	0.0759	113	37
December	1.6	0.0758	108	36

A. Calculations of the TRT System Performance

The formulas will be used in calculation of the energy and power data will be obtained from the gas passing through the turbine are:

The Universal Gas Constant, $R = 7, 82 \times 10^{-5}$ kWh / kg K
The adiabatic work;

$$[(k.R.T_1)/(k-1)]. [1 - (P_2/P_1)^{(k-1)/k}] \quad (1)$$

The turbine outlet temperature;

$$P_1/P_2 = (T_1/T_2)^{k/(k-1)} \quad (2)$$

The heat capacity coefficient is heat capacity under the constant pressure (C_p) ratio to heat capacity under the constant volume (C_v).

$$k = C_p / C_v \quad (3)$$

Here, the C is given specific heat capacity under constant pressure (P) and constant volume (V) conditions.

The ideal gas relations:

The enthalpy;

$$\int_{H_1}^{H_2} dH = \int_{p_1}^{p_2} C_p \cdot dT \quad (4)$$

The energy;

$$\int_{U_1}^{U_2} dU = \int_{T_1}^{T_2} C_v \cdot dT \quad (5)$$

The state equation on an adiabatic system;

$$p \cdot v^k = constant \quad (6)$$

The specific volume;

$$v = V' / m' \quad (7)$$

Here, V' (m^3/s); The volumetric flow rate, m' (kg/s); the mass flow rate is constant in the system;

$$p \cdot m'^k = constant \quad (8)$$

$$P_1 / m_1^{1k} = P_2 / m_2^{1k} \quad (9)$$

The mass flow rates for the flow equation;

$$Q_1'/Q_2' = m_1'/m_2' \quad (10)$$

$Q_1'/Q_2' = m_1'/m_2'$ with the equation $P_1/m_1^{1k} = P_2/m_2^{1k}$ as a result of the equations;

$$Q_1'/Q_2' = (P_2/P_1)^{1/k} \quad (11)$$

The percentage increase between two flows;

$$r = \frac{Q_1^t - Q_2^t}{Q_1^t} \cdot 100 \quad (12)$$

The equation obtained in this case is the functional change of top pressure that the BF has during production;

$$\frac{r}{100} = \left(\frac{P_2}{P_1}\right)^{\frac{1}{k}} - 1 \quad (13)$$

The maximum work that can be achieved when the ideal reversible isentropic expansion takes place (kJ/kg);

$$(W_{t12'})_{rev} = h_1 - h_2 = \Delta h_s \quad (14)$$

The work that can be achieved in irreversible adiabatic expansion conditions (kJ/kg);

$$W_{t12} = h_1 - h_2 = \Delta h \quad (15)$$

The work loss caused by isentropic expansion (kJ/kg);

$$W_{v12} = (W_{t12'})_{rev} - W_{t12} = h_2 - h_2' \quad (16)$$

The isentropic turbine efficiency;

$$\eta_s T = W_{t12} / (W_{t12'})_{rev} = W_{t12} / (W_{t12} + W_{v12}) = (h_1 - h_2) / (h_1 - h_2') = \Delta h / \Delta h_s \quad (17)$$

The turbine power on shaft (kW);

$$P_{12} = m'. (W_{t12'})_{rev} \cdot \eta_s T = m'. W_{t12} \quad (18)$$

The turbine power on shaft (kW);

$$P_{w12} = m'. W_{t12} \cdot \eta_m = P_{12} \cdot \eta_m \quad (19)$$

The generator terminal power (kW);

$$P_{G12} = P_{w12} \cdot \eta_G \quad (20)$$

B. The Carbon Emission Amount

The carbon emissions which allied with electricity consumption in a plant is calculated by multiplication of electricity consumption and emission factor. The country-specific emission factor is determined by the ratio of the country-wide emission of electricity generated by that country to the total amount of electricity produced in the country.

For our country, according to the International Energy Agency publication dated 2011(b), the amount of release per unit kWh electricity consumption is determined as "0.865664547" kgCO₂;

$$Emission\ Amount\ (kgCO_2) = Elec.\ Consp.(kWh) \times 0,865664547 \quad (21)$$

IV. RESULTS OF RESEARCH AND DISCUSSION

The adiabatic work, the thermodynamic power, the turbine power and the generator power are calculated of the TRT system from the 0.8 to 2 bars in 0.1 bar increments. The data which will be used for TRT power calculation on sample plant:

The heat capacity ratio (k):1,4
 The gas constant, R : 7,82x10⁻⁵ kWh / kg K
 P₁ : The turbine inlet pressure (0.8 bar)
 P₂ : The turbine outlet Press. (0.078 bar)
 T₁ : The turbine inlet temp. (40 °C)
 T₂ : The turbine outlet temp. (10 °C)
 The gas density : 1,27 (kg/Nm³)
 C_p : 0,00029424 (kWh/kg°C)
 The turbine efficiency : 0,90
 The generator efficiency : 0,95
 The BFG flow rate : 295.000 (Nm³/h)

The efficiency of the turbine and generator is given from the Shanguu plant reference list for TRT systems turbines. The efficiency is examined by dividing the produced energy to consumed energy of the turbine system. In addition, changing of the diameter of inlet and outlet gas pipeline, the velocity of the gas, the losses due to the friction and the other equipments of the system are also used for calculation of the efficiency of the turbine.

The adiabatic work;

$$= [(k.R.T_1) / (k - 1)]. [1 - (P_2/P_1)^{\frac{k-1}{k}}] \quad (21)$$

$$= [(1,4 \times 7,82 \times 10^{-5} \times 313) / (1,4 - 1)]. [1 - 1,078 / 1,8]^{(1,4 - 1) / 1,4}$$

$$= 0,011673 \text{ (kWh/kg)}$$

The thermodynamic power;

$$= \text{Work (adiabatic)} \times \text{Flow Rate} \times \text{Density} \quad (22)$$

$$= 0,011673 \times 295.000 \times 1,27$$

$$= \mathbf{4.373 \text{ kW}}$$

The turbine power;

$$= \text{Turbine Eff.} \times \text{Thermodynamic Power} \quad (23)$$

$$= 0,90 \times 4.373 \text{ kW}$$

$$= \mathbf{3.936 \text{ kW}}$$

The generator power;

$$= \text{Generator Eff.} \times \text{Turbine Power} \quad (24)$$

$$= 0,95 \times 3.936 \text{ kW}$$

$$= \mathbf{3.739 \text{ kW}}$$

The output of the generator and the calculation of the annual return of the system depend on the turbine inlet pressure from the 0.8 bar to 2 bar up to 0.1 bar. The calculation results are shown in Table 4.

The BF gas flow rate : 295.000 Nm³/hour
 The turbine gas inlet pressure : 40°C
 The annual operating hour of the system: 8.000 hour/year

The electricity price : 0,11 USD/kWh (Energy Institute, 2014)

Table 4. Generator output power and annual gain

BF Top Pressure (Bar g)	Generator Output Power (Mwe)	Annual Gain (x1000 TL)	Annual Gain (x1000 USD)
0.8	3.739	12.213	3.290
0.9	4.102	13.399	3.610
1.0	4.442	14.510	3.909
1.1	4.760	15.548	4.189
1.2	5.060	16.528	4.453
1.3	5.342	17.449	4.701
1.4	5.609	18.322	4.936
1.5	5.863	19.151	5.159
1.6	6.103	19.935	5.371
1.7	6.332	20.683	5.572
1.8	6.550	21.395	5.764
1.9	6.759	22.078	5.948
2.0	6.958	22.728	6.123

The generator output power which depends on the BF top pressure and annual gain is given in Figure 9. As can be seen from the Figure 9, the generator output power and the annual gains are calculated in case of operating at the indicated pressures in 2014.

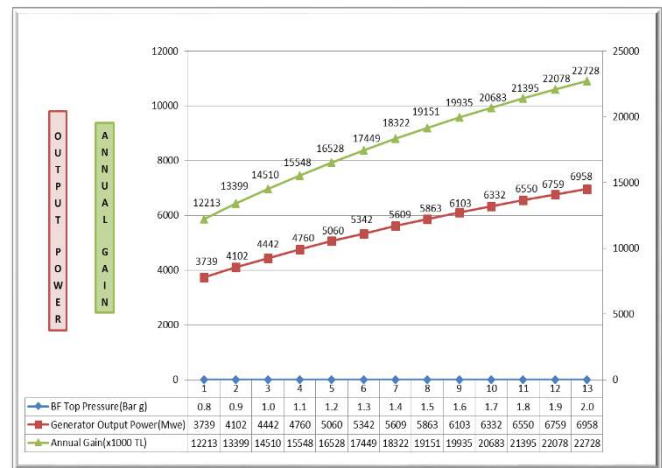


Figure 9. The generator output power belongs to the top pressure of the BF and annual gain

The investment cost analysis of TRT system is obtained by collecting direct materials (construction, steel construction, machinery and electricity), direct labor, transportation, depreciation expenses and overheads (about 20% of total production costs). The total amount of savings based on energy and cost is calculated by the return of the plant after a year of production.

The data obtained at the end of the cost analysis of the TRT system;

The total savings energy : 3.490 TOE/year
 The total saving amount energy: 40.568 MW/year

The total savings cost : 9.655.000 TL/year
 The total investment amount : 15.500.000 TL

Considering the cost and energy calculations related to the system, it is seen that the pay back period of the project is 1,6 year.

The carbon emission reduction due to annual operating hours and the electricity generation is given in Table 5. The annual working time is taken as 8.000 hours, the annual production is 40.568 MW and the amount of C reduction due to this production amount is calculated as 35.118 tons / year.

Table 5. Annually carbon emission decreasing belongs to turbine work time and electric generation.

System	Annually Work Time (Hour)	Generated Power (MW/year)	Carbon Emission (ton/year)
TBT	8.000	40.568	35.118

The Blast Furnace hourly top pressure and the generated power in January 2014 is given Table 6. As can be seen in Table 6 in January 2014, the generated power of the TRT system depends on the top pressure. It has been determined that there is a decrease in the average power output during the six days in January. Because of the blast furnace coolers damage on the 27th January, the furnace was operated at the low top pressure and the day average was realized as 1.0 bar. During the day, the average BF gas flow was realized 300.000 Nm³/hour and the average gas temperature of the turbine inlet was 33°C. The generated power of the turbine is an average of 5.8 MW on days with a daily pressure average of 1.5 bar. On the 27th day with a daily average of 1.0 generated power is to about 3.7 MW.

Table 6. The Blast Furnace hourly top pressure and the generated power in January 2014

Day	1	2	3	4	5	6	7
Top Pressure(Bar)	1.6	1.6	1.6	1.5	1.6	1.6	1.6
Generated Power(MW)	6.1	6.1	6.0	5.8	6.1	6.1	6.1
Day	8	9	10	11	12	13	14
Top Pressure(Bar)	1.6	1.6	1.6	1.5	1.6	1.6	1.6
Generated Power(MW)	6.1	6.1	6.1	5.8	6.1	6.1	6.1
Day	15	16	17	18	19	20	21
Top Pressure(Bar)	1.4	1.6	1.6	1.6	1.6	1.5	1.6
Generated Power(MW)	5.6	6.1	6.1	6.1	6.1	5.9	6.1
Day	22	23	24	25	26	27	28
Top Pressure(Bar)	1.6	1.6	1.6	1.6	1.6	1.0	1.6
Generated Power(MW)	6.1	6.1	6.1	6.0	6.1	3.7	6.1
Day	29	30	31				
Top Pressure(Bar)	1.6	1.5	1.6				
Generated Power(MW)	6.1	5.9	6.1				

The Blast Furnace hourly top pressure and the generated power chart in July 2014 is given Table 7. As can be seen in Table 7, the turbine system was stopped parallel to the blast furnace failure and the turbine system was stopped between 8th and 13th July. The monthly turbine power generation averaged 4.8 MW due to a six-day stance in July.

Table 7. July 2014 Blast Furnace hourly top pressure and generated power chart

Day	1	2	3	4	5	6	7
Top Pressure(Bar)	1.6	1.6	1.6	1.5	1.6	1.6	1.6
Generated Power(MW)	6.1	6.1	6.1	5.9	6.1	6.1	6.1
Day	8	9	10	11	12	13	14
Top Pressure(Bar)	0.0	0.0	0.0	0.0	0.0	0.0	1.1
Generated Power(MW)	0.0	0.0	0.0	0.0	0.0	0.0	4.3
Day	15	16	17	18	19	20	21
Top Pressure(Bar)	1.6	1.6	1.6	1.6	1.6	1.6	1.5
Generated Power(MW)	6.1	6.1	6.1	6.1	6.1	6.0	5.9
Day	22	23	24	25	26	27	28
Top Pressure(Bar)	1.5	1.6	1.6	1.6	1.6	1.6	1.6
Generated Power(MW)	5.9	6.1	6.0	6.1	6.1	6.1	6.1
Day	29	30	31				
Top Pressure(Bar)	1.6	1.5	1.6				
Generated Power(MW)	6.1	5.9	6.1				

The Blast Furnace hourly top pressure and the generated power chart in August 2014 is given Table 8. As can be seen at Table 8, there was no breakdown except for the pressure drops between 0.1 and 0.7 bar that occurred during the day and there was no stance programme planned. An average of 6.1 MW electricity was generated in August when electricity production was the most.

Table 8. The Blast Furnace hourly top pressure and generated power chart in August 2014

Day	1	2	3	4	5	6	7
Top Pressure(Bar)	1.6	1.6	1.6	1.6	1.6	1.6	1.6
Generated Power(MW)	6.1	6.1	6.2	6.1	6.0	6.0	6.1
Day	8	9	10	11	12	13	14
Top Pressure(Bar)	1.6	1.6	1.6	1.6	1.6	1.6	1.6
Generated Power(MW)	6.2	6.1	6.1	6.2	6.1	6.1	6.1
Day	15	16	17	18	19	20	21
Top Pressure(Bar)	1.6	1.6	1.6	1.6	1.6	1.6	1.5
Generated Power(MW)	6.1	6.1	6.1	6.1	6.1	6.1	6.0
Day	22	23	24	25	26	27	28
Top Pressure(Bar)	1.6	1.6	1.6	1.6	1.6	1.6	1.6
Generated Power(MW)	6.1	6.1	6.1	6.1	6.1	6.1	6.1
Day	29	30	31				
Top Pressure(Bar)	1.6	1.6	1.6				
Generated Power(MW)	6.1	6.2	6.0				

The TBT system reference list, which has been installed in China, has been specified in the Table 4. When the chart is examined, it is seen that this system can be used in blast furnace installations up to 450 m³ in volume.

Table 9. Sinosteel Mecc. Plant TRT system referance list (Anonymous 2014)

No	Plant	Power Produced (MW)	Type of Turbine	Gas Flow (Nm ³ /h)	Max.	Established Date
1	Xuanhua Iron&Steel Company, Zhangjiakou	3	Dry Type	450	2.580	Dec,2004
2	Xuanhua Iron&Steel Company, Zhangjiakou	7,5	Wet Type	1.350	2.500	Dec,2004
3	Xuanhua Iron&Steel Company, Zhangjiakou	10	Wet Type	330.000	1.800	Nov.,2005
4	Guofeng Iron&Steel, Tangshan	3	Dry Type	120.000	450	Sept.,2006
5	Pingxiang Iron&Steel Company, Pingxiang	3	Dry Type	120.000	450	Febr.,2007
6	Jiujiang Iron&Steel Company, Jiujiang	3	Dry Type	120.000	450	Febr.,2008
7	Changzou Iron&Steel Company, Changzou	18	Dry Type	460.000	2.350	April,2009
8	Jiujiang Iron&Steel Company, Jiujiang	12	Dry Type	330.000	1.780	March,2009
9	Iskenderun Iron and Steel Plant, Turkey	16	Wet Type	450.000	2.500	July, 2016
10	Eregli Iron and Steel Plant, Turkey	7	Wet Type	300.000	1.850	Jan., 2017

V. CONCLUSION

It is evident that the TRT system plays a big role in terms of these enterprises and the fact that TRT system has a large proportion of the integrated iron and steel plants operating in the world countries. The TRT system which plays a major role in energy saving as well as in the environmental factor, in reducing the carbon emission rate due to electricity consumption.

The sample BF was selected from iron and steel industry. The inlet temperature, the BF gas density, the BF gas flow entering the TRT system after the cleaning and the cooling process of the BF at the gas cleaning plant of one year hourly, daily, monthly and yearly top pressure, the BF gas parameters were examined and the data were recorded.

In this study, the annual average top pressure of the BF was 1,55 bar and the output power of this connected generator was calculated as 5.071 kWh for 2014 data. When the annual working time was taken as 8.000 hours, annual production amount was 40.568 MWh, equivalent value of petroleum was 3.490 TOE. The investment cost of the facility was 15.500.000 TL and the annual saving amount was 9.655.000 TL. The amount of C release reduction due to this production amount

was calculated as 35.118 tons / year, and the release of this amount of C was avoided each year by the fact that the plant was commissioned. Considering the cost and energy calculations related to the system, it was seen that the pay back period of the project is 1,6 year.

REFERENCES

- [1] Wu P. and Yang C., 2011. Identification and Control of Blast Furnace Gas Top Pressure Recovery Turbine Unit, ISIJ International, Vol. 52, No. 1, p. 96–100.
- [2] Guo Z.C. and Fu Z.X., 2010. Current Situation Of Energy Consumption And Measures Taken For Energy Saving In The Iron And Steel Industry In China, Energy, 35, p.4356-4360.
- [3] Wu Y., 1994. Actuality Analysis And Potentiality Exploration of WISCO No.3 Blast Furnace, WISCO Technology, Vol.3, p. 58-64.
- [4] World Energy Council, 2010. Energy Efficiency Policies around the World; Review and Evolution.
- [5] Zhang L., 1994. On Establishment And Operation Of Top Pressure Recovery Turbine Of Blast Furnace No.1 in Tangshan Iron & Steel Co., Metallurgy Energy, Vol.13 No.5, 52-55.
- [6] Xu W., 1998. Several Attentive Problems In The Process Of Expanding Of National TRT", Ironmaking, Vol.17 No.1, 31-33.
- [7] Xu C. and Cang D., 2010. Brief Overview of Low CO₂ Emission Technologies for Iron and Steel Making, Journal of Iron and Steel Research. International. 17(3), P.1-7
- [8] Liu X. and Gao X., 2016. A Survey Analysis Of Low Carbon Technology Diffusion In China's Iron&Steel Industry. Journal of Cleaner Production 129 (2016) p.88-101.
- [9] Cai L., Xiao J., Wang S., Goa S., Duan J. and Moa J., 2016. Gas-Particle Flows And Erosion Characteristic Of Large Capacity Dry Top Gas Pressure Recovery Turbine. Energy, 2016, p.1-9.
- [10] Arens M., Worrell E. and Schleich J., 2012. Energy Intensity Development Of The German Iron And Steel Industry Between 1991 And 2007, Energy, 45, 2012, p.786-797.
- [11] Oda J., Akimoto K., Sano F. and Tomoda T., 2007. Diffusion Of Energy Efficient Technologies And CO₂ Emission Reductions In Iron And Steel Sector, Energy Economics, 29 (2007) p.868–888.
- [12] Johansson M.T. and Söderström M., 2010. Options For The Swedish Steel Industry Energy Efficiency Measures And Fuel Conversion, Energy, 36 (2011), p.191-198.
- [13] BSIET, 2010-10. Introduction of Technical Proposal for Technology of BF TRT Unit.

The Investigation of Microstructure of Duplex Stainless Steel Welded by FCAW Method

M. Tümer¹, R. Yılmaz²

¹Kocaeli University, Department of Welding Technology, Uzunçiftlik Nuh Çimento Vocational High School, Kocaeli, Türkiye, mustafa.tumer@kocaeli.org.tr

²Sakarya University, Department of Metallurgical and Materials Engineering, Technology Faculty, Sakarya University, Esentepe, Sakarya, Türkiye, r.yilmaz@sakarya.edu.tr

Abstract — In this study, AISI 2205 duplex stainless steel material welded using E2209T1-1 / 4 wire with flux cored arc welding (FCAW) welding method. The austenite and ferrite phase contents of the duplex stainless steel structure was characterized. The image of the weld metal and inclusions was taken with transmission electron microscopy (TEM), and its characterization was obtained with energy-dispersive spectrometry (EDS). Characterization processes were supported with elemental mapping and selected field diffractions. In particular, the effect of ferrite and austenite former elements in grain structure is investigated.

Keywords — Duplex stainless steel, FCAW, microstructure, ferrite, austenite

I. INTRODUCTION

Duplex stainless steels (DSS) are based on Fe-Cr-Ni alloy system and consist of nearly equal amounts of ferrite and austenite phases at room temperature. Those type of steels offer an excellent combination of mechanical properties, general corrosion, pitting corrosion and stress-corrosion cracking resistance, which are superior to that of austenitic stainless steels. Due to the significant improvements both in material design and weldability of duplex stainless steels, those materials are involved in many applications in which especially stress corrosion cracking and pitting corrosion are required since 1980. Duplex stainless steels have been widely used in offshore oil and gas, chemical petrochemical and pulp and paper industries, high velocity injection in geothermal wells and gas transmission lines, power generation due to their superior combination properties mentioned above (1-10).

Since the usage of duplex stainless steels in some construction system often requires welding as a fabrication process. The joining of duplex stainless materials with conventional welding techniques has been studied by various researchers [8–16]. In terms of welding techniques during fabrication of those materials is very important for reducing cost and time consuming. Flux-cored arc welding (FCAW) has a number of advantages such as outstanding productivity, deep penetration, spatter reduced welding behavior, higher deposition rates and

high welding speed over the other common welding techniques. FCAW should also have cost advantages over other welding processes (17-21). FCAW method has received great attention from welders and contractors recently compare to conventional GMAW due to its advantages mentioned above, therefore, its usage is increasing year by year. FCAW method is also suitable for mechanization and robotization and easy for applying, thus provide efficiency and speedy during welding process of the sheets having high thickness such as DSS used in the shipbuilding industry (19-24).

In this study, DSSs was welded by FCAW. Characterization of the austenite and ferrite phases in the microstructure of the obtained weld metal is performed.

II. EXPERIMENTAL STUDIES

AISI 2205 grades duplex stainless steel (ferritic-austenitic) were used in this study. E2209T1-1/4 duplex stainless steel flux cored wire with diameter of 1.2 mm was used as a filler material. The chemical composition of base materials and filler materials were given in Table 1. S32205 grades duplex stainless steels plates were prepared for joining of FCAW with dimension of 400x150x11 mm³. V shaped groove were used and four passes of FCAW were performed using ceramic backing strips to ensure proper shape of the root of weld during the process, without necessary cutting out and re-welding of the weldments.

The welding parameters used were selected according to suggestions of product catalogue prepared by flux cored wire consumable producer and experiences obtained earlier. As seen from the table, welding current and voltage were between 200-230 and 32-34 volt respectively. Heat input varies between 1,3-2 kJ/mm.

Multipass welding was carried out (4 passes) in flat position (PA). The plates were welded firstly in the root pass later second pass and then third pass, finally cover pass respectively were conducted. Welding process were carried out under gases pure CO₂ with gas flow rate of 15 lt/min. The interpass temperature was maintained lower than 150 °C .

TEM study was performed on the section parallel to the fusion zone using thin foils prepared by mechanical polishing followed by twin-jet electro polishing using an electrolyte consisting of a mixture of 80% methanol and 20% perchloric acid, which was held at a temperature of $-30\text{ }^{\circ}\text{C}$.

determined by other analysis methods.

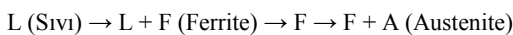
TABLE I.

DSS AND FILLER METAL CHEMICAL COMPOSITION

Elements (%)	Filler Metal	DSS
C	0.027	0,0186
Si	0.58	0,313
Mn	0.78	1,44
P	0.019	0,022
S	0.008	0,008
Cr	23.34	23,41
Ni	9.42	4.804
Mo	3.42	2.71
N	0.14	0,228
Cu	0.02	0,229

III. III. RESULTS AND DISCUSSION

All duplex stainless steels are solidified through the formation of a ferrite phase from the liquid phase first and the solidification is completed in fully ferritic form. Depending on the composition, ferrite is stable at some high temperature intervals before the start of ferrite dissolution and austenite transformation temperatures. The transformation from ferrite to austenite depends on the composition and the rate of cooling of both. Ferrite-austenite balance and the diffusion of austenite in the weld metal determines this transformation. This transformation sequence occurs in duplex stainless steels as follows (Lippold ve Kotecki 2005).



The ferrite/austenite ratio depends on the energy input in welding, since it controls the cooling rate and ferrite/austenite transformation. Cooling time has strong effects on the toughness that the ferrite content and microhardness decreases with the increasing of cooling time. On the other hand, such conditions also tend to produce coarse grained weld deposits and possibly precipitation of brittle intermetallic phases. Then it is desirable to control welding conditions such that cooling is slow enough for adequate austenite formation, but fast enough to prevent deleterious precipitation [9,11].

Figure 2 shows the TEM images taken from the weld metal of the DSS material welded by the FCAW method in order to see the detailed microstructure of the phases formed in the weld metal during the welding of the duplex stainless steels and to investigate some of the depositions or phases which cannot be

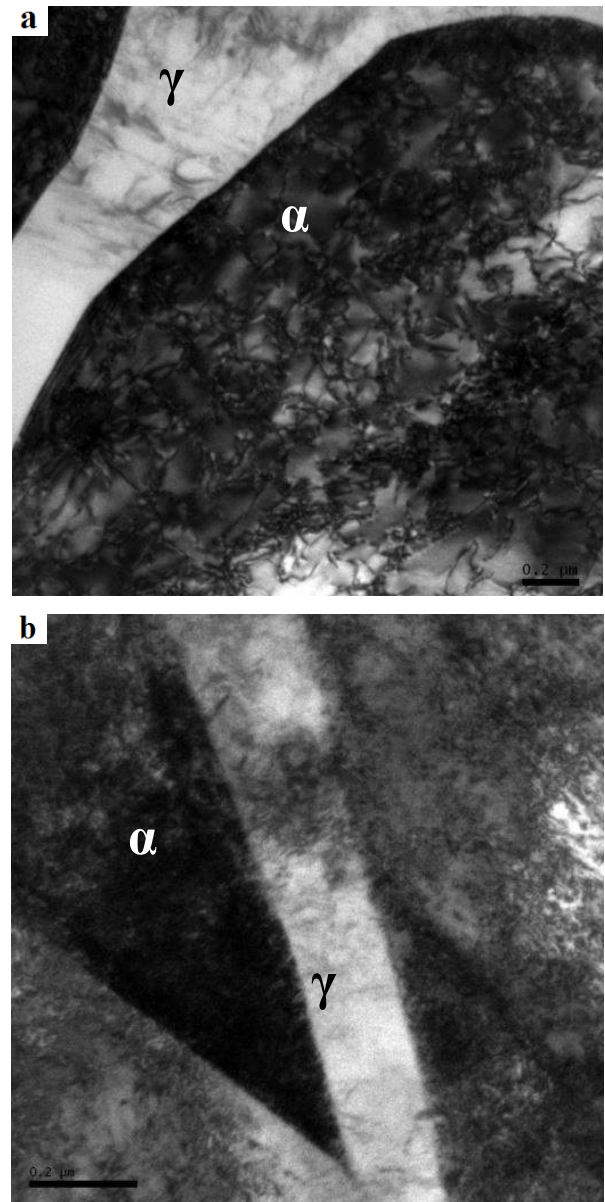


Fig.1. Weld metal microstructure

Looking at the microstructures, light colored areas represent austenite and dark colored areas represent ferrite. There were no indication in the literature about the depositions of Cr_2N , M_{23}C_6 , σ (sigma), χ (chi), etc. Although the joining process is carried out with many passes, keeping the temperature difference between the passes below $150\text{ }^{\circ}\text{C}$ and lack of any heat treatment prevented the formation of these depositions. Figure 2 shows the TEM image of the DSS weld metal, the selected area diffraction pattern and the EDS spot analysis results of the marked areas. Looking at the figures, it is seen that the arrangement of the atoms in the crystal lattice plane differs. The percentage distribution of the elements in EDS analysis from dark and light colored regions gives more accurate results about

the crystal lattice structure of the phases.

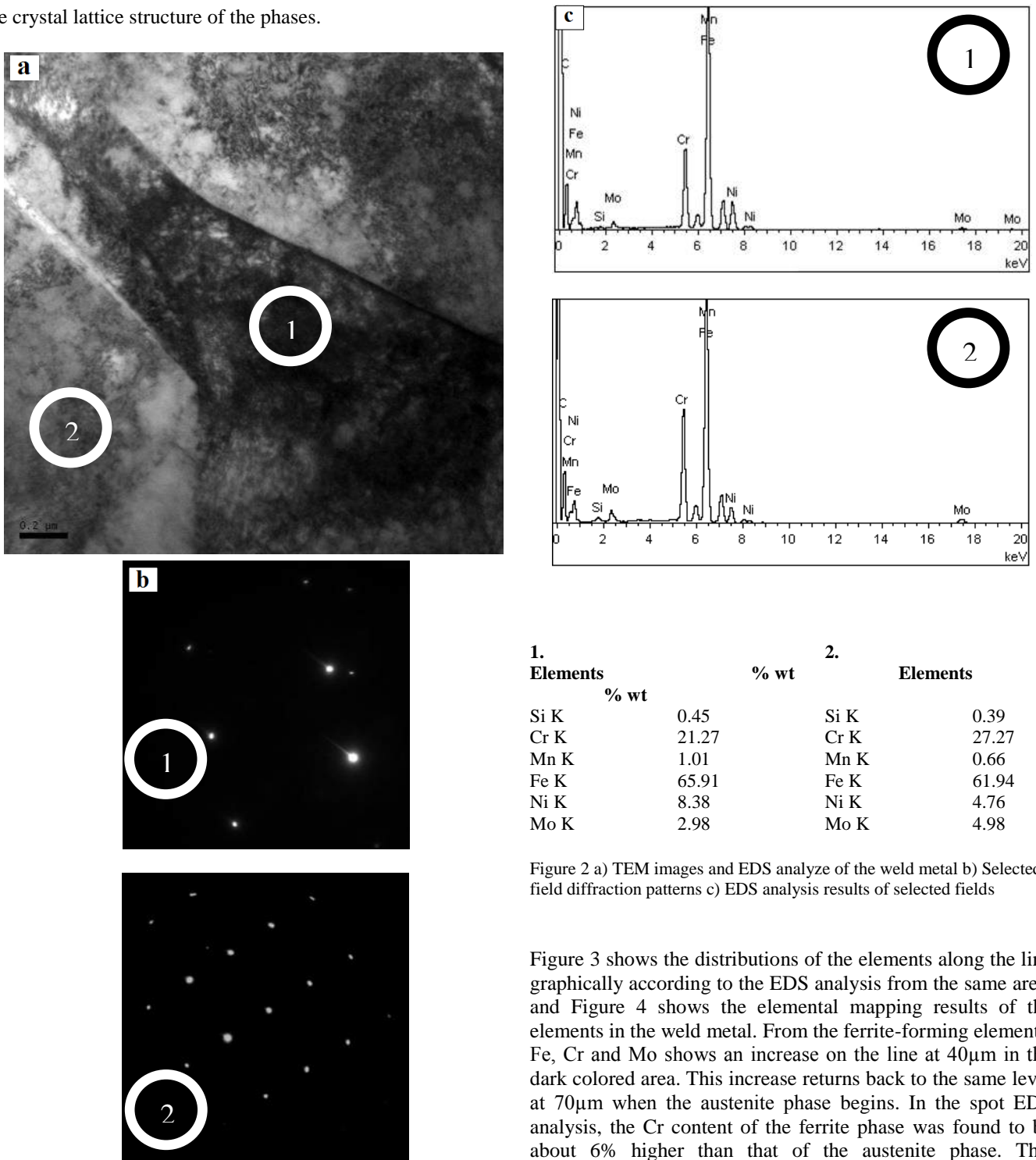


Figure 2 a) TEM images and EDS analyze of the weld metal b) Selected field diffraction patterns c) EDS analysis results of selected fields

According to EDS spot analysis results obtained from the 1st area, the Cr and Ni amounts were 21% - 8.4% respectively, whereas the Cr and Ni values obtained from 2nd area were found to be 27% - 4.8%. Cr ferrite is known to be the most effective element in Ni austenite formation (5,9) In these results, area 1 shows austenite, and area 2 shows ferrite phase.

Figure 3 shows the distributions of the elements along the line graphically according to the EDS analysis from the same area, and Figure 4 shows the elemental mapping results of the elements in the weld metal. From the ferrite-forming elements, Fe, Cr and Mo shows an increase on the line at 40μm in the dark colored area. This increase returns back to the same level at 70μm when the austenite phase begins. In the spot EDS analysis, the Cr content of the ferrite phase was found to be about 6% higher than that of the austenite phase. This difference is supported by the results of linear analysis and graphs. The Ni element shows an increase in austenite areas and a decrease in ferrite areas. When the graphs of Mn and Si elements are examined, it is seen that the peaks representing the density do not provide clear results.

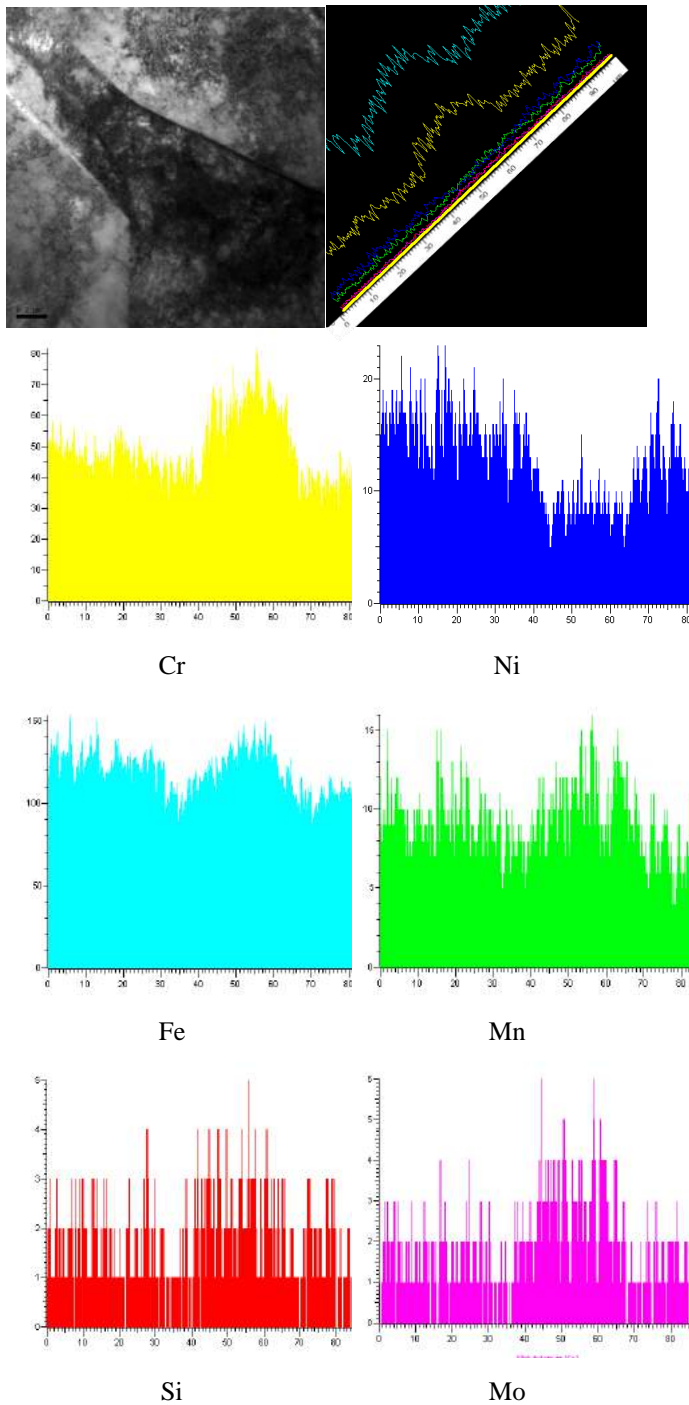


Figure 3. TEM-EDS line scan showing variation alloying elements across the weld metal and EDS analysis of linear graphs of the elements

According to the results of elementary mapping performed to see elementary distribution in weld metal, Cr and Ni elements increase and decrease according to phase formation in matrix. While the Cr element clearly increases in the ferrite phase, the other ferrite-forming elements, Si and Mo, increase only slightly. The austenite and ferrite balance of the microstructure of the weld metal affects the mechanical and corrosion properties. Ferritic structure provides strength and resistance to

tensile corrosion cracking and austenitic structure provides toughness and general corrosion resistance. Thus, a two-phase fine-grained, high-strength weld metal with good corrosion resistance is obtained.

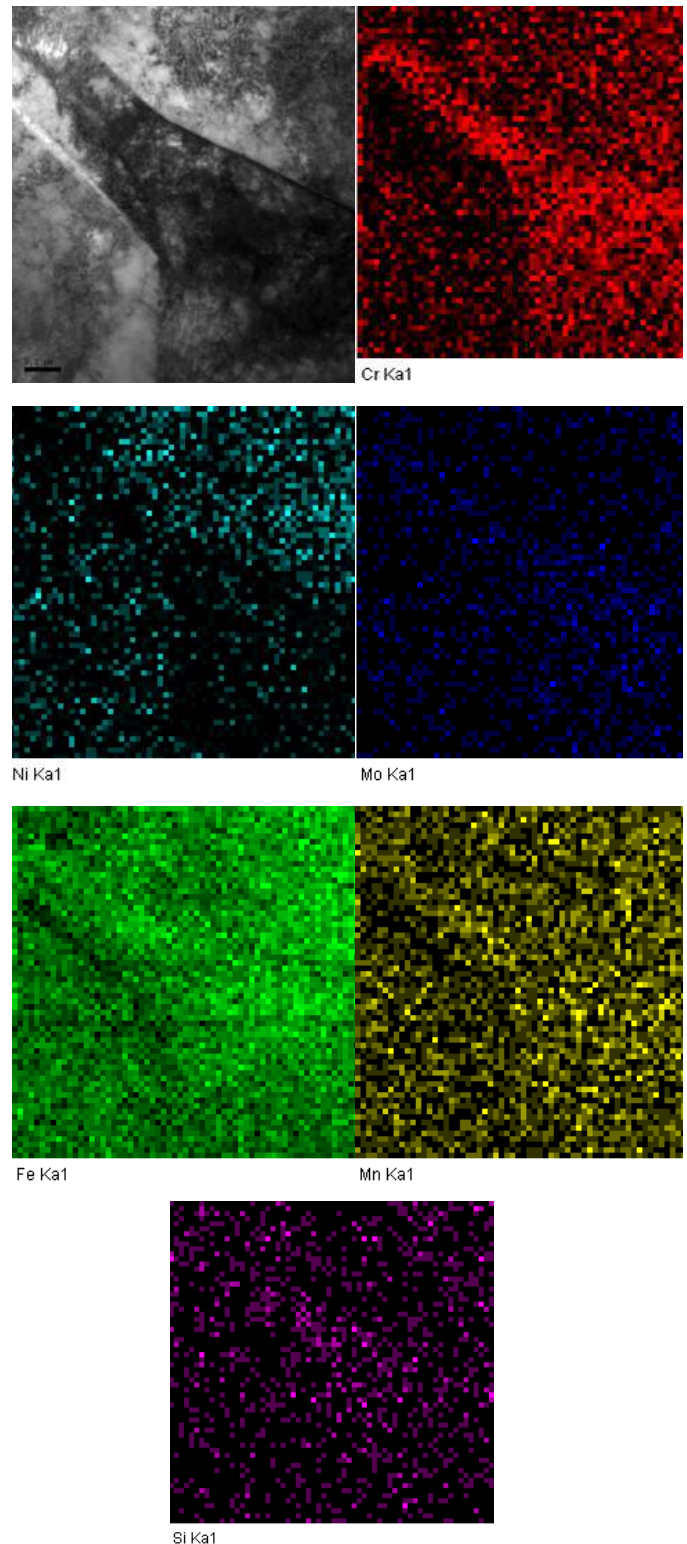
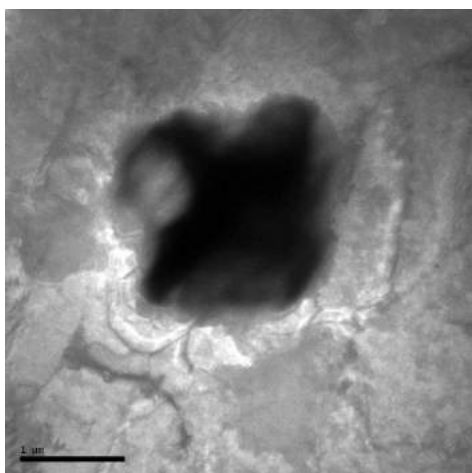
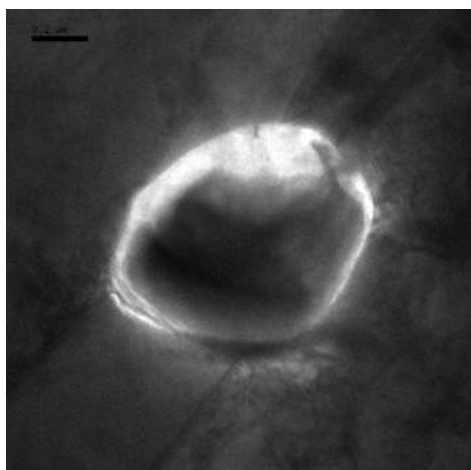


Figure 4. TEM mapping analysis taken from the weld metal

Figure 5 shows the inclusions in the DSS weld metal. The forms of the inclusions vary within the structure. There are micro inclusions with sharp angular, spherical or undefined forms.



IV.

Figure 5. TEM image of inclusions

V. CONCLUSIONS

Characterization of ferrite/austenite phases and inclusions was carried out with TEM/EDS analysis. Fe, Cr, Mo, which are the most significant ferrite forming elements, and the most significant austenite forming element Ni were detected both in linear analysis and mapping analysis. The inclusions identified by TEM are generally in spherical form in the microstructure.

VI. ACKNOWLEDGMENT

This work was carried out as a part of Project (grant no: Commission for Scientific Research Project (BAPK) 2011-50-02- 018) supported by the Sakarya University. Both authors would like to thank the University, and M. Tümer would like to thank the Gedik Welding Inc.

VII. REFERENCES

- [1] N. R. Gunn: Duplex Stainless Steels, Abington Publishing, 110, (1997), England
- [2] J.R. Davis: ASM Speciality Handbooks: Stainless Steels; Davis Assoc., OH: American Society for Metals Materials Park, (ASM), Ohio, 1994.
- [3] J. A. Jimenez, M. Carsi, O. A. Ruano: Characterization of a δ/γ duplex stainless steel, Journal of Materials Science 35 (2000) 907– 915
- [4] E. Folkhard: Welding Metallurgy of Stainless Steels; Springer-Verlag: Vienna, New York, 1984; pp. 186.
- [5] J.C. Lippold , D.J. Kotecki : Welding Metallurgy and Weldability of Stainless Steels, John Wiley&Sons, USA, 230–253, 2005
- [6] Z. Sun, M. Kuo, I. Annergren, D. Pan: Effect of Dual Torch Technique on Duplex Stainless Steel Welds, Materials Science and Engineering A356 (2003) 274-282
- [7] H. Sieurin, R. Sandstrom: Austenite Reformation in the Heat-Affected Zone of Duplex Stainless Steel 2205, Materials Science and Engineering A 418 (2006) 250–256
- [8] E. Capello, P. Chiarello, B. Previtali, M. Vedani: Laser Welding and Surface Treatment of a 22Cr-5Ni-3Mo Duplex Stainless Steel, Materials Science and Engineering, A351 (2003) 334-343
- [9] E. Taban : Joining of Duplex Stainless Steel by Plasma Arc, TIG, and Plasma Arc+TIG Welding Processes, Materials and Manufacturing Processes, Materials and Manufacturing (2008) Processes, 23: 871–878
- [10] E. Taban, Toughness and microstructural analysis of superduplex stainless steel joined by plasma arc welding. Journal of Materials Science, 2008 43 (12) 4309–4315.
- [11] P.B. Srinivasan, V. Muthupandi, W. Dietzel, V.Sivan: An Assessment of Impact Strength and Corrosion Behaviour of Shielded Metal Arc Welded Dissimilar Weldments Between UNS 31803 and IS 2062 Steels, Materials and Design, 2006 27 182–191
- [12] J.D. Kordatos, G. Fourlaris, G. Papadimitrou: The Effect of Cooling Rate on the Mechanical and Corrosion Properties of SAF 2205 (UNS 31803) Duplex Stainless Steel. Scripta Materialia 2001 44 401–408.
- [13] V. Muthupandi, P.B. Srinivasan, S.K. Seshadri, Sunderasan, S: Effect of weld metal chemistry and heat input on the structure and properties of duplex stainless steel welds. Materials Science and Engineering, 2003 A358 9–16.
- [14] S.S.M.Tavares, J.M. Pardal, L.D. Lima, I.N. Bastos, A.M. Nascimento, J.A. de Souza: Characterization of Microstructure and Toughness of a Multipass Weld Joint of Superduplex Stainless Steel UNS S32750, Materials Characterization, 2007, 58, 610–616.
- [15] A.Urena, E. Utero, M.V. Utrilla, C.J. Munez: Weldability of a 2205 Duplex Stainless Steel Using Plasma Arc Welding, Journal of Materials Processing Technology, 2007 182 624–631.
- [16] P. Sathiya, S. Aravindan , R. Soundararajan, A. Noorul Haq: Effect of shielding gases on mechanical and metallurgical properties of duplex stainless-steel welds, J Mater Sci (2009) 44:114–121
- [17] J Nowacki: Duplex-steel welding problems in the building of chemical cargo ship, Welding International 2004 18 (7) 509–515
- [18] J. Nowacki, M. Urbanski, P. Zaja: FCAW welding of duplex steel in construction of chemical cargo carriers, Welding International 2009 23 (7) 34–42.
- [19] A. Aloraier, R. Ibrahim, P. Thomson: FCAW Process to Avoid the Use of Post Weld Heat Treatment, International Journal of Pressure Vessels and Piping, 2006 83 394–398
- [20] D. Dunne, H. Tsuei, H. Li: Structural Characteristics of Multipass Flux Cored Arc Steel Welds, Science and Technology of Welding and Joining, 2003 8 2 123-132
- [21] B. Arivazhagan, S. Sundaresan, M. Kamaraj: A study on influence of shielding gas composition on toughness of flux-cored arc weld of modified 9Cr–1Mo (P91) steel, Journal of Materials Processing Technology, 209 2009 5245–5253
- [22] M.T Liao, P.Y. Chen: A Comparison of Gas Metal Arc Welding with Flux-Cored Wires and Solid Wires Using Shielding Gas, Int J Adv Manuf Technol (1999) 15:49–53
- [23] F. Hägg, H. Åström: Welding duplex stainless steel”, LDX 2101® using a matching positional flux cored wire, 625-630
- [24] DW Stainless – Flux Cored Stainless Wires, DOC. No.032001-N046, Kobelco Steel, LTD. Welding Company.

An Investigation into the Effect of Welding Parameters on Mechanical Properties of Dissimilar Resistance Spot Welded DP1000–QP1180 Steel Joints

Imren OZTURK YILMAZ*, Abdullah Yasin BILICI*, Hakan AYDIN⁺

**Beycelik Gestamp Inc.*

*BTSO Organize Sanayi Bolgesi Kahverengi cad. No:13 Nilufer/BURSA/TURKEY
{imrenyilmaz, abduallahbilici}@beycelikgestamp.com.tr*

⁺*Mechanical Engineering Department, Uludag University
Gorukle Kampusu 16059 Nilufer/BURSA/TURKEY
hakanay@uludag.edu.tr*

Abstract— In recent years, steel manufacturers have been focused to develop the 3rd Generation Advanced High Strength Steels (AHSS) for automotive industry. In this study, parametric studies have been done on the electrical resistance spot welding of the DP1000 steel, which is widely used in the automotive industry, with the newly developed QP1180 steel. Welding studies were carried out by the process window method with different welding time and welding current while keeping other parameters constant. The effects of welding current and welding time on the mechanical properties of spot welded joints were investigated. In order to determine the mechanical properties of spot welded joints, welding specimens were subjected to tensile shear tests. In this context, the relationships between welding parameters, nugget size and mechanical properties of the spot welded joints were established.

Keywords— DP1000 steel, QP1180 steel, Electrical Resistance Spot Welding, Welding Parameters, Mechanical Properties, Nugget Size.

I. INTRODUCTION

Throughout the world there is increasing interest in the development of new Advanced High Strength Steels (AHSS) with enhanced combinations of strength and ductility to provide sheet materials for demanding applications in future vehicles [1]. In recent years, global steel manufacturers have been focused to develop the 3rd Generation AHSS for automotive industry in order to reduce vehicle weight due to strict regulations of fuel efficiency for lower CO₂ emission and improve passenger safety standards [2,3]. QP1180 steel sheet combining excellent strength and formability is one of the 3rd Generation AHSS for cold stamping. Quenching & Partitioning (Q&P) has been proposed recently as a new way of producing martensitic steels containing enhanced levels of retained austenite [1,4-6]. As a result of the development of new commercial 3rd Generation AHSS for applications in car body manufacturing, QP1180 steel sheets will become popular in

automotive body structure applications in the near future. Currently, several grades of Dual Phase (DP) steel, a class of AHSS, are strong contenders for fabrication of lightweight automobile parts, which can meet the demands of weight, ductility and strength [7]. DP1000 sheet steels are also gaining popularity in manufacturing automotive body components where a higher strength is necessary, e.g. A and B pillars and bumpers [8-10]. DP steels are mainly composed of dispersed islands of martensite in a ferritic matrix [8,11-15]. The ductility is controlled by the ferrite, while the strength is controlled by the martensite [8,15,16].

The use of steel sheets for car body manufacturing in the automotive applications inevitably involves welding [8,17]. Resistance spot welding (RSW), which is a cost effective way to join two or more overlapping pieces of metal sheet together, is a common and large-scale joining method in the automotive industry. Car bodies are built by assembling several sheet steel parts by RSW. Therefore, performing dissimilar RSW of DP1000 and QP1180 steels is an inevitable demand within a few years in the modern automotive industry because of their superior functional capabilities. Many studies have been conducted to investigate the weld properties of dissimilar RS welded AHSS [8,18-23], but there is not available work on dissimilar RS welded DP1000-QP1180 sheet steels. The application of these steel sheets, especially QP1180 steel, in the automotive industry requires a more complete understanding of the issues associated with the RSW of dissimilar DP1000–QP1180 steel sheets. Therefore, the present study aims to examine the effect of welding current and welding time on the mechanical properties of RS-welded dissimilar DP1000–QP1180 joints. The mechanical properties of the spot welds were evaluated through tensile shear tests.

II. EXPERIMENTAL DETAILS

In the present study, 1.2 mm thick QP1180 steel sheet and 1 mm thick DP1000 steel sheet were used as the base metals. In order to determine the mechanical properties of the base metals, the tensile test specimens were cut along the rolling direction of the sheets. ASTM E8M sheet type specimen was taken into consideration as shown Fig.1 while the dimension of the tensile test specimen of the base metals was determining [24]. So, the mechanical properties of the base metals is given in Table I.

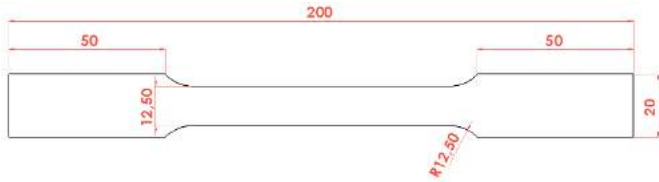


Fig. 1 Dimension of the tensile test specimen of the base metals (ASTM E-8M sheet type specimen) [24].

The steel sheets were cut into pieces for welding process laser cutting machine with the dimensions 100 mm x 40 mm. These cut sheets were cleaned properly with ethanol to remove dirt, oil, oxide and surface scale before welding. Welding was performed by overlapping the sheets using a RSW machine, as shown in Fig. 2. Cu alloy electrodes with tip diameter of 6 mm were used in the RSW process. Welding studies were carried out by the process window method with different welding time and welding current while keeping other parameters constant. The welds were performed with welding currents of 7 kA, 8 kA, 9 kA, 10 kA and 11 kA, with welding times of 12 cycle, 20 cycle and 28 cycle, and with the electrode force of 2.5 kN.

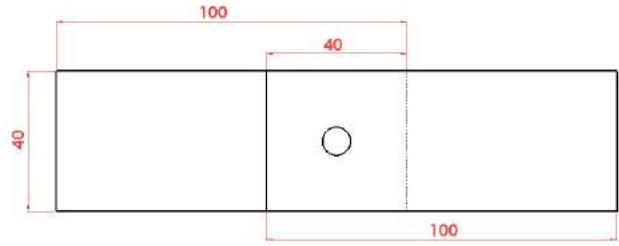


Fig. 2 The welded tensile shear test sample.

III. RESULTS AND DISCUSSION

In the tensile shear tests of the joints, all resistance spot-welded QP1180/DP1000 joints exhibited a full button pull-out failure mode referring to higher deformation energy, in which fracture occurs in the HAZ at the around of the spot weld. The effect of welding parameters on the NS of the spot welded joints is shown in Fig. 3. The NS increased almost linearly with an increasing of the welding current: The coefficient of determination (R^2) for the correlation between the NS and the welding current varies between 0.83 and 0.95 by fitting a linear model using regression analysis to the obtained results, as shown in Fig. 3a. However, at 28 cycle of welding time, NS decreased at 11 kA of welding time owing to the highest heat input. The increase in NS with increasing welding current from 7 kA to 11 kA at relatively lower welding times is around 30%, whereas this increase with increasing welding current from 7 kA to 10 kA at highest welding time is relatively limited, roughly 18%. Similarly, at lower welding currents (7 and 8 kA), the NS increased almost linearly with an increasing of the welding time: The coefficient of determination (R^2) for the linear correlation between the NS and the welding time is 0.99 and 0.93, respectively Fig. 3b. With an increasing of welding time from 12 cycle to 28 cycle, the increase in NS at 8 kA of welding current is 8.1%, whereas the increase in NS at 7 kA is rather lower, 1.2%. On the other hand, at higher welding currents (9 and 10 kA), the NS decreased almost linearly with an increasing of the welding time: The coefficient of determination (R^2) for the correlation between the NS and the welding time is 1.0 and 0.87, respectively Fig. 3b. With an increasing of welding time from 12 cycle to 28 cycle, the decrease in NS at 9 kA and 10 kA of welding currents is around 6%. However, at 11 kA of welding current, a linear relationship between the NS and the welding time is very weak ($R^2=0.40$). With an increasing of welding time from 12 cycle to 28 cycle, the decrease in NS at 11 kA is roughly 9%. Finally, it is possible to say that the effect of welding current on the NS of the resistance spot-welded QP1180/DP1000 joints is greater than that of welding time.

The effect of welding parameters on the tensile shear load (TSL) of the spot welded joints is shown in Fig. 4. The TSL values obtained with the welding parameters used in this study varies roughly between 16 kN and 20 kN and the maximum TSL (19.81 kN) was obtained with the parameter combination of 10 kA and 20 cycle. The TSL of the spot welded joints

TABLE I
MECHANICAL PROPERTIES OF THE BASE METALS USED IN THIS STUDY (MEAN VALUES).

Steel	Yield Strength (Rp0.2) [MPa]	Ultimate Tensile Strength (UTS) (Rm) [MPa]	Total Elongation (A) [%]
DP1000	788	1012	17,6
QP1180	1022	1224	14,5

In order to evaluate the mechanical properties of the spot welds and base metals, the tensile tests were carried out on a fully computerized Zwick tensile testing machine, at room temperature and with a crosshead displacement speed of 5 mm/min. The nugget size (NS) of the spot welds was measured through the fractured specimens in all welding conditions using a digital calliper.

increased almost linearly with an increasing of the welding current: The coefficient of determination (R^2) for the linear correlation between the NS and the welding current varies between 0.81 and 0.93, as shown in Fig. 4a. This increase could be attributed to the increase of the NS owing to the higher heat input with increasing of welding current. At 12 and 20 cycle, the TSL reached the maximum value at 10 kA of welding

current: With an increasing of welding current from 7 kA to 10 kA, the increase in TSL at 12 and 20 cycle of welding time is 21% and 24%, respectively. On the other hand, with an increasing of welding current from 7 kA to 11 kA, the increase in TSL at 28 cycle is 18%. On the other hand, in general, at lower welding currents (7 kA, 8 kA and 9 kA), the welding time

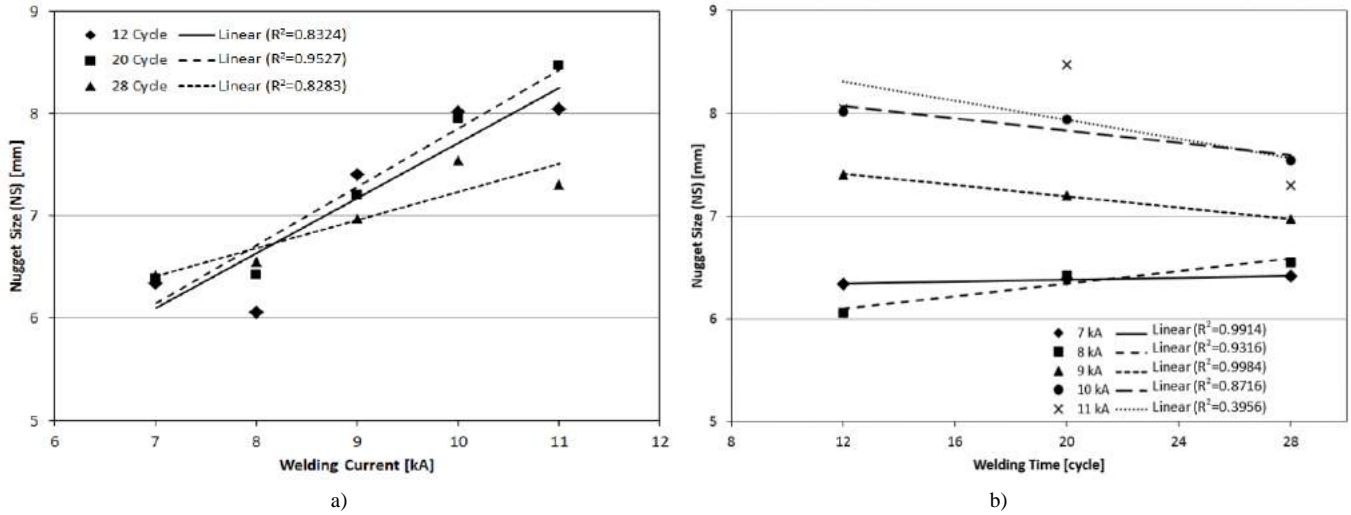


Fig. 3 The effect of welding current (a) and welding time (b) on NS of the resistance spot-welded QP1180/DP1000 joints.

did not significantly affect the TSL of the joints: TSL values in different welding times are too close to each other. It should also be noted that TSL value was relatively higher at 20 cycle of welding time. At higher welding currents (10 kA and 11 kA), it can be said that TSL of the joints decreased at the highest welding time (28 cycle). This decrease could be associated with the decrease of NS and increase of the indentation depth with excessive expulsion due to the overheating of welding zone.

A remarkable relationship was obtained between the NS and the TSL of the spot welded joints: As shown in Fig. 5, the coefficient of determination (R^2) for the correlation between the NS and the TSL is 0.88 by fitting a linear model using regression analysis to the obtained results in Fig. 5. So, it can be said that TSL of the joints increased almost linearly with an increasing of NS. The maximum TSL was obtained with 8 mm of NS.

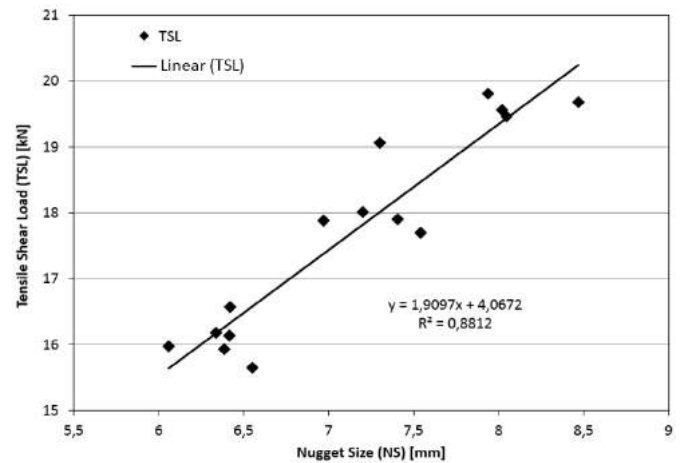


Fig. 5 The effect of nugget size (NS) on tensile shear load of the resistance spot-welded QP1180/DP1000 joint.

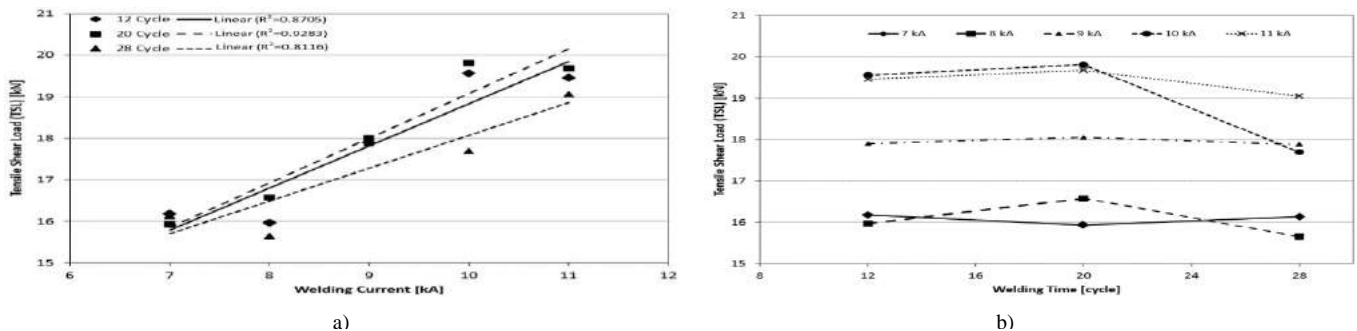


Fig. 4 The effect of welding current (a) and welding time (b) on tensile shear load of the resistance spot-welded QP1180/DP1000 joints.

IV. CONCLUSIONS

The present study was focused to examine the effect of welding parameters on mechanical properties of dissimilar resistance spot welded DP1000/QP1180 steel sheet joints. The conclusions derived from this study can be given as follows:

- The NS of the spot welded joints increased almost linearly with an increasing of the welding current. However, NS started to decrease at a combination of highest welding current and welding time (11 kA and 28 cycle).
- The increase in NS with increasing welding current at a relatively lower welding times is more effective, whereas this increase at the highest welding time is relatively limited.
- At relatively lower welding currents, the NS increased almost linearly with an increasing of the welding time, whereas at higher welding currents the NS decreased almost linearly with an increasing of the welding time. In addition this, at the highest welding current there is not a linear relationship between the NS and the welding time, but the NS tends to decline with the increase of welding time.
- The effect of welding current on the NS is greater than that of welding time.
- The parameter combination of 10 kA and 20 cycle lead to maximum TSL with 19.81 kN.
- The TSL of the joints increased almost linearly with an increasing of the welding current.
- At relatively lower welding current, there is not any significant effect of welding time on the TSL of the joints, but TSL is relatively higher at 20 cycle. At relatively higher welding current, TSL of the joints is relatively lower at 28 cycle.
- TSL of the joints increased almost linearly with an increasing of NS and around 8 mm of NS lead to the maximum TSL.

REFERENCES

- [1] D. K. Matlock, J. G. Speer, E. De Moor, and P. J. Gibbs, "Recent developments in advanced high strength sheet steels for automotive applications: an overview," *Jestech*, vol. 15, no. 1, pp. 1–12, 2012.
- [2] N. K. Tewary, S. K. Ghosh, S. Bera, D. Chakrabarti, and S. Chatterjee, "Influence of cold rolling on microstructure, texture and mechanical properties of low carbon high Mn TWIP steel," *Mater. Sci. Eng. A*, vol. 615, pp. 405–415, 2014.
- [3] O. Grässel, L. Krüger, G. Frommeyer, and L. W. Meyer, "High strength Fe-Mn-(Al, Si) TRIP/TWIP steels development - properties - application," *Int. J. Plast.*, vol. 16, no. 10, pp. 1391–1409, 2000.
- [4] F. G. Caballero and C. Garcia-Mateo, "Ultra-high – strength Bainitic Steels," *ISIJ Int.*, vol. 45, no. 11, pp. 1736–1740, 2005.
- [5] J. Speer, D. K. Matlock, B. C. De Cooman, and J. G. Schroth, "Carbon partitioning into austenite after martensite transformation," *Acta Mater.*, vol. 51, no. 9, pp. 2611–2622, 2003.
- [6] J. G. Speer, E. De Moor, K. O. Findley, D. K. Matlock, B. C. De Cooman, and D. V. Edmonds, "Analysis of microstructure evolution in quenching and partitioning automotive sheet steel," *Metall. Mater. Trans. A Phys. Metall. Mater. Sci.*, vol. 42, no. 12, pp. 3591–3601, 2011.
- [7] I. Rocha, I. Machado, and C. Mazzaferro, "Mechanical and metallurgical properties of DP 1000 steel square butt welded joints with GMAW," *Int. J. Eng. Technol.*, vol. 4, no. 1, p. 26, 2014.
- [8] H. Aydin, "The mechanical properties of dissimilar resistance spot-welded DP600-DP1000 steel joints for automotive applications," *Proc. Inst. Mech. Eng. Part D J. Automob. Eng.*, vol. 229, no. 5, pp. 599–610, 2015.
- [9] D. Anand, D. L. Chen, S. D. Bhole, P. Andreychuk, and G. Boudreau, "Fatigue behavior of tailor (laser)-welded blanks for automotive applications," *Mater. Sci. Eng. A*, vol. 420, no. 1–2, pp. 199–207, 2006.
- [10] D. Parkes, W. Xu, D. Westerbaan, S. S. Nayak, Y. Zhou, F. Goodwin, S. Bhole, and D. L. Chen, "Microstructure and fatigue properties of fiber laser welded dissimilar joints between high strength low alloy and dual-phase steels," *Mater. Des.*, vol. 51, pp. 665–675, 2013.
- [11] Y. G. Ko, C. W. Lee, S. Namgung, and D. H. Shin, "Strain hardening behavior of nanostructured dual-phase steel processed by severe plastic deformation," *J. Alloys Compd.*, vol. 504, no. SUPPL. 1, pp. S452–S455, 2010.
- [12] M. . Xia, E. Biro, Z. L. Tian, and Y. N. Zhou, "Efectos de la entrada de calor y martensita en ZAC reblandecimiento de soldadura láser de aceros Dual Phase," *ISIJ Int.*, vol. 48, no. 6, pp. 809–814, 2008.
- [13] M. Pouranvari and S. P. H. Marashi, "Key factors influencing mechanical performance of dual phase steel resistance spot welds," *Sci. Technol. Weld. Join.*, vol. 15, no. 2, pp. 149–155, 2010.
- [14] M. J. Molaei and A. Ekrami, "The effect of dynamic strain aging on fatigue properties of dual phase steels with different martensite morphology," *Mater. Sci. Eng. A*, vol. 527, no. 1–2, pp. 235–238, 2009.
- [15] D. L. Chen, Z. G. Wang, X. X. Jiang, S. H. Ai, and C. H. Shih, "The dependence of near-threshold fatigue crack growth on microstructure and environment in dual-phase steels," *Mater. Sci. Eng. A*, vol. 108, no. C, pp. 141–151, 1989.
- [16] S. Kuang, Y. Kang, H. Yu, and R. Liu, "Effect of continuous annealing parameters on the mechanical properties and microstructures of a cold rolled dual phase steel," *Int. J. Miner. Metall. Mater.*, vol. 16, no. 2, pp. 159–164, 2009.
- [17] H. Aydin, M. Tutar, and A. Bayram, "The Influence of Welding Time on Mechanical Properties of Resistance Spot Welded TWIP Steel Sheets," in *XIII INTERNATIONAL SCIENTIFIC CONGRESS MACHINES. TECHNOLOGIES. MATERIALS. 2016 SUMMER SESSION 14–17.09.2016 VARNA, BULGARIA*, pp. 16–19.
- [18] B. V. H. Hernandez, M. L. Kuntz, M. I. Khan, and Y. Zhou, "Influence of Microstructure and Weld Size on Mechanical Behaviour of Dissimilar AHSS Resistance Spot Welds," *Sci. Technol. Weld. Join.*, vol. 13, no. 8, pp. 769–776, 2008.
- [19] M. Pouranvari, S. M. Mousavizadeh, S. P. H. Marashi, M. Goodarzi, and M. Ghorbani, "Influence of fusion zone size and failure mode on mechanical performance of dissimilar resistance spot welds of AISI 1008 low carbon steel and DP600 advanced high strength steel," *Mater. Des.*, vol. 32, no. 3, pp. 1390–1398, 2011.
- [20] D. S. Safanama, S. P. H. Marashi, and M. Pouranvari, "Similar and dissimilar resistance spot welding of martensitic advanced high strength steel and low carbon steel: metallurgical characteristics and failure mode transition," *Sci. Technol. Weld. Join.*, vol. 17, no. 4, pp. 288–294, 2012.
- [21] M. Pouranvari, "Susceptibility to interfacial failure

- mode in similar and dissimilar resistance spot welds of DP600 dual phase steel and low carbon steel during cross-tension and tensile-shear loading conditions,” *Mater. Sci. Eng. A*, vol. 546, pp. 129–138, 2012.
- [22] M. S. Khan, S. D. Bhole, D. L. Chen, E. Biro, G. Boudreau, and J. van Deventer, “Welding behaviour, microstructure and mechanical properties of dissimilar resistance spot welds between galvanized HSLA350 and DP600 steels,” *Sci. Technol. Weld. Join.*, vol. 14, no. 7, pp. 616–625, 2009.
- [23] S. T. Wei, D. Lv, R. D. Liu, L. Lin, R. J. Xu, J. Y. Guo, and K. Q. Wang, “Similar and dissimilar resistance spot welding of advanced high strength steels: welding and heat treatment procedures, structure and mechanical properties,” *Sci. Technol. Weld. Join.*, vol. 19, no. 5, pp. 427–435, 2014.
- [24] ASTM E8/E8M standard test methods for tension testing of metallic materials, “ASTM E8/E8M standard test methods for tension testing of metallic materials,” *Annu. B. ASTM Stand.* 4, pp. 1–27, 2010.

Effect of Tempering Time and Temperature on Wear Performances of Cr-W steels

Fatih AYDIN^{1*}, Yavuz SUN¹, Muhammet Emre TURAN¹, Mustafa ACARER², Hayrettin AHLATCI¹, Yunus TÜREN¹

1. Karabuk University, Metallurgy and Materials Engineering Department, Karabuk-TURKEY Corresponding Author Email: fatih.aydin@karabuk.edu.tr

2. Selcuk University, Metallurgy and Materials Engineering Department, Konya-TURKEY

Abstract- In this study, Cr-W steels were produced by casting then heat treatment was applied for specimens. After the normalization process at 1100 °C for 1 hour, samples were heated up 660 °C and 760 °C to evaluate the effect of tempering temperature. One group of steel were waited at 1 hour and the other group were waited at 2 hours in these temperatures. Hardness of specimens was measured according to the Vickers test method. Wear tests were performed for all specimens under the loads of 10N, 20N and 40N in dry sliding conditions. Microstructure analysis was carried out using Light Optical Microscope (LOM), Scanning Electron Microscope (SEM). Results show that, tempering temperature significantly affects the wear behaviors of samples. These effects can be seen especially under higher loads. And also there is a direct proportion between wear and hardness results.

Key words: Cr-W steels, Wear, SEM, XRD

I. INTRODUCTION

Cr-Mo steels are widely used in power generation and petrochemical industry due to their good elevated temperature properties. In 1940's, 2.25Cr-1Mo (T22) and 9Cr-1Mo (T9) steels were started to be used for power plant applications. Addition of V, Nb, N to these steels cause to form stable carbides, nitrides and carbonitrides. Stable carbides and solid solution hardening provide high strength at elevated temperatures. In the 1990s, T23 steel was developed replacement of Mo by W. According to nuclear calculations, reduced activation steels were

produced by reducing Mo, Nb, Ni, Cu and N elements. Therefore, Mo was replaced with W and/or V [1, 4, 9].

In recent years, Oak Ridge National Laboratory developed new steels with 3% Cr, 2-3% W, 0.25% V. These steel has good strength and toughness due to bainitic structure after normalization and tempering [3]. Also, Acarer et.al. produced 2.9 %Cr, 3.5%W, 3.1%Co steel. [8] In the Cr-W steels, Cr is ferrite stabilizer element that provides good oxidation and corrosion resistance. Cr forms M_7C_3 type carbide in low Cr steels (<7%Cr). W is ferrite stabilizer element and generates solid solution hardening. In tempered conditions, W forms $M_{23}C_6$ and MX type carbides [2]. W also improve the creep resistance in Cr-W steels [13].

There are several studies about creep [4, 1], fatigue [12] fracture [5], welding [6] and mechanical properties [7] on Cr-Mo (Cr-W) steels. There are also several studies on wear behavior of Cr-Mo steel in the literature [10, 11]. But there is no study about wear properties on Cr-W steel. Wear is one of the most important issues in all materials today. Therefore, wear properties of Cr-W steel was chosen as research area in this study.

In this study, Cr-W steel was produced by casting method. Casted sample were normalized at 1100°C for 1 h and tempered 660/760°C for 1/2 h. Hardness measurement was realized after normalization and tempering treatment. The reciprocating wear test was applied to as-cast and normalized and tempered specimens with different temperature and time. Therefore, different tempering temperature and time on wear behavior of Cr-W steel was investigated.

Wear tests were realized under 10, 20, 40 N loads. To understand wear mechanisms, worn surfaces

were investigated with Scanning Electron Microscope.

II. MATERIALS AND METHODS

A. Experimental Methods

In this study, Cr-W steel was manufactured by casting method. Chemical composition of steel is given Table 1.

Table 1. Chemical composition of Cr-W steel (wt. %)

%	C	Si	Mn	P	S	Cr	Mo
Cr-W Steel	0.11	0.08	0.14	0.02	0.01	2.5	0.04
	V	Ti	W	Ta	N	B	Co
	0.15	0.02	3.6	0.02	0.02	0.005	1

Casted sample was normalized at 1100 °C for 1 h. Samples were separated as four categories (660 °C-1h, 660 °C-2h, 760 °C-1h and 760 °C-2h) to investigate effects of tempering time and temperature on tribological performance in Cr-W steel. Metallographic processes including grinding from 60 to 2000 mesh and polishing 6 μ and 1 μ were applied for all samples. Etching process was also carried out by Vilella's reagent (Picric acid, hydrochloric acid and ethanol). Microstructures of specimens were examined by Light Optic Microscope (LOM) and Scanning Electron Microscope (SEM). Hardness measurement was performed with HV 2 by Qness Q10 A+ Hardness Test Machine.

Reciprocating wear tests were conducted for all specimens under loads of 10, 20 and 40 N. Sliding distance and speed were kept constant and they were 500 m and 60 mm/s respectively. AISI 52100 steel ball was used for counterface material. Worn surfaces were investigated by SEM for lowest and highest loads to understand the nature of wear mechanism.

III. RESULTS AND DISCUSSIONS

A. Hardness Results

Table 1 shows hardness values depending on different tempering time and temperature. According to hardness results, the highest value of hardness was obtained at as-cast specimen (247.8 HV). It is observed that the hardness values are close to each other at 660°C-1h and 660°C-2h tempering parameters. Hardness value of 760 °C-1h tempering was significantly reduced because of grain coarsening (Fig.1).

Table 1. Hardness values of cast sample, 660°C-1/2h and 760°C-1/2h tempered specimens

	Hardness
As-cast	247.8
660 °C-1h	238.0
660 °C-2h	234.6
760 °C-1h	201.0
760 °C-2h	177.2

B. Microstructure Characterization

Fig. 1 shows that microstructures of normalized (1100°C/1h) and following tempering at 660°C-1h, 660 °C-2h, 760 °C-1h, 760 °C-2h. As seen in Fig. 1, inhomogeneity was observed in as-cast sample. When the microstructure of the tempered samples are examined, it can be said that the structure is generally ferritic-bainitic. Grain coarsening was observed with the increasing of tempering temperature and time. Some carbides (M_7C_3 and $M_{23}C_6$) can occur after different tempering temperature, time and transform to new carbides [6]. Therefore, SEM and TEM analysis provide clear and detailed information about relationship of microstructure, hardness and wear.

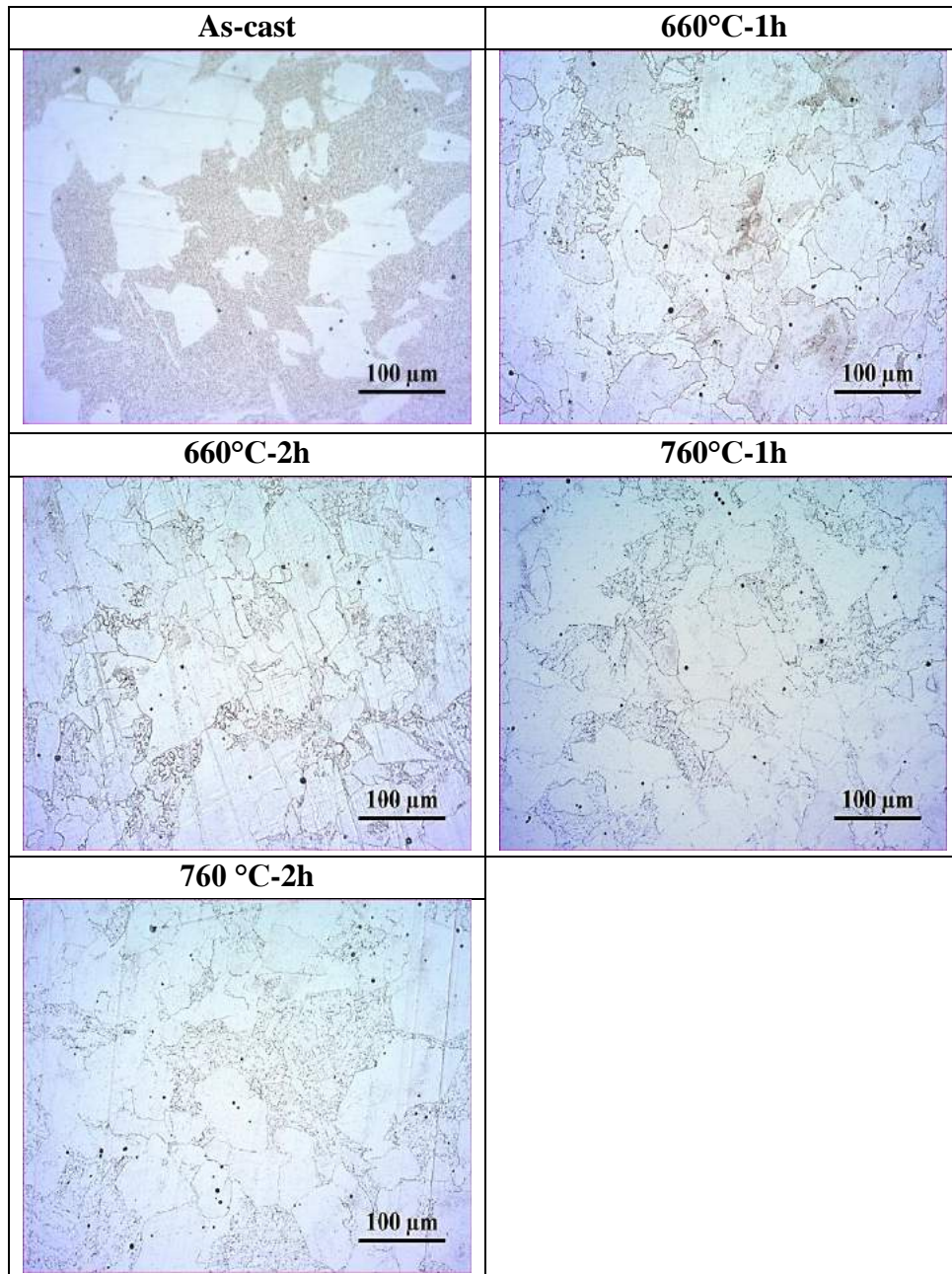


Fig. 1. Microstructures of specimens (as-cast and after different tempering time and temperature)

C. Wear Results

Wear rates belonging to the samples are given in Figure 2. Wear volume loss values were taken into account to calculate wear rates of samples. Non-heat treatment specimen has low wear rate when the wear volume loss values are compared for all samples. A specimen tempered at 660° during for 1 hour exhibits

best wear performance among the heat-treated samples. Once temperature and time increases, the wear performance is negatively affected. This is because high temperature might lead to grain growth so this situation effects the mechanical behavior. However, there is direct relationship between hardness and wear results. According to the Archard laws, softer materials has higher wear rate than harder materials.

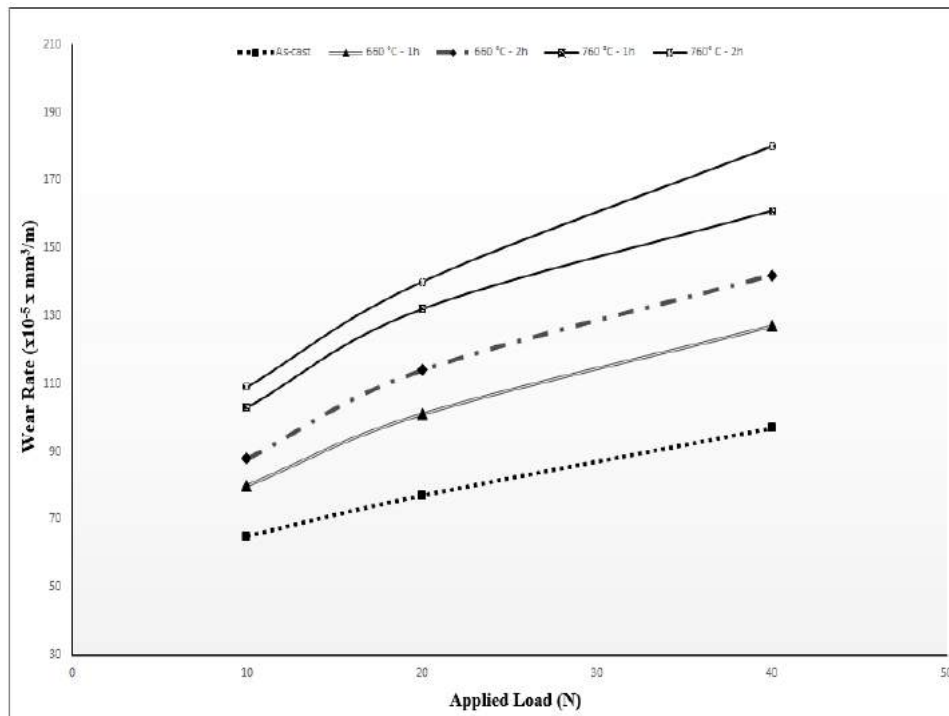


Fig. 2. Wear Volume Loss of samples

Figure 3 presents the coefficient of friction under three loads for all specimens. Coefficient of friction generally decreases when the applied loads increases. The lowest coefficient of friction is belonging to the as cast samples under the load of 10N. Furthermore, this specimen exhibits best wear resistance so it may be concluded that when the wear rate is decreased, coefficient of friction is lower. The

sample which was exposed to heat treatment at 660° during for 1 hour has lower friction coefficient. On the other hand, it can not be said that there is a significantly change among the applied loads for each sample. Generally, modest decreases can be seen when the applied loads are enhanced.

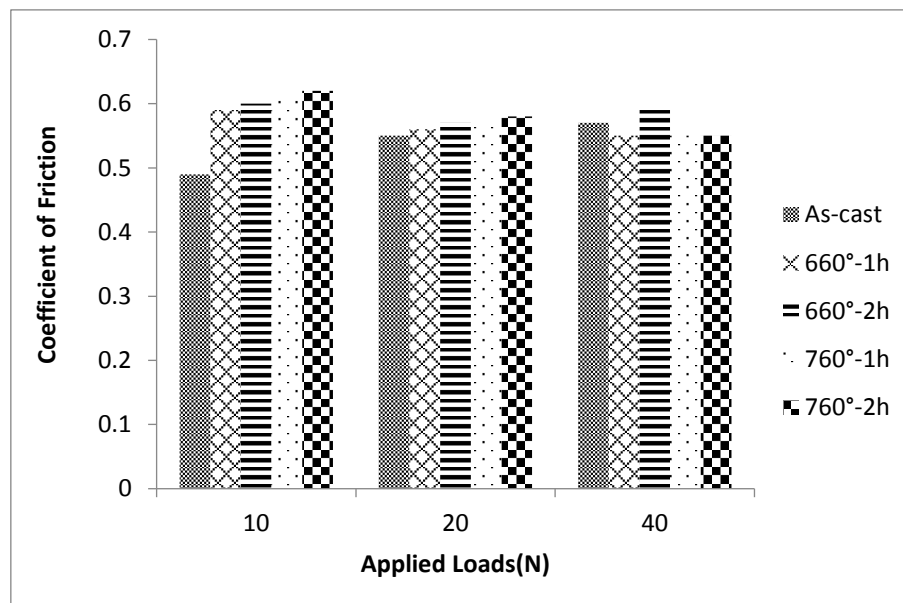
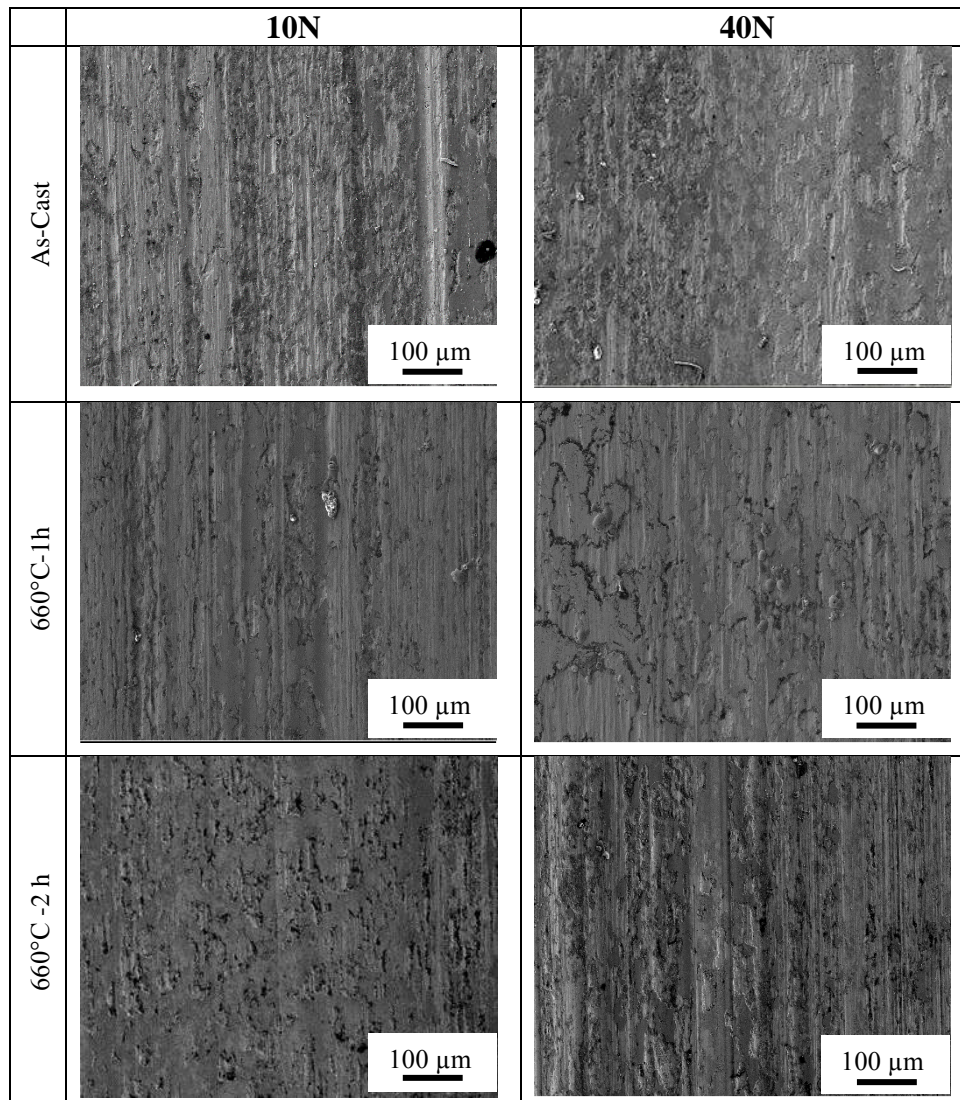


Fig. 3. Coefficient of friction versus applied loads

The worn surfaces of specimens are given in Figure 4. As cast steel has best wear morphology and wear rate is lower can be seen due to the lubricant effect. As 10N loads are examined, there are some scratches and marks on the worn surfaces of all specimens. These scratches are parallel to the sliding direction. So, abrasive wear mechanism is dominant mechanism. Also, oxidation mechanism is an effective especially for as-cast specimen. This is because reapplied loads cause the friction heat on the worn surface. When the applied loads are enhanced up to 40N, scratches are more obvious. The sample tempered at 760° during for 2 hours has grooves in

addition to marks so delamination might be occurred because of lower mechanical properties caused by grain coarsening with the elevated tempering temperature and time than other specimens. Adhesive wear can also be observed but this mechanism is minimized due to lower sliding speed during wear tests. However, scratches formation and wear rate is lower for tempered at 660° during for 1 hour than other tempered specimens can be seen from the worn micrographs clearly. Therefore, worn microstructures support the wear volume loss value which are as mentioned above.



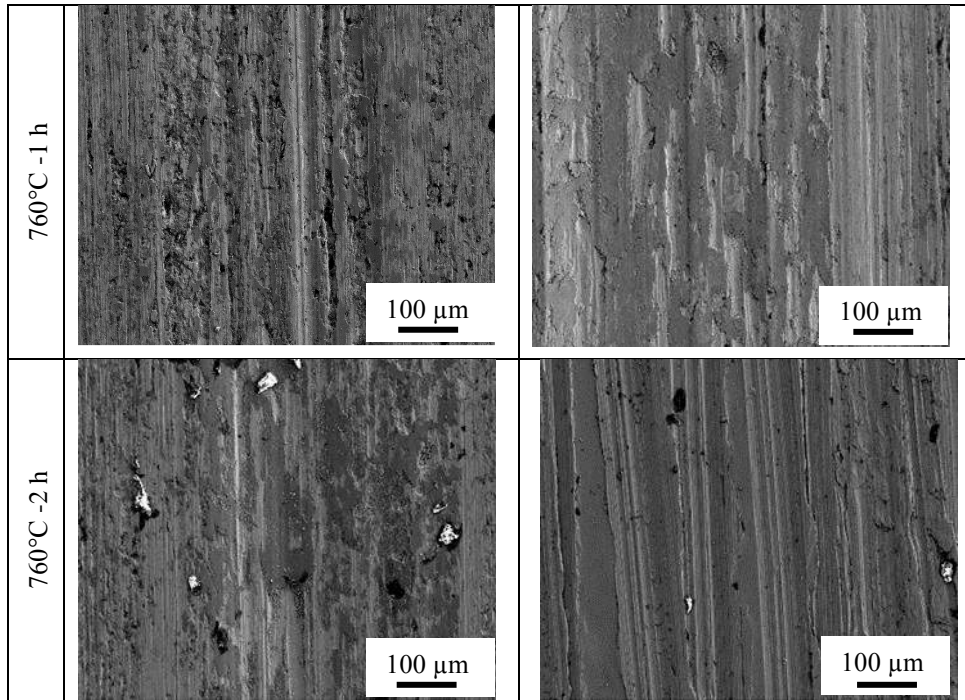


Figure 4. SEM microstructures of worn surfaces

Line EDX were taken for as cast specimen to understand the change of chemical analysis during the line spectrum. Partially oxide formation might be found as mentioned above. When the composition during the line is examined, oxide peak is increased

in some regions while the peak of Fe is decreased. Thus, FeO formation is occurred in specimens so oxide wear mechanism is an effective in as cast specimen.

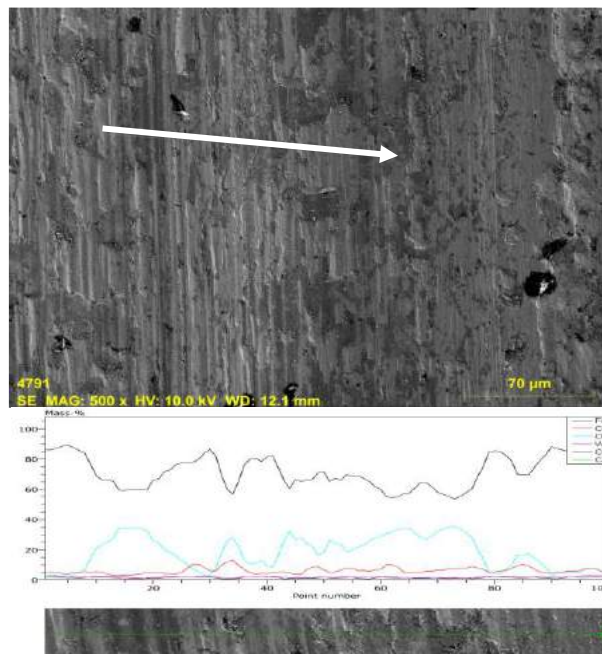


Figure 5. Line EDX of As-cast sample under the load of 40 N

To sum up, wear rate and the coefficient of friction are lower for specimen tempered at 660° during for 1 hour than other tempered specimens. Abrasive, oxidation and adhesive wear mechanisms are found for all specimens.

IV. CONCLUSIONS

The results obtained from this study are listed below.

- Wear and hardness performance of Cr-W steel could change with tempering time and temperature.
- Hardness values were decreased by tempering process especially there was a significant change in hardness for tempered at 760° during for 2 hours.
- Wear performance is getting poor once the temperature and time are enhanced due to grain coarsening.
- There is direct relationship between hardness and wear resistance.
- The lowest coefficient of friction is belonging to the as cast specimens.
- Optimum tempering time and temperature is obtained at 660°C for 1 hour. Because wear resistance of this situation is much more than other parameters.

ACKNOWLEDGEMENTS

The authors thank to Karabuk University Iron and Steel Institute due to supplying mechanical analysis.

REFERENCES

- [1] R.L. Klueh, N.D. Evans, P.J. Maziasz, V.K. Sikka, Creep-rupture behavior of 3Cr-3W-V bainitic steels, *International Journal of Pressure Vessels and Piping*, 84 (2007) 29-36.
- [2] R. L. Klueh, Elevated-temperature ferritic and martensitic steels and their application to future nuclear reactors, 2004, ORNL/TM-2004/176.
- [3] R. L. Klueh P. J. Maziasz J. M. Vitek N. D. Evans N. Hashimoto Alloy Design and Development of Cast Cr-W-V Ferritic Steels for Improved High-Temperature Strength for Power Generation Applications, CRADA FINAL REPORT, 2006.
- [4] S. Chaudhuri, R.N. Ghosh, Creep behavior of 2.25Cr1Mo steel-Effects of thermal ageing and pre-strain, *Materials Science and Engineering A*, 510-511 (2009) 136-141.
- [5] R. L. Klueh, D. J. Alexander and P. J. Maziasz, Fracture behavior of bainitic chromium-tungsten and chromium-molybdenum steels, *Metals and Ceramics Division Oak Ridge National Laboratory*.
- [6] Benjamin King Welding and post weld heat treatment of 2.25Cr-1Mo steel, University of Wollongong 2005.
- [7] Mann Jawad and Vinod K. Sikka, Development of a New Class of Fe-3Cr-W(V) Ferritic Steels for Industrial Process Applications, Final Technical Report, ORNL/TM-2005/82.
- [8] Acarer, M., Arici, G., Aydin, F., Uyaner, M., Çolak, M., Kayıkçı, R., Production of 3Cr-3W Steel by investment casting, *Livarski Vestnik*, 63(3), 2016, 124-131.
- [9] Mohsen Asadi Asadabad, Shahram Kheirandi, Abdul Javad Novinrooz, Tempering Behavior of 4.5Cr-2W-0.25V Steel, *Journal of Iron and Steel Research International*, 2010, 17(10) : 57-62
- [10] A. Shafiee, M. Nili-Ahmadabadi, H.M. Ghasemi, E. Hossein-Mirzaei, Wear behaviour of a Cr-Mo steel with different microstructures, in comparison with austempered ductile iron, *International Journal of Material Forming*, 2009.
- [11] A. Molinari, G. Straffelini, P. Campestrini, Influence of microstructure on impact and wear behaviour of sintered Cr and Mo steel, *Powder Metallurgy*, 42:3, 235-241.
- [12] Hideo Kobayashi , Akira Todoroki , Toshikazu Oomura , Takeru Sano , Tatsumi Takehana, Ultra-high-cycle fatigue properties and fracture mechanism of modified 2.25Cr-1Mo steel at elevated temperatures, *International Journal of Fatigue*, 28 (2006) 1633-1639.
- [13] J.C. Vaillanta, B. Vandenberghe, B. Hahn, H. Heuser, C. Jochum, T/P23, 24, 911 and 92: New grades for advanced coal-fired power plants-Properties and experience, *International Journal of Pressure Vessels and Piping*, 85 (2008) 38-46.

Investigation of Determination the Non-Recrystallization Temperature (T_{nr}) by Thermo-Mechanical Simulation Methods

Ekrem AKÇAI, Barış AVAR, M.

1 Uzunkum cd. No:7, Karadeniz Ereğli, 67300, Turkey/ERDEMİR, akcaek@hotmail.com

Uzunkum cd. No:7, Karadeniz Ereğli, 67300, Turkey/BEUN, barisavar@gmail.com

ABSTRACT

In order to determine the hot rolling processes, it is necessary to determine the temperature of T_{nr}. There are many formulations to determine this temperature. These formulations vary according to the microalloys found in the composition. Simulation equipments and methods are used in determination of temperature. In this study, T_{nr} temperature determination of X70 quality Nb micro alloy steel material was performed by using Gleeble 3500 thermal mechanical simulation device. T_{nr} temperatures found by formulations and thermal mechanical simulation methods were compared and the closest formulation was tried to be determined.

Keywords: Non-Recrystallization Temperature (T_{nr}), Thermo-mechanical simulation, Microalloyed steels.

Residual Stress Distribution in R220 and R260 Grade Grooved Rails

M. Emre Turan¹, Yavuz Sun, Fazıl Husem

*1Karabuk University, Metallurgy-Materials Engineering Department, Karabuk-TURKEY,
memreturan@karabuk.edu.tr, ysun@karabuk.edu.tr, fazilhusem@karabuk.edu.tr*

ABSTRACT

This study aims to determine residual stress distribution in head, web and foot parts of two different quality grooved rails and also to understand effect of carbon content on residual stress in rails. Strain gauges were glued on three regions of specimens and cutting method was applied for residual stress measurement according to the TS EN 13674-1 railway rail standard. Scanning Electron Microscope (SEM) and Optic Microscope (OM) were used for microstructure analysis of regions where the residual stress measurements were performed. Results show that, compressive residual stress is an effective stress type compared to the R260 grade rails. However, R260 grade grooved rails have higher residual stress value than R220 grade grooved rails especially in head parts of specimens.

Keywords: Residual stress, Strain gauge, SEM, Grooved, TS EN 13674-1

Dry Sliding and Corrosive Wear Performances of Head Hardened Rails

M. Emre Turan¹, Fazıl Husem, Yasin Akgul, Yavuz Sun, Hayrettin Ahlatci
¹Karabuk University, Metallurgy-Materials Engineering Department, Karabuk-TURKEY,
memreturan@karabuk.edu.tr, ysun@karabuk.edu.tr, fazilhusem@karabuk.edu.tr, yasinakgul@karabuk.edu.tr,
hahlatci@karabuk.edu.tr

ABSTRACT

In this study, head hardening process was applied for R260 quality rails. Microstructures of rails were carried out using Scanning Electron Microscope (SEM). Hardness distribution of head parts were also evaluated for two category samples (heat treatment and non heat treatment). Wear tests were performed under three different loads (10N, 20N and 40N) in both %3.5NaCl solution and dry conditions. Worn surfaces were characterized by Nikon Shuttlepix, Profile projector and SEM. Results clearly show that, head hardened rails exhibited better wear performance especially under load of 10N in dry conditions.

Keywords: Head hardening, SEM, Wear, Hardness

Steel and Defense: Success to the Successful

Bahar AŞCI

*Karabuk University, Economics and Administrative Sciences Faculty, Economics Department, Karabuk-TURKEY,
baharasci@karabuk.edu.tr*

ABSTRACT

As long as Turkey's Strategic Vision 2023 strategy map targeted iron and steel industry to be among the top 10 countries in the World at all stages of production and defense industry as a blockbuster industry, the connection between this two industries gained importance. Steel which is produced in many forms, including flat-rolled and long products, carbon pipe and tube products, wire and other fabricated products are all segments of the domestic steel industry contribute directly or indirectly to the defense industrial base. In this study, domestic and international iron and steel sources has compared with one of the system archetypes of system thinking theory which is success to the successful archetype and simulated by Insight maker – a general purpose tool for web-based modeling and simulation – and as a result found that increasing domestic production capacity and technology increases the success of defense industry and in total increases the defence capacity of homeland security. To make this simulation real, Turkey must pursue economic policies that encourage continued investment in both manufacturing and technology and give importance to local resources for defence industries' needs.

Keywords: System archetypes, systems thinking, mental models, system dynamics, future scenarios

Determination of the Individual Level of Financial Literacy: A Study in Kardemir Inc.

¹Murat YILDIRIM, Fatih BAYRAM, Ahmet OĞUZ, Gülay GÜNAY
Karabuk University, Faculty of Economic and Administrative Sciences, Karabuk-TURKEY
¹muratyildirim@karabuk.edu.tr, fatihbayram@karabuk.edu.tr, ahmetoguz@hotmail.com
ggunay@karabuk.edu.tr

ABSTRACT

Developments and innovations in financial market, product variety and the complexity of the products' content entail people to take part in financial system consciously. Recently, the importance of financial literacy dramatically increased due to some factors such as the rise in people's responsibility on decisions, innovations information and communication technology, swift changes in retirement and taxing policy, demographic changes in population, the failure of individual attempts and financial fraud. Each individual should be financially literate for financial security and comfort. Individuals' self-consciousness on financial issues will not only prepare them for prospective hard economic conditions that may emerge in the future but also supports the development of the country on strong basis. In this perspective, the awareness of financial literacy will help to use the limited sources more affectively. In addition to this, it will also prevent the waste of sources by contributing the economy and improving the life-standards of the citizens. In this regards, the aim of the study will examine individuals' who are working in Kardemir Inc., financial literacy levels. The sample consists of individuals, who are working in Kardemir Inc. Data were collected through a demographic information form, Financial Literacy Index developed by Van Rooji et al. (2011). The obtained data will be evaluated by "SPSS for Window" statistical program. Finally, the findings are compared with the literature and some recommendations are suggested for individuals, executives and researchers.

Keywords: finance, financial literacy, personal finance.

A Study on the Financial Behaviour of Kardemir Inc. Employeeer

Gülay Günay¹, Ahmet Oğuz², Fatih Bayram³, Murat Yıldırım⁴

¹ Karabuk University, Department of Social Work, Karabuk/TURKEY ggunay@karabuk.edu.tr

² Karabuk University, Department of Economics, Karabuk/TURKEY ahmetoguz@hotmail.com

³ Karabuk University, Department of Public Relations and Publicity, Karabuk/TURKEY fatihbayram@karabuk.edu.tr

⁴ Karabuk University, Department of Business, Karabuk/TURKEY muratyildirim@karabuk.edu.tr

Abstract— Families act in an environment of financing system which includes the pressure of the economic powers like the changing economic balances, increasing unemployment rate, changing purchasing power of money, inflationist pressures, increasing tax load, changing government policies, increasing interest rates, complicating consumer market, and the competence gradually increasing between the businesses. In such an environment, the behaviours of family related to usage of the income on one hand affect the social and economic welfare of family itself, and on the other hand the national economy and welfare. In this context, economic functions are of a significant center for the families to obtain their wishes and needs and to maintain their lives better and happier. In this article we focus on families' financial behaviours. For this purpose we have observed 1) financial status of families, 2) financial decision making forms of families', 3) families' financial status evaluation. The sample consists of individuals, who are working in Kardemir Inc. (n=245). A total of 245 employees are participated in the study on a voluntary. Findings indicated that 65.3% of the responses keep record for income and expenses every month. Economic decision making are always shared by couple (47.3%). The rate of monthly income scarcely satisfies needs (46.1%) are higher among the reasons for not saving. The majority of participants (89.0%) have stated that their monthly incomes are not sufficient or scarcely sufficient to satisfy the needs of families and thus, they cannot make savings. Finally, some recommendations are suggested for individuals, families, executives and researchers.

Keywords— finance, financial behaviour, family finance, financial status, family financial decision

I. INTRODUCTION

Family is one of the most important things in one's life. Because family is people who have grouped themselves into families to find trust, love, emotional, physical and collective support. Therefore family is the most basic and most important institution that creation social consciousness of individual's, which are required to develop and sustain the communities. The multifaceted function performed by it in a society makes it a much-needed institution. Therefore both of traditional and modern culture family ties are considered to be the most important factor that holds people together.

Family underlying the life should offer its members a satisfactory quality of life in order to continue its existence [1]. Therefore, economic functions of families are extremely crucial for family members to obtain their requests and needs and increase and maintain the quality of life. Accordingly, the quality of family life and marriage depends largely on the function of economic resources to be obtained for the individuals and families. If the resources owned are abundant, they enable it to easily reach the desired luxury and comfort. Financial welfare of families is a more complex issues [2], and families economic behaviours are most important determinants of life quality and family welfare [3,4]. Most of study displayed that income and financial resources are positively affected quality of family life and welfare [5,6,7,8,1]. However, economic resources of many families are limited today. Herein, families should carefully and accurately manage the economic resources which they own in order to meet their demands and needs and to reach to a desirable quality of life [5].

Much of the literature on family financial management is prescriptive in nature, including extensive discussion of what families should do in managing their financial resources. Despite the importance of effective financial management in families' lives, relatively little empirical research has focused on what families actually do. For instance, how meet family their needs? Is their income enough for meet their needs? How they use their income? Are they making saving with their finances resources? Why don't make savings? Did they debts? Are they satisfied with their financial situation? In other words, it's obvious that the financial decisions and behaviours of families will affect the macro - micro - economic decisions of families' life. The economic problems of the last few years have hit families hard. Unemployment and uncertainty about the future have resulted in financial challenges for many families.

Therefore today's family, income organization is a central resource for welfare of family members. Hira and Mueller (1987) [9] reported that improved money management practices are more important than increasing the resources. Because improving money management could be help families cope with financial difficulties and meet family needs. Thus, it is necessary to plan the usage of income for today and future,

and to create a successful balance between consumption and saving in order to develop the quality of life and provide the financial welfare [9].

Incomes are undoubtedly the ones of the major elements of quality of life [10]. The family should distribute its income balanced to economic activities in order to preserve its existence and level of welfare. Hence, income organization underlies resource management for the welfare of family members in today's family [3,11] because the income is crucial not only for meeting the basic needs (sheltering, nutrition, clothing, etc.) but also for enhancing close relationships [11]. Therefore, improving the practices of money management is more important than increasing the resources because improving money management helps families cope with financial difficulties and meet the needs of family and family members during those difficulties [9]. The budget is the statement which indicates the balance between income and expenses of a person or a family in a certain period of time. The aim of budget is to meet the largest numbers of requests and needs with the current income of the family in order to increase the quality of life of family members. In other words, the budget tries to provide the wise distribution of the income of family to expenses of family and family members [12]. In a family, the primary subjects of budget management consist of how the monetary resource has been obtained and shall be distributed to various requests and needs of family and what kind of abilities family members have related to the use of money and budget management [3]. In practice, these subjects covers the income administration, the management of bank accounts, the ways of using the savings, and the expenses made to meet requests and needs of family members [3,13,12]. Financial administration and budget in the family are affected by many demographic and socio-economic factors such as the marriage status, the family income, the educational background and ages of family members, the numbers of children in the family, the employment status of spouses, the needs of family members, the city where family lives, the life cycle in which family lives [10,14,3,15,13]. Considering needs and demands of family members and the changes between these overtime, family's transition from one life cycle to another financial management and budget administration also changed [16]. For this reason, the use of income is planned for today and for the future, a successful balance between consumption and saving is essential for the development of quality of life and financial well-being [6].

According to Yadollahi et al. (2009) demographic variables affect family economic status, but the relationship between management function and family economic status is not explained [17]. Sumarwan and Hira (1993) found that socioeconomic variables directly affect perceived income adequacy. Their results showed that gender, age, and household income have significant direct effects on perceived income adequacy [14]. Hira and Muller (1987) found that of five demographic variables only one, household size, is significantly related to financial satisfaction [9]. Çopur et al. (2009) [18] examined the relationship between adequacy of resources and socioeconomic and family composition

characteristics in Turkey. Their results indicated that individuals perceived their financial resources to be less adequate than other resources. In this study also education, income, marital status, number of children, and family life stage significantly affected scores on the perceptions of adequacy of resources inventory. Beak and De Vaney (2010) [19] examined how families manage their economic hardship. The results of the study showed that unemployment, education, income, net worth, emergency funds, credit limit, number of children, race, and expectation for future income were important on coping with the economic hardship. Chuan et al. (2011) [20] reported that the higher the level of financial satisfaction, the more likely would be the individual's level of income. Xiao et al. (2009) [21] conducting a survey among a sample of undergraduate students at a major state university in USA, reported that positive financial behaviours contribute to financial satisfaction and financial satisfaction in turn contributes to life satisfaction. Parrotta and Johnson (1998) [22] have investigated the impact of financial attitudes and knowledge on financial management and satisfaction with financial status in a sample of 194 recently married individuals. The results of this study showed that higher income and positive attitudes about finances, predicted use of recommended financial management practices. Higher income and the use of recommended financial practices were related to increased satisfaction with financial status.

Considering the requests and needs of families, and the changes of those over time, it is an expected situation that financial management practices and budget management change during the transition of families from a life cycle to another [16]. Therefore, planning the use of income for today and the future, and successfully balancing between consumption and the saving are essential to improve the quality of life and provide financial welfare [6]. In this study we investigated families' demographic variables and economic decision making and financial behaviour.

II. METHOD

A. Participation

The study has been done in the province Karabuk. The population of the study consists of all the employees who are married and work at Kardemir Inc. The list, which was taken from Kardemir Inc Human Resources Department and includes all the employees working in different service classes in the incorporation, has been used. Approximately 3924 employees work in Kardemir Inc based on the data of the year 2016 [24]. The employees, who voluntarily accepted to participate in the study and are married, have been included into the study sample. Within this scope, it was tried to reach 350 employees.

Before collecting the data of the study, talks were held with Kardemir Inc. Human Resources Department and the official approvals required by the incorporation were received in the practice stage. The participants were given information primarily about the aim of the study and how to fill in the questionnaire form, and the ones, who accepted to participate in the study after the questions, if any, had been answered, were included into the study. Within this scope, 350 employees were made fill in the questionnaire form. However, since some

questionnaire forms were filled in wrongly and incompletely (63 questionnaire forms), did not provide the necessary requirements (such as not being married) for the study (42 questionnaire forms), total 245 questionnaire forms were evaluated in the study. The data of the study were collected during the periods allowed by the incorporation in January of 2017.

B. Instruments

In order to determine the perceptions of families related to the financial behaviours, a questionnaire form was prepared by the researchers in line with the literature. The mentioned questionnaire form was prepared short so as not to bore and tire the individuals. The questionnaire form consists of two parts.

The first part of the form consists of the questions asked in order to get information about demographic matters such as gender, age, the number of family members, average monthly income, employment status of the spouse, additional income source.

In the second part, there are questions prepared in order to determine financial behaviours of the individuals. In order to determine financial behaviours of the individuals in this part, there are closed-end questions related to the frequency of keeping a record for income and expenses, the way of taking decisions related to financial matters in the family, the evaluation of the current financial position, the reasons of not achieving savings and how it shall be satisfied when cash is needed.

C. Data Analysis

The analysis of data was evaluated by using the software "SPSS for Windows 19.0" based on the responses of 245 employees of Kardemir to questions in the questionnaire form.

As the criterion in determination of financial behaviours of employees, crosstabs were formed based on the employees' ages, lengths of marriage, educational backgrounds, monthly income levels and the spouses' employment status. It was tested by using the "Chi-Square" analysis whether the difference between the questions related to financial behaviours of employees and independent variables. The Chi-Square test could not be applied when the degree of freedom was higher than one ($df > 1$), the number of pores less than 5, the expected value, exceeded 20%. In such cases, interpretations were made by using only frequency and percentages [24].

III. RESULTS AND DISCUSSION

The rate of male participants (96.3%) is seen to be higher than that of female ones. This is caused by the fact that, in the population from which the sample has been taken, woman labour is benefited less in iron and steel sector, described as heavy industry. Hence, the rate of women working in industrial sector is only 16.1% based on the data of Household Labour Force Survey (2014) conducted by the Turkish Statistical Institute [17].

The ages of employees vary between 23 and 58 and the average age has been calculated 39 ($S=6.8$). The rate of the ones between "35 and 46" years of age (58.0%) is higher than the other age groups. Among the employees (46.5%), the ones,

who have stated that the number of members in family is four, lead. The average marriage duration of individuals is 14 ($S=7.7$) years. Average monthly income level varies between 1.300 TL and 10.000 TL. While the average monthly income is 3.211 TL ($S=1.430,8$), a bit more than half of the employees (57.1%) falls into the "2.001 TL – 3.500 TL" income group; 21.6% of them falls into the "less than 2.000 TL" income group and 21.2% of them falls into the "more than 3.501 TL" income group. Among the employees, the ones stating that they are high school graduate (54.7%) rank first, they are followed respectively by the ones stating that they are college graduate (18.0%), graduate of bachelor's degree and more (13.9%) and primary school graduate at the most (13.5%). 69.8% of the individuals has stated that their spouses do not work. A very high rate of the employees (83.3%) has stated that they do not have any additional income apart from their salaries (Table 1).

TABLE XL
DEMOGRAPHIC VARIABLES

Demographic variables	F	%	Demographic variables	F	%
Gender			Monthly family income		
Female	9	3,7	Low (Less than 2000 TL)	53	21,6
Male	236	96,3	Middle (2001 TL – 3500 TL)	140	57,1
Age (M=39.1; S=6.8)			High (More than 3501 TL)	52	21,2
23 – 34	68	27,8	Spouse' work status		
35 – 46	142	58,0	Working	74	30,2
47 – 58	35	14,3	Non-working	171	69,8
Number of family member			Duration of marriage (M=14.0; S=7.7)		
2 member	25	10,2	< 6	61	24,9
3 member	62	25,3	7 – 13	50	20,4
4 member	114	46,5	14 – 20	86	35,1
5 member	31	12,7	≥ 21	48	19,6
6 member	13	5,3	Other income sources		
Education			Rent	24	9,8
Primary school (8 years)	33	13,5	Interest	1	0,4
High school (11 years)	134	54,7	Agricultural production	1	0,4
Vocational college	44	18,0	Commercial revenue	11	4,5
Bachelor's (15 years and more)	34	13,9	No other income sources	204	83,3
			Pension	4	1,6

Income plays a determinant role in formation of savings and borrowing opportunities, consumption trends and patterns. Therefore, the way of using the income in family is one of the vital elements of family life. Planning the use of money for today and the future and successfully balancing between consumption and the saving are essential to improve the quality of life [18].

It has been found that 65.3% of the employees of Kardemir, included into the study, keep records for income and expenses every month and 26.1% of them do not keep records at all. This result reveals that individuals try to balance between income, saving and borrowing behaviours. As a result of the statistical analysis carried out, it has been found that the relationship

between individuals' states of keeping records for income and expenses and their ages is significant ($X^2=15.916$, $df=8$, $p<0.05$). Individuals should be planned for their expenditures and savings in order to achieve their aims they want to accomplish for today and the future. Management of financial resources is the first and the most important step especially for low-income families and families with unstable level of income to achieve their aims. Making a budget and developing an expenditure plan for financial stability of family make it easier to discharge debts and help make savings [25]. The study results of researchers such as Kenyon, and Borden [26], Mullis and Schnittgrund (1982) [27], Schnittgrund & Baker (1983) [28], Titus, Farnslow & Hira (1989) [15], Scannell (1990) [29] related to family budget planning support the findings obtained in the present study.

In order to determine by whom of the family members the decisions are taken related to economic activities conducted in family, the question "By whom are the decisions generally taken related to economic activities in your family?" was addressed to the individuals included into the study. Frequency and percentage distributions of responses of the individuals were analysed. Based on the results obtained, the rate of the ones, stating that the spouses always take decisions together related to economic activities conducted in family, (47.3%) is high. This finding is followed by the ones stating that they decide with the family members (18.8%). Based on the results of statistical analysis carried out, it was detected that there was a significant relationship between by whom the decisions are generally taken related to economic activities in family and the ages of employees ($X^2=6.323$, $df=8$, $p<0.05$) and the relationship with duration of marriage, monthly income, educational background and employment status of the spouse was insignificant (Table 2). Various studies having been done support the result obtained in the present study. It has been observed in the studies that as educational levels of men and women, their professional status, levels of income and duration of marriage all increase, participation of women in economic decisions in family also increases [30-34].

When the perceptions of individuals related to their current financial status are examined, the rate of the ones (46.1%), stating that their monthly income scarcely satisfies their needs, is high. They are followed by the ones (29.4%) stating that their monthly salary is not sufficient to satisfy the needs of family. Moreover, the rate of the ones, stating that their incomes satisfy the needs of family readily (13.5%) and that they can make some savings from their monthly incomes (11.0%), is low in the study. Based on results of the Chi-Square test, it has been found out that the relationship between perceptions of employees related to their financial position, and their levels of monthly income ($X^2 =66.274$, $df=8$, $p<0.05$) and educational backgrounds ($X^2=29.621$, $df=12$, $p<0.05$) (Table 2). Families carry out activities in the environment of financial system in which there is pressure of economic forces, such as the change of economic balances, the increase in unemployment rate, the changes in the purchasing power of Money, the inflationist pressures, the increasing tax burden, the change of government policies, the increase in tax rates, the complexification of

consumer markets and the increasing competition among businesses [3,10,36,37]. In such an environment, the behaviours of the family related to the use of income affect both its social and economic welfare, and the country economy and welfare [6,38]. Accordingly, depending on all of these conditions, the income which individuals earn in working life makes it possible to scarcely maintain their own and families' lives and makes it difficult for them to make any savings for the future.

TABLE 2. FINANCIAL BEHAVIOUR AND CHI-SQUARE RESULTS

How often do you keep records of your income and expenses	F	%	Chi-square
Never	64	26,1	A ¹ : $X^2=15.916$, $df=8$, $p=.044^*$ M.D. ¹ : $X^2=14.937$, $df=12$, $p=.245$ I. ¹ : $X^2 =$ Does not valid E. ¹ : $X^2 =$ Does not valid S.W. ¹ : $X^2 =$ Does not valid
Once a year	7	2,9	
Every 6 months	11	4,5	
Once in 3 months	3	1,2	
Monthly	160	65,3	
Economic Decision Making	F	%	Chi-square
Always male	66	26,9	A ¹ : $X^2=15.141$, $df=6$, $p=.019^*$ M.D. ¹ : $X^2= 11.470$, $df=9$, $p=.245$ I. ¹ : $X^2 = 10.233$, $df=6$, $p=.115$ E. ¹ : $X^2 = 8.042$, $df=9$, $p=.530$ S.W. ¹ : $X^2 = 3.518$, $df=3$, $p=.318$
Always male and female together	116	47,3	
Sometimes female, but mostly male	17	6,9	
Together with family members	46	18,8	
Perceive of competence of income	F	%	Chi-square
Our monthly income does not meet our needs	72	29,4	A ¹ : $X^2 =6.323$, $df=8$, $p=.611$ M.D. ¹ : $X^2=$ Does not valid I. ¹ : $X^2 = 66.274$, $df=8$, $p=.000^*$ E. ¹ : $X^2 = 29.621$, $df=12$, $p=.003^*$ S.W. ¹ : $X^2 = 5.393$, $df=4$, $p=.249$
We meet our needs on a monthly basis	113	46,1	
Monthly income makes it easier to meet our needs	33	13,5	
We can save a bit on our monthly income	27	11,0	

* $p<0.05$ ¹A:Age; MD:Marital Duration; I:Income; E:Education; SW:Spouse' Work Status

The majority of participants (89.0%) have stated that their monthly incomes are not sufficient or scarcely sufficient to satisfy the needs of families and thus, they cannot make savings. The reasons why employees cannot make savings are present in Table 3 in general. When Table 3 is examined as a whole, the rate of the ones, who cannot balance between incomes and expenses, in other words, who have stated that they can scarcely satisfy the needs of their families with their monthly incomes, is high (%55.1). They are followed respectively by the ones stating that they cannot make savings for they owe "various debts" (19.6%), "housing loan" (18.8%) and "consumer loan" (12.7%). When the relationship between the reasons of participants' not being able to make savings and their levels of monthly income and educational background is examined statistically; it has been found that there is a significant relationship between "I can only meet my family needs with my monthly income" ($X^2=28.639$, $df=2$, $p<0.05$),

“Housing loan” ($X^2=14.316$, $df=2$, $p=.001$); “car loan” ($X^2=13.017$, $df=2$, $p=.001$) and the level of monthly income, out of the reasons of not making savings (Table 3).

Using foreign exchange deposit	8	3,3	I: $X^2 =$ Does not valid E: $X^2 =$ Does not valid
Selling valuable items such as gold, jewelers	34	13,9	I: $X^2 =$ Does not valid E: $X^2 =$ Does not valid

* $p<0.05$; I: Income; E: Education

TABLE 3. THE REASONS THAT FAMILIES CANNOT FINANCIAL SAVING

The Reasons for not saving	F	%	Chi-square
I can only meet my family needs with my monthly income	135	55,1	I: $X^2 = 28.639$, $df=2$, $p=.000*$ E: $X^2 = 0.245$, $df=3$, $p=.970$
Credit card debt	48	19,6	I: $X^2 = 1.006$, $df=2$, $p=.605$ E: $X^2 = 2.318$, $df=3$, $p=.509$
Housing loan	46	18,8	I: $X^2 = 14.316$, $df=2$, $p=.001*$ E: $X^2 = 2.979$, $df=3$, $p=.395$
Consumer loan	31	12,7	I: $X^2 = 0.667$, $df=2$, $p=.716$ E: $X^2 = 5.686$, $df=3$, $p=.128$
Car loan	13	5,3	I: $X^2 = 13.017$, $df=2$, $p=.001*$ E: $X^2 =$ Does not valid
I cannot see any reason to save money	4	1,6	I: $X^2 =$ Does not valid E: $X^2 =$ Does not valid
I do not trust financial institutions that will evaluate my savings	1	0,4	I: $X^2 = 0.720$, $df=2$, $p=.698$ E: $X^2 =$ Does not valid
I cannot stop spending money	11	4,5	I: $X^2 =$ Does not valid E: $X^2 =$ Does not valid
I don't know	7	2,9	I: $X^2 =$ Does not valid E: $X^2 =$ Does not valid

* $p<0.05$; I: Income; E: Education

In order to determine in the study how individuals shall be able to satisfy their cash needs during uncertain or emergency cases, the question “How do you satisfy when you are in need of urgent cash?” was addressed to the individuals. The response of a bit more than half of the individuals (51.8%) was “We decrease our expenses”, the response of 24.5% of them was “We take out loan from bank”, the response of 23.7% of them was “We work overtime” and the response of 20.8% of them was “We withdraw cash from the credit card account”. However, the relationship of the ways of individuals’ satisfying their cash needs with neither levels of monthly income nor educational background was statistically significant (Table 4).

TABLE 4. THE WAY TO MEET THE URGENT NEED AND CHI-SQUARE RESULTS

The Way to Meet The Urgent Need	F	%	Chi-square
By reducing expenditures	127	51,8	I: $X^2 = 0.795$, $df=2$, $p=.672$ E: $X^2 = 1.609$, $df=3$, $p=.657$
Taking borrowed money from relatives, friends and relatives	58	23,7	I: $X^2 = 5.577$, $df=2$, $p=.062$ E: $X^2 = 1.077$, $df=3$, $p=.783$
Work overtime	16	6,5	I: $X^2 =$ Does not valid E: $X^2 =$ Does not valid
Working in an additional job	23	9,4	I: $X^2 =$ Does not valid E: $X^2 =$ Does not valid
Withdrawing cash on credit card	51	20,8	I: $X^2 = 3.641$, $df=2$, $p=.162$ E: $X^2 = 0.550$, $df=3$, $p=.908$
Using term deposit	11	4,5	I: $X^2 = 1.582$, $df=2$, $p=.453$ E: $X^2 = 1.054$, $df=3$, $p=.788$
Using credit from the bank	60	24,5	I: $X^2 = 4.715$, $df=2$, $p=.095$ E: $X^2 = 4.402$, $df=3$, $p=.221$

IV. CONCLUSION

Rapid change of socio-economic structure has affected behaviours and values of social institutions. Family, the primary unit of the country economy, is one of the most important institutions affected by this change. Families need effective management of economic resources such as income in an environment of financial system in which there is pressure of economic forces [38]. Therefore, the present study has been conducted with 245 married individuals who work at Kardemir Inc., in order to determine the individuals’ frequency of keeping a record for balancing between income and expenses, ways of taking decisions related to financial matters, competence perceptions related to expenditure and savings of their incomes, the reasons of not making savings and financial behaviours related to how they shall be able to satisfy their cash needs during uncertain or emergency cases.

The level of income is directly related to determining the levels of meeting the needs of the family, as well as the health, education, social interaction, house, free time and general life style conditions. Therefore financial security is an important goal of families worldwide. However, in developing countries, it is often difficult to meet even basic needs, especially within the uncertainty of an inflationary condition in the economy [39,40]. It is possible to discover numerous researches analyzing the economic activities of the families and the results of the economic activities in the developed and developing countries.

In conclusion, based on the findings obtained in the present study, the individuals keep records (budget) in order to balance between incomes and expenses of their families. However, the fact that they make a budget in order to be able to satisfy current requests and needs of the family indicates that they are in the opinion of satisfying their daily needs and they do not do future financial planning. This may result from the fact that the individuals included into the study do not have enough knowledge levels about financial matters and budget planning. This also makes it necessary to provide the individuals in family with trainings for financial matters for those individuals to effectively use incomes they shall earn today and in the future and to maintain and increase their quality of life.

The present study serves as a pilot study having been done on financial behaviours of the individuals. Repeating the study with the sample groups with different characteristics, by using different demographic, socio-economic and socio-cultural characteristics shall both enable the comparison and shall be useful for the determination of effects of the newly-used variables used.

As in all the studies, the present study also has certain limitations. The first of them is the fact that the study covers only married individuals. It is recommended that different demographic variables (being married or divorced or remarrying, etc.) be included into the new studies to be done.

Moreover, the present study has been done with the individuals who have the same economic conditions and work in a corporation. In the new studies to be done, as well as different socio-economic and socio-cultural characteristics, the individuals with different economic conditions, who work in different institutions or do not work and are retired, and the financial behaviours surviving in different countries can be compared.

Moreover, the present study is limited by questionnaire questions applied based on the subject. In the new studies to be planned; knowledge of, attitudes and behaviours towards the subject can be measured or comparisons can be made with different questions (For example, scales related to financial problems, stress sources, economic conditions of the country and/or financial behaviours in family) which may affect budget administration and financial behaviours. The present study is thought to set up a good substructure for the new studies to be made on the subject.

V. REFERENCES

- [1] Aydiner Boylu, A. and G. Terzioğlu, Ailelerin Yaşam Kalitelerini Etkileyen Bazı Subjektif Göstergelerin İncelenmesi. *Hacettepe Üniversitesi İktisadi ve İdari Bilimler Fakültesi Dergisi*, 2008;26(2),1-28.
- [2] Bailey, A.W., Social and Economic Factors Affecting The Financial well-Being of Families. *Journal of Home Economics*, 1987;79;2,14-18.
- [3] Raijas, A., Money Management in Blended and Nuclear Families. *Journal of Economic Psychology*, 2011;(32),556-563.
- [4] Marzieh, K.T., Z.H. Zare, M.T. Seyyed and R. Abdoreza, (2013), The relation between financial literacy, financial wellbeing and financial concerns. *International Journal of Business and Management*, 2013;8(11), 63-75.
- [5] Bartholomae, S. and J. Fox, *Economic stress and families*. In Patrick C. McKenry and Sharon J. Price (Eds.). *Families and Change: Coping with Stressful Events and Transitions* (3rd Edition). Thousand Oaks, CA: Sage. 2005,p:76-123.
- [6] Çopur, Z. and Ş. Şafak, Ailelerin Tasarruf Eğilimlerinin İncelenmesi. *Ekonomik ve Teknik Dergi*, 2003;42(508),68-72.
- [7] South S.J., The geographic context of divorce: Do neighborhoods matter? *Journal of Marriage and Family*, 2001(63),755-766.
- [8] Stanley S.M., P.R. Amato, C.A. Johnson and H.J. Markman, Premarital education, marital quality, and marital stability: Findings from a large, random household survey. *Journal of Family Psychology*, 2006(20):117-126.
- [9] Hira, T. K. and M.J. Mueller, The application of managerial systems to Money management practices. *Iowa State Journal of Research*, 1987;62(2),219-233.
- [10] Godwin, D. D., Family financial management. *Family Relations*, 1990(39),221-228.
- [11] Heimdal, R. and S.K. Houseknecht, Cohabiting and Married Couples Income Organization: Approaches in Sweden and the United States. *Journal of Marriage and the Family*, 2003(65),525-538.
- [12] Varghese, M.A., Ogale, N.N. and K. Srinivasan, Home Management, New Age International (P) Ltd., Publishing New Delhi. 1996, p:238-276.
- [13] Nyman, C. (2003), The Social Nature of Money – Meanings of Money in Swedish Families. *Women's Studies International Forum*. 2003;26(1),79-94.
- [14] Sumarwan, U. and K.T. Hira, The effects of perceived locus of control and perceived income adequacy on satisfaction with financial status of rural households. *Journal of Family and Economic Issues*, 1993;14(4),343-364.
- [15] Titus, P. M., A.M. Fanslow and T.K. Hira, Changes in Financial Status Influencing Level of Satisfaction in Households. *Lifestyles: Family and Economic Issues*, 1989(10),107-121.
- [16] Davis, E. and R.A. Carr, Budgeting practice over the life cycle. *Financial Counseling and Planning*, 1992;3, 3-16.
- [17] TUIK (2010). Hanehalkı İşgücü Araştırması <http://www.tuik.gov.tr/> Accessed: 27 January 2017.
- [18] Yadollahi, M., L. Hj Paim, M. Othman, and T. Suandi, Factors Affecting Economic Status. *European Journal of Scientific Research*, 2009;37,99-109.
- [19] Copur Z., Ş. Safak, G.R. Terzioğlu, and R. Dodder, Perception of Adequacy of Resources with a Turkish Sample. *Journal of Family Issues*, 2009;30(12),1624-1650.
- [20] Baek, E. and S.A. DeVaney, How Do Families Manage Their Economic Hardship? *Family Relations*, 2010;59,358-368.
- [21] Chuan, C.S., S.B. Kai and N.K. Kok, Resource Transfers and Financial Satisfaction: A Preliminary Correlation Analysis. *Journal of Global Business and Economics*. 2011;3(1),146-156.
- [22] Xiao, J.J., C. Tang and S. Shim, Acting for Happiness: Financial Behavior and Life Satisfaction of College Students. *Social Indicators Research*, 2009; 92,53-68.
- [23] Parrotta, J.L. and P.J. Johnson, The Impact Of Financial Attitudes And Knowledge On Financial Management And Satisfaction Of Recently Married Individuals. *Financial Counseling and Planning*, 1998;9(2),59-75.
- [24] Kardemir A.Ş., İnsan Kaynakları. <https://www.kardemir.com/Info.aspx?Sec=Bilgi&Lng=tr-TR&W=1> Accessed: 02 January 2017
- [25] Büyükoztürk, Ş., *Sosyal Bilimler İçin Veri Analiz El Kitabı* Pegem Akademi Yayıncılık Ankara, Baran Ofset. 2007, p:145
- [26] Kenyon, D.B. and L.M. Borden, Family Financial Management — Planning for the Future (2003). <http://cals.arizona.edu/pubs/family/az1341/az1341i.pdf> Accessed :14 January 2017.
- [27] Mullis, R. and K. Schnittgrund, Budget behavior: Variance over the life cycle of low income families. *Journal of Consumer Studies and Home Economics*, 1982;6,113-120.
- [28] Schnittgrund, K. and G. Baker, Financial Management of Low Income Urban Families. *Journal of Consumer Studies and Home Economics*, 1983;7,261-270.
- [29] Scannell, E., Dairy Farm Families Financial Management. *Financial Counseling and Planning*. 1990;1,133-146.
- [30] Erbil, N. and T. Pasinlioğlu, Kadının Ailede Karar Vermeye Etkisi. *Atatürk Üniv. Hemşirelik Yüksekokulu Dergisi*, 2004;7,2, 1-11.
- [31] Şener A. and G.R. Terzioğlu, G.R. (2005), Determining the Expenditure, Investment and Saving Patterns in Respect of Family Life Cycles. *Aile ve Toplum Dergisi*, 2005;2,8,53-59.
- [32] Ashby, K.J. and C.B. Burgoyne, Separate financial entities? Beyond categories of money management. *The Journal of Socio-Economics*, 2008;37,458-480.
- [33] Kabaklı Çimen, L., Bir Faktör Olarak Eğitimin Kadının Aile İçi Kararlara Katılımı Üzerine Etkisi. *International Journal of NewTrends in Arts, Sports and Science Education*, 2012;1(2),78-90.
- [34] Hopper, J.S., Family financial decision making: implications for marketing strategy. *Journal of Services Marketing*, 1995;9(1)24 - 32.
- [35] Goldsmith, E.B. (2000). *Resource Management for Individuals and Families*. Second Edition. Florida State University Wadsworth Thomson Learning U.S. 2000, p:345-368.
- [36] Rosen, D. and D. Granbois, Determinants of Role Structure in Family Financial Management. *Journal of Consumer Research*, 1983;10,253-258.
- [37] Becker, G.S., Family Economics and Macro Behavior. *American Economic Review*, 1988;78(1)1 - 13.
- [38] 2001 Yılı Aile Raporu, *Ailenin Ekonomik ve Sosyal Güvenlik Sorunları*. 2001 Yılı Aile Raporu (Ed.Çaylıoğlu, İ.). T.C. Başbakanlık Aile Araştırma Kurumu Yayınları, Yayın No:120. Ankara. Beyda Ofset. (ISBN 975-19-3235-1). 2002, s: 367.
- [39] Diener E and R. Biswas-Diener, Will Money Increase Subjective Wellbeing? *Social Indicators Research* 2002;57, 119-169.
- [40] Ormsby, P. and G.T. Fairchild, Perceived Income Adequacy And Selected Financial Management Practices Among Families in Chile And Mexico. *Social Indicators Research*, 1987; 19,317-327.

Turkey's Magnesite for Production of Fused Magnesia, Properties and Uses in Refractory Applications

Asım Bilge*, Cemalettin Yaman⁺, Nuri Sarioğlu*

*Kümaş Manyezit San. A.Ş.
Eskişehir Yolu 9.km, Kütahya, Turkey
asim.bilge@kumasref.com
nuri.sarioğlu@kumasref.com

⁺Metallurgical and Materials Engineering, Yıldız Technical University
Turkey
yaman@yildiz.edu.tr

Abstract— Magnesite (MgCO₃) is natural source for production of caustic calcined, dead burned and fused magnesia. Turkey's magnesite sources have a well-known reputation internationally with high purity, cryptocrystalline structure and suitability for refractory applications.

For high temperature processes, there is a great need for refractory raw materials that can withstand oxidative environment at elevated temperatures. Fused magnesia (FM) is the most important material for these purposes with melting point 2800 °C and one of the key element of the refractory heat resistant materials especially for steelmaking refractory bricks. Fused magnesia is considered to be one of the best thermal and electrical insulators with high density, high purity and large crystals.

Fused magnesia (FM) is produced by electric arc melting of magnesite or CCM in a traditional Higgins furnace or in tilt-type furnace at >2800°C. Quality of the electrically fused magnesia is determined by choosing magnesite source, beneficiation processes, arc furnace electrical parameters and sorting. Final product were characterized by using chemical analysis, scanning electron microscope and EDX. Samples from different process parameters were investigated according to their crystal size, bulk density and impurity formation.

Keywords— Magnesite, magnesia, fused magnesia, refractory raw materials, magnesia-carbon bricks, steelmaking refractories

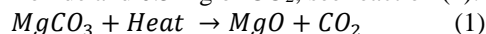
I. INTRODUCTION

Magnesite (MgCO₃) is the main raw material of fused magnesia production. Magnesite resources in the world are mainly in China, North Korea, Russia, Greece, Austria and Turkey. Magnesium carbonate (MgCO₃) occurs naturally as the mineral magnesite in two physical forms, macrocrystalline (spathic) and cryptocrystalline (amorphous, compact) [1].

Turkey mostly has cryptocrystalline magnesite reserves. Cryptocrystalline magnesite is generally of higher purity than macrocrystalline magnesite and generally contains less iron oxide but deposits are usually smaller and have a lower yield of ore to waste material, which makes them more expensive to

extract. The ore deposits often occur as an alteration product in ultrabasic rocks, typically serpentine (magnesium silicate).

Magnesite processing (Fig. 1) can be divided into crushing, sizing and beneficiation stages. The degree of beneficiation required depends on the quality of the ore and its intended end use. Cryptocrystalline ores may only need crushing, screening, washing and hand-sorting to produce a material suitable for caustic calcined magnesia (CCM), dead burned magnesia (DBM) or fused magnesia (FM). After beneficiation, purity level can reach 98%wt MgO. Calcination reaction that occurs during heating is the loss of carbon dioxide from magnesite, with the corresponding formation of magnesium oxide, the full decomposition of 1kg of pure magnesite yields 0.48kg of magnesium oxide and 0.52kg of CO₂; see reaction (1):



Fused magnesia is an essential material that has been widely used in many industries, such as the chemical industry, metallurgical industry, heating elements industry and aerospace industry [2]. Fused magnesia is considered to be one of the best thermal and electrical insulators with high density, high purity and large crystals. High-purity fused magnesia is mainly produced by the three phase AC arc furnace (Fig. 2).

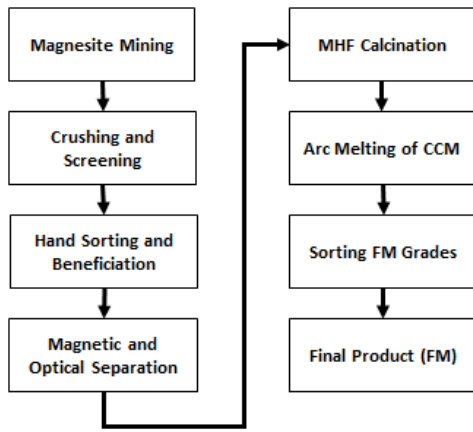


Fig. 1 Flow diagram of fused magnesia production

TABLE XLI
PRODUCTION TEMPERATURES AND PHYSICAL PROPERTIES OF MGO PRODUCTS

Material	Temp. (°C)	Crystal Size (µm)	Porosity (%)	Density (g/cm ³)
Caustic Calcined	700 - 900	<0,5	75	-
Dead Burned	1600 - 2000	>75	<0,3	3,10 – 3,40
Fused	>2800	>800	<0,1	>3,48

Fusion furnaces can be operated on both one-step and two-step processes depending on energy costs and quality. Magnesite is used in the one-step and CCM in the two-step process. FM is characterised by very large periclase crystals of more than 800µm (compared to 75µm for DBM) and a density approaching 3.55 g/cm³.

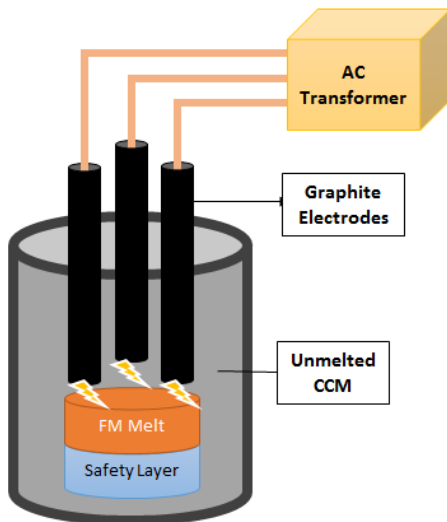


Fig. 2 Arc furnace for production of fused magnesia

After melting and cooling process, fused magnesia ingot is formed in the furnace [3]. Ingot (Fig. 3) will be broken into pieces with crushers to desired grain size and the last step in the

process is the separation of fused magnesia from the crust material.

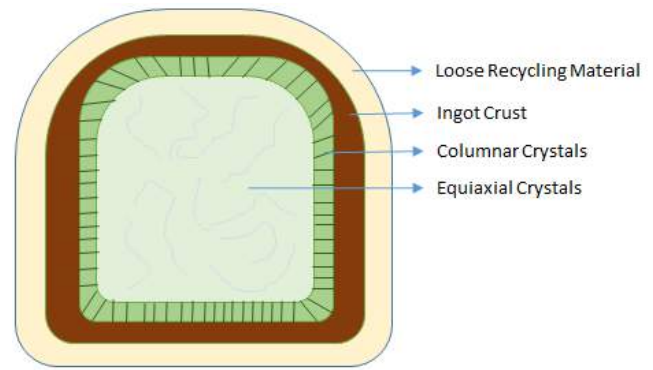


Fig. 3 Zonal structure of fused MgO ingot

II. EXPERIMENTAL

In this investigation, two type of CCM material which is processed from Turkey's magnesite reserves from Kütahya region are fed into fusion furnaces and samples are taken from the melted ingots. Feeding materials' properties are given in the Table 2.

TABLE 2
TWO TYPE OF CCM MATERIALS FOR FUSION EXPERIMENTS

Material	SiO ₂ (wt%)	CaO (wt%)	Fe ₂ O ₃ (wt%)	Al ₂ O ₃ (wt%)	MgO (wt%)
CCM-1	0,92	1,75	0,42	0,04	96,87
CCM-2	1,74	2,11	0,57	0,05	95,53

Fusion furnace secondary voltage was 180 V and secondary current was 7,5 kA. Melting time was 11 hours. Specific energy consumption for FM production is 2500 – 3500 kWh [4]. After few days cooling period, ingots are crushed and sized for further investigation.

Sampling was done based on 10 kg for different testing and samples are taken from different zones of ingots. Chemical analysis of each sample was done by X-ray fluorescence (XRF) against appropriate standard at KÜMAŞ Laboratories. Grain bulk density was measured by boiling water method using coarse grains.

For average grain size measurement and distribution of impurities present in fused magnesia, scanning electron microscope (SEM) was conducted for different fused magnesia samples at Ceramic Research Centre, Eskişehir.

III. RESULTS AND DISCUSSION

Three zones of fused magnesia ingots labeled as A, B, C are used in the experiments (Fig. 4). Sample A is the equiaxial fused magnesia crystals and the most amount of FM material from ingots. Sample B is the columnar crystals which is formed during slow cooling period. Sample C is the semifused/sintered material from ingots.

Chemical analysis and bulk densities of FM samples are given in Table 3 referred to feeding CCM-1 and CCM-2 materials.

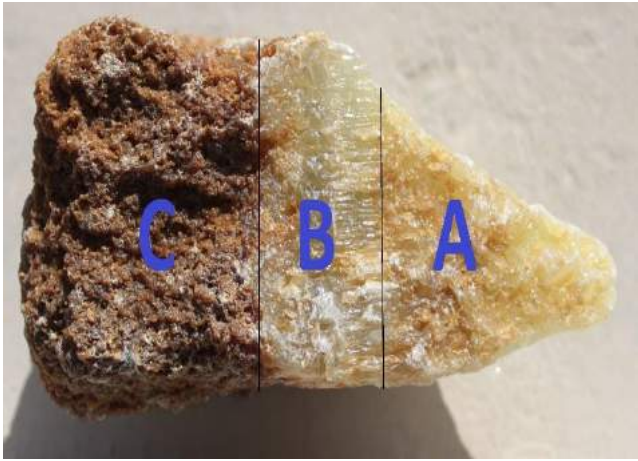


Fig. 4 Sample labels of different zones from FM ingots

TABLE 3
CHEMICAL AND PHYSICAL PROPERTIES OF FUSED MGO SAMPLES

Zone	FM-1 (CCM-1 Feed)			FM-2 (CCM-2 Feed)		
	A1	B1	C1	A2	B2	C2
SiO ₂ (wt%)	0.58	0.42	1.62	0.96	0.57	1.86
CaO (wt%)	1.44	0.85	2.12	1.93	1.18	2.25
Fe ₂ O ₃ (wt%)	0.38	0.25	0.53	0.44	0.34	0.61
Al ₂ O ₃ (wt%)	0.02	0.01	0.05	0.02	0.02	0.06
MgO (wt%)	97.58	98.47	95.68	96.65	97.89	95.22
Density (g/cm ³)	3.50	3.52	3.41	3.49	3.52	3.39
C/S ratio	2.48	2.02	1.31	2.01	2.07	1.21

As expected, CCM-1 feed results are better than CCM-2 feed in terms of purity level. As shown in the Table 3, ingots are heterogeneous in terms of chemical analysis and all zones have different properties. Samples from A and B zones are the main FM material and its purity is higher than starting materials. The purest zone of ingot is Sample B1 and B2 for both experiments due to single crystal forming.

Sample C has high impurity level compared to feeding material because of the migration of the impurities to the outside of the ingot with thermocapillary transfer mechanism and it occurs by density difference between periclase and silicate phases [5].

Lime/silica ratio is also important indicator of phase formation. C/S ratio for Samples A and B are above 2, whereas for Samples C this value is below 2 in the results. These test results always indicate that silica present in A and B is expected to exist mostly as C₂S (dicalcium silicate, T_m= 2130 °C) [6].

As shown in the Table 4, lower C/S ratio causes the formation of the low melting point phases on the grain boundaries. Samples C have a low C/S ratio and it is expected to be formed mostly as CMS (monticellite) and C₃MS₂ (merwinite) phases on grain boundaries.

TABLE 4
PHASES IN EQUILIBRIUM WITH MGO IN THE MGO – CaO – SiO₂ SYSTEM

C/S Weight Ratio	Phase Name	Composition	Melting Temp. (°C)
0.90 – 1.40	Monticellite	CaO.MgO.SiO ₂	1488
1.40 – 1.86	Merwinite	3CaO.MgO.2SiO ₂	1576
1.86 – 2.80	Dicalcium Silicate	2CaO.SiO ₂	2130
>2.80	Tricalcium Silicate	3CaO.SiO ₂	1899

The bulk density (BD) of the grains of Samples A1-2 and B1-2 varies from 3.49 to 3.52 g/cm³. These materials are suitable for steelmaking bricks as raw materials whereas corrosive slags occur. High bulk density indicates low porosity and highly compact material. However, density of Samples C varies from 3.39 to 3.41 g/cm³ and it is comparable with high quality dead burned magnesite.

In the SEM examination, it is found that average crystal size for Samples A1, A2, B1, B2, C1 and C2 are 800 μm, 745 μm, 2100 μm, 1950 μm, 420 μm, 395 μm respectively.

Periclase crystal size is important for refractory bricks because it reduces surface area and penetrability of corrosive slags into the refractory bricks. For that reason, high quality fused magnesite is essential raw material for high performance magnesite-carbon bricks. These MgO-C bricks are specially used at basic oxygen furnace (BOF) vessels, ladles and electric arc furnace (EAF) slag liners [7].

As shown in the Fig. 5, for Sample A1, darker areas are the periclase crystals, lighter areas are mostly dicalcium silicate impurities on grain boundaries and very thin impurity formation which enhances the refractory properties.

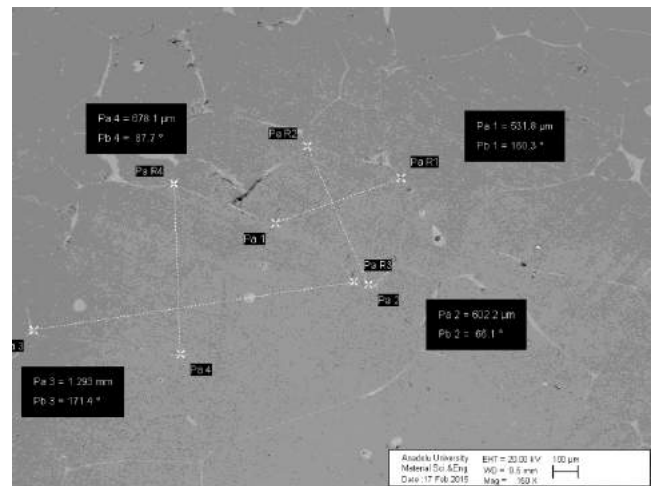


Fig. 5 SEM image of A1 fused magnesite sample

As shown in the Fig. 6, for Sample C1, periclase crystals are smaller than Sample A1. It is expected that impurity phases are mostly monticellite and merwinite and these phases have lower melting points than dicalcium silicate.

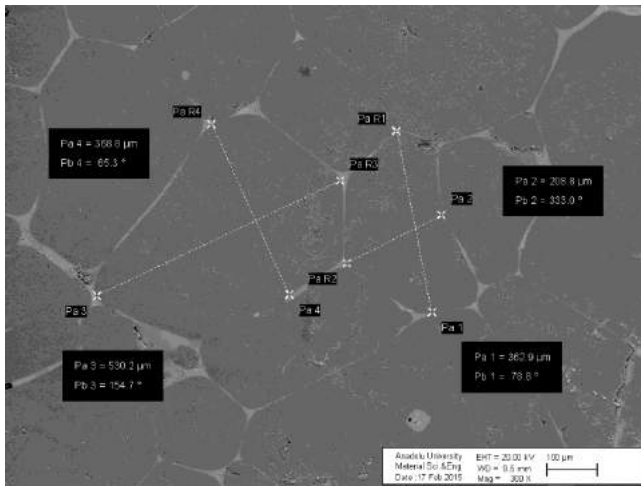


Fig. 6 SEM image of C1 magnesia sample

As shown on the Fig. 7 and Fig. 8, EDX analysis applied on Sample A1. Spectrum shows that 98.16% MgO and 1.84% CaO were found so material is nearly pure with very low content of lime.

Samples from A and B zones of ingots have low silica content, high lime/silica ratio, with high density.

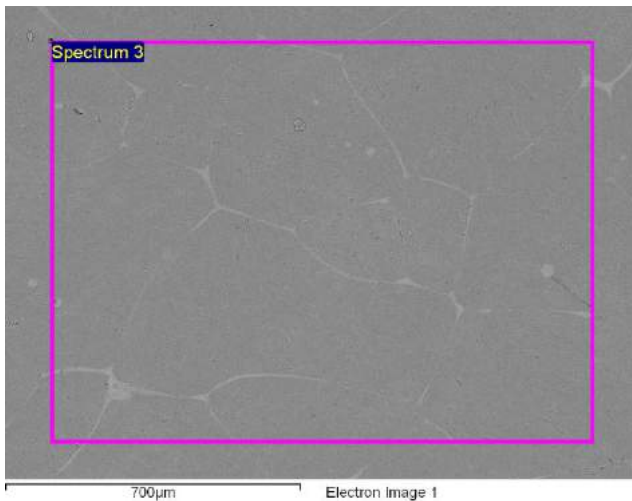


Fig. 7 SEM EDX area of A1 fused magnesia sample

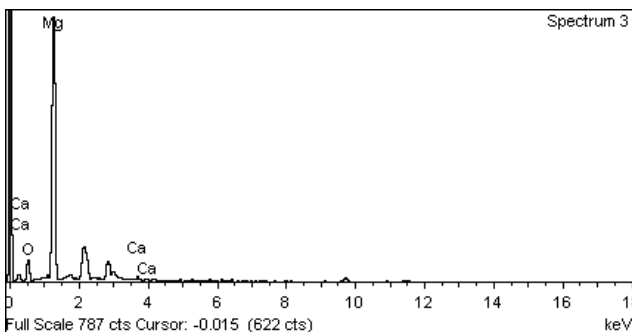


Fig. 8 EDX spectrum of A1 fused magnesia sample

IV.

V. CONCLUSIONS

This paper focused on fused magnesia derived from Turkey's cryptocrystalline magnesite reserves. It was shown that the main factors in obtaining high quality fused periclase are the purity of the raw materials, determining the high MgO concentration in periclase; occurrence of impurity transfer into the skin of the ingots.

The specification of columnar and center crystals of fused magnesia ingots derived from the present study can give high performance in magnesia-carbon bricks and subsequently longer campaign life for better converter and electric arc furnace hot spots/slag line applications.

VI. ACKNOWLEDGMENT

This work supported by Kūmaş Manyezit San. A.Ş. Kūtahya/Turkey.

VII. REFERENCES

- [1] Mark A. Shand, *The Chemistry and Technology of Magnesia*, Wiley-Interscience, 2006.
- [2] Y. Fou, N. Wang, Z. Wang, Z. Wang, B. Ji, X. Wang, "Smelting condition identification for a fused magnesium furnace based on an acoustic signal," *Journal of Materials Processing Technology* 244, 231–239, 2017.
- [3] S. Hoda, I. Zeqiri, M. Sadiku, M. Kelmendi, B. Baruti, "Preparation of Electrically Fused Magnesium Oxide from Calcined Magnesite for Use in Electrothermics," *Chemistry in industry : Journal of Chemists and Chemical Engineers*, Vol.63 No.1-2, January 2014.
- [4] G. Qi, F. Shan, Q. Li, J. Yu, "Energy Saving by Applying 3000kVA Electric Arc Furnace in Fused Magnesia Production," *Materials Science Forum* Vol. 749 pp 299-302, 2013.
- [5] V. A. Bron, I. A. Stepanova, N. A. Mityushov, V. A. Perepelitsyn, I. S. Raeva, V. G. Sivash, E. A. Egorov, "Production technology and quality of fused periclase," *Refractories*, 1979, doi:10.1007/BF01281932.
- [6] L. Redecker, A. Sax, P. Quirnbach, H. Jansen, "Reactions of Secondary Phases with Carbon in Magnesia-Carbon Bricks," *J. Am. Ceram. Soc.*, 1–9, 2016.
- [7] S. Pal, A. K. Bandyopadhyay, "Suitability of Different Grades of Fused Magnesia for Magnesia-Carbon Refractories for Critical Applications," *Transactions of the Indian Ceramic Society*, 66:2, 103-105, 2014.

Investigation of Dry Sliding Wear Resistance of AISI 52100 Steels under Different Tribological Conditions

Enbiya Türedi*, Merve Yılmaz[†]

*Kocaeli University, Faculty of Engineering, Dept. of Metallurgical and Materials Eng.
Umuttepe Campus, TR-41380, Kocaeli, Turkey
enbiya.turedi@kocaeli.edu.tr

[†]Kocaeli University, Faculty of Engineering, Dept. of Metallurgical and Materials Eng.
Umuttepe Campus, TR-41380, Kocaeli, Turkey
merve.yilmaz@kocaeli.edu.tr

Abstract—AISI 52100 is a well-known and commonly used bearing steel in manufacturing industry, today. The wear phenomenon in this type of steel may play a critical role in service life. Likewise a bearing steel part running under heavily dynamic loads could be out of service in a short time when tribological conditions particularly turned into boundary film lubrication or even worse into unlubricated condition etc. On the other hand, their tribological properties can be enhanced by heat treatment conditions. Thus the service life can be extended since they became more wear resistant. However hardness and wear resistance are normally increased at expense of toughness which is another key factor in bearing steels. Therefore it is important that optimizing heat treatment conditions in terms of not only hardness and wear resistance but also toughness. In this study, the tribological properties of three groups of AISI 52100 bearing steel specimens heat treated in different conditions were compared in terms of wear volume, wear factor, hardness and friction coefficient values. For this purpose dry sliding tests were performed in according to ASTM G99-05 standard using a “ball-on-disk” type equipment. The results showed that tempered martensitic specimens heat treated at relatively higher temperatures yielded almost same wear characteristics with harder and less tougher specimens under given tribological conditions.

Keywords—Bearing steel, dry sliding test, heat treatment, tribology, wear

I. INTRODUCTION

Bearing steels must meet a number of requirements in order to be able to operate safely in the system in which they are used. These include rolling or sliding contact, axial load and fatigue resistance in case of crack growth, furthermore hardness, strength, toughness, hydrogen resistance, ductility and corrosion resistance [1-6]. Essentially developed for machining tools, steels with a carbon content of between 0.8-1.1 wt.-% and a total dissolved atom content of less than 3.0 wt.-% are widely used for bearings [1]. The steels used for bearings are transformed into a martensitic matrix structure by quenching in

various mediums including oil and salt baths. Following this process, the tendency to excess brittleness can be eliminated by tempering at relatively low temperatures. The hardened section may vary depending on the wall thickness of the bearing component. For example, low-wall thickness parts can be hardened throughout the section as the hardenability depth is sufficient. For larger sections, the hardenability depth can be improved by pack cementation or by increasing the content of the alloy element [1,3,6].

Bearing steels have pre-eutectoid cementite formation during solidification or cooling as they also have hypereutectoid composition. When the pre-eutectoid cementite precipitates on the austenite grain boundaries during cooling, it becomes an undesirable state in the microstructure, and wear resistance is negatively affected by this structure especially for rolling contact [1,3]. For this reason spheroidization annealing is a heat treatment especially applied before machining and hardening in bearing steels [3,6-8].

In this study, the wear characteristics of microstructures obtained under different heat treatment conditions in AISI 52100 type bearing steels under different tribological conditions are investigated and it is aimed to determine which heat treatment condition have a tribological advantageous hardness, wear resistance and toughness properties which are important for operating conditions of bearing steels.

II. MATERIALS AND METHOD

The chemical composition of the studied AISI 52100 steel is presented in Table I as received from the manufacturer. The specimens were obtained as sliced disks with dimensions of 12-15 mm in height and 40 mm in diameter.

MM. Heat Treatments and Specimen Preparation

All specimens were first austenitized at 900 °C for 1/2 hour, then quenched in water to room temperature. The specimens

TABLE XLII
THE CHEMICAL COMPOSITION OF AISI 52100 STEEL SPECIMENS SUBMITTED BY THE MANUFACTURER (WT-%)

C	Si	Mn	Cr	Mo	Ni	Cu	Al	P	S	Fe
0.95	0.21	0.36	1.44	0.01	0.07	0.19	0.01	0.008	0.002	rest

were divided into three groups in terms of heat treatment conditions, see Table II. After metallographic surface preparation, specimens were etched with 3.0 vol.-% nital and microstructures were examined in SEM (Fig. 1-3). Vickers hardness values were also measured.

In the first group with coded as S01, the specimens were tempered at 795°C for half an hour, cooled at 370 K/h cooling rate in a furnace to 680°C and then cooled to room temperature in the air in according to Verhoeven's thermal cycle [8]. The purpose was to create a reference material that can be compared to the other group of specimens, in order to demonstrate the effect of modification of the pre-eutectoid cementite because of the spheroidization annealing. As a result, there are very fine grained spherical cementite grains in the ferrite matrix so-called "spherical pearlite" in the microstructure (Fig. 1). This structure, which has a very low hardness (213 HV₁₀) (see Table II), is the most advantageous in terms of machining and ductility.

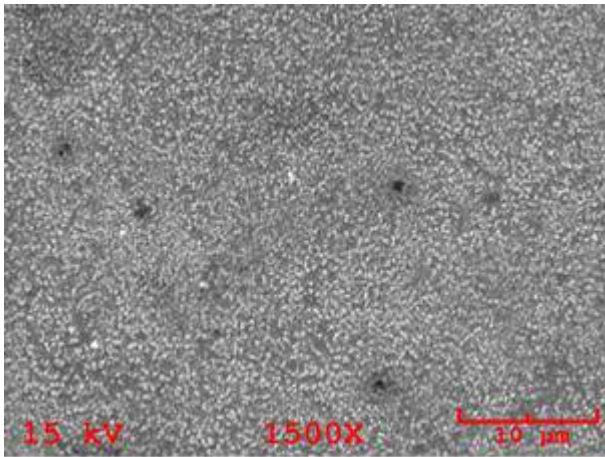


Fig. 1 "Spheroidal pearlite" structure of S01 specimen etched with Nital (3 vol.-%) in SEM/SEI mode: very finely dispersed cementite particles in ferritic matrix

The S02 microstructure exhibits a typical full-tempered martensitic matrix obtained by annealing at 400 °C for half an hour after water quenching (Fig. 2). It reveals a characteristic that the plate type martensitic morphology changes markedly and thin carbide precipitates are often seen which is locally similar to upper bainite structure. Measured average hardness value is 552 HV₁₀. In Figure 2, on the microstructure taken in the "compo mode" of the BEI contrast used in the image formation of the backscattered electrons at SEM, the spot EDX analysis on one of the particles visible as black tinted shows the

iron oxide structure. This is considered to be the local and very thin oxide layer on the surface despite the metallographic surface preparation process due to tempering in the air atmosphere.

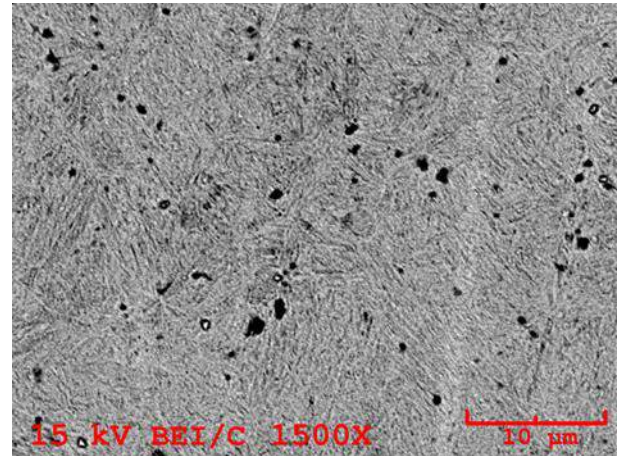


Fig. 2 Tempered martensitic structure of S02 specimen etched with same etchant mentioned above in SEM/BEI-Compo mode: mainly tempered martensitic matrix as well as resembling locally upper bainitic structure

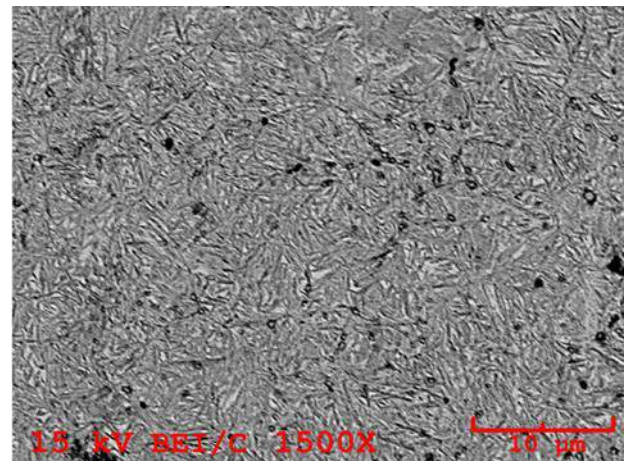


Fig. 3 Tempered martensitic structure of S03 specimen etched with same etchant mentioned above in SEM/BEI-Compo mode: a microstructure including retained austenite in a matrix, which still preserving martensitic morphology

The specimen S03 reveals a microstructure that has stress relief annealing rather than the full tempering effect. Also, after quenching, specimens are tempered at 200°C for 1/2 hour, and it can be seen that change of the plate type martensite morphology starts and first stages of the tempering effect

TABLE IXLIII
THE HEAT TREATMENT CONDITIONS APPLIED TO AISI 52100 STEEL SPECIMENS AND HARDNESS VALUES OBTAINED

Specimen	Austenitizing	Quenching	Tempering	Remarks	Hardness (HV ₁₀)
S01	900°C (1/2 h)	aqueous	795°C (1/2 h)	Cooling in furnace to 680°C with a cooling rate of 370 K/h, then cooling in air to RT.	213.0±08.3
S02	900°C (1/2 h)	aqueous	400°C (1/2 h)	Cooling in air to RT	552.7±04.1
S03	900°C (1/2 h)	aqueous	200°C (1/2 h)	Cooling in air to RT	779.2±12.1

TABLE III
DRY SLIDING TEST CONDITIONS AND TRIBOLOGICAL PARAMETERS

Load (N)	Counterpart (ball)			Temp.	Relative Humidity	Sliding	
	material	diameter (mm)	hardness (HV ₁₀)			speed (m/s)	distance (m)
10 20 30	100Cr6	5.00	843.8	RT	N/A	0.063 0.159 0.249	100

begins. Retained austenite can be seen in the section. Average hardness value was measured as 779 HV₁₀. It has the hardest microstructure in comparison. If the study by Martinez et al. [9] is considered, this group of specimens must also be had the lowest toughness value among others. Here again, images were taken in a BEI/Compo mode in SEM due to better contrast enhancement.

NN. Dry Friction Tests

A series of dry friction tests was performed on a “ball-on-disk” type tribometer according to ASTM G99-05 standard [10] for wear characterization. The tribological test parameters are summarized in Table III. The specimens were subjected to wear

tests under three different loads and three different sliding speed levels, while the other parameters were kept constant.

OO. Wear Characterization

After the dry friction test, the worn surfaces on both the specimens and the counterparts (ball) were examined in light microscope, and the wear track dimensions (width or diameter) were measured by calibrated image analysis software and their average values were calculated. By using the mathematical formulae given in ASTM G99-05 [10], wear track width on the specimen surface and the worn tip diameter values on the counterparts’ surface as well as their wear volume and wear factor [11] values were measured and calculated, accordingly.

TABLE IV
THE RESULTS AFTER DRY SLIDING TEST PERFORMED WITH DIFFERENT TRIBOLOGICAL PARAMETERS

Specimen	Load (N)	Coefficient of friction (-)	Wear volume (×10 ⁻³ mm ³)		Wear factor (×10 ⁻⁶ mm ³ /N·m)		Sliding speed (m/s)
			in specimen	in counterpart	in specimen	in counterpart	
S01	10	0.22	13.38	0.11	13.38	N/A	0.063
	20	0.25	54.17	0.12	27.08	N/A	
	30	0.23	78.61	0.13	26.2	N/A	
	10	0.31	104.22	2.71	104.22	2.71	0.159
	20	0.24	400.02	17.68	200.01	8.84	
	30	0.21	858.08	10.30	286.03	3.43	
	10	0.28	597.61	0.33	597.61	0.33	0.249
	20	0.18	1308.43	1.94	654.22	0.97	
	30	0.24	4246.31	37.49	1415.44	12.50	
S02	10	0.25	5.44	23.22	5.44	23.22	0.063
	20	0.24	9.01	34.24	4.51	17.11	
	30	0.29	11.95	37.1	3.98	12.37	
	10	0.39	54.90	5.74	54.90	5.74	0.159
	20	0.24	124.63	8.96	62.31	4.48	
	30	0.37	362.87	28.48	120.96	9.49	
	10	0.40	146.07	6.60	146.07	6.60	0.249
	20	0.36	295.45	6.78	147.72	3.39	
	30	0.45	814.52	29.98	271.51	9.99	
S03	10	0.26	5.72	13.08	5.72	13.08	0.063

20	0.28	8.92	24.04	4.46	12.02	
30	0.23	9.4	36.34	3.13	12.11	
10	0.15	59.77	12.97	59.77	12.97	0.159
20	0.18	139.83	22.42	69.92	11.21	
30	0.19	237.39	34.72	79.13	11.57	
10	0.22	30.68	8.11	30.68	8.11	0.249
20	0.12	156.93	15.12	78.47	7.56	
30	0.46	455.06	24.41	151.69	8.14	

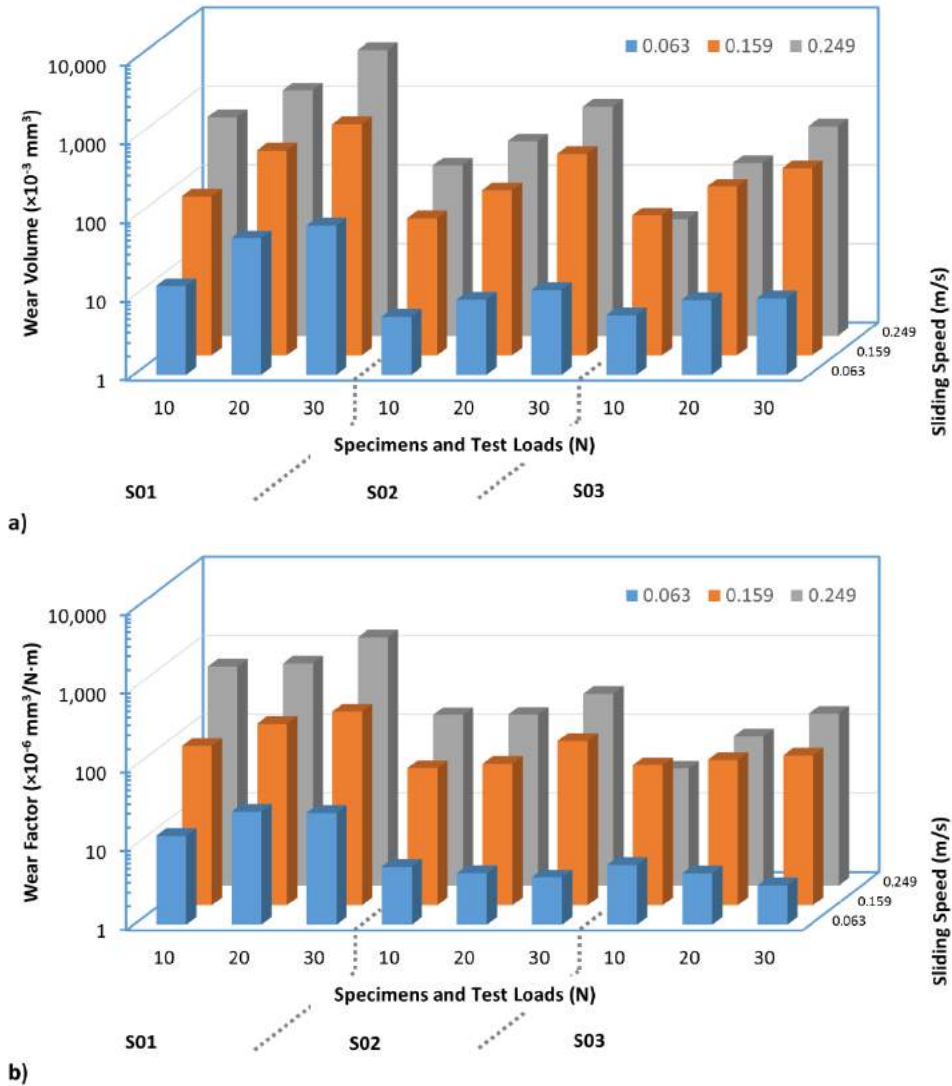


Fig. 4 The change of wear volume (a) and wear factor calculated in specimens with test load and sliding speed

III. RESULTS AND DISCUSSION

The data obtained and calculated after dry friction tests are listed in Table IV. As seen in the Table, 27 specimens were tested for three sets of specimens, three different test loads and three different sliding speed values. In each test, the friction coefficient values in the “steady-state” condition were recorded and the wear volumes as well as the wear factors of the specimens and counterparts were calculated. If the variation of

the coefficient of friction values is considered, the values obtained for the S01 specimens varied in a narrower range (0.18-0.31) than the values for S02 and S03 and thus yielded relatively a lower standard deviation (0.04). The distribution range of S02 specimens is between 0.24-0.45 and their standard deviation is about 0.08. S03 group showed relatively the widest range (0.12-0.46) with a standard deviation of 0.10. The wear volume values were measured for both the specimens and counterparts, and a series of diagrams were prepared to reveal

how the tribological parameters are changed quantitatively (see Fig. 4-6). Volumetric wear losses in the specimens at different test loads and different sliding speed conditions were compared in Fig. 4a and the effect of the same tribological parameter changes on the wear factor is shown graphically in Fig. 4b. Fig. 5 shows the relationship between the wear volume and the test load at different sliding speeds, the resulting curves are expressed by exponential functions and the determination coefficients (R^2 values) are measured.

In Fig. 6, the wear volume values were converted to the wear factor values by normalizing them to the test load and friction distance values, and the change between the specimens at different test load and sliding speed values was observed and transferred into the diagram. Using the similarly calculated exponential functions and the determination coefficients, the wear resistance and characteristics between the specimens were compared.

The wear surface images of least and most worn specimens from groups of S01, S02 and S03 were taken in SEM (a) and LM (b) and presented in Fig. 7-9, respectively. Light microscopy images were taken under bright field contrasting method using a 20x objective while SEM images taken in secondary electron imaging (SEI) mode.

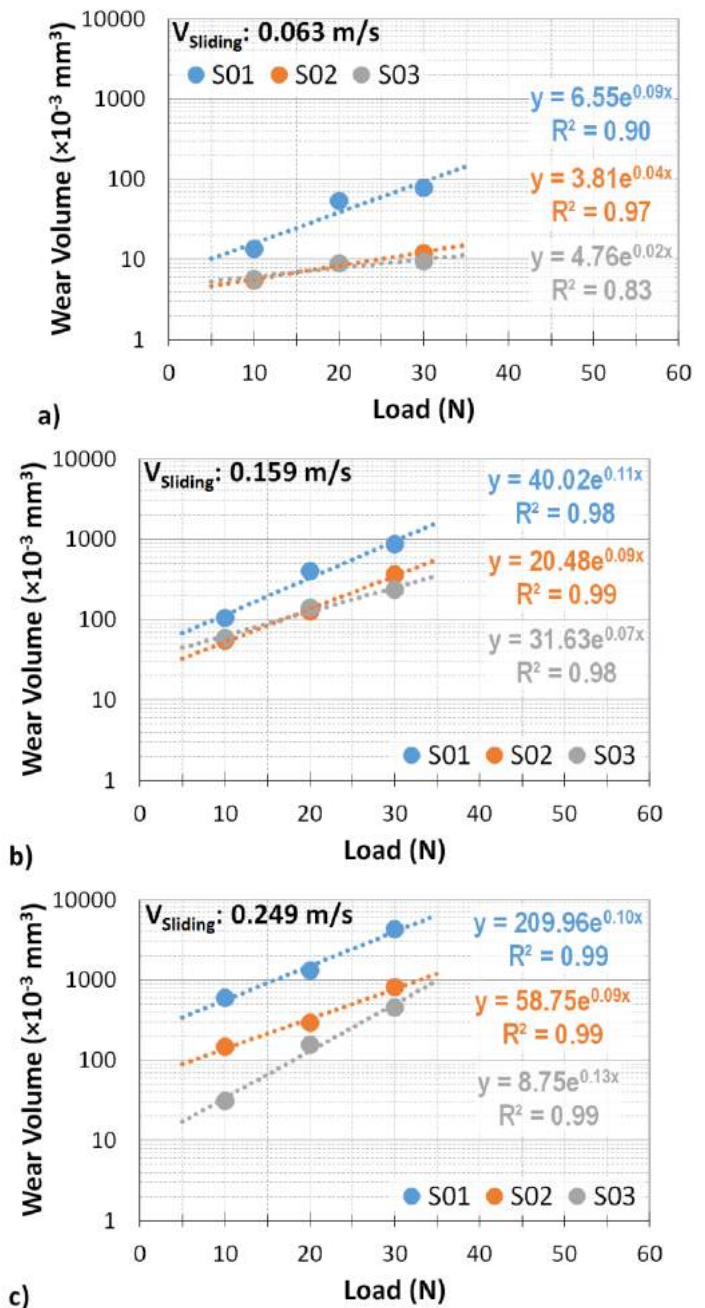


Fig. 5 Wear volume and test load relationship obtained by bearing steel specimens at different sliding speed levels; a) 0.063 m/s, b) 0.159 m/s and c) 0.249 m/s

According to the main results of the wear test summarized in Table IV and Fig. 4, it is understood that the results in the specimen groups are the same as predicted from the literature [12]. In his study which investigates grooving and sliding wear mechanisms, Zum Gahr [12] emphasized that wear resistance increases on one of the pairs in which the hardness is increased. He also stated that the abrasive wear plays an important role in the former mechanism, while the adhesive wear stands out in the latter case. However, he added that the both mechanisms take place in different shares in the same tribological condition,

and moreover these may also be accompanied by tribochemical and fatigue wear. As a matter of fact, similar findings

congruity and exhibit highly reliable math functions representing a close relation between given tribological parameters.

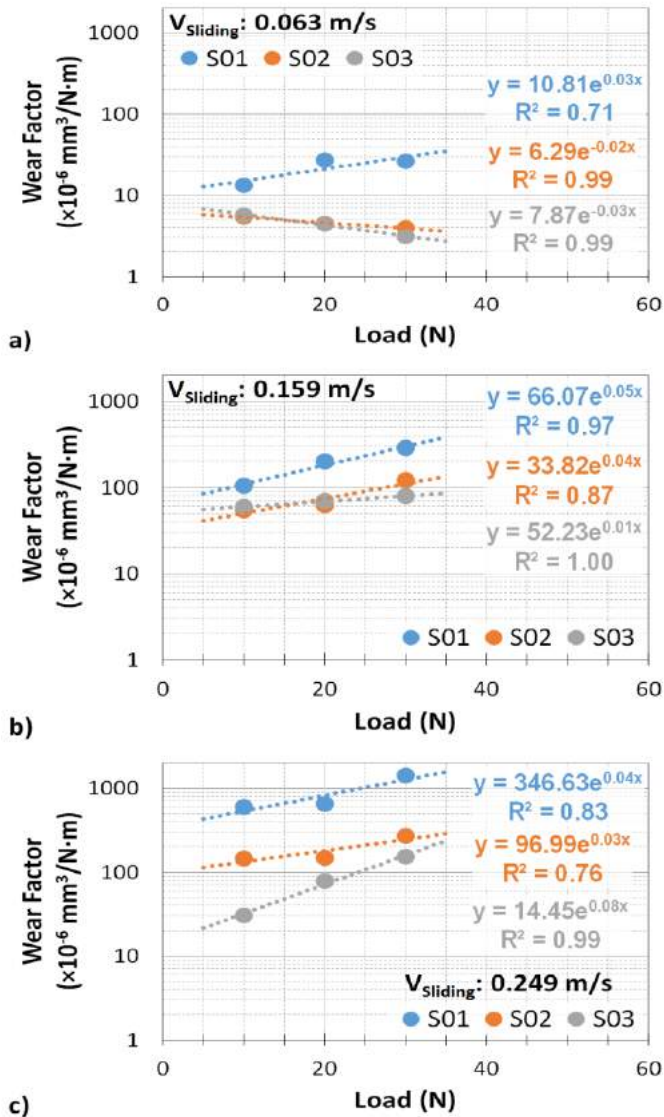


Fig. 6 Wear factor and test load relationship obtained by bearing steel specimens at different sliding speed levels; a) 0.063 m/s, b) 0.159 m/s and c) 0.249 m/s

were determined in this study. In the case of an increase in load as well as sliding speed, it is observed from Table IV and Fig. 5-6 that an increment in the hardness of the specimens leads to an increase in their wear resistance. In addition, since S01 specimens contain spheroidized carbides in a ferritic matrix called the “spheroidite” structure and have the lowest hardness, their wear resistance remains relatively lower compared to the other two groups. However, it is important to note that the specimens S02 and S03 perform very close to each other in terms of wear resistance. If the changing wear volume loss values with load and sliding speed in Fig. 5 is considered, the exponential equations and their coefficient of determination (R^2) values described for S02 and S03 specimens, except for one which takes place in Fig. 5a, S03 equation, show high

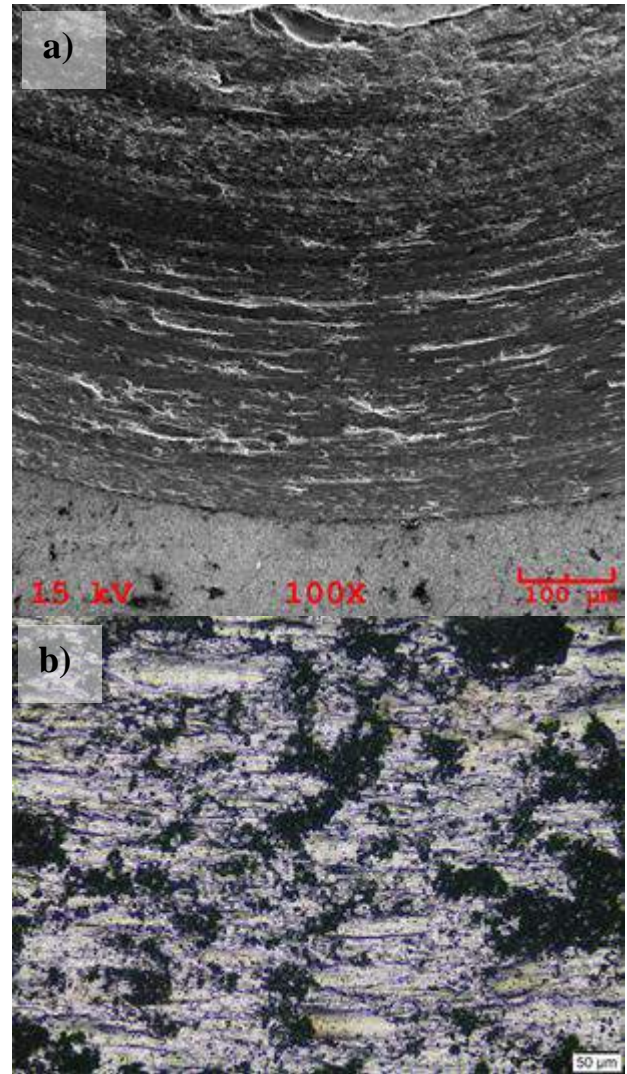


Fig. 7 Worn surfaces in S01 group; a) at least (10 N and 0.063 m/s) in SEM, and b) at most (30 N and 0.249 m/s) in LM

When the variation of the wear factor values at different load and sliding speed levels in Fig. 6 is considered, it can be seen that, the exponential equations with high determination coefficients were obtained except for two specimens (see functions between S02 specimens in Fig. 6b and c). Another exceptional point is that wear volume loss levels for S02 and S03 specimens, which tested at sliding speed of 0.249 m/s under 10 N load. However, this difference is considered to be a statistical deviation rather than a general tendency.

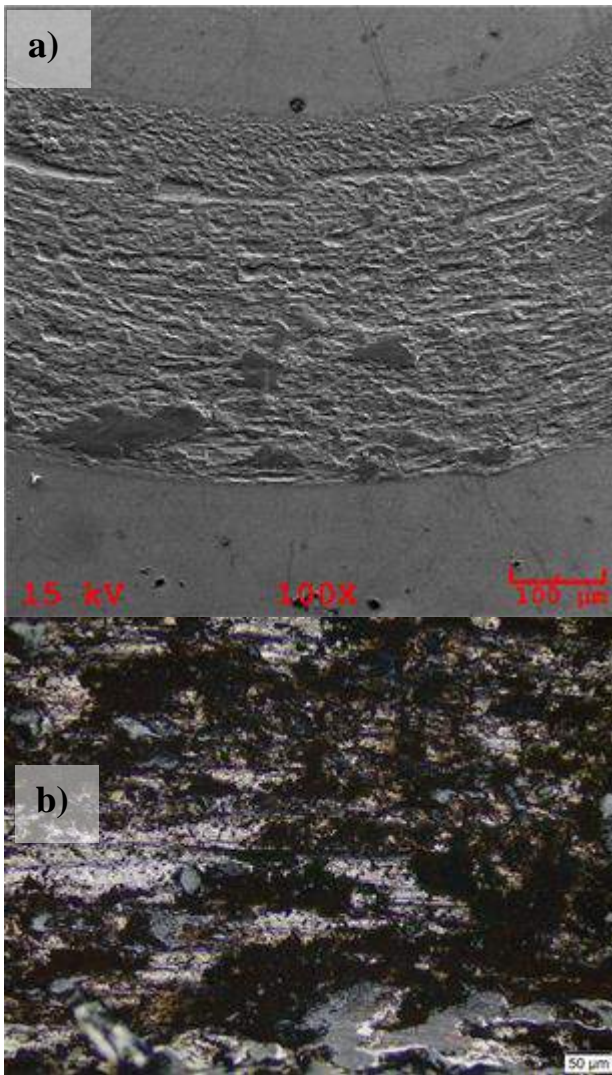


Fig. 8 Worn surfaces in S02 group; a) at least (10 N and 0.063 m/s) in SEM, and b) at most (30 N and 0.249 m/s) in LM

SEM (a) and LM (b) images of the specimens, which worn least or most ones in S01, S02 and S03 groups, were presented in Fig. 7-9, respectively. Since it is not possible to stop the sliding contact during the test according to standard [10], the wear surfaces are here shown in conditions after the tests. The common point in images is that more or less a tribo-chemical layer is scattered on the wear surfaces. From some spot EDX analysis evaluations taken during SEM study, elemental analysis results indicate oxidic content. However, it is known that not all of the layers are in the oxidic composition, but also in the parts which are detected as bare metallic [6]. Therefore, the particles separated from the surfaces by adhesive and abrasive wear, are partly oxidized and smeared by friction at the interface to form a tribo-chemical film [12]. On the other hand, different levels of scuffing occurred on the specimen surfaces. It is predicted that the galling plays a critical role at the beginning macroscopically on the wear surfaces, particularly at lower sliding speed levels and under relatively lower loads, while the scoring takes place at relatively higher sliding speed levels and under higher loads [11]. The initial

conditions of the wear surfaces were however covered since the tribo-chemical layer spreads all over surfaces with the effect of smearing, in time. It was seen that, these smeared layers with the help of well-known work hardening effect [13-16], were embrittled during test and then spalled from the surface under tribological loads, in time. This is especially apparent in light microscope images (see Fig. 7b, 8b and 9b).

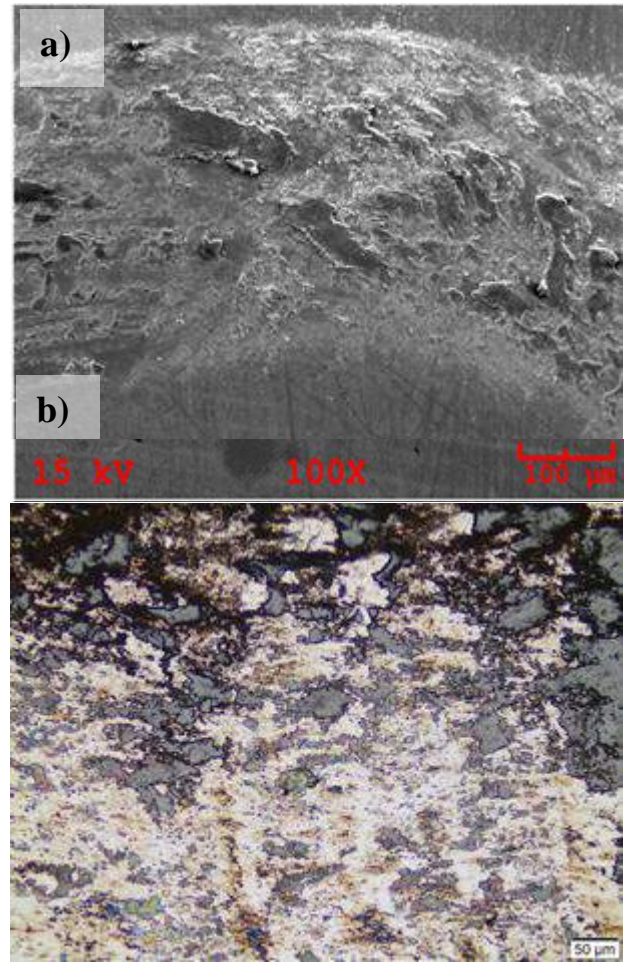


Fig. 9 Worn surfaces in S03 group; a) at least (10 N and 0.063 m/s) in SEM, and b) at most (30 N and 0.249 m/s) in LM

IV. CONCLUSIONS

As results of the study, the following statements can be outlined;

a) Since its relatively lower hardness, higher toughness and easy machinability, the S01 group, which were spheroidization annealed and involved into the study for comparison purposes as a reference specimen, represents an important production stage in the manufacturing of AISI 52100 type bearing steels. If it is not a problem in terms of dimensional tolerances, these steels can be optimized for wear resistance by hardening and tempering treatments after machining.

b) In order to meet the requirements by the chosen material in bearing applications, in which not only hardness and wear resistance, but also toughness or fracture toughness play critical role, its heat treatment parameters must be optimized. In the

bearing applications where the toughness and fracture toughness are also considered as an important criterion group, the heat treatment conditions are optimized in order that the material can be advantageous not only in terms of high hardness and abrasion resistance but also in the characteristics mentioned. It was revealed that the S02 group of specimens, which possess tempered martensitic microstructure obtained annealed at 400°C for ½ hour after water quenching, show almost equal wear resistance level with the S03 group of specimens, which were harder than S02 specimens and applied the stress-relieving treatment rather than tempering.

c) It has been concluded that the S02 group of specimens can be used instead of S03 specimens, since the former group has relatively better values in terms of toughness and providing more advantageous combinations of material properties under low and moderate tribological load levels.

V. REFERENCES

- [1] H.K.D.H. Bhadeshia, "Steels for bearings", *Progress in Materials Science*, vol. 57, pp. 268-435, 2012.
- [2] Y. Wang, T.C. Lei, C.Q. Gao, "Influence of isothermal hardening on the sliding wear behaviour of 52100 bearing steel". *Tribology International*, vol. 23, pp.47-53, 1990.
- [3] H.K.D.H. Bhadeshia (2010), Mechanical bearings webpage on Uni. of Cambridge. [Online]. Available: <http://www.msm.cam.ac.uk/phase-trans/2010/types/>
- [4] E. V. Zaretsky, "Rolling Bearing Steels—A Technical and Historical Perspective", NASA/TM Tech. Rep. 2012-217445, April 2012.
- [5] I. A. Polonsky and L. M. Keer, "On white etching band formation in rolling bearings", *Journal of Mechanics and Physics of Solids*, vol. 43, pp. 637-669, 1995.
- [6] E. Türedi, "The Effect of Heat Treatment on Tribological Behavior of AISI 52100 Steels under Dry Sliding Condition", in *Proc. 4th International Conference of Engineering Against Failure (ICEAF IV)*, 24-26 June, Skiathos, Greece, pp. 98-104, 2015.
- [7] S. Chattopadhyay and C. M. Sellars, "Kinetics of pearlite spheroidisation during static annealing and during hot deformation", *Acta Metallurgica*, vol.30, pp. 157-170, 1982.
- [8] J. D. Verhoeven, *Metallurgy of Steel for Bladesmiths & Others*, Access free e-book, Iowa State University, USA, 2005.
- [9] V. Martinez, R. Palma, J. M. R. Ibabe, and J. J. Urcola, "The relation of toughness to hardness and retained austenite in sintered high speed steels", in *Proc. the 8th Biennial European Conference on Fracture*, October 1-5, Torino, pp. 433-438, 1990.
- [10] *Standard Test Method for Wear Testing with a Pin-on-Disk Apparatus*, ASTM Std. G99-05, 2005.
- [11] *Standard Terminology Relating to Wear and Erosion*, ASTM Std. G40-15, 2015.
- [12] K. H. Zum Gahr, *Microstructure and Wear of Materials*, Elsevier Science Publishers BV. Amsterdam, 1987.
- [13] E. Türedi, "Effect of heat treatment on the wear resistance of cast irons", *Materials Testing*, vol. 58, pp. 306-311, 2016.
- [14] Ş. Polat, E. Türedi, Ş. H. Atapek, and M. Köseoğlu, "Wear behaviour of Heat Treated 100Cr6 Steels", *Materials Testing*, vol. 55, pp. 290-293, 2013.
- [15] Ş. Polat, Ş. H. Atapek, E. Türedi and G. Aktaş, "Wear behavior of Heat Treated Hot Work Tool Steels at Dry Sliding Conditions", *Materials Testing*, vol. 55, pp. 163-167, 2013.
- [16] O. Birbaşar, E. Türedi, Ş. H. Atapek and M. Zeren, "Dry sliding wear behaviour of cast roller materials", *International Journal of Surface Science and Engineering*, vol. 9(2/3), pp. 253-263, 2015.

Influence of Head Hardening Process on Fracture Toughness in Rails

F.Husem¹, M. Emre Turan, H.Ahlatci

*¹Karabuk University, Metallurgy-Materials Engineering Department, Karabuk-TURKEY,
fazilhusem@karabuk.edu.tr, memreturan@karabuk.edu.tr, hahlatci@karabuk.edu.tr*

ABSTRACT

This study aims to investigate fatigue crack growth and fracture toughness behavior in grooved rails. R260 grade and R260 grooved grade rails were used for analysis to understand effect of rail geometry on fracture properties of specimens. Fracture surfaces and microstructures of specimens were examined by the use of Scanning Electron Microscope(SEM) and Nikon Shuttlex Digital Microscope. Results show that, fracture toughness and fatigue crack growth behavior are effected by the geometry of specimens due to plastic deformation mechanism on head parts.

Keywords: Fatigue Crack Growth(FCG), Fracture Toughness, SEM, Grooved Rail

Influence of Cooling Conditions on Fracture Toughness of 1040 Quality Steel

F.Husem¹, M. Emre TURAN

*¹Karabuk University, Metallurgy-Materials Engineering Department, Karabuk-TURKEY,
fazilhusem@karabuk.edu.tr, memreturan@karabuk.edu.tr*

ABSTRACT

In this study, heat treatment was applied for four 1040 quality steels and then cooling process was performed in different conditions. One of the specimens was cooled in furnace and the other specimens were cooled in air, oil and water respectively to determine the effect of cooling conditions on fracture toughness. Fracture and precrack surfaces were examined by Nikon Shuttlepix Digital microscope during analysis and Scanning Electron Microscope(SEM) after fracture toughness measurement. Results show that, cooling conditions significantly effect the fracture toughness value of specimens.

Keywords: Heat treatment, Fracture Toughness, SEM

The Numerical Simulation of the Fatigue Analysis of UIC60 and 49E1 Rails for High Speed Moving Trains

İsmail ESEN¹, Mehmet Akif KOÇ^{*2}, Mustafa EROĞLU², Yusuf ÇAY²

²Karabük University, Mechanical Engineering, Karabük, Turkey

iesen@karabuk.edu.tr

²Sakarya University, Mechanical Engineering, Sakarya, Turkey

*makoc@sakarya.edu.tr

Abstract— In this study, fatigue analyses of rails UIC60 and 49E1 were carried out numerically using a special program written in the MATLAB environment, considering the maximum dynamic stresses for two different rail systems under the effect of high-speed trains. Each sleeper region of the railway rail system is modelled as a simple supported Euler-Bernoulli beam. The high-speed train system is defined as a moving oscillator with fixed distances between them. For motion equations, the Lagrange function is determined by using kinetic and potential energies of the system and then Hamilton principle is applied. These differential equations are solved by using the fourth order Runge-Kutta method in time domain to determine the value of the maximum stresses generated, and its position on the rail. For a 40 tons of vehicle load the fatigue behaviour of UIC60 rail is found greater than the 49E1 rail. Using these data, the life determinations of these two different rails could then be numerically determined without the need for laborious, time consuming and costly experimental methods.

Keywords— Fatigue, UIC60, 49E1, Dynamic stresses, Euler-Bernoulli

I. INTRODUCTION

The dynamic behaviour of structures under the influence of moving loads, as an important issue in engineering, has taken place in the literature. For analytical solution of various problems of moving loads, the studies[1,2] are essential in this field. Considering dynamic behaviour of structures under moving loads with variable velocity,[3–5] have studied the dynamic behaviour under the influence of accelerating mass on beams of different types. Studying a flexible structure without neglecting the effects of damping and inertia of the mass is a moving mass problem case, and some accurate solutions of these kind of problems using Finite element method (FEM) can be found in [6–9]. One of the main applications of the vehicle bridge interaction are such problems that studies in this field are generally divided into nine categories. The effect of the suspension systems, road surface roughness effects, bridge length, the vehicle braking, the vehicle mass, vehicle speed,

bridge damping, bridge unit length of the mass, the effect of the acceleration of the vehicle [10]. Despite early simple cases of a moving concentrated force on a simply supported beam with constant speed[1], the vehicle bridge interaction, particularly in bridge engineering applications, are quite important. The early studies in the literature in this area are focused the dynamics of bridges but vehicle dynamics is neglected[11,12]. Later, moving mass with constant or variable velocity over a railway bridge is an important research topic today and some useful solutions of some simple cases of them can be found in [13]. A vehicle-bridge interaction in terms of passenger comfort of a vehicle on a flexible structure for constant velocity has been given in [14]. One of the major applications of train / rail interaction, for example, [15] proposed a two-axle vehicle interaction with an Euler-Bernoulli beam-bridge using finite element model. The other Wheel/rail interaction applications using FEM can be found in[16–18]. Another research interest in this field is on the effect of road roughness.

In general, modeling of train rail interaction (TRI) system is very complicated and in the interaction between train and rail, the train model reduced to a two degree of freedom with one axis, and the rail region is limited to a part between two traverses. Using these assumptions, the interaction system is numerically modeled and the results are compared with the results obtained from a commercial (ANSYS) program.

II. THEORETICAL

PP. TRI Model

In this study, a two-degree-of-freedom single-axle half-vehicle model and a rail model which considered Euler-Bernoulli beam with simple supported boundary conditions, shown in Figure 1, was used to analyze the dynamic interaction between the rail and the train. The rail model used in the study was only two traverse zones in terms of convenience in mathematical modeling; and simple supported end conditions

were applied as boundary conditions in both cases. Apart from this, while constructing the TRI mathematical model in this study the main assumptions made are:

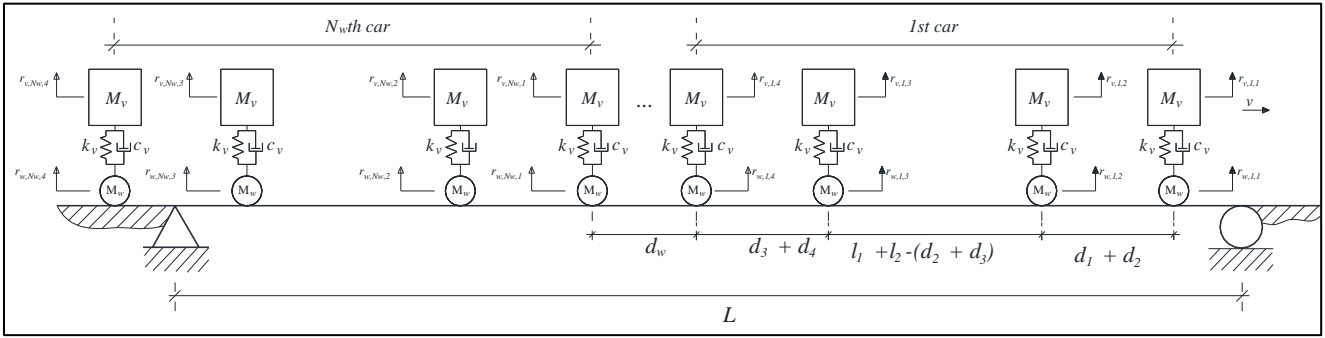


Fig. 1. Multiple train and bridge interaction model used in this study.

- The rail is modeled using the Euler-Bernoulli beam theory,
- The effect of stiffness's of traverse, ballast and basement under the rail are not considered in this study. However, if desired, these effects can be incorporated into the motion equations of the system as spring or damping elements with linear or non-linear characteristics.
- It is assumed that the speed of the train in motion on the rail is assumed to be constant and there is no positive or negative acceleration.
- It is considered that the train passing over the rail has more than one wagon.
- The transverse deformations that occur on the rail are small displacements and are considered to occur within the elastic zone in accordance with Hooke's law and without any plastic deformation.
- Numerical calculations have been made considering perfect rail without any roughness and wearing on the rail.

With these assumptions, the kinetic and potential energies of the TRI interaction, as shown in Fig. 1, are expressed as follows respectively:

$$E_k = \frac{1}{2} \left\{ \int_0^L \mu [\dot{w}_b^2(x,t)] dx + M_w \dot{y}_w^2(t) + M_v \dot{y}_v^2(t) \right\}, \quad (1a)$$

$$E_p = \frac{1}{2} \left\{ \int_0^L EI [w_b''^2(x,t)] dx + k_d [y_s(t) + d_t \theta(t) - y_d(t)]^2 \right\}, \quad (1b)$$

Here μ represents the mass per unit length of the rail beam. In Eq. (1b), EI represents the rigidity of the rail beam, and $H(x)$ represents Heaviside shape functions. Approaches, such as the principle of virtual work, Hamilton's principle, and D'Alembert's principle can be used for the equation of motion of the system, as shown in Fig. 1a. This study uses Lagrange's

equations, formed using the kinetic energy and potential energy equations of the train-rail integrated system, and the mode expansion method. The Galerkin equation for the

deflection $w_b(x,t)$ of any point x on the beam at time t is expressed as follows:

$$\begin{aligned} w_b(x,t) &= \sum_{i=1}^n \varphi_i(x) \eta_i(t), \\ \dot{w}_b(x,t) &= \sum_{i=1}^n \dot{\varphi}_i(x) \dot{\eta}_i(t), \\ w_b''(x,t) &= \sum_{i=1}^n \varphi_i''(x) \eta_i(t), \end{aligned} \quad (3)$$

$$\varphi_i(x) = \sqrt{\frac{2}{L}} \sin\left(\frac{i\pi x}{L}\right), \quad i = 1, 2, \dots, n. \quad (4)$$

Here, η_i is the generalized coordinate representing the deflection of the rail beam element, and φ_i is the shape of oscillation that is obtained with the boundary conditions of the beam. Orthogonality conditions between these shapes of oscillation are expressed, as in Eq. (5).

$$\int_0^L \mu \varphi_i(x) \varphi_j(x) dx = N_i \delta_{ij}, \quad \int_0^L EI \varphi_i''(x) \varphi_j''(x) dx = \Pi_i \delta_{ij}, \quad (5)$$

In Eq. (5), δ_{ij} represents the Kronecker delta where ($i, j=1, 2, \dots, n$) and N_i and Π_i are defined by setting $i=j$ in Eq. (5). The axle load of the vehicle during contact with the bridge is expressed with Heaviside functions, over time, as follows:

$$f_c(x,t) = -(f_{c1} H(x - \xi_1(t))), \quad (6a)$$

$$f_{c1} = (M_w + M_v) g, \quad (6b)$$

Rayleigh dissipation function for system is expressed as follows:

$$D = \frac{1}{2} \left\{ \int_0^L c \dot{w}_b^2(x,t) dx + c_v [\dot{r}_v(t) - \dot{r}_w(t)]^2 H(x - \xi(t)) \right\}, \quad (7)$$

In Eq. (7), c is the equivalent damping function for the beam. In addition, the Lagrange equation ($L_g = E_k - E_p$) of the system is equal to the difference between the kinetic energy and the potential energy. If the Lagrange equation is rearranged for two independent coordinates, the following is obtained:

$$\frac{d}{dt} \left(\frac{\partial L_g}{\partial \dot{p}_k(t)} \right) - \frac{\partial L_g}{\partial p_k(t)} + \frac{\partial D}{\partial \dot{p}_k(t)} = 0, \quad k = 1, 2. \quad (8a)$$

$$\frac{d}{dt} \left(\frac{\partial L_g}{\partial \dot{\eta}_i(t)} \right) - \frac{\partial L_g}{\partial \eta_i(t)} + \frac{\partial D}{\partial \dot{\eta}_i(t)} = Q_i, \quad i = 1, 2, 3, 4, \quad (8b)$$

State variables are expressed in vector form as follows:

$$p(t) = \{ r_w, r_v \}^T, \quad (9a)$$

$$\eta(t) = \{ \eta_1(t), \eta_2(t), \eta_3(t), \eta_4(t) \}^T, \quad (9b)$$

In addition, the generalized forces of the system Q_i is written as follows:

$$Q_i = \int_0^L \varphi_i(x) f_c(x,t) dx, \quad i = 1, 2, 3, 4, \quad (9c)$$

When above equation is represented in a state-space form the below first order motion equation is obtained for whole system.

$$\dot{X}(t) = A(t)X(t) + f(t), \quad (10)$$

QQ. Modelling of multiple train cars

Solution steps of multiple cars:

- Define the parameters $N_w, d_w, d_i (i=1, \dots, 4), l_i (i=1, 2)$, see Fig. 1.
- For the parameters make a vector for each axle. Remember for N_w cars there should be $4N_w$ axles.
- Calculate arrival times each axle using the distances and the constant velocity of train.
- Using the last two steps, calculate the coefficients of Eq. (11) for all axles.

$$D_{car}(i) = \sum_{j=1}^{4N_w} \sum_{k=1}^n \sqrt{\frac{2}{L}} \sin \frac{j p x_i}{L} \frac{\dot{w}}{\dot{\theta}} (j+k) \quad (11)$$

$$k = \begin{matrix} 1, j = 1 \\ \vdots \\ M \\ \vdots \\ 4N_w - 1, j = 4N_w \end{matrix}$$

$$DD_{car}(i) = \sum_{j=1}^{4N_w} \sum_{k=1}^n \sqrt{\frac{2}{L}} \sin \frac{j p x_i}{L} \frac{\dot{w}}{\dot{\theta}} (j+k) \quad (12)$$

- For axles, calculate equations (13) using above equations (11 and 12). Finally, solve the equation (10).

$$V_{car}^{mode,1} = \sum_{i=1}^{4N_w} \frac{\sqrt{\frac{2}{L}} \sin \frac{j p x_i}{L} \frac{\dot{w}}{\dot{\theta}} (DD_{car}(i) - x(7+2i))}{N(j)} + c_v (DD_{car}(i) - x(8+2i)) + M_{v,g} \quad (13)$$

$$V_{car}^{mode,n} = \sum_{i=1}^{4N_w} \frac{\sqrt{\frac{2}{L}} \sin \frac{j p x_i}{L} \frac{\dot{w}}{\dot{\theta}} (DD_{car}(i) - x(7+2i))}{N(j)} + c_v (DD_{car}(i) - x(8+2i)) + M_{v,g}$$

The parameters ξ, D_{car}, DD_{car} in Eq. (13) represent the position of the train axle on the bridge relative to the reference point from the left side of the bridge, the bridge deformation at the axle contact point, and the deformation velocity, respectively.

III. ANSYS SIMULATION MODELLING

In this study, the 3D model of the parts to be analysed are created in computer environment. Two different assemblies, UIC60 (Fig. 2) and 49E1 (Fig. 3) are modelled for comparison. UIC515 is the preferred model for the wheel.

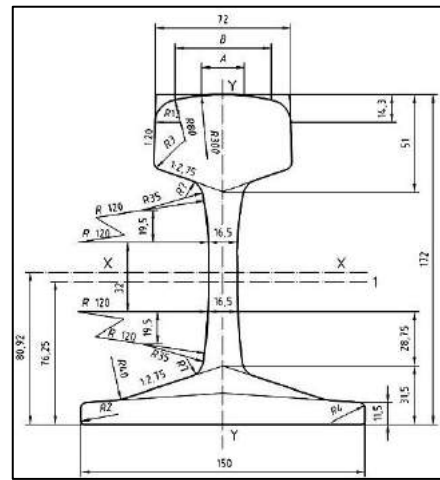


Fig. 2. Technical drawing of UIC 60 rail [14]

After assembling the rail and vehicle, the analysis process was performed in the transient structural module in ANSYS program, using a train speed of 300 km/h. for each wheel a pay load of 91036 N was applied in the vertical direction. Between the wagon and the axle, spring and damping elements are used with coefficients of 530kN/m and 80. 2kN.s/m respectively.

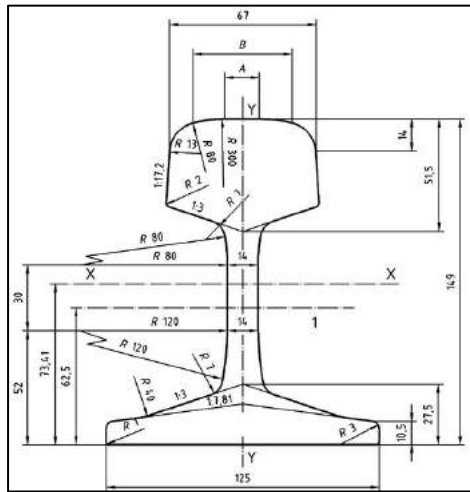


Fig. 3. Technical drawing of 49E1 rail [13]

TABLE XLIV
CHEMICAL COMPOSITION OF RAIL STEEL USED IN THIS STUDY.

Chemical composition (%)							
C	Si	Mn	Cr	Mo	P	S	Fe
0.74	0.25	1.09	0.03	0.02	0.07	0.02	Remain

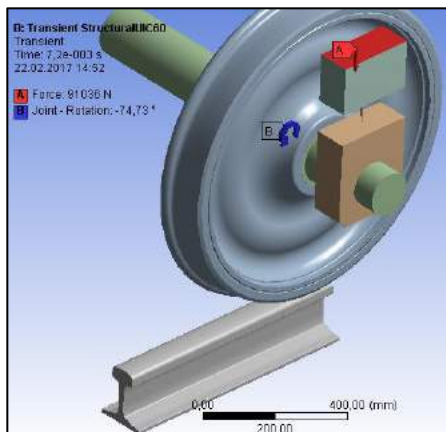


Fig. 4. Boundary conditions of the ANSYS model

The rail length is 750 mm. Since the train speed is 300 km / h, the analysis time is very short. The analysis time was taken as 0,0072sn and 600 mm on the rail. In the analysis, the surface of the wheel and the rail are made of fine mesh to give precise results. The hex dominant method was applied to both elements to prevent the wheel and the rail, from triangular meshes. Thus, for the rail model 18625 meshes were obtained with 11058 nodes. Finally, for all the modelling has 54526 nodes and 93333 meshes (Fig. 5).

For boundary conditions, a planar joint has been added so that the axle and the wheel is free for two translations and one rotation degree of freedom. The part on which the axle is attached, is limited only to move vertically and horizontally (Fig. 4). There is a frictional contact between the rail and wheel

with a dry friction coefficient of 0.3. The Axle and wheel are connected to each other by bonded contact so they cannot move independently. A frictionless contact is used between the axle and part on which the force from the pay load is applied (Fig. 4).

IV. NUMERICAL AND SIMULATION RESULTS

RR. Comparisons of the ANSYS and MATLAB models

Fig. 6 shows the comparisons of the results for two different rail models 49E1 and UIC60, using a single-axis simple train model. In these analyzes, the elasticity modulus of rail is $E = 207$ Gpa, and masses of unit length of 49E1 and UIC60 rails are taken as $\mu_{49} = 49$ kg, $\mu_{60} = 60$ kg respectively. Figure 2 shows the change of maximum stress of the rail midpoint versus the reference position of the train wheel from the rail left end. In numerical calculations for the 49E1 rail, the maximum stress was calculated as 81 Mpa at 55% the rail length.

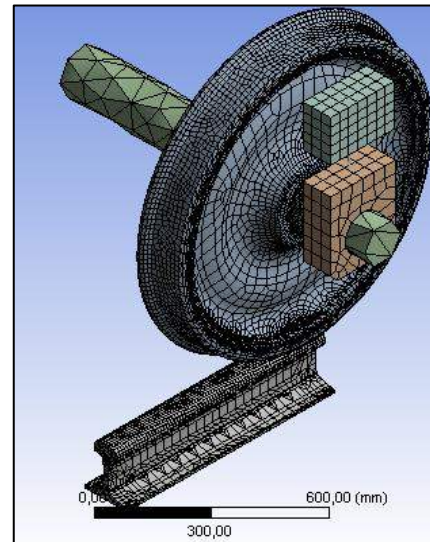


Fig. 5. Mesh structure of ANSYS model

In the analyses performed in the ANSYS program, the maximum stress was calculated as 250 Mpa at 48% of the rail length. For the UIC60 rail, in numerical calculations, the maximum stress at the rail midpoint was achieved at 74 Mpa at 52% rail distance. For this rail model, the ANSYS simulation yielded 135 MPa at 41% track distance. But except for small deviances the trends of the both results are similar as can be seen from the figure.

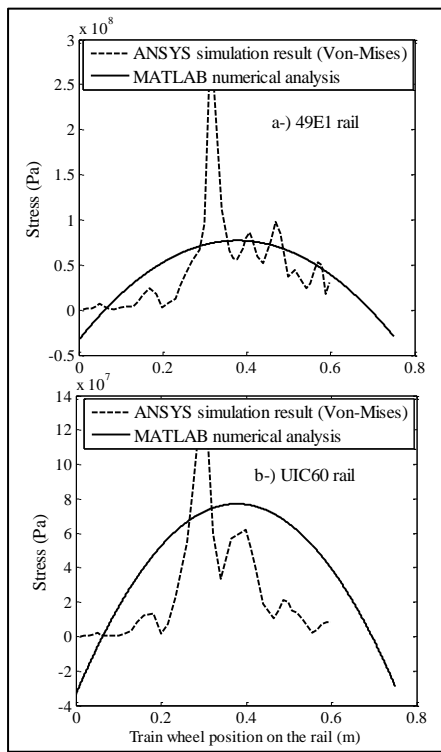


Fig.6. Comparison of the two models for rail midpoint stresses.

SS. The Fatigue Analysis of UIC60 and 49E1 Rails

Considering the whole length of both 49 and 60 rails, dynamic stresses are presented in Figures 7 and 8, considering the regions in Fig. 9.

As can be seen from Figures, dynamic stresses are increased while the wheel moves on the rail surface, especially after passing the middle of the rail, the stresses reached to the maximum level.

Fatigue analyses of the UIC60 are given in Figures 11-13 that safety factor for the rail is 1.8834 at the rail base near the supports, whereas, the safety factor of the middle zone of the rail is 5.315 when the wheel is moving on the rail. It appears that the lower portion of the rail has a lower safety factor than the upper portion. Since the rail has a safety factor greater than one million cycles, this type of rail is found suitable for the given loading condition. Whereas the results of fatigue analysis of the 49E1 rail are given in Figures 14-16. The whole safety factor of this rail is found as 0.19282. Also, the behaviour of the portions of the rail were resembles the previous UIC60 rail. When the upper portions of the rail are examined, it can be seen that the security factor of the middle zone of the rail is 1.4264. The fatigue life of the UIC60 rail was one million cycles, but the fatigue life of the 49E1 rail is only found as 1930.5 cycles.

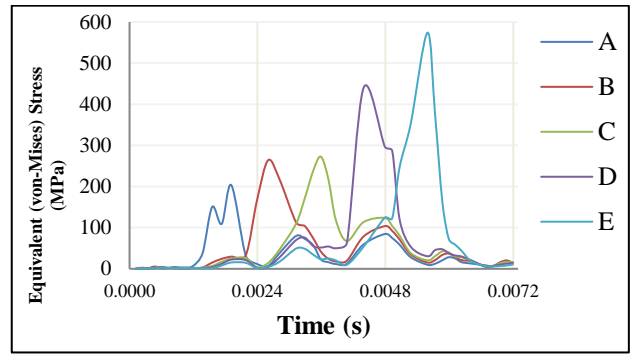


Fig. 7. Dynamic stresses in UIC60 rail

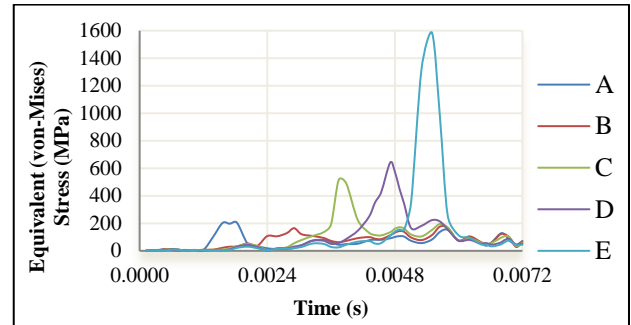


Fig. 8. Dynamic stresses in 49E1 rail

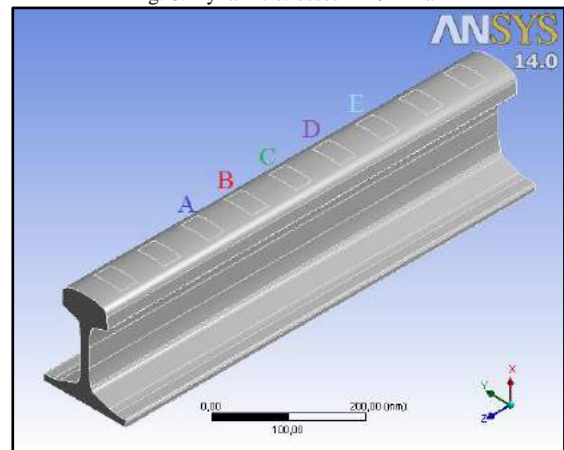


Fig. 9. The regions of stress calculation.

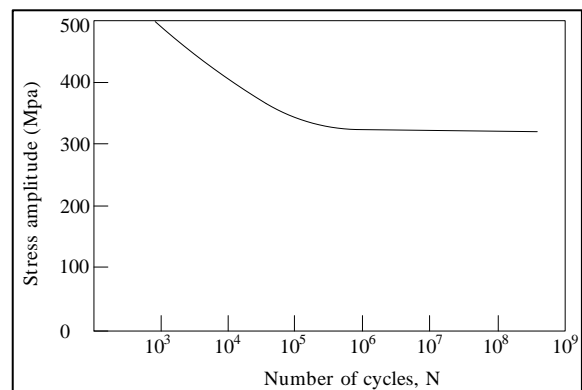


Fig. 10. A specific Wohler Curve of rail steel

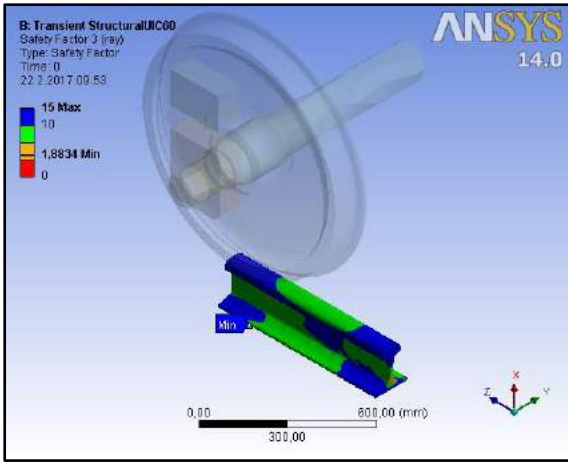


Fig. 11. Safety factor of UIC60 rail

When the fatigue sensitivity of both rails are examined, it is seen that the fatigue life of the UIC60 does not change for the given loading condition. Whereas, for 49E1 rail, the life expectancy increases when the loading is decreased. For the same loading condition the performance of UIC60 rail is more preferable than 49E1.

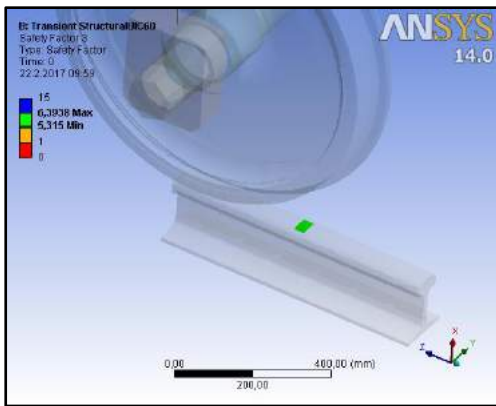


Fig. 12. Safety factor of the middle zone of the UIC60 rail

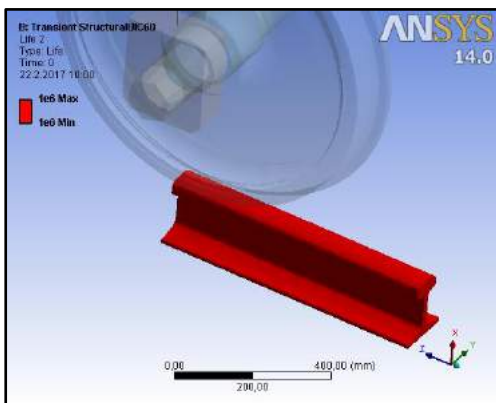


Fig. 13. Fatigue life UIC60 rail

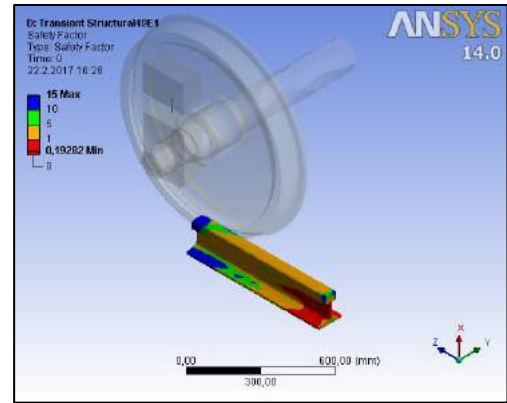


Fig. 14. Safety factor of 49E1 rail

TT. The effect of the multiple wagon train on the rail stresses

In this section, the effect of the multi-train wagon passage over the rail on the rail center point maximum stresses for 49E1 and UIC60 rails is investigated. To carry out this analysis, the model given in Fig. 1 is considered, the number of train wagons $N_w = 9$, the distance of train axle $d_1 = d_2 = 2.5$ m, the distance between the cars is $d_w = 3$ m. Otherwise, the wheel masses, the axle loads and body masses of the train were taken as in previous case. In Figure 3a, the effect of the multi-wagon carriage over the rail, on the midpoint stress is shown for 49E1. As it can be seen, when the first wagon passes, 97 Mpa stress is occurred at the middle point of the rail, whereas when the seventh wagon passes, this value increases to 107 Mpa, with an increase of 10.3%. For the UIC60 rail when the first wagon entered the rail, it reached to 55 MPa, while the seventh wagon passed it increased to 61 MPa. For this rail, an increase of about 9.8% was observed. High speed train passages produce additional stresses due to the vibration caused by the previously passed wheel.

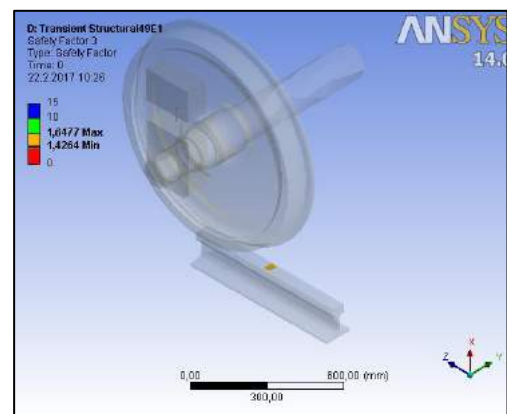


Fig. 15. Safety factor of the middle zone of the 49E1 rail

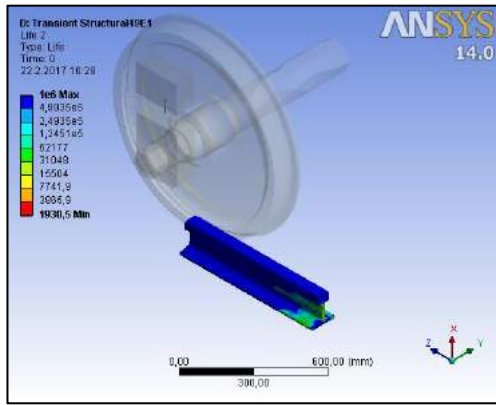


Fig. 16. Fatigue life 49E1 rail

V. CONCLUTIONS

From fatigue analysis results, it can be said that the UIC60 rail has better fatigue behaviour than the 49E1 rail. The safety factor on the UIC60 rail was 1.8834 while it was 0.19282 for the 49E1 rail. The upper regions of the both rails have greater safety factor than the lower regions. In the upper regions, the safety factor for UIC60 was 5.315 while it was 1.4264 for 49E1. In the total, it was observed that the fatigue life of the UIC60 has an acceptable lifetime (for one million cycle) while it was 1930.5 cycles only for the 49E1. From this results, it can be understood that the lower portions of a rail should be redesigned in order to increase life expectancy of the both rails.

When the passage of multiple train cars are considered the dynamic stresses have been increased at least at a rate of 10 percent due to the dynamic interaction. The reason for this is that when the wheel moves on the rail, both rail and wheel vibrates from the interaction. Thus the un-damped vibration increases the dynamic stresses.

VI. ACKNOWLEDGEMENT

VII. The authors gratefully acknowledge support from the Scientific and Technical Research Council of Turkey (TUBITAK), for this work under Grant No. 112G081.

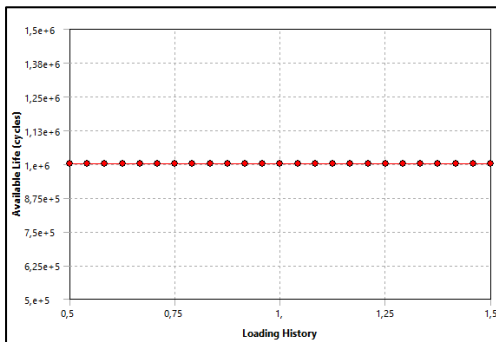


Fig. 17. Fatigue sensitivity of UIC60 rail

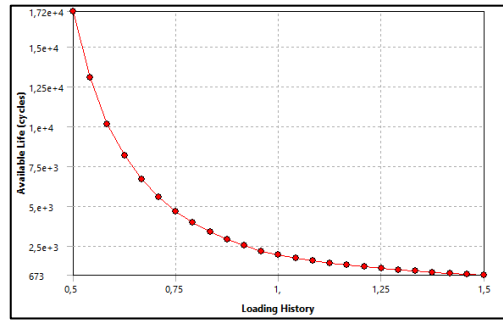


Fig. 18. Fatigue sensitivity of 49E1 rail

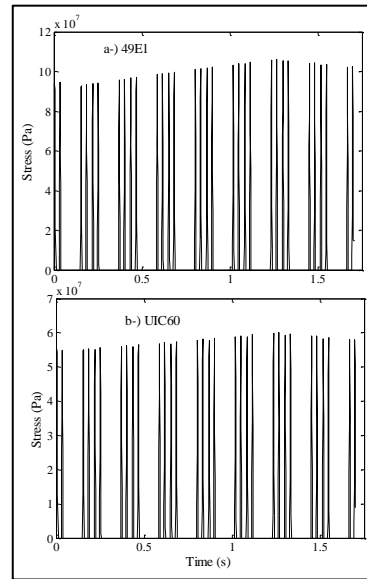


Fig. 19. Effect of the multiple train wagon moving on the rail upon rail midpoint maximum stress.

VIII. REFERENCES

- [1] L. Fryba, Vibration solids and structures under moving loads, Thomas Telford House, 1999.
- [2] C.I. Bajer, B. Dyniewicz, Numerical Analysis of Vibrations of Structures under Moving Inertial Load, Springer, New York, 2012. doi:10.1007/978-3-642-29548-5.
- [3] İ. Esen, İ. Gerdemeli, Hareketli yükler altındaki köprülü kren kirişlerinin dinamik davranışı, İtÜdergisi/d. 9 (2010) 145–156.
- [4] B. Dyniewicz, C.I. Bajer, New Consistent Numerical Modelling of a Travelling Accelerating Concentrated Mass, World J. Mech. 2 (2012) 281–287. doi:10.4236/wjm.2012.26034.
- [5] S. Timoshenko, Vibration problems in engineering, second, D. Van Nostrand Company, Inc., New York, 1929. doi:10.1016/S0016-0032(29)91051-6.
- [6] İ. Esen, A new finite element for transverse vibration of rectangular thin plates under a moving mass, Finite Elem. Anal. Des. 66 (2013) 26–35. doi:10.1016/j.finel.2012.11.005.
- [7] I. Esen, Dynamic response of a beam due to an accelerating moving mass using moving finite element approximation, Math. Comput. Appl. 16 (2011) 171–182.
- [8] V. Kahya, Dynamic analysis of laminated composite beams under moving loads using finite element method, Nucl. Eng. Des. 243 (2012) 41–48. doi:10.1016/j.nucengdes.2011.12.015.
- [9] İ. Esen, A new FEM procedure for transverse and longitudinal vibration analysis of thin rectangular plates subjected to a variable velocity moving load along an arbitrary trajectory, Lat. Am. J. Solids Struct. 12 (2015) 808–830.

- [10] S.S.Ā. Law, X.Q. Zhu, Bridge dynamic responses due to road surface roughness and braking of vehicle, *J. Sound Vib.* 282 (2005) 805–830. doi:10.1016/j.jsv.2004.03.032.
- [11] Y.A. Dugush, M. Eisenberger, Vibrations of non-uniform continuous beams under moving loads, *J. Os Sound Vib.* 254 (2002) 911–926. doi:10.1006/jsvi.2001.4135.
- [12] G. Michaltsos, D. Sophianopoulos, A.N. Kounadis, The Effect of a Moving Mass and Other Parameters on the Dynamic Response of a Simply Supported Beam, *J. Sound Vib.* 191 (1996) 357–362. doi:10.1006/jsvi.1996.0127.
- [13] H.P. Lee, Transverse vibration of a Timoshenko beam acted on by an accelerating mass, *Appl. Acoust.* 47 (1996) 319–330. doi:10.1016/0003-682X(95)00067-J.
- [14] E. Esmailzadeh, N. Jalili, Vehicle–passenger–structure interaction of uniform bridges traversed by moving vehicles, *J. Sound Vib.* 260 (2003) 611–635. doi:10.1016/S0022-460X(02)00960-4.
- [15] M. Fafard, M. Bennur, M. Savard, A general multi-axle vehicle model to study the bridge- vehicle interaction, *Eng. Comput.* 14 (1997) 491–508. doi:10.1108/02644409710170339.
- [16] Y.B. Yang, M.C. Cheng, K.C. Chang, Frequency Variation in Vehicle–Bridge Interaction Systems, *Int. J. Struct. Stab. Dyn.* 13 (2013) 1350019. doi:10.1142/S0219455413500193.
- [17] H. Azimi, K. Galal, O. a. Pekau, A numerical element for vehicle-bridge interaction analysis of vehicles experiencing sudden deceleration, *Eng. Struct.* 49 (2013) 792–805. doi:10.1016/j.engstruct.2012.12.031.
- [18] P. Lou, F.T.K. Au, Finite element formulae for internal forces of Bernoulli-Euler beams under moving vehicles, *J. Sound Vib.* 332 (2013) 1533–1552. doi:10.1016/j.jsv.2012.11.011.

The European Coal and Steel Community as a Trivet for Peace After the Second World War

Umut KEDIKLI*

#Assistant Professor

The Department of International Relations, Karabuk University
TURKEY

umutkedikli@karabuk.edu.tr

Abstract— The Alsace Lorraine region, which was taken from Germany and given to France after World War I, is rich in iron-coal mines; and The Saar Region, which has the coal, iron and steel industry controlled by the League of Nations until 1935, are important geographical regions in the economic and political conflict between Germany and France. Moreover, when Germany had a difficulty to pay their debt for reparations to France after World War I, the Ruhr region of Germany, which is a coal-rich basin developed by the iron and steel industry, was occupied by France from 1923 to 1925. When the Second World War began, these regions, which were strategic for the German heavy industry, were seized again by Germany. History shows that the struggle to have coal and iron ore, important raw materials in the development of the economies of the states, is also an important reason for the emergence of wars between states. For this reason with the end of World War II, there was a need to go to an international organization that would provide and develop cooperation in the states so that a war originating from these raw materials would not come out again in European geography. European leaders, who came together after the war including France, West Germany, Italy, Belgium, Holland and Luxemburg, agreed not to develop strategic raw materials like iron and steel in the war industry to use against each other in the battlefield. Uniting the coal and steel industries is proposed with a declaration historically known as the Schuman Declaration, to end the historic rivalry over the mines between France and West Germany. As a result of these initiatives, the European Coal and Steel Community (ECSC) was established with Paris Treaty on 18 April 1951. The aim of this study is to demonstrate how the ECSC served a function in reconstruction of peace in Europe, which has been developed with the cooperation of the member states in extraction, operation and marketing of important raw materials such as coal and iron. In this study, the organization phase, organizational structure and organs of ECSC and their activities will be examined by emphasizing its battle preventive effect on the development of economic integration of the European states.

Keywords—European Coal and Steel Community, International Organizations, European Integration, European Communities, Schuman Declaration

I. INTRODUCTION

Alsace – Lorraine Territory with the rich coal and steel mining areas retroceded to France in the aftermath of WWI, and the Saar territory under control of the League of Nations until 1935 with significant coal, iron and steel industries, are

considered important territories between Germany and France in terms of economic and political conflict. Moreover, upon failure of Germany in fulfillment of its obligations towards France after the WWI, Ruhr, the rich coal field, under German sovereignty was invaded by France in the period of 1923-1925. In the beginning of the WWII, these territories were re-captured by Germany since they were substantially strategic for heavy industry of Germany. As it has been pointed out by history, coal and iron ore substantial ingredients of development of countries are important causes of wars between them. Therefore, an international organization to ensure peace and cooperation across the European continent was found necessary to prevent wars related with sharing raw materials in the continent.

Fig. 1 The Alsace Lorraine Region



<https://global.britannica.com/place/Alsace-Lorraine>

The European Coal and Steel Community (ECSC) founded in 1952 emerged on the basis of this need. ECSC, consisted of 28 members as of today, constituted the preliminary core of the European Union (EU). In order to comprehend foundation of such organization among the European countries, it is necessary to realize vitality of steel for those countries in the

past. In the beginning of the 19th Century, steel production was essential for industrial revolution and economic growth. In fact, steel and coal industries were in the core axis of international agreements in the pre-WWII period. [1]

In the post WWII period, it was observed that the ECSC was founded to institutionalize peace and to develop cooperation among European countries on the basis of production and processing of these commodities vitally important for their heavy industries. Accordingly, the Schuman Declaration suggested unifying coal-steel industries to cease historical competition on quarries of these strategic commodities between France and Western Germany. In the present study, first the Schuman Plan was explained and approaches of constituent states of the ECSC were expressed. Then, structure of the organization and its functional mechanism and their impact on the market were considered.

A. The Schuman Plan

In September 1949, the Foreign Ministers of France, the Great Britain and the U.S., Robert Schuman, Ernest Bevin and Dean Acheson met in Washington to establish a common policy regarding Ruhr and Saar issues with Germany. Following this meeting, during the second meeting held in May 1950, Minister Schuman requested from Jean Monnet a plan for re-building of French economy in the post-WWII period. Six fundamental industries were determined in this plan one of whom was coal and steel. [1]

The European integration emerged with the Schuman Plan in 1950. The plan, prepared with the initiative of Jean Monnet, was aiming weakening the dominant position of Germany on coal and steel in order to prevent Germany to turn into a war machine which could endanger re-building efforts in the Europe.[3] Yet, it was necessary to prohibit Germany to take advantage of steel shortage in the post-war period by the leverage of its steel industry and Ruhr territory's coalmines and to act in a way that it could hinder re-building efforts of other European countries for their economies. The plan was suggesting establishment of a common coal – steel community under common High Authority including Germany and France. This organization was to be open for participation of other European countries. [1] Furthermore, Robert Schuman was aiming that the unity under coal – steel industries was to constitute the first step towards more comprehensive unity which could expand and deepen other areas of interests.

As it was indicated in a neo-functional theory suggested by Ernest Haas, an integration process started with certain industries in economical aspect would lead to political coalescence and transformation. According to Haas, as capital holders, unions and workers related especially with coal – steel industries capitalize on policies of the ECSC, they would support the organization and they would find their future in the success of the ECSC. Players from other industries, who observe positive results in the coal-steel industry, would be willing to be part of similar integration process. Thus, a supranational integration would be acquired. Thus, the ECSC was the initial step of such integration process.[2] At this point, it would be useful to expose opinions of the European countries

concerning foundation of an organization regulating the coal and steel industry.

B. Attitudes of the European Countries towards Foundation of the ECSC

One of the prominent statesmen of the Great Britain, Winston Churchill, shown his support to an organization establishing unity in Europe during his speech made in Switzerland by his words “the first step to re-formation of the European family must be partnership between France and Germany” in 1946.[1] On the other hand, from the official point of view, it was observed that the Great Britain was against the ideology of continental integrity across the Europe. Yet, the Great Britain was keeping distance to such opinion since such union could affect its export negatively; the GB was considering itself as the prevailing country of the WWII; and such union could be a competitor in the future. Moreover, the Great Britain refused to participate in this organization since it was against the binding decision making authority of the High Authority, one of the bodies of the ECSC, and against the supra-national characteristic of the organization. [1]

The most significant factor which motivated Belgium, Holland and Luxemburg, founder members of the ECSC, to join the community was their national interest. Whereas these countries sharing the same geographical territory have a special economic relationship among them, each has multi-lingual demography within themselves.[3] In the post-WWII period, these three countries came to conclude that taking joint action in international arena with regard to economic dimension were more suitable to their interest instead of acting individually. Benelux countries were in the opinion that being part of such unions was sort of measure to protect their national economic interests against other stronger countries in the Europe such as France, Germany and the Great Britain.[3] Paul Henri Spaak, one of the architects of European integration who defended that no political resolution could be concluded without an economic solution and that prosperity and security issues of small countries in the continent would conflict with each other.[3] In terms of coal and steel industry, while Belgium and Luxemburg were the countries yielding production surplus, Holland was the one lacking these resources. However, Holland did not have adequate currency reserve to fund import of those resources. This situation was an adverse impact on commercial balance among Benelux countries.

Belgium accepted the Schuman Plan on the condition that foundation of the ECSC would not be allowed to influence its coal and steel manufacturers negatively by the competitive environment that would emerge in the Europe. Similarly, Luxemburg was in pursuit of preserving exclusive position with Belgium on the basis of effective economic agreement while it was joining into the ECSC. On the other hand Holland was of the opinion that activities of the High Authority, one of the bodies of the ECSC, were to be monitored by the Council of Ministries established by European governments since it was concerned about that the supra-national structure of the organization was to serve to the interests of strong members of

the organization.[3] Finally, since all three countries were of the opinion that economic integration was necessary for liberalization of commerce and political integration across Europe, they were eager to take initiative in foundation of the ECSC.

Afterwards of disclosure of the Schuman's Plan, Germany's approach towards foundation of ECSC was that extended European economic community would bring economic advantages to the country; Coal – Steel Community was to be preliminary step for European integration which was meant to be leverage for peace and favorable relations with France and a guarantee for security against Russia.[4] Chancellor of the Federal Republic of Germany, Konrad Adenauer, viewed ECSC as remarkable step for institutionalization of intimate relationship between Germany and France. Thus, a new order relying on peaceful cooperation across Europe would be established. [5]

Finally, although the U.S., the one who gained strength at the end of the WWII, is not located in the Europe, its policy concerning European integration and foundation of ECSC, needs to be mentioned. While European economies collapsed in the post-war period, the American economy was at its peak. George C. Marshall, American Ministry of Foreign Affairs, was claiming that serious economic aids must be provided to European countries in order to prevent Soviet expansion upon break out of the Cold War.[6] Within this framework, the U.S. launched the European Recovery Program, known as the Marshall Plan. This program also contributed into establishing foundation of the European integration which paved the way for creating of the EU. According to the U.S., the European countries whose economies recovered through American economic aids were to prevent potential recession in the American economy in the post-war period. Moreover, political and economic union that would be created among European countries would also prevent armament of Germany once again and a strong Europe would restrain Soviet dominance in the continent.[6] If the Europe was left in small pieces, the continent would then have a weakness towards Soviet intervention. Therefore, whereas it was necessary to integrate European economic market and to minimize cost of massive production so as to enhance prosperity across the continent, the ECSC was seen as one of the material tools of this target.

Within scope of the economic aids of the Marshall Plan, steel production concerning our subject was influenced positively as well. Such that Western Germany's steel production increased from 2.5 million tons to 14.5 million and this contributed significantly to resolve unemployment in Germany in the period of 1946-1953.[6] Founder members of the ECSC, Federal Germany, France, Belgium, Holland, Luxemburg and Italy as well as the Great Britain received 75% of Marshall Aids. Since ECSC member witnessed the benefits of integration in terms of economic recovery, they took initiatives to deepen the integration among them in line with foundation of the European Economic Community core of the EU.[6]

C. Structure and Function of the European Coal and Steel Community

The founder agreement of the European Coal and Steel Community was executed by the founder members at the meeting in Paris in April 1951. Upon endorsement of the act by the France, Germany, Italy and Benelux countries, the Paris Act took effect on July 24th, 1952. The ECSC is considered as a milestone in the history as the first supranatural community. National governments of the founder countries transferred their ruling authority in coal and steel industry to the High Authority, a body of the supranatural organization of ECSC. Jean Monnet, one of the architects of the European integration, was assigned as the first president of the High Authority.[7] [10]

High Authority was consisted of independent experts authorized by governments of member states. High Authority was taking regulative decisions on the coal and steel market and these decisions were binding member states. The Authority was regulating the competition in the industry and making planning to eliminate dysfunctions. In this sense, the Authority was assigned tasks such as suggesting investment decisions regarding the coal-steel industry to member states and evaluating such investment requests, taking measures to increase production. According to the founder agreement, each member state is allowed to assign two members to the board of directors of the High Authority. However, while France, Germany and Italy sent two members to the board, Benelux countries sent one member each. The supranatural characteristic of this body was based on the 9th article of the agreement. This article was entailing assigned members of the High Authority to act independent from their countries and to observe interests of the Community.[8]

Another body of the Community was the Council in which governments of the member states were represented. The Council was presenting opinion to the High Authority regarding various political issues and was authorized to endorse suggestions of High Authority. There was weighted voting system functioning in the Council. According to this system, acceptance of a decision in the Council was requiring approval of a member state that manufacture minimum 20% of coal and steel in the community. The countries with such capacity were Germany and France. [7]

Another body required by the founder agreement and established to ensure transparency and accountability of activities of the High Authority was Parliamentary Assembly. Total number of members in the Assembly where member states were represented proportional to their populations was 78. The basic function of the Assembly was to audit the High Authority which was reporting to the Assembly members annually regarding activities and expenditures of the Community. [7]

Finally, establishment of the Court of Justice was stipulated in order to prevent the High Authority to breach the provided authority in the scope of the agreement. The agreement was to anticipate assignment of seven judges to the Court which was not only authorized to monitor the High Authority but also to

conduct legislative auditing of the ordinance enacted by the Council or Parliamentary Assembly.[8]

In the introduction of the founder agreement of the ECSC built upon aforesaid basic bodies, the relationship between economic integration and political integration was emphasized as a tool consolidating peaceful relationships as motive for foundation of the Community.[8] Since the Community was designed as a tool for integration among European countries, it was open to participation of other countries as well. The Great Britain, Ireland and Denmark became new members of the Community in 1973. Founder members of the Community, upon the positive consequences of the integration, founded European Economic Community (ECC) with the Rome Act (1957) after five years and the European Atomic Energy Community (EURATOM). Following the foundation of the ECC, some obligations of the High Authority were transferred to the European Communities Commission by the Brussels Act (the Fusion Act) enacted among the member states in 1965.[9] Member states coalesced bodies of these three communities and reorganized their structures and tasks on the basis of the Single European Act in 1986.

On the other hand, as it was anticipated by the 97th article of the founder agreement of the ECSC, the agreement was to be in effect for 50 years. Moreover, founder states also agreed in the meeting held in 1998 that the agreement period was not extended. Therefore, regulations on coal and steel manufacturing have been governed by the relevant EU acts afterward of the July 2002, the expiry date of the Paris Act. The Addendum of the ECSC Protocol was included in the Nice Act endorsed on February 27th, 2002 in order to involve the Coal - Steel Community into the EU.[9]

D. Impact of the ECSC to the Market in Coal – Steel Manufacturing

In 1958, at the end of the transition period, a common market was structured for coal and steel commodities and restrictions imposed on coal, iron ore, scrap iron and steel items were totally banished among the member states. Thus, free circulation of commodities was provided. In terms of imports of these commodities, a common customs tariffs were imposed against third countries.[10] Moreover, employees who were considered to work in this industry were allowed to circulate freely among member states so as to develop employment; and this made positive contribution to the unemployment problem within the Community.

The regulatory role of the ECSC on steel products is also important. For instance, when the U.S. was concerned about dumping on European steel products, existence of a single institution representing all member states was a factor facilitating functionality of the market. Additionally, when prices of steel products decreased due to redundant production in the market, the ECSC was an effective tool to regulate the market effectively.[11] When the first decade of the Community is assessed, it could be seen that High Authority was succeeded to infuse in European steel market and organ member states to back up common targets. On the other hand,

it was observed that while High Authority's spent efforts for removing commercial restrictions in order to regulate the industry, member states blocked these efforts to create employment in their countries and grow the sector; and they made government contributions to domestic companies by violating the ECSC regulations. For instance, France supported its own iron – steel industry with loans with low interest rates and guaranteed by the government. Furthermore, France regulated merger and acquisitions of its companies in spite of the anti-cartel policies of the ECSC; and regulated steel prices in the domestic market contrary to the relevant act. [11]

Besides, the High Authority audited function of the market in member states and strived to enhance transparency in shipment and sales prices. However, when a recession occurred in 1960s due to the intensified competition of foreigners in the European steel industry, member states resisted to intervention of High Authority.[11] Upon oil crisis occurred in the world aftermath of the 1974 Arab – Israel War, increasing energy prices, increasing supply of steel products around the world and developing countries' efforts to build their own steel industries resulted in another crisis in the steel industry because of decreasing steel prices. However, unlike the attitude of the ECSE members during the 1960 crisis, the Community adopted an action to increase their dominance in the steel industry.[11]

As a result, it was seen that the ECSC persisted for fifty years as it has maintained coordination among member states and exerted efforts in employment market to develop labor conditions for unions and employees. Upon termination of the ECSC's legal entity in 2002, its budget in size of 1.6 billion Euro was transferred to the EU budget; and it was agreed upon that the relevant budget was to reserved for researches on coal and steel industry.[10]

II. CONCLUSION

If it is taken into consideration that the elemental objective of the European Coal – Steel Community was preventing Germany to be a dominant power in the continent once again, it could be concluded that this objective was accomplished by providing the Europe to integrate. Yet, in the introduction of the ECSC, the relationship between political integration and economic integration was emphasized as a founding rationale of the Community.

In spite of the deficiencies experienced with the ECSC, it was seen that Shuman Plan constituted the core of the new supranational Community referred as the EU by providing cooperation in iron – steel industry between France and Germany. When contribution of the ECSC into the foundation of the EU whose members of European countries participated in the Union progressively was considered, ECSC's role in prevention of the expansion of the Soviet Union across the European continent could not be underestimated. From the economic point of view, it was observed that the High Authority was effective in terms of maintenance of a joint foreign policy in terms of industrial meaning against the pressure from especially the U.S. and international steel markets and that it protected the interior market. Furthermore,

it was realized that the Community made significant contribution in terms of enhancing employment opportunities in mining industry across the Europe.

III. REFERENCES

- [1] M. Berger, "Motives for the Foundation of ECSC", Poznan University of Economics, Working Paper, WP/2012/07, 2012.
- [2] K. J. Alter and D. Steinberg, *The Theory and Reality of the European Coal and Steel Community*, S. Meunier and K. R. McNamara, Eds., Oxford:Oxford University Press, 2007.
- [3] E. Jones, *The Benelux Countries: Identity and Self-Interest*, S. Bulmer and C. Lequesne, Eds., Oxford:Oxford University Press, 2003.
- [4] L. Kriesberg, "German Evaluations of the European Coal and Steel Community, 1950-1956", *Kolner Zeitschrift fur Soziologie und Sozialpsychologie*, vol. 11, pp. 496-516, 1959.
- [5] G. Buchstab and R. Schreiner, Eds. , *Konrad Adenauer and the European Integration*, Sankt Augustin, Germany: Konrad Adenauer Foundation Archive for Christian Democratic Policy, 2007.
- [6] H. A. Simmons. (2007), *The Marshall Plan and European Unification*, [online]. Available: https://scholar.vt.edu/access/content/user/has1285/Portfolio%20Public/Documents/PDFs/EPS_Marsahll_Plan.pdf
- [7] I. Glockner and B. Rittberger, *The European Coal and Steel Community (ECSC) and European Defence Community (EDC) Treaties*, F. Laursen, Ed. New York, USA: Palgrave MacMillan, 2012.
- [8] (2017). ECSC Treaty website. [online]. Available: <https://www.consilium.europa.eu/uedocs/cmsUpload/Treaty%20constituting%20the%20European%20Coal%20and%20Steel%20Community.pdf>
- [9] B. Ubertazzi, "The End of the ECSC", *European Integration online Papers*, vol. 8, pp.1-36, 2004.
- [10] (2016) Yirmisekiz net website. [online]. Available: <http://yirmisekiz.net/2016/10/10/avrupada-ikinci-economic-birlesme-avrupa-komur-ve-celik-toplulugu-akct/>
- [11] K. J. Alter and D. Steinberg, "*The Theory and Reality of the European Coal and Steel Community*", Northwestern University, Working Paper, WP 07-001, 2007.

An Investigation into the Machinability of Hot Work Tool Steel (Toolox 44)

Rüstem BİNALI¹, Halil DEMİR¹, İbrahim ÇİFTÇİ²

¹Manufacturing Engineering Department, Technology Faculty, Karabuk University, Karabuk, Turkey
rstmbinali@gmail.com

¹Manufacturing Engineering Department, Technology Faculty, Karabuk University, Karabuk, Turkey
hdemir@karabuk.edu.tr

¹Mechanical Engineering Department, Engineering Faculty, Cankiri Karatekin University, Cankiri, Turkey
iciftci@karatekin.edu.tr

Abstract— In this study, machinability tests were carried out on Toolox 44 hot work tool steel (44 HRC) an important material in developing industry. The tests were carried out dry through milling method at four different cutting speeds (150, 180, 210, and 240 m/min), four different feed rates (0.4, 0.8, 1.2 and 1.6 mm/tooth) and at two different depth of cut (0.2 and 0.4 mm). Cutting forces developed during milling and surface roughness of the machined surfaces were measured. The results showed that increasing feed rate increased the surface roughness while increasing cutting speed decreased the cutting forces. The lowest surface roughness value (0.533 µm) was obtained at 180 m/min cutting speed, 0.4 mm/tooth feed rate and 0.2 mm depth of cut while the highest one (3.126 µm) was obtained at 180 m/min cutting speed, 1.2 mm/tooth feed rate and 0.2 mm depth of cut. The lowest cutting force was obtained at 0.4 mm depth of cut, 0.4 mm/tooth feed rate and 180 m/min cutting speed.

Keywords— Tool Steel, TOOLOX 44, Machinability

I. INTRODUCTION

Machining processes are widely used in manufacturing processes. In order obtain the final product geometry, excessive materials are removed through machining processes. Milling, turning, drilling, grinding and threading are some of the machining processes [1,2].

Milling is one of the most commonly used machining processes. In milling, the cutting tool rotates around its axis and the workpiece moves under the cutting tool. In this process, the cutting tool usually has more than one tooth. Each of these teeth has capacity to remove some chips from the workpiece. Production of numerous machine parts is carried out using milling process. Appropriate milling conditions must be selected in order to obtain the parts with the required dimensions, tolerances and surface quality [3-9].

Machining parameters are the most important factors in machining. These are cutting speed, feed rate and depth of cut. These parameters influence the resulting cutting forces, surface roughness and tool wear significantly. For this reason, suitable machining parameters must be determined depending on the

chemical and mechanical properties of the workpiece material in milling processes. Suitable cutting tool material and cutting tool geometry must also be determined depending on the workpiece material [10-13].

The steels used in die and moulds are generally hardened after machining through a suitable heat treatment process. With this heat treatment, the die and moulds become more durable under higher temperatures and higher stresses encountered their service life. However, Toolox 44 steel is supplied directly in prehardened conditions and after machining heat treatment is not required. It is known that hardened and tempered Toolox 44 has higher dimensional stability during machining. Although this steel has 40-45 HRC hardness values, its machinability is good in terms of surface quality and therefore it has wide application areas. Mechanical properties of Toolox 44 are given in Table I [14].

Table I. Mechanical properties of Toolox 44 steel [14].

	+20 C ⁰	+200 C ⁰	+300 C ⁰	+400 C ⁰	+500 C ⁰
Tensile Strength R _m (MPa)	1450	1380	-	-	-
Yield Strength R _{p0.2}	1300	1200	-	-	-
Elongation (%)	13	10	-	-	-
Compression Yield Strength R _{c0.2} (MPa)	1250	1120	1120	1060	930
Impact toughness (J)	30	60	80	80	-
Hardness (HBW)	450	-	-	-	-
Hardness (HRC)	45	-	-	-	-

Work to date has shown that less work is available in machining of Toolox 44 steel as it is a relatively new material. In this study, machining tests were carried out on Toolox 44 steel through milling process at four different cutting speeds, four different rates and two different depths of cut. The influence of these milling parameters on surface roughness and cutting forces will be aimed to be investigated.

II. MATERIALS AND METHOD

The machining tests in this work are carried out on a CNC vertical machining centre at Gazi University Technology Faculty. Schematic test setup is shown in Fig. 1.

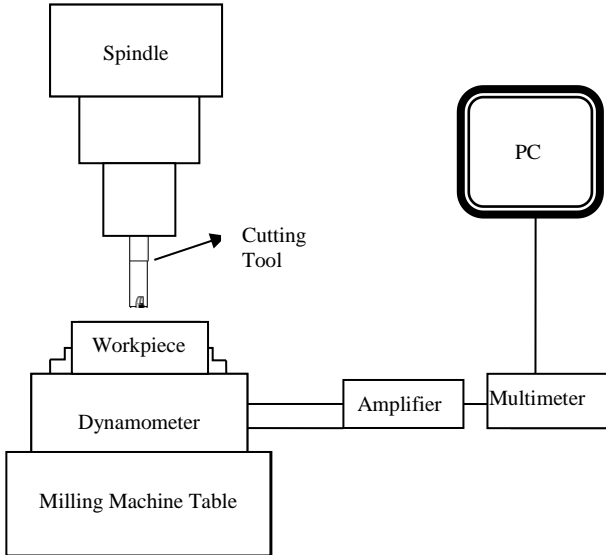


Fig. 1 Machining test setup

Toolox 44 steel is generally used in manufacturing of plastic injection and rubber moulds, form and stamping dies, metal injection moulds and hot forging dies [15]. Chemical composition of Toolox 44 is given in Table II. The dimensions of Toolox 44 workpiece material is 50x50x100 mm and given in given in Fig. 2.

Table II. Chemical composition of Toolox 44 steel [16].

Material	C	Si	Mn	P	S	Cr	Ni	Mo	V
Toolox 44	0,30	0,61	0,89	0,010	0,0009	1,23	0,66	0,79	0,145

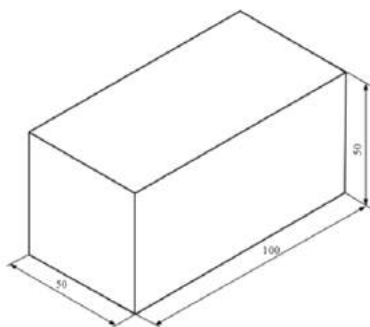


Fig. 2 Workpiece material dimensions

The cutting tools used were commercially available carbide inserts and produced by Kennametal in the form of WPGX 030204 LD. These inserts were TiAlN coating by PVD method. Table III gives some details of the cutting tool inserts.

Table III. Details of cutting tool insert

Cutting tool code	Grade	Relief angle	Included angle	Cutting tool geometry
WPGX 030204 LD 080	KC522M	12°	80°	

The cutting forces were measured using a Kistler 9257B type dynamometer during the tests, Fig. 5 while surface roughness values were measured using a Marsurf PS1 surface roughness measurement device. Specification of this device is given in Table IV. The milling parameters used are given in Table V.

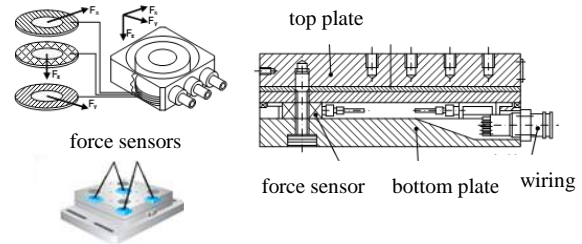


Fig. 5 Components of Kistler 9257B dynamometer [17].

Table IV. Specification of surface roughness measurement device

Model	Mahr (Marsurf PS1)
Measurement method	Stylus method
Traverse speed	0.5 mm/s (while measuring) 1 mm/s (while retracting)
Measuring force	4 mN (0.4 gf)
Stylus material	Diamond
Measurement temperature	20 °C ± 1 °C
Cut-off length	0.8 mm
Sampling length	4 mm
Stylus radius	5 µm

Table V. Milling parameters

Workpiece material	Toolox 44
Cutting speed (v)	150-240 m/min
Feed rate (f)	0,4-1,6 mm/tooth
Depth of cut	0,2-0,4 mm
Cutting tool material	TiAlN coated carbide

III. EXPERIMENTAL RESULTS AND DISCUSSION

Average surface roughness values (Ra) obtained after milling Toolox 44 steel using TiAlN coated carbide tools at four different cutting speeds (150, 180, 210 and 240 m/min) four different feed rates (0.4, 0.8, 1.2 and 1.6 mm/tooth) and two different depth of cuts (0.2 and 0.4 mm) were determined.

Fig. 7 gives the variation of average surface roughness values obtained at 0.4 mm depth of cut.

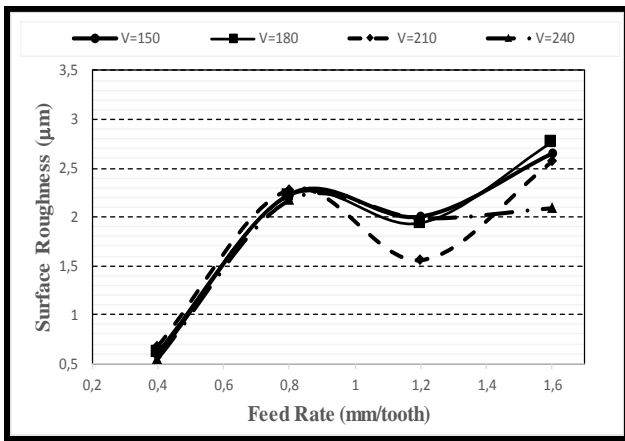


Fig. 7 Average surface roughness values obtained at 0.4 mm depth of cut

When the curves in Fig. 7 are examined, it is seen that cutting speed has not much influence on surface roughness values especially at the lower feed rates. However, the difference in surface roughness values becomes apparent at higher feed rates. A significant increase in surface roughness is seen when the feed rate is increased to 0.8 mm from 0.4 mm. Further increase in feed rate does not increase the surface roughness significantly. The highest surface roughness value is obtained at 1.6 mm/tooth feed rate and 180 m/min cutting speed. While the lowest one is obtained at 0.4 mm/tooth feed rate and 240 m/min cutting speed.

Fig. 8 gives the variation of average surface roughness values obtained at 0.2 mm depth of cut.

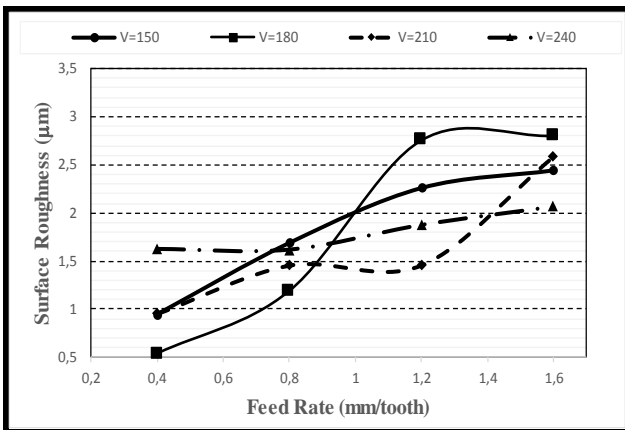


Fig. 8 Average surface roughness values obtained at 0.2 mm depth of cut

At lower depth of cut, the influence of cutting speed on surface roughness becomes more obvious at all the feed rate values. Although increasing feed rate increases the surface roughness, there is no steep increase in surface roughness with increasing feed rate as in Fig. 7. Increasing surface roughness with increasing feed rate is an expected situation. That is because, increasing feed rate increases the distance between the marks left by the cutting tool.

Increasing surface roughness with increasing feed rate and depth of cut in milling operations are also reported in Refs. [18,19].

The lower surface roughness values at 1.2 mm/tooth can be explained by the burnishing effect of the cutting tool due to the higher temperature.

The lowest surface roughness value of 0.533 µm was obtained at 180 m/min cutting speed and 0.4 mm/tooth feed rate while the highest one of 2.806 µm was obtained at 180 m/min

cutting speed and 1.6 mm/tooth feed rate. The surface roughness values obtained at 0.8 and 1.6 mm/tooth feed rates were quite close to each other at all the cutting speed.

According to the cutting speed, the most obvious difference in surface roughness values were seen at 1.2 mm/tooth feed rate. At 240 m/min cutting speed, a decrease in surface roughness was seen when feed rate increased to 0.8 mm/tooth from 0.4 mm/tooth. Apart from this, increasing feed rate increased the surface roughness for all the tests.

Fig. 9 gives the cutting forces obtained when milling Toolox 44 steel at 0.2 mm depth of cut. As can be seen from Fig. 9, increasing feed rate increases the cutting forces at all the cutting speed. However, increasing cutting speed decreases it.

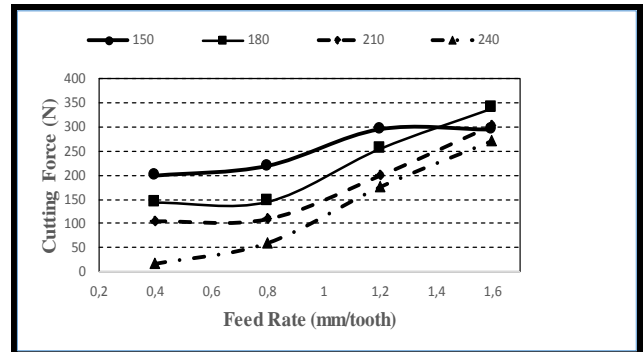


Fig. 9 Cutting forces (Fz) obtained at 0.2 mm depth of cut.

The cutting forces obtained at 0.4 mm depth of cut are given in Fig. 10.

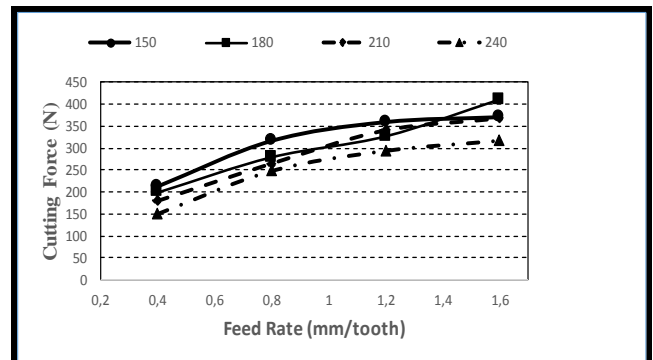


Fig. 10 Cutting forces (Fz) obtained at 0.4 mm depth of cut.

All three components of the cutting forces were measured during the tests. However, only Fz forces are analysed here as they are the highest among the others.

When the curves given in Figs. 9 and 10 are examined, it is seen that cutting forces generally increase with increasing feed rate and depth of cut. It can clearly be seen from Fig. 9 that cutting forces decrease with increasing cutting speed at all the feed rates. This situation is usually seen in machining operations and this decrease in the forces can be attributed to the decreasing tool-chip contact length on the rake face and also to decreasing shear yield strength of the adhered metal with increasing temperature as the result of increasing cutting speed [20]. The lowest cutting force of 16.3 N is obtained at 240 m/min cutting speed, 0.4 mm/tooth feed rate and 0.2 mm depth of cut while the highest one (410.7 N) is seen at 180 m/min cutting speed, 1.6 mm/tooth feed rate and 0.4 mm depth of cut.

IV. CONCLUSIONS

The influence of cutting parameters (cutting speed, feed rate and depth of cut) on surface roughness and cutting forces were investigated when milling Toolox 44 hot work tool steel using TiAlN coated carbide cutting tools. The following conclusions can be drawn from the present study:

- Increasing feed rate and depth of cut was generally found to increase the cutting forces.
- The lowest surface roughness of 0.533 μm was obtained at 180 m/min cutting speed, 0.4 mm/tooth feed rate and 0.2 mm depth of cut while the highest one of 2.806 μm was obtained at 180 m/min cutting speed, 1.6 mm/tooth feed rate and 0.2 mm depth of cut.
- The lowest cutting force of 16.3 N was obtained at 240 m/min cutting speed, 0.4 mm/tooth feed rate and 0.2 mm depth of cut while the highest one of 410.7 N was obtained at 180 m/min cutting speed, 1.6 mm/tooth feed rate and 0.4 mm depth of cut.

ACKNOWLEDGEMENT

This work was supported by Scientific Research Projects Coordination Unit of Karabük University. Project Number: KBÜ-BAP-15/2-YL-043

REFERENCES

- [1] Goetsch, D. L., "Modern manufacturing process", *Cengage Learning*, 1991.
- [2] Demir, H., Mihmat, F., Ulaş, H. B., "DIN 1.2344 sıcak iş takım çeliğinin testere freze çakılarıyla işlenebilirliğinin araştırılması", *Erciyes Üniversitesi Fen Bilimleri Enstitüsü Dergisi*, 26, 170-178, 2010.
- [3] T.S. Lee, Y.J. Lin, *Int. J. Adv. Manuf. Tech.* 16 (2000) 773–783.
- [4] Y. Altıntaş, *Int. J. Mach. Tool Manuf.* 34 (4) (1994) 461–472.
- [5] J.Z. Zhang, J.C. Chen, E.D. Kirby, J. Mater. *Process. Technology* 184, 233–239, 2007.
- [6] P. Fabricio José, P. Anderson Paulo de, B. Pedro Paulo, F. João Roberto, S. Messias Borges da, *Expert Systems with Applications* 39, 7776–7787, 2012.
- [7] Y. Karpat, T. Özel, *International Journal of Advanced Manufacturing Technology* 35, 234–247, 2008.
- [8] Demir, H., Ulaş, H., B. Ve Zeyveli, M., "Stavax Esr çeliğinin yüzey pürüzlülüğü ve kesme kuvvetleri açısından değerlendirilmesi", *5. Uluslararası İleri Teknolojiler Sempozyumu (IATS 09)*, 13-15 Mayıs 1270-1273, Karabük, Türkiye, 2009.
- [9] Demir, H., Çiftçi, İ., Zeyveli, M., Ulaş, H. B., "Eğik yüzeyleri frezelemede işleme yönlerinin yüzey pürüzlülüğüne etkileri", *UTIS09*, İstanbul, 2009.
- [10] Duran, A. Ve Acır, A. "HSS torna kalemindeki talaş açısının kesme kuvvetlerine etkisi", *Politeknik Dergisi*, 7: 3, 211-215, 2004.
- [11] Lin, W.S., Lee, B.Y., Wu, C.L., "Modeling the surface roughness and cutting force for turning", *Journal of Materials Processing Technology*, 108: 286-293 2001.
- [12] Zeyveli, M. ve Demir, H. "AISI 01 "Soğuk iş takım çeliğinin işlenebilirliğinin kesme kuvvetleri ve yüzey pürüzlülüğü açısından araştırılması", *e-Journal of New World Sciences Academy*, Vol 4, (2), 323-331, 2009.
- [13] Alaattin KAÇAL, Mahmut GÜLESİN Hasan Basri ULAŞ 2008. "Azdırma yöntemi ile dişli çark açma işleminde kesme kuvvetlerinin ölçülmesi için sistem tasarım ve imalat", *Gazi Üniversitesi Mühendislik Mimarlık Fakültesi Dergisi*, 4, 795-800, 2008.
- [14] (2017) SSAB. Available: <https://www.ssab.com/products/brands/toolox/products/toolox-44>
- [15] (2017) Arascalik. Available: http://www.arascalik.com.tr/plastik_toolox44.html
- [16] Persson, U. And Chandrasekaran, H., "Machinability of martensitic steels in milling and the role of hardness", *6th International Tooling Conference*, 2012.
- [17] Kistler, "Kistler Type 9257B Three Component Dynamometer Operating Instructions", 1 1997.

- [18] Kavak, N. and Üstel, N., "The Investigation of Surface Roughness on AISI 1040 steel with dry turning", *Karalmas Science and Engineering Journal* 2 (2), 24-29, 2012.
- [19] Kılıçkap, E. ve Çelik, Y. H., "Cam elyaf takviyeli plastik kompozitlerin frezelemede kesme parametrelerinin yüzey pürüzlülüğüne etkisinin incelenmesi", *3. Ulusal Talaşlı İmalat Sempozyumu*, Ankara, 04-05 Ekim 2012.
- [20] Çakır, M.C., "Modern talaşlı imalat yöntemleri", *Vipaş A.Ş.*, Bursa, 350-390, 2000.

Simulation and analysis of the solidification characteristics of a cast austenitic stainless steel

G. Aktaş Çelik¹, M. I. T. Tzini², Ş. H. Atapek¹, Ş. Polat¹, G. N. Haidemenopoulos²

¹Kocaeli University, Department of Metallurgical and Materials Engineering, Turkey
gulsahaktas@gmail.com, hatapek@gmail.com, sydpolat@gmail.com,

²Thessaly University, Department of Mechanical Engineering, Laboratory of Materials, Greece
margiannatz@gmail.com, ghaidemenopoulos@gmail.com

Abstract— In automotive applications, especially in exhaust systems, cast ferrous materials (cast iron, stainless steels, mild or carbon steels etc.) are preferably used due to their excellent mechanical properties, creep, oxidation and corrosion resistance at high temperatures. In diesel and gasoline engines, the manifold materials are subjected to 950°C, at which cast austenitic stainless steels (CASSs) are preferred due to their superior physical and chemical properties. The desirable properties of CASSs are basically determined by their as cast microstructures, hence it is important to identify the solidification path revealing out the microstructural features, stability of the phases and elemental partitioning during all phase transformations. In this study, a Nb-stabilized Fe-Cr-Ni austenitic stainless steel was selected as a candidate alloy for exhaust manifold material. Both its solidification behavior and microsegregation were investigated using thermodynamic calculations by Thermo-Calc. The studied composition was also cast and thermal analysis studies were carried out in order to reveal the sequence of phase formation and the phase transformations during solidification. The present study not only consists of thermal modeling and analysis but also determination of matrix phases by using microscopy. The data obtained will be useful to understand the high temperature behavior of the studied alloy.

Keywords—Cast austenitic stainless steel, Thermo-Calc, thermal analysis, characterization.

I. INTRODUCTION

Cast austenitic stainless steels (CASSs) occupy critical positions in the working conditions having high temperature and corrosive environments such as chemical, nuclear and petroleum industries as well as exhaust systems in automotive applications [1]-[7]. Especially in exhaust systems where temperature exceeds of 900 °C, Nb-stabilized cast austenitic stainless steels are attractive candidates among all cast irons and cast stainless steels due to their excellent mechanical properties, creep and corrosion resistance at high temperatures [5]-[7].

The desirable properties of CASSs are basically determined by their as-cast microstructures, hence it is important to identify the solidification path, revealing out the microstructural features, stability of the phases and elemental partitioning during all phase transformations. Studies indicate that, obtaining delta ferrite in solidified structure develops the

mechanical properties and corrosion resistance and minimizes the occurrence of hot cracks [1]-[4]. Therefore most austenitic stainless steels are modified in order to obtain primary δ -ferrite and secondary austenite during solidification [1]-[3]. This solidification sequence is named as ferritic-austenitic solidification mode (FA mode). For austenitic stainless steels, there are four types of solidification modes which can produce different solidification microstructure with various δ -ferrite morphologies [8]. Compositional variations, Ni and Cr equivalent values and non-equilibrium cooling conditions specify the solidification mode producing either primary austenite or primary delta-ferrite [8]-[10].

In this study, the solidification characteristics of Nb-stabilized cast austenitic stainless steel (CF8C) were investigated, using thermodynamic calculations by Thermo-Calc, thermal analysis and microscopic examinations.

II. EXPERIMENTAL STUDY

UU. Material

The alloy (0.03C, 17.2Cr, 10.2Ni, 1.0Mn, 0.7Si, 0.4Nb, 0.2Mo wt.-%) was produced by sand mold casting in Gedik Casting Co, Turkey. It is well known that Cr, Nb, Si are ferrite stabilizing elements while Mn, C, Ni and N have strong effect on the stabilization of the austenite phase [11]. However, Nb forms NbC and improves mechanical properties via precipitation hardening mechanism [5], [6]. In order to estimate the possible solidification mode, Ni_{eq} and Cr_{eq} values were calculated with equations (1) and (2) where the concentrations are in wt.-% [8] and Cr_{eq}/Ni_{eq} value was found as 1.61. According to this value, the solidification sequence of this composition corresponds to the FA mode [8].

$$Ni_{eq} = Ni + 30C + 0.5Mn \quad (1)$$

$$Cr_{eq} = Cr + Mo + 1.5Si + 0.5Nb \quad (2)$$

VV. Computational Method

The solidification characteristics of CF8C stainless steel were investigated by using thermodynamical calculations in ThermoCalc software according to CALPHAD approaches.

Equilibrium phase diagram and the critical temperatures of the studied composition were computed using TCFE6 database. Solidification path and the microsegregation during solidification were calculated using the Scheil module. The simulation started from the liquid phase at casting temperature (T_C) and ended at solidification temperature (T_S). The most important assumption of the Scheil simulation is the absence of diffusion in the solid phases.

WW. Thermal Analysis and Microscopic Examinations

In order to reveal out both the critical temperatures and the final microstructure of the studied CF8C stainless steel, thermal analysis and microscopic examinations were applied. The thermal analysis was carried out by using differential scanning calorimeter (DSC) method on Netzsch STA 409 PG Luxx. The DSC samples were heated to 1460 °C at a heating rate of 5 K.min⁻¹, held at that temperature for 5 min, and then cooled to room temperature (T_R) at rate of 5 K.min⁻¹.

For microscopic examinations, cast sample was prepared metallographically. Sample was ground with 320, 600, and 1000 mesh size SiC abrasives, respectively, and then polished with 3 µm diamond solution. Polished surface was etched electrochemically using %10 sodium metabisulphite for 25 sec. under 7 V. Microstructural characterization was carried out using light microscope (LM, Olympus BX41M-LED), scanning electron microscope (SEM, Jeol JSM 6060) and energy dispersive spectrometer (EDS, IXRF).

III. RESULTS AND DISCUSSION

XX. Modelling of The Solidification Sequence

The solidification path and the C isopleth of studied composition are depicted in Fig. 1 and Fig. 2, respectively. According to solidification path, (i) solidification starts at 1446.06 °C (T_L) with δ -ferrite precipitation from liquid, (ii) continues with austenite transformation at 1433.09 °C and (ii) finishes at 1021.85 °C (T_S) (Fig. 1). When temperature is decreased further, the subsequent solid state transformation occurs as MC carbide precipitation and final microstructure consists of ferrite, austenite and MC type carbide (Fig. 2). The computed solidification sequence corresponds to the FA mode given in the literature [8].

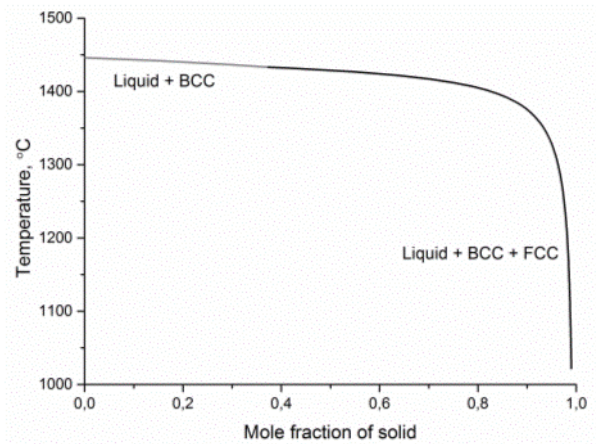


Fig. 1. Solidification path of the studied alloy.

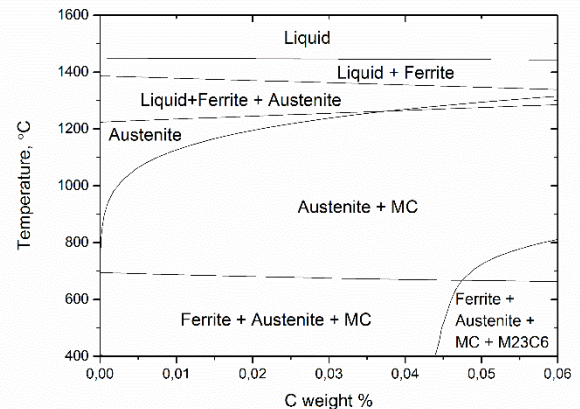
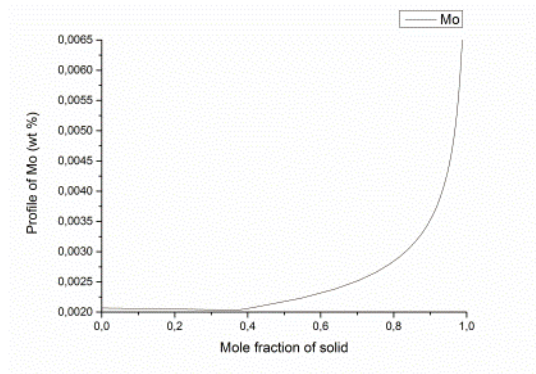


Fig. 2. Isopleth section of the studied alloy.

In order to understand microsegregation during solidification, element composition profiles in the ferrite phase were calculated against mole fraction of solid and graphs are depicted in Fig. 3 and Fig. 4. Concentration profiles of elements start at liquid phase where the mole fraction of solid is 0 and end when the solidification finishes. Increasing in mole fraction of solid means that ferrite dendrites grow into the liquid and consume the liquid phase when the mole fraction of solid becomes 1. Element compositions in the profiles start at the composition values in the liquid phase. During solidification, elements segregate through the ferrite/liquid interface, therefore compositions of the elements rise as the mole fraction of solid increases. When solidification ends, elements exhibit the highest values at the ferrite cell boundary. These microsegregation characteristics of elements affect the critical temperatures of the solid state transformations and the final microstructure of alloys [11]. Studies indicate that when solidification starts with δ -ferrite, Ni is rejected by the ferrite matrix ahead of the ferrite/liquid advancing interface during solidification and liquid becomes enriched by Ni. When Ni enrichment is enough to form austenite, austenite transformation occurs at δ -ferrite/liquid interface [8]-[10].

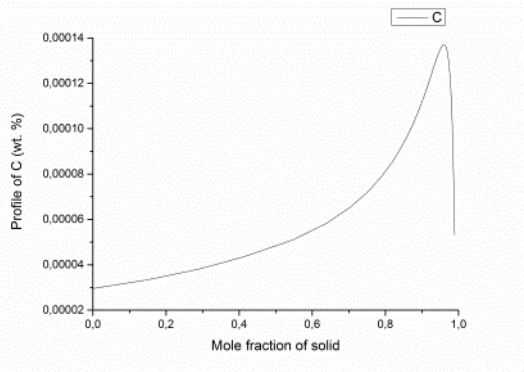
YY. Evaluation of DSC Curve

The DSC thermogram of the studied stainless steel is given in Fig. 5. The thermogram indicates the sequence of phase transformations in the studied alloy during cooling from 1460 °C to room temperature. According to the thermogram, solidification starts at 1402 °C, austenite transformation occurs at 1327 °C and solidification ends at about 1024 °C. During cooling, MC type carbide precipitates at 1024 °C. These temperatures are in agreement with Thermo-Calc data. This phase transformation sequence indicates that final microstructure may consist of δ -ferrite, MC carbide and austenite.

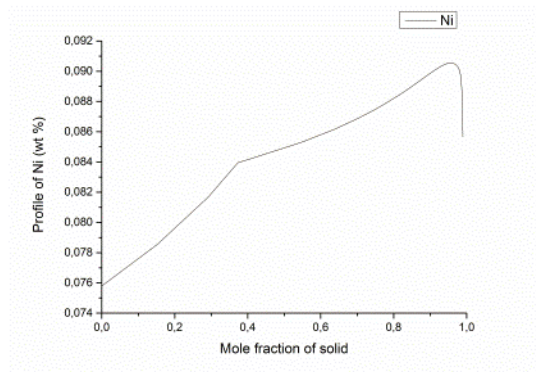


(d)

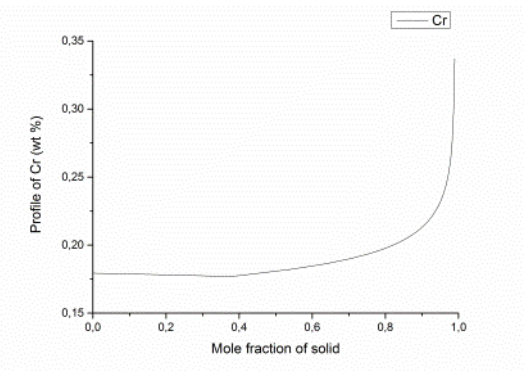
Fig. 3. Composition profiles of elements in ferrite phase during solidification; (a) carbon, (b) chromium, (c) niobium and (d) molybdenum.



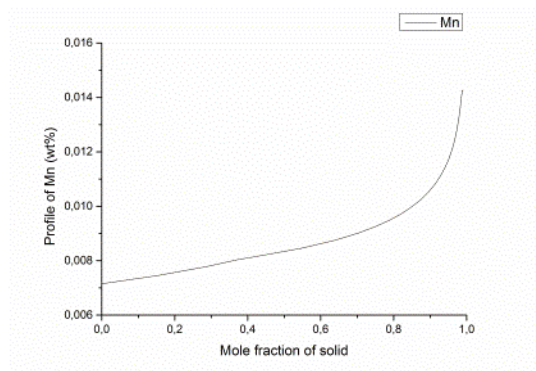
(a)



(a)

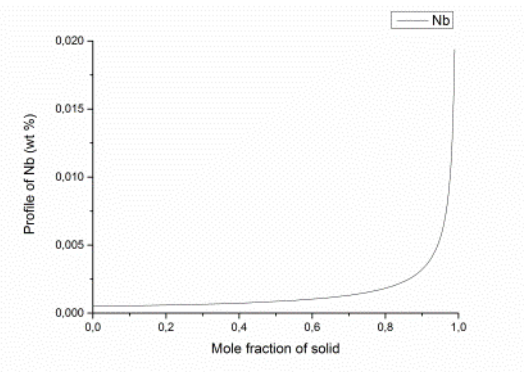


(b)



(b)

Fig. 4. Composition profiles of elements in ferrite phase during solidification; (a) nickel and (b) manganese.



(c)

ZZ. Microstructural Characterization

According to the thermodynamic calculations, the solidification path of the studied alloy corresponds to the FA solidification mode. Therefore it is expected that the microstructure contains δ -ferrite and MC carbide in the austenite matrix. Literature indicates that δ -ferrite forms in skeletal or lathy morphology depending on the solidification rate [8]-[10]. Fig. 6 shows the LM micrograph depicting the as cast microstructure of studied cast stainless steel. Steel has skeletal type δ -ferrite in the austenite matrix.

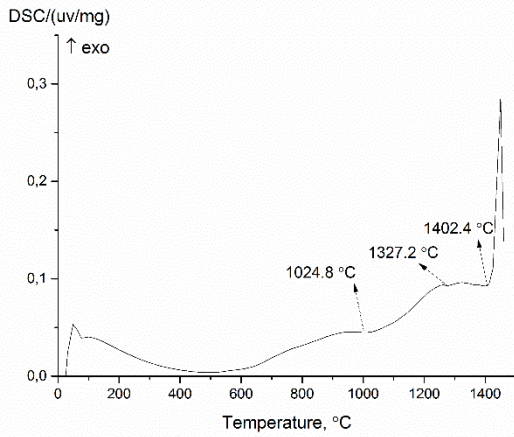


Fig. 5. Thermogram indicating the sequence of phase transformations in studied alloy.

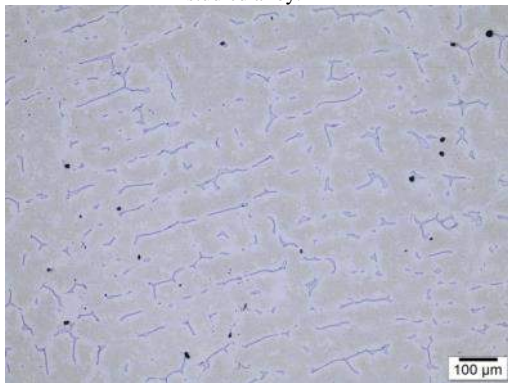


Fig. 6. LM micrograph showing the as cast microstructure of studied alloy.

SEM micrograph given in Fig. 7 indicates that cast alloy has also MC carbides precipitated near the δ -ferrite phase. These microstructural features are in agreement with the results of the thermodynamic calculations.

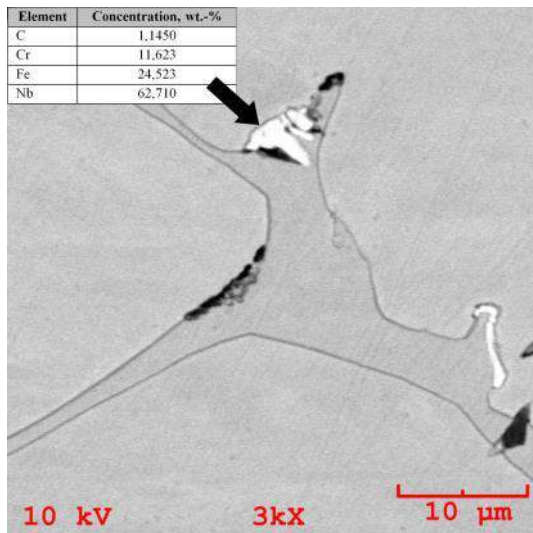


Fig. 7. SEM micrograph showing the as cast microstructure of studied alloy.

IV. CONCLUSIONS

In the present study, the solidification characteristics of a cast austenitic stainless steel were investigated using computational thermodynamics, DSC analysis and microstructural characterization. The obtained solidification path by DSC was in agreement with the Scheil solidification simulations. Solidification started with δ -ferrite precipitation from the liquid and finished after the austenite transformation. The C isopleth showed that the MC carbide precipitates on further cooling. This result is in agreement with the microstructural features determined microscopically, i.e. the final microstructure consisted of skeletal δ -ferrite, MC type carbides in austenitic matrix.

V. REFERENCES

- [1] W. Y. Chen, M. Li, M. A. Kirk, P. M. Baldo, and T. Lian, "Effect of heavy ion irradiation on microstructural evaluation in CF8 cast austenitic stainless steel", *Journal of Nuclear Materials*, vol 471, pp. 184-192, Aug. 2015.
- [2] J. S. Cheon, and I. S. Kim, "Evaluation of thermal aging embrittlement in CF8 duplex stainless steel by small punch test", *Journal of Nuclear Materials*, vol. 278, pp. 96 – 103, Aug. 1999.
- [3] M. Li, M. K. Miller, and W. Y. Chen, "Phase stability in thermally-aged CASS CF8 under heavy ion irradiation", *Journal of Nuclear Materials*, vol. 462, pp. 214 – 220, March 2015.
- [4] H. Jang, S. Hong, C. Jang, and J. G. Lee, "The effects of reversion heat treatment on the recovery of thermal aging embrittlement of CF8M cast stainless steels", *Materials and Design*, vol. 56, pp. 517 – 521, Dec. 2013.
- [5] J. P. Shingledecker, P. J. Maziasz, N. D. Evans, and M. J. Pollard, "Creep behavior of a new cast austenitic alloy", *International Journal of Pressure Vessels and Piping*, vol. 84, pp. 21 – 28, 2007.
- [6] Y. H. Zhang, M. Li, L. A. Godlewski, J. W. Zindel, and Q. Feng, "Effective design of new austenitic cast steels for ultra-high temperature automotive exhaust components through combined CALPHAD and experimental approaches", *Materials Science & Engineering A*, vol. 683, pp. 195-206, Dec. 2016.
- [7] B. Piekarski, "Effect of Nb and Ti additions on microstructure, and identification of precipitates in stabilized Ni-Cr cast austenitic steels", *Materials Characterization*, vol. 47, pp. 181 – 186, July 2001.
- [8] J. W. Fu, Y. S. Yang, J. J. Guo, J. C. Ma, and W. H. Tong, "Microstructure evolution in AISI 304 stainless steel during near rapid directional solidification", *Materials Science and Technology*, vol. 25, pp. 1013 – 1016, 2009.
- [9] H. Inoue, and T. Koseki, "Solidification mechanism of austenitic stainless steel solidified with primary ferrite", *Acta Materialia*, vol. 124, pp. 430 – 436, 2017.
- [10] A. Hunter, and M. Ferry, "Phase formation during solidification of AISI 304 austenitic stainless steel", *Scripta Materialia*, vol. 46, pp. 253 – 258, 2002.
- [11] H. K. D. H. Bhadeshia, and R. W. K Honeycombe, "Steels - Microstructure and Properties", 3rd ed., Oxford, UK: Elsevier, 2006.

Experimental study on tribological performance of SiC composite coating layers

Koray KILIÇAY*, Mustafa ULUTAN⁺, Esad KAYA[#], İsmail BAYAR^ˆ

*Mechanical Engineering Department, Eskişehir Osmangazi University, Turkey kkilicay@ogu.edu.tr

⁺Mechanical Engineering Department, Eskişehir Osmangazi University, Turkey [mulutan@ogu.edu.tr](mailto:mulutun@ogu.edu.tr)

[#]Mechanical Engineering Department, Eskişehir Osmangazi University, Turkey esatkaya@ogu.edu.tr

^ˆMechanical Engineering Department, Eskişehir Osmangazi University, Turkey ismailbayar@ogu.edu.tr

Abstract—In this study, silicon carbide (SiC) composite coating layer was produced with Plasma Transferred Arc (PTA) welding methods. Microstructure, hardness, and tribological performance were investigated on the composite coating layers. The results showed that the silicon carbide powders are completely dissolved during the PTA cladding process and the microstructures consisted of dendrites and interdendritic eutectic structure. SiC composite coatings have significantly increased the hardness due to the eutectic structures. PTA cladding processes improved the wear resistance 3.8-fold compared to the substrate.

Keywords— PTA (Plasma Transferred Arc), SiC (Silicon Carbide), Composite Coating, Friction and Wear.

I. INTRODUCTION

Wear is an important problem in moving machine parts. Surface engineering technologies are widely used to increase wear resistance of machine elements. The methods used in surface engineering technologies for coating on substrate materials include laser cladding [1], thermal spray coating [2], and plasma transferred arc (PTA) cladding [3]. The PTA cladding method is commonly used surface modification methods to increase wear resistance of materials. The PTA cladding method is based on the melting of alloy powders with suitable properties on the surface of the coating material [4-6]. When the PTA is applied to the sample surface, the energy from the plasma arc can rapidly melted the surface of substrate and coating powders to produce an alloyed molten pool. In this process, the new alloyed molten pool can generated and this new layers can rapidly solidified. As a result, a new coating layer with improved surface properties is obtained [7]. The PTA method has significant advantages such as high deposition rate, low heat input and low distortion [4, 8]. Additionally, the PTA method has advantages such as easy of application, no need for additional surface treatments, and completion of one-time processing, as well as low cost and high productivity compared to thermal spray coatings [9]. It is also a surface treatment in which a wide variety of wear resistant and hard surfaces can be formed [10].

Carbide powders are widely used in order to improve the surface properties of the metals during the surface cladding. Silicon carbide (SiC) are preferred for coating applications as

it contribute to increased wear resistance due to their high hardness values [11]. Several researches have been performed with the welding method of SiC composite coatings. Islak et al. [11] investigated the effect of Cr₃C₂ and SiC coating powders on the microstructure and hardness of the coatings produced by PTA method. They determined that microstructure is composed of dendrite and interdendrite eutectics and the coating layers appeared to be metallurgically bonded to the substrate material. They indicated that microhardness value increased with the increase of the amount of SiC added and the microhardness value of the coating layers was found to be about 2.5-3.5 times higher than the substrate material. Buytoz and Ulutan [12] investigated the silicon carbide coatings on austenitic stainless steel surface with the tungsten inert gas (TIG) method. They indicated that SiC coating powders completely melted during coating process and microstructures are composed of dendritic and interdendritic regions. They found that high powder contents produce the hard M₇C₃ primary carbides in the coating layers. They measured the highest hardness value as 1210 HV and proved the presence of M₇C₃ carbides in the matrix. Buytoz [13] investigated the effects of TIG parameters on the SiC coating layers. Author concluded that at lower powder contents, the microstructures consisted of dendrites, however, at high powder contents, the microstructures consisted of M₇C₃ primary carbides, Fe₃Si, SiC, and the graphitic carbon precipitates. Author measured the hardness value of the coating layers was between 744 and 1135 HV. It has increased the hardness value by about 5 times compared to the base material.

In this study, the effects of PTA parameters on microstructure, hardness, and wear resistance of SiC carbide coating layers were investigated.

II. MATERIALS AND METHODS

38MnVS6 microalloyed steel was selected as substrate material, and SiC powder (Alfa Aesar, at least 99.5% purity, average grain size 7 μm) was used as a coating powders. The chemical compositions of substrate steel are given in Table 1. Steel samples were prepared by cutting them to 20x10x100 mm³. 3x1 mm² channels were milled onto one surface of each sample. SiC coating powders were mixed with alcohol on these channels

and the samples were kept at 150°C for 1 hour. The surface of the samples were melted using a Fronius Plasma (Plasma Transferred Arc) welding machine. Argon gas was used as a plasma and shielding gas. PTA cladding conditions are given in Table 2.

TABLE XLV
THE CHEMICAL COMPOSITIONS OF MICROALLOYED STEEL

Element	wt. %	Element	wt. %	Element	wt. %
C	0.39	Ni	0.04	Mn	1.36
Si	0.22	V	0.11	Cr	0.07
Ti	0.003	Al	0.021	S	0.044

TABLE XLVII
PTA PROCESS PARAMETERS

Parameters	Value	Unit
Tungsten 2% Thorium electrode	Ø3.2	mm
Arc current	100-120	A
Arc voltage	22	V
Shielding gas flow rate	10	l/min
Plasma gas flow rate	0.4-0.5	l/min
Coating feed rate	40	mm/s
Working distance	2.5	mm

After the PTA process, the samples were cut using the Struers Discotom 5 wet-cutting device for microstructural, microhardness and, wear tests. The microstructure samples were ground using Struers MD Dac 220 and 600 grit discs and were polished with 3 µm diamond solutions. After polishing, to obtain clear microstructural images, the samples were etched with 2% Nital and 2 g of CuCl₂+10 ml HCl+80 ml pure ethyl alcohol solutions. The prepared samples were examined by Nikon optical and Jeol-JSM-5600LV SEM microscopes. Additionally, EDS analysis was performed using a Jeol JSM-5610 Instruments X-ray EDS instrument.

Vickers microhardness measurements were performed with a Future Tech microhardness tester. The hardness measurements parameter was selected as 100 gf (HV_{0.1}) load and 10 s dwell time. Dry sliding wear tests were performed using a CSM-Tribometer test instrument with the ball on disk (ASTM G99 test standard) wear geometry. Surfaces of sample were polished to provide similar surface properties. In all tests, ø3 mm WC balls (Wolfram Carbide - certified sphericity) were used as a counterbody and the coefficients of friction and wear distance were simultaneously recorded. The experiments were conducted at 20°C, 35-40% relative humidity, 5 N load, 100 m wear distance, and at a linear speed of 3 cm/s. After the wear experiments, the surface roughness profiles of the worn surface were measured with a Mitutoyo SurfTest SJ-400 profilometer. The wear rates were calculated from these measured values. Additionally worn surface were examined with SEM and EDS analyses for the determination the wear behaviour.

III. RESULT AND DISCUSSION

The microstructure of microalloyed steel substrate consisting of ferrite and perlite phases. The microstructures of the samples varied greatly due to the SiC coating powders used after the PTA process and the different energy inputs created by the process conditions. In the macro and micro analyses made after the PTA process, hardly any cracks, voids, and porosity were observed.

An intermediate layer was formed between the substrate and the composite coating layers (Fig. 1). The intermediate layer consisted of a planar and columnar structure. The planar structure in this intermediate layers changes as a columnar structure as it goes towards the upper surface of the coating. The solidification that started in the columnar structure in the alloying zone continued dendritically. No tertiary dendritic arms were formed in samples where the rate of cooling was partially high. Depending on the direction of cooling, the dendrites oriented towards the coating surface. In general, most vertically oriented dendritic solidification was seen from the substrate material to the coating surface. The main image of the microstructure contains dendritic arms and eutectic structures formed in the interdendritic regions. Figure 1 shows dendrites and eutectic structures in the microstructure.

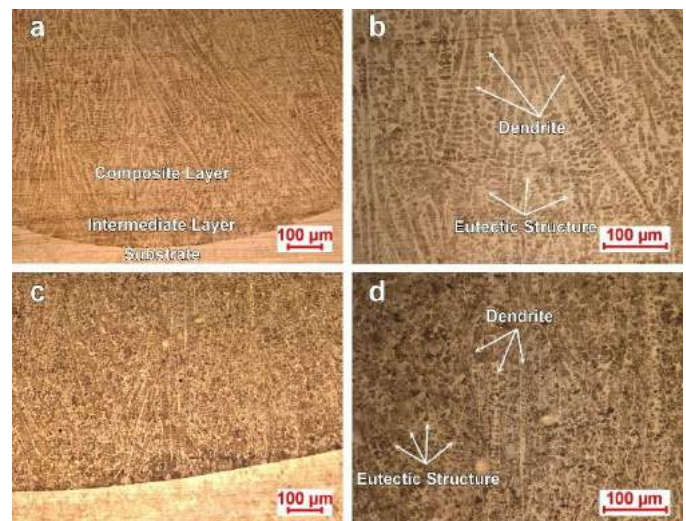


Fig. 23 Optical microscope images of SiC composite layers: a) 100A-100x, b) 100A-200x, c) 120A-100x, and d) 120A-200x.

Formations and dimensions of dendrites changed with increasing energy input. The increase in energy input caused the alloying zone to cool more slowly. For example, when Figure 1-b and Figure 1-d are examined, it is observed that only the main dendrite arms are formed in the alloying region and the dendritic arms of the 120 A-treated specimen are grow and coarse. The slower cooling of the sample with increased heat input in 120A sample led to the growth of the dendrites. For this reason, the amount of interdendritic region containing eutectic structures decreased.

The SEM photographs and EDS analyses of the samples are given in Figure 2. When the Figure 2 are examined, it was seen

that the Si and C elements diffused through the surface after the PTA process. This increase in the 38MnVS6 microalloyed containing 0.39% C and 0.22% Si (wt.%) in the composition indicates that the alloying process is successful. The microstructure consists of dendrite and interdendritic eutectic structures. Another reason for the dendritic solidification is the large difference between the melting points of the other phases formed by iron and silicon carbide dissolution. The microstructure of the coatings is mainly composed of equal-axis dendritic primer phases and thin-layered eutectics between the dendrites. According to EDS analyses, the dendritic primer phase (Figure 2-a Region 4) contains 1.896% C, 6.087% Si and 89.634% Fe (wt.%). The eutectic structure between dendrites (Figure 2-a Region 3) contains 0.952% C, 5.018% Si and 92.807% Fe (wt.%). A similar distribution of the elements in the dendrites and interdendritic regions can be explained by the rapid solidification theory of steels [12, 14]. The dendrites grow in the same direction as the heat flow of the solidification. In addition, there are variations in the composition between the dendrite and the interdendritic region due to the dissociation of atoms during rapid solidification.

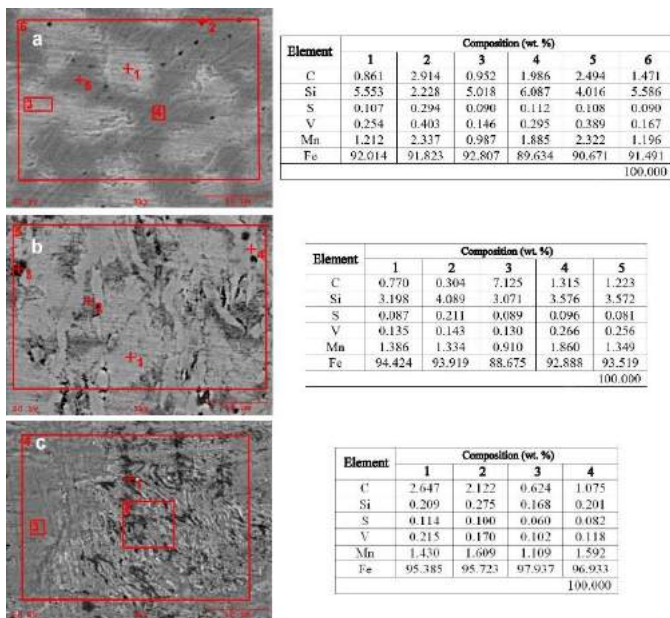


Fig. 2 SEM and EDS results of samples: a) 100A, b) 120A, and c) Substrate.

XRD analysis of SiC composite coatings are given in Figure 3. The solid phase reaction of Fe and SiC occurs due to the high temperature of the weld pool during the PTA process. The dissolution of SiC particles in the molten pool leads to enrichment of iron, silicon, and carbon in the matrix, and consequently, iron silicon compounds, SiC and iron carbides were formed in the solidified structures. In the XRD analyses of the samples, as expected after SEM and EDS analyses, the different composition of iron-silicon compounds, SiC and iron carbides were determined. The iron-silicon compounds are in different composition as $Fe_{0.94}Si_{0.06}$ and Fe_3Si which contain high iron. By the XRD analysis, it was determined that the PTA composite coatings consisted of the $Fe_{0.94}Si_{0.06}$ in the dendritic

region and the Fe_3Si , SiC, and $FeC_{0.053}$ iron carbides in the interdendritic region.

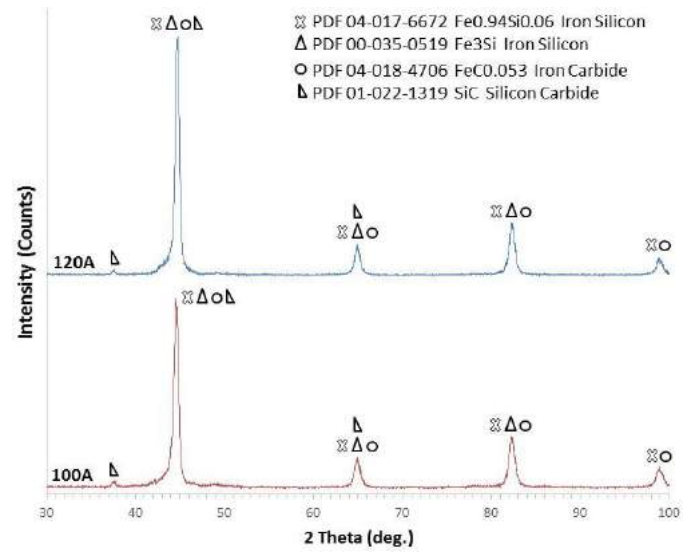


Fig. 3 XRD results of SiC composite layers

The graphs of the microhardness measurements of samples are given in Figure 4. After the surface alloying process, the hardness of the samples was determined to be notably high (258 HV) compared to the substrate material due to the effect of eutectic structures found in the interdendritic region. The average hardness value of the coating layer was calculated as 604.3 $HV_{0.1}$. After microhardness measurement, the highest hardness values in the alloying region was 711.4 $HV_{0.1}$ (100A sample) while the lowest hardness value was measured at 539.5 $HV_{0.1}$ (120A sample). As moving inwards from the surface, the hardness values decreased in all of the samples. The hardness values of the samples decreased considerably in the transition zones. However, the hardness of the transition zone is greater than the hardness of the microalloyed substrate. The hardness values are fluctuated from the surface to the inside and the suddenly increase in some points due to the interdendritic carbide. Furthermore, due to the differences in dendritic solidification, the eutectic structures formed around the dendritic arms and in the different components cause changes in the hardness values.

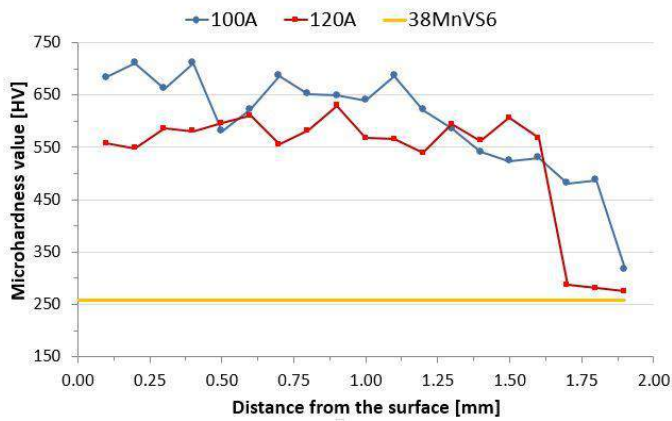


Fig. 4 Microhardness value of samples.

The wear rates and average coefficient of friction values of SiC composite coatings are given in Figure 5. Similar coefficient of friction values were determined in the composite coating samples produced from different PTA currents. The average coefficient of friction value of all samples was higher than the main material (0.37). The average coefficient of friction for these samples are 0.49 and 0.5. The low friction coefficient of the substrate material is related to the iron oxides formed on the contact surface. When Figure 5 is examined, the wear rates were reduced by about 3.6 - 3.8 times compared to the main material. These results show that wear behaviours of the composite coating are improved significantly.

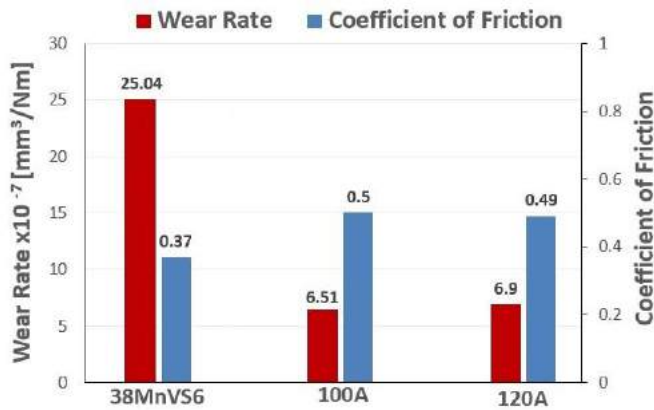


Fig. 5 Wear rate and average coefficient of friction value of samples.

In order to determine the tribological behaviour of SiC composite coatings, wear channels were investigated by SEM and EDS analysis (Figure 6). When the wear surfaces of these samples are examined, abrasive wear traces and oxide layers are seen. Therefore, wear losses were caused by surface abrasion with hard counterbody and ruptured of the oxides formed after the tribochemical reaction. In the EDS analyses of these samples, a high amount of W element that comes from the counter body was detected. This indicates that the system is stable in terms of load and wear resistance during wear tests.

Tribochemical reactions occurred on the wear surfaces of composite coatings to form Fe and W-containing oxide layers

(Figure 6). These oxide layers ruptured from the surface at the increased wear distance and caused an abrasive effect as the third body at the contact interface. Silicon and iron carbides on the contact surfaces of the samples have partially reduced this negative effect. However, these wear particles in the tribological system increased the coefficient of friction slightly. It is evident by the increase of the W element in the analyses that these oxides formed during the wear come into direct contact with the WC counter body. When the worn surface of the composite coatings was examined by SEM and EDS analysis (Figure 6), it was determined that the oxide layers formed were less than the substrate material. Therefore, the coefficient of friction of composite coatings are slightly increased compared to the base material.

The low friction coefficient of the 38MnVS6 microalloyed steel specimen relates to thick iron oxides spontaneously formed by tribochemical reactions on the contact surface. During the wear test, these thick oxide layers on the surface reduced the friction coefficient by preventing metal-metal contact. However, these oxide layers were broken at increasing wear distances and separated from the surface, therefore increased the wear rate. In this sample, the oxide layers breaking and ruptured from the surface by the load applied at increasing wear distances formed delamination zones (Figure 6-c). In addition, the broken oxide layers remain at the interface, forming abrasive particles and residues. These third bodies in the tribological system caused the abrasive wear to intensify at the contact points. For this reason, wear is greatly increased due to delamination and three-body abrasive wear in the substrate steel specimen.

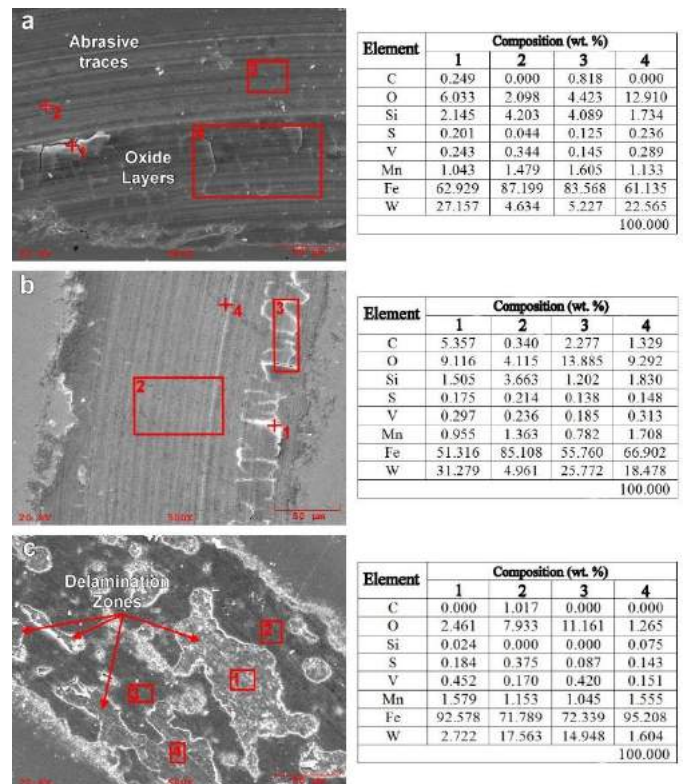


Fig. 6 SEM and EDS results of worn surfaces: a) 100A, b) 120A, and c) Substrate.

The main wear mechanism of samples treated at 100A and 120A are abrasive and oxidative wear mechanism. In interdendritic regions of SiC composite coating samples, hard silicon carbides and iron carbides were determined as a result of microstructure studies. The high abrasive wear resistance of these carbides and the protective layer formed by tungsten oxide on the surface reduced the wear rate compared to the base material. SEM photographs and EDS analyses of worn surface of the 100A sample reveals abrasive wear traces and oxide layers (Figure 6-a). In the microstructure studies of this sample, the silicon and iron carbides formed in the interdendritic regions significantly increased the wear resistance compared to the substrate. In a region of contact with these carbides on the surface, a large layer containing high W element (coming from the counterbody) and strong oxides formed by this element are seen in Fig. 6-a-4. Similar wear and friction behaviours were obtained for 120A sample. In the SEM surface photograph of this sample (Figure 6-b) again the abrasive wear traces and the oxide layers formed by W coming from the counter body are seen. The amount of dendritic structures formed in the microstructure increased due to the high heat input of this sample. This reduced abrasive wear resistance by reducing the amount of eutectic carbides formed in the interdendritic region.

IV. CONCLUSIONS

In this study, surface of 38MnVS6 microalloyed steel was alloyed with SiC powder using PTA method. The phases, microhardness distributions and tribological behavior of the samples were investigated. The results obtained as a result of the experimental investigations made are summarized below:

- Microstructures of SiC coatings consist of dendritic primer phase and thin layered interdendritic eutectic structures. The dissolution of SiC particles in the molten pool during PTA welding resulted in the formation of iron-silicon compounds, large amounts of SiC and iron carbides in the solidified structures. Increased energy input has led to the growth and coarsening of dendrites. Therefore, the amount of eutectic carbide reduced in the interdendritic region.

- All of the hardness values of the composite coating layers were measured to be higher than the microalloyed steel substrate. The high concentration of hard carbides (SiC and iron carbide) are the main reason for the high hardness of the composite coating layers. A decrease in the hardness values were detected as the composite coating layers moved from the surface to the substrate material.

- The main wear mechanism of composite layers produced with PTA cladding method were abrasive and oxidative wear. The wear rate of these samples are considerably reduced compared to the base microalloyed steel due to trioxides and hard eutectic carbides. The highest wear resistance was detected at 100A composite coatings. Wear resistance of this sample was high as 3.8-fold compared to the substrate. Increased energy input reduced wear resistance as it reduces the amount of eutectic carbide.

- The SiC composite coatings using with the PTA method improved tribological properties due to the formation of the eutectic carbides. For this reason, SiC composite coatings by PTA method can be used to improve tribological performance of 38MnVS6 microalloyed steel.

V. ACKNOWLEDGMENT

This study was financially supported by the Scientific Research Council of Eskisehir Osmangazi University (Project No: 2015-766) and Tübitak (2211/A).

VI. REFERENCES

- [1] N. Sun, H. Y. Shan, H. Zhou, D. R. Chen, X. Y. Li, W. Xia, and L. Q. Ren, "Friction and wear behaviors of compacted graphite iron with different biomimetic units fabricated by laser cladding ", *Applied Surface Science*, 258 19 7699-7706 2012.
- [2] L. M. Berger, " Application of hardmetals as thermal spray coatings ", *International Journal of Refractory Metals & Hard Materials*, 49 350-364 2015.
- [3] H. Zhao, J. J. Li, Z. Z. Zheng, A. H. Wang, D. W. Zeng, and Y. F. Miao, " The microstructures and tribological properties of composite coatings formed via PTA surface alloying of copper on nodular cast iron ", *Surface & Coatings Technology*, 286 303-312 2016.
- [4] S. Buytoz, A. Orhan, A. K. Gur, and U. Caligulu, " Microstructural Development of Fe-Cr-C and B4C Powder Alloy Coating on Stainless Steel by Plasma-Transferred Arc Weld Surfacing ", *Arabian Journal for Science and Engineering*, 38 8 2197-2204 2013.
- [5] Q. Y. Hou, " Influence of molybdenum on the microstructure and properties of a FeCrBSi alloy coating deposited by plasma transferred arc hardfacing ", *Surface & Coatings Technology*, 225 11-20 2013.
- [6] P. F. Mendez, N. Barnes, K. Bell, S. D. Borle, S. S. Gajapathi, S. D. Guest, H. Izadi, A. K. Gol, and G. Wood, " Welding processes for wear resistant overlays ", *Journal of Manufacturing Processes*, 16 1 4-25 2014.
- [7] W. Dai, Y. Miao, J. Li, Z. Zheng, D. Zeng, and Q. Huang, " Investigation on morphology and micro-hardness characteristic of composite coatings reinforced by PTA copper alloying on nodular cast iron ", *Journal of Alloys and Compounds*, 689 680-692 2016.
- [8] C. Sudha, P. Shankar, R. S. Rao, R. Thirumurugesan, M. Vijayalakshmi, and B. Raj, " Microchemical and microstructural studies in a PTA weld overlay of Ni-Cr-Si-B alloy on AISI 304L stainless steel ", *Surface & Coatings Technology*, 202 10 2103-2112 2008.
- [9] R. Veinthal, F. Sergejev, A. Zikin, R. Tarbe, and J. Hornung, " Abrasive impact wear and surface fatigue wear behaviour of Fe-Cr-C PTA overlays ", *Wear*, 301 1-2 102-108 2013.
- [10] L. Bourithis and G. D. Papadimitriou, " The effect of microstructure and wear conditions on the wear resistance of steel metal matrix composites fabricated with PTA alloying technique ", *Wear*, 266 11-12 1155-1164 2009.
- [11] S. Islak, O. Eski, S. Buytoz, M. Karagoz, and J. Stokes, " Microstructure and Microhardness Characterization of Cr3C2-SiC Coatings Produced by the Plasma Transferred Arc Method ", *Materials Testing*, 54 11-12 793-799 2012.
- [12] S. Buytoz and M. Ulutan, " In situ synthesis of SiC reinforced MMC surface on AISI 304 stainless steel by TIG surface alloying ", *Surface & Coatings Technology*, 200 12-13 3698-3704 2006.
- [13] S. Buytoz, " Microstructural properties of SiC based hardfacing on low alloy steel ", *Surface & Coatings Technology*, 200 12-13 3734-3742 2006.
- [14] C. T. Kwok, K. I. Leong, F. T. Cheng, and H. C. Man, " Microstructural and corrosion characteristics of laser surface-melted plastics mold steels ", *Materials Science and Engineering a-Structural Materials Properties Microstructure and Processing*, 357 1-2 94-103 2003.

Investigation of Tribological and Mechanical Performance of Cryogenic Treated Medium Carbon Steel, 38MnVS6

Esad Kaya*, Mustafa Ulutan[†], Koray Kılıçay[#], İsmail Bayar^ˆ

* Department of Mechanical Engineering, Eskisehir Osmangazi University, Turkey, esatkaya@ogu.edu.tr

[†] Department of Mechanical Engineering, Eskisehir Osmangazi University, Turkey, mulutan@ogu.edu.tr

[#] Department of Mechanical Engineering, Eskisehir Osmangazi University, Turkey, kkilicay@ogu.edu.tr

^ˆ Department of Mechanical Engineering, Eskisehir Osmangazi University, Turkey, ismailbayar@ogu.edu.tr

Abstract— In this study, cryogenic treatments (-160°C) were applied to medium carbon Vanadium content 38MnVS6 steel. The mechanical, and tribological behaviours of steel were investigated. The effects of cryogenic treatment soaking time on the specimens were evaluated in terms of mechanical and tribological performance including impact toughness, hardness, and wear resistance, and microstructural analyses. The results showed that the longer soaking times of cryogenic treatment improved the wear resistance and hardness. But besides the increase of these properties, cryogenic treatment also reduced the impact toughness compared to that of the conventional method, due to the increased in the distribution of martensitic transformation.

Keywords— Cryogenic treatment, Impact Toughness, Wear, Friction, Martensitic Transformation

I. INTRODUCTION

Wear is a major problem in mechanisms parts that are in contact with each other and in motion. High wear resistance and toughness in terms of fatigue are desirable traits in industrial equipment's. To obtain these desired properties, different heat treatments are used in industry. Examples can be made such as; processes include quenching in different cooling media, tempering at different temperatures, carburizing and various diffusion methods. These processes are now being used intensively. One of these methods is the cryogenic treatment, which started in the early of 1960s and continuously developing today [1]. Cryogenic treatment is a one-time complementary process for heat treatment process that affects the entire cross section of the material, rather is not an alternative to conventional heat treatments. In the cryogenic treatment cycle, the material is cooled to subzero temperatures and held. It is heating back to the room temperature after the soaking time. Thus, this process can be reduce the retained austenite content and residual stresses due to phase transformations [2]. In

addition, cryogenic treatments also ensures that alloying elements such as Cr, V and Ti in the material form secondary wear resistant carbides in microstructure. Previous studies have shown that cryogenic treatment provides outstanding improvements in service life of machine parts and cutting tools exposed to high wear and impact work [3-6]. The literature reports cryogenic treatment methods using different steels and soaking times, soaking temperature, application orders. The effect of cryogenic treatment soaking time on the tribological properties of the cold work tool steel examined in one of past studies [7]. Authors applied cryogenic treatment and tempering processes to the conventional heat treated materials at 6 different soaking time periods of 6, 24, 48, 72, 168 hours. The highest hardness value and the lowest wear resistance were obtained in samples subjected to deep cryogenic treatment for 48 hours.

Senthilkumar and Rajendran [8] investigated the effects of different soaking temperature of cryogenic treatments on the tribological properties of EN 19 steel which had been subjected to conventional heat treatment by austenitization at 875°C and quenching in oil media at 30°C. The samples that cryogenic treatment applied 118% increase in wear resistance compared to the conventional method.

Zhirafar et al. [9] applied cryogenic treatment and tempering processes to the specimen's subjected to conventional heat treatment made from 4340 steel. They investigated the effects of cryogenic treatment on hardness values, fracture toughness and fatigue strength properties of samples. Results show that, hardness and fatigue resistance of the cryogenically treated specimens were a slightly higher whereas the impact toughness of the cryogenically treated specimens was lower when compared to that of the conventionally heat treated.

Micro-alloy steels are used in the automotive industry to manufacture crankshafts, pistons, connecting rods, axles and steering parts [10-12]. Micro-alloy steels are the new area of interest due to the elements it contain and the mechanical properties that can be improved by the different heat treatments to be applied. Hence, phases that will be formed after cryogenic

treatment are important in determining the mechanical and tribological properties.

In this study, the effects of cryogenic treatment with different soaking times micro-alloy on steel specimens to hardness, wear resistance, coefficient of friction and impact toughness of the samples were investigated.

II. EXPERIMENTAL PROCEDURE

Chemical composition and experimental scheme was shown in Table 1. The samples were machined from the diameter of 40 mm- and 500 mm-length steel bar.

TABLE XLVII
CHEMICAL COMPOSITION AND EXPERIMENTAL SCHEME

Chemical Composition of 38MnVS6 (wt. %)						
Element	C	Mn	V	Cr	Ni	Mo
wt. %	0.39	1.4	0.16	0.08	0.06	0.01
Experimental Scheme						
CHT	Conventional Heat Treatment, 850°C for 40 min + oil quench					250°C for 1 hour tempering
CT 8H	CHT+ 8 hour deep cryogenic treatment at -160°C					
CT 12H	CHT+ 12hour deep cryogenic treatment at -160°C					
CT 24H	CHT+ 24 hour deep cryogenic treatment at -160°C					

45° V-shaped Charpy impact test specimens were obtained from bar materials in accordance with ASTM A370 standard using machining techniques. All samples were heated from 20°C to a temperature of 850°C at a heating rate of 0,70°C/sec and quenching at this temperature in the oil medium after 40 minutes of austenitizing time. Cryogenic heat treatments were carried out at -160°C and three different soaking times as 8, 12 and 24 hours. Cooling and heating process were carried out by waiting for the samples to cool down to the desired subzero temperature of 2°C/min from room temperature, followed by heating at the same rate. The samples used in the experimental studies were tempered for 1 hour at 250°C following cryogenic treatment. Notch impact tests were done in pursuance of ASTM A370 using impact tester MFL system PSW 300. The impact test results were presented in terms of fracture energy per unit cross- sectional area. The hardness tests were carried on the samples in accordance with ASTM E18 standard with Zwick Rockwell hardness tester by using C scale. The total load was 150 kgf for measurements. Specimens were ground using 220 grit abrasive papers to eliminate surface defects. Three measurements were done in each sample and results presented as average value. Microstructural and wear test samples were produced using the wet-cutting method. The microstructure samples were ground using Struers MD dac 220 and 600 grit magnetic grinding discs and were then polished with 3 µm diamond solutions. To obtain

clear microstructural images, the samples were etched with 2% nital solution. Prepared samples were examined by JEOL JSM-5600LV SEM microscopes. Concurrently, EDS analysis was performed.

Wear experiments were done with CSM-Tribometer instrument with the ball on disk type that is defined in the ASTM G99. Surface of specimens were polished to have a surface roughness of nearly 0.1 µm prior the wear tests. During the tests, the coefficients of friction and wear distance were simultaneously recorded. In all tests, WC balls a diameter of 3 mm were used as a counter body. The experiments were performed for, 5 N nominal load, 100 m wear distance, and at a linear speed of 5 cm/s (189 rpm). Contact pressure was calculated respect to hertz contact theory and as 2,534 GPa. Having completed the wear experiments, the roughness of worn surface were measured with a Mitutoyo Surf Test SJ-400 profile device. Cross-section values of the worn surfaces were determined by using these measured values. The wear rates were calculated using area values. After the experiments, the samples were compared in terms of calculated wear rates, the coefficients of friction, and the EDS analyses performed on the worn surfaces.

III. RESULTS AND DISCUSSION

A. Microstructure

Fig. 1 presents an EDS micrographs of the conventional and deep cryogenically heat treated specimen. The microstructure of conventional heat treated specimens consists of plate martensite, partly retained austenite phases. For cryogenic treated specimens, the microstructure exhibits an appearance with needle like tempered martensite and carbides. The amount of martensite formed in the microstructure depends on the amount of carbon in the microstructure and the kinetics of the austenite transformation. The transformation occurs by precipitation of excess carbon element contained in the austenite phase at low temperature or by ejection through the austenite lattice. Detailed examination of Fig. 1 reveals that as the cryogenic treatment soaking time increases, the amount of martensitic phase in the microstructure increases. It is also seen that the amount of needle like martensitic formation increases as the cryogenic treatment soaking time increased.

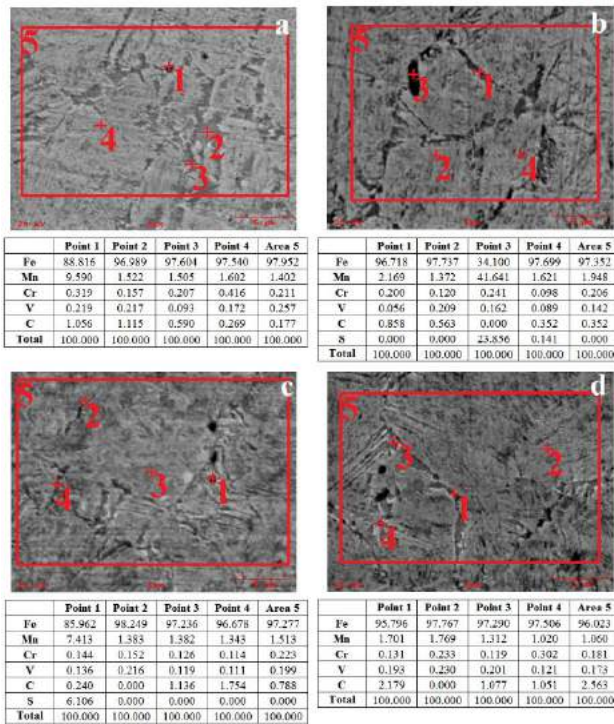


Fig.1. EDS images of samples; a) CHT, b) CT 8H, c) CT 12H, d) CT 24H

B. Impact Energy and Hardness

In Fig.2, the impact toughness of the cryogenic treated of 38MnVS6 micro-alloyed steel are given. As can be seen Fig.2, the impact toughness energy of conventional heat treated specimen is calculated as 0.174 joules/mm². The cryogenic treatment applied for 24 hours was found to have a 9% decrease in impact toughness compared to the conventional method. It was also seen that, 8 and 12 hours soaking time of cryogenic treatments did not make any dramatic effect on impact toughness.

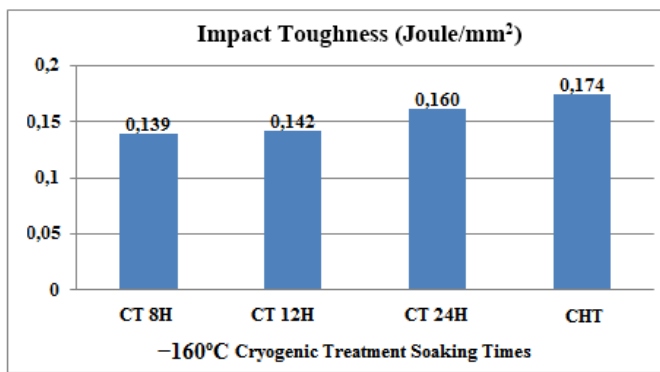


Fig.2. Impact toughness values of the samples

Fig. 2 presents that the application of cryogenic heat treatment, decreased the impact energy values about 20-40%

compared to the conventional heat treated specimen. The reason for this decrease is the complete transformation of austenite to martensite and precipitation of fine carbides by subsequently applied cryogenic treatment. As a result, the hardness of the material increases slightly while the ductility and toughness properties decrease for the cryogenic treated samples. Due to this circumstances the lowest impact toughness energy values were obtained on cryogenic treated specimens.

The SEM photos of fracture surface of heat treated samples are shown in Fig.3. The cryogenically treated samples were observed to have only regional gaps (dimples) relative to the samples subjected to conventional heat treatment. It was seen that these pits formed on the ruptured section surfaces are under influence and around of precipitated vanadium and iron carbide compounds. The formation and growth of this hollow (gap) structure in metal matrix are the reason of precipitated secondary particles due to cryogenic treatment. It was understood that the gaps first occur around the precipitated carbides formations and weaken the cross section under dynamic loads.

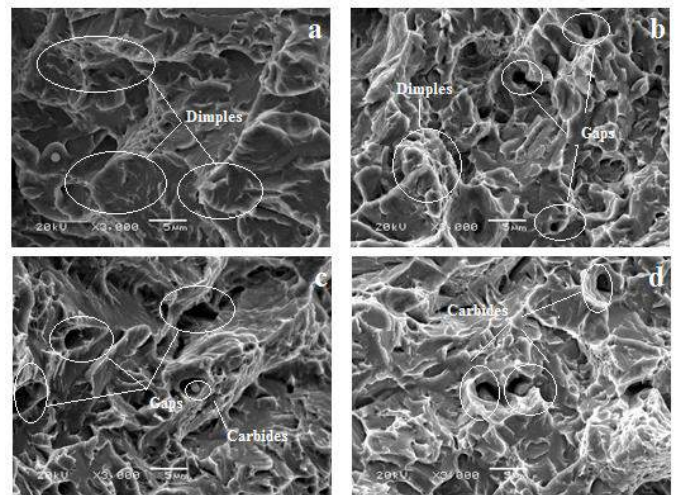


Fig.3. Fracture SEM photos of the samples; a) CHT, b) CT 8H, c) CT 12H, d) CT 24H

The macro hardness values measured of the heat treated micro-alloyed steels are given in Fig.3. Cryogenic heat treatments increased the hardness values slightly. The lowest hardness values were observed in conventional heat treated ones. The retained austenite cannot be distinguished from the SEM images because of the low carbon element and alloy content of the steel. But, cryogenic treatment increased the hardness of the resulting by transformation of retained austenite to martensite and precipitation of fine carbides. This case leads to partially increase the overall stiffness of steel matrix.

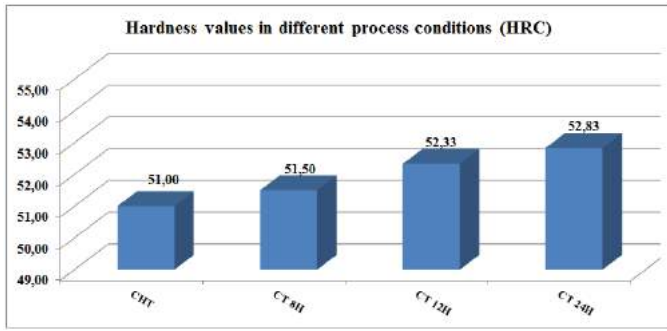


Fig.4. Hardness values in different process conditions

C. Wear and Friction

Fig. 5 shows the specific wear rates and mean friction coefficient values for the heat treated 38MnVS6 steel. As can be seen from the graph, the lowest wear rate was obtained as $5,34 \times 10^{-7} \text{ mm}^3/\text{Nm}$, which sample was cryogenically treated for soaking time of 24 hours.

Similarly, specific wear rate was obtained as $5,80 \times 10^{-7} \text{ mm}^3/\text{Nm}$ for the 12 hour cryogenic treated sample. Wear resistance was improved 10% compared to that of conventional one. The highest specific wear rate was obtained at $8,07 \times 10^{-7} \text{ mm}^3/\text{Nm}$ for 8 hours cryogenic treated specimen. When comparative studies of other samples were made, it was found that the wear rate was decreased drastically in the 12 and 24 hour cryogenic samples. The specific wear rate of the 8 hour cryogenic treated sample was obtained as $8,07 \times 10^{-7} \text{ mm}^3/\text{Nm}$. When the friction coefficient-wear distance diagram of this specimen is examined (Fig. 6), it is seen that the friction of this sample is stable up to 40 meters. At the remaining 60 meters of wear test, it is thought that hard oxide particles that ruptured from the both surface and are included in the tribological system. This case caused the exacerbation of wear.

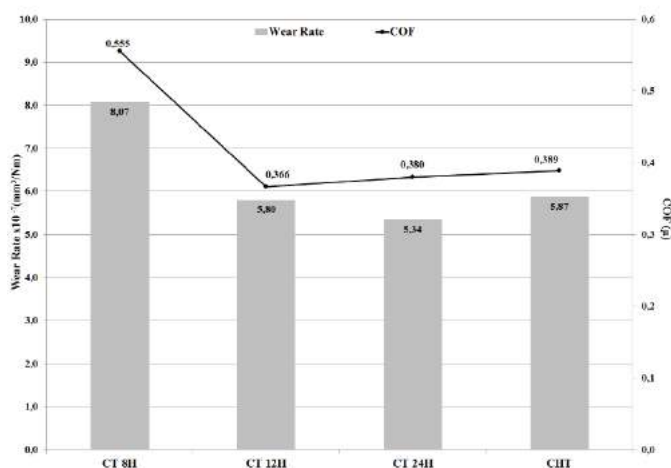


Fig.5. Specific wear rate and COF values of the samples

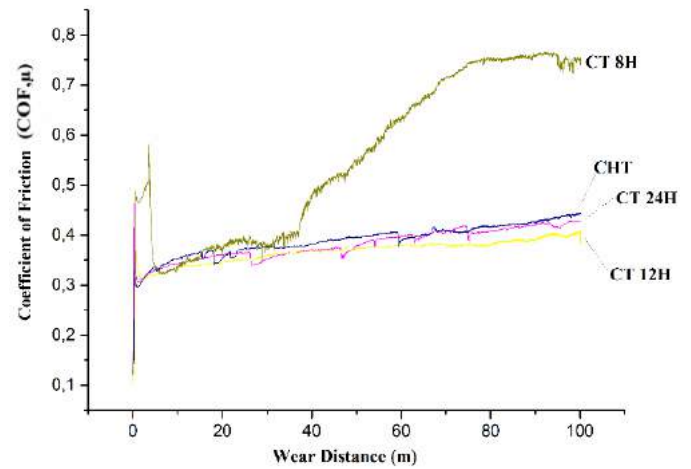


Fig.6. COF vs wear distance of the samples

The lowest coefficient of friction was obtained at 0.366 for CT 12H. When the EDS analysis of this worn surface (Fig.7) is examined, it was seen that a large oxide layer formed on the surface (Fig.7-c-Point 1). This oxide layer, occur at the beginning of the experiment, it reduces the contact surface area between counter body (WC Ball) and steel specimen surface which this event makes the mean friction coefficient lower as 0.366. This layer also provide behavior of friction steady state during the wear test (Fig.6). Besides, the though W and Fe content oxide layer are formed in this type of wear test reduce the effect of abrasive wear. It is known in the literature that, such oxides are the lubricating effect in wear.

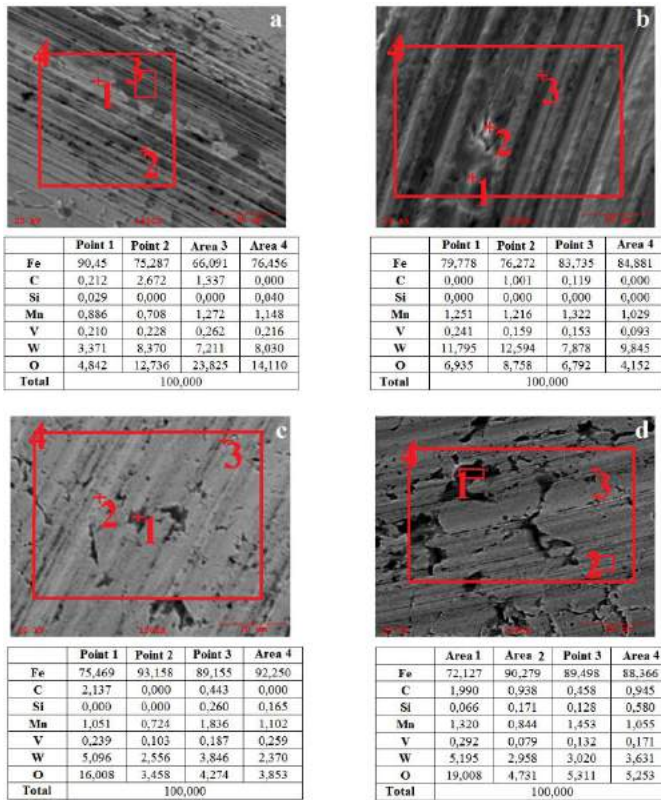


Fig.7. EDS analyses of the samples; a)CHT, b)CT 8H, c)CT 12H, d)CT 24H

IV. CONCLUSIONS

In the present study, medium carbon micro-alloy steel 38MnVS6 was cryogenically heat treated at different soaking time. The effect of the different soaking time were investigated in terms of mechanical, microstructural and tribological properties According to the experimental results, main conclusions was drawn as follows.

- It has been observed that the mean hardness values of micro-alloy steels increase with increasing cryogenic treatment soaking time. It is understood that the transformation of the retained austenite phase to the martensitic phase and the formation of finer carbides are the trigger effect of increase.
- Macro hardness of conventional and cryogenic treated samples has changed. While the average hardness was 51 HRC in the conventional heat treated, higher hardness values were obtained in the cryogenic treated. Highest mean hardness values were observed for 24 hours (52,83 HRC)
- According to Charpy impact toughness test results, the lowest fracture toughness values were obtained in samples that cryogenic treated. This incident is

correlated to increasing hardness values with increasing cryogenic treatment soaking time.

- As a result of the wear tests, specimens subjected to cryogenic treatment for 12 and 24 hours were found that reduced specific wear rates compared to conventional heat treated specimens. Best wear resistance within the cryogenic treated control group; was observed in the 24-hour cryogenic treated specimen, which also had the highest toughness value. This indicates that the wear resistance are not only related to hardness, but also toughness values at the same time.

VII. ACKNOWLEDGMENT

This study was supported by the Scientific Research Council of Eskisehir Osmangazi University, Project No: 201515D20

VIII. REFERENCES

- [1] F. K. Arslan and A. Şelte, *Takım Çeliklerinde Sıfırlıt İşlem Mekanizması*, Metalurji, (167) (2013) s.37-40.
- [2] D. Senthilkumar, I. Rajendran, M. Pellizzari, and J. Siirainen, *Influence of shallow and deep cryogenic treatment on the residual state of stress of 4140 steel*, Journal of Materials Processing Technology, 211 (3) (2011) 396-401.
- [3] M. R. D. Merac, *The effect of cryogenic treatment on the microstructure and mechanical properties of AISI D2 tool steel*. 2005, University of Calgary. p. 243p.
- [4] D. Mohan Lal, S. Renganarayanan, and A. Kalanidhi, *Cryogenic treatment to augment wear resistance of tool and die steels*, Cryogenics, 41 (3) (2001) 149-155.
- [5] M. Pérez and F. J. Belzunce, *The effect of deep cryogenic treatments on the mechanical properties of an AISI H13 steel*, Materials Science and Engineering: A, 624 (2015) 32-40.
- [6] F. Meng, K. Tagashira, and H. Sohma, *Wear resistance and microstructure of cryogenic treated Fe-1.4Cr-1C bearing steel*, Scripta Metallurgica et Materialia, 31 (7) (1994) 865-868.
- [7] K. Amini, S. Nategh, and A. Shafyeci, *Influence of different cryotreatments on tribological behavior of 80CrMo12 5 cold work tool steel*, Materials & Design, 31 (10) (2010) 4666-4675.
- [8] D. Senthilkumar and I. Rajendran, *Influence of Shallow and Deep Cryogenic Treatment on Tribological Behavior of En 19 Steel*, Journal of Iron and Steel Research, International, 18 (9) (2011) 53-59.
- [9] S. Zhirafar, A. Rezaeian, and M. Pugh, *Effect of cryogenic treatment on the mechanical properties of 4340 steel*, Journal of Materials Processing Technology, 186 (1-3) (2007) 298-303.
- [10] D. J. Naylor, *Microalloyed Forging Steels*, Materials Science Forum, 284-286 (1998) 83-94.
- [11] C. Chattopadhyay, S. Sangal, K. Mondal, and A. Garg, *Improved wear resistance of medium carbon microalloyed bainitic steels*, Wear, 289 (2012) 168-179.
- [12] G. Krauss, *Steels Processing, Structure, and Performance*. 2005: ASM International.

An Investigation on Machinability of Hardened AISI H10A Steel with CBN insert

Rıfat Akdere¹, Halil Demir², Gültekin Uzun³, Mustafa Günay⁴

¹Graduate School of Natural And Applied Sciences, Karabük University, Turkey, rifatakdere@hotmail.com

²Faculty of Technology, Karabük University, Turkey, hdemir@karabuk.edu.tr

³Faculty of Technology, Gazi University, Turkey, uzun.gultekin@gazi.edu.tr

⁴Faculty of Engineering, Karabük University, Turkey, mgunay@karabuk.edu.tr

Abstract— In this study, machinability experiments on hardened AISI H10A hot work tool steel with CBN inserts were performed in dry and minimum quantity lubrication (MQL) conditions. Hard turning experiments were conducted according to Taguchi L₉ orthogonal array. The effects of cutting parameters (cutting speed, feed rate and depth of cut) and cutting conditions on surface roughness were analysed. The analysis of variance (ANOVA) in 95% confidence level was applied in order to effects of cutting parameters surface roughness. It was observed that average surface roughness (Ra) increased with increasing feed rate and depth of cut in dry cutting condition with CBN inserts. In dry and MQL cutting conditions, the most important parameter on surface roughness were determined as depth of cut with 51.79% PCR and 69.68% PCR, respectively.

Keywords— AISI H10A, MQL, Surface roughness, CBN, ANOVA

I. INTRODUCTION

Hardened steels are preferred due to their high wear resistance and strength in many industrial applications. Hot work tool steels having high temperature strength, high toughness and thermal fatigue resistance, thermal shock gain a place in hardened steel categories. The chromium hot work steels are widely used for extrusion of aluminium, die casting of light metals and steel forging applications [1]. On the other hand, these steels due to chemical composition, microstructure, inclusions and thermo-mechanical properties are difficult to machine. When a die casting die is hardened and tempered some distortion normally occurs. By leaving some machining allowance on the die prior to hardening it is possible to adjust the die to the correct dimensions after the hardening and tempering by, for example, grinding or hard machining.

The main concerns of hard turning are the tool materials cost and the effect of the cutting conditions on machinability criteria. The machining of hardened steels using CBN, PCBN and ceramic tools is commonly known as a best replacement instead of grinding cost in order to reduce the tooling time and keep off the lubrication [2]. However, it is very hard to develop a comprehensive model with related to any machinability criteria involving all cutting conditions due to contain many factors. As, the machinability criteria such as cutting force, surface roughness, tool life, dimension stability can be

significantly affected by cutting parameters, mechanical properties of workpiece material, rigidity of machine tools, cutting tool, tool wear and coolant technique [3-5]. The control of the machinability criteria can be primarily provided by choosing suitable values of cutting speed, feed rate and depth of cut in hard turning. However, improper cutting parameters have negative effects on the machining time and cost. In this regard, design of experiment and analysis for machining process then optimization of it is great importance with regards to decrease in machining cost [6]. In the meanwhile, some scientists observed that there is a disagreement between the researchers in terms of the use of coolants in hard turning. Therefore, some more experimental investigations are required to identify eco-friendly alternatives to conventional cutting fluids during hard turning [7]. Recently scientists used nanoparticles in conventional lubricants because of its remarkable improvement in thermo-physical, and heat transfer capabilities, reduce the coefficient of friction and wear effect to enhance the efficiency and reliability of machine tools [8].

In recent years, there are performed various statistical and experimental studies which are based on design and analysis of experiment methods to determine the effects of cutting conditions on machinability criteria [9]. Aouici et al. conducted response surface methodology in hard turning of DIN 1.2343 steel with CBN tool in order to obtain mathematical models for the cutting force components and surface roughness. The authors stated that the depth of cut and workpiece hardness are the most important factor on cutting force components while the feed rate and workpiece hardness have the most significance on surface roughness [10]. Boy et al. focused on optimizing the cutting conditions to minimize the surface roughness, inner-diameter error and roundness in bearing rings produced by hard turning of bearing steel with coated CBN tool. The analysis of variance results showed that the feed rate is the major factor for the surface roughness while the cutting speed is the major factor for the roundness and inner-diameter error [11]. Bouacha et al. investigated the relationships between cutting parameters and tool wear, surface roughness, cutting force and chip volume by using variance analysis in turning of AISI 52100 steel with CBN cutting tool. It was determined that the depth of cut affects the cutting force but does not affect the

surface roughness [12]. Islam examined the surface roughness and dimensional accuracy properties (diameter error and circularity) by dry, wet and MQL turning processes applied to different materials. The author indicated that surface roughness and dimensional values are affected by different cooling methods and the best result is obtained with MQL application in general. [13]. Sarıkaya and Güllü focused on the use of the Taguchi based grey relation analysis to optimize the MQL process parameters such as cutting fluid, flow rate and cutting speed in terms of tool wear forms and surface roughness during the turning of cobalt base super alloy Haynes 25. According to the results of ANOVA, the contribution percentage of process parameters were found as the cutting fluid, fluid flow rate and cutting speed, respectively [14]. Paul et al. analysed parameters of minimum fluid application for minimization of surface roughness, flank wear, cutting force, tool vibration and cutting temperature of AISI4340 steel which was hardened to 46HRC. The researchers were compared the performance of conventional dry, wet and MQL turning applications. Hard turning with minimal fluid application reduces tool vibration and provides better cutting performance as compared with dry turning and wet turning where a commercial cutting fluid was applied at a rate of 5 l/min [15]. Mia et al. studied surface roughness obtained in turning of hardened steel of 600 BHN with uncoated carbide tool under the application of MQL. The authors focused on the use of variable time-controlled pulse in delivering coolant at flow rates of 500–1100 ml/h. It has been determined that the cutting speed is insignificant factor surface roughness while feed rate is important factor for roughness. Consequently, the minimum surface roughness has been discovered at the 1 s time-gapped MQL pulsing, although herein the highest amount of fluid is consumed [16].

II. MATERIAL AND METHOD

AAA. Material and Equipment

AISI H10A hot work tool steel was used as workpiece in experimental studies. The chemical composition of workpiece was given in Table 4.1. AISI H10A is a hot work tool steel having high toughness, high thermal shock resistant and high wear resistance in high temperatures. The hardness of AISI H10 workpiece was increased to 54-55 HRC with vacuumed hardening method. The surface roughness was based on as the machinability criteria of AISI H10 steel. Mahr Perthometer M1 type roughness device was used to measure surface roughness in hard turning experiments. The average surface roughness (Ra) was taken into consideration in roughness assessments. CNGA120404 coded uncoated CBN (KB1610) cutting tools provided by Kenna Metal Company were used as cutting tools in machining experiments. PCLNR 2525M12 coded Kenna Metal tool holder was used to fix the tool rigidly.

Hard turning experiments were performed in two different cutting conditions namely, dry and minimum quantity lubricant (MQL). UFB20-Basic cooling system branded SKF was preferred as MQL applicator. The LubriOil was used as lubricant type because of AISI H10A steel. It was decided after preliminary tests used MQL that the flow rate should be 16.25 ml/min.

BBB. Experimental Design

The cutting parameters directly effecting machinability criteria were determined in experimental design according to Taguchi method. For this purpose, three factors were chosen as depth of cut (a), feed rate (f) and cutting speed (V). The levels of these parameters were confirmed according to cutting tool firm and hard turning experiments in literature. Taguchi L₉ orthogonal array was used for experimental design in terms of these factor and levels (Table I). Moreover, experiments conducted with uncoated CBN tools were performed in two cutting conditions named as dry and MQL.

TABLE I
FACTORS AND THEIR LEVELS ACCORDING TO TAGUCHI L₉

Exp. no	a (mm)	f (mm/rev)	V (m/min)
1	0.1	0.05	100
2	0.1	0.1	150
3	0.1	0.15	200
4	0.2	0.05	150
5	0.2	0.1	200
6	0.2	0.15	100
7	0.3	0.05	200
8	0.3	0.1	100
9	0.3	0.15	150

III. RESULTS AND DISCUSSION

The surface roughness values after each hard turning process have been determined by taking arithmetic average of three measurements taken from three positions of 120°. The variations of Ra values obtained with uncoated CBN tools in dry and MQL conditions were given in separate graphs. Variations of Ra depending on feed rate (f), cutting speed (V) and depth of cut (a) were given in Fig. 1 and 2.

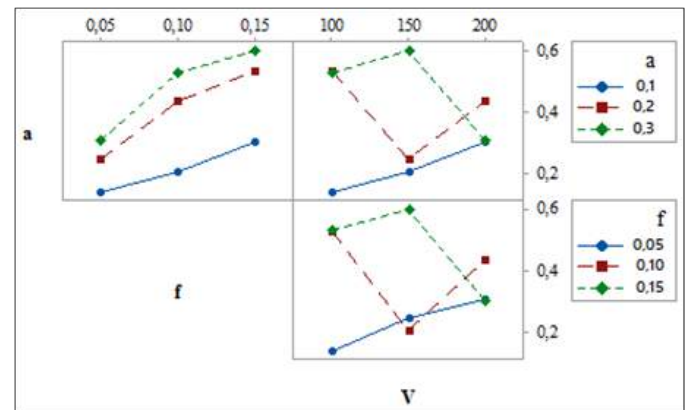


Fig. 1. Variations of Ra in dry cutting conditions.

When examining Fig. 1, it was observed that average surface roughness (Ra) generally increase with increasing feed rate and depth of cut. It was attracted from Fig. 1 that surface roughness values have irregularities in terms of cutting speed-depth of cut and cutting speed-feed rate interactions. In machining processes, it is known from literature [2-6] that Ra values

decrease with increasing cutting speed. However, it can be seen from Table I that distribution of Ra with cutting speed is complicated. Therefore, variation of Ra with increasing cutting speed was not match with literature. The lowest surface roughness value was obtained as 0.141 μm with feed rate of 0.05 mm/rev, cutting depth of 0.1 mm and cutting speed of 100 m/min in dry cutting conditions with uncoated CBN inserts. The highest surface roughness value was obtained as 0.578 μm with feed rate of 0.1 mm/rev, cutting depth of 0.2 mm and cutting speed of 200 m/min.

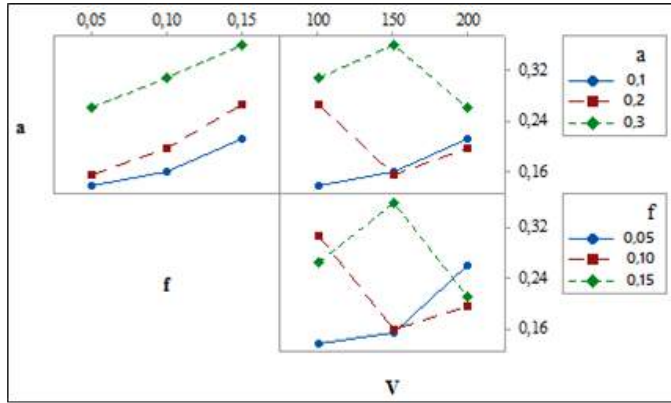


Fig. 2. Variations of Ra in MQL cutting conditions.

It was observed from Fig. 2 that MQL conditions have similar tendencies to dry cutting conditions. Average surface roughness (Ra) values increase with increasing feed rate and depth of cut. In a similar way, it was determined that Ra values does not decrease with increasing cutting speed because of hybrid experimental design. The lowest surface roughness value was obtained as 0.139 μm with the lowest feed rate, depth of cut and cutting speed in MQL cutting conditions with uncoated CBN inserts. The highest surface roughness value was obtained as 0.36 μm with feed rate of 0.05 mm/rev, cutting depth of 0.3 mm and cutting speed of 200 m/min.

This results show that better surface quality can be obtained with MQL conditions in hard turning experiments. On the other hand, achieving of the lowest Ra values in dry and MQL conditions on different levels of parameters indicate that the effects of parameters on Ra will show distinctness. For this purpose, analysis of variance (ANOVA) were performed with 95% confidence level in order to determine the effects of cutting parameters on surface roughness. ANOVA results of Ra were given in Table II and III for dry and MQL conditions, respectively. Here, the probability (P) values indicating the importance level of each factor, degree of freedom (DF), the sum of squares (SS), mean square (MS), F ratios and the percent contribution ratio (PCR) was shown. P value should be lower than 0.05 in 95% confidence level in order to determine that any factor acting on surface roughness is effective on it.

TABLE II
ANOVA RESULTS FOR DRY CUTTING CONDITIONS.

Factors	DF	SS	MS	F ratio	P value	PCR (%)
a	2	0.111498	0.055749	37.36	0.026	51.79
f	2	0.095218	0.047609	31.91	0.030	44.22

V	2	0.005591	0.002795	1.87	0.348	2.60
Error	2	0.002984	0.001492			1.39
Total	8	0.21529				100

TABLE III
ANOVA RESULTS FOR MQL CUTTING CONDITIONS.

Factor s	DF	SS	MS	F ratio	P value	PCR (%)
a	2	0.031993	0.015996	465.91	0.002	69.68
f	2	0.013454	0.006727	195.93	0.005	29.31
V	2	0.000393	0.000196	5.72	0.149	0.86
Error	2	0.000069	0.000034			0.15
Total	8	0.045908				100

It was shown from Table II that the most important factor on surface roughness in dry conditions with uncoated CBN inserts is depth of cut with 51.79% PCR. Feed rate followed this factor's effect with 44.22% PCR. Due to the fact that parameters whose P values smaller than 0.05 are important factor for ANOVA results, cutting speed is not an important factor for this experimental conditions.

It was displayed from Table III that the most important factor on surface roughness in MQL conditions with uncoated CBN inserts is depth of cut with 69.68% PCR. Feed rate followed this factor's effect with 29.31% PCR. Cutting speed is not also an important factor for MQL cutting conditions like dry condition. This result showed that effect of cutting speed is very low or statistically insignificant [10,11] and proved that experimental design is suitable.

IV. CONCLUSIONS

In this study, machinability experiments on hardened AISI H10A hot work tool steel with CBN inserts were performed in dry and minimum quantity lubrication (MQL) conditions. The effects of cutting parameters (feed rate, depth of cut and cutting speed) on the Ra were analyzed according to Taguchi experimental design. Obtained results were summarized below.

It was determined that average surface roughness (Ra) increase with increasing depth of cut and feed rate in dry cutting conditions with uncoated CBN inserts. MQL cutting conditions had similar tendencies and this situation was referred to increasing chip cross-section with increasing feed rate and depth of cut. The lowest surface roughness value was obtained in MQL conditions as 0.139 μm with the lowest feed rate, depth of cut and cutting speed with uncoated CBN inserts. The most important factor on surface roughness in dry and MQL conditions with uncoated CBN inserts was determined as depth of cut. According to ANOVA results, cutting speed was not an important factor for both dry and MQL cutting conditions. However, selection of cutting speed values was thought as an important criterion in order to decrease machining costs. As a result of this evaluations, MQL application is strongly suggested in order to increase efficiency in hard turning processes.

V. ACKNOWLEDGEMENT

This study is supported by Scientific Research Project Unit of Karabük University (KBÜ-BAP-14/1-YL-019) and the authors express their appreciation for this support.

VI. REFERENCES

- [1] R. Shivpuri, Dies and die materials for hot forging, ASM Handbook, Metalworking: Bulk Forming, USA, 2005.
- [2] I. Meddour, M.A. Yallese, R. Khattabi, M. Elbah, L. Boulanouar, Investigation and modeling of cutting forces and surface roughness when hard turning of AISI 52100 steel with mixed ceramic tool: cutting conditions optimization, *Int J Adv Manuf Technol*, 77, 1387–1399, 2015.
- [3] T. Özel, T.K. Hsu, E. Zeren, Effects of cutting edge geometry, workpiece hardness, feed rate and cutting speed on surface roughness and forces in finish turning of hardened AISI H13 steel, *Int J Adv Manuf Technol*, 25, 262–269, 2005.
- [4] J.E. Stahl, Metal Cutting - Theories and models, Lund University in cooperation with Seco Tools AB, Lund/Fagersta, Sweden, 2012.
- [5] H.B. Ulaş, F. Mihmat, H. Demir, DIN 1.2344 sıcak iş takım çeliğinin testere freze çakılarıyla işlenebilirliğinin araştırılması, *Erciyes Üniversitesi Fen Bilimleri Enstitüsü Dergisi*, 26(2), 170-178, 2010.
- [6] E. Yücel, M. Günay, Modelling and optimization of the cutting conditions in hard turning of high-alloy white cast iron (Ni-Hard), *Proc IMechE Part C: J Mech Eng Sci*, 227(10), 2280-2290, 2013.
- [7] S. Chinchankar, S.K. Choudhury, Machining of hardened steel- Experimental investigations, performance modeling and cooling techniques: A review, *Int J Mach Tools Manuf.*, 89, 95–109, 2015.
- [8] N.A.C. Sidik, S. Samion, J. Ghaderian, M.N.A.W.M. Yazid, Recent progress on the application of nanofluids in minimum quantity lubrication machining: A review, *Int J Heat Mass Transf*, 108, 79–89, 2017.
- [9] H. Yurtkuran, M.E. Korkmaz, M. Günay, Modelling and Optimization of the Surface Roughness in High Speed Hard Turning with Coated and Uncoated CBN Insert, *Gazi Uni J Sci*, 29(4), 987-995, 2016.
- [10] H. Aouici, M.A. Yallese, K. Chaoui, T. Mabrouki, J.F. Rigal, Analysis of surface roughness and cutting force components in hard turning with CBN tool: prediction model and cutting conditions optimization, *Measurement*, 45, 344–353, 2012.
- [11] M. Boy, I. Ciftci, M. Gunay, F. Ozhan, Application of the taguchi method to optimize the cutting conditions in hard turning of a ring bore, *Materials and Technology*, 49 (5), 765–772, 2015.
- [12] K. Bouacha, M.A. Yallese, S. Khamel, S. Belhadi, Analysis and Optimization of Hard Turning Operation Using Cubic Boron Nitride Tool, *Int J Refract Met Hard Mater*, 45, 160-178, 2014.
- [13] M.N. Islam, Effect of additional factors on dimensional accuracy and surface finish of turned parts, *Machining Science and Technology*, 17, 145–162, 2013.
- [14] M. Sarıkaya, A. Güllü, Multi-response optimization of minimum quantity lubrication parameters using Taguchi-based grey relational analysis in turning of difficult-to-cut alloy Haynes 25, *Journal of Cleaner Production*, 91, 347-357, 2015.
- [15] P. Sam Paul, A.S. Varadarajan, R. Robinson Gnanadurai, Study on the influence of fluid application parameters on tool vibration and cutting performance during turning of hardened steel, *Engineering Science and Technology, an International Journal*, 19, 241-253, 2016.
- [16] M. Mia, M.H. Razi, I. Ahmad, R. Mostafa, S.M.S. Rahman, D.H. Ahmed, P.R. Dey, N.R. Dhar, Effect of time-controlled MQL pulsing on surface roughness in hard turning by statistical analysis and artificial neural network, *Int J Adv Manuf Technol*, 1-13, 2017.

Design and Simulation of an Apparatus for the Post-Weld Controlled Accelerated Cooling of R350HT Head Hardened Rail Joints

Nizar Ramadan¹, Kazım Tur², Erkan Konca³

Department of Metallurgical and Materials Engineering, Atılım University, Ankara, Turkey

¹nezar_e@yahoo.com

²kazim.tur@atilim.edu.tr

³erkan.konca@atilim.edu.tr

Abstract— Controlled accelerated cooling of R350HT head hardened rail joints immediately after their welding is critical in order to secure that these joints have similar mechanical properties with the rest of the rail. In practice this accelerated cooling can be achieved by sending forced air through an apparatus placed over the welded area of the rail joint just after welding operation. The apparatus should be designed in a way to create homogenous and effective cooling around the railhead. For this purpose, airflow and cooling simulations were performed in order to optimize the design of such apparatus. Number and diameter of air nozzles, their positions, nozzle-to-rail surface distance and airflow rate were employed as the main input parameters for the simulations performed using ANSYS 15 (thermal and fluid flow). The main focus was on finding the design and operation parameters that give homogenous air flow around the rail head which in turn would produce uniform cooling. In this publication, the results of the simulations run under various conditions will be compared and an optimum set of design and operating parameters will be offered.

Keywords— Simulation, Head Hardened Rail, Controlled Cooling, Welding, Airflow.

I. INTRODUCTION

Nowadays, the current economic growth trend in all world predicts an increase in the role of railway transportation in the coming years. Such a growth would also raise the loads and stress on the railways that would have drastic effects on the humanity, economics and environment. Therefore, the railway companies are looking for new technologies to decrease rail related problems and hence improve rail service life [1]. Use of head hardened rails in curves, where there is significant wear, is suggested for increased service life of rails. However, the expected benefit from the use of head hardened rails will be possible only if their welded joints have similar mechanical properties as the rest of the rails. For flash butt welding, accelerated cooling of the welded region just after joining is suggested for this purpose [2].

Using surface response during compressed air, the cooling process conditions are obtained through calculation, and then the properties of materials after compressed air are analysed. Computational fluid dynamics method of compressed air process on R350HT rails was simulated on the constructed three-dimensional model by using ANSYS Fluent 15 [1, 3]. The most commonly name of Computational Fluid Dynamics is CFD [4].

II. OBJECTIVES

This study focuses on the computational fluid dynamics (CFD) analysis of a cooling unit that will be used for the accelerated cooling of flash butt welded R350HT rail joints immediately after their welding so that the design and operation parameters that give homogenous airflow around the rail head which in turn would produce uniform cooling would have been obtained. In present work, the results of the simulation runs under various conditions are compared and an optimum set of design and operating parameters are outlined. The process parameters include the air velocity, distance between rail and cooling unit, number of holes and their positions, and dimension of holes.

III. METHODOLOGY

CCC. Modeling and Material

Material properties of rails requiring verification are set out in European standard EN 13674-1 [5]. EN 13674-1 exclusively covers pearlitic steels for rails, those being R220, R260, R320Cr and R350HT, whose carbon content lies between 0.6 and 0.8 %. The main chemical composition of R350HT rails are shown in Table I.

TABLE XLVIII
CHEMICAL COMPOSITION OF R350HT RAILS [5]

C	Cr	Si	Mn	P	S
0.70-0.82	0.30 max	0.13-0.6	0.65-1.25	0.025max	0.008-0.03

compute heat transfer between air at room temperature and rail at 850°C.

1) *Solution*: After boundary conditions, next step was the solution methods, which runs as coupled. Once, all the boundary conditions and the solution methods are apparent for simulation, then the model was run and some surface monitors such as total pressure, velocity and total temperature, etc., were requested.

2) *Materials*: The working cooling fluid in this simulation is air and is considered to act as compressed air with density (1.225 kg/m³), thermal conductivity (0.0242 W/m-s), specific heat CP (1006.43 J/kg-K), and gravity (-9.81 m/s²) in Y-axes, and air temperature was room temperature. And for the material

it was R350HT rail with a chemical composition as shown in Table I.

3) *Boundary Conditions*: The important boundary conditions in Fluent Flow Analysis are inlet air velocity through the holes of the cooling unit, pressure outlet and internal walls of cooling unit. Based on previous experimental work by the authors for the cooling unit specifications and process conditions, such as air velocity, distance between holes, distance between rail and inner walls of the cooling unit, number and diameter of air holes in the cooling unit. Table II shows a selection of the simulation process parameters used in the simulations.

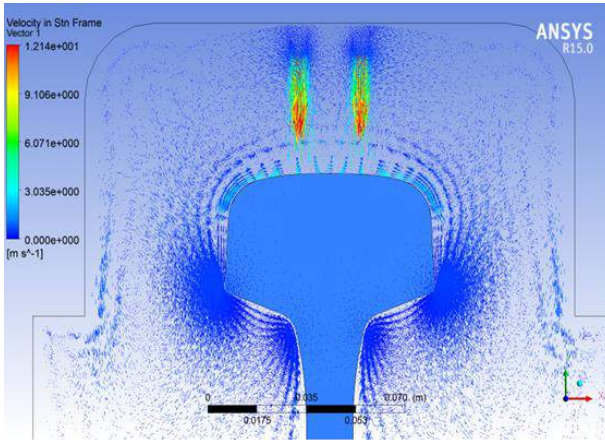
TABLE XLIX
SELECTED PROCESS PARAMETERS EMPLOYED IN AIR FLOW AND COOLING SIMULATIONS

Air velocity (m/s)	0.5	1	5	8	12	5
Distance between rails and cooling unit (cm)	3	4	5	8	10	5
No. of holes and position	1 top	1 top & 3 side	2 top & 3 side	8	10	8
Hole diameter (cm)	0.2	0.5	0.7	1	1.5	0.5
Distance between holes (cm)	0.5	1	1.5	2	3	2

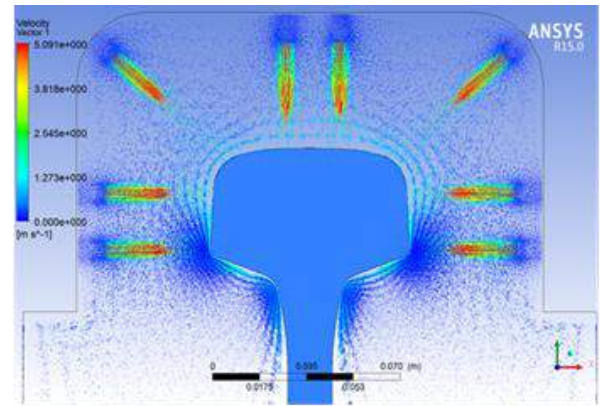
IV. RESULTS AND DISCUSSIONS

FFF. Parameters comparing graphs

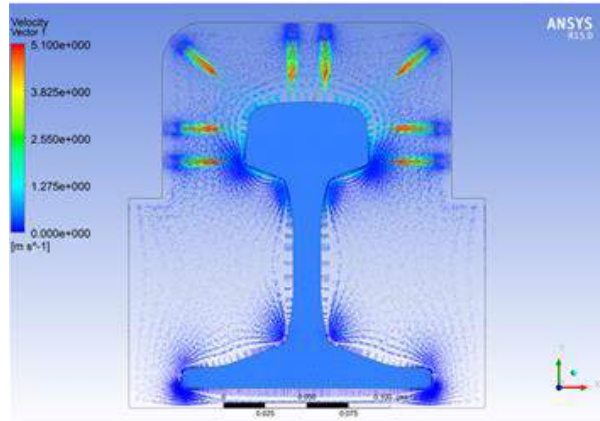
1) Air velocity: As seen in Fig. 4.a-d, it is noted that at some places pressure and velocity is highly different with different number of holes due to the shape of rail section. Simulation runs were carried out by using 1 to 8 holes on a single row to reduce the computing time. It is clear that air distribution is more homogeneous on the rail surface when air is sent through 8 holes and this gives more homogeneous cooling.



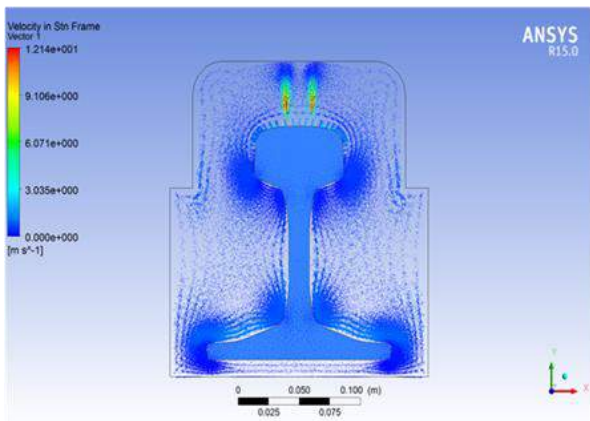
a)



c)



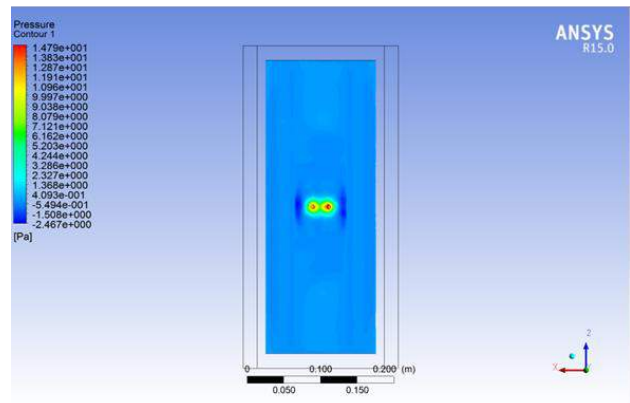
d)



b)

Fig. 4 Air velocity distribution on rail a) 2 holes on top of rail head, b) 2 holes on top, air velocity distribution over entire rail section c) 8 holes on top of rail head and d) 8 holes on top, air velocity distribution over entire rail section

2) Air Pressure: Fig. 5 shows the differences in air pressure on rail head and in entire rail profile. It is clear that with 8 holes the air pressure is more homogeneous on rail surface. Therefore, cooling is more homogeneous as well.



a)

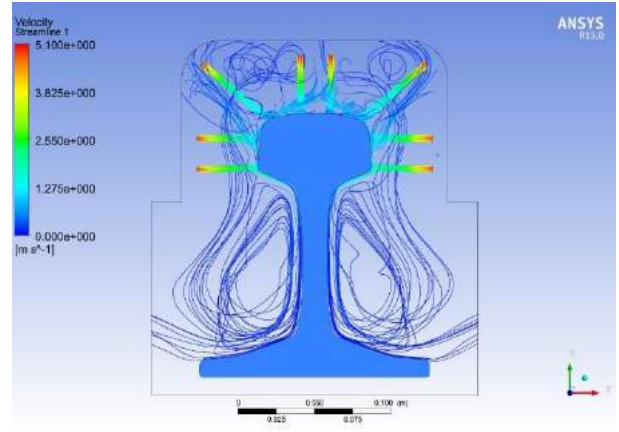
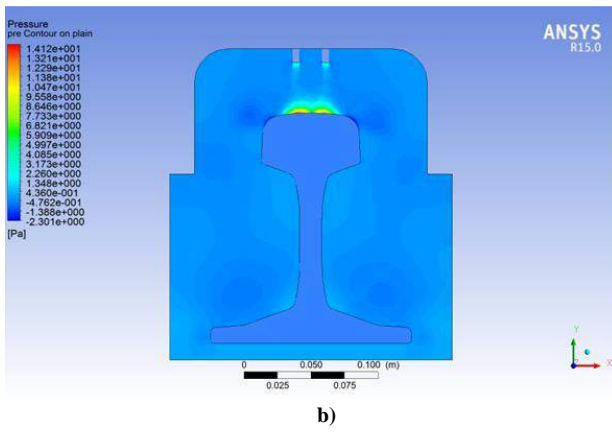


Fig. 6 Air velocity (streamline).

2) Air velocity vector:

Fig. 7 shows the air velocity in the area between rails and cooling unit, where best distribution of compressed air in rail surface is with 8 holes.

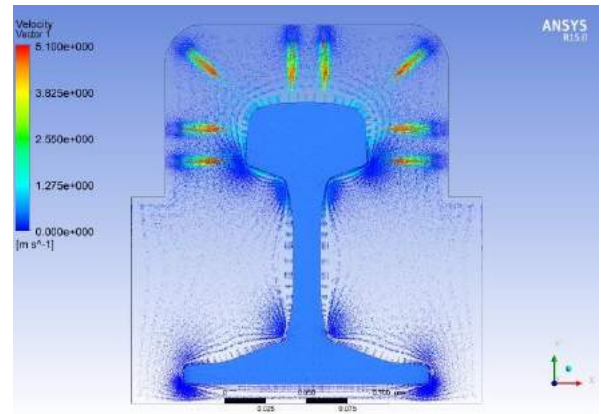
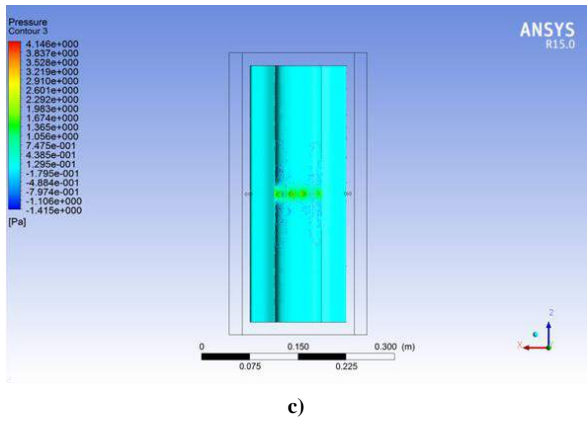


Fig. 7 Air velocity vector in cooling unit.

3) Contours

Fig. 8 shows the air velocity in the area between rails and cooling unit, where it is noted that best distribution of compressed air on the rail surface is with 8 holes.

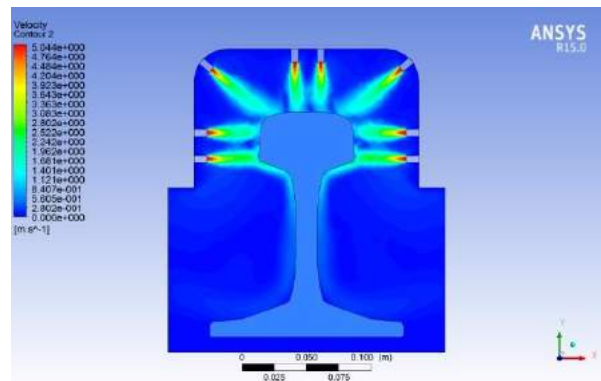
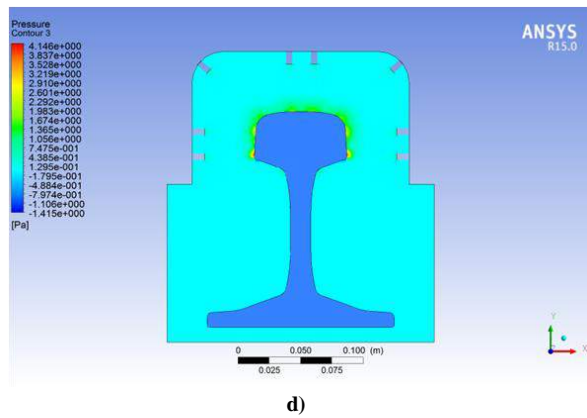


Fig. 8 Air velocity contour in cooling unit

Fig. 5 Air pressure distribution a) on rail head with 2 holes over rail head, b) over entire rail section with 2 holes, c) on rail head with 8 holes over rail head, and d) over entire rail section with 8 holes.

GGG. Best Results

1) Streamline: Fig. 6 shows that with cooling unit having 8 holes in a row has given best result where air is flowing over the all areas of the rail section.

Fig. 9 shows pressure on the head surface due to the compressed air, where best distribution of compressed air in rail surface is with 8 holes.

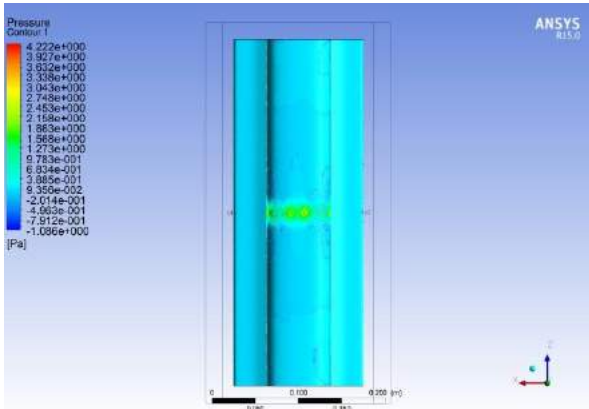


Fig. 9 Air pressure contour in cooling unit.

Fig. 10 shows the temperature distribution in the area between rails and cooling unit, where the minimum temperature is in the top area due to the forced air cooling.

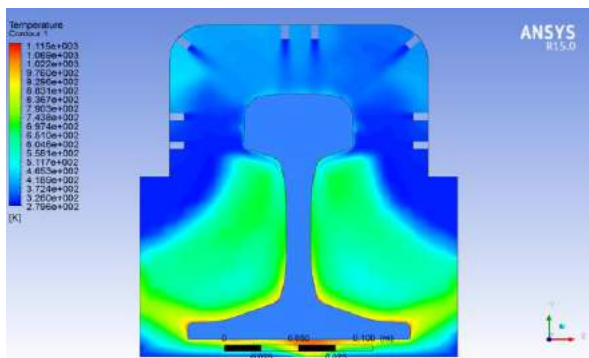


Fig. 10 Cooling unit temperature distribution.

Fig. 11 showing the temperature (volume rendering) in the area between rails and cooling unit where the minimum temperature is in center of the cooling unit due to the forced air cooling.

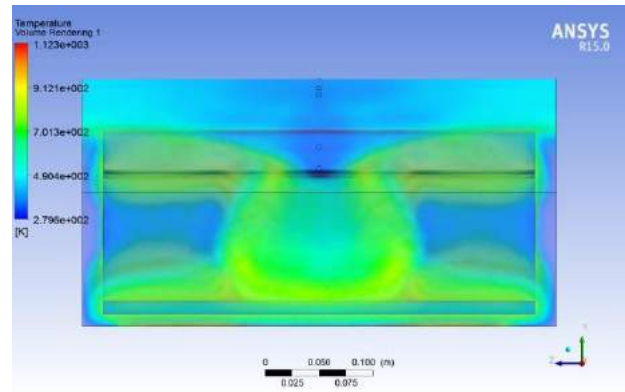
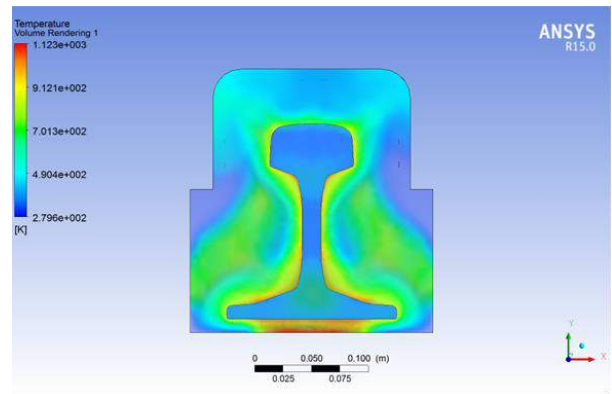


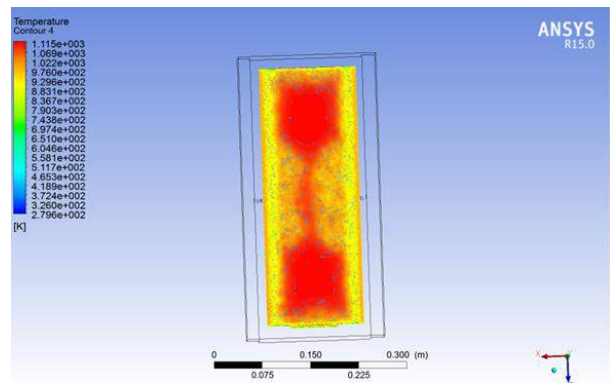
Fig. 11 The temperature (volume rendering) of cooling unit.

HHH. Some Comments

The results of simulations show that the foot of rail is still warm while the rest part of the rail section is cooled as shown in Fig. 12 a-d. Thus, we recommend to apply some means to cooling unit (such as extended side walls with air inlets) to facilitate faster cooling of rail foot in order to avoid the formation of additional residual stresses.



a)



b)

VI. REFERENCES

- [1] N. Ramadan, K.Tur., E. Konca, "Process Design Optimization For Welding of The Head Hardened R350 HT Rails and Their Fatigue: A Literature Review", International Journal of Engineering Research and Development, 2017, 13(1), pp. 49-55.
- [2] Li, G., et al., "Numerical Simulation of Heavy Rail Quenching Process", JCP, 2012. 7(10): pp. 2439-2445.
- [3] L. Gongfa, et al., "Numerical Simulation of Flow, Temperature and Phase Fields in U71Mn Rail-Head Quenching Process".
- [4] M. Sharma, T.R. Reddy, and C.I. Priyadarsini, "Flow Analysis Over An F-16 Aircraft Using Computational Fluid Dynamics", International Journal of Emerging Technology and Advanced Engineering, 2013. 3(5).
- [5] EN 13674-1:2003, Railway Applications–Track–Rail–Part 1: Vignole Railway Rails 46 kg/m and Above,

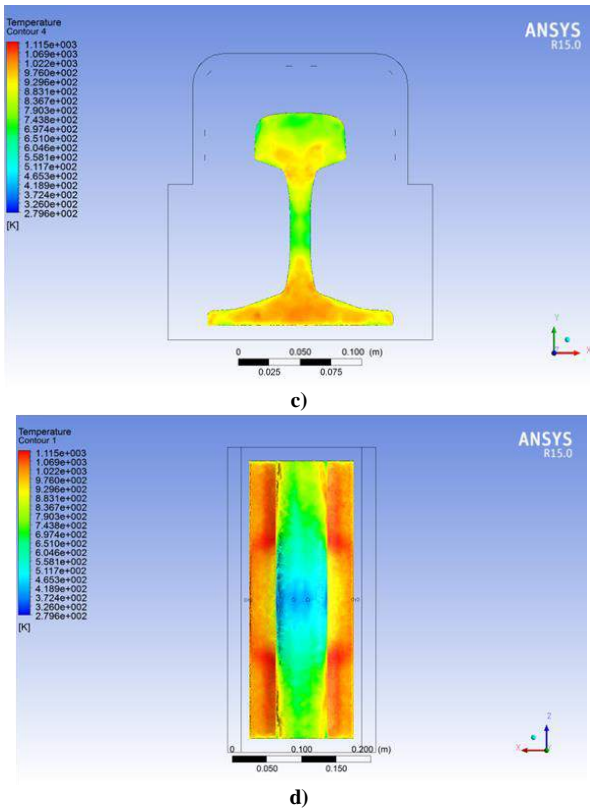


Fig.12 a) The temperature (volume rendering) of cooling unit, b) temperature contour of cooling unit, c) the temperature contour bottom side of cooling unit, and d) showing the temperature contour top side of cooling unit

V. CONCLUSIONS

The airflow and temperature distribution over a rail section is very important for the production of head hardened rails and post-weld accelerated cooling of the weld joints of those rails

The working conditions of cooling unit and the required pressure and temperatures for each part of this device were defined. The basic dimensions and parameters of cooling unit were verified. The inlet and outlet temperatures of the cooling unit using simulation in this model using ANSYS Fluent. The following process parameters were predicted by the simulation runs: the best air velocity is 5 m/s; distance between rails and cooling unit 5 cm; number of holes and position are 8 holes positioned as shown in the figures; and dimension of air inlet holes is 0.5 cm in diameter. It was also noted that the foot of rail still warmer where the rest part of rail are cooled down, yet most of the studies have focused the temperature distribution only in rail head. The results of the present study indicate the importance of the temperature distribution studies over the entire rail section.

More simulation studies using CFD software would obviously help to reduce time for the design and production of tools and materials whose processes incorporate cooling or heating cycles by means of a fluid to improve their properties.

The Effect of Prior Austenite Grain Size on Microstructure of Medium Carbon Dual Phase Steels

Ersoy ERİŞİR, Özge ARARAT¹, Oğuz Gürkan BİLİR

Kocaeli Üniversitesi, Mühendislik Fakültesi, Metalurji ve Malzeme Mühendisliği Bölümü,
Umuttepe Yerleşkesi, 41380 Kocaeli
eerisir@kocaeli.edu.tr, ozgeararat@gmail.com¹,
oguz.bilir@kocaeli.edu.tr

ABSTRACT

Finer martensitic and ferritic microstructures are demanded to obtain high strength and toughness for dual phase steels. In this study, reducing of prior austenite grain size selected as an effective method to reduce the size of dual phase microstructure. The effect of prior austenite grain size on microstructure of medium carbon dual phase steel produced by intercritical annealing were investigated for different austenitizing conditions. Annealing experiments were performed to fully austenitize the steel at different austenitizing temperatures (900, 950, 1000°C) and times (5, 10, 15 min) and followed by quenching. Finally, as-quenched martensitic microstructures were intercritical annealed at 760°C for 15 min to attain martensitic and ferritic dual phase steel. The microstructures were analyzed using light microscopy and image analysis methods. It is concluded that grain size of dual phase steel is reducing by decreasing of the austenitizing temperature and the holding time.

Keywords: Dual phase steel, intercritical annealing, prior austenite grain size, microstructural characterization

Examination of Solid State Nitrogen Absorption for Production of Nickel Free Stainless Steel

Oğuz Gürkan BİLİR¹, İsmail GÜVENİR, Ersoy, ERİŞİR
Kocaeli University Metallurgy and Materials Engineering Kocaeli, 41300 Turkey
oguzgbilir@gmail.com¹, ismailguvenir@gmail.com, eerisir@gmail.com

ABSTRACT

Co-Cr and 316L are the commonly used alloys in biomedical industry. However, both 316L and mostly used Co-Cr alloys as F-562, L-605 contain large portions of Ni as alloying element. Ni may cause allergic and toxic impacts on human health. In recent years, N-alloyed Ni free stainless steels seemed as good candidate for replacing Ni contained metals. However, liquid steel has a limited N solubility at atmospheric pressure. Thus, high pressured melting techniques are required. In this study, N alloying of ferritic 430 stainless steel sheet was performed in solid state. Nitrogen absorption of stainless steel was performed in a furnace filled with nitrogen gas with atmospheric pressure at 1200°C. Solid state N absorption was applied in four different time periods as 4, 8, 12, 24 hours. Microstructure after absorption process was investigated by Scanning Electron Microscope and Light Microscope. Fully austenitic structure was observed in surface of specimens. However, duplex microstructure of ferrite and austenite was seen in the center of specimen. Vickers hardness was carried out to evaluate of phases. It was concluded that optimum microstructure is achieved by 4 hours of N absorption.

Keywords: High Nitrogen, Stainless Steel, Metallic Implant, Heat Treatment.

Effect of Carbon Content on The Wear Behaviour of Eutectoid Steel Wire Rod

Semih Gezer*, Hayrettin Ahlatci*, Çağatay Aslan*, Yunus Türen*, Yavuz Sun*, Melike Birinci*, Meryem Yıldız*,
Neşe Çağlayan*, Hüseyin Koymatçık⁺,

⁺Engineering Faculty, Karabuk University, 78200, Turkey

semihgezer6463@gmail.com, hahlatci@karabuk.edu.tr (corresponding author), cgyaslan93@gmail.com,
melikebrnc@gmail.com, mrymyildz@hotmail.com, nesecaglayn@hotmail.com,

+Kardemir A.Ş. Karabuk, Turkey
hkoymatcik@kardemir.com

Abstract— In this study, the effect of carbon content in the range of 0,7-0,9 on wear resistance was investigated. The examined specimens in 5.5 mm diameter are manufactured with drawing process. Wear tests of the cylindrical samples with a length of 20 mm were examined in pin-on-disc type wear tester on counter face of 1.2379 cold work tool steel under the load of 30-60 N. The weight losses of the samples examined increase with the increase of carbon content and hardness. Wear Mechanism is mild wear to oxidative wear.

Keywords— Eutectid steel, Wire Rod, Wear

I. INTRODUCTION

Wire Rods are steel side products which are suitable for wire production by cold drawing processes. The steel is carbon alloy and iron that contains less than 1.8% carbon in its structure; it can acquire very variety properties with mechanical and thermal processes. Ribbed wire rods can be used in round construction iron steel equipments such as stirrup, distance piece miter, iron square, pile reinforcements. Smooth wire rods can find possibilities to use in many field such as automotive, construction industry, generally in the industry wire, nail, bolt, nut, steel wire mesh, welding electrode [1-9].

The purpose of this study is to evaluate surface properties of the C70, C80 ve C90 quality steel wire mechanical properties and wear resistance of used in friction-wear environments. In addition in this study, it is also aimed to classify the types of inclusions that cause damage in wire drawing operations service performance and determine the inclusions causing break in the wires by optical microscopy and SEM studies with EDS connection.

II. EXPERIMENTAL STUDIES

The specimens used in the experimental studies are prepared 5.5 mm in diameter and 20 mm in height. The surfaces of the samples were sanded under water with 200, 400, 600, 800, 1000, 1200 mesh sandpaper respectively according to the

metallographic procedure and then they were polished using 1 µm and 3 µm diamond paste suspensions. The specimens were washed with alcohol, dried with warm air stream, and then made ready for microstructured studies. The Microstructural studies were made using Nikon Epiphot 200 model optical microscope connected to computer hardware. Images and of the EDS elemental analysis nonetched specimens prepared with metallographic techniques was performed with scanning electron microscope (SEM) CARL ZEISS ULTRA PLUS GEMINI FESEM brand. The polished specimens taken on the SEM device were etched with 3% Nital.

In the hardness test, Brinell hardness tester of Bulut brand was used with 5 mm diameter steel balls in the device, by using 187.5 kg weight of hardness measurements were made.

In order to determine the wear behaviour, the wear test of the examined specimens was carried out at room temperature, on a pin-on-disc type adhesion apparatus, under a load of 30 N and 60 N, and at a constant sliding rate of 0.5 m/s. As the counter-disc, 1.2379 quality cold work tool steel was chosen. At every 2000 meters, the mass loss of the sample was measured and a total of 12000 meters was taken way. The samples were weighed before and after the wear test on an electronic scale with a sensitivity of 0.1 mg. The wear loss obtained from the wear test was evaluated by the sliding distance and carbon content. Worn specimens were examined on a SEM microscope to determine the wear mechanism.

III. RESULTS AND DISCUSSION

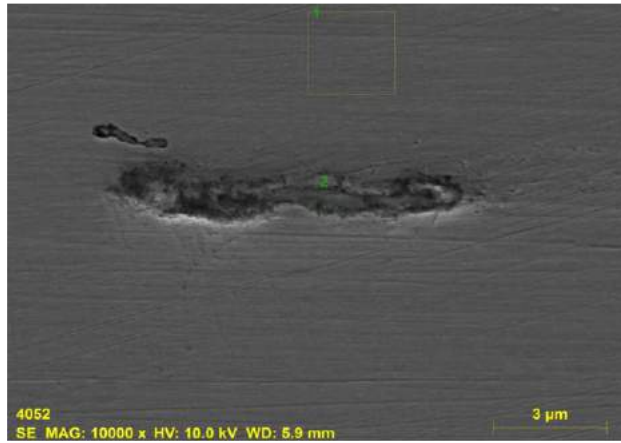
In Fig. 1, SEM images of the samples are given that are buried longitudinal bakelite and polished. Round and longitudinal black stains are observed in the matrix as seen in the SEM. The EDS results from received in these stains are given in Fig 2.

As seen in Fig. 2, wire rod of the 0.9 carbon contains inclusions in which Si, Mn and S elements are in high amounts [10,11]. These inclusions are significantly decreased by the reduction in the carbon content of the sample being examined. The microstructures of the etched samples are given in Fig. 3. The

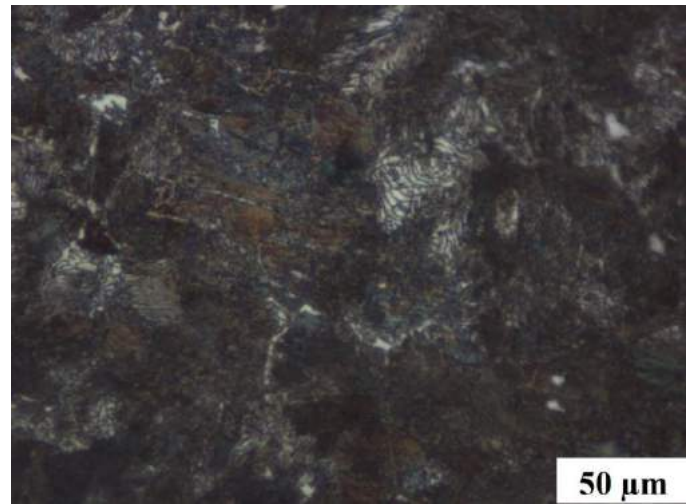
structural analyzing showed the steel pearlitic. The grain size of the samples examined increases somewhat with increasing carbon content.



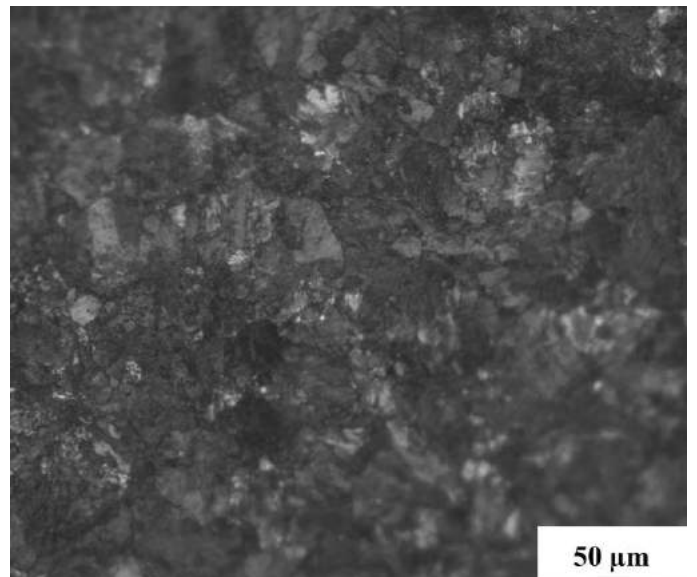
(a)



(b)



(a)



(b)

Fig. 1 (a) Round and (b) longitudinal inclusions observed in wire rod of the 0.9 carbons.

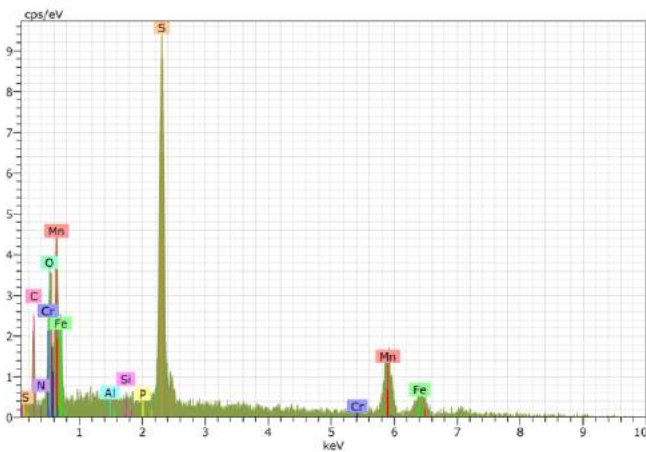
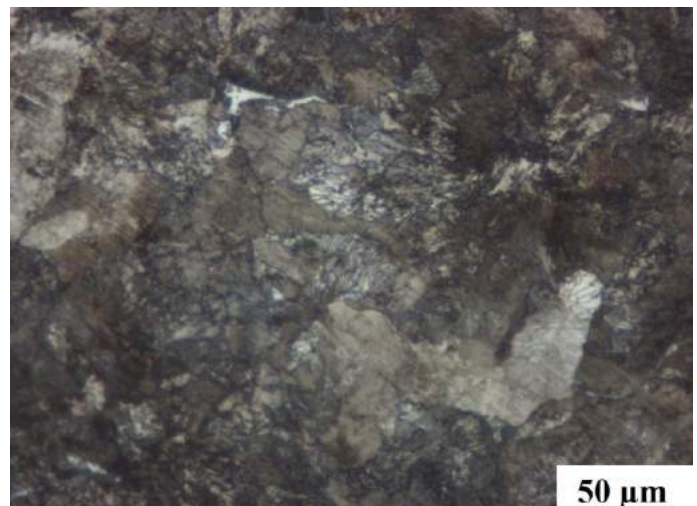


Fig. 2 EDS results from received in longitudinal inclusions in wire rod of the 0.9 carbons.



(c)

Fig.3 Microstructure of the (a) 0.7, (b) 0.8 and (c) 0.9 carbon samples.

The hardness of the examined samples are given in Fig. 4 When the carbon content of the steel is increased, the hardness increased from 320 HB to 345 HB. The increase in hardness is due to the carbon content of the steel.

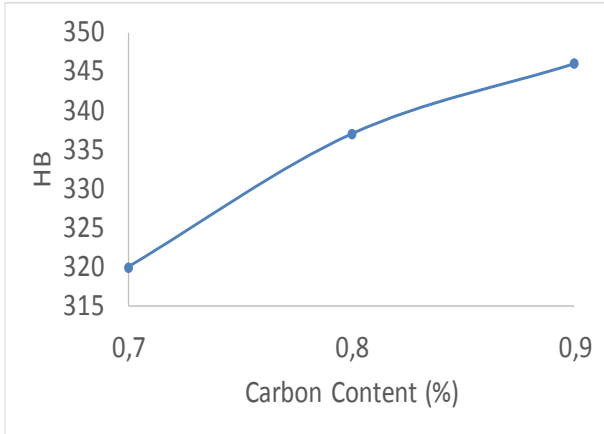
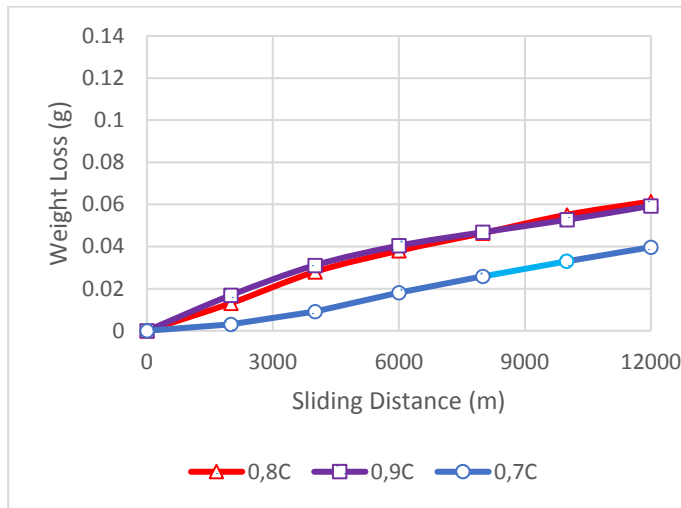
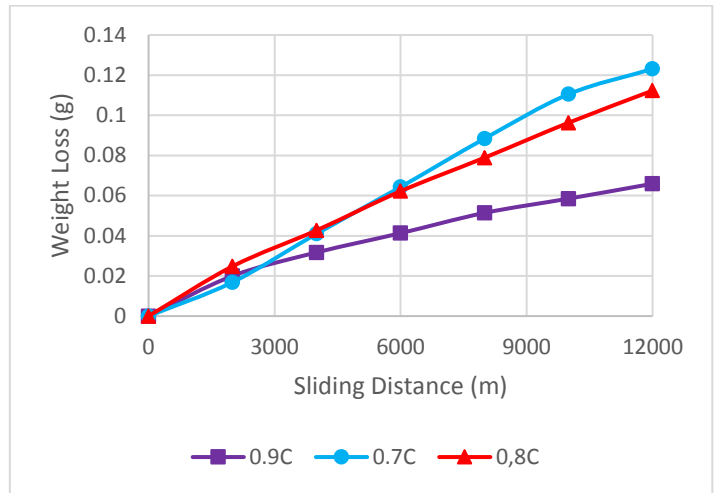


Fig.4 Hardness values of the samples with different carbon content



(a)



(b)

Fig.5 The results of the weight loss of the examined specimens under the (a) 30N and (b) 60N loads.

Fig. 5 were showed the results of weight loss obtained from the wear tests and evaluations were made on the specimen properties. The variation of the weight loss of the specimens studied in (Fig. 5) is given by the sliding distance. Weight loss according to sliding distance has been changed linearly. With an increase in the load applied within a sliding distance of 12000 meters, the amount of weight loss has increased. The lowest weight loss under a 30N load at a given sliding distance exhibits 0.7C steel, while under 60N load, the 0.9C steel has low weight loss. With the increase of the hardness of the samples examined weight loss, despite an increase in carbon content has also increased at low loads. This can be attributed to inclusions in the microstructure of the high carbon steels at low loads.

At high loads, the wear behaviors of the specimens examined have changed in accordance with their hardness. As the hardness of the examined specimens increased, the weight loss decreased.

After adhesion tests, a macro image of the traces on the counter disk is shown in Fig. 6. The wear macro images show that marks occurring at low loads are more oxidative then at high loads (Dark Mat reddish brown) At high loads, the traces appear bright reddish brown.



Fig.6 Macro view of low and high load wear on the counter disk.

The wear rates in (g/ N.m) were calculated by using the weight loss values corresponding to the 12000 meters slip distance given in Fig. 5. In Fig. 7 the variation of wear rates is plotted depending on the carbon content of the samples.

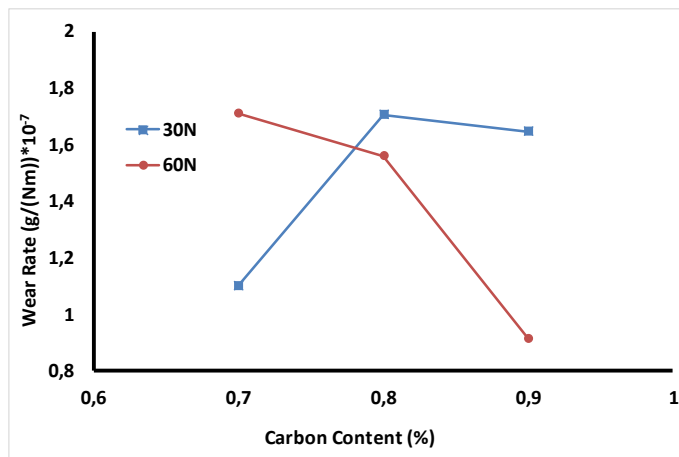
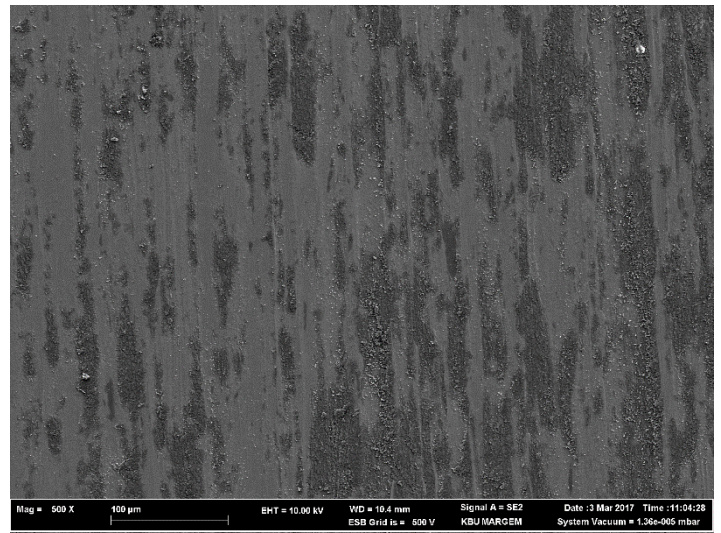


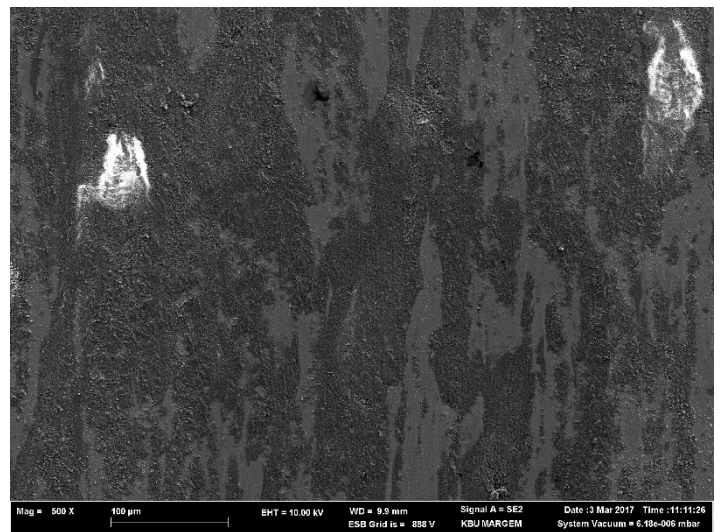
Fig.7 Variation of the wear rates of the examined samples relative to the carbon contents.

As can be seen from Fig. 7, wear rates of the specimens examined should be between $0.9 \cdot 10^{-7}$ and $1.7 \cdot 10^{-7}$. The inspected of wear on the samples examined are very low and are intercalated. Despite this, as the carbon content increases, the wear rate increases at low loads but at high loads vice versa.

The wear surfaces of the specimens subjected to the wear test and their cross sections parallel to the rolling direction were examined and SEM photographs were taken. (Fig 8 , Fig 9)



(a)



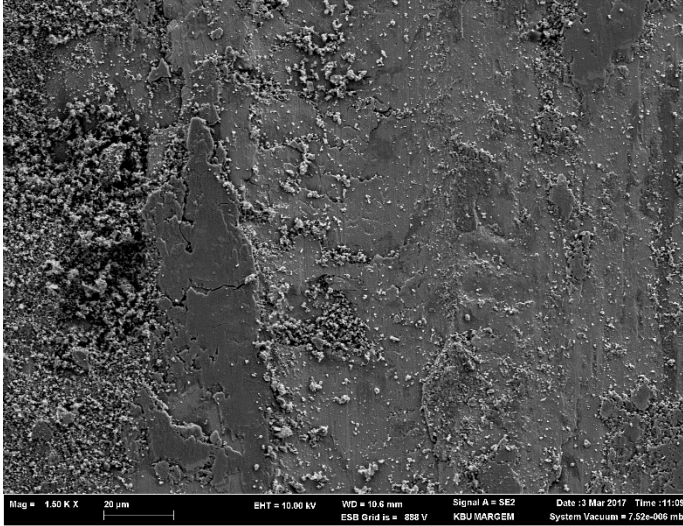
(b)

Fig 8 : At low loads 30N SEM photograph of the wear surface of the (a) 0.7C (b) 0.9C samples

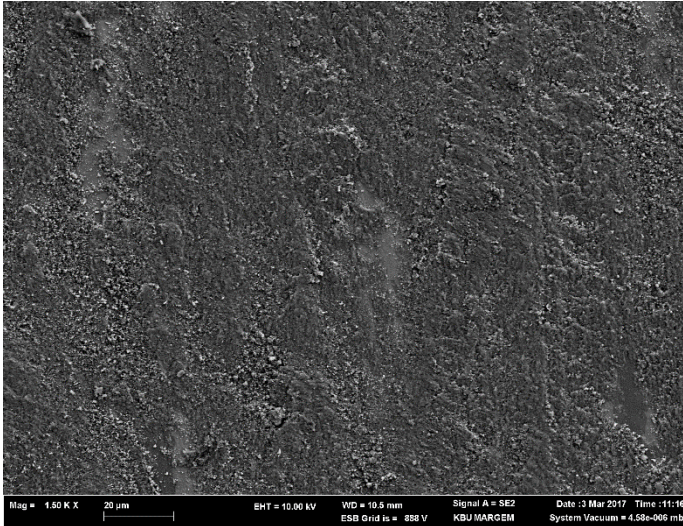
Fig. 8 shows oxidations in certain regions in the direction of flow under the 30N load. It was observed that the amount of oxidation increased in dark colored areas but, oxidation decreased and iron increased in dark colored areas. It can be said that there is little wear due to oxidation.

In Fig. 9 (c), the wear in the direction of flow under the 60N load is high and the oxidation is observed in low amount. It has been observed that a large area of the wear surfaces undergoes plastic deformation due to the interfacial pressure and the effect of shear, and that superimposed plaster occurs. It has been a matter of breaking into the area where the plaster on the worn surfaces of the 0.7C sample. (d) Under high load the wear flow direction of the sample 0.9C is low and high amount oxidation observed.

VI. REFERENCES



(a)



(b)

Fig 9 : At high loads 60N SEM photograph of the wear surface of the (a) 0.7C (b) 0.9C samples

IV. CONCLUSION

Results of the wear behavior of the examined alloys were listed below;

1. It should be examined that the wear rate with carbon content was increased under light load although the hardness was increased by carbon content of the samples.
2. Due to inclusion in the microstructure of the high carbon steel at low load the weight loss was high.
3. At high loads the wear behaviors of the specimens examined have changed in accordance with their hardness.
4. It has been observed that a large area of the wear surfaces undergoes plastic deformation due to the interfacial pressure and the effect of shear, and that superimposed plaster occurs.

V.

- [1] ASTM E 2948; Standard Dennis W. and Norwich, P.E., "A Comparison of Zero Mean Strain Rotating Beam Fatigue Test Methods for Nitinol Wire", SMST 2013 Norwich Rev Test Method for Conducting Rotating Bending Fatigue Tests of Solid Round Fine Wire.
- [2] <http://www.bekaert.com/en/functional/product-sistema>.
- [3] SAU Fen Bilimleri Enstitüsü Dergisi 6.Cilt, 3 .Sayı (Eylül 2002) – Tel Çekme Prosesi Ve İnküzyon Hasarları Ümit ŞENYÜREK, Hüseyin CÖMERT.
- [4] 5.Uluslar arası Kırılma Konferansı Bildiriler Kitabı, 310-311, (2001).
- [5] Çapan L., Metallere Plastik Şekil Verme İTÜ Yayını, 249-270, (1990)
- [6] Ünal L. M., Çelik Üretiminde İnküzyon ve Azaltılması Erdemir Yayınları, 9-48, (2001)
- [7] Kiessling R. , Lange N. " Nonmetallic Inclusions in Steel ", T.Metal Society, (PartIII) , London, 1978
- [8] Uzun İ. , "İnküzyonlar, Mekanik Özelliklere Etkileri, Giderilmesi ve Saptanma Yöntemleri", İTÜ Sakarya Mühendislik Fakültesi Metalurji Mühendisliği Bölümü Bitirme Ödevi 1991
- [9] <http://www.kromancelik.com.tr/tr/urun-detay/7/duz-filmasin>
- [10] ASTM E 45 – 05 - Standard Test Methods for Determining the Inclusion Content of Steel
- [11] ASTM E 1245 - Practice for Determining Inclusion or Second-Phase Constituent Content of Metals by Automatic Image Analysis

Analysis of the Effect of the Continuous Slab Casting Parameters on Mould Friction

Hakan KAPUSUZ*, Selçuk MISTIKOGLU⁺

**Iskenderun Iron & Steel Works, Turkey*

⁺Department of Mechanical Engineering, Iskenderun Technical University, Turkey

E mail:hkapusuz@gmail.com, selcukmistikoglu@gmail.com

Today steel is one of the most common material used in almost everywhere from seat belt mechanism to petroleum pipeline. Steel production requires many steps including the steel making and continuous casting plants. Starting with first drafts in 1856 continuous casting machines has evolved today's modern machines. One of the most important part of continuous casting machines effecting the quality, productivity and yield is the open-ended copper mould. With time there is needed more control over casters due to the increasing quality demand and machine yield. When liquid steel is poured through the mould first solidification occurs around slab strand. When the strand of steel is continuously withdrawn from the mould through roller, friction happens between strand shell and mould. Mould friction should be kept in optimum range. Beyond this range there can be breakout or produced slab having bad surface quality. Variety of continuous casting parameters effect mould friction such as casting speed, steel grade, mould level, mould powder viscosity, mould oscillation parameters, etc. In this research there can be found how different slab caster parameters effects the mould friction.

Key words: Continuous casting, slab, mould friction

I. INTRODUCTION

After ingot casting invention of the continuous casting it takes important role of steel production. Nevertheless continuous casting machines needed a 100 years to find itself in steel industry[1]. Mass production is enabled in the form of semi-final product such as billet, bloom, slab, round, beam blank. From first draft to today's modern continuous casting machine many demands have arisen from increasing quality demands, productivity and also overall yield of machine.

Casters have many common following equipment in the world, Figure 1 [2] :

- o Turret
- o Tundish
- o Mould
- o Strand Guide Rolls
- o Pinch Rolls
- o Spray Water
- o Cutting Machine

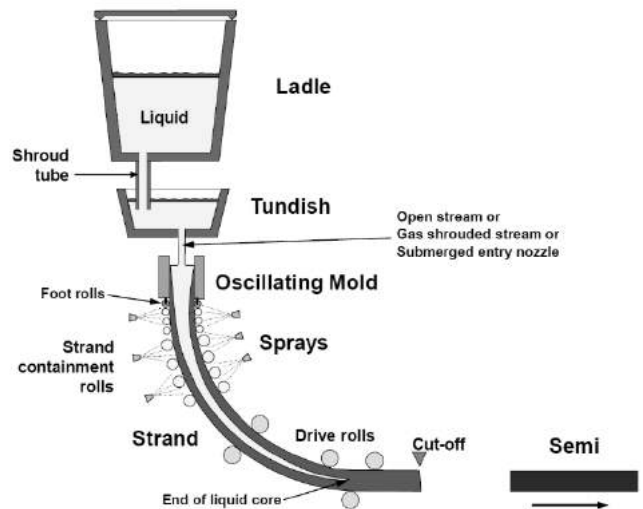


Figure 2 Side View of a Typical Continuous Casting Machine [2]

When liquid steel is prepared regarding chemical composition and temperature it is transferred to caster via ladle. Ladle is placed onto turret arms. A typical turret rotates with helping of hydraulic or electrical power. After ladle slide gate which is at bottom of the ladle is opened liquid steel is poured to the tundish through the ladle shroud. Tundish acts as a reservoir for liquid steel. Inclusions are separated from liquid steel to the surface during the residence time of liquid steel. Thus the more residence time leads less residuals. There are different tundishes used in the steel plant such as called type of B, T, V, C and H [3]. Each of them has its own advantageous and disadvantageous.

After tundish liquid steel is transferred to the open-ended mould. The mould properties play very important role on heat extraction [4]. First solidification occurs at the meniscus in the mould, wherein the cooling is called primary cooling. The strand having solidified shell is withdrawn through strand guide rolls. Whole strand guide rolls are split into parts called segment zones. Generally, every zone has its own control unit regarding the pressure of roll, position of segment and cooling pattern. The strand is cooled down to the certain limits during its movement. Liquid steel transferred by the help of gravity, on the other hand to control casting speed there is needed control unit. Most of the rolls are idle but some of them driven by electrical motors named pinch rolls to control casting speed.

When fully solidified strand exit from the strand guide rolls it is cut into semi-final product named slab.

From initial point to end of caster every stage of process contributes to productivity and quality. Among them the copper mould is assumed hearth of machine because of its crucial roles on productivity and product quality [6], Figure 2 [5].

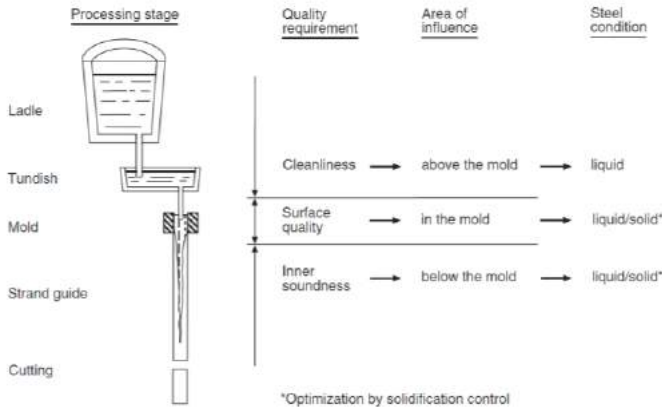


Figure 3 Main Processing Stages and Their Relevance to Product Quality [5]

II. Mould Friction

Mould friction is one the most important phenomenon occurring in the mould. Interaction between strand shell and mould wall leads to friction. Many continuous slab caster parameters effect friction less or more. Monitoring this can give many useful information regarding quality and process optimization. During time mould friction is measured by many techniques but very few studies have been done about the role of casting parameters on mould friction [7].

Mould friction is govern by following equations[15][11]:

$$F_f = A \times \eta \times \frac{v_m - v_c}{d_p} \quad [1]$$

$$F_s = \eta \times H \quad [2]$$

F_f = Friction between mould and shell (upper part of mould),

A =Mould active surface area,

η = Mould flux viscosity,

v_m = Mould oscillation velocity,

v_c = Casting speed

d_p = Mould flux thickness

F_s = Friction between solid flux layer and shell (lower part of mould),

η =Solid flux friction coefficient,

H =Ferrostatic pressure of molten steel,

Mould friction can be measured and monitored many ways without needed mould flux properties. Placing accelerometers on mould, getting pressure feedback from hydraulic oscillation cylinder, force sensor method, load cell ,

analysing power of oscillation motor are some known methods [7] [8] [9] [12].

Apart from hardware calculation methods also differ from each other due to the feedback signal types such as acceleration, pressure, and current. At the end, the mould friction can be extracted from mould-shell interaction.

Mould friction is result of interaction of mould wall and strand shell, Figure 3 [10]. Whatever effect this interaction effects mould friction. Main purpose of this research is to give a brief summary to reader how these casting parameters effecting interaction being between mould and shell.

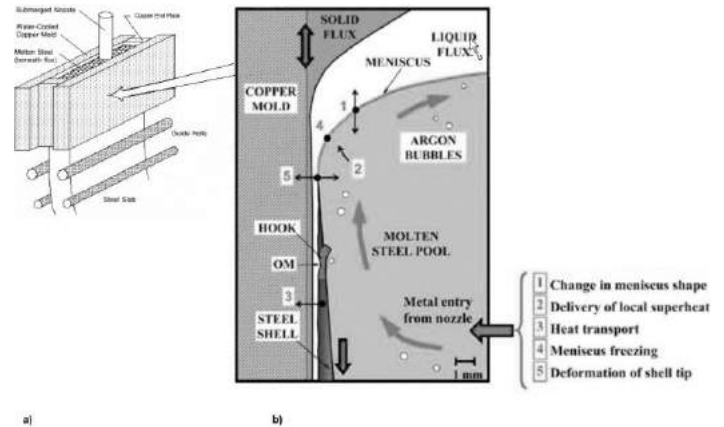


Figure 4 Continuous Casting of Steel a) Slab Mould and b) Meniscus Region [10]

III. Parameters of Steel Slab Casting Effecting Mould Friction

It is said before mould friction is result of interaction between mould wall and shell. There are many parameters contribute to this interaction.

III.1. Casting Speed

Casting speed is the measure of throughout rate of steel from mould unit m/min. When the speed increases mould powder consumption is decreased. Then lubrication between mould and shell weakens. This leads to increasing mould friction, Figure 4 [19]. In addition to this higher casting speed causes smaller shrinkage of strand leading more contact area, in other words it leads higher friction [24]. Casting speed and oscillation wave of mould have a very close relationship, wherein relative motion effects directly lubrication.

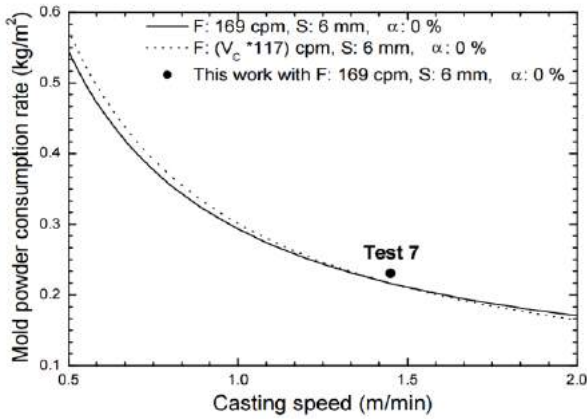


Figure 5 Mould Powder Consumption vs Casting Speed Variation [19]

Under different conditions same results are taken back again, Figure 5 [13]. This explains well why the increasing speed gives rise increasing frequency of breakout. To compensate this effect to a certain limit oscillation parameters are also changed.

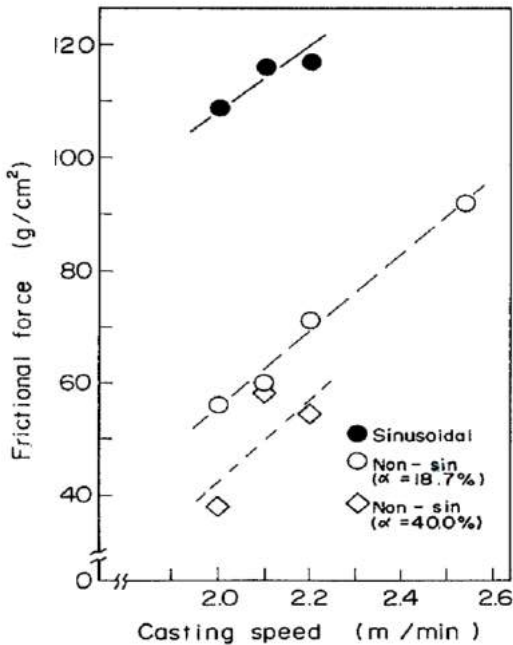


Figure 6 Mould Friction vs Casting Speed [13]

III.2. Mould Powder

Mould powder provides a liquid film between mould and shell to ensure adequate lubrication between them. Physical and chemical properties of mould powder have a very big effect on mould friction. The behavior of mould powder very depends on viscosity, basicity and break temperature [15], Figure 6 [14]. Powder A and C have different viscosity and break temperature [14].

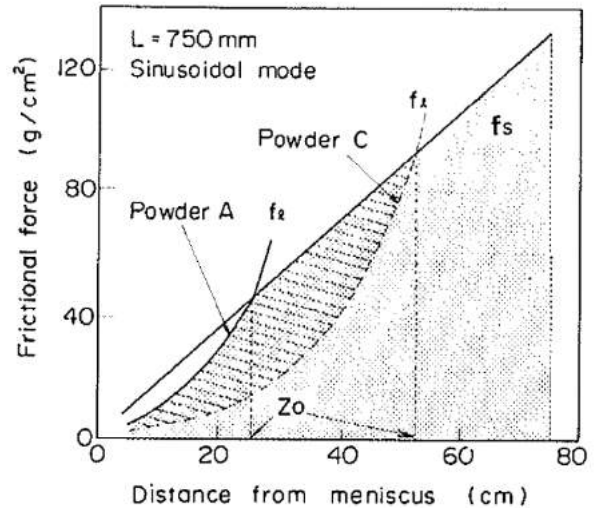


Figure 7 Comparison of Different Mould Powders [14]

It can be concluded from equation [1] that friction decreases as viscosity increases and liquid flux film depth increases [15] [11].

$$F_f = A \times \eta \times \frac{v_m - v_c}{dp} \quad [1]$$

Apart from its own physical and chemical properties almost every casting conditions contributes to lubricant properties in a way. Casting speed, Al₂O₃ content, oscillation pattern ... etc. can change behavior of mould powder. Main requirements are at the usage point to get a balance between liquid slag pool and melting rate, a good slag infiltration and control of heat transfer.

III.3. Oscillation Pattern

The oscillation of mould results in a relative motion between mould wall and strand shell. The motion of mould creates a sine function. The properties of sine wave contributes to infiltration of liquid slag (mould powder), in other words it contributes to lubrication and reduces friction.

From lubrication view there are 2 main phase in a cycle of mould's up and down motion. First phase is named (t_N) negative strip time where mould slag is infiltrated into between mould and shell. During t_N compression force is applied to shell. Other phase is named (t_P) positive strip time where tensile force is applied to shell accompanied by infiltrated mould slag [16] [17]. During 1 cycle of mould motion friction changes according to relative motion of mould and strand, Figure 7 [16] [18]

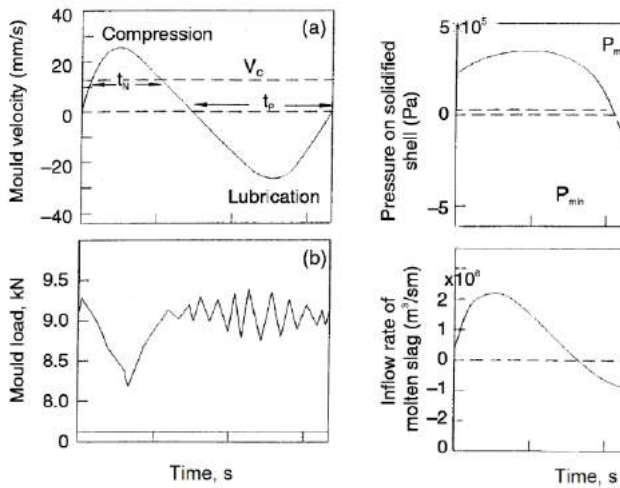
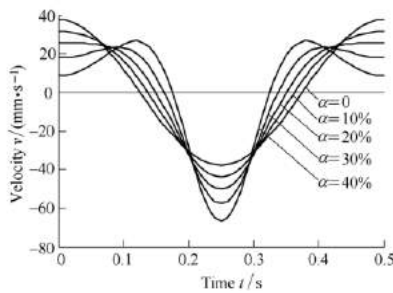


Figure 8 Effects of Mould Oscillation on a) t_N and t_p b) friction c) slag pressure on strand shell d) inflow rate of liquid slag [16][18]

Apart from sinusoidal motion, there is non-sinusoidal motion which gives user 3th. parameter except stroke and frequency. The new parameter is named distortion, modification ratio (α), Figure 8[21].



Şekil 9 Mould Velocity in Non-sinusoidal Oscillation [21]

It allows plants to optimise t_N and t_p effectively [17], in other words mould powder consumption rate, Figure 9 [19].

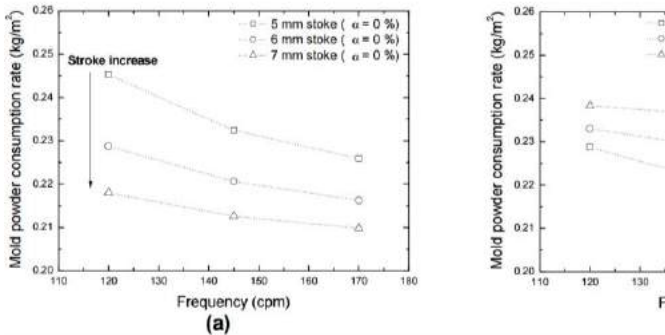


Figure 9 Effect of a) Stroke and b) Modification Ratio on Mould Powder Consumption [19]

III.4. Chemical Analysis of Steel

Friction behavior depends on steel chemistry. High friction and large fluctuation occurs in especially in peritectic

grades due to the fast phase transformation after solidification [23]. In high carbon mould friction is more stable than peritectic grades, Figure 10 [23]. On the other hand according to a research higher carbon content results in higher friction[25].

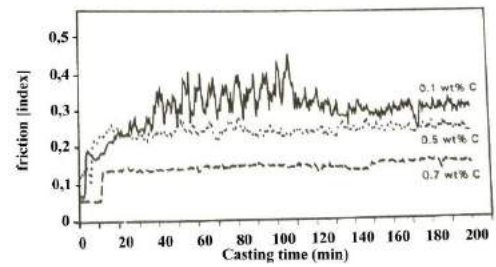


Figure 10 Carbon Content Effects On Friction [23]

Mould powder and slag interacts with each other continuously. Viscosity, basicity and solidification temperature of infiltrated slag can be changed during casting according to steel chemistry due to the steel slag interaction. Change in Al_2O_3 content of slag both effects important temperatures, viscosity and basicity, Figure 11 [20]. In other words, steel chemistry components also define lubrication behavior of slag

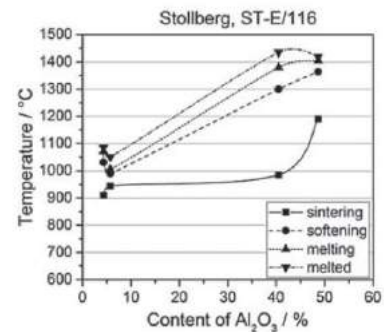


Figure 10 Al_2O_3 Effects on Important Temperatures [20]

The infiltrated liquid slag film controls friction and the solid layer controls the heat transfer [15]. It is very hard to control medium due to the dynamic slag - steel interaction.

III.5. Mould Taper

When the steel solidified it shrinks according to its carbon content [24]. Especially at narrow sides of mould the shrinkage gaps should be compensated with suitable mould powder and taper. Otherwise at worst scenario breakout occurs due to improper lubrication and heat transfer. There are many types of mould taper design in plants such as single, multi, parabolic or customized taper. It is well known that excessive taper results in higher friction [22] due to lack of lubrication. On the other hand inadequate taper results in poor heat transfer[24].

III.6. Liquid Steel Temperature

Ferrostatic force is applied to strand shell towards mould wall. If the superheat is higher shell is thinner then mould

friction increases, Figure 12 [7]. Higher superheat results in late solidification leading smaller friction which causes higher friction [24]

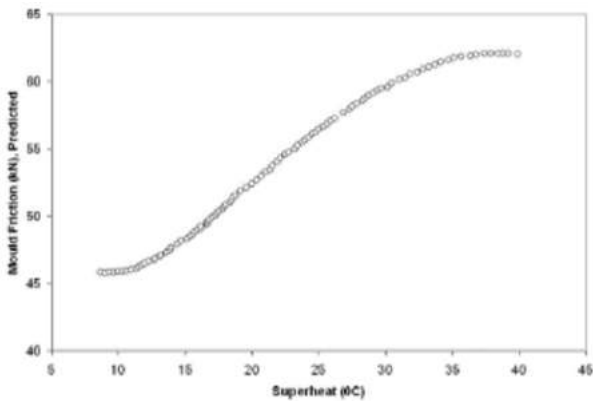


Figure 11 Superheat Effects On Mould Friction [17]

Steel temperature also changes viscosity of mould powder due to melting with heat of liquid steel. This leads to change of lubrication behavior.

III.7. Mould level

Mould level is correlated with mould friction due to surface area. If mould level is higher then friction is higher [7] [17]. Besides, mould level fluctuation caused by whether abrupt casting speed changes or other reasons disturbs infiltration of slag into mould-shell gap. If the distribution of liquid slag film is not uniform there will be uneven lubrication and shell thickness. In the worst case steel sticks to wall and cause breakout of slab. At the measurement point of view electromagnetic measurement has better results than rodometric measurement regarding mould level control.

III.8. Steel Flow In Mould

Steel jet pattern through the SEN should be double-roll for optimum casting condition. Surface velocity and level fluctuation is lower in double roll flow pattern [1][25]. Clogging, argon gas injection, position and design of SEN[26], dimensions of slab mould, control mode of stopper, steel height in tundish, electromagnetic forces contribute to flow characteristic of steel in mould.

III.9. Mould

Mould surface profile has an influence on friction. There is found correlation between heat number one mould and friction, Figure 13 [27]. This is linked to wear of mould surface.

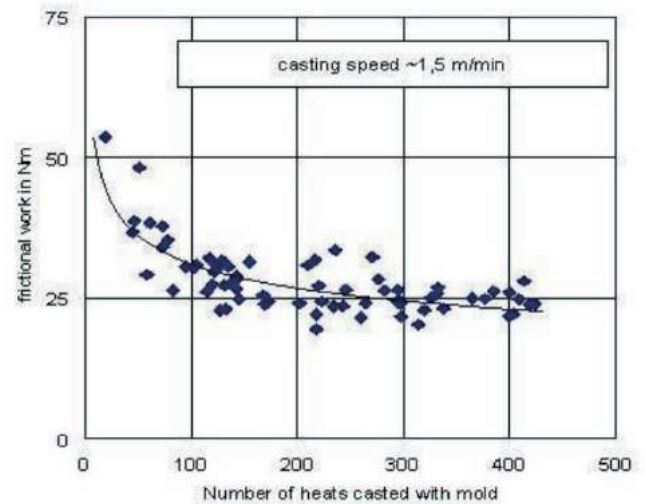


Figure 13 Frictional Work versus Heat Number [27]

Liquid steel heat extraction is done by the help of mould cooling water. Water flows through the mould continuously. Water flow rate, pressure, temperature controls heat extraction from liquid steel.

Additionally mass of total resonance part, surface coating and misalignment of mould, spring forces have influence on friction due to extra work for oscillation system.

VII. CONCLUSION

A brief summary is given about mould friction in continuous casting of steel. Although there are many theoretical approaches to reduce friction such as mould powder viscosity, casting speed, oscillation pattern etc. main concern at casting platform is to get a stable casting. Due to the dynamic nature of liquid steel in mould many parameters effecting mould friction also effect each other. Thus to optimize mould friction all parameters should be considered together. Additionally reduction mould friction and quality results should be in harmony especially for surface quality.

VIII. REFERENCES

- [1] The AISE Steel Foundation, The Making, Shaping and Treating of Steel, 11th Edition Casting Volume
- [2] E.S. Szekeres, Continuous Casting Systems-An Introduction
- [3] Sahai, Y. And Emi, T. "Tundish Technology for Clean Steel Production", World Scientific Publishing 2008, pp. 9-11
- [4] I.V. Samarasekera, and J.K. Brimcombe, "The Thermal and Mechanical Behaviour of Continuous Casting Billet Moulds"
- [5] M.M. Wolf, "Continuous Casting Operation and Metallurgy," Metallurgy of Iron, 4th ed., Vol. 11, Continuous Casting (Gmelin Handbook of Inorganic and Organometallic Chemistry, 8th Edition), edited by H. Hieberl (Berlin:Springer-Verlag, 1992)
- [6] C.Li, and B.G. Thomas, "Analysis of Potential Productivity of Continuous Cast Molds," Brimacombe Memorial Symposium, Vancouver, Canada, 2000, Met Soc., CIM, pp. 595-611
- [7] P.P. Sahoo, and S. Basu, "Use of Artificial Neural Network to Determine the Effect of Different Casting Parameters on Mould Friction in a Continuous Slab Caster," 7th. Metec. In. Steel Con. 2011
- [8] Kenneth E. Blazek, Ismael G. Saucedo1, "Characterization Of The Formation, Propagation, And Recovery Of Sticker/Hanger Type Breakout," ISIJ International Vol. 30 (1990), No. 6, P 435-443

- [9] Y. Ma, F. Wang, B. Fang, and W. Gui "Discussion and Analysis on Measurement Methods for Mould Friction During High Efficiency Continuous Casting," Int. Semp. On Material, Energy and Environment Eng. (ISM3E 2015)
- [10] Thomas, B. G., "Application of Mathematical Models to the Continuous Slab Casting Mold," Iron and Steelmaker, 16:12, 53-66, 1989; also in ISS Transactions, Iron and Steel Society, Warrendale, PA, 11, 143-156, 1990
- [11] Lin-ping LI, Xin-hua WANG, Xiao-xuan DENG, Chen-xi JI, "Process and Quality Control during High Speed Casting of Low Carbon Conventional Slab," Journal of Iron and Steel Research, International Volume 22, Supplement 1, November 2015, Pages 1-9
- [12] S. Itoyama, M. Washio, H. Nishikawa, H. Yamanaka, S. Tanaka, Tetsuya Fujii: Tetsu-to-Hagane Vol. 74 (1988) no. 7 p 1274-1281
- [13] M. Suzuki, H. Mizukami, T. Kitagawa, K. Kawakami, S. Uchida, Y. Komatsu, "Development of a New Mold Oscillation Mode for High-speed Continuous Casting of Steel Slabs," ISIJ International Vol. 31 (1991) No. 3 P 254-261
- [14] Ho Jung Shin, Seon Hyo Kim, Brian G. Thomas, Go Gi Lee, Je Min Park, Joydeep Sengupta, "Measurement And Prediction Of Lubrication, Powder Consumption, And Oscillation Mark Profiles In Ultra-Low Carbon Steel Slabs," ISIJ Int., 2006
- [15] Mills, K.C., Fox, A.B., Thackray, R.P., and Li, Z. "The Performance and Properties of Mould Fluxes," VII Con. On Moten Slags Fluxes and Salts, The South African Institute of Mining and Metallurgy, 2004
- [16] S. Mazumdar, S.K. Ray, "Solidification Control in Continuous Casting of Steel," Sadhana, Vol 26 Parts 1&2, 2001, pp. 179-198
- [17] A.K. Bhattacharya and D. Sambasivam, "Optimization of Oscillation Parameters in Continuous Casting Process of Steel Manufacturing: Genetic Algorithms versus Differential Evolution," Automation Division Tata Steel, Evolutionary Computation, 2009
- [18] J.L. Brendzy, I.A. Bakshi, I.V. Samarasekera, J.K. Brimacombe, "Mould Strand Interaction in Continuous Casting of Steel Billets, Part 2: Lubrication and Oscillation Mark Formation," Ironmaking and Steelmaking 1993, 20: 63-69
- [19] Shin, H.J., G.G. Lee, W.Y. Choi, S.M. Kang, J.H. Park, S.H. Kim and B.G. Thomas, "Effect of Mold Oscillation on Powder Consumption and Hook Formation in Ultra Low Carbon Steel Slabs" AISTech 2004, Nashville, TN, Sep. 15-17, 2004
- [20] B. Arh, F. Tehovnik, J. Burja, F. Vode, "Change of Mould Flux Properties During Continuous Casting of Ferritic Stainless Steel," Metalurgija 56 (2017) 1-2, pp.27-42
- [21] Yao Yunfeng, Li Junxia, Fang Yiming, "Motion Stability Analysis of Non-sinusoidal Oscillation of Mold Driven by Servomotor," Chinese Journal of Mechanical Engineering Vol.28, No. 6, 2015
- [22] Undergrad Consulting Team, advisor by Brian Thomas, "Thin Slab Continuous Casting Mould Taper Design," Mechanical Engineering Lab. 2009
- [23] J. Lagerberg, W. Moonen, D. Van Der Plas y J. Cijssouw, "Mechanical and thermal behaviour of billets in the mould during continuous casting", 13th PTD Conference Proceedings, The Iron and Steel Society of AIME, Warrendale, PA, 1995, pp.201-208
- [24] Zhao-zhen Cai, Miao-yong Zhu, "Thermo-mechanical Behavior of Peritectic Steel Solidifying in Slab Continuous Casting Mold and A New Mold Taper Design," ISIJ International Vol. 53 (2013) No. 10 p. 1818-1827
- [25] L. Zhang, B.G. Thomas, "State of the Art in Evaluation and Control of Steel Cleanliness" ISIJ International Vol. 43 (2003) No. 3, pp.271-291
- [26] B. Thomas, "Modeling of Continuous Casting Defects Related to Mould Fluid Flow," AIST Transactions Vol.3 No.5
- [27] G. G. Stephens, B. Seher, N. Link, A. Sormann, M. Ridolfi, A. de Vito, A. Diaz, L. F. Sancho, J. Barco, R. Kloeppel, "CASTDESMON: Improvement, Control And Prediction Of Cast And Rolled Product Quality By The Development Of An Understanding Of How The Casting Machine Design And Condition Affects Solidification And The Development And Application Of Novel Engineering Monitoring Techniques," Luxembourg: Office for Official Publications of the European Communities (2009)

Determining Retained Austenite Quantity and Composition with Heat Treatment Parameters in SAE52100 Steels

*Ersoy ERİŞİR, Oğuz Gürkan BİLİR, Ahmet Efe GEZMİŞOĞLU**

*Yahya Kaptan Mah.Salkım Söğüt Cad. Şelale Sok. C31 Blok Daire 29 KOCAELI, 41050 Turkey
eerisir@kocaeli.edu.tr, oguzgbilir@gmail.com, efegezmisoglu@gmail.com*

ABSTRACT

Influence of different austenitization conditions on retained austenite quantity and composition investigated on SAE 52100 steel. SAE 52100 steels are being widely used as bearing component regarding to their hardness and wear resistance. Traditional production cycle includes hot rolling, spheroidization, cold rolling, quenching from two phase region and tempering steps. This cycle results with martensitic matrix and undissolved coarse carbides. Coarse carbides maintain adequate wear performance but due to coarse carbides providing appropriate nucleation sites for crack propagation and growth this structure shows poor fatigue behavior. Previous studies showed better carbide size and distribution with experimental two step hardening cycle. This cycle results with considerable increase at retained austenite fraction. It's well known that mechanically unstable retained austenite improves fatigue resistance in this type of steel. Transformation retained austenite to martensite caused by deformation eliminates local stresses and retards crack propagation and growth. XRD studies are carried on to determining retained austenite quantity with various austenitizing conditions. Computational simulations with Thermo-Calc and Dictra are used for predicting carbon concentration gradient of austenite during austenitization which determines retained austenite fraction at the end. A good correlation between XRD data and simulation results was obtained.

Keywords: Bearing Steel, Sae 52100, Retained Austenite, XRD

Assessment of the Austempering Process Parameters to Improve the Wear Resistance of GG-25 Gray Cast Iron

Abdulsamet YILDIRIM*, Yunus TUREN, Hayrettin AHLATCI, Yavuz SUN, Mustafa GUÇLU, Hamza Serhat AYDEMİR, Mehmet Sami TAKVA

*Karabuk University, Department of Metallurgy and Materials Engineering, Turkey
a.samet.yildirim@hotmail.com, yturen@karabuk.edu.tr, hahlatci@karabuk.edu.tr, ysun@karabuk.edu.tr,
mustafa.gcl16@gmail.com, hserhataydemir@gmail.com, mehmetamitakva@mehmetyumak.com

Abstract— In this work, the wear resistance behavior of GG-25 gray cast iron was investigated. Three specimens with different austempering time (120, 90 and 60 minutes) and one specimen, which is not austempering, were used. With this manner it has been tried to examine the effect of the parameters of austempering process on each specimen. Pin-on-disc wear resistance test with one loads (20N) on every specimens has been applied according to of ASTM 99 standards. SEM to observe the microstructures characterized the austempered specimens. In addition, brinell hardness test was applied. With the results of the wear resistance test, as the austempering time increased, wear resistance also increases.

Keywords— Austempering, GG25 cast iron, Wear, Bainite, Hardness.

1. INTRODUCTION

Gray cast iron under class of cast irons. At the present time, gray cast irons are suitable material for wide range of products such as automotive, kitchenware, railway, agrarian materials, heavy industry etc. Therefore, the crankshaft, locomotive wheel, truck air compressors, auto brake discs etc. are used in some structural elements where wear resistance should be good. Ferrite and pearlite phases forming the microstructure of gray cast irons, affected to the mechanical properties of gray cast iron. Austempering treatment was applied to increase wear resistance of gray cast iron increase.

The main purpose of the application of the austempering process is to obtain the bainite phase and reach the wear resistance to the maximum level. In the conventional austempering process, gray cast iron is allowed to stand for a sufficient time (60-120 minutes) until fully austenite matrix is obtained at a temperature range of 850-950 °C. Then, the gray cast iron is cooled rapidly to among 350-450 °C temperature. Conventional austempering process is shown in Figure 1. The austempering process is actualized two stage. In first stage, gray cast iron decompose to austenite, ferrite and high-carbon austenite.

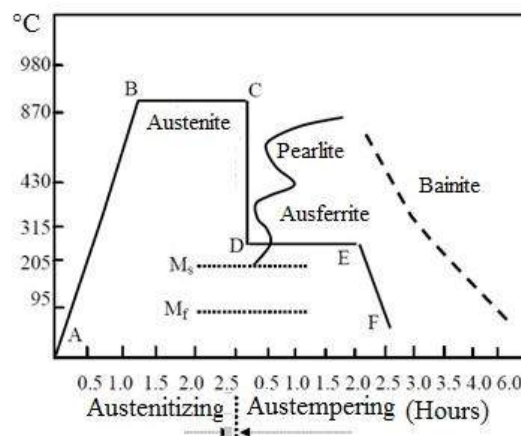


Figure 1. Conventional (single stage) austempering process

Optimum mechanical properties are obtained before the first stage reaction is completed and the second stage reaction is started. The time between of the first stage and the start of the second stage reaction is called the “distance of process”. It can be expanded by the addition of impurity element such as copper, nickel and molybdenum in the distance of process. The product obtained by the austempering process at above 350°C is named as upper ausferrite whereas the product obtained by this austempering process under this temperature is named as lower ausferrite.

Putatunda et al. [1,2] applied the two-stage process differently from other researchers and improved the fracture toughness of the spherical graphite bulk material by increasing the temperature of the salt bath in the austempering process. Prado et al. [3] and Owadi et al. [4] investigated the effects of heat treatment variables on the wear resistances of cast iron. It has been reported that the austempering temperature and the duration of wear resistance of spherical graphite cast irons are a complex function. The effect of the two-step heat treatment process on spheroidal graphite cast iron has not yet been investigated in detail. In this study, the effect of different austempering conditions on wear behavior will be determined and the effect of cooling rate on spherical graphite cast iron tribological behavior will be investigated in the two-stage

austempering process. The compound, heat treatment procedure and microstructure play a key role in the spheroidal graphite cast iron wear behavior [3, 4].

For this purpose, the effect of cooling rate on abrasive wear behaviours of ferritic and pearlitic spheroidal graphite cast iron was investigated in this study in the traditional austempering temperature and gradual austempering procedure.

2. EXPERIMENTAL STUDIES

In this study, ferritic and pearlitic GG-25 gray cast iron alloy was used. The chemical composition of the test samples is given in Table 1.

Table 1. The Chemical Composition of the samples

C%	Si%	Mn%	P%	S%	Cr%	Mo%	Ni%	Nb%
3.194	1.848	0.796	0.107	0.035	0.213	0.238	0.252	0.023
Al%	Cu%	Co%	B%	Ti%	Sn%	V%	W%	Mg%
0.008	0.580	0.061	0.0019	0.025	<0.005	0.020	<0.005	<0.005

The test specimens were first cut to a length of 100 mm and a thickness of 10 mm. It was then brought into cylindrical form with a diameter of 6 mm and a length of 20 mm by machining operations. For microstructure processing, samples were taken into bakelite mould. The microstructure samples were sanded with 240-400-600-800-1000-1200 Mesh SiC sandpaper, respectively, and polished with 6 µm diamond polish, followed by 2% Nital. The microstructures of the samples were examined with a Nikon LV-EPILED optical microscope and transferred to the computer via a CCD camera and software program. Then SEM images were taken.

The samples was prepared for the hardness test. Then, hardness test was placed on the hardness table. It was opened with 3 different spots with a 2.5 inch diamond. Then, the hardness was taken from the width-length limits by traces with the imaging device. Hardness tests was made with BMS brinell hardness device with 187.5 load and ball diameter 2.5 mm. Metal-adhesive wear tests of gray cast iron specimens were carried out on a disk-on-pin device under load of 20N and a cold work tool steel of 1.2379 quality at 8000 meters at a slip rate of 1 m / sec. Weight losses were measured at 2000 meters each. Wear samples on the disc were moved perpendicular to the wear direction so that each new sample was contacted with a non-scratched part of the disc for wear testing.

3. EXPERIMENTAL RESULTS and DISCUSSIONS

3.1 Microstructure Results

According to the results obtained from the microstructures, the sample without the austempering heat treatment has a pearlitic matrix as shown in Fig. 2. In the specimens deposited in the salt bath for 120 minutes, the ferritic structure reached its finest and a much better sub-bainitic structure was obtained here (Figure 3.).

As reported by Putatunda et al. [2] and Bosnjak et al. [5] in their spheroidal graphite cast iron studies, the austenitizing heat treatment in general involves microstructure of spherical ferrite plates and residual austenite in the spherical carbon matrix.

In this study samples with austempering at 400 °C are roughened with needle-like ferrite and the edge thickness is increased. In addition, regions that do not react with the intercellular region are visible, and in eutectic cells, blocky austenite colonies are already present in the microstructure, and these microstructural features appear in Fig. 2. and 3.

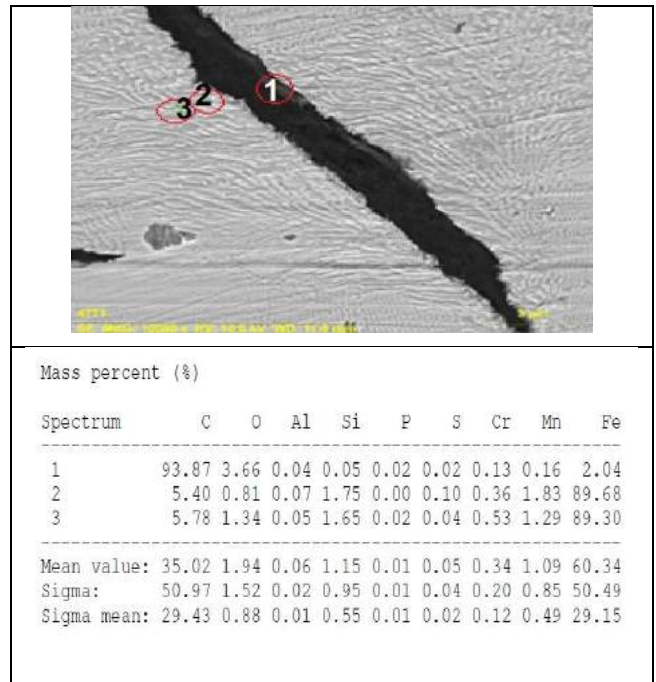


Figure 2. Microstructure and EDX of as Cast GG-25 Sample.

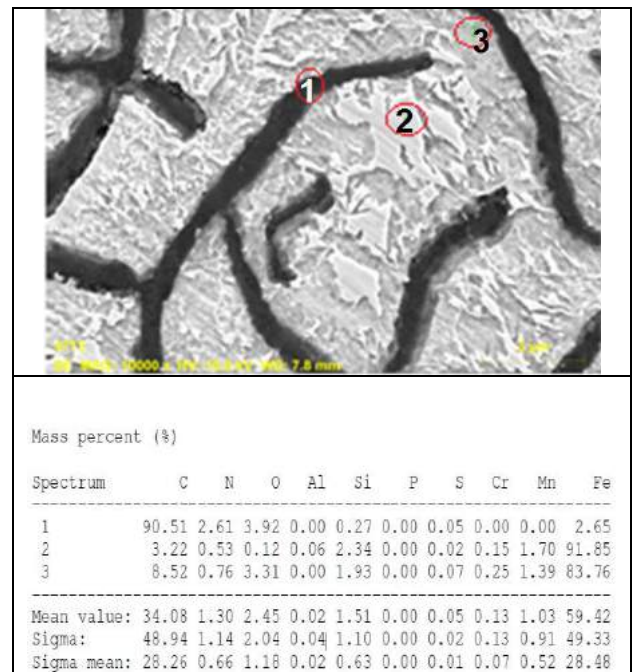


Figure 3. Microstructure and EDX of Austempered GG-25 Sample.

3.2 Hardness Results

The hardness results are shown graphically in Fig. 4. As seen in Figure 4, the hardness of the samples increased as the holding time in the salt bath. The formation of the lower bainitic structure affects hardness. As can be seen in the figure 4, the thinnest ferritic needles, that is, the lower bainite structure, of the sample held in a salt bath for 120 minutes is the hardest material. Therefore, as the lower bainitic structure becomes finer, that is, the lower bainitic structure, the hardness increases.

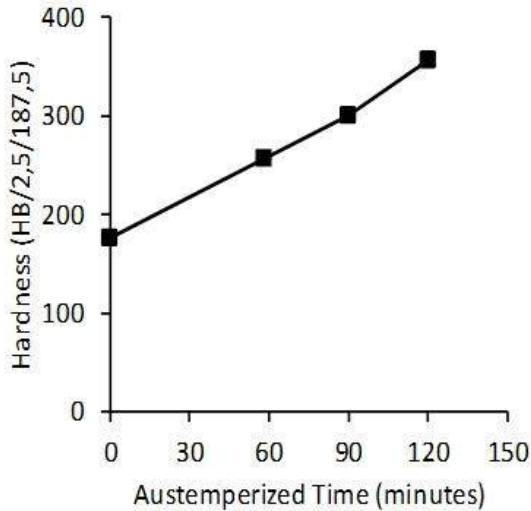


Figure 4. Hardness versus austempering times.

3.3 Wear Results

The weight losses of the GCI samples, depending on the different austempering time applied (60-90-120 minute samples of salt left in the bath) are given in Figure 5. As shown in Figure 5, the weight losses of the samples vary depending on the applied austempering time and 20N load.

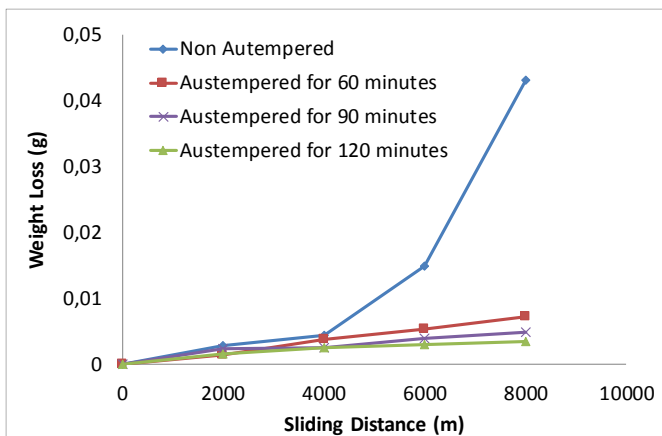


Figure 5. Weight loss changes as function of shear distance of samples as different austempering time

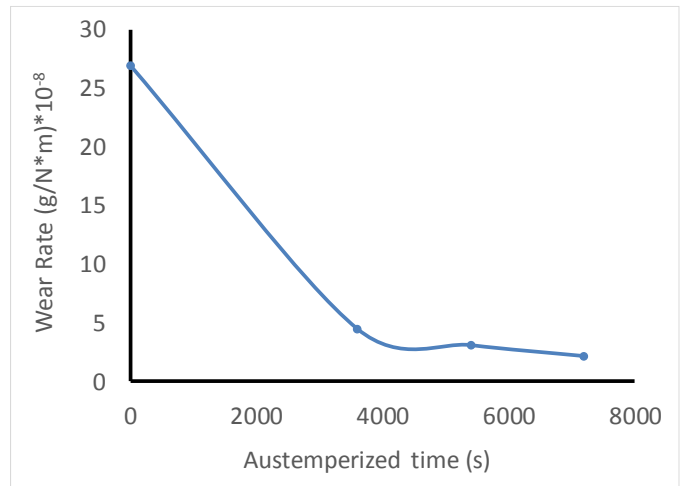


Figure 6. Wear Rate Changes as Function of Austempered Time

Change in the wear rate with regard to austempered time is shown in Fig. 6. As seen in Fig. 6., lower wear rate occurred in the 120 minutes austempered sample than the other. In the literature, the high carbon austenite on the surface is converted to martensite during wear, which means that the surface hardness of GCI increases and consequently the surface hardness increases and the weight loss decreases [5,7]. Shepperson and Allen [8] also pointed out that GCI's excellent wear resistance is due to the ferrite-austenite dual-phase morphology of this material. Because during the wear test of the structure, the austenite shows martensite transformation behavior due to deformation. This transformation does not bring any loss to the hoop of the material as it only occurs on the wear surface [7]. Thus, GCI material exhibits a combination of rare high strength, toughness and abrasion resistance. After the all wear test, seem of the worn surface of the counter disc is given in Fig. 7. Oxidative wear occurs on the counter disc. As a results wear and wear mechanism is approximately mild.



Figure 7. Wear Tracles on of the Counter Disc after Wear Test

4. CONCLUSIONS

1. With the two-stage austempering process, the hardness of the GCI material was increased with respect to the samples without the austempering heat treatment.
2. The samples subjected to the conventional and two-step austempering process suffered less wear damage than the sample without the austempering heat treatment. The least weight loss occurred for 120 minutes on a sample held in a salt bath at 400 ° C. The most weight loss occurred in the sample without the austempering heat treatment.
3. The rate of wear is higher on the non-austempered heat treated sample. In a sample held in a 400 ° C salt bath for 60 minutes, the wear rate is slower than the untreated sample.

REFERENCES

- [1]. Jianghuai Yang, J., Putatunda, S.K., "Improvement in Strength and Toughness of Austempered Ductile Cast Iron by a Novel Two-Step Austempering Process", *Materials and Design* 25, 219–230, 2004.
- [2]. Putatunda, S.K., "Development of Austempered Ductile Cast Iron (ADI) with Simultaneous High Yield Strength and Fracture Toughness by a Novel Two-Step Austempering Process", *Materials Science and Engineering A* 315, 70-80, 2001.
- [3]. Prado, J.M., Oujol, A., Culllell, J., and Tartera, J., "Dry Sliding Wear of Austempered Ductile Iron", *Materials Science and Technology*, 11, 294-298, 1995.
- [4]. Owhadi, A., Hedjazi, J., Davami, P., "Wear Behavior of 1.5Mn Austempered Ductile Iron", *Journal of Materials Science*, 14, 245-250, 1998.
- [5]. Bosnjak, B., Verlinden, B., and Radulovic, B., "Dry Sliding Wear of Low Alloyed Austempered Ductile Iron", *Materials Science and Technology*, 19, 650-656, 2003.
- [6]. Johansson, M., "Austenitic-Bainitic Ductile Iron", *AFS Transactions*, 77-73, 117-122, 1977.
- [7]. Zimba, J., Simbi, D.J., Navara, E., "Austempered Ductile Iron: An Alternative Material for Earth Moving Component", *Cement & Concrete Composites*, 25, 643-649, 2003.
- [8]. Shepperson, S., and Allen, C., "The Abrasive Wear Behavior of Austempered Spheroidal Cast Irons", *Wear*, 121, 271-287, 1988

Effects of Alloying Elements (Mo, Ni and Cu) on the Austemperability of GGG-60 Ductile Cast Iron

Erkan KONCA*, Kazım TUR*, Erkin KOÇ⁺

*Atılım University, Department of Metallurgical and Materials Engineering, Ankara, TURKEY

erkan.konca@atilim.edu.tr, kazim.tur@atilim.edu.tr

⁺Ay Döküm Machine Industry and Trade Inc., Ankara, TURKEY

ekoc@aydokum.com

Abstract—The interest in austempered ductile irons (ADI) is continuously increasing due to their various advantageous properties over conventional ductile irons and some steels. This study aimed at finding the roles of alloying elements, namely Ni, Cu and Mo, on the austemperability of GGG-60 ductile cast iron. Two different sets of GGG-60 (EN-GJS-600-3) ductile iron samples, where one set was alloyed with Ni and Cu and the other set was alloyed with Mo, Ni and Cu, were subjected to austempering treatments at 290-350°C. A custom design heat treatment setup, consisting of two units where the top unit (furnace) serving for austenitizing and the 200-liter capacity bottom unit (stirred NaNO₂-KNO₃ salt bath) serving for isothermal treatment, was used for the experiments. It has been found that austempering treatment at 290°C increased the hardness of the Ni-Cu alloyed GGG-60 sample by about 44% without causing a loss in its ductility. In the case of Mo-Ni-Cu alloyed sample, the increase in hardness due to austempering reached to 80% at the same austempering temperature while some ductility was lost. Here, the microstructural investigation and mechanical testing results of the austempered samples are presented and the role of alloying elements (Mo, Ni, and Cu) on the austemperability of GGG-60 is discussed.

Keywords— ADI, austempering, molybdenum, nickel, copper, alloying, GGG-60, cast iron

I. INTRODUCTION

Austempering is an attractive process as it can turn a cast iron of appropriate composition into a new engineering material with significantly increased strength and usable ductility. Wear resistance and fatigue properties of ADIs are also superior so that they can replace wrought alloys in certain engineering applications [1].

Austempering consists of three stages/steps: i) austenitizing ii) quenching to the isothermal treatment temperature and iii) isothermal treatment usually in the range of 250-450°C [2].

During the austempering of ductile iron, part of the austenite matrix transforms into ferrite and therefore the remaining part of the austenite becomes carbon enriched. The resulting microstructure, known as ausferrite, is responsible for the outstanding mechanical properties of austempered ductile

irons. If the part is kept at the austempering temperature too long then the carbon rich austenite decomposes into ferrite and cementite and mechanical properties deteriorate.

The primary purpose of adding copper, nickel or molybdenum to ADI is to increase the hardenability of the matrix to ensure that the formation of pearlite is avoided during the austempering process [3-15].

The objective of this work is to investigate the relative roles of alloying elements, namely Mo, Ni and Cu, on the austempering behavior of ductile cast iron.

II. EXPERIMENTAL

III. Materials

Two spheroidal graphite cast iron alloys (Alloy O and Alloy M) conformal to GGG-60 were cast in rectangular blocks at Ay Döküm Machine Industry and Trade Inc., Ankara, Turkey. Then these blocks were sliced (**Fig. 1**) in order to get samples for tensile testing after austempering under various conditions. The chemical compositions (in wt. %) of these two cast iron alloys are given in **Table 1**. Basically, Alloy O contains Ni (0.37 %) and Cu (0.52 %) as alloying elements whereas Alloy M contains 0.21 % Mo in addition to Ni (0.21 %) and Cu (0.41 %). As Alloy M is alloyed with Mo and it has reduced Ni content the comparison of its austempering behavior with those of Alloy O should indicate the role of Mo in austemperability.

III. Austempering Setup

The sample to be austempered needs to be quickly cooled from the austenitizing temperature down to the austempering temperature such that there will be no time allowed for any phase transformation to take place between these two temperatures. Use of an agitated salt bath is a very effective method for this purpose. In addition, salt bath provides a suitable medium for isothermal treatment. In this study, a custom design heat treatment setup, shown in **Fig. 2**, was used for the austempering treatments.

This setup contains two units where the top unit serves for austenitizing while the bottom unit serves for isothermal

treatment. The top unit is placed on a motorized tilting stage that allows quick transfer of the samples to the bottom unit through the guides (Fig. 2.a). The bottom unit is a 200 liter

capacity temperature controlled salt bath filled with Petrofer AS135 heat treatment salt (NaNO₂-KNO₃).

TABLE L
CHEMICAL COMPOSITIONS (WT %) OF THE DUCTILE CAST IRON ALLOYS STUDIED

Alloy	C	Si	Mn	P	S	Ni	Cu	Mo	Mg	Cr	Al	Ti	Fe
O	3.64	2.20	0.03	0.039	0.010	0.37	0.52	<0.001	0.05	0.01	0.01	0.004	bal.
M	3.76	2.19	0.14	0.041	0.013	0.21	0.41	0.21	0.04	0.01	0.01	0.008	

All samples were austenitized for 90 minutes at 850°C.

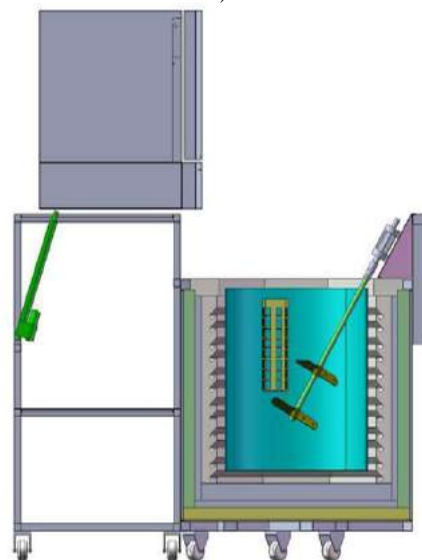


Fig. 24 The photo of some samples before austempering treatment

The salt bath is continuously stirred during operation using a motorized mixer which ensures both efficient heat removal from the sample at the time of quenching and uniform temperature in the bath during the isothermal treatment (Fig. 2.b). A PC connected to the setup records the furnace temperatures of the top and bottom units and those of the thermocouples immersed into the salt bath.



a)



b)

KKK. Austempering Conditions

In this study, the temperature and duration of austenitization for all samples were 850°C and 90 minutes, respectively. Three different austempering temperatures of 350°C, 320°C and 290°C were used for a fixed duration of 90 minutes. Austempering conditions, which are listed in Table 2 and graphically presented in Fig. 3, are in line with previous studies on similar materials [1, 3-6].

TABLE LI
AUSTEMPERING CONDITIONS

	Temperature (°C)	Duration (min)
Exp. 1	350	90
Exp. 2	320	90
Exp. 3	290	90

Fig. 25 a) Custom design heat treatment setup used in this study, b) Top unit (austenitizing) is tilted for quick transfer of the samples to the bottom unit (salt bath – isothermal treatment) through the guides, and c) Computer drawing of the setup showing the impeller and the sample basket in the salt bath

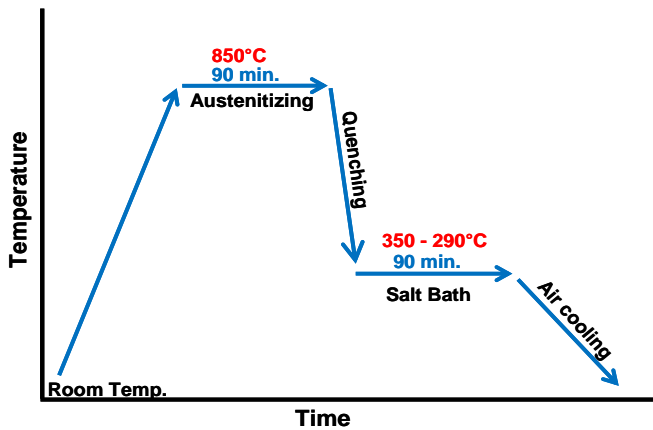


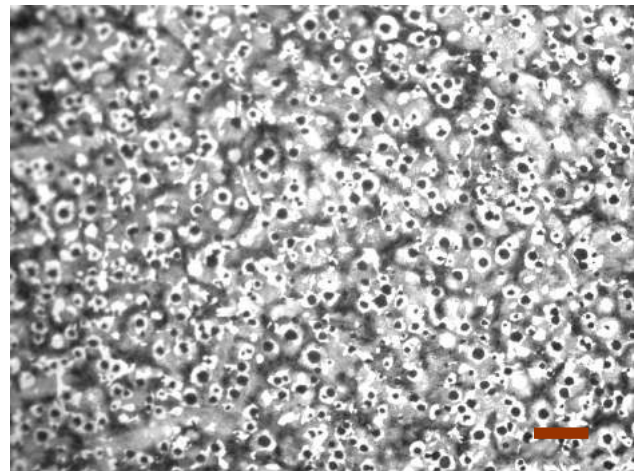
Fig. 26 Graphical representation of the heat treatment conditions

Metallographic examinations were performed on unetched and 2% nital etched sample surfaces using a Nikon LV 150 optical microscope. Brinell hardness measurements (HBW 2.5/187.5) were taken using an EMCO M4U 025 G3 universal hardness testing machine. Tensile testing of the samples were done using Alşa brand tensile testing machine at Ay Döküm.

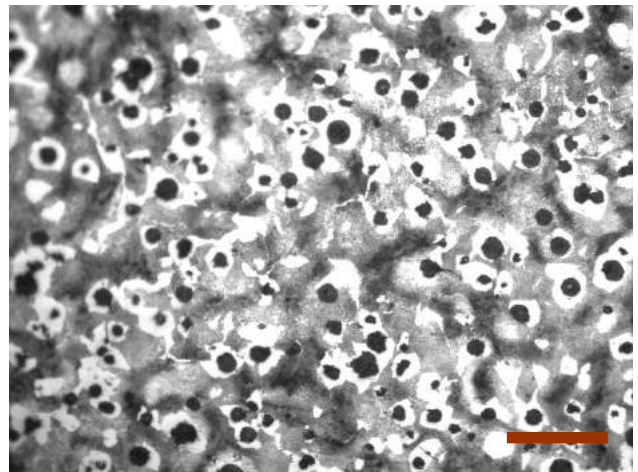
III. RESULTS AND DISCUSSION

LLL. As-Cast Samples

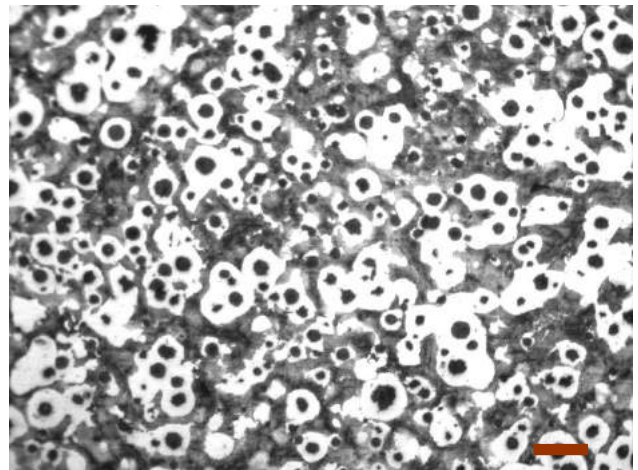
The as-cast microstructures of Alloy O and Alloy M samples are presented in **Fig. 4**. It is seen that both samples have typical bull's eye structures but to different extents. Alloy M has a lower graphite nodule density and more ferritic matrix surrounding them. It is known that Mo has an adverse effect on nodule count [10]. With a higher density of graphite nodules and a more pearlitic microstructure as a matrix, the average as-cast hardness of Alloy O, as measured from cross-section, was 236 HB whereas Alloy M has a hardness of 215 HB. The surface hardness of the samples, as measured after 0.5 mm grinding, were 243 and 202 HB, respectively. Tensile tests showed that the as-cast Alloy O has a tensile strength of 677.4 MPa with 5.7 % EL. whereas Alloy M has a tensile strength of 575.6 MPa with 11.3 % EL.



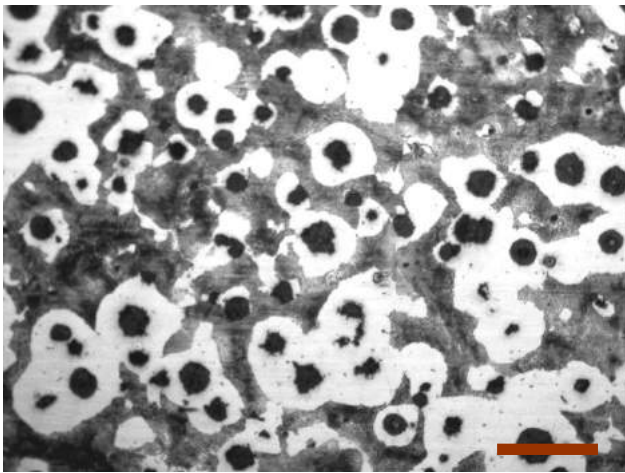
a)



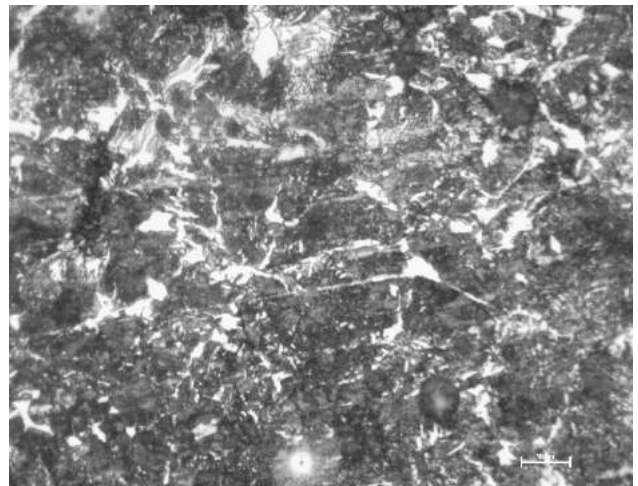
b)



c)



d)

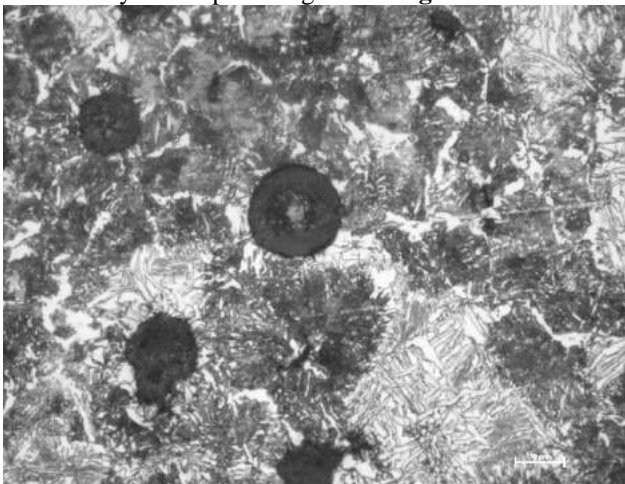


b)

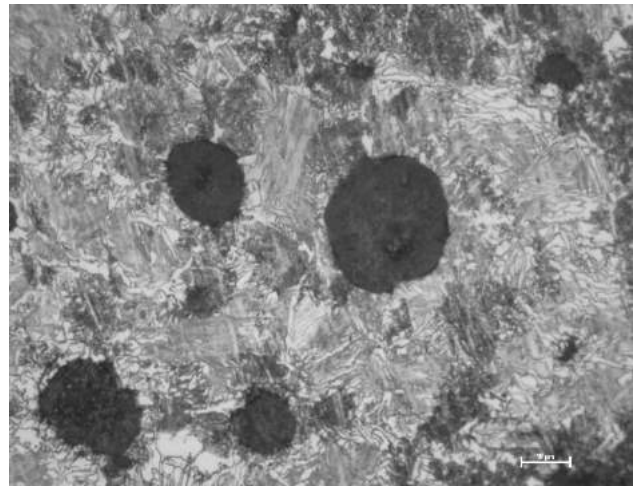
Fig. 27 Optical images of the nital etched as-cast microstructures of a) Alloy O (100x), b) Alloy O (200x), c) Alloy M (100x) and d) Alloy M (200x). (scale bars = 100 μ m).

MMM. Austempered Samples-Microstructural Examination

Optical images of the microstructures of Alloy O samples austempered at 350, 320 and 290°C are given in **Fig. 5** and those of Alloy M samples are given in **Fig. 6**.



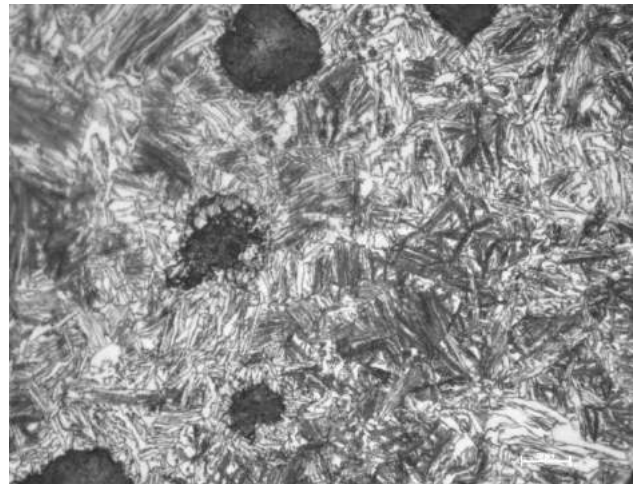
a)



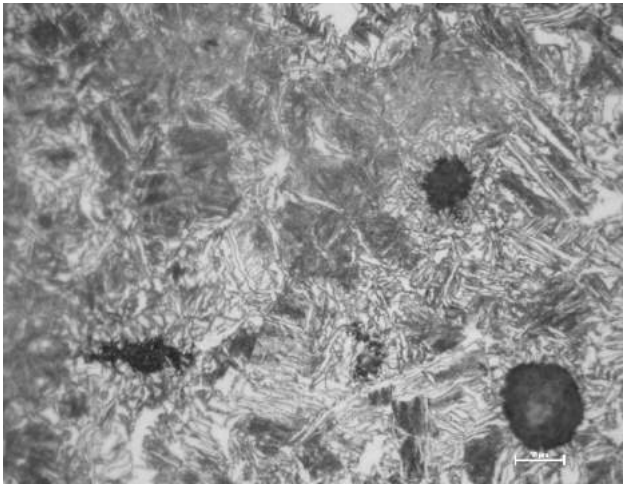
c)

Fig. 28 Optical images of the microstructures of Alloy O samples austempered at a) 350, b) 320 and c) 290°C (1000x, nital etched, scale bars = 10 μ m).

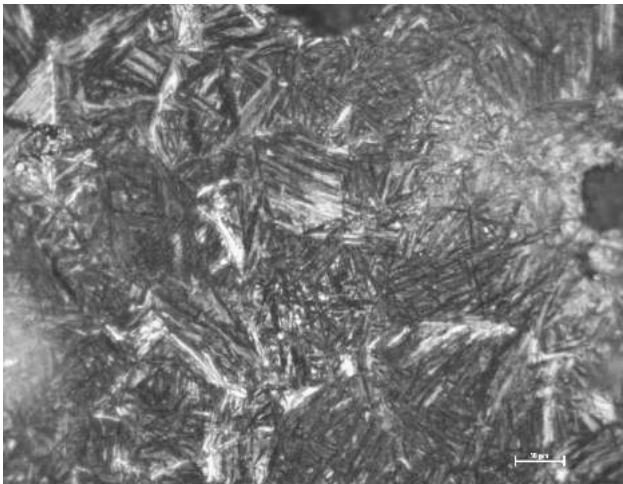
Obviously, as a result of the austempering treatment, the ferritic-pearlitic matrix of the as-cast samples shown in **Fig. 4** transformed into new complex microstructures with mainly ausferritic character.



a)



b)



c)

Fig. 29 Optical images of the microstructures of Alloy M samples austempered at a) 350, b) 320 and c) 290°C (1000x, nital etched, scale bars = 10 µm).

NNN. Austempered Samples-Hardness

The hardness values of the Alloy O and Alloy M samples after austempering are given in **Table 3**. Apparently; the austempering treatment drastically increased the hardness of all samples. The hardness of Alloy O samples were measured as 298.6, 321.8 and 340.7 HB after austempering at 350°C, 320°C and 290°C, respectively. When compared to the as-cast hardness of 236 HB, these values correspond to 26.5%, 36.4%, and 44.4% increase, respectively.

The hardness values of austempered Alloy M samples exhibited even more dramatic increases. The hardness of Alloy M samples were measured as 335.3, 336.0 and 388.5 HB after austempering at 350°C, 320°C and 290°C, respectively. When compared to the as-cast hardness of 215 HB, these values correspond to 55.9%, 56.3%, and 79.9% increase, respectively.

TABLE LII
HARDNESS VALUES OF AS-CAST AND AUSTEMPERED SAMPLES

	Brinell Hardness	
	Alloy O	Alloy M
As-cast	236	215
Exp. 1	298.6	335.3
Exp. 2	321.8	336.0
Exp. 3	340.7	388.5

OOO. Austempered Samples-Tensile Tests

The tensile test results of the austempered Alloy O and Alloy M samples are given in **Table 4**. For the Alloy O samples, the tensile strength values were 992.2, 1017.9 and 1027.2 MPa after austempering at 350°C, 320°C and 290°C, respectively. When compared to the as-cast tensile strength of 677.4 MPa, these values correspond to 46.5%, 50.2%, and 51.6% increase, respectively. Noticeably, the improvements in tensile strengths of the samples were not accompanied by decreases in % EL. On the contrary, % EL. values also improved from 5.7% for the as-cast sample to 5.8%, 6.7% and 6.3% for the samples austempered at 350°C, 320°C and 290°C, respectively.

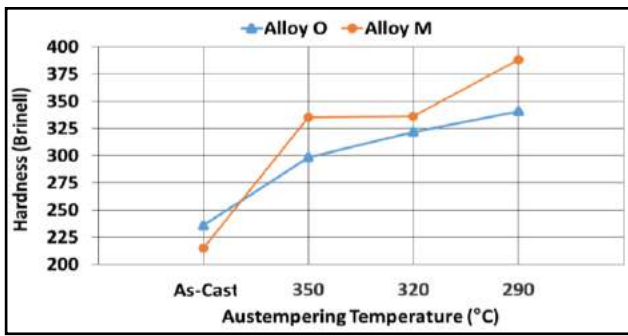
The increases in tensile strength values of the austempered Alloy M samples were even more significant; after austempering at 350°C, 320°C and 290°C, the tensile strengths of the Alloy M samples increased to 1034.5, 1065.3 and 1311.4 MPa, respectively. These values correspond to 79.7%, 85.1%, and 127.8% respective increases when compared to the as-cast tensile strength of 575.6 MPa. On the other hand, the %EL values of the Alloy M samples decreased from 8.3% EL. for austempering at 350°C to 3.5% EL. for austempering at 290°C.

PPP. Effects of Austempering Temperature and Alloying

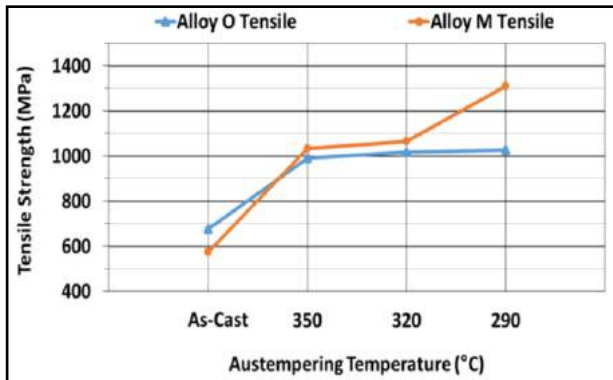
In order to have a clear picture of the results, the variation of hardness, tensile strength and %EL. values of the as-cast and austempered samples are visually presented in **Fig. 7.a, b and c**, respectively. From **Fig. 7.a**, it is evident that Mo has a higher hardenability promoting effect than Ni and Cu. In all three austempering temperatures, Mo alloyed Alloy M with reduced Ni and Cu contents reached higher hardness values than Alloy O which was alloyed only with Ni and Cu.

TABLE LIII
TENSILE TEST RESULTS OF THE AS-CAST AND AUSTEMPERED SAMPLES

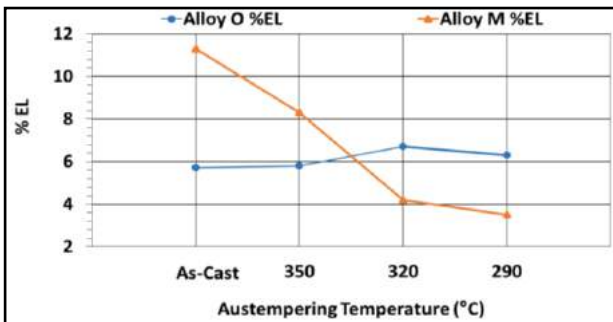
	Alloy O		Alloy M	
	Tensile Strength (MPa)	% EL.	Tensile Strength (MPa)	% EL.
As-cast	677.4	5.7	575.6	11.3
Exp. 1	992.2	5.8	1034.5	8.3
Exp. 2	1017.9	6.7	1065.3	4.2
Exp. 3	1027.2	6.3	1311.4	3.5



a)



b)



c)

Fig. 30 a) Hardness, b) tensile strength and c) %EL. values of the as-cast and austempered samples.

The effect of Mo on hardenability is also reflected in tensile strength values; 1311.4 MPa of tensile strength attained by Alloy M after austempering 290°C is significantly higher than that of Alloy O (1027.2 MPa) treated at the same temperature.

It should be noted that Alloy M austempered at 290°C comfortably meets the strength and ductility requirements of ADI Grade 1200 of European standard EN 1564 [16] and it falls in between ADI Grade 2 and 3 of ASTM A897/A897M-03 [17].

When austempered at 350°C, Alloy M exhibits higher ductility than Alloy O (8.3% EL. vs. 5.8%EL.) for a comparable strength (1034.5 MPa versus 992.2 MPa). These results mean that a wider range of mechanical properties can be attained by Alloy M by choosing the appropriate austempering conditions.

Another observation to point out is that relatively higher Ni and Cu content of Alloy O enables the conservation of its ductility even after austempering at lower temperatures, which is not the case for Alloy M.

IV. CONCLUSIONS

Two sets of ductile cast iron samples, one alloyed with Ni and Cu and the other alloyed with Mo, Ni, and Cu were cast and then subjected to austempering treatments at 350, 320 and 290°C.

When their as-cast states are compared, Mo-Ni-Cu alloyed ductile iron was softer due to its more ferritic microstructure.

After austempering, the Mo-Ni-Cu alloyed ductile iron had higher hardness and tensile strength than Ni-Cu alloyed ductile iron for all three austempering temperatures proving the better performance of Mo as a strengthener.

The ductility of the Mo-Ni-Cu alloyed ductile iron decreases as the austempering temperature is lowered. On the other hand, the ductility of Ni-Cu alloyed ductile iron slightly increases rather than decreasing with decreasing the austempering temperature.

V. ACKNOWLEDGMENT

The authors are thankful to Mr.Özdemir Dinç for his help with the metallographic sample preparation.

VI. REFERENCES

- [1] Thein TUN and Kay Thi LWIN, *Optimizing the Microstructure and Mechanical Properties of Austempered Ductile Iron for Automobile Differential Gear*, Journal of Metals, Materials and Minerals, vol.18 No.2 pp.199-205, 2008
- [2] P. A. Blackmore and R. A. Harding, *The Effects of Metallurgical Process Variables on the Properties of Austempered Ductile Irons*, Journal of Heat Treating, v. 3, n.4, pp. 310-325, 1984
- [3] S. Yazdani and R. Elliott, *Influence of molybdenum on austempering behaviour of ductile iron Part 1 – Austempering kinetics and mechanical properties of ductile iron containing 0.13%Mo*, Materials Science and Technology, vol. 15, pp. 531-540, May 1999
- [4] S. Yazdani and R. Elliott, *Influence of molybdenum on austempering behaviour of ductile iron Part 2 – Influence of austenitising temperature on austempering kinetics, mechanical properties, and hardenability of ductile iron containing 0.13%Mo*, Materials Science and Technology, vol. 15, pp. 541-546, May 1999
- [5] S. Yazdani and R. Elliott, *Influence of molybdenum on austempering behaviour of ductile iron Part 3 – Austempering kinetics, mechanical properties, and hardenability of ductile iron containing 0.25%Mo*, Materials Science and Technology, vol. 15, pp. 885-895, August 1999
- [6] S. Yazdani and R. Elliott, *Influence of molybdenum on austempering behaviour of ductile iron Part 4 – Austempering behaviour of ductile iron containing 0.45%Mo*, Materials Science and Technology, vol. 15, pp. 896-902, August 1999
- [7] D.S.Padan, *Microalloying in Austempered Ductile Iron (ADI)*, AFS Proceedings, 12-019, 2012
- [8] C. Akça, *Effect of Alloying Elements on the Austenite-Martensite Transformation in Austempered Spheroidal Graphite Cast Iron (in Turkish)*, PhD Thesis, Yıldız Technical University, 2005
- [9] B.Y. Lin, E.T.Chen and T.S. Lei, *The Effect of Alloy Elements on the Microstructure and Properties of Austempered Ductile Irons*, Scripta Metallurgica et Materialia, vol. 32, no. 9, pp. 1363-1367, 1995
- [10] Hernandez et. al., *The Effect of Molybdenum on the Microstructure of Nodular Iron*, European Scientific Journal, December 2015 edition vol.11, No.36, pp. 377-388, 2015
- [11] U. Batra, S. Ray, and S.R. Prabhakar, *The Influence of Nickel and Copper on the Austempering of Ductile Iron*, Journal of Materials Engineering and Performance, v.13 pp.64-68, 2004

3rd Iron and Steel Symposium(UDCS'17)3-5April 2017 Karabuk-TURKEY

- [12] Y. Mi, *Effect of Cu, Mo, Si on the Content of Retained Austenite of Austempered Ductile Iron*, Scripta Metallurgica et Materialia, Vol. 32, No. 9, pp. 1313-1317, 1995
- [13] K-H Lee, Y-W Park, *Effects of Molybdenum on the Microstructure of Austempered Ductile Iron*, Journal of Korea Foundry Society, (in Korean). Feb, 14(1), pp. 35-44, 1994
- [14] Ductile Iron Society, *Molybdenum in Ductile Iron*, Hot Topics Issue #1, 2007
- [15] P. Saal, L. Meier, X. Li, M. Hofmann, M. Hoelzel, J.N. Wagner, W. Volk, *In Situ Study of the Influence of Nickel on the Phase Transformation Kinetics in Austempered Ductile Iron*, Metallurgical and Materials Transactions A, v 47A, Feb., 2016, 661-671
- [16] EN 1564:2011 *Founding - Ausferritic spheroidal graphite cast irons*
- [17] ASTM A897 / A897M – 03 *Standard Specification for Austempered Ductile Iron Castings*

Use of Submerged Arc Welding Technique in Iron & Steel Industry for Coating

Mehmet Fatih Kahraman^{a,b}, Sabri Öztürk^a

*a, Department of Mechanical Engineering, Abant İzzet Baysal University,
Golkooy Campus, 14280 Bolu, Turkey*

mfkahraman@ibu.edu.tr, sabriozturk@ibu.edu.tr

*b, Department of Mechanical Engineering, Sakarya University
Serdivan, Sakarya, Turkey,*

mfkahraman@ibu.edu.tr

Abstract— In this study, submerged arc welding (SAW) method is applied for coating. Experimental results showed that Stellite-6 coating material was suitable for shafts and bearings. Stellite-6 materials can lead to improving the surface features of the shafts used in iron and steel plants. Also Stellite-6 coating materials have good resistance to impact. After coating of the shafts by using Stellite-6 materials, it was observed that the hardness of the shafts increases nearly 250 pct. Coating and machining operations of the used shafts is more economical in iron and steel plants.

Keywords— Submerged Arc Welding, Stellite-6, Coating, Iron and Steel, Hardness

I. INTRODUCTION

Steel is the crucial material of the business world. Manufacturing steel and iron have affected wholly economic and infrastructural growth. Turkey is among the top ten countries producing crude steel in the world, showing Turkey's achievement in iron and steel production. In Turkey, iron and steel production reached 31.5 million tons in 2015 [1,2]. In production line of the iron and steel process many shafts are used, specialists focused on how to carry out use of shafts economically. Because new shafts are expensive to buy, submerged arc welding is preferred for coating.

Submerged arc welding (SAW) can be used for surface alloying and coating [3,4,5]. Coating produced by this method is widely used for spare parts in continuous casting and both hot and cold rolling to reduce the expenditure.

Ceramic coatings produced are used in many industries to protect the components against corrosion, wear and erosion resistance [6–9]. The coating method applied on the materials surface can reduce the production cost by ten times [10]. Their hardness of alloys based on Co remain constant and obtain perfect thermal fatigue, wear and oxidation endurance at high temperatures [11,12]. Birol, Y. [13] investigated the effect of Stellite-6 coating on the thermal fatigue performance of the hot work tool steel. Stellite-6 coatings offer excellent thermal fatigue.

In this study, the life of the shafts produced by SAW was investigated and the effects of coating materials on the surface

hardness were utilized. This work shows that coated of Stellite-6 with SAW is a feasible method for obtaining a more shaft life.

II. MATERIALS AND EQUIPMENTS

The coating material used in the experiments is a Stellite-6 cobalt base alloy, the chemical composition of the coating material is summarized in Table 1. This material has resistant to wear and corrosion and retain these properties at high temperatures. In addition, it has good resistance to impact and cavitation erosion and can be used at pump shafts and bearings. Hardness of the coated materials is measured using a Krautkramer ultrasonic hardness measurement device. Measurement force is 10 Kgf and a square-based diamond pyramid is 136° angle. The conversion into HB (Brinell Hardness) is made according to DIN 50150 on the basis of the HV (Vickers hardness) values. Coated and manufactured shafts were compared in a slab-casting machine having one strand.

TABLE LIV
CHEMICAL COMPOSITION OF STELLITE-6 (COATING)[WT.-%]

Grade	Base	C	Cr	W
Stellite-6	Co	1	30	5,5

III. RESULTS AND DISCUSSION

Stellite-6 is commonly carried out for coating material applications. Stellite-6 is a suitable option, in order to prevent impact and cavitation erosion. It is employed in diverse surface hardening processes because it improves the mechanical properties of material as well as it may be applied with carbide tools. Hard super alloy's machinability is generally uneasy. Therefore, machinability of Stellite-6 is going to be more worthy with rising apply of the alloy for welding electrodes in the next decades. For the purpose of preventing wear resistance, Stellite-6 can be applied on material's surface by welding application.

Fig. 1 demonstrates method of submerged arc welding application. For the purpose of removing atmospheric contamination, the molten weld and arc zone are covered below a bed of granulated flux. The weld metal area may be cleaned by the flux as well as the flux causes to change the weld metal area's chemical constituents. Therefore, the submerged arc welding can be economically used in many other areas such as a coating. The manufactured weld zones have not only a uniform structure but also it has large amount of impact resistance. For this reason, this may result in developing the surface quality and increase the ring life.

Hardness values of the shafts were measured with an ultrasonic hardness measurement device. Before the machining of the base material's hardness value was 125 HB and coated material hardness was measured as 423 HB.



Fig. 31 Shaft coated with submerged arc welding method

Submerged arc welding (SAW) method creates heat produced by an electric arc generated between a continuously fed bare wire electrode and the work piece.

Increasing the rate of protection of welding zone from atmospheric gas contamination, the quality of the welding connection will improve.

Due to the deposition of welding metal in the welding zone, the feeding of the continuous welding metal from spool and the operation of the system under the 100% duty cycle, these make submerged arc welding (SAW) method has great productiveness.

Because of its high depth of penetration, it is possible to weld thick materials.

SAW method is applied without sparks, smoke and spatter, there will be not seen stress accumulation in the welding zone. Therefore, smooth weld bead is manufactured.

There are two crucial features of the weld bead; these are geometry of bead and penetration size are affected by dimension of electrode for a given welding current setting. Preventing the weld pool in SAW application is supplied by molten stratum of flux covering to the weld pool.

Lifetimes for the uncoated shafts reached values between 1500 and 2000 casts, average value used in the experimental results was 1750 casts.

Fig. 2 illustrates the coated shafts used in the continuous casting after 2485 casts. Scales can be seen on the shaft surfaces. Life of the coated shaft increases of up to 43 %, while average life of the manufactured (uncoated) shafts is 1750 cast. The high performance of the coated shafts can be attributed to the superior oxidation resistance of Stellite-6 alloy and with high thermal fatigue resistance [13].



Fig. 32 The coated shaft after use

Based on the obtained results, it is concluded from the tests that the performance of the Stellite-6 coated shafts is much better with respect to the uncoated shafts.

IV. CONCLUSION

An experimental study on coating with Stellite-6 materials has been carried out under continuous casting machine. Number of the casts between two shifts was accepted as the lifetime of the shafts. Examinations demonstrated that coating affected the life of the shafts. The lifetimes of coated shafts were longer than those of the uncoated ones. 43 pct. increases in service use was observed after coating of the shafts. Life of the shafts can be increased coating with Stellite-6 materials.

V. REFERENCES

- [1] <http://www.dunyaekonomi.com>
- [2] <http://www.dcu.org.tr>
- [3] M. F. Buchely, J. C. Gutierrez, L. M. Leon, and A. Toro, "The effect of microstructure on abrasive wear of hardfacing alloys." *Wear*, vol. 259, pp. 52-61, 2005.
- [4] R. A. Jeshvaghani, M. Jaberzadeh, H. Zohdi, and M. Shamanian, "Microstructural study and wear behavior of ductile iron surface alloyed by Inconel 617" *Materials & Design*, 54, pp. 491-497, 2014.
- [5] S. Ozturk, "Machinability of stellite-6 catings with ceramic inserts and tungsten carbide tools," *Arabian Journal for Science and Engineering*, 39 10, 7375-7383, 2014.
- [6] H. Herman, C. C. Berndt, H. Wang, "Plasma sprayed ceramic coatings," in: J.B. Wachtman, R. A. Haber (Eds), *Ceramic Films and Coatings*, Noyes Publications, New Jersey, 1993.
- [7] M. Shell. *The Science and Engineering of Termal Spray Coatings*, Wiley, New York, 1995.
- [8] T. S. Sidhu, D. Puri, S. Prakash, "Mechanical and metallurgical properties of plasma sprayed and laser remelted Ni-20Cr and Stellite-6 coatings," *Journal of Materials Processing Technology*, 159,3; pp. 347-355, 2005.
- [9] T. S. Sidhu, S. Prakash, R. D. Agrawal, "Studies of the metallurgical and mechanical properties of high velocity oxy-fuel sprayed stellite-6 coating on Ni- and Fe- based superalloys," *Surface and Coating Technology*, vol. 201.1: pp.273-281, 2006.
- [10] Matthews, R. J. Artley, & P. Holiday, "The future's bright for surface

- [11] engineering.” *Materials world*, 6(6), pp. 346-347, 1998.
- [12] J.C. Shin, J.M. Doh, J.K. Yoon, D.K. Lee, J.S. Kim, *Surf. Coat. Technol.* Vol. 166, pp 117 – 126, 2003.
- [13] J. C., Shin, J. M. Doh, J. K. Yoon, D. Y. Lee, & J. S. Kim, “Effect of molybdenum on the microstructure and wear resistance of cobalt-base Stellite hardfacing alloys.” *Surface and Coatings Technology*, vol. 166(2), pp 117-126, 2003.
- [14] I Radu., D. Y., Li, & R. Llewellyn, “Tribological behavior of Stellite 21 modified with yttrium.” *Wear*, 257(11), pp. 1154-1166. 2004.
- [15] Y. Birol, “Thermal fatigue testing of Stellite 6-coated hot work tool steel” *Materials Science and Engineering: A*, 527(21), pp. 6091-6097, 2010.

Effect of friction stir process on mechanical properties of DP600 steel

Onur SARAY*, İmren Ö. YILMAZ*+, Mümün YILMAZ*

*Bursa Technical University Department of Mechanical Engineering Bursa Turkey
onur.saray@btu.edu.tr,mumunyilmaz89@gmail.com

+ Beyçelik Gestamp R&D Center Bursa Turkey
imrenyilmaz@beycelikgestamp.com.tr

Abstract— Friction stir processing (FSP) is a thermo-mechanical process in which severe plastic strains are imposed by aid of transverse movement of non-consumable rotating tool inserted into the material. Tool friction also increases temperature of the local deformation region. This leads occurrence of the dynamic recrystallization leading to extensive grain refinement and consequently improvement of strength without a considerable loss of ductility. This improvement may be beneficial to light-weighting of the automobile bodies. However, this also requires application of FSP to the thin metal sheets. On this point of view, current study mainly focuses on FSP of 1.1 mm thick DP600 steel which is widely used in body-in-white applications. SEM investigations revealed that FSP caused both grain refinement and morphological changes. Micro-hardness mapping of the FSP region revealed nearly two fold increase in hardness. Similar improvements were also detected tension tests. By selection of proper FSP parameters, yield strength and UTS of the steel was reached to about 720 MPa and 1050 MPa respectively. This strength improvement was achieved with a considerably high uniform elongation of 7%.

Keywords— Friction stir processing, DP600, Strengthening, Grain refinement

I. INTRODUCTION

Establishing weight reduction accompanied with superior mechanical strength and enhanced crash safety is one of the most important design strategy of the modern automotive industry. This strategy leads to the increasing adoption of high-strength materials for automobile body parts. Advanced high strength steels (AHSS) are mainly developed to satisfy high strength material needs of the automotive industry. Currently, dual-phase (DP)-steels in various level of strength is one of the most widely used members of this steel family. DP steel also provides great advantage due to their adequate formability. DP steel mainly characterized with their unique microstructure that consists of ferrite and martensite phases. Morphologically, martensite phases are mainly distributed within the ferrite matrix like small islands. Hence, volume fraction of the martensite phase mainly, directly related to the strength of the

DP steel. DP steels are annealed by holding the strip in the $\alpha+\gamma$ (ferrite+austenite) temperature region for a set period of time and then quenched so that the austenite is transformed into martensite and the ferrite remains on cooling. The amount of martensite in the steel can be controlled to determine the strength level ranging from 350 to 1000 MPa. [4].

Friction stir processing (FSP) is a relatively new solid-state process to be used to microstructural modification of the metallic materials. This process is mainly developed based on principles of friction stir welding, in which solid state joining of the plates are established by synergetic effects of severe plastic deformation and frictional heat. In the FSW process solid non-consumable tool is inserted into the materials to be joined and transferred through joining line while it is rotated. During this movement, friction between the tool surface contacting to the surrounding material increases temperature of the work piece to range of about 0.5—0.8 Tm. This leads to softens and/or plasticizes a column of material. FSP uses the same methodology as friction stir welding (FSW), but FSP is used to modify the local microstructure and does not join metals together. A schematic illustration of FSP is shown in Fig. 1.

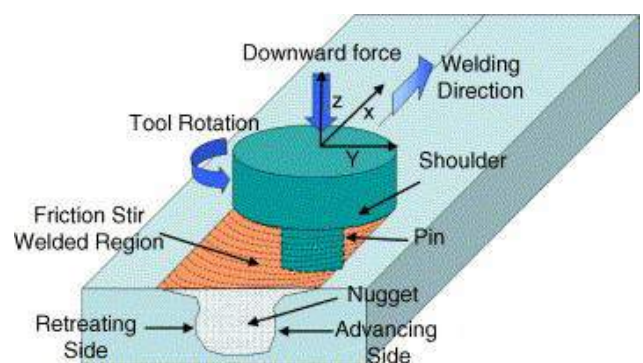


Fig. 33 Schematic representation of FSP [1, 2]

It has been well documented that, FSP may be considered as an effective and useful tool for microstructural modification and grain refinement. Generally, combined effects of the high

level of deformation and thermal input cause occurrence of dynamic recrystallization. Hence, resultant microstructure of a FSP processed metal mainly consisted of equiaxed fine grains [3-11]. It is also well known that the stir zone (SZ) consists of such fine and equiaxed grains exhibit superior mechanical properties like enhanced hardness and wear resistant compared to that of the coarse grained counterparts [12-14].

To date, research attempts have been focused mainly on face-centered-cubic (fcc) metals, namely on aluminium alloys [3]. In contrast, considerably less attention has been given to body-centered-cubic steels, despite their significant industrial importance. There are a few investigations conducted on the FSP of different steels such as stainless steels [10, 15-17], IF-steels [5, 18], carbon steels [4, 7, 8, 19-21], HSLA steels [22] and tool steels [6, 11, 23]. Considering these publications, FSP was mainly applied to thick plates in the thickness range of 1.5-10 mm or bulk materials. Also, effect of FSP on the structure and mechanical properties of the Advances High Strength steel (AHSS) have not been investigated. On the other hand, considering needs of the automotive industry application of FSP on the thin AHSS sheets may be noteworthy. On this point of view current study mainly concentrated on application of the FSP to thin DP600 steel to show effect of the FSP on the structural properties and mechanical performance of the dual phase (DP) steels.

II. EXPERIMENTAL PROCEDURE

The DP-600 steel with the composition of Fe-0.14C-0.5Mn-0.1P-0.22Ti-0.015Al-0.09Nb-0.0015S-0.5Si-1.0Cr (in wt.%) was used for this study. As DP-steels are widely used in forming of structural parts of automobile body parts, a relevant thickness of 1.1 mm was selected to investigate possibility of application of the FSP to the thin AHSS. Work-pieces for FSP was blanked and cleaned with acetone. A WC toll with a shoulder and pin diameter of 14 mm and 5 mm was utilized for the FSP processes. A conical pin with a length of 0.9 mm was used to increase depth of the microstructural modification that aimed to obtain after the FSP processes. Tool rotation speed and transfer speed was selected as 1000 rpm and 1.6 mm/s respectively. Tool shoulder tilt angle was set at 2.5° . Rotation speed, transfer speed and shoulder-pin penetration depth was kept constant using PLC driven servo electric motors and precise position sensors. These parameters were mainly determined on the results of the several experimental trials. All FSP processes were performed using a specially designed friction stir processing/welding test rig with advanced control units and 7.5 kW mechanical power (Fig. 2).

Microstructure of the as-received DP-steel was examined with optical microscope. Microstructural evolution after processing of the DP steel was examined with scanning electron microscopy. Samples for this examinations were extracted from the same workpiece as shown in Fig. 2 and prepared with standard techniques and etched with %5 Nital solution for 10 s. Zeiss Evo 50 SEM was operated at 15 kV for the microstructural examination of the FSPed samples.



Fig. 2. Photograph of Friction stir processing/welding test rig used in the study.

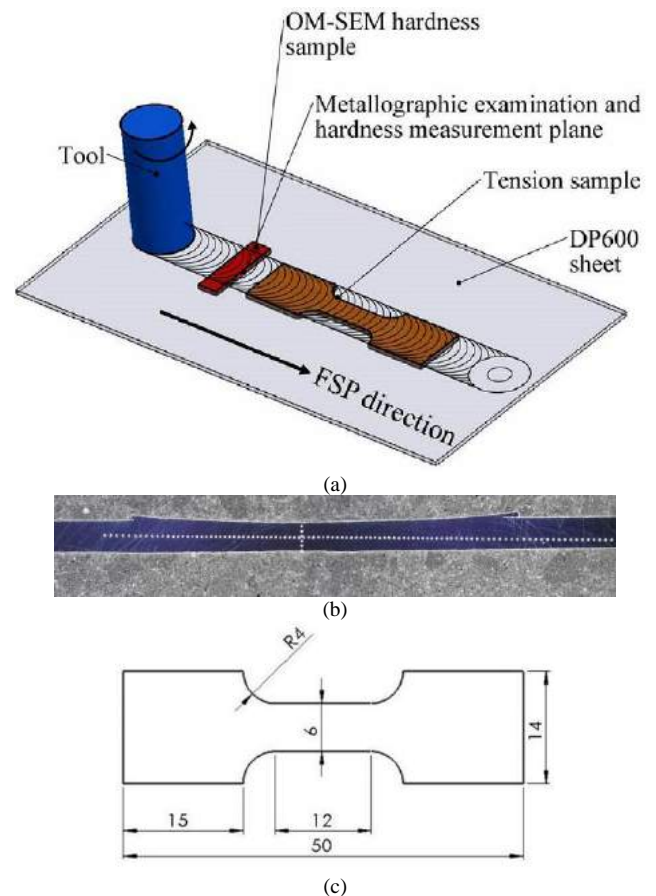


Fig. 3. (a) Schematic representation of the FSP process and location of the microstructure investigation, hardness and tension samples (b) Location of hardness measurements performed on the cross-section of the FSP processed DP-600 sheet (c) Dimensions of the tension test specimen.

Mechanical properties of the samples before and after FSP were determined with hardness measurements and tensile test using dog-bone shaped specimens. To determine variation of the hardness within the processed regions, vertical and horizontal scans were performed at the geometrical symmetry axis of the sample (Fig 2(b)). Hardness measurements were performed using a Vickers micro-hardness tester under a load of 0.5 N and for 10 s dwell time. Mechanical properties of the samples before and after FSP were determined with tensile test using dog-bone shaped specimens. Dimensions of the samples were selected to be 1.0 mm X 6 mm 12 mm (Fig. 2(c)). The test was performed using a SHIMATZU electro-mechanic tension test machine at a strain rate of 0.01 s⁻¹. Flow curves and basic mechanical properties like yield strength, ultimate tensile strength, uniform elongation and elongation to failure were determined as mean values of the results obtained from at least three companion specimens.

III. RESULTS AND DISCUSSION

3.3. Microstructural evolution

Microstructure of the as-received DP-600 steel consists of ferrite and martensite phases (Fig. 4). Morphologically, ferrite phase grains are mainly equiaxed with a mean grain size $15 \pm 5 \mu\text{m}$ (Fig. 4(a)). Size distribution of the ferrite grains were somehow homogeneous but finer grains in the size range of 5-10 μm were also evident in the microstructure (Fig 4(b)). Very fine martensite phase grains (particles) are placed at the vicinity of the ferrite phase grain boundaries constituting nearly continuous network through the structure (Fig. 4(a)-(b)). In other words, as-received microstructure of the as-received DP steel can be described as homogeneously distributed network of a hard martensite phase particles within ferrite matrix (Fig. 4(a)-(b)).

Single pass friction stir processing strongly affected as-received microstructure of the DP-600 steel. Generally, severe plastic deformation imposed by the FSP tool is found to be effective on an area with a depth and width nearly equal to the sheet thickness and shoulder diameter (Fig. 5(a)) However, variations in the plastic deformation imposed to the sample and consequently heat generation during the process formed three deformation regions namely stir zone (SZ), thermo-mechanically affected zone (TMAZ) and heat affected zone (HAZ). In SZ FSP process mainly reorganized microstructure of the DP steel (Fig. 5(b)-(c)). From Fig. 5 (b)-(c), it is obvious that martensite phase become more bulky and ferrite grains are somehow refined. It is also obvious that, ferrite grain size was not homogeneous through the microstructure. As can be understood from Fig. 5(b) fine ferrite grains with a size of 4-5 μm are formed in the microstructure of DP-steel. Also coarse ferrite grains with a size of about 20 μm exist in the SZ (Fig. 5(c)). The stir zone is subjected to the greatest strain and strain rates, as well as the highest temperatures. This combination of parameters apparently results in formation of refined ferrite grains via the dynamic recrystallization (DRX). However, existence of coarser ferrite grains may also indicate occurrence

of the static recrystallization due to the extensive heat generation and high deformation temperature reaching to about 850-950°C which may lead to coarsen of the refined microstructure.

A transition region between the SZ and the HAZ known as thermo-mechanically affected zone (TMAZ) reflect similar microstructural properties with that of the SZ zone. Mainly bulky martensite phase along with refined ferrite phase formed in the TMAZ. Also ferrite phase morphology seems to be somehow elongated (Fig 5(d)). By the end of the TMAZ, grain morphology gradually became alike with that of as-received material. However, grain size of the ferrite phase somehow coarsened compared to that of the as-received steel. This may be occurred due to deactivation of the dynamic recrystallization at regions farther from the stir pin. These regions are not deformed as effective as the SZ and TMAZ zones. However, heat generated by the shoulder and pin frictions rapidly transfer in the surrounding material. This leads HAZ to experience a thermal cycle, but not undergo any plastic deformation [1].

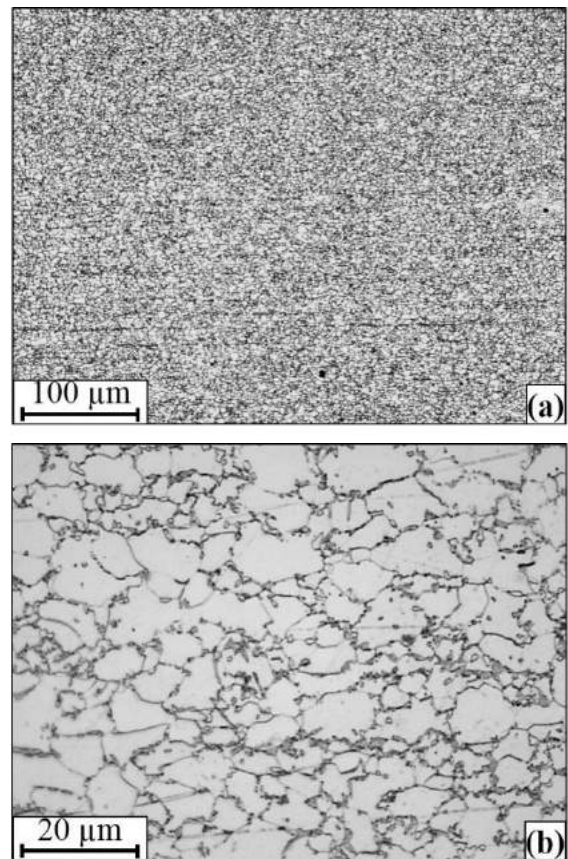


Fig. 4. Microstructure of as received DP-600 steel (a) low magnification, (b) High magnification.

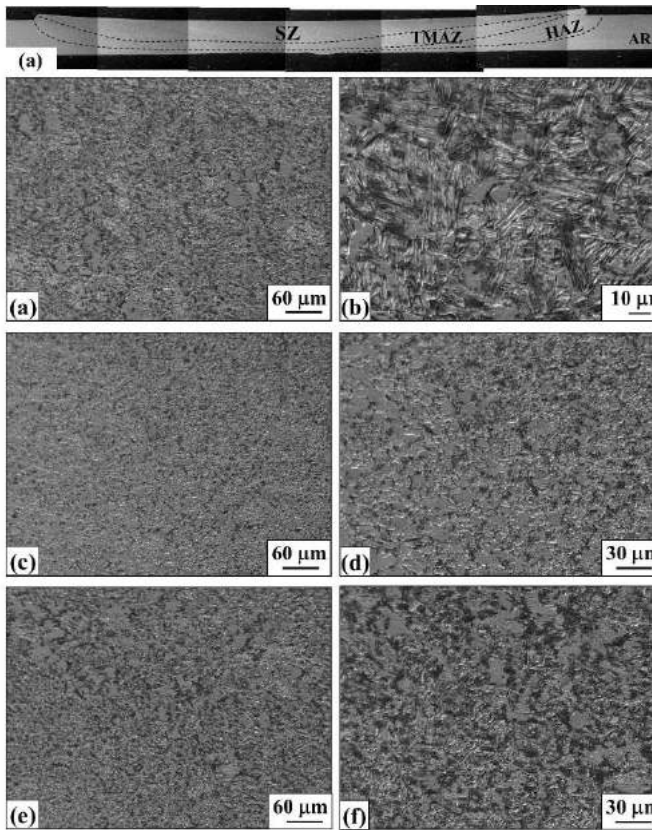


Fig. 5. Microstructure of DP-600 steel after FSP (a)-(b) Stir zone, (c)-(d) Thermo-mechanically affected zone, (e)-(f) Heat affected zone.

RRR. Mechanical properties

Hardness evolution of DP-600 steel after FSP is represented in Fig. 6 (a)-(b). Generally, FSP considerably enhanced hardness of the steel. As can be seen from the horizontal scan profile (Fig. 6(a)), hardness of the DP-600 steel sharply increase within the thermo-mechanically affected zone and reached to its peak value at the SZ. At this zone hardness of DP steel was measured as 290 ± 20 Hv0.5 which is 1.6 fold higher than that of the as-received counterpart. Also, such a considerable hardness enhancement is established in a large deformation are within a width of about 8 mm (Fig. 6(a)). It is evident from the horizontal scan profile that, enhanced hardness values are more or less symmetrical by the tool axis. However, hardness values measured at the HAZ are slightly lower than that of the as-received steel. As can be seen from Fig. 6(a), hardness values slightly decreased to about 170 Hv0.5 at the HAZ region through a distance of about 2 mm. Vertical hardness scan of the FSP processed seel also revealed similar trend of hardness enhancement (Fig. 6(b)). As can be understood from Fig. 6(b), peak hardness values were measured at the surface contacting to tool shoulder and hardness of the steel and remained stable through a depth of about 0.6 mm. Beyond this depth, however, hardness values sharply decreased to the levels of the as-received steel (Fig. 6(b)). Such increase in hardness of the SZ may be considered as an expected result of the microstructural evolution including both

grain refinement of ferrite phase and morphological alteration of the martensite phase. In accordance to the microstructural examination (Fig. 5), transformation of the martensite phase from uniformly distributed fine particles to more bulky grains may be effective on the local hardness enhancement. Also, an increase in dislocation density induced by intensive plastic deformation is may also be effective in the enhancement of hardness [1–6]. Variations in hardness values inside the SZ and TMAZ may be related to the variations in deformation temperature, strain state and inhomogeneous cooling leading to formation of heat flux within the deformation region. [2-6].

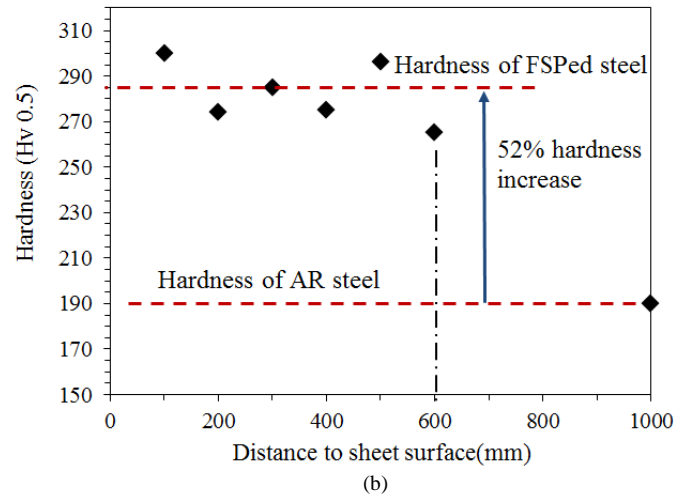
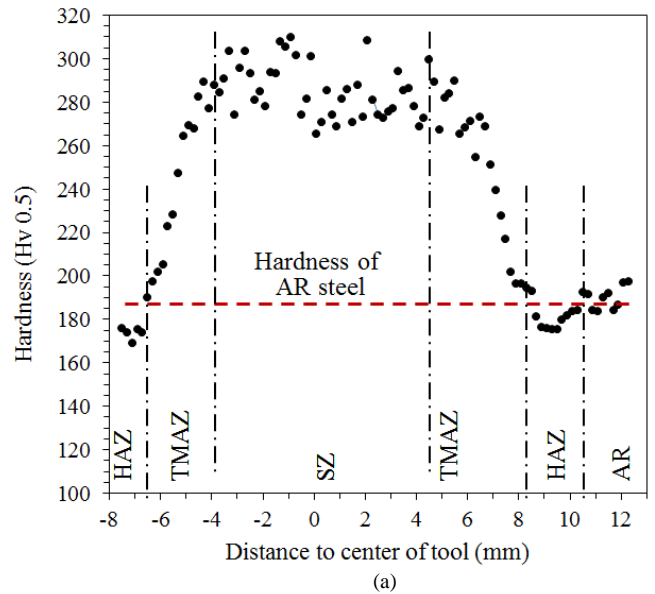


Fig. 6. Hardness evolution of DP-600 steel (a) Horizontal profile (b) Vertical (through thickness) profile.

Engineering stress-engineering strain curves of the as-received and FSPed DP-600 steel are represented in Fig. 7 .As received DP-600 steel reflected deformation behaviour mainly dominated by the strain hardening behaviour with a large strain hardening region with constitutes nearly equal to about half of the total elongation. This deformation behaviour of somehow

changed after the FSP. Generally as can be observed from Fig. 7 that, strain hardening region and ductility of the DP-600 steel decreased after FSP. However, strain hardening behaviour is still evident in the deformation curve of FSPed and dominated deformation behaviour.

Yield strength (σ_y) and ultimate tensile strength (UTS) of the as received DP-600 steel was determined to be 345 MPa and 643 MPa respectively. These strength values as-received DP-600 steel was increased drastically by the effect of single pass FSP to 721 MPa and 1054 MPa respectively. However, uniform elongation and elongation to failure of the as-received material decreased from 18.2% and 30.5% to 7.1% and 13% respectively after the FSP process. Such improvement in strength of the FSPed sample is assumed to be primarily from the considerably refined microstructure leading to grain size strengthening and transformation of the uniformly distributed martensite phase particles in to bulky grains. These microstructural changes may also be effective on the decrease in uniform elongation and consequently elongation to failure of the FSPed steel due to the increased cracking tendency of the microstructure.

It is also important to note that obtained mechanical properties of the FSPed DP-600 steel is quite close and/or slightly higher than that of the commercially available DP-980 steel with a yield strength, UTS and elongation to failure of 638 MPa, 986 MPa and 15% respectively [24]. Hence nearly two fold increase in strength values with accompanied with comparable formability achieved by a single practical FSP procedure can be capable to increase grade of the DP steels.

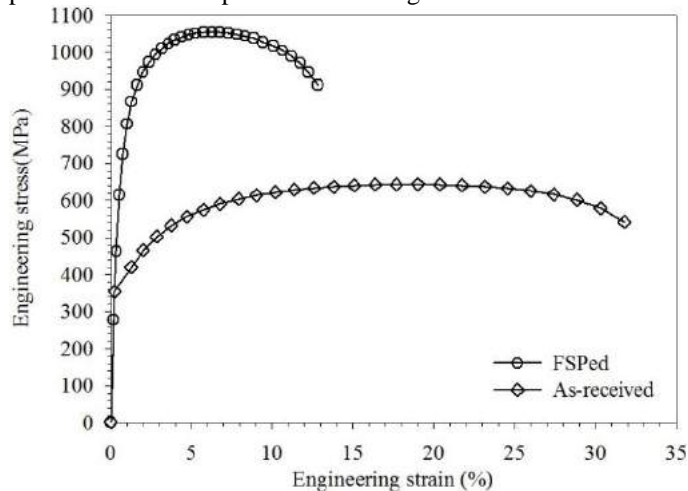


Fig. 7. Engineering stress-engineering strain curves of as-received and FSPed DP-600 steel.

IV. CONCLUSIONS

In the present study, the effect of friction stir processing (FSP) on the microstructure and mechanical properties of thin DP-600 steel sheets was investigated. The main conclusions of this study can be summarized as follows:

1. Friction stir processing was successfully applied to thin (1.1 mm) high strength DP-600 steel sheets using displacement controlled operation without formation of any defects.

2. Fine grained microstructure having mean ferrite grain size of 5 μm and bulky martensite phase were obtained after one pass FSP process.
3. Microstructural modification obtained by intense thermo-mechanical treatment of FSP increased hardness of the DP-600 steel from 190 Hv0.5 to about 290Hv0.5.
4. Deformation behavior of DP-600 steel found to be strain hardening dominated. This behavior remained unchanged after the FSP process.
5. Grain refinement and formation of the bulky martensite phase after FSP significantly enhanced strength DP steel without sacrificing the formability. Ultimate tensile strength of the DP-600 steel was increased from 643 MPa to 1054 MPa. This strength levels obtained by application of the one pass FSP to DP-600 steel is higher than that of the commercially available DP-980 steel.

VI. ACKNOWLEDGMENT

This work was supported by Scientific and Technical Research Council of Turkey (TUBITAK) under Grant No. 115M649.

REFERENCES

- [1] Z. Y. Ma and R.S. Mishra, "Friction stir welding and processing", *Mater. Sci. Eng. R*, vol.50, pp. 1-78, 2005.
- [2] Z. Y. Ma, "Friction stir processing technology: A review", *Metall. Mater. Trans. A*, vol. 39 A, pp. 642-658, 2008.
- [3] S. Mironov, Y. S. Sato and H. Kokawa, "Microstructural evolution during friction stir-processing of pure iron", *Acta Mater.*, vol. 56, pp. 2602-2614, 2008.
- [4] S. H. Aldajah, Ajayi, O. O., Fenske and G. R. David, "Effect of friction stir processing on the tribological performance of high carbon steel", *Wear*, vol. 267(1-4), pp. 350-355, 2009.
- [5] A. D. Chabok, "Formation of nanograin in if steels by friction stir processing", *Mater. Sci. Eng. A*, vol. 528(1), pp. 309-313, 2010.
- [6] M. I. Costa, Verdera, D., Vieira and M. T. Rodrigues, "Surface enhancement of cold work tool steels by friction stir processing with a pinless tool", *App. Surf. Sci.*, vol. 296(0), pp. 214-220, 2014.
- [7] L. Cui, Fujii, H., Tsuji, N. Nogi, "Friction stir welding of a high carbon steel", *Scripta Mater.*, vol. 56(7), pp. 637-640, 2007.
- [8] H. Fujii, Cui, L., Tsuji, N., Maeda, M., Nakata and K. Nogi, "Friction stir welding of carbon steels", *Mater. Sci. Eng. A*, vol. 429(1-2), pp. 50-57, 2006.
- [9] C. Meran, Kovan, V. Alptekin, "Friction stir welding of aisi 304 austenitic stainless steel", *Materialwissenschaft und Werkstofftechnik*, vol. 38(10), pp. 829-835, 2007.
- [10] Y. S. Sato, Nelson and T. W. Sterling, "Recrystallization in type 304L stainless steel during friction stirring", *Acta Mater.*, vol. 53(3), pp. 637-645, 2005.
- [11] N. Yasavol, Abdollah-zadeh, A., Vieira and M. T. Jafarian, "Microstructure evolution and texture development in a friction stir-processed aisi d2 tool steel", *App. Surf. Sci.*, vol. 293(0), pp. 151-159, 2014.
- [12] R. Bauri, Yadav, D., Shyam Kumar and C. N. Balaji, "Tungsten particle reinforced al 5083 composite with high strength and ductility", *Mater. Sci. Eng. A*, vol. 620(0) pp. 67-75, 2015.
- [13] D. Ni, D. Wang, A. Feng, G. Yao and Z. Ma, "Enhancing the high-cycle fatigue strength of Mg-9Al-1Zn casting by friction stir processing", *Scripta Mater.*, vol. 61(6), pp. 568-571, 2009.
- [14] P. Xue, B. L. Xiao and Z. Y. Ma, "Enhanced strength and ductility of friction stir processed cu-al alloys with abundant twin boundaries", *Scripta Mater.*, vol. 68(9), pp. 751-754, 2013.

- [15] M. B. Bilgin and C. Meran, "The effect of tool rotational and traverse speed on friction stir weldability of AISI 430 ferritic stainless steels", *Mater. Design*, vol. 33, pp. 376-383, 2012.
- [16] H.-H. Cho, Hong, S.-T., Roh, J.-H., Choi, H.-S., Kang, S. H., Steel and R. J.Han, "Three-dimensional numerical and experimental investigation on friction stir welding processes of ferritic stainless steel ", *Acta Mater.*, vol. 61(7), pp. 2649-2661, 2013.
- [17] S. H. C. Park, Sato, Y. S., Kokawa, H., Okamoto, K., Hirano, S.Inagaki, M. , "Rapid formation of the sigma phase in 304 stainless steel during friction stir welding", *Scripta Mater.*, vol. 49(12), pp. 1175-1180, 2003.
- [18] K. Dehghani and A. Chabok, "Dependence of Zener parameter on the nanograins formed during friction stir processing of interstitial free steels", *Mater. Sci. Eng. A*, vol. 528, pp. 4325-4330, 2011.
- [19] S. A. Khodir, Morisada, Y., Ueji and R. H.Fujii, , "Microstructures and mechanical properties evolution during friction stir welding of sk4 high carbon steel alloy", *Mater. Sci. Eng. A*, vol. 558(0), pp. 572-578, 2012.
- [20] T. Lienert, Stellwag Jr, W., Grimmett and B.Warke, "Friction stir welding studies on mild steel", *Welding Journal* vol. 82(1), pp. 1-S., 2003.
- [21] P. Xue, B. L. Xiao, W. G.Wang, , Q.Zhang, , D.Wang, Q. Wang and Z. Y.Ma, , "Achieving ultrafine dual-phase structure with superior mechanical property in friction stir processed plain low carbon steel", *Mater. Sci. Eng. A*, vol. 575(0), pp. 30-34, 2013.
- [22] P. J. Konkol, J. A.Mathers, R. Johnson and J. R. Pickens, "Friction stir welding of hsla-65 steel for shipbuilding", *Journal of Ship Production*, vol. 19(3), pp. 159-164, 2003.
- [23] Y.C. Chen and K. Nakata, "Evaluation of microstructure and mechanical properties in friction stir processed SKD61 tool steel", *Mater. Charact.*, vol. 60(12), pp. 1471-1475, 2009.
- [24] Q. Jia, W. Guo, W. Li, Y. Zhu, P. Peng and G. Zou, "Microstructure and tensile behavior of fiber laser-welded blanks of DP600 and DP980 steels", *J. Mater Proc. Tech.*, vol. 236, pp. 73-83, 2016.

Using a Nickel Coated Mold Wall in Continuous Casting Machine

Mehmet Fatih Kahraman^{a,b}, Habibullah Bilge^{a,b}, Sabri Öztürk^a

*a, Department of Mechanical Engineering, Abant İzzet Baysal University,
Golkooy Campus, 14280 Bolu, Turkey*

mfkahraman@ibu.edu.tr, habibullahbilge@ibu.edu.tr, sabriozturk@ibu.edu.tr

*b, Department of Mechanical Engineering, Sakarya University
Serdivan, 54187 Sakarya, Turkey*

mfkahraman@ibu.edu.tr, habibullahbilge@ibu.edu.tr

Abstract— In continuous casting process, avoiding crack formation is very important for the producers. This paper examines the effect of nickel-coated mold wall upon the cracks during casting of steel. Casting products are analyzed in this study and the test reveals nickel coating is the best possible output on the basis of slab quality. Moreover, molds coated by nickel have more service life than copper based molds.

Keywords— Continuous casting, Mold, Nickel coating, Cracks, Lifetime

I. INTRODUCTION

Turkey is the 9nd largest steel producing country in the world. In 2015, Turkey produced 31.52 million metric tons of the global production of crude steel [1]. Steel from the basic oxygen furnace is tapped into a ladle and teemed from the ladle to the tundish, after than slabs are produced by slab-casting machine. In this process, molten steel becomes a solid into a "semi-finished casting product" slab.

Formation of crack on the rolling mills is a crucial problem for iron and steel industry. Therefore, it is very significant to keep away from this damage throughout continually production. On the other hand, these crack formation can lead to rising expenditure for strand conditioning prior to rolling or defective goods can be come up. Consequently, detection and mending of damages in continuous casting slabs becomes much more difficult. This study particularly observes the star cracks occurred during the continuous casting of steel.

Many authors have interested in crack formation [2]. Therefore, they have created mathematical model of crack formation. Excellence production for iron and steel industry is related to controlling the crack formation [3-6].

Most of researchers [7-12] investigated continuous casting steel process experimentally and theoretically. As known that the mold heat flow operation includes many complicated mechanisms and most surface defects in casting originate in the mold at the meniscus. The solidifying shell is very thin at the meniscus, because of this reason many surface defects can be

occurred in this region. Changing meniscus heat transfer has an interrelation with risen surface or subsurface damage.

The fluid flow and heat transfer in the mold affect the quality of the slab in continuous casting process [13, 14].

Construction and material properties of the mold plates forthrightly affected the star crack defects. Nickel and/or chromium are used as a coating material, it protects against copper pickup, also keeps away from star cracks. Coating with nickel plays a crucial role in continuous casting molds. The purpose of these experiments was to investigate the effects of star defects and to preserve surface defects on the slabs made of steel by casting.

II. PLANT TESTS

The production line in iron and steel plant is used for the tests. The width of the cast slabs manufactured in the casting process was 200 mm. The mold walls were changed 41 to 36 mm, and their lengths were 800 mm. Average casting speed was 1 m/min. Experiments were applied in the curve slab-casting machine, which has 9.8-meter radius as shown in Fig. 1. The oscillation stroke of the casting machine was 12 mm. The metal level observation method was determined by using non-contact electromagnetic indicators. Also casting speed of the machine can be controlled by this method. The mold powder machine supplied the powder for casting with a uniform dispersion. Thermocouples were used to assess temperature in the mold wall.



Fig. 34 One stand continuous casting machine

The tests employed basically consisted two different steel grades. One of the grades used for the tests contains 0.20 C, 0.2 Si, 0.5 Mn, 0.010 P, 0.021 S and 0.02 Al (in wt.%) and it can be named as Grade A. Chemical component of the other one is 0.19 C, 0.3 Si, 0.9 Mn, 0.012 P, 0.020 S and 0.03 Al (in wt.%) as can be called Grade B.

For the tests, two different mold plate materials were used under the constant casting speed. One of the mold plate materials was nickel-coated copper, and the other one was uncoated copper. Due to high coating expenditure, only the half size of the mold plate walls was covered with 3 mm thickness nickel as seen in Fig. 2.



Fig. 2 Nickel-coated mold wall

III. RESULTS AND DISCUSSION

The casting speed rates applied in the experiments are determined according to the quality of the material. In these experiments environment circumstances and other parameters like cooling water curves, mold powder, and the time of casting were applied uniformly for the similar grades. Steels including %0.08-%0.14 carbon atoms are very sensitive to surface cracks, in addition including high carbon steel and high alloy steels are much more sensitive to surface and subsurface cracks.

As known star crack which is a kind of defects are located in slabs. This failure is shown up after oxide layer has been taken away from slab surface by heating. This application, which

causes the surface temperature to enhance, changes the nature of the crack, also it causes to disappear sign that could lead to clarify its formation mechanism.

The cause of this crack type is explained with the existence of Cu, which could coming from inside the steel or from continuous casting mold. When rising of the Cu percentage in the slab lead to resolution in austenite, Cu in liquid phase precipitates at the steel surface as long as it is exposed to oxidation at high temperature.

Two different mold plate materials were used in the experiments. The mold walls made of copper may lead to crack extension on the surface of the slabs in the continuous casting process. Cracks are spread on the top layer of the slabs. After beginning to employ nickel-coated mold, star cracks approached zero, as well as there is no damage was seen when visually checking of slabs.

The specimens picked up from the slabs were analyzed, and just two images were chosen for the clarifying in the present paper due to the mandatory space restriction. The visual observation of the cracks found in steel slabs can be seen in Figs. 3 and 4. The slabs were carefully examined, the cracks were gathered on the surface like capillary lines and can be visible on surfaces after conducting a scarfing operation as can be seen in Figs. 3 and 4.

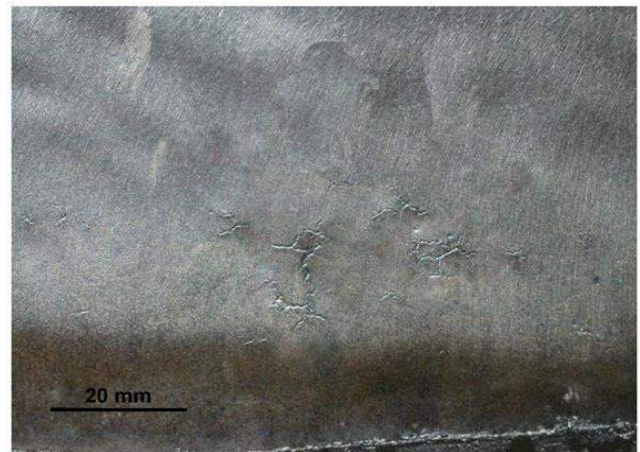


Fig. 3 A representative star crack for Grade A

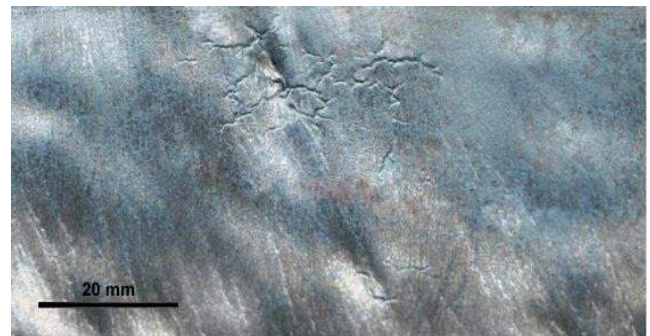


Fig. 4 A representative star crack for Grade B

Investigation indicates that number of star crack defects was diminished by coating of walls of mold plate.

To protect from the star crack formation, nickel coating was applied on the mold elements, performing nickel coated on the mold wall literally evolved mechanical properties of the slabs, and moreover star crack defects weren't seen in casting molds coated by nickel.

The nickel coated mold service life was longer than uncoated ones. The nickel coated increased service life more than %9 percent when comparing the uncoated molds for two different grades named as Grade A and B.

The number of casting between two shift periods was considered as the mold service life. Service life of mold plates with nickel-coated achieved amount between 326 and 350 casts, though the using range of uncoated mold plate (copper-base) only reached between 300 and 320 casts. The average of casting number was 310 for uncoated mold plate (base-copper) and average number of use of nickel-coated mold was 338 casts.

IV. CONCLUSION

The purpose of the work was to assess the impact of the different mold materials on star cracks defect in continuous casting, and the most suitable combination of mold materials was selected. Selected mold plate materials are nickel coated copper and uncoated copper, respectively, for casting trials. Due to the copper pick up, mold walls coated by nickel are used for casting. When the test sample taken from the slab is observed, there are no defects to be seen. Nickel offers enough protection against wear on the top layer of the copper. Using nickel-coated mold wall is the best method preserving star crack effectively. To reduce the formation of star cracks, the most important point to attention must be choosing of mold wall materials. Therefore, nickel used as a coating material was carried out to the slab caster mold plates to enrich their lives as well as prevent the formation of the star crack. Half of the area of the copper based mold plate walls can be coated by nickel. Thickness of the nickel can be selected 3 mm. The mold walls could be used until nickel coated thickness were reached up to 0.5 mm.

REFERENCES

- [1] <http://www.worldatlas.com>
- [2] S. Ozturk, M. M. Arikian, and Y. Kacar, "Effects of nickel coating of mold plates on star crack defects." *Metallurgical and Materials Transactions B*, 44(3), 706-710, 2013.
- [3] L. Guo, X. Wang, H. Zhan, M. Yao, & D. Fang, "Mould heat transfer in the continuous casting of round billet." *ISIJ international*, 47(8), 1108-1116, 2007.
- [4] Y. Meng, & B. G. Thomas, "Simulation of microstructure and behavior of interfacial mold slag layers in continuous casting of steel." *ISIJ international*, 46(5), 660-669, 2006.
- [5] K. Schwerdtfeger, & H. Sha, "Depth of oscillation marks forming in continuous casting of steel." *Metallurgical and Materials Transactions B*, 31(4), 813-826, 2000.
- [6] M. O. El-Bealy, "Transient Simulation of Mold Heat Transfer and Solidification Phenomena of Continuous Casting of Steel." *Metallurgical and Materials Transactions B*, 47(5), 3013-3038, 2016.
- [7] C. A. M. Pinheiro, I. V. Samarasekera, J. K. Brimacombe, & B. N. Walker, "Mould heat transfer and continuously cast billet quality with mould flux lubrication Part 1 Mould heat transfer." *Ironmaking & Steelmaking*, 27(1), 37-54, 2000.

- [8] Y. A., Meng, & B. G. Thomas, "Heat-transfer and solidification model of continuous slab casting: CON1D." *Metallurgical and Materials Transactions B*, 34(5), 685-705, 2003.
- [9] M. Jesiotr, D. Myszk, & W. Trzaskowski, "The Analysis of Molding and Modification of the Ceramic Surfaces and Its Impact on the Roughness of Castings." *Archives of Foundry Engineering*, 14, 47-50, 2014.
- [10] M.O. El-Bealy: *Proc. 6th European Conference on Continuous Casting*, 2008, 3-6 June 2008, Riccione, Italy.
- [11] X. Y. Tian, F. Zou, B. W. Li, & J. C. He, "Numerical analysis of coupled fluid flow, heat transfer and macroscopic solidification in the thin slab funnel shape mold with a new type EMBr." *Metallurgical and Materials Transactions B*, 41(1), 112-120, 2010.
- [12] M. Herrera-Trejo, J. J. Ruiz, M. Castro-Roman & H. Solis, "Star cracks in continuously cast peritectic steel slabs", *Ironmaking & Steelmaking*, 37:6, 452-457, 2010.
- [13] B.G. Thomas, "Modeling of Continuous Casting Defects Related to Mold Fluid Flow." *3rd International Congress on Science & Technology of Steelmaking*, Charlotte, 9-12 May 2005, 847-861, 2005.
- [14] R. Miranda, M. A. Barron, & C. A. Hernandez, "Velocity Monitoring of Molten Steel in a Continuous Casting Mold Using Three Submerged Entry Nozzle Designs." *Modeling and Numerical Simulation of Material Science*, 6(04), 59, 2016.

Tribological Behaviors of Nitrided and Nitroxed Tool Steels

M. Emre Turan, M. Acarer, M.Karakus, H.Ahlatci, Y.Turen, Y.Sun

Karabuk University Iron and Steel Institute Karabuk, 78050 Turkey

memreturan@karabuk.edu.tr, macarer@selcuk.edu.tr, akkomustafa@gmail.com, hahlatci@karabuk.edu.tr,

yturen@karabuk.edu.tr, ysun@karabuk.edu.tr

ABSTRACT

The aim of this study is to investigate the effect of nitration and nitrox process on wear performances of tool steels. For this purpose, samples were separated as two categories. One group was exposed to nitration process in salt bath at 530 0C during 6 hours. For other group, nitrox process was applied at 4900C during 2 hours after nitration. Reciprocating wear test was performed for all specimens under the loads of 10N, 20N and 40N according to the ASTM G99 standard. Microstructures and worn surfaces of specimens were analysed using Scanning Electron Microscope (SEM). Results show that, wear performances of specimens exhibit difference when they are exposed nitration and oxidation process. And also they show better performance under the lower loads.

Keywords: Tool steels, SEM, Wear, Nitration, Nitrox

Microstructural Evolution and Mechanical Properties of Friction Stir Processed TRIP780 Steel

İmren Öztürk Yılmaz^{##}, Mümün Yılmaz^{*}, Onur Saray^{*}

[#] Beyçelik Gestamp R&D Center Bursa Turkey

imrenyilmaz@beycelikgestamp.com.tr

^{*} Bursa Technical University Department of Mechanical Engineering Department Bursa Turkey onur.saray@btu.edu.tr, mumunyilmaz89@gmail.com

Abstract—Friction stir processing (FSP) is a method which refines microstructure of metals by localized plastic deformation. This microstructural evaluation brought a remarkable increase in mechanical properties with an acceptable loss of ductility. In the literature there are several publications on the microstructural and mechanical evolution of FSPed steels. However, there limited number of studies on the effect of FSP on the microstructure and mechanical properties of Transformation-Induced Plasticity (TRIP) steel as a widely used material with unique properties like excellent formability and strain hardenability. In order to close this gap, current study is mainly concentrated on the effect of FSP on the microstructural evolution and mechanical properties TRIP 780 steel. The microstructural evaluation was analysed scanning electron microscopy (SEM) techniques. Mechanical properties were investigated by microhardness test and tensile test. Results indicated that a two-fold increase in the hardness was achieved after FSP. Also, yield strength and UTS of the TRIP-780 steel reached to 1280 MPa and 1475 MPa respectively. This strength increase was also obtained with an acceptable uniform elongation of % 9, which is concluded that a good balance of strength, ductility and strain hardenability.

Keywords— Transformation induced plasticity steel, TRIP effect, Friction stir processing.

I. INTRODUCTION

Friction stir processing (FSP) is an emerging engineering technology [1, 2] developed on the basic principles of friction stir welding [3, 4]. FSP can make localized microstructure modification and also phase transformation in the friction stir processed zone. A rotating tool consisting of a shoulder and a pin is plunged into a work piece and then travels in the interested direction. The tool has two primary functions, heating and deforming the material. After extreme levels of plastic deformation and thermal exposure, the processed zone normally exhibits significant microstructural refinement and homogeneity. As a result the material properties such as strength, wear and corrosion resistance are improved [4-6].

FSP is a thermomechanical process. Phase transformations and grain refinement occurs during these thermomechanical process inside the stir zone through. Consequently, the phase

transformation and grain refinement should also be controlled by the FSP conditions and parameters like tool rotation speed and the process speed which have great impact on cooling rate and heat input leading to fine tuning of the grain growth and/or grain size. [4, 5, 7-9]. FSP uses the same methodology as friction stir welding (FSW), but FSP is used to modify the local microstructure and does not join metals together. A schematic illustration of FSP is shown in (Fig.1)

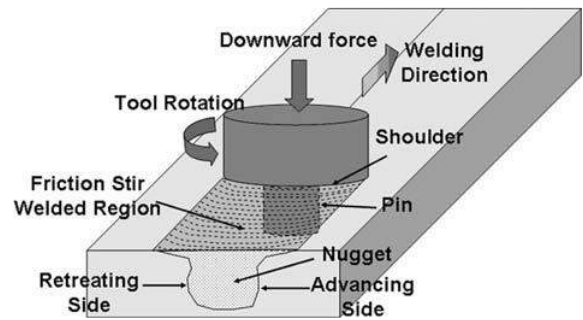


Fig. 35 Schematic representation of FSP [2, 4]

Many studies have reported friction stir processing or friction stir welding. FSP has been mainly employed for microstructural modification of low melting temperature materials like; aluminum, copper and magnesium [1, 10-17]. However, in recent years much attention has been paid to FSP/FSW of ferrous alloys such as carbon steels [18-20] high strength low alloy steels [21, 22] ductile irons, tool steels [23-26] and stainless steels [27-34]. There are a few study in automotive steels used of friction stir processed.

In recent years, the automotive industry has developed a new generation of high strength steels (AHSS) to meet the need to produce lighter vehicles while maintaining strength values. Transformation induced plasticity (TRIP) steel is one of these sheet materials. It has received significant research effort because it's high strength to ductility ratios. Considering the microstructural and mechanical properties, TRIP steel provides great advantages like excellent formability and high capacity of shock absorbance. On the other hand strength levels of this steel basically and mainly related to plastic strain imposed. In other words it is required to trigger martensitic transformation with a

certain amount of plastic strain to get higher level of strength. TRIP steels have been found beneficial in forming of body parts with complicate geometrical details. Also, increasing strength of the TRIP steel may provide great advantageous considering the lighweighting goals.

On this point of view, strengthening of the TRIP steel via FSP may be seem to be meet this basic requirements and expand the usage of TRIP steel in automotive applications. However, effect of FSP on the structure and properties of the TRIP-steel have not been investigated. Further investigations are needed to identify the mechanical properties of the FSPed TRIP-steels in order to reveal possible advantages of FSP on the strength and ductility.

In view of above, literature contains a range of studies examining FSPed behavior of different materials including some kind of steels, but there has not yet been a systematic study concerning of (AHSS). Therefore, the aim of this study was to clarify the microstructural change during FSP and its effects on the microstructure formation and mechanical properties of TRIP-steels.

II. EXPERIMENTAL PROCEDURE

A commercially available plate of tool TRIP 780 steel was used in this study. The chemical composition of the TRIP 780 steel is shown in Table 1. Samples with the dimensions of 200mm x 400mm x 1.95 mm were sheared. Samples fixed between the holders of the machine. TRIP-steel samples were subjected to one-pass FSP using a WC tool shoulder having a diameter of 16 mm and a cylindrical pin with a diameter and length of 6 mm and 0,8 mm, respectively. The tool was tilted at an angle of 3° from the normal to the processed plate. Tool rotation speed and processing speed was set at 1000 rpm and 80 mm/min, respectively.

Table1. Chemical composition of the as-received TRIP780 steel.

TRIP780	Chemical compositions (mass%)					
	C	Si	Mn	P	S	Al
	0,209	1,68	1,65	0,001	0,001	0,035

Processing temperature was determined with a thermal camera during the processing surface of the sample. Peak temperature was determined to be 850–900°C. Scanning electron microscope (SEM) and optical microscope (OM) were used to observe the microstructure of TRIP-steel samples before and after FSP. The metallographic specimens were sectioned perpendicular to the process direction (Fig. 1) and then etched in 2% Nital for 20s after standard metallographic preparation. Hardness measurements were performed using a Vickers micro hardness tester under a load of 500 g and for 10s dwell time (Fig. 2)

Tensile properties were determined on dog bone-shaped specimens with strain rate of 0.01 s⁻¹. The tensile axis of the samples was oriented parallel to the processing direction (Fig. 2 (a)). At least three tests were conducted to check the

repeatability of both hardness and tensile test results for each point.

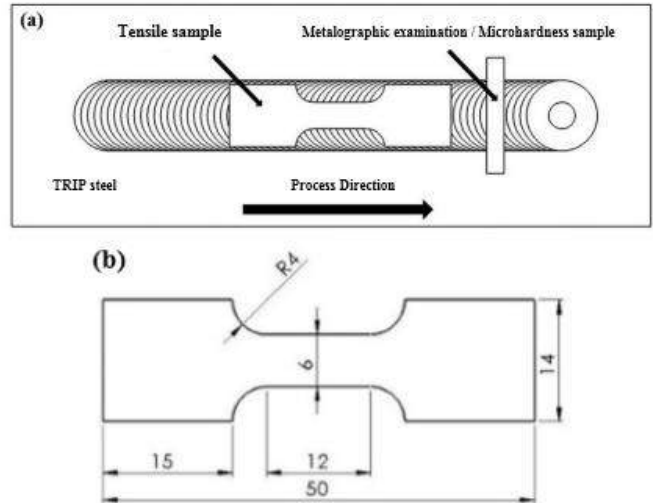


Fig. 2 (a) Schematic illustrations of the FSPed plate and the position of the specimens inside the FSPed zone (b) Dimensions of tensile sample

III. RESULTS AND DISCUSSION

A. Microstructure Observations

(Fig. 3 (a)-(d)) shows the microstructural features for the as-received (AR) TRIP steel. Microstructure of TRIP steel mainly consists of ferrite, bainite and retained austenite phases. Retained austenite phase is an important element in designing TRIP steel. Its morphology and amount of other phases are also a vital factor that influencing the mechanical properties and behavior of retained austenite. Transformation of retained austenite into martensite during deformation ceases beyond a critical strain. The grain size of the ferrite and the retained austenite phases is about 12 μm -14 μm.

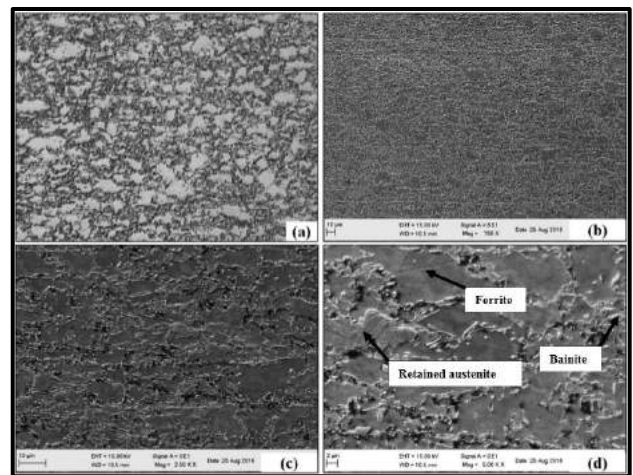


Fig. 3 Microstructure of as-received TRIP steel (a) Optical micrographs . (b)-(c)-(d) Different high magnification micrographs showing the SEM micrographs



Fig. 4 Macrograph of the FSPed zone of TRIP Steel

(Fig. 4) shows a cross-sectional macrograph of the FSPed zone. FSP formed a process region with depth of about 1,9mm and width close to diameter of the tool shoulder (16mm). In the cross section, the right and left sides of the process center correspond to the retreating side (RS) and advancing side (AS) of the rotation tool, respectively (Fig.5 (a)). Also, thermomechanical process condition variations based on the changes plastic strain and deformation temperature formed some deformation regions that can be distinguished by the microstructural differences. These deformation regions are well defined and named in previous studies and indicated on the (Fig. 5 (a)). The FSP zone consists of an as-received TRIP steel (Fig. 5 (b)-(c)-(d)), SZ (Fig. 5 (f)-(g)), transition region, (TMAZ), and a heat affected zone (HAZ) (Fig. 5 (e)). As can be seen from (Fig. 5 (a)), in FSP zone, some of the characteristic areas include, the stir zone (SZ), which under goes material flow introduced by the shoulder or probe. Grain structure evolution was found to be a process continuous dynamic recrystallization and phase transformation. A needle-shaped martensites were observed in most parts of the SZ. (Fig. 5 (f)-(g)). Therefore, as-received microstructure effectively transformed into a martensite dominated microstructure via occurrence of phase transformation within the SZ. . The heat-affected zone (HAZ), which has a microstructure that is only affected by the heat generated during the FSP and reflects features of grain growth. Also, thermo-mechanically affected zone (TMAZ) (Fig. 5 (e)) which is the transition area between the SZ and the HAZ is formed. In this region transformation of retained austenite to martensite partly occurs but the ferrite phase also remains in the structure. It is important to note that , the HAZ are difficult to identify after applied FSP conditions.

In fact, it is known that the most important feature of TRIP steels is the transformation of the retained austenite into the martensite structure during the applied plastic deformation. This transformation is particularly effective in the SZ. Also it is obvious from (Fig. 5 (f)-(g)) that morphological properties of the structure grains varied in the SZ. This may be occur due to the formation of the heat flux as a natural result of the nonuniform heat transfer within the deformation region.

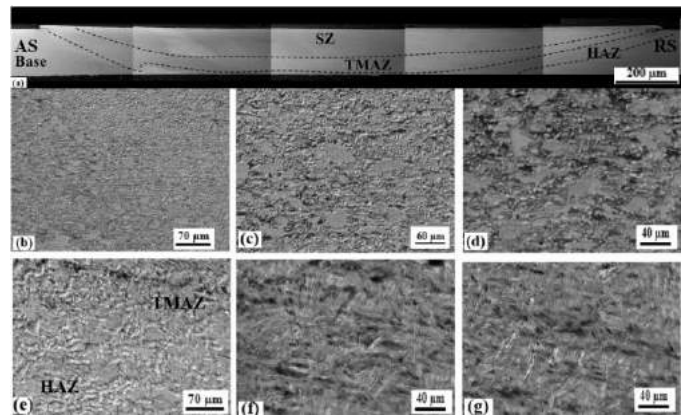


Fig. 5 (a) A general view of cross-section of the sample perpendicular to the advancing direction of the FSP (b)-(c)-(d) Different high magnification SEM micrographs of microstructure of as-received TRIP-steel (e) TMAZ-HAZ (f)-(g) SEM micrographs of SZ

B. Mechanical properties

Effect of microstructural evolution by FSP on the hardness of TRIP-steel was summarized in (Fig.6 (a)-(d)). Fig 6 (a)-(d) indicate that the hardness of the stirred layer is much higher than that of base material. There is almost a two-fold increase in hardness, reaching to 488 Hv 0.5 compared to that of the base material (260 Hv 0.5). SZ of the FSPed workpiece experiences the most severe deformation and phase transformation. Consequently, the highest hardness values in the range of 435Hv 0.5-488Hv 0.5 (Fig. 6 (a)-(d)) were measured in this region. Towards TMAZ hardness values sharply decreased and reached to base metal hardness as a natural result of decreased level of plastic deformation and martensitic transformation.

As can be understood from Fig. 6 (c)-(d), peak hardness values were measured at the surface where tool shoulder contacts to workpiece surface. The peak hardness value remained stable through a depth of about 1.15 mm. Beyond this depth, however, hardness values sharply decreased to the levels of the as-received steel (Fig. 6 (d)). This variation may be considered as an expected result of decrease in deformation and phase transformation degree from the top surface towards the center of the sheet.

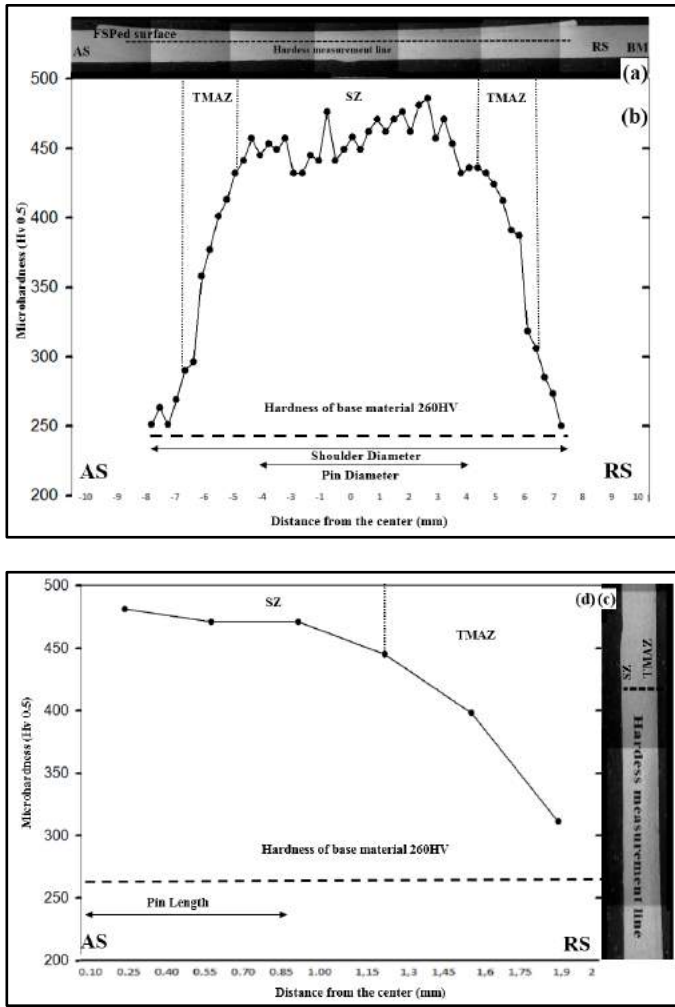


Fig. 6 Cross-sectional view micro-hardness distributions of FSPed sample through (a)-(b) horizontal and (c)-(d) vertical directions.

The stress-strain curves of as-received and FSPed TRIP-steel samples are shown in (Fig.7) The yield strength (YS), ultimate tensile strength (UTS), uniform elongation (UE), and elongation to failure (EL) taken from this curves are summarized in Table1.

Table2. Mechanical properties of as-received and FSPed FM TRIP-steel samples.

TRIP-STEEL	YS(MPa)	UTS(MPa)	UE(%)	EL(%)
As-received	415	829	23	34
FSPed	1280	1475	11	22

As-received TRIP steels showed low strength and high elongation with a very large strain-hardening region (Fig. 7).

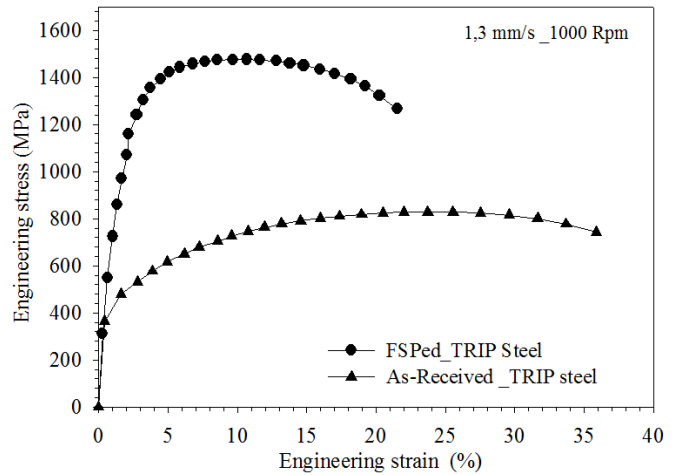


Fig. 7 Stress-strain curves of the as-received and FSPed TRIP-steel samples.

Strength of as-received TRIP steel was increased drastically by the effect of FSP. The YS and UTS of the BM steel increased from 415MPa and 825MPa to about 1280MPa and 1475MPa, respectively, after FSP. This strength increase was also obtained with an acceptable uniform elongation of % 9, which is concluded that, a good balance of strength, ductility and strain hardenability. More importantly, the strengthening was achieved without decline of ductility, which is a crucial parameter considering the engineering applications of the steels for sheet metal forming.

It is also important to note that obtained mechanical properties of the FSPed TRIP 780 steel is quite close and/or slightly higher than that of the commercially available 22MnB5 steel with a yield strength, UTS and elongation to failure of 1010 MPa, 1478 MPa and 10% respectively [35].

IV. CONCLUSION

Friction-stir processed thin TRIP steel has been studied. In the process region microstructure of TRIP steel is strongly affected by the FSP and important microstructural evolutions including both grain refinement and phase transformation observed. In these experiments, can be summarized as follows;

- Friction stir processing was successfully applied to thin (1.95 mm) high strength TRIP-780steel sheets using displacement controlled operation without formation of any defects.
- Microstructural modification obtained by intense thermo-mechanical treatment of FSP increased hardness of the TRIP-7800 steel from 260 Hv0.5 to about 488Hv 0.5.
- Especially due to phase transformation Grain after FSP significantly enhanced strength TRIP steel without give away the formability. Ultimate tensile strength of the

TRIP 780 steel was increased from 825 MPa to 1475 MPa. This strength levels obtained by application of the one pass FSP to TRIP 780 steel is higher than that of the commercially available 22MnB5 steel.

VII. ACKNOWLEDGMENT

This work was supported by Scientific and Technical Research Council of Turkey (TUBITAK) under Grant No. 115M649. We would like to thank to support of Beyçelik Gestamp and Borçelik.

VIII. REFERENCES

- [1] Mishra, R.S., et al., *High strain rate superplasticity in a friction stir processed 7075 Al alloy*. Scripta Materialia, 1999. **42**(2): p. 163-168.
- [2] Ma, Z.Y., R.S. Mishra, and M.W. Mahoney, *Superplastic deformation behaviour of friction stir processed 7075 Al alloy*. Acta Materialia, 2002. **50**(17): p. 4419-4430.
- [3] Thomas WM, N.E., Needham JC, Murch MG, and D.C.G.B. Templesmith P, *Patent Application No:9125978.8*, Dec. 1991.
- [4] Mishra, R.S. and Z.Y. Ma, *Friction stir welding and processing*. Materials Science and Engineering: R: Reports, 2005. **50**(1–2): p. 1-78.
- [5] Mishra, R.S. and M.W. Mahoney, *Friction Stir Welding and Processing*. 2007: ASM International.
- [6] Ma, Z.Y., F.C. Liu, and R.S. Mishra, *Superplastic deformation mechanism of an ultrafine-grained aluminum alloy produced by friction stir processing*. Acta Materialia, 2010. **58**(14): p. 4693-4704.
- [7] Thomas, W.M., P.L. Threadgill, and E.D. Nicholas, *Feasibility of friction stir welding steel*. Science and Technology of Welding and Joining, 1999. **4**(6): p. 365-372.
- [8] Cui, L., et al., *Friction stir welding of a high carbon steel*. Scripta Materialia, 2007. **56**(7): p. 637-640.
- [9] Tsujikawa, M., et al., *Microstructural Evolution of Friction Stir Processed Cast Mg-5.9 mass%Y-2.6 mass%Zn Alloy in High Temperature Deformation*. Materials Transactions, 2007. **48**(3): p. 618-621.
- [10] Garcia-Bernal, M.A., et al., *Influence of friction stir processing tool design on microstructure and superplastic behavior of Al-Mg alloys*. Materials Science and Engineering: A, 2016. **670**: p. 9-16.
- [11] Patel, V.V., V. Badheka, and A. Kumar, *Effect of polygonal pin profiles on friction stir processed superplasticity of AA7075 alloy*. Journal of Materials Processing Technology, 2017. **240**: p. 68-76.
- [12] Kapoor, R., et al., *Effect of friction stir processing on the tensile and fatigue behavior of a cast A206 alloy*. Materials Science and Engineering: A, 2013. **561**: p. 159-166.
- [13] Yang, Q., et al., *Achieving high strain rate superplasticity in Mg–Zn–Y–Zr alloy produced by friction stir processing*. Scripta Materialia, 2011. **65**(4): p. 335-338.
- [14] Ni, D., et al., *Low cycle fatigue properties of friction stir welded joints of a semi-solid processed AZ91D magnesium alloy*. Materials & Design, 2014. **56**: p. 1-8.
- [15] Zhang, D., et al., *Superplastic tensile behavior of a fine-grained AZ91 magnesium alloy prepared by friction stir processing*. Materials Science and Engineering: A, 2012. **556**(0): p. 100-106.
- [16] Xue, P., B.L. Xiao, and Z.Y. Ma, *High tensile ductility via enhanced strain hardening in ultrafine-grained Cu*. Materials Science and Engineering: A, 2012. **532**(0): p. 106-110.
- [17] Chang, C.I., X.H. Du, and J.C. Huang, *Achieving ultrafine grain size in Mg–Al–Zn alloy by friction stir processing*. Scripta Materialia, 2007. **57**(3): p. 209-212.
- [18] Fujii, H., et al., *Friction stir welding of carbon steels*. Materials Science and Engineering: A, 2006. **429**(1–2): p. 50-57.
- [19] Sun, Y.F., et al., *Microstructure and mechanical properties of mild steel joints prepared by a flat friction stir spot welding technique*. Materials & Design, 2012. **37**: p. 384-392.
- [20] Cho, H.-H., et al., *Microstructural evolution in friction stir welding of high-strength linepipe steel*. Materials & Design, 2012. **34**: p. 258-267.
- [21] Ghosh, M., K. Kumar, and R.S. Mishra, *Friction stir lap welded advanced high strength steels: Microstructure and mechanical properties*. Materials Science and Engineering: A, 2011. **528**(28): p. 8111-8119.
- [22] Xue, P., et al., *Enhanced mechanical properties in friction stir welded low alloy steel joints via structure refining*. Materials Science and Engineering: A, 2014. **606**: p. 322-329.
- [23] Reynolds, A.P., et al., *Friction stir welding of DH36 steel*. Science and Technology of Welding and Joining, 2003. **8**(6): p. 455-461.
- [24] Chen, Y.C. and K. Nakata, *Evaluation of microstructure and mechanical properties in friction stir processed SKD61 tool steel*. Materials Characterization, 2009. **60**(12): p. 1471-1475.
- [25] Yasavol, N., et al., *Microstructure evolution and texture development in a friction stir-processed AISI D2 tool steel*. Applied Surface Science, 2014. **293**(0): p. 151-159.
- [26] Yasavol, N. and A. Ramalho, *Wear properties of friction stir processed AISI D2 tool steel*. Tribology International, 2015. **91**: p. 177-183.
- [27] Reynolds, A.P., et al., *Structure, properties, and residual stress of 304L stainless steel friction stir welds*. Scripta Materialia, 2003. **48**(9): p. 1289-1294.
- [28] Park, S.H.C., et al., *Rapid formation of the sigma phase in 304 stainless steel during friction stir welding*. Scripta Materialia, 2003. **49**(12): p. 1175-1180.
- [29] Sato, Y.S., T.W. Nelson, and C.J. Sterling, *Recrystallization in type 304L stainless steel during friction stirring*. Acta Materialia, 2005. **53**(3): p. 637-645.
- [30] Meran, C., V. Kovan, and A. Alptekin, *Friction stir welding of AISI 304 austenitic stainless steel*. Materialwissenschaft und Werkstofftechnik, 2007. **38**(10): p. 829-835.
- [31] Bilgin, M.B. and C. Meran, *The effect of tool rotational and traverse speed on friction stir weldability of AISI 430 ferritic stainless steels*. Materials & Design, 2012. **33**: p. 376-383.
- [32] Rezaei-Nejad, S.S., et al., *Formation of Nanostructure in AISI 316L Austenitic Stainless Steel by Friction Stir Processing*. Procedia Materials Science, 2015. **11**: p. 397-402.
- [33] Tinubu, O.O., et al., *Friction stir processing of A-286 stainless steel: Microstructural evolution during wear*. Wear, 2016. **356–357**: p. 94-100.
- [34] Cho, H.-H., et al., *Three-dimensional numerical and experimental investigation on friction stir welding processes of ferritic stainless steel*. Acta Materialia, 2013. **61**(7): p. 2649-2661.
- [35] Karbasian, H. and A.E. Tekkaya, *A review on hot stamping*. Journal of Materials Processing Technology, 2010. **210**(15): p. 2103-2118.

Achieving Ultrafine Grain Structure with Superior Mechanical Properties by Friction Stir Processing of Interstitial-free Steel (IF-steel) Sheets

Mumun Yilmaz*, Imren Ozturk Yilmaz⁺, Onur Saray*

**Department of Mechanical Engineering, Bursa Technical University
Bursa, Turkey
onur.saray@btu.edu.tr*

*⁺Beyçelik Gestamp R&D Center
Bursa, Turkey
imrenyilmaz@beycelik.com.tr*

Abstract— Grain refinement is a unique approach to improve physical and mechanical properties of metallic materials without need to change their chemical compositions. Friction stir processing (FSP), is technique for microstructural refinement of metallic materials down to micrometer levels. In this process, a specially designed rotating tool is plunged into the sheet to be processed and traversed along the line of interest. The most important advantage of process is providing weight reduction by effectively strengthening of metals. However, applicability of this process to thin sheets have been found difficult. In this study; thin interstitial-free steel (IF-steel) was subjected to FSP using a carbide-tungsten tool with the diameter of 14 mm. Ultrafine grain structure was successfully achieved in 1.2 mm thick IF steel sheet via position controlled processing technique and selection of the proper tool dynamics. The microstructural evolutions were characterized using scanning electron microscopy (SEM) techniques. The results show that the FSP of IF-steel resulted with the fine grains with a mean grain size of 5 μm (initial grain size was 35 μm). FSP steel exhibited a good combination of yield strength of 500 MPa with uniform elongation of 16%.

Keywords— Friction stir processing, IF-steel, Grain refinement, Severe plastic deformation

I. INTRODUCTION

Friction stir processing (FSP) is a effective severe plastic deformation technique developed based on the principles of friction stir welding (FSW) [1], [2]. In FSP, a non-consumable rotating tool with a shoulder and pin is inserted into a metal plate and traversed through a direction of interest. Heat generated by the friction between rotating tool and metal surface locally softens the volume to be processed. By traversing the rotating tool, the material flowing around the pin and the tool shoulder under goes severe plastic deformation and thermal exposure [3]. Mainly, plastic deformation with frictional heating up to 0.6-0.7 T_m leads to dynamic recovery (DRV) and dynamic recrystallization (DRX) assisted microstructural refinement [4]–[6]. In many cases, the FSP

leads to transformation of the coarse-grained (CG) initial microstructure into equiaxed fine-grained (FG) and/or even ultra-fine grained (UFG) structure [1]–[5], [7].

On the other hand, dendritic structure of the as-cast alloys can be successively broken-up, and casting defects like solidification micro-porosities, cavities and inclusions are eliminated with FSP [6], [7]. Furthermore, this method has been successfully used for producing metal matrix surface composites on plate-type samples. In corporation of reinforcement components like ceramic particles, multi-walled carbon nanotubes into the metal matrix have been done with the aid of intense plastic deformation and stirring during FSP [1], [2].

Given the potential technological advantages of this effective and flexible technology, several research efforts have been made to understand the mechanical response and engineering performance of the FSPed materials. To date, considerable attention has been paid especially to the light metals namely wrought and cast Al, Mg, Cu and Ti alloys [1], [2], [8]. It has been demonstrated in these studies that mechanical properties of CG metallic materials could be enhanced by microstructural refinement and reorganization [1], [2], [8]. Generally, enhanced hardness and strength can be achieved for variety of material groups according to Hall-Petch type strengthening [1], [2], [8], [9].

In limited studies, mainly microstructural evolution and texture formation of FSPed steels were investigated [3], [10]–[13]. It has been reported that the microstructures of FSPed steels consisted of nearly equiaxed grains with the sizes of micron levels [3], [14]. Also, hardness of FSPed steels increased in the stir zone (SZ) compared to that of the base material [3], [10]–[13]. Considering these publications, relatively less attention has been given to Interstitial-free (IF-steel) steel sheets, despite their significant industrial importance [14]–[18]. Especially in these studies, the lowest thickness of the IF-steel sheets was 1.5 mm due to application of FSP in force controlled mode. In order to expand application areas of FSPed IF-steels into the automotive industry thinner

sheets need to be processed, in order to sustain lightweighting goals. Therefore, the purpose of this study is to investigate systematically the effect of processing parameters on the mechanical properties of thin IF-steel sheets via position controlled FSP applications.

II. EXPERIMENTAL PROCEDURE

Cold rolled and continuously annealed IF-steel sheets with the chemical composition of 0.004 C, 0.012 Si, 0.2 Mn, 0.012 P, 0.009 S, 0.1 Ti (in wt%) and balance Fe was used in this study. 1.2 mm thick samples with the dimensions of 400 mm x 100 mm x 1.2 mm were cut from the as-received CG sheets. They were subjected to FSP using a carbide-tungsten tool with a flat shoulder diameter of 14 mm and a conical pin with a diameter and length of 5 mm and 0.8 mm, respectively.

The effects of different rotation speed (800, 1000 and 1200 rpm) and processing speed (48, 60 and 78 mm/min) on the mechanical properties of FSPed IF-steel were investigated. The shoulder tilt angle was 3° and the tool plunge depth was kept constant at 0.1 mm by position controlled servo mechanical system. Processing temperature was determined with an infrared thermal imaging camera, as shown Table I. Peak temperatures of the various processing conditions were measured in the range of 840-970 °C.

TABLE LV
PROCESSING TEMPERATURE

Sample Number	Rotation Speed, rpm	Processing Speed, mm/min	Temperature, °C
1	1200	78	895±48
2	1200	60	977±19
3	1200	48	918±11
4	1000	78	866±16
5	1000	60	887±13
6	1000	48	878±39
7	800	78	865±32
8	800	60	867±15
9	800	48	842±11

Optical microscope (OM) scanning electron microscopy and (SEM) were used to observe the microstructure of IF-steel samples before and after FSP. The metallographic specimens were sectioned perpendicular to the process direction (Fig. 1) and then etched in 2% Nital for 20 s after standard metallographic preparation.

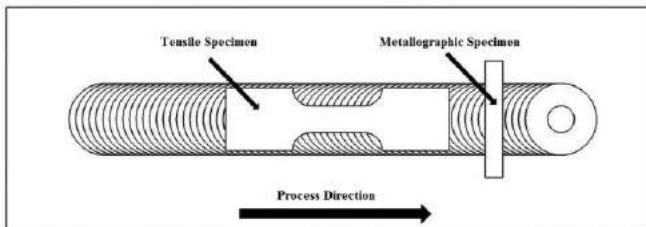


Fig. 36 Schematic illustration of the FSPed plate and the position of the specimens inside the FSPed zone

III. RESULTS AND DISCUSSION

SSS. Microstructural Evolutions

The OM images regarding the cross section microstructure of specimen subjected to various rotating and processing speeds are presented in Fig. 2. Generally, intense plastic deformation and complicated material flow around the stirring pin formed a SZ at the central parts of the process region (PR) with a darker contrast (Fig. 2). Also, as a well-known result of the FSP, variations in plastic straining and amount of the heat generation led to formation of thermo-mechanically affected zone (TMAZ) and heat affected zone (HAZ). In TMAZ grain morphology was elongated due to the decrease effectiveness of the dynamic recrystallization. Microstructure within the heat affected zone mainly characterized with coarse grain sizes compared to that of SZ and TMAZ or even than that of the as-received condition. This mainly due to the HAZ region is only affected from the thermal exposure without plastic straining. A closer look to deformation regions formed after FSP process indicates a strong relationship between the tool rotation speed (TRS), tool transverse speed (TTS) and existence and dimensions of the deformation regions (Fig 2). Mainly, increasing the tool rotation speed and decreasing the transverse speed resulted with formation of a more widespread heat affected zone (Fig. 2). Also, grain refinement within the TMAZ and SZ become more and more limited with increasing values of the TRS and TTS. It is well known that increasing TRS values increases heat generated during the FSP process [15]. Therefore excessive heat generation is mainly cause occurrence of the static recrystallization rather than favoured dynamic recrystallization. Moreover, selection of the lower TTS together with high TRS values allows high amount of heat to be transferred. This leads to increase in temperature of the deformation regions at the vicinity of SZ and causes to formation of HAZ, coarsening grain size of TMAZ and/or extending the boundaries of the HAZ. On the point of view of the current results obtained from the microstructural investigations indicates that, basic requirement to achieve more effective grain refinement is selection of the lowest possible TRS and highest possible TTS. In the current study lowest possible TRS and highest possible TTS were applied as 800 rpm and 78 mm/min respectively. Application of the FSP based on these process parameters formed a deformation region with the microstructure given in Fig. 3.

As-can be understood from Fig. 3, single-phase ferritic microstructure having a mean grain size of 35 µm was strongly refined and transformed in to a FG microstructure inside the SZ as a result of intense plastic deformation (Fig. 3 (b)-(c)). It is evident from Fig. 3 (b)-(c) that microstructure of the SZ was mainly consisted of equiaxed grains with a mean size of about 5 µm. A transition region between the SZ and the unaffected zone known as thermo-mechanically affected zone (TMAZ) as

seen in Fig. 3 (d)–(e). By the end of the TMAZ, grain morphology gradually became a like with that of as-received material.

Generally, continuous dynamic recrystallization (CDRX) is reported to be operative mechanism grain refinement in warm deformation of high stacking fault energy materials like ferritic steels [3], [11], [19], [20]. In this mechanism, new grains are not formed by a classical nucleation mechanism; the recrystallised microstructure develops instead by the progressive transformation of subgrains into new grains, with in the deformed original grains [20]. This mainly leads to the formation of homogenous microstructure having mainly equiaxed fine grains at the SZ where the highest level of frictional heat and plastic straining were achieved. However, static recrystallization (SRX) may lead to coarsen of the refined microstructure due to the extensive heat generation and high deformation temperature by increasing the rotating speed. In contrast, occurring of HZ can be avoided by employing lowest possible rotating speed as seen Fig. 3 (a).

TTT. Effect of Processing Parameters on Tensile Properties

The effect of rotating speed on the tensile behaviour of FSPed specimens are presented in Fig. 4, respectively, for the processing speeds of 48, 60 and 78 mm/min. The yield strength (σ_y), ultimate tensile strength (UTS), uniform elongation (ϵ_u), and elongation to failure (ϵ_f) taken from this curves are summarized in Table 2. As-received CG sample showed low strength and high elongation with a very large uniform elongation region (Fig. 4). Therefore, it is obvious from the stress-strain curves, deformation behaviour of the as-received IF-steel is dominated by the strain hardening.

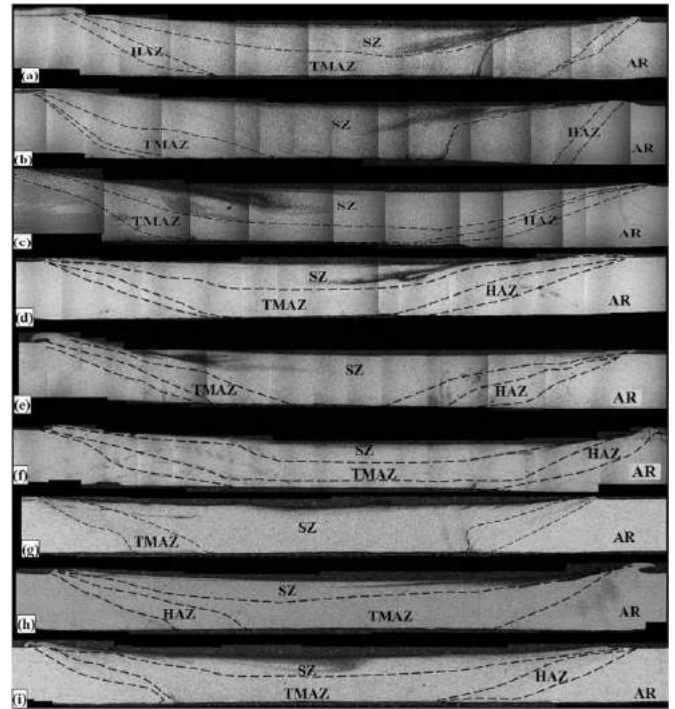


Fig. 2 A general view of cross-sections of the sample's perpendicular to the advancing direction of the FSP.

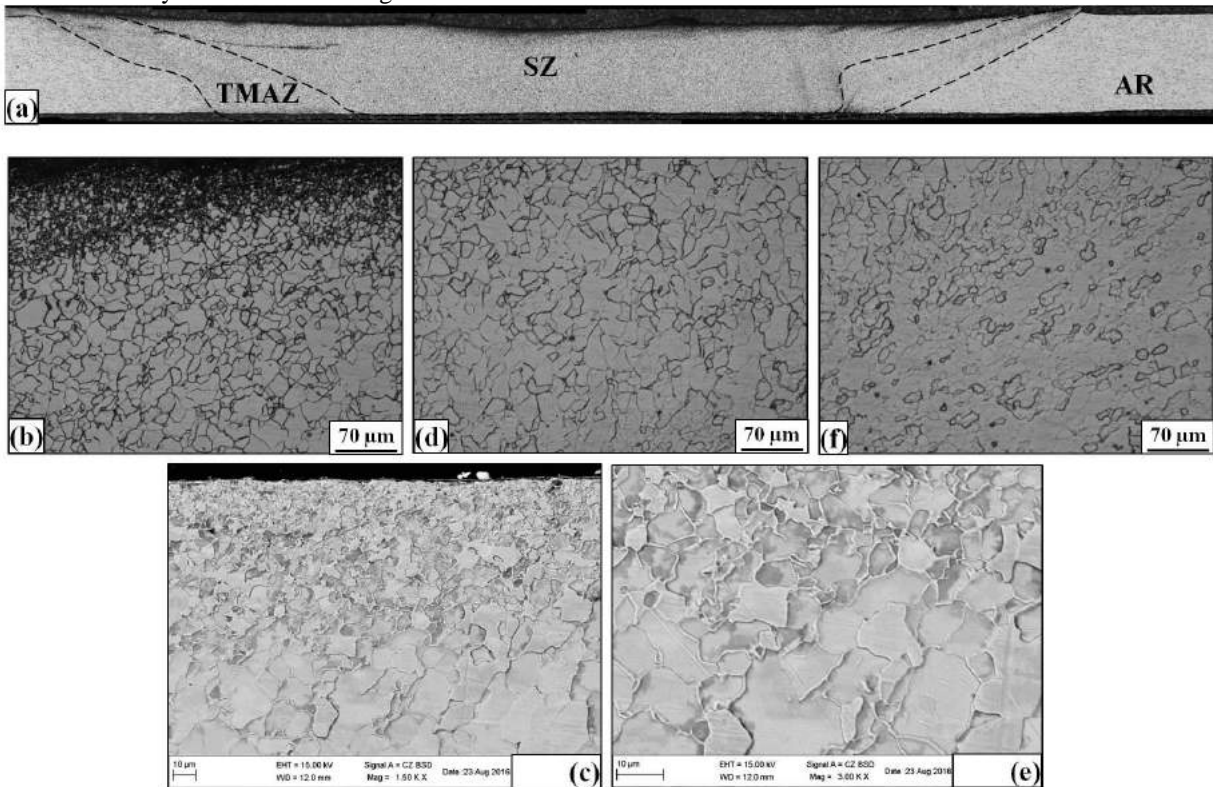


Fig. 3 (a) A general view of cross-section of the sample 7 perpendicular to the advancing direction of the FSP. High magnification micrographs showing the: (b)-(c) SZ optical and SEM micrographs, (d)-(e) optical and SEM micrographs of transition zones between the SZ and TMAZ, (f) optical micrograph of HAZ

Actually, this behaviour is one of the most important design criteria and the characteristic feature of the IF-steels considering the engineering applications that mainly concentrated on the sheet metal forming. This important behaviour is still evident after the applied FSP following various process parameters (Fig. 4(a)-(c)). However, it is also obvious that, FSP somehow constricted the uniform elongation region and/or strain hardening capability. This is mainly due to the more-or-less grain refinement after the FSP processes leading to reduce of the free dislocation path and decrease effectiveness of dislocation-dislocation interactions. However, even after the reduction of the strain hardenability, FSPed IF-steel still undergo deformation with a considerable domination of the strain hardening behaviour.

As-received IF-steel mainly reflected limited strength and excellent ductility. The yield strength and ultimate tensile strength of the as-received IF-steel was determined to be 156 MPa and 279 MPa respectively. FSP have been found effective in enhancing strength of the IF steel. However, process parameters also found to be effective on the achieved strength enhancements. Generally, FSP processes applied at higher TRSs like 1000 rpm and 1200 rpm resulted in limited strength enhancements (Fig. 4(a)-(c)). This argument become more pronounced when low TTS are applied. For example, the

process applied at 1200 rpm and 48 mm/min resulted in a limited strength enhancement with yield strength and UTS of 237 MPa and 334 MPa respectively. These values are nearly close to that of as-received IF-steel. Application of the lowest possible process TRS and highest possible TTS, on the other hand, resulted in a most effective strength increment. As can be seen in Table 2 and Fig. 4(a), yield strength and UTS of the as-received IF steel reached to 382 MPa and 501 MPa via setting TRS and TTS to 800 rpm and 78 mm/min respectively. More importantly, the strengthening was achieved without a considerable decline of ductility, which is a crucial parameter considering the engineering applications of the steels. In CG state, the ϵ_u and ϵ_f were measured as 24.5% and 45.8%, respectively. After FSP applied following the process condition where the most effective strength enhancement achieved (TRS=800 rpm and TTS 78= mm/min), the ϵ_f value decreased to about to 21.8%. However, considerably high uniform elongation of about 16.6% was still retained (Table 2). As an expected result, other process conditions leading the lower strength enhancement resulted in higher elongation values (Table 2). Such improvement in strength of the FSPed sample is assumed to be primarily from the considerably refined microstructure leading to grain size strengthening (Fig. 3 (c)-(d)) [21].

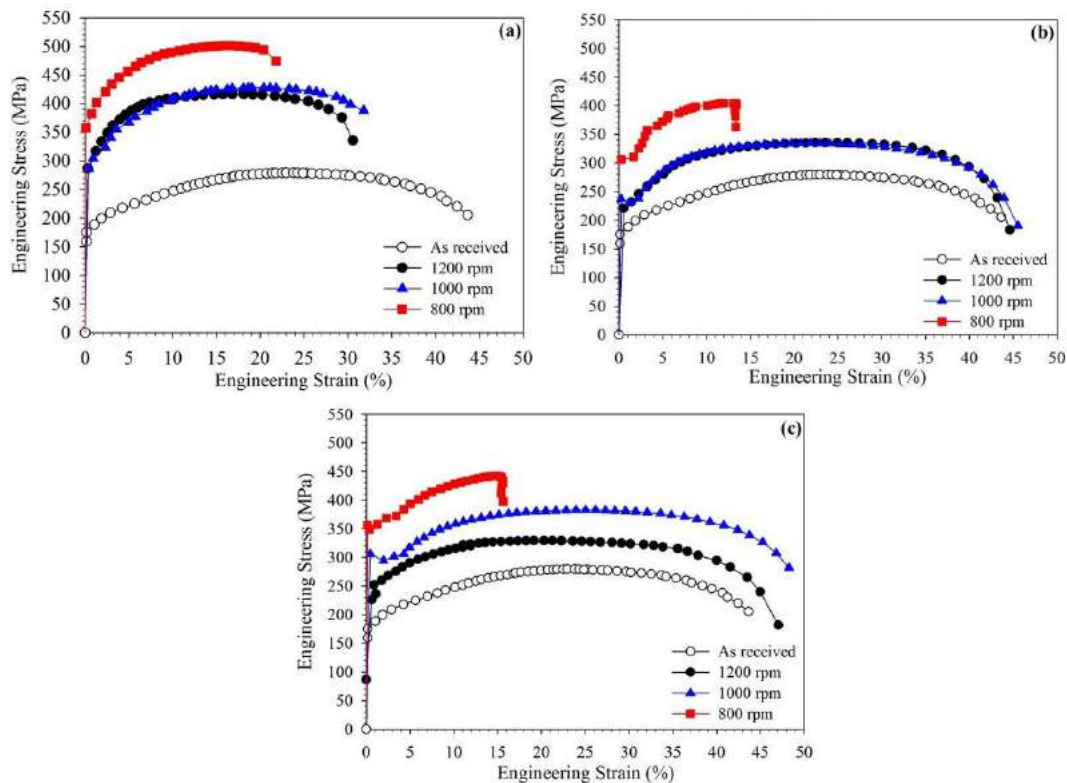


Fig. 4 Tensile stress-strain curves of FSPed IF-steel at processing speed of (a) 78 mm/min, (b) 60 mm/min and (c) 48 mm/min

TABLE ILVI
THE MECHANICAL PROPERTIES OF AS-RECEIVED CG AND FSPED FG IF-STEEL SAMPLES

Sample Number	Rotating Speed, rpm	Processing Speed, mm/min	Yield Strength, MPa	Ultimate Tensile Strength, MPa	Uniform Elongation, %	Total Elongation, %
1	1200	78	305.9	416.5	16.8	30.5
2	1200	60	234.2	329.0	21.2	48.2
3	1200	48	231.9	294.0	23.5	44.6
4	1000	78	304.0	427.7	18.6	31.8
5	1000	60	237.5	334.4	22.3	46.2
6	1000	48	282.8	335.7	26.1	48.2
7	800	78	382.6	501.0	16.6	21.8
8	800	60	310.0	404.4	13.0	13.5
9	800	48	356.3	442.3	14.8	15.0

IV. CONCLUSIONS

In the present study, the effect of friction stir processing (FSP) parameters on the microstructure and mechanical properties IF-steel was investigated. The main results and conclusions of this study can be summarized as follows:

- 1.2 mm thick IF-steel sheets successfully processed by position controlled FSP.
- A fine grained microstructure having mean grain size of 5 μ m were obtained from the coarse-grain (CG) (35 μ m) IF-steel with FSP.
- Deformation behavior of IF-steel found to be strain hardening dominated. This behavior remained unchanged after the FSP.
- Grain refinement by position controlled FSP significantly enhanced strength of IF-steel without sacrificing the formability. Ultimate tensile strength of the IF-steel was increased from 279 MPa to 501 MPa. This strength level is higher than all reported improvements until to this date.

IX. ACKNOWLEDGMENT

This research was supported by The Scientific and Technological Research Council of Turkey (TUBITAK), under Grant No: 115M649.

X. REFERENCES

- [1] R. S. Mishra, and Z. Y. Ma, "Friction stir welding and processing." *Materials Science and Engineering: R: Reports*, vol. 50.1, pp. 1-78, 2005.
- [2] Z. Y. Ma, "Friction stir processing technology: a review." *Metallurgical and materials Transactions A*, vol 39.3, pp. 642-658, 2008.
- [3] S. Mironov, Y. S. Sato, and H. Kokawa. "Microstructural evolution during friction stir-processing of pure iron." *Acta Materialia*, vol. 56.11, pp. 2602-2614, 2008.
- [4] C. G. Rhodes, et al. "Fine-grain evolution in friction-stir processed 7050 aluminum." *Scripta Materialia*, vol. 48.10, pp. 1451-1455, 2003.
- [5] J. Q. Su, T. W. Nelson, and C. J. Sterling, "Friction stir processing of large-area bulk UFG aluminum alloys." *Scripta materialia*, vol. 52.2, pp. 135-140, 2005.
- [6] M. L. Santella, et al. "Effects of friction stir processing on mechanical properties of the cast aluminum alloys A319 and A356." *Scripta Materialia*, vol. 53.2, pp. 201-206, 2005.
- [7] Z. Y. Ma, et al. "Microstructural refinement and property enhancement of cast light alloys via friction stir processing." *Scripta Materialia*, vol. 58.5, pp. 361-366, 2008.
- [8] R. Nandan, T. DebRoy, and H. K. D. H. Bhadeshia, "Recent advances in friction-stir welding-process, weldment structure and properties." *Progress in Materials Science*, vol. 53.6, pp. 980-1023, 2008.
- [9] C. I. Chang, C. J. Lee, and J. C. Huang, "Relationship between grain size and Zener-Holloman parameter during friction stir processing in AZ31 Mg alloys." *Scripta Materialia*, vol. 51.6, pp. 509-514, 2004.
- [10] Y. C. Chen, and K. Nakata, "Evaluation of microstructure and mechanical properties in friction stir processed SKD61 tool steel." *Materials characterization*, vol. 60.12, pp. 1471-1475, 2009.
- [11] P. Xue, et al. "Achieving ultrafine dual-phase structure with superior mechanical property in friction stir processed plain low carbon steel." *Materials Science and Engineering: A*, vol. 575, pp. 30-34, 2013.
- [12] N. Yasavol, et al. "Microstructure evolution and texture development in a friction stir-processed AISI D2 tool steel." *Applied Surface Science*, vol. 293, pp. 151-159, 2014.
- [13] S. H. Aldajah, et al. "Effect of friction stir processing on the tribological performance of high carbon steel." *Wear*, vol. 267.1, pp. 350-355, 2009.
- [14] D. M. Sekban, et al. "Microstructure, mechanical properties and formability of friction stir processed interstitial-free steel." *Materials Science and Engineering: A*, vol. 642, pp. 57-64, 2015.
- [15] A. Chabok, and K. Dehghani, "Effect of processing parameters on the mechanical properties of interstitial free steel subjected to friction stir processing." *Journal of materials engineering and performance*, vol. 22.5, pp. 1324-1330, 2013.
- [16] A. Chabok, and K. Dehghani, "Formation of nanograin in IF steels by friction stir processing." *Materials Science and Engineering: A*, vol. 528.1, pp. 309-313, 2010.
- [17] A. Chabok, and K. Dehghani, and M. A. Jazani, "Comparing the Fatigue and Corrosion Behavior of Nanograin and Coarse-Grain IF Steels." *Acta Metallurgica Sinica (English Letters)*, vol. 28.3, pp. 295-301, 2015.
- [18] A. Chabok, and K. Dehghani, "Dependence of Zener parameter on the nanograins formed during friction stir processing of interstitial free steels" *Materials Science and Engineering: A*, vol. 528.13, pp. 4325-4330, 2013.
- [19] D. M. Sekban, et al. "Impact toughness of friction stir processed low carbon steel used in shipbuilding." *Materials Science and Engineering: A*, vol. 672, pp. 40-48, 2016.
- [20] H. Fujii, et al. "Friction stir welding of carbon steels." *Materials Science and Engineering: A*, vol. 429.1, pp. 50-57, 2006.

S. Gourdet, and F. Montheillet, "A model of continuous dynamic recrystallization." *Acta Materialia*, vol. 51.9, pp. 2685-2699, 2003.

Study of the Compacting and Pre-Sintering of Dental Zirconia Waste Powders

*Handan Turan Matik, Mustafa Boz, Ulaş Matik
Karabuk University, Department of Manufacturing Engineering Karabuk, 78050 Turkey
handantrnmtk@gmail.com, mboz@karabuk.edu.tr, matik@karabuk.edu.tr*

ABSTRACT

This study aims to determine the optimum parameters for production of zirconia block from dental zirconia waste powders. For this purpose, zirconia blocks obtained by uniaxial pressing of waste powders under different pressures (200, 300, 400, 550 and 600 MPa) were pre-sintered at different temperatures (950, 1050, 1150 and 1250 °C) for 2 h. Pre-sintered zirconia blocks were characterized density and hardness tests. The phase structure and chemical composition of zirconia blocks were determined by SEM-EDX and XRD analysis. The density and hardness of zirconia blocks increased depending on increasing pressing pressure and pre-sintering temperature. Also, it has been found that high pressing pressures cause cracks in the blocks.

Keywords: Zirconia presintering characterization

The Tribological Characteristics of Electroless Ni-P Coated AISI1020 Carbon Steel

Ulaş Matik¹ and Ramazan Çıtak²

¹TOBB Technical Science Vocational School, Karabuk University, Karabuk, 78050, TURKEY,
matik@karabuk.edu.tr

²Gazi University, Technology Faculty, Department of Metallurgical and Materials Engineering., Ankara, 06500,
TURKEY, citak@gazi.edu.tr

ABSTRACT

The effects of phosphorus content of electroless Ni-P (EN) coatings on the tribological and morphological properties of AISI1020 carbon steel were investigated. For this purpose, AISI1020 carbon steel substrates were coated with low, medium and high phosphorus EN coatings. Coated samples were characterized using surface roughness and micro hardness measurements, pin-on-disc wear tests, optical microscopy and scanning electron microscopy with energy dispersive X-ray spectroscopy (SEM/EDX). The hardness and wear resistance of the EN coatings increased depending on decreasing phosphorus content of the coatings. Also, it has been found that the increase in the phosphorus content of the coating improves its friction properties.

Keywords: Electroless nickel; Carbon steel; Ni-P; hardness; wear; tribology

The Influence of Heat Treatment on Structural Transformations of NiTi alloy

Yüksel Akinay, Fatma Meydaneri TEZEL, Yasin AKGUL

Karabuk University Iron and Steel Institute Karabuk, 78050 Turkey

yukselakinay@karabuk.edu.tr, yasinakgul@karabuk.edu.tr, fatmameydaneri@karabuk.edu.tr

ABSTRACT

In this study, effects of heat treatment on microstructure and structural properties of NiTi alloy were investigated. In this sence, the depence of shape memory behavior of NiTi alloy was examined by changes of heat treatment temperature and cooling conditions. Two group of specimens were used. One group was deformed by 50% and the other group was deformed 75%. Heat treatment temperatures were chosen 5000C and 600 0C. All specimens were cooled both in air and water to investigate the influence of cooling conditions. Microstructures were examined using Scanning Electron Microscope (SEM). Also DSC and XRD analysis were carried out for thermal and structural characterization.

Keywords: Shape memory, NiTi alloy, SEM, DSC, XRD

The Influence of Heat Treatment on Structural Transformations of NiTi alloy

Yüksel Akinay, Fatma Meydaneri TEZEL, Yasin AKGUL

Karabuk University Iron and Steel Institute Karabuk, 78050 Turkey

yukselakinay@karabuk.edu.tr, yasinakgul@karabuk.edu.tr, fatmameydaneri@karabuk.edu.tr

ABSTRACT

In this study, effects of heat treatment on microstructure and structural properties of NiTi alloy were investigated. In this sense, the dependence of shape memory behavior of NiTi alloy was examined by changes of heat treatment temperature and cooling conditions. Two groups of specimens were used. One group was deformed by 50% and the other group was deformed 75%. Heat treatment temperatures were chosen 500°C and 600 °C. All specimens were cooled both in air and water to investigate the influence of cooling conditions. Microstructures were examined using Scanning Electron Microscope (SEM). Also DSC and XRD analysis were carried out for thermal and structural characterization.

Keywords: Shape memory, NiTi alloy, SEM, DSC, XRD

Effect Of SiC Particle Size on the Tribological Properties of AA6061-SiCp Composite Prepared By Hot Pressing

Mert Yakışık, Ulaş Matik
Karabük Üniversitesi Meslek Yüksekokulu Karabük, 78050 Turkey
mertyakisik@gmail.com, matik@karabuk.edu.tr

ABSTRACT

The aim of this study is to investigate the effect of SiC particle size on the hardness and wear behaviour of AA6061-SiCp composites. For this purpose, various size (8, 32 and 82 μm) with 30wt.% amount of SiC particles have been added into AA6061 aluminum alloy powders and $\text{Ø}35 \times 10$ mm cylindrical blocks were produced by hot pressing at 525°C. Then, T6 heat treatment was applied to AA6061-SiCp composites aged at 180 °C for 18 h after solution heat treatment at 540 °C for 1 h. In order to identify the hardness and wear tests were performed to all samples under same conditions. Experimental results showed that with the increase of SiC particle size in the composites, the hardness decreased and wear resistance increased.

Keywords: AA6061, SiC particle, Composite, Hot pressing, Hardness, Wear

Investigation of Cutting Forces and Surface Roughness in Hard Turning of Bearing Ring with CBN Insert

Mehmet Boy*, İbrahim Çiftçi**, Feridun Özhan***

* Karabük University, TOBB Technical Sciences Vocational College, Karabük, Turkey

mboy@karabuk.edu.tr

** Çankırı Karatekin University, Department of Manufacturing Engineering, 18100, Çankırı, Turkey

iciftci@karatekin.edu.tr

*** ORS Bearing, Ankara, Turkey

Abstract—The most important components of the bearings are the inner and outer bearing rings. The raceway is the most important feature constituting the bearing rings. Grinding and super finishing operations are applied to attain tight tolerances and very low surface roughness in the raceway. In this study, the effect of the cutting parameters on the cutting forces and surface roughness in turning of the outer bearing ring raceway, made from hardened AISI 52100 steel, was investigated by using cubic boron nitride (CBN) cutting tool instead of grinding. The cutting forces occurred in hard turning of the outer bearing rings were measured using a piezoelectric cutting force measurement unit. It was seen that the radial cutting forces acting on the outer ring raceway were higher than the primary forces. The feed force at the end of the raceway form was higher than that at the start point of the form. The lowest surface roughness was obtained at 0.04 mm/rev feed rate.

Keywords— Cutting force, surface roughness, hard turning CBN insert, bearing ring

I. INTRODUCTION

Ball bearings are used to support rotating shafts in mechanical equipment due to their versatility and overall performance. Ball bearings are manufactured to a very high precision level in high volume quantities. A ball bearing consists of inner and outer rings, rolling elements and cage. The outer diameter of the inner ring and the inner diameter of the outer ring have a groove in which the balls roll on and contact. This groove is commonly called the raceway. The surface of this raceway is precision finished to extremely tight tolerances and is honed to a very smooth surface finish. Ball bearings are generally made of high carbon chromium steels such as AISI 52100. From raw material, the bearing rings can be made either by tube rolling or forging process. After this the rings are annealed for a longer period which is called spheroidised annealing process. After annealing the

soft rings are turned to get a desired shape of the races followed by heat treatment for hardening and tempering. The final geometry and surface quality are achieved through grinding and super-finishing processes [1-2].

The finishing operations determine the surface quality of the contacting elements, which is fundamental for stress resistance and lubrication. For this reason, finishing operations of the bearing rings are conventionally carried out through grinding process. The hard turning has been increasingly used as an alternative to grinding operations. Because of the advances in machine tools and cutting tool technology, hard turning becomes an effective manufacturing process to produce parts with high precision and surface quality. Hard turning, compared to grinding operations, has some benefits such as a high material-removal rate, more flexibility, lower energy consumption and production costs, a shorter cycle time, an improved overall product quality, and a lower environmental impact [3-7].

Hard machining requires special tool materials, with high wear-resistance and high hardness at elevated temperatures. Mixed ceramic and cubic boron nitrides (CBN) are the most commonly used tool materials. Their hardness and chemical stability enable them to withstand the high thermal and mechanical loads of such machining operations. CBN has a higher hardness than ceramic tools at both low and high temperatures. Other CBN properties, such as high thermal conductivity and low thermal expansion coefficient, are also important when using such tools in hardened steel turning. CBN tools are usually classified as high CBN content (around 90%) and low CBN content (around 60%) grade. The high CBN content tools show higher toughness than low CBN content tool. Therefore, high CBN content tools are usually recommended for interrupted cutting operations. Also, the high CBN content makes them harder than the low

content one. The ceramic phase in CBN tools drops hardness and toughness of the tool, but increase chemical stability [8-10].

Cutting forces and surface roughness on the machined surface are greatly influenced by the cutting parameters chosen. Cutting forces acting on the tool and surface roughness produced during finish hard turning of the workpiece may be used to evaluate the performance of the selected range of cutting parameters. For successful implementation of hard turning, selection of suitable cutting parameters for a given cutting tool; workpiece material and machine tool are important steps. Study of cutting forces is critically important in turning operations because cutting forces correlate strongly with cutting performance such as surface accuracy, tool wear, tool breakage, cutting temperature and forced vibrations, etc.

The cost of machining is strongly dependent on the rate of material removal, and costs may be reduced by increasing the cutting speed and/or the feed rate. There are limits to the speed and feed above which the tool life is shortened excessively. Another important output in machining is surface roughness. The surface roughness affects the performance of mechanical parts and their production costs and indicates the irregularities of a surface texture. Machined surface characteristics are important in determining the functional performance such as frictional and corrosion resistance, ease of holding the lubricant, electrical and thermal conductivities, fatigue strength and tribological properties of machined components. The surface roughness is affected by several factors including the cutting tool geometry, the cutting speed, the feed rate, the microstructure of a workpiece and the rigidity of a machine tool [11-15].

In recent years, there have been many statistical and experimental studies concerning the effect of cutting conditions on the surface roughness, cutting force and tool wear occurred in hard turning of various steels. Yücel and Günay investigated the effect of cutting conditions on cutting forces and surface roughness. They found that depth of cut and feed rate are the most significant factor on surface roughness and cutting force for both the ceramic and CBN cutting tool. Also, they obtained the lowest surface roughness with CBN insert during machining of Ni-Hard with 62 HRC [16]. Thiele and Melkote investigated the effect of workpiece hardness and cutting edge geometry on surface roughness and cutting forces in finish hard turning of AISI 52100 steel using CBN tools. They found that increasing the edge hone radius tends to increase the average surface roughness and the effect of edge hone radius on the surface roughness decreased with an increase in workpiece hardness. It is also shown that the two-factor interaction of the workpiece hardness and cutting edge preparation on the surface roughness is very significant [17]. Bouacha et al. investigated the Ra values in hard turning AISI 52100 bearing steel with CBN cutting tool. They found that surface roughness was mainly influenced by feed rate and cutting speed. Also, the radial force was the highest of cutting force

components, and it was highly sensitive to workpiece hardness, negative rake angle and tool wear evolution. The depth of cut exhibited maximum influence on cutting forces as compared to the feed rate and cutting speed [14]. Chen experimentally investigated the machining of hardened steel with CBN insert that the radial cutting force was the largest among the three-cutting force components [18]. Singh and Rao carried out an investigation to determine the effects of cutting conditions and tool geometry on the surface roughness in hard turning of AISI 52100 [19]. Moreover, the cutting forces as the surface roughness are also influenced by the insert cutting edge geometry as it was mentioned by Özel et al [20]. Boy et al. studied the effects of cutting tool edge geometry, feed rate and cutting speed on surface roughness and the resultant cutting forces in the hard turning of AISI 52100 steel with ceramic cutting tools. The interaction of the cutting parameters on the surface roughness and cutting forces was determined by using ANOVA. The results showed that the feed rate and tool edge geometry were the most significant factor on the resultant cutting forces and surface roughness. In a further work, they found that the cutting-edge geometry, cutting speed and feed rate were the most significant factors on the resultant cutting force while the cutting insert edge geometry and feed rate were the most significant factor for the surface roughness [].

Until now only straight turning or facing operations were carried out on cylindrical parts in these studies. However, ball bearing rings produced mainly from AISI 52100 steel have circular grooves in addition to cylindrical features. Both the outer and inner rings of a ball bearing have circularly grooved raceways. Essentially the conditions of turning circularly grooved cylindrical surfaces differ quite considerably from those of straight cylindrical surfaces. In this study, hard turning tests were carried out on AISI 52100 steel ball bearing rings using CBN cutting tools. The circularly grooved raceway of an outer ring was hard turned. The influences of cutting speed and feed rate on surface roughness and cutting forces were investigated.

II. EXPERIMENTAL

UUU. Workpiece Material

In this study, the hard turning tests were performed on the bearing rings of AISI 52100 steel with hardness of 60 ± 2 HRC, the composition of which is given in Table 1. The outer rings used in the experiments were brought in suitable dimensions and tolerances for hard turning after hot forging, spheroidising, cold roll forming, soft turning, heat treatment and face grinding. The outer bearing ring used in the experiments is shown in Fig. 1.

TABLE LVII
CHEMICAL COMPOSITION OF AISI 52100 STEEL (WT%)

C	Si	Mn	P	Ni	Cr	Mo	Cu	Al	Fe
0,99	0,24	0,36	0,016	0,06	1,43	0,02	0,10	0,017	Balance

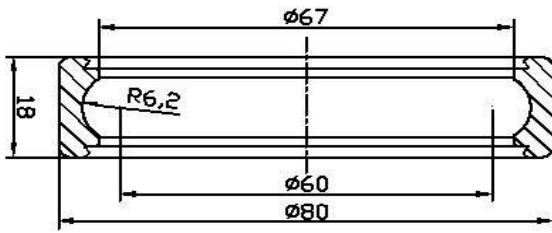


Fig. 1 Geometry of the outer ring used for hard turning tests

VVV. Cutting Tool and Geometry

The cutting tools used were commercial grade TiN coated low content CBN inserts produced by Sandvik Coromant with the geometry of DCGW 11T304 S01020. These inserts are recommended for machining hardened steel by Sandvik and had CB7015 Sandvik grade (ISO H15) with chamfered + honed edge geometry. A25T SDXCR 11 ISO coded internal tool holder was used for hard turning of the raceway.

WWW. Experimental Design

The hard turning tests were carried out on a twin spindle CNC chucker equipped with a pair of highly precise collet chucks. Three cutting speeds (120, 140 and 160 m/min) and three feed rates (0,04, 0,06 and 0,08 mm/rev) were used. Selection of these cutting conditions was based on a series of preliminary tests. It was found that, at a depth of cut of 100 μm , the resulting out of roundness values were quite high. Therefore, the depth of cut was reduced to 50 μm .

At each condition, a total of 12 rings were hard turned. Surface roughness measurement was carried out on the hard turned raceway using a Form Talysurf PGI instrument capable of measuring contours. The surface roughness measurements were carried out on 1, 4, 8 and 12th hard turned rings and the readings were averaged. Cutting force was measured with a Kistler 9121 three components piezoelectric dynamometer and associated 5070 A charge amplifiers connected to PC employing Kistler Dynoware force measurement software.

III. RESULTS AND DISCUSSIONS

Cutting forces and average surface roughness values were measured during hard turning of circularly grooved cylindrical surfaces of raceways of ball bearing outer rings.

A. Evaluation of cutting forces

In precision hard turning of various components, magnitude of cutting force components is crucial in meeting the design specifications such as roundness and squareness. Excessive cutting forces require higher clamping forces and the higher clamping forces, in turn, lead to the roundness error especially in the case of ring shaped parts like bearing rings. In addition, the higher forces make the workpiece change its position during cutting, which results in more inaccuracy. The force components arising from hard turning are the cutting force, feed force and radial force. Among the hard turning parameters, cutting speed, feed rate and

workpiece geometry have effects on the magnitude and direction of these force components.

The outer ring raceway was machined in two passes using CBN cutting tools. Two different depth of cut were used 0.1 mm and 0.05 mm at each pass, respectively. Cutting forces can be divided into three components: feed force (F_f), radial force (F_p) and tangential cutting force (F_c). The cutting force components that measured in hard turning of raceway were given Fig 2. In Fig 2., similar tendencies were seen in the cutting forces formed in 1st and 2nd pass. When evaluating the cutting forces, the data obtained in hard turning of the second pass was considered. While evaluating the cutting forces, the average of the forces occurred at the start and end of the raceway for feed force and the middle of the raceway for the tangential and radial force were taken.

A quite different force pattern was observed in hard turning of the raceway. As can be seen from Fig. 2, there are substantial differences in the magnitude and direction of the cutting force components obtained for the raceway.

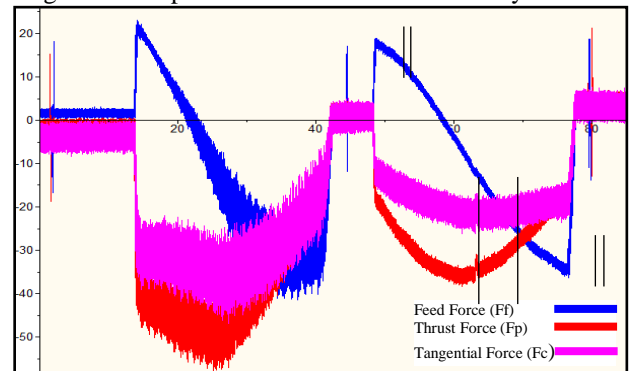
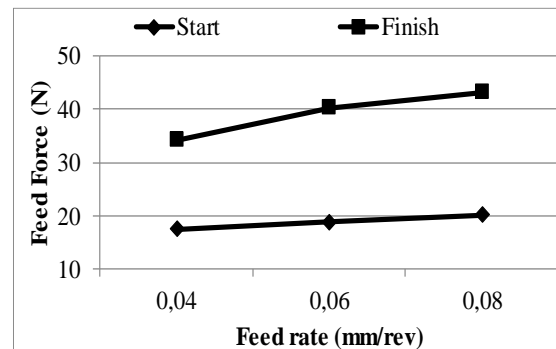
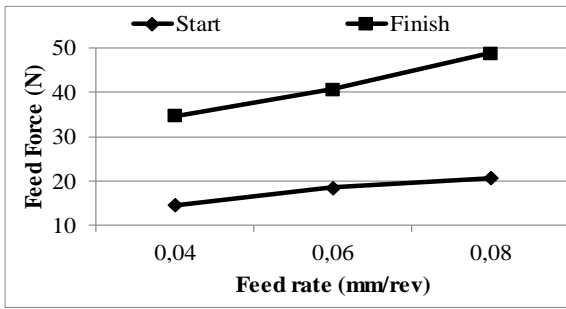


Fig.2 Cutting force components in hard turning of outer ring raceway

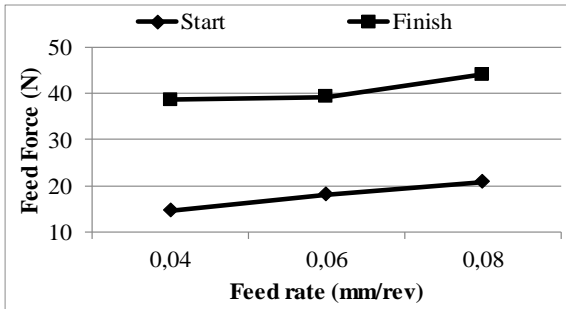
In hard turning of the raceway, the tangential force and the radial force are in negative directions. Direction of the feed force changes depending on the position of the cutting tool with respect to the raceway.

a)





b)



c)

Fig.3 Effect of feed rate on feed force: a) 120, b) 140 c) 160 m/min

Fig.3 shows the effect of feed rate on feed force at three different cutting speeds. It is seen from Fig.3 that the feed force increases with increasing the feed rate. The increase in the feed force with increasing the feed rate is due to increasing chip load. Also, it is seen that the feed forces occurring at the end of the raceway are greater than those at the beginning. Because of the form of the raceway, the contact area of the cutting edge changes with the motion of the cutting tool, resulting in changes in the chip cross section and tool-chip contact length.

Fig. 4. and Fig. 5. show the variation of the radial and tangential forces, with respect to cutting speed. With an increase in cutting speed, the radial force showed a decrease. This reduction is usually seen when machining of most metals. This reduction is explained by the plastic softening of machined material under the effect of the increase in the cutting temperature and in part to a decrease in tool-chip contact area owing to a thinner chip. It was seen that, at a feed rate of 0.04 mm/rev, radial force decrease when the cutting speed increasing to 140 m/min. However, an increase in the radial force was observed at 160 m/min cutting speed. The same trend was seen for the tangential cutting force. The lowest radial and tangential forces were obtained at a feed rate of 0.04 mm/rev and cutting speed of 140 m/min. It is seen that the radial force is greater than the tangential force which occurred in hard machining of the raceway. Because of the low depth of cut, chip formation occurs at the tip of the cutting tool, which causes the radial forces to increase. The increase in radial force can lead to instability through vibration. Therefore, the tool nose radius should be kept as small as possible. In addition, this may also cause temperature concentration at the tool nose and increase the tool wear, resulting in a short tool life.

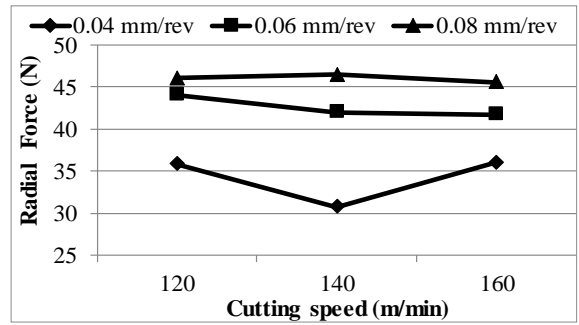


Fig.4 Effect of cutting speed on radial force

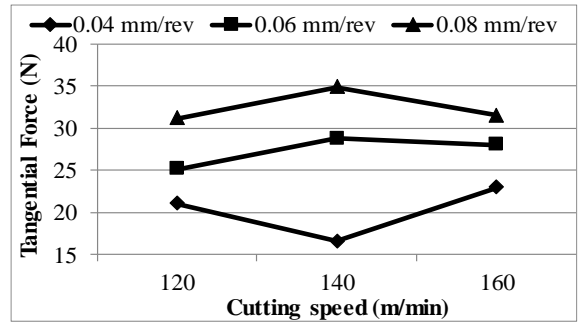


Fig.5 Effect of cutting speed on tangential cutting force

B. Evaluation of surface roughness

Surface roughness in hard turning is influenced by many factors such as cutting speed, depth of cut, tool nose radius, workpiece hardness, feed rate, and tool geometry. As surface roughness is critical to the functionality of hard turned components, low feed rates were selected to reduce the surface roughness values. Low feed rates also reduce the mechanical and thermal impacts on the workpiece and the cutting tool. Fig. 6 shows the variation in average surface roughness with different cutting parameters. The surface roughness values obtained in all cutting parameters are below 0.6 μm required for the raceway.

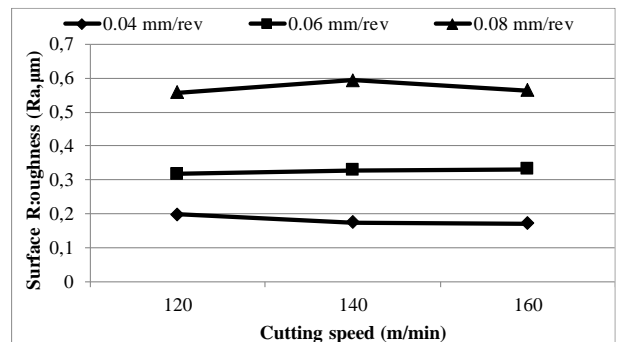


Fig.6 Effect of cutting parameters on surface roughness

Specially, the surface roughness increases as the feed rate increases, the surface roughness proportional to the square of the feed rate. For the raceway, surface roughness increases with increasing feed rate as expected. Surface roughness values are close to each other at same feed rates, which have obtained in hard turning with CBN cutting tool.

Similar trends and the range of changes were revealed for the average surface roughness, as shown in Fig. 6. In general, average surface roughness decrease with increasing cutting speed as expected, but there is some irregular relationship between cutting parameters and surface roughness. It was observed that with increasing cutting speed there was a decrease in surface roughness at 0.04 mm/rev, while an increase at 0.06 mm/rev. The highest Ra value has obtained at 0.08 mm/rev and 140 m/min. These variations can be attributed to the variable chip cross section of the hard turning of the raceway. At same time, the adhered workpiece material on the worn areas of the flank land of the cutting tool used to hard turn the raceway cause the higher surface roughness for the raceway as reported by Boy et. al [22]. The authors were documented that during hard turning, the deposits of workpiece material increased the adhesion to the newly generated surface, so increases surface roughness.

IV. CONCLUSIONS

In this study, the effects of cutting speed and feed rate on surface roughness and cutting forces in hard turning of outer bearing ring raceway were investigated. The results obtained from this study are presented below:

1. In terms of cutting force, different patterns were observed in hard turning of the raceway.
2. Radial forces were found to be higher than tangential forces in hard turning of the raceway.
3. The lowest radial and tangential forces were obtained at a feed rate of 0.04 mm/rev and cutting speed of 140 m/min.
4. Feed rate is the most significant factor on surface roughness in hard turning of the raceway. The lowest surface roughness was obtained at 0.04 mm/rev. and 160 m/min.
5. All the surface roughness values obtained were below 0.6 μm .

REFERENCES

[1] (2017) ORS bearing website. [Online]. Available: <http://www.ors.com.tr/index.php/home>

[2] M. Boy, "Machining of hardened bearing rings with ceramic and CBN cutting tools", Ph. D. thesis, Graduate School of Natural and Applied Sciences Indian Institute of Science, Karabük, Jan. 2015.

[3] J. P. Davim, *Machining of Hard Materials*, London: Springer-Verlag, 2011.

[4] H.K. Tönshoff, C. Arendt, R.B. Amor, "Cutting of hardened steel", *Annals of the CIRP*, vol. 49 (2), pp. 547-566, 2000.

[5] G. Byrne, D. Dornfeld, B. Denkena, "Advancing cutting technology", *Annals of the CIRP*, vol. 52 (2), pp. 483-507, 2003.

[6] W. Köntig, A. Berktold, K.F. Koch, "Turning versus grinding - a comparison of surface integrity aspects and attainable accuracies", *Annals of the CIRP*, vol. 42 (1), pp. 39-43, 1993.

[7] F. Klocke, E. Brinksmeier, K. Weinert, "Capability profile of hard cutting and grinding processes", *Annals of the CIRP*, vol. 54 (2), pp. 22-45, 2005.

[8] Sadik, M.I., "Wear development and cutting forces on CBN cutting tool in hard part turning of different hardened steels", *Procedia CIRP*, vol.1, pp. 232-237, 2012.

[9] Diniz, A. E. and Oliveira, A.J., "Hard turning of interrupted surfaces using CBN tools", *Journal of Materials Processing Technology*, vol.195, pp. 275-281, 2008.

[10] Li Qian, L. and Hossan, M.R., "Effect on cutting force in turning hardened tool steels with cubic boron nitride inserts", *Journal of Materials Processing Technology*, vol. 191, pp. 274-278, 2007.

[11] G. Bartaryaa, S.K. Choudhuryb, "Effect of cutting parameters on cutting force and surface roughness during finish hard turning AISI 52100 grade steel", *Procedia CIRP*, Vol 1. 651-656, 2012.

[12] C. J. Raoa, D. Nageswara Raob, P. Sriharic, "Influence of cutting parameters on cutting force and surface finish in turning operation", *Procedia Engineering*, vol. 64, pp. 1405-1415, 2013.

[13] V. S. Sharma, S. Dhiman, R. Sehgal, S. K. Sharma, "Estimation of cutting forces and surface roughness for hard turning using neural networks" *J Intell Manuf*, Vol.19, pp. 473-483, 2008.

[14] Bouacha K., Yallese M.A., Mabrouki T., Rigal J.F. "Statistical analysis of surface roughness and cutting forces using response surface methodology in hard turning of AISI 52100 bearing steel with CBN tool", *Int. J. Refract. Met. Hard.*, vol. 28(3), pp. 349-361, 2010.

[15] H. Aouici, M. A. Yallese, K. Chaoui, T. Mabrouki, J.F. Rigal, "Analysis of surface roughness and cutting force components in hard turning with CBN tool: Prediction model and cutting conditions optimization", *Measurement* 45 (2012) 344 - 353

[16] E. Yücel, M. Günay, "Modelling and optimization of the cutting conditions in hard turning of high-alloy white cast iron (Ni-Hard)", *Proc IMechE Part C: J Mechanical Engineering Science*, vol. 227 (10), pp. 2280-2290, 2013.

[17] J.D. Thiele, S.N. Melkote, "Effect of cutting edge geometry and work piece hardness on surface generation in the finish hard turning of AISI 52100 steel", *Journal of Materials Processing Technology*, vol. 94, pp. 216-226, 1999.

[18] W. Chen, "Cutting forces and surface finish when machining medium hardness steel using CBN tools" *Int J Mach Tools Manuf*, vol.40 (3), pp. 455 - 66, 2000.

[19] D. Singh, P.V. Rao, "A surface roughness prediction model for hard turning process". *Int J Adv Manuf Technol*, vol. 32, pp.1115 - 1124, 2007.

[20] T. Özel, T.K. Hsu, E. Zeren, "Effects of cutting edge geometry, workpiece hardness, feed rate and cutting speed on surface roughness and forces in finish turning of hardened AISI H13 steel", *Int J Adv Manuf Technol*, vol.25 (3 - 4), pp. 262 - 269, 2005.

[21] M. Boy, H. Demir, M. Günay, İ. Çiftçi, "Optimisation of tool edge geometry and cutting parameters in hard turning of AISI 52100 using Taguchi method" *International Conference on Engineering and Natural Science*, 2015, 334-342.

[22] M. Boy, İ. Çiftçi, F. Özhan, "Sertleştirilmiş Rulman Bileziğinin İşlenmesinde Kesme Parametrelerinin Kesme Kuvveti ve Yüzey Pürüzlülüğüne Etkisi," 6. Talaş İmalat Sempozyumu, 2015, 273-281.

An Application Example for Electric Power Production with Organic Rankine Cycle from Waste Heat of Basic Oxygen Furnace Process

Mustafa KARAGÖZ^a, Aytaç AYDIN^b, Emrah DENİZ^c

^aTOBB Tech. Sciences Vocational School, Karabuk University, Turkey
mustafakaragoz@karabuk.edu.tr

^bGraduate School of Natural & Applied Sciences, Department of Mechanical Engineering, Karabuk University, Turkey.
ayaydin@kardemir.com

^cFaculty of Engineering, Department of Mechanical Engineering, Karabuk University, Turkey
edeniz@karabuk.edu.tr

Abstract—Today, rapid industrialization, manufacturing innovations and the growing population rate has caused an increase in energy needs in many countries. This increase in energy needs of people to produce more energy, energy efficiency and led the search for renewable energy. The next few centuries studies renewable energy sources and focus on the efficient use of energy has been caused because of run out of fossil origin fuels. The industrial sector of energy consumption of fossil origin energy sources are widely used and especially in countries that are dependent on foreign energy supply of increased production costs and causes it to fall of its competitiveness of firms. How much more energy if the benefit is reduced to that amount of production costs and emissions, emission caused environmental problems by reducing wastes, imply avoided.

In the study, both the iron & steel industry is being used in basic oxygen converter process occurring from organic rankine cycle from waste heat produced electricity with satisfying the energy needs of a partition and use in order to prevent negative environmental impacts have been studied. To this end, the waste heat from power generation system with organic rankine of cycle designed and production capacity was calculated. The data from the potential for producing electricity system designed fairly high level, and that substantial financial resources through the application of recycling have been identified that can be instantiated.

Keywords— Electric power, Organic rankine cycle, Waste heat, Basic oxygen furnace, Iron and Steel

I. INTRODUCTION

It is known that in our country, between 90 °C and 125 °C, there is a lot of hot water source which is not suitable for electricity generation at large capacity. These sources that remain idle in this way or can only be used for heating purposes can be converted to electricity by the Organic Rankine Cycle.

Traditionally, utilizing low temperature heat brings about various challenges. The technical difficulty and lack of economic are some of these difficulties. Heat power generation is traditionally accomplished through steam

turbines, but steam turbines require high temperature and pressure. The way to utilize heat from low temperatures is Organic Rankin Cycle (ORC). This name has been taken in the ORC system because it uses low temperature (<150 °C) and organic fluid instead of high temperature and pressurized steam [1]. Waste heat, engine cooling water, solar pools, biomass energy, geothermal heat, oil and so on. Heat sources are among the heat sources of the ORC [2-3-4-5].

An ORC system that produces waste heat source electricity is shown in Fig. 1 and the system works as follows. The heat from the waste heat source (red line) is used to vaporize the organic working fluid (Green line) in the evaporator. Organic fluids can be silicone based, hydrocarbons or refrigerant based fluids [6]. The pressurized steam is then sent to the turbine and electricity is generated in the turbine-generator set. Steam from the turbine is condensed in the condenser and liquidified again. Ground water, river water or cooling tower (Blue line) can be used to cool the hot organic fluid in the condenser. The cooled organic fluid is sent back to the evaporator pump and this closed cycle process is repeated. The waste heat is used as a fuel source, so there is no fuel cost. Furthermore, since combustion does not occur, there is no oscillation in the atmospheric circulation in the ORC cycle.

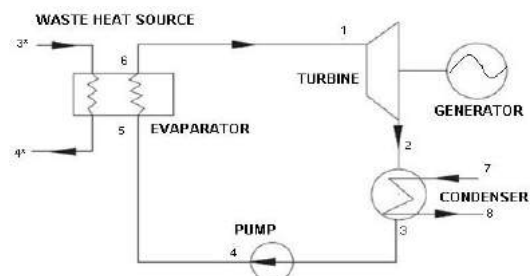


Fig. 1 ORC System diagram [7].

The thermodynamic cycle of the ORC is schematically shown in Fig. 2. The left part is called the Temperature-Entropy or T-S diagram. The hot organic fluid from the turbine heats up some of the organic fluid entering the

evaporator through the preheater (2 → 3 → 4). Electricity is produced when the organic fluid evaporating in the evaporator passes through the turbine-generator set (3 → 4 → 4_{is}). The steam is then condensed in the condenser by cooling with water or air (4_{is} → 1). The organic liquid is finally pumped into the preheater and evaporator (1 → 2); So that the series of operations in the closed circle circuit end [1].

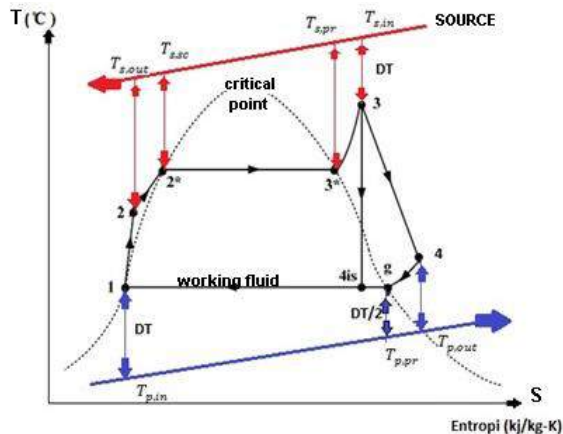


Fig. 2 Closed Thermodynamic ORC Cycle (T-S Diagram) [1].

Wang et al. have emphasized the increasing interest in low-temperature waste heat recovery in recent years. Engine exhaust gases, industrial process gases, solar energy potentials are promising and the use of ORC in waste heat recovery processes is quite widespread. The authors have mentioned two basic advantages of the ORC system in their study. These; The organic fluid used in the system is more adaptive to water than at low temperatures and the possibility of using local and small units different from conventional rankine cycle is possible with ORC [8]. Börrnert and his colleagues have stated in their work that waste heat is released in large quantities while the main processes of the plants such as oil refining, steel production, glass industry are being carried out. Approximately 20-50% of the energy used in the production process is released to the atmosphere and the energy consumption can be increased between 10% and 50% by using waste heat. It is also stated that the use of waste heat can reduce the annual CO₂ emission of 10,000 tons per year by 20% [9]. Li and his colleagues point out that industrialization and population growth together with the increasing need for energy have become one of the important problems for people. Limited reserves of primary sources (coal, oil, natural gas, etc.) for sustainable development have been adversely affected, and waste heat released to the environment has caused serious energy loss and environmental pollution [10]. The gases emitted from the lime kilns (kilns) are thrown into the atmosphere as exhaust gases. In 4-stage pre-heaters, the exhaust gas temperature is 300-350 °C, while 5- and 6-stage preheaters are 200-300 °C. The clinker's lime oven temperature is about 1000 °C and it is cooled to 100 ~ 120 °C by the atmosphere (atmosphere). During this time, hot air is obtained at 200 ~ 300 °C. It has been shown in the work of Bundela et al. [11]

that the energy of the exhaust gases from the cooling air and the lime oven can be recovered using organic rankine conversion technology. The thermal efficiency of a spark-ignition engine with a cylinder volume of 1.4 varies from 15 to 32%, depending on operating conditions. The remaining 60-70% of the energy is absorbed by the radiator (18 ~ 42%) and the exhaust gases (22 ~ 46%) [12]. This heat, which is lost in Rankin cycle, can be recovered to provide thermal comfort inside the cabin or to power generation. Honda designed and tested a prototype that used water as a fluid. The prototype demonstrates that the thermal efficiency increases from 28.9% to 32.7% under constant speed conditions of 100 km/h [13].

It has been shown that the ORC system, which was used in different studies above, can benefit from many areas for both electricity generation and comfort. In this study, the feasibility of electricity production from basic oxygen furnace waste heat using Organic Rankin Cycle was investigated. The quantity of the waste heat source was calculated in the work done and the financial value was derived by selecting the appropriate ORC unit. Simple payback period is calculated by calculating the financial value of the electricity to be generated by the system to be installed.

II. BASIC OXYGEN CONVERTER SYSTEM AND RECOMMENDED ORC SYSTEM

Waste heat sources are available in sizes that can not be overlooked in the basic oxygen furnace (converter) process. The most potent of these sources is the high-flow, high-pressure and high-temperature cooling water circulating in the converter water-cooled chimneys for the flue gas discharge. In Fig. 3, the system is shown schematically.

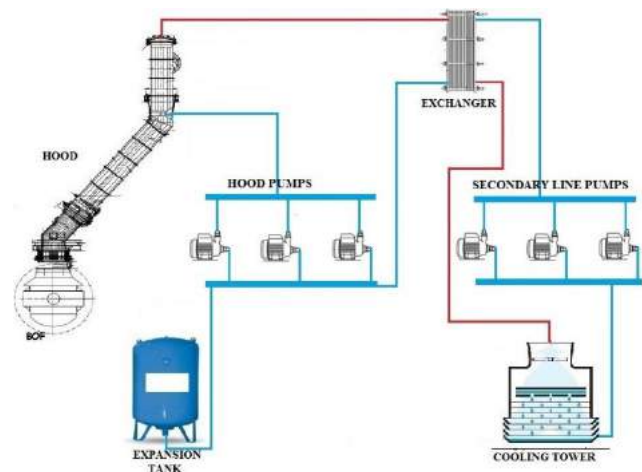


Fig. 3 Basic Oxygen Converter Process [14].

The water used in the cooling stack works according to the closed cycle principle. The hot water is returned to the system by passing through a heat exchanger circulating the cooling water in the secondary line. The cooling water used for cooling completes the cycle from the cooling tower. This means that the waste heat is released into the environment without being evaluated. This waste heat,

which has a high potential in steel production, must be evaluated. In the case of converters, it is possible to define the steel production process in three basic stages depending on the temperature change of the flue water.

Phase 1: Liquid Mine and Scrap Charge

At this stage, the liquid raw mine from the blast furnaces and the prepared scrap charge are made. At this time, the circulating water flow in the cooling pit is $960 \text{ m}^3 / \text{h}$, the pressure is 1.4 MPa and the temperature is around $75 \text{ }^\circ\text{C}$.

Phase 2: Oxygen Blowing in Converters

At this stage, pure oxygen is blown into the mixture of liquid mine and scrap, which is charged to the converter. During this time, the water circulating in the cooling stack takes the maximum temperature value and can reach $110 \text{ }^\circ\text{C}$. Flow and pressure are constant. ($960 \text{ m}^3 / \text{h}$ 1,4 Mpa)

Phase 3: Steel Casting in Converters

At this stage, steel production took place at the temperature of about $1650 \text{ }^\circ\text{C}$, at the end of the blowing step. The ready steel is poured into steel crucibles. At this time, the amount of water circulating in the cooling pits is nearly $960 \text{ m}^3 / \text{h}$, the pressure is 1.4 MPa and the temperature is around $85 \text{ }^\circ\text{C}$.

The steel production process covered in this study is composed of 3 converter systems. Independently from 3 different converters are produced. In order to maximize the blowing steps at which the water temperature is at its maximum level in order to maximize the waste heat, the 3-hour working processes of these 3 (BOF) converters have been simulated. It is accepted that this 3-hour work schedule will be maintained for 24 hours. The time from casting to casting for a converter is about 40 min. The highest temperature of the waste heat generated in the converters is the oxygen blowing phase. The oxygen blowing stage lasts about 15 minutes for a converter. For this reason, the oxygen blowing stages for 3 converters are brought forward and the stabilization of the high heat source of heat is ensured. In the present case, there are

exchangers and chimney pumps separately for each converter. With the progress of the blowing stages, the system must be made selective so that the hot water can run on a single line. A line will be drawn for the waste heat evaluation system that will be installed next to the normal line, and this line and normal line will be selected by automatic valves. In this case, it would suffice to install a single waste heat evaluation system for 3 converters. Waste heat will be provided by passing hot water through the waste heat evaluation system at the time when the amount of waste heat generated in the converters is highest depending on the temperature. Fig.4 shows the temperature changes of the 3-converter system coolant.

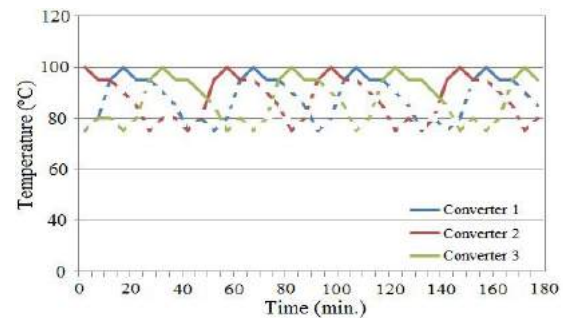


Fig. 4 Temperature change of 3-BOF system

As can be seen from the graph, it is possible to stabilize the hot water, which is a waste heat source, at certain temperature values. The waste heat value to be taken as basis in the scenario to be considered in the study shall be calculated from the hot water at $95 \text{ }^\circ\text{C}$ and $960 \text{ m}^3 / \text{h}$. Waste water will be used at the temperature of $65 \text{ }^\circ\text{C}$ in order to be used again in the process.

III. ESTABLISHMENT PREDICTED ORC SYSTEM AND REFRIGERANT FLUID COMPARISONS

It has been determined that electricity generation by the organic rankine cycle of the waste heat evaluation methods based on BOF. The chimney will transfer waste heat from the waste heat to an evaporator by means of an evaporator. The proposed system is schematically shown in Fig.5.

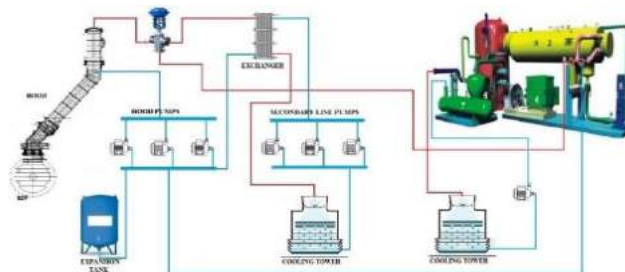


Fig. 5 Schematic representation of the ORC system foreseen.

In this part of the work, comparisons are made of the net power that can be obtained from the thermal efficiency, the efficiency of the exergy, and the refrigerant systems used at different pressure values of the refrigerant, using the waste heat source for R245fa refrigerant on the same conditions. The GENETRON and REFPROP programs were used when this comparison study was conducted.

The following assumptions have been adopted for the modeling of the proposed system:

- Each component was considered to be an open system in steady state;
- In addition to friction and heat losses, kinetic and potential energies were neglected;
- The specific heat of the welding and cooling water was considered constant;
- At the outlet of the condenser, the working fluid was accepted as saturated liquid;
- The specific volume of working fluid remains constant during pumping;
- The efficiency of the turbine and the pump was considered constant for all working fluids.
- The waste heat source;
 - ✓ Temperature ($T_{s,in}$)= 95 °C,
 - ✓ Waste heat source hot water system output temperature ($T_{s,out}$)= 65 °C,
 - ✓ Mass flow rate (m_{source})= 960.000 kg/ h,
 - ✓ DT= 10 °C,
 - ✓ Ambient temperature ($T_{ambient}$)= 20 °C,
 - ✓ Coolant inlet temperature ($T_{p,in}$)= 20 °C, is accepted.

Accepted parameters are shown in Table 1.

TABLE 1.
ACCEPTED PARAMETERS

Parameters	Value	Unit
Waste heat inlet temperature	368.15	K
Waste heat outlet temperature	338.15	K
Mass flow of waste heat	960	m ³ /h
Condensation temperature	293.15	K
Cooling water inlet temperature	293.15	K
Cooling water outlet temperature	313.15	K
Ambient temperature	293.15	K
Ambient pressure	100	kPa
Isentropic efficiency of turbine	80	%
Isentropic efficiency of pump	75	%
Efficiency of generator	96	%

When a low-grade waste heat recovery system was simulated, the method of evaluation of system performance used the method of exergy analysis.

Exergy balance for an open thermodynamic system can be expressed as:

$$\Sigma E_{in} - \Sigma E_{out} = I \tag{1}$$

Evaporator heat is transferred from the heat to the working fluid in the heat region 2-3.

$$Q = m(h_3 - h_2) \tag{2}$$

The loss of exergy in the evaporator can be given as:

$$I_{evp} = E_{in} + E_2 - E_{out} - E_3 \tag{3}$$

Expansion in turbine 3-4

$$\eta_{tbn} = \frac{(h_3 - h_4)}{(h_3 - h_{4is})} \tag{4}$$

The power generated by the turbine can be given as:

$$W_{tbn} = m(h_3 - h_4) \tag{5}$$

The loss of exergy on the side of the turbine can be expressed as:

$$I_{tbn} = E_3 - W_{tbn} - E_4 \tag{6}$$

The loss of exergy in the condenser is as follows:

$$I_{cond} = E_4 - E_1 \tag{7}$$

Exergy loss at the pump is as follows:

$$I_{pump} = W_{pump} + E_1 - E_2 \tag{8}$$

The heat generation of the ORC system is expressed as follows according to the 1st law of thermodynamics:

$$\eta_{thm} = \frac{(W_{tbn} - W_{pump})}{Q} \tag{9}$$

Thermal efficiency does not reflect the ability to convert low-grade waste heat energy into usable work. For this reason, we must take into account the efficiency of exergy that can evaluate the performance of waste heat recovery. The exergy of the ORC system can be given as follows:

$$\eta_{exg} = \frac{(E_{in} - \Sigma I - E_{out})}{E_{in}} \tag{10}$$

The temperatures of the refrigerant used for comparison are assumed to be 85 °C at the evaporator outlet and the thermal efficiency changes at different evaporator pressures are shown in Fig.6.

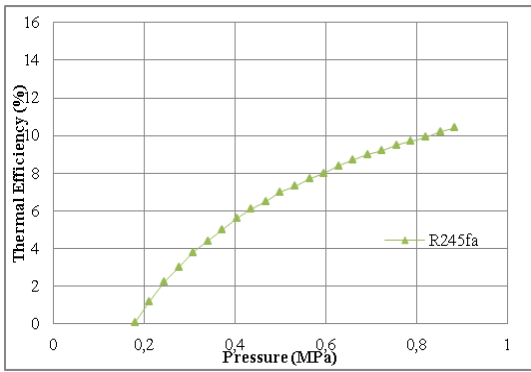


Fig. 6 Thermal effluent values for different evaporator pressures of R245fa

As seen in Fig. 6, R245fa have higher thermal dissipation at lower evaporator pressures with an 85 °C constant evaporator inlet temperature. Higher thermal efficiency at low pressure as the system cost and performance directly affected, the most suitable fluid in terms of thermal efficiency at the inlet temperature of the evaporator was seen as R245fa. Fig.7 shows the changes in the exergy yields at different evaporator pressures for the 85 °C evaporator inlet temperature of the refrigerant used in comparison.

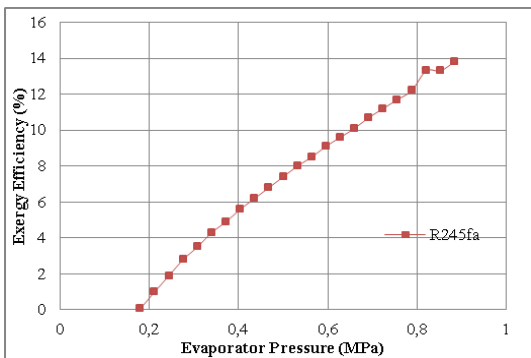


Fig.7 Exergy efficiency of R245fa for different evaporator pressure

Exercise production is important in terms of effective operation of the system to be established. Given system cost and efficiency, it is important to work at low evaporator pressures. For this reason, R245fa is the one of the most efficient from the fluids considered in terms of giving exergy.

Thermal efficiency and exergy efficiency of R245fa exchange with W_{net} are shown in Fig.8 and Fig.9.

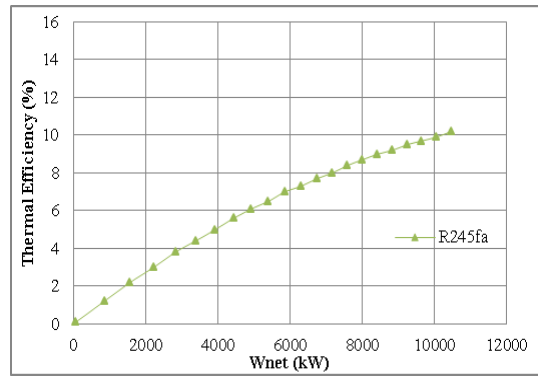


Fig. 8 Exchange of thermal efficiency of R245fa with W_{net}

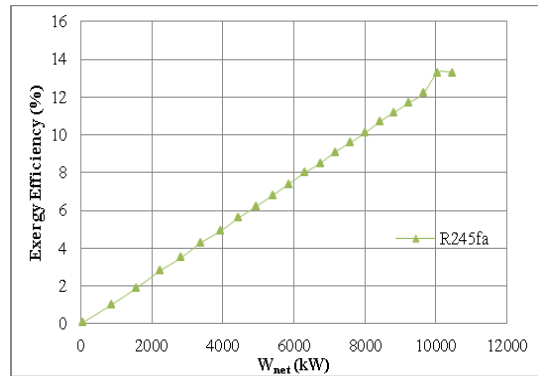


Fig. 9 Exchange of exergy efficiency of R245fa with W_{net}

IV. ELECTRICITY GENERATION AND WASTE HEAT RECOVERY

In the study, thermal efficiency, exergy yield, max W_{net} , comparison was made at variable evaporator pressures, depending on the fixed evaporator temperature. In these comparisons, the most suitable fluid for system cost and efficiency is R245fa. The Organic Rankin Cycle Unit, which uses any of these fluids in its system, has reached a usable result in the assessment of waste heat released during the BOF process.

The investment to be made is that Infinity Turbine will take the ORC unit model IT2MW using R245fa refrigerant. As a result of the investigations, it was found that the IT2MW DROPS unit and installation cost is about \$ 3.000.000. In Table II, the feasibility study of electric power and cost that can be produced is included. The payback period of the investment is calculated.

TABLE II.
FINANCIAL VALUE OF INVESTMENT AND COST OF INVESTMENT

Parameters	Value	Unit
Working hours	8200	hours/year
Waste heat capacity	33.494	kW
System efficiency	8	%
Net electricity generation	21.972.064	kW

Annual electricity production	21.972.064	kWh/ year
Financial value of production*	1.227.850	\$/ year
Investment cost**	3.000.000	\$

*Electricity unit price 0.05\$ / kWh

V. CONCLUSIONS

In this study, waste heat source and amount in Basic Oxygen Converter process were determined and necessary calculations were made and Organic Rankin was determined for the system. The price for the specified ORC unit has been investigated and the system cost has been deducted. System installation cost is 3.000.000 \$. With the designed system, 21.972.064 kWh of electricity can be generated annually from waste heat. The financial value of the electricity generated by the system is about 1.227.850 \$/ year. If a simple payback period is calculated, it is seen that the system has amortized itself in 2.4 years. The system has more than twenty years of life and shows the appeal of the system for a short period of depreciation. By means of this exemplary work, it was aimed to show how valuable the unused waste heat is, how long it can be achieved with short depreciation times and to create awareness. Increasing use of waste energy in the meeting of increasing energy demand in the world and our country will make a significant contribution to our economy. These and similar activities should be increased to encourage businesses that are not aware of waste heat and do not invest in the environment, and should be aware of the environment and productivity.

REFERENCES

[1] H. Özden, D. Paul, "Organik Rankine Çevrim Teknolojisiyle Düşük Sıcaklıktaki Kaynaktan Faydalanılarak Elektrik Üretimi. Örnek

Çalışma: Sarayköy Jeotermik Santrali", X. Ulusal Tesisat Mühendisliği Kongresi, 2011/İzmir.

[2] D. Wang, X. Ling, H. Peng, Performance analysis of double organic Rankine cycle for discontinuous low temperature waste heat recovery. *Appl Therm Eng* 2012;48: 63–71.

[3] E. Ksayer, Design of an ORC system operating with solar heat and producing sanitary hot water. *Energy Proc* 2011;6: 389–95.

[4] M.D. Agustín, G. Lourdes, Analysis and optimization of the low-temperature solar organic Rankine cycle (ORC). *Energy Convers Manage* 2010;51: 2846–56.

[5] M. Astolfi, L. Xodo, M.C. Romano, E. Macchi, Technical and economical analysis of a solar–geothermal hybrid plant based on an Organic Rankine Cycle. *Geothermics* 2011;40: 58–68.

[6] M. Eyidoğan, "Organik Rankine Çevrimli Güç Üretim Sisteminin Enerji Ve Ekserji Analizi" Karabük Üniversitesi Fen Bilimleri Enstitüsü, Doktora Tezi, 2014.

[7] V.L. Le, A. Kheiri, M. Feidt, S. Pelloux-Prayer, Thermodynamic and economic optimizations of a waste heat to power plant driven by a subcritical ORC (Organic Rankine Cycle) using pure or zeotropic working fluid *Energy* 78 (2014) 622–638.

[8] J.F. Wang, Y.P. Dai, "Exergy analyses and parametric optimizations for different cogeneration power plants in cement industry", *Appl Energy* 2009;86(6):941–8.

[9] T. Börmert, T. Bürki, ABB's flexible ORC power plant. ABB Switzerland Ltd., 2010

[10] M. Li, J. Wang, M. Wang, J. Xia, Y. Dai, "Multi-objective optimization design of condenser in an organic Rankine cycle for low grade waste heat recovery using evolutionary algorithm", *International Communications in Heat and Mass Transfer* 45 (2013) 47–54

[11] P. S. Bundela, V. Chawla, "Sustainable development through waste heat recovery", *American Journal of Environmental Sciences*, 6 (1): 83-89 (2010)

[12] R. El Chalmas, D. Clodic, "Combined cycle for hybrid vehicles", *SAE World congress*, 1171 (1): 1-5 (2005).

[13] T. Endo, S. Kawajiri, Y. Kojima, K. Takahashi, T. Baba, S. Ibaraki, T. Takahashi, M. Shinorama, "Study on maximizing exergy in automotive engines", *SAE World Congress*, Detroit, Michigan, 257 (1): 1-6 (2007).

[14] <http://ietd.iipnetwork.org/content/basic-oxygen-furnace> (12.02.2015)

An Application Example for Demineralized Water Production from Waste Heat of Basic Oxygen Furnace Process

Aytaç AYDIN^a, Mustafa KARAGÖZ^b, Emrah DENİZ^c

^aGraduate School of Natural & Applied Sciences, Department of Mechanical Engineering, Karabuk University, Turkey.
ayaydin@kardemir.com

^bTOBB Tech. Sciences Vocational School, Karabuk University, Turkey
mustafakaragoz@karabuk.edu.tr

^cFaculty of Engineering, Department of Mechanical Engineering, Karabuk University, Turkey
edeniz@karabuk.edu.tr

ABSTRACT

Today, the most important factors in the evolution of people's living standards are the development of industrialization and production capabilities. In the industrial sector, fossil-based energy sources are widely used and cause production costs to increase and competitiveness to decline, especially in countries that are dependent on energy supply. In addition to this, the use of energy as efficiently as possible and the recycling of waste energy can reduce both costs and adverse environmental problems.

In the study, the use of the waste heat from the basic oxygen converter process used in the iron and steel industry has been examined again to meet the demand for demineralized water and to convert the overproduced water into a financial resource and to avoid adverse environmental effects. For this purpose, a demineralized water production system that operates on the basis of a humidification-dehumidification method compatible with the amount of waste heat, whose investment costs are more advantageous than other methods, is designed and the production capacity is calculated. It has been determined that the obtained data is at a very high level of demineralized water producing potential of the designed system and that this recycling application can be funded considerably.

Keywords: Demineralize water, Humidification-Dehumidification, Waste heat, Basic oxygen furnace, Iron and Steel.

Fabrication and Mechanical Behavior of Aluminum-Matrix Composites Reinforced With Boron Nitride Particles

Yasin AKGULI, Yuksel AKINAYI, Fazil HUSEMI, Hamza SIMSIRI, Safa POLATI
1 Karabuk University, Iron and Steel Institute, 78050, Karabük, TÜRKİYE
yasinakgul@karabuk.edu.tr

ABSTRACT

In this study, effect of boron nitride particles on the mechanical properties of aluminum composites reinforced with BN particles was investigated. Experimental procedure was started with mixing of powders in the turbula mixer. Hot press was applied at 550 C in argon atmosphere. For characterization of microstructure, scanning electron microscope (SEM) analysis was done. Compression test was applied for determination of strength. Vickers hardness was used to measure hardness of samples.

Keywords: Powder metallurgy, Aluminium, Boron nitride

Investigation of the Effect of TiC Content on the Mechanical Properties of the Aluminum/TiC Composites

*Yasin AKGUL¹, Muhammet Emre TURAN¹, Yuksel AKINAY¹,
1 Karabuk University, Iron and Steel Institute, 78050, Karabük, TÜRKİYE
yasinakgul@karabuk.edu.tr*

ABSTRACT

Aim of this study is to investigate effect of titanium carbide nanoparticle contents on the mechanical properties of the Aluminum/TiC composites. Aluminum and titanium carbide nanoparticles were mixed in the turbula mixer. After mixture process, samples were produced using Hot Press in argon atmosphere. Scanning Electron Microscope (SEM) and X-ray diffraction were used for characterization. Compression test was performed for determination of strength and also vickers hardness tests were carried out to understand mechanical effects of TiC particles on pure aluminum.

Keywords: Powder metallurgy, Aluminium, TiC, Compression

Experimental Investigation of Effect of Processing Parameters on the Surface Roughness during the Brass Alloy Turning with Abrasive Water Jet

Fuat KARTAL^{*}, Hasan GÖKKAYA⁺

^{*}Mechanical Engineering Department, Kastamonu University,
Turkey

fkartal@kastamonu.edu.tr

⁺Mechanical Engineering Department, Karabük University,
Karabük, Turkey,

hgokkaya@karabuk.edu.tr

Abstract— This study investigates the impact of processing parameters on the surface roughness in the process of machining brass alloy of \square 14 and 230 mm in size using abrasive water jet. The sample was machined using abrasive water jet for four different parameters of Nozzle feed rate (5, 15, 25 and 35 mm/min), abrasive flow rate (100, 150, 200 and 250 g/min), spindle speed (50, 100, 150 and 200 rpm) and nozzle distance (2, 6, 10 and 14 mm). Pump pressure (380 MPa), abrasive size (80 Mesh, in Garnet form), and nozzle diameter (0.75 mm) are kept constant throughout the empirical study. According to the results obtained from the experiment, increasing machining parameters, namely nozzle feed rate and nozzle approach distance, resulted in increased average surface roughness. On the other hand, increased spindle spin and abrasive flow rate result in enhanced average surface roughness (Ra).

Keywords— Brass Alloy, Turning, Abrasive Water Jet, Machining Parameters, The Average Surface Roughness.

I. INTRODUCTION

The abrasive jet technology has gained widespread use recently, the process and parameters of the technology have been widely investigated. Nevertheless, there is a lack of studies focused on machining and turning using abrasive water jet [1]. Overall, it can be said that there is no material, which cannot be machined using abrasive water jets regardless of the type of the material to be machined. As tool wear and overheating is not an issue, it is rather easier to cut a material using abrasive water jet. Rough and hard-to-machine materials are easily machined using this method Momber and Kovacevic (1998).

The literature survey made in order to drive this study involved the work of Zong and Han (2002) observed the impact of several machining parameters (spindle speed, nozzle feed rate, nozzle approach rate, water pressure, and abrasive flow rate) on the surface roughness of glass with a 25mm diameter using the abrasive water jet. The data obtained was then compared against the date obtained from

a standard turning lathe. The results showed that increased feed rate was responsible for increased roughness and fluctuations. In addition, it was determined that surface roughness was improved when the distance between water jet nozzle and work piece is decreased. According to the results obtained from the experiments, the best surface roughness results were obtained from 300 g/min abrasive flow rate. It was found that low nozzle feed rate and higher cutting speeds of turning lathe contributed to improved surface roughness [3]. Hashish found that the most significant parameters during the material removal process applied to a cylindrical work piece using abrasive water jet turning were the nozzle feed rate and the depth of cut [4]. Kartal and Gökkaya (2012) have developed a turning mechanism suitable for abrasive water jet machining by designing a hybrid experiment mechanism, which prevents the impact of abrasive particles on the turning mechanism during abrasive water jet turning process [6]. Kartal and Gökkaya (2013) conducted a literature review on academic studies involving AWJT [6]. Kartal et al. (2012) studied the impact of machining parameters on surface roughness, macro surface characteristics and material removal for the turning of a copper alloy (Cu-Cr-Zr) using abrasive water jet. P (350 MPa) value, abrasive type (Garnet) and size (80 Mesh), and nozzle diameter (1.2 mm) are kept constant throughout the experiments. A copper alloy of \varnothing 30 and 240 mm is machined using the parameters of nozzle feed rate (10, 15, 20 and 25 mm/min), abrasive feed rate (50, 150, 250 and 350 g/min), SS (25, 50, 75 and 100 rpm) and nozzle approach distance (2, 5, 8 and 11 mm). According to the empirical results, nozzle feed rate and nozzle approach distance led to an increase in average surface roughness giving an Ra value of 2.5- 5.5 μ m [9]. Kartal and Gökkaya studied the impact of abrasive water jet parameters on both material removal rate and depth of AISI 1040 steel. Pump pressure (350 MPa), abrasive size (80 Mesh, Garnet), and nozzle diameter (1.2 mm) are kept constant throughout the experiments. AISI 1040 steel of \varnothing 30 and 240mm was machined using parameters of four different abrasive flow rate (50, 150, 250 and 350 g/min), nozzle distance (2, 5, 8

and 11 mm), nozzle feed rate (5, 15, 25 and 35 mm/min) and spindle spin (25, 50, 75 and 100 rpm). According to the findings, highest material volume was found to be 1387.25 mm³ at 5 mm/min nozzle feed rate. Optimal cutting depth of 0.94 mm was obtained at a spindle speed of 100 rpm [8].

Processed low-density polyethylene material is using abrasive water jet processing parameters with L18 orthogonal array. Polyethylene work piece processed using classic milling was investigated for surface roughness and thread generation due to melting surface material. Work piece processed using AWJT has provided machining with no thermal deformation and melting [9].

The cutting power of abrasive water jet is rather low. As it operates with a lower cutting power, it is ideal to work with when machining brittle, flexible, easy to deform materials (glass, ceramics) [10]. No matter the diameter of the work piece to be machined using abrasive water jet, it is not sensitive to the cutting power as it is the case for classic turning processes. The turning process of work pieces larger in size results in adverse situations such as increased momentum, vibration and backlash. Machining with abrasive water jet eliminates adversities such as deviation deformations caused by vibration and power. Nevertheless, it eliminates the need for changing the cutter gear and powerful connector parts while reducing the waste of time [10]. It is possible to machine work pieces of different shapes and sized using a single nozzle [10]. Classical turning lathes, on the other hand, require different cutter gears for machining of work pieces with different shapes. As a relatively recent machining method, abrasive water jet offers ease of use with the possibility to work on work pieces of all forms and shapes using only one nozzle. Fig. 1 shows the cutter nozzle moving through the X, Y, and Z coordinates and allowing for lengthwise machining.

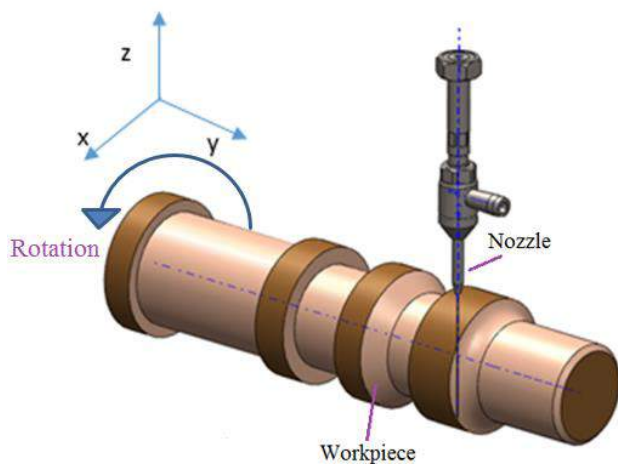


Fig.1 Turning with abrasive water jet

II. MATERIALS AND METHODS

This study applies the special turning lathe setup developed in order to be used in abrasive water jet. An electric motor with 0.37kW power was selected for the turning setup and a ATV 12 380V-220V control card was used in order to control the speed of the motor. This card is able to control the 3-phase motor with 220V electricity system and to adjust the turning speed and direction while keeping the torque at a constant. Another advantage brought in with this card is that it can keep the motor speed at a constant. The turning direction is set using the control knob available on the card. The system was built using belt, pulley, and spline shaft connections. Fig. 2 shows the components of the hybrid turning lathe setup developed in order to be used in abrasive water jet machining.

The work piece used in the experiments is a low lead brass alloy of Ø 14 and 230 mm size. It constitutes of approximately 57% Copper, 2.5% lead and 40% zinc.

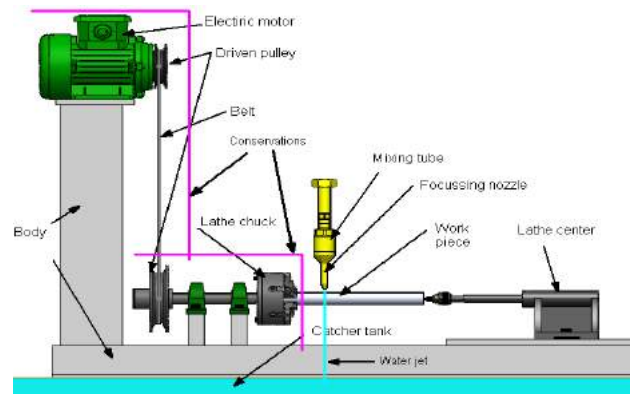


Fig. 2 The experimental setup was developed for use in turning with abrasive waterjet.

The following process parameters were investigated: nozzle feed rate, abrasive flow rate, spindle speed and nozzle distance Pump pressure (350 MPa) abrasive size (80 Mesh, in Garnet form), and nozzle diameter (0.75 mm) are kept constant throughout the empirical study (Table I).

This study investigated the material removal of a brass alloy machined using abrasive water jet for four different parameters of nozzle feed rate (5, 15, 25 and 35 mm/min), abrasive flow rate (100, 150, 200 and 250 g/min), spindle speed (50, 100, 150 and 200 rpm) and nozzle distance (2, 6, 10 and 14 mm). The impacts of process parameters on surface roughness and the usability of abrasive water jet on the brass alloy for machining purposes were investigated. Parameters such as abrasive flow rate, spindle speed and nozzle distance were processed with abrasive water jet. Pump pressure (380 MPa), abrasive size (80 Mesh, in Garnet form), and nozzle diameter (0.75 mm) are kept constant throughout the empirical study.

TABLE I. MACHINING PARAMETERS AND THEIR LEVELS

Parameters	Units	Levels			
Feed Rate	mm/min	5	15	25	35
Abrasive Flow Rate	g/min	100	150	200	250
Spindle Speed	mm/min	50	100	150	200
Standoff Distance	mm	2	6	10	14

CNC abrasive water jet lathe offering perpendicular processing feature and 415 MPa SL-V 50 KMT pump pressure with 0.01 precision was preferred for the material removal process. The surface roughness measurement was then taken using “Mitutoyo” SJ-301, a desktop-type surface roughness measurement device that also allow for bar chart or text printouts. Technical properties of the surface roughness device are shown in Table II.

Only the Ra values were taken into consideration during the measurements and Ra values were taken from four points located in the mid part of the workpiece. Ra values were then converted into graphs in average.

III. RESULT AND DISCUSSION

The pump pressure (380 MPa), abrasive size (80 Mesh), and nozzle diameter (0.75 mm) were kept constant during the abrasive water jet machining process of the work piece of Ø14 and 230 mm in size with the predefined abrasive water jet processing parameters. Fig. 3 shows the machining process of the cylindrical brass alloy using abrasive water jet.

The correlation between the spindle speed and Ra because of the abrasive water jet machining of the brass work piece are shown in Fig. 4. The Ra improves by 7% (3,53 µm-3,25 µm) as the spindle speed increases from 25 rpm to 50 rpm while increasing the spindle speed from 50 rpm to 200 rpm further improved the Ra by 23% (3,53 m-2,69 µm). With the increasing spindle speed, the average roughness value improves because of the increased abrasion effect of the abrasive water jet on the unit surface. Values obtained comply with the values found in the literature [11].

TABLE II. Machining parameters and their levels

Model	SJ-301
Scanning speed	0.25, 0.5 mm/s
Pin tip radius	2 -5 µm
Measurement ranges	350µm (-200µm... +150µm)

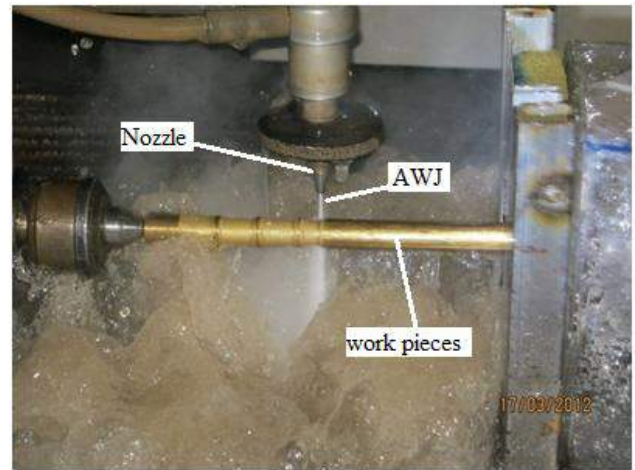


Fig. 3 The brass alloy specimen turning with abrasive water jet.

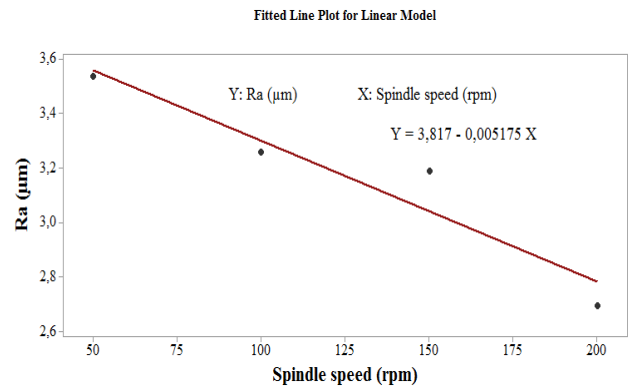


Fig.4 The effect of spindle speed on the Ra

Fig. 5 shows the Ra values obtained from the material removal process carried out using four different nozzles feed rates. As the nozzle feed rate increases from 5 to 35 mm/min Ra increases by 60% (3.18 µm-5.10 µm). The reason behind the increase in the Ra is that the impact of the abrasive water jet on the surface is not homogenous and the machining time is reduced. Values obtained comply with the values found in the literature [1], [5], [6], [7].

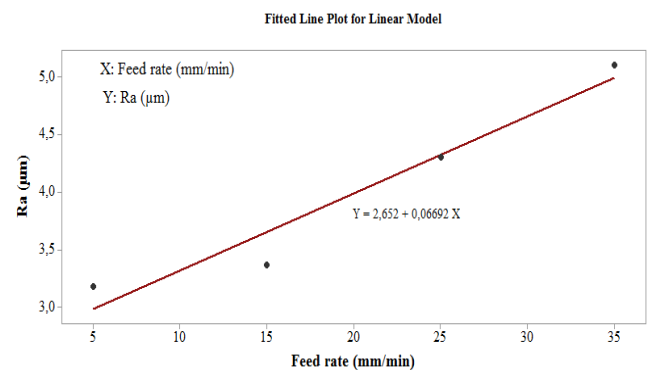


Fig. 5: The effect of nozzle feed rate on the Ra

IV. CONCLUSION

Figs. 6 and 7 shows the Ra values obtained from the material removal process carried out using four different abrasive flow rates and nozzle approach distances. Ra is improved by 16% ($4,30 \mu\text{m}$ - $3,60 \mu\text{m}$) as the abrasive flow rate was increased from 100 g/min to 250 g/min. Ra is improved by 39% ($4,30 \mu\text{m}$ - $2,59 \mu\text{m}$) as the abrasive flow rate was increased from 100 g/min to 250 g/min. Increased abrasive flow rate results in improved Ra values [1], [5], [6], [7].

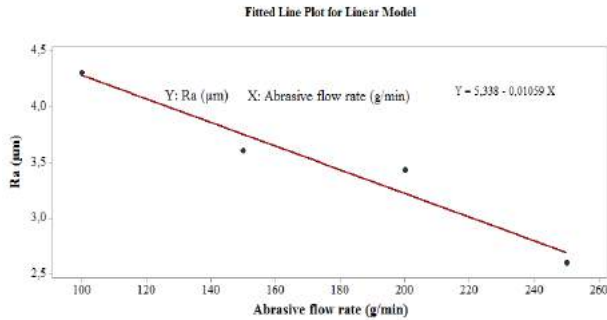


Fig. 6 Effect of abrasive flow rate on the Ra

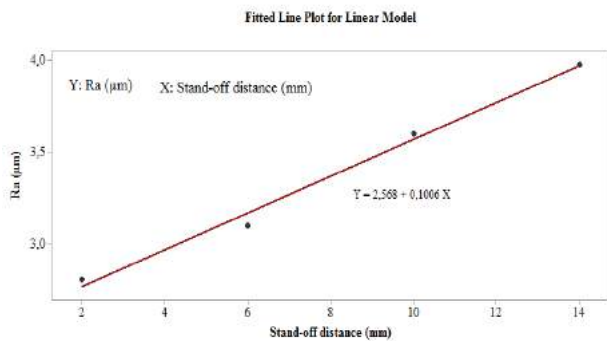


Fig. 7 The effect of nozzle standoff distance on the Ra

It was found that the increased nozzle approach distance had an adverse effect on the average surface roughness Hashish (1984). The reason behind this may be attributed to the feature of the beam produced by the nozzle (Fig. 7). The beam is bigger than the impact of the jet, which results in even rougher surfaces. It would be fair to say that nozzle approach distance is one of the most important factors having an impact on the surface roughness when machining the work piece using abrasive water jet [1].

Brass alloy was successfully machined using abrasive water jet. Results obtained from the experiment parameters are as follows;

- It was found that machining using abrasive water jet with appropriate turning lathe setup is possible.
- Surface roughness improves with the increased spindle speed.
- Ra increases with the increased nozzle feed rate.
- Ra decreases with the increased abrasive flow rate.

Ra increases with the increased distance between nozzle and the work piece.

REFERENCES

- [1] Axinte, D. A., Stepanian, J. P., Kong, M. C., Mc Gourlay, J. , 2009, Abrasive Water Jet Turning-An Efficient Method to Profile and Dress Grinding Wheels, *International Journal of Machine Tools and Manufacture*, 49(1-3), 351-356.
- [2] Momber, A., Kovacevic, R., 1998, Principles of Abrasive Water Jet Machining, Springer-Verlag, London.
- [3] Zhong, Z. W., and Han, Z. Z., 2002, Turning of Glass with Abrasive Water Jet, *Materials and Manufacturing Processes*, 17(3), 339-349.
- [4] Hashish, M., 1984, A Modeling Study of Metal Cutting with Abrasive Water Jets, *ASME J. of Eng. Mat. And Tech.*, 106(1), 88-100.
- [5] Kartal, F. and Gokkaya, H., 2012, Aşındırıcı su jeti ile tornalama deney düzeneği tasarımı, *International Iron & Steel Symposium, Karabük*.
- [6] Kartal, F. and Gokkaya H., 2013, Turning with Abrasive Water Jet Machining-A Review, *Engineering Science & Technology, an International Journal*, 16(3), 113-122.
- [7] Kartal, F., H. Gökaya, and M. Nalbant. 2012, Turning of (Cu-Cr-Zr) alloy with abrasive water jet, 21st International Conference on Water Jetting, Ottawa, Canada.
- [8] Kartal, F., Gokkaya H., 2014, The Effect of Process Parameters on Machining Volume and Depth of Cut in Turning Operation of AISI 1040 Steel with Abrasive Water Jet, *Pamukkale J Eng Sci.*, 20 (1), 20-24.
- [9] Kartal, F., et al. ,2014, Optimization of Abrasive Water Jet Turning Parameters for Machining of Low Density Polyethylene Material Based on Experimental Design Method, *International Polymer Processing*, Vol. 29.4 535-544.
- [10] Hashish, M. ,2001, Macro characteristics of AWJ turned surfaces, Proceedings of 2001 WJTA American Waterjet Conference, Minneapolis, Minnesota.
- [11] Hashish, M. ,1995, Effect of abrasive waterjet parameters on volume removal trends in turning, *Journal of engineering for industry*, 117, 475.
- [12] Kartal, F., & Gökaya, H., 2015, Effect of abrasive water jet turning process parameters on surface roughness and material removal rate of AISI 1050 steel, *Materials Testing*, 57(9), 773-782.
- [13] Mitutoyo SJ-301 Surface Roughness Tester, User's

Optimization of Process Parameters for Abrasive Water Jet of Cast A319 Aluminium Alloy by Taguchi Method

Fuat KARTAL*, Hasan GÖKKAYA+, Refik POLAT+
*Mechanical Engineering Department, Kastamonu University,
Kastamonu, Turkey
fkartal@kastamonu.edu.tr
+Mechanical Engineering Department, Karabük University,
Karabük, Turkey,
hgokkaya@karabuk.edu.tr

Abstract— In this paper, Taguchi technique is selected in order to explore ideal process parameters for abrasive water jet machining (AWJM). The goal of this exploratory research is to explore the effects of machining parameters on MRR and SR of a work piece made of aluminum a356 alloy. Our approach is based on Taguchi's technique, ANOVA and the SN ratio in order to optimize AWJ machining process parameters for successful machining and to establish optimal values of each AWJM parameter, namely, abrasive stream rate, traverse speed, standoff distance and abrasive grit size. L9 orthogonal array is utilized for varying values of A, B, C, D and three tests were conducted for each combination. Using the SN ratio, it was possible to find the optimal parameter values for AWJM. It was concluded that, in actual practice, the ideal combination of AWJM process parameters fulfill the requirements for machining of cast A 356 aluminum alloy.

Keywords— Abrasive Water Jet Machining (AWJM), Taguchi method, ANOVA, SN Ratio, MRR

I. INTRODUCTION

AWJ machining is an untraditional machining process which involves high-pressure and high-speed water jet and abrasive material included in this water jet in order to remove materials from the workpiece with the impact of erosion [1-3]. As an advanced production technology, AWJM is finding increasingly wide range of use in many industries. A water jet with a slim go section inclusive of exceptional-grained abrasive particles jumbled together right ratios is transferred onto the workpiece via a nozzle and material removal is executed due to the erosive effect of the abrasive particle on the workpiece. AWJM has been utilized in one-of-a-kind industries for a long term now [2,3]. AWJM is ideal for cutting brittle materials such as glass, ceramics, and stone, along with materials containing iron and composites. The surface properties obtained using this technique depend on a number of factors such as nozzle standoff distance, abrasive flow rate, traverse speed and the material properties of the workpiece [3]. The fact that nozzle is not in contact with the workpiece, there are no surfaces under thermal effects, the cutting power applied on the workpiece is rather low, and the ability to machine a wide range of materials

make it easier to prefer AWJM over other cutting processes. Nevertheless, it is possible to use AWJM in a number of applications such as drilling, surface cleaning, turning and milling [1-6].

Erosion caused by the impact effect of robust abrasive particles is one of the many types of material deformation generally classified as abrasion [2-4]. A water jet cutter, additionally known as a water jet or waterjet, is an industrial device capable of reducing a huge form of materials using a completely high-stress jet of water, or a aggregate of water and an abrasive substance [1-6]. The term abrasive jet refers particularly to using a aggregate of water and abrasive to reduce tough substances which include metallic or granite, whilst the terms natural waterjet and water-handiest reducing talk to waterjet reducing without using added abrasives, frequently used for softer materials consisting of wooden or rubber. AWJM has been commonly used in industry for cutting ductile and brittle materials such as glass, stone, and ceramics [1-5]. There are several AWJM process parameters and factors which may have an impact on the surface quality of the workpiece being machined [1-3]]. Material removal increases with the increasing abrasive mass flow rate. As it does not require different combinations to be subjected to confirmation tests, full factorial design is ideal for optimization efforts [3-6]. Many authors have conducted researches on different AWJM parameters [1-6].

II. MATERIALS & METHOD

Taguchi method It was developed by Genichi Taguchi in the 1950s as a process optimization technique. The most striking contribution Taguchi brings to quality is that it is closely related to the quality and customer satisfaction of a product and the excellence of design and development in the pre-production phase, by separating the quality system into pre-production (off-line) and production It shows. 3 different S/Ns are used namely, Nominal-the-best, Smaller-the-better, and Larger-the-better. It was selected as our purpose is to achieve minimum surface roughness and the relevant equation is given in Eq.1. ANOVA and F-Test were used for the analysis of the experimental data. Larger-the-better S/N approach was used

for MRR. The data sequence of the performance properties of Larger-the-better approach was run as shown in Eq. 2. Experiments conducted for different levels of the factors were then assessed in the 95% confidence level [7].

$$S/N = -10 \log (y/s^2y) \quad (1)$$

$$S/N = -10 \log ((1/n) ((1/y^2))) \quad (2)$$

An A356 aluminium alloy sample plate of 100x40x10mm size was used in this study as it is commonly used in the automotive industry. Chemical composition of A356 aluminium alloy is shown in Table 1. A356 aluminium alloy is one of the most commonly used cast alloys both in chill casting and sand casting.

TABLE I. CHEMICAL COMPOSITION OF A356 ALUMINIUM ALLOY [8]

Si	Mg	Cu	Fe	Mn	Ti	Al
7.13	0.389	0.023	0.135	0.002	0.114	91.990

80-Mesh Garnet of 7.5 Mohs hardness is used as the abrasive material in this study. A number of abrasive waterjet cutting attempts were made on a CT2.5 axis AWJ machining system using KMT SL-V100D ultra high-pressure pump which can deliver up to 413.7 MPa water pressure through a sapphire orifice. The lathe size was 1,000x2,000mm, nozzle diameter was 0.76mm and diamond orifice diameter was 0.4mm. Figure 2 shows the image from the machining of A356 aluminium alloy on the waterjet lathe.



Fig. 1. Waterjet machining system used in this study



Fig. 2. An image from the machining of A356 aluminium alloy on the waterjet lathe.

Taguchi L9 experimental design which uses Taguchi L9 orthogonal array was preferred for the cutting parameters. This experimental procedure involves four control parameters and three levels as shown in Table 2. Observed according to Taguchi method, the values are calculated using 'larger the better' and 'smaller the better' approaches. The pressure was held constant at 240MPa. Thus, the observed maximum and minimum values for MRR and SR were defined. Then, the experiment was run for each value defined with a single run. The optimization of observed values (Table 3) was done using ANOVA and S/N ratio comparisons and in accordance with the Taguchi method.

TABLE II. PROCESSING PARAMETERS AND LEVELS

Code	Abrasive Turning Parameters	Unit	Level 1	Level 2	Level 3
A	Nozzle speed	mm/min	100	200	300
B	Abrasive flow rate	g/min	250	350	450
C	Standoff distance	mm	2	5	8
D	Abrasive grit size	(µm)	80	100	120

TABLE III. EXPERIMENTAL VALUES OF MRR AND SR

Traverse speed (mm/min) A	Abrasive flow rate (g/min) B	Stand of distance (mm) C	Abrasive grit size (µm) D	Ra (µm)	MRR (mm ³ /min)
100	250	2	80	3,39	46,98
100	350	5	100	3,08	47,74
100	450	8	120	2,62	48,95
200	250	5	120	4,48	45,02
200	350	8	80	4,29	45,74
200	450	2	100	4,28	46,75
300	250	8	100	4,97	43,17
300	350	2	120	4,87	43,76
300	450	5	80	4,86	44,46

III. RESULTS AND DISCUSSION

ANOVA is used in order to define the impact of process parameters and their interactions on the quality characteristics, i.e. surface roughness. ANOVAs conducted on averages and signal-noise ratios are shown in Tables 4 and 5, respectively.

The significance of a relevant process parameter in ANOVA is calculated using the ratio of the variance value of that parameter to the variance of deviation which is called an F-Test. Having compared this value with the F-Table value at a specific confidence level, the significance of this parameter on the quality characteristic is identified. If the F-Test value is greater than the F-Table value, then the parameter is significant. The last columns of the tables show the percentile distribution of each parameter. Accordingly, Table 4 shows that nozzle traverse speed and abrasive flow rate have a statistically significant impact, while nozzle standoff distance and abrasive size do not have a statistically significant impact. On the other hand, nozzle traverse speed has the greatest impact on the material removal rate by 85% which was followed by the abrasive flow rate by 14%. Table 5 shows the average impact of process parameters on the average surface roughness. According to the Table 5, nozzle traverse speed has the only statistically significant impact. When the factors are listed for their level of impact on the average surface roughness values, nozzle traverse speed is the most effective factor by 89.29%. Abrasive flow rate follows by 3.31%.

TABLE LVIII. ANOVA AND F-TEST FOR MRR

Source	DF	Adj SS	Adj MS	F-Value	P-Value	Contr. (%)
Traverse Speed (mm/min)	1	25,1331	25,1331	1051,9	0	85,33
Abrasive Flow rate (g/min)	1	4,15	4,15	173,69	0	14,09
Stand of Distance (mm)	1	0,0228	0,0228	0,95	0,384	0,07
Abrasive Grit size (µm)	1	0,0504	0,0504	2,11	0,22	0,17
Error	4	0,0956	0,0239			0,32
Total	8	29,4519				100

TABLE V. ANOVA AND F-TEST FOR SR

Source	DF	Adj SS	Adj MS	F-Value	P-Value	Contr. (%)
Traverse Speed (mm/min)	1	5,24535	5,24535	68,06	0,001	89,29
Abrasive Flow rate (g/min)	1	0,1944	0,1944	2,52	0,187	3,31
Stand of Distance (mm)	1	0,0726	0,0726	0,94	0,387	1,24
Abrasive Grit size (µm)	1	0,05415	0,05415	0,7	0,449	0,92
Error	4	0,3083	0,07708			5,25
Total	8	5,8748				100,00

Figure 3 shows the main effects of each factor involved in AWJM on Material Removal Rate (MRR) with respect to the level conditions shown in Table 1. Fig. 4 shows the main effects plot for processing parameters on the average surface roughness.

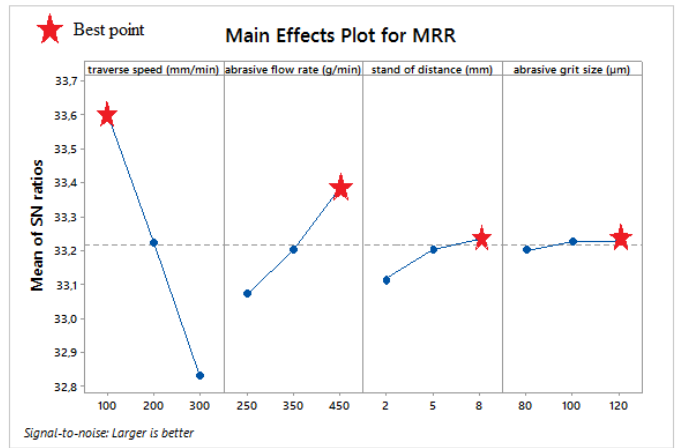


Figure 3. The main effects plot of AWJ machining parameters on material removal rate.

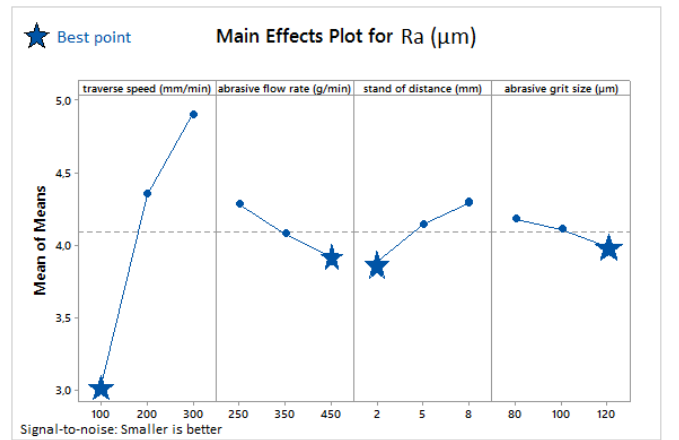


Figure 4. The main effects plot of AWJ machining parameters on surface roughness.

According to Fig. 3, MRR decreases with the increasing nozzle traverse speed; the lowest MRR was obtained from the level 3, 300mm/min nozzle traverse speed. The ideal value that should be assigned to nozzle traverse speed is 100mm/min. Taking Abrasive flow Rate into consideration, it was found that level 3, 450 g/min results in the highest MRR. Material removal increases to a point with the increasing abrasive flow rate. When it comes to standoff distance, level 1, 8mm standoff distance results in the highest MRR however it leads to kerf formation at the inlet and outlet points of the workpiece. Kerf formation is unwanted. While the main purpose is to achieve the specified material removal rate, increasing standoff distance does not significantly increase MRR as the abrasion at the sides is calculated. When it comes to abrasive size parameter, it was found that 120 mesh abrasive grit size results in the highest MRR, however, there is cost differences between 80 mesh and 120 mesh abrasives; AWJ users who are not concerned widely with surface roughness may prefer 80 mesh abrasive to machine mildly hard material. 120 mesh abrasive can be preferred for the machining of brittle material and for precision cutting. Thus, the optimal parameter selection for the MRR was found to be A1B3C1D1. Fig. 3 shows the main effects of each factor at all the levels for surface roughness. According to Fig.

4, the average surface roughness increases when A and C are increased and decreases when B and C is increased. In order to obtain low average surface roughness and with consideration into operational costs, nozzle traverse speed of 100mm/min, abrasive flow rate of 450g/min, standoff distance of 2mm and abrasive size of 120 mesh can be selected.

Confirmation Test:

A final validation test was conducted to check the reliability and efficiency of the Taguchi method. The estimated process combination was found to be A1B3C1D1 for MRR, while it was A1B3C1D3 for SR and it resulted in MRR, 48,64 mm³/min and SR, 2,84 μm . Table 6 shows that the difference between estimated and actual S/N Ratios of material removal rate was not more than 6%, while the Estimated MRR was not more than 3.5%. According to Table 7, the difference between estimated and actual S/N Ratios of surface roughness was not more than 6%. Similarly, the difference between estimated and actual Ra was not more than 9%, as shown in Table 7. The difference between estimated and actual values of both MRR and Ra was not more than 10% and it is recognized as an acceptable difference.

TABLE VI: S/N RATIO FOR MRR (LARGER THE BETTER)

MRR (mm ³ /min)	Estimated MRR (mm ³ /min)	% change	S/N Ratio MRR (mm ³ /min)	Estimated S/N Ratio MRR (mm ³ /min)	% change
46,98	45,53	3,08	33,43	31,54	5,60
47,74	46,29	3,03	33,57	31,68	5,62
48,95	47,5	2,96	33,79	31,90	5,59
45,02	43,57	3,22	33,06	31,17	5,71
45,74	44,29	3,17	33,20	31,31	5,69
46,75	45,3	3,10	33,39	31,50	5,65
43,17	41,72	3,35	32,70	30,81	5,77
43,76	42,31	3,31	32,82	30,93	5,75
44,46	43,01	3,26	32,95	31,06	5,73

TABLE VII: S/N RATIO FOR SR (SMALLER THE BETTER)

S/N Ratio Ra (μm)	Estimated S/N Ratio Ra (μm)	% dif.	Ra (μm)	Estimated Ra (μm)	% dif.
-10,603	-11,104	-4,72	3,39	3,16	6,78
-9,771	-10,271	-5,12	3,08	2,85	7,47
-8,366	-8,866	-5,98	2,62	2,39	8,78
-13,025	-13,525	-3,84	4,48	4,25	5,13
-12,649	-13,149	-3,95	4,29	4,06	5,36
-12,628	-13,128	-3,96	4,28	4,05	5,37
-13,927	-14,427	-3,59	4,97	4,74	4,63
-13,750	-14,250	-3,64	4,87	4,64	4,72
-13,732	-14,232	-3,64	4,86	4,63	4,73

Regression Analysis

First order regression equation obtained for Ra values is given in Eq. (3). Regression coefficients of first order equation are shown in Table 8 for Ra. First order regression equation obtained for MRR values is given in Eq. (4). Regression coefficients of first order equation are shown in Table 9 for Ra.

$$Ra(\mu m) = 3,512 + 0,009 \text{ traverse speed (mm/min)} - 0,001 \text{ abrasive flow rate (g/min)} - 0,0367 \text{ stand of distance (mm)} - 0,00475 \text{ abrasive grit size } (\mu m) \quad (3)$$

TABLE VIII. REGRESSION COEFFICIENTS OF FIRST ORDER EQUATION FOR RA.

Term	Coef	SE Coef	T-Value	P-Value
Constant	3,512	0,758	4,63	0,01
Traverse speed (mm/min)	0,00935	0,00113	8,25	0,001
Abrasive flow rate (g/min)	-0,0018	0,00113	-1,59	0,187
Stand of distance (mm)	-0,0367	0,0378	-0,97	0,387
Abrasive grit size (μm)	-0,00475	0,00567	-0,84	0,449

$$MRR(\text{mm}^3/\text{min}) = 46,463 - 0,020467 \text{ traverse speed (mm/min)} + 0,008317 \text{ abrasive flow rate (g/min)} + 0,0206 \text{ stand of distance (mm)} + 0,00458 \text{ abrasive grit size } (\mu m) \quad (4)$$

TABLE IX. REGRESSION COEFFICIENTS OF FIRST ORDER EQUATION FOR MRR.

Term	Coef.	SE Coef.	T-Value	P-Value
Constant	46,463	0,422	110,13	0
Traverse speed (mm/min)	-0,02047	0,000631	-32,43	0
Abrasive flow rate (g/min)	0,008317	0,000631	13,18	0
Stand-off distance (mm)	0,0206	0,021	0,98	0,384
Abrasive grit size (μm)	0,00458	0,00316	1,45	0,22

III. RESULTS

This study analyzed the interactions between process parameters of abrasive water jet machining at different levels using Taguchi technique. The following results can be reached for the effective machining of Aluminium using AWJM process:

The most important factor in AWJM with respect to MRR is the nozzle traverse speed (A). The second most important factor is the abrasive flow rate. Nozzle Standoff Distance and Abrasive Size have insignificant effects. The parameter combination recommended for optimal material removal is A1B3C1D1.

For optimal parameter combination recommended for the best surface roughness is A1B3C1D1. Considering the cost aspect of the process, the selection can be abrasive flow rate at 350g/min, abrasive size at 80 Mesh, and nozzle traverse speed at 200mm/min. A mathematical model is developed, having identified the parameters impacting on the cutting power, vibration level and surface roughness values. It was found that both models can be used at a confidence level of 95%. It is possible to identify the process parameter levels after finding the sufficient values at the confidence level of 95% using the surface roughness estimation equation for the cutting process.

ACKNOWLEDGEMENTS

The authors would like to thank CT Cutting Technologies in Istanbul from Turkey.

REFERENCES

- [1] Bitter, J. G. A. "A study of erosion phenomena part I." wear 6.1 (1963): 5-21.
- [2] Levy, Alan V. "The solid particle erosion behavior of steel as a function of microstructure." Wear 68.3 (1981): 269-287.
- [3] Çaydaş, Ulaş, and Ahmet Haşçalık. "A study on surface roughness in abrasive waterjet machining process using artificial neural networks and regression analysis method." Journal of materials processing technology 202.1 (2008): 574-582.

- [4] Kk, Metin, Erdogan Kanca, and mer Eyercioęlu. "Prediction of surface roughness in abrasive waterjet machining of particle reinforced MMCs using genetic expression programming." *The International Journal of Advanced Manufacturing Technology* 55.9-12 (2011): 955-968.
- [5] Selvan, M. Chithirai Pon, N. Mohana Sundara Raju, and H. K. Sachidananda. "Effects of process parameters on surface roughness in abrasive waterjet cutting of aluminium." *Frontiers of Mechanical Engineering* 7.4 (2012): 439-444.
- [6] Kolahan, Farhad, and A. Hamid Khajavi. "Modeling and optimization of abrasive waterjet parameters using regression analysis." *International journal of aerospace and mechanical engineering* 5.4 (2011): 248-253.
- [7] Aruna, S. T., et al. "Optimization of the properties of electrodeposited Ni-YSZ composites using Taguchi method and regression analysis." *Portugaliae Electrochimica Acta* 29.1 (2011): 23-37.
- [8] Emamy, M., et al. "The Effect of Sr and Grain Refining Elements on the Microstructure and Tensile Properties of A356-10% B4C Metal Matrix Composite." *Mechanics of Advanced Materials and Structures* 18.3 (2011): 210-217.
- [9] ..

Influence of Grain Size on Susceptibility to Intergranular Corrosion of AISI 316 Austenitic Stainless Steel

Hüseyin Zengin*, Yunus Türen*, Hayrettin Ahlatcı*, Yavuz Sun*, Burak Dursun Ünsever*

*Karabuk University, Department of Metallurgy and Materials Engineering, Turkey

huseyinzengin@karabuk.edu.tr, yturen@karabuk.edu.tr, hahlatci@karabuk.edu.tr, ysun@karabuk.edu.tr, burakunsever@gmail.com

Abstract— In this study, influence of grain size on degree of sensitization and susceptibility to intergranular corrosion of AISI 316 austenitic stainless steel was investigated. As-received AISI 316 austenitic stainless steel samples were first solution heat treated at 1050 °C for 0.5 h, 1.5 h and 3 h in order to obtain different grain sizes and then, each of them was heat treated for sensitization at 700 °C for 1h followed by water quenching. Grain size measurements of the first set of samples were performed by linear intercept method according to ASTM E112 standard and the degree of sensitization was measured by double loop electrochemical potentiodynamic reactivation (DLEPR) test. The results showed that grain size increased as the solution heat treatment time increased. A decrease in the degree of sensitization was observed for the samples having larger grains. That is to say, the increase in grain size improved intergranular corrosion resistance.

Keywords— austenitic stainless steel, solution treatment, sensitization, intergranular corrosion, DLEPR

I. INTRODUCTION

Austenitic stainless steels are extensively used in mainly chemical and nuclear industries since they have an excellent combination of mechanical properties and corrosion resistance at both low and elevated temperatures. Nickel and manganese as austenite stabilizers, are the major alloying elements in order to provide stable austenite structure in stainless steels resulting in improved toughness, formability, weldability and corrosion resistance [1]. However, when austenitic stainless steels are undergone a slow heating or cooling in the temperature range of 450 °C to 850 °C (welding, heat treatment etc.), Cr-rich carbide (Cr_{23}C_6) precipitates are formed along grain boundaries leading to Cr-depleted zones (below 13%) in the vicinity of grain boundaries which called sensitization. When sensitized austenitic stainless steels are subjected to corrosive environment, they become susceptible to intergranular corrosion (IGC) and intergranular stress corrosion cracking (IGSCC) that may cause failure in service [1]-[3]. Researchers have extensively studied the corrosion monitoring conditions and methods on IGC [4]-[6]. A modification of electrochemical potentiokinetic reactivation (EPR) test described by ASTM G 108 was called double loop

electrokinetic repassivation test (DLEPR). This method has been widely used to assess the degree of sensitization (DOS) with being less dependent on surface finish and grain size.

Several studies investigated the effects of strain rate and heat treatment on susceptibility to intergranular corrosion of austenitic stainless steels [7]-[11]. It was reported that DOS increased with increasing strain in 316 stainless steel [7]. Parvathavarthini et al. [8] showed that DOS increased with increasing effective grain boundary energy but decreased beyond a critical value. They also reported that presence of copper in 316L stainless steel effectively decreased chromium carbide precipitation and DOS. It was revealed that decreasing grain size promoted chromium carbide precipitation and increased DOS [8]-[10]. However, there is still limited information about the effect of grain size in a specific electrochemical condition on the extent of susceptibility to IGC in 316 stainless steel. In the present study, the 316 stainless steel samples with various grain sizes that produced by solution heat treatment at 1050 °C for different durations were equally sensitized at 700 °C for 1 h. %DOS was determined by performing DLEPR test and a correlation between the grain size and DOS was found.

II. EXPERIMENTAL PROCEDURE

The AISI 316 stainless steel was supplied from the market as sheet form. Samples with a dimension of 10 mm x 10 mm x 3 mm were cut for microscopic and corrosion tests. The samples were solution heat treated at 1050 °C for 0.5 h, 1.5 h and 3 h in order to obtain different grain sizes. After that, each sample was heat treated equally for sensitization at 700 °C for 1h followed by water quenching. For microstructural investigations, all samples were mechanically ground with 240, 400, 600, 800, 1000, 1200 and 2000 grit emery papers followed by polishing with 6 μm and 1 μm diamond paste. Then, the samples were electrochemically etched in 10% oxalic acid solution at 6 V for 1 min. Grain size measurements of the first set of samples were performed by linear intercept method according to ASTM E112 standard. The degree of sensitization was measured by double loop electrochemical potentiodynamic reactivation (DLEPR) test. The samples for corrosion test were mounted in epoxy resin with brass

wire connection. The electrochemical testing system consisted of a graphite rod as counter electrode, a saturated calomel electrode (SCE) as reference electrode and the sample with exposed area of 0.25 cm² as working electrode in a working solution of 0.5 M H₂SO₄ + 0.01 M KSCN. The polarization curves were obtained by Gamry model PC4/300 mA potentiostat/galvanostat with DC105 corrosion analysis controlled by a computer. After monitoring open circuit potential for 300 s, the specimens were polarized anodically from E_{OC} to +0.3 V and immediately reversed to E_{OC}. The degree of sensitisation (%DOS) were determined by multiplying 100 and the ratio of the maximum current generated in the reactivation or the reverse scan (I_R) to that generated in the anodic scan (I_A) as illustrated in Fig. 1.

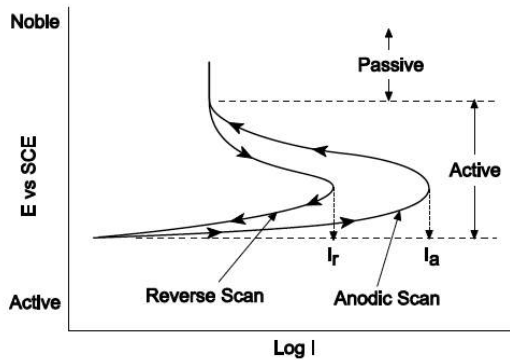


Fig. 1 A schematic diagram for the procedure of DLEPR test [6].

III. RESULTS AND DISCUSSION

Fig. 2 shows the microstructures of the as-received and heat treated samples with various grain sizes that measured by linear intercept method and listed in Table 1. The average grain size of the as-received sample was 21.82 μm. After solution heat treatment at 1050 °C for 0.5, 1.5 and 3 h, the average grain size gradually increased to 35.65 μm, 72.71 μm and 88.75 μm respectively. It can be seen in the microstructures that the grain size distribution became uneven as the duration of solution heat treatment increased in which the microstructures consisted of mostly huge grains with several tiny grains. It should also be noted that all the samples showed single phase austenitic structure with no second phase.

mentioned

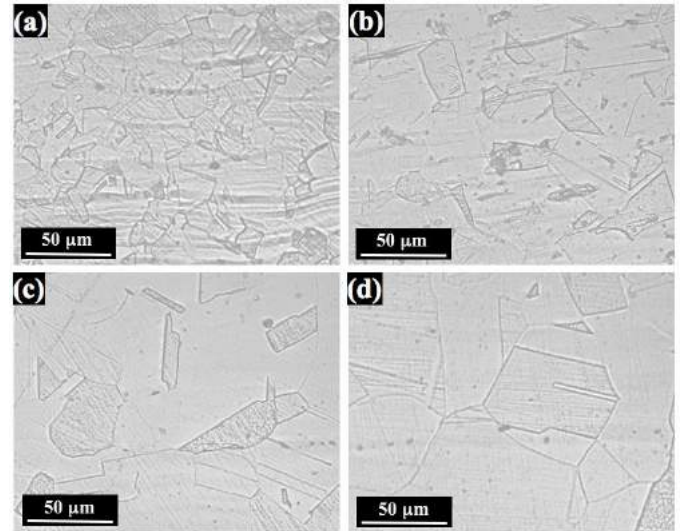


Fig. 2 Optical micrographs of 316 SS with various grain sizes by solution heat treatment at 1050 °C for (a) as-received, (b) 0.5 h, (c) 1.5 h and (d) 3 h.

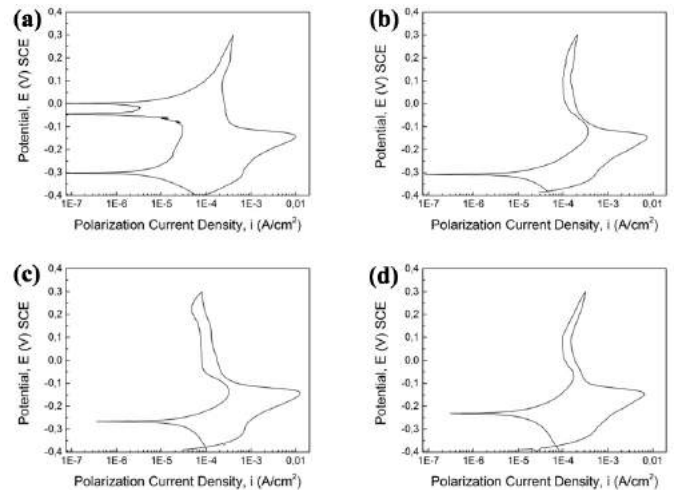


Fig. 3 DLEPR polarization curves of 316 SS with various grain sizes by solution heat treatment at 1050 °C for (a) as-received, (b) 0.5 h, (c) 1.5 h and (d) 3 h after sensitization at 700 °C for 1h.

The as-received samples unexpectedly showed a %DOS of 0.3 which means a low amount of sensitization was present in as-received condition. This might have occurred as a result of

TABLE LIX
GRAIN SIZES AND %DOS VALUES OF AS-RECEIVED AND SOLUTION HEAT TREATED 316 STAINLESS STEEL SAMPLES.

In Fig. 3, DLEPR polarization curves of the samples were presented. The %DOS values as listed in Table 1, were calculated by obtaining the maximum currents of both anodic and reverse scans from the polarization curves as

Condition	Time (h)	Average Grain Size (μm)	Reactivation Current, I_R (A/cm^2)	Activation Current, I_A (A/cm^2)	%DOS (I_R/I_A)x100
As-Received (Unsensitized)	-	21.82	2.9×10^{-5}	96.3×10^{-4}	0.30
Solution Heat Treated + Sensitized at 700 °C for 1h	0.5	35.65	36.4×10^{-5}	75×10^{-4}	4.85
	1.5	72.71	35.1×10^{-5}	121.4×10^{-4}	2.89
	3	88.75	16.8×10^{-5}	63.8×10^{-4}	2.63

earlier. The as-received sample without any solution or sensitization heat treatment was also tested as shown in Fig. 3a in order to evaluate %DOS of the as-received condition and to compare with heat treated samples some heat treatment processes during production. After sensitization at 700 °C for 1 h, %DOS values were found as 4.85, 2.89 and 2.63 for the samples solution heat treated for 0.5, 1.5 and 3 h respectively. The %DOS values were not high which indicated a partial sensitization. According to time-temperature-sensitization (TTS) diagram of 316 stainless steel [12], heat treatment at 700 °C for 1 h results in a partial sensitization and longer durations at this temperature lead to full sensitized structure. Therefore, it can be said that the calculated DOS values were compatible with the TTS diagram of 316 stainless steel.

Fig. 4 shows the change of %DOS with increasing austenite grain size. It can be clearly seen that %DOS significantly decreased as the grain size increased. This behaviour was attributed to the decreased nucleation sites for Cr-carbide precipitation with increased grain size leading to less Cr-depleted zones in the vicinity of grain boundaries. DOS is inversely proportional to grain size. However, the calculated %DOS values are not only dependent on grain size but also the testing parameters and texture [10]. Further investigations for longer durations of both solution and sensitization heat treatments at certain testing parameters and texture intensities can help to establish a more precise relationship between DOS and grain size.

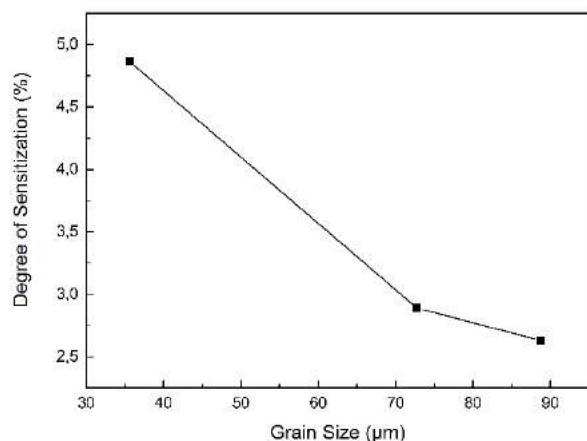


Fig. 4 The change of %DOS values of the sensitized alloys as a function of various grain size.

IV. CONCLUSIONS

The effect of grain size on susceptibility to intergranular corrosion of 316 stainless steel was investigated. DLEPR tests showed that the 316 stainless steel has less DOS and susceptibility to intergranular corrosion with increasing grain size meaning that DOS is inversely proportional to grain size. It is also suggested that keeping the grain size at an optimal level can be an effective way to decrease susceptibility to intergranular corrosion of 316 stainless steel although it is challenging without sacrificing the mechanical properties.

REFERENCES

- Parvathavarthini, N., 2002. *Sensitization and Testing for Intergranular Corrosion*, in: Khatak, H.S., Raj, B. (Eds.), *Corrosion of Austenitic Stainless Steels*, Woodhead Publishing Series in Metals and Surface Engineering, Woodhead Publishing, pp. 117–138.
- Taiwade, R.V., Ingle, A.V., Khatirkar, R.K., 2014. *Assessment of Inter-granular Corrosion Susceptibility of 304L Stainless Steel Using Non-destructive Electrochemical Techniques*. ISIJ International 54, 1898–1905.
- Taiwade, R.V., Patil, A.P., Patre, S.J., Dayal, R.K., 2012. *A Comparative Study of Intergranular Corrosion of AISI 304 Stainless Steel and Chrome-Manganese Austenitic Stainless Steel*. ISIJ International 52, 1879–1887.
- Parvathavarthini, N., Mudali, U.K., 2014. *Electrochemical techniques for estimating the degree of sensitization in austenitic stainless steels*. Corrosion Reviews 32, 183–225.
- Rahimi, S., Engelberg, D.L., Marrow, T.J., 2011. *A new approach for DL-EPR testing of thermo-mechanically processed austenitic stainless steel*. Corrosion Science 53, 4213–4222.
- Aydođdu, G.H., Aydinol, M.K., 2006. *Determination of susceptibility to intergranular corrosion and electrochemical reactivation behaviour of AISI 316L type stainless steel*. Corrosion Science 48, 3565–3583.
- Murr, L.E., Advani, A., Shankar, S., Atteridge, D.G., 1997. *Effects of Deformation (Strain) and Heat Treatment on Grain Boundary Sensitization and Precipitation in Austenitic Stainless Steels*. Materials Characterization 39, 575–598.
- Parvathavarthini, N., Mulki, S., Dayal, R.K., Samajdar, I., Mani, K.V., Raj, B., 2009. *Sensitization control in AISI 316L(N) austenitic stainless steel: Defining the role of the nature of grain boundary*. Corrosion Science 51, 2144–2150.
- Beltran, R., Maldonado, J.G., Murr, L.E., Fisher, W.W., 1997. *Effects of strain and grain size on carbide precipitation and corrosion sensitization behavior in 304 stainless steel*. Acta Materialia 45, 4351–4360.
- Li, S.-X., He, Y.-N., Yu, S.-R., Zhang, P.-Y., 2013. *Evaluation of the effect of grain size on chromium carbide precipitation and*

- intergranular corrosion of 316L stainless steel. Corrosion Science* 66, 211–216.
- [20] Trillo, E.A., Murr, L.E., 1998. *Effects of carbon content, deformation, and interfacial energetics on carbide precipitation and corrosion sensitization in 304 stainless steel. Acta Materialia* 47, 235–245.
- [21] Voort, G.F.V., 1991. *Atlas of Time-temperature Diagrams for Irons and Steels*. ASM International.

Improving the Energy Efficiency in Iron and Steel Industry by Electric Motor Retrofit

Mehmet AKBABA *

*Computer Engineering Department, College of Engineering, Karabuk University
Balıklar kayası mevki 78050 Karabuk, Turkey
mehmetakbaba@karabuk.edu.tr

ABSTRACT

In iron and steel industry electric motor systems consume around 7% of total energy use. This rate is even more in some special applications. Motor systems include motor driven units such as rolling mills, pumps, conveyors, fans and material handling equipment. In many cases motors used in this industry are aged motors of standard efficiency class that are consuming much more energy than the new generation energy efficient motors. Solution to this problem is to retrofit the existing even healthy standard efficiency motors by the new generation energy efficient motors. In some countries governmental regulations makes it mandatory to retrofit the standard efficiency motors with the new generation energy efficient class motors, where in most countries around the globe this matter remains as recommendation. Depending on the energy cost in each country the pay-back periods varies between 2 years to 6 years. For the countries such as Turkey where the energy prices are very high the pay-back periods for electric motor retrofits will be about 2 to 3 years or less than that. This means that a motor retrofit will cover the installation and new motor cost mostly within approximately 2 to 3 years or less and then energy and cost saving will start for free thereafter. Retrofit means replacing and old but operating healthy motor of standard efficiency with a new higher efficiency motor. In this investigation several scenarios will be presented on the energy and cost saving by motor retrofit and pay-back periods will be determined in details. Importance of the dependency on the energy prices, benefits of motor retrofit to the iron and steel industry and environmental pollution will be explored with several examples when using different sizes of electric motors. It will be shown that the size of the motor plays an important role on the pay-back period and that the energy and cost saving is more significant for retrofitting small and medium size motors up to 100 kW, which are more commonly used motor sizes in the iron and steel industry.

Keywords: Energy efficiency, iron and steel industry, motor retrofit

From Waste Management in Iron and Steel Sector to Zero Waste

Aslan ÜNAL¹, Prof. Dr. Mustafa ÖKSÜZ²,
Prof. Dr. Onuralp YÜCEL³, Esma YILMAZ³,

¹ MATIL Material Test and Innovation Laboratories A. S., Istanbul Technical University Ayazağa Campus, Sarıyer, 34469 İstanbul, Turkey

² Yalova University, Faculty of Engineering, Department of Polymer Engineering, 77200, Yalova, Turkey

³ Istanbul Technical University, Faculty of Chemistry and Metallurgy, Department of Metallurgical and Materials Engineering, Sarıyer, 34469, Istanbul, Turkey

aslan.unal@matil.org mustafa.oksuz@yalova.edu.tr
yucel@itu.edu.tr esma.yilmaz@itu.edu.tr

ABSTRACT

There is no doubt that the iron and steel sector plays an important role in the determination of the development level for countries. Especially the production and export values of this sector has the key role of progress for countries. According to year of 2016 data, the annual production of iron and steel in the world is 1.6 billion tonnes. On the other hand, Turkey is a remarkable spot in the iron and steel industry in the world with an output of 33 million tons. Raising profit margins by lowering production costs has become the most important issue all over the world, given the progress of the industry and the decline in available resources. For this reason, waste management will be one of the leading factors for both reducing manufacturing costs and bringing other new profit items. In addition, the developing environmental consciousness has brought new concepts and trends in waste management. In this context, "zero waste" is taken seriously in many countries and many commercial or non-commercial institutions. Especially in Europe, it is predicted that these countries and institutions will switch to zero-waste production technologies after a certain period of time. According to the year 2016, when iron and steel sector is evaluated in terms of waste production, it will be seen that the slag production is 0,375 tons in the integrated system and 0,075 tons in the electric arc furnaces. Attempts to restore these wastes to the economy must be made in accordance with the waste hierarchy. This is also important in terms of sustainable development. Reducing slag production, investigation to utilization in different application should be analysed considering to scope of zero waste. This study is focused on especially the EAF slags. First of all, the ways of recovery metal and then the utilization of these slags in alternative applications were investigated.

Keywords: Waste management, EAF slug, zero waste

Application of Taguchi Method for Optimization AWJ Machining of AISI 316 Stainless Steel

Fuat KARTAL*, Hasan GÖKKAYA⁺

*Mechanical Engineering Department, Kastamonu University,
Kastamonu, Turkey

fkartal@kastamonu.edu.tr

+Mechanical Engineering Department, Karabük University,
Karabuk, Turkey,

hgokkaya@karabuk.edu.tr

Abstract—A non-conventional material removal process, Abrasive Water jet (AWJ) machining is also an ideal manufacturing process for very hard materials. This study aims to optimize the parameters involved in AWJ machining of 316 stainless steel material such as abrasive material grain size, nozzle speed, standoff distance, abrasive mass flow rate and pumping system pressure. The analysis of the impact of parameters involved in this study was conducted using the L27 Taguchi orthogonal array, S/N ratio and ANOVA. Five controllable factors were used to obtain the minimum surface roughness and each parameter was assigned with three different values in order to define the optimal factor and level combination. Results showed that the surface roughness is in strong correlation with abrasive material grain size. The findings of this study suggest that the study design used is much more effective than the full factorial design in terms of the number of experiments conducted.

Keywords— AISI 316 stainless steel, Abrasive Water jet, machining, full factorial design, Taguchi orthogonal array, stainless steel

I. INTRODUCTION

When compared to the other unconventional techniques, AWJ machining is recognized as an effective technology for cutting several materials due to its advantages such as non-thermal cutting, high cutting flexibility, minimal stress build-up on the workpiece, etc [1]. AWJ machine is an industrial device which can be used for cutting any kind of material, soft and hard. The waterjet feed in an AWJ machine is at a high-pressure between 20,000 to 60,000 psi and offers a good cutting and surface machining process [2-4]. AWJ machine is equipped with a nozzle mounted in an orifice and the waterjet is transferred through this nozzle as a cutting flow; this nozzle is able to move on x-y axis as it is the case for CNC devices. AWJ machining is also known as cold process or cold cutting process and using this cold process it is possible to cut the material in any way desired. AWJ machine uses a water pump. A mixture of 80 mesh Garnet (abrasive) and water is the case in AWJ machining in order to cut the material and provide a better surface machining. Abrasive water jet machine is much more powerful than the sole waterjet [1-5]. AWJ machining devices consist of four fundamental components: pumping system,

abrasive feed system, abrasive waterjet nozzle and the holder [2-4]. AWJ machine includes two types of pumps, a booster pump and a high concentrator pump, and it provides up to 450mpa high-speed waterjet using a high-power motor running at 50HP [2-6]. Abrasive feed system ensures the controlled abrasive feed through a port (abrasive tank)in order to mix the abrasive into the high-speed waterjet. Abrasive waterjet machines also include a nozzle which sprays the Garnet and water, having mixed them inside of it. Another component of the AWJ machine is the holder which holds the water and waste inside [5,6]. This component is placed at the bottom of the machine. Unconventional machining processes are developed in order to overcome the shortcomings of conventional machining processes. These unconventional processes offer advantages such as accuracy, quality, ability to cut hard materials, and ability to perform complicated movements on workpieces with complicated shapes. Nevertheless, these processes also have weaknesses such as lower productivity when compared to conventional cutting processes [1-3]. AWJ machining is a material removal process provided by the erosion caused by the high-pressure abrasive waterjet [3,4]. AWJ machining has become one of the most common unconventional production methods today [2, 3]. AWJ machining involves a very thin waterjet at high speeds bearing abrasive material in order to cut hard materials such as granite and titanium [4-8]. A very thin cut, also known as a kerf, is made on the workpiece during this process [4]. Jet cutting mechanism is quite complicated [2,8]. Material removal is ensured mechanically with the erosion caused by the local compression failures which occur when the local fluid pressure is in excess of the maximum compressive strength of the target material [5,6]. A number of studies have been conducted on the abrasive waterjet machining in the recent years and the process is extensively discussed [1-8].

II. MATERIAL AND METHOD

A. Materials Used in Experiments

AISI 316 stainless steel samples were used in this study. As it offers material properties acceptable for many applications, stainless steel is one of the most commonly used steel type. Stainless steel is a very hard material which is hard to machine

using other cutting methods, however, easy to machine using AWJ.

B. Abrasive

Garnet abrasive is made up of Almandine Garnet particles which are known for their natural hardness, strength and abrasive properties. Garnet abrasive is commonly used in waterjet machining devices available in the world. It was possible to produce the Garnets with the highest purity at a very precise particle size using the best machining methods. 80 mesh Garnet is the ideal abrasive for the purpose of the AWJ machines. 80 mesh Garnet has the maximum usage inn waterjet cutting when compared to other abrasives such as tungsten carbide, aluminium oxide and silicon carbide.

C. Equipment

A number of abrasive waterjet cutting attempts were made on a CT2.5 axis AWJ machining system using KMT SL-V100D ultra high-pressure pump which can deliver up to 413.7 MPa water pressure through a sapphire orifice. A gravity feed type abrasive hopper, an abrasive feed system, a pneumatic controlled valve and a lathe of 1400x1000mm were used in the machine.



Fig. 1. AISI 316 stainless steel sample being machined.

D. Material

316 Quality stainless steel offers a wide range of use and a perfect corrosion resistance. It is resistant against all the possible oxidations which may arise in architectural applications and it is sometimes used for seafront buildings, bridge connections and beams which are exposed to extreme conditions. It is preferred in spaces where food is processed as it is easy to clean. It is resistant against organic chemicals, dyes and a wide range of inorganic chemicals. Experiment design is an important tool which is used for several experiment

conditions. AISI 316 stainless steel was selected in this study as the workpiece. Chemical composition and properties of AISI 316 stainless steel is shown in Table 1.

TABLE I. CHEMICAL COMPOSITION OF AISI 316 STAINLESS STEEL [9].

C	Si	Mn	P	S	Mg	Cr	Ni	Mo	Cu	Al	V	W	Fe
0.035	0.477	1.054	0.036	0.008	0.001	16.95	10.36	2.418	0.382	0.007	0.043	0.001	68.219

The dimensions of the workpiece were 120x120mm. Tests were conducted on the AWJ machine using 80mesh Garnet. Among the control parameters were water pressure, abrasive flow rate (AFR), and standoff distance (SoD) and material removal rate (MRR) was the output.

E. Design of Experiment

Table 2 shows the process parameters and their levels while Table 3 shows the design of experiment based on the Taguchi L9 Orthogonal Array. Responses obtained were then compared with the estimated values obtained from regression equations. Trial version of the Minilab 17 statistics software was used in order to create the regression equations and to analyses the data obtained from ANOVA and Taguchi Method.

TABLE II. PROCESS PARAMETERS AND THEIR LEVELS

Parameters /Levels	Level 1	Level 2	Level 3
Pump Pressure (MPa)	150	250	350
Abrasive flow rate (g/min)	150	250	350
Standoff distance (mm)	2	5	8

TABLE III. DESIGN OF EXPERIMENT FOR ABRASIVE WATER JET MACHINING OF AISI 316 STAINLESS STEEL

Experiment no	Pump Pressure (MPa)	Abrasive Flow Rate (g/min)	Stand off distance (mm)	MRR (g/min)	S/N ratio
1	150	150	2	3,5	10,8814
2	150	250	5	4,5	13,0643
3	150	350	8	5,5	14,8073
4	250	150	5	4,5	13,0643
5	250	250	8	4,8	14,8073
6	250	350	2	5,5	13,6248
7	350	150	8	5,5	16,2583
8	350	250	2	6,5	14,8073
9	350	350	5	7,5	17,5012

III. FINDINGS & DISCUSSION

Fig. 2 shows the effects of factors on the material removal rate. It was found that increasing S/N ratio also increases the positive impact of the input variable on the output variable. According to the plot, optimal MRR value was obtained from water pressure, 350 MPa; abrasive flow rate, 350g/min; and standoff distance, 8 mm. However, as the standoff distance of

8mm leads to kerf formation, it is recommended to use the standoff distance of 2mm (Fig. 2).

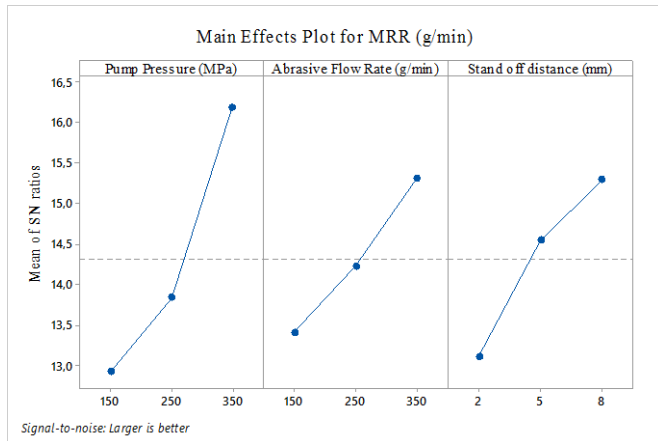


Figure 2. The effect of control factors on MRR.

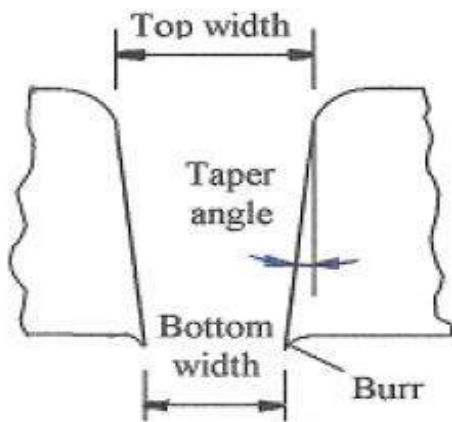


Fig. 2. Schematic of AWJ produced kerf profile and surface [10,11].

ANOVA was used to measure the extent of the effects of process parameters on the material removal rate. This analysis was conducted at the confidence level of 95%. ANOVAs conducted on averages and signal-noise ratios are shown in Table 4. ANOVA was conducted in order to analyze the effect of process parameter on the MRR and to identify the parameters with most significant effects on MRR. In Fig. 2, MRR increases as the pump pressure increases from level 1 to level 3. MRR is at a minimum when the pump pressure is 150MPa and at a maximum when the pump pressure is 350MPa. MRR increases when the abrasive flow rate is increased from level 1 to level 3. In this case, a higher abrasive flow rate is favorable in order to increase the MRR. The effect of standoff distance is found less significant when compared to the other process parameters.

TABLE LXV. ANOVA AND F-TEST FOR MRR

Source	D F	Adj SS	Adj MS	F-Value	P-Value	% effect
Pump Pressure (MPa)	1	6	6	27,98	0,003	53,72
Abrasive Flow Rate (g/min)	1	1,815	1,815	8,46	0,033	16,25
Standoff distance (mm)	1	2,282	2,2817	10,64	0,022	20,43
Error	5	1,072	0,2144			9,59

Total	8	11,16	9	100
-------	---	-------	---	-----

First order regression equation obtained for MRR values is given in Eq. (1). Regression coefficients of first order equation are shown in Table 5 for MRR.

$$MRR \text{ (g/min)} = 0,408 + 0,01000 \text{ Pump Pressure (MPa)} + 0,00550 \text{ Abrasive Flow Rate (g/min)} + 0,2056 \text{ Standoff distance (mm)} \quad (1)$$

TABLE V. REGRESSION COEFFICIENTS OF FIRST ORDER EQUATION FOR MRR.

Term	Coef	SE Coef	T-Value	P-Value
Constant	0,408	0,755	0,54	0,612
Pump Pressure (MPa)	0,01	0,00189	5,29	0,003
Abrasive Flow Rate (g/min)	0,0055	0,00189	2,91	0,033
Standoff distance (mm)	0,2056	0,063	3,26	0,022

Estimated values obtained from the regression equation for MRR were compared to the values obtained from the experiments for confirmation purposes. Fig. 3 shows the plot comparison of the MRR values obtained from the experiments and the estimated MRR values. Nevertheless, Table 6 shows the optimum parameter combinations obtained from the analysis.

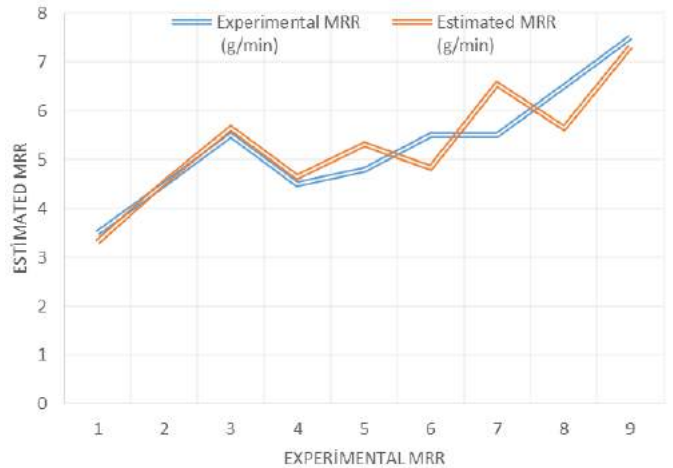


Fig. 3. Plot comparison of the experimental and estimated MRR values.

TABLE VI. OPTIMUM CONTROL PARAMETERS AND THEIR LEVELS

Response	Pump pressure (MPa)	Abrasive flow rate (g/min)	Standoff distance (mm)
MRR	350	350	2

IV. RESULTS

This study explored the straight cutting of the AISI 316 Stainless Steel plate using abrasive waterjet. Abrasive waterjet machining is an effective method for material machining. Only two of the selected parameters, pump pressure, 53.72% and abrasive flow rate, 16.25%, affect the material removal rate in

AWJ machining. Water pressure is found to be the most effective factor in terms of material removal rate for 316 stainless steel workpiece and abrasive flow rate and nozzle standoff distance followed. Therefore, water pressure of 350 MPa, abrasive flow rate of 350 g/min, and standoff distance of 2mm must be used in order to achieve maximum material removal rate when it comes to 316 stainless steel. Pump pressure is the most important factor while abrasive flow rate has a significant impact on the MRR. Moreover, AWJ will create a narrower kerf with the decreasing abrasive flow rate. The reason behind this is that decreasing abrasive flow rate will lead to decreased erosion on the target workpiece which in return creates a narrower kerf. The experimental results were similar to the literature.

ACKNOWLEDGEMENTS

The authors would like to thank CT Cutting Technologies in Istanbul from Turkey.

REFERENCES

- [1] Momber, Andreas W., and Radovan Kovacevic. Principles of abrasive water jet machining. Springer Science & Business Media, 2012.
- [2] Aich, Ushasta, et al. "Multi-objective optimisation of abrasive water jet machining responses by simulated annealing and particle swarm." *International Journal of Mechatronics and Manufacturing Systems* 7.1 (2014): 38-59.
- [3] Mahajan, Gaurav. "A Study of Effect of Various Process Parameters on Abrasive Jet Machining Using Silicon Carbide as Abrasive Material." (2014).
- [4] Youssef, Helmi A. "Nontraditional Machining Processes—An Overview." *Machining of Stainless Steels and Super Alloys: Traditional and Nontraditional Techniques* (2016): 141-177.
- [5] Tomy, Anu, and Somashekhar S. Hiremath. "A Comprehensive Review on Abrasive Jet Machining." *International Conference on Advanced Material Technologies (ICAMT)*. Vol. 2016. No. 27th. 2016.
- [6] Mardi, K. Bimla, et al. "Surface integrity of Mg-based nanocomposite produced by Abrasive Water Jet Machining (AWJM)." *Materials and Manufacturing Processes* (2017): 1-8.
- [7] Dhanawade, Ajit, and Shailendra Kumar. "Experimental study of delamination and kerf geometry of carbon epoxy composite machined by abrasive water jet." *Journal of Composite Materials* (2017): 0021998316688950.
- [8] Yuvaraj, Natarajan, and Murugasen Pradeep Kumar. "Investigation of process parameters influence in abrasive water jet cutting of D2 steel." *Materials and Manufacturing Processes* 32.2 (2017): 151-161.
- [9] Çiçek, Adem, Turgay Kıvak, and Gürcan Samtaş. "Application of Taguchi method for surface roughness and roundness error in drilling of AISI 316 stainless steel." *Strojniški vestnik-Journal of Mechanical Engineering* 58.3 (2012): 165-174.
- [10] Pappas, M., Ntziantzias, I., Kechagias, J., & Vaxevanidis, N. M. (2011). Modeling of Abrasive Water Jet Machining using Taguchi Method and Artificial Neural Networks. In *IJCCI (NCTA)* (pp. 377-380).
- [11] Wang, J., Kuriyagawa, T., & Huang, C. Z. (2003). An experimental study to enhance the cutting performance in abrasive waterjet machining. *Machining Science and Technology*, 7(2), 191-207.

Machining of Inconel 718 Using by Taguchi Methodology with Abrasive Water Jet Machining Parameters

Fuat KARTAL*, Hasan GÖKKAYA+, Refik POLAT+
 # Mechanical Engineering Department,
 Kastamonu University, Turkey
 fkartal@kastamonu.edu.tr
 + Mechanical Engineering Department,
 Karabük University, Karabuk, Turkey,
 hgokkaya@karabuk.edu.tr University

Abstract— Inconel 718 is commonly sought after for its resistance to high temperature and corrosion, however, these characteristics reduce the machinability of this material which brings forth the AWJ machining, a non-conventional material removal process, as the ideal option. The use of Abrasive Waterjet (AWJ) machining for Inconel 718 offers desired machining characteristics, therefore, has a commercial significance. The objective of this study is to optimize input parameters of AWJ machining involved in AWJ machining of Inconel 718 using the Taguchi technique. Optimization of AWJ machining parameters was conducted based on the analysis of variance (ANOVA) and Signal-to-Noise (S/N) Ratio analysis in order to obtain effective Surface Roughness and Material Removal Rate. AWJ machining parameters such as abrasive flow rate, focusing tube size, traverse speed and water pressure were calculated for optimized Surface Roughness and Material Removal Rate. It was concluded that the optimal AWJ machining parameters found in this study are satisfactory for the actual/commercial machining of Inconel 718.

Keywords— Inconel 718, Abrasive Water jet, machining, full factorial design, Taguchi orthogonal array, Material Removal Rate, non-conventional Machining, Surface Roughness

I. INTRODUCTION

The development of super alloys began in 1930s in the USA and it gained momentum with the need for heat resistant materials increased as the jet engines are developed [1-3]. Nickel-based super alloys are being developed since 1930s and they are mainly used in aviation applications [1-3]. Inconel 718 (2.4668) or commonly referred to as the alloy 718 is one of the most commonly used nickel alloys. Inconel 718 consists of nickel, chromium and molybdenum [1-4]. With the chemical formula of NiCr19Fe19Nb5Mo3, this nickel alloy is extremely resistant against corrosion [1,2]. Possible to be hardened further with aging process, this material is able to preserve its mechanical properties even at a wide range of temperature [4-8]. This nickel alloy offers a very high tensile strength. Inconel 718 is also a material with very high breaking strength and fracture resistance [1-5]. Also able to resist high temperatures, this material will assume a stronger structure when it is hardened

with aging. It is commonly used in chemical plants and power plants in preheater tubes, boilers, methane correction fibers, electrical heater parts coating, collectors, furnace tubes and many food processing equipment. As it offers high resistance, it is not possible to machine this alloy using conventional methods [2-6]. Therefore, unconventional methods such as abrasive waterjet and laser machining are commonly used [4]. Laser machining is an economical method for cutting Inconel 718 plate up to 3mm thickness, while abrasive waterjet (AWJ) machining is often preferred for thicker materials [4-10]. Abrasive waterjet machining (AWJM) is preferred over laser machining with its ability to machine workpieces resulting in the smallest kerf width [7-10]. Many studies on the use of AWJ machining on engineering materials have explored the optimal material removal rate (MRR) and surface roughness (SR) using experimental design. Optimization of process parameters involved in the machining of Inconel did not receive a lot of academic interest [7-10].

In this study it is aimed to optimize the AWJM parameters for Inconel 718 alloy using Taguchi method. Nozzle traverse speed, abrasive flow rate and standoff distance are optimized for both MRR and SR.

II. MATERIALS & METHODS

The effects of parameters were investigated in this study, having Inconel 718 alloy of 6 mm thickness machined using AWJ. The main chemical composition of Inconel 718 material used in experiment is given in Table 1.

TABLE LXI
 CHEMICAL COMPOSITION OF INCONEL 718 ALLOY (WT%) [1-9].

C	Si	Mn	S	P	Cr	Ni	Mo	Nb	Ti	Al	Fe
0.024	0.06	0.02	0.02	0.03	18.84	53.64	3.08	5.23	0.95	0.53	17.62

Among the abrasive waterjet equipment used are high-pressure pump produced by KMT, Streamline SL-V 50 Plus, mounted on a CNC lathe and an abrasive feed system

connected to this pump (Fig. 1). Figure 2 shows the image from the machining of Inconel 718 alloy on the waterjet lathe.



Fig. 37 Waterjet equipment used in this study

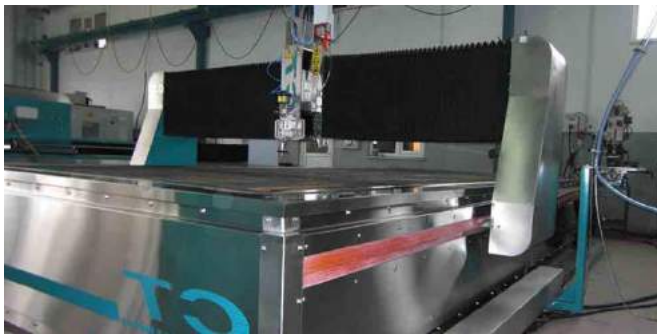


Fig. 2. Waterjet equipment used in this study

Garnet sand of 80 Mesh was used as the abrasive material. The nozzle used has an inner diameter of 0.35mm while the inner diameter of the focusing nozzle is 1.10mm. Taguchi experimental design was used. Nozzle traverse speed (mm/min), abrasive flow rate (g/min) and standoff distance (mm) were selected in this study to analyze the effects of AWJ machining parameters on MRR (g/min) and SR (μm) of Inconel 718. As shown in Table 2, selected process parameters were explored for three different levels.

TABLE LXIII
SELECTED PROCESS PARAMETERS AND THEIR LEVELS

Code	Machining Parameter	Level 1	level 2	Level 3
A	Traverse speed (mm /min)	120	220	320
B	Abrasive flow rate (g / min)	300	400	500
C	Standoff distance (mm)	2	3	4

As shown in Table 3, process parameters for each experiment were set at predefined levels in accordance with the Orthogonal Array.

TABLE LXIII
TAGUCHI L9 ORTHOGONAL ARRAY WITH MACHINING PARAMETERS

Ex p. No	Traverse speed (mm /min)	Abrasive flow rate (g / min)	Standoff distance (mm)
1	120	300	2
2	120	400	3
3	120	500	4
4	220	300	3
5	220	400	4
6	220	500	2
7	320	300	4
8	320	400	2
9	320	500	3

III. FINDINGS & DISCUSSION

Both surface roughness and material removal rate are important quality control parameters in the assessment of a production process. It was found that the surface being machined has a lower roughness where the waterjet enters and that the roughness increases gradually towards the waterjet outlet. The reason behind this is that the particles lose their kinetic energy as they move inwards which in return reduces their cutting capacity. The analysis of the experimental data of the selected material showed that the optimal selection for these three basic parameters is important in terms of the control of process outputs, i.e. MRR and SR. Effects of each one of these parameters are investigated, having taken the other parameters constant as shown in Table 2. Experimental observations for MRR (g/min) and Ra (μm) of the selected process parameters available in Table 3 are shown in Table 4.

TABLE LXIVV
EXPERIMENTAL OBSERVATION VALUES FOR MRR (G/MIN) AND RA (μM)

Exp no	Traverse speed (mm /min)	Abrasive flow rate (g / min)	Standoff distance (mm)	MRR (g/min)	Ra (μm)
1	120	300	2	6.65	3.27
2	120	400	3	6.66	3.19
3	120	500	4	6.87	3.07
4	220	300	3	6.34	3.49
5	220	400	4	6.42	3.46
6	220	500	2	6.44	3.39
7	320	300	4	5.92	3.79
8	320	400	2	5.97	3.59
9	320	500	3	6.22	3.51

This table shows the ANOVA and F-Test results for SR.

Effects of process parameters on the Material Removal Rate (MRR)

Table 5 shows the ANOVA and F-Test results for MRR. The effects of each process parameter on MRR are shown in Fig. 3 and Table 8. Nozzle traverse speed is found to have a

more significant effect on MRR (88.94%) when compared to the other parameters. According to Table 5 and Fig. 3, MRR is affected by three main parameters, namely, traverse speed, abrasive flow rate and standoff distance. MRR is found to be maximal at traverse speed level 1 (120 mm/min), abrasive flow rate level 3 (500 g/min) and standoff distance level 2 (3 mm). Thus, the optimal parameter selection for the MRR was found to be A1B3C2. Table 6 shows the MRR, S/N ratios, estimated MRR values and percentage differences.

9	6.2	6.18	0.7	15.88	15.8123	0.7
---	-----	------	-----	-------	---------	-----

First order regression equation obtained for MRR values using Table 6 in order to make estimations in a confidence level of 95% is given in Eq. (1). Regression coefficients of first order equation are shown in Table 7 for MRR. Regression coefficient of R2 97.39 was obtained.

$$MRR=6,658-0,003450*A+0,001033*B+0,0250*C \quad (1)$$

TABLE V
EXPERIMENTAL OBSERVATION VALUES FOR MRR (G/MIN) AND RA (µM)

Code	DF	Adj SS	Adj MS	F-Value	P-Value	% contr.
A	1	0.71415	0.71415	170.13	0	88.94
B	1	0.064067	0.064067	15.26	0.011	7.97
C	1	0.00375	0.00375	0.89	0.388	0.46
Error	5	0.020989	0.004198			2.61
Total	8	0.802956				100

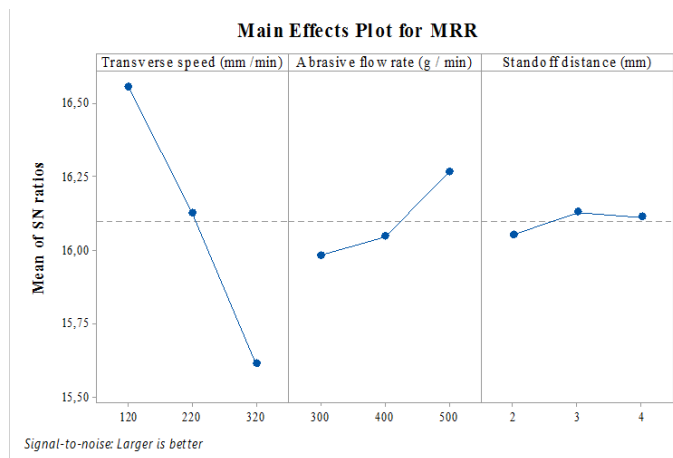


Fig. 3 The effect of control factors on MRR.

TABLE VI
MRR S/N RATIOS, ESTIMATED MRR VALUES AND PERCENTAGE DIFFERENCES.

Exp no	MR R	Estimated MRR	%	S/N Ratio MRR	Estimated S/N Ratio MRR	%
1	6.6	6.61	0.6	16.46	16.3929	0.6
2	6.6	6.71	0.7	16.47	16.5357	0.7
3	6.8	6.86	0.8	16.74	16.7364	0.8
4	6.3	6.33	0.9	16.04	16.0391	0.9
5	6.4	6.38	0.7	16.15	16.0872	0.7
6	6.4	6.49	0.7	16.18	16.2439	0.7
7	5.9	5.97	0.8	15.45	15.5127	0.8
8	5.9	5.96	0.9	15.52	15.5168	0.9

TABLE VII
REGRESSION COEFFICIENTS OF FIRST ORDER EQUATION FOR MRR.

Term	Coef	SE Coef	T-Value	P-Value
Constant	6.658	0.146	45.58	0
A	-0.00345	0.000265	-13.04	0
B	0.001033	0.000265	3.91	0.011
C)	0.025	0.0265	0.95	0.388

Effects of process parameters on the average surface roughness (Ra)

Fig. 4 shows the effects of each parameter on the surface roughness. According to Table 10 and Fig. 4, surface roughness is affected by three main parameters; traverse speed, abrasive flow rate and standoff distance. Ra is found to be minimal at traverse speed level 1 (120 mm/min), abrasive flow rate level 3 (500 g/min) and standoff distance level 2 (3 mm). Thus, the optimal parameter selection for the Ra was found to be A1B3C2. Table 9 shows the ANOVA and F-Test results for surface roughness. Table 9 shows that the traverse speed (81.30%) is the parameter with the most significant effect on Ra. Abrasive flow rate (14.78%) is the second most significant parameter. On the other hand, it was found that standoff distance has a lesser effect on Ra when compared to other process parameters. Table 6 shows the Ra, S/N ratios, estimated Ra values and percentage differences.

TABLE IX
ANOVA AND F-TEST FOR RA.

Source	DF	Adj SS	Adj MS	F-Value	P-Value	% Contr.
A	1	0.308267	0.308267	110.05	0	81.30
B	1	0.056067	0.056067	20.02	0.007	14.78
C	1	0.000817	0.000817	0.29	0.612	0.21
Error	5	0.014006	0.002801			3.69
Total	8	0.379156				100

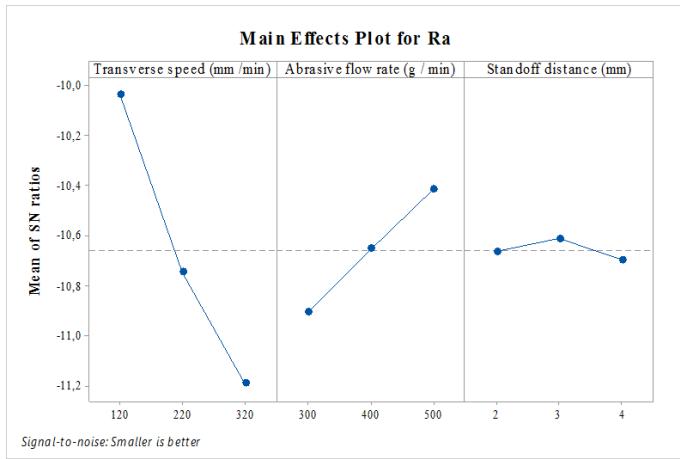


Fig. 4 The effect of control factors on Ra.

TABLE X

Ra (µm)	Estimated Ra	%	S/N Ratio Ra	Estimated S/N Ratio Ra	%
3.27	3.27	0.1	-10.2910	-10.2906	0.0
3.19	3.15	1.2	-10.0758	-9.9841	0.9
3.07	3.10	1.1	-9.7428	-9.8349	0.9
3.49	3.52	1.0	-10.8565	-10.9486	0.8
3.46	3.46	0.1	-10.7815	-10.7811	0.0
3.39	3.35	1.1	-10.6040	-10.5123	0.9
3.79	3.75	1.0	-11.5728	-11.4811	0.8
3.59	3.62	1.0	-11.1019	-11.194	0.8
3.51	3.51	0.1	-10.9061	-10.9058	0.0

First order regression equation obtained for Ra values in order to make estimations in a confidence level of 95% is given in Eq. (2). Regression coefficients of first order equation are shown in Table 11 for Ra. Regression coefficient of R2 96.43 was obtained.

$$Ra(\mu m) = 3,271 + 0,002267 * A - 0,000967 * B + 0,0117 * C \quad (2)$$

TABLE XI
REGRESSION COEFFICIENTS OF FIRST ORDER EQUATION FOR RA.

Term	Coef	SE Coef	T-Value	P-Value
Constant	3.271	0.119	27.41	0
Traverse speed (mm /min)	0.002267	0.000216	10.49	0
Abrasive flow rate (g / min)	-0.00097	0.000216	-4.47	0.007
Standoff distance (mm)	0.0117	0.0216	0.54	0.612

Confirmation Tests

Subsequently, a confirmation test is carried out to confirm that the best parameters are acquired from the study design. These confirmation tests were used to machine Inconel 718. Estimated process combination for MRR and Ra are A1B3C2 and A1B3C2, respectively. Optimal response values are MRR, 6.86 g/min and SR, 3.10µm.

IV. RESULTS

The optimization of processing parameters of abrasive waterjet machining of Inconel 718 is presented, having taken MRR and SR as outputs in this study. The findings obtained at the end of the machining of Inconel alloy 718 are briefly as follows;

As seen in ANOVA and F-Test, traverse speed is very important in terms of its effect on MRR by 88.90%. Abrasive flow rate follows by 7%. It was found that the effect of standoff distance on MRR is statistically insignificant.

Confirmation tests were conducted using the optimal combinations obtained for the process parameters in Taguchi analysis. The parameter combination recommended for optimal MRR is A1B3C2 and optimal output value of MRR is 6.86g/min. Considering the effects of these factors on Ra, traverse speed plays an important role by 81.30%. On the other hand, abrasive flow rate has a significant effect on Ra by 14.70%. Confirmation tests were conducted on Ra using the A1B3C2 combination obtained from Taguchi analysis. The optimal output value for Ra is 3,10 µm. These results offer a great deal of information for the selection of important parameters in abrasive waterjet machining of Inconel 718 in terms of outputs such as MRR and SR.

ACKNOWLEDGEMENTS

The authors would like to thank CT Cutting Technologies based in Istanbul, Turkey.

REFERENCES

- [1] Wang, Z., Zhou, D., Deng, Q., Chen, G., & Xie, W. The Microstructure and Mechanical Properties of Inconel 718 Fine Grain Ring Forging. *Superalloy 718 and Derivatives*, 343-349.
- [2] Courbon, C., Et Al. "Investigation Of Machining Performance In High Pressure Jet Assisted Turning Of Inconel 718: A Numerical Model." *Journal Of Materials Processing Technology* 211.11 (2011): 1834-1851.
- [3] Rahman, M., W. K. H. Seah, And T. T. Teo. "The Machinability of Inconel 718." *Journal Of Materials Processing Technology* 63.1-3 (1997): 199-204.
- [4] Reddy, D. Sidda, A. Seshu Kumar, and M. Sreenivasa Rao. "Parametric optimization of abrasive water jet machining of Inconel 800H using Taguchi methodology." *Universal Journal of Mechanical Engineering* 2.5 (2014): 158-162.
- [5] Escobar-Palafox, G. A., R. S. Gault, and K. Ridgway. "Characterisation of Abrasive Water-Jet Process for Pocket Milling In Inconel 718." *Procedia Cirp* 1 (2012): 404-408.
- [6] Ay, Mustafa, Ulaş Çaydaş, and Ahmet Haşçalık. "Optimization of Micro-Edm Drilling Of Inconel 718 Superalloy." *The International Journal of Advanced Manufacturing Technology* 66.5-8 (2013): 1015-1023.

- [7] Hashish, Mohamed. "Pressure effects in abrasive-waterjet(AWJ) machining." ASME, Transactions, Journal of Engineering Materials and Technology 111 (1989): 221-228.
- [8] Ay, Mustafa, Ulaş Çaydaş, and Ahmet Hascalik. "Effect Of Traverse Speed On Abrasive Waterjet Machining Of Age Hardened Inconel 718 Nickel-Based Superalloy." Materials and Manufacturing Processes 25.10 (2010): 1160-1165.
- [9] Ay, Mustafa, Ulaş Çaydaş, and Ahmet Hascalik. "Effect Of Traverse Speed On Abrasive Waterjet Machining Of Age Hardened Inconel 718 Nickel-Based Superalloy." Materials and Manufacturing Processes 25.10 (2010): 1160-1165.
- [10] Uçun, İrfan, Kubilay Aslantaş, and Fevzi Bedir. "Inconel 718 Süper Alaşımının İşlenmesinde Kaplanmış Mikro Takımların Aşınma Davranışları Ve Performans Analizi." Makine Teknolojileri Elektronik Dergisi 7.4 (2010): 47-55.

The Limitations for Plane-Strain Fracture Toughness Test of Steel Compact Tension Specimens

Sedat İRİÇİ¹, Oğuzhan DEMİR², Ali Osman AYDINI

1.Sakarya University, TURKEY

siric@sakarya.edu.tr

2.Bilecik Şeyh Edebali University

ABSTRACT

Plane-strain fracture toughness test method enables the determination of the plane-strain fracture toughness (K_{Ic}) of metallic materials by tests using a variety of pre-cracked specimens, bend, compact tension, arc-shaped, disk-shaped specimen, etc. Compact tension (CT) specimen is one of the most common type used in the literature and a standard specimen in accordance with ASTM standard test method for linear-elastic plane-strain fracture toughness, K_{Ic} , of metallic materials (E399-12). In this study, experimental fatigue pre-cracking and fracture toughness tests are performed for CT specimens made of AISI 1040 carbon steel and machined from rolled plates in the L-T rolling direction (crack plane is perpendicular to the rolling direction). Test conditions are determined as indicated in the ASTM standard and details of the experimental setup are described. Having performed experimental analyses, applicability of plane-strain fracture toughness tests to compact tension specimen of AISI 1040 steel is investigated.

Keywords- Plain-Strain Fracture, Fracture test of steel, minimum thickness calculation

Effect of Forging and Heat Treatment on Microstructure and Mechanical Properties of SAE 4140 Steel

Ahmet Asım Eser¹, Mehmet Ali Güvenç¹, Seracettin Akdı¹, Mustafa Acarer²

¹AYD Company, Aydınlar Yedek Parça Sanayi ve Ticaret A.Ş.
Konya Organize Sanayi Bölgesi İhsandede Cad. No:7 Selçuklu/Konya/Turkey
{akdi.seracettin, eser.ahmetasim, guvenc.mehmetali}@aydtr.com

²Selcuk University Technology Faculty Metallurgy and Material Engineering
Konya/Turkey
macarer@selcuk.edu.tr

Abstract— SAE 4140 steel or 42CrMo4 is widely used in automotive industry (parts of steering wheel, parts of suspension, etc.) as forged parts due to its high strength, different fatigue behaviors, and good machinability properties. In this study, the effect of post-forging heat treatment process was examined. Different heat treatment routes were applied to 4140 steel, following hot forging. Microstructure and mechanical properties including fatigue strength were determined. Microstructures of the forged changed regard as cooling rate and martensitic and martensitic/bainitic structures were observed. While the sample forged and then quenched in air has shown the highest tensile strength and fatigue cycle, optimum properties were obtained with the sample as forged-quenched in air-tempered, and forged-austenitizing-quenched-tempered conditions.

Keywords— Steel, heat treatment, quenching, tempering, SAE 4140

I. INTRODUCTION

Today, heat treatments applied to steel have gradually become important due to common usage of steels along with developing technology and accordingly for improving mechanical and microstructural properties.

SAE 4140 or 42CrMo4 is the low alloy steel type which is commonly used in automotive industry (parts of steering wheel, parts of suspension, etc.), forged parts, bolted mounting, welded parts, and in other applications as quenched-tempered condition. The dominant phase in the steels is tempered martensite after quenched and tempered condition. Due to the microstructure and mechanical properties of 4140 steel depending on quenching and tempering, numerous methods were developed to apply for the steels. These are direct quenching and reheating quenching [1]. SAE 4140 is steel with high strength, different fatigue behaviors, and good workability properties. Even though there are numerous studies [1-5] on SAE 4140, especially its fatigue behavior has still been examined [6-9]. It has been a research study lasting until today to improve fatigue strength in order to increase mechanical performance of SAE 4140 alloy. The microstructure that characterizes forged parts depends on material quality, forging and heat-treatment parameters [10]. In recent years, there is an increased interests for using direct cooled microalloyed forging

steel in place of quenched and tempered steels. In comparison to conventionally processed quenched-and-tempered steels, direct-cooled microalloy steels offer the potential for significant cost savings [11].

In this study, the effect of post-forging heat treatment on microstructure and fatigue strength of 4140 steel was examined.

II. EXPERIMENTAL STUDIES

Table 1 shows chemical composition of SAE 4140 steel used in this study. Chemical composition was determined in Spectromaxx Optical Emission Spectroscopy Unit.

Table 1. Chemical composition of SAE 4140 steel

C	0.38-0.43
Si	0.15-0.35
Mn	0.75- 1
≤ P	0.03
≤ S	0.04
Cr	0.8-1.1
Mo	0.15-0.25
Ni	≤ 0.25
Cu	≤ 0.35
Fe	Balance

After choosing profile with diameter appropriate for part to be formed via hot forging, it was cut in proper length. Following completion of the cutting process, samples heated at about 1100°C by being placed into induction heating system for forming were firstly subjected to the performing process in rolling machine and then press forging process was applied as shown in Figure 1.

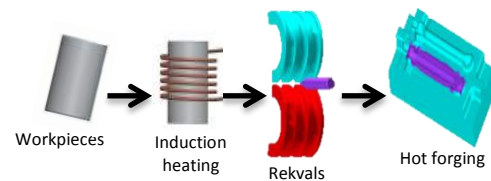


Fig 1. Hot forging process

Four different processes applied respectively are listed as forging (F) (Figure 2.a), forging and oil cooling (F+O) (Figure 2.b), forging and oil cooling and tempering (F+Q+T) (Figure 2.c), and tempering after forging and oil cooling (T+F+O) (Figure 2.d). The processes are also presented in Figure 2.

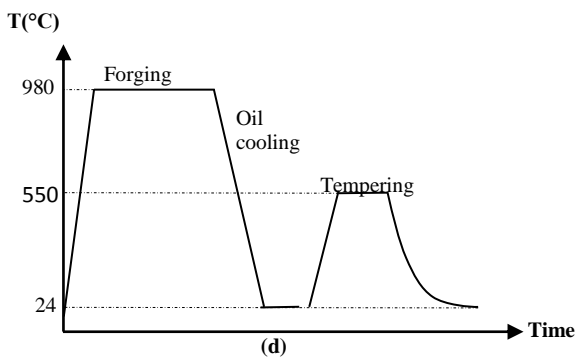
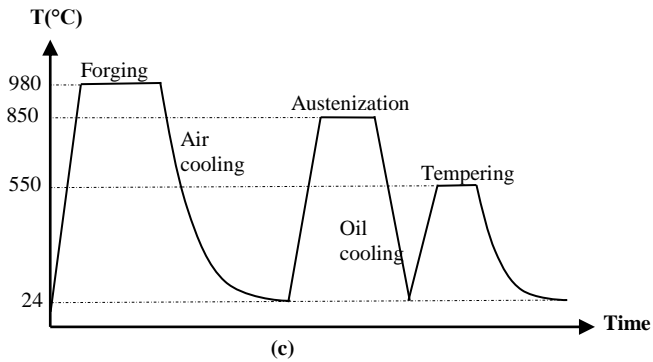
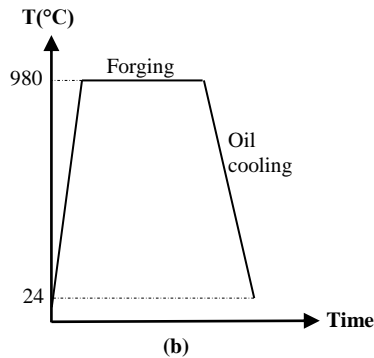
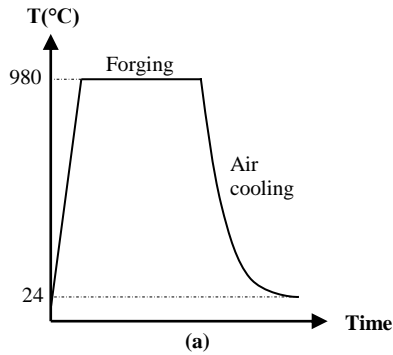


Fig 2. (a) Forging, (b) forging + oil cooling, (c) forging + quenching + tempering, (d) tempering after forging + oil cooling

Microstructural and mechanical properties of the samples were characterized after forging and heat treatment process. For microstructural examinations, the samples were prepared by using standard metallography techniques and etched with nital. Microstructural images were obtained from NIKON MA 200 Optical Microscope. Hardness measurements were performed with Innovatest Vickers Hardness device by applying 1 kg loading for 10 seconds. Tensile test was performed in 1mm/min speed in ALŞA tensile-compression test machine at room temperature in accordance with ASTM E8 standard. Elongation values were measured by using extensometer with 30 mm of measuring distance that was attached to tensile sample. 0.2% stress was taken as yield stress. Axial fatigue test was performed in order to examine fatigue behavior. For this test, samples were prepared in accordance with ASTM E466 standard. Test was performed in MTS Landmark fatigue test device, under 12 kN load and at 30 Hz.

III. RESULTS AND DISCUSSION

Figure 3 shows microstructures of 4140 steel as forged, forged and quenched in oil, forged and tempered, and forged and quenched in oil followed by tempering conditions.



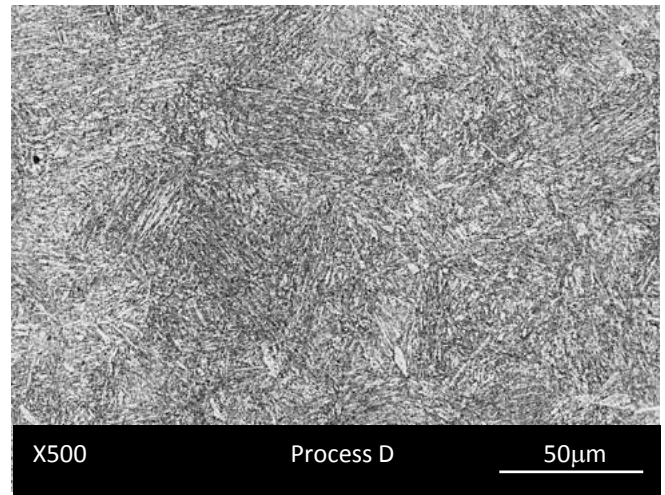
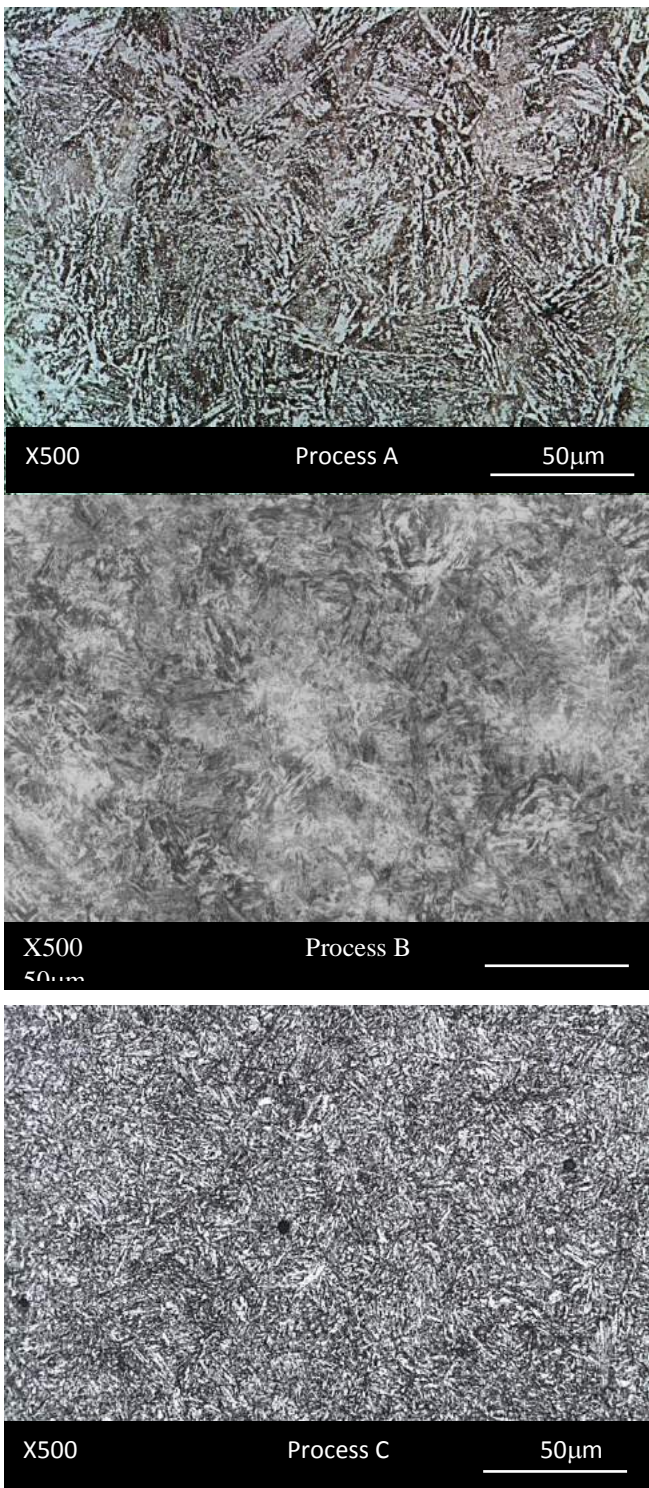


Fig 3. Microstructures of 4140 steel

In Figure 3 b, it can be seen that the microstructures of 4140 steel in case of both Process A and Process B are martensite. These microstructures are agreement with CCT diagram of the steel and literature [2, 3]. However, the samples following Process C and Process D have tempered martensitic and/or bainitic structure. In literature [1, 4] it was reported that same structures were obtained after tempering heat treatment. Hardness of 4140 steel as received, forged and following heat treatment conditions are given in Table 2. While hardness of the samples as forged and quenched in oil (Process B) condition is 63 HRC, hardness values obtained at the end of the other processes (Process A, C and D) are similar, 28-34 HRC. Also, any considerable difference between hardness of the samples forged then cooled in air (Process A) and forged then the heat treated (Process C and D) conditions was not observed. Altaweel and Tolouei-Rad [2] reported that hardness' of 4140 steel quenched in water and in air are 59 HRC and 33 HRC respectively. A.D. da Silva et al. [3] observed that hardness of 4140 steel after oil quenching process is 54-55 HRC. Also the microstructure images in which martensite and tempered martensite structure shown are confirmed by hardness values.

Table 2. Hardness' of 4140 steel as Process A, B, C and D

Process	Hardness (HRC)
Forging (Process A)	28-30
Forging and Oil Cooling (Process B)	62-63
Forging+Quenching+Tempering (Process C)	32-34
Forging+Oil cooling+Tempering (Process D)	28-32

In Table 3, tensile test results and charpy impact energy of the 4140 steel after forging and heat treating process can be seen. While the tensile strength of the samples Process C is the highest, it has the lowest elongation and impact energy values. Process C and Process D have the best tensile properties as well charpy impact energy. Tensile properties and impact energy values are agree with the microstructure as well hardness. The mechanical test results agree with literature [1]. Fatigue cycles

of the samples are shown in Table 3 in which the sample as Process B condition presents the highest fatigue cycle.

Table 3. Tensile test, fatigue test and charpy impact energy test results

Process	Fatigue cycle (N) at 12 kN	Impact energy (J)	Yield strength (MPa)
Process A	6.560	32	705
Process B	5.000.000	13	2000
Process C	83.500	103	1078
Process D	50.000	84	1020
Process	Tensile strength (MPa)	Elongation (%)	Sertlik (HRC)
Process A	860	15.33	28-30
Process B	2074	5	62-63
Process C	1172	20	32-34
Process D	1137	16	28-32

IV. CONCLUSIONS

From the present work it can be concluded that;

1. Forging and Oil Cooling (Process B) shows highest hardness, tensile strength and fatigue cycle.
2. Forging+Quenching+Tempering (Process C) has optimum properties comparing to other process.

ACKNOWLEDGEMENT

It is a pleasure to thank Ms Gamze Kucukyagliglu and Mr Ahmet Can Yasar from AYD for their help with the experimental part of the work.

REFERENCES

- [1] A.H. Meysami, R. Ghasemzadeh *, S.H. Seyedein, M.R. Aboutalebi , An investigation on the microstructure and mechanical properties of direct-quenched and tempered AISI 4140 steel, *Materials and Design* 31 (2010) 1570–1575
- [2] Ali RafaAltawe , Majid Tolouei-Rad, EFFECT OF QUENCHING MEDIA, SPECIMEN SIZE AND SHAPE ON THE HARDENABILITY OF AISI 4140 STEEL, *Emirates Journal for Engineering Research*, 19 (2), 33-39 (2014).
- [3] A.D. da Silva, T.A. Pedrosa, J.L. Gonzalez-Mendez, X. Jiang, P.R. Cetlin, T. Altan, Distortion in quenching an AISI 4140 C-ring – Predictions and experiments, *Materials and Design* 42 (2012) 55–61
- [4] A. Kamyabi-Gol, S.J. Clark, J.W. Gibbs, S. Sridhar, P.F. Mendez, Quantification of evolution of multiple simultaneous phase

- transformations using dilation curve analysis (DCA), *Acta Materialia* 102 (2016) 231-240
- [5] Nicholas E. Nanninga, Effect of microstructure and alloying elements on the resistance of fastener grade steels to hydrogen assisted cracking, Master's Thesis, Michigan Technological University, 2005.
- [6] M. Klein, P. Starke, D. Eifler, Manufacturing influences on the fatigue properties of quenched and tempered SAE 4140 specimens, *Procedia Engineering* 10 (2011) 1184–1189 .
- [7] F. Klocke, S. Schneider, L. Ehle, H. Meyer, L. Hensgen, A. Klink, Investigations on Surface Integrity of Heat Treated 42CrMo4 (AISI 4140) Processed by Sinking EDM, *Procedia CIRP* 42 (2016) 580 – 585
- [8] H. Kovacı, A.F. Yetim, Ö. Baran, A. Çelik, Fatigue crack growth behavior of DLC coated AISI 4140 steel under constant and variable amplitude loading conditions, *Surface and Coatings Technology*, Volume 304, 25 October 2016, Pages 316-324
- [9] H. Kovacı, A.F. Yetim, Ö. Baran, A. Çelik, Fatigue crack growth analysis of plasma nitrided AISI 4140 low-alloy steel: Part 2-Variable amplitude loading and load interactions, *Materials Science and Engineering: A*, Volume 672, 30 August 2016, Pages 265-275.S. M. Metev and V. P. Veiko, *Laser Assisted Microtechnology*, 2nd ed., R. M. Osgood, Jr., Ed. Berlin, Germany: Springer-Verlag, 1998.
- [10] A.H. Meysami, R. Ghasemzadeh S.H. Seyedein, M.R. Aboutalebi , An investigation on the microstructure and mechanical properties of direct-quenched and tempered AISI 4140 steel, *Materials and Design* 31 (2010) 1570–1575
- [11] D.K. Matlock, G. Krauss, J.G. Speer, Microstructures and properties of direct-cooled microalloy forging steels, *Journal of Materials Processing Technology* 117 □2001) 324±328

Calculation Of (hkl) Plane Energy Of bcc and bct Iron Using Analytical Method

Hamza Yaşar OCAK1, Gökay UĞUR2, Şule UĞUR2

1. Dumlupınar University, TURKEY.

2. Gazi University, TURKEY

hyasar.ocak@dpu.edu.tr

ABSTRACT

In this study, the (hkl) plane energies of bcc and bct Fe crystals were calculated as a function of internal interactions between atoms. The Classical Morse Potential Function applied in the theoretical studies of transition elements was used in Fortran code for analytical calculations. Since the force applied to the crystal at the equilibrium has bcc \rightarrow bct conversion, we calculated the variations of the a2 lattice parameter depending on the a1 lattice parameter. The (hkl) plane energies of bcc and bct crystals were determined using calculated lattice parameters. Calculations are limited to 9 (hkl) planes. For the bcc Fe (h00) planes, the internal energy passed through the minimum points, while the energy in the (hk0) and (hkl) planes changed parabolically. In the case of bct, no stability point was determined on any plane. Theoretical calculations show that the total energy is the nearest plane energy of the incoming feeds. In bcc \rightarrow bct phase transformation, the system has a single equilibrium point and the stability range is not very large. This calculation method can be successfully applied to cubic Fe and Fe-based alloys in the theoretical studies.

Keywords: (hkl) Planes, bcc and bct, equilibrium, stability

Microstructure Characterization and Mechanical Properties of 9Cr-1.2W Weld Metal

Fikret KABAKCI¹, Mustafa ACARER², Selcuk KESKINKILIC³ Filiz KUMDALI ACAR³ İsmail Hakkı KARA⁴

¹Bulent Ecevit University
Alapli Vocational School- Zonguldak, Turkey
fikret.kabakci@beun.edu.tr

²Selcuk University
Faculty of Technology- Konya, Turkey
macarer@selcuk.edu.tr

³Gedik Welding Company-Istanbul, Turkey
skeskinkilic@gedik.com.tr-facar@gedik.com.tr

⁴Karabuk University
Faculty of Engineering – Karabuk, Turkey
ihakkikara@karabuk.edu.tr

Abstract

High CrMo (W) steel is widely used in ultra-super critical (USC) power plant applications operation temperature up to 620 °C. The steels and their weld metal are used for tempered condition. Tempering temperature must be below A_{c1} temperature of the weld metal. Welding of the steel is generally applied by shielded metal arc welding (SMAW) with multi-pass process. In this study, stick electrodes were fabricated for high chromium tungsten steel in Gedik Welding Company. Microstructure and mechanical properties of the all weld metal produced by the stick electrodes were investigated following tempering at 760 °C for 4h. Microstructure was characterized by optical microscope (OM) and scanning electron microscope (SEM) with energy dispersive X-ray spectroscopy (EDS). Differential scanning calorimetry (DSC) analyze was used to determine transformation temperature of the weld metal. Hardness measurement, tensile test and charpy impact test were carried out. Fracture surfaces of the samples were also investigated via SEM.

Keywords— 9Cr weld metal, Fracture surface weld metal, Hardness map, Toughness of 9Cr Steels, delta ferrite.

I. INTRODUCTION

In power plant industries, the need to improve efficiency has led to develop the new materials which have good oxidation resistance, better mechanical properties at high temperature, better toughness properties, creep resistance[1, 2]. High chromium steels are widely used in the power plant industry due to having high creep strength and oxidation resistance. It is desirable to use high chromium ferritic steels because these steels have good thermal conductivity and lower thermal expansion coefficient compared to austenitic stainless steels [3-5]. T/P91 steel includes 9%Cr and 1%Mo and small amount of microalloying elements such as Nb and V, whereas T/P 92

steel contains 9%Cr and 0.5%Mo and 1.5-2%W, Nb, V and %0.001-0.006 B [6]. Both of T/P91 and T/P92 steels used normalized and tempered condition. These steels have martensitic microstructure under air cooling after normalized heat treating besides includes equiaxed ferritic grain too slow cooling. In this study, microstructure and mechanical properties of 9Cr-1,2W steel weld metal were investigated.

II. EXPERIMENTAL

Shielded metal arc welding (SMAW) was used to produce all weld metal deposit. Stick electrodes were fabricated by Gedik Welding Company in Turkey. Welding parameters used to obtain weld deposit can be seen in Table 65. Rigaku ZSX Primus II X-ray fluorescence (XRF) instrument used for identification of chemical composition of weld metal. Table 65 shows multi-pass welding condition. Fig. 38 shows weld plate configuration.

Table 65 Welding conditions

Diameter of covered electrode	3.20 (mm)
Welding current	~130 (A)
Welding voltage	~32 (V)
Welding speed	~125mm/min
Pass number	25
Preheat and interpass temperature	200-315 (°C)
Welding position	Flat
Heat input	~2.05 (kJ/mm)

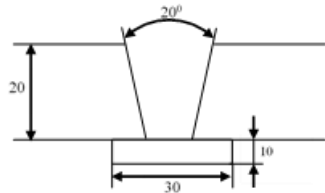


Fig. 38 Welding plate configuration

Post weld heat treatment (PWHT) was applied at 760 °C for 2, 4, 6 and 8h. to prevent crack formation (Fig. 39). Nikon MA 100 eclipse optical microscope and Zeiss EVO LS10 model Scanning Electron Microscope used for microstructural and fracture surface examination. Conventional metallographic preparation grinding and polishing up to 1µm used to weld metal. Weld metal cross section after metallographic preparation etched with picric HCl (2,5gr picric acid + 2,5ml HCl+100ml Ethanol) [7]. Also Mettler Toledo TGA/DSC 2 instrument was used to identify the transformation temperature. Tensile properties of weld metal were measured with Mohr Federhat instrument. Charpy impact to determine absorbed energy was carried out at 20 °C accordance with AWS 5.5. Hardness of weld metal, as welded and after PWHT 4h condition was identified by Qness automatic micro hardness tester applied to 2 kg load.

P	0.01
S	0.01
W	1.17
Nb	0.03
V	0.16
Cr_{Eq} (Eq. I)	10.92

$$Cr_{Eq} = (\%Cr) + 6(\%Si) + 4(\%Mo) + 11(\%V) + 5(\%Nb) + 1.5(\%W) + 8(\%Ti) + 12(\%Al) - 4(\%Ni) - 2(\%Co) - 2(\%Mn) - (\%Cu) - 40(\%C) - 30(\%N) \dots \dots \dots \text{Eq. I [8].}$$

In order to prevent the formation of fresh martensite after heat treating following welding, PWHT should be below A_{c1} transformation temperature. Fig. 40 shows DSC/TGA curve of weld metal. Transformation temperature A_{c1} is higher than 760 °C used as PWHT in this study.

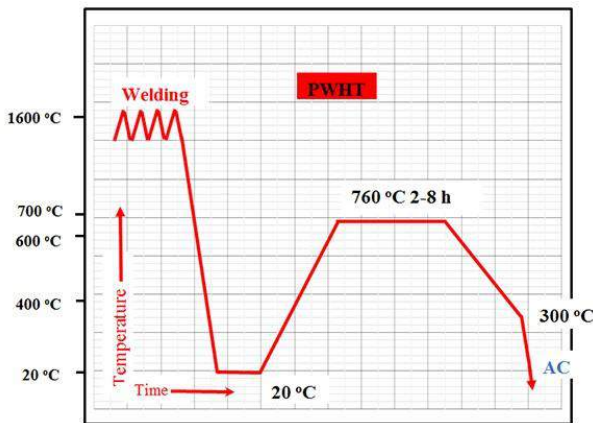


Fig. 39 PWHT cycle of Produced weld metal

III. RESULTS AND DISCUSSION

Chemical composition of weld metal is given in Table 66. For the chemical composition, Cr_{Eq} was calculated according to Eq.I calculated.

Table 66 Chemical composition of weld metal

Elements	(wt.%)
C	0.06
Si	0.18
Mn	0.81
Mo	0.58
Cr	9.20
Ni	0.33

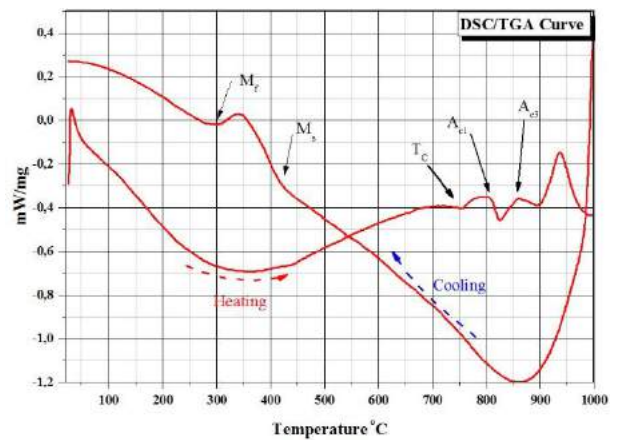


Fig. 40 DSC/TGA curve of weld metal (20 °C/min-43,22mg).

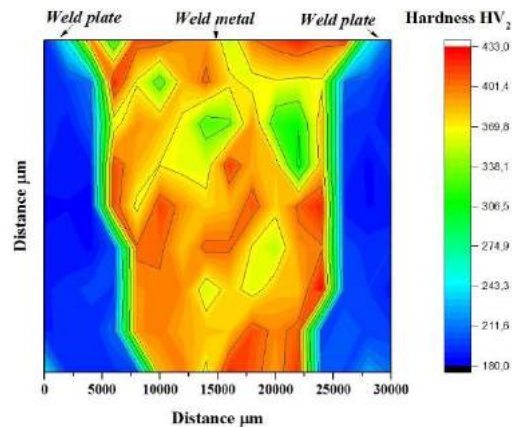


Fig. 41 Hardness map of weld metal as welded condition

There are inhomogeneity microstructures in a multi-pass welding. Since sample thickness was 25 mm, the weld metal was produced with 25pass by shielded metal arc welding (SMAW) in this study. Therefore, all weld metal (WM)has

different regions such as coarse grain (CG) and fine grain (FG) structures. In multi-pass welding, there are primary weld metal and weld metal reheated to various temperature by subsequent beads. The reheated regions can be termed as weld metal heat effected zone (WMHAZ), and it can be divided to a coarse grain zone and fine grain zone [9-11]. The variation of micro-structure constituents in WM and WMHAZ (coarse grain and fine grain zone) and localized hardness changes may play a significant role [12]. Therefore, in this paper, hardness maps were figured out throughout the WM and WMHAZ regions as seen in Fig. 41 and Fig. 42. Hardness of the weld metal changes from 270 HV to 433 HV as welded condition. However, it was not observed any considerable variations in throughout the WM and WMHAZ regions as PWHT'ed condition.

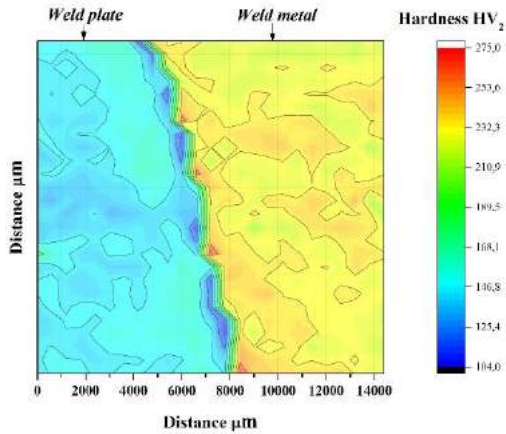
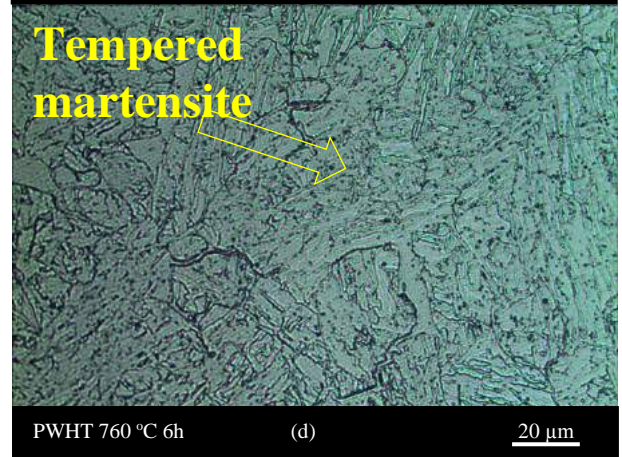
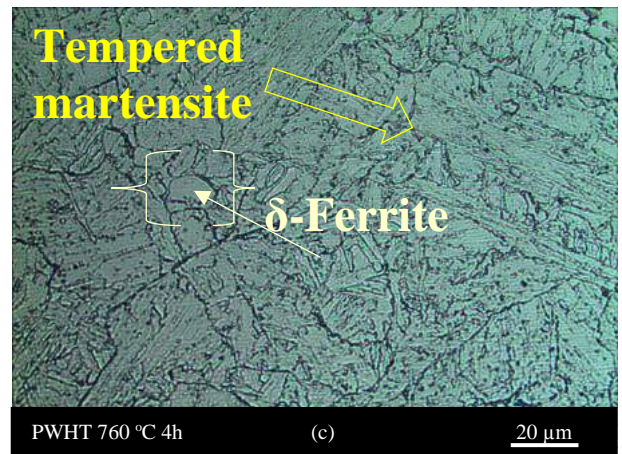
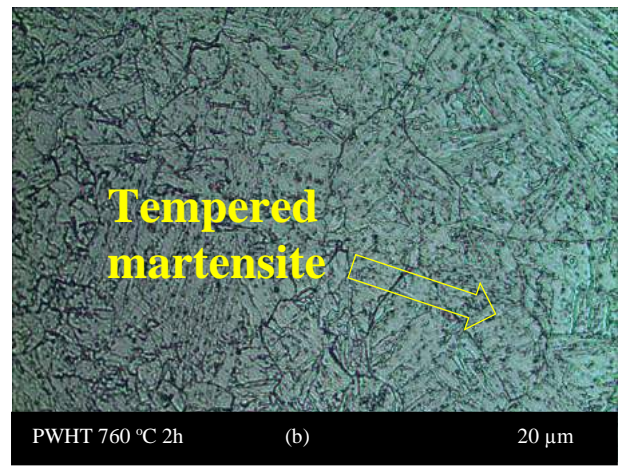
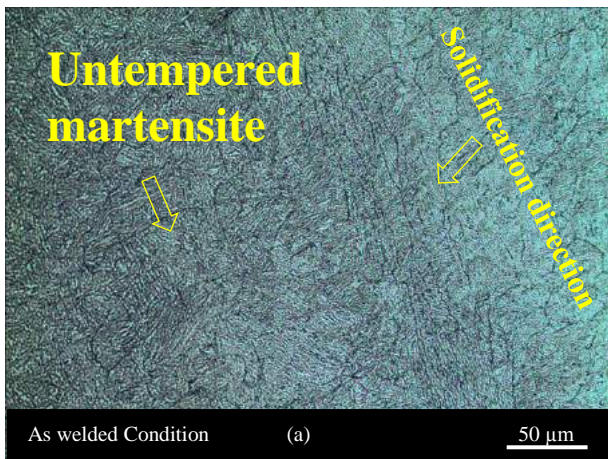


Fig. 42 Hardness map of weld metal (760 °C 4h PWHT)



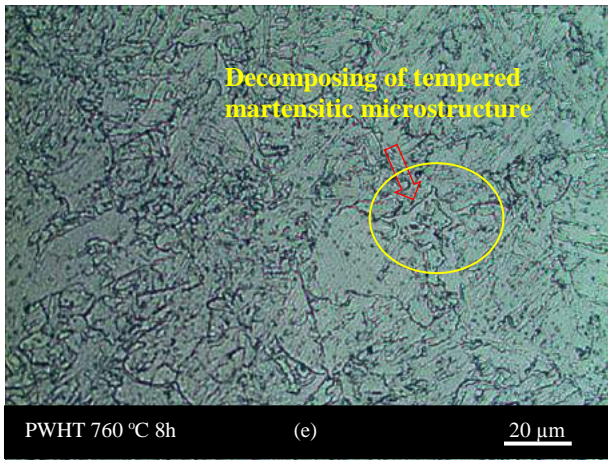


Fig. 43 Microstructures of weld metal

Microstructural observation of weld metal includes all heat treatment conditions have little delta ferrite phase and tempered martensite showed on Fig. 43 (a-e). Also tempered martensitic phase and delta ferrite phase includes small amount of oxide inclusions which detrimental effect to toughness properties of weld metal. Also delta ferrite formation on 9Cr steels and weld metal deteriorate toughness properties and creep resistance [13-15].

In Table 67 and Fig. 44, tensile test and charpy impact test results are given respectively. Elongation of weld metal was observed as 15,7 %. Yield and tensile strength of the samples subjected to PWHT at 760 °C for 4h are 450 MPa and 650 MPa respectively. According to charpy impact test results of the samples PWHT'ed at 760 °C for 4h the highest absorbed energy.

Table 67 Tensile test result 760 °C 4h heat treated weld metal.

Rp 0.2/MPa	Rm/MPa	Elongation (%)
533	694	15.7

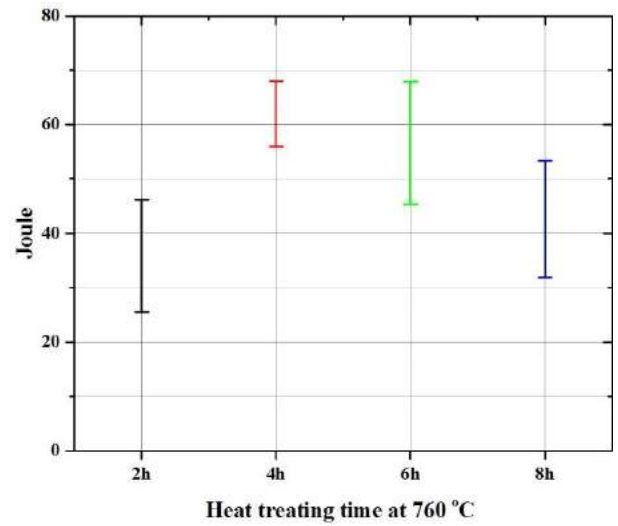


Fig. 44 Charpy impact toughness of weld metals different time at 760 °C.

In **Hata! Başvuru kaynağı bulunamadı**. Shows fracture surface of Charpy V impact test samples. The type of fracture is transgranular because of the fracture cracks pass through the grains in **Hata! Başvuru kaynağı bulunamadı**. for the sample empered at 760 °C for 4h. However, the fracture surface of the sample tempered at 760 °C for 4h has dimples evidence of ductile fracture.

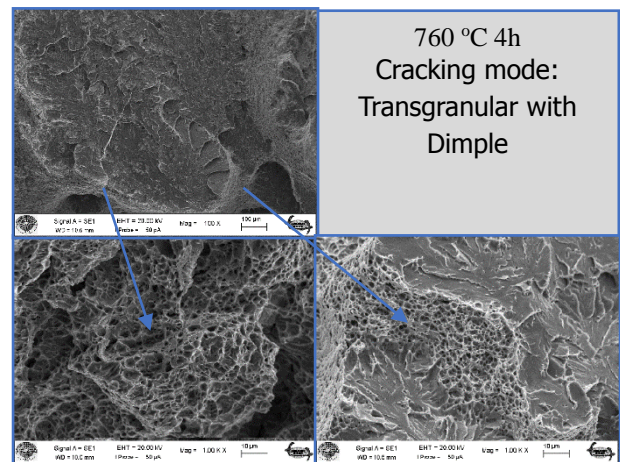


Fig. 45 Fracture surface of weld metal, PWHT at 760 °C for 4h

A few inclusions was observed in the microstructure of the weld samples. The inclusions are placed δ -ferrite grains inside (Fig. 46). The inclusions might be formed due to the fact that welding process was done at high relative humidity.

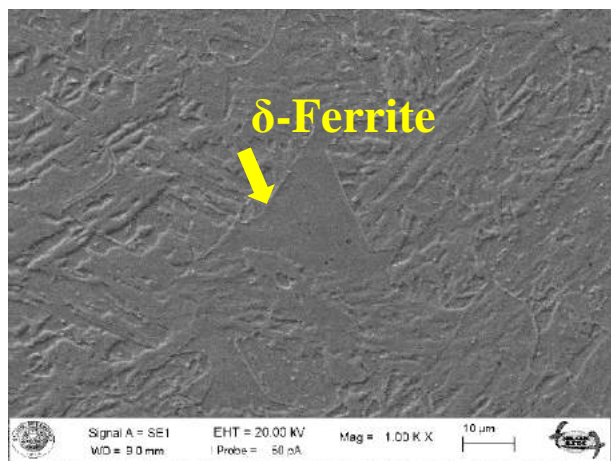


Fig. 46 SEM image of the weld metal PWHT'ed at 760 °C 8h

IV. CONCLUSIONS

Weld metal toughness was affected by PWHT time. Optimum toughness was obtained in the samples PWHT'ed at 760 °C for 4h.

The inclusions were detected which are deteriorating for the weld metal toughness and ductility. Also the inclusions are spheroidal shaped.

Inclusions are presents within δ -ferrite grains and tempered martensitic microstructure.

Samples PWHT'ed at 760 °C 4h have dimple and showed transgranular fracture mode. The dimples at the fracture surface of the weld metal by the reason of delta ferrite phase or deformation process at the test condition.

ACKNOWLEDGMENT

This study was carried out as a PhD thesis by Fikret KABAKCI in the Graduate School of Natural and Applied Science at the University of Selçuk, Konya, Turkey. This work also supported by Turkish Ministry of Science, Industry and Technology, SAN-TEZ Project under Grant Numbers 0374.STZ.2013-2

REFERENCES

- [1] R. Viswanathan, K. Coleman, and U. Rao, "Materials for ultra-supercritical coal-fired power plant boilers," *International Journal of Pressure Vessels and Piping*, vol. 83, no. 11, pp. 778-783, 2006.
- [2] B. Shanmugarajan, P. Sathiya, and G. Buvanashakaran, "Mechanical and metallurgical properties of autogenous laser welded P92 material," *Journal of Manufacturing Processes*, vol. 24, pp. 11-18, 2016.
- [3] B. Arivazhagan, S. Sundaresan, and M. Kamaraj, "A study on influence of shielding gas composition on toughness of flux-cored arc weld of modified 9Cr-1Mo (P91) steel," (in English), *Journal of Materials Processing Technology*, vol. 209, no. 12-13, pp. 5245-5253, Jul 1 2009.
- [4] R. Klueh, "Ferritic/martensitic steels for advanced nuclear reactors," *Transactions of the Indian Institute of Metals*, vol. 62, no. 2, pp. 81-87, 2009.
- [5] S. S. Wang, D. L. Peng, L. Chang, and X. D. Hui, "Enhanced mechanical properties induced by refined heat treatment for 9Cr-0.5Mo-1.8W martensitic heat resistant steel," *Materials & Design*, vol. 50, pp. 174-180, 2013.
- [6] A. A335/A335M, "Standard Specification for Seamless Ferritic Alloy-Steel Pipe for High-Temperature," no. C, pp. 1-13, 2011.
- [7] J. Oñoro, "Martensite microstructure of 9-12%Cr steels weld metals," *Journal of Materials Processing Technology*, vol. 180, no. 1-3, pp. 137-142, 2006.

- [8] P. Patriarca, S. Harkness, J. Duke, and L. Cooper, "US advanced materials development program for steam generators," *Nuclear Technology*, vol. 28, no. 3, pp. 516-536, 1976.
- [9] R. Paranhos, R. Rosenthal, and I. Bott, "Effect of charpy V notch position on impact toughness of all weld metal welds and its relevance with ASME codes," *Journal of pressure vessel technology*, vol. 128, no. 3, pp. 314-317, 2006.
- [10] Z. Zhou and S. Liu, "Influence of local brittle zone on the fracture toughness of high-strength low-alloyed multipass weld metals," *Acta Metallurgica Sinica*, no. 2, pp. 87-92, 1998.
- [11] H. Wang and K. M. Wu, "Investigation on Microstructures of Multipass Deposited Metal for 9Cr-1Mo Ferritic Steels," in *Materials Science Forum*, 2010, vol. 652, pp. 270-274: Trans Tech Publ.
- [12] H. Song, G. Evans, and S. Babu, "Effect of microstructural heterogeneities on scatter of toughness in multi-pass weld metal of C-Mn steels," *Science and Technology of Welding and Joining*, vol. 19, no. 5, pp. 376-384, 2014.
- [13] P. Mohyla and Z. Kubon, "Influence of delta ferrite on mechanical and creep properties of steel P92," presented at the 9.th Liege Conference: Materials for Advanced Power Engineering, 2010.
- [14] D. J. Abson, J. S. Rothwell, and P. Woollin, "The Influence of Ti, Al and Nb on the toughness and creep rupture strength of grade 92 steel weld metal," presented at the IOM3, London, 24-26 April, 2007.
- [15] J. Oñoro, "Weld metal microstructure analysis of 9-12% Cr steels," *International Journal of Pressure Vessels and Piping*, vol. 83, pp. 540-545, 2006.

The Flash Butt Welding Application and Inspection in Railway in Karabuk Train Station

Mustafa DURSUNLAR ^a and Harun ÇUĞ ^b

^a Karabük University, Faculty of Engineering, Railway Systems Engineering, e-mail: mustafadursunlar@gmail.com

^b Karabük University, Faculty of Engineering, Mechanical Engineering, e-mail: hcug@karabuk.edu.tr

ABSTRACT

Welding is made up of many scientific and technical works. In industrial applications, it is applied to increase work efficiency and safety, reduce size and weight, and reduce production cost. Welding in the railway is usually done at the joints of the rails. Rail junctions have caused serious problems since the early days of railroads. As a solution, durable algebras have been developed but not sufficient in this application. As a result, the request for removal of the rail joints has emerged. Accordingly, different welding techniques have been developed. Among these techniques, aluminothermite and combustion head are widely used today. In this study, ultrasonic inspection results of the incinerator application applied to the rails in Karabük train station are examined.

Key words: Railway, Rail welding, Flash Butt welding.

The Investigation of Mechanical Properties of DP 600 Cross Sheets Joint Using Resistance Spot Welding

Ibrahim SEVIM*, Burak Emre YAPANMIS*, Suleyman Cinar CAGAN*, Mustafa UGURLU*, Burhan BAYHAN*, Fatih HAYAT†

*Mechanical Engineering Department, Mersin University
Mersin, TURKEY

ibrahimsevim@mersin.edu.tr
burakemreyapanmis@mersin.edu.tr
cinarcagan@mersin.edu.tr
mustafaugurlu@mersin.edu.tr
burhanbayhan@mersin.edu.tr

†Metallurgical and Materials Engineering Department, Karabuk University
Karabuk, TURKEY
fhayat@karabuk.edu.tr

Abstract—In this study, mechanical properties of resistance spot welded cross shaped DP 600 galvanized automotive sheets is investigated. The specimens are joined by resistance spot welding at different weld currents and times. Welded specimens are examined for their mechanical properties. In addition, the hardness change of the heat effected zone is examined. Stress-strain graphs are drawn for different welding currents and for welding times of 10, 20, 40 cycles. As a result of this study, optimum welding parameters are determined for DP 600 steel.

Keywords— DP 600 steel sheet, resistance spot welding, mechanical properties, tensile strength, hardness test

I. INTRODUCTION

High-strength steels are widely used to increase the safety of passenger and decrease fuel consumption in automobile industry. Advanced high-strength steels (AHSS) are generally preferred due to their energy absorption during deformation.

High strength steels manufacturing involve non-traditional techniques by comparison with manufacturing of low strength steel. All high-strength steels are produced under controlled cooling; also coating and tempering processes are carried out.

DP steels are one of the steel developed as AHSS and it is intensively used in the iron-steel industry because of its lightweight, strength [1]. DP steels have included both ferrite and martensite composition. Fig. 1 shows the DP steel microstructure which is showing martensite in the ferrite. Martensite imparts rigidity while ferrite imparts ductility to the structure.

Hardenability and excellent elongation give DP steels much more tensile strength than conventional steels with the same yield strengths. Fig. 2 compares the stress-strain curves of High Strength Low Alloy (HSLA) and Dual Phase (DP) Steels at the same yield values [2].

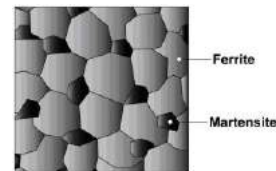


Fig. 1 DP steel microstructure

DP which is one of the AHSS has a hardening effect on the furnace compared to conventional steels. The effect of curing in the kiln is called the increase in the yield strength of the resultant high-temperature aging after prestressing. [3]

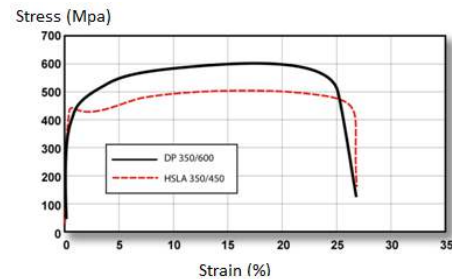


Fig. 2 Comparison of stress-strain curves of DP and HSLA steels

The cooling process carries out martensite phase owing to carbon, therefore, it contributes increasing the stiffness. Manganese, chromium, molybdenum, vanadium, phosphorus, silicon, and nickel also increase the hardenability when added alone or in combination. These attachments must carefully be added for equivalent mechanical strength and good spot welding ability [3].

The resistance spot welding (RSW) is one of the most common methods used to join steel sheets. The RSW is a welding method performed without the use of additional metal by means of pressure and welding current. The parts to be

welded are placed between two copper electrodes and a certain pressure is applied to ensure the passage of electric current. The basic components of a standard point resistance welding machine consist of a mechanical system used to apply loads to the copper electrodes, a transformer that reduces the voltage from the mains, current controllers in some machines, and a timer. In Fig. 3, the resistance spot welding machine is shown [4].

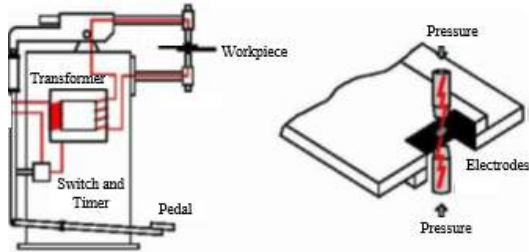


Fig. 3 Resistance spot welding machine

It has many superior features compared to other welding methods. These superior features; Fast, easy to use, suitable for automation, inexpensive method for duplicate production. Because of these superior features, the resistance spot welding method has become the primary method used to combine steel sheet parts in the automotive industry. Automotive bodies have included thousands resistance spot welding joints [5-7].

II. EXPERIMENTAL WORK

The main purpose of this study, determine optimum resistance spot welding parameters for DP 600 steel about time and current. Firstly, pieces which are combined were cut by guillotine appropriately for DIN EN ISO 14273. The surfaces of these parts, which are cut, are cleaned with ethyl alcohol. The work piece shape is cross and one piece of work piece dimension is 50x150mm. These two pieces were combined at the midpoints with the different welding parameters. These parameters are shown in Table I.

TABLE LXVIII
WELDING PARAMETERS OF SPOT WELDED DP 600CROSS SHEETS

	Welding Time	Welding Current
1	10	9
2	10	12
3	20	9
4	20	12
5	40	9
6	40	12

Tensile test and hardness test are performed to the DP 600 steels which are connected by different welding parameters.

XXX. Tensile test

The Tensile are a common standard test which is performed to determine important mechanical properties of engineering materials. A sample is exposed to uniaxial tensile forces until fractured in the tensile test. As a result of the tensile test, strength values such as the ratio limit of the material, the elastic

limit, the yield limit and the tensile strength, ductility values such as fracture length, fracture contraction and toughness are determined.

The tensile test is applied under 100 kN Alsa brand test machine. Every welding parameter is tested 3 times for repeatability. Tensile test machine photography is shown in Fig. 4.



Fig. 4 Tensile test machine

A special apparatus is designed and created by us to hold test sample in tensile test. The test samples easily are connected to tensile machine owing to this apparatus. Stress-strain graph results obtain after tensile test. The tensile strength values are read from these graphs.

YYY. Micro Hardness test

The samples which are connected by different welding time and current are cut midpoint for hardness test. After cutting, samples are sanded and buffed. To perform the hardness test, a special apparatus is used. The hardness test setup is shown in Fig. 5.



Fig. 5 Microhardness Test Machine

Hardness measurements were made diagonally according to ASW standards. Hardness measurements are carried out at 1

mm intervals for each sample. All measurement is performed three times for repeatability.

III. RESULTS AND DISCUSSION

It is observed that the welding diameter of the resistance spot welding process grows with the increase of the welding current. The results of other researcher’s studies show that the same result is achieved [8-10].

The tensile forces which are obtained from force-elongation graph in the tensile test are given by Table 2. In addition, the graphic form of the table is given in Fig. 5.

TABLE LXIXI
TENSILE STRENGTH

Tensile Stress [kN]					
Experiment Number	Input parameters	Exp. 1	Exp. 2	Exp. 3	Average
1	40 cycle-12 kA	1,20	1,07	1,23	1,17
2	40 cycle - 9 kA	1,06	0,95	1,18	1,06
3	20 cycle - 12 kA	1,22	1,28	1,26	1,25
4	20 cycle - 9 kA	1,11	1,12	1,01	1,08
5	10 cycle - 12 kA	0,83	0,91	0,80	0,85
6	10 cycle - 9 kA	0,78	0,73	0,80	0,77

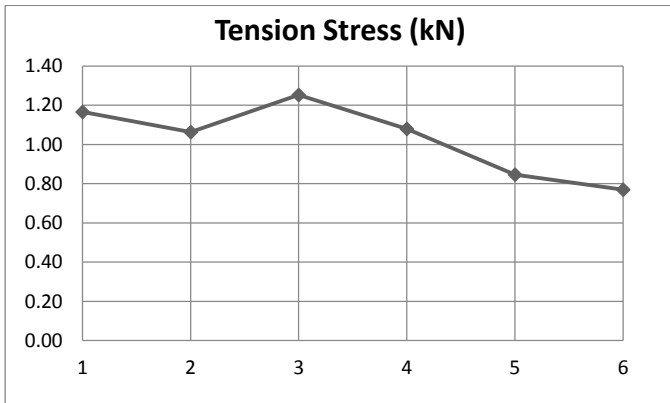


Fig. 5 Tensile test results

When the table I is taken into consideration, tensile strength is risen with increasing ampere. However, it is not valid for welding cycle. The highest tensile stress is obtained from the third experiment.

Measurement hardness values are shown in Fig. 6-10 which are categorized by cycle and current.

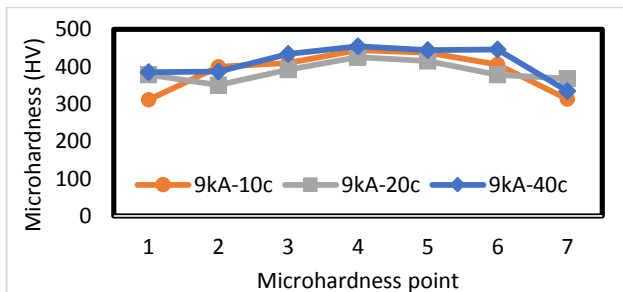


Fig. 6 Hardness values under constant ampere (9 kA) and variable cycles

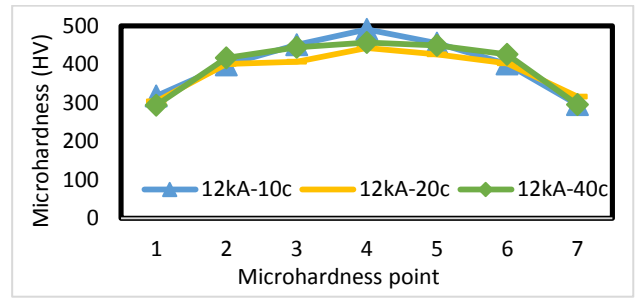


Fig. 7 Hardness values under constant ampere (12 kA) variable cycles

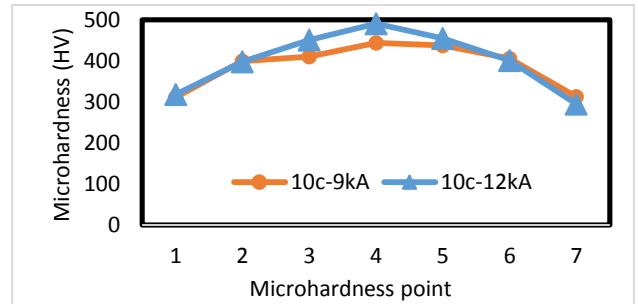


Fig. 8 Hardness values under constant cycle (10 cycles) variable ampere

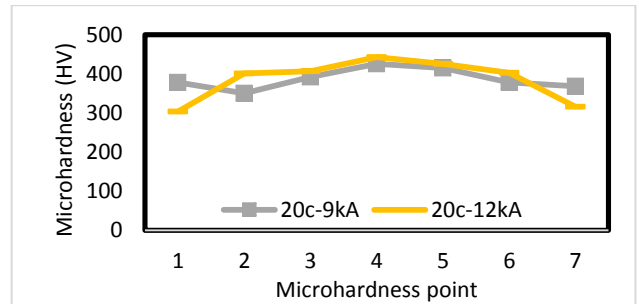


Fig. 9 Hardness values under constant cycle (20 cycles) variable ampere

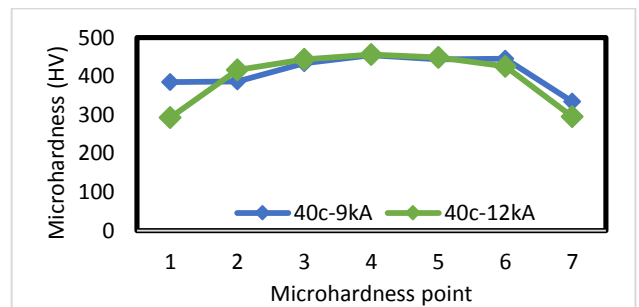


Fig. 10 Hardness values under constant cycle (40 cycles) variable ampere

DP 600 hardness value is measured between 280 - 330 HV. heat affected zone hardness value approximately is obtained 350 HV, the center of the welding hardness value is measured 450-490 HV.

IV. CONCLUSIONS

In the present study, two important resistance spot welding parameters which are welding time and welding current are

examined. The examination is performed by tensile test, micro hardness and macro structural.

Brittle fracture is observed in tensile test. This fracture is occurred in heat affected zone. It has been found that the growing up the welding diameter does not change linearly in the tensile stress.

It is observed that the centre of the welding is change welding current. In addition, hardness is increased with welding current magnitude. It is established that the centre of the welding point and heat affected zone hardness values rather are similar.

When the results are evaluated, the optimum welding parameters are determined as 20 cycle welding time and 12 kA welding current. It is considered to apply different steel thicknesses and welding strengths in future study.

ACKNOWLEDGMENT

This study is supported by Mersin University projected which is number of 2017-1-AP4-2152.

REFERENCES

- [1] Carlsson, B., "Choice of Tool Materials for Punching and Forming of Extra- and Ultra High Strength Steel Sheet", 3rd International Conference and Exhibition on Design and Production of Dies and Molds, Bursa-Turkey, 2004.
- [2] *Advanced High Strength Steel (AHSS) Application Guidelines*, International Iron & Steel Institute Committee on Automotive Applications, March 2005.
- [3] Geliştirilmiş yüksek mukavemetli çelik sacların şekillendirilmesinde takım çeliklerinden beklenen özellikler, *Available: http://www1.mmo.org.tr/resimler/dosya_ekler/e9a7776c9ae8ab7_ek.pdf*
- [4] MEGEP, "Elektrik Direnç Kaynağı", Metal Teknolojisi, Ankara, 2012.
- [5] Deng, X. Chen, W. Shi, G., "Three-dimensional finite element analysis of mechanical behavior of spot welds", *Finite Elements in Analysis and Design*, vol: 35, pp. 17-39, 2000.
- [6] Chen, X. Deng, X. "Performance of shell elements in modelling spot-welded joints", *Finite Elements in Analysis and Design*, vol. 35, pp. 41-57, 2000.
- [7] Fujii, T. Tohgo, K. Suzuki, Y. Yamamoto, T. Shimamura, Y. Ojima, Y., "Fatigue properties of spot welded and spot weld-bonded joints of steel sheet", *Engineering Procedia*, vol. 10, pp. 1075-1080, 2011.
- [8] Akkuş, A., "Nokta kaynaklı farklı çelik sacların yorulma dayanımlarının deneysel analizi", *Journal of Itu*, Vol:6 No:1, pp 37-46, 2007.
- [9] Vural, M. Akkus, A. "On the resistance spot weldability of galvanized interstitial free steel sheets with austenitic stainless steel sheets", *Material Processing Technology*, vol. 153-154, pp.1-6, 2004.
- [10] Satoh, T. Abe, H. Nakaoka, T. and Hayata, Y. "The fatigue life of the spot welded joint under a repeated load of R=-1", *Welding in The World*, pp.12, 1996.

Improvement of 16MnCr5 Steel Wear Resistance by Deformation

Hüseyin DEMİRTAŞ
Karabuk University
hdemirtas@karabuk.edu.tr

ABSTRACT

This study, in order to determine the effect of plastic deformation on the wear resistance are performed. The deformation of the 16MnCr5 steel was performed after annealing by tensile testing device with varying amounts. The changes in hardness was measured by Vickers hardness tester and the wear behavior was analysed by pin on disc test. Tests and measurements showed that when the amount of plastic deformation increased, wear resistance and hardness increased. And also, it is seen that the heat treatment applied at a temperature similar to the carburizing, significantly reduces the mechanical properties.

Keywords: 16MnCr5 Steel, Plastic deformation, wear rate

Reduction of Operation Cost and Improvement of Production by Utilizing Advance Surface Modification Technology "UNSM (Ultrasonic Nanocrystal Surface Modification)"

Young Pyun¹, Auezhan Amanov¹, Inho Cho²

1. Sun MOON University

2. DesignMecha

pyoun@sunmoon.ac.kr

ABSTRACT

UNSM (Ultrasonic Nanocrystal Surface Modification) refines the surface structure into nano grains, induces big and deep compressive residual stress, increase surface hardness, improves surface roughness and creates micro dimple textures on surface. So service life of UNSM treated trimming knives, shear pins and remanufactured bearings were extended more than 100% comparing to untreated ones. So not only the operation cost is reduced, but production time is increased. UNSM mechanism and its effect on mechanical properties and performance are explained. The changes of hardness, surface roughness and residual stress change of D2 and H13 tool steel and how much the performance of wear & friction and rotary bending fatigue are improved is explained with real field test results of trimming knives in steel mill industry. In same way, test for test specimens of AISI1045 steel and shear pins and remanufactured bearings in steel mill industry are explained. Cost reduction and increased production time in case of shear pins was explained as a case.

Keywords: UNSM, Trimming knife, shear pin, bearing manufacturing, cost reduction, production efficiency

Heat Transfer Analysis of a Reheat Furnace in Iron and Steel Industry

Adem YILDIRIM¹, Hüseyin YAĞLI², Yıldız KOÇ³, Ali KOÇ^{4*}, Furkan GÜVEN⁵

¹İskenderun Teknik Üniversitesi, Makine Fakültesi, Makine Mühendisliği, İskenderun/HATAY ademmyildirim@hotmail.com

²İskenderun Teknik Üniversitesi, Makine Fakültesi, Makine Mühendisliği, İskenderun/HATAY huseyin.yagli@iste.edu.tr

³İskenderun Teknik Üniversitesi, Makine Fakültesi, Makine Mühendisliği, İskenderun/HATAY ali.koc@iste.edu.tr

⁴İskenderun Teknik Üniversitesi, Makine Fakültesi, Makine Mühendisliği, İskenderun/HATAY yildiz.koc@iste.edu.tr

⁵İskenderun Teknik Üniversitesi, Makine Fakültesi, Makine Mühendisliği, İskenderun/HATAY guvnfurkan@gmail.com

Abstract— This document presents the heat transfer analysis of a reheat furnace which locates in a steel and iron plant in Iskenderun, Hatay. During the studies the Fourier law based analysis is made by using many assumptions.

Keywords— Reheat furnace, heat transfer, wall loss, energy saving, optimisation, iron and steel

I. INTRODUCTION

Steel and iron industry has a considerable impact on industrialization due to becoming raw materials of wide variety of durable consumer goods. Therefore, one of the indicators of the prosperity and development of a country is the consumption rate of steel and iron productions. Steel and iron consumption consistently increases especially in the developing and strong countries and these countries aims to meet consumption rates by creating new production capacity.

There is a rapid development in industries of the Turkey. Related with this growth, raw material producer sectors especially like steel and iron industry gets more importance. Iron and steel production capacity of Turkey is second-largest in Europe countries and eighth largest manufacturer in the world [1]. In 2016, raw steel and iron production in Turkey had an increase of 5.3% if compared with previous year. This proportion means that 33.2 million tons of iron and steel produced during the 2016, which means Turkey will be biggest manufacturer in Europe and seventh producer country in the world [2, 3].

Energy consumption of the steel and iron industry has 5% share in total energy consumption of the world, annually average 24 EJ (24.10¹⁸ J). Because of that, this industry takes places among the most energy consuming sectors [4]. When we get all this cases under care we should decrease the cost of production. Energy costs have the largest portion with 30 % in total cost [5]. Also iron and steel industry of Turkey consumes 20 % of total energy consumption in all industries consumption [6]. Energy of Turkey is externally dependent to the other countries. Because of this cases and rapid growing, industrialists needs to save energy consumption. Due to achieve energy saving, optimization of system equipment is becoming more and more important quantity.

Keeping the energy consumption at the desired balance is crucial for the environmental sustainability as well as the financial cost of the operator. In recent years, as a result of rapidly developing industrialization, the effect of chimney gases on the ecosystem left to the atmosphere has reached dangerous dimensions. It is stated in the report that the CO₂ emissions due to energy consumption will increase by 49% in 2030 compared to 2005 and that an international energy company, which industrial enterprises will face with serious energy costs [7].

There have been many studies on energy efficiency in reheating furnaces. In these studies, the system has been studied as a whole, as well as a specific part of the furnace. In works, it was emphasized that system design and application conditions in the plant should be determined in the most suitable way, the necessary efficiency should be provided in the most efficient way, waste water, waste gas and recycling from the boiler should be provided and periodical maintenance should be done. [8].

In this direction, the recycling of waste heat after recuperator exit of high temperature (700°C - 750°C) exhaust gases, which is opened in annealing furnace at an iron and steel production plant, which has been investigated by Yağlı in order to regain waste heat to the system. First of all, whether the waste gas temperature is properly regulated or not is examined. Organic Rankine cycle is then designed with the help of known data. At the end of the study, the electricity production capacity was calculated by energy formulas and the system was calculated for exergy [9]. Chen et al., studied the energy efficiency and performance of annealing furnaces with practical measurements and numerical analyses in their work. Numerical data show that fuel consumption is more efficient with increased production speeds in furnaces. On the other hand, it is observed that 15.7% of the heat inside the furnace is provided by the flue gas leaving the atmosphere and 80% by the combustion of the fuel. Practical measurements showed that the recovered heat yield was 47.76% and the heat exchange efficiency was 86.66% [10].

Si et al. analysed the energy efficiency of a steel plant in Canada in terms of energy efficiency, which can be achieved by waste heat recovery. It is observed that the efficiency of the annealing furnace is 60% with the calculations made by the

process heat evaluation and inspection tool. In this study, the largest energy loss in the furnace was found to be flue gas losses with a rate of 29.5%. As a result of the study it was emphasized that the billets should be heated to 315 ° C and energy efficiency should be increased [11].

In this study, a reheat furnace in iron and steel industry was analysed. The reheat furnace has two temperature zones. First zone has temperature range in between 900 °C and 1100 °C, second zone has range in between 1200 °C and 1300 °C. In a day, 850 tons of steel slabs are being heated up to the temperatures in between 1100 °C and 1200 °C. These heated slabs enter to the rolling process. By using data taken from furnace, heat transfer analysis of the reheat furnace is calculated. Results taken from calculations are expounded and amount of the heat losses and percentages are investigated in detailed manner.

II. Material and Method

A. Reheat furnace

The reheat furnace is ovens that work between 1050-1300 °C prior to rolling cold blocks, which is the varied dimensions. This heat operation is performed by the burners in the furnace wall surface. The reheat furnace is diversely designed according to movement of blocks, long and production capacity. The burner capacity and the refractor material is determined by regarding the design parameters. Isometric view of the reheat furnace is shown in Figure 1.

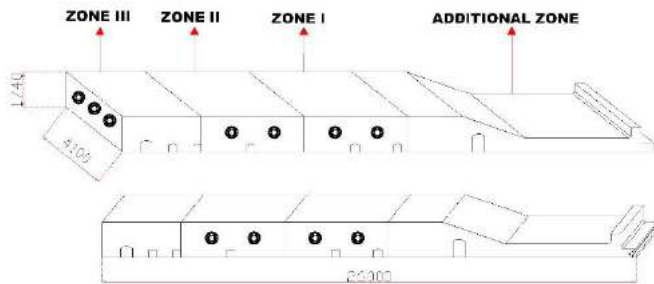


Fig. 1 Isometric view of the reheat furnace

The heat loss of heat furnace is calculated in the study. The furnace is located in bracket shape Rolling factory. Because of pushing the block on the floor surface, the furnace is called as the pusher type of heat furnace. System is designed according to 30 ton capacity and consists of four separate combustion zones. The zones are called as Additional Zone, Zone I, Zone II, Zone III, respectively. The additional zone is close to the flap area where cold block inserts into the furnace. Zone III is called as the Chapter where the heat block exits from the furnace. The length and width of the reheat furnace is 26 meter and 4.1 meter, respectively. The block, which is varied in dimension up to 4 meters, can be heated by the reheat furnace.

To perform the heating operation in the furnace, totally 11 burners used in the furnace, which are located in Zone I (4 burners with capacity of 1298 kW), in Zone II (4 burners with capacity of 1550 kW) and Zone III (3 burners with capacity of 623 kW).

B. Construction materials of the reheat furnace

The one of the most important steps in production of a reheat furnace is selection of refractory materials, after the steps of decision of operation direction, dimensions of the furnace and burner selection. The refractory materials should be selected to minimise the heat loss from the walls of furnace as much as possible. Sectional view of the reheat furnace wall layer is shown in Figure 2.

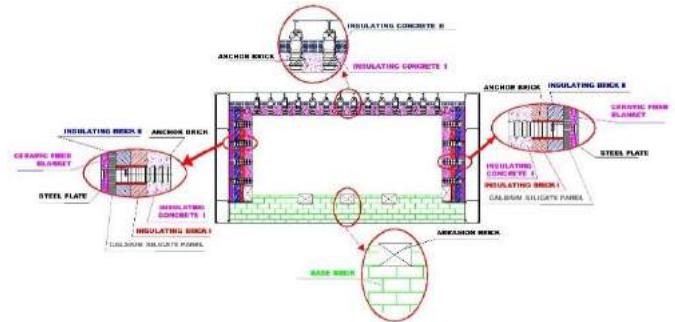


Fig. 2 Sectional view of the reheat furnace wall layer

Insulating concrete and insulating bricks were used in the construction process of the ceiling and side walls. Therefore anchor bricks were also used in construction in order for refractory materials to hold each other better. In the base of the furnace, apart from base bricks, abrasion bricks were used to minimise erosion on the base surface, that can be occur during the movement of the steel blocks. The dimensions of the refractory materials and their thermal conductivity values are given in Table I.

TABLE I
THE DIMENSIONS OF THE REFRACTORY MATERIALS AND THEIR THERMAL CONDUCTIVITY VALUES

MATERIAL STRUCTURE OF THE CEILING WALL										
MATERIAL NAME	DIMENSION (m)			THERMAL CONDUCTIVITY (W/m.K)						
	LENGTH	WIDTH	THICKNESS	200 °C	400 °C	550 °C	600 °C	800 °C	1000 °C	1050 °C
INSULATING CONCRETE I	-	-	0.1800	-	1.2000	-	-	1.2000	1.2000	-
INSULATING CONCRETE II	-	-	0.1050	-	-	-	-	0.4000	0.4300	-
ANCHOR BRICK L 350	0.1200	0.1200	0.3500	-	-	-	1.7000	-	1.7000	1.5000
MATERIAL STRUCTURE OF THE SIDE WALL										
MATERIAL NAME	DIMENSION (m)			THERMAL CONDUCTIVITY (W/m.K)						
	LENGTH	WIDTH	THICKNESS	200 °C	400 °C	550 °C	600 °C	800 °C	1000 °C	1050 °C
INSULATING CONCRETE I	-	-	0.1700	-	1.2000	-	-	1.2000	1.2000	-
INSULATING BRICK I	0.2300	0.0650	0.1150	-	0.1700	-	0.1900	0.2200	0.2500	-
INSULATING BRICK II	0.2300	0.0650	0.1150	-	0.1250	-	0.1400	-	-	-
CALSIUM SILICATE PANEL	1.0000	0.5000	0.0500	0.0600	0.1000	-	0.1500	0.1800	-	-
CERAMIC FIBER BLANKET	7.2000	0.6100	0.0500	0.0450	0.0850	-	0.1520	-	-	-
ANCHOR BRICK L 350	0.1200	0.1200	0.3500	-	-	-	1.7000	-	1.7000	1.5000
ABRASION BRICK T:200	0.5500	0.2000	0.2000	-	-	-	4.3000	4.6000	5.1600	-
INSULATING CONCRETE I	-	-	0.4000	-	1.2000	-	-	1.2000	1.2000	-
STEEL PLATE	-	-	0.0150	-	17.0000	-	-	-	-	-
AIR	-	-	0.0500	-	0.0492	-	-	-	-	-
MATERIAL STRUCTURE OF THE BASE WALL										
MATERIAL NAME	DIMENSION (m)			THERMAL CONDUCTIVITY (W/m.K)						
	LENGTH	WIDTH	THICKNESS	200 °C	400 °C	550 °C	600 °C	800 °C	1000 °C	1050 °C
ABRASION BRICK T:200	0.5500	0.3000	0.2000	-	-	-	4.3000	4.6000	5.1600	-
BASE BRICK RD AL	0.2200	0.1500	0.4200	-	-	-	2.2000	-	2.1000	2.0000
BASE BRICK RD AL	0.2200	0.1500	0.6000	-	-	-	2.2000	-	2.1000	2.0000

During the construction of the reheat furnace walls, the order of refractory materials were decided by taking into account the coefficient of thermal conductivity which obtained from manufacturer of the refractory materials. Since the coefficient of thermal conductivity of each refractory material are varied, heat loss calculations of these ordered materials should be made for each zone of the reheat furnace separately. During the reheat furnace heat loss calculations, the furnace is divided into zones

to ease investigation and reveal results accurately. Many of abbreviations are accepted for each type of refractory material and each ordered refractory groups. The accepted classification of the reheat furnace is given in Table II.

TABLE II
THE ACCEPTED CLASSIFICATION OF THE REHEAT FURNACE

THE ACCEPTED CLASSIFICATION OF THE REHEAT FURNACE				
CLASSIFICATION NAME	REFRACTORY NAME	ABBREVIATIONS	L (m)	K (W/m.K)
A	INSULATING CONCRETE I	IB1	0.1700	1.2000
	INSULATING BRICK I	IT1	0.1150	0.2200
	INSULATING BRICK II	IT2	0.1150	0.1400
	CALSIUM SILICATE PANEL	KSP	0.0500	0.1000
	CERAMIK FIBER BLANKET	SFB	0.0500	0.0525
	STEEL PLATE	CLKSC	0.0150	17.0000
B	ANCHOR BRICK L:350	ASL350	0.3500	1.5000
	AIR	HV	0.0500	0.0492
	CALSIUM SILICATE PANEL	KSP	0.0500	0.1000
	SERAMIK FIBER BATTANIYE	SFB	0.0500	0.0525
	STEEL PLATE	CLKSC	0.0150	17.0000
C	INSULATING CONCRETE I	IB1	0.4000	1.2000
	STEEL PLATE	CLKSC	0.0150	17.0000
D	ANCHOR BRICK L:350	ASL350	0.3500	1.5000
	CERAMIK FIBER BLANKET	SFB	0.0500	0.0525
	STEEL PLATE	CLKSC	0.0150	17.0000
E	INSULATING CONCRETE I	IB1	0.1800	1.2000
	INSULATING CONCRETE II	IB2	0.1200	0.4000
F	ANCHOR BRICK L:350	ASL350	0.3500	1.5000
	BASE BRICK 80 AL	TT80	0.6000	2.0000
G	ABRASION BRICK T:200	ATT200	0.2000	5.1600
	BASE BRICK 80 AL	TT80	0.4200	2.0000
H	ABRASION BRICK T:200	ATT200	0.2000	5.1600
	INSULATING BRICK I	IT1	0.0850	0.2200
I	INSULATING BRICK II	IT2	0.1150	0.1400
	CALSIUM SILICATE PANEL	KSP	0.0500	0.1000
	CERAMIK FIBER BLANKET	SFB	0.0500	0.0525
	STEEL PLATE	CLKSC	0.0150	17.0000
	INSULATING CONCRETE I	IB1	0.1000	1.2000
FLAPS	INSULATING CONCRETE I	IB1	0.1000	1.2000
	STEEL PLATE	CLKSC	0.0100	17.0000

C. Measured values

The system parameters and temperatures must be recorded correctly due to perform the best heat loss calculation of the reheat furnace. Therefore, the inside and outside temperatures of the reheat furnace are measured by thermometers for all surface the furnace by considering each zone (Additional Zone, Zone I, Zone II, Zone III) separately. The measured outside boundary temperatures of the reheat furnace are shown in Figure 3.

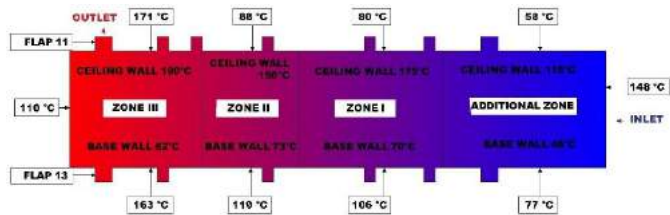


Fig. 3 The measured outside boundary temperatures of the reheat furnace

The temperatures of flaps on the reheat furnace are also measured to consider in infiltration. The outside surface temperatures of the furnace flaps are given in Table III.

TABLE III
THE OUTSIDE SURFACE TEMPERATURES OF THE FURNACE FLAPS

THE OUTSIDE SURFACE TEMPERATURES OF THE FURNACE FLAPS														
	FLAP 1	FLAP 2	FLAP 3	FLAP 4	FLAP 5	FLAP 6	FLAP 7	FLAP 8	FLAP 9	FLAP 10	FLAP 11	FLAP 12	FLAP 13	INLET FLAP
CLOSED FLAP OUTSIDE SURFACE TEMPERATURE (°C)	129	144	132	145	130	141	155	135	130	139	61.9	27.1	45.9	45.8
OPENED FLAP OUTSIDE SURFACE TEMPERATURE (°C)	0	0	0	0	0	0	0	0	0	0	56.8	0	56.5	0

The measured outside temperature values of the flaps, steel block entrance flaps and movable flaps are stated in the table above. Since the steel block exit flap and billet bayonet system

are open able, infiltration heat losses of these flaps are calculated by taking into account the temperatures recorded above. During the calculation of infiltration rate and infiltration heat losses, opening duration of the flaps and thermodynamic properties of the air around flaps are used as well as flap surface temperatures. The opening durations of the movable flaps are shown in Table IV.

TABLE IV
THE OPENING DURATIONS OF THE MOVABLE FLAPS

THE OPENING DURATIONS OF THE MOVABLE FLAPS		
FLAP NAME	TOTAL DURATION (sec)	OPENING DURATION (sec)
SIDE WALL (WEST) OUTLET FLAP-FLAP 11	50	12
SIDE WALL (EAST) PUSHER FLAP-FLAP 13	50	20

This table includes opening durations of the 11th and 13th flaps upon steel blocks exits from the furnace. The thermodynamic data used for infiltration calculations of the furnace flaps are stated in Table V.

TABLE V
THE THERMODYNAMIC DATA USED FOR INFILTRATION CALCULATIONS OF THE FURNACE FLAPS

SPECIFICATION OF ZONE III						
INTERNAL TEMPERATURE (°C)	EXTERNAL TEMPERATURE (°C)	INTERNAL PRESSURE (mbar)	EXTERNAL PRESSURE (mbar)	VOLUME(m ³)	INSIDE AIR ENTHALPY(kj/kg)	OUTSIDE AIR ENTHALPY(kj/kg)
1321	30	1009.9	1000	28.3044	30.1545	1477.4136

The inside air temperatures recorded by automation system of the plant by the thermocouples assembled to the ceiling of the reheat furnace are used during the calculation, based on the assumption that the furnace inside air temperature is equal to the Wall inside surface temperatures. The screen shot of the automation system used to measure inlet air properties are shown in Figure 4.

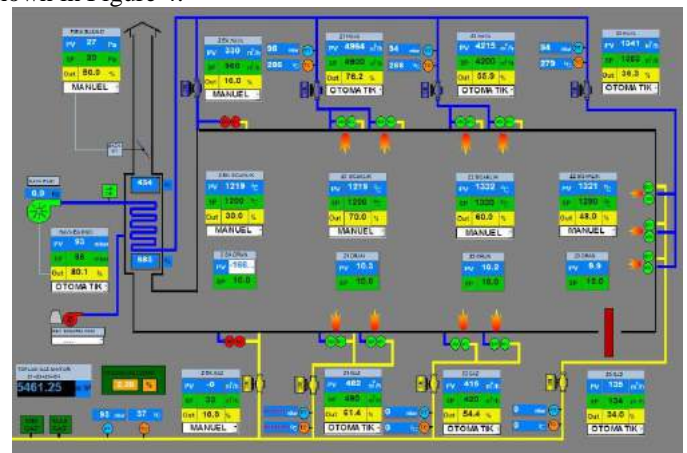


Fig. 4 The screen shot of the automation system used to measure inlet air properties

The heat transfer surface areas of the refractory groups are calculated in account of zones. The calculated surface area values of the classified reheat furnace are stated in Table VI.

$$R_{res} = R_1 + R_2 + R_3 + R_4 + \dots$$

The air lost by the flaps located on the furnace which are open at specific time intervals refers to infiltration. The heat lost by infiltration found by;

$$\dot{Q}_{inf} = \dot{m}(h_{outside} - h_{inside})$$

where \dot{m} and h refer to air mass flow rate and enthalpy of air. *Outside* and *inside* refer to outside atmosphere and inside air condition of the furnace. Consequently, the total heat loss during opened and closed time interval of the flaps is calculated by;

$$\dot{Q}_{flap} = \frac{(\dot{Q}_{inf} * t_{open}) + (\dot{Q}_{FHT} * t_{closed})}{(t_{open} + t_{closed})}$$

In order to evaluate more stable and solvable state, some acceptances are made during calculations. When we investigate these assumptions;

- The surface area of the burners is ignored, as they are relatively small compared with total wall area.

- During the heat transfer calculation, the heat loss calculation of the system is calculated up to the exit of the furnace to the chimney and the heat loss of exhaust gas inside pipes and chimney are not considered.

- The inside Wall surface temperatures are accepted as equal to the furnace inside air temperatures which is measured by thermocouples joined on ceiling

- The outer surface temperature of the furnace is assumed as equal to mean values of temperatures that measured many part of surface depending on zones and position of the walls.

- Since all open able flaps are in Zone III and opening duration of the flaps has relatively short time interval, volume of Zone III is used instead of whole inside volume of the furnace during the infiltration calculations.

- It is assumed that the combustion is complete combustion and the burners are operating at 100% efficiency during the calculations of wall heat losses.

III. Results and Discussion

In the present study, the total wall heat losses of the system and the energy ratios entering it are calculated by using assumptions and formulations given above. Distribution of the calculated total heat losses according to wall regions are given in Table VII.

TABLE VII

DISTRIBUTION OF THE CALCULATED TOTAL HEAT LOSSES ACCORDING TO

TABLE VI

THE CALCULATED SURFACE AREA VALUES OF THE CLASSIFIED REHEAT FURNACE

THE CALCULATED SURFACE AREA VALUES OF THE CLASSIFIED REHEAT FURNACE						
	CLASSIFICATION NAME	ADDITIONAL ZONE	ZONE I	ZONE II	ZONE III	
		A(m2)	A(m2)	A(m2)	A(m2)	
SIDE WALL (WEST)	A	11.6479	7.6606	7.0438	5.3825	
	B	0.6059	0.3652	0.4233	0.2822	
	I	0.0000	0.0000	0.7320	0.4780	
	FLAPS	FLAP 1	0.5209	0.0000	0.0000	0.0000
		FLAP 3	0.0000	0.1575	0.0000	0.0000
		FLAP 4	0.0000	0.1575	0.0000	0.0000
		FLAP 7	0.0000	0.0000	0.1575	0.0000
		FLAP 9	0.0000	0.0000	0.0000	0.1575
		FLAP 10	0.0000	0.0000	0.0000	0.1575
		FLAP 11	0.0000	0.0000	0.0000	0.3109
	SIDE WALL (EAST)	A	11.6479	7.6606	7.0438	5.5317
B		0.6059	0.3652	0.4233	0.2905	
I		0.0000	0.0000	0.7320	0.4780	
FLAPS		FLAP 2	0.5209	0.0000	0.0000	0.0000
		FLAP 5	0.0000	0.1575	0.0000	0.0000
		FLAP 6	0.0000	0.1575	0.0000	0.0000
		FLAP 8	0.0000	0.0000	0.1575	0.0000
		FLAP 12	0.0000	0.0000	0.0000	0.1575
		FLAP 13	0.0000	0.0000	0.0000	0.3109
		SIDE WALL (NORTH)	C	1.0035	0.0000	0.0000
D			0.0830	0.0000	0.0000	0.0000
INLET FLAP	1.6400		0.0000	0.0000	0.0000	
SIDE WALL (SOUTH)	A	0.0000	0.0000	0.0000	6.1760	
	B	0.0000	0.0000	0.0000	0.3403	
BASE WALL	H	0.0000	0.0000	3.3390	6.2910	
	G	50.5831	21.7099	18.0119	10.8580	
CEILING WALL	E	46.7621	19.0507	18.9755	14.4384	
	L	3.9508	1.8592	1.9754	1.5106	

D. Formulations and acceptance used during the heat transfer calculations

The linear heat transfer equations are used during calculations, based on the assumption that the heat transferred from the wall by conduction is equal to the heat transferred from the wall by convection. The Fourier heat conduction law is defined as [12, 13, 14];

$$Q = -kA \frac{dT}{dL}$$

where k , A and L refers to coefficient of thermal conductivity, heat transferred surface area and wall width, respectively. The equivalent heat resistance equation written as;

$$R_{res} = \frac{L}{kA}$$

When Fourier heat conduction law rearranged;

$$Q = \frac{kA}{L}(T_i - T_d) \leftrightarrow Q = \frac{1}{\frac{L}{kA}}(T_i - T_d) \leftrightarrow$$

$$Q = \frac{1}{R_{res}}(T_i - T_d) \leftrightarrow Q = \frac{(T_i - T_d)}{R_{res}}$$

where T_i is the inside surface temperature, T_d is the outside surface temperature and R_{res} is the equivalent heat resistance. The total equivalent heat resistance of the furnace calculated by;

WALL REGIONS

DISTRIBUTION OF THE CALCULATED TOTAL HEAT LOSSES ACCORDING TO WALL REGIONS							
	CLASSIFICATION NAME	ADDITIONAL ZONE	ZONE I	ZONE II	ZONE III		
		Q (Watt)	Q (Watt)	Q (Watt)	Q (Watt)		
SIDE WALL (WEST)	A	4601.1627	2968.7542	2907.0704	2106.0545		
	B	259.1408	153.2219	189.1874	119.5472		
	-	0.0000	0.0000	326.1690	201.8360		
	FLAPS	FLAP 1	6765.6147	0.0000	0.0000	0.0000	
		FLAP 3	0.0000	2040.0298	0.0000	0.0000	
		FLAP 4	0.0000	2015.6320	0.0000	0.0000	
		FLAP 7	0.0000	0.0000	2021.2623	0.0000	
		FLAP 9	0.0000	0.0000	0.0000	1859.8616	
		FLAP 10	0.0000	0.0000	0.0000	1484.5111	
		FLAP 11	0.0000	0.0000	0.0000	4979.8000	
		FLAP 13	0.0000	0.0000	0.0000	6841.6000	
SIDE WALL (EAST)	A	4525.6837	2900.9863	2907.0704	2179.4902		
	B	254.8815	149.7089	189.1874	123.9231		
	-	0.0000	0.0000	326.1690	203.2524		
	FLAPS	FLAP 2	6672.5099	0.0000	0.0000	0.0000	
		FLAP 5	0.0000	2006.2482	0.0000	0.0000	
		FLAP 6	0.0000	2023.1390	0.0000	0.0000	
		FLAP 8	0.0000	0.0000	2308.9375	0.0000	
		FLAP 12	0.0000	0.0000	0.0000	1970.5900	
		FLAP 13	0.0000	0.0000	0.0000	6841.6000	
		SIDE WALL (NORTH)	C	3215.7333	0.0000	0.0000	0.0000
			D	74.9143	0.0000	0.0000	0.0000
INLET FLAP	115237.3300		0.0000	0.0000	0.0000		
SIDE WALL (SOUTH)	A	0.0000	0.0000	0.0000	2544.7151		
	B	0.0000	0.0000	0.0000	151.8400		
BASE WALL	H	0.0000	0.0000	16899.0442	31333.6498		
	G	197442.7003	83148.9170	75589.9403	44843.5400		
	E	114723.0187	44197.6240	49842.3133	36288.5120		
CEILING WALL	F	18608.2680	8278.7520	9964.8420	7289.7240		
	I	18608.2680	8278.7520	9964.8420	7289.7240		
TOTAL		472380.9579	149883.0133	163371.1932	144522.4470		
		930157.6114					

The total heat losses of base and ceiling of the furnace are calculated more than the total heat losses of the side walls. This dramatic difference shows us that the insulation materials used in base and ceiling of the reheat furnace are inadequate to prevent from over heat loss. The table also includes infiltration losses of the 11th and 13th flaps as well as flap surface heat losses. Also, when we compared with other zones, the total heat loss of the additional zone is higher, this is, because, the total volume of the additional zone is more than the other zones.

The total energy released from burners to the furnace is calculated as 13289 kW when all burners are considered to operate at 100% efficiency. When considered the total heat loss from the reheat furnace surface (930157.61 kW), the ratio of total heat loss of the reheat furnace to the total energy input from burners is calculated as 7%. The main aim of the calculation total wall heat losses is the investigation of zones of the furnace that needs to be improved. Therefore, it is essential to find out the ratio of total heat loss and total energy input and to determine the zones that release the most heat to environment. For this reason, taking into account the zones decided at the beginning of the calculations, the heat released from zones are calculated in order to better understand system losses. Proportional Distribution of the reheat furnace wall heat losses according to zones is shown in Figure 5.

Distribution of The Reheat Furnace Wall Heat Losses According to Zones

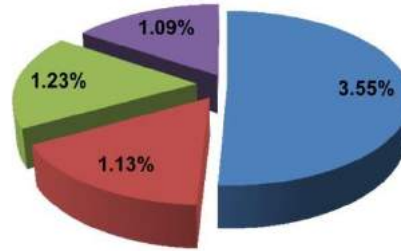


Fig. 5 Proportional Distribution of the reheat furnace wall heat losses according to zones

Considering the ratio (7%) of total wall loss of reheat furnace to the total amount of heat input, 3.55% of this ratio occurs at additional zone which is the most when compared with other zones. The minimum loss is seen at Zone III. The only reason why the most loss in the reheat furnace walls is seen in the additional region is that the additional zone volume and therefore the wall surface areas are the most. Therefore, in order to be able to analyse the system in more detail and determine the areas where the most loss is experienced locally, the percentage distribution of the calculated losses according to walls in each zone are calculated. Proportional Distribution of the zone heat losses according to walls presented in Figure 6.

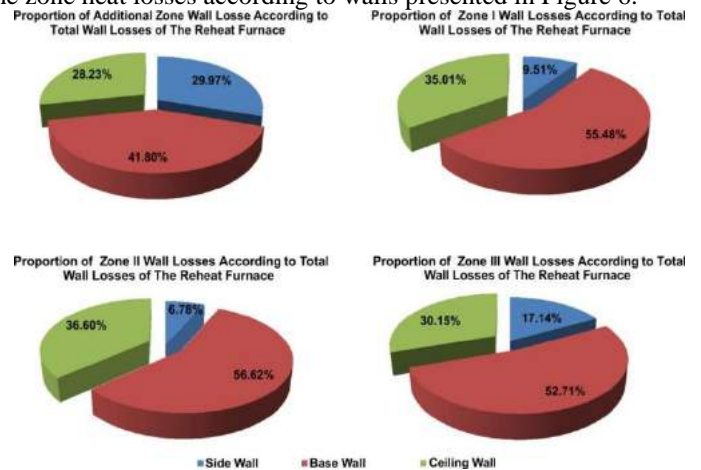


Fig. 6 Proportional Distribution of the zone heat losses according to walls

When the heat losses are examined locally, it is seen that in all regions out of the additional zone, the losses are minimum at the side walls and maximum at the base. However, it is seen that when the additional zone is examined within itself, it is the lowest loss in the ceiling, though it is still the highest loss at the base.

Since insufficient refractory material is used in the walls where the loss is maximum, it is understood that these total loss values are the greatest. The reason why the most loss in the side walls is seen in the additional region is that this zone has the movable log entrance flaps which are produced from the sheet metal. Since this inlet, which is closed with thin sheet metal, does not contain any insulation, the heat loss is calculated the most. Although the steel block exit on the Zone III is much smaller than the steel block entrance of the Additional Zone, all other open able flaps in the Zone III is increased the infiltration

heat loss of this zone. Therefore, total heat loss of the Zone III is calculated much more than Zone I and Zone II.

IV. Conclusion

When all the results are examined together, it is seen that the base and ceiling wall heat losses are the highest in all zones. This shows the inadequacy of the materials used in these zones of the reheat furnace. The total heat loss of the additional zone is bigger than the other zones, since the total surface area of the additional zone is more than others. In the reheat furnace we investigated, the heat losses especially at the base are very high. By using data obtained from plant automation and calculations made in this study, the base refractory material of the reheat furnace is improved by insulating with ceramic fiber blanket and calcium silicate panel. Ceramic fiber blanket is also placed on the ceiling wall in the same way to minimise the heat loss.

REFERENCES

- [1] Sanayi ve Teknoloji Bakanlığı, Demir-çelik sektörü raporu (2013/1)
- [2] Yüksek Enerji Maliyetleri Demir Çelik Sektörünü Yatırıma Zorluyor, Enerji Dergisi 10.12.2012
- [3] http://www.dcu.edu.tr/news.asp?news_id=797
- [4] Xu, C. ve Cang, D., "A Brief Overview of Low CO₂ Emission Technologies for Iron and Steel Making", Journal of Iron and Steel Research, International, Cilt 17, No 3, 1-7, 2010.
- [5] M.Emre Erten, Entegre demir-çelik tesislerinde enerji tasarrufu potansiyeli, mmo 1. Demir çelik sempozyum bildirileri / 121
- [6] www.ebso.org.tr/.../S.ELDEM_Presentation-2_sanayide_enerji_verim
- [7] IEA, "Global Energy Trends", World Energy Outlook 2007 Edition, International Energy Agency, 73-75, 2007
- [8] Bilgiç, M., "Endüstri kazan dairelerinde Enerjinin Etkin kullanılması için; Yakıttan baca gazına kadar dikkate alınması gereken hususlar", Türk Tesisat Mühendisleri Derneği Dergisi, Temel Bilgiler, Tasarım ve Uygulama Eki, Sayı :8
- [9] Yaglı, Huseyin, et al. "Comparison of toluene and cyclohexane as a working fluid of an organic Rankine cycle used for reheat furnace waste heat recovery." International Journal of Exergy 19.3 (2016): 420-438.
- [10] Chen, W.H., Chung, Y.C. ve Liu, J.L., "Analysis on Energy Consumption and Performance of Reheating Furnaces in a Hot Strip Mill", International Communications in Heat and Mass Transfer, Cilt 32, No 5, 695-706, 2005.
- [11] Si, M., Thompson, S. ve Calder, K., "EnergyEfficiency Assessment by Process Heating Assessment and Survey Tool (PHAST) and Feasibility Analysis of Waste Heat Recovery in the Reheat Furnace at a Steel Company", Renewable and Sustainable Energy Reviews, Cilt 15, No 6, 2904-2908, 2011.
- [12] Cengel, Yunus A. Heat transfer: a practical approach. WBC McGraw-Hill, 1998.
- [13] Özışık, M. Necati. Heat transfer: a basic approach. Vol. 1. McGraw-Hill College, 1985.
- [14] Bennett, Carroll O., and John Earle Myers. Momentum, heat, and mass transfer. New York: McGraw-Hill, 1962.

The Effects of Heat Treatment on Thermal, Mechanical and Microstructural Properties of Al based Sb - 42.4% Mg - 57.6% Al Eutectic Alloy

Fatma Meydaneri TEZEL, Yunus GENCTURK, Ugur VELİ, Mustafa Mert KULAK, Orcun OLCAY, Eren UZUN
Karabuk University, TURKEY
fatmameydaneri@karabuk.edu.tr

ABSTRACT

Al based Sb - 42.4% Mg - 57.6% Al ternary eutectic alloy was melted by vacuum melting furnace, and was casted into kokil mould. Then, in order to observe the effect of heat treatment, samples were investigated as-cast and under heat-treated conditions. Designed samples were homogenized at 573 K for 1.5 h. The values of enthalpy of fusion (ΔH) and the specific heat capacity (C_p) of the solid phase for Al based the ternary eutectic alloy were measured with DSC. The crystal structure parameters and the grain sizes for the alloys were investigated by XRD diffraction. Mechanical properties of the ternary eutectic alloy were studied with compression test. The effects of heat treatment on the microstructures and the microscopic fracture surface morphology of the aged samples were examined by FESEM. The microhardness for the alloys was measured from 5 different points with Vickers microhardness device. The compositions of the ternary alloys were determined by Energy Dispersive X-Ray (EDX) analysis.

Keywords: Heat treatment, specific heat capacity, enthalpy, microstructure, mechanical properties

Increasing Cold Forging Tool Life of M10x1.25 Welding Flange Nut by Using Finite Element Simulation

Sezgin Yurtdaş*, Cenk Kılıçaslan+, N. Emrah Kılıncdemir+, Barış Tanrikulu+, Buğra Karahan+

*Norm Civata San. ve Tic. A.Ş., 10007 Sok., A.O.S.B., Çiğli, İzmir, Turkey
sezgin.yurtdas@norm-fasteners.com.tr

+ Norm Civata San. ve Tic. A.Ş., 10007 Sok., A.O.S.B., Çiğli, İzmir, Turkey

Abstract—Cold forging of flange welding nuts requires proper design of forging stages to get tight dimensional tolerances of welding bulges and high tool life. In this study, reasons of low tool life of cold forged M10x1.25 welding flange nuts were determined by using finite element simulations and then forging stage designs were modified to decrease the tool stresses. Finite element simulations of cold forging operations were prepared in commercial finite element code Simufact.forming. Forging tests showed that two forging tools at forging stage 5 fractured due to fatigue failure during forging of 2,500 welding nuts. Numerical simulations revealed that preform of the nut before fifth forging stage was not properly formed and this led excessive increase in forging force during flow of the material in stationary tool in following forging stage. In fourth forging design, flat punch geometry was replaced by stepped punch design and closed forming case was formed on the stationary tool. It was seen that forging force in the fifth forging stage was decreased to 64 tones from 92 tones. Forging tests conducted with this design showed that tool life in fifth forging stage was increased more than 200%.

Keywords—Cold forging; nut; simulation; tool design; tool life

I. INTRODUCTION

Cold forging has a crucial role in the production of fasteners due to high mechanical properties and low material loss. Along with developing and changing technology, the use of complex fasteners is an increasing trend in the automotive, construction and aviation sectors. Complex shapes on fasteners require high forging machine capacity and tool life. These can be obtained by deep understanding of the effects of the process parameters and forging designs. Due to trial-error studies are very costly, numerical simulations become usable in metal forging process design [1]. In addition to forging station and tool designs, the effects of process parameters like tool material and surface conditions can also be investigated easily [2]. The use of CAD and CAE in the creation of new fasteners greatly shortens the product development process. Computer aided numerical simulation studies should be used to increase production and quality and reduce employment costs [3]. In the literature, many studies can be found about forging process of metals. Some of these studies were given in the followings. Geiger et al. [4] compared tool materials which were made by powder

metallurgy and ceramic and their superiority against each other examined. Tools made with powder metallurgy showed compressive resistance to ~3000 MPa while ceramic materials showed higher resistance to wear. Increasing the fatigue tool life of cold forging dies is a very curial issue. In the study of Lee et al. [5], the effect of different shrink fitting ratios on die life has been investigated. It was found that the stress amplitudes plays a critical role on determining tool life and the effects of creating pre-stress and pressure to minimize the stress amplitude was clearly revealed. In a previous study of the authors [6], It was determined that the increased shrink fitting ratios between the die components increases tool life. Carbon fiber reinforced composite material was used as the stress ring material and the shrink fitting ratios between the components was increased to 3.5%. With this innovation, up to 25% die life improvements have been achieved.

In this study, low tool life of cold forged M10x1.25 welding flange nuts were determined by using finite element simulations and then forging stage designs were modified to reduce the tool stresses to increase tool life. Forging simulations and tool analyses were conducted in simufact.forming finite element software.

II. TOOL DESIGN AND FAILURE

M10x1.25 welding flange nuts were forged from annealed 20MnB4 steel alloy. Technical drawing of the product is given in Figure 1. The forging capacity of the machine used in the cold forming of this product is 300 tons. The product is forged in total of 6 stations and the station design is given in Figure 2. Billet surface has been improved in the first two stations. While station 3 is prepared for hexagonal form, flange form preparation is made at station 4. At 5th station, the final form is given before piercing and the piercing is carried out at the last station.

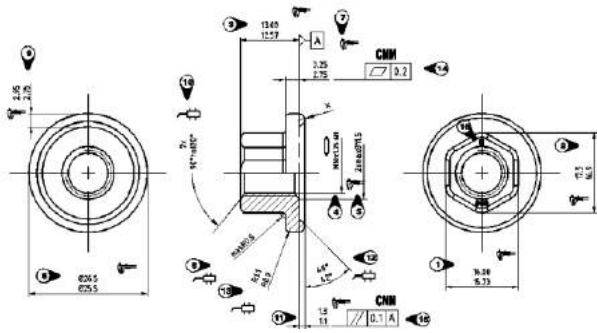


Fig. 47 Technical drawing of the M10x1.25 welding flange nut.

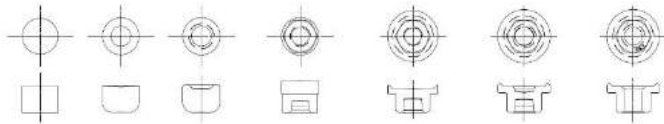


Fig. 2 Station design in production line.

2,500 numbers of the product have been cold-formed on the production line and 2 numbers of 5th station die were failed. This fracture may be formed due to ineffective preparation form in the 4th station. Technical drawing of stage 4 die couple is shown in Figure 3. While the stationary die is given on the right side, moving die is given on the left side

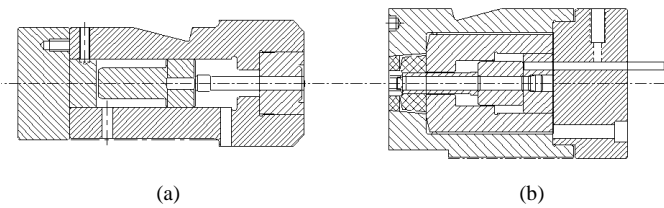


Fig. 3 Die system of stage 4; a) moving, b) stationary die.

III. NUMERICAL SIMULATIONS

Based on the station design given in Figure 2, die models were created. Numerical models of cold forging operation were prepared in Simufact.forming finite element software. Thermal effects and raw material's mechanical properties have been considered in simulations. Beside this, temperature dependent Coloumb friction coefficient was defined to the software. By this way, it was aimed to get more realistic results. Stage 1 and 2 were simulated with 2D models due to the axisymmetry while 3D models were used for stage 3, 4 and 5. As an illustration of numerical models, example of the model is shown in Figure 4. Rigid dies were used in simulations and workpiece material, 20MnB4, was modelled as plastic material. True stress-true plastic strain curves of the workpiece between temperatures of 20 and 400 °C and strain rates between 1 and 50 s-1 were defined to the software. While in 2D models, quad elements were used in the mesh of the workpiece, in 3D models hex elements were used. In 3D models, workpiece geometry is modelled 180° and symmetry plane was determined to reduce solution time. After the forming simulations, the forming forces were determined at each station.

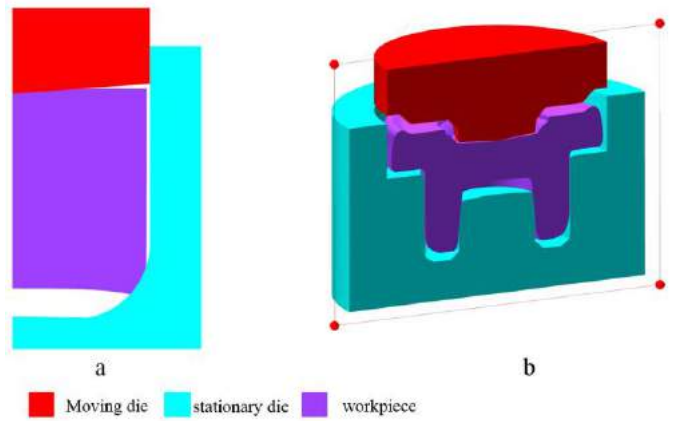


Fig. 4 Examples of numerical models; a) 2D axisymmetric and b) 3D models.

IV. RESULTS AND DISCUSSIONS

In the beginning of the study, simulations have been done to clarify the accuracy of the current design. In this respect, forging operations have been carried out according to the station designs given in Figure 2. Simulation forms in each station (ST) are given in Figure 5.

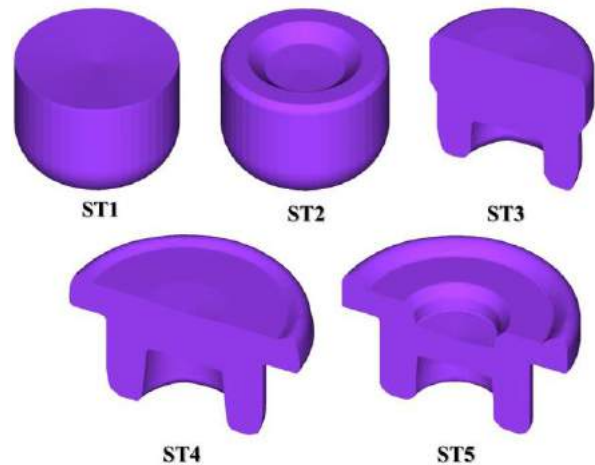


Fig. 5 Station forms obtained from simulations

Simulations revealed that welding ring form at 4th station was not properly formed. As seen in Figure 2, the height of the welding ring has to be 1.83 mm. However, the simulation showed that height of the welding ring is changing between 0.3 and 0.5 mm. Welding ring of the forged part was also measured as shown in Figure 6, and it was seen that results of simulation and forging trial are in good agreement.

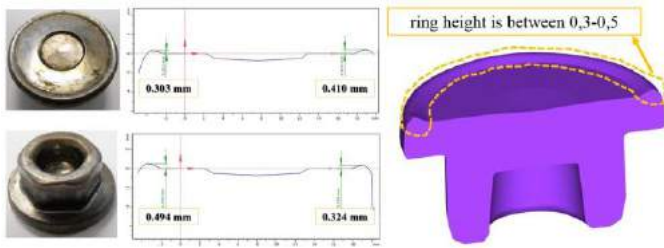


Fig. 6 Production and simulation measurement comparisons.

As followings, the forging force on 5th station was determined due to forging force has a great influence on die failure. As can be seen from the forging force graph shown in Figure 7, the forging force increased rapidly after workpiece contacted with case section of the stationary die. On each forging cycle, this high load evolution causes early breakage of the die.

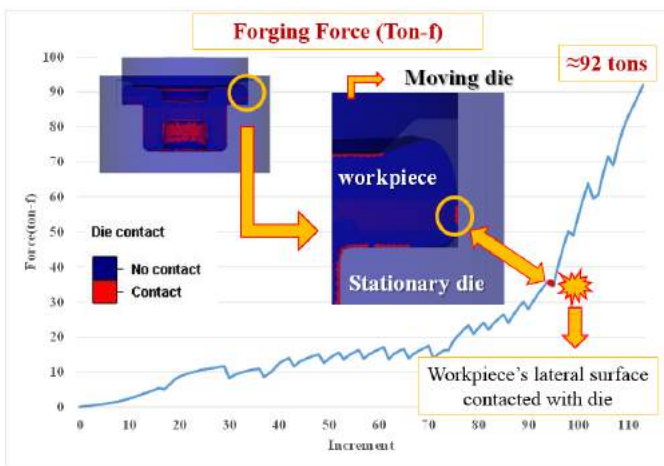


Fig. 7 Forging force versus increment graph at 5th station.

During alternative studies on the forging station design, it was aimed to make ring welding in required height by making various revisions in stationary and moving dies. In the 4th station, the case form on the moving side was replaced by the stationary side and the punch diameter was reduced from 20.2 mm to 18.5 mm as depicted in Figure 8. The revised form of stationary and moving dies were given in Figure 8.

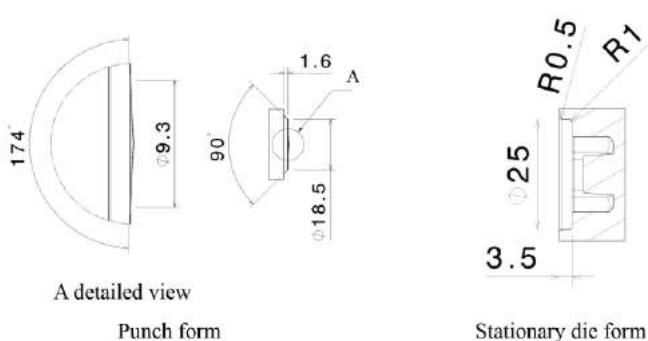


Fig. 8 Revised punch and stationary die form of 4th station.

Simulations were repeated after the design change. The ring height at the 4th station was obtained between 1.22-1.39 mm. In the current design, the forging force, which was approximately 92 tons in the 5th station, was reduced to 64 tons by the revised preparation form. Forging force experienced a decrease about 30%. The 5th station semi-finished form obtained from the simulation is shown in Figure 9. When the simulation form was checked according to Figure 1, it was determined that all the measurements were within the tolerances. In the current and revised design, difference between maximum forging force on the 5th station of current and revised design is given in Figure 10.



Fig. 9 5th station simulation form obtained from revised forging design.

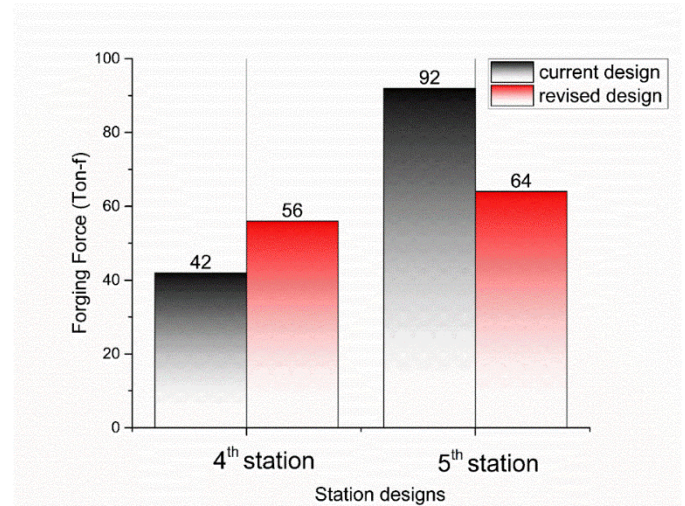


Fig. 10 Forging forces comparison between current and revised design.

Cold forging dies were manufactured according to the revised design, and forging trial was carried out. It was seen that 515,000 numbers of product have been cold-formed on the production line and only 2 numbers of 5th station die were failed. Therefore, tool life was improved more than 200%.

Conclusions

In this study, cold forged M10x1.25 welding flange nuts were investigated numerically to analyze the reasons of low cycle tool life. Simulations have been done to clarify the accuracy of the current design. The forging force on 5th station was identified due to forging force has a strong effect on die failure. The forging force during cold forging was seen to increase immediately after the workpiece contacted with case section of the stationary die. As a result of each forging cycle, this high load evolution leads early damage of the die. In the ring preparation form at 4th station, revisions were made on stationary die and punch geometry to flow of the material. In the current design, the forging force, which was roughly 92 tons in the 5th station, was decreased to 64 tons with the revised preparation form. Forging force was reduced about 30%. The forging trial was carried out and 2 numbers of 5th station die were failed when 515.000 forging cycles have been completed. It was seen that proper revisions on forging stage designs lead to increase of tool life more than 200% in production.

REFERENCES

- [1] Hsia, S.-Y. and Y.-T. Chou, Fabrication Improvement of Cold Forging Hexagonal Nuts by Computational Analysis and Experiment Verification. *Mathematical Problems in Engineering*, 2015. 2015.
- [2] Vazquez, V., D. Hannan, and T. Altan, Tool life in cold forging-an example of design improvement to increase service life. *Journal of Materials Processing Technology*, 2000. 98: p. 90-96.
- [3] Hsia, S.-Y. and P.-Y. Shih, Wear Improvement of Tools in the Cold Forging Process for Long Hex Flange Nuts. *Materials*, 2015. 8(10): p. 6640-6657.
- [4] Geiger, M., M. Arbak, and U. Engel, Material adapted tool design in cold forging exemplified by powder metallurgical tool steels and industrial ceramics. *Production Engineering*, 2008. 2(4): p. 409-415.
- [5] Lee, H.C., et al., The effect of shrink fitting ratios on tool life in bolt forming processes. *Journal of Materials Processing Technology*, 2009. 209(8): p. 3766-3775.
- [6] Yurtdaş, S., et al., A Case Study for Improving Tool Life In Cold Forging: Carbon Fiber Composite Reinforced Dies. *Research on Engineering Structures & Materials*, 2016.

Experimental Investigation on Self-Loosening of Preloaded Stainless Steel Fasteners

Umut Ince*, Barış Tanrıkuşu+, N. Emrah Kılıncdemir+, Sezgin Yurtdaş*, Cenk Kılıçaslan+

*Norm Civata San. ve Tic. A.Ş., 10007 Sok., A.O.S.B., Çiğli, İzmir, Turkey
umut.ince@norm-fasteners.com.tr

+ Norm Civata San. ve Tic. A.Ş., 10007 Sok., A.O.S.B., Çiğli, İzmir, Turkey

Abstract— Use of stainless steel bolts has become widespread due to their high resistance to corrosive environment. However, the widespread use of stainless steel bolts brought together many unknowns in assembly conditions. In particular, there are not many studies present in the literature that concerning the behaviour of stainless steel fasteners under transverse vibration conditions. Within the scope of our work, Junker vibration tests were carried out on M12x1.75x40 A2-70 bolts with a combination of axisymmetric nut, double nut and prevailing nuts which all have a locking mechanism. Then, the vibration loosening rates were compared. In addition, Torque-Clamp load tests on existing bolts were performed to obtain friction coefficients and torque-clamp load graphics. The result of the study shows that stainless bolts and nuts with different mechanical locking mechanisms behave differently under vibrational conditions.

Keywords— Stainless steel; Fastener; Vibration; Loosening; Friction coef.

I. INTRODUCTION

Stainless steel fasteners have a huge range of application area in the industry, especially where the corrosive atmospheres are dominant. Stainless steel fasteners differ in mechanical behaviour from conventional bolts. Exposure of the bolts to vibration which results severe loss of clamp load causing undesired problems. The most frequently encountered problems in fastener industry were the loosening due to vibration because of insufficient clamp loads and breakage due to over torqueing. For this reason, it is necessary to determine as much as possible the torque value at desired clamp load before the assembly operation. Inspection of transvers vibration effects on fasteners has begun with Junker et al. [1]. According to Junker, vibration in transvers direction has a critical role in loosening process. Researches on vibration have continued and it was found that friction coefficient has a key role in loosening processes [2]. Many other studies based on the transvers vibration has been conducted with different combinations of fastener-nut-washers to determine the effects of these on loosening. [3–8]. Researchers mainly focused on finding a mathematical model for describing the behaviour of loosening processes. Nassar and Yang [9], generated a mathematical model which is used for predicting the preload loss in a vibrational condition.

In this study, Junker vibration tests were carried out on M12x1.75x40 A2-70 bolts with a combination of axisymmetric nut, double nut and prevailing nuts which all have a locking mechanism. Then, the vibration loosening rates were compared.

II. EXPERIMENTAL TEST PROCEDURE

In the study three different type of stainless steel nuts, double nut, axisymmetric nut and prevailing nuts, were used. These nuts were mainly used in the industry for providing better loosening solutions in corrosive environment. In the first part of the study, torque tension test were conducted for determining the friction coefficient and preload value for 30 Nm torque. The pictures of each specimen is given in Figure 1. During the tests, only one specimen was used for each test to eliminate the effects of friction coefficient increase after one use. Bolts used for the tests were classified as M12x1.75x40 A2-70 stainless steel bolts.



Fig. 48 M12 x 1.75 x 40 A2-70 fasteners with double nut, axisymmetric nut and prevailing nut

Friction coefficient values were calculated based on the preload value which has been measured during torque-tension tests according to EN ISO 16047:2005, which was given in Equation 1;

$$\mu_{total} = \frac{T/F - P/2\pi}{0,577d_2 + 0,5d_b} \quad (1)$$

In the second part of the study, Junker vibration tests according to DIN 65151 were conducted on stainless steel bolts with nuts. Junker test machine was a special device for

simulating the vibration condition in the bolts which were clamped on the bench with a desired torque. The principle of the test device is based on measuring the preload loss of the clamped fastener under transverse displacement. All fasteners were clamped at a same preload value of 16 kN which was measured in torque tension test for 30 Nm. Junker tests were conducted on 5 different specimens for each nut combination.

III. RESULTS AND DISCUSSIONS

Torque-tension test for double nuts were conducted with 2 step torquing. Firstly, smaller nut which was called as "1.Nut" was torqued at a value of 12 Nm which was the %40 of the desired torque. Secondly, the ticker nut which is called as "2. Nut" was torqued at a value of 30 Nm. The result of the double nut torque tension test was given in Figure 2.

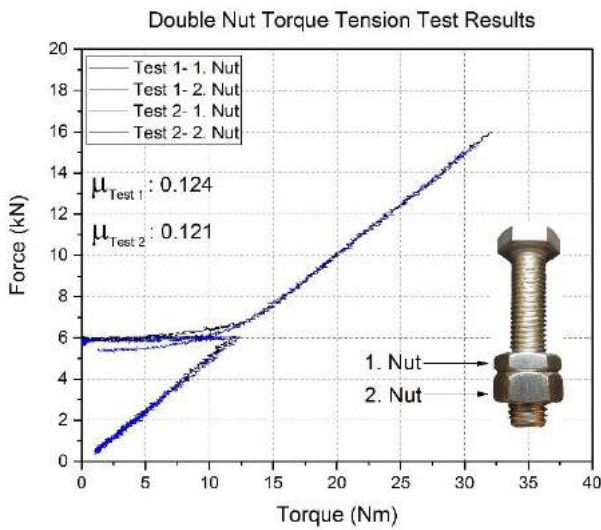


Fig. 2 Double nut torque-tension test results.

According to the test results, friction coefficient was found around 0.12 which was an ideal value for bolts. It was also found that 30 Nm torquing value gives 16 kN clamp load on the fastener. Clamp load values which was then used in the junker vibration test for the starting point. Torque tension test of axisymmetric nuts were also conducted with 2 times torquing. Test result for the axisymmetric nut tests were given in Figure 3.

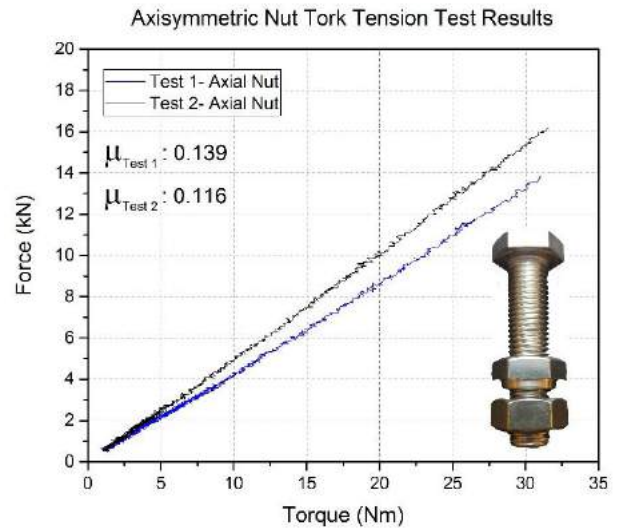


Fig. 3 Axisymmetric Nut torque-tension test results.

According to the test result, it is clearly seen that the clamp load value for 30 Nm was approximately same with the double nut value. Desired clamp load at a same torque value can be only changed by adjusting the friction coefficient in these conditions. The last torque tension were conducted with prevailing nut. The result for prevailing nuts were given in Figure 4.

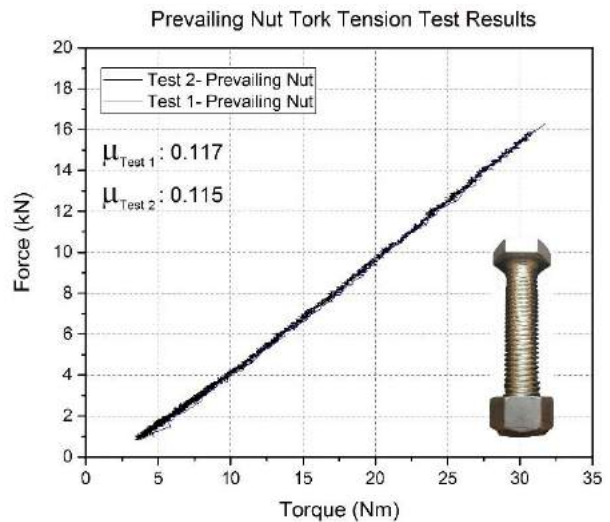


Fig. 4 Double nut torque-tension test results.

Result for the prevailing nut torque tension test showed that the friction coefficient value for all three type nut was between 0.11-0.13 and the clamp force values were between 14-16 kN. For the junker vibration test 15 kN clamp load forces was used as the starting references for all three type of nuts. Junker tests were conducted with 0.9 mm relative displacement at 3 Hz in transverse direction. The preload loss was measured during the test and results were graphically shown in a preload loss-cycle

plot. Five tests were conducted for each nut type and the average values were taken. Test results for double nuts were given in Figure 5.

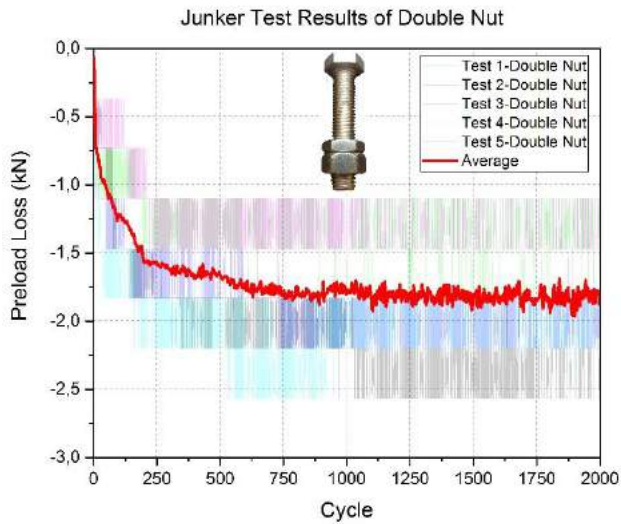


Fig. 5 Double nut Junker vibration test results.

Result of the junker vibration test of double nuts shows that there has been a very sharp preload loss in the first 250 cycle of the test which was seen around 1.6 kN. The lost in 2,000 cycle which is considered as the limit of loosening cycle in junker vibration test was around 2 kN.

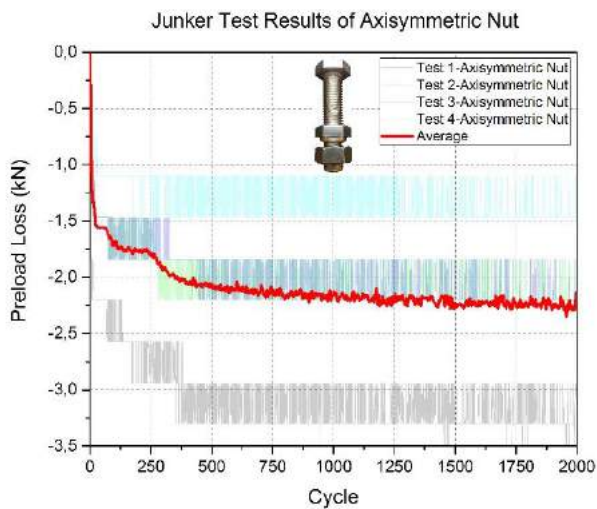


Fig. 6 axisymmetric nut Junker vibration test results.

The result of the axisymmetric nut on junker vibration test given in Figure 6 shows that sudden preload loss also happened in the first 250 cycle with a value of 1.8 kN. The total loss for the nut in 2,000 cycle was around 2.2 kN.

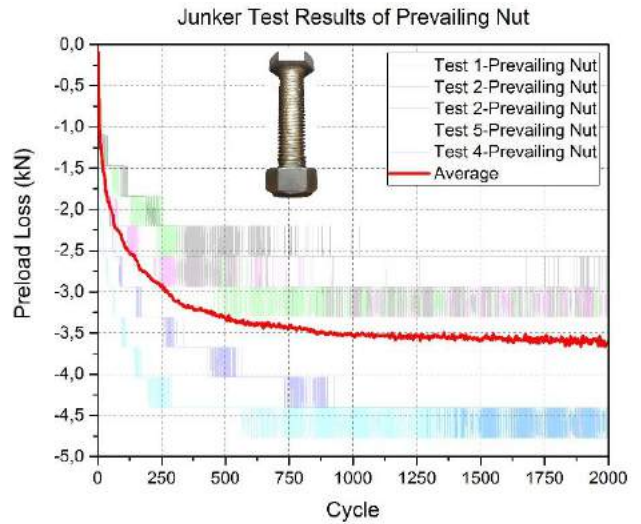


Fig. 7 Prevailing nut Junker vibration test results.

From the test result given in Figure 7, it is clearly seen that the preload loss at the first 250 cycle was around 3 kN. The total loss was approximately 3.5 kN for 2,000 cycle. For understanding the loosening behaviour of both nuts, preload loss averages have been comparatively drawn in the same plot which was given in Figure 8.

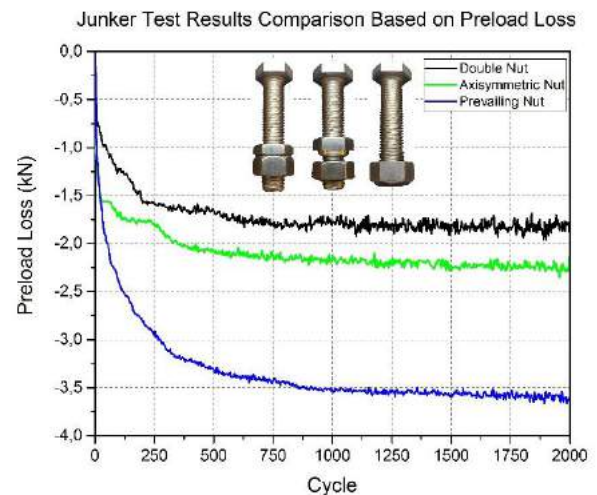


Fig. 8 Junker vibration test preload loss comparison

According to the comparative test results, it was clearly seen that prevailing nut showed the highest loss in preload loss during the junker vibration test in contrast to rest of the nuts. It can be also seen that sudden drop in preload during the test continues up to 500 cycle. As a result of that, it can be concluded that fasteners which has a double nut or axisymmetric nut have higher resistance to vibration loosening.

Conclusions

In this study, vibration loosening performances of stainless steel double nut, axisymmetric nut and prevailing nuts were investigated experimentally and comparative test results based on the preload loss has been given. Torque-tension tests were showed that friction coefficient for all three type bolt-nut combination has approximately the same, ~0.12. Clamp load was found as 16 kN in average for torque value of 30 Nm. Junker vibration tests were showed that all nuts except prevailing nut showed sudden drop in preload during the first 250 cycle of the tests. It was found that prevailing nut has the highest drop in clamp force of 3.5 kN in contrast to double and axisymmetric nuts which were experienced 2 kN and 2.2 kN loss in clamp force, respectively. Experimental study conducted on stainless steel M12x1.75x40 A2-70 bolts and nuts had clearly showed that double nut has the higher vibration resistance among others.

REFERENCES

- [1] G.H. Junker, New Criteria for Self-Loosening of Fasteners Under Vibration, SAE Trans. 78 (1969) 314–335. doi:10.4271/690055.
- [2] T. Hattori, M. Yamashita, H. Mizuno, Loosening and Sliding Behaviour of Bolt-Nut Fastener under Transverse Loading, in: EPJ Web ofConferences 6, 2010. doi:10.1051/epjconf/20100608002.
- [3] P. Gutowski, M. Leus, Tribology International The effect of longitudinal tangential vibrations on friction and driving forces in sliding motion, Tribol. Int. 55 (2012) 108–118. doi:10.1016/j.triboint.2012.05.023.
- [4] G.E. Ramey, Experimental Analysis of Thread Movement in Bolted Connections Due to Vibrations, Res. Proj. NAS8-39131, Auburn Univ. (1995).
- [5] B.A. Housari, S.A. Nassar, Effect of Thread and Bearing Friction Coefficients on the Vibration-Induced Loosening of Threaded Fasteners, 129 (2014). doi:10.1115/1.2748473.
- [6] M. Holland, D. Tran, Effects of Vibration on a Coulomb Friction System, Sch. ACME, Victoria Univ. (2007).
- [7] D.P.Hess, O.P.Keifer, C.B. Moody, Tests on Loosening of Aviation Threaded Fasteners with Different Washer Configurations, J. Fail. Anal. Prev. 14 (2014) 683–689. doi:10.1007/s11668-014-9873-8.
- [8] T. Yokoyama, M. Olsson, S. Izumi, S. Sakai, Investigation into the self-loosening behavior of bolted joint subjected to rotational loading, Eng. Fail. Anal. 23 (2012) 35–43. doi:10.1016/j.engfailanal.2012.01.010.
- [9] S.A. Nassar, A Mathematical Model for Vibration-Induced Loosening of Preloaded Threaded Fasteners, 131 (2009) 1–13. doi:10.1115/1.2981165.

Wear Characteristics of H13 Hot Work Tool Steel at Elevated Temperatures

Zafer Can TEOMAN, Faiz MUHAFFEL, Huseyin CIMENOGLU
Istanbul Technical University, TURKEY
zcanteoman@gmail.com

ABSTRACT

H13 (DIN-X40CrMoV) is one of the well-known steels for utilization at elevated temperatures owing to its good resistance to softening at high temperatures and thermal shock resistance along with a relatively low cost. In the present study, sliding wear performance of H13 hot work tool steel at room and elevated temperatures has been examined against Al₂O₃ ceramic counter-material. Based on the observations and analyses of the contact surfaces, wear track profiles, and friction curves, the role of varying temperatures on the operative wear mechanism has been examined.

Keywords: Hot work tool steel, hardness, elevated temperature, wear resistance

Research and Developments in Iron and Steel Industry

Oguz ISIK, Aslan UNAL, Huseyin SOYKAN
MATIL Material Test and Innovation Laboratories A.S.
oguz.isik@matil.org

ABSTRACT

The iron and steel industry has a big role which is related to development level for countries. Therefore, all over the world, big companies are interested in this industry. Not only production values but also export data is as a key role for countries. Hence, especially in recent years, the concept of innovation has gained importance due to increasing globalization, developments in raw material markets, increasing social consciousness towards the environment and changing competition conditions depending on these developments. For this reason, research and development (R&D) became more important and critic topic especially in developing countries. Turkey has also a significant capacity in this sector thus R&D and innovation should become more important issue for us. According to these facts, major iron and steel production factories, research centres and universities which are focused on steel research are brought together in a big platform which is called European Steel Technology Platform. This platform has developed various policies which are related safer, eco-friendly and more efficient steel production. This review, what has Turkey made up to this time in the scope of R&D studies and discuss the position of turkey in the world when focusing about the concept of innovation. In addition, in this review discuss the importance of R&D for especially in the iron and steel industry according to not only world but also Turkey. This study has also look for answers to a number of questions such as what can be done on the basis of innovative concept for iron and steel industry and which roles the private sector and universities should be in these Research and Development studies. As well as Research and Development itself, a bridge from R&D to innovation and efficient utilizations to approach solution is also reviewed.

Keywords: Research and Development, Iron and Steel, European Steel Technology Platform

The Optimization of the Coating Process Parameters by Electro-Spark Deposition (ESD) Technique Using Steel/Inconel Couple

Mustafa Safa YILMAZ, Kemal KORKMAZ, Ali CAKIR, Cengiz DOGRU
Gebze Technical University
msyilmaz@gtu.edu.tr

ABSTRACT

The aim of the study is searching for the best parameters for St-37 steel surface by Electro Spark Deposition (ESD) method with using Inconel 718 alloy electrode. ESD process was carried out in different voltages (30-62 volt), different frequents (75-130 Hz) and different atmosphere (in air and in silicon oil pool). For varying electrical and ambient conditions, samples were prepared and their coating thickness (9,30 μm - 14,39 μm) and surface roughness (2,043 μm - 5,891 μm) values were measured. The coating thickness was determined higher in the air experiments. Also, thickness and roughness values were increased with the increased voltage, but there were not certain effect of the frequent on thickness and roughness. In addition, SEM images, linear and local EDX analysis, cross-sectional hardness test and XRD analysis were also obtained. It was detected that all coatings have iron-nickel based alloys and CrFe alloy were found in silicon oil pool experiments. Moreover, the cross-sectional hardness tests presented that the coating is two times harder than the steel substrate. By the SEM experiments, it was determine that coating layer had micro pores and good bonding with substrate.

Keywords: Hard Coatings, Novel Coating Materials, Processing and Characterization, Tribology

Unpressurized Gating System Design and Simulation in Sand Casting of Ductile Iron

Atahan Erbul, Ali Serdar Vanli

Componenta Dokumculuk A.S., Engineering Department, Bursa, Turkey
atahan.erbul@componenta.com

Yildiz Technical University, Mechanical Engineering Department, Istanbul, Turkey
svanli@yildiz.edu.tr

Abstract— Casting, one of the oldest manufacturing techniques, is based on the basis of phase changing. Even if there are different types, sand casting is most preferred one. Casting processes have many parameters and due to that for obtaining the products which have the best quality, those parameters should be adjusted as optimal. Simulation is a useful way for determining the optimum values, estimating the risks and avoiding the defect possibilities before the production. Each part is unique and gating systems have to be designed according to part geometry to get better results. In this study, unpressurized gating system design is investigated for ductile iron. Dimensions of the critical areas as the cross-section of the runner and gates which are very important for determining pouring time and liquid metal velocity, are calculated precisely.

Keywords— Sand casting, gating system, simulation, optimization, ductile iron.

I. INTRODUCTION

Casting is the manufacturing technique that has many process parameters. Because of that, meeting the customer requirements is very difficult. In order to reach the desirable quality in casting, well designed gating system is the first step. Dimensions of the gating system's members need to be calculated according to product geometry since each part has different shape and an incorrect design is the root cause of the defects which can be detected on the surfaces or within the parts, mostly. There is a wide variety of casting defects. Shrinkage porosity, gas porosity, sand defects, slag defects, short run and cold shut are the common ones. High molten metal velocity, long pouring time, low permeability, poor feeding system and filtration or incorrect vent placement can cause these kind of defects [1,2]. Therefore, all process should be investigated in detail.

Today, there is a fierce competition between the companies for gaining a place in the market. Therefore, the companies should serve the best at the cheapest cost. Predicting the possible risks before the pouring is important to avoid the defects and decrease the scrap rate. Simulation is helpful way for obtaining that. Basically, a simulation program creates a virtual reality and provides an opportunity to observe the processes before production. It makes the risks detectable and under favour of that, the precautions can be taken, earlier. It reflects on the scrap rate and production cost, positively.

In this study, a gating system is calculated for a cast iron project part and simulations for molten metal velocity, porosity, temperature are run and simulation outputs are evaluated. The tooling which is designed according to data is manufactured and then the production is realized. Visual and x-ray inspections are done and one part is sectioned. Results are compared with the simulation outputs.

II. GATING SYSTEM

Gating system serves different purposes and the most important one is conveying the molten metal into the mold cavity. Choke area is the tightest area of the system and it controls the filling time and liquid metal velocity. There are two types of gating systems according to choke area location. If it is located at the sprue, then this system is called unpressurized gating system. If the choke location is at the gate, it is called pressurized gating system.

Gating system is composed of various parts. Those are pouring basin, sprue and sprue well, runner and gates (e.g. Fig 1). Pouring basin is the first location where the molten metal flows in the mold cavity. Molten metal reaches the sprue after passing through pouring basin. Sprue conveys it to the sprue well. If the system is unpressurized, the velocity and filling time are controlled by the sprue where the choke is.

Sprue well is the place where the flow direction is changed to horizontal from vertical. Besides, it provides a laminar flow to molten metal to avoid sand erosion and air entrapment. Liquid metal flows in runner and then reaches the gates. Since sand erosion that can be occurred during the molten metal flowing in the runner and gates can affect the part quality directly, the liquid metal velocity should be kept under control in those areas.

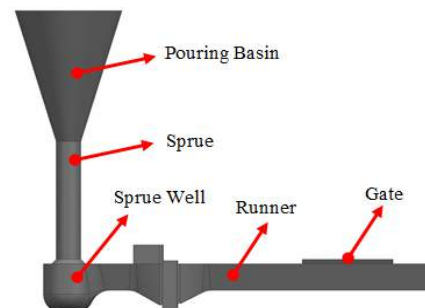


Fig. 49 Schematic drawing of a gating system in sand mold casting

TABLE LXX
REQUIREMENTS OF IDEAL GATING SYSTEM [3]

Requirements	Example
The molten metal velocity should be kept between the critical limits by gating system.	If the velocity is high, it can cause sand erosion and gas entrapment or if the velocity is slow, solidification can start before the cavity is fully filled.
Gating system should be designed optimal in the point of flow rate.	If the system design is not optimal, waste of metal increases and the fettling operations gets harder.
Gating system should provide a laminar flow and minimize turbulence	If the flow is turbulent, it can cause gas entrapment and sand erosion.
The gating system should convey the molten metal to mold cavity and solidify after the part.	If the gating system can't convey the molten metal to mold cavity or it solidifies before the part, metal flow be precluded and the mold cavity does not fill.
Gating system should prevent entry of slag, dross, inclusions to mold cavity.	Slag, dross and inclusions scrap the casting parts.

TABLE II
ADVANTAGES AND DISADVANTAGES OF UNPRESSURIZED GATING SYSTEM [4]

Advantages	Disadvantages
Since the sections are enlarged after choke, liquid metal velocity is lower than pressurized gating system at runners and gates.	Due to the larger gates, fettling operations are more difficult.
Because of the lower velocity, sand erosion possibility is less than pressurized gating system.	During the pouring, whole system has to be kept filled with molten metal until the pouring is done. Because of its difficulty, the gas entrapment possibility occurs.

III. GATING SYSTEM DESIGN

Gating system is to provide a laminar flow for molten metal from ladle to mold cavity and also to avoid the entry of inclusions to mold cavities. Design of the gating system starts with calculation of the choke area.

$$C_A = \frac{22,6 \times W}{\rho \times \xi \times t \times \sqrt{H}} \quad Eq. (1)$$

- C_A: Choke area (cm²)
- W: Total metal weight (kg)
- ρ: Density of liquid metal (g/cm³)
- ξ: Friction factor (dimensionless)
- t: Pouring time (s)
- H: Effective pouring height (cm)

The tables and formulas help to determine the parameters which are needed for calculation the choke area. There are three types of effective pouring height calculation. It depends on part layout in mold. The entire part can be in

drag (e.g. Fig. 2). The 'H' is calculated by the formula which is stated below, in this case.

$$H = h \quad Eq. (2)$$

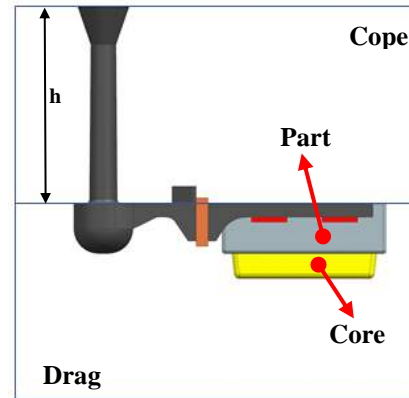


Fig. 2 The part is in drag completely

The entire part can be in cope (e.g. Fig. 3). The 'H' is calculated by the formula which is indicated below, then.

$$H = h - \frac{c}{2} \quad Eq. (3)$$

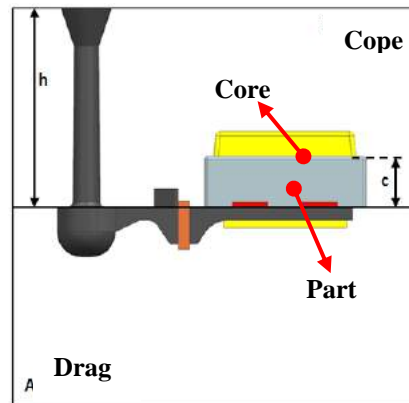


Fig. 3 The part is in cope completely

The part can be in cope and drag (e.g. Fig. 4). To calculate the 'H', the following formula can be used, in the present case.

$$H = h - \frac{a^2}{2c} \quad Eq. (4)$$

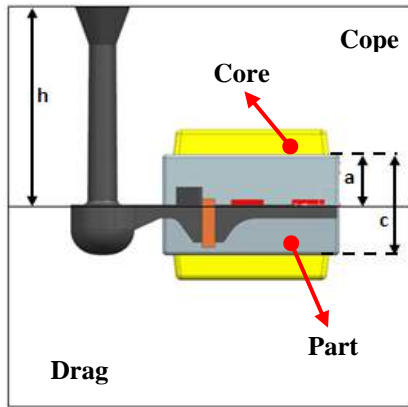


Fig. 4 The part is in cope and drag

Another parameter is pouring time. In order to determine it approximately, the diagram which is shown in Fig. 5 can be used.

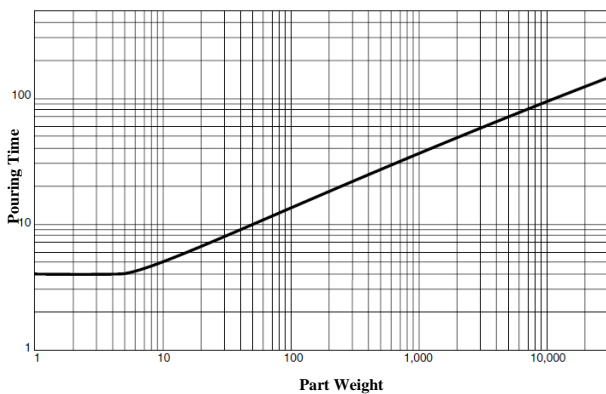


Fig. 5 Part weight – Pouring time diagram [5]

Friction factor is between 0,2 - 0,6 in generally. It depends on mold geometry and metal type [6]. 0,4 is an acceptable assumption. Cast iron is the metal type of this project which is the member of the ferrous alloys. It is one of the most preferred material in casting since its good mechanical properties and low production cost. There are different grades of cast iron and the density parameter depends on material type as known [7-10].

Total metal weight, in another saying gross weight, is connected with the part geometry, gating system design and feeders. After determining the all values, C_A can be calculated by the formula. Cross section dimensions of runner and gates should be calculated after finding C_A . As mentioned before, the sections enlarge from choke to gates. The gating system can be designed according to recommended rates for choke's, runner's, and gate's section areas.

TABLE III
RECOMMENDED RATES FOR SECTION AREAS OF UNPRESSURIZED GATING SYSTEM [4]

Choke	Runner	Gate
1	1,1	1,2
1	1,2	1,6
1	1,5	2
1	2	2

1	3	3
1	4	4

Filtration is needed for production quality. During pouring, sands, inclusions, slag can enter the mold cavity within liquid metal. The filters are used for avoiding this problem. As the others, the filter dimensions have to be calculated according to gross weight and material type (e.g. Tab. 4). Besides that, filter's pore intensity depends on the material fluidity.

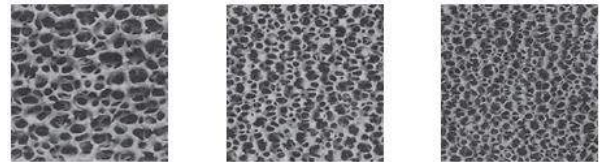


Fig. 6 10 ppi – 20 ppi – 30 ppi filters' images [6]

TABLE IV
FOSECO FILTER CHARACTERISTICS ACCORDING TO MATERIAL TYPE [6]

Material	ppi	Filtration Capacity (kg/cm ²)
Ductile Iron	10	1,5
Grey Iron	20	4
Malleable Cast Iron	30	4

Filter section area is calculated with the formula which is stated below.

$$A_{filter} = \frac{W}{n \cdot fk} \quad Eq. (5)$$

- A_{filter} : Filter section area (cm²)
- W: Gross weight (kg)
- n: Filter quantity (dimensionless)
- fk: Filtration capacity (kg/cm²)

IV. GATING SYSTEM DESIGN OF PROJECT PART

This project is supported by Componenta Dokumculuk A.S. and planned according to Componenta production lines. The project part is chosen as differential housing (e.g. Fig. 7.) The part weight is 23 kg and its material is EN-GJS-450-10 [11]. That material is ductile iron grade.

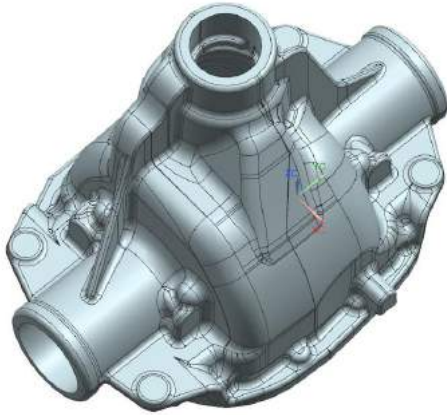


Fig. 7 The project part

Componenta Dokumculuk A.S. has several production lines and these have different dimensions and pouring basin geometries (e.g. Fig. 8). According to the part geometry and weight, line 3 is chosen as a production line. As shown in Fig. 9, the layout is with two cavities.



Fig. 8 The pouring basing geometries of Line 7 - 6 - 3 - 2, respectively

To determine the gross weight approximately, a rough gating system design is required. It is created by CAD software (e.g. Fig. 9).



Fig. 9 The rough gating system design

The gross weight can be calculated by CAD software. But the density value has to be inputted to the program, firstly. The part material is EN-GJS-450-10 [11] as stated before. Its density value is 7,1 gr/cm³. The gross weight equals to 62,5 kg according to the result (e.g. Fig. 10).

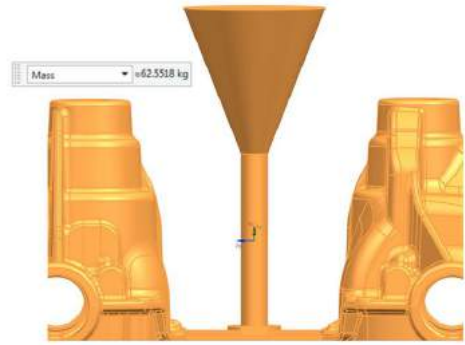


Fig. 10 The gross weight

Determination of the parting line is important for calculation of the effective pouring height. According to the part design (draft angles etc.), the parting line is as shown in Fig. 11. And it seems that the part is in drag and cope.

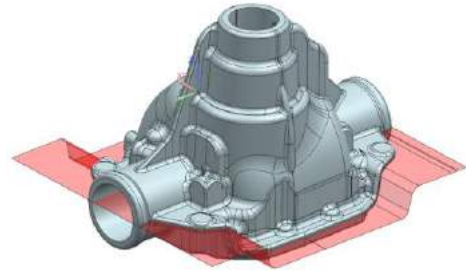


Fig. 11 The parting line

To calculate the effective pouring height, h , a and c dimensions have to be determined. According to the measurement results from CAD data, ' c ' dimension is measured 279 mm and ' a ' dimension is measured 265 mm. The ' h ' dimension is the cope height. And the cope height is 360 mm for Line 3 at Componenta Dokumculuk A.S.. After determining the required dimensions, the ' H ' can be calculated.

$$H = h - \frac{a^2}{2c} = 360 - \frac{265^2}{2 \times 279} = 234 \text{ mm} = 23,4 \text{ cm} \quad \text{Eq. (6)}$$

$$\sqrt{H} = \sqrt{23,4 \text{ cm}} = 4,83 \text{ cm} \quad \text{Eq. (7)}$$

Another parameter pouring time can be determined from the Part weight - Pouring time diagram as shown in Fig. 5. According to 62,5 kg gross weight, the pouring time is found about 11 s, if the lines that are plotted from the values are intersected. The friction factor value can be considered as 0,40. As stated before, this value is acceptable assumption for this project. Density of EN-GSJ-450-10 [11] is 7,1 gr/cm³. Since all the parameters are ready, C_A (e.g. Fig. 12) can be calculated now.

$$C_A = \frac{22,6 \times 62,5}{7,1 \times 0,4 \times 11 \times 4,83} = 9,36 \text{ cm}^2 \quad \text{Eq. (8)}$$

$$9,36 \text{ cm}^2 = 936 \text{ mm}^2 \quad \text{Eq. (9)}$$

$$936 = r_{sprue}^2 \times \pi \quad \text{Eq. (10)}$$

$$r_{sprue} = 17,26 \text{ mm} \approx 17 \text{ mm} \quad \text{Eq. (11)}$$

1:1,2:1,6 rate is used to calculate section areas of gating system. This rate depends on the designer. It can be selected different. 'R_A' is the section area value of the runner and 'a_R' is the length of short base of trapezoid (e.g. Fig. 13).

$$C_{A,pattern} = r_{sprue,pattern}^2 \times \pi \quad \text{Eq. (12)}$$

$$C_{A,pattern} = 17^2 \times \pi = 907,9 \text{ mm}^2 \quad \text{Eq. (13)}$$

$$R_A = C_{A,pattern} \cdot 1,2 = 907,9 \cdot 1,2 \approx 1089,4 \text{ mm}^2 \quad \text{Eq. (14)}$$

$$1089,4 = \frac{(a + 2a) \cdot 2a}{2} = 3a^2 \quad \text{Eq. (15)}$$

$$a_R \approx 19 \text{ mm} \quad \text{Eq. (16)}$$

As defined 'G_A' is the total section area value of the gates. The gates' dimensions are considered as same. Therefore, the total area is divided by four to find one of them (e.g. Fig. 14).

$$G_A = C_{A,pattern} \cdot 1,6 = 907,9 \cdot 1,6 = 1452,6 \text{ mm}^2 \quad \text{Eq. (17)}$$

$$MG_{A,1} = MG_{A,2} = MG_{A,3} = MG_{A,4} \quad \text{Eq. (18)}$$

$$\frac{1452,6}{4} = 363,1 \text{ mm}^2 \quad \text{Eq. (19)}$$

Dimensions of the gate are determined 8 mm and 45 mm according to consideration of section area value and optimization of the fettling operations. After the simulations, these dimensions can be optimized if any risks are detected.

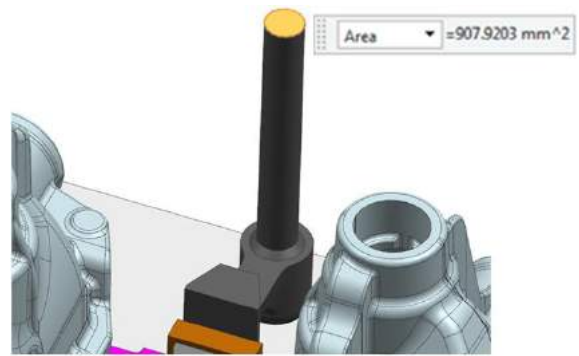


Fig. 12 Measurement of choke area

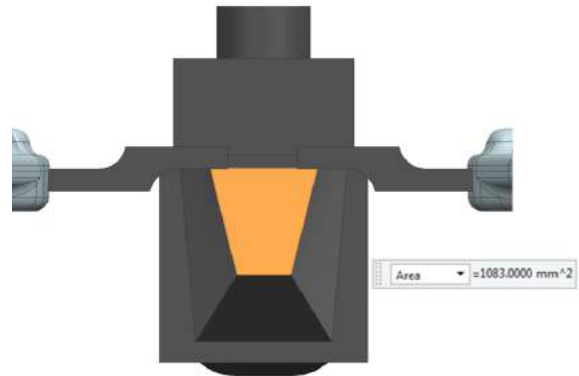


Fig. 13 Measurement of runner section area

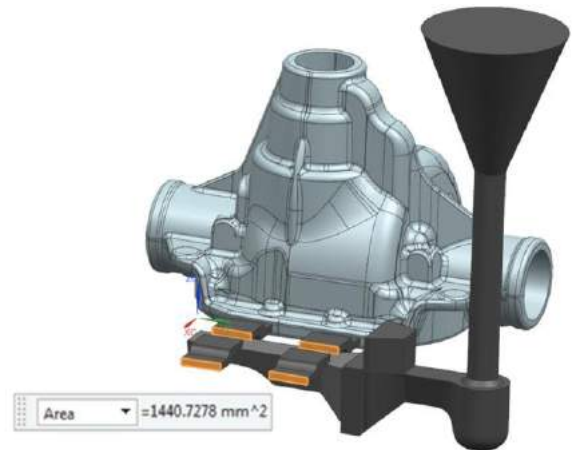


Fig. 14 Measurement of gates section areas

Another decision that has to be taken is filter type. The filter selection is made according to following formula. A_{filter} value gives an idea about the minimum limit of filter section area that should be. According to result, a proper filter should be chosen from the related catalog. In this project, Foseco Sedex 75x75x22 mm filter is used. But it can be changed due to tight layout or high slag possibility.

$$A_{filter} = \frac{62,5}{1,1,5} \approx 41,6 \text{ cm}^2 \quad \text{Eq. (20)}$$

$$A_{filer} = 4160 \text{ cm}^2 < 75 \times 75 \\ = 5625 \text{ mm}^2 \quad \text{Eq. (21)}$$

V. SIMULATION OF THE PROJECT PART

The gating system is created by CAD software according to calculations. The simulation is run with the CAD data. MAGMA 5.2 is used in this project as simulation software. Before running simulations, some basic adjustments have to be made. These basic adjustments are alloy type, process mode, sand type, pouring temperature and material type. In addition, the program has to be calibrated according to foundry conditions for getting accurate results. By the way, the chemical composition can be adjusted if a specific study is required. In this project, adjustments are as shown below.

- Alloy type: Iron alloys
- Process mode: Sand mold casting
- Sand type: Green sand
- Pouring temperature: 1400 °C
- Material: EN-GJS-450-10 [11]

According to Fig. 15, the velocity values are about 1 m/s. The velocity value is important for erosion but at this velocity there is no risk detected. According to Fig. 16, cold shut risk is detected because the purple colored areas stay cold during solidification. According to Fig. 17, porosity risks are detected for several areas.

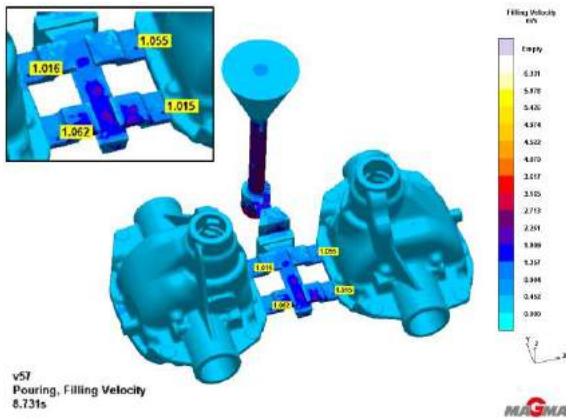


Fig. 15 Molten metal velocity at the gates

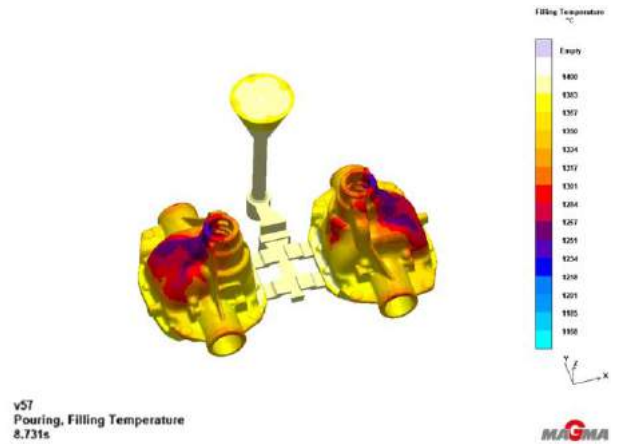


Fig. 16 Filling temperature

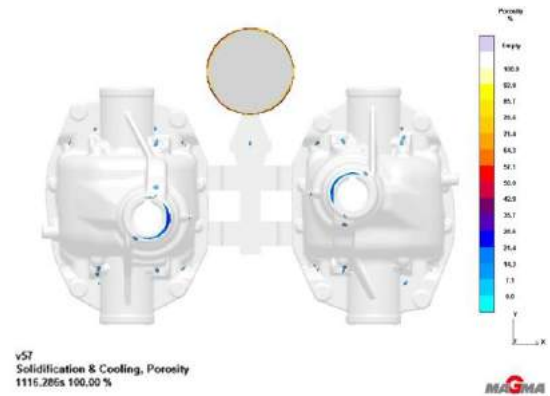


Fig. 17 Porosity

VI. PRODUCTION AND SCRAP ANALYSIS

Production is realized for 5 boxes / 10 parts according to conditions which are determined before (e.g. Fig. 18, 19). The cold shut defect is detected during the scrap analysis (e.g. Fig. 20). After the production of 10 pieces, whole parts are investigated with X-ray (e.g. Fig. 21) and one of them is sectioned (e.g. Fig. 22). Investigations show that the simulation overlaps with the results of production. Cold shut defects are detected on the area which is predicted by simulation. In addition, the CC3-4 level [12] shrinkage porosities are observed with x-ray and after sectioning (e.g. Fig. 23). The locations of the porosities are estimated by simulation, precisely.

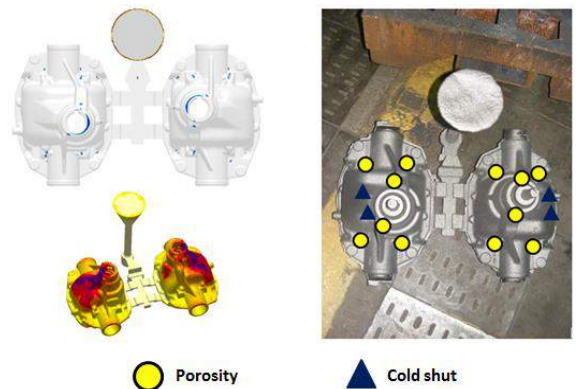


Fig. 18 Comparison of the simulation and production results

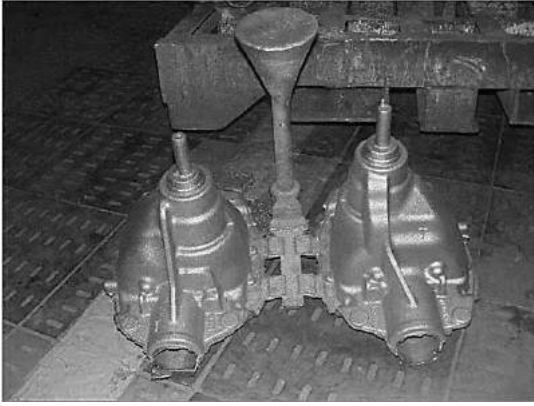


Fig. 19 The parts with gating system after production



Fig. 20 Cold shut

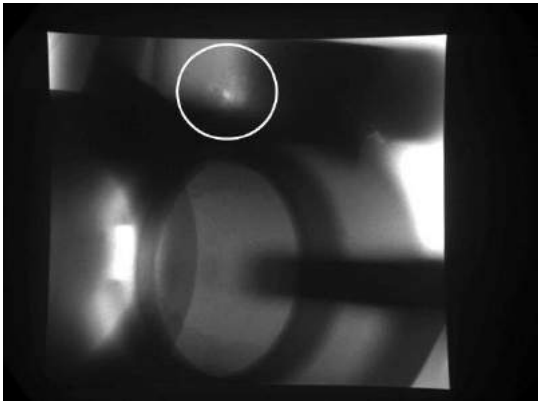


Fig. 21 X-ray image



Fig. 22 The part section

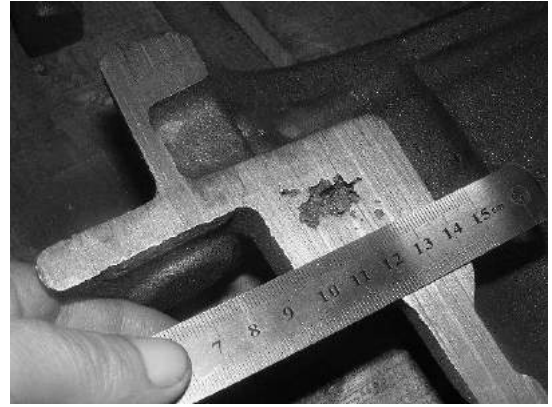


Fig. 23 The part section

VII. CONCLUSIONS

According to the comparison of the results, the well calibrated simulation software estimates the possible defects before the productions. It creates opportunities to avoid wasting of material, energy, time etc. Besides that, it enables to find solutions quickly for improving the current processes.

For this case, to find a solution for shrinkage porosity, a feeding system is needed. According to part geometry and consideration of fettling operations, risers or side feeders can be chosen. Besides, to avoid the cold shut, pouring temperature can be increased and/or another gate which can keep warmer to the cold area can be added the system but simulation results which is run with new inputs should be checked and repeated until the results are satisfying.

ACKNOWLEDGMENT

Authors are thankful to "Componenta Dokumculuk A.S." for their support to put in practice this project.

REFERENCES

- [1] AFS, *Döküm Hataları Atlası*, İstanbul, Türkiye: Tüdoksad, 1999.
- [2] AFS, *Analysis Of Casting Defects*, Chicago, USA, 1947.
- [3] ASM International, *ASM Handbook Volume 15 Casting*, Ohio, USA, 1998.
- [4] N.S. Demircioğlu, *Dökümcülük ve Modelcilik Teknolojisi 1*, Ankara, Türkiye: Pozitif Matbaacılık, 2013.
- [5] Rio-Tinto Iron and Titanium Inc., *Ductile Iron: The Essentials Of Gating And Riser Design*, Montreal, Canada, 2000.
- [6] J.R. Brown., *Foseco Foundrymen's Handbook*, London, England: Butterworth, 2000.
- [7] E.N. Çavuşoğlu, *Döküm Teknolojisi 1*, İstanbul, Türkiye: İTÜ Gümüşsuyu Matbaası, 1981.
- [8] A. Odabaşı, *Kokil ve Kum Kalıba Döküm Yöntemleriyle Üretilen Yüksek Kromlu Beyaz Dökme Demirlerin X-ışınları ve Taramalı Elektron Mikroskobu Çalışmalarıyla Karakterize Edilmesi*, Yüksek Lisans Tezi, İTÜ Fen Bilimleri Enstitüsü, İstanbul, Türkiye, 2004.
- [9] J.R. Davis, *ASM Speciality Handbook Cast Irons*, Ohio, USA: Materials Park, 1996.

- [10] C. Bodsworth, *British Iron and Steel AD1800-2000 and Beyond*, London, England: IOM Communications, 2001.
- [11] EN 1563:2011, *Founding - Spheroidal graphite cast irons*, European Standard, 2011.
- [12] ASTM E446-15, *Reference Radiographs for E446 Steel Castings Up to 2 in. (51 mm) in Thickness - Vol II + Active Standard*, ASTM International, West Conshohocken, 2015.

Effect of Nb Content on Microstructure and Mechanical Properties of Nb-V Added Microalloyed Steel Produced By Powder Metallurgy Method

^{1*}Mehmet Akif ERDEN, ²Ferhat KAHVECİGİL, ²Özkan KARAOĞLU

^{1*}Corresponding Author Karabük University, Karabük TOBB TS Vocational School, Karabük, 78050, Turkey, makiferden@karabuk.edu.tr

²Karabük University, Department of Manufacturing Engineering, Karabük, 78050, Turkey, ferhatkahvecigil@gmail.com, ozkankaraoglu94@gmail.com

Abstract— In this work, the effect of Nb content on the microstructures and tensile behaviors of Nb-V added microalloyed powder metallurgy (PM) steels were investigated. The samples were pressed at 700 MPa and sintered at 1400°C temperature in argon atmosphere for 1 hour. Nb-V added PM microalloyed steels with different niobium ratio were analyzed by tensile test. The microstructure of the PM steels was characterised by optic microscope. Results indicated that 0.075 wt. % Nb added PM steel showed the highest values in yield strength (YS) and ultimate tensile strength (UTS). However, when the amount of Nb content increased from 0.075 to 5 wt.%, yield strength and ultimate tensile strength decreased. Elongation also tends to decrease with increasing Nb content.
Keywords— Powder metallurgy, powder metallurgy steels, Nb-V, Microstructure.

I. INTRODUCTION

The tendency to produce new materials for specific purposes has been increasing because no simple material is able to meet the needs which have risen up in the last 20 years [1]. Microalloyed steels are the material group having superior properties such as; high strength and toughness, low ductile-to-brittle transition temperature, excellent weldability and corrosion resistance which are obtained by applying various hardening mechanisms and proper thermomechanical procedures. The main roles of microalloying elements are to refine the grain size, prevent recrystallization and facilitate precipitation hardening. The effect of microalloying elements on the grain boundary movement and recrystallization is a result of carbo-nitride precipitates [1-5]. One of the features of the microalloyed elements is that they restrict grain size by formed carbide and nitride during the austenitizing or sintering process. NbC(N) and VC(N) are the microalloying precipitates which decrease the grain size and increase the toughness.

Powder metallurgy (P/M) paves the way for the economical production of high quality and sophisticated tools. This production method turns the metal powders that are different in size, shape and packaging features into resistant, precise and high performance tools [6]. A great proportion of the microalloyed steels are produced as flat and tube products and in the recent years, along with

microalloyed steels for forging purpose. Although it is not at the desired level, microalloyed steel is produced with powder metallurgy method [7-8]. Certain studies are available in the literature about the relationship between the production of PM steel and microstructure mechanical properties. For instance, Erden et al. produced Ti and V microalloyed steel with PM method. They carried out the sintering process at 1150°C for 60 minutes and confirmed that yield strength and tensile strength increase as Ti and V ratios (% 0,1- % 0,2) increase. They based it on the formation of precipitates like TiC(N) and VC(N) during the sintering and post-sintering cooling period [1-2].

In the present study, PM steel has been produced in the targeted compound by adding different proportions of Nb into the Fe matrix with the powder metallurgy method and the output microstructural mechanical features have been compared.

II. EXPERIMENTS

In this investigation the effect of the Nb's amount, added in different proportions, on microstructural and mechanical properties is investigated. Fe, V, graphite and Nb powders by Aldrich were used. The size of graphite, iron, niobium and vanadium powders were <20, ≤180, <45, and <44 μm, respectively. These powders were supplied by Aldrich. The purities of graphite, Fe, Nb and V are 96.5 %, 99.9 %, 99.8 % and 99.5 %, respectively. Before the mixing process, powders were prepared in the proportions given in Table 1 by weighing by a digital scale having 0.0001 g precision. The powders was mixed in an industrial conic mixer for 1 h. Steel is produced by mixing the chemical compounds given in the Table 1. Tensile test is made on the produced samples after microstructural characterisation. The results are compared. After mixing homogeneously, the powders were pressurized under 750 MPa unidirectionally with Hidroliksan brand device which has 96-ton pressure capacity. Samples of the tensile experiments were turned into blocks by squeezing with the mould prepared according to ASTM (E 8M) standards of powder metal material tension sample.

TABLE I CHEMICAL COMPOSITIONS OF POWDER METAL STEELS

Compound	Graphite (%wt.)	Nb (%wt.)	V (%wt.)	Fe (%wt.)
Alloy 1	0.45	-	-	Rest
Alloy 2	0.45	0.05	0.075	Rest
Alloy 3	0.45	0.075	0.075	Rest
Alloy 4	0.45	0.1	0.075	Rest
Alloy 5	0.45	0.5	0.075	Rest
Alloy 6	0.45	3	0.075	Rest
Alloy 7	0.45	5	0.075	Rest

The pressed samples were sintered in argon atmosphere at 1400 °C for 1 hour. After sintering, density and pore values were measured. The sintered samples were subjected to standard metallographic procedures. Having sintered at 1400 °C, the microstructures of the PM steel were examined under a Nikon Epiphot 200 optical microscope with X50-X1000 zoom capacity. Tensile test was carried out at 1 mm/min crosshead speed with a Shimadzu tensile testing device with 50 KN capacity. The yield strength (% 0.2), tensile strength and % (percentage) values of elongation of the tensile test samples were determined. Vickers hardness value was determined by applying 0.5 kg weight on a Shimadzu unit hardness device. The density of the samples was determined according to Archimedes' principle. Likewise, the pearlite proportions of the powder metal steels were calculated using Gladman and Woodhead's metallographic point counting method [11]. Along with it, NbC, NbN, VC and VN precipitates were detected with the help of the point and line EDS.

III. RESULTS AND DISCUSSIONS

III.I. MICROSTRUCTURE RESULTS

The microstructural images of the samples are demonstrated in the Figure 1. As can be seen from the figure, the structure contains ferrite and pearlite phases in the whole alloy. Microstructure images given in Figure 1 shows that there are pores in the grain borders. Although it is stated that porosity affect the strength of many materials negatively, it is also reported that tiny and spherical pores do not reduce the strength [12-13].

It is inferred from the images of microstructure that as the proportion of the Nb in the samples increases, the grains get smaller gradually. It is observed that the average grain size becomes larger in the alloy that contains 0.1 % Nb. For instance, the size of the grain decreased to 25.8 μm and 24.22 μm respectively with 0.1 and 0.2 percentage of weight increase in the amount of the Nb while the average size of grain in the non-alloyed PM steel sample in the Fe+0.25C compound is 29.7 μm. It is observed to be 27.16 μm when the amount of Nb is calculated as 3% by weight.

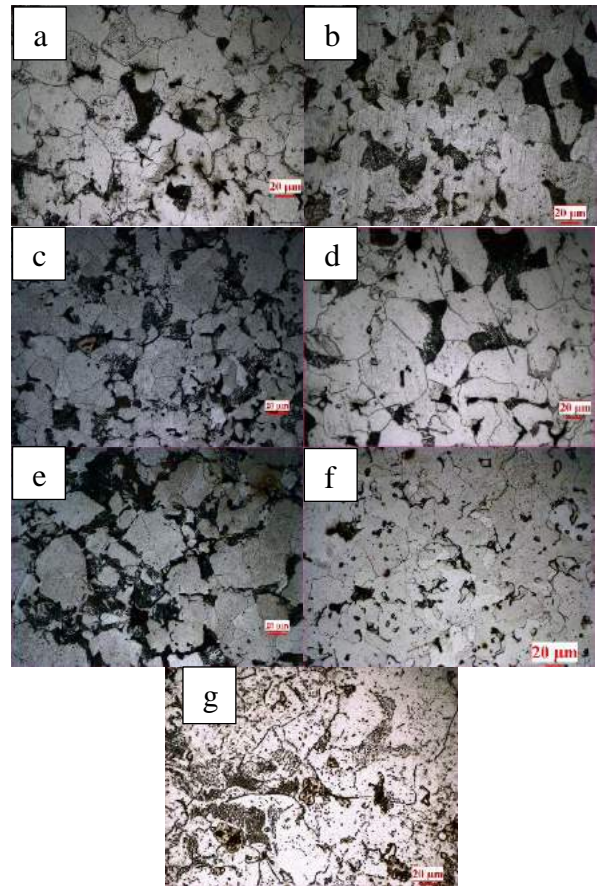


Fig. 1 Micrographs of PM steel specimens (500 x). (a) Alloy 1, (b) Alloy 2, (c) Alloy 3, (d) Alloy 4, (e) Alloy 5, (f) Alloy 6 and (f) Alloy 7.

TABLE II RELATIVE DENSITY, MEAN GRAIN SIZES AND VOLUME FRACTIONS OF PEARLITE PHASES IN PM STEEL SPECIMENS

Alloy	Relative Density (%)	Porosity (%)	Pearlite (%)	Grain Size (μm)
Alloy 1	91.11	8.89	30	49
Alloy 2	92.43	7,57	33	39
Alloy 3	93.26	6,74	50	33
Alloy 4	92.46	7,54	37	51
Alloy 5	90.64	9,36	37	48
Alloy 6	88.74	11,26	36	48
Alloy 7	90.37	9,63	21,94	50

In the Table 2, it is seen that the average grain size decreases with a 0.075 % increase in the proportion of the Nb. This situation takes place when NbC, NbN, VC, VN, VC(N) and NbC(N) precipitates that formed during the sintering process prevent the austenite grains from getting bigger. One of the properties of microalloyed elements is that they restrict grain size by forming carbide and nitride in the austenitizing or sintering processes. Formation of small precipitates during the austenitizing process prevents austenite grains from growing and leads to the development of small ferrite grains [3-12].

It is observed that the average grain size increases slightly with an increase in Nb amount from 0.075 % to 5 %. This can be attributed to formation of large

precipitates within the grain boundaries [12-14]. These large precipitates lead to an increase in the average size of the grains as they cannot restrict grain size sufficiently.

III.II. Mechanical properties

While Figure 2 shows the stress-strain diagrams of the sintered samples, Table 3 shows the yield strength, tensile strength, percentage elongation and hardness results. The yield and tensile strength with the percentage elongation and hardness values are observed to increase when Nb proportion increases to %0.075. Being formed by the niobium and vanadium, the carbide, nitride and carbonitride precipitates ensure the material to be small grained by way of restricting the size of the austenite grain and re-crystallisation of the austenite. Resistance to dislocation movement is increased by increasing grain boundaries in the small grained structure. The decrease of the grain size also contributes to the percentage elongation of the material. Along with these, the formed precipitates contributed to the increase in the yield and tensile strength via various strength increasing mechanisms like precipitation hardening and dispersion hardening [1-3; 11-14].

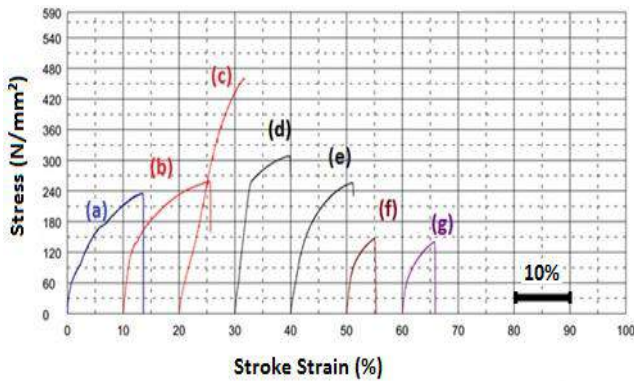


Fig. 2 Variation of stress–strain curves of PM steel specimens (a) Alloy 1, (b) Alloy 2, (c) Alloy 3, (d) Alloy 4, (e) Alloy 5, (f) Alloy 6 and (f) Alloy 7.

TABLE III MECHANICAL PROPERTIES OF SINTERED PM STEEL AND MICROALLOYED PM STEELS

Alloys	Yield Strength (MPa)	Ultimate Tensile Strength (MPa)	Elongation (%)	Hardness Hv0.5
Alloy 1	137	240	14	83
Alloy 2	179	260	16	95
Alloy 3	270	460	12	133
Alloy 4	250	309	10	118
Alloy 5	155	257	11	100
Alloy 6	90	147	5	75
Alloy 7	69	141	6	71

It is thought that Nb(N) and VCN like precipitates lead to development of small austenite grains by restricting the

grain size during the sintering process, thereby improving the resistance of the material. Similarly, Erden et al. [1-2] produced Ti microalloyed steel with PM method. They conducted the sintering process at 1150 °C for 60 minutes and determined an increase in the yield and tensile strength as the proportion of V (% 0,1-% 0,2) rises. The author demonstrates in the study that VC(N)-like precipitates lead to the development of small austenite grains by restricting the grain size during sintering and as a result of this, the resistance of the materials improves. In the other studies [11-14], it is stated that the carbide and nitrite formed in the microalloyed steels lead to an increase in the toughness and strength. In the same study, it is pointed out that solid solution hardening remains at low percentage because of the precipitation of carbide and nitrite [1-3]. In addition, presence of NbC, NbN, VC, VN, VC(N) and NbC(N) in steel at a high proportion makes the material brittle and leads to the decrease of strength by causing over-hardening of the precipitate.

III.III. SEM-EDS Analysis

It is determined from the SEM image that the sample given in Figure 3 containing 0.075 % of Nb results in different sizes of precipitates. In addition, the analysis results of the point EDS show that Nb VC(N) precipitates form because these precipitates contain niobium, vanadium, carbon and nitrogen and that Fe₃C precipitates form because they contain iron and carbon. It can be said that these formed precipitates restrict the growth of austenite grain size, re-crystallization and improve the strength of the material with precipitation hardening [11-14].

The effect of the microalloying elements in precipitates on the re-crystallization of the austenite is not much. The prevention of the grain boundary movement via the precipitated grains is more than that of the dissolved atoms [11-16].

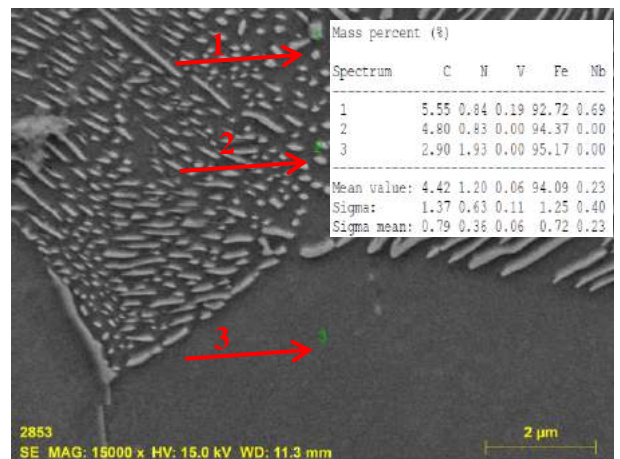


Fig. 3 SEM micrograph Alloy 3 and corresponding EDS of the indicated points.

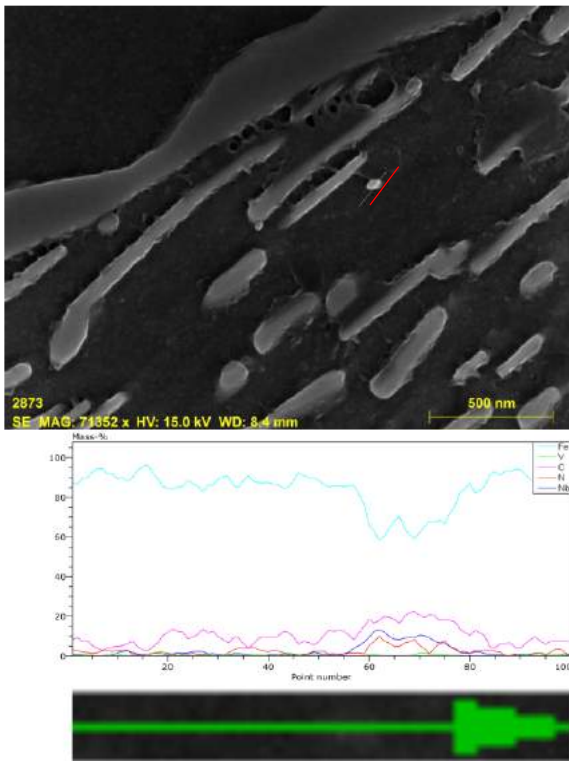


Fig. 4 SEM micrograph for Alloy 3 sintered at 1400 °C and EDS line scan of the indicated particle.

Figure 4 shows the line EDS analysis results that were taken from the matrix and precipitates of the 0.075 % of Nb including PM steel sample which was sintered at 1400 °C. When the results of the line EDS analysis of 0.075 % of Nb including PM steel are examined, it is observed that there is a difference in the element type and amount along the stripe that cut the matrix and the precipitate. It is determined that matrix phase is iron-rich but round-shaped precipitate is niobium-rich. In addition, when the stripe which comes from the matrix cuts the sediment, there has been a sharp increase in the amount of niobium. The results of the point and line EDS analysis that were obtained in this investigation demonstrates that the precipitates like NbCN and VCN develop in the titanium PM steels.

IV. CONCLUSION

The non-alloyed and Nb-V alloyed PM steel which has seven different volume ratios (0–0.05 – 0.075–0.1 – 0.5–3 Nb % and 5 Nb %) is produced by cold pressing and sintering at the argon environment and the following results are obtained from this study.

Composite materials which contain Nb, V and Fe matrix can be produced with powder metallurgy. Solid solution hardening and precipitation hardening which arise during the sintering process or after-sintering cooling process increase the resistance of the steel.

Composite materials that are added 0.05 -and 0.075 % Nb by weight compared to non-alloyed steels showed smaller grain structure. This situation stems from the restriction of

grain size by the carbide and nitrite which alloy elements has created.

Usually, there has been an increase in the yield strength, tensile strength, percentage (%) elongation and hardness values of the compounds which have Nb ratio by 0.075 % as the alloy ratio rises. This situation is a result of the development of the precipitates like NbCN during sintering process and after-sintering cooling process. These precipitates lead to the creation of small austenite grains by preventing grain size and thus improving the resistance of the materials.

After-sintering density of the nonalloy and Nb-V added alloyed steel is observed to be generally at about 92 %. After-sintering density of the produced PM steels showed a little increase.

The strength of the steels gets lower when the amount of Nb is more than 5 % by weight. This indicates that like VC, NbC precipitates are present in the grain boundary as well as in the grain and caused excessive hardening and brittleness.

SEM and EDS analyses show that VC, VN, VCN, NbC, NbN and NbCN occurred in the NbC added PM steels. These different precipitates formed affect the mechanical properties of the PM steels.

ACKNOWLEDGMENT

This work was supported by Scientific Research Projects Coordination Unit of Karabük University. Project Number: KBÜ-BAP-15/2-KP-058.

REFERENCES

- [1] M. A. Erden, S. Gündüz, M. Türkmen, H. Karabulut, "Microstructural characterization and mechanical properties of microalloyed powder metallurgy steels", *Materials Science and Engineering: A*, vol. 616, pp. 201-206, August 2014
- [2] M. A. Erden, S. Gündüz, M. Türkmen, H. Karabulut, "The Effect of V Addition on the Microstructure and Mechanical Properties of Low Carbon Microalloyed Powder Metallurgy Steels", *Materials Testing*, vol. 58(5), pp. 433-437, May 2016
- [3] M. A. Erden, "Effect Of Pressing Pressure On Microstructure And Mechanical Properties Of Non-Alloyed Steels Produced By Powder Metallurgy Method" *Omer Halisdemir University Journal of Engineering Sciences*, vol. 6(1), pp. 257-264, Jan. 2017
- [4] A. Kaçal, M. Gülesin H. B. Ulaş "System Design And Manufacturing For Measurement Of Cutting Forces In Gear Hobbing Process", *J. Fac. Eng. Arch. Gazi Univ.*, vol. 23(4), pp. 795-800, Sept. 2008.
- [5] T. Gladman, *The physical metallurgy of microalloyed steels*, *The Institute of Materials*, England, 1997
- [6] M. A. Erden, H. Gökçe, "The Effect of Sintering Atmosphere on Mechanical Properties of Nb V Bsaed Microalloy Steels Produced by Powder Metallurgy Method", *Sylwan*, vol. 160(8), pp. 362-375, August. 2016
- [7] A. G. Kostyryzhev, A. Al Shahrani, C. Zhu, J. M. Cairney, S.P. Ringer, C. R. Killmore, E. V. Pereloma "Effect of niobium clustering and precipitation on strength of an NbTi-microalloyed ferritic steel", *Mater. Sci. Eng. A*, vol. 607, pp. 226-235, Oct. 2014
- [8] M. A. Erden, "The Effect of Ni on the Microstructure and Mechanical Properties of Nb V Microalloyed Steels Produced by Powder Metallurgy", *Sylwan*, vol. 160(10), pp. 362-375, Oct. 2016
- [9] A. M. Sage, "An overview of the use of mikroalloys in hsla steels with particular reference to vanadium and titanium, processing,

- properties and applications”, *Proceedings of the Second International Conference on HSLA Steels*, p. 51, May 1992
- [10] M. A. Erden, Effect of C Content on Microstructure and Mechanical Properties of Nb-V Added Microalloyed Steel Produced by Powder Metallurgy Method”, *European Journal of Science and Technology* Vol. 5, No. 9, pp. 44-47, December 2016
- [11] T. Gladman, and J. H. Woodhead, “The accuracy of point counting in metallographic investigations”, *Journal of the Iron Steel*, vol. 194, pp.189, Jan. 1960
- [12] M.A. Erden, 2015. An Investigation On the Relation Between Microstructure and Mechanical Properties of Microalloyed Steels Produced by Powder Metallurgy, PhD. Thesis, Institute of Science and Technology, Karabuk University, Karabuk, Turkey
- [13] S. Sarıtaş, M. Turker, N. Durlu, Powder Metallurgy and Particulate Materials Processing, Turkish Powder Metallurgy Association, 2 nd ed., Ankara, 2007
- [14] C Schade, T. Murphy, A. Lawley, R. Doherty “Microstructure and mechanical properties of microalloyed PM steels”, *Int. J. of Powder Metall.*, vol. 48, pp. 51-59, April 2012
- [15] R. D. K. Misra, K. K. Tenneti, G. C. Weatherly, G. Tither, “Microstructure and texture of hot rolled Cb-Ti and V-Cb microalloyed steels with differences in formability and toughness”, *Metall. Mater. Trans. A*, vol. 34A, pp. 2341, 1 Oct. 2003
- [16] M. A. Erden, E. Özkurt, A. N. Tanrıverdi, A. Yılmaz, M. Türkmen, H. Karabulut, S. Gündüz “Investigation Of The Effect Of Carbon Content On Microstructure And Mechanical Properties Of AlC Added Powder Metallurgy Steels” *Technological Applied Sciences*, 11(4), 139-145, Oct. 2016

Effect of Cr Content on Microstructure and Tensile Strength Properties of Cr Added Steel Produced By Powder Metallurgy Method

¹*Mehmet Akif ERDEN, ²Rıfat GÜNDÜZ

*1**Corresponding Author Karabük University, Karabük TOBB TS Vocational School, Karabük, 78050, Turkey, makiferden@karabuk.edu.tr

*2*Karabük University, Department of Manufacturing Engineering, Karabük, 78050, Turkey, rgunduz1649@gmail.com

Abstract— In this work, the effect of Cr content on the microstructures and tensile behaviors of nonalloyed powder metallurgy (PM) steels were investigated. The samples pressed at 700 MPa and sintered at 1400°C temperature in the sintering argon atmosphere for 1 h were produced. Nonalloyed PM microalloyed steels with different Cr ratio were analyzed in terms of tensile test. The microstructure of the PM steels was characterised by optic microscope. Results indicated that 5 wt. % Cr added PM steel showed the highest values in yield strength (YS) and ultimate tensile strength (UTS).

Keywords— Powder metallurgy, powder metallurgy steels, Cr, Microstructure.

I. INTRODUCTION

Steels are the material group having superior properties such as; high strength and toughness, low ductile-to-brittle transition temperature, excellent weldability and corrosion resistance which are obtained by applying various hardening mechanisms and proper thermomechanical procedures. The main roles of alloying elements are to refine the grain size, prevent recrystallization and facilitate precipitate hardening. The effect of alloying elements on the grain boundary movement and recrystallization is a result of carbo-nitride precipitates. [1-4].

While chromium forms unstable carbides in steel, it is cheap, common and, it increases corrosion resistance, especially to intercrystalline corrosion. It can also delay transformation during tempering [5]. It is commonly added to steel to increase corrosion resistance and oxidation resistance. It increases hardenability and improves high temperature strength. Chromium is normally used with a toughening element such as nickel for superior mechanical properties. Chromium is a strong carbide former element. Chromium is an essential alloying element in steel with increased hardness and wear resistance. Besides that, chromium prevents the transformation of austenite into pearlite during cooling, and affects the structure of the metallic matrix of steel, closing γ -area in the phase diagram Fe-Fe₃C. Chromium does not increase hardenability but, in combination with higher carbon content, has a beneficial

effect on the depth of hardened layer. The important parameter for hardening is the ratio Cr/C and, the higher the ratio, the higher the hardenability [7].

Powder metallurgy (P/M) paves the way for the economical production of high quality and sophisticated tools. This production method turns the metal powders that are different in size, shape and packaging features into resistant, precise and high performance tools [6]. Certain studies are available in the literature about the relationship between the production, and microstructure or mechanical properties. Erden [7] studied the effect of Ni content on microstructure and mechanical properties of Nb-V added microalloyed steel produced by powder metallurgy method. It was concluded that, as the amount of Ni content increased, which resulted in the enhancement of yield and tensile strength.

In the present study, PM steel has been produced in the targeted compound by adding different proportions of Cr into the Fe matrix with the powder metallurgy method and the output microstructural mechanical features have been compared.

II. EXPERIMENTS

In this investigation, having been added in different proportions, the effect of the Cr's amount on microstructural and mechanical properties is researched. Fe, graphite and Cr powders by Aldrich were used. The size of graphite, iron, niobium and vanadium powders were <20, ≤180, <45, and <44 μm, respectively. These powders were supplied by Aldrich. The purities of graphite, Fe and Cr are 96.5 %, 99.9 %, 99.8 % and 99 %, respectively. Before the mixing process, powders were prepared in the proportions that had been given in Table 1 by weighing on a digital precision scale which has 0.0001 g precision. The powders were mixed in an industrial conic mixer for 1 h. Steel is produced by way of mixing in the chemical compounds given in the Table 1. Tensile test has been implemented on the produced samples after microstructural characterisation is performed. The results have been compared. Having been mixed

homogeneously, the powders were pressurised under 750 MPa unidirectionally with Hidroliksan branded device which has 96-ton pressure capacity. Samples of the tensile experiment were turned into blocks by squeezing with the mould which had been prepared according to ASTM (E 8M) standards of powder metal material tension sample.

TABLE I CHEMICAL COMPOSITIONS OF POWDER METAL STEELS.

Compound	Graphite (%wt.)	Cr (%wt.)	Fe (%wt.)
Alloy 1	0.55	-	Rest
Alloy 2	0.55	0.1	Rest
Alloy 3	0.55	1	Rest
Alloy 4	0.55	3	Rest

The pressed samples were sintered in argon atmosphere at 1400 °C for 1 hour. After sintering, density and pore values were measured. The sintered samples were subjected to standard metallographic procedures. Having sintered at 1400 °C, the microstructures of the PM steel were examined under a Nikon Epiphot 200 optical microscope of X50-X1000 zoom capacity. Tensile test was carried out at 1 mm/min crosshead speed with a Shimadzu tensile testing device of 50 KN capacity. The yield strength (% 0.2), tensile strength and % (percentage) values of elongation of the tensile test samples were determined. The density of the samples was determined according to the principle of Archimedes. Likewise, the pearlite proportions of the powder metal steels were calculated using Gladman and Woodhead's metallographic point counting method [8].

III. RESULTS AND DISCUSSIONS

IV. III.I. MICROSTRUCTURE RESULTS

The microstructural images of the samples are demonstrated in the Figure 1. As can be seen from the figure, the structure comprises of ferrite and pearlite phases in the whole alloys. When the images of the microstructure in the Figure 1 are examined, it is detected that there are pores in the grain borders.

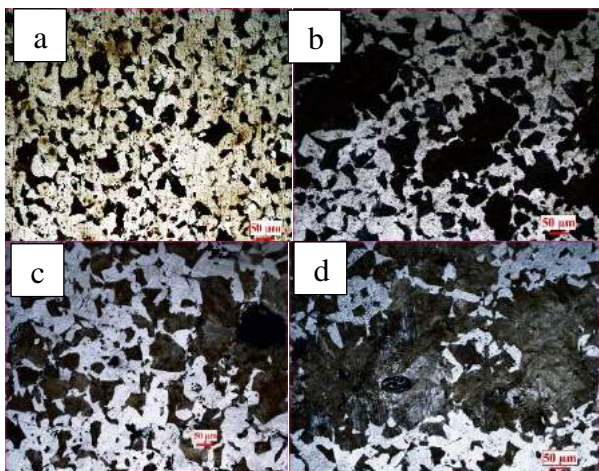


Fig. 1 Micrographs of PM steel specimens (500 x). (a) Alloy 1, (b) Alloy 2, (c) Alloy 3, (d) Alloy 4 and (e) Alloy 5.

Although it is stated that porosity affect the strength of many materials negatively, it is reported that tiny and spherical pores do not reduce the strength [9-11].

TABLE II RELATIVE DENSITY, MEAN GRAIN SIZES AND VOLUME FRACTIONS OF PEARLITE PHASES IN PM STEEL SPECIMENS

Alloy	Relative Density (%)	Porosity (%)	Pearlite (%)	Grain Size (µm)
Alloy 1	92	8	25	33
Alloy 2	91.5	8,5	28	29
Alloy 3	90	10	33	25
Alloy 4	91	9	38	21

It is inferred from the images of microstructure that as the proportion of the Cr in the samples increases, the grains get smaller gradually. For instance, the size of the grain decreased to 29 µm and 21 µm respectively with 0.1 and 3 percentage of weight increase in the amount of the Cr while the average size of grain in the non-alloyed PM steel sample in the Fe + 0.55 Graphite compound is 33 µm.

III.II. MECHANICAL PROPERTIES

Table 3 shows the yield strength, tensile strength, percentage elongation and hardness results. The yield, tensile strength and hardness values are observed to increase when Cr proportion increases to %3. Being formed by Cr, the carbide, nitride and carbonitride precipitates ensure the material to be small grained by way of restricting the size of the austenite grain and re-crystallisation of the austenite. The improvement of the resistance to dislocation movement is fulfilled thanks to the increasing grain boundaries in the small grained structure. The decrease of the grain size also contributes to the percentage elongation of the material. Along with these, the formed precipitates contributed to the increase in the yield and tensile strength via various strength increasing mechanisms like precipitates hardening and dispersion hardening [1-3; 11-12].

TABLE III MECHANICAL PROPERTIES OF SINTERED PM STEEL AND MICROALLOYED PM STEELS

Alloy	Yield Strength (MPa)	Ultimate Tensile Strength (MPa)	Elongation (%)
Alloy 1	102	270	16
Alloy 2	112	306	12
Alloy 3	134	351	11
Alloy 4	171	434	9.2

Yield strength of the Cr added PM steels shows similar kind of behavior to that of tensile strength as seen in both Table 3. However elongation (%) of Cr added PM steels decreased when the Cr content of PM steels increased from 0.1-1 % to 3%. This is a result of the differences in the amount of pearlite content and precipitate particles occurred

during sintering or cooling after sintering. It is thought that precipitates like CrC(N) lead to the development of small austenite grains by way of restricting the grain size during the sintering process, thereby improving the strength of the steels.

Similarly, Meigui et al. [13] study, investigated the influence of Cr content on the microstructure and properties of spring steel 60Si2CrVA (treated with quenching tempering and quenching partitioning tempering (QPT) processes) was studied. Heat treatment parameters were optimized, and the appropriate Cr content was determined. Optimal microstructure and mechanical properties of 60Si2CrVA steel were obtained at 1.45 wt% Cr or 1.55 wt% Cr. QePeT treatment with its strength toughness combinations is beneficial for 60Si2CrVA spring steel. With increasing Cr content, hardness shows no significant change, whereas the strain hardening exponent increases. This result implies that increased Cr content could improve the ability for plastic deformation.

Surian et al. [14], when the Cr content increased in low-alloy low-hydrogen iron powder AWS E10018, E11018 and E12018-M electrode all-weld-metal, the following was found. There was a monotonic increase of yield and tensile strengths for the two levels of Mn studied. Yield strength showed an increase when Mn varied from 1.0 to 1.4%, although tensile strength did not change significantly. Elongation was adversely affected, particularly when Cr exceeded 1.2%. Elongation was adversely affected, particularly when Cr exceeded 1.2%.

V. CONCLUSION

The non-alloyed and Cr added PM steel which has seven different volume ratios (0–0.1 – 1 Cr % and 3 Cr %) is produced by cold pressing and sintering at the argon setting and the following results listed below are obtained from this study.

- Composite materials which contain graphite, Cr and Fe matrix can be produced with powder metallurgy. Solid solution hardening and precipitation hardening which arise during the sintering process or after-sintering cooling process increase the resistance of the steel.
- Composite materials that are added 0.1 -1 and 3 % Cr as weight compared to non-alloyed steels showed smaller grain structure. This situation stems from the restriction of grain size by the CrC(N) precipitates.
- Usually, there has been an increase in the yield strength, tensile strength, percentage (%) elongation and hardness values of the compounds which have Cr ratio by 3 % as the alloy ratio rises. This situation is a result of the development of the precipitates like CrC(N) during sintering process and after-sintering cooling process. These precipitates lead to the creation of small austenite

grains by preventing grain size and thus improving the resistance of the materials.

- After-sintering density of the nonalloy and Cr added alloyed steel is observed to be generally at about 92 %. After-sintering density of the produced PM steels showed a little bit increase.

ACKNOWLEDGMENT

This work was supported by Scientific Research Projects Coordination Unit of Karabük University. Project Number: KBÜ-BAP-15/2-KP-058 and KBÜ-BAP-17-LÖAP-086.

REFERENCES

- [1] M. A. Erden, S. Gündüz, M. Türkmen, H. Karabulut, "Microstructural characterization and mechanical properties of microalloyed powder metallurgy steels", *Materials Science and Engineering: A*, vol. 616, pp. 201-206, August 2014
- [2] M. A. Erden, H. Gökçe, "The Effect of Sintering Atmosphere on Mechanical Properties of Nb V Bsaed Microalloy Steels Produced by Powder Metallurgy Method", *Sylwan*, vol. 160(8), pp. 362-375, August 2016
- [3] M. A. Erden, "Effect Of Pressing Pressure On Microstructure And Mechanical Properties Of Non-Alloyed Steels Produced By Powder Metallurgy Method" *Omer Halisdemir University Journal of Engineering Sciences*, vol. 6(1), pp. 257-264, Jan. 2017
- [4] A. Kaçal, M. Gülesin H. B. Ulaş "System Design and Manufacturing for Measurement Of Cutting Forces In Gear Hobbing Process", *J. Fac. Eng. Arch.Gazi Univ.*, vol. 23(4), pp. 795-800, Sept. 2008
- [5] E. Lichańska, M. Sułowski, A. Ciał "Mechanical properties and microstructure of PM Mn-Cr-Mo steels with low carbon concentration" *Arch. Metall. Mater.*, vol. 61(1), pp. 109–114, Jan. 2016
- [6] M.D. Cikara, D.D. Cikara, "Wear resistance, structure and application possibilities of high chromium iron alloys", *Journal of Metallurgy*, vol. 7 (1) pp. 45-59, Jan. 2001
- [7] M. A. Erden, "The Effect of Ni on the Microstructure and Mechanical Properties of Nb V Microalloyed Steels Produced by Powder Metallurgy", *Sylwan*, vol. 160(10), pp. 362-375, Oct. 2016
- [8] T. Gladman, and J. H. Woodhead, "The accuracy of point counting in metallographic investigations", *Journal of the Iron Steel*, vol. 194, pp.189, Jan. 1960
- [9] S. Sarıtaş, M. Turker, N. Durlu, Powder Metallurgy and Particulate Materials Processing, Turkish Powder Metallurgy Association, 2 nd ed., Ankara, 2007
- [10] C Schade, T. Murphy, A. Lawley, R. Doherty "Microstructure and mechanical properties of microalloyed PM steels", *Int. J. of Powder Metall.*, vol. 48, pp. 51-59, April 2012
- [11] A. M. Sage, "An overview of the use of mikroalloys in hsla steels with particular reference to vanadium and titanium, processing, properties and applications", *Proceedings of the Second International Conference on HSLA Steels*, p. 51, May 1992
- [12] R. D. K. Misra, K. K. Tennen, G. C. Weatherly, G. Tither, "Microstructure and texture of hot rolled Cb-Ti and V-Cb microalloyed steels with differences in formability and toughness", *Metall. Mater. Trans. A*, vol. 34A, pp. 2341, 1 Oct. 2003
- [13] O. Meigui, Y. Chunlin, Z. Jie, X. Qifan, Q. Huina "Influence of Cr content and QePeT process on the microstructure and properties of cold-coiled spring steel" *Journal of Alloys and Compounds*, vol.697 , pp. 43-54. Dec. 2017
- [14] E. Surian, J. Trotti, A. Cassanelli And L. A. De Vedia "Influence of Chromium on the Mechanical Properties and Microstructure of Weld Metal from a High-Strength SMA Electrode" *Welding Journal*, pp.45-53, March 1994

The Mechanical Properties of Carburized and Uncarburized AISI 8620 Steel by Powder Metallurgy Method

¹Mehmet Akif ERDEN, ²Özcan TOPÇU

¹*Corresponding Author Karabük University, Karabük TOBB TS Vocational School, Karabük, 78050, Turkey, makiferden@karabuk.edu.tr*

²*Karabük University, Department of Manufacturing Engineering, Karabük, 78050, Turkey, topcu.ozcan67@gmail.com*

Abstract— In this work, the relation between microstructure and mechanical properties of carburizing steel produced by powder metallurgy method were investigated. The samples pressed at 700 MPa and sintered at 1400 °C temperature in the sintering argon atmosphere for 1 h were produced. Steels which have carburized and uncarburized were analyzed in terms of tensile and hardness test. The microstructure of the PM steels was characterized by optic microscope. Results indicated that carburizing steel can be produced.

Keywords— Powder metallurgy, powder metallurgy carburizing steels, Microstructure, Mechanical properties.

I. INTRODUCTION

The steels are manufactured in different specifications according to the purpose of use of the industry [1-5]. The mechanical properties of the steels vary considerably depending on the alloying elements in the chemical composition, their construction, the grain sizes and the heat treatments applied [6]. To this end, steel is subjected to many more operations such as carburizing, normalization, annealing, austempering, martempering, boring. Properties are developed and materials suitable for the intended purposes are produced. One of the most important of these processes is the cementation surface hardening process. It is a heat treatment applied on the inside of the hardened steel, where high toughness is required on the high toughness surface. Carburizing can be carried out in solid, liquid or gaseous media. At the end of the process, the surface of the part is hard and resistant to abrasion, while the core part is soft but firm with respect to the surface [7].

Carburizing process is a method to disperse carbon into the steel surface in order to enhance its mechanical properties such as hardness and wear resistance. Low-carbon steel parts are produced, by machining, into finished shapes and then are transformed by carburizing into a composite material creating of a high-carbon steel case and low-carbon steel core. When this steel composite is quenched to martensite and tempered, the superior hardness and strength of the case microstructure, compounded with the favourable case compressive residual stress developed by interactions between the case and core during quenching, produce very high resistance to wear, bending fatigue, and rolling-contact fatigue. Recently, there are many researches

on the development of surface treatment process in order to improve the mechanical properties, wear resistance of steels [8].

Patidar et al [9] studied the carburized mild steel at 950 °C with soaking time of 2 h and then tempered with different temperature range for different soaking time. After this, the carburized and tempered mild steel are subjected for various kind of test such as abrasive wear test at different load and mechanical properties test like hardness, and tensile. Finally it was analysed that wear resistance and mechanical properties increased with increase in tempering temperature.

Singh et al. [10] studied three heat treatment processes namely quenching, carburizing, and tempering. After this the carburized and tempered mild steel are subjected for various kind of test such as abrasive wear test at different load and hardness test, and tensile test, Finally it was concluded that as wear rate increases, hardness increases for different soaking time. Also tensile strength increases with increasing the soaking time.

Emamian [11] studied the effect of solid carburization on mechanical and tribological properties of powder metallurgy parts. The effects of austenitization and quenching are investigated on some specimens and concluded that wear resistance can be increased with moderate toughness.

Powder metallurgy varies greatly between metal processing technologies is a production technique. It is economically feasible to produce powder metallurgically attractive, high-precision parts with very high precision. One of the advantageous sides of the powder metallurgy parts is that it is more there is a short cycle-to-manufacturing cycle, because some process steps are not applied, it is possible to manufacture parts which are suitable for direct use. Metals with high melting temperatures can be easily formed with powder metallurgy [1-3].

Certain studies are available in the literature about the relationship between the production, and microstructure or mechanical properties. For instance, Erden [10] studied the effect of C content on microstructure and mechanical properties of Nb-V added microalloyed steel produced by powder metallurgy method. It was concluded that, the proportion of pearlite increased as the amount of C content increased, which resulted in the enhancement of yield and tensile strength.

Erden et al. produced in their studies Ti and V microalloyed steel with the method of PM. They carried out the sintering process at 1150°C during 60 minutes and confirmed that yield strength and tensile strength increase as Ti and V ratios (% 0,1-% 0,2) increase. They based it on the formation of precipitates like TiC(N) and VC(N) during the sintering and post-sintering cooling period [1-2].

In the present study, AISI 8620 PM steel has been produced in the targeted compound by adding different proportions of alloy elements into the Fe matrix with the powder metallurgy method and have been compared the mechanical properties of carburized and uncarburized AISI 8620 PM steel by powder metallurgy method.

II. EXPERIMENTAL METHOD

In this study, the AISI 8620 PM steel samples were produced in the desired compositions with the PM method. Fe, Mo, Ni, Cr and graphite powders by Aldrich were used. The size of graphite, iron, Mo, Ni and Cr powders were <20, ≤180, <150 μm, <5 μm and <44 μm, respectively. These powders were supplied by Aldrich. The purities of graphite, Fe, Mo, Ni and Cr are 96.5 %, 99.9 %, 99.9 %, 99.7 % and 99 %, respectively. The samples were produced by way of mixing in the chemical compounds given in the Table 1.

TABLE 1 CHEMICAL COMPOSITIONS OF AISI 8620 STEEL.

Graphite (%wt.)	Cr (%wt.)	Mo (%wt.)	Ni (%wt.)	Fe (%wt.)
0.27	0.45	0.15	0.4	Rest

Tensile test was carried out on the produced samples after the microstructural characterisation. The results were compared. Before the mixing process, the powders were prepared in the proportions given in Table 1 by weighing on a digital precision scale of 0.0001 g precision. The mixing process was conducted without ball using a Turbula T2F mixer for 1 hour. Having mixed homogeneously, the powders were pressed under 700 MPa unidirectionally with a Hidroliksan press of 96 ton pressure capacity. The samples of the tensile experiment were shaped into blocks by squeezing with the mould prepared according to ASTM (E 8M) standards of powder metal material tension test sample. The pressed samples were sintered in argon atmosphere at 1400 °C for 1 hour. After sintering, density and pore values were measured. The sintered samples were subjected to standard metallographic procedures. Having sintered at 1400 °C, the microstructures of the PM steel were examined under a Nikon Epiphot 200 optical microscope of X50-X1000 zoom capacity. Tensile test was carried out at 1 mm/min crosshead speed with a Shimadzu tensile testing device of 50 KN capacity. The yield strength (% 0.2), tensile strength and % (percentage) values of elongation of the tensile test samples were determined. Vickers hardness value was determined through applying 0.5 kg weight under a Shimadzu unit hardness device. The density of the samples was determined according to the principle of Archimedes. Likewise, the pearlite proportions of the powder metal steels were calculated using Gladman and Woodhead’s metallographic point counting method [12].

The carburizing process was carried out. The carbon was adsorbed the samples for 4 hours in a sodium cyanide salt bath containing 0.8C at 925°C. The samples were taken in heat treatment oil (oil: 70°C) Then it was tempered at 200 degrees for 2 hours.

III. RESULTS AND DISCUSSIONS

III.I. Microstructure results

Figure 1 shows microstructure of (a) pure AISI 8620 PM steel and samples that were carburized AISI 8620 PM steel. It could be seen in Figure 1(a) that the microstructure consists of ferrite and pearlite phases. After carburizing, it was found that there are presences of carbon layer on the surface. Figure 1(b) shows the thickness of carbon dispersion. The measured dark layer in the figure is the carbon layer at the outer surface of AISI 8620 steel.

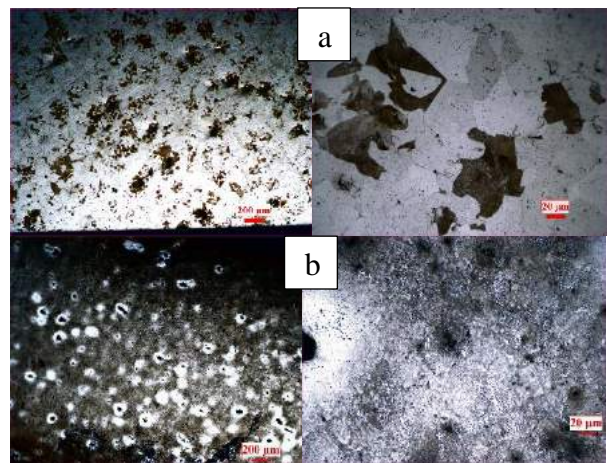


Fig. 1 Micrographs of PM steel specimens (50x-500 x). (a) Pure AISI 8620 PM steel, (b) Carburized AISI 8620 PM steel.

TABLE II RELATIVE DENSITY, MEAN GRAIN SIZES AND VOLUME FRACTIONS OF PEARLITE PHASES IN AISI 8620 PM STEEL SPECIMENS

Alloy	Relative Density (%)	Porosity (%)	Pearlite (%)
Pre carburizing Alloy	90.11	9.89	28.45
After carburizing Alloy	90.66	9.34	-

Similar studies were recorded. For example, Li and Dong et al [13] which found that the thickness of the surface-treated layers increased with the treatment temperature. The reason is that with increased processing temperature, besides atomic diffusion of carbon, there is other reactions occur in the carburized layer [14].

When the images of the microstructure in the Figure 1 are examined, it is detected that there are pores in the grain borders. Although it is stated that porosity affect the strength of many materials negatively, it is reported that tiny and spherical pores do not reduce the strength [15-17].

III.II. HARDNESS AND TENSILE STRENGTH

While Figure 2 shows the stress-strain diagrams of the sintered samples, Table 3 shows the yield strength, tensile strength, percentage elongation and hardness results. The yield and tensile strength with the percentage elongation and hardness values are observed to increase after carburizing process.

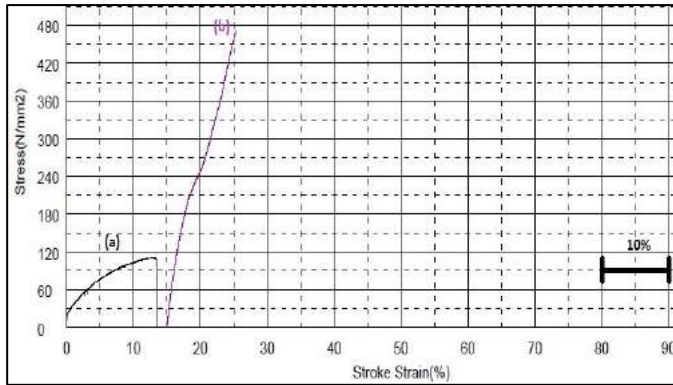


Fig. 2 Variation of stress–strain curves of AISI 8620 PM steel specimens (a) Pure AISI 8620 steel, (b) Carburized AISI 8620 steel.

TABLE III MECHANICAL PROPERTIES OF SINTERED AISI 8620 PM STEELS

Alloy	Yield Strength (MPa)	Ultimate Tensile Strength (MPa)	Elongation (%)	Average of Hardness for surface (HV0.5)
Pre carburizing	137	112	13.22	106
After carburizing	254	473	10.33	461

Table 3 show the comparison of hardness for different samples which are pure AISI 8620 steel and carburized AISI 8620 steel 900°C. Hardness of untreated sample indicates the hardness value of 106 HV. When the carburized treatment applied the sample, the hardness value increase from 106 to 461 HV. As the temperature applied, the heat caused carbon atom to diffuse into the metal surface. The applying of carburizing temperature causes carbon atoms to diffuse into the metal surface and this will increased the hardness of the sample [18]. A new element which is carbon that has been added to AISI 8620 PM steel gives better hardness characteristics to improve the properties of AISI 8620 PM steel. Yong Luo et. al [19] also reported that after carburization process, there is a significant increase in hardness of the samples.

Figure 5 shows the variation of tensile strength for different samples. The tensile strength of pure AISI 8620 PM steel was averaged at 112 MPa. A significance increased in the tensile strength were recorded when the carburizing treatment applied. The tensile strength were 473 MPa respectively. It was observed that as the hardness increases, the tensile strength also increases. This is due to the increasing amount of carbon in the carburized samples [20]. The presence of carbon on the AISI 8620 PM steel steel

affects the tensile strength. Carbon element increased the toughness, however because of the carbon brittleness, the elasticity of the carburized samples decreases.

IV. CONCLUSION

AISI 8620 PM Steels are produced by cold pressing and sintering at the argon setting. Same of AISI 8620 PM Steels have been carburized at 925°C. It was found that with the applying carburizing heat treatment, the average carbon dispersion layer increases. As the carbon dispersion layer increases, the amount of carbon that diffuses into the surface of AISI 8620 PM Steels increases and resulted in an increase in hardness and tensile strength of the sample.

ACKNOWLEDGMENT

This work was supported by Scientific Research Projects Coordination Unit of Karabük University. Project Number: KBÜ-BAP-15/2-KP-058 and KBÜ-BAP-17-DS-029.

REFERENCES

- [1] Y. Ozcatalbas, F. Ercan, "The effects of heat treatment on the machinability of mild steels", *Journal of Materials Processing Technology*, vol. 136, pp. 227–238, Feb. 2003
- [2] M. A. Erden, S. Gündüz, M. Türkmen, H. Karabulut, "Microstructural characterization and mechanical properties of microalloyed powder metallurgy steels", *Materials Science and Engineering A*, vol. 616, pp. 201-206, Agust. 2014
- [3] M. A. Erden, S. Gündüz, M. Türkmen, H. Karabulut, "The Effect of V Addition on the Microstructure and Mechanical Properties of Low Carbon Microalloyed Powder Metallurgy Steels", *Materials Testing*, vol. 58(5), pp. 433-437, May 2016
- [4] M. A. Erden, "Effect Of Pressing Pressure On Microstructure And Mechanical Properties Of Non-Alloyed Steels Produced By Powder Metallurgy Method" *Ömer Halisdemir Üniversitesi Mühendislik Bilimleri Dergisi*, vol. 6(1), pp. 257-264, Ocak 2017
- [5] A. Kaçal, M. Gülesin H. B. Ulaş "System Design And Manufacturing For Measurement Of Cutting Forces In Gear Hobbing Process", *J. Fac. Eng. Arch.Gazi Univ.*, vol. 23(4), pp. 795-800, Sept. 2008
- [6] B. Pekgöz, S. Saridemir, İ. Uygur, Y. Aslan "The Effects of Carburisation Process on the Hardness Values and Microstructure for Steels", *Electronic Journal of Machine Technologies*, vol. 10(1), pp. 19-24, April 2013
- [7] N. Mebarki, D. Delagnes, P. Lamelse, F. Delmas, C. Levaillant, "Relationship Between Microstructure And Mechanical Properties of a 5% Cr Tempered Martensitic Tool Steel", *Materials Science and Engineering A*, vol. 387–389, pp. 171–175, 2004
- [8] S. Ahmad, S.K. Alias, B. Abdullah, M. H. M. Bakri, M. H. Jumadin, M. Amir M. Shah, "Enhancement of Stainless Steel's Mechanical Properties via Carburizing Process" *IOP Conf. Series: Materials Science and Engineering*, vol. 160(1), pp. 1-7, 2016
- [9] S. Patidar, A. Jain, and D. Singh, "Effect of tempering temperature and applied load on various wear environment of carburized mild steel", *IOSR Journal of Mechanical and Civil Engineering*, pp. 62–69, 2012
- [10] S. Singh, D. Singh, K. Sachan and A. Arya, "Effects of soaking time and applied load on Wear Behaviour of Carburized mild steel", *IOSR Journal of Engineering (IOSRJEN)*, pp. 10 – 19, 2013
- [11] A. Emamian, "Study on wear resistance, Hardness, and impact behaviour of Carburized Fe-Based Powder Metallurgy parts for automotive applications", *Materials Sciences and Applications*, pp. 519 – 522, 2012
- [12] T. Gladman, and J. H. Woodhead, "The accuracy of point counting in metallographic investigations", *Journal of the Iron Steel*, vol. 194, pp.189, Jan. 1960

- [13] X.L. Wei Li, D. Hanshan, Effect of Tensile Stress on the Formation of S-phase during Low -temperature Plasma Carburizing of 316L foil, *Acta Materialia*, vol. 59, pp. 5765-5774, 2011
- [14] Y.Sun, Kinetics of Low temperature Plasma Carburizing of Austenitic Stainless Steel. *Journal of Materials Processing Technology*, vol. 168, pp. 189-194, 2005
- [15] M.A. Erden, An Investigation On the Relation Sheep Between Microstructure and Mechanical Properties of Microalloyed Steels Produced by Powder Metallurgy, PhD. Thesis, Institute of Science and Technology, Karabuk University, Karabuk, Turkey, 2015
- [16] S. Sarıtaş, M. Turker, N. Durlu, Powder Metallurgy and Particulate Materials Processing, Turkish Powder Metallurgy Association, 2 nd ed., Ankara, 2007
- [17] M. A. Erden, H. Gökçe, “The Effect of Sintering Atmosphere on Mechanical Properties of Nb V Bsaed Microalloy Steels Produced by Powder Metallurgy Method”, *Sylwan*, vol. 160(8), pp. 362-375, Agust. 2016
- [18] E. Hesham, “The Effect of Carburization on Hardness and Wear Properties of the Mild Steel Samples” *International Journal of Innovation and Applied Studies*, vol. 6(4), pp. 995-1001, Jul. 2014
- [19] Y. Luo, H. Jiang , G. Cheng, H. Liu, “Effect of Carburization on the Mechanical Properties of Biomedical Grade Titanium Alloys” *Journal of Bionic Engineering*, vol. 8(1), pp. 86-89, March 2011
- [20] S.A.I. Fatai Olufemi Aramide, “Effects of Carburization Time and Temperature on the Mechanical Properties of Carburized Mild Steel using Activated Carbon as Carburizer”, *Materials Research*, vol. 12, pp. 483-487, Dec. 2009

Effect of Graphite Content on Microstructure and Mechanical Properties of Mo Added Steel Produced By Powder Metallurgy Method

¹Mehmet Akif Erden, ^{1x}Hasan Karabulut, ²Süleyman Gündüz

¹Karabük University, Karabük TOBB TS Vocational School, Karabük, 78050, Turkey, makiferden@karabuk.edu.tr

^{1x}Corresponding Author Karabük University, Karabük TOBB TS Vocational School, Karabük, 78050, Turkey,

²Karabük University, Department of Manufacturing Engineering, Karabük, 78050, Turkey, sgunduz@karabuk.edu.tr

Abstract— In this work, the effect of graphite content on the microstructures and tensile behaviors of Mo added powder metallurgy (PM) steels were investigated. The samples pressed at 700 MPa and sintered at 1400°C temperature in the argon atmosphere for 1 h were produced. Mo added PM microalloyed steels with different graphite ratio were analyzed in terms of microstructure and tensile test. Results indicated that as the amount of the graphite in the PM steels increases, the volume fraction of the pearlite increases gradually. Mo added PM steel contained 0.6 wt. % graphite showed the highest values in yield strength (YS) and ultimate tensile strength (UTS).

Keywords—Powder metallurgy, Mo added steels, Microstructure, Tensile strength.

I. INTRODUCTION

Steels are the material group having superior properties such as; high strength and toughness, excellent weldability and corrosion resistance. These properties are obtained by applying various hardening mechanisms and proper thermomechanical procedures. The main roles of alloying elements are to refine the grain size, prevent recrystallization and increase the precipitate hardening [1-5].

Molybdenum prevents the grain growth and increases the strength of steels when it presents in solid solution or as precipitate particles. More than half of molybdenum produced is used in metallurgy, with the rest used in chemical applications [6]. Most high-strength steel alloys contain 0.25 to 8% molybdenum, Because of its lower density and more stable price, molybdenum is sometimes used in place of tungsten, Molybdenum can also be used as a flame-resistant coating for other metals. It was reported [7] that Mo in small amount increase the hardenability of steels when it was dissolved in austenite. Some work [8] showed that molybdenum increased the effect of precipitation hardening in Nb added HSLA steels. Junhua et al. [6] investigated the effect the Mo content on the microstructure and mechanical properties of high strength pipeline steel X80. It was concluded that, the volume fractions of acicular ferrite raised as the amount of

Mo content increased, which resulted in an increment in yield and tensile strength.

Powder metallurgy (PM) is the way for the economical production of the samples with high quality. This production method turns the metal powders into resistant, and high performance tools [9]. Clock parts, electrical connection components, railway parts, nuclear power plants, aircraft parts, automotive components, armor-piercing materials, orthopedic materials, high temperature filters, jet engines, high power lightening are some of the areas that parts are produced by powder metallurgy method. PM method is preferred for its economy, manufacturability, homogeneity and quality as well as high performance and low cost of the produced parts [3].

Certain studies are available in the literature about the relationship between the production, and microstructure or mechanical properties. For instance, Erden at al. produced Ti, V, Ti-V and Nb-Al microalloyed steel with PM method. They carried out the sintering process at 1150°C and 1350°C for 60 minutes and confirmed that yield strength and tensile strength increased as the amount of microalloying elements increased from 0.1 % to 0.2 %. They concluded that this is due to the formation of precipitates like TiC(N), TiVC(N), VC(N) and AlN during the sintering or cooling after sintering [3-9]. Erden [10] studied the effect of C content on microstructure and mechanical properties of Nb-V added microalloyed steel produced by powder metallurgy method. It was concluded that, the proportion of pearlite increased as the amount of C content increased, which resulted in the enhancement of yield and tensile strength.

In this study, Mo added PM steels was produced by adding 0.5 % Mo powder and 0.4-0.6 % graphite as weight percentage into the Fe powder. Sintering process for the produced tensile test samples was carried out at 1400°C during 1 hour in argon atmosphere. Along with the analysing of the microstructure specifications of samples like proportion of pearlite, density and porosity, mechanical properties were determined by using tensile test.

II. EXPERIMENTS

In this experiment, steel samples were produced in the desired compounds with the method of powder metallurgy. The effect of graphite ratio on the microstructure and mechanical properties was examined. Fe, graphite, and Mo powders of ≤ 180 , < 20 and < 150 μm supplied by Aldrich were used. Analysis indicated that the purity of Fe, graphite and Mo was 99.9 %, 96.5 % and 99.9 % respectively. Before the mixing process, powder was weighed in the different ratios on a digital precision scale which has 0.0001 g precision. The chemical composition of powders is given in Table 1. The weighed powders were mixed with a three axis Turbula brand mixer without marbles during one hour. The alloyed powders were pressed in to the shape of tensile specimen at 700 MPa according to ASM (E8M) standarts.

Table 1: Chemical compositions of powder metal steels.

Compound	Graphite (%wt.)	Mo (%wt.)	Fe (%wt.)
Fe +0.4 Graphite+ 0.5 Mo (Alloy 1)	0.4	0.5	rest
Fe +0.5 Graphite+ 0.5 Mo (Alloy 2)	0.5	0.5	rest
Fe +0.6 Graphite+ 0.5 Mo (Alloy 3)	0.6	0.5	rest

The pressed samples were sintered at 1400 °C for 1 hour in argon atmosphere. After sintering, density (%) and porosity (%) were measured. Microstructure examinations were carried out with Nikon Epiphot 200 brand optical microscope which has X50-X1000 zooming capacity. These images are intended to be qualified enough to represent the whole microstructure by capturing different size of images from the different parts of each sample. Etching process was carried out by sinking the samples into 2% Nital solution during 2-6 seconds. After the etching process was completed, etched surfaces were cleaned with methanol and dried for the examination under optical microscope. Density of the samples was measured with the density measurement tool according to Archimedes principle. Pearlite ratios of the PM steels were determined by using the metallographic point counting method according to suggestions of Gladman and Woodhead [11]. Tensile test was made at 0.5 mm/min crosshesd speed with Shimadzu tensile device that has 50 KN capacity. The yield strength (0.2%), tensile strength and elongation % of the tensile test samples were determined.

III. RESULTS AND DISCUSSIONS

III.I. Microstructure results

The microstructures of the samples are seen in the Figure 1. As can be seen, the structure consists of ferrite and pearlite phases in the different proportions. When the microstructure in the Figure 1 are examined, it is detected that there are partially uncovered pores on the borders of the grains. Although porosity affect the strength of materials negatively, tiny and spherical pores do not reduce the strength [12]. It is also seen from the microstructure that as the amount of the graphite in the PM samples increases, the volume fraction of the pearlite increases gradually. For instance, the volume fraction of the pearlite in 0.4-0.5 and 0.6 graphite added PM steels

are 29.7%, 38.7% and 49.5 % respectively. Similar studies support this conclusion. For example, Erden studied the effect of C content on the microstructures and tensile behaviors of Nb-V added microalloyed PM steels. Results indicated that the volume fraction of pearlite increases by the increase in C content to 0.35% which showed the highest values in yield strength (YS) and ultimate tensile strength (UTS) [10].

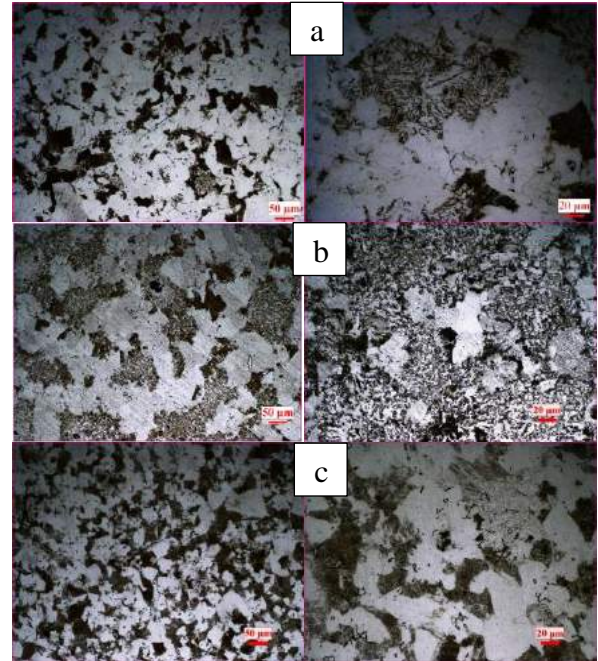


Fig. 1: Micrographs of PM steel specimens (200x-500 x). (a) Alloy 1, (b) Alloy 2, (c) Alloy 3.

Table 2: Relative density, mean grain sizes and volume fractions of pearlite phases in PM steel specimens

Alloy	Relative Density (%)	Porosity (%)	Pearlite (%)	Grain Size (μm)
Alloy 1	93.7	6.3	29.7	53.5
Alloy 2	93.4	6.6	38.1	45.7
Alloy 3	93	7	49.5	39.3

Table 2 shows microstructure analyses of PM steels. As can be seen, the average grain sizes decrease when the graphite content increases from 0.4% to 0.5 or 0.6%. This is due to more precipitation of MoC in the PM steels after sintering or cooling after sintering which prevent the grain growth. One of the features of alloy elements is that they restrict grain size by creating carbide and nitride in the austenitizing or sintering processes. Development of small precipitates during the austenitizing process prevents austenite grain growth and leads to the development of small ferrite grains Also relative density of the Mo alloyed PM steels with different amount of graphite is observed to be generally at about 93%. After sintering Mo alloyed PM steels showed slight increase in density.

III.II. Mechanical properties

While the Figure 2 shows the stress-strain diagrams, Table 3 gives the yield strength, tensile strength and elongation (%) values in percentage. It is seen from Figure 2 and Table 3 that yield strength and tensile strength increases as the amount of the graphite in the PM samples increases. For instance, the tensile strength of 0.4, 0.5 and 0.6 % wt. graphite added Mo alloyed PM steel is 275 MPa, 307 MPa and 391 MPa respectively. Similar studies support this conclusion. For example, Erden et al. investigated, the effect of C content on the microstructures and tensile behaviors of AIC added microalloyed PM steels. Results indicated that as the amount of the C in the PM samples increases, the volume of the pearlite increases gradually and 0.35 wt. % C added PM steel showed the highest values in yield strength (YS) and ultimate tensile strength (UTS) [13]. Guo et al., the influence of carbon content on the mechanical properties of high yield strength bridge steel has been investigated. The results show that the excellent mechanical properties and corrosion resistance are obtained for the steel. Strength of the high performance weathering steel is influenced by carbon content. If the carbon content is less than 0.003 6%, the steel cannot be strengthened by accelerated cooling, even by microalloying approach; if the carbon content is in the range of 0.03% - 0.05%, the yield strength of the steel can reach 600 -700 MPa by the proper TMCP and cooling rate [14]. De la concepción et al. studied the effect of carbon content on microstructure and mechanical properties of DP steels. Samples of steels with different carbon content were heat treated at different intercritical temperatures, obtaining DP steels with different fractions of martensite. Microstructural characterization, microhardness and tensile test were made for each condition. Increasing carbon content and martensite fraction hardness and strength were increased. The best properties combination was reach for steels with a carbon content of 0.1 to 0.15% and 50% of martensite [15].

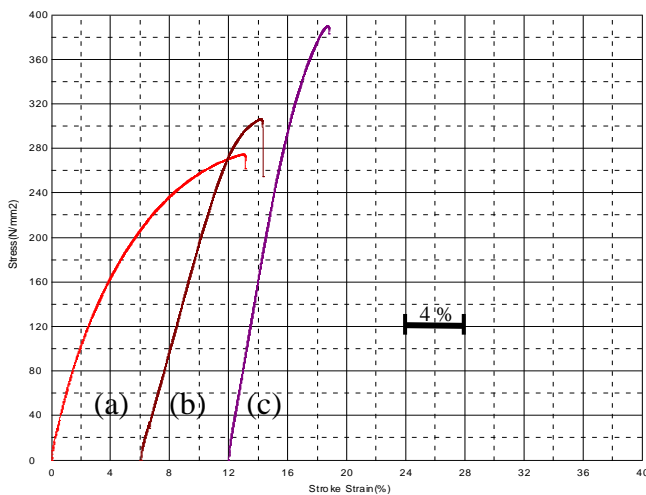


Fig. 5: Variation of stress–strain curves of the PM steel and microalloyed PM steels at different percentages of Mo content (a) Alloy 1, (b) Alloy 2 and (c) Alloy 3.

Table 3: Mechanical properties of sintered PM steel and microalloyed PM steels

Alloy	Yield Strength (MPa)	Ultimate Tensile Strength (MPa)	Elongation (%)
Alloy 1	105	275	13.05
Alloy 2	181	307	8.15
Alloy 3	221	391	6.65

Yield strength of the Mo added PM steels shows similar kind of behaviour to that of tensile strength as seen in both Figure 1 and Table 3. However elongation (%) of Mo added PM steels decreased when the graphite content of PM steels increased from 0.4 % to 0.5% or 0.6%. This is a result of the differences in the amount of pearlite content and precipitate particles occurred during sintering or cooling after sintering. It is thought that precipitates like MoC(N) lead to the development of small austenite grains by way of restricting the grain size during the sintering process, thereby improving the strength of the steels. However, elongation decreases due to higher pearlite content in Mo added PM steel with 0.5 or 0.6% graphite.

Erden et al., produced Ti and V microalloyed steel with PM method. They sintered the steel at 1150 °C for 60 minutes and observed that yield and tensile strength show an increase when the amount of Ti and V (0.1-0.2%) rises. They concluded that this is due to the precipitation of TiC(N) and VC(N) which prevented grain growth during sintering. As a result of this, the strength of the steels improves. The other work that was carried out by different authors indicated that the carbides and nitrides which occur in the alloy steels lead to an increase in the strength [16-17]. In these works, it was pointed out that strength increments due to solid solution hardening is less compared to the precipitation hardening [1-3].

IV. CONCLUSION

The Mo alloyed PM steels containing different amount of carbon (0.4, 0.5 and 0.6%) are produced by cold pressing and sintering at 1400 °C for 1 hour in argon atmosphere and the following results are obtained from this study.

- Fe matrix alloyed with C and Mo can be produced with powder metallurgy method. Solid solution hardening and precipitation hardening which arise during the sintering process or cooling after sintering increase the strength of the steel.
- As the amount of the graphite in the PM samples increases, the volume fraction of the pearlite increases gradually. Mo alloyed PM steel contained 0.6 wt. % graphite showed the highest values in yield strength (YS) and ultimate tensile strength (UTS).
- Relative density of the Mo alloyed PM steels with different amount of graphite is observed to be generally at about 93%. After sintering Mo alloyed PM steels showed slight increase in density.

ACKNOWLEDGMENT

This work was supported by Scientific Research Projects Coordination Unit of Karabük University. Project Number: KBÜ-BAP-15/2-KP-058.

microalloyed steel”, *J. of Iron and Steel Res Int.*, vol.20 (9) pp. 105-110, 13 Sept. 2013.

REFERENCES

- [1] M. A. Erden, S. Gündüz, M. Türkmen, H. Karabulut, “Microstructural characterization and mechanical properties of microalloyed powder metallurgy steels”, *Materials Science and Engineering: A*, vol. 616, pp. 201-206, Agust. 2014.
- [2] M. A. Erden, S. Gündüz, M. Türkmen, H. Karabulut, “The Effect of V Addition on the Microstructure and Mechanical Properties of Low Carbon Microalloyed Powder Metallurgy Steels”, *Materials Testing*, vol. 58(5), pp. 433-437, May 2016.
- [3] M. A. Erden, “Effect Of Pressing Pressure On Microstructure And Mechanical Properties Of Non-Alloyed Steels Produced By Powder Metallurgy Method” *Ömer Halisdemir Üniversitesi Mühendislik Bilimleri Dergisi*, vol. 6(1), pp. 257-264, Ocak 2017.
- [4] A. Kaçal, M. Gülesin H. B. Ulaş “System Design And Manufacturing For Measurement Of Cutting Forces In Gear Hobbing Process”, *J. Fac. Eng. Arch.Gazi Univ.*, vol. 23(4), pp. 795-800, Sept. 2008.
- [5] T. Gladman, The physical metallurgy of microalloyed steels, *The Institute of Materials*, England, 1997.
- [6] K. Junhua, Z. Lin, G. Bin, L. Pinghe, W. Aihua, X. Changsheng “Influence of Mo content on microstructure and mechanical properties of high strength pipeline steel”, *Materials and Design* 25 (2004) 723–728, April 2004.
- [7] H. W. Paxton, E. C. Bain “Alloying elements in steels” *Metals Park, OH: ASM*; 1966. p. 274.
- [8] WB Lee, SG Hong, “Influence of Mo on precipitation hardening in hot rolled HSLA steels containing Nb” *Scr Mater.*, vol. 43(4), pp. 319–24, 2000.
- [9] A. M. Sage, “An overview of the use of mikroalloys in hsla steels with particular reference to vanadium and titanium, processing, properties and applications”, *Proceedings of the Second International Conference on HSLA Steels*, 11.05.92, p. 51.
- [10] M. A. Erden, Effect of C Content on Microstructure and Mechanical Properties of Nb-V Added Microalloyed Steel Produced by Powder Metallurgy Method”, *European Journal of Science and Technology* Vol. 5, No. 9, pp. 44-47, December 2016.
- [11] T. Gladman, and J. H. Woodhead, “The accuracy of point counting in metallographic investigations”, *Journal of the Iron Steel*, vol. 194, pp.189, Jan. 1960.
- [12] R. D. K. Misra, K. K. Tenneti, G. C. Weatherly, G. Tither, “Microstructure and texture of hot rolled Cb-Ti and V-Cb microalloyed steels with differences in formability and toughness”, *Metall. Mater. Trans. A*, vol. 34A, pp. 2341, 1 Oct. 2003.
- [13] M. A. Erden, E. Özkurt, A. N. Tanrıverdi, A. Yılmaz, M. Türkmen, H. Karabulut, S. Gündüz “Investigation Of The Effect Of Carbon Content On Microstructure And Mechanical Properties Of AlC Added Powder Metallurgy Steels” *Technological Applied Sciences*, 11(4), 139-145, 2016.
- [14] GUO Jia', SHANG Cheng-jia' • YANG Shan-wu' • WANG Ying' •, WANG Lien-wei", HE Xin-lai 1 “Effect of Carbon Content on Mechanical Properties and Weather Resistance of High Performance Bridge Steels” *Journal Of Iron And Steel Research. International*. 2009.16(6),63-69.
- [15] Valeria L. de la Concepcióna, Hernán N. Lorussoa,b, Hernán G. Svoboda “Effect of carbon content on microstructure and mechanical properties of dual phase steels” *Procedia Materials Science*, vol. 8, pp. 1047 – 1056, Oct. 2015.
- [16] M. A. Erden, The Effect of Mixing Time On Microstructure and Mechanical Properties of Non Alloyed Steels Produced by Powder Metallurgy Method”, *European Journal of Science and Technology* Vol. 5, No. 9, pp. 62-65, December 2016.
- [17] H. Xiang-dong, M. Xin-ping, L. Sheng-xia, “Effect of annealing temperature on recrystallization behavior of cold rolled Ti-

Precipitating of Sinter Powder by ESP And Effects of Sinter Powder on ESP Efficiency

Ahmet BALIK , Hüseyin DEMİREL* , Muhammed Esad ÇAYIR

Kardemir A.Ş., Karabük, Turkey, abalik@kardemir.com

Karabük University, Karabük, Turkey, hdemirel@karabuk.edu.tr

Karabük University, Karabük, Turkey, muhammed_esad_93@hotmail.com

Abstract – Changes in operating conditions (ESP chemicals and changes in the physical properties of the gas in) the ESP field strength, the emission current and the corona current in order to determine the relationship on the number of spark, an understanding of the effect it would cause both the operational variability.

Keywords – Sinter, ESP “electrostatic precipitator”, Corona, Voltage

I. INTRODUCTION

Electrostatic filter, the most simple definition of the post-combustion hot gas in the holding of dust is equipment. The operating principle of the system in general, Is based on the principle that the solid or liquid particles in the flue gas are separated from the flow by the influence of electric force.

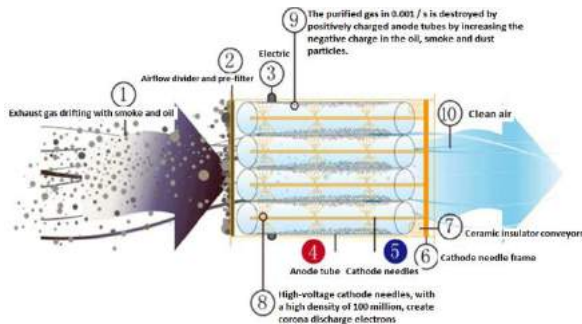


Figure 1. The ESP Working Principle example.

Electro-filters utilize two flow electrostatic ash holders to utilize the ash in the flue gas from the electric field. Sheet metal plates are placed in a closed body. Between these plates the strands are stretched. Each flow becomes a half dust trap. The 225 k VA transformer, which converts 380 Volt DC current for each section, is supplied from the rectifier group. The wires (-) electrode on the electro-filter is plate electrodes (+) electrodes. When voltage is applied to the electrodes, the electrons extracted from the wires collide with the unarticulated dust particles to make them (-) ion. (-) loaded dusts are attracted by (+) charged electrons, so dust particles adhere to the sheet metal and are separated from the

gas. There are cam mechanisms to shake the plates from the dust. With the cam, the plates are shrunk at certain periods. Electric motors provide this motion to the cams. The ashes are drain to the ash silos under the electro-filter. The gas is thrown out of the chimney at about 1600 C by means of a gravitational pulling ventilator. The efficiency of the Electro-Filters is about 98% [1].

II. WORKING PRINCIPLE

According to a very well-known law of elementary electricity information, a pulling force between the two particles having different, i.e., oppositely labeled electric charges, becomes apparent, which tend to approach each other. This principle is based on the realization of electrostatic dust collectors. The dirty air is passed through the thin wires which acquire a high level of electrostatic charge due to being connected to a direct current source having a positive regression of about 13000 Volts. These wires are separated from each other by rods and pipes connected to the ground. The particles gain a positive charge during passage from the electrostatic area between the wires and the rods. The air-to-dust mixture then passes through a series of parallel plates or plates with apertures of about 8 mm between them. Each of these plates is connected to a direct current source having a positive voltage of about 6000 Volts. Positively charged dusts, dusts deposited on a surface coated with a viscous substance, are removed by washing or other method. This type of air cleaning device, which has a very effective structure, allows very fine dust particles to be retained [2].

III. PARTICLE SIZE AND EFFICIENCY IN ESP

The efficiency of collecting dust from the electro-filter depends on the electrical resistance of the collected dust. High-resistance powder can reach an abnormal back corona, which reduces ESP collection efficiency. Effective methods for improving ESP performance

- Reduction of dust resistance
- Advanced flue gas failure system

It can be said as. [3].

A. Design of Electrostatic Filter

The migration rate of the particles and the specific collection area is the determining factors of the efficiency of the electrostatic dust holder. A statistical design approach has been used to establish the effect of changes in the electrical resistivity of the dust on the performance of the electrostatic dust collector. A reliable design methodology comes from the real tests on similar installations equipped with an electrostatic dust collector. However, the ideal electrostatic dust collector should be designed based on the theoretical relationships taking into account all the variable parameters [4].



Figure 2. ESP Overview.

B. Performance in applications

Many factors determine the performance of the electrostatic dust trap in practice. Both research work and experience have shown that particle collection efficiency for electrostatic dust collector is affected by the size of the dust particle. The operating temperature also has an important effect on the efficiency of the electrostatic dust collector. Electrical conditions also play an important role in determining the performance of the electrostatic dust collector. An important electrical parameter is the apparent corona power, defined as the corona power per unit volume of the processed gas. In addition, electrostatic dust collector efficiency, voltage current characteristics, applied voltage is also affected by the wave and gas components [3].

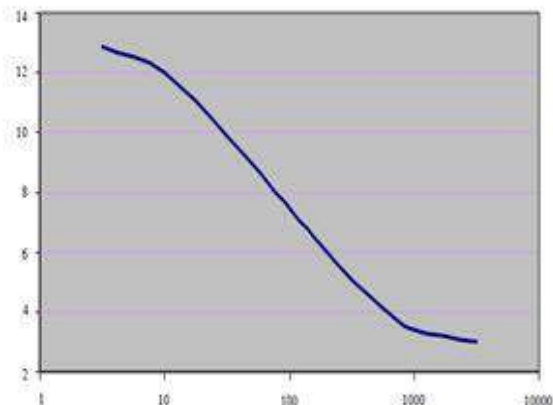


Figure 3. Migration Rate Change by Particle Resistance

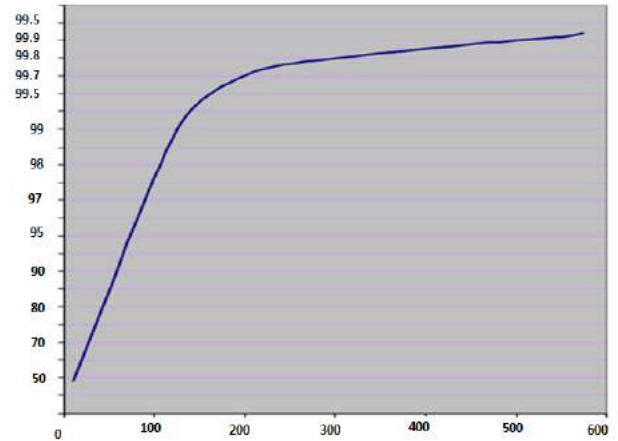


Figure 4. Corona Retention Efficiency.

C. Factors Affecting Electrostatic Filter Efficiency

There are many factors affecting the electrostatic filter efficiency and working style. These are basically as particle size distribution, particle resistance, temperature, gas flow rate and particle density. In an electrostatic filter, large particles are generally easier to hold. Particles with a diameter of 0.2-0.4 μm are the most difficult to hold. This is because the space charge for small particles leads to diffusional loading with thermal ions. A large fraction of small particles ($<1 \mu\text{m}$) in the gas stream reduces the number of particles loaded by reducing corona discharge at the inlet section. In electrostatic filter installation, design should be made by determining the particle size for full capacity processing conditions. The filter is a function of the emission particle size. If the operating temperature is 155° C, particle size and electrostatic filter efficiency appear [4,5].

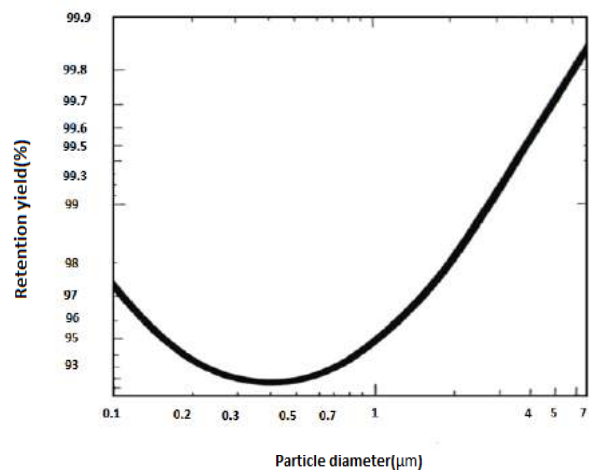


Figure 5. Particle Diameter and Retention Efficiency.

D. Development and Innovation Investigations in Electrostatic Filters

The latest trends that are electrically designed in electrostatic filters focus on low sulphur content, high-resistance cake retention, energy savings and the development of material input from structural materials. Innovations include broad electrode spacing, cut-off feed, pulsed feed, preload and microprocessor and power and shake control.

The most commonly used replacement in electrostatic filters is the use of a wider electrode gap. Instead of the weighted electrode system, a constant corona electrode is used, less collection electrodes and more convenient structural connections are used, with less maintenance and financial savings. The use of a large electrode area has the disadvantage of increasing the process voltage. This can cause insufficient insulation [3].

IV. ELECTROSTATIC FILTER APPLICATION AREAS

- Steel Works
- Sugar Factories
- Chemical Facilities
- Chrome Magnesite Facilities [6].

V. ADVANTAGES AND DISADVANTAGES OF ELECTROSTATIC PRECIPITATOR (ESP)

They have good retention efficiency on small particles due to strong electrical forces. They can be used if the gas pollutants are not explosive and the dusts are not damp or sticky. The composition of the dusts is important because they affect the electrical conductivity (resistance) in the powder layer on the collecting surfaces. As the resistance increases, the holding efficiency decreases.

ESPs work on all resistors, but the best yield is 108-1010 ohm-cm [1,4].

VI. CONCLUSION

Legal requirements oblige operators to determine the quality of atmospheric air. Limit values that are legally controlled and determined may fall to lower levels in the years to come. These legal obligations, including the penalties that will go on until the production plant is shut down, will lead to continual improvement of industrial plants in their filtration systems.

Legally, the first priority of businesses is to increase the efficiency of the filters they use and determine the parameters that affect the filter efficiency. The most important parameter that determines the efficiency of the electrostatic powder holder is the knowledge of the conditions under which the system will work in the design phase and what kind of powder characteristic it will work with. Choosing an incorrect electrode-plate geometry design can lead to undesirable consequences, such as process stoppage, when the false air flow control check will make it difficult to achieve the desired values.

In our industry, electrostatic filters which have continuous operation feature, different operation algorithms, low operating cost and high efficiency are still widely used in the industry. The way to obtain the best efficiency from electrostatic filtration is

generally possible by properly determining the initial parameters of the filter parameters and geometry.

The distance between the plates and the electrode and the different geometries of the electrodes affect the electric field distribution and the maximum electric field strength, as well as the electric field distribution in the physical and chemical structure of the retained powder, thus changing the efficiency of ESP.

It was observed that the grain size of the sintered powder studied in the application was increased as well as the electric field distribution of the water particles inside. It was seen that the water particle approaching the corona electrode increased the maximum electric field intensity.

Under operating conditions, it has been found that the moist material in the filter adheres to the collecting and corona electrode, forming a layer on the electrodes, which prevents the corona discharging to occur at the appropriate level. At the same time, in the short circuits that may occur in the filter, it is observed that the current does not increase due to the high values and the voltage does not increase. In the line failure, the voltage is high and the current does not increase.

The parameters affecting the ESP performance include the gas temperature, moisture, the powder charge in the gas and the components of the powder charge (eg limestone) as well as the fact that the use of reprocessing ESP powder will increase the ESP load and that the ESP powders are more sticky than the normal operating powders. It is difficult to reduce ESP dust through the use of hammers.

As a result of the investigations made, the resistance between the plate and the wire which passes through the ESP directly prevents the undesired cleaning of the plate and the wires, and as a natural result, prevents the emission and corona current as well as the corona tension to be desired. That is why the plates and the wires are either hammered continuously or shaken (Scrubbing) means that it is more appropriate to clean it. If the ESP yield is used in operating processes with different chemical structure, it is foreseen to be increased by controlling the distance between the plate and the wire [3].

REFERENCES

- [1] Ö. Alaca " Electrostatic Filters and Industrial Applications" , Master Thesis , Gazi University Science Institution , Ankara 2007.
- [2] L. Stephen, Francis, Andreas Bäck, Per Johansson " Reduction of Rapping Losses to Improve ESP Performance" Alstom Power Inc, Francis 2009.
- [3] A. BALIK, Precipating Of Sinter Powder By Esp And Effects Of Sinter Powder On Esp Efficiency, Master Thesis, Karabük Üniversitesi Fen Bilimleri Enstitüsü, June 2015.
- [4] Nazaroff & Alvarez-Cohen, Electrostatic Precipitators, pages 447-453.
- [5] D. Xiaoqing, et al. "Experiment Study on Optimization of Electric Field Performance for Electrostatic Precipitator by Using Finite Element Method." Electrostatic Precipitation. Springer Berlin Heidelberg, 169-174, 2009.
- [6] Y. E. Balgün " Elektrostatik Filtre Verimini Artırıcı Çözümlerin İncelenmesi" , Yüksek Lisans Tezi , İstanbul Teknik Üniversitesi Fen Bilimleri Enstitüsü , İstanbul, 11-66, 2009.

Microstructural and Mechanical Characterization of 9Cr -1Mo -1W Weld Metal

Emin SALURI, Mustafa ACARER1, Fikret KABAKCI2, Selcuk KESKINKILIC3, Filiz KUMDALI ACAR3

1.Selcuk University, TURKEY

2.Bulent Ecevit University, TURKEY

3. Gedik Welding, TURKEY

esalur@selcuk.edu.tr

ABSTRACT

A number of studies have been conducted to reduce the use of fossil fuels and gas emissions in power generation industry. In recent years new material technology has emerged depending on this quest. CrMo steels are widely used at power plant constructions as piping and tubing. They are known as heat resistant materials due to high creep strength, as well as their low thermal expansion and high conductivity. During the few decades, high chromium steels have been developed by alloying with elements such as W, Ni, Nb, V, Ti as a result of extensive studies carried out in some countries with the participation of various project partners. In Europe E911 steel was developed which includes 9% Cr, 1% Mo and 1-2% W. E911 steel has martensitic microstructure under air cooling after normalizing. Therefore it is used as tempered condition following normalizing. This paper presents microstructural and mechanical characterization of E911 weld metal. The types and transformations of phase and microstructures of all-weld metal have been investigated through scanning electron microscopy, optical microscope, x-ray diffraction analysis. The elemental analysis of weld metal was determined by x-ray fluorescence and mechanical tests of the weld metal were carried out. In this study it was observed that the microstructure of E-911 steel consisted of tempered martensite, and in some regions δ -ferrite phases were present. According to examined of thermal analysis, in the heating A1, A3, Tcurie temperatures are 850, 890, 750 oC respectively and in the cooling Mf temperature is 650 oC, Ms temperature is 690 oC. When X-ray analysis was examined, carbides (Cr₇C₃, Cr₂₃C₆) in the microstructure were detected. In SEM examinations, in addition to these carbides, Mo₂C, W₂C and VC were observed inside grain and grain boundary. The Brinell hardness test was carried out at room temperature and under a load of 187,5 kgf. The average Brinell hardness is 230 HB. The micro hardness tests were applied for 20 seconds under 50 gram load. The average micro hardness of δ -ferrite zone in microstructure was determined as 165 HV (~ 164 HB). Yield strength, tensile strength and elongation were determined as 550 MPa, 712 MPa, % 18 respectively according to tensile test results at room temperature.

Keywords: Microstructure, E-911 steel, All weld metal, mechanical characterization

Corrosion Behaviour of Steel Wire Rod

Medine KILINÇ*¹, Gülseher DOĞANCIK², Yunus TÜREN³, Yavuz SUN⁴, Hayrettin AHLATCI⁵, İbrahim AFŞAR⁶, Serhat ÖZDEMİR⁷, Hüseyin KOYMATCIK⁸, Hüseyin ZENGİN⁹

^{*}Karabuk University, Department of Metallurgy and Materials Engineering, Turkey

¹medineklnc@gmail.com, ²gulloanck67@gmail.com, ³yturen@karabuk.edu.tr, ⁴ysun@karabuk.edu.tr,

⁵hahlatci@karabuk.edu.tr(corresponding author), ⁶komi_nick@hotmail.com, ⁷srht41534@gmail.com,

⁸hkoymatcik@kardemir.com, ⁹huseyinzengin@karabuk.edu.tr,

Abstract - In this study, the effect of C addition on the corrosion behavior of wire rods of 5.5 mm in diameter was investigated. The horizontal and vertical cross sections of the wire rods with 0.7, 0.8, 0.9 C ratio were taken during the metallographical process. The microstructure of the examined specimens was examined by light optical (LOM) and scanning electron microscopy (SEM). Hardness test of steel containing 0.7-0.9 C was carried out in shimadzu brand micro hardness tester. Corrosion tests of the prepared samples were evaluated according to both the weight loss and the Potentiodynamic Polarization measurements in 3.5% NaCl solution. Despite the increased hardness of the specimens examined, the corrosion resistance decreased. This can be caused by inclusions in the microstructure.

Keywords- Wire rod, Carbon content, Corrosion

I. INTRODUCTION

It is the name given to coil spun metal which is traditionally used in wire rod, coiling-wrap construction. Copper and steel are produced abundantly in this way [1-5]. Karabük Demir Çelik Sanayi ve Ticaret AŞ (Kardemir), one of Turkey's major integrated steel production facilities, a significant investment in wire rod production, which is a semi-finished steel wire for vehicle tires. Kardemir Inc. produces semi-finished product of this material and gives a product which is very special and high value added in industrial area to our country. In this article, the corrosion behaviors of wire rod, which is used in the automotive sector, of semi-finished and high value added cord steel are investigated according to different carbon ratios.

II. EXPERIMENTAL

In this study 0.7 % mm, 0.8 % mm, 0.9 % mm carbon content and 5.5 mm diameter wire rods cut into 10 mm lengths were molded from horizontal and vertical sections for microstructure and hardness scanning. Molded samples were abraded with 200-1200 mesh sandpaper and then polished with diamond solution. The polished samples were examined both in etched and unetched conditions. Examination of the unetched samples was carried out on

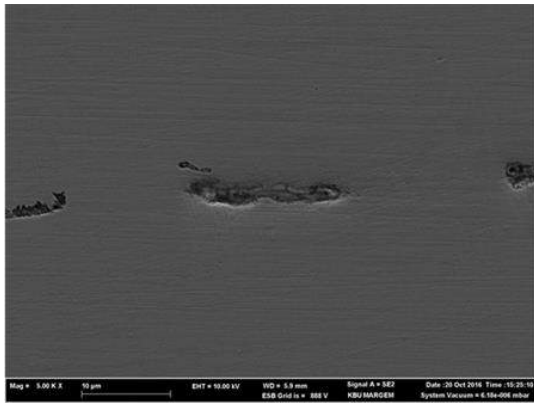
Carl Zeiss Ultra Plus Gemini Fesem brand SEM equipped with EDS apparatus. Microstructure photographs were photographed under a Nikon brand optical microscope.

Weight loss test and potentiodynamic and polarization test were carried out to determine corrosion behavior of the test specimens. The specimens were prepared in 5.5 mm diameter and 1 mm height cylinders in order to determine corrosion behavior by immersion method. Prior to the corrosion test, all surfaces of the samples were polished to 1000 mesh sandpaper according to the metallographic procedure. Before and after the test, the samples were ultrasonically cleaned in pure water for 5 minutes and then rinsed with alcohol and dried. The weight losses of the samples were measured on an electronic scale with a total of 72 mg of 0.1 mg sensitivity. The test results were evaluated in mg / cm² according to the loss of weight per unit surface area of the samples. The experiment was carried out in a 3.5% NaCl solution in a potentiodynamic tester. In the experiment, corrosion test specimens (working electrode) were soldered copper wire 1.5 mm in width and 150 mm in length to the back surface to provide conductivity. It was covered with resin so that only the desired surfaces of electrolyte and contact were exposed. Potentiodynamic corrosion experiments were performed using a computer-controlled Gamry model PC4 / 300mA potentiostat / galvanostat with DC105 Corrosion Analysis software. Experiments were carried out at room temperature and wire rods having a specific surface area in cm² as a working electrode, a 6 mm diameter carbon electrode serving as a counter electrode and a saturated calomel electrode (SCE) as a reference electrode were placed in the test cell. The working electrode and carbon electrode surfaces were placed at a certain distance from each other and the reference electrode was placed as close as possible to the working electrode. To determine the mechanism of the corrosion test specimens on the corrosion surfaces, images were taken with a Carl Zeiss Ultra Plus Gemini Fesem model ZEISS SEM imager.

III. RESULTS AND DISCUSSION

SEM and EDS analysis was carried out on polished samples which are given in Figure 1. The EDS analysis taken from the inclusions were observed longitudinally at the microstructure of the 0.9 %C sample which is shown in Fig. 1 that Manganese and sulfur-rich inclusions were present. In

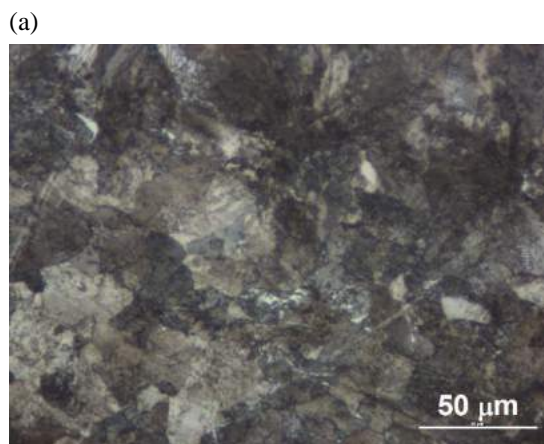
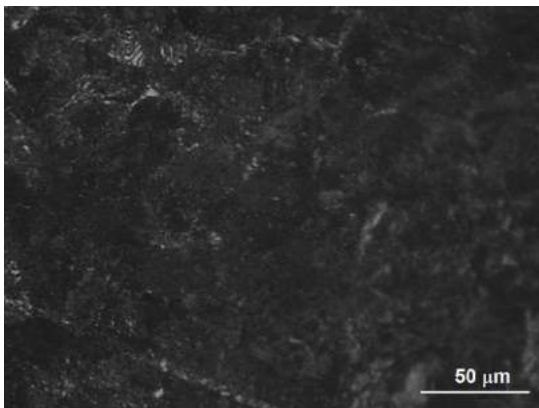
addition, inclusions with bright and circular corners inclusions are found to be rich in Silicium. Observed in the structure of the 0.7%C sample hardness of the investigated samples increased with increasing carbon content.



(a)

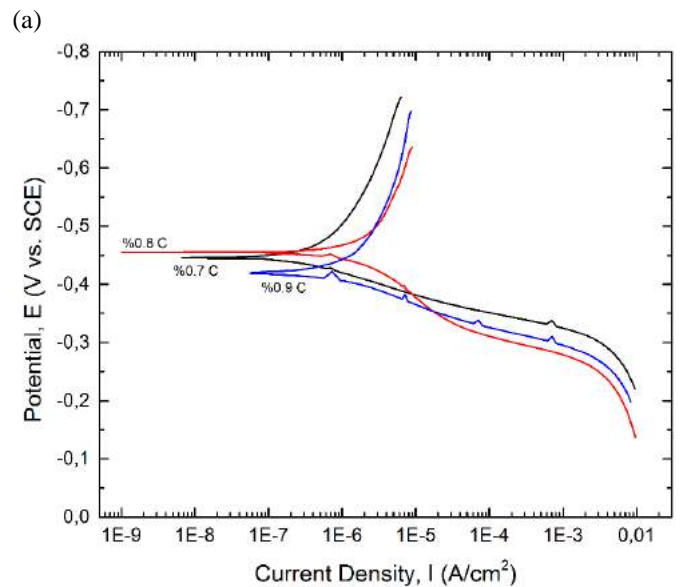
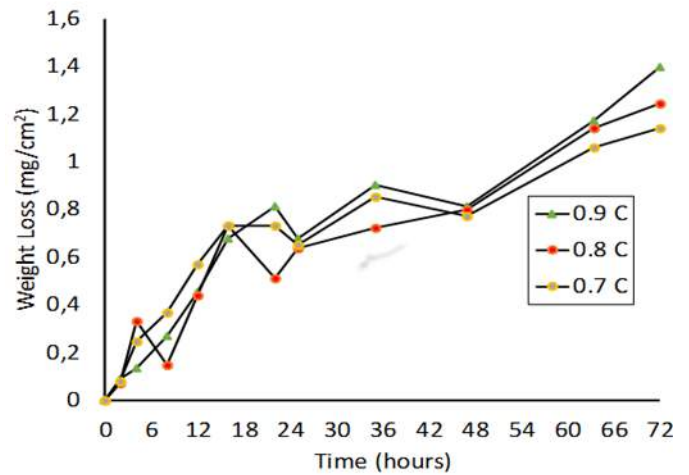
Mass s Percent	C	N	O	AL	Si	P	S	Cr	Mn	Fe
		9.40	0.49	4.83	0.00	0.10	0.00	16.17	0.73	44.86

(b) Figure 1. (a) Polished image of sample with 0.9 C and (b) EDS result of prolonged inclusion



(b) Figure 2. (a) 0.7%C images of and (b) 0.9% C steel microstructure of images

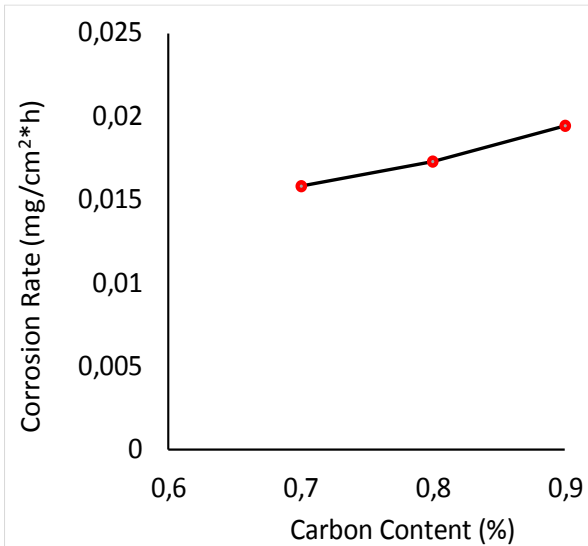
Microstructure images of the specimens examined are given in Figure 2. It has been revealed from the microstructure images that the pearlitic structure and grain boundary cementite are not observed. It is also observed that the grain structure is slightly tapered as the carbon content increases. The results of the weight loss versus time of the samples examined after the immersion methods are given in Figure 3a. The lowest weight loss of 0.7 %C steel after 72 hours, while the most weight loss of 0.9 %C steel. Figure 3b gives the results of the potentiodynamic polarization test. From the results of the potentiodynamic polarization test it is observed that the steel of 0.9 C has higher current density than the others.



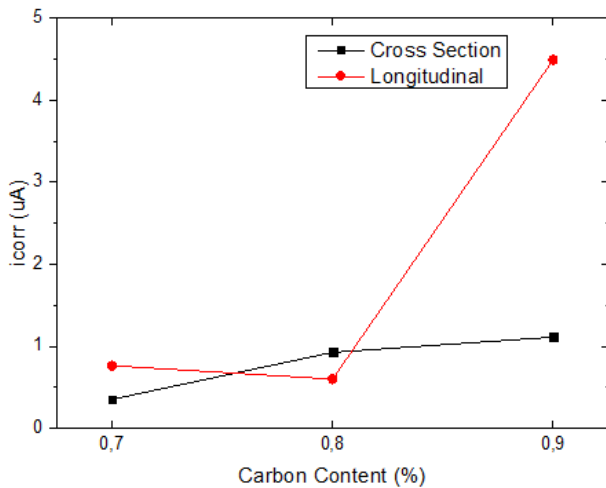
(b) Figure 3. (a) Immersion method and (b) potency test results of the dynamic polarization test

Corrosion rates were calculated in $\text{mg}/(\text{cm}^2 \cdot \text{h})$ [6,7] by taking advantage of the weight loss results of the samples

examined after the immersion method in Fig. 3a. In Figure 4a, change the corrosion rate change were drawn into the graph of the samples investigated due to the carbon content. Figure 4b shows the change in corrosion current density with carbon content by determining the corrosion current values from the tafel curves obtained from the potentiodynamic polarization tests. The results of the changes in the corrosion rates obtained after the two test methods are compatible with each other. An increase in carbon content and an increase in corrosion rates were observed. This can be attributed to the presence of more inclusions in the microstructure of the 0.9% C steel that in other steels.



(a)

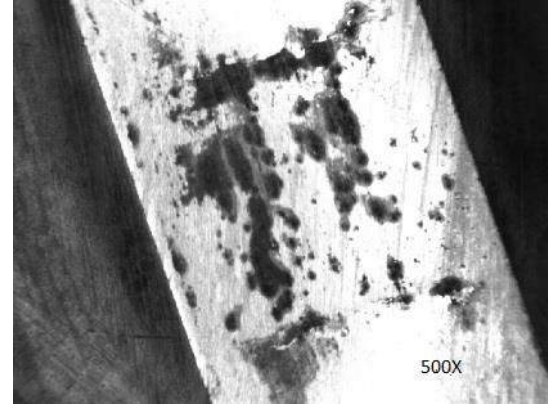


(b)

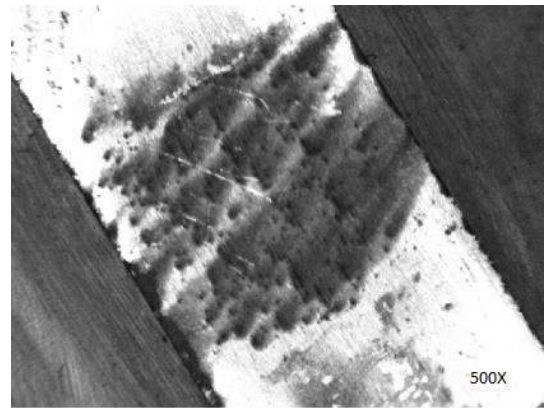
Figure 4. Change in corrosion rate in terms of (a) mg/(cm²*h) and (b) icorr due to the carbon content.

Figure 5 shows the appearance of the samples after corrosion tests. Macro corrosion develops homogeneously. However Figure 5 shows occurrence of pitting corrosion after the test. As increasing carbon

content, pitting failures increased severely.



(a)



(b)

Figure 5. Appearance of corrosion on the surfaces of (a) 0,7% C and (b) 0,9 % carbon steels.

IV. CONCLUSION

The results of the corrosion behavior of wire rods with 0.7 %, 0.8%, 0.9 %C are given below.

1. When the microstructures of wire rods are examined, manganese and silicon rich inclusions are encountered in the structure. Increased inclusion rate with increasing carbon content.
2. Corrosion resistance was higher at 0.7 C and less at 0.9 C. This is based on the inclusions in the microstructure.

V. ACKNOWLEDGMENTS

V. Firstly we would like to thank Karabük Demir Çelik Sanayi ve Ticaret AŞ (Kardemir), one of the most important integrated steel production facilities of Turkey which supports this scientific research, ARGE Coordination Engineer Çağıl KOYMATCIK, Furkan

ÇETİNKAYA, Business Engineer who helped us to see the wire rod production line, thank you to Karabük University Department of Metallurgical and Materials Engineering which provides our researches.

References

[1] Ochiai, I., Nishida, S., Tashiro, H., Wire J. Int. 26(12), 50 (1993)

[2] Takahashi, T., Ochiai, I., Tashiro, H., Ohashi, S., Nishida, S., Tarui, T.: Shinnittetsu Giho. (354), 39(1994)

[3] Tarui, T., Takahashi, T., Tashiro, H., Nishida, S.: Metallurgy , Processing and Applications of Metal Wires. TMS, 1996, P.87

[4] Balin, B., 2004. Seçilen Karakteristiklerin Tel Çekme İşlemi Üzerindeki Etkileri. Yıldız Teknik Üniversitesi Fen Bilimleri Enstitüsü, Y. Lisans Tezi, 71 s, İstanbul.

[5] Bitkov, V. 2006. Research of Wire Drawing Under Conditions of Hydrodynamic Friction, Wire and Cable Technology, 94- 97.

[6] YALÇIN Hayri, Timur KOÇ, Korozyon ve Katodik Koruma, ANKARA, 1991.

[7] ERDEN Seyit, M. Caner DEĞERTEKİN, Korozyon ve Katodik Koruma Kocaeli - EMO -Şubesi, 2004.

A Literature Review to Design of 60 Metres Aerial Work Platform

Yasin Yaman*, İlhan Asilturk⁺

*Hidrokon, Selcuklu \ Konya, Turkey
yasin.yaman@hidrokon.com

⁺Faculty of Technology, Selcuk University
Selcuklu, Konya, Turkey
iasilturk@selcuk.edu.tr

Abstract— In this paper, a literature review was conducted for the development of the aerial work platform with a working height of 60 meters, which was installed on the truck. And mentioned to why needed for work platforms, how they were developed, and their history as well as areas of use. In the near future, this study has been thought that the platform to be designed will help to be secured, technologically and low cost.

Keywords— Aerial work platform (AWP); access platform; structure; cherry picker; mobile elevating work platform (MEWP)

I. INTRODUCTION

An aerial work platform is a mechanical structure used to provide temporary access to inaccessible areas. Scaffoldings have been built, which were developed to provide people to access and work at these heights before the platforms. A scaffolding building process could be laborious and costly as well as taking a long time depending on the altitude and the environment to be worked on.

The first platform (e.g. Fig. 1), which was similar to today's work platforms, was invented by Jay Eitel in 1944. In the summer of 1944, Eitel has found trouble to move stairs and climbing to staircase countless times for collecting cherries, and began to search for a solution that could make it easier. He has developed a simple steel construction with high maneuverability, which can be controlled by a single arm, mounted on a van chassis working. Finally, he named his invention as a "cherry picker" that is still being used. In this way, Eitel laid the foundations for that mobile elevating work platform industry. [1]

Same like in many sectors, aerial work platform sector watches the developments in the iron and steel industry closely. With the development of the iron and steel industry in the period from the first platform to the present day, high-strength steels have been started to use in the construction of aerial work platforms. Lighter and more efficient aerial work platforms have been manufactured with using of high strength steels, which has yield strength 960 MPa and 1100 MPa. Today there are platforms up to 100 meters working height. The future of the iron and steel industry can carry this height even higher.



Fig.1 An aerial work platform designed by Eitel in 1944

ZZZ. Aerial Work Platform Usage Areas

Work platforms are purchased oftenly by rental companies, in order to lease to construction companies, institutions or individuals who has special needs. Development of technology is leading to the growth of the construction and industry in the world, so the demand for energy in the global sense is constantly increasing. Wind turbine systems, which are becoming increasingly common in many countries, are predicted to be the most used energy sources of the future. According to Turkey National Renewable Energy Action Plan, in 2023 Turkey's wind turbine systems will be 8 times bigger than year 2013. Consequently, Aerial work platforms are absolutely necessary for the installation, maintenance and repair of wind turbines (e.g. Fig. 2); it is just a sign which will increase to the demands day by day, even in this sector. [2]



Fig.2 Maintenance of wind turbine with an aerial work platform

The aerial work platforms market is going to reach a market value of US\$ 15.3 Billion by 2026. That growth equals to Compound Annual Growth Rate (CAGR) of 6.5% in 10-year forecast period (2016-2026). [3]

II. MATERIAL AND METHOD

A comprehensive literature review was conducted to design a 60 meters platform. In addition, standards and regulations that would create design constraints were researched.

AAAA. Literature Review

In the study of Y. Hong and his colleagues, the boom structure of a 42m weather platform was developed. As a design input, they have argued that the hexagonal boom section is more resistant to bending moment and stress intensity. And they study in design and finite element analysis (FEA), for applying to verify the stress distribution, stress concentration, deflection, natural frequencies. In these analyses, the boom system has been analysed at critical loads and working positions. Consequently, they found that highest values of the stress concentration and deflection. Besides, the safety coefficient has been determined according to the obtained data. At the end of the study, after the boom design, they had been compared their prediction with the analysis results. [4]

In the study of Y. Guder, the optimal construction design of the superstructure of 8x8 mobile crane with 100 tons of capacity, with the numerical calculations and system's finite elements method the statical and dynamical analyses have

been done (e.g. Fig. 3). By the studies realized within the context of the thesis, by taking the macro and thickness written in the analysis environment, material yield strength and security parameter values into consideration the strain optimisation is automatised, and made appropriate for all the product sorts. [5]



Fig.3 Mobile crane design

BBBB. Standards and Regulations

Increasing number of work platform manufacturers, competition conditions are getting harder every day. As a result, in order to increase their profits and at the same time to reduce their costs, some companies may compromise from safety precautions. Some standards and regulations have been established for the production of security of aerial work platforms. The main standards and regulations are;

- TS EN 280 Mobile elevating work platforms - Design calculations - Stability criteria - Construction - Safety - Examinations and tests,
- Occupational Safety and Health Regulation,
- Road Transport Regulation,
- Regulation on Safety of Machinery (2006/42/EC)

4) *TS EN 280*: This European Standard is to explain rules for safeguarding persons and objects against the risk of accidents associated with the operation of Aerial Work Platforms (AWPs). In addition to, this standard includes the structural design calculations and stability criteria. Also it is applicable in construction, safety examinations and tests before AWPs. It describes the hazards arising from the use

ACKNOWLEDGMENT

of AWP's and shows the technical ways for the elimination or reduction of these hazards. [6]

2) *Occupational Safety and Health Regulation*: The occupational safety and health programs intend to create a safe and healthy work environment. In the "Occupational Health and Safety Regulation in Construction Work" published in the Official Gazette dated October 5, 2013 and numbered 28786, if there is possibility of injury or fall down in every level of work, it is called high work. Precautions to be taken in order to create safely and healthily work at high altitude are explained. In short, it is an important regulation about the aerial work platform designs and applications in terms. [7]

3) *Road Transport Regulation*: The purpose of this Regulation is to regulate road transport activities as required by the national economy; To provide order and safety in transportation activities; In accordance with the principles of financial adequacy, professional competence and professional respect for transportation, agency, transportation works commission, transportation business organizer, transportation warehouse operation, cargo operation, logistics operation, terminal operation, distribution operation and similar transportation activities, , Determining the rights, responsibilities and obligations of the senders, the passengers, the employees; To determine the qualifications of the persons employed in transportation activities and the vehicles, equipment, structures, facilities and the like used in transportation activities; To ensure that road transport serves as a complement to each other and with other transport systems, and that the available facilities are used in a more beneficial way. Briefly, the dimensions, weight and axle loads of the truck mounted aerial work platform, should not prevent it from getting into traffic. The truck must comply with the provisions of this directive. [8]

4) *Regulation on Safety of Machinery (2006/42EC)*: This regulation covers the conformity assessment of the machine, interrogation of the suitability of the components and safety components used in the machines. It also includes the safety of machines, replaceable equipment, safety components, lifting accessories, chains, ropes and belts, removable mechanical transfer devices, partially completed machinery. [9]

III. CONCLUSIONS

In this study, a literature review study for the platform to be designed in the forthcoming period is presented. The importance of the iron and steel industry has been emphasized in order to produce aerial work platforms that can reach high areas. The development of the aerial work platform industry in history and the design constraints for platform production, which can enable safe operating today, are shortly described.

This study was supported by Hidrokon Ind. Trade. Co. Ltd.

This article is derived from Yasin YAMAN 's master thesis.

REFERENCES

- [1] (2012) Lift and Access Magazine website [Online.] Available: <http://www.liftandaccess.com>
- [2] "Turkey National Renewable Energy Action Plan data sheet" Ministry of Energy and Natural Resources, Ankara, Turkey.
- [3] (2016) Future Market Insight Magazine website [Online.] Available: <http://www.futuremarketinsights.com/>
- [4] Y. Hong, S. Han, J. Lee, D. Hong and Y. Kim, "Structural analysis of boom system in 42m aerial platform truck," Chonbuk National University, Jeonjusi, Jeonbuk, South Korea, Boom System Tech. Rep. 2007.
- [5] Y. Guder, "Telescopic boom and jib boom mechanism of mobile cranes desing, analysis and optimization" M. Eng. thesis, The Graduate School of Natural and Applied Science of Selcuk University Konya, Turkey, Nov. 2014.
- [6] Mobile elevating work platforms - Design calculations - Stability criteria - Construction - Safety - Examinations and tests, TS EN 280, 2015.
- [7] (2013) Official Gazette website. [Online]. Available: <http://www.resmigazete.gov.tr/>
- [8] "Road Transport Regulation data sheet", Ministry of Transport, Maritime Affairs and Communication, Ankara, Turkey.
- [9] (2009) Official Gazette website. [Online]. Available: <http://www.resmigazete.gov.tr/>

Tribological Damages on Projectile Steel Tip Surface after Ballistic Impact

Mehmet Baki KARAMIŞ

Erciyes University, Engineering Faculty, Department of Mechanical Engineering

KAYSERİ, TURKİYE

karamisb@erciyes.edu.tr

Abstract- This study investigates the some tribological behaviour of the steel tip surface of armor projectiles after ballistic impact. For this purpose many ballistic tests were performed with steel projectile tip on Metal Matrix Composites (MMCs) such as 5083, 6063 and 7075 aluminum alloys as matrix reinforced with SiC and Al₂O₃ particles. Terminal ballistic tests with AP 7.62 and 9 mm projectiles were performed on these composites. The mean velocities of AP 7.62 and 9 mm projectiles are 710-800 and 400 m/s, respectively. The distances between the armor and running position of the projectiles were 5 and 15 m for the 9 mm and AP 7.62 mm projectiles, respectively.

It is observed that The projectile nose is broken or deformed plastically when it impacts the composite target. If the composite has hard reinforcement particles such as Al₂O₃, the friction between projectile tip and hole surface becomes greater and the projectile surface is scratched by ploughing. Plastic damage or breaking of the tip nose leads to increasing the resistance to the projectile movement through the target hole. The predominant wear mechanism of the tip surface is abrasion. Microcutting and plastic yielding as bulging are also observed on the tip surface as wear mechanisms. Deep valleys on the tip nose and deep grooves on the main surface of the projectile tip are also observed. This shows that a the composite manufactured from Al and Al₂O₃ has good ballistic performance against AK-47 (7.62mm×39mm Armour Piercing) and G3 (7.62mm×51mm Armour Piercing) projectiles.

Keywords—Ballistic test, Projectile tip, Projectile tribology, Impact wear, composite material

I. INTRODUCTION

Ceramic materials have been considered for armor applications for over 30 years. Generally, these materials are very strong in compression and weak in tension. They are also very brittle, but can have significant strength after failure when under compression. Metal matrix composites (MMCs) are widely used in the manufacturing of some machine elements and in armor systems. Therefore, the research on these composites has been intensified. As the need for these composites in wider application areas increases due to their high stiffness and strength properties, the dynamic deformation characteristics of these composites

must also be investigated. Although these materials have high modulus, hardness, wear resistance, good oxidation and corrosion resistance, they also have some poor properties such as lower strain to failure, higher cost and difficulty of processing. However, particle reinforced MMCs have good properties of both ceramic and metal. The relatively high complexity of impact problems is caused by the large number of intervening parameters like relative velocity of projectile and target, shape of colliding objects, relative stiffness and masses, time-dependent surface of contact, geometry and boundary conditions and material characteristics.

II. MATERIALS AND METHODS

CCCC. Materials

The material used in this investigation is 5083, 6063 and 7075 aluminum alloys as matrix reinforced with SiC and Al₂O₃ particles. The matrix material is extensively used in defense applications due to its favorable ballistic properties, moderate strength, high corrosion resistance and super plastic potential.

TABLE 1
THE CHEMICAL COMPOSITION OF THE AL MATERIALS
USED IN BALLISTIC TESTS

Material	% Si	% Fe	% Cu	% Mn	% Mg	% Cr	% Zn	% Ti
5083	0.4-0.7	0.4	0.1	0.4-1	4.0-4.9	0.05-0.25	0.25	0.15
7075	0.4	0.5	1.2-2	0.3	2.1-2.9	0.18-0.28	5.1	0.2
6063	0.2-0.6	0.35	0.1	0.1	0.45	0.1	0.1	0.1

DDDD.

Methods

Manufacturing of the composite is performed by the squeeze casting method. SiC and Al₂O₃ particles were incorporated into the matrix material in different volume fractions. They were solidified under a pressure of 180 MPa in a steel mold with a 650–700 C temperature range.

The manufactured MMC specimens were disc shaped with a diameter of 120 mm and a thickness of 20 mm. Any heat treatments have not been applied to the MMCs. Namely, the samples were tested with T0 conditions. The flashes on the samples generated during casting were removed by machining

Terminal ballistic tests with AP 7.62 (Fig.1-a) and 9 mm (Fig.1-b) projectiles were performed on these composites. The mean velocities of AP 7.62 and 9 mm projectiles are 710-800 and 400 m/s, respectively. The distances between the armor and running position of the projectiles were 5 and 15 m for the 9 mm and AP 7.62 mm projectiles, respectively.



Fig. 1 a) AP 7.62 b) 9 mm projectiles

DISCUSSION

The microstructure of MMC can be seen in Figure 2. It is obvious that the SiC particles are distributed homogeneously. In the interface of particles and the matrix, direct reaction of SiC and Al occurs to form hexagonal platelet-shaped Al₄C₃ crystals and free Si.

TABLE 2
REINFORCEMENTS PROPERTIES

Reinforcement	ParticleSize (mm)	Density (gr/cm ³)
SiC	0.25 – 0.5	3.1
Al ₂ O ₃	0.5-1, 1-2, 4-8	3.6

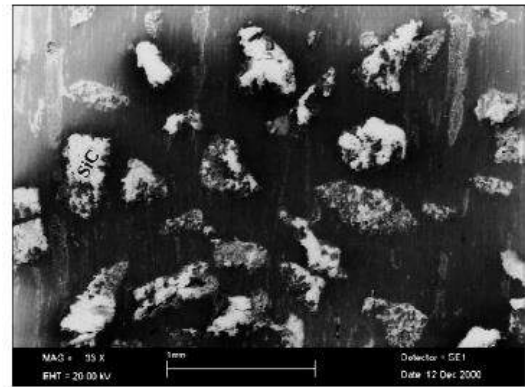
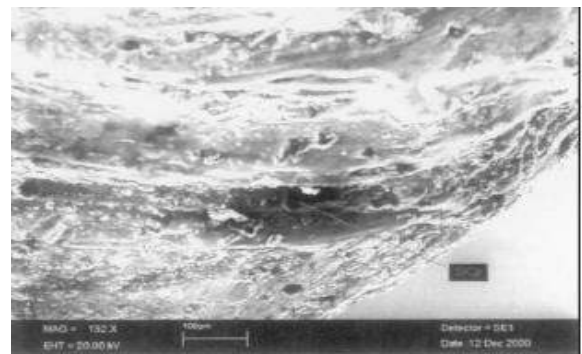
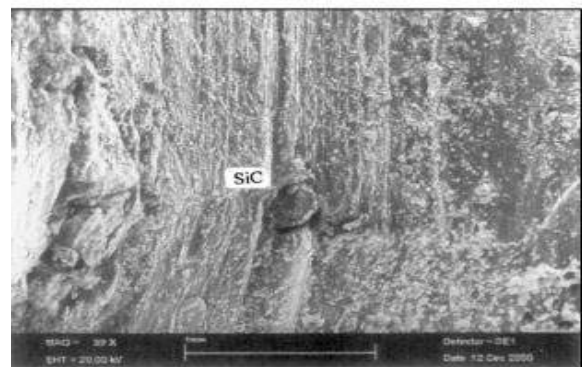


Fig. 2 Micro structure of SiCp composites

The strong friction between the particles and the penetrator generally lowers the penetration depth. It can be seen in Figure 3(a) that the SiC particles scratch the projectile surface by ploughing mechanism. By this friction mechanism, the kinetic energy of the projectile is dissipated and thus the penetration depth is reduced. The main purpose of MMC usage in armour applications is to prevent perforation. The prevention is also provided by scratching the hole surface (Figure 3 b). When the projectile enters the target, it meets with some particles and transfer them to another zone on the surface by ploughing. If the particles are brittle such as SiC, they are sometimes shattered into smaller pieces and buried into the frictional surfaces and this increases the frictional forces between frictional pairs.



(a)



(b)

Fig. 3 (a)The projectile surface scratched by SiCp (b) The hole surface scratched by SiCp (material AA6063 15%).

It is obvious that some particles have been pulled out of their locations and buried either to hole or to its surface by projectile (Fig. a). On the other hand, some of these particles, close to the surface, have been shaken only and consequently gaps in their surroundings have been formed due to particle displacement or the breaking up of the particles (Fig. b). It is obvious that the projectile is plastically deformed when it impacts against the armour surface.

However, it follows its direction itself in the MMC matrix. It can be seen in Figure 4 that a projectile nose, shot at 710 m/s a speed of, has lost the sharpness and swell after impacting and stopped by in the matrix. While the nose was plastically deformed, some coarse and finer SiC particles were transferred to the projectile surface by adhering to the projectile. On the other hand, some of the large particles become free by being broken from the worn surfaces. These events cause dissipation of the kinetic energy of projectile and decrease in the penetration depth. There is evidence that friction behaviour of the projectile in the MMC is an important factor for its ballistic performance. It can be claimed that the stronger the friction, the smaller the penetration depth.

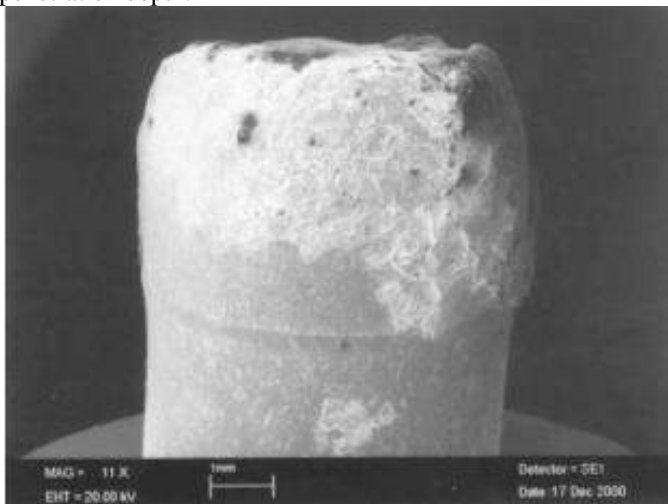


Fig. 4 The swelling and failure of projectile nose shot at 710 m/s speed

The projectile is slowed down by particle friction initially but stopped by others embedding to both surfaces. Examples for these friction mechanisms can be seen in Figure. The figures show that embedded particles cause the projectile to stop in the matrix.

It can be easily supposed that a big crater can result from impact leading to the plastic deformation of the nose (Fig.5 a). Also many deep grooves can be seen on the transition areas between the nose and the vertical surface of the projectile (Fig.5 b).

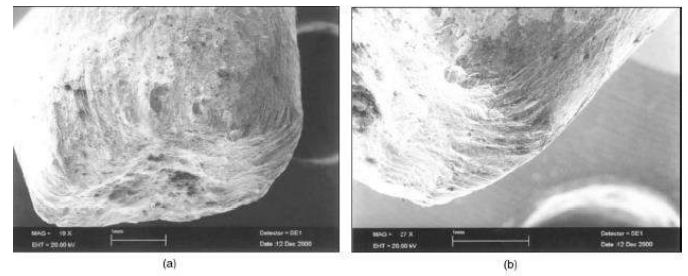


Fig. 5 The crater, land and deep grooves caused by plastic yielding, and SiC particles. (a) Crater and land after impact; (b) deep grooves caused by frictioning of SiC particles

The projectile surface is scratched by the SiC particles and the plastic deformation is also occurred during the scratching while some wear debris is generated by frictional effect. Fig. c also shows evidence that there are many deep grooves caused by reinforcing particles on the friction surface parallel to the propagation direction. The strong friction leads to the deceleration of the projectile in the armours.

Only 10% of the groove volume is wear debris, while the other 90% is swelled by the occurrence of plastic yield [26]. Some cracked SiC particles are also observed on the grooves adhering loosely to the surface (Fig. d). It is possible that the wear debris generated by the abrasion can be melted over the surface.

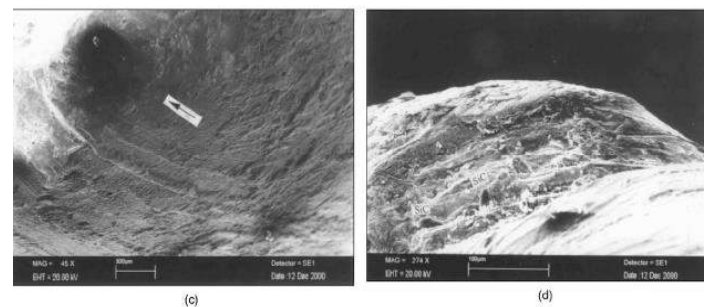


Fig. 5 The crater, land and deep grooves caused by plastic yielding, and SiC particles (c) the wear tracks occurred by reinforcing particles on the nose surface (d) scratching and swelling edge of the deep grooves with SiC particles.

The surface characteristics of the AK-47 (7.62mm×39mm Armour Piercing) and G3 (7.62mm×51mm Armour Piercing) projectile tips (Fig.6 a and b) were also investigated after impacting an Al alloy reinforced with Al₂O₃ particles at high velocity. The composite samples were manufactured from Al-7075 by the squeeze casting method and they were subjected to ballistic impact tests as defined in related ballistic standards of the National Institute of Justice standards.

One factor affecting the ballistic performance of armour is the friction between the surface of the armour hole and the projectile. The more friction occurs, the better performance is created. On the other hand, the frictional characteristic of the armour heavily depends on the reinforcement particle volume fraction and type. Strong friction causes damage to the surface of the projectile tip. Damage types occurring on the tip surface are predominantly macro deformation and breaking of the tip, micro cutting, scratching, and adhesion

of the matrix material by melting and embedding of particles in the projectile surface.

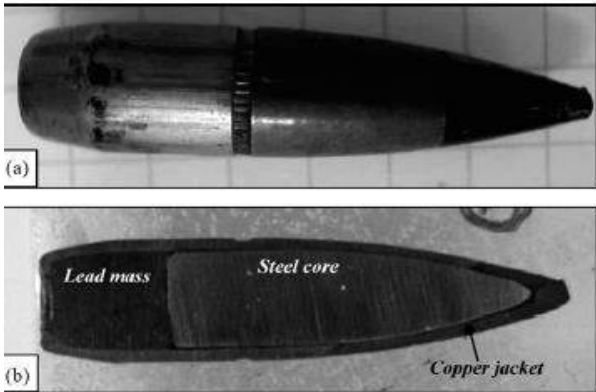


Fig 6 (a) AK-47 Armour Piercing projectile (b) projectile cross section.

Figure shows the some macro damage on the projectile tip caused by armour plate during impact. It can easily be seen that the projectile tip may have been broken and blunted (Fig. 7 a). This breaking often occurs if the projectile impacts a hard zone generated by collecting the hard Al₂O₃ particles onto the target surface. After the projectile tip enters the armour plate, it has to pass among the hard and coarse Al₂O₃ particles.

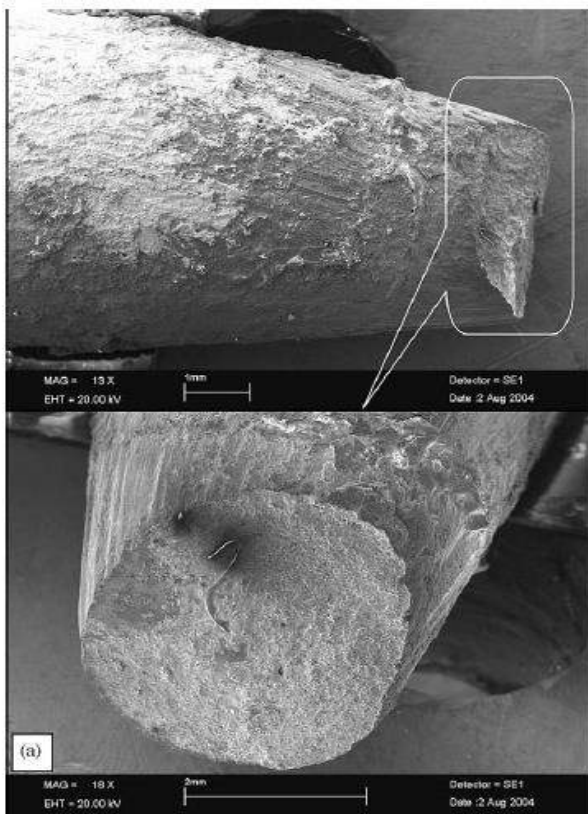


Fig 7 Damage on the projectile tip after impacting (a) broken AK-47 steel projectile tip

Sometimes, this interaction caused to asymmetric forces on the nose of the projectile. These forces deflect projectile line of flight inside the target and may be bend projectile nose (Fig. 7 b). This phenomenon may be resembled projectile impact to an inclined Plate.



Fig. 7 Damage on the projectile tip after impacting (b) plastic deformation of the tip by bending.

It may also detach some parts from projectile nose by breaking, and big craters can be formed (Fig.7 c). Even when the projectile is very sharp, the interception capability of the composite target is very satisfactory. It can be seen from the figure that penetration of the projectile tip to the target is too hard and the projectile lost some parts from its nose. Some deep valleys generated from friction with Al₂O₃ particles can also be observed on the tip nose (Fig.7 d).

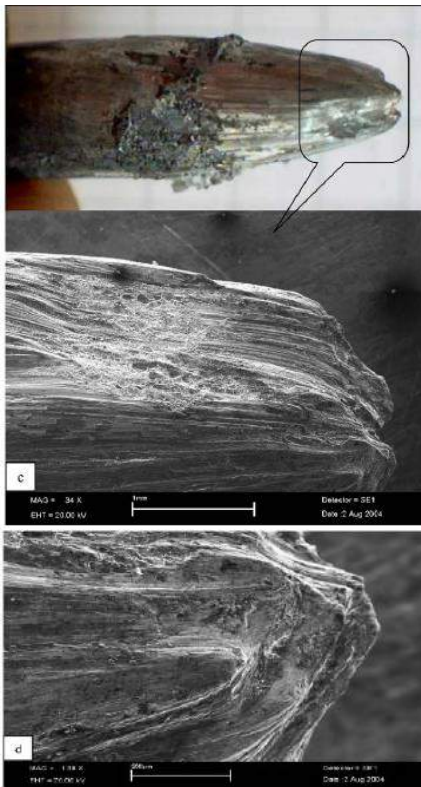


Fig. 7 Damage on the projectile tip after impacting: (c) crater on the tip nose by breaking, and (d) deep valleys on the tip nose.

On the other hand, some composite material with reinforcement is transferred by adhering or embedded to the tip surface as shown in Fig.8 a. When the projectile enters the target, it meets hard Al₂O₃ particles some of which embed into the surface (Fig.8 b). With subsequent movement, the surface of the projectile tip is scratched by ploughing. As explained above, deep grooves are formed together with microcutting, yielding and bulging (Fig.8 c).

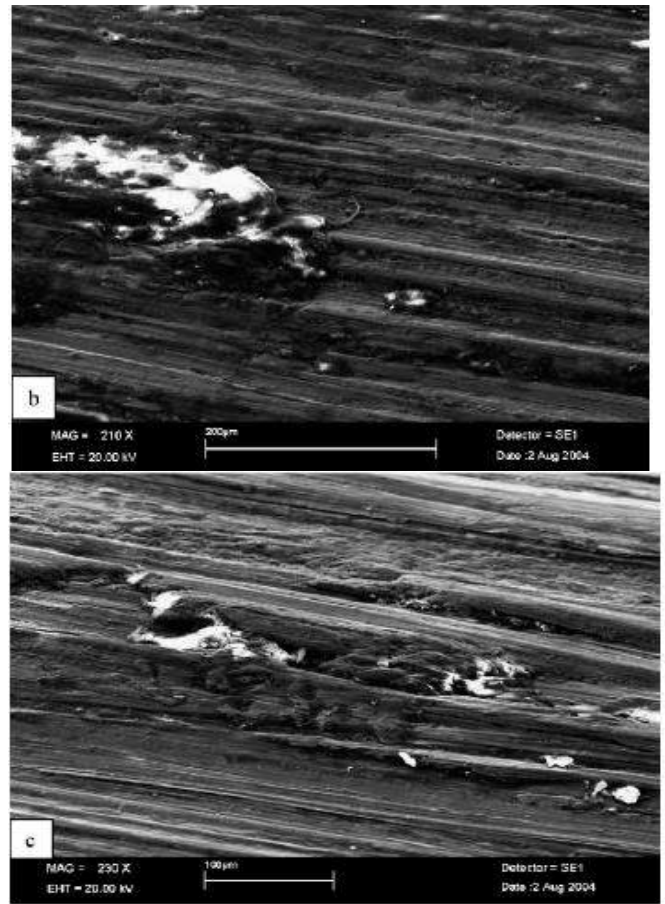
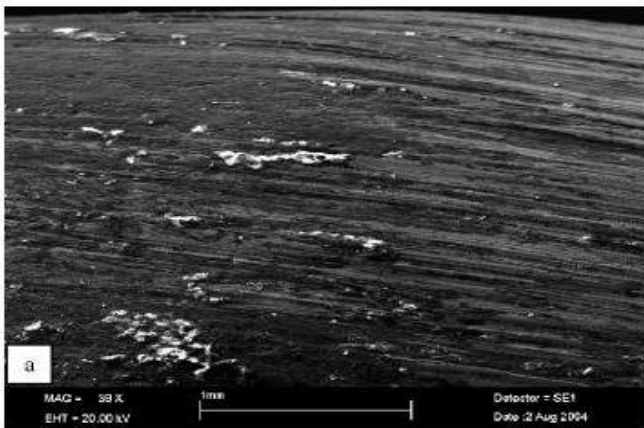


Fig. 8 SEM observation of the tip surface: (a) transferred composite material on the tip surface, (b) Al₂O₃ reinforcement particle transferred by embedding, and (c) deep grooves on the tip surface

It can be seen that the wear mechanism on the tip nose is predominantly abrasion and microcutting and plastic yielding is also observed. Surprisingly that some matrix material can be observed adhered to the nose. It is easily estimated that this adhering material can be yielded plastically by the effect of frictional heating during the strong friction and high pressure and shear stresses involved. This situation can be seen clearly from Fig.9 a. This adhering material is thick and may include some reinforcing particles too (Fig. b).



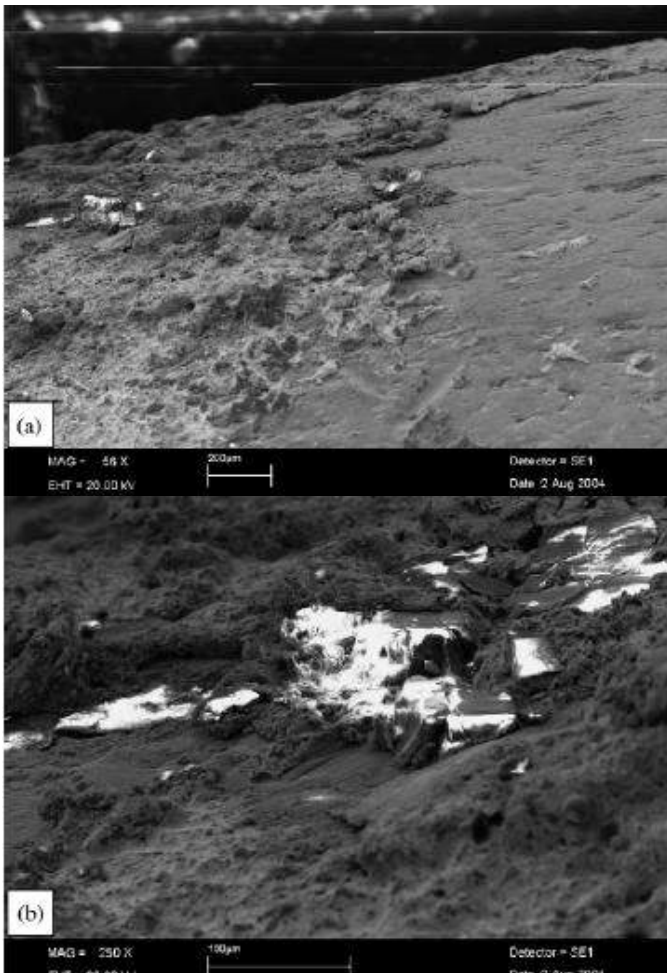


Fig. 9 Adhered material on the projectile tip surface: (a) matrix material adhered to the tip surface, (b) Al₂O₃ reinforcing particles.

However some melted areas can also be observed in this thick yielded layer (Fig.10 a). So,during the high-velocity friction, the Al matrix material melted, adhered to the surface and resolidified rapidly there. After this rapid solidification, it is hot cracked (Fig.10 b), and Karamis area occurs (Fig.10 c).

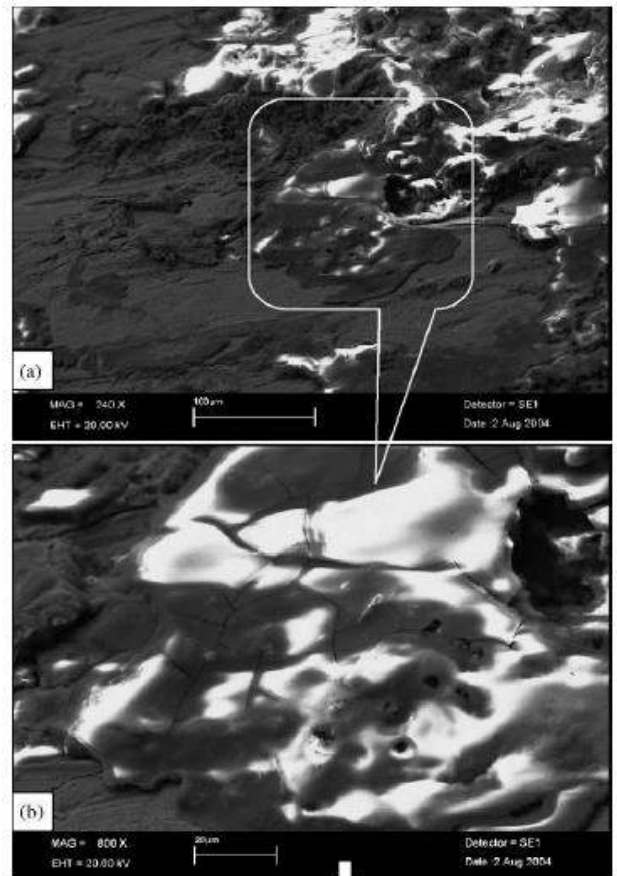
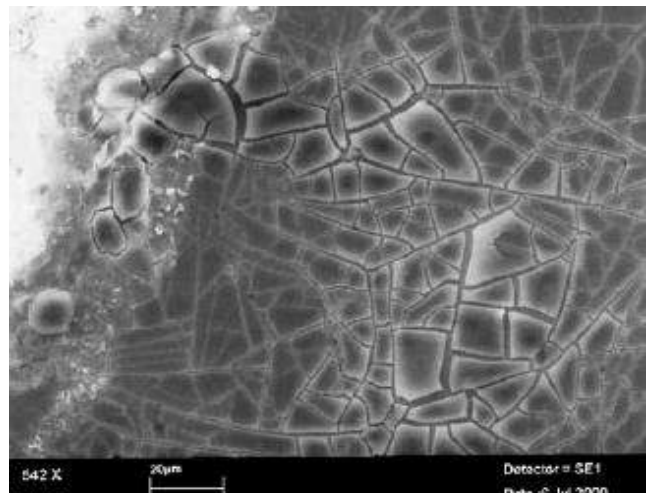


Fig. 10 (a)Melted zone in the adhered layer on tip surface (b) hot cracking on the melted zone Karamis area

This was explained elsewhere for a hole surface created by projectile impact on MMC. This covering material is also observed on the projectile back surfaces Although there is dramatic abrasion damage to the projectile tip surface, some melted and yielded matrix material adhered to the tip surface. After the melted Al material adhered to the surface, it oxidized and solidified rapidly there (Karamis area). Therefore, these areas have Al₂O₃ caused by oxidation .



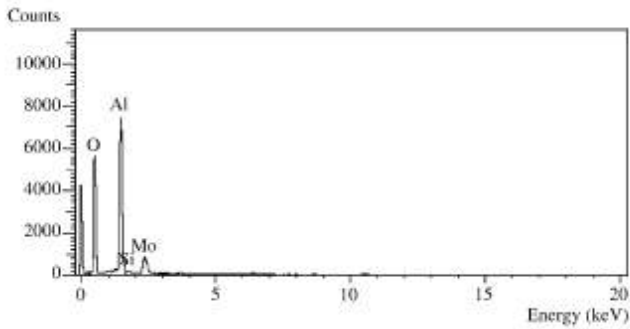


Fig. 10 Karamis area and ED-X analysis of Karamis area

Some matrix material and some melted Pb generated from lead mass at the back side of the projectile tip also adhered to the surface by plastically yielding from areas at temperatures lower than the melting point of Al (Fig.11 a). Area a on the layer consists of fully melted and solidified Pb (Fig.11 b). This Pb on the layer is due to the Pb, contained in the projectile jacket so that the mass of the projectile could be increased.

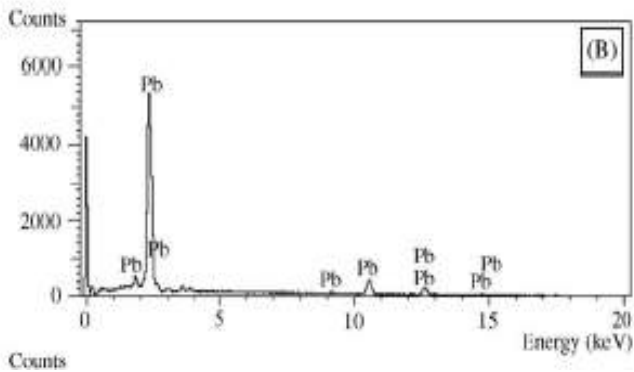
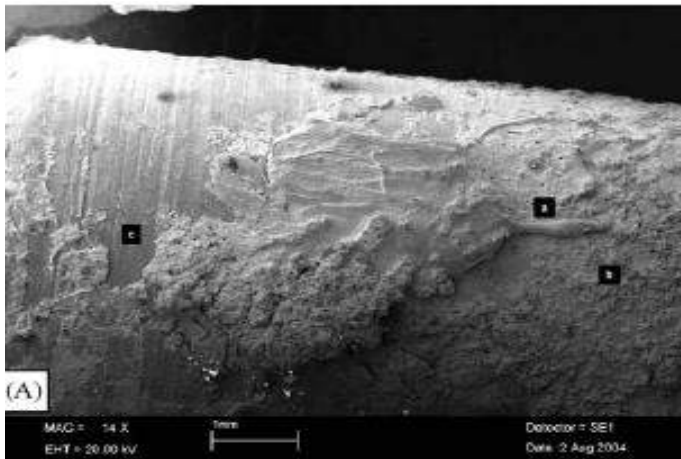


Fig. 11 (A) Layers adhered by plastic yielding and by melting on the tip surface, (B) ED-X analysis of point a,

When the projectile tip impacts the target, its jacket made from a copper alloy and containing some Pb interacts with the hole surface through friction while the tip goes on into the composite (Fig. C). Therefore, some Pb stuck to the tip

surface from the inner side of the copper jacket is melted easily by frictional heating and resolidifies on the tip surface. The same phenomenon happens with the melted matrix material. It is interesting that matrix material at point b also has a major Pb component, generated from the back side of the projectile tip (Fig. D). It is estimated easily that point c on the tip surface mainly consists of Fe because tip material is steel (Fig. E).

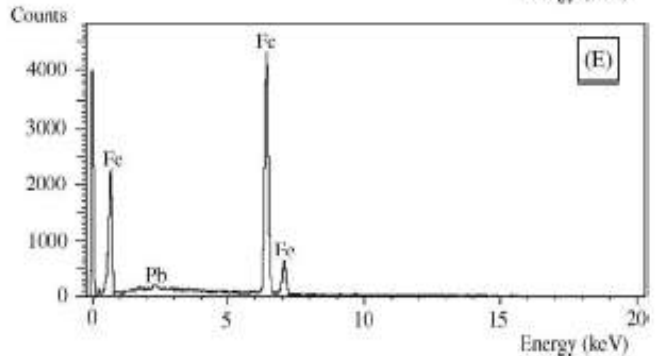
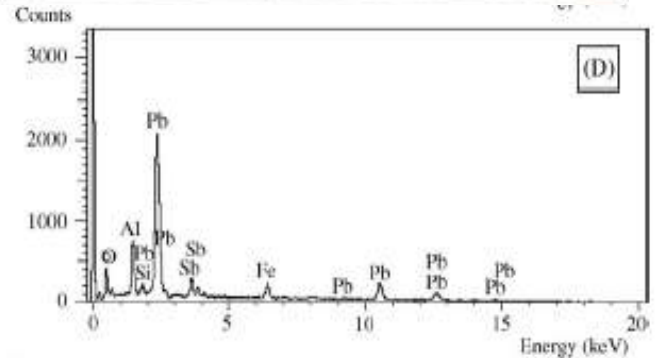
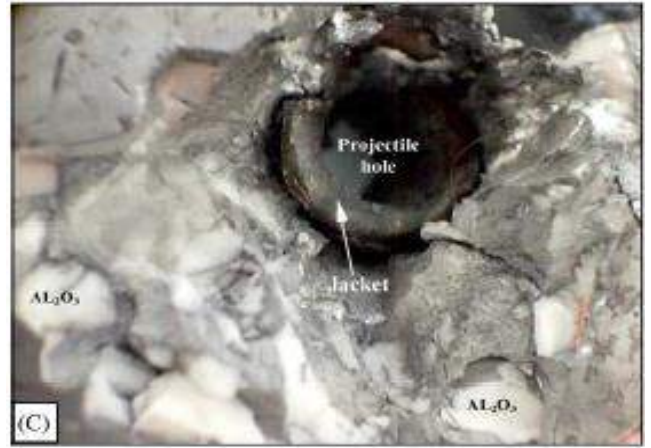


Fig. 11 C) intercepted projectile jacket by composite, (D) ED-X analysis of point b, and (E) ED-X analysis of point c.

When the projectile surface is examined by SEM, it is seen that the surface is scratched dramatically by the reinforcement particles in the composite. It is understood that the Al₂O₃ reinforcement particles scratch the surface by ploughing due to the strong friction (abrasion) between the particles and projectile tip (Fig.12)

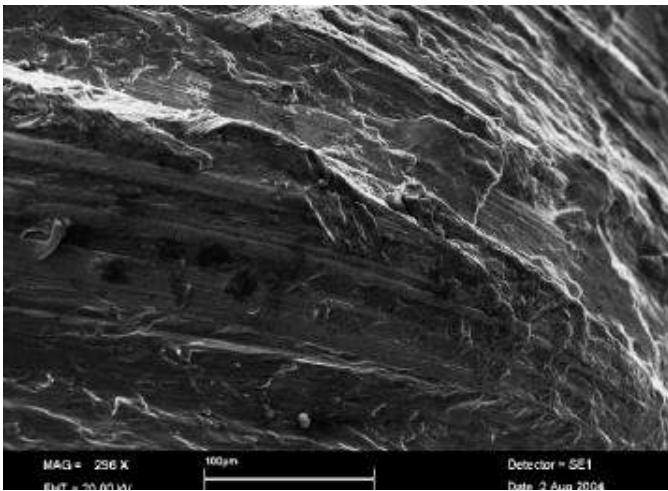


Fig. 12 SEM examination on the projectile tip surface.

This strong friction leads to a reduction in the velocity of the projectile, and thus the penetration depth is reduced when compared to that of the matrix alloy. For example, the G3 projectile could not pass the layered composite (Fig.13 a), while it could pass throughly to the unreinforced Al alloy and it penetrated to the backing material (Fig.13 b). The shallower the penetration depth, the better the performance of the armour. Indeed the main purpose of using MMC in armour is to prevent perforation as given an evidence in Fig.13 a.

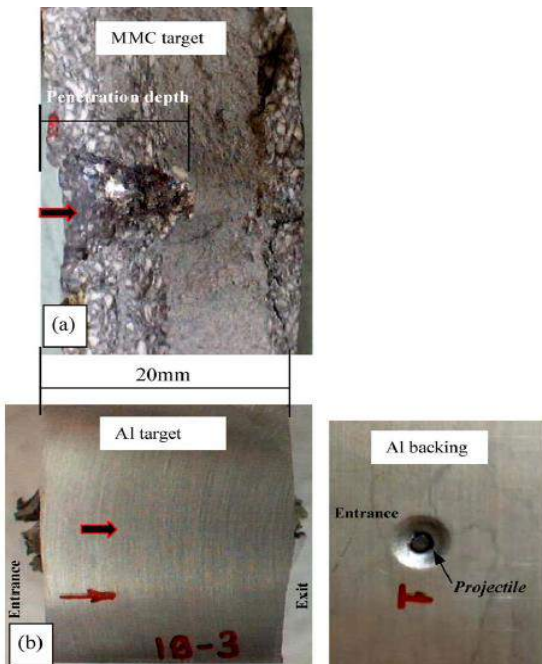


Fig. 13 Penetration properties of targets: (a) MMC target (b) Al target.

As an addition to the effects mentioned above, strong friction also causes the breaking of some reinforcement particles the hole surface or transfer to the tip surface. Figure 14 shows the breaking of an Al₂O₃ particle transferred to

the tip surface. If the particles are brittle such as Al₂O₃, they are shattered into smaller pieces or are cracked and buried in the frictional surface (i.e. The tip surface) and this increases the frictional force between the frictional pairs in favor composite performance.

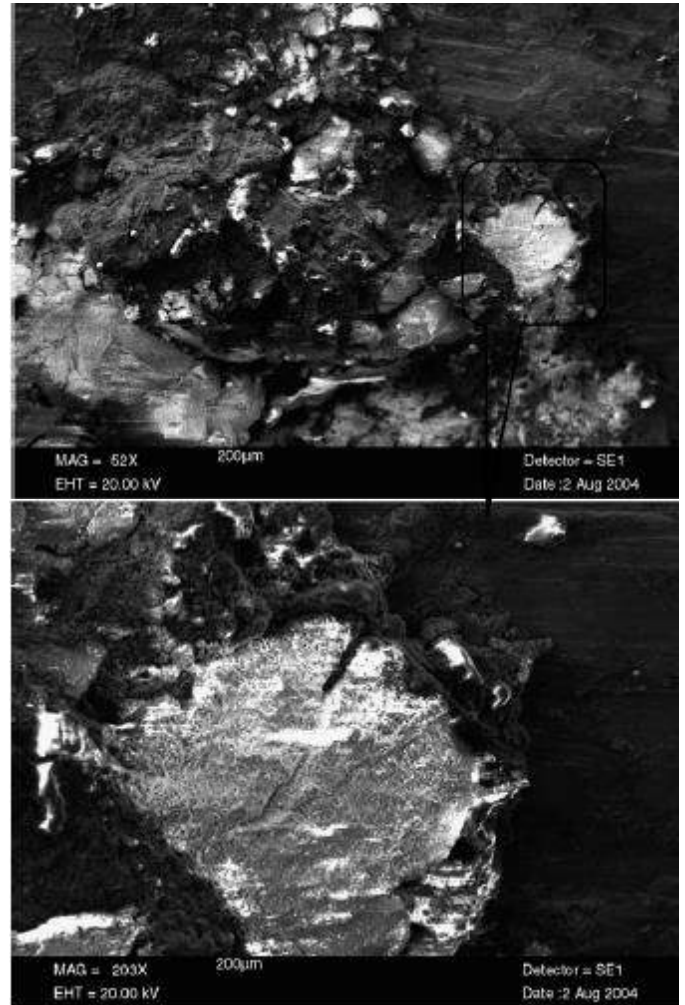


Fig 14 Broken Al₂O₃ particles on the tip surface.

CONCLUSIONS

- The high velocity of the projectile leads to melting of some surface layers because of the excess heating resulting from high velocity friction. Because of high friction, some melted regions have porous structure as a result of the shrinkage during the rapid solidification caused by the high-speed projectile at the hole surface. Because the velocity of the projectile is slowed down by the material, the hole surface is coarsened from the lower velocity friction at the exit side of the hole.
- The type and the speed of projectile have an important role on the damage created on the composite. If the velocity of the projectile is higher, it can pass throughly

the thickness of the composite with or without its jacket and may be without any damages on the sample. The projectile leaves the jacket in the composite if it has a slower velocity relatively. It can pass the composite thoroughly or it is stopped by the composite in its body according to composite properties such as toughness.

- The frictional behaviour of MMC armour is strongly affected by the contact conditions between projectile and the matrix of the composite. The more reinforcement particles the projectile comes into contact, the greater is the friction. This will reduce the penetration depth of the projectile. If the particles are brittle, such as SiC, they are sometimes broken up into smaller pieces and buried into the frictional surfaces, thereby increasing the friction between the projectile and the MMC armour. This further reduces the penetration depth.
- The projectile nose is plastically deformed when it impacts the MMC armour. Because of swelling and the presence of SiC particles in the matrix, the sliding of the projectile through the armour hole surface is now more difficult. This reduces the penetration depth.
- The projectile nose is broken or deformed plastically when it impacts the composite target. If the composite has hard reinforcement particles such as Al₂O₃, the friction between projectile tip and hole surface becomes greater and the projectile surface is scratched by ploughing. Plastic damage or breaking of the tip nose leads to increasing the resistance to the projectile movement through the target hole.
- Some composite material with reinforcements is transferred to the tip surface by adhering. This adhered layer on the tip surface can be melted due to the high frictional heating and subsequently resolidified rapidly. This causes to hot cracking of the layer and to the formation of Karamis, area. If the layer has reinforcement, these particles can be embedded in the tip surface and they can either scratch the surface by ploughing or be cracked by being compressed between the hole and tip surface.
- The predominant wear mechanism of the tip surface is abrasion. Microcutting and plastic yielding as bulging are also observed on the tip surface as wear mechanisms. Deep valleys on the tip nose and deep grooves on the main surface of the projectile tip are also observed. This shows that a the composite manufactured from Al and Al₂O₃ has good ballistic performance against AK-47 (7.62mm×39mm Armour Piercing) and G3 (7.62mm×51mm Armour Piercing) projectiles.

- M. Baki Karamiş, “**Tribology at high-velocity impact**”, Tribology International, Volume:40, Issue:1, January 2007, 98-104
- M. Baki Karamiş, “An evaluation of the Macro Damage on Metal Matrix Composites after High Velocity Impact”, Journal of Composite Materials, SAGE, first published on Mar 23, 2006
- M. Baki Karamiş, A. Alper Cerit and Fehmi Nair ”Surface characteristics of projectiles after frictional interaction with metal matrix composites under ballistic condition” Wear, 261, Issue:7-8, 20 October 2006, 738-745
- M. B. KARAMIŞ, F. NAİR AND A. TAŞDEMİRÇİ, "Analyses of metallurgical behavior of Al-SiCp composites after ballistic impacts", Composite Structure, 64 (2004) 219-226.
- M. B. KARAMIŞ, A. TAŞDEMİRÇİ , F. NAİR, “Failure and tribological behaviour of the AA5083 and AA6063 composites reinforced by SiC particles under ballistic impact”, Composites Part A: Applied Science and Manufacturing, Volume 34, Issue 3, March 2003, Pages 217-226.

IV. REFERENCES

Enhancement of Engine Oil Life with Vaccination Method

İsmail Varol Tarakçı İlhan Asiltürk+*

** Soma Aegean Lignite Organization*

Manisa, Turkey

tarakcii@eli.gov.tr

+Department of Mechanical Engineering, University of Selçuk, Campus, 42250

Konya, Turkey

iasilturk@yahoo.com

Abstract - Machine parts must lubricate each other in order to fulfill their performances while working with each other and to increase their life span. The oils used can meet the expected lubrication property for a certain period of time and then have to be replaced. In this study, instead of 200-hour periodic maintenance of engine oil for pickling trucks, New oil is added instead of used oil taken from engine oil every 50 hours of use. And it is aimed to extend the oil change period to the warning change time. The results of this practice, which is more advantageous in terms of economy and environmental health, are given in detail.

Keywords - Engine oils, TBN (Total Base Number), Oil analysis, Oil change, Oil life, Oil drain-add, Pickling trucks

I. INTRODUCTION

A wide variety of oil groups are used in a work machine. The oil group which is the most consumed most of these oils and which is changed most periodically is motor oils. Because the engine oil, hydraulic, gearbox, etc., loses its feature faster than other oils. Frequent replacement of engine oil increases the amount of use and costs accordingly. Besides the cost, the destruction of used oils in the nature also causes great harm to the environment. Because of these two reasons, maximum use of engine oils is of great importance both in terms of costs and environmental health [1-3].

II. OIL USED IN ENGINE

Oils obtained from crude oil are called mineral oil or machine oil. Such oils are not suitable for the operating conditions of the motor and are subject to enrichment with a number of additives and become available [1-3].

A. Main Tasks of Oils Used in Engines

- Reducing parts wear and power loss by avoiding direct contact between moving metal parts.
- Helping to cool down engine parts
- Clearing the contaminants between parts
- Preventing compression eccentricity between piston, Ring and cylinder walls
- Reduce the noise and voices by destroying the knockout with the reason of the gap between the housing and the (swivel) cylinder.

B. Classification of Engine Oils

Engine oils are classified by their viscosity (according to S.A.E serial number). S.A.E; refers to the initials of the United States Society of Automotive Engineers.

There are three types of engine oils. ; Summer, winter and combined oils (all-season oils)

a) Summer Oils: S.A.E10, S.A.E20, S.A.E30 etc.

b) Winter Oils: S.A.E0W, S.A.E5W, S.A.E etc.

c) Combined Oils: S.A.E0W-30, S.A.E10W-30, S.A.E20W-40, etc.

C. Engine Oil Replacement

The engine oils in work machines and pickling trucks are changed under the following conditions:

- During periodic maintenance
- Problems in analysis results
- When the operator or the repair supervisor sees a problem in his examination by hand, eye or smell according to his experience.

When we examine these three substances in turn; Most of the oil change is not done periodically. The oil changes made during periodic maintenance are determined entirely in the direction of the machine manufacturer and do not depend on any fault or problem.

When the other two items are examined; The oil changes are made due to the deterioration of the engine oil due to the failure of the vehicle. According to the analysis results, oil

change is made when the following conditions are encountered.

- Viscosity change in engine oil
- There is water in engine oil
- There is fuel in engine oil
- Engine oil is dusty
- There are sawdust accumulation in the engine oil
- TBN drop due to oxidation

Except for the last item, all other items appear as the result of faults coming into play. If any malfunction occurs on the engine, the oil is replaced when the faulty oil becomes dirty and loses its characteristic. Due to this, when the oil change is made, the problem is not caused by losing its property due to the end of the oil life but it is a great advantage to distinguish it from the faulty source.

Because simply changing the oil as a solution will not solve the problem. Since the new engine oil is also fueled, it is necessary to put the new engine oil after removing the fuel oil.

What we are trying to explain above is that changing the engine oil as a result of malfunction does not mean that the engine oil life is over. The purpose of this article is to find the answer to the question of what happens to the actual life of motor oil without any breakdown and without a liquid mixture from the outside into the engine oil.

D. Engine Oil Degradation

1) Chemical Deterioration of Oil:

Minerals in the oil combine with oxygen in the air at high temperatures to oxidize. In addition, other chemical substances, which are formed as combustion products, combine with oil to bring organic acids to the water.

2) Physical Deterioration of Oil:

The dust in the air entering the cylinder at the time of sucking, the bodies coming to the end of the combustion, the chips coming from the wear of the parts, the fuel in the gasses escaping from the oil pan will cause the pollution and the deterioration of the oil.

III. METHODS OF OIL SAMPLING

Points to note when sampling:

- The sample should be at the operating temperature or the sample should be taken within maximum 30 minutes after the machine has been stopped. Thus, the sample taken is homogeneous and will show the actual performance of the oil in the system.
- It should be adjusted so that it can be taken from the middle point of the oil level when sampling with the vacuum pump. Accumulated accumulations should not be withdrawn by reaching the bottom of the hose or the anesthetic of the carotene. Otherwise the amount of particles found in the analysis result will be misleading.
- The sample container should be clean and dry.

- Sampling is finished the finished sample cap must be tightly closed immediately and precautions must be taken to avoid spillage during shipment.
- The sample vessel should be filled up to $\frac{3}{4}$ of the container, It shouldn't be filled completely.
- The label information must be completely filled. (Brand, model, working time, date etc.)
- Samples should be sent to the relevant organization for analysis without delay [4].

A. Sampling Method with Vacuum Pump

- The most popular method used in sampling for systems without sampling valves or plug.
- Samples can be taken from every unit like gearbox, motor, axle, and Traction.
- The unused and clean hose is cut at an angle of 45° and passed over the vacuum pump. The cut end must be clean. Foreign particles that may remain on the end may be misleading as a result of the analysis.
- The sampling vessel connected to the vacuum pump should be clean and unused. The hose should be inserted into the sample vessel approximately 4 cm.
- If a level control bar is present, the length of the hose must be determined accordingly. If there is no level bar, the length of the hose must be set to the middle of the oil tank.
- The motor must be stopped and the machine must be stopped. The oil to be sampled must be at the operating temperature to ensure homogeneity.
- The hose must be adjusted so that it does not touch the bottom of the tank or the oil tank at the midpoint level. The sample container should be filled up to $\frac{3}{4}$ and not completely filled.
- Label information must be filled and affixed on the cabinet.
- The hose must be removed after sampling. However, by pulling the hose upwards, the removal pump can become contaminated. To prevent this, the hose should be removed by cutting it from the top of the pump and pulling it down.
- Sampling vessel and hose are disposable.

B. Sampling Method from Drain Tap or Drain fountain

- It should be preferred to examine the oil performance in oil changes.
- When taking samples with this method, the technician should pay attention to cleanliness. The plug should be thoroughly cleaned, washed and thoroughly cleaned with compressed air. The smallest amount of dirt that can enter the sample vessel changes the analysis results unexpectedly.
- While the machine is newly stopped, the sample to be taken will give the best result.
- During emptying, samples should not be taken from the first mouth or the last flowing oil. Towards the middle of the stream, the sample vessel must be carefully filled while the oil is relatively clear.
- The sample container should be immediately sealed tightly. The label information must be filled in correctly.

- No sample should be taken from the collection container placed under the plug.
- It should be preferred to examine the oil performance in oil changes.
- When taking samples with this method, the technician should pay attention to cleanliness. The plug should be thoroughly cleaned, washed and thoroughly cleaned with compressed air. The smallest amount of dirt that can enter the sample vessel changes the analysis results unexpectedly.
- While the machine is newly stopped, the sample to be taken will give the best result.
- During emptying, samples should not be taken from the first part or the last flowing oil. Towards the middle of the stream, the sample vessel must be carefully filled while the oil is relatively clear.
- The sample container should be immediately sealed tightly. The label information must be filled in correctly.
- No sample should be taken from the collection container placed under the plug.

IV. OIL ANALYSIS

Oil analysis is a preventive maintenance program that is being used and is being implemented to increase the life and productivity of business machines, to prevent maintenance costs and waste of time. All used oils with oil analyzers; Engine, differential, cer and hydraulic system oils can be tested. These tests have been developed not only to assess the state of the oil, but also to evaluate the condition of motors and machines. The success of a nursing care program can be measured by the financial gain to the user. The application of oil analysis is cheap, quick and easy, and at the same time it can save a lot of money. The oil analysis application forms the basis of the best possible maintenance program for the machines when combined with the high performance characteristics of the original oil and filters used [5].

A. Analysis of wear elements

In every system that works with oil (engine, hydraulic, gearbox etc.), normal wear and tear elements wear out. The acceleration of wear, ie the increase in the concentration of wear elements, is a sign of a problem. With the analysis of wear elements, the problem is found before the unit fails. By means of wear elements analysis, particles in the size of approximately 10 μ are detected. 8 elements are evaluated in oil analysis. These are; Copper (Cu), iron (Fe), chromium (Cr), lead (Pb), aluminum (Al), morden (Mo), silicon (Si) and sodium (Na). All elements except silicon (powder inlet) and sodium (water inlet) are located on the engine's structure. Some of the elements in the sample may also be sourced from oil additives, which are not abrasive in the system [6].

B. Oil Condition Analysis

When the oil analysis program is first started and a new engine oil is introduced, a clean oil sample or reference oil is required. The new clean oil is examined with a special product that uses infrared radiation. The information is stored in the device memory. The used oil sample is sent to the laboratory at every oil change. The oil status analyzer records the data from the used oil in the case of a thin film layer. The device uses mathematical formulas to compare the amount of difference between the used oil and the new oil.

This analysis, which is part of the oil analysis program, saves money and time by preventing large size faults [5].

C. Particle Counting Analysis

The counting of particles in the oil allows the determination of harmful pollutants and large particles which shorten the life of the unit. It is applied to other units except motor. Metal or non-metallic particles formed as a result of wear or pollution from the outside are identified and counted. When these measurements are evaluated together with the results of wear elements, possible failures can be determined in advance.

The particle count is one of two tests that determine the particles of the oil analysis program. It detects all metal and non-metal particles between 2-100 μ . Laser analytical laboratories use laser beam technology to count particles. The specimen is passed through a beam of light emitted from a particular light source. As the particle in the oil passes through it, the change in light is displayed by the sensor, the particles are counted and their dimensions are recorded. This test can detect an increase in the number of particles that can cause wear or costly problems [6].

V. DETERMINATION OF LIFE SPAN TIME OF ENGINE OIL

The engine oils in work machines are changed under the following conditions:

- During periodic maintenance
- Problems in analysis results
- When the operator or the repair supervisor sees a problem in his examination by hand, eye or smell according to his experience.

A pickling truck engine takes 135 Lt oil. When the causes of oil change are examined, the most change occurs at periodic maintenance time. In other vehicles in the market or in personal vehicles, engine oil change is mostly due to periodical maintenance, and even this is almost exclusively due to the fact that the engine oil which is not running out of service has been exhausted. So why do not we use the alert change method according to the sample? And why do we use the method of periodic change? How accurate is to change the implementation of the oil with a vehicle the same make and model, in every point of Turkey, with the same conditions and in every periodical time?

One of the biggest factors that pollute engine oil is fuel. Because the sulfur in the fuel brings the sulfuric acid to the water by combustion and this sulfuric acid is mixed with the lubricating oil in some ways and causes the oxidation of the oil. So the more sulfur in the fuel, the more the fat will be oxidized. Likewise, consider two identical vehicles with the same engine and using the same fuel. One of these two cars is located in a place where traffic density is high and other traffic is very low. The average amount of fuel consumed by these two vehicles will not be the same and the amount of oil contamination cannot be the same. In that case, the engine oil change times and the kilometers of these two vehicles should not be the same. How to clean the oil to be oxidized in each case? Here, additives are included in the engine oils. In order to neutralize the oxidation, a base additive is added to the oil, and TBN (total base number) is defined in these oils. When this additive is depleted, it is decided that the engine oil should now change.

The TBN value of motor oils sold on the market is between 6-14. And the unit is mg KOH / g. The TBN value is checked for the first oil change, which means that the additive is exhausted when it reaches the end of the first value. For example, if the TBN rating of our first engine oil is 12, this indicates that no more base additive is left in our engine oil and the engine oil should be replaced.

VI. ENHANCEMENT OF ENGINE OIL LIFE WITH VACCINATION METHOD

When talking about the life of motor oils; We emphasized the importance of TBN value. Based on the TBN value we have investigated that it is possible to use our engine oil much more efficiently. Is it possible to use engine oil which has been depleted in base additive for a while? It may not be possible to use the same oil, but it is possible to use our engine oil more efficiently by the grafting method.

Vaccination method: The base oil is a process of adding a new oil in the same amount of oil at the optimum amount when a TBN value reaches a critical value from a consuming engine oil.

By means of the grafting method it is possible to keep the TBN value at the upper level all the time by adding new oil in parts instead of renewing the engine oil completely. It will be seen that the amount of oil added after this operation is much less than the amount of oil which changes completely during the same working hours. This environmentally and financially important method is used in shipbuilding machines, and yields are obtained in profitable results on pickling trucks that have been tested.

VII. OIL ANALYSIS AND LIFE SPAN TIME DETERMINATION OF PICKLING TRUCK ENGINES

In the following tables, pickling truck engine and oil information of Aegean Lignite Organization is given. It also shows the results of engine oil analysis as a result of controlled maintenance of pickling truck number 415, as an example.

TABLE I
ENGINE POWERS AND LOAD CAPACITIES OF TRUCKS

Make	Engine Model	Engine Power		Capacity	
630 ES	KT-50	1600	HP	170	Tons
HD 785-1	KT-2300 C	877	HP	85	Tons
HD 785-2	KT-2300 C	877	HP	85	Tons
HD 465-3	SA6D170A	702	HP	50	Tons

TABLE II
OIL VARIANTS - CHARACTERISTICS AND CHANGE PERIODS USED IN THE ENGINE OF TRUCKS

Make Model	Oil Type	Oil Standard	Oil Cap. (Lt.)	Oil Change Period (Hour)
KOM.HD 785-1	MOT.	SAE 15W-40	135	200
KOM.HD 785-2	MOT.	SAE 15W-40	135	200
KOM.HD 465-3	MOT.	SAE 15W-40	71	200
KOM. 630 ES	MOT.	SAE 15W-40	180	200

TABLE III
INFORMATION OF TRUCK WHICH WAS ANALYZED FOR OIL

Vehicle Door No	Machine type	Machine Model	Engine Serial No	Working Area
415	Komatsu truck	785-1	CY-34	Soma

TABLE IV
ELEMENT ANALYSIS RESULT OF 415 DOOR NUMBERED TRUCK (SAE15W/40)

Sample receive date	Oil working hour	Fe	Cr	Pb	Cu	Al	Si	Na
		1,28	0,12	2,35	0,05	1,92	10,3	4,17
13.06.16	52	1,63	0,37	7,98	1,62	1,51	3,44	3,18
29.06.16	131	6,21	0,40	6,99	2,10	3,72	3,41	4,33
25.07.16	189	10,68	0,72	2,55	2,79	5,58	2,59	86,25
17.09.16	303	17,80	0,79	5,18	3,59	6,97	5,90	70,57
29.09.16	363	14,96	0,93	10,5	3,83	5,03	5,17	5,75
08.10.16	414	25,30	0,87	13,5	4,99	7,56	9,18	6,22
19.10.16	492	23,45	0,77	14,4	5,56	6,61	6,31	74,31
26.10.16	551	17,51	0,60	13,7	3,88	5,64	6,08	80,81
08.11.16	591	18,90	0,84	14,2	6,06	3,98	5,65	5,76
13.12.16	645	20,43	1,28	12,9	5,65	4,72	5,74	5,73
17.12.16	656	19,81	1,27	14,1	5,65	4,58	6,08	70,86

TABLE V
MOLECULAR ANALYSIS RESULT OF TRUCK WITH 415 DOOR NUMBER (SAE15W / 40)

Sample receive date	Oil working h.	Water (0-12)	Fly ash (0-1)	Oxidation (0-12)	Nitration (0-9)

13.06.16	52	10,67	-0,23	7,68	6,22
29.06.16	131	10,71	-0,20	8,41	6,86
25.07.16	189	13,37	-0,17	8,60	7,07
17.09.16	303	9,42	-0,13	9,53	7,44
29.09.16	363	9,93	-0,08	9,27	7,37
08.10.16	414	10,34	-0,10	10,11	7,75
19.10.16	492	10,24	-0,07	10,38	7,85
26.10.16	551	9,69	-0,09	9,45	7,25
08.11.16	591	10,08	-0,15	9,64	7,44
13.12.16	645	10,79	-0,06	10,31	7,95
17.12.16	656	11,20	-0,90	10,26	7,94

TABLE VI

MOLECULAR ANALYSIS RESULT OF TRUCK WITH 415 DOOR NUMBER (SAE15W / 40)

Sample receive date	Oil working h.	Diesel (0-260)	Suffixation (0-17)	Glyco l (0-1)	TBN (6-14)
13.06.16	52	255,10	15,93	0,37	10,41
29.06.16	131	256,30	16,73	0,59	9,52
25.07.16	189	254,70	17,42	0,65	8,94
17.09.16	303	257,40	17,99	0,69	8,76
29.09.16	363	256,40	18,32	0,70	8,59
08.10.16	414	256,70	19,08	0,77	8,31
19.10.16	492	256,00	19,29	0,89	7,76
26.10.16	551	256,90	18,19	0,79	9,93
08.11.16	591	257,60	18,64	0,75	8,22
13.12.16	645	256,10	19,29	0,85	8,57
17.12.16	656	257,20	19,38	0,80	8,23

TABLE VII

VISCOSITY ANALYSIS RESULT OF TRUCK WITH 415 DOOR NUMBER (SAE15W / 40)

Sample receive date	Oil working hours	Viscosity Index	40°C	100°C
			102,0	13,7
13.06.2016	52	134	96,8	13,1
29.06.2016	131	134	99,2	13,3
25.07.2016	189	134	98,7	13,3
17.09.2016	303	134	98,0	13,2
29.09.2016	363	134	101,3	13,5
08.10.2016	414	134	100,1	13,4
19.10.2016	492	134	97,0	13,1
26.10.2016	551	134	94,6	12,9
08.11.2016	591	134	98,4	13,2
13.12.2016	645	134	97,0	13,1
17.12.2016	656	134	97,0	13,1

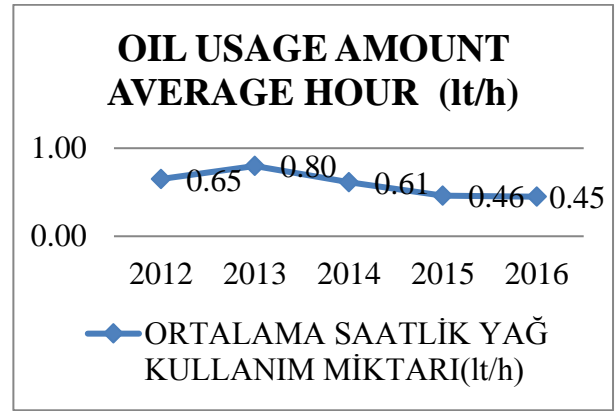


Fig. 1 Change in the amount of engine oil consumed per hour in the last 5 years for all pickling trucks in the Aegean Lignite Organization.

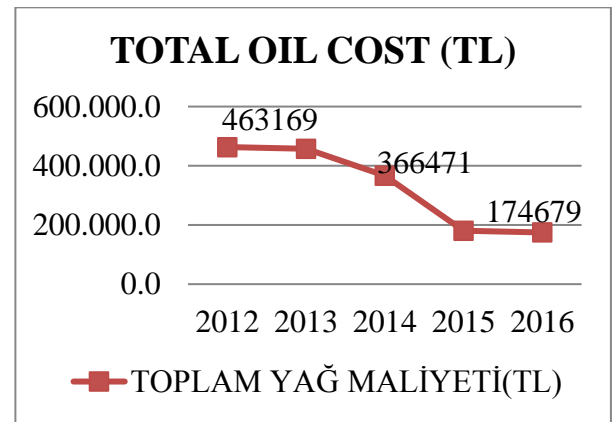


Fig.2 Change in the cost of engine oils for all pickling trucks in the Aegean Lignite Plant over the past 5 years.

VIII. RESULTS AND INTERPRETATION

Oil change is made for 3 reasons. These are;

- Physical and chemical changes due to oxidation (deterioration in oil),
- Contamination with materials mixed in the combustion chamber (deterioration in oil),
- Periodic maintenance.

If none of the first and second reasons were present, the oils would have to be changed due to a third reason, i.e., and periodic maintenance time. Well how accurate method is this?

In this study, the Komatsu 785-1 model pickling truck numbered 415, operating in the Aegean Lignite Organization Soma open pit mine, was followed up. Table IV, Table V, Table VI and Table VII show the results of 15W / 40 engine oil analysis of pickling truck numbered 415 with 50 hour periods between 13.06.2016 and 17.12.2016. If engine oil does not show any damage due to physical - chemical changes and contamination; the engine oil, which

should be renewed periodically in 200 hours, was canceled for truck number 415. And continued to work according to the TBN value of engine oil.

The first TBN value of engine oil used is 10.5; the depletion of the basic effect is only possible when the TBN value falls to 5.25. When Table VI is examined, the first periodic control TBN measurement value is reduced to 10.41. Again, the TBN value was only 8.94 when the oil on the same chart approached 200 hours. So, the result of this analysis clearly shows us that the motor oil on the cam is used for much longer than 200 hours. When we continued to study the same table, oil working hours increased to 656 hours in the sample taken on 17.12.2016, but the TBN value did not reach the critical point and the TBN value was 8.23. It is clear to us that it is possible to increase the oil life for more than 3 times as long as there is no physical-chemical change and contamination in engine oil.

Fig.1 shows the average amount of engine oil in 1 hour of last 5 years for 104 pickling trucks in Aegean Lignite Plant. It is understood from the graph that oil change according to TBN value started in 2014. In 2012, 1 truck consumed 0,65 Lt of motor oil per hour on an average, this ratio decreased to 0.61 Lt in 2014 and this rate decreased to lower levels (0,45 Lt) as the operation continued.

Fig.2 shows the cost of engine oils used by the 104 Aegean Lignite Trucks for the last 5 years. As the graph implies; after the oil change was started to be applied according to the TBN value of the engine oil which cost about 460.000 TL in 2012, it decreased to 360.000 TL and the cost of engine oil decreased to 170.000 TL as this application continued.

ACKNOWLEDGMENT

This study was produced by İ.Varol TARAKÇI's seminar work entitled "Oil Analysis and Lifetime Assessment in Pickling Truck Engines". I would like to thank Mr. Rifat KARATAŞ, Director of Machine Operation Branch Manager of Aegean Lignite Works, Işıklar Workshop Chief Engineer Mustafa DEMİR and his colleagues.

REFERENCES

- [1] Standard Test Method for Acid and Base Number of Petroleum Products by Color-Indicator Titration, ASTM Designation D-974, Annual Book of ASTM Standards, Vol.5.01 (1995)
- [2] Standard Test Method for Base Number of Petroleum Products by Potentiometric Perchloric Acid Titration, ASTM Designation D-2896, Annual Book of ASTM Standards, Vol.5.01 (1995)
- [3] Çağlayan H., 2003. Oil Analysis and Importance in Working Machines. TMMOB Chamber of Mechanical Engineers, Work Machinery Symposium and Exhibition, September 6-7, 2003
- [4] Gökalp B., 2005. Improvement of Used Engine Oils. Kocaeli University, Graduate School of Natural and Applied Sciences, M.Sc. Thesis, Kocaeli, 180 p.

- [5] Gökalp B., Saraç H. İ., Çelik C., 2007. Damage analysis due to abrasion with oil analysis program. 8th International Conference on Fracture, November 7-8, 2007
- [6] İpek R., Erdoğan M., 2006. Experimental Investigation of the Effects of Engine Oil Reinforcements on Wear Mechanisms. Dumlupınar University, Graduate School of Natural and Applied Sciences, M.Sc. Thesis, Kütahya, 12 p.
- [7] Kauffman, R. E., "Rapid, Portable Voltammetric Techniques for Performing Antioxidant, Total Acid Number (TAN) and Total Base Number (TAN) Measurements," *Lubr. Eng.* 54, 1, pp. 39-46 (1998).
- [8] Megep Motor Vehicle Technology Periodic Care, Ankara, 2011
- [9] Orhan A., 2009. Determination of Engine Failure Predictive Maintenance by Oil Analysis done. Celal Bayar University, Graduate School of Natural and Applied Sciences, M.Sc. Thesis, Manisa, 152 p.
- [10] Wohltjen, H., Jarvis, N.L., Klusty, M., Gorin, N., Fleck, C., Shay, G. and Smith, A., "Solid State Microsensors for Lubricant Condition Monitoring: ", & Quot; *Lubr. Eng.* 50, 11, pp. 861-866 (1994)
- [11] Yıldırım A., 1988. Spectrometric Oil Analysis. Anadolu University, Institute of Science, M.Sc. Thesis, Eskişehir, 78 p.

Iron Powder Recovery from Steel Plant Red Mud

Mehmet Ozkaymak*, Selcuk Selimli*, Cagil Koymatcik

*Energy Systems Engineering, Karabuk University, Turkey

mozkaymak@karabuk.edu.tr, selcukselimli@karabuk.edu.tr

Kardemir Iron and Steel Co., Turkey

cyaman@kardemir.com

Abstract— Environmental susceptibility, increasing energy costs, and competitive conditions in the market require the saving and recovery of energy and energy related facts. In this respect, red mud which is discharged from an industrial facility production waste water treatment plant was studied due to the rate of recoverability of magnetic materials. The mud sample was experimentally studied by wet high intensity magnetic separation method. Magnetic field intensity was chosen 17,000 Gauss to maximize the separated iron powder level. Results presented that, unit mass of red mud sample includes about 70% of magnetized materials and 45% of the magnetized material composition is elemental iron (Fe). This rates are seeing satisfactory to get profit from the recovery process. The size of the gaining by the recovery of iron dust is about 22,075,200/years.

Keywords— red mud, recovery, iron

I. INTRODUCTION

Energy is the dominant necessity of the heavy production processes such as iron and steel production facilities. Increase in unit cost of energy, and environmental respects directs the decision makers through the saving of energy and so less energy source usage. Similar approximations with this scope of paper have been discussed in the studies were given in this part of the paper. Delgado et al. discussed about the recovery of iron from the pickling waste water. They claimed the 97% of iron recovery form the waste water [1]. Samouhos et al. studied the separation of iron oxide from red mud. They subjected to magnetic separation the samples and obtained about 54% magnetite concentration [2]. Liu, and Li discussed about red mud magnetic recovery processes. It is concluded that multiple recovery or incorporation of the extraction of Al, Na, Ti, Sc, rare earth elements into iron recovery process is possible [3]. Samouhos et al. researched the separation of magnetic materials from red mud by wet magnetic separation. It is determined that the optimum concentrate contains 31.6% iron with a 69.3% metallization degree [4]. Li et al. presented a technique using magnetizing roasting process followed by magnetic separation. Optimum parameters, the grade of magnetic concentrate was 61.3% Fe and recovery rate of 88.2% [5]. Tang et al. studied the recovery of magnetic materials from ferritungstite ore. Results showed that an iron concentrate with an Fe content of 55.65% and recovery of 83.30% was obtained after magnetic separation [6]. De-qing et al. studied the recovery of iron from red mud by magnetic separation. The results showed that an overall iron recovery about 95.76% [7].

Li et al. applied high gradient superconducting magnetic separation to separate the extreme fine magnetic particles from the red mud. The iron oxide concentration is about 45% in the sample and they separated only 10% of the content [8].

Experimental wet high intensity magnetic separation by the subjected 17000 Gauss magnetic field intensity on 52.8 gr wet mud sample with %52 moisture content diluted with 200 gr water and evaluated results presented in this paper.

II. TESTING AND PROCEDURE

Taken samples from the plant were preliminary studied to have an idea about the magnetic content and particulate size of this content. Samples were dried in a dehumidifier. Then, samples granulated and subjected to a magnet. Obtained magnetised content was separated from the waste mud and sieved. Sieved magnetic dust was classified in sizes as in Table 1.

Table 1. Sieved magnetic particulate sizes and rates.

Magnetic Dust Particulate Sizes (μ)	%
+100	6.06
+50	27.27
-50	66.67

In the second stage of the study 25 gr of sample was expired with a moisture analyser and about 52% of it is determined as moisture. In this respect, about 52 gr of sample (25 gr of it is solid content) diluted with 200 gr water. Dilution was mixed sufficiently and magnet balls met with the dilution. Imposed magnetic field is about 17,000 Gauss. 18.6 gr magnetised particulate was separated, also 6.4 gr solid nonmagnetic content was determined. This result showed that about 70% of the waste mud could be recovered sufficiently and could be earned into economy.

In the plant about 50 tones/day red mud has been gotten and if about 48% of this mass is dry base. We could have 24 tones/day dry base red mud and if we recover the magnetic materials with approximately about 70% efficient. 45% of the magnetic particles that is separated by magnetic method is iron. This rate means about 7.56 tones/day iron recovery. Iron dust cost is about \$8 in the market. We simply conclude that \$60,480/day economical profit could be possible. Annually, this economical gaining could be aggregated approximately about \$22,075,200/years.

III. CONCLUSIONS

Red waste mud of an iron steel production plant recovery process is the subject of this paper. In this respect, a prestudy has been done with wet high intensity magnetic separation method. About 17,000 Gauss magnetic effect applied on water-mud dilution, and magnetic particles in the dilution separated with 70% efficiently and 45% of this rate compost of iron particles. This rate corresponds almost 7.56 tones/day iron dust. Daily saving potential could be determined about \$60,480/day, and annually about \$22,075,200.

REFERENCES

- [1] A. L. Delgado, F.J. Alguacil, and F.A. Lopez, "Recovery of iron from bio-oxidized sulphuric pickling waste water by precipitation as basic sulphates," *Hydrometallurgy*, vol. 45, pp. 97-112, 1997.
- [2] M. Samouhos, M. Taxiarchou, G. Pilatos, P. E. Tsakiridis, E. Devlin, and M. Pissas, "Controlled reduction of red mud by H₂ followed by magnetic separation," *Miner. Eng.*, vol. 105, pp. 36-43, 2017.
- [3] Z. Liu, and H. Li, "Metallurgical process for valuable elements recovery from red mud—A review," *Hydrometallurgy*, vol. 155, pp. 29-43, 2015.
- [4] M. Samouhos, M. Taxiarchou, P. E. Tsakiridis, and K. Potiriadis, "Greek red mud residue: A study of microwave reductive roasting followed by magnetic separation for a metallic iron recovery process," *J. HAZARD MATER.*, vol. 254-255, pp. 193-205, 2013.
- [5] C. Li, H. Sun., J. Bai, and L. Li, "Innovative methodology for comprehensive utilization of iron ore tailings Part 1. The recovery of iron from iron ore tailings using magnetic separation after magnetizing roasting," *J. Hazard Mater.*, vol. 174, pp. 71-77, 2010.
- [6] H. Tang, W. Sun, Y. Hu, and H. Han, "Comprehensive recovery of the components of ferritungstite base on reductive roasting with mixed sodium salts, water leaching and magnetic separation," *Miner. Eng.*, vol. 86, pp. 34-42, 2016.
- [7] Z. De-qing, C. Tie-jun, P. Jian, and H. Zhen, "Recovery of iron from high iron red mud by reduction roasting with adding sodium salt," *J. Iron Steel Res. Int.*, vol. 19(8), pp. 1-5, 2012.
- [8] Y. Li, J. Wang, X. Wang, B. Wang, and Z. Luan, "Feasibility study of iron mineral separation from red mud by high gradient superconducting magnetic separation," *Physica C*, vol. 471, pp. 91-96, 2011.

Accelerated Cooling Heat Treatment of Equilateral Angle and Hea-Heb Profiles

Fatma KÖZ*, Furkan ACAR*, Emre DEMİRÇİ*, Hayrettin AHLATÇI*, Yavuz SUN, Yunus TÜREN, Mustafa DEMİRKAZIK+, Mesut KAYMAZ+, Şerafettin ÖNER+

*Karabuk University, Department of Metallurgy and Materials Engineering, Turkey

+Çelsentaş, Çelik Mamulleri San.Tic.A.Ş. Turkey,

fkoz.kbu@gmail.com , acarfurkan@gmail.com, demirciemree@gmail.com, hahlatci@karabuk.edu.tr, ysun@karabuk.edu.tr, yturen@karabuk.edu.tr, mustafademirk@gmail.com, mesutkymz@gmail.com, serafettin.oner@celsentas.com.tr

Abstract— Heat treatment methods are the most commonly used production steps because they can interfere with all the mechanical properties of the material without altering the chemical composition of the metal in industry. Accelerated cooling is also one of the most prominent points in the series production process in these heat treatment methods. This method is used in the manufacturing process of thin pearlitic steel, double phase steel, rayon sheet steel which is used for bainitic steel production, from construction bar to profile in many different quality and size products. In this study, S355J2 corrugated corrugations and S275JR quality HEA-HEB structural section steels were produced from hot rolled billets produced by open casting method. Intensive inclusions were found in both of the materials examined and it was seen that they could not meet the mechanical strength values in the sizes with low crushing rates. These materials, especially those with low impact strength, have been subjected to accelerated cooling to increase their impact strength.

Key words: S355J2 quality steel, S275JR quality steel accelerated cooling, impact test, ductile fracture, brittle fracture
[9]

I. INTRODUCTION

The accelerated cooling process in steel production has changed drastically during the 30-35 years and has become an important process. This process was first used in the 1960s to shorten rolling-out stages of hot rolled strips, but unexpected benefits were detected. Started an intensive research work on this field and this process has been taken under a different perspective. Properties of double-phase steels, perlite-bainite steels and so on were developed by the accelerated cooling process [1-3].

In our country, especially after the great disasters such as Marmara Earthquake on 17 August, the strength of the steel products used in reinforced concrete structures has been on the agenda. The research done in order to improve the mechanical properties of the steels used in construction sector in

our country has gained momentum. It is known that accelerated cooling heat treatment contributes to significant increases in toughness values and other mechanical properties of steel structure products.

Accelerated cooling process is also used to increase the wear and fatigue resistance of pearlitic rails in today's railway materials. The abrasion resistance of coarse pearlitic rails in the eutectoid compound known as R260 quality is insufficient in bends with a radius of curvature less than 2000 metric tons. In this context, a special cooling regime was determined and the distances between the perlite lamellae were reduced by adding material [4]

In this study, the changes in properties were investigated by applying hot-rolling 100x100x10 mm cross-section angles and HEA140 profiles with accelerated cooling heat treatment by using open casting produced billets. S355J2 grade and S275JR grade steels are preferred as structural steels used in the production of all kinds of machine and machine parts, general construction and energy transmission lines. Equilateral bridges (S355J2 quality) and HEA-HEB (S275JR quality) profiles, which are used in a wide range of fields from high temperature environments to very harsh winter conditions, are especially used in important points such as energy transmission lines and bridge projects in our country. These steels have a minimum impact energy of 27J at the expected room temperature and or -20 ° C.

II. EXPERIMENTAL PROCEDURE

In this study, 100x100x10 section equilateral angles and HEA-HEB profilers manufactured from the quality steel billet with 130X130 mm cross section, which were produced by continuous casting method without any vacuum process which is called as open casting were used. Chemical compositions are given in Table-I.

TABLE-I
CHEMICAL COMPOSITION

	C	Mn	Si	S	P	Nb	V
S355J2	0,12	1,36	0,20	0,01	0,01	0,0022	0,085
S275JR	0,07	0,70	0,14	0,035	0,01	0,0005	0,0052

A laboratory-scale accelerated cooling system was fabricated in order to observe changes in toughness and other mechanical properties of the equilateral angles and HEA-HEB profiles used in this study by accelerated cooling heat treatment. The nozzles to perform the cooling were placed in accordance with the heat treatment of both the corners and the profiles. Fig.1

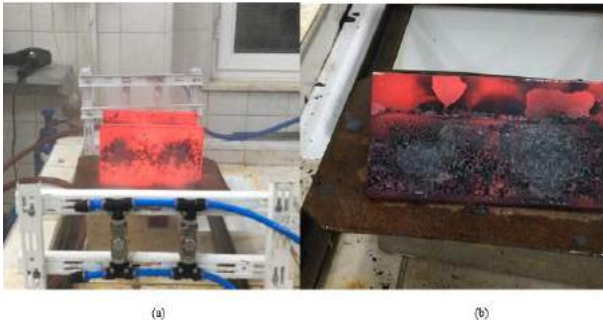


Fig.1. HEA-HEB (a) and Equilateral Angle (b) profiles Heat Treated By Accelerated Cooling.

200 mm long specimens cut from S355J2 grade steel equilateral steel with 100x100x10 mm cross-section and S275JR grade steel profiles with 140 mm cross-section were held in a furnace set at 950°C, the final draft bench outlet temperature, for 30 minutes to pass through the austenite structure. During accelerated cooling process, time parameters and pressure of water+air are given in Table II.

[11] TABLE-II
HEAT TREATMENT PRESSURES AND TIMES

	PRESSURE(BAR)		TIME(sec)
	WATER+AIR		
S355J2	4 BAR	5 second	
	2 BAR	7 second	
S275JR	4 BAR	60 second	
	4 BAR	7 second	
	2 BAR	15 second	
		60 second	

To obtain microstructural images, the samples were etched with 2% nital after sanding and polishing according to the standard metallographic procedure. The microstructural images of the investigated samples were taken with a Nikon LV-EPILED optical metal microscope.

After accelerated cooling heat treatment, Brinell Hardness test was performed on samples taken from each material cooled at different times and pressures. The hardness measurements were carried out with a ball of 5 mm in diameter and a force of 250 kg.

or notch impact tests, equilateral angle brackets and profiles according to TS EN 10025-1 standard, according to TS EN10045-1 standard, at -20 ° C for equilateral angles and at room temperature for profiles (20 ° C) was made with a Zwick / Roell brand notch impact tester.Fig.2

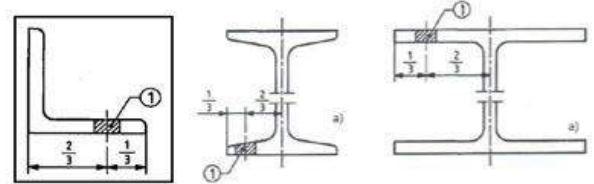


Fig.2 Impact Test for TS EN 10025-1 and EN10045-1 standards

III. RESULTS AND DISCUSSION

AYDIN at all [4] reported that, in accordance with this study, the square shaped angles and profiles do not exhibit impact properties at 80x80x8 mm, produced from open poured logs. The inclusions in the profiles produced by the open cast [4] billet were elongated square and circular form shown in Fig.3.

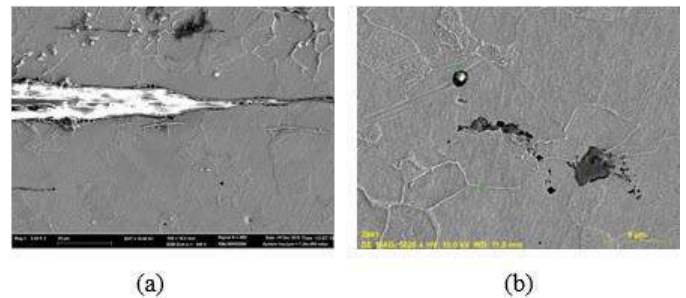


Fig.3 SEM image of elongated (a) and circular/square (b) inclusions of 80x80x8 mm equilateral angles [4].

The microstructures of the S355J2 and S275JR quality steels investigated in this study are shown in Fig.5 after accelerated cooling for 7 seconds. While the microstructure of the S275JR steel is ferritic and pearlitic after the heat treatment processes, the microstructure of the S355J2 subjected to the accelerated cooling processes is bainitic.

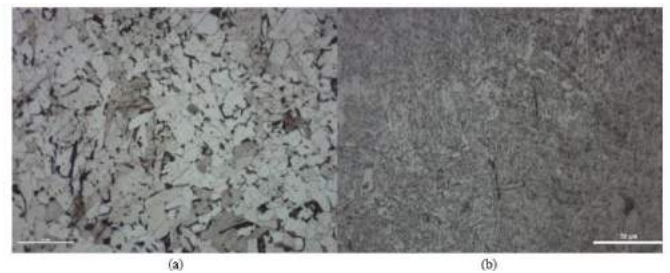
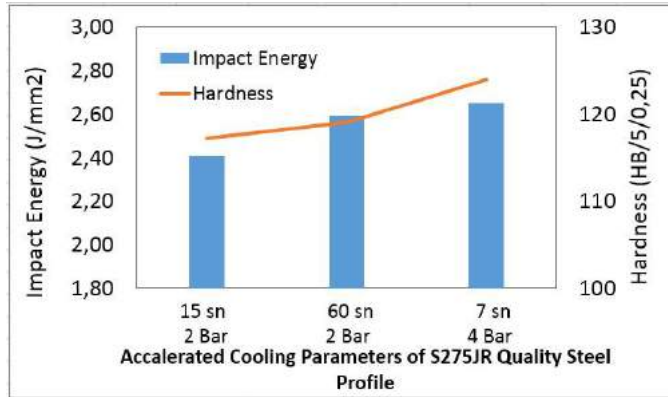


Fig.4 Microstructure of the S275JR (a) and S355J2 (b) after the accelerated cooling heat treatment.

Before the accelerated cooling heat treatment, the expected impact-notch energy at -20 ° C for the

equilateral angle brackets and at 20 ° C (room temp.) for the profiles was 27 J, approximately 0,45J/mm². Results of the hardness and impact tests are shown in Fig.5. As seen in Fig.5, equilateral angles and profiles subjected to accelerated cooling at different (water+air) pressures (2 and 4 bar) and times (7 and 60 s) exhibited high impact energy upper than 1,8J/mm².

Impact energies of all investigated steels are higher than 0,45J/mm² which reported in standards. As pressure (water+air) increases and times decreases, high impact energy was obtained.



[12]

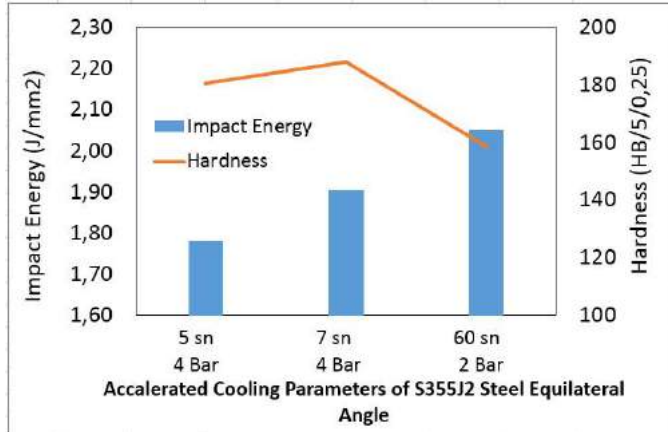


Fig.5 Hardness and impact energy results with respect to accelerated cooling parameters

IV. CONCLUSIONS

In this study the general results obtained from the investigated S355J2 100x100x10 square corners and the S275JR quality HEA-HEB profiled specimens for accelerated cooling process with different pressure values for 5-7-15-60 seconds are as follows:

1) In the microstructure of the investigated steels before accelerated cooling process, there were elongated and spherical inclined inclusions in the direction of the rolling line.

2) While the microstructure of the S355J2 subjected to the accelerated cooling process for 5-60 s at 2 and 4 bar water+air pressure is bainitic, that of the S275JR steel is ferritic and thin pearlitic.

3) At conditions of high pressure (water+air) + low time and low pressure + high time during accelerated cooling processes high impact energy obtained on the investigated alloys.

4) Impact energy of the S355J2 quality steel is higher than that of the TS EN 10025-1 and TS EN10045-1 standards by accelerated cooling processes.

ACKNOWLEDGMENT

The authors would like to express thanks to Karabuk University Coordination of Scientific Research Projects (BAP) Project code coded as KBÜ-BAP-16/2-YL-076 and 17-LÖAP-121 for supplying steel wires and supporting this work financially.

REFERENCES

- [1] A.J. DeArdo, Accelerated cooling: A Physical Metallurgy Perspective, *Proceeding of the International Symposium on Accelerated Cooling of Rolled Steel*, August 24-25, 1987.
- [2] O. Çelik, *Nervürlü İnşaat Çeliklerinin Mekanik Özelliklerinin İncelenmesi, Yüksek Lisans Tezi, Karabük Üniversitesi, Karabük 2015.*
- [3] E. Devrim, *İzmir Demir Çelik Sanayi A.Ş. Eğitim Yayınları İZMİR, 2000.*
- [4] S. Aydın, O. C. Candoğan, S. Özçelik, H. Ahlatci, Y. Türen, Y. Sun, H. Zengin, A. Ertan, Ş. Uğurlu, R. Yıldız, M. Demirkazık, Ş. Öner, *The Effect of Accelerated Cooling on Microstructure and Impact Strength of S355J2 Quality Steels Used in Power Transmission Line Construction. International Conference on Material Science and Technology, 6-8 April 2016, Kapadokya, Türkiye, 2016.*

Investigation of Hot Rolled AISI 4140 Steels Subject To Large Strains

Sedef ŞİŞMANOĞLU*, Ali GÜNGÖR*

*Karabuk University, Engineering Faculty, Metallurgical and Materials Engineering Department, Karabuk-Turkey

Abstract— The mechanical and microstructural properties of hot rolled AISI 4140 steels subject to large strains were investigated in this study. The steels heated at 1200°C were hot rolled. The initial thickness of the steel plate, 160 mm, was reduced to 15 mm, 10 mm and 6 mm after multiple-pass. After hot rolling, normalization and hardening heat treatments were applied to one group of the steels. Mechanical and microstructural properties of as-hot rolled and heat treated steels were determined experimentally. Tensile properties, hardness values and wear properties of the steels were determined with room temperature tensile tests, Brinell hardness measurements and wear tests, respectively. In addition, scanning electron microscope (SEM) was used to analyze the surface morphology of the steels. It was seen that yield and tensile strength, hardness and wear resistance of the steel increased, but ductility and toughness decreased significantly after hardening.

Keywords—AISI 4140, hot rolling, normalization, hardening, tensile properties, wear

I. INTRODUCTION

AISI 4140, medium carbon and low alloy steel, is a high strength steel with chrome and molybdenum and it is mainly supplied as hardened and tempered. AISI 4140 steel has a very good balance of strength, ductility and wear resistance. Therefore, AISI 4140 is extensively used in many industry sectors for a wide range of applications such as; axles, bolts, conveyor parts, crankshafts, crow bars, gears, guides, logging parts, spindles, shafts, pins, piston rods, pump shafts, rams, ring gears, torsion bars, valves, etc.

In hot deformation, microstructural evolution occurs and it influences the mechanical properties of metals and alloys. Therefore, it is important to understand the relationship between thermo mechanical parameters and microstructure of the materials to improve the quality of hot deformed products [1–5]. Extensive studies have been done over the years to understand the hot deformation behavior of AISI 4140 steel [6–13]. Lin et al. [14] presented the flow stress constitutive equations of the work hardening-dynamic recovery and dynamic recrystallization periods. Kim et al. [7] investigated the effect of deformation mode on constitutive relation by hot torsion and compression tests. Kim and Yoo [9] established the quantitative

relationships between the flow stress and the volume fraction of dynamic recrystallization as a function of thermomechanical process parameters for AISI type 4140.

It is well known that the microstructure of this alloy steel is very sensitive to the thermomechanical process parameters such as strain, strain rate and temperature. Therefore, effects of amount of hot deformation (% strain) at a constant temperature on the microstructure and mechanical properties of hot rolled AISI steel with and without hardening were investigated in this study.

II. MATERIALS AND METHODS

A. Experimental Methods

In this study, microstructure, mechanical and wear properties of hot rolled AISI 4140 medium carbon low alloy steel were investigated. The steel was heated to 1200°C and kept at that temperature for an hour to obtain a uniform temperature distribution. After that the steel with 160x150x300 mm (in width, thickness and length respectively) was hot rolled. After a few pass, 165x46x1030 mm plate was obtained. Later, this plate was heated at 1200°C for 20 minutes and hot rolled to 142x15x3600 mm after a few pass. Hot rolled plate was cooled in a well to prevent wind effect and allow to cool slowly. After that, it was cut 500 mm in length and the rest of the steel was heated at 1200°C for 15 minutes. The steel was hot rolled to 10 mm in thickness and then cooled in the well. Another 500 mm piece was taken and thickness of the rest of the steel was reduced to 6 mm with the same process. As a result, hot rolled AISI 4140 steels with 6, 10 and 15 mm in thickness were obtained. In other words, AISI 4140 steel was hot rolled to 90.6%, 93.75% and 96.25% strain.

B. Heat Treatments

The hot rolled plates were cut 200 mm in length and 20 mm in width to get specimens for characterization. One specimen was taken of each thickness and normalization heat treatment was applied. Normalization heat treatment was carried

out at 860°C for 2 hours in normal atmosphere. Later, the specimens were cooled in air. Right after normalization heat treatment, the specimens were hardened. Hardening heat treatment was done by heating the steels at 835°C for 2 hours in normal atmosphere and quenching into water.

C. Tensile Test

Room temperature mechanical properties of the hot rolled steels with and without hardening heat treated were determined according to ISO 6892-1 standard using Zwick/Roell Z600 static/dynamic test machine The strain rate was of $6,7 \times 10^{-3} \text{ s}^{-1}$.

D. Microstructure Analysis

The microstructure of the alloys and chemical composition of the phases were characterized using scanning electron microscope (SEM, Carl Zeiss Ultra Plus Gemini FESEM) with attached energy-dispersive X-ray spectrometer (EDS).

E. Hardness Test

Brinell hardness of the hot rolled steels with and without hardening heat treatment was measured. A tungsten carbide ball with 2.5 mm in diameter and 187.5 kg load were used. Brinell hardness was measured from three different points on the Rolling surface of the specimens and average hardness was determined for each specimen.

F. Wear Test

All specimens were initially grinded to 1000 grit paper and then mechanically polished. Wear resistance of the hot rolled steels with and without hardening heat treatment was measured with reciprocating type wear test. During the wear tests, 10 N load was applied. The sliding distance was 500 m, stroke was 10 mm and sliding speed was 240 mm/s.

III. RESULTS AND DISCUSSIONS

Microstructures of as-hot rolled steels and hardened steels were investigated using FEG-SEM. Micrographs were taken both from the Rolling direction and Normal direction. Figure 1 shows the microstructures of the hot rolled steel before and after hardening. Micrographs in the first row represent the microstructures of hot rolled AISI 4140 steel from normal direction. Micrographs in the second row represent the microstructures of hot rolled AISI 4140 steel from Rolling direction. Similarly, micrographs in the third and fourth rows represent the microstructures of hot rolled and hardened AISI 4140 steel from Normal and Rolling directions, respectively. The microstructure of as-hot rolled steel consists of proeutectoid ferrite (formed above the eutectoid temperature) and fine eutectoid

perlite that contain eutectoid ferrite and cementite. Eventhough grain structure of the steels is not very clear in Normal direction, it is clearly seen in Rolling direction. All as-hot rolled steels have very similar microstructure and it looks like that microstructures of the steel are independent from the degree of deformation. This might be due to severe deformation (more than 90 % strain) that the steels experienced. When we looked at the microstructure of the hardened steels from Normal and Rolling directions, we see that martensitic transformation occured in the hardened steels and microstructures consist of martensite and small amount of retained austenite. Amount of retained austenite increases with decreasing deformation.

Brinell hardness of the steels is given in Table 1. As it is seen, hardness of the steels increases between 71 % and 135 % on hardening. Before hardening, hardness of the hot rolled steel with 10 mm thickness (93.75 % strain) showed the highest hardness among the other hot rolled steels. After hardening heat treatment, the hot rolled steel with 5 mm thickness (96.25 % strain) exhibited the highest hardness among the hardened steels.

TABLE LXXI
AVERAGE BRINELL HARDNESS OF THE HOT ROLLED STEELS

	96.25 % Strain (5 mm in thickness)	93.75 % Strain (10 mm in thickness)	90.6 % Strain (15 mm in thickness)
As-hot rolled	273	298	292
Hardened	642	639	498
%Increase	135	114	71

Tensile test results of the hot rolled steels are given in Table 2 and stress-strain curves are given in Fig. 2. All steels have very high yield and tensile strength and they increase significantly after hardening, while strain at break decreases significantly after hardening hot rolled steel.

As it is seen from the figure, ductility and toughness of the as-hot rolled steel decrease with increasing amount of hot deformation. Both tensile stress and strain of the steels increase with decreasing amount of hot deformation. Therefore, it can be said that the strength, ductility and toughness of the steel increase with decreasing amount of deformation. In addition, the shape of the stress-strain curves of hardened steels indicates that the hardened steels show brittle behavior, while as-hot rolled steels show ductile behavior.

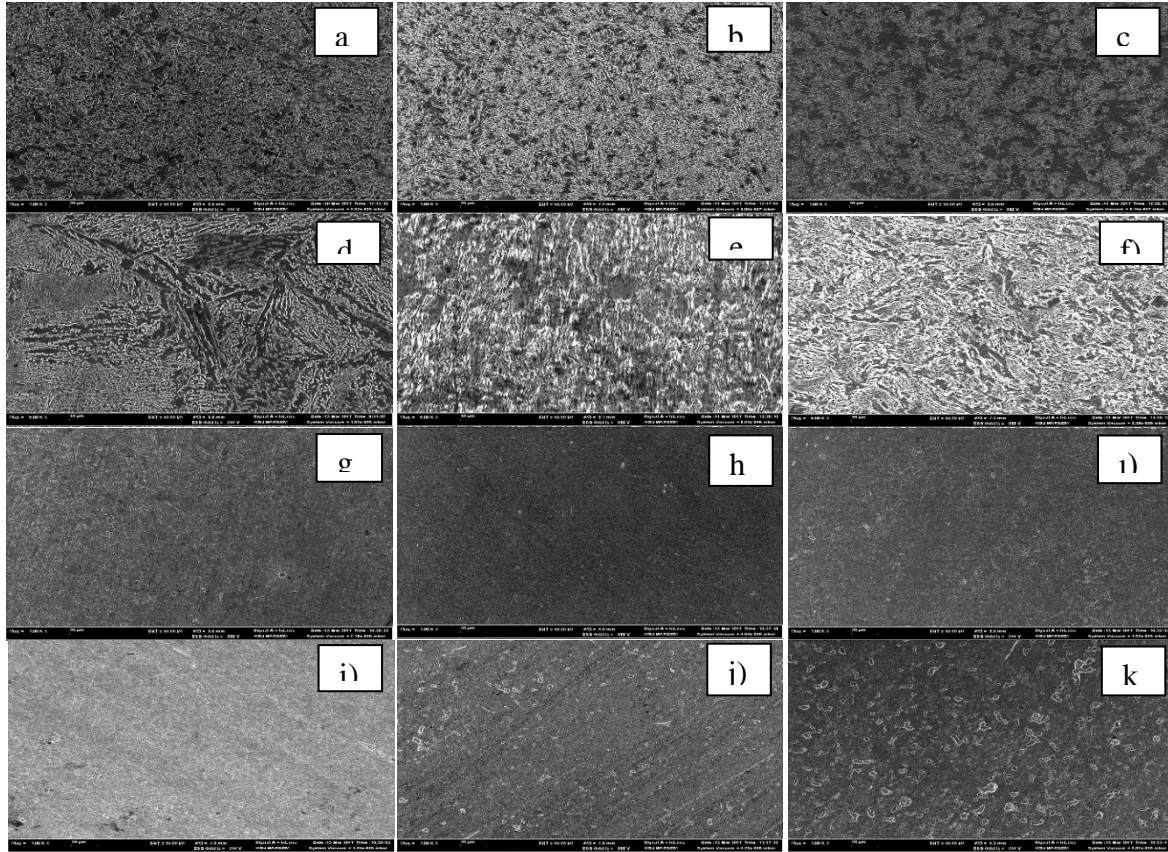


Fig. 1 Microstructures of hot rolled steels before (a-f) and after (g-k) hardening. a-c and g-i) from Normal direction, d-f and i-k) from Rolling direction

TABLE ILXXII
TENSILE PROPERTIES OF HOT ROLLED AISI 4140 STEEL

Degree of Deformation		Modulus of Elasticity (GPa)	Yield Stress (MPa)	Tensile Stress (MPa)	Strain at Break (%)
As-hot rolled	96.25 % Strain (5 mm in thickness)	178	655	906	3.37
	93.75 % Strain (10 mm in thickness)		630	876	4.06
	90.6 % Strain 15 mm in thickness		679	1019	4.92
Hardened	96.25 % Strain (5 mm in thickness)	178	1224	1590	0.48
	93.75 % Strain (10 mm in thickness)		1247	1414	0.31
	90.6 % Strain 15 mm in thickness		1173	1282	0.27

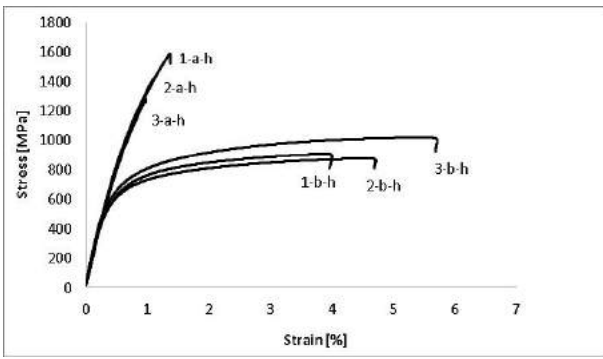


Fig. 2 Stress-strain curves of the hot rolled steels for different degree of deformations (96.25 %, 93.75 % and 90.60 %), b-h: before hardening and a-h: after hardening

Wear properties of the hot rolled steels before and after hardening heat treatment were determined using reciprocating wear test. Wear rate (g/m) and friction coefficient given in Table 3 were determined from experimental data. Wear rate and friction coefficient of the steels are given in Fig. 3.

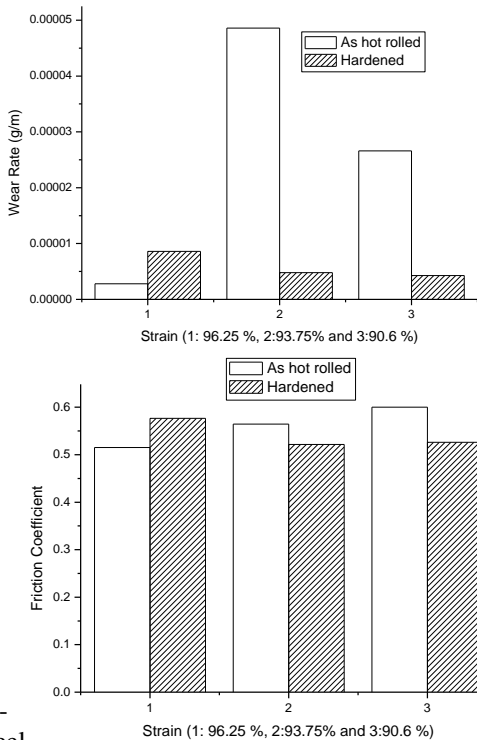


Fig. 3 Wear rates and friction coefficients of hot rolled steels

Wear rate of hot rolled steel does not change regularly with the amount of hot deformation. However, wear rate of hardened steels increases with the amount of hot deformation. Although friction coefficient of as-hot rolled steel increases with the amount of deformation, friction coefficient of hardened steels decreases slightly with the amount of deformation.

TABLE LXXIII II

WEAR RATE AND FRICTION COEFFICIENT OF HOT ROLLED STEEL

Degree of deformation (%)	Wear Rate (g/m)	
	As-hot rolled	After hardening
96.25	2.8×10^{-6}	8.6×10^{-6}
93.75	4.9×10^{-5}	4.8×10^{-6}
90.60	2.7×10^{-5}	4.2×10^{-6}
Friction Coefficient		
96.25	0.52	0.58
93.75	0.56	0.52
90.60	0.60	0.53

IV. CONCLUSIONS

Mechanical properties and microstructure of hot rolled AISI 4140 steel with and without normalization and hardening heat treatments were investigated as a function of degree of deformation at constant temperature. It was seen that:

1. Microstructure consists of martensite and small amount of retained austenite after hardening. Amount of austenite increases with decreasing degree of deformation.
2. Hardness of the steel increases after hardening. Among the hardened steels, the steel rolled to 5 mm thickness or deformed at 96.25 % has the highest Brinell hardness.
3. Yield and tensile stress also increase significantly after hardening, but strain at break decreases significantly.
4. The strength, ductility and toughness of the hardened steels increase with increasing amount of hot deformation.
5. Wear rate of the hardened steels also decreases with increasing amount of hot deformation.

ACKNOWLEDGMENT

The author would like to thank Avcılar Demir ve Çelik Çekme Sanayii for providing AISI 4140 steel and Arda HAYAT, Mehmet BÜLBÜL, Toprak YARAN, Research Asistant Alper İNCESU, Research Asistant Yasin AKGÜL, Research Asistant Emre TURAN and Research Asistant Yüksel AKINAY for their help in experimental part.

REFERENCES

[1] B. Eghbali, Mater. Lett. 61 (2007) 4006–4010.
 [2] X.G. Fan, D.M. Jiang, Q.C. Meng, L. Zhong, Mater. Lett. 60 (2006) 1475–1479.
 [3] J.T. Liu, H.B. Chang, R.H. Wu, T.Y. Hsu, X.Y. Ruan, Mater. Charact. 45 (2000) 175–186.
 [4] J. Huang, Z. Xu, Mater. Lett. 60 (2006) 1854–1858.
 [5] S. Bruschi, S. Poggio, F. Quadrini, M.E. Tata, Mater. Lett. 58 (2004) 3622–3629.
 [6] H. Holzzapfel, V. Schulze, O. Vöhringer, E. Macherauch, Mater. Sci. Eng. A 248 (1998) 9–18.
 [7] S.I. Kim, Y. Lee, S.M. Byon, J. Mater. Process. Technol. 140 (2003) 84–89.
 [8] F. Sarioglu, Mater. Sci. Eng. A 315 (2001) 98–102.
 [9] S.I. Kim, Y.C. Yoo, Mater. Sci. Technol. 18 (2002) 160–164.
 [10] Y.C. Lin, M.S. Chen, J. Zhong, Comput. Mater. Sci. 42 (2008) 470–477.
 [11] Y.C. Lin, M.S. Chen, J. Zhong, Comput. Mater. Sci 44 (2008) 316–321.

- [12] P. Uranga, A.I. Fernandez, B. Lopez, J.M. Rodriguez-Ibabe, Mater. Sci. Eng. A 345 (2003) 319–327.
- [13] X. Huang, K. Suzuki, A. Watazu, I. Shigematsu, N. Saito, Mater. Sci. Eng. A 488(2008) 214–220.
- [14] Y.C. Lin, M.S. Chen, J. Zhong, Mech. Res. Commun. 35 (2008) 142–150.

Effect Of Deformation on the Mechanical Properties of Hot Rolled AISI 4140 Steel

Gökhan ATAY*, Ali GÜNGÖR*

*Karabuk University, Engineering Faculty, Metallurgical and Materials Engineering Department, Karabuk-Turkey

Abstract— The effects of deformation on the mechanical and microstructural properties of hot rolled AISI 4140 steel were investigated. The steel heated at 1200°C was hot rolled from the initial thickness of 160 mm to 15 mm, 10 mm and 6 mm after multiple-pass. Later, normalization and tempering heat treatments were applied to the hot rolled steels. Mechanical and microstructural characterization of as-hot rolled and tempered steels were determined experimentally. Tensile properties, hardness values and wear properties of the steels were determined with room temperature tensile tests, Brinell hardness measurements and wear tests, respectively. In addition, scanning electron microscope (SEM) was used to analyze the surface morphology of the steels. After tempering heat treatment, yield stress increases with increasing amount of hot deformation, while wear rate, ductility and toughness of the steels decrease with increasing amount of hot deformation. In addition, the hardness of the steels decreases after tempering heat treatment.

Keywords—AISI 4140, hot rolling, normalization, tempering, tensile properties, wear

I. INTRODUCTION

AISI 4140, medium carbon and low alloy steel, is a high strength steel with chrome and molybdenum and it is mainly supplied as hardened and tempered. AISI 4140 steel has a very good balance of strength, ductility and wear resistance. Therefore, AISI 4140 is extensively used in many industry sectors for a wide range of applications such as; axles, bolts, conveyor parts, crankshafts, crow bars, gears, guides, logging parts, spindles, shafts, pins, piston rods, pump shafts, rams, ring gears, torsion bars, valves, etc.

Microstructural evolution occurs during hot deformation and it influences the mechanical properties of metals and alloys. Therefore, it is important to understand the relationship between thermomechanical parameters and microstructure of the materials to improve the quality of hot deformed products [1–5]. Extensive studies have been done over the years to understand the hot deformation behavior of AISI 4140 steel [6–13]. Lin et al. [14] presented the flow stress constitutive equations of the work hardening-dynamic recovery and dynamic recrystallization periods. Kim et al. [7] investigated the effect of deformation mode on constitutive relation by hot torsion and compression tests. Kim

and Yoo [9] established the quantitative relationships between the flow stress and the volume fraction of dynamic recrystallization as a function of thermomechanical process parameters for AISI type 4140.

Since the microstructure of AISI 4140 steel is very sensitive to the thermomechanical process parameters such as strain, strain rate and temperature, it is important to understand the effect of degree of deformation (% strain) on the microstructure and mechanical properties of hot rolled AISI steel. Therefore, the effect of deformation on the mechanical and wear properties of hot rolled steel with and without heat treatment was investigated in this study.

II. MATERIALS AND METHODS

A. Experimental Methods

In this study, microstructure, mechanical and wear properties of hot rolled AISI 4140 medium carbon low alloy steel were investigated. The steel was heated at 1200°C for an hour to obtain a uniform temperature distribution in the steel. After that the steel with 160x150x300 mm (in width, thickness and length respectively) dimensions was hot rolled. After a few pass, 165x46x1030 mm plate was obtained. Later, this plate was heated at 1200°C for 20 minutes and hot rolled to 142x15x3600 mm after a few pass. Hot rolled this plate was cooled in a well to prevent wind effect and allow to cool slowly. After that, it was cut 500 mm in length and the rest of the steel was heated at 1200°C for 15 minutes. The steel was further hot rolled to 10 mm in thickness and then cooled in the well. Another 500 mm piece was taken and thickness of the rest of the steel was reduced to 6 mm with the same process. As a result, hot rolled AISI 4140 steels with 6, 10 and 15 mm in thickness were obtained. In other words, AISI 4140 steel was hot rolled to 90.6%, 93.75% and 96.25% strain.

B. Heat Treatment

The hot rolled plates were cut 200 mm in length and 20 mm in width to get specimens for characterization. One specimen was taken of each thickness and normalization heat treatment was

applied. Normalization heat treatment was carried out at 860°C for 2 hours in normal atmosphere. Later, the specimens were cooled in air. Right after normalization heat treatment, the specimens were tempered. Tempering heat treatment was done by heating the alloys at 540°C for 2 hours in normal atmosphere and quenching into water.

C. Tensile Test

Room temperature mechanical properties of the hot rolled steels with and without tempering heat treatment were determined according to ISO 6892-1 standard using Zwick/Roell Z600 static/dynamic test machine. The strain rate was of $6,7 \times 10^{-3} \text{ s}^{-1}$.

D. Microstructure Analysis

The microstructure of the alloys and chemical composition of the phases were characterized using scanning electron microscope (SEM, Carl Zeiss Ultra Plus Gemini FESEM) with attached energy-dispersive X-ray spectrometer (EDS).

E. Hardness Test

Brinell hardness of the hot rolled steels with and without tempering was measured. A tungsten carbide ball with 2.5 mm in diameter and 187.5 kg load were used during hardness measurement. Brinell hardness was measured from three different points on the Rolling surface of the specimens and average hardness was determined for each specimen.

F. Wear Test

All specimens were initially grinded to 1000 grit paper and then mechanically polished. Wear resistance of the hot rolled steels with and without tempering was measured with reciprocating type wear test. During the wear tests, 10 N load was applied. The sliding distance was 500 m, stroke was 10 mm and sliding speed was 240 mm/s.

III. RESULTS AND DISCUSSIONS

Microstructures of as-hot rolled steel and tempered steel were investigated using FEG-SEM. Micrographs were taken both from the Rolling direction and Normal direction. Figure 1 shows the microstructures of the hot rolled steel before and after tempering. Micrographs in the first row represent the microstructures of hot rolled AISI 4140 steel from Normal direction. Micrographs in the second row represent the microstructures of hot rolled AISI 4140 steel from Rolling direction. Similarly, micrographs in the third and fourth rows represent the microstructures of hot rolled and tempered AISI 4140 steel from Normal and Rolling directions, respectively. The microstructure of as-hot rolled steel consists of proeutectoid ferrite (formed

above the eutectoid temperature) and fine eutectoid perlite that contain eutectoid ferrite and cementite. Eventhough grain structure of the steels is not very clear in normal direction, it is clearly seen in rolling direction. All as-hot rolled steels have very similar microstructures. Therefore, it can be said that the microstructures of the steel are independent from the degree of deformation. This might be due to severe deformation (more than 90 % strain) that the steel experienced. The microstructure of hot rolled and tempered steels consist of ferrite and layered perlite structures.

Brinell hardness of the steels is given in Table 1. As it is seen, hot rolled and tempered steels have lower Brinell hardness. The decrease in Brinell hardness of the steels changes between 0.37 % and 17.45 %. Among the as-hot rolled steel, the highest hardness was observed in 93.75% deformed steel. After tempering, the highest hardness was observed in 96.25% deformed steel.

TABLE LXXIV
AVERAGE BRINELL HARDNESS OF THE HOT ROLLED STEELS

	96.25 % Strain (5 mm in thickness)	93.75 % Strain (10 mm in thickness)	90.6 % Strain 15 mm in thickness
As-hot rolled	273	298	292
Tempered	272	246	249
% Decrease	0.37	17.45	14.73

Tensile test results of the hot rolled steels are given in Table 2 and stress-strain curves are given in Fig. 2. As-hot rolled steels have very high yield and tensile strength. Although the strain at break decreases with the amount of deformation, the stress does not change regularly with the degree of deformation. A significant softening occurs after tempering heat treatment. It is seen that tempered steels have either comparable or higher yield stress than as-hot rolled steels. However, tensile stress of tempered steels is lower than those of as-hot rolled steels.

As it is seen from Figure 2, ductility and toughness of both as-hot rolled and tempered steels decrease with increasing amount of hot deformation. When the ductility and toughness of the as-hot rolled and tempered steels are compared, it is seen that tempering significantly increases the ductility and toughness of the steel.

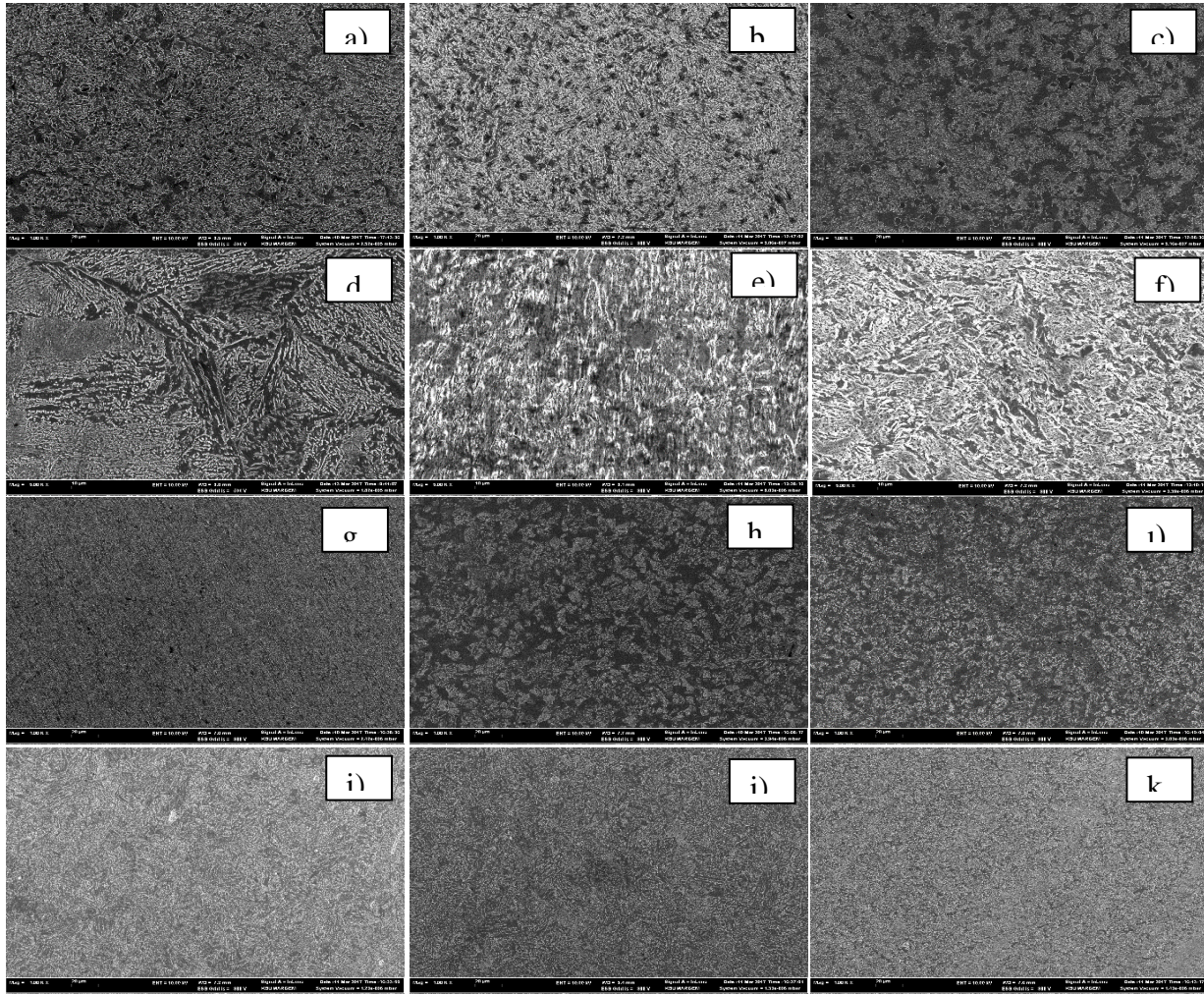


Fig. 1 Microstructures of hot rolled steels before (a-f) and after (g-k) tempering. a-c and g-i) from Normal, d-f and i-k) from Rolling directions.

TABLE LXXXV
TENSILE PROPERTIES OF HOT ROLLED AISI 4140 STEEL

Degree of Deformation		Modulus of Elasticity (GPa)	Yield Stress (MPa)	Tensile Stress (MPa)	Strain at Break (%)
As-hot rolled	96.25 % Strain (5 mm in thickness)	178	655	906	3.37
	93.75 % Strain (10 mm in thickness)		630	876	4.06
	90.6 % Strain 15 mm in thickness		679	1019	4.92
Tempered	96.25 % Strain (5 mm in thickness)	185	694	851	156.9
	93.75 % Strain (10 mm in thickness)		691	861	238.6
	90.6 % Strain 15 mm in thickness		662	820	402.6

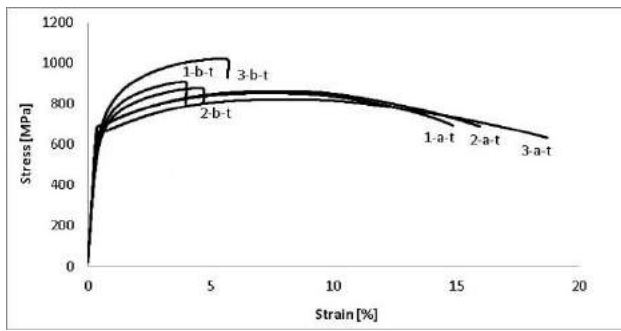


Fig. 2 Stress-strain curves of the hot rolled steels for different degree of deformations (96.25 %, 93.75 % and 90.60 %), b-h: before tempering and a-h: after tempering

Wear properties of the hot rolled steels before and after tempering were determined using reciprocating wear test. Wear rate (g/m) and friction coefficient given in Table 3 were determined from experimental data. Wear rate and friction coefficient of the steels are given in Fig. 3.

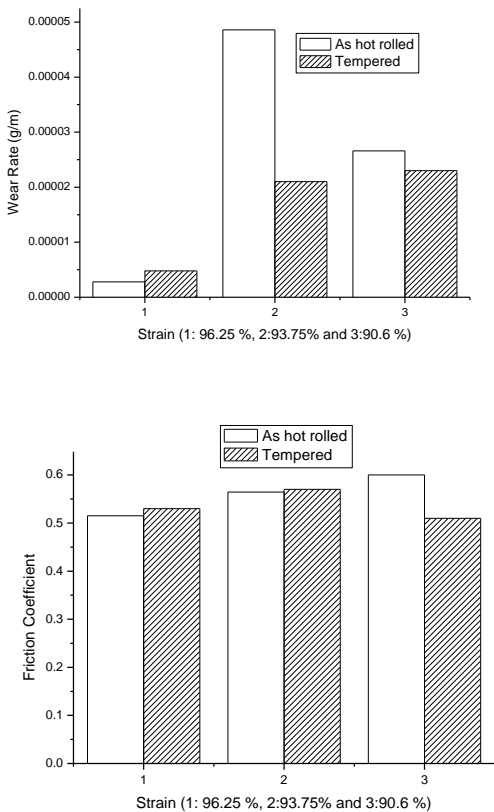


Fig. 3 Wear rates and friction coefficients of hot rolled steels

It is seen that wear rate of as-hot rolled steels does not change regularly with the amount of hot deformation. However,

wear rates of tempered steels are lower than that those of as-hot rolled steels. In addition, wear rate of tempered steels decreases with increasing amount of hot deformation. Friction coefficient of as-hot rolled steels decreases with the amount of hot deformation. The friction coefficient of tempered steels is slightly higher than those of as-hot rolled steels except 90.6 % hot deformed and tempered steel.

TABLE LXXVI
WEAR RATE AND FRICTION COEFFICIENT OF HOT ROLLED STEEL

Degree of deformation (%)	Wear Rate (g/m)	
	As-hot rolled	After Tempering
96.25	2.8×10^{-6}	4.8×10^{-6}
93.75	4.9×10^{-5}	2.1×10^{-5}
90.60	2.7×10^{-5}	2.3×10^{-5}
Friction Coefficient		
96.25	0.52	0.53
93.75	0.56	0.57
90.60	0.60	0.51

IV. CONCLUSIONS

Microstructure, mechanical and wear properties of hot rolled AISI 4140 steel with and without normalization and tempering heat treatment were investigated as a function of degree of deformation at constant temperature. It was seen that:

6. Hardness of the steels decreases after tempering.
7. Ductility and toughness of as-hot rolled and tempered steels decrease with increasing amount of hot deformation.
8. Wear rate of tempered steels decreases with increasing amount of hot deformation.

ACKNOWLEDGMENT

The author would like to thank Avcılar Demir Ve Çelik Çekme Sanayii for providing AISI 4140 steel and Arda HAYAT, Mehmet BÜLBÜL, Toprak YARAN, Research Asistant Alper İNCESU, Research Asistant Yasin AKGÜL, Research Asistant Emre TURAN and Research Asistant Yüksel AKINAY for their help in experimental part.

REFERENCES

[1] B. Eghbali, Mater. Lett. 61 (2007) 4006–4010.
 [2] X.G. Fan, D.M. Jiang, Q.C. Meng, L. Zhong, Mater. Lett. 60 (2006) 1475–1479.
 [3] J.T. Liu, H.B. Chang, R.H. Wu, T.Y. Hsu, X.Y. Ruan, Mater. Charact. 45 (2000) 175–186.
 [4] J. Huang, Z. Xu, Mater. Lett. 60 (2006) 1854–1858.
 [5] S. Bruschi, S. Poggio, F. Quadrini, M.E. Tata, Mater. Lett. 58 (2004) 3622–3629.
 [6] H. Holzzapfel, V. Schulze, O. Vöhringer, E. Macherauch, Mater. Sci. Eng. A 248 (1998) 9–18.
 [7] S.I. Kim, Y. Lee, S.M. Byon, J. Mater. Process. Technol. 140 (2003) 84–89.
 [8] F. Sarioglu, Mater. Sci. Eng. A 315 (2001) 98–102.
 [9] S.I. Kim, Y.C. Yoo, Mater. Sci. Technol. 18 (2002) 160–164.
 [10] Y.C. Lin, M.S. Chen, J. Zhong, Comput. Mater. Sci. 42 (2008) 470–477.

- [11] Y.C. Lin, M.S. Chen, J. Zhong, *Comput. Mater. Sci* 44 (2008) 316–321.
- [12] P. Uranga, A.I. Fernandez, B. Lopez, J.M. Rodriguez-Ibabe, *Mater. Sci. Eng. A* 345 (2003) 319–327.
- [13] X. Huang, K. Suzuki, A. Watazu, I. Shigematsu, N. Saito, *Mater. Sci. Eng. A* 488(2008) 214–220.
- [14] Y.C. Lin, M.S. Chen, J. Zhong, *Mech. Res. Commun.* 35 (2008) 142–150.

Influence of Aging on Residual Stress, Wear and Hardness behaviour in Al-Cu-Ni Heusler Alloys

F. HUSEM¹, F. M. Tezel¹
1. Karabuk University, TURKEY
fazilhusem@karabuk.edu.tr

ABSTRACT

Although many parameters for metallic alloy systems can be obtained in the literature, there are limited studies about the relationship between residual stress and tribological performance of the metallic alloy systems. In this study residual stress measurement was performed by strain gauge method to investigate on residual stress, hardness and wear behaviours of Al-Cu-Ni Heusler Alloys before and after aging process. Wear tests were carried out using two different loads (10N and 20N) in dry sliding conditions. Results show that aging time effects mechanical behaviour of heusler alloys. Also Best wear resistance is belonging to the aged samples under load of 10N.

Key Words: Heusler Alloys, Wear Performance, Residual Stress, Aging

Investigation of Wear and Mechanical Behaviors of Damascus Steels

Eren SALISI, Umit YAVUZI, Nurdan KUCUKI, Fazil HUSEMI, Hayrettin AHLATCI, Memis ISIKI, Pinar UYAN

1. Karabuk University, TURKEY

2. Bilecik Seyh Edebali University, TURKEY

erensals@gmail.com

ABSTRACT

Damascus steels are produced by traditional methods and mostly used in the construction of decorative tools. This study aims to investigate wear and mechanical behaviors of damascus steels which are exposed different forging type. Wear tests were applied for two different category of samples under the loads of 30N and 40N. In addition to wear tests, tensile test was carried out to understand the influence of forging type on mechanical behavior in this quality steel. Results show that, wear performances are changed with forging process and best wear resistance could be seen under loads of 30N for all samples.

Keywords: Damascus steels, forging, wear, tensile

An innovative study: Developing of a continuous coating method for steel sheets or plates

Mehmet Eroglu
Firat University, TURKEY
[*meroglu@firat.edu.tr*](mailto:meroglu@firat.edu.tr)

ABSTRACT

Innovation is the application of an idea, item or a new process to the real life for income. In coating sector, it is possible to talk about some new and innovative processes for different kind of parts, especially for small parts. However, the subject of coating for steel sheets or plates having large surfaces with Fe-based alloys, especially for resistance to wear, is still open for investigation. For coating of large steel surfaces, common method is welding using different kind of electrodes. However, coating with welding has some disadvantages such as; dependent on electrodes, low coating rate, high surface roughness and so on. However, in the continuous coating method that was invented under this study has more advantages. In the experimental study, st 37 steel plates having dimensions of 4 x 800 x 800 mm were coated using continuous coating method with three different kinds of Fe-based alloys, austenitic manganese steel, high chromium-

high carbon alloy and nodular cast iron, with the thickness of 4 mm. After coating process, microstructural investigation was conducted using optical and scanning electron microscope (SEM) with EDS analysis and microhardness measurements were obtained from coating to substrate. The results showed that there is a good bond between substrate and coting layers and the continuous coating method is much more suitable for coating the surfaces of large sheets or plates safely and economically.

Keywords: Continuous coating, Hardfacing, Hardness, Microstructure, Wear

Recycling and Reuse Potential of Solid Wastes Produced in Iron and Steel Industry

Sakine UGURLU KARAĞAÇ¹

¹*Karabuk University Engineering Faculty, Environmental Engineering Department, Demircelik Kampusu, 78050 -
Karabuk-Turkey*

sakineugurlu@karabuk.edu.tr

ABSTRACT

Iron and steel is one of the important tools for the economy of countries. Iron and steel industry uses energy and high quantity of raw material. Iron and steel production has a number of impacts on the environment, including air emissions, wastewater contaminants, hazardous wastes, and solid wastes. Sources of solid wastes for steel industries may be identified as coke oven by product plant, sinter plant, refractory materials plant, blast furnace, basic oxygen furnace, steel melting shop and rolling mill. In steel industry, solid waste management is aimed to provide maximum benefits from waste products and to generate the minimum amount of waste. To achieve this goal “4Rs” i.e. reduce, reuse, recycle and restoring the materials are being considered as strategies of solid waste management. For minimizing the sources of solid wastes and maximizing the recycle of collected wastes can be opted in the following ways: Identification of sources, quantities and types of solid wastes generated from different sub-processes of steel manufacturing process. To find out the reasons of generation of solid wastes. To use advanced technology for minimizing waste. In efforts to prevent environmental pollution, the priority is to evaluate waste materials for recycle and reuse. Thus waste and damage to the environment are minimized and also provides economic benefits.

Key Words: Reuse, recycling, solid waste, iron and steel industry environment

Abrasion Resistant Steels

*Oktay Elkoca
ArcelorMittal USA
oktay.elkoca@arcelormittal.com*

In general, design of abrasion resistant steel is based on the assumption that abrasion resistance increases with hardness. However, in practical use, some problems are created with an increase in hardness exceeding 500 HB. Therefore, abrasion resistant steels should have a combination of high abrasion resistance, good cold formability and sufficient impact toughness. Relia® is ArcelorMittal's new range of high hardness, low-alloyed martensitic steels, offering outstanding resistance to wear and abrasion. Despite their extreme hardness, the properties of Relia® plates are specifically designed for improved workability such as cutting, forming, drilling and welding to realise any kind of applications and designs.

Keywords: Steel, abrasion resistant, cutting

Metallurgical Challenges in Resistance Spot Welding of Advanced High Strength Steels

Majid Pouranvari

Department of Materials Science and Engineering, Sharif University of Technology, Tehran, Iran
pouranvari@sharif.edu

Abstract—The successful implementation of advanced high strength steels (AHSS) requires improving fundamental understanding regarding metallurgical response and failure behaviour of these materials during resistance spot welding, the key crucial joining process in automotive industry. The present paper briefly reviews the fundamental challenges regarding microstructure/failure behavior relationship in AHSS steels resistance spot welds. Finally, the unresolved scientific challenges are highlighted.

Keywords— Resistance spot welding, advanced high strength steel, microstructure, failure mode

I. INTRODUCTION

The use of advanced high strength steels (AHSS) is a key strategy to address the conflicting demands on the automotive industry to simultaneously improve crash safety and fuel economy [1]. As resistance spot welding (RSW) is crucial manufacturing technology in sheet metal joining, the weldability of AHSS is one of the key factors governing their widespread application in the automotive industry. The well-designed microstructure of the base metal is destroyed in the fusion zone (FZ) and heat affected zone (HAZ) [2-7] affecting the mechanical performance of the resistance spot welds (Fig. 1a). As the weld failure during a crash is a critical issue for crashworthiness, stiffness and NVH (Noise, Vibration and Harshness) performance of the vehicle [8-9], there is need to improve load bearing capacity and energy absorption capability of the resistance spot welds. In this paper, the metallurgical challenges during RSW of AHSS are briefly reviewed and the future research needs are highlighted.

II. CHALLENGES IN RSW OF AHSS STEELS

A. Challenges in RSW of AHSS steels

Microstructure evolution in FZ is governed by chemical composition and cooling rate during RSW process. The heating and cooling rate of RSW is significantly higher than conventional arc welding and laser welding processes. It is shown that the cooling rates during RSW vary between 8000 to 2000 Ks⁻¹ for the sheet thickness ranging from 0.8 to 2 mm [10]. These extremely high cooling rates are due to the presence of water cooled copper electrodes and their quenching effect as well as short welding cycle. The critical cooling rates for AHSS

are below 500 Ks⁻¹. The critical cooling rates for DQSK and IF steel are below 3000 Ks⁻¹ [2]. Depending on the sheet thickness, the cooling rate experienced by FZ can be higher than the critical cooling rate of all steels. Therefore, martensite formation in FZ is not surprising even in the case of low carbon steels (Fig. 1b).

Hardness of the FZ is a key metallurgical factor in determining weld ductility and failure mode transition [11]. Generally, the FZ hardness of steel resistance spot welds dictated by the carbon content and alloying element of the weld metal [12, 13]. It is shown that there is linear relationship between Yurioka carbon equivalent and FZ hardness for AHSS welds [13]. The carbon equivalence is increased in order of IF, DQSK, DP and TRIP steels. Therefore, it can be concluded that TRIP steels exhibits the highest FZ hardness [14]. The high FZ hardness promotes brittle failure during cross-tension loading [15].

B. HAZ Softening

Reduction in the HAZ hardness (softening) with respect to the BM has been reported in ferrite-martensite dual phase steel and martensitic steels. HAZ softening play important role in interfacial to pullout failure mode transition as well as mechanical properties. Significant HAZ softening can promotes pullout failure; however, it can reduce the peak load

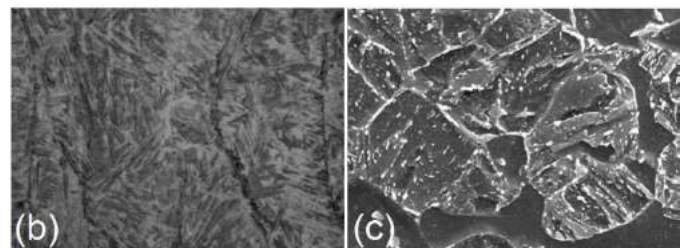
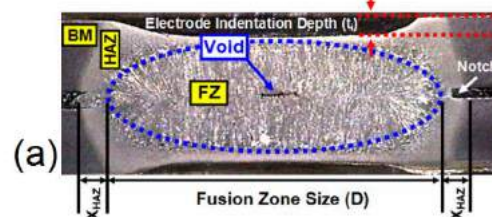


Fig.1: (a) Typical macrostructure of resistance spot welds showing the weld physical attributes including FZ size D , electrode indentation depth t_i and the width of HAZ X_{HAZ} . The joint can be divided into three distinct Microstructural zones including FZ, HAZ and BM. The presence of a natural notch at the

sheet/sheet interface significantly affects the mechanical behaviour of resistance spot welds.

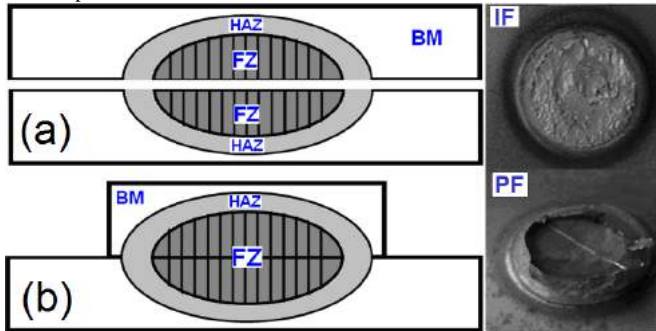


Fig. 2: Schematic representation of two distinct failure modes of resistance spot welds (a) interfacial, (b) pullout.

of the welds [16-20]. HAZ softening in DP steels is due to the tempering of the pre-existing martensite in the sub-critical areas of the HAZ (Fig.1c) [16]. In the case of martensitic steels, the HAZ softening can be related to (i) the formation of ferrite phase in ICHAZ leads to hardness reduction in respect to fully martensitic BM and (ii) the occurrence of martensite tempering in sub-critical HAZ [18]. The degree of the HAZ softening depends on the volume fraction of martensite in the BM, chemical composition of the steel, sheet thickness, heat input and welding process. document. The only two level-1 headings which must not be numbered are “Acknowledgment” and “References”.

C. High susceptibility to fail in interfacial failure mode

Failure mode of resistance spot welds (RSWs) is a qualitative measure of mechanical properties. Basically, spot welds can fail in two distinct modes described as follows:

Interfacial failure (IF) mode in which, the fracture propagates through the fusion zone (Fig.2a). It is believed that this failure mode has detrimental effect on the crashworthiness of the vehicles.

Pullout failure (PF) mode in which, the failure occurs via withdrawal of the weld nugget from one sheet. In this mode, fracture may initiate in the BM, HAZ or HAZ/FZ depending on the metallurgical and geometrical characteristics of the weld zone and the loading conditions (Fig.2b). Generally, the PF mode exhibits the most satisfactory mechanical properties. The failure mode of resistance spot welds is controlled by following factors:

(1) FZ size: The FZ size is the most important parameter governing the failure mode of RSWs [21, 22]. The larger the FZ size (i.e. larger bond area) the lower the stress experienced by sheet/sheet interface (i.e. the higher the resistance to the interfacial failure).

(2) Porosity and shrinkage voids in the weld nugget: Porosity and shrinkage voids in the weld nugget decrease the area of the load bearing surface in IF mode (i. e. sheet/sheet interface area). This leads to the development of much higher stress at the interface and consequently promotes IF mode.

From material's chemistry point of view, it is shown that materials with rich chemistry promote the formation of shrinkage voids [23]. Richer chemistry of AHSS compared to low carbon steel can partly explain the more susceptibility of AHSS to interfacial fracture in comparison with the mild carbon steels.

(3) Segregation of P and S in grain boundaries: The higher carbon equivalent from elements of carbon, manganese, etc., makes the weld hard and brittle, which congregated in the grain boundaries and increased the boundary energy to easily cause the solidification cracks. Segregation of trace elements such as S and P in the material composition to the grain boundaries induces intercrystalline fracture [24].

(4) Hardness characteristics: The dependence of failure mode on the weld hardness characteristics depends on the loading condition. In cross-tension and coach peel loading conditions, the transition behavior is controlled by the ratio of FZ fracture toughness to pullout failure location (BM or HAZ) hardness. Since the FZ hardness and HAZ hardness both depend on the carbon equivalent of the steel, the tendency to fail in interfacial mode increases as the carbon equivalence increases. The higher carbon equivalence of AHSS steel compared to low strength steels explain their higher tendency to fail in IF mode. The failure mode transition in tensile-shear loading depends on the hardness ratio of FZ to pull-out failure location. For a constant sheet thickness and porosity level, those spot welds having low H_{FZ}/H_{PFL} exhibit higher susceptibility to the interfacial failure mode. Higher hardness value of the fusion zone relative to the hardness of failure location encourages the failure initiation in the base metal or HAZ. Accordingly, (a) increasing the FZ hardness and (b) HAZ softening can reduce the tendency to fail in PF mode during the TS failure mode. Typically, fusion zone hardness value of the mild steel RSWs is about 2-3 times higher than the base metal hardness. Therefore, in the case of low carbon steel, PF mode should be the dominant failure mode. However, in the case of AHSS spot welds, the H_{FZ}/H_{PFL} is lower than that of the low carbon steel RSWs due to the higher BM hardness of AHSS. This explains the high susceptibility of the AHSS to interfacial failure mode in comparison with the low carbon steels. Accordingly, it is of great importance to study the effect of this metallurgical factor on weld failure mode [2].

III. APPROACHES TO REDUCE THE TENDENCY TO FAIL IN INTERFACIAL MODE

Weld fracture of the AHSS spot welds is a complicated phenomenon which involves interaction among the geometrical factors, weld metallurgical properties and loading mode. To reduce the tendency to fail in IF mode, several factors should be controlled:

A. Adjusting welding parameters

As mentioned above, there is a minimum FZ size to ensure pullout failure mode. Therefore, welding parameters, viz. welding current, welding time and electrode force, which determine weld heat input, should be adjusted so that the sufficient weld size is obtained.

B. Adjusting chemical composition of FZ

Chemical composition of FZ can affect the hardneability of the FZ and its susceptibility to formation of solidification defects. Both factors largely depend on the carbon equivalence of the FZ. The lower CE the lower tendency to formation of martensite and solidification defects is leading to higher tendency to fail in PF mode. The adjusting the FZ chemical composition can be achieved through two techniques: (1) introducing a low carbon steel shim insert and [25] (2) dissimilar welding of high alloyed steel to lean alloyed steels.

C. Controlling the hardness characteristics

The hardness characteristic of steel spot welds can be engineered via controlling the thermal cycle using some techniques such as in-process tempering, pre-heat treatment, post heat treatment and controlling the cooling rate by down slope and post heating [26-34].

The use of down slope or introducing a low current pulse immediately after the welding current pulse can reduce cooling rate. Thus, this may provide more time to austenite decomposition into softer products rather than hard martensite. However, the time required to prevent martensite formation depends on the steel chemistry. For example, based on the CCT diagrams, the required times to prevent martensite formation for TRIP steel (Fe-0.3C-0.29Si-1.53Mn), dual phase steel (Fe-0.15C-0.32Si-1.42Mn) and martensitic steel (Fe-0.19C-0.4Si-0.47Mn) are 20, 10 and 1.5 s. Therefore, to effectively modify the microstructures of these steels, down sloping times ranging from roughly 120 cycles (martensitic steels) to over 600 cycles (dual phase steels) to 1200 cycle for TRIP steel are required. Therefore, the use of down sloping in AHSS spot welds is not practical and economic [26].

One of the proven methods of alleviating the problem of high sensitivity to IF mode is in-process quench and tempering of the weld. After the weld has been made, it is held between the electrodes long enough to sufficiently quench to martensite. A subsequent temper pulse is then applied to soften the microstructure of the weld. Although the concept is simple, the behavior of steels of varying composition and processing particularly AHSS during tempering is not fully understood.

To perform a proper quench and tempering treatment on the weldment, the following criteria should be satisfied [32, 34]: (1) the quenching time should be selected such that the weldment cooled to a temperature slightly below the martensite-finish temperature (M_f) before being heated for tempering. If this temperature is above M_f , there can be untransformed austenite left in the FZ and it can re-decompose to un-tempered martensite upon cooling to room temperature

after tempering. For a particular tempering time and tempering current, there is a minimum cooling time to achieve pullout failure mode. (2) the tempering time and tempering current should be adjusted such that the martensite tempering process is occurred in sufficient extent to reduce FZ hardness.

IV. OUTLOOK

Unlike the conventional low strength automotive steels, the metallurgical behaviour of AHSSs during RSW plays an important role in their mechanical behaviour. The sophisticated designed microstructure of AHSSs is destroyed in the FZ and HAZ during RSW, which calls for detailed investigations of microstructure evolution during welding process. From the preceding analyses, it was understood that AHSSs experience more complicated microstructural transformations (e.g. martensite formation in the FZ and softening of the HAZ in some grades) during RSW. As it was emphasised above, the IF to PF mode transition is strongly influenced by the hardness characteristics of the welds which in turns is controlled by microstructural evolution in FZ and HAZ. Therefore, there is a need to develop mathematical modelling for prediction phase transformation during fast cooling rate of RSW. Despite the fact that the current models are capable to predict the microstructural evolution during austenite decomposition in FZ and HAZ, much work should be directed towards understanding of physical mechanism of HAZ softening during RSW of AHSS (e.g. non-isothermal tempering of martensite/bainite) and develop models for predicting the hardness of softened zone.

Increased tendency to fail in interfacial mode is prominent in AHSS resistance spot welds. Sizing based on conventional recommendation of $4t0.5$ and $4t0.5$ [35] cannot produce PF mode in AHSS resistance spot welds. Therefore, there is a need to define new weld quality criteria for AHSS welds. As discussed above, the failure mode transition is governed by several factors including loading mode, sheet thickness, hardness characteristics of the weld, FZ toughness, HAZ softening, shrinkage voids and decreased coherency of columnar grains in FZ voids. Therefore, the metallurgical characteristics of welds should be considered to predict and analyze the spot weld failure mode more precisely. There is a lack of systematic studies regarding the numerical modelling of failure mode transition accounting the weld metallurgical phenomena including material properties mismatch in the joint region, hardness gradient in HAZ and HAZ softening. The brittle IF of the AHSS spot weld is more likely to occur during impact loading which calls for more comprehensive investigations regarding fundamental understanding of the role of microstructure/properties gradient in the failure behaviour of the similar and dissimilar AHSSs spot welds.

Resistance spot welding of AHSSs with existing welding practices for the conventional steels may not be the preferred approach to achieve the full benefits of AHSS. The possibility of in situ controlling of thermal cycle during RSW (e.g. preheating and post-heating heat treatment) provides significant opportunity for modification of weld microstructure and hence improving failure mode transition behaviour and

enhancing the mechanical properties. However, the success of these techniques is highly depended on precise controlling the temperature distribution during pre-/post-heat treatment which can be predicted using sophisticated numerical modelling and in detailed understanding of metallurgical response of FZ and HAZ (including upper critical HAZ, inter-critical HAZ and subcritical HAZ) to in situ post-heat treatment of the weld.

REFERENCES

- [1] [C. C. Tasan, M. Diehl, D. Yan, M. Bechtold, F. Roters, L. Schemmann, C. Zheng, N. Peranio, D. Ponge, M. Koyama, K. Tsuzaki, D. Raabe, An overview of dual-phase steels: advances in microstructure-oriented processing and micromechanically guided design, *Annu. Rev. Mater. Res.*, 2015, 45, 391–431.
- [2] M. Pouranvari, S. P. H. Marashi, Critical Review of Automotive Steels Spot Welding: Process, Structure and Properties, *Sci. Technol. Weld. Join*, 2013, 18, 361–403.
- [3] S. Dancette, D. Fabregue, V. Massardier, J. Merlin, T. Dupuy, and M. Bouzekri 'Experimental and modeling investigation of the failure resistance of Advanced High Strength Steels spot welds', *Eng Fail Anal*, 2011, 78, 2259-2272.
- [4] M. Pouranvari, Fracture toughness of martensitic stainless steel resistance spot welds, *Materials Science and Engineering: A*, 680 (2016), 97-107.
- [5] S. T. Wei, R. D. Liu, D. Lv, L. Lin, X. F. Lu, S. W. Ding, Effect of joint configuration on resistance spot weldability of galvanised DP780 steel sheets, *Sci Technol Weld Join*, 2016, 21:178-185.
- [6] V Rajinikanth, K Mukherjee, S Ghosh Chowdhury, A Schiebahn, A Harms & W Bleck, Mechanical property and microstructure of resistance spot welded twinning induced plasticity-dual phase steels joint, *Sci. Technol. Weld. Joining*, 2013, 18: 485-491.
- [7] M. Pouranvari, M. Alizadeh-Sh, S. P. H. Marashi, Welding metallurgy of stainless steels during resistance spot welding Part I: fusion zone, *Sci Technol Weld Join*, 2015, 20: 502-511.
- [8] H. Zhang and J. Senkara: 'Resistance welding: fundamentals and applications'; 2005, London, Taylor & Francis CRC Press
- [9] Y. P. Yang; J. Gould; W. Peterson; F. Orth; P. Zelenak; W. Al-Fakir, 'Development of spot weld failure parameters for full vehicle crash modelling', *Sci. Technol. Weld. Joining*, 2013, 18, 222-231.
- [10] J. E. Gould, S. P. Khurana, and T. Li, Predictions of microstructures when welding automotive advanced high-strength steels, *Weld J*, 2006, 85, 111-s-116-s.
- [11] M. Pouranvari, S. P. H. Marashi, and D. S. Safanama: 'Failure mode transition in AHSS resistance spot welds. Part II: Experimental investigation and model validation', *Mater. Sci. Eng., A*, 2011, 528, 8344-8352.
- [12] M. I. Khan, M. L. Kuntz, E. Biro, and Y. Zhou: 'Microstructure and mechanical properties of resistance spot welded advanced high strength steels', *Mater Trans*, 2008, 49, 1629-1637.
- [13] N. J. Den Uijl, H. Nishibata, S. Smith, T. Okada, T. Van Der Veldt, M. Uchihara, and K. Fukui: 'Prediction of post weld hardness of advanced high strength steels for automotive application using a dedicated carbon equivalent number', *Weld World*, 2008, 52(11-12), 18-29.
- [14] H. K. D. H. Bhadeshia, Problems in the Welding of Automotive Alloys, *Sci Technol Weld Join*, 2015, 20, 451-453.
- [15] M. Pouranvari: 'Susceptibility to interfacial failure mode in similar and dissimilar resistance spot welds of DP600 dual phase steel and low carbon steel during cross-tension and tensile-shear loading conditions', *Mater. Sci. Eng., A*, 2012, 546, 129-138.
- [16] V. H. Baltazar Hernandez, M. L. Kuntz, M. I. Khan, and Y. Zhou: 'Influence of microstructure and weld size on the mechanical behaviour of dissimilar AHSS resistance spot welds', *Sci. Technol. Weld. Joining*, 2008, 13(8), 769-776.
- [17] X. Sun, E. V. Stephens, and M. A. Khaleel, Effects of fusion zone size and failure mode on peak load and energy absorption of advanced high-strength steel spot welds, *Weld J*, 2007, 86, 18s-25s.
- [18] M. Tamizi, M. Pouranvari, M. Movahedi, Welding metallurgy of martensitic advanced high strength steels during resistance spot welding, *Sci. Technol. Weld. Join.*, 2017, 22, 327-335.
- [19] M. Pouranvari, S. P. H. Marashi, Key factors influencing mechanical performance of dual phase steel resistance spot welds, *Sci. Technol. Weld. Join.*, 2010, 15, 149-155.
- [20] M. Pouranvari, S. P. H. Marashi, Failure mode transition in AHSS resistance spot welds. Part I. Controlling factors, *Mater. Sci. Eng. A*, 2011, 528, 8337-8343.
- [21] M. Pouranvari, H. R. Asgari, S. M. Mosavizadch, P. H. Marashi, and M. Goodarzi: 'Effect of weld nugget size on overload failure mode of resistance spot welds', *Sci. Technol. Weld. Joining*, 2007, 12, 217-225.
- [22] D. J. Radakovic and M. Tumulu: 'Predicting resistance spot weld failure modes in shear tension tests of advanced high-strength automotive steels', *Weld J*, 2008, 87, 96-s-105-s.
- [23] A. Joaquin, A. N. A. Elliott, and C. Jiang: 'Reducing shrinkage voids in resistance spot welds', *Weld J*, 2007, 86, 24-27.
- [24] N. J. D. Uijl and S. Smith: 'Resistance spot welding of advanced high strength steels for the automotive industry', *Proc. 4th Int. Semin. on 'Advances in resistance welding'*, Wels, Austria, November 2006, 30–60, SWANTEC Software and Engineering ApS and FRONIUS International GmbH.
- [25] W. Peterson: 'Dilution of weld metal to eliminate interfacial fractures of spot welds in high and ultra-high strength steels', *Proc. ICAWT 1997 Int. Conf. on 'Advances in welding technology'*, Columbus, OH, USA, September 1997, 331–346, Woodhead Publishing Ltd.
- [26] G. Shi and S. A. Westgate: 'Techniques for improving the resistance spot weldability of 1.6–2.0 mm ultra-high strength steels for automotive applications', TWI report, TWI, Cambridge, UK, 2005.
- [27] VH Baltazar Hernandez, Y Okita, Y Zhou Second Pulse Current in Resistance Spot Welded TRIP Steel—Effects on the Microstructure and Mechanical Behavior, *Weld J*, 2012, 91, 278-285.
- [28] A. R. Jahandideh, M. Hamed, S. A. Mansourzadeh, A. Rahi, An experimental study on effects of postheating parameters on resistance spot welding of SAPH440 steel, *Sci. Technol. Weld. Joining*, 2011, 16, 669-675.
- [29] G. Shi, S. A. Westgate, Techniques for improving the resistance spot weldability of 1.6-2.0 mm ultra-high strength steels for automotive applications, TWI report. 2005.
- [30] R. Duan, Z. Luo, Y. Li, Y. Zhang, Z. M. Liu, Novel postweld heat treatment method for improving mechanical properties of resistance spot weld, *Sci Technol Weld Join*. 2015; 20:100-105
- [31] S. T. Wei, D. Lv, R. D. Liu, L. Lin, R. J. Xu, J. Y. Guo, K. Q. Wang, Similar and dissimilar resistance spot welding of advanced high strength steels: welding and heat treatment procedures, structure and mechanical properties, *Sci Technol Weld Join*, 2014, 19: 427-435
- [32] W. L. Chuko, J. E. Gould, Development of appropriate resistance spot welding practice for transformation-hardened steels, *Weld J*, 2002, 81, 1s-7s.
- [33] C. Wakabayashi, S. Furusako, Y. Miyazaki, Strengthening spot weld joint by autotempering acceleration at heat affected zone, *Sci. Technol. Weld. Joining*, 2015, 20, 468-472.
- [34] W. Chuko and J. E. Gould: 'Development of appropriate resistance spot welding practice for transformation-hardened steels', U.S. Department of Energy, Report to the American Iron and Steel Institute, 2002.
- [35] H. Zhang and J. Senkara: 'Resistance welding: fundamentals and applications'; 2005, London, Taylor & Francis CRC Press.

Trends In Steel Usage In The Automotive Industry

Fatih HAYAT

Karabük University, Department of Metallurgy Materials Engineering, Karabük,
TURKEY, fhayat@karabuk.edu.tr

Abstract- In this study, used materials in the automobile industry and steel trend has been discussed. In addition, contributions to the country's economy and statistical information are presented. The material and engineering requirements used in the production of motor vehicles and automobiles are very different. The most important elements of security needs, CO₂ emissions and fuel savings need to be met in the best way. Other factors are comfort, manufacturability, cost, driving performance, fuel efficiency and weight. When all these factors are considered, the difficulties in automobile production and the diversity of materials attract attention. In recent years, it has been observed that the types of steel used in the production of vehicles in the world have changed, the demands of automotive manufacturers and the weight reduction efforts have accelerated. For this purpose, it might be an important objective to produce steel for the automotive industry that has come into prominence in our country with a high level of added value and income. Production of light and advanced high-strength steel for Turkish and World industries is a very critical technology.

Key words : Automotive, steel, advanced high strength steel, emission

1. Automotive Industry and its Importance

Motorized road vehicles are four or more wheeled vehicles that are driven by a combustible or explosive motor, carry goods or passengers, and are produced in accordance with certain technical regulations for driving in road traffic. The industry that produces these tools is called "Automotive Main Industry" [1]. Figure 1 shows the sectors related to the automotive industry.

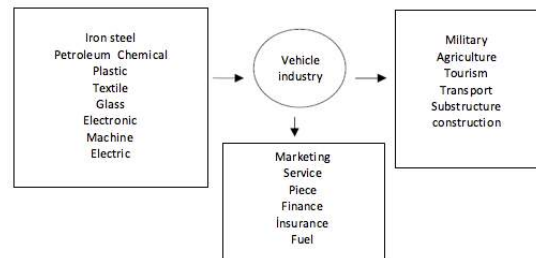


Figure 1. The sectors related to the automotive industry.

It is clear that all the developments and changes in the automotive sector affect other sectors as well. Today, the study of the developments in the automotive sector, which is at the heart of many countries' economies, is of great importance. Today, the automotive industry is a "key" sector for developed and developing countries. A strong automotive industry is striking

as one of the common characteristics of industrialized countries. The main reason of the automotive industry has such an importance is its close relationship with other sectors. The automotive sector benefits from many other industries such as iron and steel, glass, plastics, textiles, electronics and electricity sectors. In addition, the automotive sector provides efficient operation of some sectors with production. It is also known that the automotive sector contributes to construction, tourism and agriculture, the defense sector and also indirectly to the national security of the country.

1.1. Production In Turkey

Automotive main and sub-industry is one of the locomotive sectors of Turkish manufacturing industry today. Auto main and sub industry also constitute the infrastructure of defense industry and shipbuilding industry. Today, Turkey is the largest producer of light commercial vehicles in Europe and the second largest bus manufacturer. In the January-December period of 2016, Turkey ranked 6th in the list of European automotive sales [2]. In domestic automotive production, 12 main industrial firms operate in 18 factories. Of these 12 companies, only 4 are cars, 6 are only commercial vehicles (trucks, vans, minibuses, midibuses, tractors and buses), and 2 are automobiles and commercial vehicles.

According to the report of the Automotive Industrialists' Association; 2006-2016 total and automobile production growth (January-December) (x1000) [4].

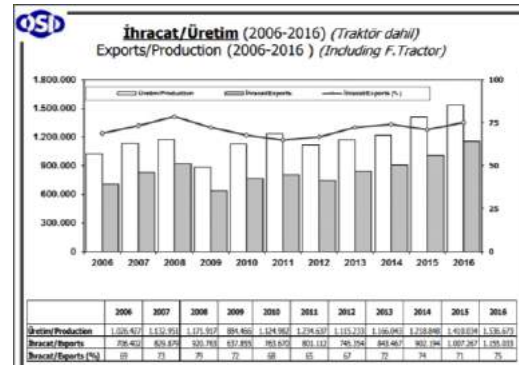


Figure 2. Number of vehicles produced in Turkey.

It is observed that vehicle production in our country has risen steadily and balancedly from 2006 onwards, but declines during crisis periods. It is reported that 1 million 537 thousand vehicles were produced in 2016. It has been reported that most of the vehicles produced are exported. It is similar in production to the world. According to the OECD (Organization for Economic Co-operation and Development) report, changes in the number of vehicles to be produced by 2020 are given in the world (Figure 3).

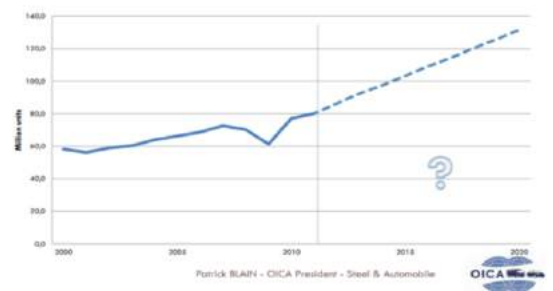


Figure 3. The change of vehicle production in the world between 2002-2020 [5].

According to the graph in Figure 3, it is stated that the vehicle production will reach a rapid increase until 2020. According to the report, it is predicted that there will be an increase in production in the world and the number of vehicles produced in 2020 will increase to over 120 million.

1.1. Required specification in Automotive

The most important things in the automotive industry for the advanced vehicle concept in production are given in Figure 4.



Figure 4. Features of a car [6].

As you can see from the graph, the features required from a car are primarily safety, fuel consumption, fuel efficiency and economics. In addition to the provision of these three basic elements from the other side, CO2 emissions have become important with the decisions taken in recent years. In addition, comfort, car weight, driving performance, cost / price relationship is important.

2. Materials used in automobile production

In all industrial areas where materials are used, producers desire to use materials that have superior mechanical properties, light weight, high strength, good shaping ability and good after-forming strength and suit to service conditions. In the automotive industry in recent years, it is desired to improve passenger safety, driving safety, fuel economy and mitigate the vehicles due to environmental factors [6]. Especially when energy and oil crises are experienced, this issue is at the forefront. The five most frequently used and indispensable materials in automobile production are; Steel, non-ferrous metals (aluminum, magnesium), plastic, glass, composite materials.

Approximately 20% of the world's carbon dioxide emissions come from automobiles. This ratio is expected to increase further in the coming years. The automotive sector is shown as responsible for 77% of the greenhouse gases that cause global warming. Therefore, in the European Union and the United States, there are legal regulations governing the reduction of carbon dioxide emissions by automobiles [7]. Figure 5 shows the rates of greenhouse gases emitted to nature during the production of materials used in automobiles.

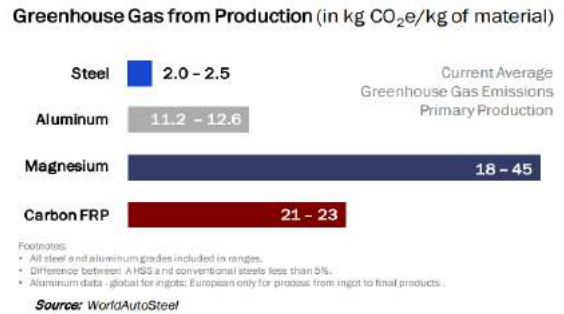


Figure 5. Greenhouse gas released to nature during the production of materials used in automobiles.

In the production process, aluminum and magnesium release about 5 to 20 times more CO₂ than the environment. In addition, Al and Mg are 3 to 10 times more expensive than steel alloys. In this frame, all the parameters are taken into consideration and given in Table 1 as a comparative example.

Table 1. Weight reduction and unit price comparison of materials [7].

HAFIF MALZEME	DEĞİSTİRİLEN MALZEME	ACIRLIKÇA AZALMASI %	FİYAT (PARÇA BAŞINA)
Yüksek Mukavemetli Çelik	Yumuşak Çelik	10-25	1
Alüminyum	Çelik,Dökme Demir	40-60	1.3-2
Magnezyum	Çelik,Dökme Demir	60-75	1.5-2.5
Magnezyum	Alüminyum	25-35	1-1.5
Cam,FRP,Kompozit	Çelik	25-35	1-1.5
Karbon,FRP,Kompozit	Çelik	50-60	2-10+
AL matris, Kompozit	Çelik veya Dökme Demir	50-65	1.5-3+
Titanyum	Alegimli Çelik	40-55	1.5-10+
Paslanmaz Çelik	Karbon Çeliği	20-45	1.2-1.7

According to this table, steel is the most cost-effective material per piece. Steel has long been the material of choice for automakers worldwide. The use of steel has allowed automobile manufacturers to achieve the desired standards of strength and safety for their vehicles at relatively low costs vis-a-vis other materials [8].

Greenhouse gas emissions should be reduced within the Paris Climate Summit (December 2015) agreement [9]. Our country has also ratified this agreement. Different sectors around the world are working to ensure a sustainable reduction in CO2 emissions. The automotive sector is taking more than that. The Ford Global reported forecasts of CO2 emissions from automobiles (Figure 6).

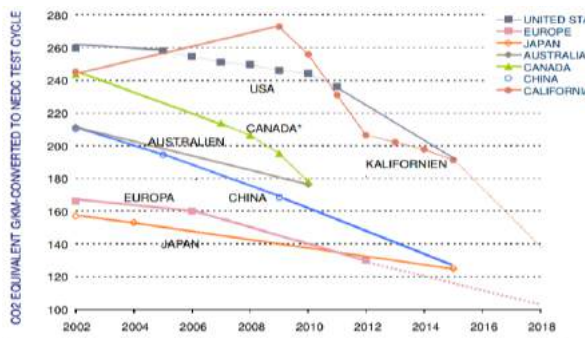


Figure 6. Estimated reduction in CO2 emissions.

Figure 6 shows the predictions of greenhouse gas emissions by vehicles in different countries until 2018, stating that emission values should be reduced rapidly in accordance with the decisions

taken. The gas emission in the USA is estimated to be 260 g in 2002 and 140 g in 2018. The OECD [5] reported that in 2020 these values would be 95 gr in Europe, 107 gr in China and 105 gr in the USA.

2.1. Types of Steel Used in Automotive Industry

Different types of steel are used in the automotive industry. Figure 7 gives the strength and% elongation ratios of steels used in automobile construction.

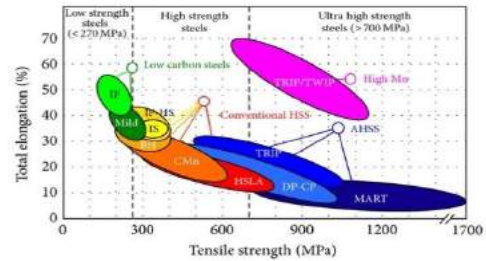


Figure 7. Schematic comparison of mechanical properties of conventional and advanced steel alloys. [10].

Reducing vehicle weight by using high strength steels;

In addition to reducing vehicle weight, at the present time the car body part of the vehicles is at least alleviated due to the increasing driving safety requirements and environmental factors. That is, the thickness of the sheets used in automobiles is gradually decreasing. However, the strength of these sheets is increasing to meet the security requirement. The most commonly used steels in the group of Advanced High Strength Steel (AHSS) used in weight saving operations are: Double-phase (DP), conversion-welded plasticity-winning (TRIP) and twinned plasticity-winning (TWIP) steels. The aim is to reduce the strength and performance of existing parts without lowering and even increasing them by using high strength steels in thinner sections and thicknesses.

Uses of high-strength steels in automobiles:

- Bumpers
- Impact Emitters
- Door Profiles
- A Pillar
- B Pillar
- C Pillar
- Ceiling Frames
- Door Strengths
- Door Mechanics
- Suspension Headgear

When the automotive producers and iron-steel producers are investigated, In the report of the AISI's steel development institute, AISI's Steel Market Development Institute (SMDI) reported that the use of AHSS steels between 2007 model and 2009 model vehicle increased from 10% to 15%. with an increase in the use rate of AHSS steel has been reported to reduce overall body weight by 70 kg.

In the Corus 2008 report it was reported that the weight of the car would be reduced by 60 kg by increasing the use of AHSS steel and that this weight saving could be increased to 100 kg by using more AHSS steel and that 1 ton of savings would be achieved during the use of each vehicle from CO2 emission [11]. The world's number one steelmaker, Arcelor Mittal, reported in its 2008 report that the use of ultra-light high strength steels reduced the weight by 50% in gas cylinders and by 40% in automobile parts, resulting in reduced gas emissions [12]. Arcelor Mittal reported that by intensifying work on advanced steels, it could replace conventional steels and produce 20% lighter vehicles [13].

In another study, Arcelor Auto reported that the weight reduction with the use of advanced steels in automobiles differs between the regions of

the car [13,14]. If an example is given from a region of the car; (TRIP, DP steel, etc.) in the backplane area reduced weight from 22 kg to 17 kg and saved 24% weight savings. At the front, the weight saving was reported to be 28%, while the rear and front doors reported a weight loss of 18%.

In the BMW-6 (2009 model) car series produced worldwide, the body structure and the AHSS steel ratio, including the main parts, have been increased to 32%. Other new models that use above average AHSS are Chevrolet Traverse, Ford F-150, Chrysler Town and Country [15]. In addition, Corus 2007 [16] reported that the Volvo C30 uses weight-saving, high-strength steel developed in door frames and white hulls, considering lateral loads, impacts.

For the first time in 2011, an iron-steel maker Posco produced a commercial TWIP steel sheet called "Dream Steel" [17]. At the Detroit Auto Show in 2016, Posco recommended TWIP steels for many products [18]. Posco's report states that by using TWIP steel in place of other steels in European vehicle tampons, a 28% weight saving and a 22% price saving will be achieved [19]. The FIAT company, the automobile manufacturer, reported that instead of the DP600 double-phase steel combined with the Boron steel in the Panda model, TWIP steel was used to achieve a weight gain of 0.88 kg (Figure 8).

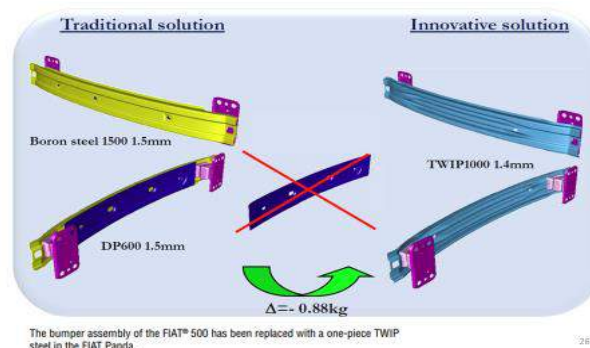
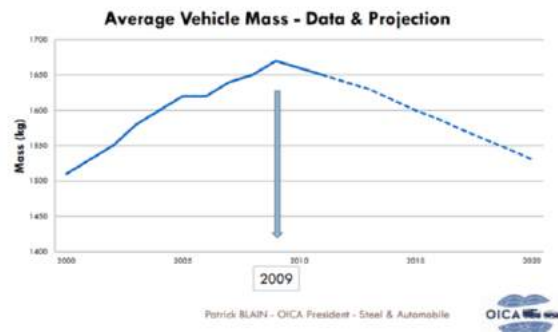


Figure 8. Saving weight from the use of TWIP steel [20]

TWINNING Induced Plasticity (TWIP) steels, which are the predecessors of high strength steels, have high strength values as well as high formability properties. Due to its mechanical properties it is an unrivaled steel, with high ductility and unrivaled steel type with an elongation value approaching 100%.

According to the OECD (Organization for Economic Co-Operation and Development) report, estimates of changes in vehicle weight have been given since 2009 (Figure 9).



Şekil 9. Change of vehicle weight between 2000 and 2020 [5].

The OECD report reports that the work of reducing vehicle weight is accelerating and producing lighter vehicles.

CONCLUSIONS

In recent years, emissions reduction and fuel saving efforts have accelerated. Energy crises and conservation efforts can be seen as the main causes, albeit for different reasons. Depending on this result, the pressure on the automotive producers is directly reflected in the steel producers. Steel producers are working to improve and improve the new steel they produce. The main objective was to produce steel with higher mechanical properties by reducing low quality steel products. For this reason, increasing interest in High, Advanced High and Ultra High Strength

steels pushed steel manufacturers to produce and develop these steels. The production of these steels in our country is very small, DP steel production is limited in our country, and TRIP and TWIP steels are not produced. Increasing the number of steel qualities produced in our country and making it compatible with the world automotive sector is essential. Automotive manufacturers' demand for advanced steels with high strength / ductility ratio is increasing day by day. This is because the first condition is the use of steel with higher strength and ductility as much as possible, while reducing the overall strength of the vehicle, even increasing it.

KAYNAKLAR

1. http://www.dtm.gov.tr/dtmadmin/upload/IHR/OtomotivElektrikDb/otomotiv_sektoru.doc
2. <http://www.odd.org.tr/folders/2837/categorial1docs/1764/ODD%20Sekt%C3%B6rel%20De%C4%9Feriendirme%20Ocak'2017.pdf>
3. http://osd.org.tr/Sites/1/upload/files/Otomotiv_Sektor_Raporu_TSKB-2208.pdf
4. http://www.osd.org.tr/sites/1/upload/files/2016-12_OSD_RAPOR_SB_1-2203.pdf
5. <https://www.oecd.org/industry/ind/50498824.pdf> (May 31st 2012)
6. SSAB Swedish Steel, "Higher Strength-Lower Weight: Educating the Body Weighty Using Extra and Ultra High Strength Steel", GB 2000 Lygner Form& Tryck 2004
7. <http://analizsimulasyon.com/2016/05/10/otomotiv-yuksekk-mukavemetli-celiklerin-kullanimi/>
8. <https://www.forbes.com/sites/greatspeculations/2015/05/20/trends-in-steel-usage-in-the-automotive-industry/#6278f45f1476>
9. The Paris Protocol – A blueprint for tackling global climate change beyond 2020,30 Kasım- 11 Aralık 2015, Paris, Fransa. İnternet adresi: http://ec.europa.eu/priorities/energy-union/docs/paris_en.pdf., Son erişim tarihi: 20/12/2015. - See more at: <http://www.makinatek.com.tr/arsiv/yazi/161-otomotiv-endustrisinde-twip-celiklerin-gelecegi#sthash.L69Httv0.dpuf>
10. <http://gooa.las.ac.cn/external/share/1239879>
11. "Environmental Case Study Automotive: an Advanced High-Strength Steel Family Car", World Steel Association, 2006. (www.worldsteel.org).
12. Corus Research, Dev.&Technology, Corporate Responsibility Report 2007/08.
13. ArcelorMittal, "How Will We Achieve: Safe Sustainable Steel?", Corporate Responsibility Report, 2008.

14. Flat Carbon Europe, "Client Magazine", ArcelorMittal, September, 2007. (www.arcelormittal.com/fce/repository/Update/EN_UpdateFCE_aug07.pdf)
15. "New Study Finds Increased Use of Advanced High-Strength Steels Helps Decrease Overall Vehicle Weight", Automotive Applications Council, 2010. (http://www.steel.org/AM/Template.cfm?Section=Press_Releases9&TEMPLATE=/CM/ContentDisplay.cfm&CONTENTID=32077)
16. "Arcelor Body Concept", Arcelor Auto, Arcelor Group.
17. <http://globalblog.posco.com/posco-announces-new-steel-sheets-at-detroit-motor-show/>
18. <http://globalblog.posco.com/tag/twip/>
19. http://309fbf2c62e8221fbaf0-b80c17cbaf20104b072d586b316c6210.r88.cf1.rackcdn.com/Gangzhao%20Presentations/09_China%20Automotive%20Steel%20Conference_POSCO_Ja-e-Bok%20Nam.pdf
20. <http://www.autosteel.org/~media/Files/Autosteel/Great%20Designs%20in%20Steel/GDIS%202013/On%20the%20Role%20of%20Body-in-White%20Weight%20Reduction%20in%20the%20Attainment%20of%20the%20US%20EPANHTSA%20Fuel%20Economy%20Mandate.pdf>

Bainitic Rail Steel Production from Perlitic Rails In Eutectoid Alloy And Investigation Of Wear Behaviour

Harun ÇUĞ^a, Hayrettin AHLATCI^b, Derya BULGAN^c and Mustafa DÖNMEZ^c

^a Karabük University, Faculty of Engineering, Mechanical Engineering, e-mail: hcug@karabuk.edu.tr

^b Karabük University, Faculty of Engineering, Metallurgy and Materials Engineering, e-mail: hahlatci@karabuk.edu.tr

^c Karabük University, Faculty of Engineering, Railway Systems Engineering, e-mail: deryahira25@gmail.com, musttaaffaa@gmail.com

ABSTRACT

While rail steels are being developed, the main objective is to improve wear performance. For this purpose we are continuing to work harder on the production of rail steel. However, a certain degree of hardness can be obtained by conventional methods. Bainitic microstructural rail steels can achieve higher hardness than conventional perlitic rail steels. In this study, it has been tried to obtain a bainitic structure with isothermal transformation to this steel with hardened rayon steel of eutectoid alloy. Two different austenite temperatures (850°C and 900°C) and two different bainitic transformation temperatures (350°C and 450°C) were determined. Abrasive abrasion tests have shown that the specimen with a bryitic structure at 350°C was annealed at 900°C compared to perlitic rayon steel, resulting in higher wear resistance.

Key words: Perlitic and bainitic rail steel, Eutectiod alloy, heat treatment.

Investigation of the Effect of Vanadium Addition and Cycling Heat Treatment on Mechanical Properties and Wear Behaviors of Casting Steel

Harun ÇUĞ^a, Hayrettin AHLATCI^b and Ercan CANDAN^c

^a Karabük University, Faculty of Engineering, Mechanical Engineering, e-mail: hcug@karabuk.edu.tr

^b Karabük University, Faculty of Engineering, Metallurgy and Materials Engineering, e-mail: hahlatci@karabuk.edu.tr

^c Bilecik Şeyh Edebali University, Engineering Faculty And Manufacturing Engineering Department e-mail: e.candan@yahoo.com

ABSTRACT

Train wheels are manufactured by forging and casting method. Cast iron wheels have advantages in terms of cost. When vanadium element is added to the steel, it has mechanical properties enhancing properties. Repetitive heat treatment contributes to the breakdown of the carbides in the grain boundaries and an increase in strength can be observed at this point. In this study, microstructure, mechanical properties and wear behaviors of train wheel steel produced by casting method under laboratory conditions with a train wheel obtained by forging method were investigated.

Key words: Train wheel, casting, heat treatment, wear.

The Flash Butt Welding Application and Inspection in Railway in Karabuk Train Station

Mustafa Dursunlar, Harun ÇUĞ
Karabuk University, TURKEY
mustafadursunlar@gmail.com

ABSTRACT

Welding is made up of many scientific and technical works. In industrial applications, it is applied to increase work efficiency and safety, reduce size and weight, and reduce production cost. Welding in the railway is usually done at the joints of the rails. Rail junctions have caused serious problems since the early days of railroads. As a solution, durable algebras have been developed but not sufficient in this application. As a result, the request for removal of the rail joints has emerged. Accordingly, different welding techniques have been developed. Among these techniques, aluminothermite and combustion head are widely used today. In this study, ultrasonic inspection results of the incinerator application applied to the rails in Karabük train station are examined.

Keywords: Railway, rail welding, flash butt welding

Climate Change Effect by Road Transportation in Karabük Province

Ali CAN

Karabük University, Faculty of Engineering, Mechanical Engineering Department 78050, Karabük, Turkey
alican@karabuk.edu.tr

Abstract—Anthropogenic air pollution is increasing in the earth. And highest portion of the anthropogenic air emission is caused by energy consumption. The biggest section of the energy consumption in the transport sector is originated from the road transportation. Therefore, the road transportation is highly emitting direct and indirect GHGs caused by gasoline, diesel and LPG consumption on the roads. This sector is needed to be examined in detail for climate change studies. The uncertainties in road transportation emission calculations are very high, because the other sources emissions, meteorological conditions, vehicle using behaviour and age of vehicles have some pressures on the emissions.

Direct greenhouse gases, including CO₂, N₂O and CH₄, emitted by the road vehicles are the key sectors for Turkey. In long-term struggle with climate change, Turkey should reduce emissions from this sector. Therefore, the studies related to the emission control on road transportation are supporting climate change mitigation.

In this study, the direct GHGs emissions from the road vehicles in Karabük province have been calculated and the effect on the climate change is considered. The IPCC methodology was used for calculating the emissions. The vehicles were classified in different categories and the CO₂, N₂O and CH₄ emissions were calculated as time series for each category. The road vehicle statistics of Karabük province were obtained from TURKSTAT and the total fuel consumption was estimated due to the average km covered by vehicles and total consumption of fuels taken from the energy balance tables.

The final results are showing that the diesel consumption on the road is increasing CO₂ equivalent (CO₂ equ.) emission until the 0.22 million tonnes in 2014. It is just 0.5% of total Turkey's road emission. Moreover, the gasoline consumption in the city is remaining constant although the number of automobile is increasing in the city. The main reason is the people living in the city prefer diesel or LPG automobiles. Consequently, the emission related to the diesel vehicle is highest and it is concluded that 75% of total CO₂ equ. emission from road vehicles in Karabük province is coming from the diesel vehicle. The GHGs emissions caused by automobiles, van and caterpillar are causing highest pollution in Karabük province. The CO₂ equ. emissions from these three type vehicles are 83% of total city's road emissions.

Keywords—Climate Change, Direct Greenhouse Gases, CO₂ equivalent, CH₄ and N₂O emissions, IPCC Methodology

I. INTRODUCTION

The GHGs' emissions to the atmosphere have been increasing considerably according to the scientific studies [1]. And the most of the scenarios are also showing that the emission will continue to increase due to the high rate consumption of fuels [2]. In Paris Agreement, the parties reached a landmark agreement to combat climate change and to accelerate and intensify the actions. The investments are needed for a sustainable low carbon future of the earth [1]. One of the main reasons of the global Climate Change problem is the transportation. Approximately, 25 % of climate change problem is due to the consumption of fuels in the transportation sector. And the big portion of emission is coming from the road transportation. However, the improved technologies were used in new generation cars in order to decrease the emission. Although, technological improvement has shown that the CO₂ emissions will be tightened and decreased until 95 g CO₂/km until 2020, the road transportation will still be considered as one main GHGs source [3].

The climate change studies are considered as important for Turkey as being one of the Annex (I) countries of UNFCCC and Kyoto Protocol. The GHGs emissions are increasing in earth. The percentage of road transportation is around 18% throughout the years. According to the TurkStat statistical data [4], the number of road vehicles is increased to 19 million in 2014 and the CO₂ equ. emission from road vehicles was around 67 million tonnes CO₂ equ. emission which is corresponding to 90% of total transport CO₂ equ. emission.

For this study, the Karabük province, one of the industrial cities of Turkey, has been studied to determine the direct GHGs emission from road transportation due to different type of vehicles, and it was compared with Turkish National Emission Inventory [5]. The time series vehicles data for the years between 2004 and 2014 was gathered from transport statistics produced by TurkStat and energy balance tables produced by MENR [6]. In this study, the main aim is to investigate the climate change problem which is caused by road transportation in province Karabük.

The IPCC [7; 8] emission factors (EF) for different types of fuels for the direct greenhouse gases are given below Tables 2, 3 and 4.

II. METHODOLOGY

The CO₂, CH₄ and N₂O emissions estimation process is divided into two steps that lead to figures for CO₂ and non-CO₂ emissions from fuel consumption according to the (IPCC - Tier 1) methodology. The general formula (1) for the CO₂ emission is given as [7; 8].

$$CO_2 \text{ Emiss.} = \sum (U_n + I_n - H_n - IB \pm SC) * EF * CF * E * C - CO_2 \quad (1)$$

- U_n : The fuel production quantity
- I_n : Imported fuel quantity
- H_n : Exported fuel quantity
- IB : International Bunkers
- SC : Stock changes
- CF : Conversion Factor
- N : Fuel type
- EF : Emission Factor
- E : Efficiency (99%)
- C-CO₂ : Carbon to CO₂ emission

And the general formula (2) for the CH₄ and N₂O emissions is given by IPCC Guidelines [7; 8].

$$Non-CO_2 \text{ Emiss.} = \sum (U_n + I_n - H_n - IB \pm SC) * EF * CF \quad (2)$$

For the GHGs emission calculations, the following steps are considered:

- a) The energy units are converted into Net Calorific Values (NCV).
- b) The fuel data consumption of road vehicles in Karabük province is estimated according to the Can [9] studies. Total and province base data (household numbers, car numbers and consumption of fuels) are used for calculating emission.
- c) The number of road vehicles and transport distance per year (km/year) for each type of vehicles was used for estimating consumed fuel data in province basis. The following table was estimated by using for sale car's age and mileage in internet (Table 1).

Table 1. Average mileage of road vehicles per year

Vehicles type	Average mileage per year (km/year)
Otomobile	10000
Minibus	20000
Bus	60000
Van	20000
Truck	40000
Motorcycle	4000
Caterpillar	1500
Special Purpose	2000

Table 2. CO₂ Emission Factors

Fuel Types	CO ₂		
	EF	Efficiency	C-CO ₂
	Unit: tC/TJ		
Diesel Oil	20.2	0.99	3.6666667
Gasoline	18.9	0.99	3.6666667
LPG	17.2	0.99	3.6666667

Table 3. CH₄ Emission Factors

Fuel Types	Transport
	EF (Kg/TJ)
Diesel	5
Gasoline	20
LPG	50

Table 4. N₂O Factors

Fuel Types	Transport
	EF (Kg/TJ)
Diesel	0.6
Gasoline	0.6
LPG	0.1

III. RESULT AND DISCUSSION

The CO₂ emission from diesel-oil consumption in Turkey is around 32.18 million tonnes in 2014. It is different than Turkish official (TurkStat) emission inventory (EI) value. Approximately 0.5% of this emission is contributed by province Karabük with a value of 0.17 million tonnes CO₂. For the same year, the CO₂ emission from gasoline consumption by road vehicles is 5.7 million tonnes in Turkey and the value is around 0.035 million tonnes in Karabük with a 0.6% of total CO₂ emission. In Karabük, entire LPG was used by automobiles. The CO₂ emission from LPG is 0.021 million tonnes with an 0.027% of total Turkey's emission which is 7.74 million tonnes.

The following annual CO₂, CH₄ and N₂O emissions from road vehicles in Karabük province are given in Table 5 as time series. The GHGs emissions are increasing throughout the years as seen in table 5.

Table 5. The GHGs emissions from road vehicles in Karabük province (unit:kt)

Emission	2004	2005	2006	2007	2008	2009	2010	2011	2012	2013	2014
CO ₂	119.30	129.65	141.58	151.91	159.83	167.80	176.45	186.92	197.89	209.79	220.59
CH ₄	0.0140	0.0164	0.0182	0.0201	0.0220	0.0239	0.0258	0.0278	0.0297	0.0320	0.0338
N ₂ O	0.0008	0.0009	0.0010	0.0011	0.0011	0.0012	0.0012	0.0013	0.0014	0.0015	0.0016

Table 6. The road vehicles distribution rates according to the fuel type in Karabük province

Fuel type	2004	2005	2006	2007	2008	2009	2010	2011	2012	2013	2014
Gasoline	0.37	0.34	0.34	0.32	0.31	0.30	0.28	0.27	0.25	0.25	0.24
Diesel	0.58	0.59	0.59	0.59	0.60	0.59	0.60	0.61	0.62	0.62	0.62
LPG	0.05	0.07	0.08	0.08	0.10	0.11	0.12	0.13	0.13	0.14	0.14

The contributions of Karabük province to the CH₄ emission in unit thousand tonnes are 0.011 from diesel-oil, 0.006 from gasoline and 0.017 from LPG. For Karabük, the respective N₂O emission values for diesel-oil, gasoline and LPG are 1.35, 0.17 and 0.03 tonnes in 2014. The total CO₂ equivalent (CO₂ eq.) emissions of direct GHGs are given in the following Figure 1. In Figure 1, the total CO₂ eq. emission calculated by Turkstat has showing some fluctuations due to the methodological changes after year 2011 [8].

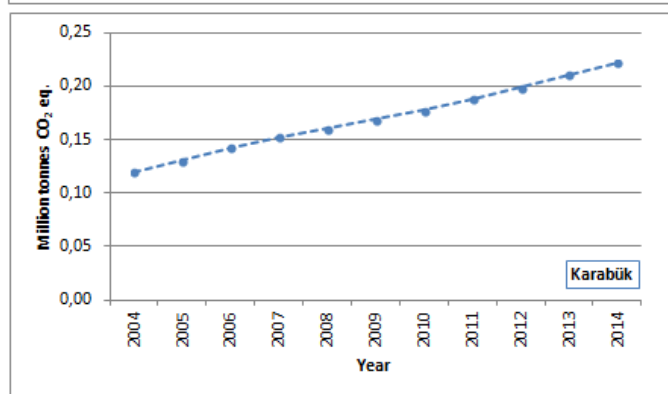
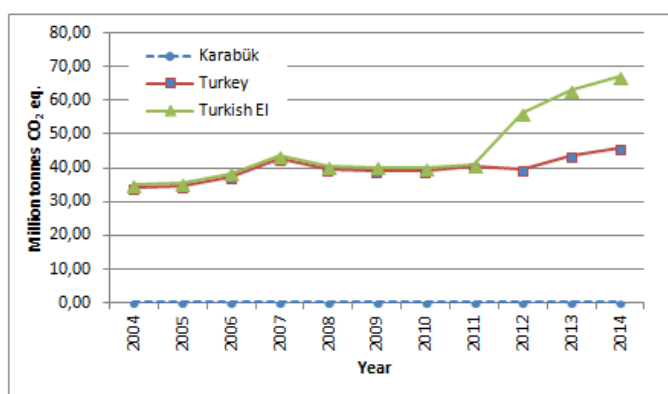


Fig. 1 The contribution of Karabük province to GHGs emissions from road transportation

In Turkish National Emission Inventory prepared by TurkStat is showing some fluctuations on the figure after year 2011. The main reason is changing EF made by Ministry of Transport, Maritime Affairs and Communications.

For province Karabük, the CO₂ eq. emission trend is increasing steadily for the period 2004 and 2014. Although, the numbers of road vehicles are increased 83% during this time, the technological improvement has also causing a stable emission trend. The road vehicles distribution according to the fuel type was given on the Table 6. The data are gathered from TurkStat.

The people living in the city prefer diesel or LPG automobiles. Therefore, the increasing diesel consumption is causing an increasing emission trend until year 2014 and reaching the 0.165 million tonnes CO₂ eq. emission value. The total CO₂ equivalent emission according to the fuel type in Karabük Province (Figure 1 and Figure 2) is showing that the GHGs emission is parallel to the diesel consumption in Karabük province. In figure 2, the total CO₂ eq. emission from gasoline is not showing any trend between year 2004 and 2014. However, the LPG consumption on the roads is slightly

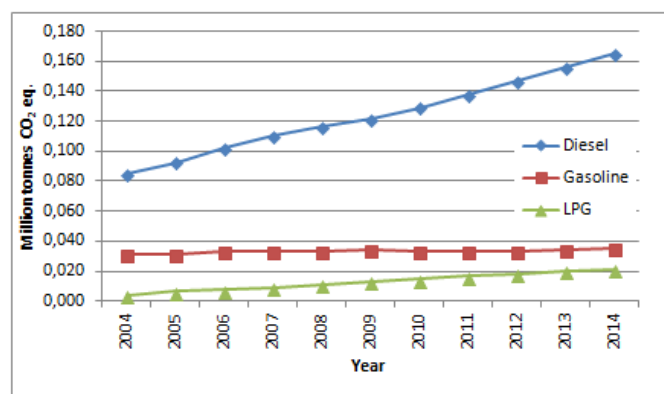


Fig. 2 The total CO₂ eq. emissions according to the fuel type in road transportation

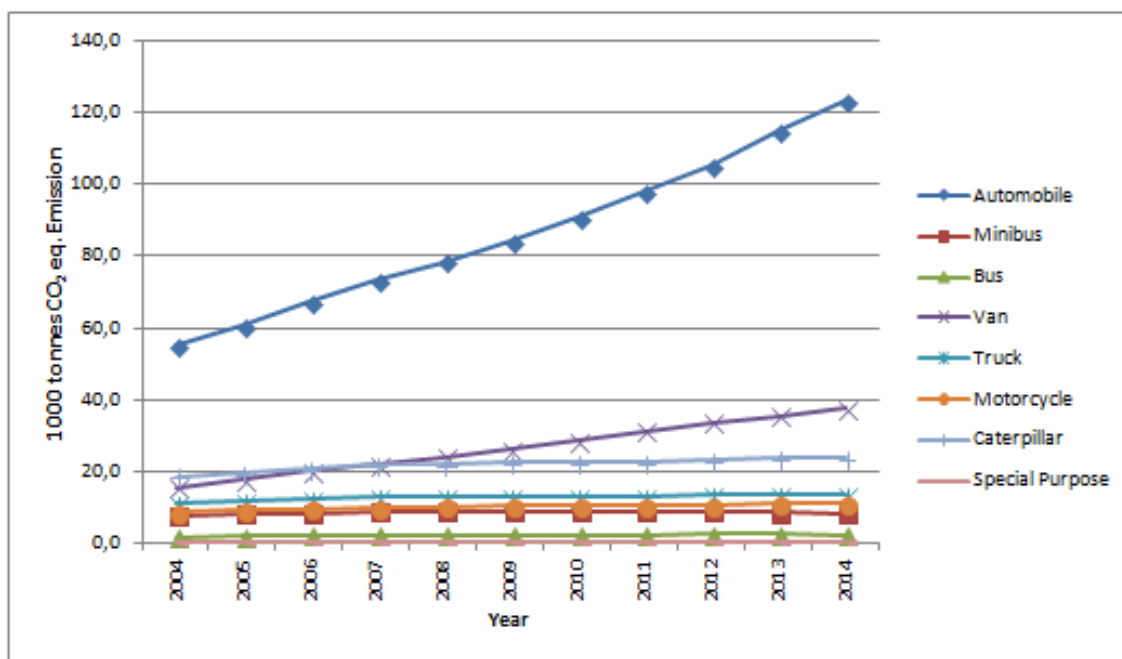


Fig. 3 The total CO₂ eq. emissions caused by vehicle type in Karabük province

increasing. Related to the LPG consumption, the emission trend is also showing increasing trend for diesel and LPG. However, the CO₂ eq. emission from gasoline is constant for years with an average value of 0.033 million tonnes.

The highest CO₂ eq. emission was created by automobiles in Karabük Province. The average value is around 0.08 million tonnes CO₂ eq. emission (Figure 3). Following automobiles, the vans and caterpillars in Karabük province are emitting highest with values of 0.037 and 0.024 million tonnes CO₂ eq. emission, respectively.

According to these analyses; the emissions caused by automobiles, van and caterpillar are key factors in Karabük province. The CO₂ eq. emissions from these three type vehicles are 83% of total city's road emissions.

IV. CONCLUSION

During the study period, the gasoline consumption by road vehicles is staying constant; however, the diesel-oil consumption is considerably increasing in Karabük province. The emissions caused by automobiles, van and caterpillar are key factors in Karabük province. The CO₂ eq. emissions from these three type vehicles are 83% of total city's road emissions. The average CO₂ eq. emission from road transportation is 0.22 million tonnes for study period. This average value is approximately 0.5% of Turkey's road GHGs emissions as in unit CO₂ eq.

REFERENCES

- [1] UNFCCC – United Nations Framework Convention on Climate Change web page: https://unfccc.int/national_reports/annex_i_ghg_inventories/national_inventories_submissions/items/9492.php date:10.09.2016.
- [2] IPCC, 2013. Climate Change 2013: The Physical Science Basis, Working Group I contribution to the Fifth Assessment Report of the Intergovernmental Panel on Climate Change, Cambridge University Press. www.ipcc.ch/report/ar5/. Date: 17.09.2016.
- [3] EEA - Towards a resource-efficient transport system - TERM 2009: indicators tracking transport and environment in the European Union. P.14-17.
- [4] TurkStat, - TÜİK - Transportation Statistics Databases (2004-2014). <http://tuikapp.tuik.gov.tr> date:09.08.2016.
- [5] TurkStat, National Greenhouse Gas Inventory Report, 1990-2014. Annual Report submission under the "Framework Convention on Climate Change", 2014.
- [6] MENR, The annual Energy and Petroleum Balance Sheets 1970-2014, Ministry of Energy and Natural Resources, 2014.
- [7] IPCC Greenhouse Gas Inventory Reference Manual – Revised 1996 IPCC Guidelines for National Greenhouse Gas Inventories – Volume 3 – Intergovernmental Panel on Climate Change – Edited by Houghton J.T., et al., 1996.
- [8] IPCC Greenhouse Gas Inventory Reference Manual – IPCC Guidelines for National Greenhouse Gas Inventories - Intergovernmental Panel on Climate Change, 2006.
- [9] Can A., 2006. Investigation of Turkey's Carbon Dioxide Problem by Numerical Modeling. (Ph.D.Thesis) – METU.

The Integration of Plate Heat Exchangers to Heating System in an Iron & Steel Plant

Murat Demirhan¹, Mehmet Özalp², Mutlucan Bayat²

1. ASELSAN, TURKEY

2. Karabuk University, TURKEY

muratdemirhan@gmail.com

ABSTRACT

In this study, an analysis has been performed to increase the energy efficiency of existing natural gas boilers which have been adapted to a heating system. For this analysis, it has been investigated to what extent the plate heat exchangers can be used to reduce the adverse effects of water in the system and to make the working regime more uniform than the existing conditions. The system consists of 3 natural gas boilers, circulation pumps and other boiler equipment in the old case and it is necessary to heat 500 tons of water in a single cycle. Because of the use of well water, limestone formation is observed in the boiler and other equipment, and the capacity of the reverse osmosis system that treats the reduced water is not enough to reduce the water hardness. In order to overcome these problems in the system, it has been considered to separate the suction and discharge lines and create a new cycle with 2 plate exchangers and additional pumps. Therefore, this new system which has a lower mass ratio is fed with soft and purified water coming from the treatment system to prevent the formation of limestone and consequently the decrease of the lifecycle. As a result of the cost analysis of the new system formed by the plate heat exchangers, the payback period of 6 months has been determined with some acceptances.

Keywords: Plate heat exchangers, energy saving, energy efficiency, payback period, Iron&Steel plant

Solution Casting Polyvinyl alcohol (PVA) Functionalization Graphene Nanocomposites

Kamal Yusoh¹, Zulhelmi Ismail², Abu Hannifa Abdullah¹, Anis Sakinah Zainal Abidin¹

¹Faculty of Chemical Engineering and Natural Resources, Universiti Malaysia Pahang, Lebuhraya Tun Razak, 26300 Gambang, Pahang, MALAYSIA

²Faculty of Manufacturing Engineering, Universiti Malaysia Pahang, 26000 Pekan, Pahang, MALAYSIA
Email: *kamal@ump.edu.my*

Abstract

Graphene materials have attracted enormous academics and industries to explore due to its outstanding thermal and mechanical properties. In this work, the solution-casted polyvinyl alcohol (PVA) film reinforced with shear exfoliated graphene and its properties such as hardness and mechanical behaviour were studied. The compatibility between graphene and PVA was enhanced by the functionalization of graphene with gum Arabic. The decoration of OH groups on graphene allowed better interfacial interactions with PVA through H-bonding chains. As been observed during morphological study by scanning electron microscopy (SEM) and x-ray diffraction (XRD), agglomeration of graphene sheets was detected at highest graphene loading (0.15 wt.%). Improvement of mechanical properties was observed by nanoindentation for sample with lowest graphene contents (0.05 wt.%). The enhancement of nanoindentation modulus sample was contributed by homogenously distributed graphene in the matrix of PVA.

PANEL SPEECHES

SPEECH OF ERCÜMENT ÜNAL

(General Manager of KARDEMİR A.Ş)

İlk olarak " 1995 yılında çelik sektöründe göreve başladığımda sektörün geleceğine ilişkin projeksiyonların yapıldığı bir birimde çalıştım. Mühendislikten direktörlüğe kadar bu görevlerde bulundum. Burada geçmişteki 3-5 yıllık verilere göre projeksiyonlar yapardık. Kullandığımız datalar ile tahmin ettiğimiz sonuçları, gerçekleşen ile kıyasladığımızda % 98,5'lara ulaşan tahminlerimiz ve fiyat projeksiyonlarımız olurdu. 2015 yılından itibaren piyasalar değişti. Eskiden sektör 3 yıl iyi gider 1 yıl dip yapardı. Sonra tekrar toparlanırdı. Bunu bizler çok iyi tahmin edebilirdik. Global çelik endüstrisinde şu an kapasite fazlalığı nedeniyle arz talep dengesinde 2015'den bu yana sıkıntı yaşıyor. Bu sıkıntının temel sebebi Çin'deki kapasite fazlalığıdır. Çin'deki tesislerin devlet destekleri ile zararına da olsa mal satması fiyatları aşağı çekti. Türkiye'nin ciddi pazarları arasında yer alan Ortadoğu bölgesindeki karışıklıklarda pazar kayıplarına neden oldu.

Geçmişte 3-5 yıllık, hatta 10 yıllık verilere göre yaptığımız tahminler de artık 3 aya inmiş durumda. Eskiden 3 yılda yaşadıklarımızı 3 ay içerisinde yaşar hale geldik. Örneğin bundan iki ay önce hurda fiyatları 300 \$'dı. Sonrasında bir panikle 260 \$ mertebesine düştü ve kısa bir süre sonra yeni bir hareketle tekrar 300 \$'a çıktı. Şimdilerde tekrar indi. Oysa eskiden sağlıklı bir şekilde yükselir ve düşüş gösterirdi. Şimdi ise talep ve mamul fiyatları girdi fiyatlarını destelemiyor ve fiyatlar geri kırılıyor. Sektör kendi yönünü belirleyemiyor.

2015 ve 2016 yılında Çin'in Türkiye'ye, Avrupa'ya ve Amerika'ya ciddi tehditleri sebebiyle Çin'e büyük oranda vergiler kondu. Baktığımız zaman bu vergiler Çin için önemli olmadı çünkü, devlet desteği ile önemli oranda çelik satışlarını sürdürdüler. Örneğin referans bir sayı olarak 400 \$ olan bir malı Çin, üzerine navlunu da ödeyerek Türkiye'ye 350 \$ a getirebildi. Oysa ki bu malın global girdi maliyeti zaten 350 \$. Devlet desteklerini ve koruma duvarlarını dikkate aldığımızda Amerika'da ciddi vergiler var. Türkiye'deki üreticiler maliyetlerini düşürüp Amerika'ya mal sattığında hemen bir dumping soruşturması açılıyor.

Şu andaki çelik kapasitesinin % 50'sini üreten ve dünya ya ihracat yapan Çin, son 3-4 aydır politikasını değiştirerek ihracatını kesti. Şimdiki sıkıntımız ise gelişmekte olan ülkelerdeki talebin zayıflaması oldu. Ortadoğu'da bir hareket yok. Avrupa'ya gidiyorsunuz otomotiv sektörü dışında inşaat sektörü yok. Büyümeler % 2- 2,5 seviyelerin üstünde değil. Bakıldığında Çin ve ABD'nin ayrıışmış olmasına rağmen talepte ciddi sıkıntılar var. Talepteki sıkıntılara rağmen fiyatlar aşağı doğru hareket etmiyor, fiyatlar sabit ama yönü belirsiz.

Türkiye'de 50 milyon tonun üzerinde çelik üretim kapasitesi var. Geçen yıl ise fiili üretim 33,5 Milyon ton seviyesinde oldu. Yani kapasitelerimizin önemli bir kısmı atıl kaldı. Burada nihai ürün tüketimini artırmak için politikalar geliştirmeliyiz. Bir taraftan atıl kapasitelerimizi kullanamıyoruz, diğer yandan ise ihraç ettiğimiz kadar çeliği ithal ediyoruz.

Çok hızlı gelişen ve küresel gelişmelere karşı çok duyarlı bir sektörün içerisindeyiz. Ülkemiz çelik sektörü ufak bir daralma ile ya hasta oluyor ya da grip. Oysa yaşanan gelişmelerden Çin ayrıışıyor, ABD ayrıışıyor.

Ancak ülkemizde, yaşanan gelişmeler karşısında aksiyon almak için gecikiyoruz ve bu zaman kaybı da sektöre rekabetçiliğini kaybettiriyor"

SPEECH OF UĞUR DALBELER
(General Director of Çolakoğlu Metalurji)

Öncelikle herkese iyi günler. Karabük'ün Kardemir'in 80.yaşını kutlayarak başlamak istiyorum. Böyle özel bir günde de beni aranızda davet etmiş olmanızdan dolayı ayrıca teşekkür ediyorum. Önce kendimi tanıtayım. İsmim Uğur DALBELER. 1986 Orta Doğu Teknik Üniversitesinden Metalurji Mühendisi olarak mezun oldum. Diplomamı aldıktan 1 ay sonra başladığım şirkette hala devam ediyorum. Çeşitli kademelerde değişik sorumluluklar aldıktan sonra 2005 yılından bu yana şirketin genel müdürü olarak görevi sürdürmeye çalışıyorum. Anlayacağınız 30 yıl içerisinde bu sektörün nasıl değiştiğine, nasıl geliştiğine bizzat şahit oldum. İlk başlarda sürekli zarar eden tamamen politikaya batmış verimsiz devlet kontrolü altında fabrikalar, diğer yanda da henüz emeklemekte olan yeteri kadar sermaye biriktirememiş bir özel sektör vardı. Ama bugün geldiğimiz noktada gerçekten sektör öyle bir aşama kaydetti ki bugün dünyada çelik ile ilgili her yıl toplantı olsa, her yıl konferans yapılırsa adı geçen 5 ülkeden biri Türkiye'dir. Dünyanın 8. Büyük üreticisi konumuna ulaştık. Dünyanın en büyük 7. ihracatçısı olduk. Bu tabii gurur verici. Bu performansın arkasında birçok sebep var ama bana göre en büyüğü sahip olduğu insan gücüdür. Zira bu ülkede gerçekten özverili, çalışkan, ciddi bir birikim mevcuttur. Ama öncelikle, aslında en büyüğü bu işe kendini, hayatını vakfetmiş girişimcilerdir. En büyük örneklerinden biri KARDEMİR'dir. Bundan yıllar önce kapatılmasına karar verilmiş artık tamamen umudu kesilmiş bir tesisin bütün olanaksızlıklarına bakmadan devralan ve bu süreçte büyütüp misliyle katlayarak, bugünlere getiren bir girişimci grubudur. Bu insanlar bu işi sadece parayla yapmadılar. Bu işin arkasında ciddi bir gönül birliği, gönül bağlılığı var. Diğer yandan, o dönemde çok küçük haddehaneleri bugün dünya ölçeğinde, çok ciddi çelik devlerine dönüştürmüş bir özel girişimci grubu var. Ve bunları yaparken de, nerdeyse 15 yıldır en ufak bir teşvikten, en ufak bir devlet yardımından da yararlanmadan tamamen kendi kaynakları ile sektörü bu duruma getirdiler. Ercüment Bey biraz bahsetti. Sektör bu gelişme içerisinde son 3 senedir maalesef biraz sıkıntılar yaşıyor. Ve ciddi de bir küçülme yaşadı. Fakat 2016 yılı ile birlikte tekrar açıkçası büyüme trendine girdik. 2004 ile 2008 arasında birçok sebepten ötürü, Çin'in yaratmış olduğu talep, petrol fiyatlarındaki artıştan dolayı, dünyada yaşanan büyümeyle birlikte çelik talebinde ciddi bir patlama yaşadık. Ve o güne kadar 200 dolar mertebelerinde olan çeliğin ton fiyatı, bir anda 1500 dolarları buldu. Fakat 2008 sonrası global krizin ardından bir anda bu 1500 dolarlar tekrar 300 dolarlara geriledi. Tabii böyle şokları kaldırmak pek kolay değil. Sektörde bundan ciddi anlamda etkilendi. Bazı ülkeler bu dönemde sektörleri destekleyebilmek için direk teşvikler verdiler. Bazıları ise kendi sektörlerini dışarıya karşı koruma altına alarak indirekt olarak desteklediler. Bir de bunun üzerine son

dönemde yaşamış olduğumuz, coğrafyadaki, politik çalkantılar savaşlar vs. sebeplerle çelik sektörü oldukça zor bir dönemden geçti. Örnek vermek gerekirse, biz 2013 yılında, 4 milyon tonluk bir satışa ulaşmışken geçen sene ancak bunun % 60 'ını gerçekleştirebildik. Fakat tekrar bir olumlu havaya girdiğimizi düşünüyoruz. İşte Ercüment Bey biraz bahsetti. Çinlilerin içerisindeki politika değişikliği, kendi iç tüketimlerini arttırmaya yönelik, almış oldukları bir takım kararlar ile dünya piyasalarından o fazla arzı göreceli olarak şu an için çekmeleri ile bir denge oluştuğunu söyleyebiliriz. İşte bütün bu gelişmeler yaşanırken benim üzerinde durmak istediğim asıl konu bizim kendi içimizde sektöre yönelik ortaya çıkan tartışmalar. Önce sektörün dışa bağımlılığı, gündeme geldi. Ardından aslında çok da fazla katma değer yaratamadığı tartışılmaya başlandı. Aslında çok fazla istihdam sahibi olmadığımız kalitesinin dünya ölçeğinde yeteri kadar yer bulamadığı çevreye olan zarar vs. gibi gündemleri tartıştık biz aslında gelişmek veya ilerlemek için neler yapılması gerektiği konusunu araştırmak varken bunları düşünüp çok fazla zaman harcadık. O yüzden ben biraz bu konulara, açıklık getirmek istiyorum. Şimdi hep katma değerden bahsediliyor. Katma değer düşük olduğundan bahsediliyor. Ben de ısrarla aynı şeyi vurguluyorum. Çelik sanayinin temel girdisidir. Yaşamın her alanında, çelik olmazsa olmaz. Yani artık vücudumuzun bir parçası haline dönüştü. O yüzden biz sektör olarak aslında katma değeri yaratılacak malzemeyi üretiyoruz. Siz çeliği üretirsiniz ondan sonra bu çeliği neye dönüştürdüğünüz asıl önemli olandır. Katma değer asıl o zaman önemlidir. Eğer, üretmiş olduğunuz çeliği, bir otomobile dönüştürebiliyorsanız veya bir gemiye veya bir makineye işte katma değer orda ortaya çıkar. Yurtdışına bağımlıyız evet. Haklılar. Ama şu örneği vereyim. Yani, karnınız aç helva yapmak istiyorsunuz ununuz şekeriniz yağınız yoksa yapamazsınız. O zaman bunu bir yerden bulmak zorundasınız. Yoksa aç kalırsınız. Türkiye'de maalesef doğal kaynak olarak fakir bir ülke. Yeteri kadar, ne cevherimiz var, ne kömürümüz var. Hani derler ya vardı da biz mi kullanmadık diye. Ama bütün bu olumsuzluklara rağmen, Sektör dediğim gibi dünyanın 8. Büyüğü konumuna gelmiştir. Hammaddeyi buluyoruz, asıl malzemeyi biz burada kendi imkanlarımızla üretiyoruz. Eğer yeteri kadar hurda yoksa bence düşünülmesi gereken şey şudur. Demek ki Türkiye'deki sanayi yeteri kadar hurdayı yaratabilecek büyüklüğe ulaşmamıştır. O zaman biz bunun üzerine kafa yorabiliriz. 1995 e kadar Japonlar hurdayı ithal ederlerdi. 1995 ten bu yana, yarattıkları hurda artık kendilerine yetti ve dünyaya hurda ihraç etmeye başladılar. Çine bakıyoruz. Dünyanın %50 üretimine sahip ülke büyük bir ihtiyacını yine yurt dışından karşılıyor. Biz dediğim gibi, yeterliliğimizden çok burada neler yaratabileceğimiz üzerine odaklanmalıyız. Çeliği üretmek önemlidir ama asıl üzerinde ısrarla durulması gereken konu, çeliği tüketebilmektir. Bizler bugün 500 kg a yakın kişi başına çelik tüketimine sahip bir ülkeyiz. Aslında bu rakam dünya ortalamasının üzerindedir. Ama gelişmiş ülkelere bakıldığında, yeterli değildir. 500 kg ın aslında yarısı sabit belli yatırımların, inşaatla kullanılan çeliktir diğer yüzde ellisi sanayide tüketilen çeliktir. Biz

onun üzerine odaklanmalıyız. Bugün bir Koreli yaklaşık 1000 kg çelik tüketiyor. Baktığımız zaman dünyanın her yerinde Kore'de üretilmiş otomobilleri görüyorsunuz. Dünyanın en büyük gemi imalatçılarından biridir. Beyaz eşyada aynı şekilde. O zaman hedefimiz biz çeliği nasıl tüketebiliriz. Ve bu çeliği neye dönüştürüp o katma değeri yaratabiliriz? Rekabet üzerine de çok tartıştık. Rekabetçilik söz konusu olduğunda, bizi Çin ve Rusya ile kıyaslıyorlar. Ben de diyorum ki: Niye Amerika, Almanya, İtalya ile kıyaslamıyorsunuz? Şartları eşitleyerek kıyaslayabilirsiniz. Bizlerde aynı imkanlara sahip olalım. O zaman kıyaslayabilirsiniz. Çin'in sağında bankalar yer alıyor. Ne zaman kaynak ihtiyacı olsa sonsuz kaynak imkanlarını elde ediyor. Veya başı darı düştüğünde, diğer tarafında da devlet istediği imkanları ona sağlıyor. Herşeye rağmen şunu söyleyebilirim. Bizim ülkemizde çeliğin fiyatı, dünyanın birçok ülkesinden daha ucuzdur. Yani bir yarış içindeyiz. Maalesef biz her gün ilave bir ağırlıkla dolaşıyoruz. Çünkü maliyet en önemli unsurlardan biri ve bu ağırlıklarla bu ilave yükümlülüklerle rekabet konusunda bu tür ülkelerle kıyaslandığında, maça 1-0 maalesef mağlup başlıyoruz. Ama bunun artı tarafı da var. Bugün Çin'in Rusya'nın bu imkanlardan yararlanarak, dünyada elde etmiş olduğu rekabetçilik onlara bir çok ülkede, telafi edici vergiler gibi kısıtlayıcı önlemler olarak karşılımları çıkıyor. Halbuki Türk çelik sektörü aynı sınavı son 20-25 senedir başarıyla veriyor. Ve birçok ülkede birçok pazarda uzun yıllardır varlığını sürdürüyor. Çelik için şöyle bir tabir kullanılır. 3D business. Dirty difficult dangerous ve düşünülenin aksine aslında bugün Türk çelik sektörü çevreye çok duyarlı bir sektördür. Sadece çevre için yapmış olduğumuz yatırımlar, birçok sektörde toplam yatırım maliyetlerinin kat ve kat üzerindedir. Bütün bunları dile getirmişken, ayrıca ithal ettiğimiz hammaddeyle çevre katkı fonu ödemekle karşı karşıyayız. Sektör enerji yoğun bir sektör. Türkiye'de sanayide tüketilen, enerjinin yaklaşık % 20 sini çelik sektörü tüketir. Birçok ülkede çelik üreticileri özel tarifelerle elektriği satın alırlar. Bizde de bu 2002 yılına kadar mevcuttu. Türkiye'de elektrik ve indüksiyon ocakları diye bir tarife vardı. Daha sonra Avrupa topluluğu anlaşmasını imzaladıktan sonra, bu tarifenin adı devlet teşviği olarak yorumlanabilir. Biz de bakanlığa tarifenin adını değiştirdik. Onlar tarifeyi kaldırdılar. Saat 17 ile 22 arası puan saati dediğimiz bir saat var. Elektriğin fiyatı kw saat başına 30 kuruştur. Dünyada yaklaşık 8-9 cent e denk gelmektedir. Dünyada genelde 3-4 cent arasındadır. Fabrikalar daha çok çalışabilsin diye, gece ve hafta sonları onlara özel tarifeler uygulanır. Büyük tüketiciyseniz daha ucuz fiyatla alırsınız. Çünkü daha fazla tüketiyorsunuzdur. Eğer Türkiye'de tekrar gözden geçirilirse, puan saatlerinde birçok tesis maalesef çalışmıyor. Çünkü maliyetler kurtarmıyor. Hem onların çalışması sağlanacak hem üretimleri artacak, hem de elektrik tüketimi artacağından dolayı, elektrik piyasasında üreticilerin yaşamış oldukları sıkıntıların bir kısmı bertaraf edilebilecektir. Ödediğimiz fiyattan ayrıca biz TRT payı ödüyoruz. Bugün TRT'nin bütçesinin %20 sini Türk demir çelik sektörü karşılıyor. Belediye vergisi, kayıp kaçak oranı,

kaçak kullananların bedelini biz ödüyoruz. Yenilenebilir enerjiyle ilgili, devletten teşvik alıyorlar. Aslında sonuçta bizlerin cebinden çıkıyor.

Diğer yandan yoğun bir sermaye ihtiyacı var. Özel sektör bugüne kadar Kardemir, Erdemir, veya İsdemir'i kuramamıştır. Geçmişe bakarsak devletin kaynakları da buna yeterli olmamış. Kardemir'i 1937 de İngilizler, Erdemir'i 65 te Amerikalılar, İsdemir'i 75 te Ruslar kurmuştur. Bugün böyle bir tesisi kurmanın bedeli milyarlarca dolardır. Türkiye'de sermaye yapısı o seviyelere ulaşmamıştır. Ulaşabilmesi için sağlıklı bir ortamda, makul bir kar marjıyla bu sektörün ayakta faaliyetlerine devam etmesi gerekir. Bugüne kadar kazandığı her kuruşu tekrar oturup aynı işe yatıran sermayedar sağlıklı büyüyebilir ve ülkenin ihtiyacına yönelik gelişimleri gerçekleştirebilir. Bana artık dert olan bir konu var. Bu da hurdadan çelik üretimi. Artık bu konunun sonlandırılmasını talep ediyorum. Çünkü her ortamda hurdadan üretilen çelik sorgulanır halde. Bugünün dünyasında bu tartışmanın sonuna gelinmesi gerekiyor. Çünkü çeliği neden ürettiğiniz değil ne üretmek istediğiniz önemlidir. Siz sonuçta neyi elde etmek istiyorsanız, ona göre bir hammadde kullanırsınız. Son üç yılda, Kars'tan Edirne'ye kadar yaklaşık 1200 km yaklaşık doğalgaz boru hattı döşendi. Toplam 1.2 milyon tona yakın çelik kullanıldı. Bunun içinde Türkiye'nin payı sadece 100 tondur. Bir Almanın, Çinlinin veya Korelinin birkaç haftada geçebildiği bir süreci biz maalesef 3 senede geçemedik. 5 yıldır biz bu çeliği üretebiliriz diye yeri göğü inlettik. Her mercide bu konuyu gündeme getirdik. Ama inandıramadık ikna edemedik. Aynı dökümantasyonları testleri defalarca yaptık. Her seferinde sonuç pozitif olarak sonuçlandı. Nihayet ikna olup bize dediler ki ya projenin sonuna geldik. bütün hepsini kullandık. Sizin hatırınız için 100 ton alalım. İnat ettik yapcaz. Halbuki bu projenin devamı Yunanistan sınırından İtalya'ya kadar olan boru hattında, ihaleye girmeye çalıştık. Avrupa bizi ihaleye bile sokmadı. Söylemeye çalıştığım şey, burada birbirimiz ne kadar desteklediğimiz de çok önemli. Bugün Amerika da sac üreten yerler yassı çelik üreten, yassı çelik üretimine başladıktan sonra, sık sık gündeme geliyor. Yassı çelik üretilir mi diye? 5 tane üretici vardır bunların 3 tanesi elektrik ark ocağı ile hurdadan yassı çelik üretirler. Başkan Trump diyor ki; ben Amerika'da Amerika çeliği kullanırdım. Amerikan çeliğinin tanımı da şudur. Eğer çeliği Amerika'da ergitiyorsanız bu Amerikan çeliğidir. Biz maalesef Türkiye'de ürettiğimiz çeliğin daha henüz yerli malı tanımına sokamadık. Şimdi bu kadar negatif şeyden bahsettikten sonra, biraz da olumlu konuşmak lazım. Sonuç olarak, bu sektör ihtiyaç olan her türlü çeliği üretebilecek aslında kapasiteye birikime, teknolojiye ve donanımına sahiptir. Ürünlerimiz bir çok ülkede kabul gördü. Ve talep ediliyor. Çünkü 30 yıldır, çok ciddi yatırımlar yapıldı. Hem teknolojik anlamda, hem bilgi birikimi anlamında ve büyük de avantajlarımız var. Sonuçta genç bir sanayimiz var. Büyük potansiyele sahip yani tükettiğimiz fazlasıyla kullanabilecek önümüzde bir imkan var. Dünyanın öyle bir yerinde oturuyoruz ki, tam anlamıyla çelik ticaretinin merkezi. Hem doğuya hem batıya eşit mesafedeyiz. Türkiye 1983 te başladığı, ihracat

macerasını başarıyla, hala geliştirerek sürdürebiliyor. 2002 ye kadar en büyük, pazarımız güney doğu asya , uzak doğu ülkeleriydi. Sonra oradaki konjunktürün değişmesinden sonra batı taraflarına ağırlık verdik. Ama bu son geçtiğimiz 6 ay içerisinde tekrar doğuya girdik. Şunu söylemeye çalışıyorum. Çelik sektörü o esnekliği o beceriyi kazandı ve biz bugün dünyanın en büyük 7. İhracatçısı, konumuna geldik. Temsilcilerimizin hepsi çok iyi. Teknolojik anlamda, birçok ülkeden çok daha ileri inanılmaz özverili ve iş sahibi olan bir emek güzü var. Bütün tesisler nerdeyse limanlarda çok büyük bir avantaj sağlıyor. Büyük bir potansiyel var. Bu da çelik sektörünün önünde, ciddi imkanların olduğunu gösteriyor. Bu sektöre gerçek anlamda gönül vermiş biri olarak, bu sektörün geleceğinin çok daha iyi olacağına bütün kalple inanıyorum. Teşekkür ederim. Amerika' da biz kapıdan giriyoruz, bacadan kovuluyoruz. Fakat diğer taraftan kendi evimizin kapılarını sonuna kadar açmışız, gelen geçen giriyor. Fiyatı düşünerek sanki bir avantaj elde ettiğimizi düşünüyoruz ama işin sonunda şu gerçek ortaya çıkıyor: biz gidip Çin'inin veya Rus işçinin maaşını ödüyoruz. Gerektiği zaman belki biraz pahalıya da mal olsa sonuçta ürettiğimiz değer ülkede kalabilmeli. Aynı şartlar, aynı imkanlar verildiği sürece bu sektörün rekabet edemeyeceği en ufak bir konu mevcut değil. Zira 1990 yılında demir perde yıkıldığında döviz ihtiyaçlarını giderebilmek için ilk yaptıkları şey komünist rejim zamanında kurdukları devasa kapasiteli tesislerini dünyaya arz etmek oldu. Ve biz o zamanlar ayakta kaldık. O zamanlardan bu zamanlara 27 sene geçmiş ve bu zaman içerisinde Türk Çelik Sektörü bırakın gerilemeyi katlanarak büyümüştür. Şimdi bir Çin tehlikesi var. Rahmetli Latif Anbarlı 'nin bir lafı var hiç unutmuyorum. Bu konuyu bundan 15-20 sene önce konuşurken aynı şeyi söylemişti ; "Bizi Ruslar ezip geçemedi, dünyanın öbür tarafındaki Çinlilerden mi korkuyoruz?" Gerçek budur. Yani Çinlilerin ürettiği çeliğin maliyeti ile bizim ürettiğimiz çeliğin maliyeti arasında bir fark yok. Ama orda ki fark nedir? Dara düştüklerinde devlet bankaları istedikleri kadar kredi veriyor. Hatta öyle bir şey var ki (bir başka anıyı anlaticam) Yönetim Kurulu Başkanımız Hasan Çolakoğlu (aynı zamanda TEB Yönetim Kurulu Başkanı) yıllar önce diyor ki "Çin'e gittim ve bir Çin Devlet Bankası Yönetim Kurulu Başkanı ile görüşürken "Batik kredileriniz hangileri?" diye sordum. Başkan "Batik kredi nedir?" diye sordu. Yani dedim "Verdiğin kredinin geri dönmediği oluyor mu?" Şöyle cevap verdi. "Ben devletim. Kredi verdiğim adam da devlet. Burada batma durumu nasıl oluşabilir ki?" Çin' de böyle bir mantıktan bahsediyoruz. Burada ise son birkaç yıldır bankacılık sektörü çelik ürünlerine cüzzamlı gibi bakıyor. Kaçmaya çalışıyorlar. Bu koşullar altında biz rekabetten bahsediyoruz. Buna rağmen bu sektör her halukarda tüm zorlukların altından kalkabilecek bir potansiyele sahip. Çünkü o kadar çok dayak yedik ki artık direncimiz son derece güçlü.

Aslında çok genç bir sektörüz. Aşama aşama ilerliyoruz. Benim çalıştığım firma başladığım zaman yılda yaklaşık 750 bin ton çelik ürettiyordu ve ürettikleri çelik sadece insana yönelikti. 2013 yılında ise 4 milyon tonluk satışa ulaştık ve özel sektörde yassı çelik üretimi yapan ilk gruplardan birtanesiyiz. Bu bize çok şey

öğretti. Bugün artık biz Amerika'ya bizim kabul edemediğimiz veya buradaki otoritelere kabul ettiremediğimiz kalitede çelik ihraç edebiliyoruz. Otomotiv yan sanayi olsun, birçok makina imalat sanayi olsun artık o noktalara ulaştık. Bir sonraki hedefimiz kendi ölçeğimizde paslanmaz çeliklerle başlamak istiyoruz. Martenzitik Paslanmaz çeliklere başlamak için belli bir yatırım yaptık. Bir süre sonra gerçekleştireceğimize inanıyorum. İşte 30 yıl önce Almanya 'ya, İtalya'ya veya Japonya'ya baktığımızda onlar da bu yollardan geçtiler ama biz de evrile evrile o noktalara yavaş yavaş ulaşıyoruz. İnşaat çeliğinde dünyada en bilinen markadır Türkiye... Bugün dünyanın neresine giderseniz gidin Türkiye birinci tercih sebebidir. Yaklaşık olarak her sene 100 ülkeye ihracat gerçekleştiriyoruz. Biz firma olarak 30-35 ülkenin altına asla düşmüyoruz. Genelde 50 civarında ülkeye ihracat yapıyoruz. Bunu süreklilik arzedecek şekilde yapma gayreti içerisindeyiz. Çünkü bana göre en önemli şey süreklilik. Bir kere yapmakla başarmış olmuyorsunuz. İsveçli patentini almış zamanında, oldukça erken yola çıkmış. Fakat bu demek değildir ki, Türkiye o noktaya ulaşamayacak. Biz yolu hemen hemen yarılдық. Daha önümüzde bir süreç var ama o süreci daha hızlı geçeceğimize inanıyorum.

Biz çelik ihracatçıları birliği olarak ARGE projesi sonucunda bir merkez oluşturduk. Üniversite Sanayi işbirliğini de ne kadar hızlı geliştirebilirsek bu süreçte o kadar hızlı geçebileceğimizi düşünüyorum. Sermaye tarafından baktığımızda son derece mütevazî, kendi işinden başka bir şey düşünmeyen fakat diğer taraftan da kendini göstermekte zorlanan bir profilimiz var. Ankara 'ya ben hafta da bir gitmek zorundayım. Ve her seferinde de her karşılaştığım bürokrata tekrar tekrar sektörü baştan anlatmak zorundayım. Çünkü o algıyı bir türlü maalesef kıramıyoruz. Biz koruma istemiyoruz aslında biz vergi gelsin de istemiyoruz. Biz normal şartlar altında eşit rekabet koşulları altında çalışmak istiyoruz. Sermaye yoğun bir sektör, bugün bir fabrikanın kurulması için en az bir milyar dolarlık bir yatırım gerekir. Şimdi öyle bir kaynağımız olması lazım ki sonraki aşamaya geçebilesiniz. Ama 2008 sonrası global krizin en fazla etkisi Demir Çelik sektöründe görüldü. Ve biz ancak mevcudu korumaya yönelik bir takım hareketler yapabildik. Halbuki ortam Avrupa'daki ve Amerika'daki gibi bu sektörü sağlıklı bir şekilde götürebilecek şekilde sağlanabilse, o zaman o sermaye oluşur ve bir sonraki aşamaya daha rahat geçebiliriz diye düşünüyorum. Birikimimiz var, teknolojiye var fakat biraz kaynak sıkıntımız var. Sektörün su anda yaşadığı sıkıntıların başında bu kaynak problemi geliyor. Şu anda Türkiyenin gerçekleştirmiş olduğu 140 milyar dolarlık ihracatta çeliğin kilogram fiyatı yaklaşık 1.5 doların altında. Eğer siz o çeligi otomotiv çeliline dönüştürürseniz değeri misli ile katlanıyor.

Otomotiv sektöründe Erdemir bizden fersah fersah ilerde ama biz bu işe daha yeni başladık. Yavaş yavaş ilerliyoruz. Bugün Renault der ki; Senin ülkende otomotiv üreteceğim ama çeliği Fransa'dan alacağım. İstediginizi söyleyin, istediğiniz fiyatı verin hayir derler. Japon da aynı şeyi söyler. Demek ki Fransızın

otomobilini değilde kendi yerli otomobilinizi yapacak duruma geldiğimizde ancak kendi çeliğimizi kullandırmayı kabul ettirebiliriz. Ticari kaygılar yüzünden ufak tasarrufları bir kazanç gibi görüyoruz. Fakat ben 30 yıldır çelik ihrac ediyorum.

Fransızlara çelik satamıyorum. O kapıdan bir türlü sokmuyorlar. Diyorlar ki kendi ülkemizde ürettiğimiz çeliği kullanırız. Almanları ikna etmek için otuz tane takla atıyorsunuz yine ikna olmuyorlar. Bir Japonu ikna etmek için ise oradaki kalite onay belgesini almayı düşündüğümüzü söyledim. Ciddi olup olmadığını sordu. Ciddi olduğumu söyledim. Bana bir kitapçık verdi Japonca. İngilizce çevirisinin olup olmadığını sordum. Hayır yok dedi. Burada yatırım yapmak istiyorsan Japonca öğrenmelisin. Şimdi o aşamayı katedebilsen bile oradaki bir tane adama mal satamayız. Çünkü bir tane adam o çeliği aldığı zaman o adamın işi bitmiştir Japonya'da. İşte onlarda böyle bir kültür var. Yani kendi içimizde biz kendi kendimizi ne kadar destekleyebiliriz mesele bu. Bizim asıl üzerinde durmamız gereken husus budur. Biz malzemeyi üretiyoruz bu sektörde. Bunu tüketebilecek alanları yaratabilsek gerisi kendiliginden gelecektir. Israrla söylüyorum, üzerinde durmamız gereken konu çelik sektörünün ne yaptığından çok, üretilen çeliğin nerede nasıl tüketilebileceği olmalıdır.

Avrupa'da çelik sektörü ölüyor. Çünkü onların rekabet gücü ortadan kalkıyor. Son dönemde kendilerini korumak için izole olmaya çalışıyorlar; sektör yaşayabilsin diye. Malzemeniz olmazsa bir şey yapamazsınız. Keza Amerika da öyle. 80 'lerden bu yana zor durumdadılar fakat hala ayakta; çünkü sektörün yaşaması için gerekli ortamı önceden oluşturmuşlardı. Türkiye bence önümüzdeki 15-20 sene içerisinde Avrupa Çelik Sektörünün yerini alabilecek potansiyele sahip ve bizim hedefimiz bu. Avrupada bir çelik firmasını gözümüze kestirdik. Onlara 15-20 yıl sonra Çolakoğlu Metalurji 'nin karşısında tutunma şanslarının olmadığını söyledik.

Geçenlerde bir toplantıda sektörün sorunlarını anlatmamı istediler. Dedim ki on senedir aynı şeyleri söylüyorum. Tekrar etmeye gerek yok. Fakat yine de önemli bir husus üzerinde durmamız gerekiyor. Enerji maliyetlerimiz... Aslında sadece bu sektöre yönelik değil Türkiye'nin enerji sektörüne de yönelik bir takım çözümler içerdiğine inandığımız için dile getiriyoruz. İnşallah bundan sonra birer birer bu aşamaları geçerez. Umudumuzu hiçbir zaman yitirmiyoruz.

SPEECH of NAZIM ÇAPRAZ

(Head of KAHDER)

Sevgili gençler ve sayın hocalarım konuşmama, Türkiye'nin belki de hayatta kalmış en eski haddecisi ve sanayicisi olarak ve aynı zamanda Demir Çelik'in kuruluşunda aileden devraldığım hikâyemden kısaca söz ederek başlayacağım. 1937 yılında Demir Çelik Fabrikası, İsmet Paşa'nın Başbakanlık, Fevzi Çakmak'ın Mareşal ve Genelkurmay Başkanı ve Celal Bayar'ın da Sanayi Bakanı olduğu dönemde, Mustafa Kemal'in emriyle Ereğli'de böyle büyük bir Demir Çelik Sanayisi kurulması teklif ediliyor. Fakat günümüzde de olduğu gibi o zamanda da Türkiye için iyi bir teşebbüs, iyi niyetle hazırlanmış girişimler tepki görüyor. Bu tepkilerin kaynağı sadece içerdeki muhalifler değil dışarıdan, içerdeki maşalar tarafından yapılan tepkilerdir. Buna dikkat etmek lazım. Türkiye'nin ilerlemeye kalkınmaya çok ihtiyacı vardır. Şimdi o zaman da kömür madeni, özellikle bu Entegre tesislerde kullanılacağından, bir de demir cevheri de kullanılacağından dolayı demir cevheri Sivas Divriği de var fakat orası da uzak ama en azından kömür madeni yakın Zonguldak'ta var ama çok önemli bir şey de var ki deniz ve Liman da var. O tarihte mühendislerimizin, üniversitelerimizin, teknolojinin yaygın olmadığı o günkü dönemde bile hükümet istemedi. Osmanlı Döneminde de istenmediğinden Ereğli'de temeli atılmıyor. Karabük' e kurulma kararı alınıyor ve itiraz edecek kimse yok. En sonunda Karabük'e kuruluyor.

Büyüklerimden dinlediğim bir şey var ama doğruluğu hakkında kesin bir şey söyleyemiyorum. Bu Demir Çelik'in kurulumunda Çanakkale ve İstiklal Harbi'nde en fazla şehit veren iki vilayet var; Kastamonu ve Çankırı. Bu vilayetlerin Karabük'e yakın olduğundan Fevzi Çakmak Paşa'nın bu fabrikanın şehit evlatlarının iş sahası bulmasını düşündüğünden dolayı kurulmasından bahsederler ama ben bunun doğruluğu hakkında pek emin değilim. Demir Çelik Fabrikaları ile ilgili bir rapor yazması istenir. Biliyorsunuz o zaman Alman harbi var. Demir Çelik'in temeli atıldığı zaman hava boşluğu var. Bu arada bombardıman uçakları fabrikanın üzerinden geçemeyecek raporu vardır. O hikâye ile beraber buraya temeli atıldı. İngilizler buraya kurduğu zaman genellikle İngilizleri çalıştırdı tabii. Türkiye'nin yetişmiş mühendisi falan çok yok son dönem Sultan Hamit döneminde kurulan üniversitelerimiz var. Ondandır sonra Cumhuriyet döneminde başlıyor üniversiteler kurulmaya teknik elemanlarımızla çok yok Sanat okulundan yetişmiş pratikten yetişmiş iki tane genç diyorlar ki o zaman en genel müdürüne “Yeter artık biz bu haddehaneleri çalıştırırız” ve onlar deniyorlar ikisini de birer vardiyanın başına veriyorlar. Haddehanelerin başına ustabaşı olarak tayin ediyorlar birini, bugünkü belediye başkanının babasıdır. Benim eniştemdir. 9 Kişi bir araya geliyor minyatürünü yaptırıp buraya koyduğum öyle bir 2 toplu hadde Karabük'te ilk defa kuruluyor. Celal Bayar Başbakan kurdelesini kesiyor ve ben talebeyim ve kurdele kesildiğinde orada seyirci idim bunun yaşadım. Yani onun için

Türkiye'nin özel en eski haddecileri arasında 1960 yılında özellikle işveren olarak, teknik adam olarak başladım ve baştan beri ben bu işin içinde varım. İkinci haddehane Balat da iki ortaklı kuruluyor. Bunun birisi yine benim eniştem Mehmet Vergili ilk defa Özel sektör olarak Demir Çelik ile ilgili haddehane kuruluyor. Bu haddehane iki toplu bir haddehane ve inşaat demiri çekiyor. O günün şartlarında yuvarlak, sekizlik, onluk vb. bunları Karabük demir çeliğini çekerken bozuğa çıkmış 35'lik 40'lık dört köşelerinden yani hadde bozuğu diye tabir edilen malzemeler çekiyor. Tabi bu zamanla gelişmeye başlıyor.

Karabük'te devam eden Demir çelikten faydalanılarak Demir çelikten hammaddesi alınarak devam eden bu Tesisler Türkiye'de yayılmaya başlıyor. Evvela bu Tesisler İstanbul'da kurulmaya başlıyor sonra İzmir'e ve Ereğli'ye doğru gidiyor. Hatta Ankara'da bile bunlar kurulmaya başlanıyor. Türkiye'nin ilk kurulduğu yerler bu yerler sonra Ankara tamamen bu işi bırakıyor. İzmir devam ediyor İskenderun devam ediyor ve Karabük devam ediyor. İstanbul devam ediyor ve bu Tesisler büyüyor. Uzun müddet büyüyerek gelişerek devam ediyor. İlk defa ark ocağı diye tabir ettiğimiz izabe tesisi Demokrat Parti son döneminde Demokrat Parti milletvekillerinin bir araya gelerek Ziraat Bankası'ndan almış olduğu bir teşvik Kredi ile İstanbul'da bu tesisin kurulmasına başlanıyor. Fakat tesisin kurulmasına yakın ihtilal oluyor daha sonra bu tesisi birisi satın alıyor ve izabe tesisinin Hadde tesisi ilgili kurulumunda bir hata yapmışlar. Beni çağırdı ben kendim ona bir proje verdim proje ile beraber motorun ve şanzımanların yönünü değiştirerek bir sıra düz inşaat çeliği çekerek hadde üretimine başladı.

Az önce Hocanın bahsettiği Entegre Tesisler ve izabe ve tesislerinin avantaj ve dezavantajlarından önemli bir şey de ben hatırlatmak istiyorum. İzabe Tesisleri avantajlı değil. Entegre Tesisler esas önemli olan. Peki, neden avantajlı değil? Bugün artık hızlı tren rayları da Türkiye'de yapılıyor. Bunu Karabük Demir Çelik üretiyor haddeleme tesisi yeterli mi değil. Ark ocaklarında bu kalitede çeliği üretme ihtimaliniz yok. Dinlenmiş maden yüksek fırın ve çelikhane olmadığı müddetçe bu analizi verme şansımız yok. İzabe fırınlarında İnşaat çeliğinin en kalitelisini verebilirsiniz, beton çeliğine en iyi şekilde üretebilir analizini tutturabilirsiniz onun üzerinde bunu kolayca tutturamazsınız. Tabi Karabük Demir Çelik fabrikası burayı uzun zamandır yapıyor 12 metreden 24 metreye çıktı. Tabii ben bu sürecin içinde tamamen varım Haddeciler Derneği 1960 yılında kuruldu O zamandan beri varım. 1980 altıya kadar bu yükü taşıdım ben 1986 da geri çekildik bu işin başına gençler otursun dedik. İki sene önce bu işin tekrar bana devredilmesi demir çelik sektörü ile Özel sektör arasında bazı kavgalar ve gürültüleri önlemek, Karabük'teki huzuru yakalamak için yaşım itibariyle “Sen bizim aramızı bul” diyerek tekrar beni bu işin başına getirdiler. Şu an bu sebeple Başkanım yoksa yaşım icabı ile başkanlık edecek bir insan değilim.

Karabük'te ihracata yönelik çalışır vaziyette 52 tane hadde tesisi var iken hammadde sıkıntısı çekilmeye başlandı. Bu haddehanelerin çoğu Karabük'ten gittiler. Kimisi İzmir'deki kimisin İstanbul'da arkadaşlarımız bende Ummanda ve Cezayir'de tesis kurmuştum zamanla birbirimizden ayrılınca aileler dağılınca herkes bir tarafa çekildi. Bu mesleği yapmak istemiyordu benim yeğenlerim tekrar Karabük'e döndüm Karabük'teki tesis üzerine devam ettim benden sonra Oğlum ne kadar devam eder onu da bilmiyorum Karabük'teki haddehane Tesisleri 12-13 e indi.

13 Tane tesisten şu an 6-7 tanesi çalışır vaziyette. En ince malzemeden en kalın malzemeyi yaklaşık 100 çeşit malzeme üretmeye başladık. 6-7 tane haddehanenin çalışabilme nedeni de bu. Hammadde sıkıntısı var. Bu hammaddeyi nereden temin ediyoruz? Kardemir'in piyasaya verdiği bu hammadde yetmiyor. Biz ihracata yönelik çalıştığımız için Ukrayna'dan ve benzeri yerlerden gelen hammaddeler ile yarı mamuller ile çalışıyor ve bunlarla üretim yaparak Karabük ekonomisine katkıda bulunmaya çalışıyoruz.

Türkiye'de olması gerekenler için de mücadele verdik. 1960 yılında Demokrat Parti yönetiminde iken ilk ark ocağı Çolakoğlu firmasıdır. Çolakoğlu'ndan sonra İÇDAŞ, Yazıcı vesaire gelişerek İskenderun ve İzmir'deki Ark ocakları kurulması ile devletten alınan teşviklerle bir yere kadar geldik. Hatta yakında Entegre tesis kuracak bütçelere kavuşacağız. Bunları bakanlıklarla yapılan toplantılarda her yerde bu konuları ben anlattım. Ya ortak olarak ya da tek başına bu Entegre Tesisleri kurulması gerekmektedir.

2015 yılında Çin dünyaya ve Türkiye'ye mal sattı. Ucuz mal sattı rekabet edemedik. Türkiye sıkıntılara girdi. Türkiye'nin yüzde 23'ü Entegre Tesis yüzde 77'si Ark ocağı, dışarıya bağımlı çalışıyoruz. 2000 yılında Demir Çelik krize girdiği zaman Zonguldak TTK ya üç arkadaşım ile beraber gittim. Kardemir'e borç olmaması için Demir Çelik'i kurtarmak için bu mücadeleyi verdik. %25 kapasite ile çalışarak ocakları dondurmak için mücadele veriyordu Demir Çelik o zamanın Genel Müdürü bize bir şey söyledi: "Siz çok büyük bir mücadele veriyorsunuz ve aslında üç şeyi kurtarıyorsunuz. Bunlardan birincisi bizim kömür satışımızın yüzde 35'ini sadece Karabük Demir Çelik fabrikası sağlıyor. Eğer Karabük Demir Çelik kapanırsa bizim ocaklarımız kapanır ve işçilerimizin işten çıkarılması gerekir. İki Devlet Demir Yollarının nakliyesini %50'sini Karabük karşılıyor. Bu tesisin kapanması devlet demiryollarında sıkıntıya sokuyor. Üç, Sivas Divriği madenini en çok Karabük kullanmaktadır. Böylece Karabük'e kömürü verdi. O zaman eski başkan Şinasi Kardemir'in genel müdür iyiydi eğer o gece oraya kömür ulaşmasaydı ocaklar duracak ve Türkiye'ye bir buçuk milyon ton üretim yapan bu Entegre tesis 72 metreden çeken en uzun profilleri üreten bu Demir Çelik olmayacaktı.

Bu Demir Çelik'in Türkiye'ye çok büyük faydalar oldu. Tansu Çiller'in Başbakanlığı zamanında çok mücadele verdik bu Demir Çelik'in yaşamaya devam etmesi çok önemliydi. İstanbul'daki İSKİ skandalı Karabük Demir Çelik fabrikasının boru fabrikasının da kapanmasına sebep oldu.

İzabecilere buradan sesleniyorum etmeyin gitmeyin bu ülkenin bütün imkânlarını kullanıp bundan sonra Türkiye'ye faydalı olmak için Türkiye'nin dışarı ile rekabet edebilmesi için dönün. Millettin elindeyken 21-22 bin işçiyle çalışıyordu, bu politik bir çalışmaydı. Tek tabanca idi kar etme çabası yoktu. Şu an 3500 4000 kişi ile yapılan üretim daha fazla bu siyasi parti çıkar politikaları yanlış bir politika idi.

Asil Çelik KOÇ'u batırabilecek kadar büyük bir sıkıntıya girdi ve devlet el atıp bunu kurtardı. Bunların yanında Türkiye'nin büyük iş adamları Sabancılar vesaire demir-çelik özelleşirken buna el atmaya korktular. O zamanın başbakanının: "Bu demir-çelik bizim sırtımızda bir kambur vergilerle yaşıyoruz. Biz başka bir yere yatırım yapamıyoruz." cümleleri insanları korkuttu. Eğer öyle olmasaydı 1 liraya devre edilmeyecekti. Bu fabrikaya kalkındırmak için birisi taşın altına elini koyacaktı ve bu canı yanan insanların eline geçecekti. Fabrikayı ortaklı veya ortaksız birileri satın alacak 1998 ve 2000 yıllarında fabrika zarar etmeyecekti.

Hatta Kardemir 0-0 devam etti işçilerin tazminatları ödendi. Hatta 44 milyon dolar revartman bedeli Tansu Çiller'e ödendi. Maalesef Uzakdoğu problemleri vesaire gibi sorunlar yüzünden Demir Çelik zarar etmeye başladı ve yine de 7500 8000 işçinin altına inmedi ama Demir Çelik istihdamına ayarlar ve üretimini artırırsa pazarında bulabilirse bu her zaman para kazanacaktır. Şu an Kardemir 650 bin tondan iki buçuk milyon 3 milyon üretime geçti. Kardemir'in şu an profil üretmemesi demek 300 bin ton bizim dışarıdan ağır profil almamız dışarıya borçlanmamız anlamına gelmektedir. Eğer Kardemir üretim yapmasaydı 150-200 bin ton ray dışarıdan alınması gerekecekti. Eğer Türkiye Entegre tesis olarak yüzde 70'lere çıkarsa ülkenin kurtuluşu olacaktır. Bizim evler için de sıkıntılarımız var. Elektrik üretimimiz de kömür dışarıdan alıyoruz. S dışarıdan alım yapmak zorundayız. Nükleer santral vesaire istemeyenlerin bu yaptıkları anlaşılabilir değil. Daha dün Marzinc hava kirliliğine sebep oluyor diyip istemeyen Ereğli Demir Çelik, fabrikasını kurdu. Bu istemezük olaylarının artık değişmesi gerekmektedir. Bu sebeple böyle yatırımlara köstek olunmamalı önü açılmalıdır. Özellikle böyle yatırımlar teşvik edilmelidir. Demir Çelik üretimi Türkiye'nin lokomotif sektörüdür.

SPONSORS

KARDEMİR KARABÜK DEMİR ÇELİK SANAYİ VE TİCARET A.Ş.

3 Nisan 1937 tarihinde kurulan, Türkiye'nin ilk entegre demir çelik fabrikasıdır.

Türkiye ve bölge ülkeler arasındaki tek ray üreticisidir.

Yüksek fırınlardan gelen sıvı madenin işlendiği, bünyesinde kükürt giderme, konverterler, pota fırını, vakum tesisi ve sürekli döküm makineleri bulunan çelikhane prosesi, Kardemir'i ray piyasalarında öne çıkaran gelişmiş teknolojik altyapıya sahiptir.

2007 yılında devreye aldığı ray profil haddehanesinde ciddi bir tecrübe ve bilgi birikimi edinen Kardemir, ray piyasasında bölgesel bir güç haline gelmiştir. Şekil ve ölçü kontrollerinin online lazer sistemi ile yapıldığı bu tesiste, milimetrenin yüzde biri hassasiyetle üretim gerçekleştirilir. % 95'in üzerinde kalite oranı ile çalışan tesiste, 72m.'ye kadar müşteri isteklerine uygun boyutlarda ray üretimi gerçekleştirilmektedir.

Ray üretiminde en önemli istasyonlardan biri olan test merkezi, geometrik kontrollerin yapıldığı lazer, yüzey kontrollerinin yapıldığı girdap akımları ve iç kontrollerin yapıldığı ultrasonik test ünitelerinden oluşur. Üretim hattında olduğu gibi test merkezinin tüm operatörleri de en az seviye-2 kullanıcı sertifikalarına sahiptir.

Avrupa'da sadece birkaç ray üreticisinin sahip olduğu uluslararası geçerliliğe sahip HPQ belgesini de almaya hak kazanan Kardemir, 2017 yılının başında Ray Sertleştirme Tesisi yatırımını da tamamlayarak mantarı sertleştirilmiş ray üretimine başlamıştır.

Halen stratejik teşvik kapsamında yapımı devam eden 200.000adet/yıl kapasiteli demiryolu teker üretim tesisi ile birlikte Kardemir, raydan sonra demiryolu tekeri üretiminde de Türkiye ve bölge ülkeler arasındaki tek üretici olacaktır.

550mm. genişliğe kadar ağır profil üretimi ile yapısal çelik üretiminde Türkiye'nin tek üreticisi olan Kardemir, ürünlerini katma değeri yüksek yeni çelik kaliteleri ile çeşitlendirecek olan Çubuk ve Kangal Haddehanesini de 2016'da devreye almıştır. 700 bin ton /yıl kapasitesi ve teknolojik üstünlükleriyle ayrıcalıklı bir konuma sahip olan bu tesiste, ø5,5mm - ø55 mm arası kangal ve ø20-100 mm arası çubuk üretimi yapılmaktadır.

3 Nisan 2017 tarihinde 80. kuruluş yıldönümünü kutlayan Kardemir, köklü sanayi kültürünün vermiş olduğu birikimle ve toplam kalite felsefesine inanarak daha fazla değer yaratmaya devam etmektedir.

İLETİŞİM:

KARDEMİR KARABÜK DEMİR ÇELİK SANAYİ VE TİCARET A.Ş.

78170 / KARABÜK

Tel: +90 370 418 23 25

Fax: +90 370 419 10 40

İstanbul Ofis: +90 216 576 20 01

www.kardemir.com

KARDEMİR

Established on 3 April 1937, Kardemir is Turkey's first integrated iron and steel factory.

Kardemir is the only rail producer in Turkey and the region.

Steelshop, where the liquid metal from the blast furnaces is processed, has desulphurisation, converters, ladle furnace, vacuum plant and continuous casting machines, It has the technological infrastructure that makes Kardemir stand out on the rail market. In addition, Kardemir has developed his own experience in the production of rail steel.

Kardemir, renewed its production technologies with new investments made after privatization, became a regional power in the rail market by acquiring a considerable experience and knowledge in the rail profile rolled in 2007. With the online laser system of shape and size controls, production is done with precision of one per cent of the millimeter. With a quality ratio of more than 95%, rail is produced in dimensions suitable for customer requests up to 72m.

The test center, which is one of the most important stations in rail production, consists laser, where the geometric controls are made and the eddy current made by the surface controls, and the ultrasonic test units. In the production line, all of the testing center operators have level-2 user certificates.

Kardemir is entitled to receive the HPQ document with international validity, only a few rail producers in Europe have this document. Also at the beginning of 2017, the rail hardening plant was completed and the hardened cork rail production started.

Kardemir will be the only producer between Turkey and the countries of the region in the production of railway wheel with the investment of 200.000 unit / year capacity railway wheel which is still under construction within the scope of the strategic incentive.

Kardemir, the only manufacturer in Turkey in structural production with steel with heavy profile production up to 550mm. wide, was also commissioned in 2016 for the Bar and Wire Rod Mill, which will diversify its products with new high quality steel products. This facility, which has a privileged position with 700.000 tons/year capacity and technological superiorities, produces ø5,5 mm - ø55 mm coils and ø20 - 100mm. rod productions.

Celebrating its 80th anniversary on April 3, 2017, Kardemir continues to create more value by believing in the philosophy of total quality and the accumulation of deep-rooted industrial cultures.

CONTACT:

KARDEMİR KARABÜK IRON STEEL INDUSTRY TRADE & COMPANY INC.

78170 / KARABÜK, TURKEY

Tel : +90 370 418 23 25

Fax : +90 370 419 10 40

İstanbul Office : +90 216 576 20 01

www.kardemir.com

ERDEMİR GRUBU **Destekleyen Kuruluş**

Erdemir Grubu, modern teknolojiye sahip tesislerinde, tecrübeli ve dinamik çalışanları ile kaliteli, güvenilir ve yüksek standartlarda çelik üretip dağıtımını gerçekleştiriyor. AB-28 ülkelerinin en büyük 3. çelik üreticisi* olan Erdemir Grubu, yıllık 9,65 milyon ton sıvı çelik ve yaklaşık 11 milyon ton nihai ürün üretim kapasitesiyle çalışıyor. Erdemir Grubu toplam varlıkları bakımından Türkiye'nin en büyük sanayi şirketlerinden biri.

Erdemir Grubu, ürün ve hizmetlerini aralarında otomotiv, enerji, inşaat, boru, gemi üretimi, ev aletleri, elektronik aletler, zirai makineler, ısı, ağır sanayi, gıda ve ambalaj sektörlerinin de bulunduğu pek çok sektöre sunan, çelik endüstrisinde küresel bir oyuncu. Yassı ve uzun çelik üretimi, çelik servis merkezi hizmetleri, madencilik, mühendislik ve proje yönetimi konularında engin bir deneyime sahip. Türk otomotiv sektörünün de ana çelik tedarikçisi konumunda.

Grup 12 bini aşkın çalışanıyla Türkiye'nin en çok istihdam yaratan kuruluşları arasında yer alıyor. Erdemir Grubu; Erdemir, İsdemir, Erdemir Maden, Erdemir Çelik Servis Merkezi, Erdemir Mühendislik, Erdemir Romanya ve Erdemir Asia Pacific'ten oluşuyor. Grubun Ereğli ve İskenderun'da iki büyük limanı da bulunuyor.

Türk sanayine yarım asrı aşkın süredir hizmet veren ve Türkiye'nin en büyük entegre yassı çelik üreticisi olan Erdemir; levha, sıcak haddelenmiş, soğuk haddelenmiş, galvanize/galvenile ve kalay/krom kaplı yassı çelik ürünleri üretiyor. Ayrıca Erdemir, Türk çelik sektörüne bakanlık onaylı ilk Ar-Ge Merkezi'ni kazandırdı.

Türk sanayine 47 yıldan bu yana hizmet veren İsdemir, Türkiye'nin hem yassı hem de uzun çelik üreten tek entegre çelik üreticisi. İsdemir'in Erdemir Grubu bünyesine katılmasının ardından tesiste yürütülen yatırımlar Türkiye Cumhuriyeti Tarihi'ndeki en büyük sanayi yatırımları arasında yer alıyor. İsdemir, yassı çelik ürün yelpazesine ek olarak, hasır, tel, çivi, cıvata, yay, elektrot ve kaynak teli üretiminde kullanılan pik demir, kütük ve kangal da üretiyor.

*2015, Dünya Ham Çelik Üretimi Sıralaması, Dünya Çelik Birliği ("worldsteel")

ERDEMİR GROUP **Supporting Firm**

Erdemir Group manufactures and delivers high-quality and reliable steel at high standards in facilities equipped with state-of-the-art technology with an experienced and dynamic staff. Erdemir Group; 3rd biggest steel producer in EU-28 countries*, operates with 9,65 million tons liquid steel and around 11 million tons final product capacity per annum. Erdemir is one of the biggest industrial corporations in Turkey in terms of total assets.

Erdemir Group is a global player in the steel industry that renders its products & services to many industries like automotive, energy, construction, pipe, ship-building, home appliances & electronics, agricultural machinery, heat, heavy industry, food and packaging. It has a proven expertise in the fields of flat and long steel production, steel service center, mining and engineering & project management. It is the major steel supplier of the automotive industry in Turkey.

The Group is among the largest employers in Turkey with its employees more than 12,000 and continues its operations through the companies Erdemir, İsdemir, Erdemir Mining, Erdemir Steel Service Center, Erdemir Engineering, Erdemir Romania and Erdemir Asia Pacific. The Group also has two ports which are located in Ereğli and İskenderun.

Erdemir, serving to the Turkish Industry for the last 52 years, is the biggest integrated flat steel producer in Turkey that produces plate, hot rolled, cold rolled, hot dip galvanized / galvanized and tin/chromium coated flat steel products. Additionally, Erdemir brought the first R&D Center of the steel industry to Turkey.

İsdemir, serving to the Turkish Industry for the last 47 years, is the only integrated steel producer in Turkey that produces both flat and long products. The investments executed in İsdemir after the acquisition of the company by Erdemir Group is among the largest scale industrial investment projects in Turkey. İsdemir also produces pig iron, billet and wire rod which are used in the production of mesh, wire, nail, bolt, spring, electrode and welding wire in addition to its flat steel product range.

*2015, by crude steel production, World Steel Association (worldsteel)



Kendi aralarında Türkiye'nin en uzman, eğitimli ve tecrübeli kadrosu ile MAK Elektronik, Otomotiv, Havacılık, Demir Yolları ve Tren Aksamları, Demir-Çelik ve Demir-Dışı metal hammadde/ürün üretim ve imalat, Plastik/Lastik ürün üretimi/imalatı, Petrol Doğalgaz hatları, Rafineri Depolama ve Dağıtım Tesisleri gibi sektörlerde, yüksek kalite ve yüksek verim ihtiyacının bilincinde olarak sizlerin kalite kontrol, AR-GE, servis ve bakım-onarım çalışmalarınızda her zaman sizlerden biri gibi ihtiyaç ve gereksinimlerinize çözüm ortaklığı yapmaktadır.

Uzman ve tecrübeli kadromuz, en temel tehlikelerden, en yüksek dizayn ve teknik çalışma gerektiren uygulamalara kadar sizlere en uygun ve gelişmiş sistemler ile çözüm ve ihtiyaç odaklı hizmet etmeye her zaman hazırdır. Müşteri odaklı çalışmalarda hedefimiz, müşterilerimiz için "MAK Elektronik" departmanı (kalite çalışmalarında çözüm ortağı/çalışanı) olmaktır.

MAK ELEKTRONİK has made solution partnership for requirements and needs in quality control, service and maintenance works by taking fully account of high quality control and high efficiency requirement in sectors like Automotive, Aviation, Railways, Rolling Stock, Iron-Steel and Nonferrous Metal raw material / product and manufacture, Plastic / Rubber production, Petrol, Neutral Gas pipelines, Refinery Storage and Distribution Systems.

It experienced personnel have given solution and requirement focused service with the most advanced systems from the most basic dangers to the applications requiring highest design and technical study.



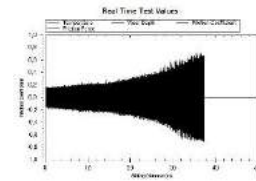
Malzeme Analiz ve Kalite Kontrol Cihazları Dış Tic. Ltd. Şti.



QNESS GmbH - AVUSTURYA
SERTLİK ÖLÇÜM CİHAZLARI



ATM GmbH - ALMANYA
METALOGRAFİK NUMUNE HAZIRLAMA CİHAZLARI



UTS DESIGN - TÜRKİYE
TRIBOLOJİ TEST CİHAZLARI



ANKA ANALİTİK MEKATRONİK SAN. TİC. LTD. ŞTİ.

Anka Analitik, kimyasal analiz, kalite kontrol, laboratuvar cihazları ve dökümhane ihtiyaçlarına bütünüyle cevap veren bir firmadır. Satış, teknik servis, kalibrasyon, personel eğitimi ve yedek parça temini konularında hizmet vermekteyiz.

Anka Analitik, bünyesinde metal&metalurji, kimya, boya, çimento, seramik&porselen, madencilik, çevre ve kalite kontrol laboratuvarları, üniversiteler, enstitüler ve kamu kuruluşlarına yönelik; Spektral Analiz Cihazları, Optik Emisyon Spektrometreleri, Numune Hazırlama Cihazları, Üiversal Test Cihazları, NDT Tahribatsız Muayene Cihazları, Tane Boyutu Analiz Cihazları, XRF Spektrometreleri, X-Ray Difraktometreleri, Mikroskoplar, Taramalı Elektron Mikroskopları ve ICP-OES/ICP-MS, Atomik Absorbsiyon, XRF cihaz sarfları başta olmak üzere birçok alanda hizmet sunmaktadır.

Anka Analitik, Türkiye temsilciliğini yaptığı dünya çapında saygın firmaların ürünlerinin satış sonrası servisini de bünyesinde barındırarak, müşterileriyle sürekli ve sağlıklı ilişkiler kurma prensibini taşımaktadır.

.....
Anka Analitik delivers solutions to customers in needs of chemical analysis, quality control, foundry and laboratory equipments etc. We serve and provide technical service, sales, calibration, personnel training and spare parts services.

Anka Analitik offers a wide range of services to diversified industries and establishments such as the metal & metallurgy, chemistry, paint, cement, ceramics & porcelain, mining, environment and quality control laboratories, universities, institutes and public institutions, within its scope mainly for XRF spectrometers, X-ray Diffractometers, Microscopes, Scanning Electron Microscopes and ICP-OES / ICP-MS, Atomic Absorption Spectrophotometers, Spectral Analyzers, Optical Emission Spectrometers, Sample Preparation Instruments, Universal Testing Instruments, NDT Non Destructive Testing Instruments, Particle Size Analyzers , XRF device consumables.

Anka Analitik has the principle of establishing continuous and healthy relations with its customers by incorporating the after sales service of the products of reputable companies in Turkey which Anka Analitik represents.



GNR was established in 1984 in Milan (Italy).

G.N.R. S.r.l., thanks to its 30 years of experience, is a worldwide market manufacturer of advanced analytical instruments, developing procedures of analysis for various applications, supplying the corresponding laboratory equipment and providing consulting and Customer support worldwide, through its well established sales and postsale network.

G.N.R. S.r.l. projects and manufactures Optical Emission Spectrometers (OES) and Rotating Disc Electrode Optical Emission Spectrometers (RDE-OES) for the measurement of elemental composition of metal alloys and the analysis of contaminants, additives and wear metals in oils and lubricants, coolants and hydraulic fluids.

G.N.R. S.r.l. develops and produces X-Ray Diffractometers (XRD) and X-Ray Fluorescence Spectrometers (XRF) for the study of material structure and elemental composition for both academic and industrial applications.

GNR 1984 yılında Milan, İtalya' da kurulmuştur.

G.N.R. S.r.l. 30 yıllık tecrübesiyle, güçlü satış ve pazarlama ağı ile gelişmiş analitik cihazların dünya çapında üreticisi, çeşitli uygulamalar için analiz prosedürleri geliştiren, ilgili laboratuvar ekipmanlarını tedariki ve dünya çapında danışmanlık ve müşteri desteği sağlayan bir firmadır.

G.N.R. S.r.l. metal alaşımlarının element bileşiminin analizi için Optik Emisyon Spektrometreleri (OES) ve, yağlardaki ve yağlayıcılar, soğutucular ve hidrolik sıvılardaki kirletici madde, katkı maddeleri ve aşınma metallerinin analizi için Dönen Disk Elektrotlu Optik Emisyon Spektrometrelerini (RDE-OES) projelendirir ve üretir.

G.N.R. S.r.l. hem akademik hem de endüstriyel uygulamalar için malzeme yapısı ve element kompozisyon çalışması için X-Ray Diffractometers (XRD) ve X-Ray Fluorescence Spektrometre (XRF) geliştirir ve üretir.



Founded in 1890, a private company owned by Galdabini family.

Galdabini manufactures and provides service material testing machines, straightening machines and hydraulic presses.

The company is composed by two corporate headquarters located in Italy and Switzerland, providing you high technologies, quality and a long lasting know how. Specialised in material testing machines to analyze mechanical properties of various materials and components – suitable to carry out material tests as tensile, flexure, compression, bending and impact. Leader in straightening machines for testing shafts, profiles, rings, tubes and bars. The company offers a wide range of straightening machines and solutions is suitable for application in automotive and non-automotive fields. In addition high efficiency and performances in hydraulic presses and turn-key production lines to satisfy a large range of requirements for steel and aluminium forming. A qualified staff supports you on-site during installation, training and calibration on a world-wide scale. Galdabini is an official European Calibration Centre for load, deformation, resilience hardness and other typical units.

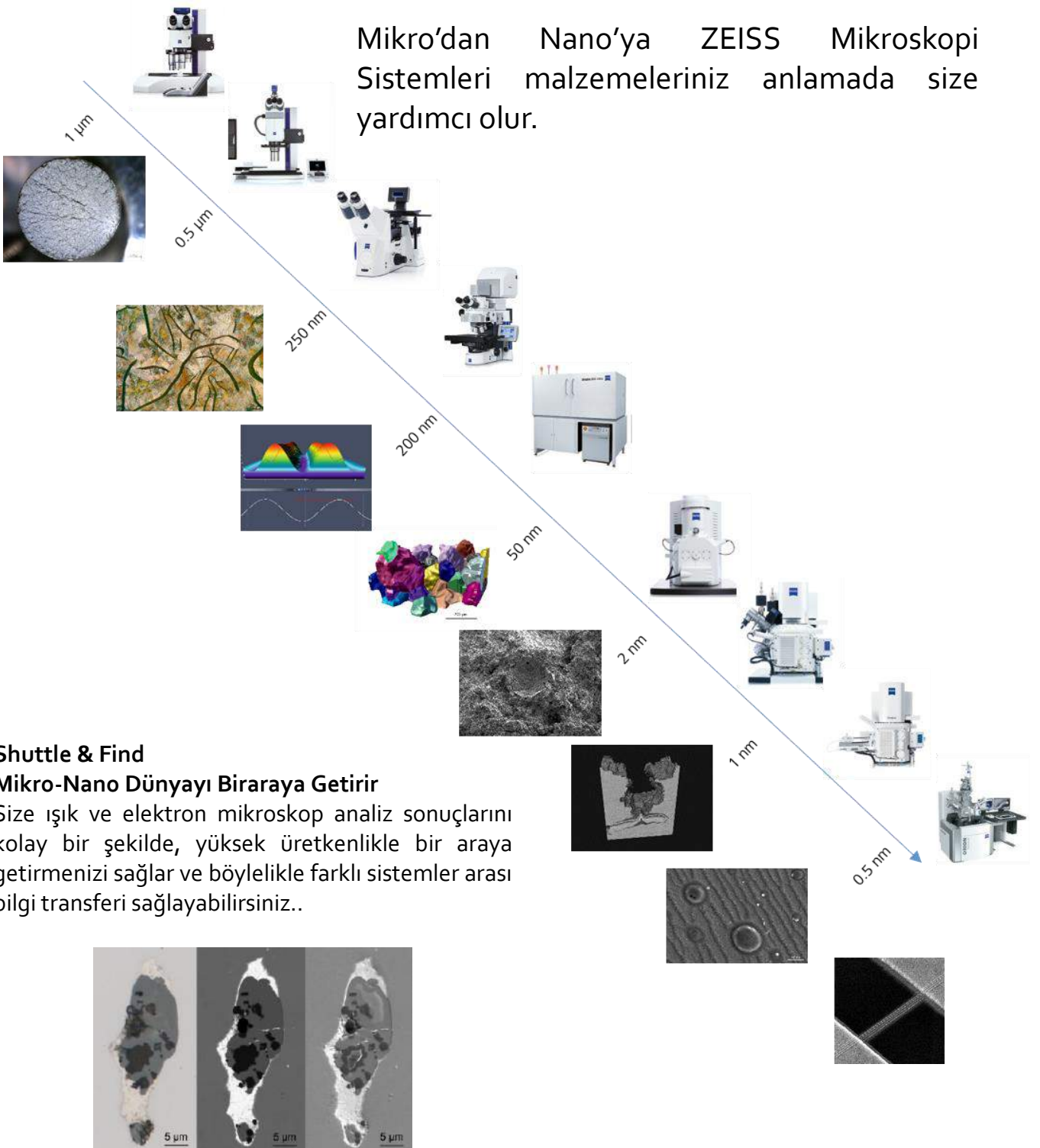
Galdabini ailesinin 1890 yılında kurduğu özel bir firmadır.

Galdabini, malzeme test makineleri, doğrultma makineleri ve hidrolik presler üretmektedir.

Şirket, İtalya ve İsviçre'de bulunan iki şirket merkezi tarafından oluşturulmuş olup size yüksek teknolojiler, kalite ve uzun ömürlü bir uygulama hizmeti sunmaktadır. Çekme, bükülme, sıkıştırma, bükme ve darbe gibi malzeme testlerini yapmak için uygun çeşitli malzeme ve bileşenlerin mekanik özelliklerini analiz eden malzeme test makinalarında uzmanlaşmıştır. Şaftlar, profiller, yüzükler, borular ve çubukların testinde kullanılan doğrultucu makinelerde liderdir. Firma, otomotiv ve otomotiv dışı alanlar için çok çeşitli doğrultma makineleri ve çözümleri sunmaktadır. Çelik ve alüminyum şekillendirme için kullanılan çok çeşitli gereksinimleri karşılamak için hidrolik presler ve anahtar teslimi üretim hatlarında yüksek verimlilik ve performans sağlar. Kalifiye personeli, kurulum, eğitim ve kalibrasyon sırasında dünya çapında destekler. Galdabini, yük, deformasyon, esneklik sertliği ve diğer tipik üniteler için resmi bir Avrupa Kalibrasyon Merkezi'dir.

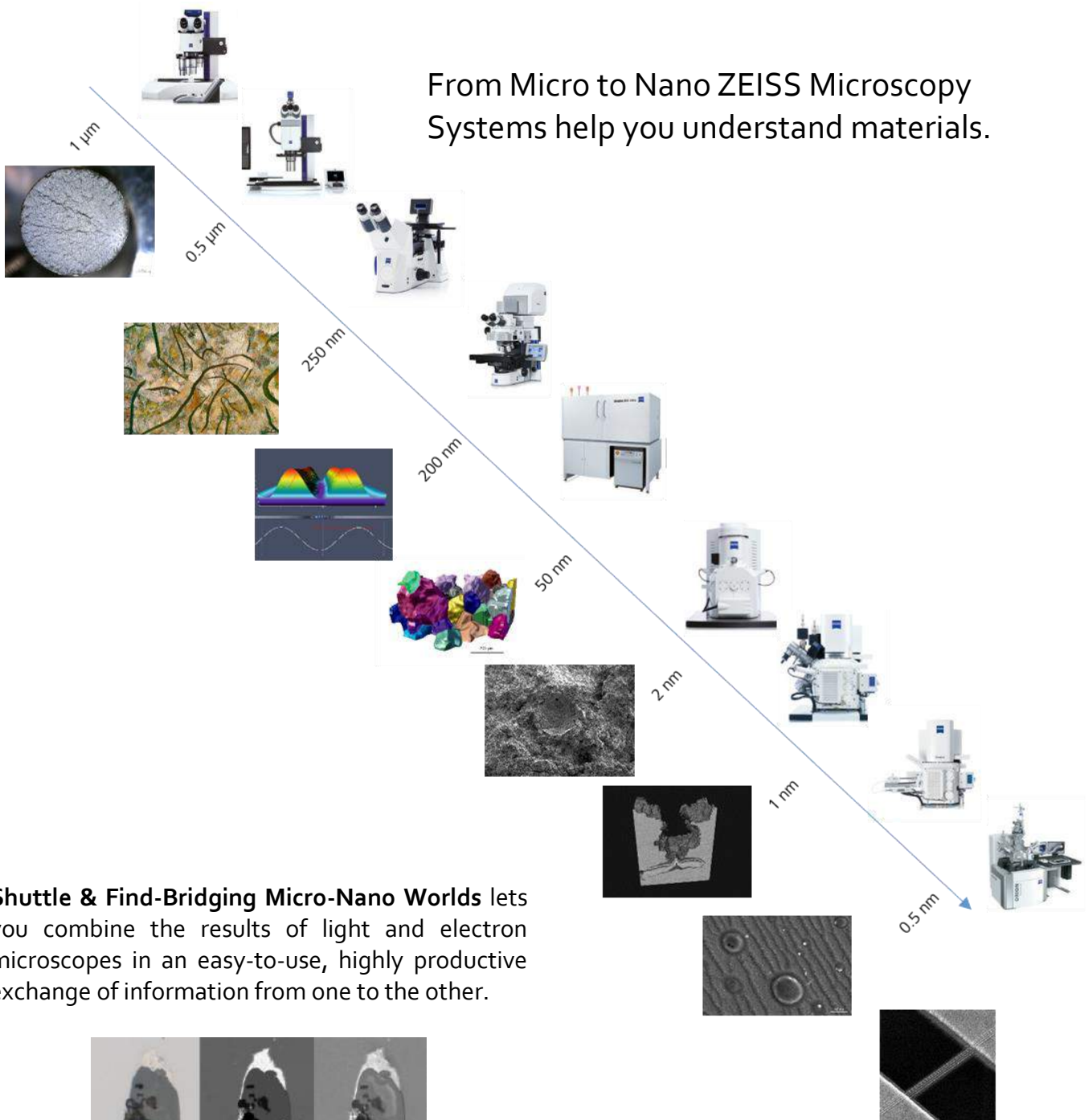
ZEISS Çok Ölçekli Korelatif Mikroskopi

Mikro'dan Nano'ya ZEISS Mikroskopi Sistemleri malzemeleriniz anlamada size yardımcı olur.

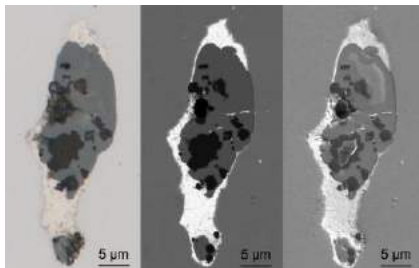


ZEISS Multiscale Correlative Microscopy

From Micro to Nano ZEISS Microscopy Systems help you understand materials.



Shuttle & Find-Bridging Micro-Nano Worlds lets you combine the results of light and electron microscopes in an easy-to-use, highly productive exchange of information from one to the other.



KARABÜK ÖZEL SEKTÖR DEMİR-ÇELİK HADDECİLERİ DERNEĞİ

Derneğimiz 1962 yılında; MustafaYAZICI, İbrahim SÖZEN, Osman YÜCEL, İhsan KES, Ziya GÜLTEKİN, Sümer GÜVEN, AliHATİPOĞLU, Azmi ÖZÇATAL, Mustafa SAKA, Aziz SÜRMEK, Mehmet VERGİLİ, Yaşar KAPTAN ÇEBİ, Mehmet IŞIK ve Halis ÇEBİ den oluşan ve Türkiye'nin Demir-çelik sektörü alanındaki ilk yatırımcıları olan 14 değerli girişimci büyüğümüz tarafından kurulmuştur. Aynı zamanda bu alandaki önderlerimiz olan bu sanayici iş adamlarımızdan vefat edenleri rahmetle ve hasretle anıyor, sağ olanlarına sağlıklı uzun ömürler diliyoruz.

Derneğimiz çatısı altında faaliyet gösteren Özel Demir-Çelik tesisleri 200 bin m2 kapalı ve 280 bin m2 açık olmak üzere toplam 480 bin m2 alanda üretim faaliyetlerini sürdürmekte olup, 5 firma hem sıcak çekme hem de soğuk çekme, 14 firma sıcak çekme, 2 firma İndüksiyon ocağı olarak kütük demir üretimi yapmakta, 1 firma ise makine imalatı yapmakta olup, yıllık kapasitemiz 3 milyon ton'a ulaşmış durumdadır.

Tesislerde her nevi İnşaat Çelikleri, muhtelif ebat ve boyda lama, silme, kare, Köşebent, profil, altı köşe, asansör rayı ve özel siparişler üretilmekle birlikte Soğuk çekme imalatı yapan tesislerde ise kabuk soma, kumlama gibi işlemlerde ileri teknoloji ürünü makinelerde başarı ile üretilmekte ve 6 kıtada 160 a yakın ülkeye ihraç edilmektedir.

ÜYELERİMİZ

S.NO FİRMA ADI TELEFON FAX

- 1 AYGÜNSAN D.Ç.SAN VE TİC.LTD ŞTİ. 712 02 70 712 12 43
- 2 BAŞARAN HADDECİLİK 424 15 50 424 75 68
- 3 BEŞA HAD.SAN.TİC.A.Ş. 424 73 08 424 35 34
- 4 BEŞBAŞLAR HD.SAN.VE TİC A.Ş. 424 24 40 424 15 91
- 5 BOSKAY METAL SAN VE TİC.LTD ŞTİ 412 87 17 412 72 25
- 6 ÇAPRAZOĞLU D.Ç.SAN VE TİC.A.Ş. 424 20 50 424 65 73
- 7 ÇELİKOĞLU HADDECİLİK 415 78 00 415 78 05
- 8 ÇELSENTAŞ SAN VE TİC.A.Ş. 415 50 50 415 50 57
- 9 ERHALLAR D.Ç.SAN VE TİC A.Ş. 415 52 00 424 18 36
- 10 GÜVEN D.Ç.SAN VE TİC.A.Ş. 424 10 78 424 25 58
- 11 IŞIK ÇELİK SAN VE TİC.A.Ş. 424 20 77 424 11 29
- 12 KAPTAN D.Ç.END.TİC.A.Ş. 415 47 00 424 47 08
- 13 MESCİER D.Ç.SAN.VE TİC.LTD ŞTİ 415 63 00 424 26 76
- 14 KAYIKÇI D.Ç.SAN VE TİC.LTD ŞTİ. 452 01 01 452 01 03
- 15 VERGİLİ D.Ç.SAN VE TİC.A.Ş. 447 60 36 447 60 34
- 16 SAKA D.Ç.SAN VE TİC.A.Ş. 413 02 33 424 73 59
- 17 SERHAT HADD.SAN VE TİC.A.Ş. 415 51 10 424 22 31
- 18 S.Y.M.D.Ç.SAN VE TİC.A.Ş. 424 30 13 412 38 80
- 19 YEŞİLYURT D.Ç.SAN VE TİC.A.Ş. 424 25 37 412 92 83

MARZINC A.Ş (TR)

Marzinc Dünyada ve ülkemizde gelişen çevre bilincinin bir yansıması olan Marzinc yatırımı, hurda süreci sonucu ortaya çıkan baca tozunu bertaraf etmek üzere Türkiye'nin önde gelen 5 demir çelik şirketi olan Çolakoğlu, Diler, İçdaş, Kaptan ve Kroman tarafından kuruldu. Ana amacı ortak şirketlerin üretiminden çıkan EAF tozunu çevreci ve ekonomik bir şekilde geri kazanmak olan tesis, yılda 200.000 tona yakın baca tozundan 50.000 ton civarı çinko oksit elde etme kapasitesine sahiptir. İleri ve modern bir teknolojiyle kurulan Marzinc dünya üzerindeki benzerlerine göre çok daha çevreci ve verimli bir şekilde üretim yapmaktadır. İyi kalitede ürünlerinin tamamını yurtdışı pazarlarına ihraç eden tesis, Ocak 2013'ten bu yana geri dönüşüme ve Türkiye ekonomisine katkı sağlamaktadır.

Çevre ve Şehircilik Bakanlığı, çelik üreticilerinden, üretimleri sonucu ortaya çıkan atıkların sağlıklı ve ekonomik bir şekilde geri dönüştürülmesi için Marzinc ve benzeri tesislerin kurulmasını Türkiye Çelik Üreticileri Derneği aracılığıyla teşvik etmektedir. Ülkemizin çelik üretiminin yaklaşık yarısının gerçekleştirildiği 5 çelik üreticisi, Bakanlığın da desteği ve talebiyle Marzinc'in kurulmasına öncülük ederek bu önemli tesisi ekonomimize kazandırılmıştır. Tesis aynı zamanda bakanlık tarafından verilen "ÇED Olumlu Kararı" belgesine ve "Çevre İzin ve Lisans Belgesi"ne sahiptir. Marzinc'i hayata geçiren 5 çelik üreticisi firma, gelecek kuşaklara daha yaşanabilir bir Türkiye bırakmak için, üretimlerinin her aşamasında çevreyi ve ekolojik dengeyi korumaktadırlar. Dünyada gelişen ISG ve çevre algısına tamamen paralel hareket eden ortaklar, bu alandaki çözümleri de ileriye taşımaktadırlar.

Baca tozu geri kazanımında dünyada kendisini kanıtlamış tek yöntem olan "Waelz Prosesi", Avrupa'daki çelik üretiminde açığa çıkan baca tozunun geri kazanımında da kullanılmaktadır. Avrupa Birliği ülkelerinde toplamda 750.000 ila 1.200.000 ton/yıl aralığında baca tozu ortaya çıkmakta ve Birlik, Marzinc muadili tesislerle, bu tozların dönüşümü desteklemektedir. Marzinc kurucuları, AB'nin bu deneyimleri ve birikimlerinden faydalanmak amacıyla İtalya'da kurulu olan ve 30 yıldır geri kazanım faaliyetinde bulunan bir tesis ile işbirliği yaparak çözüm ortağının teknoloji ve teknik bilgisini Türkiye'ye transfer etmiştir. Ayrıca çeşitli alt tedarikçilerinin desteğiyle sistem en son teknolojiyle kurulmuştur. Marzinc modern ve çevreci üretim sürecini 2013 yılının Ocak ayında başlatmıştır.

MARZINC A.Ş. (EN)

Being a reflection of the environmental conscience improving in our country in parallel to the environmental perception in the world, Marzinc investment was established by 5 leading steel producers of Turkey, namely Çolakoğlu, Diler, İçdaş, Kaptan and Kroman, in order to recover the zinc metal in the flue dust resulting from the scrap process. Aiming to recover the EAF (electric arc furnace) dust resulting from the production of the associated companies in an eco-friendly and economical way, the company has a capacity to obtain around 50.000 tons of zinc oxide from approximately 200.000 tons of flue dust per year. Because Marzinc was established with an advanced and modern technology, it produces in a much more environmental and effective way than its equivalents around the world. Exporting its good quality products to the foreign markets, the facility has been contributing to recycling and Turkey's economy since January 2013.

The Waelz Process run by Marzinc is implemented in Europe and eco-friendly countries such as USA. This process requires a great deal of know-how, tools and devices as well as machinery equipments. Assuming responsibility, Turkey's leading five steel producer companies gathered the financial potential and know-how required to run the project under a single roof, and presented Marzinc facility to Turkey. Marzinc Recovery Facility can process 200.000 tons of flue dust per year, and it will be able to process 120.000 tons of mill scales annually with the addition of a second facility that is in the feasibility stage. The Ministry of Environment and Urbanization asks steel producer companies to establish Marzinc-like facilities in order to recycle the waste resulting from the iron and steel production in a healthy and economical way. The Ministry gives its full support to such investments through the Iron & Steel Producers' Association. The producers where almost half of the iron-steel production of Turkey is carried out, pioneered Marzinc's establishment upon request and with the support of the Ministry, and presented this important facility to the sector. This facility which was established with the support of the ministry also has "Positive Environmental Impact Assessment" and "Environmental Licence" issued by the Ministry.

5 steel producer companies running Marzinc protects the environment as well as the ecological balance at every stage of their production to leave a more livable Turkey for the next generations. Complying with all required standards, the companies are contributing to green production for Turkey's future. Being the only method that has proved itself in the field of flue dust recovery within the world, the "Waelz Process" is used in Europe to recover flue dusts resulting from the steel production. The total flue dust amount in the EU countries is between 750.000 and 1.200.000 tons/year. The Union supports the transformation of such dusts with the facilities similar to Marzinc. The founders of Marzinc cooperated with an Italian recovery plant which has been running a recovery facility since 30 years and is settled in Italy in order to benefit from the experience and knowledge of the EU. The technology information and know-how of Italian recovery plant was transferred to Turkey due to this cooperation. Marzinc started its modern and eco-friendly production process on January, 2013 thanks to this transfer.

